Electrical Contacts

Fundamentals, Applications and Technology

Milenko Braunovic
MB Interface, Scientific Consultants
Montreal, Quebec, Canada

Valery V. Konchits
National Academy of Sciences of Belarus
Belarus, Russia

Nikolai K. Myshkin
National Academy of Sciences of Belarus
Belarus, Russia

CRC Press
Taylor & Francis Group
Boca Raton London New York

CRC Press is an imprint of the
Taylor & Francis Group, an informa business

CRC Press
Taylor & Francis Group
6000 Broken Sound Parkway NW, Suite 300
Boca Raton, FL 33487-2742

Printed in the United States of America on acid-free paper
10 9 8 7 6 5 4 3 2 1

International Standard Book Number-10: 1-57444-727-0 (Hardcover)
International Standard Book Number-13: 978-1-57444-727-9 (Hardcover)

Library of Congress Cataloging-in-Publication Data

Braunovic, Milenko.
Electrical contacts : fundamentals, applications and technology / Milenko Braunovic, Nikolai K. Myshkin, Valery V. Konchits.
p. cm. -- (Electrical and computer engineering)
Includes bibliographical references and index.
ISBN-13: 978-1-57444-727-9
ISBN-10: 1-57444-727-0
1. Electric contacts. 2. Friction. 3. Tribology. I. Myshkin, Nikolai Konstantinovich. II. Konchits, V. V. (Valerii Vasil'evich) III. Title. IV. Series.

TK2821.B665 2006
621.31'042--dc22 2006015470

Visit the Taylor & Francis Web site at
http://www.taylorandfrancis.com

and the CRC Press Web site at
http://www.crcpress.com

Preface

The multidisciplinary study of the electrical contact in modern engineering is significant, but often neglected. The scientist and engineers who have spent their professional lives studying and applying electrical contacts know that these components are critical to the successful operation of all products that use electricity. In our civilization, all electricity transmission and distribution, most control, and most information exchange depends upon the passage of electricity through an electrical contact at least once. The failure of an electrical contact has resulted in severe consequences, e.g., an energy collapse of a megapolis, a failure of the telephone system, and even the crash of an airplane.

Ragnar Holm, the prominent researcher, renowned engineer, and inventor, developed the validity of "electrical contacts" as its own technical discipline with his book *Electric Contacts* (1958). The 50 years following its publication have given a firm confirmation of the accuracy of his predictions and conclusions. Since that time, however, there has been a huge increase in the application of electrical contacts. For example, the era of the information highway and the development of the integrated circuit have created new challenges in the use of electrical contacts. The use of electrical contacts on the microscopic scale presents numerous problems never considered by previous generations of researchers and engineers. The future MEMS/NEMS technology is another area where the theory and practice of the electrical contact is of critical importance.

The purpose of the authors has been to combine the progress in research and development in the areas of mechanical engineering and tribology, which Holm postulated to be key segments in electrical contacts, with the new data on electrical current transfer, especially at the micro/nanoscale.

This book complements the recent volume *Electrical Contacts: Principles and Applications* (published by Marcel Dekker, 1999). It takes a practical applications approach to the subject and presents valuable design information for practicing mechanical and electrical engineers. In fact, the information contained here will serve as an excellent source of information not only for anyone developing equipment that uses electricity, but for postgraduate students who are concerned about the passage of current from one conductor to another.

The authors of this book have many years of research and practical experience. One unusual and interesting aspect of the book's development is that it comes through the cooperation of the different approaches to the subject from the West and the East. They have succeeded in making the bulk of research and engineering data equally clear for all the segments of the international audience.

Paul G. Slade
Ithaca, New York

The Authors

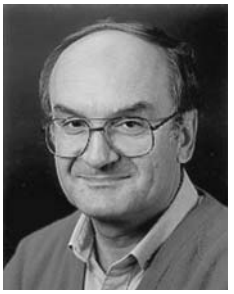

Dr. Milenko Braunović received his Dipl. Ing degree in technical physics from the University of Belgrade, Yugoslavia, in 1962 and the M.Met. and Ph.D. degrees in physical metallurgy from the University of Sheffield, England in 1967 and 1969, respectively. From 1971 until 1997, he was working at Hydro-Québec Research Institute (IREQ) as a senior member of the scientific staff. He retired from IREQ in 1997 and established his own scientific consulting company, MB Interface. From 1997 until 2000 he was consulting for the Canadian Electricity Association as a technology advisor. He is presently R&D manager with A.G.S. Taron Technologies in Boucherville, QC, Canada.

During the last 30 years, Dr. Braunović has been responsible for the development and management of a broad range of research projects for Hydro-Québec and the Canadian Electrical Association in the areas of electrical power contacts, connector design and evaluation, accelerated test methodologies, and tribology of power connections. He has also initiated and supervised the R&D activities in the field of shape-memory alloy applications in power systems. Dr. Braunović is the author of more than 100 papers and technical reports, including contributions to encyclopaedias and books, in his particular areas of scientific interests. In addition, he frequently lectures at seminars world wide and has presented a large number of papers at various international conferences.

For his contributions to the science and practice of electrical contacts, Dr. Braunović received the Ragnar Holm Scientific Achievement Award in 1994, and for his long-term leadership and service to the Holm Conference on Electrical Contacts he received, in 1999, the Ralph Armington Recognition Award. He is also a recipient of the 1994 IEEE CPMT Best Paper Award. He successfully chaired the Fifteenth International Conference on Electrical Contacts held in Montreal in 1990, and was a technical program chairman of the Eighteenth International Conference on Electrical Contacts held in Chicago in 1996. He is a senior member of the Institute of Electronics and Electrical Engineers (IEEE), the American Society for Metals (ASM), the Materials Research Society (MRS), the Planetary Society, the American Society for Testing of Materials (ASTM), and The Minerals, Metals & Materials Society (TMS).

Dr. Valery Konchits was born on January 3, 1949 in the city of Gomel, Belarus. He graduated from Gomel State University in 1972. He received his Ph.D. degree in tribology from the Kalinin Polytechnic Institute, Russia in 1981.

In 1972, he joined the Metal-Polymer Research Institute of the National Academy of Sciences of Belarus in Gomel. In 1993, he became the head of the laboratory in the Tribology Department. Since 2001, Dr. Konchits has been Deputy Director of the Metal-Polymer Research Institute.

The scientific interests of Dr. Konchits lie mainly in electrical contacts' friction and wear, contact phenomena at their interfaces, and electrophysical diagnostic methods of friction. He is the author of more than 80 papers and holds 10 patents. He is also the co-author of a monograph in Russian, "Tribology of electrical contacts" (authors: Konchits V.V., Meshkov V.V., Myshkin N.K., 1986, Minsk).

Prof. Nikolai Myshkin was born on May 12, 1948 in the city of Ivanovo, Russia. He graduated from the Power Engineering Institute in 1971 with a degree in electromechanics. Has received his Ph.D. from the Institute for Problems in Mechanics of the Russian Academy of Sciences in 1977. The same year, he joined the Metal-Polymer Research Institute in Gomel where since 1990 he has been Head of the Tribology Department. He has also been the director of MPRI since 2002. He earned his Dr.Sc. degree in tribology in 1985 and became a full professor of materials science in 1991. He was elected as a correspondent member of the Belarus National Academy of Sciences in 2004.

He received the USSR National Award for Young Scientists in 1983, the Award for Best Research given by the Belarus National Academy of Sciences in 1993, and the Award of the Russian Government in Science and Technology in 2004.

The scientific interests of Prof. Myshkin lie mainly in the characterization at micro and nanoscale surfaces, the contact mechanics of solids, wear monitoring, electric phenomena in friction, tribotesting equipment, and aerospace engineering.

He has authored or co-authored more than 180 papers and 60 patents. He is a co-author of the *Tribology Handbook* (Russian edition 1979, English translation 1982), monographs *Physics, Chemistry and Mechanics of Boundary Lubrication* (1979), *Tribology of Electric Contacts* (1986), *Acoustic and Electric Methods in Tribology* (Russian edition 1987, English translation 1990), *Structure and Wear Resistance of Surface Layers* (1991), *Textbook in Materials Science* (1989), *Magnetic Fluids in Machinery* (1993), the English textbook *Introduction to Tribology* (1997), and *Tribology: Principles and Applications* (2002).

Prof. Myshkin is chairman of the Belarus Tribology Society and vice-president of the International Tribology Council. He is also assistant editor-in-chief of the *Journal of Friction and Wear*, and a member of editorial boards of *Tribology International*, *Tribology Letters*, *Industrial Lubrication and Tribology*, and the *International Journal of Applied Mechanics and Engineering*.

Acknowledgments

In the preparation of the book, the authors have used a large number of published materials, either in the form of papers in referenced journals, or from the websites of different companies and organizations. In both cases, proper permissions for using these materials have been obtained. In many instances, the authors obtained the required information directly from the authors of the papers or from the company authorities.

The authors are indebted to Dr. Paul Slade for writing the preface of the book. Special thanks go to Dr. Daniel Gagnon of Hydro-Québec Research Institute (IREQ) in Varennes, QC, Canada for providing essential reference material and fruitful discussions concerning certain topics of power connections.

The authors are grateful to Dr. Mark. I. Petrokovets for fruitful discussion and his help in preparation of Chapters 2, 3 and 5. We also thank Dr. Denis Tkachuk for his valuable assistance in preparation of the manuscript.

Acknowledgement is made to the many individuals and company authorities for permission to use the original material and, in particular, to modify the original figures to maintain the uniformity of graphic presentation throughout the book. The following is a list of these individuals and company authorities.

Prof. George M. Pharr, Department of Materials Science and Engineering, University of Tennessee, Knoxville, USA for providing the papers on nanoindenation testing methods and instrumentation and allowing modification of some of the figures appearing in these papers.

Prof. Doris Kuhlmann-Wilsdorf, Department of Materials Science and Engineering, University of Virginia, Charlottesville, USA for permission to use the information on fiber-brushes and dislocation nature of the processes occurring during friction.

Dr. Roland Timsit of Timron Scientific Consulting, Inc., Toronto, Canada for permission to use the relevant material from his papers and publications.

Dr. Robert Malucci of Molex, Inc., Lisle, IL, USA, for permission to use the relevant material from his papers and publications and modify some of the figures from his original publications cited in this book.

Dr. Bill Abbott of Batelle, USA for helpful suggestions and discussions regarding the problems of corrosion in electrical and electronic connections.

Dr. Sophie Noel, Laboratoire de Génie Electrique, Supélec, Gif sur Yvette, France for helpful discussions concerning the lubrication of electrical contacts and permission to use some of data from the publications cited in this book..

Dr. Magne Runde of the Norwegian University of Science and Technology, Norway, for helpful discussions concerning the problem of electromigration in electrical contacts.

Prof. Zoran Djuric and Milos Frantlovic of the Center for Microelectronics Technologies and Single Crystals, MTM, University of Belgrade, Serbia and Montenegro for providing the information on the wireless temperature monitoring system.

Dr. Bella Chudnovsky of Square D, USA, for helpful discussions concerning the whisker formation in electrical contacts and for permission to use the information on the On-Line Wireless Temperature Monitoring System for LV, MV electrical equipment fond on the company web site (http://www.squared.com).

Prof. L.K.J. Vandamme of the Department of Electrical Engineering, Eindhoven University of Technology, The Netherlands for providing and allowing the use of reference materials concerning the noise in electrical connections.

Mr. Larry Smith of USi, Armonk, NY, USA, for permitting the use of the images and descriptions of the Power-donut unit found on the company web site (http://www.usi-power.com).

Dr. Young-kook (Ryan) Yoo, Director of Global Sales and Marketing of PSIA Corp. Sungnam 462-120, Korea, for permission to use descriptions of different surface analytical equipment as posted on the company web site (http://www.psiainc.com.).

Dr. G. Palumbo of Integran Technologies, Inc., Toronto, Canada for providing the information on the grain size effects in nanocrystalline materials (http://www.integran.com).

Mr. J. Renowden of Transpower New Zealand, for providing the information concerning the field applications of the microohmeter Ohmstik on power lines (http://www.transpower.co.nz).

Mr. J. Lebold of Boldstarinfrared, Canada for permission to use the infrared images from the company web site (http://www.boldstarinfrared.com).

R.N. Wurzbach of Maintenance Reliability Group (MRG), York, PA, USA for permission to use description of the web-based cost benefit analysis method for predictive maintenance (http://www.mrgcorp.com).

ndb Technologie, Inc., Québec, Canada for permission to use the information about the microohmeters found on their web site (http://www.ndb.qc.ca).

In addition, the authors would like to acknowledge the courtesy of the following companies for allowing the use of the information found on their respective websites: Omega Madge Tech., Inc., (http://www.omega.com), FLIR Systems (http://www.flirthermography.com), Mikron Infrared, Inc**.** (http://www.irimaging.com), Electrophysics Corp. (http://www.electrophysics.com), Infrared Solution, Inc. (http://www.infraredsolutions.com), Elwood Corp. (http://www.elwoodcorp.com), Sensolink Corp., (http://www.sensorlink.com).

Lastly, it is a pleasure to acknowledge and express our gratitude to Mrs. K. Braunović for her generous hospitality shown to the authors during the preparation of the book manuscript.

Introduction

This book provides detailed analytical models, state-of-the-art techniques, methodologies and tools used to assess and maintain the reliability of a broad class of moving and permanent electrical contacts in many technological devices, such as automotive and aerospace components, high- and low-power contact joints, sliding and breaking contacts, electronic and control apparatus, and electromechanical systems. It provides a comprehensive outline of the tribological behavior of electrical contacts that is rarely discussed in the existing literature; these are problems of considerable interest for researchers and engineers.

Focusing on the main mechanical and electrical problems in connections with the field applications and the relationship between structure and properties, this volume provides a well-balanced treatment of the mechanics and the materials science of electrical contacts, while not neglecting the importance of their design, development, and manufacturing. The book provides a complete introduction to electric conduction across a contacting interface as a function of surface topography, load, and physical-mechanical properties of materials, and the interrelation of electrical performance with friction and wear; it takes into account material properties and lubricant effects. Consideration is given to the deleterious effects of different degradation mechanisms, such as stress relaxation/creep, fretting, differential thermal expansion, and the formation of intermetallics, as well as their impacts on operating costs, safety, network reliability, power quality. Various palliative measures to improve the reliability and serviceability of electrical contact at macro-, micro-, and nano-levels are also discussed.

This book diminishes a large gap between engineering practice widely utilizing empirically found methods for designing and optimizing the contact characteristics and theory relating to tribological and electromechanical characteristics of the contacts. The main trends in the practical solutions of the tribological problems in electrical contacts are discussed in terms of contact design, research and development of contact materials, coatings and lubricants and the examples of practical applications in various fields are given throughout the book.

Covering a wide range of references, tables of contact materials, coatings and lubrication properties, as well as various testing procedures used to evaluate these properties, the book will be an indispensable practical tool for professional, research, design and development engineers. The book (or parts of it) can be used not only as a reference, but also as a textbook for advanced graduate students and undergraduates, as it develops the subject from its foundations and contains problems and solutions for each chapter.

Table of Contents

Part I
Fundamentals of Electrical Contacts 1
Milenko Braunović, Valery V. Konchits, and Nikolai K. Myshkin

Chapter 1
Introduction to Electrical Contacts 3
1.1 Introduction 3
1.2 Summary of Basic Features 6

Chapter 2
Contact Mechanics 9
2.1 Surface of Solids 9
2.2 Surface Topography 11
2.3 Modern Techniques of Measuring Surface Parameters 17
2.4 Contact of Smooth Surfaces 21
2.4.1 Plastic and Elastoplastic Contacts 23
2.5 Contact between Rough Surfaces 27
2.5.1 Greenwood–Williamson Model 27
2.5.2 Multilevel Model 29
2.5.3 Transition from Elastic to Plastic Contact 33

Chapter 3
Tribology 35
3.1 Friction 35
3.1.1 Laws of Friction 35
3.1.2 Real Contact Area 38
3.1.3 Interfacial Bonds (Adhesion Component of Friction) 38
3.1.4 Deformation at Friction 41
3.1.5 Friction as a Function of Operating Conditions 42
3.1.6 The Preliminary Displacement 44
3.1.7 Stick-Slip Motion 46
3.2 Wear 47
3.2.1 Stages of Wear 48
3.2.2 Simple Model of Wear 48
3.2.3 Basic Mechanisms of Wear 50
3.2.4 Abrasive Wear 52
3.2.5 Adhesive Wear 56
3.2.6 Prow Formation 57
3.2.7 Fatigue Wear 57
3.2.8 Corrosive Wear 59
3.2.9 Fretting Wear 59
3.2.10 Delamination 62
3.2.11 Erosion 64
3.2.12 Combined Wear Modes 64
3.3 Lubrication 65
3.4 Current Trends in Tribology 67

Chapter 4

Contact Materials 71
4.1 Metallic Contact Materials 71
4.1.1 Properties of Contact Materials 71
4.1.1.1 Copper 71
4.1.1.2 Aluminum 75
4.1.1.3 Silver 76
4.1.1.4 Platinum 78
4.1.1.5 Palladium 78
4.1.1.6 Gold 79
4.1.1.7 Rhodium 79
4.1.1.8 Tungsten 79
4.1.1.9 Nickel 80
4.1.2 Metals and Alloys for Heavy- and Medium-Duty Contacts 80
4.1.3 Metals and Alloys for Light-Duty Contacts 83
4.1.4 Materials for Liquid-Metal Contacts 85
4.1.5 Spring Contact Materials 87
4.1.6 Shape-Memory Alloys and Their Applications in Electrical Contacts 88
4.2 Coatings for Electrical Contacts 89
4.2.1 Basic Requirements 89
4.2.2 Surface Engineering Technologies 91
4.2.2.1 Surface Segregation 92
4.2.2.2 Ion Implantation 94
4.2.2.3 Electroplating 94
4.2.2.4 Electroless Plating 97
4.2.2.5 Cladding 97
4.2.2.6 Chemical Deposition 99
4.2.2.7 Plating by Swabbing 99
4.2.2.8 Physical Vapor Deposition Technology 99
4.2.2.9 Electro-Spark Deposition (ESD) 100
4.2.2.10 Intermediate Sublayers 101
4.2.2.11 Multilayered Contacts 101
4.2.3 Coating Materials 102
4.2.3.1 Coatings for Power Connectors (Copper and Aluminum Joints) 102
4.2.3.2 Coatings for Electronic/Electrical Applications 104
4.3 Composite Contact Materials 111
4.3.1 Composite Materials for Contacts of Commutating Apparatuses 111
4.3.2 Self-Lubricating Composites for Sliding Contacts 118
4.4 Nanostructured Materials 125
4.4.1 “Bulk” Properties Nanomaterials 127
4.4.2 Mechanical Properties 127
4.4.3 Electrical Properties 131
4.4.4 Magnetic Properties 136
4.4.4.1 Giant Magnetoresistance (GMR) 136
4.4.4.2 Ballistic Magnetoresistance (BMR) 138
4.4.5 Nanotubes 140
4.4.6 Thermal Stability 142
4.4.7 Characterization Techniques for Nanostructured Materials 143
4.4.7.1 Nanoindentation 143
4.4.7.2 Scanning Probe Microscopes 144

Chapter 5

Current and Heat Transfer across the Contact Interface 149
5.1 Contact Resistance 149
5.1.1 Circular and Noncircular *a*-Spots 149
5.1.2 Effect of Signal Frequency 154
5.1.3 Size Effects, Nanocontacts 157
5.1.4 Effect of Surface Films 160
5.1.5 Effect of Contact Geometry 166
5.1.6 Conductivity of Rough Contact 172
5.2 Interfacial Heating 180
5.2.1 Principles of Heat Conduction Theory 181
5.2.2 Simple Problems of Heat Conduction Theory 183
5.2.3 Contact Spots Heated by Electrical Current 188
5.2.3.1 Film-Free Metal Contact 188
5.2.3.2 Heating of Contact Spots Having Surface Films 190
5.2.3.3 Field Intensity in the Contact Clearance with Tunnel-Conductive Films 194
5.2.4 Formulation of Heat Problem with Friction 195
5.2.5 Flash Temperature of Electrical Contact 198
5.2.6 Thermal Instability of Friction Contact 200
5.2.6.1 Thermoelastic Instability 201
5.2.6.2 Instability Caused by Temperature-Dependent Coefficient of Friction 202
5.2.6.2 Instability Related to Friction Mode Variation 202

Chapter 6

Reliability Issues in Electrical Contacts 205
6.1 Significance of Electrical Contacts Reliability 205
6.2 Electrical Contact Requirements 206
6.3 Factors Affecting Reliability 206
6.4 Connection Degradation Mechanisms 208
6.4.1 Contact Area 209
6.4.2 Oxidation 211
6.4.3 Corrosion 212
6.4.4 Fretting 214
6.4.4.1 Mechanisms of Fretting 217
6.4.4.2 Factors Affecting Fretting 219
6.4.4.3 Fretting in Electrical Contacts 219
6.4.4.4 Contact Load 221
6.4.4.5 Frequency of Motion 223
6.4.4.6 Slip Amplitude 224
6.4.4.7 Relative Humidity 224
6.4.4.8 Temperature 226
6.4.4.9 Effect of Current 226
6.4.4.10 Surface Finish 228
6.4.4.11 Hardness 229
6.4.4.12 Metal Oxide 230
6.4.4.13 Coefficient of Friction 230
6.4.4.14 Electrochemical Factor 230
6.4.5 Intermetallic Compounds 230

6.4.5.1 Effect of Electrical Current 232
6.4.6 Electromigration 237
6.4.7 Stress Relaxation and Creep 240
6.4.7.1 Nature of the Effect of Electric Current 241
6.4.7.2 Effect of Electric Current on Stress Relaxation 242
6.4.8 Thermal Expansion 247
6.5 Impact of Connection Degradation 248
6.5.1 Prognostic Model for Contact Remaining Life 250
6.5.2 Economical Consequences of Contact Deterioration 256
6.5.3 Power Quality 258

Part II
Applications of Electrical Contacts 261
Milenko Braunović, Valery V. Konchits, and Nikolai K. Myshkin

Chapter 7
Power Connections 263
7.1 Types of Power Connectors 263
7.2 Design Features and Degradation Mechanisms 263
7.2.1 Bolted Connectors 263
7.2.1.1 Fretting in Bolted Connectors 269
7.2.1.2 Fretting in Aluminum Connections 271
7.2.1.3 Intermetallics 272
7.2.1.4 Creep and Stress Relaxation 275
7.2.2 Bus-Stab Contacts 276
7.2.3 Compression Connectors 279
7.2.3.1 Degradation Mechanisms in Compression Connectors 281
7.2.3.2 Corrosion 282
7.2.3.3 Fretting in Compression Connectors 283
7.2.4 Mechanical Connectors 284
7.2.4.1 Binding-Head Screw Connectors 285
7.2.4.2 Insulation Piercing Connectors 289
7.2.4.3 Wedge Connectors 289
7.2.5 Welded Connectors 290
7.3 Mitigating Measures 292
7.3.1 Contact Area–Connector Design 292
7.3.2 Contact Pressure 294
7.3.3 Surface Preparation 296
7.3.4 Mechanical Contact Devices 297
7.3.4.1 Retightening 300
7.3.4.2 Bimetallic Inserts 301
7.3.4.3 Transition Washers 301
7.3.4.4 Multilam Contact Elements 302
7.3.4.5 Shape-Memory Alloy Mechanical Devices 302
7.3.4.6 Self-Repairing Joints 303
7.3.5 Lubrication: Contact Aid Compounds 304
7.4 Installation Procedures 306

Chapter 8

Electronic Connections 309
8.1 Types of Electronic Connections 309
8.2 Materials for Electronic Connections 309
8.2.1 Solder Materials 310
8.2.2 Lead-Free Solders 312
8.2.2.1 Tin 312
8.2.2.2 Tin–Silver 312
8.2.2.3 Tin–Silver–Bismuth 313
8.2.2.4 Tin–Silver–Copper 313
8.2.2.5 Tin–Silver–Copper–Antimony 314
8.2.2.6 Tin–Silver–Antimony 314
8.2.2.7 Tin–Bismuth 314
8.2.2.8 Tin–Copper 315
8.2.2.9 Tin–Indium 315
8.2.2.10 Tin–Indium–Silver 316
8.2.2.11 Tin–Zinc 316
8.2.2.12 Tin–Zinc–Silver 316
8.2.2.13 Tin–Zinc–Silver–Aluminum–Gallium 317
8.3 Degradation Mechanisms in Electronic Connections 317
8.3.1 Porosity 319
8.3.2 Corrosion/Contamination 322
8.3.2.1 Pore Corrosion 322
8.3.2.2 Creep Corrosion 323
8.3.2.3 Tarnishing 324
8.3.3 Fretting 327
8.3.4 Frictional Polymerization 334
8.3.5 Intermetallic Compounds 336
8.3.6 Creep and Stress Relaxation 348
8.3.7 Electromigration 353
8.3.8 Whiskers 357
8.4 Mitigating Measures 361
8.4.1 Effect of Coating 361
8.4.1.1 Gold Coatings 361
8.4.1.2 Palladium and Palladium Alloys 362
8.4.1.3 Tin Coatings 364
8.4.1.4 Nickel and Nickel-Base Alloys 364
8.4.2 Effect of Lubrication 364

Chapter 9

Sliding Contacts 369
9.1 Tribology of Electrical Contacts 369
9.1.1 Interrelation of Friction and Electrical Processes 370
9.1.2 Role of Boundary Films 371
9.1.3 Main Means of Improving Reliability of Sliding Contacts 371
9.1.4 Tribophysical Aspects in the Development of Sliding Contacts 373
9.2 Dry Metal Contacts 376
9.2.1 Low-Current Contacts 376
9.2.1.1 Effects of Low Current and Electrical Field on Friction 377
9.2.1.2 Effect of Interfacial Shear 378

9.2.1.3 Adhesion, Transfer, Wear Debris Formation, and Surface Transformation 380
9.2.2 High-Current Contacts 386
9.2.2.1 Effects of Electrical Current on Tribological Behavior 386
9.2.2.2 Influence of Electric Fields 390
9.2.2.3 Effect of Velocity 392
9.2.2.4 Effect of Material Combination of Contacting Members 393
9.2.2.5 Electroplastic Effect in Sliding Contact 394
9.2.2.6 Friction and Current Transfer in Metal Fiber Brush Contacts 396
9.2.3 Stability of the Contact Resistance. Electrical Noise 400
9.2.3.1 Contact Noise in Closed Connections 400
9.2.3.2 Electrical Noise in Sliding Contacts 402
9.3 Lubricated Metal Contacts 414
9.3.1 Introduction. Lubrication Factors 414
9.3.2 Electrical Properties of Lubricating Boundary Layers 415
9.3.3 Conductivity of Lubricated Contacts 419
9.3.3.1 Effect of Lubricant on Conductivity near the Contact Spots 419
9.3.3.2 Effect of Lubricant on Conductivity of Contact Spots 420
9.3.3.3 Experimental Studies of Electric Conductivity of Lubricated Contacts 427
9.3.3.4 Contact Resistance between Very Smooth Lubricated Surfaces 430
9.3.3.5 Temperature Dependencies of Contact Conductivity 431
9.3.4 Lubrication Factors in Sliding Contacts 433
9.3.4.1 Effect of Lubricant Origin 434
9.3.4.2 Lubricant Durability 435
9.3.4.3 Tribochemical Aspects of Lubrication 438
9.3.4.4 Effect of Velocity in Light-Current Contacts 441
9.3.4.5 Effects of Lubricant Contact Properties 442
9.3.4.6 Current Passage and Friction in High-Current Lubricated Contacts 444
9.3.5 Lubricants for Electrical Contacts 449
9.3.5.1 Lubricants for Sliding Electric Switch Contacts 450
9.3.5.2 Lubricants for Sliding Contacts of Sensors 451
9.3.5.3 Selection of Contact Lubricants 454
9.4 Composite Contacts 454
9.4.1 Effect of Intermediate Layers on Electrical Characteristics 455
9.4.1.1 Structure and Electrical Properties of Intermediate Films 456
9.4.1.2 Mechanism of Current Passage through the Contact with Intermediate Films 460
9.4.1.3 Influence of Polarity on Conductivity in Composite–Metal Contact 467
9.4.2 The “Lubricating” Effect of Electrical Current 471
9.4.2.1 Effect of Current on Friction Characteristics 471
9.4.2.2 Mechanism of the “Lubricating” Action of the Electric Current 473
9.4.2.3 Effect of Brush Material on Friction Behavior with Electric Current 477
9.4.3 Electrical Wear 479
9.4.3.1 Wear of Currentless Contacts 479
9.4.3.2 Effect of Current on Wear 480
9.4.3.3 Factors Leading to Electrical Wear in the Absence of Sparking 483

9.4.3.4 Influence of the Electric Field in the Clearance 489
9.4.3.5 Wear with Sparking and Arcing 491
9.4.3.6 Some Ways to Reduce Electrical Wear 493

Part III
Diagnostic and Monitoring Technologies 495
Milenko Braunović, Valery V. Konchits, and Nikolai K. Myshkin

Chapter 10
Electrical Methods in Tribology 497
10.1 Surface Characterization 497
10.2 Diagnosis of Contact Area and Friction Regimes 503
10.2.1 Formation of Contact Area 503
10.2.2 Control of Sliding Contact with the Presence of Oxide Films 508
10.2.3 Experimental Study of Metallic Contact Spots Formation 509
10.3 Evaluation of Tribological Performance of Materials and Lubricants 511
10.3.1 Evaluation of Load-Bearing Capacity and Lubricity of Surface Films 511
10.3.2 Estimation of Lubricant Interlayer Shear Strength under Imperfect Lubrication 515
10.3.3 Evaluation of Thermal Stability of Materials and Lubricants by Electrical Methods 517
10.3.4 Control of Surface Coatings and Films 519
10.3.5 Novel Systems for Measuring and Analysis of Contact Characteristics 521
10.3.5.1 Method of "Triboscopy" 523

Chapter 11
Monitoring Technologies 529
11.1 Thermal Measurements 530
11.1.1 Infrared Thermography 532
11.1.2 Basic Features of Infrared Thermography 532
11.1.3 Types of Infrared Thermal Systems 534
11.1.4 SME Temperature Indicators 538
11.1.5 Temperature Stickers (Labels) 540
11.1.6 Remote Temperature Sensors 541
11.2 Resistance Measurements 542
11.3 Monitoring Contact Load (Pressure) 545
11.4 Ultrasonic Measurements 546
11.5 Wireless Monitoring 548
11.6 Cost Benefits of Monitoring and Diagnostic Techniques 552

Appendix 1: Methods of Description of Rough Surface 555

Appendix 2: Shape-Memory Materials 565

Appendix 3: Electrical Contact Tables 585

References 599

1 Introduction to Electrical Contacts

1.1 INTRODUCTION

An electrical contact is defined as the interface between the current-carrying members of electrical/electronic devices that assure the continuity of electric circuit, and the unit containing the interface. The current-carrying members in contact, often made of solids, are called *contact members* or *contact parts*. The contact members connected to the positive and negative circuit clamps are called the *anode* and *cathode*, respectively.

Electrical contacts provide electrical connection and often perform other functions. The primary purpose of an electrical connection is to allow the uninterrupted passage of electrical current across the contact interface. It is clear that this can only be achieved if a good metal-to-metal contact is established. The processes occurring in the contact zone are complex and not fully explained within the limits of present knowledge. Although the nature of these processes may differ, they are all governed by the same fundamental phenomena, the most important being the degradation of the contacting interface and the associated changes in contact resistance, load, temperature, and other parameters of a multipoint contact.

Electrical contacts can be classified according to their nature, surface geometry, kinematics, design and technology features, current load, application, and by others means.[1–3] In general, electrical contacts can be divided into two basic categories: stationary and moving. Figure 1.1 represents the most general classification of electrical contacts according to contact kinematics, functionality, and design features.

In stationary contacts, contact members are connected rigidly or elastically to the stationary unit of a device to provide the permanent joint. Stationary contacts are divided into *nonseparable* or *all-metal* (welded, soldered, and glued), and *clamped* (bolted, screwed, and wrapped). Nonseparable (permanent) joints have a high mechanical strength and provide the stable electrical contact with a low transition resistance. A nonseparable joint is often formed within one contact member. For example, in commutating devices, only materials with a complex composition and arc-resistant working layers are used as the contact members. They are made by contact welding, soldering, coating, deposition, electrospark alloying, and mechanical methods of joining.

Clamped contacts are made by mechanically joining conductors directly with bolts or screws or using intermediate parts, specifically, clamps. These contacts may be assembled or disassembled without damaging the joint integrity. The simplest case of a clamped contact is the joint of two massive conductors with flat contact surfaces, such as busbars. A more complex joint configuration is a contact comprising several conductors, such as joints of a multistrand wire and clamp that are used for joining wire conductors in transmission lines.

The nature of clamped and all-metal contacts is different. This is because in the all-metal contacts there is no physical interface between conductors, whereas in clamped contacts the interface is controlled by the contact pressure and the ability of the material to undergo plastic

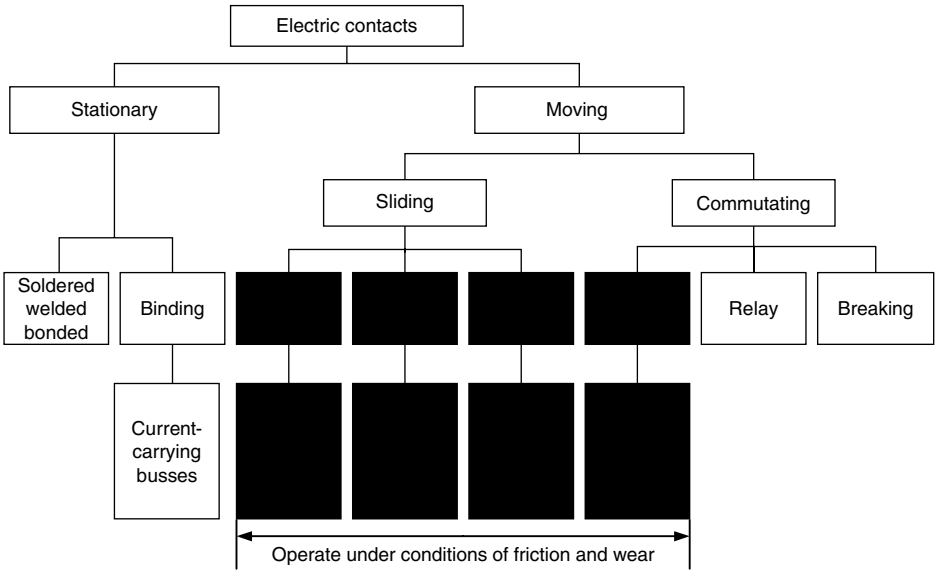

FIGURE 1.1 Classification of electrical contacts.

deformation. The lower the specific resistance and hardness of a material, the higher its corrosion resistance and, consequently, the lower the contact transition resistance. For this reason, contact surfaces are usually covered with soft, corrosion-resistant materials such as tin, silver, cadmium, or similar materials. Different surface cleaning techniques are often used to improve the joint connectability.

In *moving contacts*, at least one contact member is rigidly or elastically connected to the moving unit of a device. Depending on their operating conditions, these contacts are divided into two categories: commutating and sliding. Commutating contacts intermittently control the electric circuit. They fall into two categories: separable (various plug connectors, circuit breakers) and breaking. The latter are used for a periodical closing and opening of an electrical circuit, such as in different switches, contactors, relays, and similar devices. Because of differences in breaking power, current, and voltage, there is a great variety of breaking contacts. The breaking contacts can be classified as light-, medium- and heavy-duty:

- *Light-duty* contacts carry very low currents, operate at voltages up to 250 V, and display no appreciable arc-related electrical wear. The successful operation of these devices depends mainly on maintaining relatively low and stable contact resistance and also on the selection of the contact materials. The factors that must be taken into account are tendency to oxidize (tarnish); presence of dirt, dust or other contaminants on the contact surface; and contact design (form, size, contact pressure, and finish). Light-duty contacts are intended for use in instrument controls, general automation, radio and data communication, and telecommunication systems.
- *Medium-duty* contacts carry appreciably higher currents (see 5A above) and operate at voltages up to 1000 V. For this group, electrical wear is of prime importance. The factors governing contact material selection to meet the very severe operating conditions include tendency to welding, material transfer, and erosion (pitting). Applications of medium-duty contacts are control devices for industrial, domestic, and distribution network applications.

- *Heavy-duty* contacts carry very high currents (tens of kA) and operate at very high voltages (hundreds of kV). The most common types of these connectors are contactors, starters, and circuit breakers.

In *sliding contacts*, the contacting parts of the conductors slide over each other without separation. Current passage through the contact zone is accompanied by physical phenomena (electrical, electromechanical, and thermal) that produce changes in the state (characteristics) of surface layers of the contacting members that differ when operating without current (see Figure 1.2). The severity of the processes occurring at contact interface depends on the magnitude and character of the current passing through the contact, the applied voltage, operating conditions, and contact materials.[4,5] The physical processes occurring in the contact zone of sliding contacts can be classified as follows:

- *Sliding contacts with a heavy electrical contact load* are contacts whereby currents or voltages are commutated, inducing mechanical, thermal or electrical effects including sparking and arcing. These effects thus produce changes in the state (properties) of the contact members. The necessary condition of such an operating regime is that the voltage across disclosed contacts exceeds the minimal electric arc voltage for the materials used;
- *Sliding contacts with a moderate electrical contact load* are contacts where mechanical, thermal or electrical effects, excluding sparking and arcing, change the state of the mated surfaces. The voltage across opened contacts is between the softening voltage and the minimal electric arc voltage for the material used;
- *Sliding contacts with a low electrical contact load* are contacts where no additional physical phenomena and changes are induced in the state of the mated surfaces. In this case the voltage across open contacts is less than the softening voltage.

The most important and widely used types of sliding contacts include contacts of electrical machines, current pick-offs of transport and lifting machines, and of radio-electronic devices, and control and automatic systems. As a rule, sliding contacts for electrical and transportation machines are intended to commutate currents of a moderate and high intensity while those for radio-electronic devices and control and automatic systems are usually low-current level contacts.

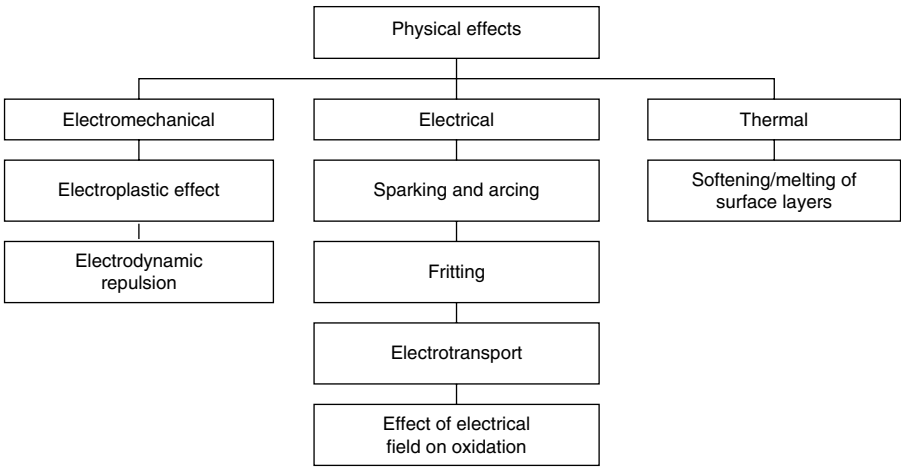

FIGURE 1.2 Possible effects on the passage of electrical current through the interface.

For electrical machines, there are two types of sliding electrical contacts: brush-collector and brush-collector ring, in which the brushes with different polarities slide over one friction track (brush-collector) or different rings (brush-collector ring).[1,6] Collectors are commonly made of electrolytic copper or copper with small additions of cadmium, silver, magnesium, zirconium, or tellurium. Collector rings are made of copper alloys with zinc, lead, and aluminum and, in some cases (very high peripheral velocities), of ferrous metals and their alloys. Brush materials are based mainly on multicomponent composites of graphite, soot, copper, and coke powders.[7]

Sliding contacts are very important components in many devices used in automatic, telemechanical, and communication equipment, such as different potentiometers serving as electromechanical sensors.[8,9] Their design is wide ranging and, despite their low material consumption, they are expensive parts of machines and devices due to an extensive use of noble metals in their production. From a mechanical viewpoint, the operating conditions of low-current sliding contacts are quite favorable because sliding velocities are low and loads on the contact members are light; thus, as a rule, these devices are protected against harmful environment factors.

1.2 SUMMARY OF BASIC FEATURES

It has been established that real surfaces are not flat but comprise many asperities.[1] Therefore, when contact is made between two metals, surface asperities of the contacting members will penetrate the natural oxide and other surface contaminant films, establishing localized metallic contacts and, thus, conducting paths. As the force increases, the number and the area of these small metal–metal contact spots will increase as a result of the rupturing of the oxide film and extrusion of metal through the ruptures.

These spots, termed *a*-spots, are small cold welds providing the only conducting paths for the transfer of electrical current. A direct consequence of this is a porous contact where infiltrating oxygen and other corrosive gases can enter to react with the exposed metal and reduce the metallic contact areas. This will eventually lead to disappearance of the electrical contact, although the mechanical contact between the oxidized surfaces may still be preserved. The real contact area A_r is only a fraction of the apparent contact area A_a, as illustrated in Figure 1.3.

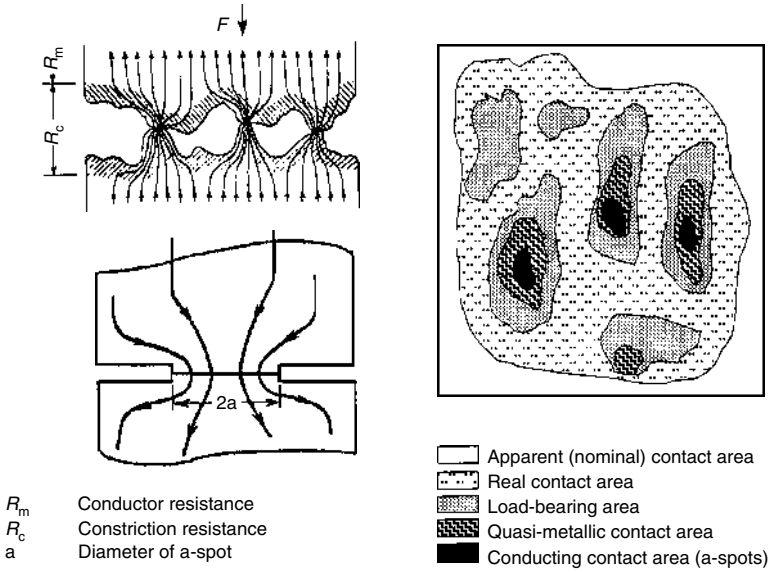

FIGURE 1.3 Schematic of current constriction and real contact area.

The relationship between the applied normal load F_c, hardness of the metal, H, and the apparent contact area, A_a, is given by the following expression:

$$F_c = \xi H A_a. \tag{1.1}$$

The hardness, H, in this expression represents a measure of the ability of a metal to resist deformation due to point loading; ξ is the pressure factor and depends on the amount of deformation of the asperities and is equal to 1 in most practical contact systems. On the other hand, Holm[1] has shown that hardness is related to the yield stress (σ_y) by the following expression:

$$H = 3\sigma_y. \tag{1.2}$$

The results, shown in Table 1.1, express the real contact area as a percentage of the apparent contact area, A_a, at various normal loads. It should be noted, however, that the real contact area calculated in this manner includes the load-bearing area which is covered with the oxide film and is not, therefore, a dependable path for transfer of electrical current. Therefore, the conducting contact area will be only a small fraction of the calculated real contact area, generally considered to be much smaller than 1%.

It should be pointed out that the electrical interface of an *a*-spot is far different from the single circular contact spot. Current passing across a contact interface is constricted to flow through *a*-spots. Hence, the electrical resistance of the contact due to this constricted flow of current is called *constriction resistance* and is related to the basic properties of metals such as hardness and electrical resistivity. Holm[1] has shown that the constriction resistance for a single *a*-spot can be expressed as

$$R_s = (\rho_1 + \rho_2)/4a, \tag{1.3}$$

where ρ_1 and ρ_2 are resistivities of the contacting metals, and a is the radius of the metal-to-metal contact area. If the two contacting metals are the same, then the constriction resistance becomes

$$R_s = \rho/2a. \tag{1.4}$$

Because the metals are not clean, the passage of electric current may be affected by thin oxide, sulphide, and other inorganic films usually present on metal surfaces. Consequently, the total contact resistance of a joint is a sum of the constriction resistance (R_s) and the resistance

TABLE 1.1
Effect of Normal Load on Real Area of Contact for Clean Surfaces

	Real Contact Area/Apparent Contact Area (A_r/A_a) (%)		
Alloy[a]/Applied Load	**10 N**	**100 N**	**1000 N**
Al (H-19)	0.01	0.1	1.0
Al (H-0)	0.05	0.5	5.0
Al+0.75% Mg+0.15% Fe (H-19)	0.01	0.1	1.0
Al+0.75% Mg+0.15% Fe (H-0)	0.02	0.2	2.0
Cu (H-0)	0.008	0.08	0.8

[a] (H-0), fully annealed; (H-19), fully hardened.

of the film (R_f)

$$R_c = R_s + R_f$$
$$R_f = \sigma/\pi a^2, \tag{1.5}$$

where σ is the resistance per area of the film. Both tunnelling and fritting are considered operative mechanisms for the current transfer across the film. In most practical applications, the contribution of these films to the total contact resistance is of minor importance because the contact spots are usually created by the mechanical rupture of surface films.

The contact resistance is the most important and universal characteristic of all electrical contacts and is always taken into account as an integral part of the overall circuit resistance of a device. Therefore, although it is significantly smaller as compared with the overall circuit resistance, the changes in the contact resistance can cause significant malfunctions of the device. This is because the contact resistance can vary significantly with the changes in the real contact area, contact pressure variations, resistive film nonuniformity, and other factors. This results in large voltage increases, thus making the fine adjustment or good operation of devices difficult. For instance, the instability and high values of contact resistance are especially noticeable in bulk DC potentiometers, whose resistive members are relatively thick and have a high specific resistance.

There are many parameters that can be used to assess the operating efficiency of electrical contacts. Among these parameters, perhaps the most important are electric (the transition voltage drop, commutation noise, erosion resistance), tribological (the wear resistance and friction coefficient) and chemical (corrosion resistance). In the following chapters, detailed analyses of the factors affecting the properties and performance of electrical contacts will be given.

2 Contact Mechanics

2.1 SURFACE OF SOLIDS

The features of a solid surface as a physical object are governed by its spatial arrangement as a boundary between two phases.[10] The atoms and molecules belonging to the surface have fewer neighbors than those in the bulk. This simple fact has far-reaching consequences for geometry and physics of a surface: the interactions between its atoms and their neighbors vary, distorting the force field that penetrates to the depth of several interatomic distances. Given this fact, the excess of energy to surface energy appears; consequently, the surface interacts with the environment. This process is termed *adsorption*. There are physical and chemical types of adsorption.

Physical adsorption is characterized by the van der Waals interactions between the adsorbate and the solid surface. As a rule, its energy of the interaction is below 20 kJ/mol. The polymolecular films adsorbed on the surface are removed relatively easily.

The chemical adsorption energy is quite high (80–400 kJ/mol), usually producing a monolayer on the surface that is hard to remove, even through the use of elevated temperatures. In addition, chemical reactions between the surface and the active elements, such as oxidation in the environment, should be remembered. Unlike the case for chemisoption, these reactions result in a bulk phase on the surface.

The environment exerts very different effects on a solid surface.[10] In the 1920s, A. Joffe demonstrated that halide crystals, e.g., NaCl, that are brittle in dry air, become ductile in a moist atmosphere and show an increase in strength. Joffe ascribed this effect to a water film on the solid surface, assuming that the water heals surface microcracks. This circumstance holds significance in tribological behavior of materials for which Joffe's effect takes place. For example, aluminum oxide is sensitive to water vapor, and high-strength steel exposed in pure hydrogen is sensitive to a small concentration of oxygen. An attack of some active environmental species on the solid surface of metals or nonmetals may change the mechanical behavior of surface layers because of the wedging, or Rebinder, effect (Figure 2.1). This phenomenon was first observed by P. Rebinder. As a rule, the species are of organic origin (fatty oxides, alcohols, soaps, etc.) and are present in lubricants.

The adsorbed film may have the opposite effect, producing surface hardening. This hardening occurs in, for example, oxides on certain metals (the Roscoe effect). Hence, the surface adsorptivity produces a fine boundary layer with a structure and behavior differing from those of the surface layer of the solid. Figure 2.2 shows schematically that the structure of the boundary layer is quite intricate. The appearance of each sublayer depends upon the conditions of fabrication of a part. The layers may mutually penetrate one another through the system of microcracks.

The boundary layer may be in a diversity of physical states, ranging from nearly gaseous to solid crystalline. Both the basic parameters (temperature and pressure) and the pattern of interactions with the solid phase determine its state. The mechanical behavior of boundary layers demonstrates a wide spectrum of properties ranging from viscous and viscoelastic behavior to perfect elasticity.

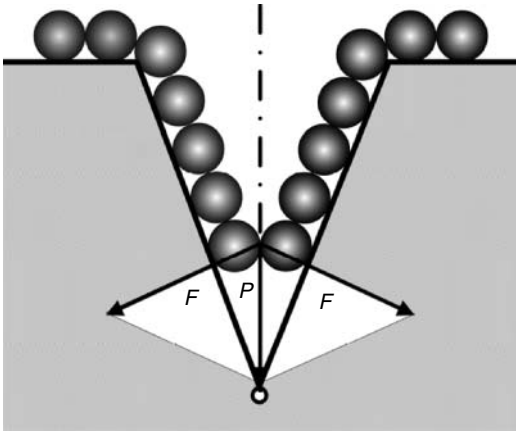

FIGURE 2.1 Effect of wedging out produced by polar molecules in surface cracks. *P*, load induced by adsorbed layer; *F*, forces of wedging out.

When two solids approach each other, only their molecular fields interact and generate the attracting force responsible for their bonding or adhesion. This latter state implies the appearance of molecular bonds between the mated surfaces. The thermodynamic work of adhesion, γ_a, between two bodies (1 and 2) is equal to the work of reversible adhesive detachment; this is frequently determined by the Dupre equation:

$$\gamma_a = \gamma_1 + \gamma_2 - \gamma_{12},$$

where γ_1 and γ_2 are the surface energies of surfaces 1 and 2 before contact (their free energies) and γ_{12} is the interface energy.

2.2 SURFACE TOPOGRAPHY

When investigating the real contact, it should be remembered that machine-part surfaces deviate to various extents from design shapes that are usually designed to be geometrically due to

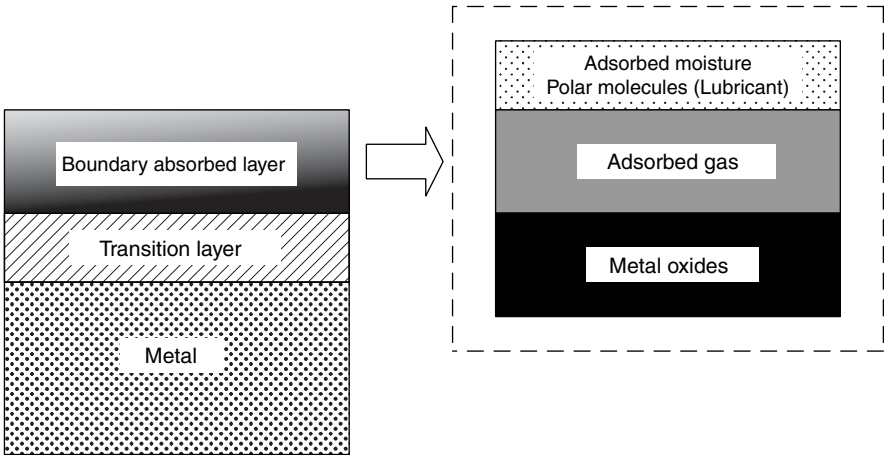

FIGURE 2.2 Structure of surface layer of metallic part.

manufacturing or other considerations.[11,12] A real surface is not ideal because of asperities appearing during machining and subsequent use. The extent of deviation particularly depends upon the structure of contacting materials. The solid surface experiences the effects of various factors that can be classified into manufacturing, operational, and structural.

The height (amplitude) dimensions of asperities range extensively from decimal fractions of a nanometer to several millimeters. The spacing parameters of the asperities are still wider and sometimes extend the length of the part itself. The lower limits of these ranges relate naturally to the dimensions of atoms and molecules; the upper limits depend on the conditions of machining and the structure of the materials in question. There are apparently no physically imposed limits of existence of the asperities within these height and spacing ranges. Nevertheless, the investigation of rough surfaces and the development of suitable measuring equipment indicate that it is methodologically reasonable to divide the asperities into four dimensional levels: errors in form, waviness, roughness, and subroughness (Figure 2.3).

Errors in form are defined as shape deviations of a real surface or profile from the simple geometry having a great spacing ($S = 1$–$5{,}000$ mm) and relatively small height ($\Delta = 1$–50 μm). As a rule, $\Delta/S \leq 0.001$. The errors in form are usually single, irregularly spaced surface departures. For cylindrical parts, they can be oval facets in the cross-section and taper, and barrel-shaped cambers in the longitudinal section; lack of rectilinearity and flatness characterize shape deviations of a flat surface.

Errors in form result from faulty machining, lack of tool precision, wear of tools, and elastic deformations in the system of lathe-tool-workpiece produced by factors such as the variable cutting force.

Sometimes shape deviations are determined quantitatively by the parameter; Δ being the greatest distance between the real surface points and the surface enveloping the latter along the normal (Figure 2.3). The *enveloping surface* is defined as the nominally shaped surface contacting with the real surface and lying outside the material of the part, so that any deviation of the point most distant from the real surface within a specified area should have the minimum magnitude.

Roughness is usually excluded when errors in form are analyzed. In reality, these errors and the roughness specified for the same surface are interrelated; therefore, a tolerance on the form error also imposes restrictions on the roughness. For example, it is accepted that the roughness, R_z, should be at least 1.5–2 times less than the highest shape deviations.

When studying a contact between real surfaces, it should be borne in mind that errors in form tend to redistribute the pressure within the apparent contact area; as a consequence, the stress concentration occurs in the relevant contact areas, and rubbing surfaces undergo uneven wear.

Waviness is a combination of n quasiperiodic asperities with a relatively large spacing along the portion exceeding the specified sampling length, l, for measuring the surface roughness. The waviness covers the following dimensional area: the spacing of asperities is 0.8–10 mm

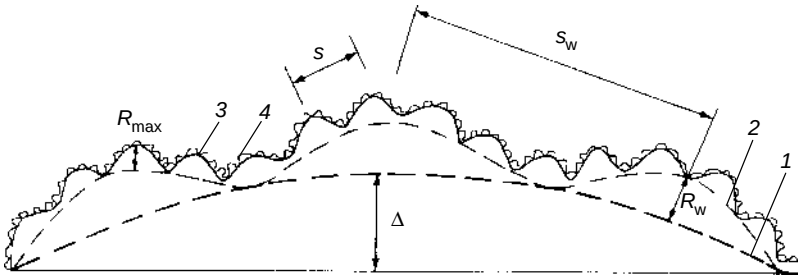

FIGURE 2.3 Components of surface profile. (1) error in form, Δ; (2) waviness; (3) roughness; (4) subroughness; S_w, R_w, waviness spacing and height; S, R_{max}, roughness spacing and height.

(bigger parts may have a larger upper limit, up to 200–300 mm); the height is 0.01–500 μm. Some countries (Germany, Switzerland, and the United States, for example) have standards for waviness.

There is no strict distinction between waviness and roughness. Conventionally, for the convenience of measurement and classification, either the waviness spacing (the lower spacing of waviness should exceed the assessment length used for roughness measurement) or the ratio between the spacing and the waviness height (assumed, as a rule, to be over 40) serves as such a separating boundary.

Vibrations (forced or self-excited) in the lathe-tool-workpiece system are the main cause of waviness that may also result from friction and wear. The cluster structure of the real contact between solids is mostly due to waviness, making the latter an important subject in studies of energy transfer across the contact zone.

Roughness constitutes a surface microrelief, and it is defined as a population of asperities with a relatively small sampling; it is measured using the assessment length, *l*, shown in Figure 2.4.

Usually, roughness is produced by tracks of machining tools (a cutter, a mill, an abrasive cutter, etc.), and the quality of roughness depends on the kinematical design, the method of machining, the mechanical properties of a material, and vibrations in the lathe-tool-workpiece system. The original roughness of working surfaces undergoes significant modification during friction and wear, and it reaches the so-called "equilibrium roughness" that is apparently reproduced under normal friction conditions.

Subroughness presents the fine (nanometer scale) structure of a real surface, and it is closely related to the so-called "physical relief." It involves the accidental and imperfect location of crystallographic planes, chaotically distributed grains, and islet-type films including oxides and adsorbed ones. For some partially crystalline polymers, the subroughness can be connected with alternating crystalline and amorphous regions of dozens of nanometers in size. Its study can provide a new insight into the theory of friction, wear, and lubrication.

Hence, the real surface has a set of topographic elements that can be divided into two groups and four levels of shape deviations: macrogeometry (errors in form and waviness) and microgeometry (roughness and subroughness). They possess different scales and patterns of distribution, and they play different roles in the processes of friction and wear. Conditionally, the regions of existence of each can be represented by some subsets in the coordinate system with the axes being the height of asperities, *H*, and the mean distance, *S*, between them (Figure 2.5). Even when the surface has the asperities of the same level, its description presents a nontrivial problem. The description can be facilitated if its objectives are clearly understood. At present, four approaches exist in tribology to describing real surfaces: deterministic, parametric, probabilistic, and fractal.

The deterministic approach presents a surface description as some periodic, continuous, or piecemeal continuous function. It is educative to compare the sketch made by Coulomb in 1821 (Figure 2.6a) with that borrowed from a contemporary monograph by Johnson in 1987 (Figure 2.6b).[13] Although such imaging of the surface may seemingly be naïve, it allows one of

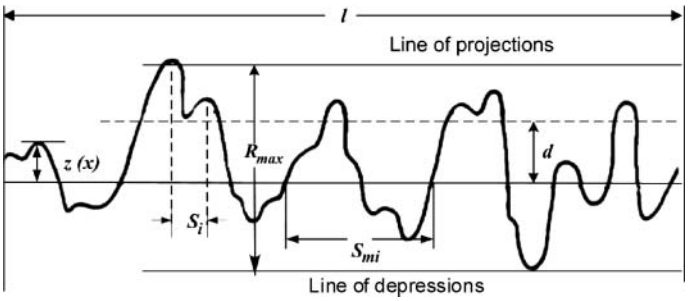

FIGURE 2.4 Rough surface profile.

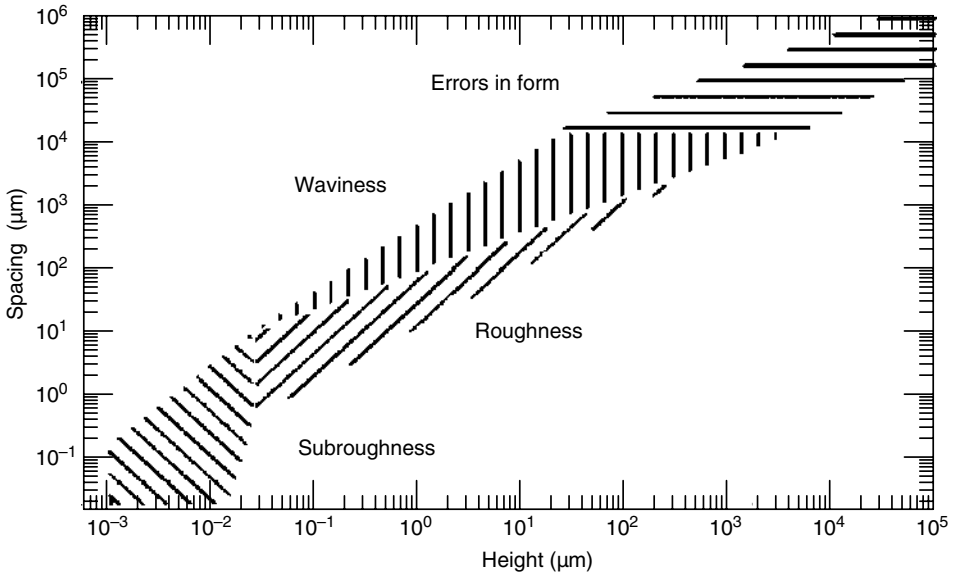

FIGURE 2.5 Relation between typical dimensions of basic topographic elements of real surface.

the fundamental features of rough surfaces—their discrete (patchy) pattern—to be reflected, whereas stochastic behavior as another feature is ignored.

The parametric method is based upon the description of a surface using a set of some parameters that are determined, as a rule, by analyzing surfaces in two or three dimensions. The roughness parameters are calculated in respect to some reference line (surface) that is plotted in a definite manner. The mean line (surface) is usually used as the reference line.

The surface profile is generally characterized by a set of parameters. There is a variety of such sets; the parameters include height (amplitude), sampling, and those of a hybrid type. A discussion follows of the basic parameters used in engineering practice and research.

The arithmetic average roughness, R_a, is defined as an arithmetic mean of the departures of the roughness profile from the mean line over one sampling length, l:

$$R_a = \frac{1}{l}\int_0^l |z(x)|\mathrm{d}x, \tag{2.1}$$

where $z(x)$ is the profile equation which is frequently set in a graphic or tabular form.

In the last case, R_a is calculated by the formula

$$R_a = \frac{1}{n}\sum_{i=1}^{n} z_i \tag{2.2}$$

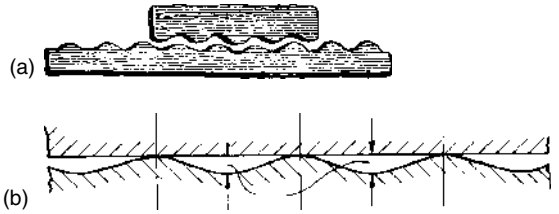

FIGURE 2.6 Fragment of sketch by (a) Coulomb and (b) Johnson.

Usually, R_a is averaged over several consecutive sampling lengths from 2 to 20 in accordance with the national standard. The parameter is identical to arithmetic average (AA) and center-line average (CLA).

The root-mean-square (RMS) roughness, R_q, is defined as the RMS deviation of the profile from the mean line over sampling length:

$$R_q = \left(\frac{1}{l}\int_0^l z^2(x)\right)^{1/2} \tag{2.3}$$

or

$$R_q = \left(\frac{1}{n}\sum_{i=1}^{n} z_i^2\right)^{1/2}.$$

The parameters R_a and R_q differ insignificantly in magnitudes. For the same surface, R_a is less than R_q by 6–30%. Thus, a regular sine-shaped profile with a single harmonics, the ratio R_q/R_a is equal to $\pi/2^{3/2} \approx 1.11$; for the Gaussian profile, $R_q = 1.25R_a$.

The 10-point height (or zone roughness), R_z, is separation of the average of the five highest peaks and the five lowest valleys within a single sampling length (peak [valley] is defined as local maximum [minimum] above [below] profile mean line):

$$R_z = \left(\sum_{i=1}^{5} |z_{ip}| + \sum_{i=1}^{5} |z_{iv}|\right) \Big/ 5, \tag{2.4}$$

where z_{ip} is the height of the ith highest profile peak, z_{iv} is the depth of the ith deepest profile valley.

The same notation, R_z, is often used for the average peak-to-valley height, which is found by averaging over five consecutive sampling lengths of separation of the highest and lowest peak in each sampling length (Figure 2.7).

The maximum peak-to-valley height, R_{max}, is the largest single peak-to-valley height in five adjoining sampling lengths. The parameter is a sensitive indicator of high peaks or deep scratches but has a large scatter due to random sampling. The standards specify some spacing parameters.

Spacing along the mean line, S_m, is the mean spacing between profile peaks at the mean line, measured over the assessment length. Here, a profile peak is the highest point of the profile between an upwards and downwards crossing of the mean line.

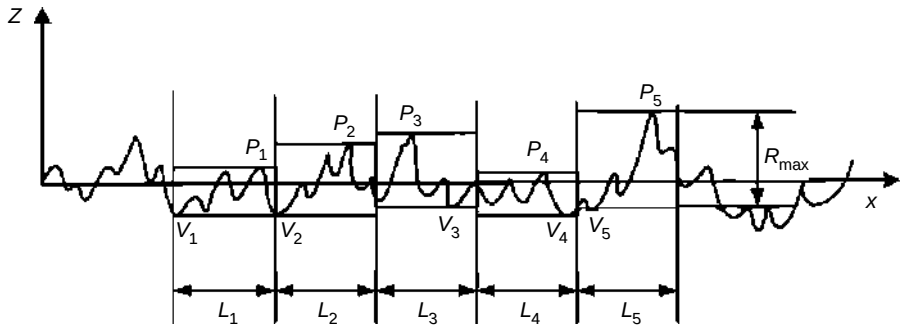

FIGURE 2.7 Consecutive basic lengths $L_1 - L_5$ making up the rating length, L.

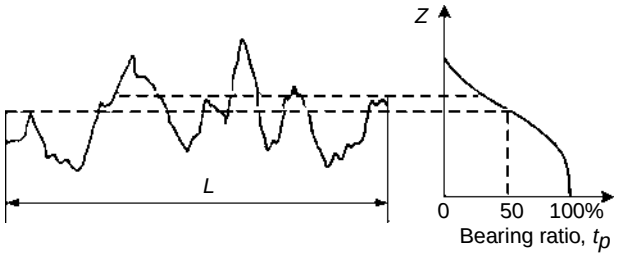

FIGURE 2.8 Schematic of bearing curve construction.

Spacing of peaks, S, is the mean spacing of adjacent local peaks, measured over the assessment length. A local peak is the highest part of the profile measured between two adjacent minima, and it is only included if the distance between the peak and its preceding minima is at least 1% of the peak-to-valley of the profile. Normally specified in a Russian standard, these parameters also exist in hybrid form.

Bearing ratio, t_p, is the length of bearing surface (expressed as a percentage of the assessment length, L) at a given height, p, below or above the reference line (Figure 2.8). A plot of bearing ratio against surface height is named the bearing ratio curve (or Abbott–Firestone curve). The curve allows one to estimate the contact area of mating surfaces and to assess the expected rate of wear. The initial portion of the curve is conveniently approximated by the exponential function:

$$\eta = b\varepsilon^{\nu}, \tag{2.5}$$

where $\varepsilon = a/R_{\max}$, a is the distance between the highest line of profile and the specified level p. b and ν are the parameters of the parabolic approximation of initial part of bearing ratio curve. They depend on the type of machining.

The probabilistic approach to describing the rough surface geometry is based on the theories of probability and random processes. As a rule, it is more labor consuming, yet the effort is partly compensated by more complete information about the surface topography. This approach allows treating two-dimensional or three-dimensional surfaces as some statistical sample of profile ordinates (or peaks of asperities) or as some realization of a random process.

In the first case, the set of heights (the ordinates) of the profile $z(x)$ is treated as a random variable that is described in the theory of probability by the cumulative probability function $F(z)$. The function is the probability that random variable $z(x)$, the profile height z, for example, takes a value less than or equal to z:

$$F(z) = P\{z(x) \leq z\}.$$

The function $F(z)$ is the integral of the probability density function $f(\xi)$, i.e.,

$$F(z) = \int_{-\infty}^{z} f(z)\mathrm{d}z. \tag{2.6}$$

The probability density $f(z)$ in this situation is the fraction of these profile ordinates that are located within the interval $(z, z+\mathrm{d}z)$. In other words, $f(z)\mathrm{d}z$ is the probability of finding an ordinate in that range. It is simplest to determine the function $f(z)$ by plotting a relevant histogram followed by its approximation. Most often these histograms are successfully approximated with the Gaussian curve:

$$f(z) = \frac{1}{\sigma\sqrt{2\pi}} \exp\left[-\frac{(z-a)^2}{2\sigma^2}\right], \tag{2.7}$$

where σ is the standard deviation of the profile ordinates (identical to the roughness parameter, R_q, described above), which characterizes the scattering of the random variable, while a is its expectation (mean value of profile ordinates). If the ordinates are normalized by σ and they are measured from the mean line of profile, then $a = 0$ and the Gaussian (normal) probability density is written as:

$$f(z) = \frac{1}{\sigma\sqrt{2\pi}} \exp\left[-\frac{z^2}{2}\right]. \tag{2.8}$$

When the ordinates of rough surfaces distribute according to the Gaussian law, they are called *Gaussian* or *normal* surfaces. A comparative simplicity of their description has provoked numerous theories of contact interactions between them. Yet, it should be remembered that in engineering, the surfaces are frequently quite different from normal surfaces. Hence, the conclusions based on the Gaussian models should be treated in a highly critical way, as some rough approximation of the real situation.

The probabilistic approach is generalized by the concept based on the theory of random fields (processes), which treats a profile as a random field. This method was developed primarily for Gaussian (isotropic and anisotropic) surfaces. Its advantages become remarkable when analyzing a three-dimensional surface.

This paper will not discuss the mathematical refinements of the method, which can be consulted in publications. Below are given the main results of applicable significance.

The probability density of summit heights is described by the following equation:

$$\begin{aligned} p(\xi_1^*) = \frac{\sqrt{3}}{2\pi}\Bigg\{ & \xi_1^* \left[\frac{3(2\alpha-3)}{\alpha^2}\right]^{1/2} \exp(-C_1\xi_1^{*2}) + \frac{3\sqrt{2\pi}}{2\alpha}(\xi_1^{*2}-1) \\ & \times \left[1 + \operatorname{erf}\left(\xi_1^* \left(\frac{3}{2(2\alpha-3)}\right)^{1/2}\right)\right] \exp\left(-\frac{1}{2}\xi_1^{*2}\right) + \left[\frac{2\pi\alpha}{3(\alpha-1)}\right]^{1/2} \\ & \times \left[1 + \operatorname{erf}\left(\xi_1^* \left(\frac{\alpha}{2(\alpha-1)(2\alpha-3)}\right)^{1/2}\right)\right] \exp\left[-\frac{\alpha\xi_1^{*2}}{2(\alpha-1)}\right]\Bigg\}, \end{aligned} \tag{2.9}$$

where $\xi_1^* = \xi_1/m_0^{1/2}$ is the dimensionless height of summit; $\alpha = m_0 m_4/m_{22}$ is the bandwidth parameter; $C_1 = \alpha/(2\alpha-3)$. This equation is termed *Nayak's distribution*. Nayak was the first to propose it exactly in this form for describing rough surfaces.[14]

The distribution p depends on the spectral moments only in some dimensionless combination α that can be determined from the surface profilogram. The bandwidth parameter α is associated with the width of the surface spectral density. The larger the parameter α, the broader the spectrum, i.e., the band of wavelengths making up the given surface is wider. A narrow band ($\alpha \to 1.5$) indicates approximate equal length of all the waves.

The bandwidth parameter varies from 1.5 to infinity; the distribution of Nayak degenerates into the known Rayleigh and Gaussian distributions at these limit values of the bandwidth parameter:

$$p_R(\xi^*) = \begin{cases} 0, & \xi^* < 0, \\ \dfrac{2\sqrt{3}}{\sqrt{2\pi}}\left[\xi^{*2} - 1 + \exp(-\xi^{*2})\right]\exp(-\xi^{*2}), & \xi^* > 0, \end{cases} \tag{2.10}$$

$$p_G(\xi^*) = \frac{1}{\sqrt{2\pi}} \exp\left(-\frac{1}{2}\xi^{*2}\right).$$

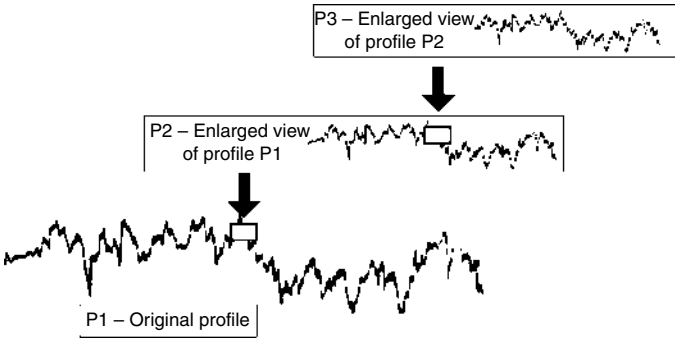

FIGURE 2.9 Fractal representation of real surface roughness.

It is obvious that the transition from the Gauss to the Rayleigh distribution (with decreasing the parameter α) increases the probability of the existence of higher summits.

The fractal approach to describing rough surfaces has attracted tribologists because the roughness parameters of a real surface proved to be substantially dependent on the resolution of available measuring instruments because of the multiscale character of roughness and its nonstationary features. These qualities of rough surfaces have stimulated the search for a method of surface characterization that could provide the structural information on roughness. Parameters would be invariant for all scale levels. By not very rigorous definition, the fractal is a structure comprising the components resembling the whole in some sense. Rough surfaces frequently satisfy this definition. If the accuracy of measurements is increased successively by registering finer and finer surface details, the fractal roughness appears the same at any scale of magnification (Figure 2.9). Hence, the fractal dimensions represent in fact the only parameter fully describing the rough surface. This fact, considered as the basic advantage of the fractal approach, has been the cause of its criticism. It is hard to imagine that such intricate objects like rough surfaces can be described with a single number.

Combined methods are usually employed in practical research: a deterministic description involves probabilistic components, or a fractal description uses spectral roughness characteristics. More detail analysis of roughness description is presented in Appendix 1.

2.3 MODERN TECHNIQUES OF MEASURING SURFACE PARAMETERS

At present there are many methods of studying surface topography.[11,15] The stylus methods remain the most popular; the results have been the foundation of modern standards. Optical methods using electromagnetic radiation have become popular. There are electrical and thermal methods using various electrical phenomena and heat transfer through the rough contact. Figure 2.10 shows capabilities of various methods for measuring the surface parameters.

An analysis of modern tendencies shows that the interests of science and technology have shifted towards obtaining data about very smooth surfaces, i.e., the micro- and nano-scale roughness and reconstruction of three-dimensional images of real surfaces. Still, as in the past, the stylus methods retain their foothold (Figure 2.11).

In these methods a fine stylus slides over the surface, replicating its relief. Displacements of the stylus in the vertical direction are converted into electrical signals that are recorded as profilograms and/or digitized for PC processing.

The height of asperities is smaller, as a rule, than their horizontal dimensions. Therefore, it is better to record a profile trace with vertical magnification greater than that in a horizontal direction (Figure 2.12a). Figure 2.12 shows that the impression on the surface profile strongly depends on the ratio between the scales of magnification and that the real roughness is inclined more steeply than

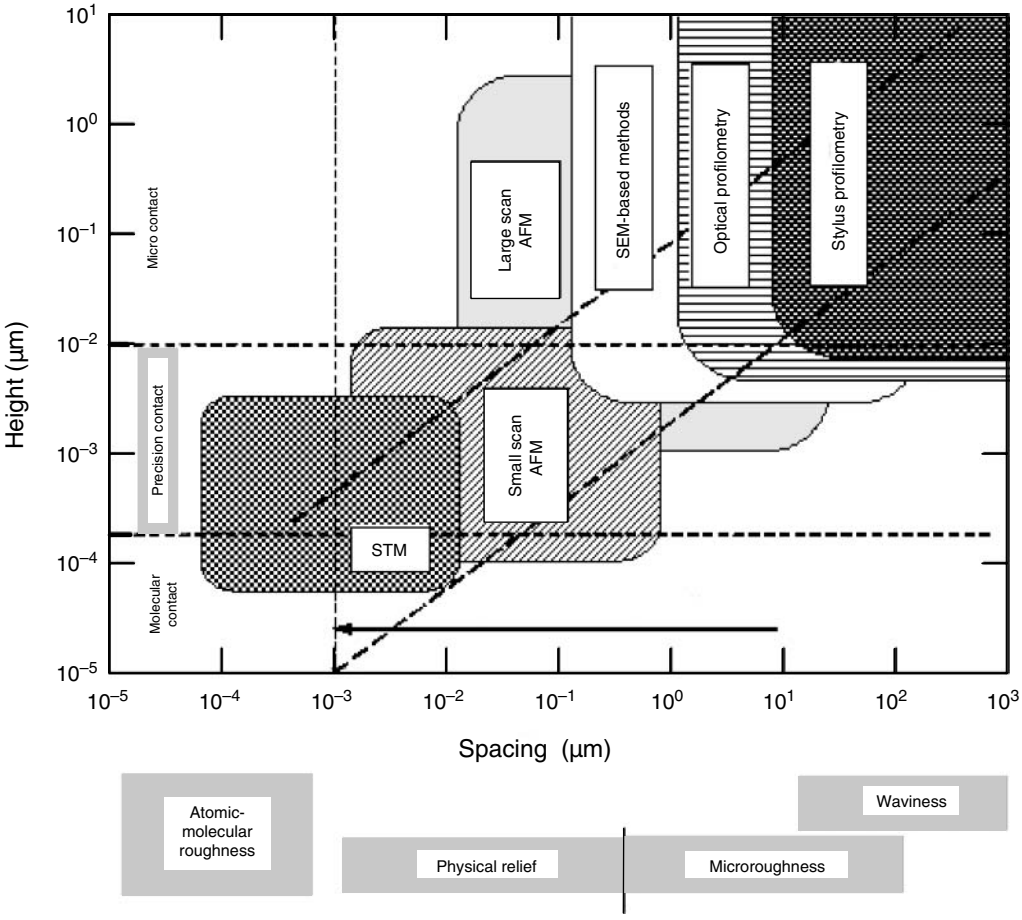

FIGURE 2.10 Diagram of the height and spacing parameters and the ranges of vertical-lateral resolution for different methods of roughness measurement.

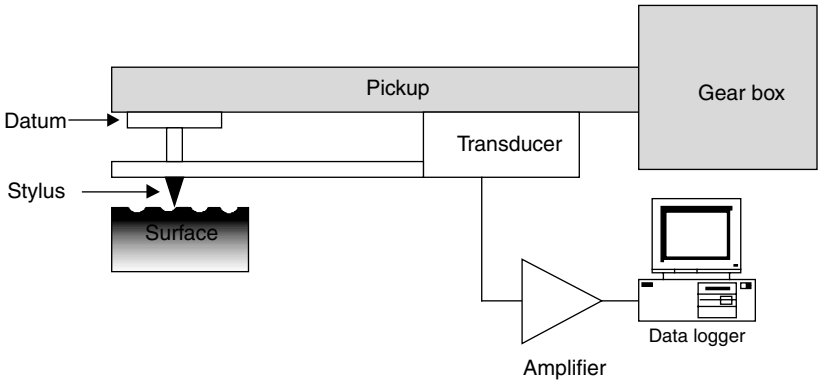

FIGURE 2.11 Schematic of stylus profilometer.

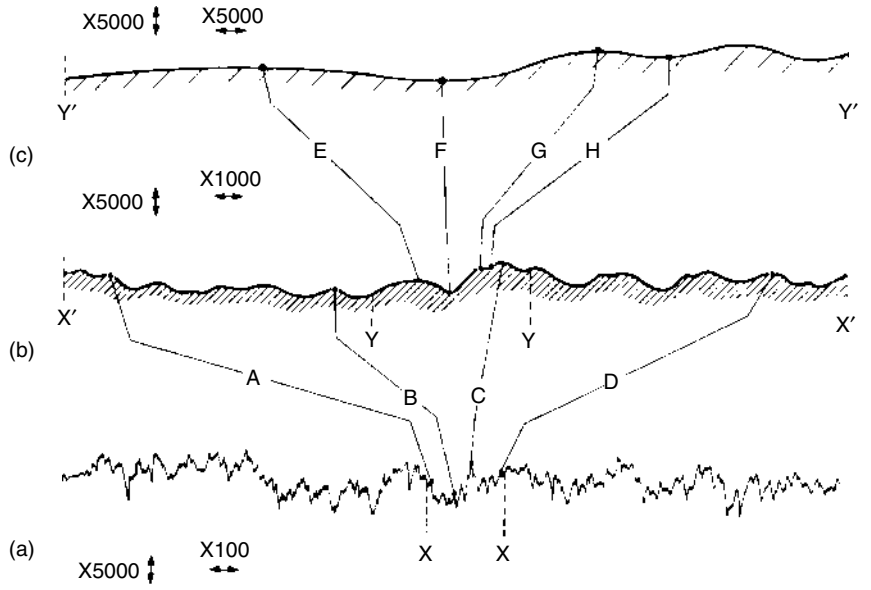

FIGURE 2.12 The profile real surface with different vertical and horizontal magnification. (a) vertical amplification exceeds horizontal amplification 50 times; (b) same surface when magnification ratio is 5:1; (c) surface with identical vertical and horizontal magnification. (Adapted from Hutchings, I. M., *Tribology: Friction and Wear of Engineering Materials*, Edward Arnold, London, 1992. With permission.)

the profile trace shows it to be. The optical methods are most popular because of their high vertical resolution (<0.1 nm). The laws of light diffusion reflected by surface asperities allow one to determine a number of essential characteristics of rough surfaces, such as the standard deviation and the radius of correlation. Efforts are known of using ellipsometry for measuring roughness parameters.[10]

Electron microscopy is a significant method of scientifically studying of rough surfaces. Actually there is a large group of noncontact methods based on transmission and scanning electron microscopy (diffusion, elastic, or secondary electrons) and techniques (processing stereo couples, installing auxiliary detectors, etc.).

Studies of very smooth subrough surfaces have been additionally stimulated after scanning tunnel microscopy (STM) was pioneered and first made public in 1982. Physically, STM is based on the tunneling of electrons between two closely spaced electrodes. The principle of operation of a tunnel microscope (Figure 2.13) implies that the displacement of the metallic needle fixed in a three-coordinate piezodrive over the target surface induces a tunnel current I_m in the clearance between them under the effect of voltage U:

$$I_T = U \exp(-A\Phi_1/2d),$$

where Φ is the potential barrier in the clearance d between the needle and the surface; A is the proportionality coefficient ($A = 1$ when Φ is measured in electron-volts and the clearance, d, is in Angstroms). When the voltage in the clearance is maintained constantly (as it is usually practiced), the clearance is varied by the feedback system controlling the displacement of the needle by the piezodrive to maintain the magnitude of the tunnel current. The surface profile is obtained by tracing the stylus travel (providing that the potential barrier along the path remains constant). Yet, studies have shown that the vibrating-electrode method allows the surfaces with a variable work function to be studied.

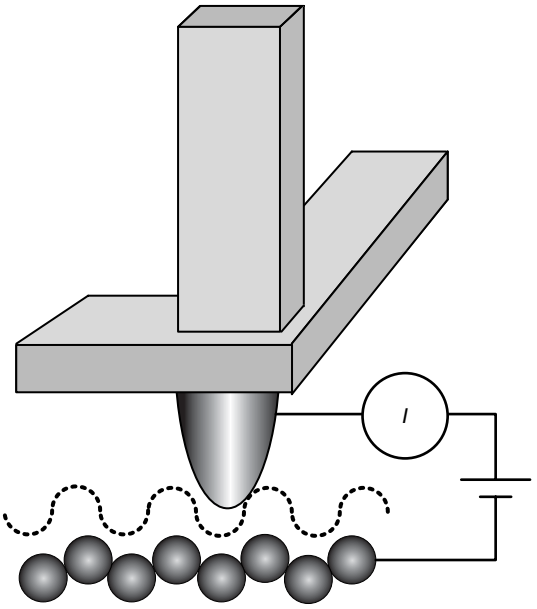

FIGURE 2.13 Schematic view of scanning tunnel microscope. The tip shaped as a rounded cone is mounted in three-coordinate piezoelectric scanner. A scan of the tip (dashed line) over the sample can show contours of the surface down to the atomic level.

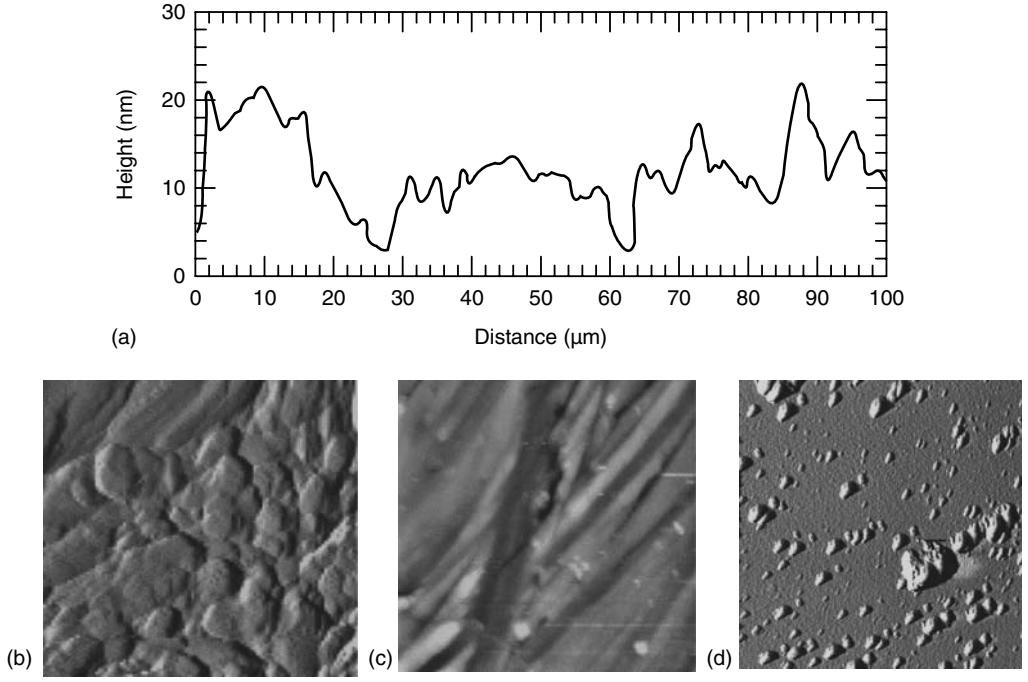

FIGURE 2.14 Application of STM and AFM: (a) STM profile of aluminum alloy machined with diamond tool ($R_a = 7$ nm) and (b) AFM images of electrolytic cobalt coating, (c) polished steel, and (d) diamond-like coating.

The resolving power of the method is very high: it amounts vertically to a hundred fractions of a nanometer. The horizontal resolution is somewhat less pronounced and depends on the stylus radius of curvature and the clearance. The STM method is extensively employed to investigate the structures of fine films, high-temperature superconductors, the processes of chemical and ion etching, and the effect of roughness on the observable surface-enhanced Raman scattering.

Essential and promising in tribological research, the STM allows one to obtain both qualitative and quantitative data about fine geometric structures of friction surfaces, such as their subroughness. The advent of STM has pushed through the development of a new class of instruments employing the same principle of operation. The scanning atomic force microscope (AFM) has good prospects and an extensive potential. It combines the STM principle with the stylus profilometer. A distinctive feature of the AFM is the use of the forces of atomic interactions between the tip and the specimen, instead of the tunnel current, when scanning, allowing studies at the atomic scale of surfaces of any material, conducting, semiconducting, or dielectric. The AFM has a high resolving power: at least 0.1 nm in the vertical direction and approximately 2–5 nm in the horizontal direction. In addition, the AFM allows investigation of both the surface topography and other processes, such as friction, electrostatic repulsion, and chemical reactions. Studies of the topographies of very smooth surfaces used in high-precision mechanics are hardly imaginable now without STM or AFM. Figure 2.14 shows a typical subrough surface scanned with AFM. Higher accuracy and the resolving power of these methods of measuring roughness enable one to obtain information on extremely fine geometrical surface structures, including the information on subroughness possibly about atomic roughness.

2.4 CONTACT OF SMOOTH SURFACES

In 1881, using the following assumptions, Hertz was the first to solve the problem of contact between two elastic bodies:[13,16] (1) mated surfaces are homogeneous and isotropic, and their initial contact is concentrated, i.e., it occurs at a point or along the straight line; (2) the deformation is small enough to be able to apply the linear theory of elasticity; (3) the characteristic dimensions of the contact region are small when compared with the dimensions of contacting bodies, factoring in calculation of local deformation to treat each body as en elastic half-space; and (4) bodies have smooth contacting surfaces.

Now consider what occurs when two bodies come in contact. For simplicity's sake, they are two balls with radii R_1 and R_2 (Figure 2.15). Initially they touch at a point, O. The distance from the plane of their contact to points A_1 and A_2 located at a short distance r from the axis z can be represented as $z_i = r^2/2R_i$ $(i = 1, 2)$, where $r^2 = x^2 + y^2$. In fact, the equation of the meridional section of sphere is $(z-R)^2 + r^2 = R^2$, whence $z = R - (R^2 - r^2)^{1/2} = R - R(1 - r^2R^2)^{1/2}$. Because $r \ll R$, then $(1 - r^2/R^2)^{1/2} \approx 1 - r^2/2R^2$ and after elementary transformations the desired equation is obtained. Therefore, before deformation of the bodies touching at the point O, the distance between

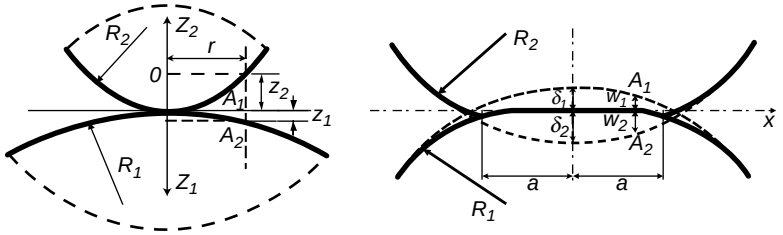

FIGURE 2.15 Contact between two balls: (a) initial touch; (b) after compression.

the points A_1 and A_2 is equal to

$$z_1 + z_2 = \frac{r^2}{2R_1} + \frac{r^2}{2R_2} = \frac{r^2}{2R}. \tag{2.11}$$

After a normal load, P, is applied, the bodies are deformed (compressed), and the remote points T_1 and T_2 shift to the original point O of the contact by distances δ_1 and δ_2, respectively. If the bodies could penetrate into one another without difficulty, their surfaces would occupy the positions showed by the dashed line. Since this is not the case, a local compression of the bodies occurs during which the plane of contact at the point O remains stationary, while the points A_1 and A_2 are displaced by w_1 and w_2 parallel to the axis z. From geometric considerations, it follows that the condition of contact between the points A_1 and A_2 is the following equality:

$$w_1 + w_2 = (\delta_1 + \delta_2) - (z_1 + z_2).$$

Let $\delta = \delta_1 + \delta_2$ be the approach of the contacting bodies, then this equation is rewritten as

$$w_1 + w_2 = \delta - r^2/2R. \tag{2.12}$$

The local deformation produces a circular contact area over which the total load P distributes with a yet unknown intensity $p(x)$. They are related by the expression:

$$P = \int_{-a}^{a} p(x)\mathrm{d}x. \tag{2.13}$$

Because the radius of the contact circle is small compared with the dimensions of the balls, they can be treated as half-spaces in the vicinity of the contact and the formula

$$w(x,y) = \frac{1}{\pi}\frac{1-\nu^2}{E}\int_{-a}^{a}\frac{p(\xi,\eta)\mathrm{d}\xi\mathrm{d}\eta}{((x-\xi)^2+(y-\eta)^2)^{1/2}},$$

can be applied. As a result, the integral equation is obtained:

$$\frac{1}{\pi}\left(\frac{1-\nu_1^2}{E_1}+\frac{1-\nu_2^2}{E_2}\right)\int_{-a}^{a}\frac{p(\xi,\eta)\mathrm{d}\xi\mathrm{d}\eta}{((x-\xi)^2+(y-\eta)^2)^{1/2}} = \delta - \frac{x^2}{2R} - \frac{y^2}{2R}$$

or

$$\frac{1}{\pi}\frac{1}{E^*}\int_{-a}^{a}\frac{p(\xi,\eta)\mathrm{d}\xi\mathrm{d}\eta}{((x-\xi)^2+(y-\eta)^2)^{1/2}} = \delta - \frac{x^2}{2R} - \frac{y^2}{2R}.$$

The unknowns in this equation are the contact pressure distribution, $p(x,y)$, the radius of contact, a, and the approach, δ. Hertz drew an analogy with the electrostatic potential and actually conjectured that contact pressure should have spherical (ellipsoidal in the general case) distribution:

$$p(x,y) = p_{\max}(1 - x^2/a^2 - y^2/a^2)^{1/2}.$$

By using also Equation 2.13, it is easy to show that the radius of contact is calculated from Equation 2.14 and the approach from Equation 2.15 (Table 2.1). Table 2.1 presents the basic relations for spherical contact (left column).

TABLE 2.1
Hertzian Contact of Balls and Cylinders

	Contact of Balls	Equation Number	Contact of Cylinders	Equation Number
Radius (semi-width) of contact	$a=\left(\frac{3}{4}\frac{PR}{E^*}\right)^{1/3}$	(2.14)	$a=\left(\frac{4PR}{\pi E^*}\right)^{1/2}$	(2.18)
Approach	$\delta=\frac{\pi}{2}\frac{p_{\max}a}{E^*}$	(2.15a)	$\delta=\frac{2P}{\pi}\left(\frac{1-\nu_1^2}{E_1}\ln\frac{4R_1}{a}-\frac{1}{2}\right)$	
	$=\frac{a^2}{R}$	(2.15b)	$+\left(\frac{1-\nu_2^2}{E_2}\ln\frac{4R_2}{a}-\frac{1}{2}\right)$	(2.19)
	$=\left(\frac{9P^2}{16RE^{*2}}-\right)^{1/3}$	(2.15c)		
Maximum contact pressure	$p_{\max}=\left(\frac{6PE^{*2}}{\pi^3R^2}\right)^{1/3}$	(2.16)	$p_{\max}=\left(\frac{PE^*}{\pi R}\right)^{1/2}$	(2.20)
Mean contact pressure	$p_m=\frac{P}{\pi a^2}$	(2.17a)	$p_m=\frac{P}{2a}$	(2.21a)
	$=\frac{2}{3}p_{\max}$	(2.17b)	$=\frac{\pi}{4}p_{\max}$	(2.21b)

Note: The effective modulus of elasticity E^* is defined by the equation.

$$\frac{1}{E^*}=\frac{1-\nu_1^2}{E_1}+\frac{1-\nu_2^2}{E_2},$$

where E_1, ν_1, and E_2, ν_2 are elastic moduli and Poisson's ratios for the contacting bodies.The effective radius is calculated as

$$\frac{1}{R}=\frac{1}{R_1}\pm\frac{1}{R_2},$$

where R_1 and R_2 are radii of the contacting bodies. The plus sign (+) stands for a contact of convex bodies, whereas the minus sign (−) stands for a contact of ball (cylinder) and spherical (cylindrical) hollow.

Similar reasoning leads to an integral equation for calculating the contact between two cylinders with radii R_1 and R_2. Its solution has allowed one to establish that contact pressure distributes over a strip with the semiwidth a in accordance with relation (2.18). Regarding the approach of the cylinders, δ, some arbitrariness of its determination is already mentioned above, which is due to the peculiarity of the solution to plane problems of the theory of elasticity. The table (right column) shows one possible formula for calculating the approach (Equation 2.19), together with the some other useful relations.

2.4.1 Plastic and Elastoplastic Contacts

Solids manifest their elastic behavior until their stresses and deformation exceed definite limits beyond which a transition to plastic deformation occurs, with the appearance of residual deformation (the element after deformation does not fully recover its shape). The condition of this transition is the relation between the stresses specified by a criterion of yield (plasticity). Two approximately equivalent criteria of yield are fulfilled well for metals:

- The French engineer Tresca (1864) concluded from his experiments of metal extrusion through a hole that the maximum tangential stress in the yield state has the same value equal to the yield stress in simple shear τ_s or to half the yield stress in simple tension (or compression) $0.5\tau_s$. Analytically this criterion is written in the following form:

$$\max\left[\frac{1}{2}|\sigma_1-\sigma_2|,\frac{1}{2}|\sigma_2-\sigma_3|,\frac{1}{2}|\sigma_3-\sigma_1|\right]=\tau_s=\frac{\sigma_s}{2},$$

where σ_1, σ_2, σ_3 are the principal stresses in the complex stress–strain state.

- In 1913, von Mises proposed a different criterion according to which yield begins when the second invariant of the stress deviator, J_2, reaches some critical value for a given material:

$$J_2\equiv\frac{1}{6}[(\sigma_1-\sigma_2)^2+(\sigma_2-\sigma_3)^2+(\sigma_3-\sigma_1)^2]=\tau_s^2=\frac{1}{3}\sigma_s^2.$$

The two criteria differ little; their application is determined by the degree of simplification of calculations when solving a specific problem.

In the case of axisymmetric loading of the halfspace (during contact between balls in particular), σ_z, $\sigma_r=\sigma_\theta$ are the principal stresses along the axis of symmetry, the maximum contact stress equal to $0.31p_{max}$ is reached along the same axis at a depth of $0.48a$ (when $\nu=0.3$). Then, according to Tresca's criterion, $\tau_{1max}=0.31p_{max}=\tau_s$; whence $p_{max}=3.2\tau_s$. In view of Equation 2.16, the load P_m that induces the flow of the material is

$$P_m=(3.2\tau_s)^3\frac{\pi^3R^2}{6E^{*2}}=169.3\frac{R^2\tau_s^3}{E^{*2}}.$$

According to the von Mises criterion, $(\sigma_z-\sigma_r)^2=3\tau_s^2$ or $\tau_{1max}=0.31p_{max}=3^{1/2}\tau_s/2$. Whence,

$$P_m=(2.8\tau_s)^3\frac{\pi^3R^2}{6E^{*2}}=113.43\frac{R^2\tau_s^3}{E^{*2}}.$$

In the case of contact between two cylinders, the maximum contact stress is equal to $0.3p_{max}$ at a depth of $0.78a$. Then, $p_{max}=3.3\tau_s$, and using Equation 2.20 it is obtained that

$$P_m=(3.3\tau_s)^2\frac{\pi R}{E^*}=10.9\frac{\pi R\tau_s^2}{E^*}.$$

To apply the von Mises criterion, the principal stresses are substituted into the condition of yield, and J_2 takes the greatest value equal to $0.104p^2{}_{max}$ at a depth $0.704a$ (when $\tau=0.3$). Then $p_{max}=3.1\tau_s$ and

$$P_m=(3.1\tau_s)^2\frac{\pi R}{E^*}=9.6\frac{\pi R\tau_s^2}{E^*}.$$

It is apparent from expressions for P_m that, by increasing the effective radius of curvature and/or by selecting a material combining a high yield stress with a small modulus of elasticity, the contact zone can be made to withstand heavier loading without transforming into the plastic state.

Thus, plastic yield appears in a softer material (with a lower yield point) at some depth under the contact area at a mean contact pressure of about σ_y. This zone of plasticity is small, and the elastically deformed material surrounds it, so that the order of magnitude of the elastic and plastic

deformations is similar. The plastic zone occupies larger and larger volumes as contact pressure goes up. The so-called "contained elastoplastic stage of deformation" occurs that terminates in the emergence of the plastic zone on the external surface. A fully plastic (uncontained) stage of deformation begins when the average pressure under the indenter reaches the value

$$p_m = c\sigma_y. \tag{2.22}$$

Studies have shown that the coefficient c is approximately equal to 3.0, depending on the geometry of the indenter and friction on the contact surface. The range of mean pressures from σ_y to $3\sigma_y$ corresponds to the stage of contained elastoplastic deformation, which is too intricate to analyze. Therefore, a simplified ball core model is frequently used for the analysis (Figure 2.16) according to which the contact surface is enveloped with a semispherical "core," having a radius a. It is assumed that a hydrostatic stress–strain state with the intensity p_m exists within the core. Analysis of this model[13] shows that, in case the material is incompressible, the mean pressure is determined by the relation:

$$\frac{p_m}{\sigma_y} \cong \frac{2}{3}\left(1.7 + \ln\frac{1}{3}\frac{aE^*}{R\sigma_y}\right).$$

The dimensional variable under the log sign is interpreted as a relation between the deformation produced by the indenter (a/R) and the elastic deformability of the material (σ_y/E^*). Expressing the mean pressure (Equation 2.17) on the Hertzian contact through this variable, one can obtain:

$$\frac{p_m}{\sigma_y} = \frac{4}{3\pi}\frac{aE^*}{R\sigma_y}.$$

Considering that for full plasticity ($p_m/\sigma_y = c - \text{constant}$), a general dependence of the mean contact pressure on the dimensionless parameter $aE^*/R\sigma_y$ for the conditions of purely elastic, elastoplastic, and fully plastic states (Figure 2.17), it is apparent that the yield state occurs at $p_m \approx 1.1\sigma_y$, while the upper limit of pressure of indentation during full plasticity equal to $3\sigma_y$ is reached at $aE^*/R\sigma_y \approx 30$.

The reasoning above relates to elasto-ideally-plastic bodies with a constant yield point σ_y in compression. Yet, real materials are hardened, as a rule, in the process of deformation. In this case, the Meyer empirical law is frequently used to describe the relation between load P applied to the indenter and the diameter of the imprint d:

$$P = gd,$$

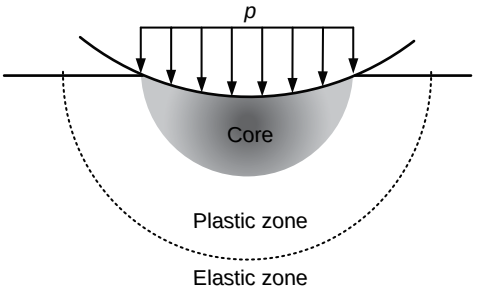

FIGURE 2.16 Model with ball core at elastoplastical indentation.

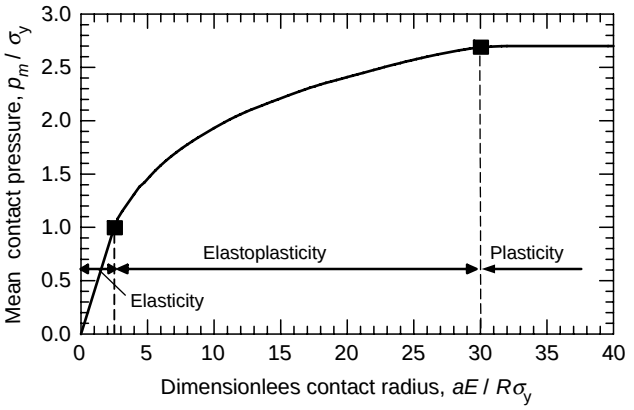

FIGURE 2.17 Generalized dependence of the mean contact pressure, p_m/σ_y, on the dimensionless contact radius, $aE/R\sigma_y$, for elastic, elastoplastic and fully plastic deformation.

where g and n are some constants of material. The diameter of the imprint is combined with indentation δ by an approximated relation $d \approx (8r\delta)^{1/2}$, where r is the radius of the sphere indented into the material. Then the Meyer hardness, or the mean contact pressure, amounts to

$$p_m = 4P/\pi d^2 = 4gd^{n-2}/\pi.$$

The coefficient g can be expressed through the maximum Meyer hardness H_{Mmax}, which corresponds to the penetration of the ball to the equator, i.e., the diameter of the imprint is equal to the diameter of the ball D: $H_{Mmax} = 4gD^{n-2}/\pi$, and upon substitution into the relation for p_m yields:

$$p_m = 2^{n/2-1} H_{Mmax} y^{1-n/2} \delta^{n/2-1}.$$

It is known that the maximum Meyer hardness relates to the Brinell hardness as:

$$H_{Mmax} = 2HB/k,$$

where $k = n^{n/2}(n-2)^{(n-2)/2}(n-1)^{(1-n)}$. For an extremely hardened material, when $n \to 2$, k also tends to 2, and $H_{Mmax} = HB$. Thus, in case of plastic contact with hardening, the mean contact pressure is equal to

$$p_m = A\delta^{n/2-1}, \tag{2.23a}$$

where $A = 2^{n/2} HBr^{1-n/2}/k$.

Contact load relates to indentation as:

$$P = \pi 2^{n/2} + 1HBr^{2-n/2}\delta^{n/2}/k. \tag{2.23b}$$

2.5 CONTACT BETWEEN ROUGH SURFACES

Real surfaces are rough. When rough surfaces approach each other, initially their highest asperities come in contact. As a rule, the high local pressure appears, resulting in their strong compression and bringing fresh asperities into contact that undertake a major portion of the total load. The process of

approaching completes itself when the number of asperities in contact becomes sufficient to withstand the applied load. It is essential that the contact appearing in this manner, and termed as the "real contact," has an area significantly smaller (almost by two orders of magnitude) than the apparent contact. Yet, its significance goes beyond the field of tribology. The real contact area is found to be necessary in a number of applications, for example, when estimating the contact electrical resistance and heat conductivity of real couples, in problems such as contact strength and corrosion. Yet, the classic methods of mechanics of deformable solids do not seem to be capable of assessing the real contact area.

The calculations of the real contact area are simplified when an idea of the equivalent rough surface is introduced. The equivalent surface accumulates the roughness of two contacting surfaces, allowing limiting analysis to the contact of between the equivalent surface and a perfectly smooth surface.

Below, the most popular models of contact between rough surfaces are discussed. It is assumed that asperities are shaped as spherical segments of the same radius.

2.5.1 Greenwood–Williamson Model

One of the specific features of the modern mechanics of friction relates to intensive use of the probabilistic methods for calculating a contact between rough surfaces. This approach is consistently and systematically implemented in the Greenwood–Williamson (GW) model, which became the starting point for numerous studies in this area.[17] An analogous approach was used by Greenwood and Tripp[18] for curvilinear surfaces.

The authors of the GW model originally assumed that the distribution law for the summit heights $\varphi(z)$ is known (it is normal, for example). The distribution function indicates a probability that the summit height, z, is located within the range $(z, z+\mathrm{d}z)$, or, in other words, it is the share of all the summits N within the apparent contact area that are thrown into this range. Then the number of the summits in contact, i.e., the summits with the ordinates exceeding the separation of mean planes d, is equal to

$$n = N\int_d^\infty \varphi(z)\mathrm{d}z.$$

Here, only the elastic contact between the asperities is considered (see Table 2.1). Now the equations for an individual contact spot are rewritten:

$$a_\mathrm{i} = \beta^{1/2}\delta_\mathrm{i}^{1/2}; \qquad A_\mathrm{i} = \pi\beta\delta_\mathrm{i}; \qquad P_\mathrm{i} = \frac{4}{3}E\beta^{1/2}\delta_\mathrm{i}^{3/2},$$

where a_i is the radius of contact spot; A_i is its area; P_i is the load on the spot; δ_i is the approach.

Bearing in mind that the approach is $\delta = z - d$ and summing the values over all contacting asperities, the average contact spot per asperity is found:

$$\bar{A}_\mathrm{i} = \int_d^\infty \pi\beta(z-d)\varphi(z)\mathrm{d}z.$$

Then the total real contact area is equal to

$$A_\mathrm{r} = \pi\beta N\int_d^\infty (z-d)\varphi(z)\mathrm{d}z.$$

Similarly the total load is determined:

$$P = \frac{4}{3}E\beta^{1/2}N\int_d^\infty (z-d)^{3/2}\varphi(z)\mathrm{d}z.$$

Going over to the dimensionless values, $\zeta = z/\sigma$ and $h = d/\sigma$; using the surface density of roughnesses $D = N/A_a$ (A_a is the apparent contact area) yield,

$$\eta = \frac{A_r}{A_a} = \pi\beta D\sigma \int_h^\infty (\zeta - h)\varphi^*(\zeta)\mathrm{d}\zeta, \tag{2.24}$$

$$\tilde{p} = \frac{P}{EA_a} = \frac{4}{3}\beta^{1/2}\sigma^{3/2}D\int_h^\infty (\zeta - h)^{3/2}\varphi^*(\zeta)\mathrm{d}\zeta. \tag{2.25}$$

Here, $\varphi^*(\zeta)$ is the normalized probability density.

The integrals included into the obtained system of equations have a similar structure and are frequently designated in the following manner:

$$F_n(h) = \int_h^\infty (\zeta - h)^n \varphi^*(\zeta)\mathrm{d}\zeta,$$

where the index n can take other values in addition to 1 and 3/2 (e.g., 0, when determining the number of contacting asperities, or 1/2 when estimating the electrical resistance of the real contact).

Using the designation $\mu = \beta D\sigma$, Equation 2.24 and Equation 2.25 can be written in the following compact manner:

$$\eta = \pi\mu F_1(h),$$

$$\tilde{p} = \frac{4}{3}\mu\left(\frac{\sigma}{\beta}\right)^{1/2} F_{3/2}(h).$$

This system yields the dependence of the real contact area on the load in the parametric form, the common parameter being the dimensionless separation, h. This representation is encumbered with some analytical difficulties, which are quite surmountable with modern computer technology. The analysis of the system was performed for the Rice distribution, which transforms in extreme cases into the Rayleigh and Gauss distributions. Figure 2.18 shows how the relative real contact area depends on the contact pressure.

It is apparent that, unlike the elastic contact between smooth bodies when the contact area increases proportionally to the load to the power 2/3, the real contact area is directly proportional to the load; it is in compliance with the Amontons–Coulomb friction law. The distribution law of summit heights does not affect the pattern of the dependence $\eta \sim p$, all things are the same (Figure 2.19a). All the calculations were performed for $2.0 \le h \le 2.5$.

However, a considerably higher load is needed to achieve the same approach (nominal separation) at the Rayleigh distribution than at the Gaussian distribution. Meanwhile the roughness parameters (within the framework of the same distribution) alter strongly the inclination of the dependence $\eta \sim p$ (Figure 2.19b). The constancy of the mean real pressure P/A_r is another sequence of the proportionality between the real contact area and the contact pressure. Figure 2.20 shows that changes in the nominal load by more than three orders of magnitude cause an insignificant change of the real pressure, independently of the pattern of distribution of the asperity heights. This circumstance gives an idea that the value $H_e = 0.05E(\sigma/\beta)^{1/2}$ can be treated as the "elastic hardness" of material, similar to the hardness of plastic materials equal to the mean pressure on the contact. As in the case of plastic contact, the real contact area at elastic deformation of roughness is determined by the ratio $A_r = P/H_e$.

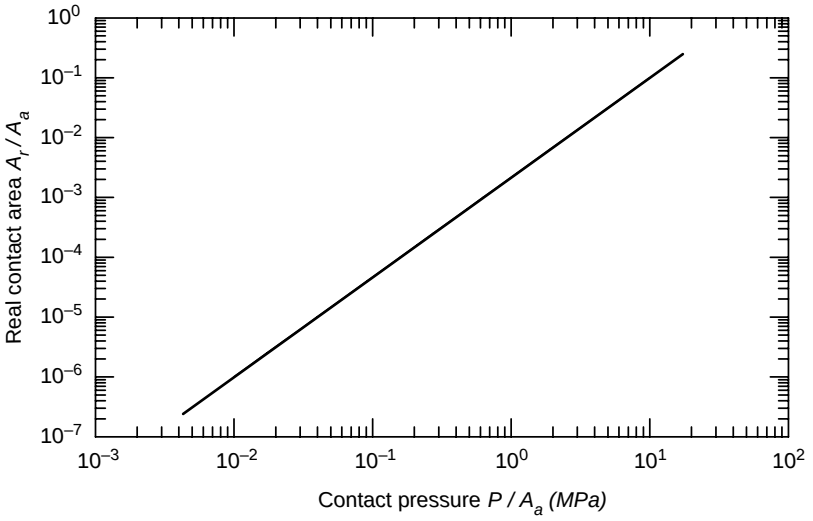

FIGURE 2.18 Dependence of real contact area on load.

2.5.2 Multilevel Model

Real surfaces, as a rule, contain at least two levels of asperities, such as waviness plus roughness, or roughness plus subroughness. The natural quest for inspection of rubbing surfaces in minute detail and advanced methods of roughness measurement gave rise to establishment of three fundamental facts: erratic arrangement of surface asperities and random distribution of their parameters (height, slope, summit curvature); multiscale character of roughness (i.e., the significant size of asperities can vary from the length of the sample to the atomic scale); and nonstationarity, i.e., a dependence of the numerical values of roughness parameters on the scale of measurement. These properties are not independent. For example, nonstationarity owes its origin to the multiscale topography, all other things being the same. Nonstationarity of surface topography was first identified by Sayles and

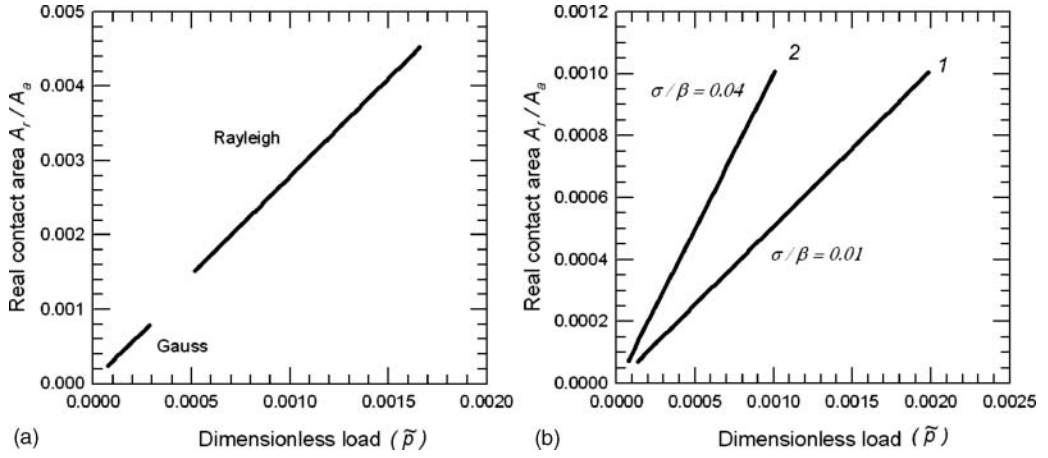

FIGURE 2.19 Dependence of actual contact area on dimensionless load: (a) effect of distribution law of peak heights ($\mu = 0.03$, $\sigma/\beta = 0.12$, $2 \le h \le 2.5$) 1, Gauss distribution; 2, Rayleigh distribution. (b) Effect of roughness: $1 - \sigma/\beta = 0.01$; $2 - \sigma/\beta = 0.04$.

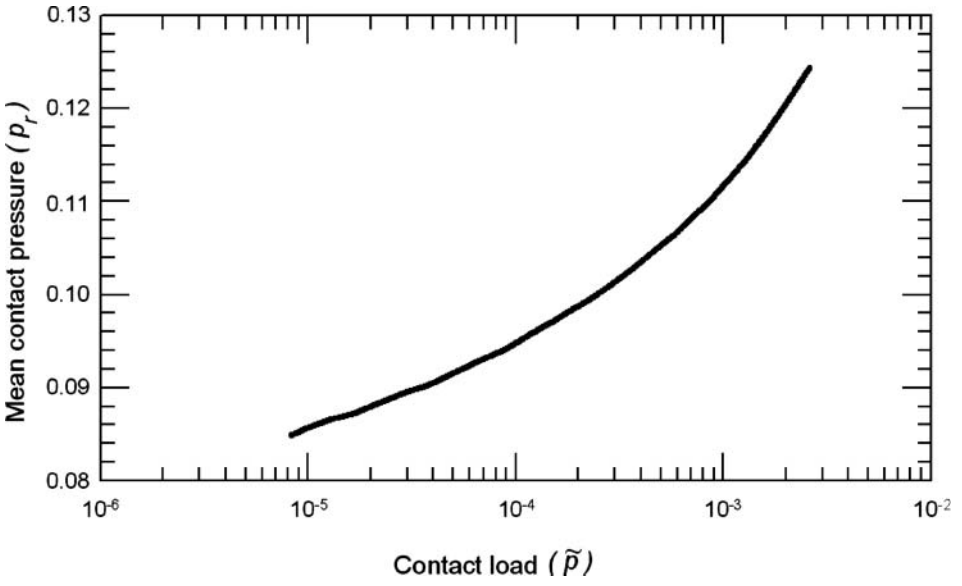

FIGURE 2.20 Dependence of mean contact pressure on load.

Thomas.[19] A crude method was proposed to separate a real topography measured by AFM into two levels, roughness and subroughness.[20] This method provides the fulfillment of at least one of two conditions for stationarity, namely, zero mean of random process. A description of the procedure follows. Preliminary analysis of AFM-image of rough surface demonstrated that the profile contains long-wave-component inherent microroughness rather than subroughness.

A development of a two-level contact model involves such important stages as determination of roughness parameters for each of the levels. This problem may be solved by the median filtration of the primary three dimensional profile as shown earlier.[20,21] Let us use the AFM-image of a very real surface to illustrate the procedure. Preliminary analysis of an AFM-image of a rough surface (Figure 2.21a) demonstrated that the profile contains long-wave component inherent to roughness rather than subroughness.

To eliminate the component, the procedure of repeated median filtration of the image was used. After each application of the procedure, utmost points of the images (on the perimeter) were cropped where heights were deformed most of all as a result of edge effects. The filtration procedure was carried out up to seven times. Computational experiment has shown that, for the images it was enough to filter out the subroughness component of the relief. A greater number of filtrations do not significantly change the spectral function for appropriate profile sections of the image. At the

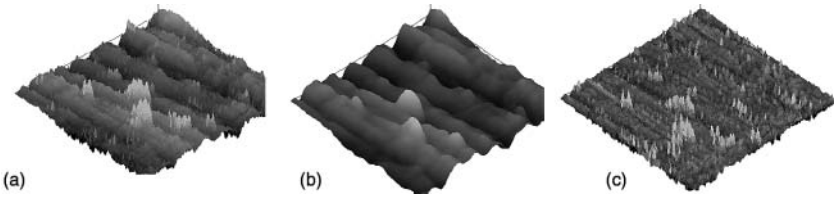

FIGURE 2.21 Image processing procedure for separation of roughness scale levels: (a) = (b) + (c), where (a) is an initial image, (b) is its long-wave component, and (c) is the subroughness image.

following stages the filtered image (Figure 2.21b) was subtracted from the initial image (Figure 2.21a) to obtain resultant image reflecting a surface subroughness (Figure 2.21c). Parameters for the sub-microrelief were determined on the basis of the subroughness image.

The proximity of the spacing parameters obtained from the subroughness image (Figure 2.21c) and that measured by Talystep on the same sample provides good indirect evidence that the above procedure is acceptable.

For considering the effect of irregularities in two levels on contact characteristics, the model of discrete contact was developed. Archard first perceived the important implication of this fact for tribology and proposed the well-known multilevel model.[22] He pioneered the application of the multiscale topography to the deduction of the friction laws for the contact conditions when deformation is entirely elastic.

The geometric and mechanical difficulties were obviated by considering either level of roughness as an object in its own geometry and mechanical behavior; in so doing the combined deformation of asperities of different levels is incorporated. The calculation procedure is a modification of conventional scheme, for example, GW model. But at the first stage, in lieu of the Hertz problem for smooth spherical asperity, a solution to problem on contact of rough sphere and plane Greenwood–Tripp problem was used.[18] On examination of combination "roughness (level 1) plus subroughness (level 2)" the rough sphere serves as a model of a real asperity carrying subroughness.

The Greenwood–Williamson approach turned out to be fruitful when developing the so-called "two-level" model that involves the above-mentioned analysis of the contact of two rough surfaces comprising asperities of two levels, e.g., roughness and subroughness.

The Greenwood–Tripp solution for the contact of rough spheres is used as the basic equation for a single asperity to consider the presence of subroughness on coarser asperities or rough ones. The solution gives the parametric dependence between the dimensionless contact area $\tilde{A}_\mathrm{i}$ and dimensionless load $\tilde{P}$ for a single contact:

$$\tilde{A}_\mathrm{i} = \frac{9\pi^2}{32}\mu_\mathrm{s}^2 \int_0^{a^*}\int_u^\infty (\xi - u^*)\Phi_2^*(\xi)\rho \mathrm{d}\rho \mathrm{d}\xi,$$

$$\tilde{P}_\mathrm{i} = \frac{3\pi\sqrt{2}}{4} \int_0^{a^*}\int_u^\infty (\xi - u^*)^{3/2}\Phi_2^*(\xi)\rho \mathrm{d}\rho \mathrm{d}\xi,$$

where μ_s is the complex roughness parameter, $\Phi_2^*(\xi)$ is the probability density of subroughness summits often assumed to be normal, and u^* is the dimensionless clearance between "rough" sphere and plane.

Extending the obtained solution over an ensemble of asperities, i.e., rough asperities, one can determine the dimensionless dependencies of the real contact area, $\tilde{A}_\mathrm{r}$, physical contact area, $\tilde{A}$, and normal load, $\tilde{P}$, if the distribution of summit heights $\Phi_1^*(\xi)$ is known:

$$\tilde{A}_\mathrm{r}(d_1^*) = 2\pi R_1 D_1 \sigma_2 \int_{d_1^*}^\infty \tilde{A}_\mathrm{ri}(\omega_0^*)\Phi_1^*(\xi)\mathrm{d}\xi,$$

$$\tilde{A}(d_1^*) = \frac{D_1}{D_2}\int_{d_1^*}^\infty \tilde{A}_\mathrm{i}(\omega_0^*)\Phi_1^*(\xi)\mathrm{d}\xi,$$

$$\tilde{P}(d_1^*) = \frac{\mu_\mathrm{s}}{2\sqrt{2}}\frac{D_1}{D_2}\left(\frac{\sigma_2}{R_2}\right)^{1/2}\int_{d_1^*}^\infty \tilde{P}_i(\omega_0^*)\Phi_1^*(\xi)\mathrm{d}\xi.$$

Here, D_1, D_2 are the surface densities of asperities and subasperities; ξ is a dimensionless asperity height; $\Phi_1^*(\xi)$ is the distribution density of summit heights; ω_0^* is the deformation

of asperity in the center of contact; R_1 and R_2 are curvature radii of asperities and subasperities; σ_1 and σ_2 are root-mean-square deviation of summit height of asperities and subasperities.

The solution of the problem gives relationships between the contact parameters. Based on the data of computer simulation, we estimated the limit values of RMS roughness below, where the surfaces can be treated as perfectly smooth ones, i.e., they form a continuous physical contact with a separation that does not exceed an interatomic spacing. Those values are about 1 nm for metals, 1–3 nm for hard polymers, and about 10 nm for elastomers. The subroughness below these values exerts no influence on the real contact.

Calculations indicate that the highest asperities of the first level come into contact and form the elementary real contact spots. Yet, contrary to traditional views, the spots are not continuous but multiply connected, i.e., each of the spots consists of a set of subspots whose total area was conditionally named "physical contact area." This area results from the contact of nanometer-scale asperities (subroughness). For electrical contacts, the physical contact area should coincide with the area of current conductivity, and its determination is very important in calculation of contact electrical resistance. Calculation of physical contact area is shown in Figure 2.22 (here A_a is the apparent contact area and A stands for RCA or physical contact area; E' is the reduced modulus of elasticity). Here, the real contact area A as a function of load is presented for comparison. The RCA is plotted for rough surfaces with the following roughness parameters: RMS roughness $\sigma_1 = 0.50$ μm, radius of peak curvature $R_1 = 13.3$ μm, and bandwidth parameter $\alpha = 6.3$ (subroughness is assumed to be absent). The remaining curves present the cases when the same roughness "carries" subroughness with $\sigma_2 = 0.1$ μm and $\alpha = 6.3$, but different values of surface density of asperities D_2 (μm^{-2}), curvature radius at asperity peak R_2 (μm) and complex parameter of topography μ_s, respectively.

Calculation shows that the physical contact area is less than the RCA by one to two orders of magnitude (Figure 2.22). The strong interaction between the mating surfaces may occur within the physical contact area. Its contribution to friction force may be very significant. Thus, the physical contact area previously known as a qualitative characteristic gains its quantitative measure owing to the two-level model.

Some calculation results are presented in Figure 2.22. The highest roughness asperities (the first level) undergo deformation and form real contact spots when the surfaces are in

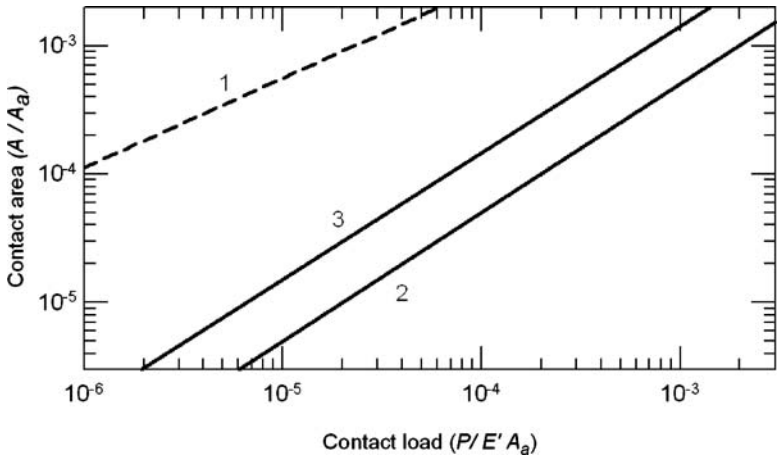

FIGURE 2.22 Real (dotted line) and physical (solid lines) contact areas vs. load: (1) $\sigma_1 = 0.50$ μm, $R_1 = 13.3$ μm; (2) $\sigma_2 = 0.1$ μm, $R_2 = 0.20$ μm, $D_2 = 3.2$ μm^{-2}, $\mu_s = 0.2$; (3) $\sigma_2 = 0.1$ μm, $R_2 = 0.10$ μm, $D_2 = 25$ μm^{-2}, $\mu_s = 1.0$.

contact. Yet, contrary to the common ideas, each spot is multiply connected and comprises several spots of so-called "physical contact" resulting from the contact of subroughness asperities.

Numerical calculations show that the physical contact area is by one or two orders of magnitude less than the real contact area but that enough strong forces can act within it. These forces contribute quite significantly to the total force of resistance to surface movement. The physical contact area formed by nanoscale asperities determines the contact resistance in electrical contact. The effect of nanoscale roughness and contact spots of nanometer size on electrical resistance of contact is considered further in Chapter 5.

2.5.3 Transition from Elastic to Plastic Contact

The equations derived in the preceding paragraph are valid for rough contact where its asperities deform elastically. But in the general case, the surface asperities are deformed both elastically and plastically. Their number depends on a critical approach of the surfaces relating to transition from elastic to plastic deformation. A variety of transition criteria have been suggested.[23,24] The Greenwood–Williamson criterion or the plasticity index has become the most popular.[17] The authors of the criterion analyze the deformation of roughness assuming that the plastic yield of an individual asperity begins when the maximum Hertzian pressure, p_{max}, reaches $0.6H$ (H is the hardness of the softer contacting material). According to Hertz, during indentation of the ball into the plane, the approaching δ is related to p_{max} by the equation:

$$\delta = \frac{\pi^2}{4}\frac{p_{max}^2 \beta}{E^2},$$

then substitution of $p_{max} = 0.6H$ yields the critical approach $\delta_p = 0.89\beta(H/E)^2$. This relation can be simplified assuming the numerical coefficient is equal to unity. This has definite meaning because the supporting effect of elastically deformed regions is taken into account. The critical approach is written in the dimensionless form in the following manner:

$$\delta^* = \frac{\delta_p}{\sigma} = \frac{\beta}{\sigma}\left(\frac{H}{E}\right)^2.$$

If h is the dimensionless nominal separation of contacting surfaces, then the asperities higher than $h+\delta^*$ are deformed plastically and the share of the real contact area made up by these roughnesses amounts to

$$\varepsilon = \frac{\tilde{A}_p}{\tilde{A}_r} = \frac{F_1(h+\delta_p^*)}{F_1(h)}.$$

It is usually believed that plastic flow begins at $\varepsilon = 0.02$. When ε is specified, the equation relates the approach δ_p^* to the critical nominal separation h_{cr} allowing the calculation of the critical nominal load when elastic contact transforms into plastic contact. It is convenient, instead of the approach δ_p^*, to use some function

$$\psi = \frac{1}{\sqrt{\delta_p^*}} = \frac{E}{H}\sqrt{\frac{\sigma}{\beta}},$$

that has come to be known as the *plasticity index*.

Analysis indicates that elastic contact occurs at $\psi < 0.6$, whereas plastic contact occurs at $\psi > 1.0$, irrespective of the load. The load cannot already be ignored if the index is in the range between these limits. In this case the curve shown in Figure 2.23 should be used where the dimensionless critical load $\tilde{p} = P/A_c H$ is plotted as ordinate.

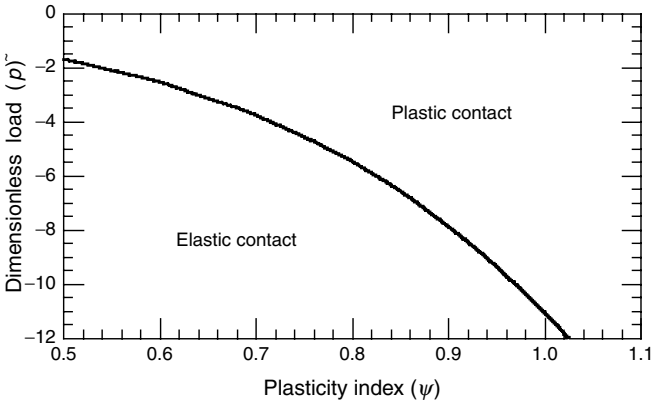

FIGURE 2.23 Deformation mode of asperities on contacting rough surfaces as function of the dimensionless load, $\tilde{p}$, and the plasticity index, ψ.

For real surfaces ψ varies between 0.1 and 100. For example, the plasticity index of steel surfaces ($E = 210$ GPa, $H = 2.5$ GPa) varies between 0.35 and 33 depending on the type of machining, its least values are achieved after finishing, i.e., the very smooth surfaces deform elastically.

3 Tribology

3.1 FRICTION

Friction is the most widespread phenomenon in daily life. Studies of friction date back to the times of Aristotle and Leonardo.[25] Friction accompanies not only any motion, but also tendency for displacement. Although the term "friction" is well-known, few people realize what it really means because of the highly intricate nature of this phenomenon.

Primarily, internal friction, as resistance to relative displacement of the components of one and same body, should be discriminated from the external friction of solids or just friction that is treated below. Friction can be considered as a formation of real contact area under normal load and shearing of the contact interface. The environment is an additional important factor influencing the process. This combination results in numerous surface effects and a variety of friction mechanisms.

Sliding friction occurs between two relatively moving bodies in contact, in which their surface velocities in the contact area are different with respect to magnitude and/or direction. It is governed by the processes that occur in thin surface layers. There are two main noninteracting mechanisms of friction: adhesion and deformation.[23,24] This idea is essential for the two-term model of friction, although the independence of these mechanisms is a matter of convention.

3.1.1 Laws of Friction

When two bodies are in contact, a tangential force must be applied to produce their relative displacement. When this force increases from zero to a finite value, microdisplacement δ occurs in the contact zone, though the bodies themselves remain motionless as a whole until the tangential forces reaches some limiting value termed the *static friction force*, F_s (Figure 3.1). The intermediate values of the applied tangential force F_{int} are termed the partial static friction force.

Apparently, there is a force that impedes the break of relative state at rest and incipient motion. The force is always nonzero and possesses a finite value. This principal fact should be treated as the fundamental law of friction that can be formulated as follows: a static friction exists when two solids form a contact.

To retain the numbering of the laws, as is accepted in the tribological literature, this law should be termed the zero law. Notwithstanding its simple formulation, this law is of great significance. It is exactly the friction at rest that is a typical feature of external friction distinguishing it from the internal friction induced by any infinitesimal tangential displacement. Moreover, without static friction the world would be queer and eerie, if it would exist at all. Humans would not be able to walk in their customary shoes. A book placed on a desk would gradually slip off as if it was sliding down a slope. The tires of any vehicle would slide.

Referring to Figure 3.1, after the body begins to move, the resistance to its motion decreases but it never vanishes completely because it remains approximately constant if the conditions for motion remain unchanged. This resistance to motion is termed *kinetic friction* and the resistance force is termed the *kinetic friction force*, F_k.

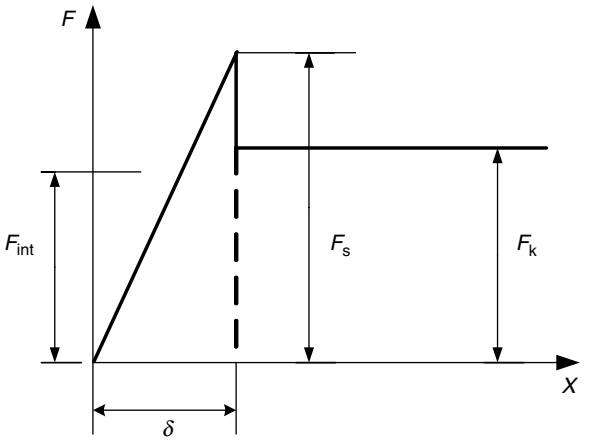

FIGURE 3.1 Transition from static friction to kinetic friction.

The relation between the friction force (static or kinetic) and normal load is commonly termed the *coefficient of friction* (static or kinetic, respectively). Leonardo da Vinci (1452–1519) believed that the coefficient of friction of smooth surfaces was constant and equal to 0.25. This viewpoint persisted in science for a very long time. Guilliom Amontons (1663–1705) assumed that the friction coefficient of iron, leather, lead, and wood was equal to 1/3. In reality, the coefficient of friction may vary over a wide range, from approximately 0.001 in rolling bearings under light loads to tens of units between thoroughly cleaned surfaces like metals contacting in vacuum.

As a rule, under normal conditions of friction in air, the coefficient of friction changes within a comparatively narrow range from 0.1 to 1. It is not the magnitude of the friction coefficient but rather its constancy that, in fact, is the essential implication of the first law of friction, frequently called the Amontons' law. Figure 3.2 shows a simple experimental design illustrating this law. If a body (for instance, a book) lies on the plane and has the weight P, the force needed to move this body is equal to F. To move a pile of n books ($n = 2$ in the figure), the tangential force should be n times larger. Therefore, the first law of friction is formulated in the following manner: the friction force is directly proportional to the normal load.

When μ designates the coefficient of friction that, from the above formulation, is constant and independent of the normal load, the first law of friction states that:

$$F = \mu P. \tag{3.1}$$

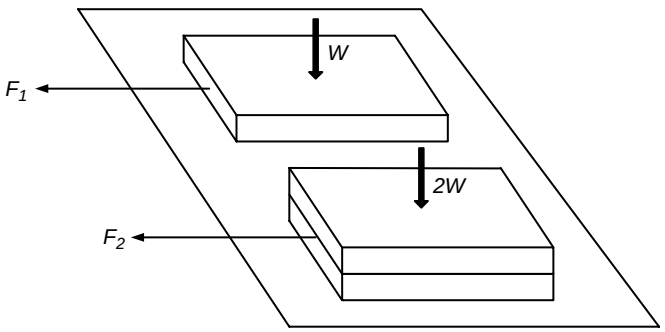

FIGURE 3.2 The friction force increases practically proportionally to the applied normal load (first law of friction.)

However, the founders of tribology realized long ago that this relation was true only for definite load and speed conditions, combinations of rubbing materials, and other friction conditions. At the time, Amontons wrote that the force of friction intricately depends on the normal pressure, time, and speed of sliding. This condition is sufficiently accurate in the case of boundary friction or for a number of nonlubricated rubbing materials.

The second law of friction is most paradoxical: the friction force is independent of both shape and size of the apparent contact area. It can be assumed that the ancient Egyptians erected giant pyramids from right-angled boulders knowing with certainty that resistance to dragging over these boulders is independent of whether they lie flat, rest on their lateral side, or stand on end. Many years have elapsed since Leonardo da Vinci established that both coiled and straightened ropes offer the same resistance to sliding. A fragment of the work by da Vinci, reproduced in Figure 3.3, shows that the force to move the body over the plane is independent of the unequally sized faces exposed to friction.

The cause of this phenomenon remained ignored for a long time until Amontons demonstrated experimentally that friction did not depend on the apparent area of contact between rubbing bodies. Amontons' statement received a cool welcome by the French Royal Academy of Sciences, which instructed senior academician De la Hire to verify Amontons' experiments. Additional tests (1699–1700) corroborated both of Amontons' laws and his formulation of the second law forestalled modern ideas that solids are in discrete contact. Expressed it in modern terms, Amontons' paradox arises because solids are in contact by individual spots because their real surfaces are rough and they are unable to contact over their entire nominal surfaces.

The total area of the spots (real contact area which is treated more thoroughly in subsequent chapters) is very small compared with the apparent area. If the latter is specified, experience shows that the real area increases linearly as a function of load. The friction force, in turn, is proportional to the real contact area. Different faces of the specimen can be arranged so that the area of the real contact is maintained and depends only on the load. Consequently, it is clear why friction does not depend on the apparent contact area.

The third law, often attributed to Coulomb (1736–1806), is added to the above two: the friction force does not depend on the sliding velocity. This law was less substantiated than the others. Incidentally, Coulomb observed in his experiments that the friction force increases or decreases as a function of velocity. Nevertheless, this law can be true within a reasonable range of velocities, provided that the contact temperature in friction varies insignificantly and the features of the contact zone remain practically unchanged.

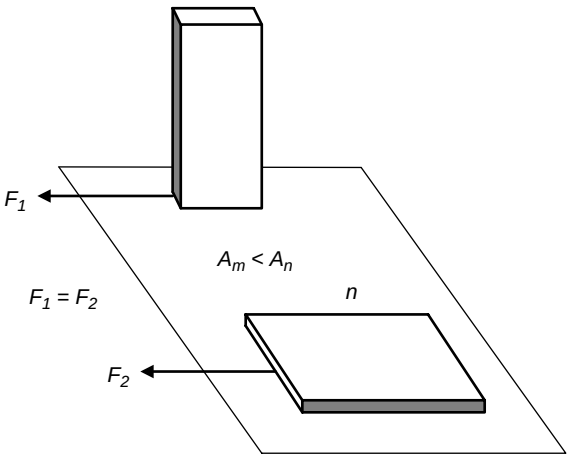

FIGURE 3.3 Fragment of Leonardo da Vinci's drawing illustrating the second law of friction.

In conclusion, it should be noted that the laws of friction are good empirical rules allowing tackling the tribological situations emerging in various applications.

3.1.2 Real Contact Area

When two surfaces approach each other, their opposing asperities with maximum height come into contact. As the load is increased, new pairs of asperities with smaller heights come into contact, forming individual spots. The overall area of these spots is known as the real contact area (see Chapter 2). The real contact area depends both on the mechanical behavior of the surface layers and their roughness. The latter may vary under compression and friction conditions. When the real contact area is built up, parts of the surface asperities elastically deform; others undergo plastic strain. In the general case, the deformation is elastoplastic with hardening. The real contact area varies in direct proportion with load to the power index in the range from 2/3 to 1. A load index very close to unity is not an indication of the contact plastic deformation because the contact behavior is also governed by statistical geometry of rough surfaces in contact.

The mean diameter of a single contact spot is scarcely affected by the applied load. The rate of the spot area growth is about an order of magnitude less than that of the real contact area. The real contact area increases with increasing curvature radius of asperity and decreases when yield point, elasticity modulus, and material hardening increase.

3.1.3 Interfacial Bonds (Adhesion Component of Friction)

If two clean surfaces are brought into contact, the forces of attraction at interatomic distances are the same as in the bulk. Several types of these forces can be differentiated (Figure 3.4).[10] The ionic bond occurs between anions and cations held together by electrostatic forces. The ionic solids have high strength; such is the case of aluminum oxide.

The covalent (homopolar) bond between neutral atoms is generated by overlap of their electron fields that results in very strong bonding forces in crystalline solids such as diamond.

The van der Waals bond may occur between any atoms and molecules due to dipole–dipole interaction (the atoms are treated as momentary dipoles because the centers of positive and negative charges are inequitable at any time). It is responsible for physical adsorption of environmental species by a solid surface.

The metallic bond is found in all metals and is realized by free electrons freely moving in ionic lattice. The bonding is generated between the rubbing surfaces only when the surface films are absent (e.g., when sliding in high vacuum or when wear rate of the film exceeds the rate of film formation).

Each individual atom in the bulk of a material interacts with its nearest neighbors through these forces. A specific amount of energy associated with the interaction is referred to as the *cohesive energy* that plays an important part in tribology. An atom in the free surface is under different conditions because the number of neighbors has been reduced and, as a result, there is no bonding outside the solid (Figure 3.5). For this reason, the surface exhibits an excess energy known as the *surface energy*. This energy controls the capacity of surfaces to form the adhesive junctions.

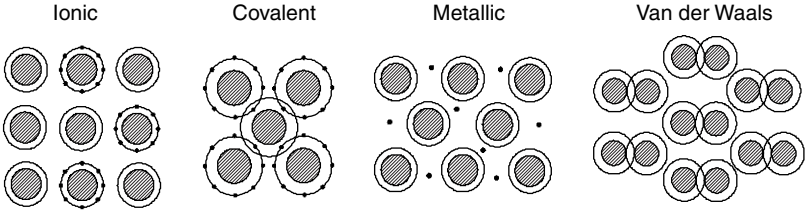

FIGURE 3.4 Main types of bonding forces.

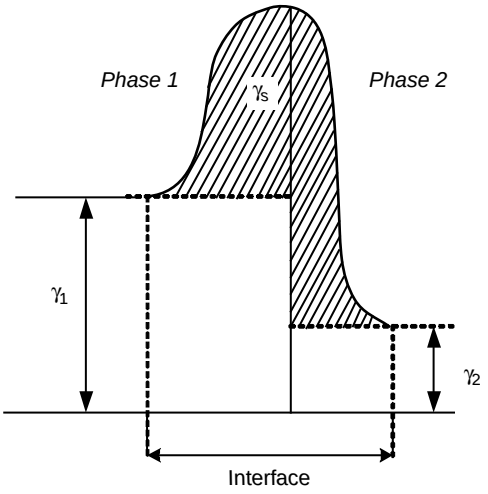

FIGURE 3.5 Surface energy γ_S (shaded region) as an excess energy of phases 1 and 2 that are brought into contact.

Adhesion refers to an atomic bonding process that occurs between contacting points on opposing surfaces. The junctions may form at both static contact and friction. Bowden and Tabor have proposed the simple model of the adhesive junction formation.[23]

It is a matter of general experience that clean iron surfaces seize in vacuum due to formation of strong adhesive bonds. This is not always the case when the surfaces come into contact at normal conditions. The junctions may appear only between very smooth surfaces under high load and, in this case, a mutual microslip of the mating surfaces is desirable. This is due to the presence of the absorbed films (including natural oxides), moisture, and other substances on the solid surface. These contaminants lower the surface energy, thereby reducing the possibility of strong junction formation.

Initially, when two rough surfaces are approaching one another, at least two asperities come into contact. Because the contact area is small, the pressure is very high, even under a very small load. The material of the softer asperity undergoes plastic flow; the surfaces continue to approach, bringing more and more asperities into contact. The process continues until the area of contact becomes sufficient to withstand the load. The area of an individual contact spot, A_n, is proportional to the load, P_n, and inversely proportional to the yield point of the softer material, p_m:

$$A_n = \frac{P_n}{p_m}. \tag{3.2}$$

This simple explanation is the basis of the model of sliding friction developed by Bowden and Tabor.[23] They assumed that the "welding bridges" (adhesive bonds) appear on each contact spot with the shear strength equal to s. These bonds fail (undergo shear) during relative sliding of the surfaces; hence, the friction force is equal to this shearing force. Analytically, the friction force can be written as

$$F = A_r s, \tag{3.3}$$

where A_r is the total real contact area equal to ΣA_n. Substituting this value instead of A_r yields

$$F = \frac{Ps}{p_m}, \tag{3.4}$$

where $P = \Sigma P_n$.

From this simple equation, it follows that the friction force is proportional to the load and independent of the apparent contact area; this is in agreement with the first two laws of friction. It is worthwhile to note that the shear strength, s, of the majority of metals is on the order of $0.2p_m$. The coefficient of friction, $\mu = F/P$, then, is equal to $s/p_m = 0.2$. This value is close to that proposed by Leonardo da Vinci, but still not sufficient with respect to real friction values. The fact is that the explanation in question is extremely simplified and ignores a large number of factors. For example, it was assumed that plastic flow during compression of a material and the shearing of adhesive bonds evolved independently. This is not quite true if the contacting rubbing materials are hardened and/or adhesive bonds (junctions) grow under the combined effect of normal and tangential forces. In reality, in accordance with the yield criterion, a relationship between normal, p, and tangential, s, stresses affecting the bonding should exist as

$$p^2 + as^2 = p_m^2. \tag{3.5}$$

Here, p_m is the yield point of a material during uniaxial compression, where $p = P/A_r$ and F/A_r. When a surface asperity undergoes complete transformation into the plastic state under normal loading, then $s = 0$ and $p = p_m$. Generally speaking, the yield criterion breaks down when a tangential load is applied. To retain its validity, the normal stresses should be reduced. This occurs when the contact area increases to a certain value A when surfaces come into a more intimate contact. Substitution of p and s shows that the contact spot area increases in the following manner:

$$A \sim \left(1 + a(F/P)^2\right)^{1/2}. \tag{3.6}$$

It might seem that the contact spot area would expand unrestricted as the tangential load increases. However, due to a number of factors, including the limited shear strength s_a of adhesive bonds, the bonds fail and sliding begins at a definite value of $F = s_a A$. It follows from the preceding equations that the friction coefficient is equal to

$$\mu = \frac{s_a}{p} = \left(a\left((s/s_a)^2 - 1\right)\right)^{-1/2} \tag{3.7}$$

Hence, it is apparent that if the shearing strength of adhesive bonds is close to the shearing strength of the metal, the coefficient of friction may take any arbitrarily large value. Yet, it drops sharply when s_a decreases, for example, when $s_a = 0.7$ (at $a = 10$) of the shear strength of the metal, the contact spot area increases 1.4 times and the coefficient of friction $\mu = 0.31$.

A similar situation occurs when the contacting surfaces move relative to each other (kinetic friction). However, rubbing may facilitate penetration of protective surface films, allowing a strong junction to form. Therefore, the nature of adhesive junctions forming at friction may be very different: from the strong metallic bonds between virgin portions of the contacting surfaces to the weak van der Waals bonds between the absorbed films protecting the rubbing bodies. The junctions will have to be sheared under the applied tangential force. This is the frictional force. That is, the work completed by the frictional force is extended for damage to the interfacial bonds.

Friction is therefore treated as a process of continuous formation and fracture of adhesive bonds. This work completed by the frictional force is extended for damage to the interfacialis essence of adhesion (molecular) component of friction. When tangential load is applied, the bonds are sheared. Their shearing strength is determined by:

$$\tau_n = \tau_0 + \beta p_r \tag{3.8}$$

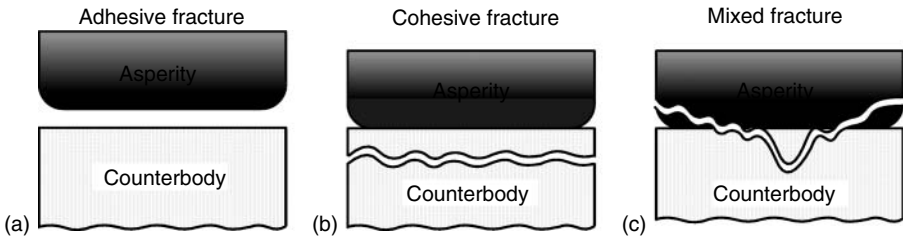

FIGURE 3.6 Fracture types of adhesion junctions forming at friction: (a) adhesive fracture; (b) cohesive fracture; (c) mixed fracture.

where τ_0 and β are empirical constants depending on character of surface interaction; p_r is pressure on a single contact spot. This relationship was first obtained by Bridgman in his study of high pressures.

The site where fracture occurs depends on the relative strength of the junction and the rubbing materials (Figure 3.6). If the interfacial bonding is stronger than the cohesive strength of the weaker material, then this material is fractured and the material transfer takes place. Otherwise, fracture occurs at the interface.

In general, the interfacial junctions (their formation, growth and fracture) are influenced by the nature and chemistry of the surface and the stress state of surface layers (the loading conditions). The interfacial junctions, together with products of their fracture and the highly deformed layers where shear deformation is localized, have been named by Kragelskii as a *third body*.[24] This term implies that the material entrapped in the friction process may possess properties that differ drastically from those of the rubbing materials.

3.1.4 Deformation at Friction

Another source from which the frictional force arises is attributed to deformation occurring when the asperities of two sliding surfaces come into contact with each other. This deformation is accompanied by dissipation of mechanical energy mechanisms that may be highly diversified, depending on deformation mode, sliding conditions, rubbing materials, environment, and other factors. In the Bowden–Tabor model for sliding friction, the asperities of the harder surface are assumed to plough through the softer counterpart. The ploughing resistance causes a force contributing to the frictional force. This contribution is referred to as the ploughing component of friction, i.e., the deformation term.

Assume that under the load P a single cone-shaped asperity with the opening angle 2ϑ (Figure 3.7) penetrates to a depth h into the plastic material with the hardness H. Under the action of the tangential force F, the cone ploughs a groove into the softer material. This groove is a triangle in the cross section with height h and base $2a$. As the cone moves, the normal load is apparently sustained by the semicircle with the radius a, i.e., the following relation should exist between the load P and the depth h to which the irregularity penetrates:

$$P = 0.5\pi h^2 H \tan 2\vartheta, \tag{3.9}$$

wherel $a = h \tan \vartheta$.

On the other hand, the tangential force (drag force) equal to the friction force should overcome the resistance of the material ahead of the indenter, i.e., it acts on the cross section of the groove with the area equal to $a_h = h^2 \tan \vartheta$, then

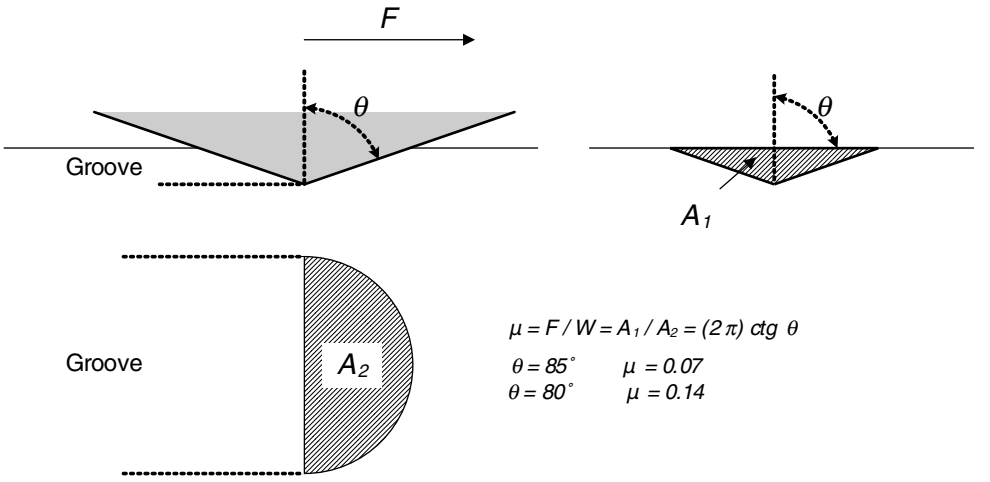

FIGURE 3.7 Deformational component of friction appearing when plastic material is ploughed with cone-shaped irregularity.

$$P = Hh^2 \cot \vartheta. \tag{3.10}$$

Hence, the coefficient of friction due to the ploughing (deformation) is recorded as

$$\mu_d = \frac{2}{\pi} \cot \vartheta. \tag{3.11}$$

As a rule, the asperities on a real surface have a slope on the order of 5–10°, i.e., the angle 2ϑ is 80–85°. Substitution of this value into the last formula yields a deformation (ploughing) component of the coefficient of friction within the range 0.07–0.14. Usually, these two components (both adhesion and deformation) are just added arithmetically, assuming that these are additive. In reality, this is not quite true because deformation, while enlarging the contact area, enhances adhesion and the stronger adhesion increases the severity of deformation during friction. Nevertheless, because the areas over which these two processes evolve change insignificantly, the assumption that these two components are additive is correct. Moreover, this is advantageous for gaining more insight into the nature of friction.

Note that, almost without exception, ploughing (Figure 3.8a) is accompanied by adhesion (Figure 3.8b) and, under certain conditions, the ploughing may result in *microcutting* (Figure 3.8c), i.e., additional work is completed and the friction is increased.

During deformation, there are other mechanisms of energy dissipation. Hence, when a polymer with viscoelastic behavior slides against a hard, rough surface, dissipation of energy occurs with high hysteresis losses. This deformation component is known as an elastic hysteresis friction. The energy may also be carried away along other channels of dissipation. For instance, due to nucleation and development of microcracks on the sliding surface and in the bulk of the material, the elastic waves are generated at the interface with a tendency towards infinity.

3.1.5 Friction as a Function of Operating Conditions

Depending upon the rubbing materials, the roughness, the operating conditions (load, sliding velocity, temperature) and the environment, the relative contribution of adhesion and deformation components to friction can vary over a wide range. This is most noticeable in the load dependence of the friction coefficient (Figure 3.9). According to Kragelscii such dependence has a minimum

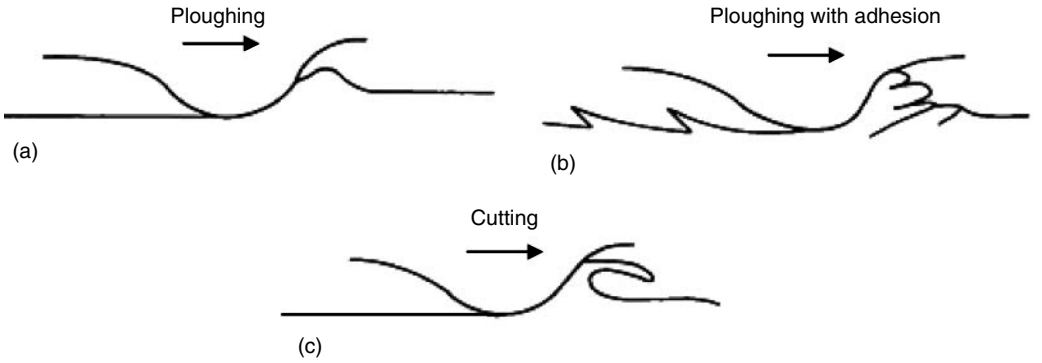

FIGURE 3.8 Deformation component of friction.

that is connected directly with the transition from elastic to plastic (increased load) contact and the associated change in the relative contributions from the friction components.

As discussed earlier, the real area of elastic contact is proportional to load with power less than 1, i.e., the adhesion component and therefore the friction coefficient will decrease with load due to negligible contribution from the deformation component. When contact becomes plastic, the real contact area and the adhesion component become load-independent. At the same time, penetration of the asperities into the counterbody increases with load and, as a result, so does the deformation component (the ploughing term). The total coefficient of friction increases. This transition from a descending to an ascending branch of the curve defines the minimum. Its position depends upon a ratio of adhesion and deformation components and is shifted towards lower values of friction with increasing μ_a/μ_d.

It should be emphasized that the minimum in this relationship is not very pronounced. The experimental evidence indicates that due to numerous factors exerting an additional influence on friction, a large number of these relationships, from a descending (or ascending) curve to a load-independent relation, exists. It is interesting to note that similar behavior is observed in the dependence of the friction coefficient on the roughness, i.e., the smaller the height of asperities, the greater

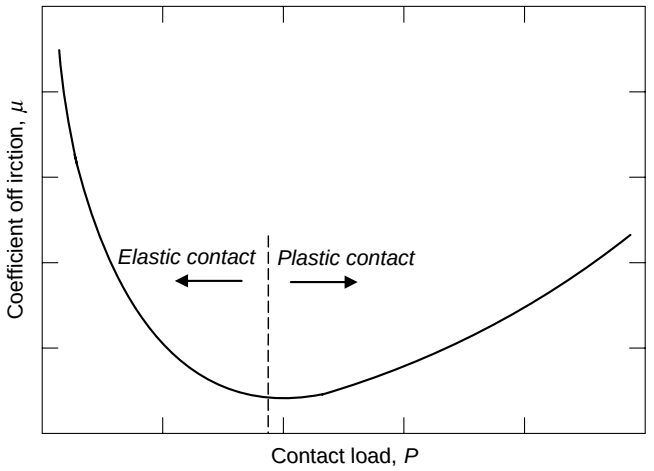

FIGURE 3.9 The dependence of friction coefficient on load.

is the real contact area and therefore the adhesion component. On the other hand, the higher the asperities and the smaller the curvature radius at their tips, the greater the deformation component.

It is interesting that the dependence of the friction coefficient on roughness has similar character: the lower the asperity height, the greater the real contact area and the adhesion component. On the other hand, the higher the asperities and the smaller the radii of peak curvature, the greater is the deformation component. However, it should be remembered that roughness itself varies during friction: a very smooth surface becomes rougher, whereas a very rough surface may be smoothed. There is a concept of *equilibrium roughness* that is independent of initial roughness; depending on the wear conditions, it may be either less than or greater than the initial roughness (Figure 3.10). Dependence of friction on sliding velocity is a complex issue because the effect of velocity is often indistinguishable from the temperature effect. Nonetheless, it is evident that when sliding is initiated, reduction of the friction coefficient may be observed (the zero law of friction).

Alternatively, the friction becomes independent of the sliding speed (the third law of friction) when a perfectly elastic body is rubbed under the conditions whereby the contact temperature remains almost unchanged. In practice, more complicated dependences may be observed because increasing the sliding speed increases the strain rate and the contact temperature.

These factors affect the mechanical behavior of the rubbing materials and, consequently, the adhesion and deformation components of friction. Therefore, because the plastic deformation is localized in a thinner surface layer, the friction force decreases. For imperfectly elastic materials, the friction is associated with the speed and is therefore also associated with generation of the hysteresis losses. In general, the speed-dependent friction passes through a maximum that may be reduced by certain conditions, resulting in a descending tendency of friction. The effect of contact temperature must be emphasized because increasing temperature weakens the strength of adhesive bonds and the contact becomes more plastic; this, in turn, enlarges the real contact area. The set of these effects may give wide-ranging effects of the friction temperature dependence.

3.1.6 The Preliminary Displacement

The kinetic friction is preceded by a process called *preliminary displacement.* The process involves relative microdisplacements of the contacting bodies, originally at rest under normal load W,

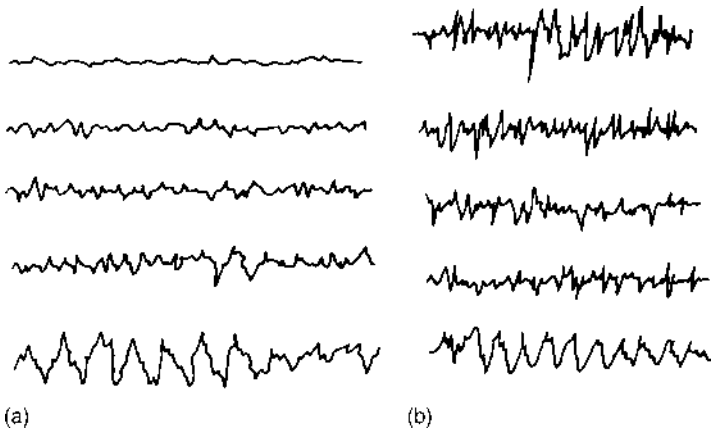

FIGURE 3.10 Change in roughness during running-in: (a) increasing the roughness when the initial roughness is less than the equilibrium one; (b) decreasing the roughness when the initial roughness is greater than the equilibrium one.

by applying and increasing the tangential load F from zero to some critical value F_s (*static friction force*) responsible for gross sliding.

This phenomenon exerts primary control over wear and serviceability of such precision engineering devices as electronic switches, magnetic head–disc contacts in computer, and so on.

Numerous experiments have revealed that microdisplacement increases monotonically with increasing tangential force only during the initial stage of the process. This microdisplacement comprises reversible and irreversible components and is smaller than the junction size (the diameter of a contact spot). Under the preliminary displacement, energy dissipation occurs jointly with storing of the mechanical energy. The mechanism of preliminary displacement can be conveniently explained using a sphere-on-flat-contact configuration (Figure 3.11).

Let the sphere be loaded by a constant force W. The contact is assumed to be elastic. The normal pressure is a Hertzian distribution:

$$p(r) = p_0\left[1 - \left(\frac{r}{a}\right)^2\right]^{1/2}. \tag{3.12}$$

Because the tangential force F is less than the static friction force F_s applied to the sphere, the contact surface traction $\tau(r)$ appears (curve 1 in Figure 3.11). If contact adhesion was very strong, the tangential displacements of all the contact points would be the same and the associated distribution of the tangential traction would be

$$\tau(r) = \frac{p_0}{(1 - r^2/a^2)^{1/2}}. \tag{3.13}$$

This equation shows that the traction rises to infinity at the contact edge. This requires an infinite coefficient of friction that is not realizable, or, alternatively, there must be some microslip. This can be explained as follows: Before the sliding commences, the tangential force F approaches its limiting value $\mu_s P$ and the tangential traction is proportional to the normal pressure:

$$\tau'(r) = \mu_S p(r). \tag{3.14}$$

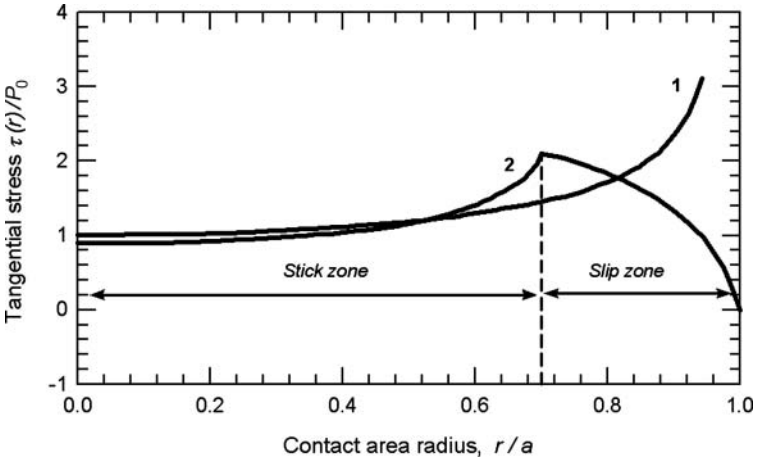

FIGURE 3.11 Distribution of tangential stresses over the contact area: (1) no slip; (2) partial slip.

Furthermore, an additional distribution of traction is considered:

$$\tau'' = -\frac{c}{a}\mu_S p_0\left(1-\frac{x^2}{c^2}\right), \tag{3.15}$$

that acts over the circular area $r \leq c$. The resultant distribution curve 2,

$$\tau(r) = \tau'(r) + \tau''(r), \tag{3.16}$$

is shown in Figure 3.11. The radius c corresponds to the peak of the traction distribution $p(r)$:

$$\frac{c}{a} = \left(1-\frac{F}{\mu_S P}\right)^{1/3}. \tag{3.17}$$

This means that the contact area consists of two zones: (1) circular stick zone of radius c, where the traction is less than the static friction and where the slip is absent, and (2) annular zone ($c < r \leq a$) where the slip takes place. In other words, if the tangential force F is increased from zero, microslip begins immediately at the edge of contact area, and the stick region decreases in size down to a single point when $F = \mu_s W$. The gross sliding begins and the static friction passes into the kinetic friction.

3.1.7 Stick-Slip Motion

The difference between the static and the kinetic friction may account for the friction-induced vibrations, often referred to as stick-slip. In many instances, the vibrations upset the normal operation of the mechanical systems, e.g., sharp jerks and appreciable chatter at automobile starting, brake squeaks at stopping, intermittent motion of carriage in a metal-cutting machine tool, and so forth. The main reason for these mechanical vibrations has to do with the positive difference between the static friction and the kinetic friction. This difference may be due to both the rise of the static friction with prolonged time of stationary contact and the descending dependence of friction force on velocity.

Figure 3.12 demonstrates a schematic of experiment with the stick-slip motion. A weight 1 tied with spring 3 lies on belt 2. When the belt begins to move with a low constant speed, the weight will first move with it and the continuously increasing elastic force of the spring is balanced by the incomplete static friction force up to the point when the latter reaches the complete static friction. Because the kinetic friction is less than the static friction, further motion of the weight occurs with varying speed under the combined action of the spring and the kinetic friction (a stage of slip).

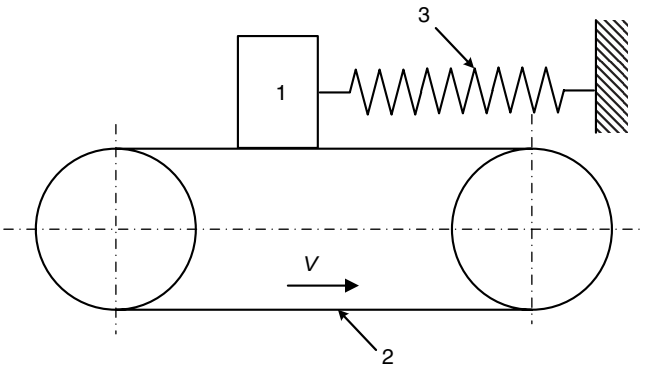

FIGURE 3.12 A simple model to study the stick-slip motion.

Due to inertia force, the weight passes over the equilibrium point and stops when its speed with respect to the belt becomes equal to zero. At this moment, the weight is picked up by the belt and they are now back to collective motion. Duration of stationary contact (stick) decreases with increasing speed, but the vibration amplitude will decrease and the frequency will increase.

The friction-induced vibrations in an elastic mechanical system can be eliminated by carefully selecting the contact materials and the finishing quality, and changing the design of the tribosystem. For dry friction, a material that exhibits a higher modulus of elasticity, a larger aftereffect rate, and a smaller relaxation rate is less susceptible to the stick-slip phenomenon. Increasing the normal load is favorable to this intermittent motion. Prevention of stick-slip in electrical contacts is very important because stick-slip can generate electrical erosion of the contact surfaces due to discharge at the moments of contact breakdown.

Effects relating to stick–slip phenomena in electrical contacts have been discussed elsewhere.[26–28] Where noble metals slide, prow formation leads to an increase in contact resistance. Prow breakage, however, is accompanied by an instantaneous excursion of both contact resistance and friction to values characteristic of unworn contact pairs. The levels quickly return as new prows form. This behavior is in agreement with observations that the contact system converts to one characteristic of the member with a larger apparent contact area because of the mechanism of prow growth. Another reason of stick-slip is the behavior of the meniscus around the contact spots. This behavior depends on many factors, including humidity of the ambient medium, materials of contact members, etc.

In stick-slip motion, friction is highest at the stick, whereas contact resistance is lowest. With severe sticks, electrical opens occur on breakaway due to surface roughness and rider inertia. Instantaneous bad variation, caused by the same factors without the extreme of contact separation, also affects contact resistance and friction force.

It was shown[28] that the stick-slip amplitude increases with increasing relative humidity and contact spot size; given this, the interfacial electrical resistance spikes at the beginning of slip exhibit hysteresis during stick-slip cycling.

3.2 WEAR

When solid surfaces are in sliding or rolling relative motion, a removal of material from one or both of these surfaces can be observed. The process is termed *wear*. There exist several definitions of wear:[29]

- Wear is the progressive loss of substance from the operating surface of a body occurring as a result of relative motion at the surface (Organization for Economic Co-Operation and Development (OECD), Research Group on Wear of Engineering Materials, Glossary, Paris, 1969).
- Wear is damage to a solid surface, generally involving progressive loss of material, due to relative motion between that surface and a contacting substance or substances (ASTM Standard G 48–83, Standard Terminology Relating to Erosion and Wear, Philadelphia, PA).
- Wear is a result of wear process, which is process of a loss of substance from a solid body surface in friction and/or build up of its permanent deformation, displayed as a gradual change of body dimensions and/or shape (ISO/DIS 4378/2 Project).

Wear is expressed in specified units (length, volume, or mass). The wear process is often described by wear rate. There is no single standard way to express wear rate. The units used depend upon the type of wear and the nature of the tribosystem in which wear occurs. Wear rate can be expressed, for example, as (1) volume of material removed per unit time, per unit sliding distance, per revolution of a component, or per oscillation of a body; (2) volume loss per unit normal force at unit sliding distance ($mm^3/(N\ m)$) that is sometimes called the *wear factor*; (3) mass

loss per unit time; (4) change in a certain dimension per unit time; or (5) relative change in dimension or volume with respect to the same changes in another (reference) substance.

The reciprocal of wear rate has come to be known as *wear resistance*, which is a measure of the resistance of a body to removal of material by a wear process. Relative wear resistance is sometimes considered using arbitrary standards.

Wear is a rather intricate phenomenon involving a large variety of mechanisms that rarely act individually or independently. Nevertheless, more often than not, there is a leading mechanism that is responsible for mode and severity of wear. Wear is affected by numerous factors, including load, sliding velocity, temperature, materials, lubrication, environment, etc.

3.2.1 Stages of Wear

Wear is a process that evolves with time. The wear of a friction pair is imaged graphically as a function of time (or friction path) at constant load and sliding speed conditions. The slope of the curve at each point characterizes the wear rate. Three stages of wear usually exist as shown in Figure 3.13.

The first portion of the curve (stage I) is the initial period of wear that lasts a short time as compared with the expected life of a friction unit. This stage is characterized by the unsteady state of the tribosystem with a high wear rate that gradually decreases. This stage is termed the *run-in* of the tribosystem that occurs rubbing surfaces adapt one to another, particularly while the so-called equilibrium roughness is reached. Friction and wear modify such that the tribosystem transforms into the steady state.

The second stage (II) lasts longer and is characterized by stable conditions of friction and a practically constant and relatively low wear rate. This stage occurs during normal operation of a friction unit after its run-in period is complete. As this stage evolves, wear intensifies gradually (almost linearly), thereby damaging the surface, altering the shapes of rubbing pairs and the clearance between them; this leads to pronounced changes in the operating conditions, when the wear rate increases strongly and catastrophic wear begins (stage III). It should be noted that real tribosystems operate with stops because during re-starts, run-in conditions occur again, although less extensively.

3.2.2 Simple Model of Wear

Unlike the laws of friction, no "laws" of wear exist, although tests and operation of friction units demonstrate the presence of some typical features. It is commonly accepted that wear increases with load and operating time; the harder the rubbing material, the smaller is its wear, etc. These rules are often confirmed experimentally and derived from the simple models proposed by Holm and Archard.[1,30]

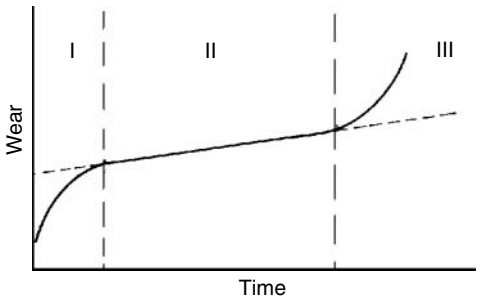

FIGURE 3.13 Typical stages of wear process.

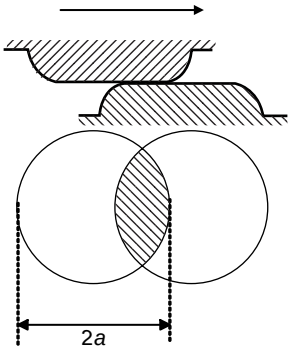

FIGURE 3.14 Simplified scheme of origination of a single contact spot.

The wear model, described by Hutchings[15] is based on the assumption that two rough surfaces are in discrete contact, i.e., the contact consists of individual spots formed by the asperities of mating surfaces. The area of each individual spot initially expands from zero to its maximum πa^2 (a is the maximum contact spot radius) and then shrinks back to zero. Figure 3.14 shows one stage of the process. The essence of the wear process is shearing of the adhesive bonds formed at these spots. In addition, the local deformation of the asperities is assumed to be plastic. It is apparent that the normal load P_n supported by a contact spot in this situation is determined by the expression:

$$P_n = \pi a^2 p_m, \tag{3.18}$$

where p_m is the yield pressure of a plastically deformed asperity that is close to the hardness H of the material.

As sliding proceeds, individual junctions are continuously formed and destroyed; as a result, detachment of the fragments of material from the asperities may occur. The volume of each such fragment (wear particle) depends on the typical dimension of the adhesive bond that conceives it. If the effect of junction growth is disregarded, then the volume of a wear particle, V_n, can be taken to be proportional to the cube of the contact radius. This assumption implies that the shape of the wear particle is independent of its size; therefore, the wear particle may be treated as a hemisphere with radius a and volume V_n given by

$$V_n = \frac{2\pi a^3}{3}. \tag{3.19}$$

Because the wear particle is produced in the friction path $2a$ (see Figure 3.14), the wear rate i_n (wear per unit distance of sliding) is $V_n/2a$, i.e., $i_n = \pi a^2/3$. The latter equality is rewritten as

$$i_n = \frac{P_n}{3p_m}. \tag{3.20}$$

If all the pairs of contacting asperities produced wear particles, the total wear rate would be equal to the total contribution from all contact spots:

$$I^* = \sum i_n = \frac{P}{3p_m}, \tag{3.21}$$

where the total normal load on the contact is $P = \Sigma P_n$.

It would appear reasonable to assume, as was done by Archard, that only a fraction k of all contact asperities produce wear particles. Notice that the coefficient k may also take into consideration a geometric similarity of wear fragments and contact spots. Hence, $I = kI^*$, that is written as

$$I = \frac{kP}{3p_m}. \tag{3.22}$$

It is convenient to designate $K = k/3$ and assume that $p_m = H$, where H is the indentation hardness. Then the equation of wear develops in the form:

$$I = \frac{kP}{H}. \tag{3.23}$$

This equation, often called the Archard wear equation, shows that the wear rate I (the volume worn per unit sliding distance) is directly proportional to the normal load P and inversely proportional to the hardness of the softer material H. The constant K, usually termed the *wear coefficient*, is dimensionless and always less than 1. K allows comparison of the severity of wear processes in different tribosystems. For engineering applications, it is often preferable to use the ratio K/H, termed the *wear coefficient*, dimensionally expressed as $mm^3/(N\ m)$. The measure of wear provided by the wear coefficient is particularly helpful when comparing wear rates in different classes of materials.

It is interesting to note that the Holm–Archard equation is easily derived from dimensional analysis. The worn volume per unit sliding distance has the dimensions of area, and the P/H ratio also represents the real contact area during plastic deformation of asperities. The only dimensionless value (wear coefficient) is obtained as the ratio between these two areas. It follows from the Archard equation that, when K is a constant for a given tribocouple, the volume (or mass) of the worn material should be proportional to the friction path. If the normal load P changes, the wear rate should change proportionally.

A large number of studies confirm that the wear of many tribocouples is truly proportional to the sliding distance. Depending on the pattern of the running-in process, exceptions can be observed at the start of sliding (during the running-in) when the wear rate can be above or below its stabilized level. Within a limited range of loads, many tribosystems exhibit this type of direct proportionality between the wear rate and the normal load. Nonetheless, an abrupt transition from a low to high wear rate, and sometimes back again, is often observed with increasing load.

Though the coefficient of wear K plays a significant role in the studies and analyses of tribosystems, its physical sense is rather implicit and its values can only be determined experimentally. This means that there are no other means, other than the trial-and-error method, to predict the wear rate of a combination of materials rubbing under certain conditions. The wear coefficient K varies over a wide range that spans about six orders of magnitude as a function of the properties of materials and conditions of friction.

3.2.3 Basic Mechanisms of Wear

Three stages of wear may be formulated: interaction of surfaces, changes in surface layer, and damage to surfaces. All the stages are interrelated and occur at individual contact spots. The surfaces interact in both mechanical and molecular ways (Figure 3.15). The mechanical interaction involves penetration and interlocking of asperities.

After relative motion of mating surfaces is initiated, the elastic and plastic pushing of material takes place by the penetrating asperities (Figure 3.15a). Interlocking of asperities leads to their deformation, and in the limiting case the softer asperity can be sheared (Figure 3.15b). The molecular interaction is manifested as adhesion of films on the mating surfaces (Figure 3.15c).

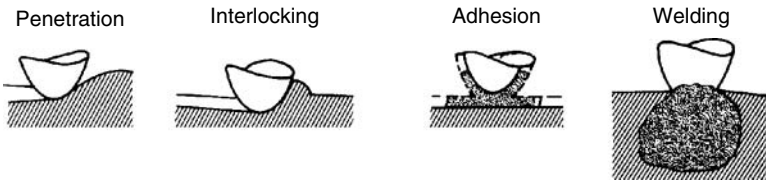

FIGURE 3.15 Mechanical and molecular interaction of surfaces resulting in wear debris formation.

In specific cases, the adhesion is so strong that a breakup of the adhesive bonds is accompanied by pulling out of coarse pieces of material (Figure 3.15d).

The changes in the surface layer arise from mechanical stresses, temperature and chemical reactions. The normal stress of plastically deformed asperities will be close to the indentation hardness of the softer body. However, if the surfaces are very smooth, closely compliant, or lightly loaded, then the contacts may be elastic. Therefore, the normal load applied to the system controls the extent of plastic flow at the asperity contacts. If the load is low enough, or if the surfaces are in compliance, wear will proceed very slowly as a result of elastic deformation.

The magnitude and position of the maximum shear stress depend on the coefficient of friction, μ (see Chapter 2). For $\mu < \sim 0.3$, the maximum shear stress and associated plastic flow will lie beneath the surface and the plastic strain accumulated by each sliding pass is small. This condition is typical for a lubricated system, or for one carrying a protective layer. For $\mu > \sim 0.3$, however, the maximum shear stress lies at the surface and large shear strains can be accumulated. Several wear mechanisms controlled by plastic flow have been proposed. These involve asperity adhesion and shear, nucleation and growth of subsurface cracks leading to the formation of lamellar wear particles (*delamination wear*), and fatigue crack propagation. At relatively low sliding speeds and high loads, these *plasticity-controlled* wear mechanisms prevail, leading to *severe wear*.

Under certain conditions, due to a nonperfect material structure, the repeated elastic deformation may result in pitting of rolling surfaces. The plastic deformation alters the structure of the surface layer. The concentration of subsurface and near-surface dislocations in a metal increases, resulting in hardening of the surface layer. This process continues until the recrystallization temperature is reached and dislocation concentration sharply falls; this leads to annealing of the surface layer. The process of strain hardening and annealing is repeated many times, initiating certain wear processes. Additionally, high temperatures and plastic deformation that occur at the rubbing surface accelerate the rate of diffusion and provoke solute enrichment of the surface.

The local temperature at the interface may be substantially higher than that of the environment and may also be enhanced at the asperity contacts by transient "flashes" or "hot-spots." *Flash temperature* increases may exceed 1,000 K, whereas a steady interfacial temperature increase due to the mean frictional power dissipation can contribute an additional hundred or so degrees. Such high-temperature transients can lead to local phase transformations. They are also responsible for rapid surface oxidation and other reactions between the surface and environment.

For almost all metals, the oxide films formed in air protect the surfaces against welding. The metallic surfaces interacting with surfactants in oil are covered with films that play a role similar to that of oxide films.

The above-listed mechanisms and many others are the basis of the wear process. Yet, the great diversity of the mechanisms and their interrelation make impossible a rigorous classification of wear processes, although many classification systems have appeared in the literature. It is generally recognized that the most common types of wear are abrasion, adhesion, fatigue, corrosion, erosion, and fretting.

3.2.4 Abrasive Wear

Abrasive wear is defined by the ASTM G 40–83 terminology standard as a wear due to hard particles or hard protuberances forced against and moving along a solid surface. Abrasive wear, also known as *abrasion*, is one of the most common forms of wear. Examples of abrasion and abrasive wear are abundant. It is a major form of damage to machinery in the mining and agriculture industries. But abrasion is also present in our daily life. Shoes are replaced if they become too "scuffed up."

The key aspect of abrasive wear is its association with the cutting or plowing of the surface by harder particles or asperities. These cutting points may either be embedded in the counterface, or lost within the contact zone. The former case is commonly called two-body abrasion; the latter case is three-body abrasion (Figure 3.16). Sometimes, the abrasion may be classified in terms of the force acting on abrasive material. If the force is so large that the abrasive particles are crushed and the working surface experiences significant cutting and deformation, then *high-stress abrasion* takes place. This form of abrasion is observed, for example, in high-load bearings, where hard particles are trapped between mating surfaces. A particular case of high-stress abrasion is *gouging abrasion*.

This term is used for abrasion by large hard lumps that remove material from the worn surface in large fragments. Yet, the situations when the term may be applied are described ambiguously. When the pressure on the abrading particles or asperities is relatively low and the particles remain unbroken, the abrasion is called *low-stress abrasion*.

Abrasion displays scratches, gouges, and scoring marks on the worn surface, and the debris produced by abrasion frequently takes on the appearance of fine cutting chips similar to those produced during machining, although at a much finer scale. Most of the models associated with abrasive wear incorporate geometric asperity descriptions, so that wear rates turn out to be quite dependent on the shape and apex angles of the abrasive points moving along the surface. The sources of the abrasive solids are numerous, and the nature of the abrasive wear in a given tribosystem will depend to some extent on the manner in which the abrasives enter the tribosystem: whether they are present in the original microstructure as hard phases, enter the system as contaminants from outside, or are generated as debris from the contact surfaces as they wear.

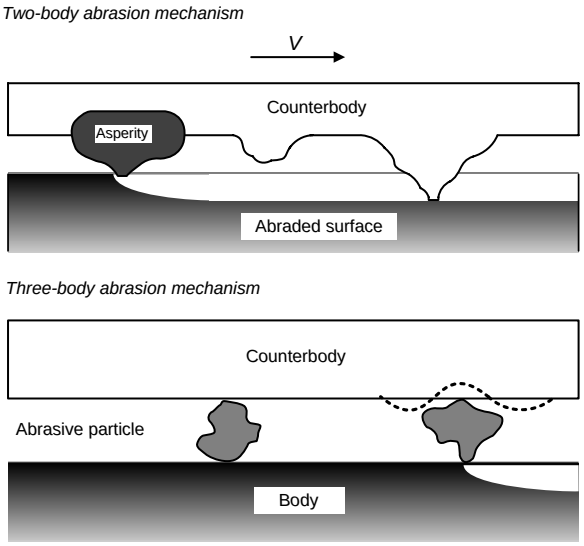

FIGURE 3.16 Two-body and three-body abrasion mechanisms.

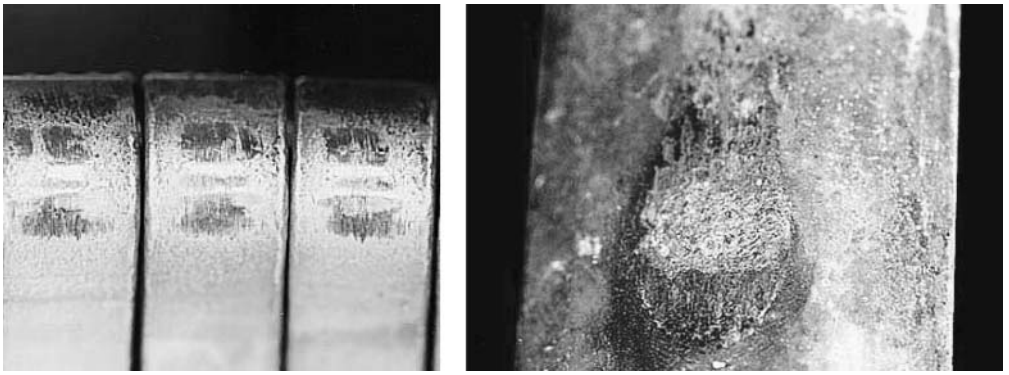

FIGURE 3.17 Typical abrasion wear features observed on silver-plated fingers and blade of a disconnect switch. Note the loss of silver plating due to abrasion. (Courtesy of RusCan, www.ruscan.com.)

Figure 3.17 shows typical abrasion wear features in silver-plated fingers and blade of a disconnect switch.

The hardness, shape, and size of particles involved in abrasion influence the rate of wear. Let H_a and H_S be abrasive and surfaces hardness, respectively. The analysis of plastic deformation at the contact between abrasive and surface shows that there is a certain value of the ratio between these hardnesses that establishes a conventional line of demarcation between two types of abrasion wears. If $H_a/H_S \ll 1.2$, abrasion is sometimes identified as *soft abrasion*, in contrast to *hard abrasion* when $H_a/H_S \gg 1.2$. Soft abrasion demonstrates a lower wear rate than hard abrasion but greater sensitivity to the ratio H_a/H_S. In hard abrasion, however, the exact hardness value of abrasive has only a slight effect.

Despite the recognition by researches that wear particle shape is important, relatively few methods for quantifying shape indices and specifying them in standard wear tests have been implemented. It should be remembered that, depending on the particle shape, the wear rate may vary by a factor of ten or more.

Fundamental mechanisms of abrasive wear are directly related to plastic flow and brittle fracture. Plastic deformation of a working surface by harder abrasive particles results in the formation of grooves from which material is removed. Let the abrasive particles be modeled by pyramids or cones indenting the surface at depth h_i (Figure 3.18). When the friction path is rather large, the volume wear per unit sliding distance, I, is proportional to a sum of the

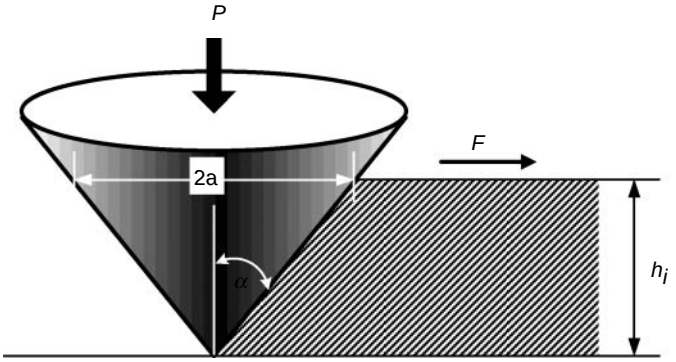

FIGURE 3.18 Contact of conical abrasive particle with a solid surface.

indentation depths:

$$I \approx \sum_i h_i^2. \tag{3.24}$$

The external load W is distributed among all particles so that $P = \sum_i P_i$. Under conditions of plastic deformation, the hardness H is then

$$H = \frac{P_i}{Bh_i^2}. \tag{3.25}$$

It follows that

$$P_i = HBh_i^2$$

Summing the equality gives

$$P = BH \sum h_i^2 \approx HI,$$

or

$$I = K\frac{P}{H}, \tag{3.26}$$

where K is the dimensionless *wear coefficient* that indicates the severity of wear. Typical values of K in the two-body abrasive wear of metals lies in the range $(5–50)\times10^{-3}$. For three-body abrasion, K is lower, typically in the range $(0.5–5)\times10^{-3}$.

Equation 3.26 is the key relation for the abrasive wear. It shows that relative wear resistance (the reciprocal of wear rate) is directly proportional to indentation hardness. For pure metals and nonmetallic hard materials, this conclusion has been demonstrated by Khruschov's experiment (Figure 3.19).[31] It should be noted that the data for steels lies on the straight lines that do not pass the origin, as expected from Equation 3.26. Sensitivity of the wear coefficient K to steel structures is the most likely explanation for this dependence. Changing the hardening and tempering conditions leads to the formation of different structures with the same hardness, thus resulting in different wear resistance. In addition, the abrasion itself changes the mechanical behavior of material by introducing high shear strain, temperatures, and strain rates.

As pointed out above, the abrasion by plastic flow is accompanied by the formation of grooves. There are two distinct modes of deformation when an abrasive particle acts on a plastic material. The first mode is plastic grooving, often referred to as ploughing, in which a prow is pushed ahead of the particle and material is continually displaced sideways to form ridges adjacent to the developing groove (Figure 3.20). No material is removed from the surface. The second mode is named *cutting* because it is similar to micromachining and all the material displaced by the particle is removed as a chip.

In two-body abrasion, some asperities produce ploughing, the rest show cutting. This is determined by two controlling factors: the attack angle of the particle and the interfacial shear strength expressed as the ratio between the shear stress at the interface and the shear yield stress of plastically deformed material. There is a critical attack angle at which the transition occurs from ploughing to cutting. The value of the critical angle depends only on the interfacial shear strength of a perfectly plastic material. For a real material, it also depends on the material work-hardening rate and elastic properties, specifically, the ratio between the Young's modulus, E, and the surface hardness, H. The higher value of E/H, the larger the critical attack angle. For most metals, the angle is in the range of 30° to 90°.

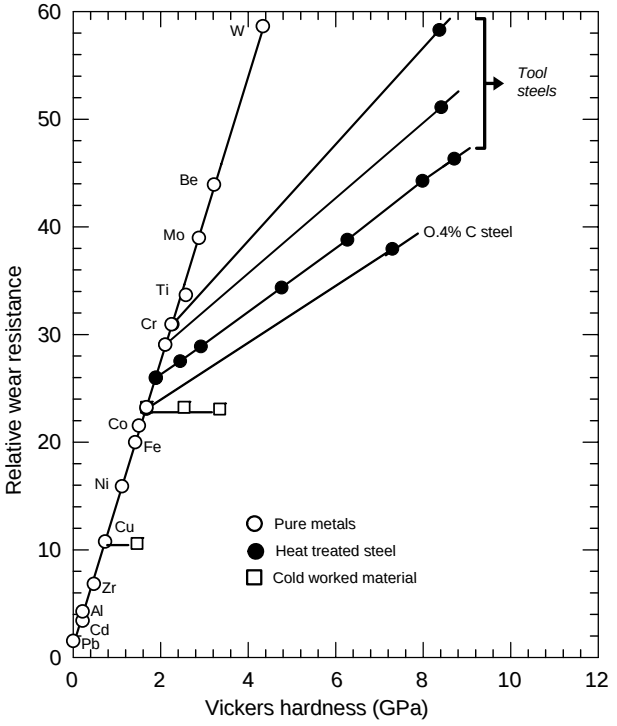

FIGURE 3.19 Relative wear resistance for pure metals and heat-treated and work-hardened steels under conditions of two-body abrasion, plotted against indentation hardness. (From Khruschov, M. M., *Proceedings of Conference on Lubrication and Wear*, Institution of Mechanical Engineering, London, 655–659, 1957. With permission.)

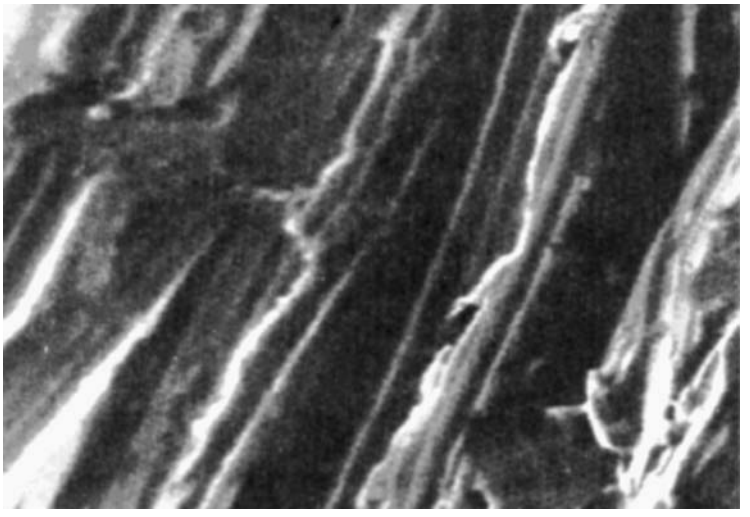

FIGURE 3.20 Grooved surface after two-body abrasion.

Abrasive wear of brittle materials, e.g., ceramics, results from microcracking whereby the contribution from plastic flow is negligible. For these materials, the tensile stresses associated with the abrasive indentation cause the median and lateral vent cracks to propagate from the plastic zone. Material is removed by fracture mechanism if the lateral cracks adjacent to the grooves intersect those from other grooves or propagate toward the surface.

Finally, it must be noted that abrasive wear should not always carry a negative connotation. The controlled use of abrasion is extremely important to the grinding and finishing processes, the polishing of optical components, and the cutting of various materials ranging from blocks of quarry stone to computer microchips.

3.2.5 Adhesive Wear

Adhesive wear results from the shear of the friction junctions. The fundamental mechanism of this wear is adhesion, an important component of friction. This wear process evolves in exactly the same manner as adhesion friction, i.e., formation, growth, and fracture of adhesion junctions. A distinguishable feature of this form of wear is that transfer of material from one surface to another occurs due to localized bonding between the contacting solid surfaces. The limiting form of adhesive wear is called *scoring* or *scuffing*. Scoring may be due to local solid-phase welding that often involves material transfer and higher friction force.

It is reasonable to assume that the adhesive wear occurs with the processes associated with other wear types (fatigue, abrasion, etc.). Although this situation applies to all types of wear (e.g., adhesion can affect abrasion), some researchers believe that replacing the term *adhesive wear* with *sliding wear* is inadequate. In our opinion, this is not necessarily the case. There are numerous cases when adhesion dominates and its manifestation through the materials transfer is easily observed. For these situations, the term *adhesive wear* should be retained, whereas the *sliding wear* can be applied to the cases when there is no single dominant process. In other words, sliding wear means that several processes occur on equal terms and that wear is a result of their competing actions.

Experiments show that adhesion occurs even at the interface between two bodies in static contact. When the bodies are pulled apart, material transfer can take place from the cohesively weaker material to the stronger one. If one body moves relative to the surface of the other, a transfer film forms on the surface of the cohesively stronger material. The amount of transferred material depends on the strength of adhesion bonds that, in turn, is governed by the electronic structure of the mating materials, their metallurgical compatibility, (i.e., the tendency to form solid solutions or intermetallic compounds with each other) as well as crystal structure and orientation. Also, the adhesion is a function of sliding conditions and other factors mentioned earlier.

The phenomenon of *friction transfer* is observed practically in all materials (metals, ceramics, and polymers) and their combinations. The question arises as to whether the tribological behavior of the friction pair is affected by this transfer. If so, this is then the case of adhesive wear whereby, as a result, material transfer may be significantly different. If small particles of micrometer size are transferred from one surface to the other, then the changes in the wear rate are insignificant.

Under certain conditions, the situations may occur when a thin film of soft material is transferred onto the hard mating surface, e.g., bronze on steel, lead on steel, steel or aluminum alloy on chromium coating, polymer on metal. The results of such a transfer may be as follows: If the transferred bronze film is carried away from the steel surface and a new surface is formed, the wear rate is increasing. If the film is held in place, the friction occurs between the similar materials and the seizure may take place. The spreading of a polymer on a steel shaft sharply increases the friction force, but is not followed by significant changes in wear.

It is known that under certain conditions the hard material can be transferred to the soft surface. For example, steel is transferred to bronze, bronze is transferred to polymer. The transferred hard particles are embedded in soft material and serve as an abrasive that scratches the parent material.

3.2.6 Prow Formation

The initial sliding of most clean contact metals is characterized by a severe adhesive process called prow formation.[26] For contacts of the same material, there is net metal transfer from the part with the larger surface involved in sliding to the smaller surface, e.g., from jaw to blade in a disconnect switch contact assembly. A lump of severely work-hardened metal (the prow) builds up and wears the flat by continuous plastic shearing or cutting, whereas the rider does not wear. Prows are lost from the rider by back-transfer to the flat or as loose debris. If the rider always traverses virgin metal, prow formation continues indefinitely. This is shown schematically in Figure 3.21.

When contact members of the same material are identical in size and shape, the initial prow can come from either member. However, after transfer occurs, the receptor then becomes the rider and the opposing surface wears. With dissimilar metals, prows form even when the flat is harder than the rider, provided this difference is not greater than a factor of about three. Friction and contact resistance characteristics of the system are determined by the prow metal. Prow formation occurs with gold, silver, copper, copper alloys, lead, aluminum, iron, titanium, and many other metals. Metals that do not work harden, such as indium at room temperature, fail to form prows. This is because the prow must become harder than the flat by the work-hardening process to be able to wear the flat, particularly by cutting.

Prow formation and delamination (see below) are fundamentally different mechanisms and are mutually exclusive. Prow formation occurs early in sliding and is a form of metal transfer, whereas delamination wear occurs only after many passes; transfer, therefore, plays no part in delamination.

3.2.7 Fatigue Wear

Fatigue is known to be a change in the material state due to repeated (cyclic) stressing that results in progressive fracture. Its characteristic feature is accumulation of irreversible changes that give rise to the generation and development of cracks. A similar process takes place at the friction contact

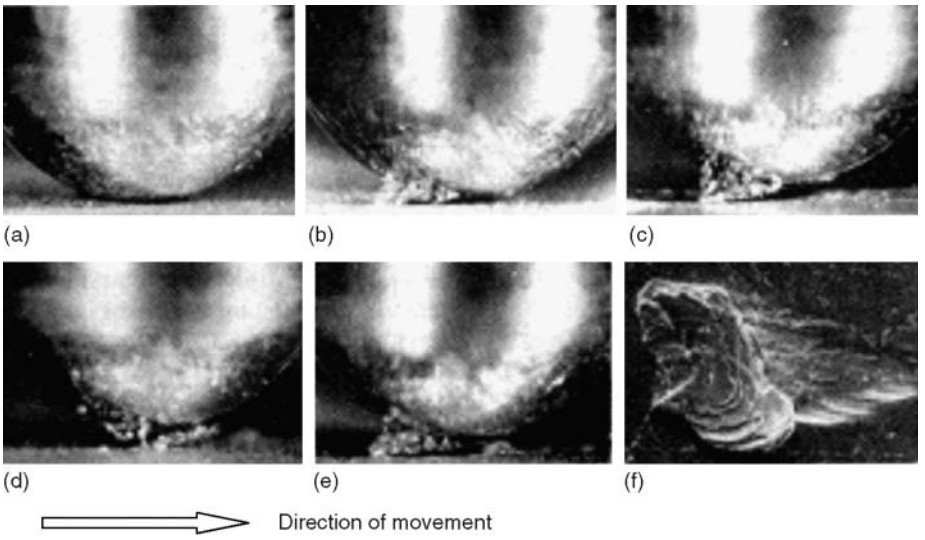

FIGURE 3.21 Prow formation mechanism in sliding rider-on-flat gold contact at 500 g load: (a) start of run; (b) well-developed prow, (c) and (d) loss of portion of prow by back transfer to flat; (e) newly formed prow consisting of overlapping thin layers of metal back-transferred; (f) SEM image of the prow debris. (From Antler, M., *Electrical contacts. Principles and Applications*, P. G. Slade, Ed. Marcel Dekker, New York, 309–402, 1999. With permission.)

that accompanies nearly all the wear modes. A friction contact undergoes the cyclic stressing during rolling and reciprocal sliding. In addition, each asperity of the friction surface is subjected to a sequential loading by the counterface asperities. As a consequence, in the surface and subsurface regions, two varying stress fields of different strengths are generated. These fields are responsible for material fatigue in these regions, leading to the generation and propagation of cracks and the formation of wear particles. This process is termed *friction fatigue*.

Unlike bulk fatigue, friction fatigue is confined to surface and subsurface regions only. The loss of material from solid surfaces due to friction fatigue is referred to as *fatigue wear*. This definition may be tautological, but it is useful in situations when the stress is accentuated as the cause and consequence of the wear process. It has been known that the fatigue cracks are initiated at the points where the maximum tangential stress or the tensile strain takes place. Theoretical and experimental studies show that, under contact loading, the maximum tangential stress position is dependent on the friction coefficient. With a low friction coefficient, the point of maximal shear stress is located below the surface ($\mu < 0.3$). When the friction coefficient increases ($\mu > 0.3$), the point of maximal shear strength emerges to the surface. On the other hand, if a solid is subjected to combined normal and tangential loading, the surface and subsurface regions appear where the tensile strain occurs. Therefore, cracks may be nucleated in the surface and/or below it.

Defects, such as scratches, dents, marks, and pits on the surface, as well as dislocations, impurities, voids, cavities, and carbides in the subsurface region, are responsible for the stress concentration and contribute to the initiation of the fatigue cracks.[24,32] Both surface and subsurface cracks that are generated as a result of repeated stressing gradually grow, coalesce, cross each other, and exit to the surface. After a certain number of cyclic loads, the wear particles, including spalls, appear on the surface (Figure 3.22).

Fatigue wear rate is affected by a number of factors, such as physical, mechanical, and chemical properties of the solid surface, lubricant (if present), environment, surface quality, temperature, etc. For example, it has been shown that the fatigue crack growth is very sensitive to the humidity in the atmosphere.

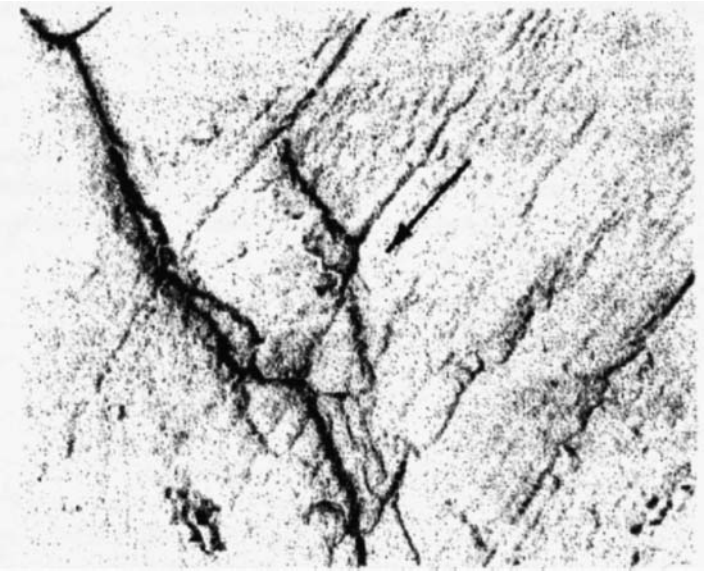

FIGURE 3.22 Fatigue cracks on the worn surface of electroplating chromium worked against bronze brush under light electric current in mineral oil (an arrow is pointed along the sliding direction.)

3.2.8 Corrosive Wear

Corrosion is defined as a failure of a solid due to its chemical or electrochemical interactions with the environment. Corrosive wear occurs as a result of the formation of corrosion products at the friction surfaces that exert significant effect on the wear behavior. Strictly speaking, the corrosive wear is not a separate wear mode because, in some situations, the contribution of the corrosion mechanism to wear is so large that the use of this term is justified.

Corrosive wear depends on many factors, such as chemical composition(s) and microstructures of the contact surfaces; rigidity and porosity of the contact surfaces, pressure or absence of surface cracks and grain boundaries; degree to which the contact surface has been work-hardened; state of stress in the surface; electrical potentials and current paths between contacting surfaces; temperature and pressure in the contact zone; and the reactivity of the medium interposed between contact surfaces. For example, higher temperatures are favorable to chemical reactions that result in corrosion.

It has often been argued that the term *corrosive wear* should be reserved for the severe wear in a "hostile" environment, whereas the mild wear in a relatively normal environment should be termed *oxidative wear*. Oxidative wear occurs when an oxide is formed on the friction surface. This film may be generated by reaction of a metallic surface with oxygen in air or lubricant; it can significantly affect friction and wear. On the other hand, the extensive deformation of the metal and the high contact temperature generated by friction significantly affect the rate of oxidation. The role of the oxide film is dual. First, the film protects the friction surface from severe wear and seizure, thereby reducing the wear process to failure of the film that recovers anew. The oxide film prevents welding of virgin surfaces that would otherwise occur in vacuum. Second, the oxidative wear products have high hardness and initiate the abrasive wear.

During the oxidative wear deformation, adsorption and chemical reactions occur simultaneously and are interrelated. Deformation activates the finest surface layers, enhancing their susceptibility to adsorption, diffusion, and chemical reactions. The latter processes, in turn, exert a profound effect on plastic strain. The layer formed as a result of localized plastic deformation contains numerous microstructure defects and areas of high dislocation density (in metals and ceramics). Under normal conditions of boundary lubrication, the thickness of the activated layer is about 100–1,000 μm. This layer interacts with a limited amount of oxygen dissolved in lubricant and transforms into an oxide film of uniform thickness strongly bonded to the base metal.

The main features of oxidative wear are: absence of any fracture in the base material, localization of fracture in the finest surface layers generated during friction, and the dynamic equilibrium of mechanical and chemical processes responsible for the generation and failure of oxide films.

Under certain conditions, the equilibrium may be disturbed, resulting in substantial changes in the wear rate intensity. In the classical work of Welsh on steels, the wear rate-load dependence demonstrates two mild–severe–mild wear-rate transitions (Figure 3.23). The first transition to severe wear occurs as the load attains the level P_1. The wear rate abruptly increases by more than two orders of magnitude. However, the increase in the local temperature results in the transformation of the surface material to martensite that supports the surface oxide. At load P_2, the tribosystem suddenly returns to the mild wear mode. The further friction with load up to value P^2 is accompanied by severe wear. Figure 3.24 shows an example of corrosion wear damage in a silver-plated disconnect switch.

3.2.9 Fretting Wear

The term *fretting* refers to small oscillatory motion between two solid surfaces in contact. The amplitude of the motion often falls in the range 1–100 μm. Wear occurring at this motion is referred to as *fretting wear*. Fretting wear occurs between components that are not intended to

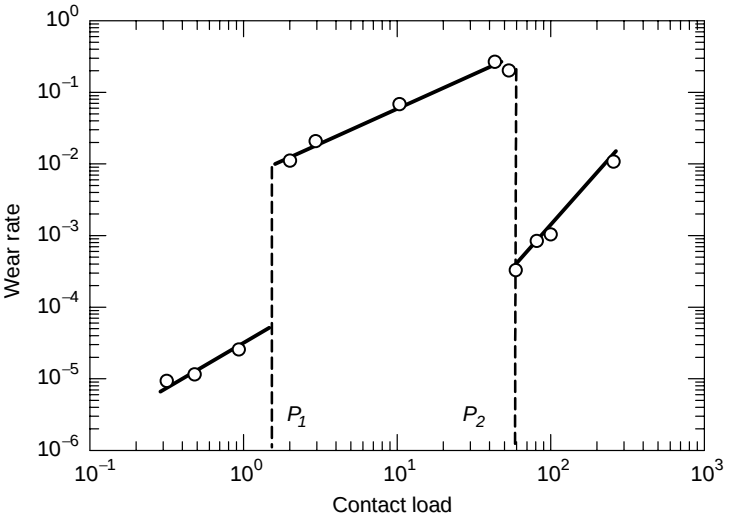

FIGURE 3.23 The variation of wear rate with load for a 0.5% plain carbon steel pinsliding at 1 m/s in air against tool steel in pin-on-ring test. (From Welseh, N. C., Phil. Trans. Roy. Soc. 257, 31–70, 1965.)

move, e.g., mechanical fasteners, electrical connectors, etc. This wear generally originates in conjunction with the operation of vibrating machinery or cyclic stressing of the stationary contact.[34]

Depending upon the nature of the mechanical and environmental factors, two general types of fretting wear are recognized. The term *fretting fatigue* is used when fretting damage is caused by cyclic loading that initiates the surface fatigue cracks and eventually leads to catastrophic failure.

The process in which chemical interaction is predominant is termed *fretting corrosion.* Usually, both types of fretting wear occur simultaneously. The cyclic microdisplacements break down the protective (e.g., oxide) film covering the metal. The exposed metal oxidizes easily and the oxidation products act as an abrasive, causing surface damage.

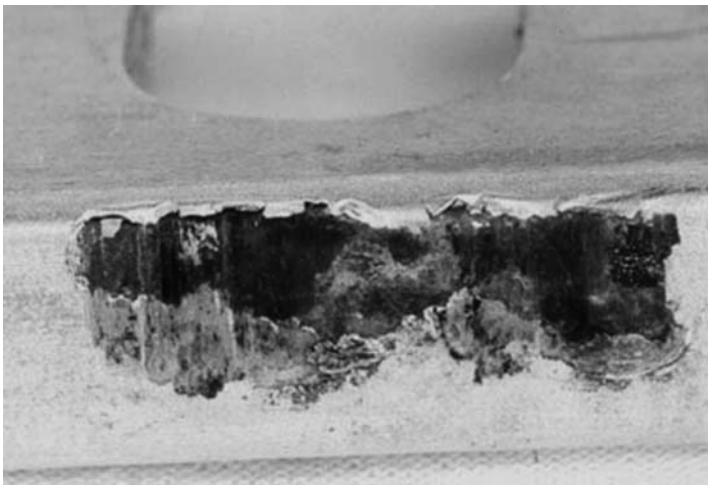

FIGURE 3.24 Corrosion wear damage in sliver-plated disconnect switch blade. (Courtesy of RusCan, www.ruscan.com.)

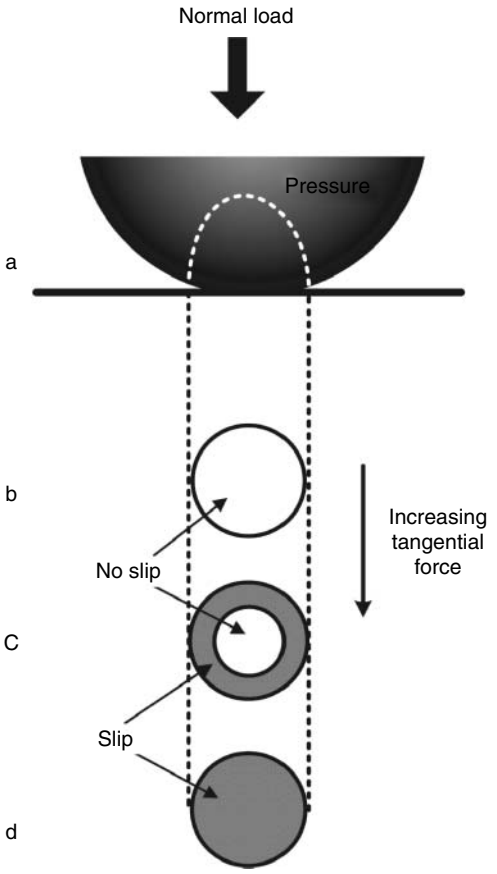

FIGURE 3.25 The distribution of elastic normal stress beneath a sphere pressed against a flat (a). Views of the contact with increasing the applied cyclic tangential force are shown in (b–d). (Adapted from Hutchings, I. M., *Tribology: Friction and Wear of Engineering Materials*, Edward Arnoid, London, 1992. With permission.)

The sphere-on-flat contact, as seen in Figure 3.25, is used to describe fretting fatigue. If contact is elastic and bears normal load, the contact pressure is distributed according to the Hertz equation with a maximum at the center of the contact circle and a zero value at the boundary. Tangential force increases the contact surface traction, which has a minimum at the center of the contact and tends to infinity at the edges. As a result, some displacement may occur in the vicinity of the edges.

The contact zone is divided into two regions: a central area ("stick zone"), inside which the static friction exceeds the traction and there is no slide, and an annular zone (the shaded regions in Figure 3.25) in which microslip occurs ("slip zone"). The stick-slip boundary circle shrinks with an increasing tangential force until it reaches zero at some value of critical force. Thus, four different regimes of contact behavior may be pointed out: complete sticking, mixed sliding and microslip, gross slip, and reciprocal sliding.

The most severe fretting fatigue occurs in the slip zone and is affected by a number of factors, including the amplitude of fretting motion. The fretting fatigue causes nucleation and subsequent crack growth. Therefore, the microstructure and properties of materials profoundly affect fretting wear. As with other wear modes, environment and temperature extensively affect fretting, both separately and synergistically. When chemical attack becomes important, this is a clear indication that fretting corrosion occurred. In air, the oxide that forms on fretting surfaces can lubricate the

surfaces and retard the progress of damage at temperatures higher than ambient. Not all oxides, however, are beneficial; their effects will depend on the materials, oxide thickness, contact conditions, and the fretting environment.

A complex interplay of mechanical and chemical phenomena in fretting, along with a great number of factors determining the rate of these phenomena, makes it difficult to develop adequate measures to prevent fretting. There are several means of reducing the fretting wear, such as decreasing the amplitude of microdisplacements, increasing the abrasion resistance of mating materials, enhancing the corrosion resistance to environment, using special devices for suppressing vibrations, etc.

3.2.10 Delamination

Delamination wear occurs as a result of repeated sliding and is a contributing mechanism to the loss of metal. The mechanisms of delamination wear involve the initiation of subsurface cracks that propagate parallel to the surface and lead to detachment of flakes 0.1–20 μm thick. These cracks are thought to initiate at voids and vacancies developed from dislocation pile-ups bellow the surface layer; at a critical length, the cracks shear to the surface.[35]

Delamination theory of wear was developed by Suh and his colleagues and was extensively discussed by tribologists since 1974.[36–40] One evident reason for the popularity of the theory is the frequent observation of wear debris in the form of flakes. The formula relating the depth of dislocations pile-up under the contact surface was proposed by Suh:

$$h = \frac{Gb}{4\pi(1-\nu)\sigma_f}, \tag{3.27}$$

where h is the depth, G is the shear modulus, b is the Burgers vector, σ_f is the stress preventing the dislocation motion, and υ is Poisson's ratio.

The delamination theory was heavily criticized by materials scientists because the behavior of the contact layer is strongly affected by plastic deformation, shear, and phase transformations in materials.[41,42]

As it stands, the delamination theory of wear is applicable only for the case of low-speed sliding, where the temperature rise at the contacting surface is so low that diffusion and phase transformation are not involved in the wear process. Figure 3.26 shows a schematic of delamination wear formation and an example of delamination damage in a silver-plated copper contact.

Rigney[43] and Alexeev and Dobychin[44] have presented the most detailed analysis of the contact surface layer behavior from the viewpoints of materials science and contact mechanics. The phenomenon of delamination appears much more complicated when other factors, in addition to dislocation transport in the continuum material near the surface boundary, are taken into consideration. One typical example of Rigney's[43] experiments is illustrated by Figure 3.27. The structure of the copper surface layer appears significantly more complicated than a continuum; certainly the presence of grain boundaries, local shear, and phase transformations at the temperature rise make the picture very difficult to analyze in terms of dislocation transport only. Moreover, fatigue is a major factor when examining this problem from a materials science perspective.

Kuhlmann-Wilsdorf has tried to combine the original simplified dislocation models with the comprehensive materials science approach. She has considered fundamentals of dislocation transport under the complex conditions of phase transformations induced by the contact heating. Phase transformation (amorphization, in particular) was considered as one of the important processes affecting the state and structure of a material under conditions of friction shear and cyclic effects of mechanical loading that are very common in electrical contacts.[39,40] It was found that shear strain in the contacting metal foils (Ag and Cu films) results in the amorphization and further formation of crystalline alloys. Shearing of the foil stacks causes a proliferation of phase boundary area between

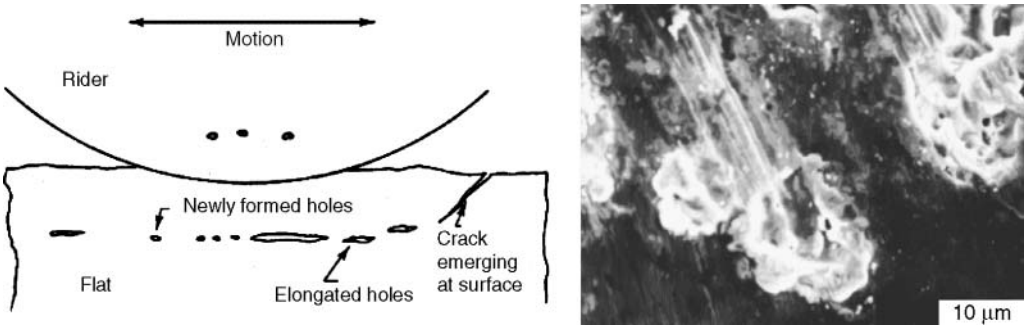

FIGURE 3.26 Schematic of delamination wear formation and an example of delamination wear damage in silver-plated copper contacts.

the contacting metals. As a result, the phase boundary spacing decreases until the free energy of the crystalline mixture exceeds the free energy of the amorphous phase. Then, the phase boundary breaks down and releases a multitude of dislocations. Further formation of a crystalline alloy of two metals can occur through the solid state nucleation on the remnant crystalline microvolumes. Figure 3.28 illustrates the phase boundary evolution at shear that promotes the above mentioned phase transitions.

The model of delamination is one example of the attractive power of clear physical explanations of complex phenomena at the boundary of materials science and mechanics. Even though it is not applicable to most of the numerous cases of wear, it has nonetheless pushed a great impulse to studies in structural transformations of materials in friction. The field of electrical contacts that are affected by mechanical, electrical, and heat phenomena continues to be a very fruitful area for

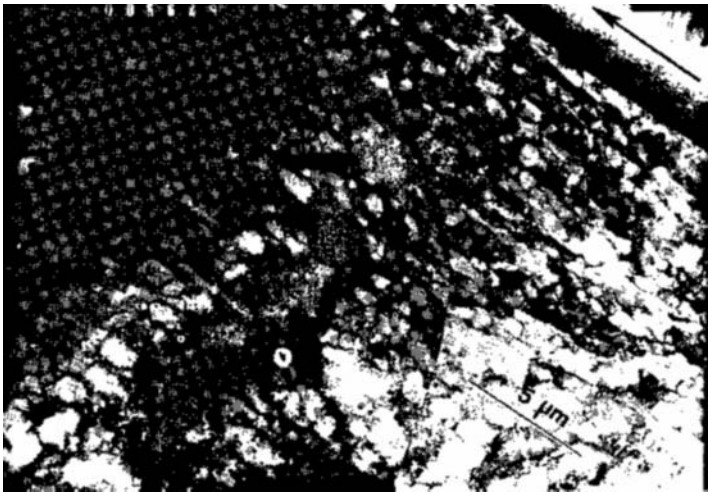

FIGURE 3.27 TEM micrograph showing part of a longitudinal section of an OFHC copper wear sample block (block-on-ring geometry). The deformation substructure varies with depth below the sliding interface. The curved line is a grain boundary; it has bent in the sliding direction. Arrow shows direction of motion of counterface. Dark material near arrow is mechanically mixed material. Experimental parameters: normal load, 67 N (6.8 kg); 100 revolutions of type 440C steel ring; 12 m total sliding distance; 1 cm/s sliding speed; argon atmosphere. (From Rigney, D. A., *Tribology in the USA and Former Soviet Union*, Belyi, V. A. Ludema, K. Myshkin, N. K. Eds. 53–65, Allerton Press, New York, 1994. With permission.)

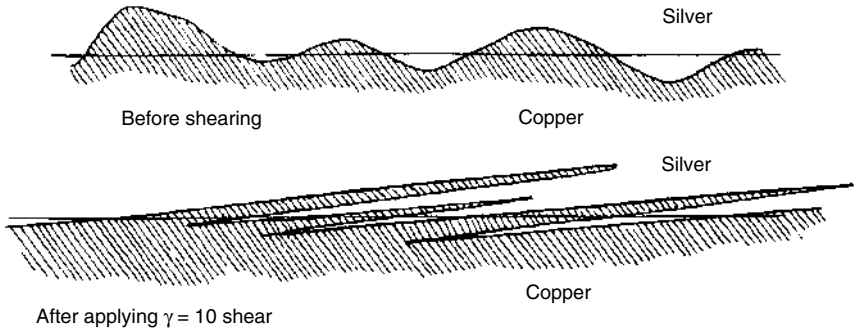

FIGURE 3.28 Semi-schematic illustration of the geometrical proliferation of interface boundaries through shearing of foil stacks in the Bridgman apparatus. it is caused by an initial mild waviness of the foils relative to the shearing plain. (From Kuhlmann-Wilsdorf, D., *Wear*, 200, 8–29, 1996. With permission.)

applications of dislocation-based mechanisms, especially in view of the increasing interest in microscale and nanoscale effects.

3.2.11 Erosion

In a broad sense, erosion is a process of damage to solid surfaces due to the action of the environment. In tribology, the term is used in a narrow sense as a wear mode involving moving streams of gases, liquids, or solids. According to ASTM Standard G 40, *erosion* is defined as the progressive loss of original material from a solid surface due to mechanical interaction between that surface and a fluid or impinging liquid or solid particles. However, because of the broad scope of this term, it is recommended that it normally be qualified to indicate the relevant mechanism or context, e.g., cavitation erosion, liquid impingement erosion, etc.

In the case of the onset of sparking or arcing, ejection of the contact material in the arc discharge takes place. The process may intensify the wear by an order of magnitude.[1,2] Damage to material resulting from electrical discharge is often classified as a variety of erosion, specifically, *electroerosion wear*. An illustration of a surface that has experienced this mode of wear is shown in Figure 3.29.

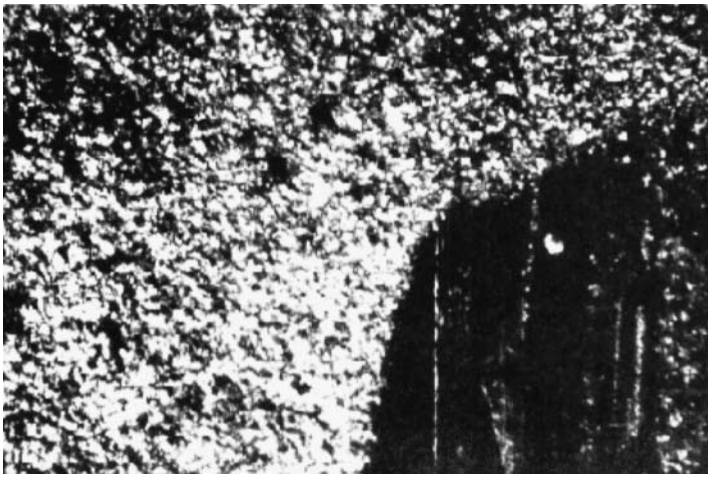

FIGURE 3.29 Typical surface of sliding electrical contact after electroerosive wear.

3.2.12 Combined Wear Modes

The wear modes described above do not exhaust the subject; their rigorous classification is absent to the present day because wear is a complex process involving a diverse array of elementary mechanisms. Therefore, identifying the "first features," according to which the wear may be classified, is rather difficult. It is conceivable that this is why many modes are encountered in the literature, e.g., deformation wear, impact wear, mechanical wear, metallic wear, polishing wear, rolling contact wear, thermal wear, etc. It is clear, however, that in real situations, a tribosystem with a single wear mode is a rare exception.

It is often found that the combined action of several wear mechanisms may be present. It is a matter of general experience that the shapes of wear particles and the appearance of worn surfaces are fair indications of the wear mode. However, "collaboration" of adhesion, plastic deformation, fatigue, delamination, heating, and current passage may take place. Even though these individual mechanisms would be studied extensively, their interactions with one another depend largely on the operating conditions, structural changes, and modifications of the physical and chemical properties of the wearing surface. This fact is very important in electrical contacts, where current passage can affect all of the basic wear mechanisms.

3.3 LUBRICATION

Lubrication is defined as a process that reduces friction and wear by applying a lubricating material. Gaseous, liquid, or solid materials may act as lubricants if they possess definite properties discussed below. This definition, however, should be made somewhat more specific. There are situations where it is more important to maintain friction (not wear) as unchanged rather than to reduce it. This is to reduce the vibration of the guides of cutting tools, to maintain a uniform feed of strips of rolling metals or to eliminate brake chatter.

Lubrication performs other functions, such as preventing the overheating of rubbing surfaces and/or protecting them against corrosion. Lubrication of rubbing surfaces radically alters the mechanism of friction. The viscosity and the thickness of the lubricating film as well as the friction operation conditions determine the extent of this change. As an example, consider a lubricated sliding bearing and the changes in the friction coefficient with the dimensionless parameter $\eta v/p$, where η is viscosity, v is the speed of rotation of the shaft, and p is the linear load on the bearing (Figure 3.30).

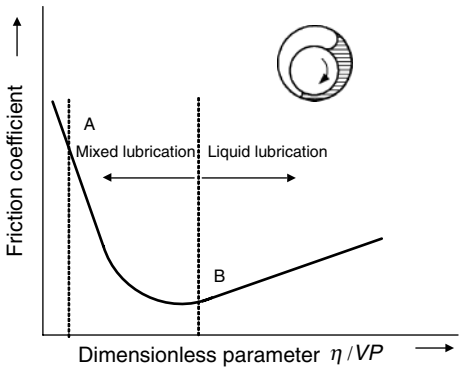

FIGURE 3.30 Stribeck curve describing relation between friction coefficient μ and dimensionless parameter $\eta V/P$.

The lubrication is assumed to be complete when the mating surfaces are completely separated and all direct contact between them is eliminated. This is unacceptable for electrical sliding contacts; therefore, only the lubrication regimes providing the direct contact of mating surfaces are considered. To more rigorously determine the lubricating conditions, the parameter Λ is frequently used as a measure of the lubricating layer thickness, h, with respect to the effective roughness of the contacting surfaces.

Because the film is thin ($1 < \Lambda < 3$), it becomes incapable of keeping the contacting surfaces apart. The conditions of mixed (semiliquid) lubrication set in with the appearance of the hydrodynamic effect (the oil wedge) in the individual areas of the contact, whereas in the other areas, metallic contact between asperities may be formed where the surfaces are separated by a very thin film (<0.1 μm). Viscosity ceases to be a significant factor in the friction processes and other characteristics emerge as the important ones. It is believed that under these conditions boundary lubrication occurs that is most effectively manifested when $\Lambda < 1$.

The term "boundary lubrication" was introduced into scientific use by the famous English researcher William Hardy (1864–1934), who laid down the foundations for this essential part of tribology. Boundary lubrication is one of the most common features to occur during friction in metals because these are, as a rule, coated with the absorbed films. This regime of lubrication is often used in sliding electrical contacts.

An effective boundary film on the friction surface can only be produced by few lubricants. For example, pure mineral oils are practically not suitable for the purpose. Therefore, small amounts of active organic substances must be added to boost their capacity to produce boundary films. The adhesion of boundary films to metals is governed by the electron structure of adsorbed molecules. Polar molecules (i.e., the molecules with active endgroups) and molecules capable of chemically reacting with the metallic surfaces show the most pronounced tendency to adhere to these surfaces. The adsorbed molecules arrange perpendicularly to the surface and produce a film structure similar to wool pile. When adsorbed, molecules with similar groups at their ends (esters, for example) arrange along the surface, producing a multimolecular crystal-like layer. Solid greases, such as graphite, can produce boundary films when they are rubbed in. As a result, a film with a laminar lattice structure appears on the friction surface.

During friction, the boundary films perform several essential functions. First, they prevent direct contact between the asperities and protect the surface layers of rubbing bodies, thereby strongly reducing their adhesion. Due to their specific structures, they possess anisotropic mechanical characteristics, as manifested by their low shear strength combined with a strong resistance to normal compression. The load-carrying capacity of a boundary film may reach several GPa.

These factors allow visualization of a simplified pattern of friction during boundary lubrication. A fine boundary film on the rough surfaces replicates their topography. Therefore, the contact is established through the lubricant rather than at the individual spots. Because the lubricating film is thin, it does not inhibit elastic or plastic deformation of contacting bodies. The most essential consequence is that shear localizes within the film that, as noted above, shows little resistance to shear, thus reducing friction. William Hardy noted that the coefficient of friction of glass on glass ($\mu = 1$) reduces to about 0.1 when their rubbing surfaces are coated with a fine film of stearic acid.

Also, strong plastic deformation or elevated temperatures can destroy the lubricating film covering the contact spots. As a result, the adhesion of contacting bodies becomes stronger and the resistance to sliding and wear increases. The fact that the boundary film is unable to prevent deformation of rubbing bodies makes their wear unavoidable. The use of an unsuitable lubricant can provoke corrosion.

In some cases, chemical reactions between ambient medium, lubricant, and metal can result in the formation of nonconductive polymer-like films. The phenomenon of friction polymerization was discovered by Hermance and Egan.[45] They suggested that polymer precursors, which can be virtually any organic compound containing more than one carbon atom, are strongly adsorbed on

the sliding surfaces. Due to severe mechanical strain and the catalytic activity of the metal, the compounds react and form high molecular weight, cross-linked solids. Hydrogen and low molecular weight species split off from hydrocarbons; however, halogenated compounds also produce polymers.

Friction polymer films demonstrate a negative effect on metallic contact. Catalysis can continue even when polymers are dispersed, as well as when the reaction involves condensed phases of simple molecules or complex lubricants.[46] Any real environment contains enough organic material for friction polymers to form in sufficient quantity to cause electrical problems at some conditions with palladium–palladium contacts. Studies of relays[47] indicate that palladium oxides can be formed on palladium–palladium contact surfaces operating in air in inactive (zero discharge) circuits when the level of organic pollutants is very low. Contact resistance increases due to the reaction product.

3.4 CURRENT TRENDS IN TRIBOLOGY

Tribology is a multidisciplinary science and technology and is interconnected with most of the natural sciences. Modern tribology derives from the mainstream of mechanics and uses its principles and methods to encompass advances in physics, chemistry, and materials science. The most recent advances in surface science were made in the field of thin films, coatings, and interface phenomena.

Presently, there is a strong trend towards a transition from macro to micro and nanoscale[12,48] that gives a new insight into the basic problems of tribology, e.g., correlation of deformation and adhesion mechanisms of friction. A new area of tribology, termed micro and nanotribology has become a basis for development of new classes of mechanical devices—microelectromechanical systems (MEMS), defined as miniature devices that combine the functions of a sensor, signal transducer, and service unit. Nanolithography has made possible the manufacture of MEMS films with dimensions of a few micrometers thick and dozens of micrometers long. An example of such a system is a microscopic drive unit made of silicon shown in Figure 3.31.

Friction, lubrication, and wear in microsystems occur on very smooth contact areas with dimensions comparable with the size of the system. In these systems, adhesion and surface forces are very important and call for novel solutions to the tribological problems. For instance, monolayers of special fluorocarbon liquids are applied to provide low friction and protect against wear. Because silicon is mainly used for MEMS, its poor lubrication ability, low mechanical

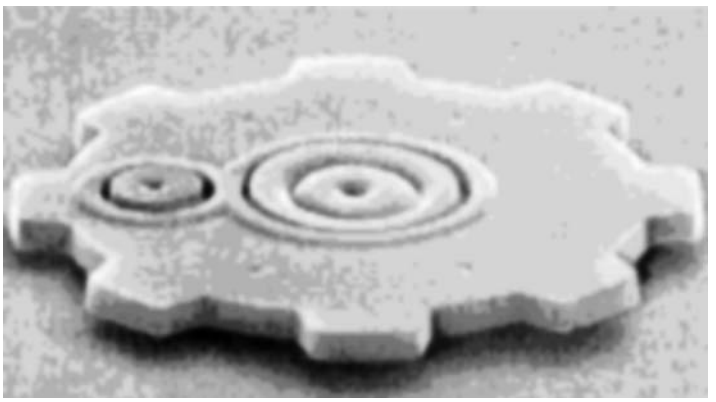

FIGURE 3.31 Silicon microdrive unit with a diameter of 50 μm.

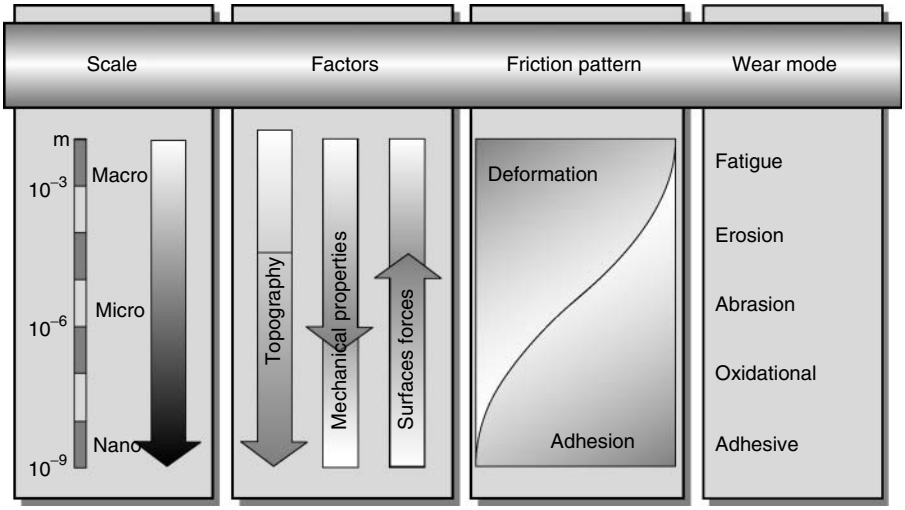

FIGURE 3.32 Combination of factors effecting friction and wear.

strength, and tendency to react with oxygen and hydrogen prompted the development of new methods of surface modification and fabrication of extremely thin coatings.

The trends in tribology from macro to nano are presented in Figure 3.32. The factors include mechanical properties of the materials in contact, surface topography, atomic and molecular force interactions, and heat dissipation in the contact.

Mechanical properties of contact materials are scale-dependent. Therefore, parameters such as Young's modulus and hardness can differ not only in magnitude, but also in their physical interpretation. Scaling from macro to nanoscale can be related to the transition from bulk properties of material to surface-layer properties, local Young's modulus, and nanoindentation data. Scanning probe microscopy offers an extraordinary potential for obtaining new promising results on the mechanical properties of the nanoscale systems. The basic problem, however, lies in the interpretation of experimental data and their self-affinity to the scale changes.

Development of new tools, such as 3D-contact and noncontact profilometers, atomic force microscopes, and new optic and ultrasonic instruments contributed to significant advancements in the surface topography analysis. Computer simulations of the contacting bodies make visualization of nanoscale processes possible. Analysis of texture has become a new successful trend in the description of surface topography.

The last century was marked as the century where extensive discussions were devoted to the subject of surface forces as a source of adhesion and their correlation to macroscopic phenomena of friction, lubrication, and wear. Today, this problem has reached the stage of practical importance and necessity in the design and development of microscopic mechanical systems.

It is generally assumed that the heat generation in friction results from the material deformation at the real contact spots. Also, heat sources may be associated with the origin and fracture of adhesion bonds. The current state of knowledge indicates that the bulk, surface, and flash temperatures are additive terms describing friction processes occurring in contact at different scale levels. Progress in this area can be achieved if the atomic and molecular levels of energy dissipation are considered.

Bearing in mind the practical importance of tribology to modern engineering, a very important problem of bridging the gap between the nano, micro and macroscales in tribology must be solved.

Inventions in MEMS and in the ever-growing areas of precision engineering and memory storage require new levels of research and applications. The importance of each step in the transition from nano to macro depends on a particular practical problem. The most important task of tribology is probably to determine what scale level and available experience should be used to satisfactory solve a particular problem. Tribological education and technology transfer can dramatically improve the efficiency of different classes of machines and devices while further research in micro and nanoscience are required to meet the challenges of the new technological era. Electrical contact, as shown below, is one of the areas of new applications of micro and nanotribology.

4 Contact Materials

4.1 METALLIC CONTACT MATERIALS

4.1.1 Properties of Contact Materials

In ordinary engineering usage, a solid conductor is a material of high conductivity. The electrical conductivity of metallic conductors is on the order of 10^6–10^8 S m^{-1} at ambient temperature and can be as high as 10^{11}–10^{12} S m^{-1} at temperatures in the vicinity of 0 K. Solid metallic conductors can be generally classified into two groups according to their applications:

- Technically pure metals, the most common and widely used of which are Cu and Al, sometimes alloyed with other metals to improve their mechanical properties.
- Alloys used as conductors with particular properties such as wear resistance and low friction, the most common materials being bronzes, brasses and some aluminum alloys.

Practical application of solid metallic conductors requires a detailed knowledge of various properties of conductor materials, such as electrical, thermal, chemical, mechanical, and tribological characteristics. This is because in service solid conductors are subjected to different mechanical and thermal stresses as well as environmental effects. Table 4.1 lists physical–mechanical and electrical characteristics of the metals used to fabricate contacts.

The metallic materials used for electrical contacts span over a wide rage. Among the listed materials, copper, aluminum, and their alloys are most widely used in heavy-current contacts while noble metals and their alloys are most widely used in low-current contacts. Pure noble metals are used mainly as coatings (see Section 4.2). Table 4.2 represents the basic physical–mechanical characteristics of the contact alloys applied most often in low-current electrical contacts.

The basic properties and applications of main contact materials are briefly discussed below, whereas the properties of copper and aluminum are summarized in Table 4.3.

4.1.1.1 Copper

Copper is a soft, malleable, and ductile metal with a high conductivity and an excellent weldability and solderability. By rolling and drawing, a variety of electrical products such as wires, sheets, tubes, shaped bars, and flat busbars can be manufactured. The high-conductivity copper useful for electrical applications must be produced by careful refining treatments such as electrolytic refining which removes Ag, Au, As, Sb, and other impurities. The most common copper used in the power industry is tough-pitch copper ETP or C11000 made by the electrolytic refining of copper.

The principal shortcoming of ETP copper is embrittlement to which it is subjected when heated in hydrogen to temperatures of 370°C or more. This results from the presence of oxygen in the metal which reacts with hydrogen to form steam, leading to internal cracking. The solution to this problem is to use copper with substantially lower oxygen content. While phosphorus is an effective

TABLE 4.1
Metals Used in Electrical Contacts and Their Characteristics

Material	Density (g/cm^3)	ρ (10^{-8} Ωm)	λ (W/(m°C))	H_B	α (°C^{-1})	E (10^5 MPa)	Temperature (°C)		Voltage (V)	
							Softening	Melting	Softening	Melting
Platinum	21.4	11.7	70	40	0.0038	1.54	540	1,773	0.25	0.65
Gold	19.3	2.3	310	20	0.004	0.84	100	1,063	0.08	0.43
Iridium	22.4	5.5	60	170	0.0039	5.3	—	2,450	—	—
Palladium	12.0	10.8	70	32	0.0033	1.2	—	1,554	—	0.57
Silver	10.5	1.65	418	25	0.004	0.75	180	960	0.09	0.37
Tungsten	19.3	5.5	190	350	0.005	3.5	1000	3,390	0.4	1.1
Copper	8.9	1.75	380	35	0.004	1.2	190	1,083	0.12	0.43
Graphite	1.8	700	160	35	0.0013	0.03	—	3,650	2	5
Aluminum	2.7	2.9	210	27	0.004	0.72	150	657	0.1	0.3
Gallium	5.9	53.4	33	—	0.00396	—	—	29.75	—	—
Cadmium	8.6	7.5	90	16	0.004	0.6	—	321	—	0.15
Cobalt	7.87	9.7	69	125	0.0066	2.1	—	1,495	—	—
Molybdenum	10.0	5.8	140	250	0.0045	3.5	900	2,620	0.25	0.75
Nickel	8.8	8	70	70	0.005	2.1	520	1,452	0.22	0.65
Tin	7.3	12	64	4	0.0045	0.4	100	232	—	—
Lead	11.3	21	35	4	0.004	0.16	200	327	0.12	0.19
Zinc	7.1	6.1	110	33	0.0037	0.84	170	419	0.1	0.17
Rhodium	12.4	4.5	88	55	0.0043	3.0	1,966	1,966	—	—
Rhenium	21.0	9.71	75	250	0.007	4.7	1,400	3,170	—	—
Iron	7.8	10	60	67	0.0065	2.0	500	1,540	0.21	0.6
Manganese	7.46	164	—	—	—	—	—	1,245	—	—
Chrome	7.0	20	67	90	0.002	9.0	—	1,615	—	—
Mercury	13.55	94	9	—	0.0092	—	—	−38.7	—	—
Tantalum	16.6	14	545	40	0.003	1.9	800	2,996	0.3	1.0
Ruthenium	11.56	7.16	—	193	0.0046	4.2	—	2,500	—	—
Osmium	22.5	9.66	—	—	0.0042	5.6	—	2,700	—	—
Indium	7.3	8.2	24	1	0.0049	—	—	156	—	—
Hafnium	1.3	44	—	—	—	—	—	2,222	—	—
Cadmium oxide	0.69	600	—	—	—	—	—	—	—	—

ρ, specific electrical resistivity; λ, thermal conductivity; H_B, Brinell hardness; α, temperature coefficient of resistivity; E, elastic modulus.

TABLE 4.2
Characteristics of Alloys for Low-Current Contacts

Alloy Composition (%)	Density (kg/m^3)	ρ (10^{-8} Ωm)	α (°C^{-1})	λ (W/(m°C))	E (10^5 MPa)	H_B	T_m (°C)
Ag–Cu 97/3	10,500	1.8	0.0035	390	—	40	900
Ag–Cu 75/25	10,100	2.0	—	325		82	779
Ag–Cu 50/50	9,700	2.1	0.003	340	—	70	730
Ag–Au 90/10	11,400	3.6	0.0016	196	—	23	—
Ag–Au 20/80	16,500	9.4	0.009	—	—	25	1,035
Ag–Au–Pd 40/30/30	12,900	22	—	34	—	65	—
Ag–Cd 95/5	10,450	2.95	0.004	—	—	35	940
Ag–Cd 80/20	10,100	5.7	0.002	—	—	60	875
Ag–Pd 95/5	10,500	3.8	—	—	0.910	26	—
Ag–Pd 40/60	11,400	42	0.00025	20	1.250	—	1,330
Ag–Pt 95/5	10,880	4.65	0.0023	30	—	99	—
Ag–Pt 70/30	12,540	20	0.0002	—	—	170	—
Ag–Ni 90/10	10,100	1.8	0.0035	—	—	90	961
Ag–Ni 60/40	9,500	2.7	0.002	310	—	115	961
Au–Ni 95/5	18,300	12.3	0.0007	—	—	100	—
Au–Pd 99/1	19,300	3.0	0.004	—	—	20	—
Au–Pt 93/7	19,600	10.2	—	70	—	40	1,080
Au–Pt 70/30	19,900	34	—	—	—	135	—
Au–Ag–Cu 70/20/10	14,300	13.2	—	—	—	114	—
Au–Ag–Ni 70/25/5	15,400	11.85	0.0009	—	—	80	1,080
Au–Ag–PI 69/25/6	16,100	14.9	—	55	—	112	—
Pd–Cu 95/5	11,400	21.6	0.0013	—	—	60	—
Pd–Cu 60/40	10,600	35	0.0032	38	—	80	—
Pd–Ag–Co 60/35/5	11,100	40.8	0.0014	—	1.300	192	—
Pt–Ni 95/5	23,000	20	0.00188	—	1.000	135	—
Pt–Ro 90/10	20,000	19.2	0.0018	—	1.500	90	—
Pt–lr 95/5	21,500	10	0.002	42	—	130	1,080
Pt–lr 75/25	21,700	33	—	16		246	1,875
Cu–Cd 99/1	8,900	2.6	—	—	—	345	—

T_m, melting temperature.

deoxidizer for copper, it degrades the conductivity too much to yield a product suitable for electrical applications. Instead, electrolytic slabs are melted and refined in a special process using oxygen-free inert gas and no metallic oxidizers. As a result, 99.98% pure copper with essentially no oxygen and less than 0.005% of any one impurity, is known as *oxygen-free high-conductivity copper* (OFHC).

The conductivity of copper is frequently referred to in terms of the International Annealed Copper Standard (IACS). Thus, percent IACS equals 100 (resistivity IACS/resistivity of sample). In absolute terms, the IACS has a resistivity of 1.7241 Σ cm. A common criterion for defining the purity of metals is the ratio of their resistivities at 273 and 4.2 K. This ratio varies between 150 and 400 for OFHC copper but can reach 1000–5000 and higher for zone-refined materials.

Under normal atmospheric conditions, copper is comparatively resistant to corrosion. At room temperature an oxide layer, Cu_2O, forms to protect the surface against further oxidation and is semiconductive. At higher temperatures, as a result of exposure to air, a CuO oxide layer is formed. The considerable corrosion of copper may be produced by air containing ammonia or chlorine

TABLE 4.3
Selected Properties of Copper and Aluminum Concluctors

	Aluminum			Copper		
Properties	**EC-0 (A)**	**Al–Mg (5005) (B)**	**Al–MgSi (6201) (C)**	**OFHC (D)**	**Phosphor Bronze 95/5 (E)**	**Brass (70/30) (F)**
Density (g/cm^3)	2.7	2.7	2.69	8.94	8.86	8.53
Melting point (°C)	660	652	654	1,083	1,060	955
Coeff. linear thermal expansion (1/10^{8}K)	23.6	23.7	23.4	17.0	17.8	20.3
Thermal conductivity (W/cmK)	2.34	2.05	2.05	3.91	0.84	1.2
Electrical resistivity (S/cm)	2.8	3.32	3.2	1.7	8.7	6.4
Thermal coeff. of electr. resistivity (1/10^{3}K)	4.46	4.03	4.03	3.93	4.0	1.0
Elastic modulus (GPa)	69	69.6	69.6	115	110	110
Yield strength (MPa)	28	193	310	69	140	110
Tensile strength (MPa)	83	200	330	220	345	330
Specific heat capacity (1/JgK)	0.9	0.9	0.9	0.38	0.38	0.38
Current carrying capacity (%)	80			100		
Hardness (H_B)	23	51	95	42	50	60

A, Annealed; B, 0.8% Mg Fully cold worked (H19); C, 0.7%Si–0.8%Mg, Solution treated cold worked, aged (T81); D, Annealed, grain size 0.05 mm; E, 94.8%Cu–5%Sn–0.2%P, annealed, grain size 0.035 mm; F, 70%Cu–30%Zn, annealed.

Source: From Braunović, M., *Electrial Contacts: Principles and Applications*, Slade, P. G., Ed., Marcel Dekker, New York, pp. 155–270, 1999.

compounds. The use of copper near sea coasts is undesirable, since the salts present in the air can cause severe corrosion. Moist atmospheres containing sulfur dioxide attack copper, resulting in the formation of a mixed oxide sulfide scale.

Spring properties of copper are poor, but alloying with beryllium or phosphorus greatly improves these properties (see Section 4.1.5).

For electrical applications, the mechanical properties of copper have to be improved, but in doing so the electrical conductivity is often reduced. Strengthening can be achieved by cold working and/or alloying copper with various elements. Cold-drawn pure copper can be softened by annealing at 200–325°C, but previous cold deformation and the presence of impurities can alter this annealing range. The higher the degree of prior cold deformation, the lower is the range of the annealing temperature, whereas the presence of impurities or the additions of various elements raise the annealing temperature. Some specific alloy families are reviewed below.

Cu–Ag. The amount of silver added is within the range 0.030–0.1% and results in improved creep strength and resistance to softening at elevated temperatures without appreciable sacrifice of the electrical conductivity. This alloy is commonly used for current collectors of electrical machines.

Cu–Be. This alloy contains 0.5–2% Be as the principal alloying element, but Ni and Co are also often added to achieve desirable properties. It is nonmagnetic and has excellent mechanical (elastic) properties. Its main application is for springs, diaphragms, switch parts, and electrical connectors. The precipitation-hardening alloy is heat-treated by annealing at 900°C followed by water quenching and subsequent aging at 425°C.

Cu–Cd. This alloy contains 0.0–1.0% Cd and has an excellent capacity for cold working and hot forming and also for soldering, brazing, and gas-shielded arc welding. It is widely used in thin wire applications for airplane electric circuitry, as well as in commutator segments and other applications.

Cu–Cd–Sn. The total amount of Cd and Sn may reach 2%. Main applications are for telephone lines, electric motor brushes, and parts for switching devices.

Cu–Cr. The Cr concentration is within the range 0.15–0.9%. This precipitation-hardened alloy has a large part of the solute contained in the second phase, which imparts an excellent mechanical resistance at elevated temperatures. Its main applications include electrode materials for welding machines, heavy-duty electric motors, circuit-breaker parts, switch contacts, current-carrying arms and shafts, and electrical and thermal conductors requiring more strength than is provided by unalloyed copper.

Cu–Te. The amount of tellurium added is 0.3–0.7% to improve machinability while retaining approximately 90% IACS. This alloy also has an excellent solderability and corrosion resistance. It can also be used at relatively elevated temperatures. Typical uses include electrical connectors and motor and switch parts.

Cu–Zr. This alloy contains 0.1–0.2% Zr. Because of its low tendency to embrittlement and improved creep behavior at elevated temperatures and mechanical stresses, it is used for switches and circuit breakers for high-temperature and high-vibration service, commutators and studs, and bases for power transmitters and rectifiers.

Bronzes. This group encompasses Cu–Sn alloys with a concentration of tin from 5% to 15%. All bronzes have superior mechanical properties but inferior electrical properties relative to copper. The electrical resistivity of bronze can be 2–20 times less than that of electrolytic copper. Bronzes are frequently ternary or quaternary alloys, containing third elements such as P, Si, Mn, Zn, Al, Cd, or Ni; the third element is usually stated in the name of the alloy. Bronzes for electrical applications contain less tin and other metals than bronzes for structural applications, for which the mechanical properties and corrosion resistance are the governing factors. Typical applications of bronzes are springs, diaphragms, bushings, face plates, connectors, and electrical machine parts.

Brasses. These are alloys containing nominally 15–40% Zn. The addition of other metals such as Mn, Ni, and Al improves their mechanical strength. Brasses are seldom used for electrical conductors due to their low conductivity. Typical electrical uses are conduits, screw shells, sockets, and receptacle contact plates where formability is important. When using some types of brass intended for mechanical or structural applications, care should be taken to avoid dezincification and stress corrosion cracking, which occur under certain conditions.

4.1.1.2 Aluminum

In recent years, aluminum has been used ever-increasingly for a number of economic and engineering reasons. Because of its light weight, relatively good electrical and thermal properties, availability, and moderate cost, aluminum is being considered as a viable alternative to copper for many conductor applications in electrical systems. In substituting aluminum for copper, however, due account should be taken of their differences in resistivity, mechanical strength, and density. For the same resistance and length, an aluminum conductor should have the cross-sectional area of 60% greater than that of an equivalent copper conductor, whereas the weight of the aluminum conductor is 48% of that of the copper conductor. The current-carrying capacity of aluminum is 80% of that of copper.

Aluminum is a ductile metal with a relatively high thermal and electrical conductivity. It is softer than copper and can be rolled into thin foils. However, because of its low mechanical strength, aluminum cannot be drawn into very thin wires.

The resistivity and mechanical strength of aluminum depend on its purity and degree of cold working. By selecting the proper fabrication process, aluminum containing 10 ppm of impurities can be obtained with a resistivity ratio surpassing 1000. Higher resistivity ratios, greater than 30,000, can be obtained by zone melting. The resistivity of high-purity aluminum (99.999%) is 2.635 Σ cm at 20°C, whereas that of the commercial grade is within the region of 2.78 Σ cm. The commercial grade of aluminum contains nominally less than 0.1% Si and less than 0.015%,

(Mn, Ti, Cr, V). To minimize further the effect of the impurities (Ti and V in particular) on the conductivity of aluminum, 0.02% boron is often added, leading to the transformation of these impurities (except Mn) into borides that have very little effect on the electrical conductivity, as they are not in a dissolved form.

Pure aluminum, even if hard-drawn, possesses inadequate mechanical properties. This shortcoming can be somewhat overcome by alloying with a variety of other metals, resulting in improved tensile and creep strengths. The alloys most frequently used for electrical applications are *Al–Mg* or *Al–Mg–Si* also containing Fe or Co.

Generally speaking, there are three main categories of the application of aluminum and its alloys. These are overhead transmission lines and underground cables, coil winding (magnet wire), and busbar conductors. For overhead transmission lines, the aluminum alloy used generally contains 0.8% Mg or 0.5% MgSi and has a high strength combined with a relatively good electrical conductivity. However, the mechanical strength of this alloy may not always be sufficient; for instance, for long spans in overhead lines, conductors of composite construction are used, in which the core of the line is composed of steel wires.

Alloys for coiled winding wire (magnet wire) have a relatively high concentration of Fe and a low Si content. This ensures rather high elongation values for the wire in the annealed condition, a higher recrystallization temperature, and higher tensile strength at elevated temperatures. Further improvements in the mechanical strength of these alloys can be achieved by adding small amounts of Mg or Cu. The use of aluminum alloys for coil winding wires requires some design alterations: motors and transformers should have larger slots to accommodate the larger gauge size of the aluminum wire if this is to have the same conductance as copper magnet wires.

For busbars, Al–Mg–Si alloys are mainly used because of their excellent corrosion resistance, good workability, and electrical and mechanical properties. When jointing the busbars, care must be taken to minimize the effect of stress relaxation. This requires the use of a special spring lock or disk spring (Belleville) washers. For busbar joints it is also desirable to use all-aluminum hardware if possible. By doing so, the effect of thermoelastic ratcheting can be avoided.

Other electrical areas where the extensive use of aluminum is made are the fabrication of capacitors for which an aluminum thin foil is used as the electrode and/or dielectric film-former, and integrated circuit electronics, where thin films of evaporated aluminum form conductive intraconnections.

Apart from the above-mentioned major applications of aluminum as a solid conducting material, there are an equally large number of other areas where aluminum is employed not because of its electrical properties, but rather because of its light weight, availability, and cost.

One of the most significant drawbacks that prevents the wider use of aluminum as a conductor material is the lack of a truly reliable and economical method of termination. To overcome this problem, many methods such as welding, plating, ultrasonic bonding, plasma spraying, bolting, clamping, and brazing have been adopted, but most of them are relatively expensive and require greater operator care; in some cases they are marginal in electrical or mechanical performance. There are a number of special problems common to aluminum that have to be considered when terminating aluminum conductors. The general problem areas when using aluminum in conductor and connector systems are discussed in the subsequent sections of this chapter.

4.1.1.3 Silver

This is the most widely used material for a considerable range of make and break contacts operating at currents from 1 to 600 A and contact forces greater than 15 g. It has the highest electrical and thermal conductivities of all metals. Because of its ductility, it can be fabricated into many designs, including solid, tubular, and composite rivets and solid buttons. However, it is widely used as plating or coating material for the contact parts of connectors. The main drawbacks of silver are low melting and boiling points, low mechanical strength, possible contact welding, and a tendency

to form sulfide films (tarnishing). Another problem with silver is the diffusion of silver atoms through certain electrical insulation materials, such as phenolic fiber, under the influence of applied electrical fields, which may cause the failure of the insulation to occur.

It should be noted that silver belongs to the most deficient chemical elements and its content in the Earth crust is only 7×10^{-6} wt%. The consumption of silver exceeds the production of the primary metal and the deficit is compensated by the secondary metal. In this connection saving silver in electrical engineering and electronics including the manufacturing and maintenance of contacts and other silver-containing materials and articles has become a crucial problem.

The most harmful drawback of silver is its ability to be sulfidized under the effect of sulfur-containing compounds which are especially reactive in the presence of moisture and such gases as NO_2, Cl_2, and O_2.[49–52] Free sulfur, which can be contained in the environment, released from rubbers and compounds used in devices, and released in reactions between some aggressive components of the environment, is especially dangerous for silver. Currently such aggressive components are present in great amounts in the atmosphere, especially in large cities, due to environmental pollution with industrial waste.

Improved mechanical properties and a higher resistance to tarnishing may be achieved by alloying silver with copper, cadmium, gold, palladium or platinum. Some of them are alloyed with nickel and iron to improve their wear resistance. Table 4.4 summarizes the effect of additions of different elements on different properties of silver.[53]

To protect silver against sulfidizing, a palladium additive is successfully used.[54] The optimal content of palladium in alloys *Ag–Pd* intended for low-current contacts is approximately 30%. However, such alloys have a high specific resistance exceeding that of pure silver by approximately an order of magnitude. For this reason contacts in which these materials are used, especially miniature contacts, have a great contact resistance. Besides, friction processes can induce the formation of insulating films on the contact surfaces because of catalytic activity typical for palladium.[55,56] This time AgPd50% (AgPd50) often used for high-speed and light-duty sliding contacts is selected for the mated material because of its excellent abrasion resistance.

Ag–Cu alloys are the least resistant to corrosive environment components among all silver alloys since copper also corrodes easily under these conditions, forming films of three kinds: Cu_2O, CuO, and Cu_2S. Alloys rich in copper are unsuitable for contacts operating under arcing conditions and low pressures because the transition resistance is unstable due to oxidation. In addition, copper is the best alloying element for silver from the viewpoint of improving its strength and wear resistance. For example, the alloy containing 15–18% of copper has a high wear resistance.[57]

Ag–Ni Alloys. Small amounts of nickel (0.2–3%) improve the wear resistance and lessen the probability of welding and tarnishing.

Ag–Cd Alloys. The addition of cadmium decreases the electrical conductivity, melting point, and oxidation resistance, but improves the resistance to tarnishing. Silver alloys with 1–10%

TABLE 4.4
Effect of Additions of Different Elements on Different Properties of Silver

Property	Additions
Arc resistance	Pd, Mg, Li, Zn, La, Sb
Abrasion resistance	Cu, Ni, Pd, Li
Lubrication	In, Zn, Sn, C
Weld resistance	In, Zn, Mn, metal oxides

Source: From Shirakawa, R., Suzuki, S., Matsuda, A., and Shibata, N., *Proceedings of 38th IEEE Holm Conference on Electrical Contacts*, Institute of Electric and Electronic Engineers, Inc., 119–124, 1992. With permission.

of cadmium are also some of the most popular materials for relatively high-speed sliding contacts such as spring contacts, sliding fingers and others because of their excellent properties like hardness, low transfer rate, wear resistance, stable resistance under small contact forces, slight resistivity to arc, and low cost. The reduction of using cadmium, which causes pollution, would be beneficial to human life and industry in light of recent environmental problems.

Ag–Li–La Alloys. An effort has been made to develop and use a substitute for silver–cadmium alloys. Shirakawa et al.[53] have reported the successful development of Ag–Li–La alloy to replace silver alloy containing 1% of cadmium (AgCd1) used as light-duty sliding contact material. The silver–lithium–lanthanum alloy shows more satisfactory properties as a sliding contact, including low contact resistance, abrasion resistance, and arc resistance compared to AgCd1. The favorable properties of silver such as workability, chemical stability, and cost efficiency are well maintained by its diluteness of added elements. Further, the test results of this alloy in a light-duty relay tester proved its possibility as relay contact use showing a low and stable contact resistance compared to other common silver alloys.

Ag–Pt Alloys. The additions of platinum, palladium or gold all harden silver, decrease its electrical conductivity, and improve the resistance to wear, tarnishing, and metal transfer.

Contacts are made of the *silver–zirconia alloy* (95/5) with a specific resistance of 0.019 μΩm and a Brinell hardness of 66. Contacts made of the alloy *Ag–MgO* (97.5/2.5 and 95/5) with a specific resistance of 0.019 and 0.023 μΩm and a Brinell hardness of 74 and 88, respectively, and of the alloy *Pd–Ag–Ni* (25/70/5) with a specific resistance of 0.105 μΩm and a Brinell hardness of 35, are also of interest.

4.1.1.4 Platinum

Platinum has an exceptional resistance to tarnishing, oxidation, and corrosion. For this reason platinum contacts provide a highly stable transition resistance. It is suitable for light-duty applications where operating currents are below 2 A, the contact-pressure is low and where the reliability is the most important parameter. The minimal arc formation current for platinum is the highest (0.9 A) compared to other noble metals (0.35–0.45 A). The voltage of arc ignition for platinum is also higher than for other metals. However, under fretting conditions, platinum contacts are susceptible to frictional polymerization.

Pure platinum is rarely used for fabricating contacts because of its low hardness. Additions of iridium, ruthenium, and osmium to form binary or ternary alloys increase the hardness, mechanical strength, melting point, resistivity, and wear resistance of platinum.

Pt–Ir alloys are used because of their low tendency to arc formation and greater resistance to electroerosion than platinum. *Pt–Ru alloys* are harder than platinum–iridium alloys with a low affinity to contact welding compared with platinum. *Pt–Ni alloys* are resistant to needling and contact welding. Compared to platinum, *Pt–Ro alloys* are harder and have a low volatility at elevated temperatures. The alloying of platinum with tungsten and molybdenum (*Pt–W* and *Pt–Mo alloys*) increases the melting point and hardness of the material.

4.1.1.5 Palladium

Palladium is less expensive than platinum but has a lower resistance to corrosion, oxidation, and tarnishing. It begins to tarnish at 350°C, but the tarnish film formed decomposes at 900°C. The additions of copper, ruthenium, silver or combinations of other metals improve the mechanical properties of palladium with some reduction in the corrosion resistance and lower its cost. Palladium and its alloys are of interest as possible low-cost substitutes for gold in separable connectors, switches, and printed-circuit boards. However, in atmospheres containing traces of organic compounds, palladium contacts subjected to motion relative to each other (fretting) tend to form an insulating frictional polymer.

Friction processes occurring in sliding contacts increase the catalytic activity of palladium. Organic compounds releasing from plastics, rubbers, composites, insulating materials, lubricants, etc. used in devices can precipitate on the contact surfaces and form thick strong insulating films under the effect of catalytically active palladium. As a result, contact conditions worsen and contact can even fully disappear.[56]

Pd–Ir alloys possess good contact properties; moreover, their cost is much less than that of platinum–iridium alloys. No sulfurous films are formed on the surface of *Pd–Ag alloys* with the palladium content in excess of 50%.

Pd–Cu alloys with copper contents of 15 or 40 wt% are commonly used as contact materials in telecommunications and automotive engineering because of their good resistance against material transfer. Palladium and copper are completely miscible with superlattice effects in the solid state. Therefore, the electrical conductivity is extremely dependent on the composition of the alloys with a distinct drop of the conductivity of copper with increasing the palladium content in the solid solution.[58]

4.1.1.6 Gold

Gold is the softest noble metal. It has an excellent tarnish and oxidation resistance but is very soft and susceptible to mechanical wear, metal transfer, and welding. It is widely used in computers and telecommunication and data transmission devices where operating currents are not more than 0.5 A. The addition of copper, silver, palladium or platinum, forming binary and ternary alloys, improves the hardness without loss of the tarnish resistance, but usage is restricted to low-current applications.

Pure gold has tendency to seizure and severe adhesive wear.[59–61] Addition of base metals (Co, Ni, Cu, Sb, Cd, In) or noble metals[61,62] increases the hardness and reduces the wear in gold alloys. Electrical contacts made of gold alloys have a high resistance to the effect of sulfur-containing compounds and some other aggressive components (H_2S, SO_2, NO_2, O_2, CO, H_2O). Only gold alloys are capable of retaining a stable contact resistance for a long time in an environment containing the above components.[63] The resistance of gold alloys to environment contamination increases with increasing the gold content.[64]

Ammonium sulfate films may appear even on pure gold in an ammonia environment.[65] Organic compounds are another kind of film that form on the surfaces of gold contacts,[56,66] especially if they operate at elevated temperatures in closed environments.

Due to susceptibility to electrical erosion, pure gold is used in precision contacts operating under light loads and at low voltages. Gold alloys have improved hardness and erosion resistance. *Au–Ag contact alloys* containing over 50% gold show no tendency to form sulfur films. Also, *Au–Pt–Ni alloys* are used. Among ternary alloys of gold, the hard, nontarnishing *Au–Ag–Pt contact alloy* is the best known. Additions of copper and nickel to *Au–Ag–Cu* and *Au–Ag–Ni alloys* improve their hardness. Hard refractory *Au–Pd–Ni alloys* are also used.

4.1.1.7 Rhodium

Rhodium is very resistant to tarnishing but is very hard and extremely useful as a contact material. However, owing to difficult fabrication, it is used exclusively as a plating material in light-duty electrical contacts where the reliability is of the utmost importance.

4.1.1.8 Tungsten

Tungsten is a very hard metal with an excellent resistance to wear, welding, and material transfer, with high melting and boiling points. Its main disadvantages are a low corrosion and oxidation resistance, high electrical resistivity, and poor formability. It is best suited to applications where currents range from 1 to 5 A and where impact on closing the contact is high. Tungsten for contact

applications is generally made by powder metallurgical processes. The advantages of tungsten contacts are their resistance to the appearance of arc discharges (tungsten has the highest minimal arcing current); resistance to electrical erosion and welding because tungsten is a refractory metal; and a low mechanical wear due to a high hardness.

4.1.1.9 Nickel

A high resistance to oxidation and corrosion of nickel and nickel alloys make them suitable for a wide variety of applications, the majority of which involve corrosion and/or heat resistance. Other applications involve low-expansion, electrical resistance, soft magnetic, and shape-memory nickel-based alloys. The low-expansion nickel alloys are used in the lamp electronic industries where glass-to-metal seals in encapsulated components are important.

Invar (Fe—36% Ni), the most common low-expansion alloy, is widely used in the electronics industry for printed circuit boards. When used in a clad composite with copper, it can provide a composite with very good controlled-expansion characteristics. The low expansion of Invar with other alloys of different expansion can provide a series of thermomechanical control and switchgear devices.

The electrical resistance nickel alloys are commonly used in instrument and control equipment to measure and regulate electrical characteristics or to generate heat in furnaces and appliances. The most common alloys in this class of alloys are *Cu–Ni* (2–45%Ni), *Ni–Cr–Al* (35–95%Ni), and *Ni–Cr–Si* (70–80% Ni). The permeability properties of soft magnetic nickel–iron alloys are used in switchgear and direct current motor and generator designs. The lower-nickel alloys ($<$50% Ni) with a fairly constant permeability over a narrow range of flux densities are primarily used in rotors, armatures, and low-level transformers. High-nickel alloys ($\sim$77% Ni) are used for applications in which power requirements must be minimized, such as in transformers, inductors, magnetic amplifiers and shields, memory storage devices, and tape recorder heads.

Molybdenum is inferior to tungsten in hardness and melting point and susceptible to atmospheric corrosion. It forms loose oxides capable of disturbing the contact conductivity; therefore, molybdenum contacts are less reliable in operation in air. Contacts made of the alloy tungsten–molybdenum with an improved hardness are intended for operation in vacuum and inert gases.

More detailed data on properties of contact metals and alloys can be found on the website located at http://www.goodfellow.com. This site provides a great amount of information on a huge number of metals, alloys, and compounds.

4.1.2 Metals and Alloys for Heavy- and Medium-Duty Contacts

Electrical Machines. Because sliding contacts of electrical machines, apparatuses, and transport pick-offs require substantial consumption of copper and its alloys, in many applications ferrous metals are also used as contact materials, as seen in Table 4.5.

In contact with carbon–graphite brushes, copper forms a complex-structured film that controls the commutating ability, contact voltage drop and wear resistance of the sliding contact. For those reasons it is used for collector rings operating at temperatures up to 130°C. The alloy of copper and cadmium (Cd 0.9–1.2%) has a Brinell hardness not lower than 95 and is commonly used as a collector ring material. Collector rings made of copper slightly alloyed with silver are suitable for applications in high-speed machines operating at temperature up to 155°C. Magnesium bronze has the most universal characteristics and is recommended for machines operating at temperatures up to 230°C over extended periods of time. For high-speed machines operating at high-temperature, collector rings are made of chrome bronze (Cr 0.4–1%) and zirconium bronze (Zr 0.3–0.5%) with a Brinell hardness not less than 100 and 115, respectively.

In addition to nonferrous metals, ferrous metals are also used in the current pick-offs in electrical machines, including turbo-generators. For example, chrome–nickel stainless steel and

TABLE 4.5
Materials for Collectors and Collector Rings of Electrical Machines

		Physical–Mechanical Characteristics				Ultimate Temperatures	
Metal or Alloy	Composition	IACS (%)	σ (MPa)	H_B	T_s (°C)	T_{po} (°C)	T_{sd} (°C)
Electrolytic copper	Cu 99.9	100	250	80	155–170	160	250
Metal–ceramic copper	Cu 99.9	85	250	70	250	180	300
Conductor bronze	Ag 0.07–0.14, balance Cu	96	250	85	240	220	300
Magnesium bronze	Mg 0.1–0.35, balance Cu	80	270	90	260	230	350
Cadmium bronze	Cd 0.9–1.2, balance Cu	80	270	95	250	230	350
Chrome bronze	Cr 0.4–1.0, balance Cu	75	380	110	325	270	425
Chrome–zirconium bronze	Cr 0.2–0.4, Zr 0.15–0.35, balance Cu	80	450	120	450	350	600
Zirconium bronze	Zr 0.2–0.4, balance Cu	85	350	100	350	250	450
Stainless steel (bars)	Cr 17–19, Ni 8–9.5, Mn 10–20, Ti 0.5–0.7, Fe- balance	2.6	550	160	—	600	680
Tin–zinc bronze	Sn 3–5, Zn 3–5, Pb 1.5–3.5, balance Cu	15	550	160	400	350	400

IACS, electrical conductivity; σ, tensile strength; H_B, Brinell hardness; T_s, softening temperature; T_{po}, temperature of prolonged operation; T_{sd}, temperature of short duration during soldering.

gray iron have good antifriction properties and strong resistance to corrosion and vibration and are used in electrical machines operating with brush current density of 15–20 A/cm^2. For the collector rings, operating with brush current density exceeding 15 A/cm^2, lead–zinc bronze is used where the addition of lead improves the antifriction properties and that of zinc the mechanical strength (Brinell hardness is 60). Collector rings made by compacting the copper powder (metal–ceramic rings) operate efficiently at temperatures up to 155°C and, from a production point of view, are promising technological innovations. The rotor of homopolar pulse generators can be made of aluminum plated with copper.[67]

Monolithic metal brushes are used in electrical machines intended for specific applications only. An example is a brush commutating electromagnetic linear motor (coilgun) used for underwater launching. The operation of coilgun commutation brushes immersed in seawater raises a number of challenging issues that must be addressed, including environmental issues (corrosion, biofouling) and commutation issues (arcing erosion, hydrodynamic lift). It was found that copper is a good material to operate in seawater since it has the right combination of low corrosion and biofouling resistance.[68] Resistively graded brushes can reduce the current in the coil to decrease arc erosion, and with fingerlike brushes no hydrodynamic lift was observed.

Another field of copper fingerlike brushes applications is in pulsed homopolar generators.[69] Solid copper fingers can be used in sliding electrical contacts at sliding speeds of 300 m/s and collector current densities above 75 MA/m^2 as compared to that of copper–graphite operating at limited brush speeds 220 m/s and current density of 7–15 MA/m^2.

Sliding wire contacts are used occasionally, mostly in the geometry of tiny violin bows on rotating axles, especially when current densities are high because dimensions have to be kept small, provided that fairly rapid wear can be tolerated.[70] Depending on the application, the materials used for modern metal wire brushes are much the same as for switches or any other releasable connectors.

For powerful electrical machines and equipment, e.g., homopolar motors, instead of wire or graphitic brushes, metal–metal sliding contacts with greatly reduced wire diameters, i.e., in

the form of low-wear metal fiber, are developed.[70–72] Different modes of experimental *metal fiber brushes* of aluminum, copper, gold, niobium, silver, and platinum were made with fiber diameters between about 3 μm and 100 μm, and "packing fractions," (the volume fraction of fiber material in the fibrous art of the brush before use) between 5% and 60%.

The basic method of making metal fiber brushes was explained by Adkins, Kuhlmann-Wilsdorf, and Kuhlmann-Wilsdorf.[73–76] Metal fiber brushes of this kind can be made by etching away the matrix material from among the fibers in filamentary materials, such as those used in superconducting devices, ultimately no doubt at modest cost. The cost of making a few small laboratory samples of the required multifilamentary materials by industrial processes is, however, prohibitive. Hence, for superconductive multifilamentary materials, methods based on the multiple drawing and bundling were developed. So far, brushes have been made with fibers of copper, gold, niobium, platinum, and silver.

A cross section of brush stock before the matrix material was etched away is shown in Figure 4.1 (note the exposed fibers). The fibers, in this case of gold, were initially one sturdy wire inserted into copper tubing which was drawn to about 0.25 mm diameter. After cutting into shorter lengths and bundling, the pieces were encased in another copper tubing, drawn down to 0.25 mm once again, and after a second cutting and bundling, were drawn down to the present size. In Figure 4.1, the light-colored material is the gold. The copper matrix is composed of the initial copper tubing which surrounds each individual gold fiber, plus the tubing into which the encased gold pieces were bundled after the first drawing and which defines the circular groupings of the gold fibers in the figure. The last copper encasement is not shown, being well outside of the field of view. In fact, it defines the outer shape of the brush. For this reason the drawing after the second bundling is commonly not severe, to leave a desirable brush area of about 0.8 cm^2. The final step is etching of the matrix material, leaving the fibers exposed.

Metal fiber brushes perform very well at high speeds and current densities.[76–79] For many years it has been widely held that metal fiber brushes cannot be used in commutators because of the chopping action of commutator bars (it would cause fiber breakage and catastrophic wear) and severe arcing on adjoining bars (it would cause fast erosion). However, experiments with bare and silver-plated copper fiber brushes in the protective argon atmosphere[72] suggest that these problems may be overcome using fibers having diameters much less than 100 μm. No fiber breakage was observed, arcing was only moderately stronger than with carbon brushes, and the total

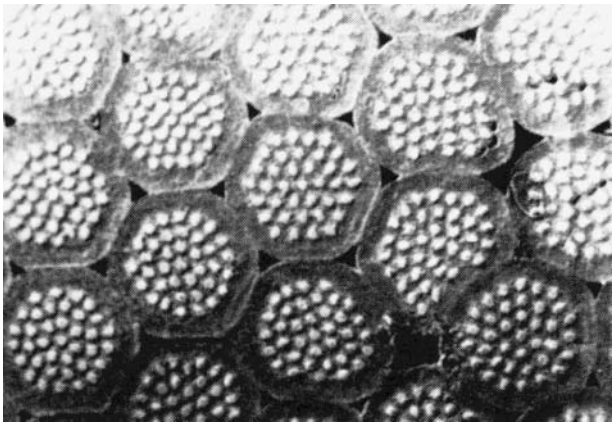

FIGURE 4.1 Micrograph of the cross section of almost finished "brush stock," comprising bundles of 20-μm gold fiber in a copper matrix. (From Kuhlmann-Wilsdorf, D., *Proceedings of 37th IEEE Holm Conference on Electrical Contacts*, Institute of Electric and Electronic Engineers, Inc., 1–24, 1991. With permission.)

dimensionless wear rate in the motor was only about twice that of a polished copper rotor under other comparable conditions.

Eventually, fiber brushes may displace monolithic brushes everywhere. Initially the most likely applications of fiber brushes will be homopolar motors/generators, but they should spread to all types of brush motors as costs come down and reliability is established. The driving forces will be (1) the extremely low noise of fiber brushes, (2) low heat loss and voltage drops of about 0.1 V and less where monolithic graphite brushes require 1 V, (3) their very high current density capability which makes them supremely suited for miniaturization, and (4) they will be irreplaceable whenever very high current density is needed, if even in short pulses.

According to Kuhlmann-Wilsdorf[79] one may not expect soon to see fiber brushes used in cheap consumer items, but eventually they should be used not only in high-tech applications but also in electric generating stations, in auxiliary car and airplane motors, in hand-held tools; in hair dryers, in large industrial and marine motors, in turbo generators, alternators, starter motors, telemetry devices, and in a host of other applications. What is still required is the test of time and experience.

Transport Current Pick-Offs. Trolleys of transport means are made of profiled hard-drawn copper. Cadmium or magnesium bronzes with the conductivity equal to 80–85% of pure copper conductivity are also used. The wear resistance of trolleys made of bronze is 1.5–2.5 times greater than that of copper trolleys. The increased mechanical strength of bronze trolleys allows designers to make suspension devices lighter. The contact slider of pantographs and current pick-offs of electric rolling stock and urban transport vehicles can be made of hard-drawn copper lubricated with graphite grease.[80]

Metallic alloys, for example chrome–zirconium bronze, are applied in some cases in the heavy-duty current pick-off of locomotives. In high-speed electrical locomotives (speeds over 160 km/h), the current pick-off in the contact line of 3000 V operates under conditions of severe wear and extensive localized heating of the contact surface exceeding 600°C. To reduce wear pick-offs made of metallic plate with grease are used. For example, Italian railways use pick-offs with a graphite or metal-carbon layer being inserted between two bronze plates.

Contacts for Electrical Apparatuses. Noble metal alloys, cadmium or beryllium bronze with a high wear and corrosion resistance and satisfactory electric conductivity, are widely used materials for sliding contacts in electrical apparatuses such as variable resistance, potentiometers, slider switches, etc. In sliding switches the slider is often made of phosphor bronze, whereas the stationary contacts are made of brass.

4.1.3 Metals and Alloys for Light-Duty Contacts

As a rule, in low-current electrical contacts pressures are light and the current produces minor effect on the durability. Therefore, if no severe electrical erosion occurs, the provision of a stable and low transition resistance is the main operation requirement.

The problem of selecting contact materials for light-current contact applications arose in the 1970s. Initially, copper and its alloys were mainly used for this application. The requirements to the stability of the contact resistance and the reliability of contacts were not strict because of a low sensitivity of various devices. As automatic control systems became more complex and automatic telephone stations, new engineering devices and equipment continued, the consumption of noble metals, primarily silver and silver-alloys in electrical contacts, increased. For example, in the 1970s, the annual silver consumption in the United States exceeded 5000 t. Over 20% of this amount was used to produce various contacts.[81] During those years, Japan alone used up to 24% of the total silver produced in contact-related applications.

The use of silver and its alloys containing copper for light-current contacts does not comply with the reliability and life requirements due to the their susceptibility to seizure and sulfidizing in the presence of sulfur-bearing compounds. For example, when technically pure silver (Ag999)

or materials with a high silver content (AgNiCu—2—20; PdAg—30; PdAg—40; PdAg—70—5; AgCu—300, etc.) are used, tarnishing films are damaged, asperities are plastically deformed, and the seizure of the virgin surfaces occurs. For this reason, in light-current devices, the contacting members of silver and its alloys are paired with dissimilar metals or protected against environmental effects and seizure by special greases (see Chapter 9, Section 2).

For the most important devices, contacts are made of platinum- and gold-based materials. Only gold alloys are capable of retaining the required contact resistance stability for a long time in an atmosphere with aggressive-bearing components. For example, electronic connectors and related components in a telecommunications central office apparatus require low and stable contact resistance over the span of their service lifetimes, often as long as 40 years. Consequently, the tendency of most metals to oxidize, tarnish, or corrode during exposure has led to the nearly universal use of gold as a connector contact material. Electroplated gold has been widely used as a contact material for conventional type connectors. Due to the corrosion and resistance to wear requirements, a minimum thickness within 0.5–1.0 μ has been adopted for gold-bearing contacts.[82]

The extensive use of noble metals in electric/electronic applications prompted numerous research activities in the search for reliable replacement materials. A number of alternate materials were developed with one of two comparable characteristics to that of gold and silver; however, most often their contact resistance stability, susceptibility to tarnishing, and life were considerably poorer. For example, according to Waine and McKarthy,[83] coatings Sn60Pb40 and Sn90Pb10 can compete with gold as far as the contact resistance is concerned, but due to their short service life and tendency to a rapid seizure during operation, they are inferior to gold-based contact materials. In addition, they have poorer corrosion resistance than gold and can be used only with lubricants in the devices where no strict reliability and service life requirements are imposed.

Taking into account the presence and properties of surface layers and their considerable effects exerted on the operation of low-current contacts, the following requirements for the contact materials can be put together:

- Physical properties: high electric and thermal conductivities; low thermal resistance and thermoelectric coefficients; high melting and evaporation temperatures; high specific heat of fusion, specific heat of evaporation, and specific heat; high voltage and current of arcing; no phase transitions in operation.
- Chemical properties: composition constancy; a high corrosion resistance; a low catalytic reactivity; resistance to various contaminations; capability of forming a thin surface film to act as a lubricant.
- Mechanical properties: a high elastic modulus, hardness, strength, and elastic limit, along with ductility, i.e., the absence of brittle fracture; a low friction coefficient; no adhesive wear; a high wear resistance.

Many of these requirements are contradictory; therefore, the selection of suitable contact materials for low-current contacts is an extremely arduous task. The best contact materials contain from four to seven components. The problem should be solved together with the development of an optimal design of the contact unit, taking into account a variety of factors controlling contact operation.

For example, sliding low-current contacts in complex devices are often grouped into a unit comprising tens of single rings or tracks. If voltages, currents, and loads and loading modes in different circuits differ, the contact materials should be different and provide reliable operation of the contacts. Since from a technological viewpoint this is inconvenient, the same contact pairs are often used both for commutating microcurrents (10^{-6}–10^{-3} A) and in circuits with currents 1–4 A. In this case, the contact quality, life, and reliability in different circuits may differ.

4.1.4 Materials for Liquid-Metal Contacts

In contacts between liquid and solid metals, the deformation of the solid member is negligible and the tarnish and chemisorbed films on its surface remain undamaged. Here the load bearing and the apparent area are equal. For this reason, the use of a liquid metal as the intracontact medium separating solid contact members significantly increases the contact area encompassing almost the whole apparent area of the solid electrode surface, thus reducing the electrical contact resistance.

If a liquid metal wets the virgin surface of the solid electrode, no transition resistance occurs provided that the metals do not produce chemical compounds. When a liquid metal moistens the oxidized surface of the solid electrode surface, the contact resistance is controlled by the resistance of the oxide film, which is on the order of 10^{-9} Ωm^2, and 10^{-8}–10^{-7} Ωm^2 for thick oxide films. The resistance caused by the presence of physically adsorbed films is insignificant and within the range of 10^{-10}–$10^{-11}\Omega m^2$ at room temperature and drops almost to zero when heating the contact to 400°C. In this case, there is no need to provide a high contact force and variation in the shape of the solid contact elements since the effect of wear on the transition resistance is negligible. Therefore, in spite of some restrictions, the contact devices with commutating and sliding contacts comprising a liquid metal intermediate medium are widely used.

Mercury has been commonly used for a long time as the intermediate liquid-metal medium due to its low melting point, quite good electric conductivity, and the behavior of the noble metal in air. In some cases, mercury was used for research purposes. For example, the contact between the film-covered metal and mercury provides means to investigate the conduction of the surface films. This is because the load-bearing (A_b) and the apparent (A_a) contact areas may be considered as being equal that is $A_b = A_a$.[1,84]

The application range of mercury contacts is quite wide and includes turbine interrupters, electrolytic tank and unipolar generator contacts, vacuum contactors, and mercury commutating components of low-current automatic devices, among other applications.[85,86] In medium-duty mercury switches, mercury is enclosed in a hermetically sealed chamber, forming a bridge between the sealed-in metal electrodes. Rupturing the liquid connection (by inclining the vessel or by means of plunging electrodes) breaks the circuit. Applications of mercury-wetted contacts are described by Spear, Lanyos, and Mort.[86] Examples are relays using mercury-wetted contacts where mercury is fed to the platinum contact through the capillary path between the parallel platinum wires. The contact is moved magnetically. The advantages are no wear and bounce and a lifetime of more than 10^9 operations.

Sliding contacts for unipolar generators were constructed with high currents and peripheral speeds (50–250 m/s).[85] In the initial arrangement, mercury was held in a rotor groove by centrifugal forces (see Figure 4.2). Since for practical purposes the friction force was too great to provide a suitable contact area, an arrangement was developed whereby separated mercury-jet contacts

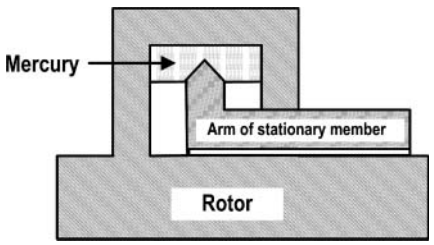

FIGURE 4.2 Mercury contact of the unipolar generator. The mercury is held in a groove by the centrifugal force.

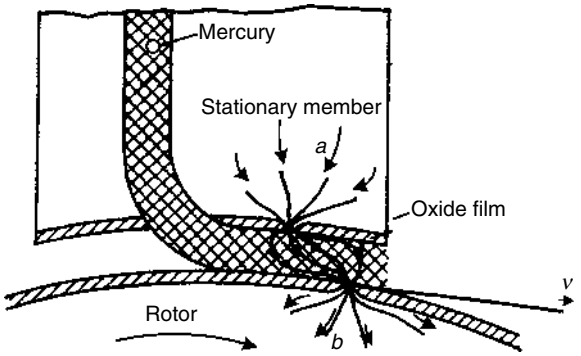

FIGURE 4.3 Mercury-jet contact: (a) and (b) are current constriction of α-spots.

were used (see Figure 4.3). The jets were forced through channels within the stator into the contact gap. With this arrangement, the contact surface is diminished but remained much greater than the real contact area under a solid, for example, carbon brush.

The toxicity of mercury is the main drawback as the intermediate liquid-metal medium, canceling its advantages. Therefore, it is an urgent problem to replace mercury contacts with similar yet nontoxic liquid-metal contacts of equal quality.

Gallium has a number of advantageous compared to mercury and other liquid metals as the intracontact-conducting medium. Among all liquid metals, gallium is the least toxic material and for that reason is used even in dentistry. It has the widest range in its liquid state: its melting temperature is 29.8°C and its boiling temperature is 1983°C. Its electric and thermal conductivities exceed those of mercury. It is known that gallium eutectic alloys with indium and tin such as GaIn and GaInSn in liquid states at temperatures above 3°C are used as an intracontact-conductive medium.[87] In recent years, the lubricating effect and electrical characteristics of gallium-based materials used as liquid-metal contact members in conducting devices materials have been extensively studied.[88] It was shown that in addition to the considerable reduction of contact resistance, such eutectics produce weak lubricating effect and maintain the efficiency of the liquid-metal contact at temperatures up to 100°C.

Eutectic alloy NaK_{78} was used successfully as a liquid-metal current collector in homopolar machines (300 kW).[89] Homopolar motors and generators are characterized by relatively low voltages and extremely high currents and, therefore, require low-loss current collectors if a high efficiency and power density are to be achieved. The current densities required are well above the capacity of conventional solid brushes. NaK_{78} is compatible with machine components and exhibits excellent electrical and physical properties. The disadvantage of NaK_{78} is that it is highly reactive with oxygen and water; therefore, exposure to normal atmosphere must be prevented, resulting in added machine shaft seal complexity.

To find a suitable low melting point alloy (LMPA) replacement for NaK_{78}, extensive investigations have been conducted.[90] Alloys with melting points below 65°C containing various proportions of bismuth, lead, tin, indium, and cadmium were found as potentially suitable replacements for NaK_{78} alloy. Table 4.6 compares the physical characteristics of NaK_{78} alloys. The trade names of alloys 117 and 136 refer to their melting point in degrees Fahrenheit.

The advantage of using the LMPA as contacting members in motors is in their relative easy handling capability compared to that of NaK alloys. In addition, although these alloys have to be covered to prevent oxidation, exposure to air for a short time can be tolerated. In fact, complete deterioration does not occur for 50–100 h.

TABLE 4.6
Characteristics of Low-Melting-Point Alloys

Alloy	Composition	Density (g/cm^3)	Resistivity (μΩcm)	Viscosity (cP)
NaK_{78}	Na-22%, K-78%	0.85	33.8 (20°C)	0.5
Alloy 117	Bi-45%, Pb-23%, Sn-8%, In-19%, Cd-5%	9.75	88.4 (77°C)	3.31
Alloy 136	Bi-49%, Pb-18%, Sn-12%, In-21%	9.23	89.2 (77°C)	3.35

Source: From Maribo, D. W. and Sondergaard, N. A., *Proceedings of 32nd IEEE Holm Conference on Electrical Contacts*, Institute of Electric and Electronic Engineers, Inc., 91–94, 1986. With permission.

A promising trend in the modern science of contact materials is related to the development of composite materials including a solid frame impregnated with a liquid metal. This topic will be considered in Section 4.3. Presently, theoretical methods of calculating characteristics of the contacts with the intermediate liquid-metal are available while the effect of liquid-metal oxidation and means of preventing it are lacking.

4.1.5 Spring Contact Materials

Copper and copper alloys are used to a very large extent in low-current engineering for current-carrying spring components. Beryllium copper (0.1–2.0% Be) is a specially suitable spring contact material for connector applications due to its good mechanical properties, electrical and thermal conductivities, and resistance to wear and corrosion. It can retain its spring characteristics up to 150°C. Phosphorous bronze (1.3–10% Sn, 0.1–0.3% P) is also widely used as a spring material for connector applications. However, it should not be used at high stress levels at temperatures exceeding 107°C, nor in salt-containing atmospheres. Low-lead brass (0.3–0.8% Pb) is primarily used as rod stock for pin contacts, notably in rack- and panel-type connectors.

Lately, the use of traditional materials, such as phosphorous bronze, nickel silver, and beryllium copper, was matched with newly developed materials that established their suitability for special applications. The selection and applicability of spring contact materials must satisfy two basic requirements: mechanical strength, namely the spring bending limit, and electrical conductivity. Other important characteristics are the elongation and yield strength, the resistance to relaxation, the fatigue strength, and miscellaneous properties.

Three groups may be distinguished[91]:

- Materials having a high spring bending limit (900–1200 N/mm^2) and low electrical conductivity are used for parts under heavy mechanical loads, such as special contact springs found in insulation displacement connectors. This group includes spinodally decomposable alloys on CuNiSn basis (C726, C727, C728, C729). However, additional production steps are necessary to achieve the high elongation characteristic of these alloys.
- Materials with a medium spring bending limit (500–700 N/mm^2), some of them with a somewhat higher electrical conductivity, are used to a very large extent for connectors and relay springs. Among the materials of this group, $CuSn_6$, a phosphorous bronze with extremely fine grain structure, must be mentioned.[92] This may be obtained either by special production steps or by very small amounts of certain alloying additions. Materials of this type meet higher strength requirements, but their electrical conductivity is below 10 m/Ωmm^2. A higher electrical conductivity with about the same strength is shown by CuCoBe; however, this alloy must be aged, making it too expensive for mass article

production. Alloy Cl9 (CuPeSnCo) in turn offers the advantage of a higher strength and good electrical conductivity without ageing treatment.
- Materials with a relatively high electrical conductivity but limited application for spring components on account of their low strength are used for less-loaded connectors or lead frames (C194, $CuFe_2$).

The growing trend toward the miniaturization of components and toward compact units imposes the need for materials with both high electrical conductivity and sufficient strength. For connectors, there is an added need for good formability. The request for easy processing plus low material and production costs can only be met by alloys requiring no expensive ageing treatment to obtain optimal properties. The material "Wieland-KV5" (96.8% Cu, 1% Ni, 1% Sn, 0.5% Ti, 0.7% Cr) fulfils these requirements to a very large extent.[93] The electrical conductivity of KV5 lies between 25 and 30 $m/\Omega mm^2$, notably higher electrical conductivity than conventional contact carrying materials while retaining a comparable strength. This favorable combination of properties can be achieved without costly ageing treatments, making the alloy attractive for application especially in the field of connector springs.

Coatings for high-temperature applications require high-performance copper alloys that fulfill the demands concerning a high stiffness and constant-contact normal force during the lifetime of a connector. Cu–NiSi alloys like C7025/K55 and CuCrTi alloys like C18080/K88 show the necessary yield strength and the relaxation behavior for applications at temperatures up to 200°C.[91]

4.1.6 Shape-Memory Alloys and Their Applications in Electrical Contacts

Metals with the ability to "memorize" their original shape, shape-memory alloys (SMA), have been used in electrical contacts for several decades.[94–99] During this time the general knowledge about these metals has reached a high enough level to permit the production of high quality materials at reasonable prices.

The base for the shape-memory effect (SME) is the ability of these alloys to transform easily to, as well as form, a martensitic phase. Unlike other types of martensite, the SMA type only results in a small change of the volume. The desired shape is formed in the austenitic state at an elevated temperature. Then the piece of metal is cooled, resulting in a phase transformation to twinned martensite. In this state, the metal is deformed. By heating to the temperature interval of austenite formation, the original shape of the piece is obtained. If there is a restraint imposed on the SMA piece, it will instead exert a force on the surrounding material.

The SME is unique to two groups of alloys: nickel–titanium (Ni–Ti) and copper-based alloys (Cu–Zn–Al and Cu–Ni–Al) whose transition temperature is highly sensitive to the alloy composition and thermomechanical treatment. In the case of Ni–Ti, the temperature can be varied from −200°C to +100°C, whereas with copper-based alloys, it can range from −105°C to +200°C.

The shape-memory effect can be utilized in different fields of conventional and novel technologies as well as in medicine, biomedicine, and orthodentistry. Comprehensive reviews of the general applications of shape-memory materials and in the electrical industry are given by Schetky[100] and Braunović.[3,101] Table 4.7 shows an overview of identified SMA products developed and used in different domains.

Typically, the SMA are used in electrical contacts as force actuators, such as an additional SMA washer in bolted joints[98] or a SMA coil-shaped clamp in electrical connectors.[99] Other practical applications are circuit breakers, switches, switching devices, fuses, locking rings for braided terminals, temperature indicators, and others.

On the market, there is a large variety of SMAs, and their properties may be varied within quite extensive ranges. The major commercial SMA types are Ni–Ti alloys and Cu-based alloys. Ni–Ti alloys have the strongest SME and are superior to Cu-based alloys in corrosion resistance. For example, SMA 50/50 atomic percent nickel and titanium[99] can undergo up to 8% strain and

TABLE 4.7
Shape-Memory Alloy Applications in Power and Electronic Industries

Electrical Power Industry	Electronic Industry
Connectors	Integrated circuit connectors (IC)
Circuit breakers	Zero-insertion force connectors (ZIF)
Fuses	Dual-in-line connectors (DIP)
Switches, switching devices	Pin grid array package (PGAP)
De-icing of transmission lines	Microstrip connectors
Sagging of transmission lines	Locking rings for braided terminals
High-power heat engines	Disk drive lift/lower recording heads
Robotic devices	
Electrical/thermal actuators	
Thermomarkers	
Overcurrent protection	
Overheating protection	
Optical fiber splices	
Contact bounce dampers	
Nuclear power plant applications	

still recover its original shape. In addition, if that recovery is constrained, this alloy can generate stresses as high as 700 MPa. The Cu-based alloys, on the other hand, are much more inexpensive as compared to Ni–Ti, a ratio of about 1–10. In recent years, new types of Cu-based alloys have been developed, having improved mechanical properties, thus being strongly competitive to Ni–Ti alloys.

A detailed description of the origin of the shape-memory effect, SMA materials, shape-memory connector and switches designs are presented in Appendix "SMA."

4.2 COATINGS FOR ELECTRICAL CONTACTS

4.2.1 Basic Requirements

Presently, electronic and electrical industries are experiencing a relentless increase in the use of protective and wear-resistant coatings for electrical contact applications. Such trends are driven not only by the cost benefit demands but also many useful functions offered by the coatings such as: corrosion and wear protection, diffusion barriers, conductive circuit elements, fabrication of passive devices on dielectric surfaces, and others. To a large extent, the contact quality of different devices and systems is controlled by the electrical and mechanical properties of the surface layers. Depending on the coating material characteristics, contact operating conditions, and intended functions, the thickness of deposited material onto the contacting surfaces varies from 0.1–0.3 to 20–30 μm and sometimes to 100 μm.

There are several critical properties that dictate the performance of the coating and its ability to become an integral part of an electrical connection. The chemical composition of the product plays a major role in its performance, but the application parameters are equally important. To understand the critical role that they play in coating performance, a review of the most important parameters is in order.

The performance of an electrical connection is basically controlled by the phenomena occurring at the surface, such as contamination, oxidation, re-oxidation, sulfide-formation, corrosion, etc. The presence of these contaminants on the surface increases the contact resistance and is

detrimental to the connection reliability. Hence, maintaining the stability and integrity of the contact surface is of prime importance in the search for reliable connections.

The characteristics of contacts that otherwise could not be realized by common metallurgical methods can be modified and engineered within a wide range of appropriate arrangements of the layers in the coating, the layer thickness and composition, the substrate material and deposition conditions.

Coating characteristics can be varied over a wide range by changing the regimes and technology of coating, thus producing a great number of contact materials with different properties. For instance, contact resistance of a connection, such as a busbar, can significantly be reduced by plating the busbar surface with a sufficiently thick low-resistivity material. Also, the use of noble metals as coating materials in low-current contact applications substantially decreases their consumption in a variety of applications without any change in the design and dimensional requirements of a coated product.

It should be noted, however, that despite the obvious advantages of the coatings, there is still a number of problem areas that have to be addressed when using coatings for electrical contacts. For instance, in low-current sliding contacts wear resistance is of prime importance. Hence, if thin coatings are used (within the micron range), they have to provide adequate mechanical strength for a connection to prevent the occurrence of severe wear between the contacting surfaces. For that reason, it is preferable to wear out the brush rather than the coating.

There are a number of factors affecting the characteristics of practically all types of coated electrical connections. Among these, the surface imperfections (porosity), hardness (softness), adherence to the substrate, and resistance to oxidation and the effects of a corrosive environment are probably the most important. Porosity provides a path for the substrate materials to protrude to the surface and chemically interact with the surrounding environment. The result is the formation of complex corrosion products such as protrusions and surface films. As exposure time increases, the films thicken and spread over the entire contact surface, thus adversely affecting the contact resistance and the overall integrity and performance of a device. In severe cases, the coating is also affected by corrosion leading to its spalling from the contact (see Figure 3.27).

One of the most important tasks in ensuring satisfactory performance of an electronic connection is the prevention of corrosion occurring as a result of an intensive diffusion of the substrate material through the coating or the penetration of aggressive components of the environment to the substrate through pores, cracks, and other defects in the coating. Porosity has been considered as one of the major failure mechanisms in electrical connectors. However, understanding corrosion behavior both at pore sites and its effects on electrical performance is still quite sketchy and controversial. Nevertheless, numerous studies have shown that surface roughness[102,103] and the presence of dust[104] on the surface before plating are most likely the major parameters affecting the porosity. The adverse effect of porosity can significantly be suppressed by smoothing the surface roughness, using thicker substrate materials and pore-blocking corrosion inhibitor coatings.

Figure 4.4 illustrates the effect of surface roughness and the coating thickness on the porosity[103] of gold plate on OFHC copper substrate. It is clear that increasing the coating thickness and decreasing the surface roughness significantly reduces the porosity of gold plating.

Although the coatings are very successful in providing the most effective and economical connectibility and corrosion protection, there are some inherent problems that make it difficult to ensure complete reliability of a connection. Some of these problems are due to the chemical, mechanical, and electrical nature of the coating materials, whereas some are related to coating applications. One of these problems is adhesion, which can be very subtle and can involve effects that would normally not be expected.

The adhesion property of a coating is integral to its performance capabilities. Proper initial adhesion and the ability of the coating to provide adequate adhesion throughout the design life of the connection are the key factors in providing adequate and reliable connection performance. In other words, adhesive strength is defined as the force required to detach the coating from

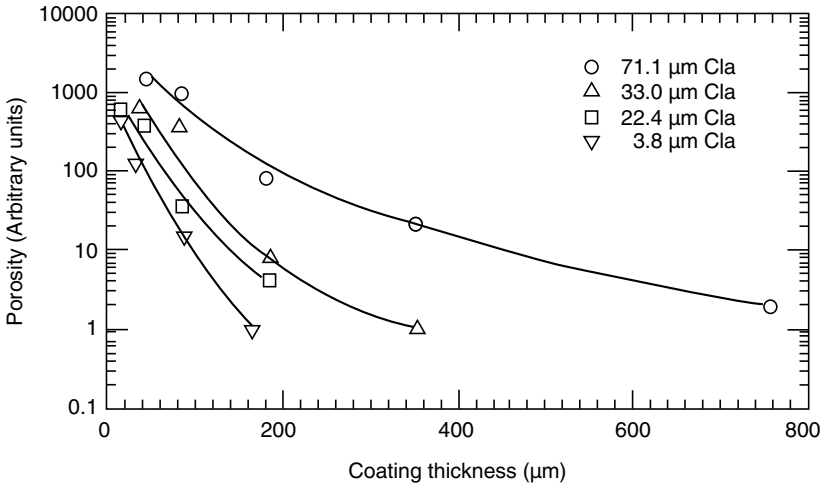

FIGURE 4.4 Effect of surface roughness and coating thickness on the porosity of pure gold plate on OFHC copper substrate polished and abraded with different grit-size papers. CLA denotes the substrate roughness in μm center line average.

the substrate. Although coatings with higher adhesive strengths are preferable, the ability to preserve their initial strength is perhaps more important, especially for connections designed for long service life. Hence, maintaining proper adhesion throughout the service life of the connection is one of the key factors in evaluating the success of the coating.

Furthermore, because the coatings may lose adhesion and separate from the substrate surface (spalling) under normal operating and environmental conditions, their ability to resist these tendencies is crucial. Therefore, the success of coatings in electrical and electronic applications lies in their ability to limit the adverse effect of environment, compatibility with the substrate material, and maintenance of the intended functionality of a device.

When selecting and depositing coating, different and often contradictory requirements have to be met. In general, the following general criteria are used: the functionality of the contact, operating conditions, the material of the main contact member (substrate), the compatibility of the coating and substrate materials, the coating cost, and environmental safety in coating deposition. For instance, development or selection of coatings for low-current contacts requires the following set of conditions to be considered: appearance of coating (bright or matte, no cracks); co-deposition of components when depositing alloys; hardness and tensile strength; property improvements (hardening, heat treatment, cold working); porosity; thickness and its uniformity; adhesion to the substrate; specific resistance; resistance to heat, corrosion, wear and electroerosion; solderability; multilayer coatings; internal stresses; and cost.[105] The combination of these requirements determines the methods to be used in the production of coatings for low-current contacts.

Detailed account of the problem areas in the coating technology can be found in the literature dealing extensively with the subject. Some of the most comprehensive references are found in Paunovi.[106]

4.2.2 Surface Engineering Technologies

The effect of surfaces has been well recognized in recent years, not only because of their effects on the surface-related phenomena in electrical contacts, but also because of the growing commercial availability of a wide range of cost-effective surface technologies now known as *surface engineering*. The success of surface engineering in electrical contacts is demonstrated by the

development and application of novel surface technologies to a variety of electrical and electronic components to improve their in-service performance, useful working lifetimes, aesthetic appearance, or economics of production.

Surface engineering is modifying the surface of a material or component to confer surface properties which are different from the bulk properties. The purpose may be to minimize corrosion, reduce frictional energy losses, reduce wear, act as a diffusion barrier, provide thermal insulation, electrically insulate, or simply improve the aesthetic appearance for the surface. Hence, under situations where components are subjected to complex external loadings, more than one surface technology needs to be employed to produce the required combination of properties to provide an adequate protection and maintain the fault-free functionality and performance of an electrical/electronic component.

There are many surface engineering methods for enhancing the corrosion resistance and/or their tribological properties that may generally be grouped into three broad categories (see Figure 4.5):[15]

- Surface modification without altering the chemical constitution of substrate
- Modifying the surface layers by altering the alloy chemistry
- Depositing the layers of material to the surface

In the case when the surface is modified without altering the chemical constitution of substrate, the metallurgical state is changed within the surface region either by thermal or mechanical means. Thermal means include techniques such as flame, induction, laser or electron beam surface treatments whereby instead of heating the whole component, only the surface is affected, so that the bulk properties remain unaffected and component distortion is minimized. These techniques are widely used to improve the hardenability of the treated materials, most often ferrous alloys.

4.2.2.1 Surface Segregation

Although not as widely documented as in the case of ferrous alloys, thermal treatments were also used to modify the surface properties of electric contact materials. This is achieved by provoking an intensive surface segregation of impurities or solute at the free surface. Segregation can be defined as the enrichment of a material constituent at a surface or internal interface of material. This segregation may intensify or moderate the tendency of surfaces to absorb active species

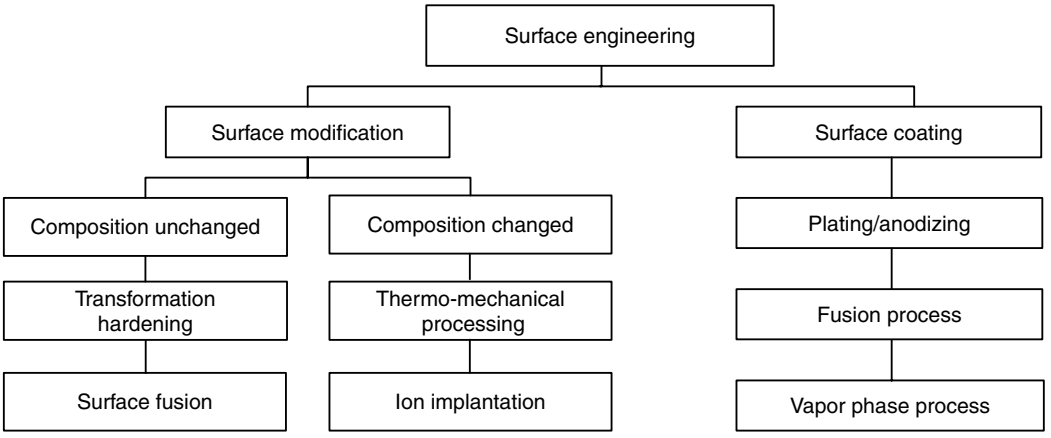

FIGURE 4.5 A summary of the methods available for surface engineering. (Adapted from Hutchings, I. M., *Tribology: Friction and Wear of Engineering Materials*, Edward Arnold, London, 1992.)

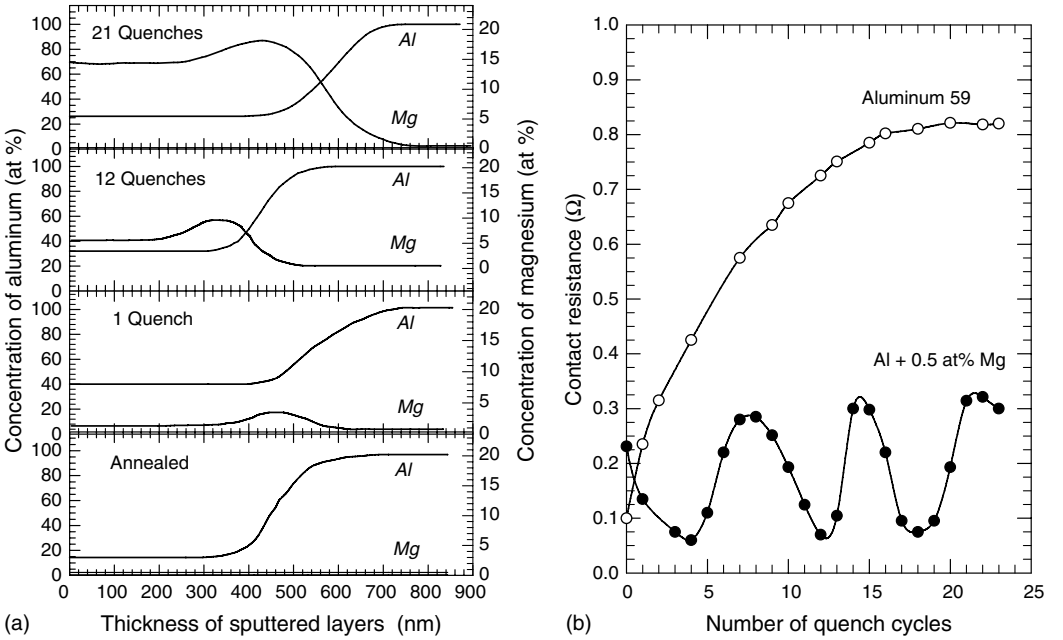

FIGURE 4.6 The effect of thermal cycling on the Auger electron spectroscopy concentration profiles of magnesium (a) and contact resistance (b) of high-purity aluminum and aluminum–magnesium alloys.

from the environment with consequent modification of the segregation of impurities from within the body.[107–112]

An example of the effect of impurity/solute segregation at the surface on the contact resistance of aluminum–magnesium alloy containing 0.5% Mg is shown in Figure 4.6. An intensive surface segregation of magnesium occurred as a result of thermal cycling as revealed by the Auger electron microscopy (AES). It appears that the enrichment of the surface with magnesium is a continuous process substantially lowering the lower contact resistance. A number of possible mechanisms were proposed to account for such beneficial effects of magnesium surface segregation. These include lowering the mechanical strength of the oxide by the presence of segregated magnesium, formation of a new phase MgO or $MgAl_2O_4$ in the oxide, and microblistering resulting from the thermal stresses during thermal cycling.

The mechanical means of surface modification include cold working by peening, shot blasting and other specialized machining processes to produce deformed layers. This process increases the stored energy and compressive stress, thereby increasing the hardness, fatigue and stress corrosion resistance. It has been established that impurity segregation in cold worked metals, as compared to annealed metals, can be enhanced by several orders of magnitude.[113] This is caused by the increased dislocation density produced during plastic deformation of the metal.

Indeed, an intensive segregation of sulfur was observed in the wear tracks formed by sliding contacts in OFHC copper.[114–115] The results of these studies indicated that the contact resistance tends to increase several orders of magnitude, eventually reaching a steady state. The coefficient of friction, however, decreased from a relatively high value to reach a low steady state value after prolonged oscillatory wear.

In the case when the surface layers are modified by altering their alloy chemistry, the new elements are diffused into the surface, usually at elevated temperatures, thus changing composition and properties of the coating as compared to those of the bulk. This technique is widely used to

improve the surface properties of ferrous alloys. There are many types of surface layer modifications, including chromising, aluminizing, siliconizing, and others.

4.2.2.2 Ion Implantation

Ion implantation is a well established process in semiconductor device technology. The ability to tailor profiles by ion implantation allows the development of novel device structures which are not achievable by conventional methods. Although the greatest attention at present is focused on the use of ion implantation for producing improved or new semiconductor devices, this surface modification technique was also used to improve wear resistance and connectability of electrical contacts.

Ion implantation is the process of introducing foreign atoms into a solid substrate by bombardment of the solid with energetic ions. Atoms of gaseous or metallic elements are ionized and pass to a high vacuum chamber where they are accelerated through a mass separator. Selected ions are then further accelerated and implanted into the target component. The implanted species occupy interstitial sites and distort the lattice. The depth of effect is very shallow, 0.2 μm, but the surface properties such as wear resistance, friction and oxidation/corrosion resistance can be enhanced.[116,117]

The results of studies of gold-, palladium-, and copper-based alloys showed that ion-implantation can significantly improve their surface and contact properties. For instance, it was shown[118] that boron implant can significantly improve adhesive and abrasive properties of 60Pd40Ag alloy and copper–nickel–tin alloy CA725, whereas the contact resistance of palladium-based alloy remains practically unaffected. The improvement in the properties was attributed to an increased superficial hardness produced by boron implantation. Similarly, Leech[119] has shown that the nitrogen ion implantation of Au26Ag3Ni, Au30Pd29.5A91.5Sn, and Au8Ag alloys significantly reduces the coefficient of friction and wear during sliding. These effects were associated with changes in the magnitude or direction of the initial adhesive transfer in sliding.

The effect of indium ion and nitrogen ion implantation on the contact resistance of copper and AgCu electrical contacts under fretting conditions showed that nitrogen ion implantation considerably reduces deleterious effects of fretting, whereas indium ion implantation had practically no effect.[120] Also, nitrogen ion-implantation significantly improves the adhesive wear and corrosion resistance of Ag-plated contacts without degrading the electrical contact behavior.[121] The beneficial effects of ion-implantation on the friction coefficient of AuAgNi[119] and contact resistance silver plated copper[120] are illustrated in Figure 4.7.

The third group of surface technology techniques is the group incorporating the widest group of coating processes, in which a material different from the bulk is deposited on the surface. Unlike the first two categories, there will be a clear boundary at the coating/substrate interface and the adhesion of the coating is a primary issue. There are numerous processes which involve coating with a layer of material, not necessarily metallic, to meet the requirements of specific service environments.

Among the main methods of this group are electroplating with or without reflow treatment, electroless plating, cladding, dip immersion, and physical vapor deposition (PVD). Chemical vapor deposition (CVD), swabbing, thermal deposition in vacuum, and electric-spark deposition are less common techniques.

4.2.2.3 Electroplating

The electroplating method is widely used in different industries, including electrical contact manufacturing. Electroplating is the deposition of metals (or alloys) on top of an electronically conductive surface from an electrolyte contains the metals ions (see Figure 4.8). The process is usually done form aqueous electrolytes at room temperature. A unique feature of the electrolytic

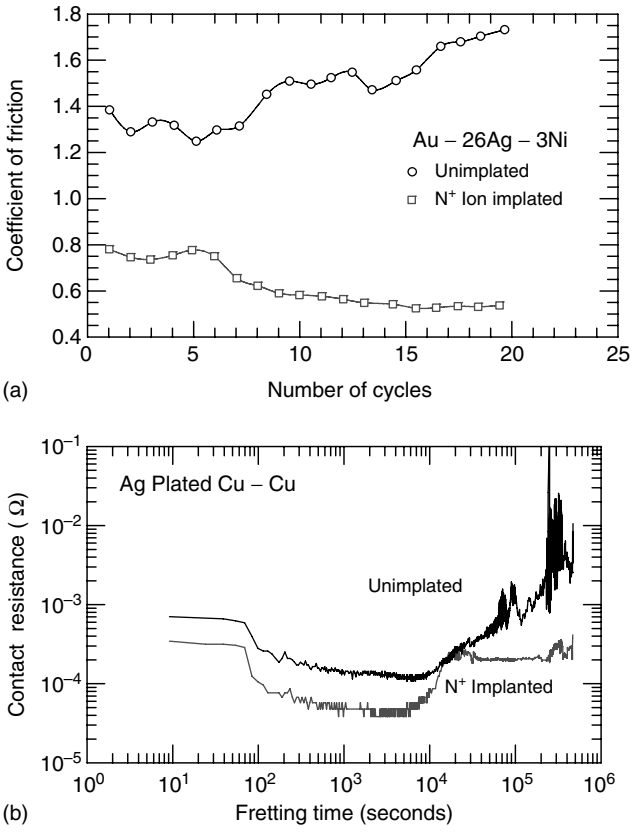

FIGURE 4.7 (a) Effect of nitrogen ion-implantation on friction coefficient of Au–26Ag–3Ni alloy (b) and contact resistance of silver-plated copper contacts. (From Leech, P. W., *Proceedings of 33rd IEEE Holm Conference on Electrical Contacts*, Institute of Electric and Electronic Engineers, Inc., 53–61, 1987; Braunović, M. and Trudeau, M. L., *Proceedings of 40th IEEE Holm Conference on Electrical Contacts*, Institute of Electric and Electronic Engineers, Inc., 195–210, 1994.)

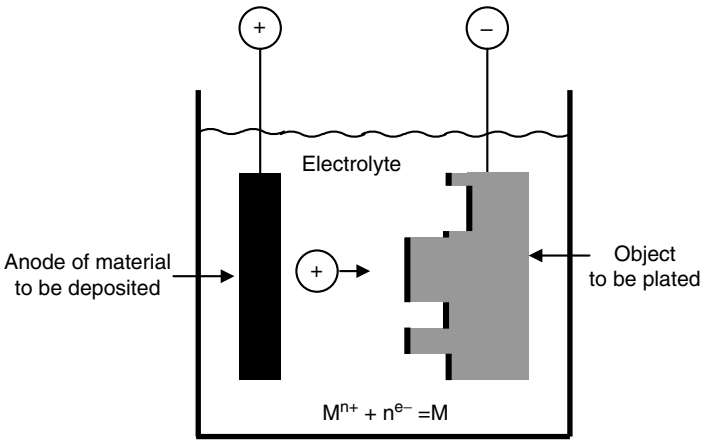

FIGURE 4.8 Schematic illustration of an electrolytic cell used to form an electroplated coating. (Adapted from Hutchings, I. M., *Trihology: Friction and Wear of Engineering materials*, Edward Arnold, London 1992. With permission.)

process is the possibility of controlling the deposition rate of the coating and its basic characteristics by changing the current density.

The coatings produced by this method possess a higher resistance to electrical erosion and hardness than corresponding bulk materials and coatings of the same composition deposited by other techniques. Electroplated rhodium and platinum show an especially high hardness (the Brinell hardness is up to 700 and 500, respectively). The hardness of palladium reaches 250, silver reaches 100, and gold reaches 70. In general, coatings with a higher hardness have higher wear resistance, providing the coating with no tendency toward brittle fracture. By varying the deposition regime, coating of different thicknesses can be obtained with characteristics otherwise not achievable by other methods.

Electroplating is very successful in reducing coating porosity. This is achieved by special substrate preparation, introduction of alloying additives, and depositing multilayer coatings. When introducing additives such as brighteners, a coating can be obtained that requires no further machining. This is especially important if noble metals are deposited. Electroplating is the basic coating method for both miniature low-current contacts and power connections with large contact surfaces.

The most common and widely used plating materials are silver, gold, tin, nickel, cadmium, palladium, platinum, and rhodium. Base materials such as copper and its alloys (bronze, brass) can readily be plated with any of these plating materials. Gold, rhodium, palladium, and platinum can be deposited on most steels, aluminum, and certain aluminum alloys, provided that a silver backing is deposited.[3]

The presence of impurities in the electroplated coating exerts strong effects on their structure and properties. This is manifested by significant increases of the specific resistance of the plating metal that otherwise would have a higher electric conductivity.

The advantages of electroplating are high deposition rate, a nonuniform thickness due to ohmic effects, a required conductive surface, a wide variety of materials that can be electroplated, low cost, and ease of control.

One of the most serious disadvantages of electroplating is the presence of high internal stresses that can lead to cracking generated in the coatings. Hence, to obtain a strong adhesive strength for the coating, careful surface preparation prior to electroplating is required. Thick coatings without internal stresses can be obtained by dipping a part to be plated into a molten metal bath rather than using a salt solution bath.

Another disadvantage of this method is the limited variations in the composition. Due to the instability of metals in different salt solutions, electrolytes for all combinations of metals are not possible. Even if the solution of two salts is stable, such as for Au and Co, the ratio of the composition cannot be varied over a wide range.

Sometimes the plated material includes several layers. The plating material can cover the substrate from one or both sides fully or partially. The possibility of producing joints of several materials with dissimilar characteristics allows developing materials which cannot be manufactured by other methods[122] for example to deposit a multicomponent gold-base alloy onto a material with good spring behavior. The problem of corrosion of plated materials is always important because the metals forming electric couples are mated. This induces electrochemical corrosion.

Plated materials are widely used for electrical contacts of a complex shape. Plating is performed simultaneously with the forging of a finished contact member; however, the method has some restrictions. For example, the manufacturing of a collector ring from a plated metal is a difficult task. This requires a stripe to be welded and the seam to be machined. As a result, the welded seam acquires properties differing from those of other materials.

In forging, characteristics of contact materials can change due to excessive work hardening and the protrusions of the substrate material at the contact edges. This reduces the corrosion resistance of the material as a whole, since the corrosion products appearing on the easily corroded substrate

metal can spread quite rapidly over the surface.[123] This phenomenon is especially pronounced if a material with discontinuous plating is used, and copper or its alloys serve as the substrate material.

4.2.2.4 Electroless Plating

This is a chemical reduction process whereby any catalytic surface in contact with the plating solution is coated uniformly regardless of part geometry. In this process the electrons still flow between the couples in the bath event in the absence of the electrodes. Several metals can be electroless plated, including palladium, copper, nickel, and silver. However, the most common are nickel and copper.

Ni Electroless Plating. Nickel is usually plated from a hypophophite bath on activated surfaces. The deposition is an alloy of nickel and phosphorous (6–18% P). The surface is activated by a colloidal mixture of tin chloride and palladium. Electroless nickel can be applied with excellent adhesion to many different substrates, including steels, aluminum; copper, bronze and brass, as well as nonconductors (ceramics, plastics), powdered or sintered metals, and magnesium, beryllium and titanium.

Cu Electroless Plating. Copper plating is limited for certain applications, such as in the semiconductor industry. The reducing agent in Cu electroless plating is formaldehyde, which is a carcinogenic material. This process can be costly due to environmental restrictions.

The hardness of an electroless nickel deposit is inversely related to its phosphorus content: increasing the phosphorus content decreases the plated hardness decreases. Electroless nickel deposits can be hardened through heat treatment which causes the formation and precipitation of nickel phosphide. When electroless nickel is heat treated to convert the deposited layer from amorphous to crystalline, the result can be very hard coating (400–500 HV).

Electroless nickel coatings have good wear resistance because of their high hardness and natural lubricity. This property, coupled with the uniformity of the electroless nickel deposit, makes it an ideal wear surface in many sliding-wear applications. Relatively soft substrates with poor abrasion resistance, like aluminum, can be given a hard, wear-resistant surface with electroless nickel. Electroless nickel has also found widespread use in antigalling applications where the use of certain desirable materials could not otherwise be used due to their mutual solubility and propensity to gall and seize.

One of the primary uses of electroless nickel in electrical contact and engineering applications is enhanced corrosion protection of critical components. Since electroless nickel is cathodic to most common metals in most environments, sacrificial mechanisms are not required to maintain its corrosion protection. Corrosion protection occurs through encapsulation of the substrate. Low porosity and resistance to many chemicals and atmospheric conditions make electroless nickel ideal for this application.

Electroless nickel is widely used in the electrical and electronic industries as coatings for aluminum and zinc connectors. The coating serves to provide corrosion protection, wear resistance, and is especially important because of the complex shape of these components. One of the major electronic applications of electroless nickel is the aluminum memory disk in computer storage devices.

4.2.2.5 Cladding

The cladding method involves the combined rolling of several layers at pressures 80–200 MPa. As a result, cold welding occurs at interfaces of different layers. Rolling is often carried out at elevated temperatures to achieve a stronger interlayer adhesion. Since surface films hamper the strong adhesion of metals, cladding is sometimes performed in vacuums or inert gas.

Cladding of common base metals such as copper and its alloys (brass, bronze), steel, and aluminum with precious metals like gold, silver, and platinum, is now a well-established technique to realize the optimal combination of functional properties. This method permits obtaining a combination of different properties, such as thermal and/or electrical conductivity, a high strength, corrosion wear and heat resistance, weldability, light weight, and springiness.

Cladding can be applied in the form of inlays, toplays, overlays, and edgelays. Typical applications of clad metals include contacts, thermostats, blades, springs, contact brackets, binding pads, lead frames, and connectors.[3] The thickness of the metallic layer deposited onto the base material can be 1 μm–2 mm.

When two metals to be joined by cladding have no tendency to cold welding but rather tend to form brittle compounds, the joint is very difficult to make. Nevertheless, if such metals are to be jointed, this can be achieved either by rolling two bars previously welded by electrocontact welding, or by rolling a multilayered joint comprised of a strongly adhering interlayer inserted between two incompatible metals.

Another form of cladding is welding of solid materials, such as silver, to a substrate like copper or aluminum [RusCan]. The advantage of using solid silver is that lubrication of the contact is eliminated and the accumulation of dust and other particles at the interfaces is reduced, thus considerably reducing the deleterious effects of wear damage. Even if damages do occur, the thickness of the silver in the contact is sufficient to maintain silver-to-silver contact, thus preventing exposure of the underlying copper to corrosion that would otherwise occur. Solid silver was used both on jaw fingers and switch blades, as seen in Figure 4.9.

The appropriate selection of materials allows equipment to endure short-circuit currents rated up to 30 times the normal current. The thick silver in the contact provides better heat distribution inside the silver itself and thus lowers the temperature of the contact zone under short-circuit conditions. Moreover, the property of silver alloys used for the contacts practically suppresses melting at the interface, and consequently no welding will occur.

Most of the high voltage disconnect switches have active contacts made of silver-plated copper contacts and structural parts of aluminum. Hence, there is a strong probability that interfacing of different materials may result in the formation of intermetallic phases between copper and aluminum due to an increased temperature of the contact interface caused by short-circuit or emergency operating conditions, for instance. The use of silver-tipped aluminum contacts eliminates this problem as well as the possibility of galvanic corrosion (see Chapter 6, Section 1 for details).

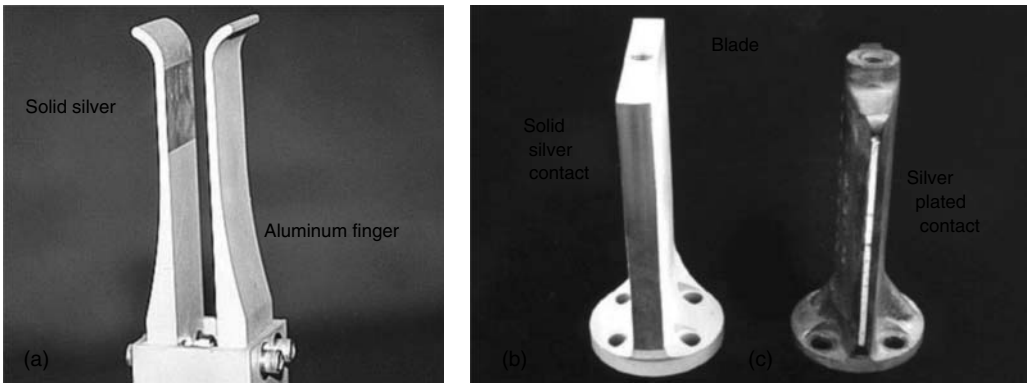

FIGURE 4.9 RusCan design for disconnect switch jaw finger and blade are shown in (a) and (b), whereas typical silver-plated blade contact is shown in (c).

The added advantage of using all-aluminum technology for disconnect switches is not only in eliminating potential deterioration problems such as corrosion or intermetallics, but also making their weight much lighter.

4.2.2.6 Chemical Deposition

Chemical deposition of metallic coatings involves the reduction of metal ions present in the solution on the active surface. The solution for chemical coating deposition includes salts of the metal being deposited, a reducing agent, a stabilizer, buffer compounds, brighteners, ligand donors, and other components. With the best developed processes of chemical silvering and gilding, coatings of up to 3–5 μm thick can be obtained. Solutions for the chemical deposition of palladium, platinum, and rhodium are available, but the deposition rate of these metals and the coating thickness obtained are low.

The hardness of chemically deposited coatings exceeds that of corresponding annealed metals, yet it is by 30–50% less than that of electroplated coatings. For this reason the wear resistance of these coatings is low. Disadvantages of the chemical deposition method lie in the instability of solutions, which require constant renewal, as well as limitations of the substrate materials. Due to these shortcomings, this method serves mainly as the first stage of the metallization of insulating materials, followed by the deposition of an electroplated coating.

4.2.2.7 Plating by Swabbing

This method is not generally recognized as an acceptable plating method since it provides merely a thin film, e.g., silver on the conductor, compared to the coating deposited on the conductor using other plating methods. However, this method is of practical importance when the contact surfaces have to be plated in the field.

4.2.2.8 Physical Vapor Deposition Technology

Although electroplating and cladding are used for the mass production of electrical contacts, vapor deposition has been suggested as an alternative method of coating.[124] The sputtering process, used in layer production, is the physical vapor deposition (PVD) technology, which is based on the processes resulting from glow discharge (see Figure 4.10). Metal atoms are sputtered from the target by bombardment with inert gas ions (argon) and deposited on the substrate placed

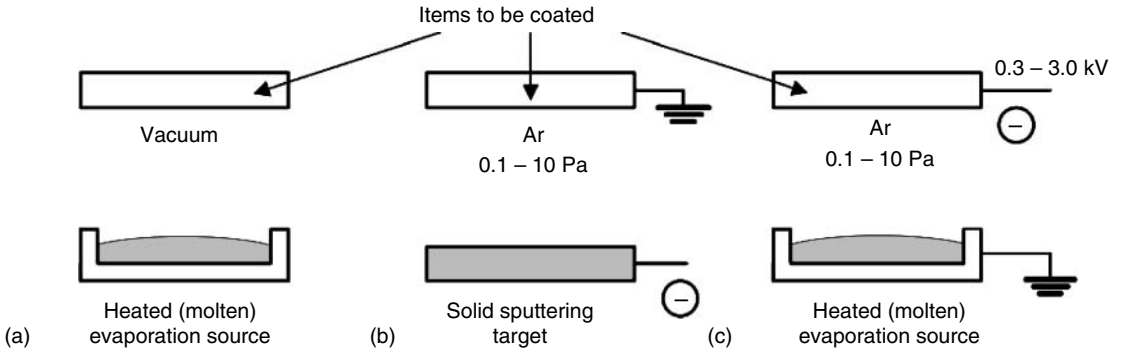

FIGURE 4.10 Schematic illustration of the principal methods of PVD: (a) evaporation; (b) sputtering; (c) ion plating. All these methods may be modified by the incorporation of a reactive gas into the system. (Adapted from Hutchings, I. M., *Tribology: Friction and Wear of Engineering Materials*, Edward Arnold, London, 1992. With permission.)

in the chamber. The mechanical, electrical, and chemical properties of the growing layer can be varied by changing deposition parameters, such as the residual gas pressure and corn position, the sputtering rate, the substrate temperature, and the substrate current.

The PVD technology has important advantages for the development of alloys because of the possibility of co-sputtering (several targets of different materials are sputtered simultaneously). The composition of the alloy can thus be varied in a wide range simply by changing the individual sputtering rates, i.e., the Ar^+ flux bombarding the target. The electron-beam evaporation process is not flexible especially for materials with a high melting point. Additionally, the adhesion of the layers and their structure are more appropriate in the case of sputter deposition because of a higher kinetic energy of the atoms impinging on the substrate surface.

The advantages of vapor deposition over electroplating are numerous. For example, vapor deposition can be used to create coating structures and compositions which are often either difficult or impossible to obtain by electroplating, including multilayers, composites, and amorphous alloys of metals and ceramics. From a processing point of view, vapor deposition is also an agile manufacturing technique; as the same vapor deposition system can be used to deposit almost any coating material onto any substrate. Furthermore, vapor deposition is an environmentally friendly manufacturing process which does not generate hazardous byproducts, such as the chemicals used in some plating baths.

The sputtering technique has been used for many years in electronics to deposit contact coatings of precious metal alloys onto microprofile wires and connector and switching contacts.[124–126] The sputtering process is characterized by a high rate. Moreover, sputtered coatings are highly pure, as there is no contamination by any other media like components of the electrolyte or residues from the rinsing and drying processes. The PVD technology opens new opportunities for the composition of contact systems and their thickness.

In addition to the PVD technology, thermal deposition and ion plating are two other methods are suitable for vacuum coating deposition. They are described and compared by Varga and Bailey.[127] Among these techniques, the ion plating method seems appropriate in contact fabrication. This method involves the application of a high negative potential to the substrate and the ionization of atoms of the metal being deposited in gas plasma discharge. These impinge on the substrate surface at a high speed and penetrate into it to a depth of 3–7 μm.[128] The substrate-coating interface almost disappears. This feature can be used at the first stage of coating deposition, especially with dielectric substrates, followed by the deposition of a plated coating with a very strong adhesion. This method is suitable for depositing any alloy and multilayer coating onto differently shaped substrates of metals, plastics, glass, and ceramics, and lead to highly homogeneous coatings.

4.2.2.9 Electro-Spark Deposition (ESD)

ESD is a capacitor discharge, micro-arc welding process that utilizes short duration electrical pulses, discharged at controlled energy levels, to create a metallurgically bonded surface modification. Electric sparks are generated at 10–1000 per second for 10^{-6}–10^{-5} seconds per spark. Direct current from the power supply will heat the electrode to 8000–25,000°C only at the contact areas and transfers a small quantity of the electrode to the work piece under an ionized state to produce a strong metallurgical bonding.

In this process very high densities of energy flows are achieved without significant heating of the specimen under treatment. Since the process is extremely nonequilibrium, principally new materials can be obtained which under common equilibrium conditions could not be produced. Moreover, in spark discharge the distance between the electrodes and substrate can be made extremely short, down to a few tens of microns. This eliminates the effect of the environment on the deposition process and excludes the necessity of a vacuum and thus significantly widens the application range of the coatings.

This process can be used to produce metallurgically bonded coatings and repairs with a minimal heat-affected zone (HAZ) and can be used to deposit a variety of engineered surface coatings. Nearly any electrically conductive cermet or metal electrode, having a melting point, may be deposited onto a substrate having the same characteristics. Electro-spark deposited coatings are typically in the range of 0.10–40-μm thick and are used to improve surface properties such as wear resistance, corrosion resistance, galling resistance, antisparking surfaces, and customized coefficient of friction.

4.2.2.10 Intermediate Sublayers

When the structures of the coating and substrate materials are considerably different, intermediate sublayers are deposited. The structure characteristics of the sublayer materials are between those of the substrate and coating materials that, in turn, improves the adhesion of the coating to the substrate. Such sublayers can produce a damping effect in the operation of low-current sliding contacts and also act as diffusion barriers to impede diffusion of the substrate material to the coating surface. The suitable selection of the sublayer material can improve the coating wear resistance. For example, it is shown[129,130] that when a hard nickel sublayer was used on copper, the wear resistance of a gold coating increased considerably. The proper choice of the coating and sublayer materials is an extremely arduous task; this explains why that multilayer coatings comprising from 3 to 5 layers have optimal performance characteristics.

4.2.2.11 Multilayered Contacts

Owing to the unavailability of a single general-purpose contact material, multilayer contacts are developed and used to obtain the intended performance within required ranges of mechanical and electrical loads. There are a great variety of methods of fabricating sandwich structures.[131–133] Figure 4.11 exemplifies such a structure. Up to 5 layers are put together to reach an optimum switching performance.

The basic idea of multilayer contacts is that materials with different conducting and erosion characteristics are combined in a single contact. Depending on the current load the contact has to switch, the suitable material is used; for example, when no load is switched, just the gold layer remains on the top. When high loads are switched, the gold and AgNi0.15 layers are eroded and the $AgSnO_2$ switches the load. Selecting the appropriate set of materials for the multilayer coatings

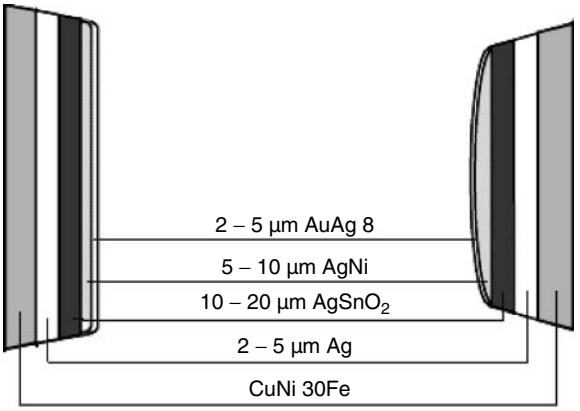

FIGURE 4.11 Multilayer contact profiles with five different layers of contact materials. (From Sauer, H., *Modern Relay Technology*, 2nd Ed., Huethig Verlag, Heidelberg, 1986.)

allows the contact to vary performance characteristics over a wide range. In practice, the number of different layers is limited by the cost.

4.2.3 Coating Materials

4.2.3.1 Coatings for Power Connectors (Copper and Aluminum Joints)

The coating of aluminum or copper by different metals is one of the most common commercial practices used to improve the stability and suppress the galvanic corrosion of aluminum-to-copper connections. The most widely used coating materials are tin, silver, copper, cadmium, and nickel. Surprisingly, very few comparative studies have been published on the efficiency of these coatings in maintaining the uninterrupted operation of aluminum-to-copper connections under different service conditions. This is because the effects of coating materials are very difficult to separate from those associated with the connector design. Much of the available data are primarily empirical in nature.

One of the first comparative studies on the efficiency of coating materials was carried out by Bonwitt, who in 1948[134] investigated the electrical performance of plated and bare bolted aluminum-to-copper connections exposed to elevated temperatures and a saline environment. The principal measurement characteristic, the contact resistance, was measured after the bolted joints were exposed to elevated temperatures and the salt spray. The coating materials investigated were cadmium, tin, and zinc deposited to copper busbars. Tin-plated copper, followed by bare copper, showed the best performance, whereas zinc-plated copper performed the worst. However, the contact resistance of both tinned and bare copper increased after exposure to the elevated temperature. It was also shown that galvanic corrosion was not eliminated by the coating and that the lubrication of bolted busbars was essential in a saline environment.

Subsequently, Hubbard et al.[135] evaluated the effect of cadmium, tin, and zinc platings on the performance of aluminum-to-copper joints of different designs under current-cycling conditions and in a saline environment. Cadmium on either aluminum or copper and hot-flowed electro-tin on copper were ranked as the most efficient plating materials. Again, lubrication was cited as essential in prolonging the useful life of plated aluminum-to-copper connections in a saline environment.

Bond and McGeary[136] assessed the effectiveness of cadmium, nickel, tin, and silver as coating materials in maintaining the stability of aluminum-to-copper bolted-type connections subjected to heat/current cycling conditions and also in a saline environment. It was demonstrated that the nickel-coated connections were superior in performance to other plating materials, as manifested by their stable contact resistance behavior under the simulated service conditions.

Although tin is widely used in the electrical industry, there is mounting evidence indicating that tin neither effectively prevents galvanic corrosion nor ensures the stability of aluminum-to-copper connections. Tin-plating, traditionally used to suppress the adverse effects of galvanic corrosion, requires no special surface preparation prior to assembly and improves the performance of joints at elevated temperatures. However, there is mounting evidence that the use of tin-plating is not as advantageous as previously thought for two main reasons. First, tin-plated contacts are very susceptible to fretting, which causes severe degradation of contact interfaces and leads to an unacceptably high contact resistance, instability and, ultimately, an open circuit. Second, tin easily forms intermetallic phases with copper even at the room temperature, rendering the contact interface very brittle, highly resistive, and susceptible to the influence of the environment. Furthermore, galvanic corrosion was not eliminated by tin coating, and therefore the lubrication of bolted busbars was essential for reducing the corrosion damage in a saline environment as illustrated in Figure 4.12.[134]

Silver is an excellent conductor and is widely used in joints for high-temperature operations in enclosed-type switchgear assemblies. The three most popular methods for coating the contact surfaces with silver are electroplating, plating by the dip immersion process, and plating by the swabbing method.

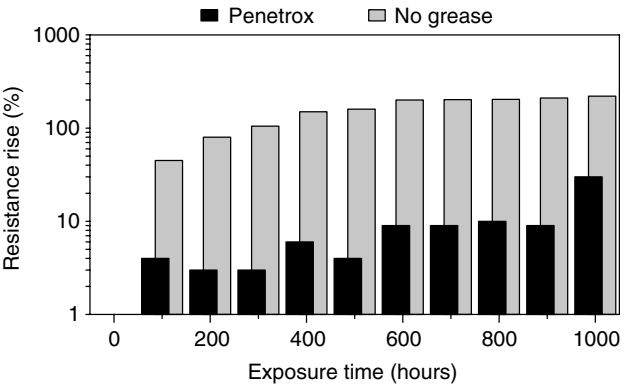

FIGURE 4.12 Effect of saline environment on the contact resistance of lubricated (Penetrox) and nonlubricated aluminum to hot-tin-dipped copper bolted joints.

Plating 5–15 μm thick for coating switchgears and enclosed buses is generally considered adequate, or even thicker than necessary. Because of the porosity of the silver plating, however, a thicker coating is required where abrasion and weather resistance are important factors. If the joint will be connected and disconnected many times during the life, for instance the operation of a disconnect switch, the silver plating must be thick enough to prevent the exposure of the aluminum or copper through wear.

Although the silver plating of electrical contacts is beneficial in maintaining a low electric resistance, it has a potential disadvantage: silver, like copper, is cathodic to aluminum and may, therefore, cause the galvanic corrosion of aluminum. Furthermore, due to the sensitivity of silver to tarnishing, the use of silver plating in environments with sulfurized contaminants has to be avoided. The coatings should be uniform and relatively thick. The use of protective contact aid compounds for the optimum performance is essential for silver-coated joints that are exposed to a high humidity or moisture. Of course, where no moisture or other contaminants exist, silver-coated joints are not subject to deterioration.

Most switchgear equipments are installed in relatively clean air with normal humidity. In such cases, the lubrication of the silver-plated joints will seal the joints adequately and protect them against the entrance of an electrolyte and the possibility of galvanic corrosion. Some manufacturers use lubrication as a regular practice, while others use high-temperature wax, such as ceresine wax dissolved in naphtha, which is easily deposited to coat the silver-coated contact surfaces. In outdoor sea coast exposures and in other strongly corrosive atmospheres where galvanic corrosion prevails, inhibitor paints should be used in addition to the contact aid compounds or wax coatings.

The problem of porosity and excessive wear of silver-plated contacts during make and break operations, as in the case of disconnect switches, can be alleviated and practically eliminated by welding thin solid silver plates or strips to the copper or aluminum contact blades or jaws.[137] The welded solid silver contact interfaces are impervious to creep or pore corrosion, less susceptible to fretting, have a superior wear resistance, and are significantly less affected by sulfur-containing environments since, as shown by Kassman et al.,[138] the presence of tarnish films can have a beneficial effect on contact behavior. In other words, an appropriate combination of silver and sulfurized film properties can produce positive effects on the wear and deformation of the contact and thus outweigh the negative effects of tarnishing on the electrical behavior of contact systems in which sliding, fretting, and make-and-brake actions are involved.

Nickel. Recent studies have clearly demonstrated that the nickel-coated connections, as manifested by their stable contact resistance behavior under the simulated service conditions, were

superior in the performance to other plating materials. From the available data, nickel appears to be the best practical coating material from the point of view of both its economy and the significant improvements of the metallurgical and contact properties of aluminum-to-copper connections.[139]

The superiority of nickel to other coating materials was confirmed by Jackson,[140] who performed current-cycling tests on tin-, silver-, and nickel-plated copper busbars bolted to 1350 grade aluminum. The nickel coatings on copper connections showed an excellent stability and low initial contact resistance. The poor performance of tin- and silver-plated connections was attributed to the effect of differential thermal expansion between the substrates of aluminum and copper that promoted progressive loss of the contact spots, leading to deterioration of the contact.

Lefebre et al.[141] showed that the instability of aluminum connections can be significantly reduced by the technology of direct nickel plating. The results of severe current-cycling tests demonstrated an excellent stability of the contact resistance of nickel-plated aluminum. Moreover, the nickel layer is stable up to reasonably high working temperatures (about 400°C). However, Aronstein[142] has shown that although nickel-coated aluminum wire conductors under different operating and environmental conditions had a better connectibility than uncoated aluminum wire conductors, but the coating/conductor interface was very susceptible to corrosion.

Furthermore, studies by Braunović[144] and Bruel et al.[145] on the effect of fretting on the contact properties of nickel-coated aluminum conductors revealed that, despite marked improvement brought about by the nickel coating, fretting still produces a considerable degradation of the contact zones. Lubrication, heavier loads, and shorter sliding amplitudes are found to mitigate these adverse effects.

Braunović[146] made a comparative evaluation of tin-, silver-, and nickel-plated copper-to-aluminum connections based on the performance of coated joints under current-cycling and fretting conditions and the ability to protect the contact against corrosion in saline and industrially polluted environments. The results summarized in Table 4.8 provide an overall assessment of the various coatings at a glance and provide a more quantitative method of comparison. The INDEX was obtained by averaging the numerical values assigned to the performance of joints under different laboratory (current-cycling and fretting) and environmental (saline and industrial pollution) conditions. The lower the INDEX number, the more efficient is the coating material.

From Table 4.8, it appears that nickel plating significantly enhances the stability of aluminum-to-copper connections (the lowest INDEX), while tin and silver coatings show the poorest performance (the highest INDEX) under different operating and environmental conditions. It should be emphasized, however, that the ranking of these coatings was obtained under the controlled conditions using laboratory equipment. Hence, it is of great importance to establish whether the difference between the coating materials tested will be significant in real operation where many extraneous and variable influences such as water, dirt, sand, acid rain, extreme ambient temperatures, pollutants, and other variables become very important.

TABLE 4.8
Summary of Comparative Evaluation of Different Coating Materials for Aluminum-to-Copper Connections

Contact Pairs	Index
Aluminum (nickel-plated)—Copper (nickel-plated)	0.7
Aluminum (copper-plated)—Copper (bare)	1.0
Aluminum (bare)—Copper (nickel-plated)	1.3
Aluminum (bare)—Copper (silver-plated)	2.0
Aluminum (bare)—Copper (bare)	2.4
Aluminum (bare)—Copper (tin-plated)	2.7

In summary, for added assurance of satisfactory performance on routine installations and for additional protection against adverse environmental effects, connections should be thoroughly sealed with a suitable contact aid compound to prevent the penetration of moisture and other contaminants into the contact zone. Detailed discussion of the types and effects of lubrication on the performance of electrical contact is given in Chapter 4, Section 4, and Chapter 9, Section 3.

4.2.3.2 Coatings for Electronic/Electrical Applications

Gold and Gold Alloys. For specific applications, such as safety components in the automotive industry or highly miniaturized electrical contacts with relatively low contact forces, the use of gold as a contact material is still indispensable. For strict safety requirements, gold coatings 0.8–4 μm thick are used.

Three different methods are used to deposit gold to the substrate material: rolling, galvanic deposition, and sputtering.[132] The performance of sputtered gold layers compared to rolled or galvanically deposited ones is superior in most applications but results in higher processing costs. Some part of the high processing cost can be saved by lower precious metal consumption.

The deposition of gold alloys by sputtering provides a combination of different elements that would not be possible to achieve by melting and ensure a much better hardness control of the gold layer. Further advantages of the sputtered gold layers are the absolute cleanness of the surface and the positive effect on material transfer. On sputtered gold layers the ignition of the arc takes place at different points distributed over the whole contact area. As a result, the contact erosion is well distributed and less severe.[147]

Rolled gold layers have comparatively low processing costs. The minimum thickness is limited to approx. 3 μm, but the metal consumption is relatively high. Another disadvantage of rolled gold layers is their low hardness and susceptibility to cold welding.

Galvanically deposited gold alloys are the most cost effective and widely used as a contact material for electronic connectors. When nearly pore-free deposits are required, the gold thicknesses are specified at 2–4 μm, whereas for less critical applications which allow for some porosity, 0.5–1.5 μm are tolerated.[82] Electroplated hard gold is widely used as a contact finish for sliding electrical contacts.[148]

The susceptibility of gold to the formation of spherical crystallites in electroplating can reduce the corrosion resistance of thick gold coatings since microcracks appear over the boundaries of single coarse crystallites and propagate through the whole coating.[149] In low-current sliding contacts, such coarse fragments on the contact surface can induce significant brush vibration that can increase the severity of coating wear and thus the probability of contact loss. For this reason, in some cases the surface is additionally machined after electroplating. For example, rolling by a steel or diamond tool smoothes the surface by plastically deforming the asperities, healing the pores and microcracks and hardening the coating. As a result, the contact quality is improved due to reduced tendency to vibration and an increased coating resistance to corrosion and wear.

The key point is to obtain a pinhole-free layer with the least possible thickness. This is possible with layers less than 1 μm thick. Diffusion of gold into the substrate material can be realized by diffusion annealing which, in turn, would further improve the performance of low-level switching.[150]

For gold-based alloys, substrate corrosion can be accompanied by coating corrosion especially at a high content of alloying elements.[52] For this reason the optimal concentration of the latter is recommended to be in the range of up to 2%.

Adhesive wear is one of the main disadvantages of gold coatings intended for sliding contact applications.[151] It can be overcome by alloying gold with other elements such as Ni, Co, Cd, Sb, Cu, Ag, and Pd. The introduction of small additives (tenth of percent) of nickel into gold, for example, increases the coating hardness several times.[152] Also, it was shown that alloying reduces the grain size by one or two orders of magnitude, i.e., from 1–100 to 0.01 μm.[152] In addition, structural

changes in the crystals, including the presence of the finest pores about 5 nm in size, increase the coating hardness. In some cases, the adhesion wear of gold coatings in dry air can be suppressed by alloying, but their corrosion resistance will be reduced. Decreasing the contact force is another means of reducing the wear resistance, but this is of limited value since this jeopardizes the vibration stability of the connection, a problem which is unacceptable in many applications.

The use of soft thick gold layers (>20 μm) in sliding contact leads to galling, whereas relatively hard coating causes brittle fracture to occur.[153] On the other hand, it was found[129] that nickel underplate minimizes the wear of the gold plate. In addition, both the adhesive and abrasive wear of pure (soft) gold platings can be markedly reduced using hard underplates and substrates rather than hard gold that is prone to brittle failure. The optimal thickness of the nickel underplate to yield stable contact resistance was found to be about 100 μm[130] so that a soft gold flash (5 μm) can be used over such an underplate. Nevertheless, the brittleness of nickel has to be taken into consideration when making connectors by stamping, bending, and other methods.

The miniaturization of components has led to higher local contact forces, ever-increasing environmental loads and operating conditions (friction and wear, temperature, corrosion), and cost reduction issues. This trend has triggered the search for alternative solutions for applications where standard gold systems are unsuitable from technical or economical viewpoints.

Among the available alternatives, a coating system involving a modified nickel-based coating and a thin gold layer 0.15 μm thick (the TRIBOR system) showed an outstanding performance, particularly at high mating cycles and under corrosive conditions. Owing to the nonmagnetic nature of the system components, this coating system offers improved performance levels for RF-applications by means of inter-modulation phenomena. In addition to its functional benefits, the reduction of applied gold thicknesses within the coating system allows overall costs to be reduced to a large extent.[154,155]

Alloying gold with another noble and base metals leads to a wide range of coating materials with different properties for electrical contact applications. For example, Table 4.9 presents advantages and disadvantages of some coatings of gold alloys for low-level switching.[132] Properties of the most often used gold alloys are discussed below.

AuCo Alloys. Electrodeposited cobalt-hardened gold has been the most widely used material for high reliability separable electronic contacts.[91,156] It is usually plated on a copper alloy substrate which may be a connector spring element, a pin or socket, or the edge of a printer circuit board. Nickel underplates and lubricants are commonly applied in the junction with gold to improve its wear resistance.[157] Clad metals are an alternative form of the contact material. They are made by roll bonding of a noble metal to a suitable substrate such as CA725 alloy (88Cu10Ni2Sn). Usually, a groove is machined in the substrate, and the noble metal on a thicker strip of nickel is placed in the

TABLE 4.9
Gold and Gold Alloys for Low-Level Switching

Contact Material	Advantages	Disadvantages
Au	High conductivity, 44 MS/m Corrosion protection	Very soft, hardness H_V 20 Tendency to cold welding
AuAg 8–10	High conductivity and reliability	Cold welding, sticking
AuNi 2–5	High hardness no and material migration in DC applications	Contact welding Formation of NiO_2
AuPd 2–4	High erosion protection	Fretting corrosion (polymerization)
Au Co 0.2–0.5	No material migration in DC applications	Oxidation of Co

Source: From Johler, W., *Proceedings of 21st International Conference on Electrical Contacts*, SEV, Fehraltorf, Switzerland, 87–100, 2002. With permission.

groove so that the resulting composite is flush with the surface. The clad sheet is subsequently stamped and formed into a connector element with the noble metal located at the point of electrical contact.

Due to cobalt's tendency to segregate, the temperature limit for AuCo layers with a small amount of Co (about 0.3%) is 160°C. Above 160°C, Co separates from Au (Co segregation) and diffuses into the surface where it oxidizes, leading to increased contact resistance and failure of the connector.[158]

Diffused gold/60Pd40Ag approved for the T & T Bellpac connector in 1980 has proved to be a successful alternate to electroplated Co-hardened Au in this and many other connector applications.[159]

AuPd Alloys. The catalytic nature of Pd makes these alloys susceptible to the formation of polymerized films on contact surfaces. For instance, organic vapors from the housing can polymerize on solid Pd deposits; under fretting or sliding conditions, these can lead to frictional polymerization and formation of a brown powder.[160] The high hardness of the pure Pd layer does not allow sharp bending operations.

Coating electroplated palladium connectors with a gold flash was found to prevent the brown powder effect.[161] Palladium with 0.2-μm hard gold surfacing is suitable for application in plug-type connectors because of very good wear characteristics of palladium balanced with good corrosion resistance of the added gold.[162]

AuPt Alloys. The AuPt1.0 and AuPt2.5 alloys with a 1-μm Ag diffusion barrier showed excellent properties in high-temperature surroundings such as in automotive electronics. The electrical and mechanical properties are stable at temperatures up to 200°C for the lifetime of a car. The ductile Ag underlayer coupled with the reduced thickness of the hard AuPt layer provides good contact bendability. Furthermore, fully coating the backside of the AuPt with Ag suppresses diffusion of Cu from the substrate material. Free stamping edges are not a problem for diffusion processes in terms of static contact resistance. Additionally, by introducing Ag as an intermediate layer, the minimum bending radius can be reduced to the thickness of the strip material and below. The contact system showed good fretting behavior in model testing and the friction coefficient was well less than 1.[91]

AuNi Alloys. In case of AuNi alloys (5% Ni) an increase in the contact resistance is observed at elevated temperatures ($T > 160$°C) due to the oxidation of nickel at the surface.

Silver and Silver Alloys. Silver-coated copper contacts are still commonly used in different types of apparatuses and connections in electrical power transmission and distribution systems. Copper and silver are sensitive both to sulfide and chlorine substances, and high corrosion rates can be expected in the paper and pulp industry. It was shown[163] that the silver coating thickness is the most important factor in maintaining the reliability of contacts operating in environments that are corrosive for both silver and copper. A cost-effective way to solve this problem is to use thick pore-free silver coatings. Another possible solution is to use a more corrosion-resistant copper alloy than the substrate, comparable to the use of brass to avoid copper creep corrosion. Inhibiting corrosion of both copper and silver with a suitable passivating chemical is an equally important task in the search for reliable silver-plated connections.

Electroplated Ag coatings are worthy coatings for temperatures up to 160°C with excellent electrical properties and good fretting behavior. Disadvantages of Ag are the reactions with sulfuric compounds, electromigration, and softening due to recrystallization at temperatures above 100°C (the hardness decreases roughly by 50%). In addition, at 180°C a very resistant oxide film is formed and, because of the hardness of the coating, very high normal contact forces are necessary to break the oxide film and maintain the stable electrical contact.[91]

An overview of the most commonly used silver contact materials for low-level switching is given in Table 4.10. Pure silver or silver–nickel alloys are the most cost-effective contact materials available. From a performance point of view, the materials listed in Table 4.10 are quite different. For example, pure silver or AgNi0.15 are only suitable for light loads and not resistant against

TABLE 4.10
Silver and Silver Alloys for Low-Level Switching

Contact Material	Advantages	Disadvantages
Ag	High conductivity, 60 MS/m Inexpensive	Formation of Ag sulfides, sticking
AgNi 0.15	High strength	Formation of Ag sulfides, sticking
AgNi 10–20	High erosion protection	Contact welding Material transfer
AgPd 60	High resistance to sulfide formation Good resistance to material transfer	Polymerization
PdRu 10	High conducting reliability	Expensive
$AgCdO/AgSnO_2$	High erosion protection at high current (power circuit breaker)	High and unstable contact resistance in low-level applications

Source: From Johler, W., *Proceedings of 21st International Conference on Electrical Contacts*, SEV, Fehraltorf, Switzerland, 87–100, 2002. With permission.

material transfer. The advantage is their high conductivity. The formation of AgS is not critical in sealed devices.

Alloys of AgNi with Ni contents between 10% and 20% are suitable for heavier loads, e.g., for higher currents, as AgNi has a good resistance against contact erosion. The disadvantage is the contact resistance stability and tendency for the welding of nickel.

Materials with palladium have a very high chemical resistance against all kinds of erosion. When materials with high palladium content are used, there is a risk of brown powder generation, as previously mentioned. The major advantage is their excellent resistance against material transfer.

AgCdO and $AgSnO_2$ alloys are used to switch high loads. Due to their heterogeneity they have unstable contact resistance at low-level switching loads. Resistance values up to 1Ω must be expected.

Standard contact materials for low-level switching contacts are gold-plated AgNi 10–30, AgPd 30–40, and PdRu 10.

Whether both or only one of the two contacts should be gold coated depends mainly on the substrate materials. Heterogeneous materials like $AgNi_2O$ should always be gold coated, whereas for homogeneous materials, such as Ag and AgPd, only one of the two contacts can be coated with gold.

Tin Coatings. In low-voltage, low-current operations tin is considered as a suitable substitute for gold plating in electrical connectors. The main applications of tin in the electronic and electrical industries are either solders or coatings to aid soldering or improve the connectibility of wires and cables with electrical equipment. Tin coatings are soft and ductile so that soldering with a thick coating can easily be performed. However, owing to its low hardness and tendency to readily oxidize and form a self-healing film, tin is less acceptable as a contact finish material.[3]

Tin coatings (pure and alloyed) are distinguished in terms of the coating process, which consists of hot dip tinning or electroplating with or without reflow treatment.[164] Tin coating performance will depend on a combination of the processing parameters used for tin plating, along with the environment to which the tin plated system is subjected to during the life of a connector system. A common plating process in Europe is hot dip tinning involving a hot air level system. Electroplating processes with or without reflow are mostly used in Japan. Depending on the design demands, both the hot dipping and the electroplating processes can provide the required thicknesses.

Tin easily forms discrete intermetallic compounds with most other metals. The solid diffusion of the substrate material into the tin coating usually occurs, causing the formation of intermetallic

compounds at the interface between the substrate and the tin coating. The diffusion process is mainly a function of time and temperature, but substantial diffusion rates can be provoked in tin-plated contacts by relatively low-density electrical current.[165] A detailed description of the crystal structure of tin intermetallides and crystal growth on solid surfaces can be found in Larson,[166] and Hammam and Sundberg.[167]

The electrical conductivity of the intermetallic compounds is almost the same as that of pure tin, while their hardness is considerably higher. The formation of intermetallic phases can cause the degradation of electrical and mechanical properties of connectors. Formation of the intermetallics in tin-plated connections should always be considered when the reliability of a tin-plated component is concerned. There have been many extensive studies dealing with the formation and growth of the intermetallics in copper–tin systems. The most comprehensive studies can be found in Timsit,[168] Bauer and Lessman,[169] Zakraysek,[170] Lindborg et al.,[171] and So et al.[172]

Tin-coated copper-based alloys are commonly used in electric connectors due to their low price and an acceptable reliability for many applications.[173] Tin-coated electric contacts are also used for separable plug-in-type connectors with a restricted number of insertion and withdrawal cycles such as printed circuit board connectors and pin-socket contacts.

Among many industrial applications, the use of tin-plated copper-based alloys for electrical terminals in the automobile industry is perhaps one of the most important.[174] Adding about 4% of silver to tin during hot dipping process improves the electrical and mechanical properties. This low alloyed tin–silver–copper coating (SnTOP) meets the engine compartment requirements in terms of temperature exposure while simultaneously providing low insertion forces.

This alloy is characterized by a hypereutectic microstructure with Ag_3Sn and Cu_6Sn_3 intermetallic phase particles in a tin solid solution matrix. Dispersion hardening and solid solution hardening effects ensure a good wear resistance combined with the necessary bendability. The dispersive Ag_3Sn particles impede the grain growth and the diffusion of tin during heating; increase the fatigue resistance, and improve the creep behavior.

Tin-coatings are normally used at temperatures up to 130°C, whereas this alloy can be used up to 160°C. They are inexpensive, corrosion-resistant, and show a high ductility. One disadvantage is the affinity of pure tin to fretting corrosion. At temperatures above 160°C softening and creeping occur, diffusion of Cu is accelerated, and eventually the entire coating is transformed into Cu_6Sn_5 intermetallics.

Palladium Coatings. Owing to its superior chemical stability and tribological properties compared to those of wrought gold, palladium is considered the most suitable substitute material for electronic connections.[175,176] Palladium coatings have a high hardness and corrosion resistance and in some cases are preferable to silver and gold. The tribological properties of palladium coatings, however, are somewhat undesirable due to the catalytic nature of palladium and its tendency to form polymers on contact surfaces, thus restricting its use in low-current contacts.[55,66,176,177] When exposed to industrial environments, chlorine has been detected in the surface films on palladium and some palladium–silver alloys.[178] Other disadvantages of palladium coatings are their susceptibility to delamination from the substrate under friction conditions and a comparatively low electric conductivity.[179] Apparently, contact materials containing palladium are the most expensive ones.

The adhesion of a palladium coating to the substrate can be improved by depositing interlayers. The high catalytic activity of palladium is reduced by covering it with rhodium or gold[177] and by developing palladium-based alloys with additives, considerably decreasing the catalytic activity of the base metal. The effect of the catalytic features of palladium can significantly be reduced by alloying with nickel and cobalt, but the corrosion resistance of the alloys formed is rather poor.

When there is doubt concerning the necessary conditions for a good performance of a device, gold finishes on copper or nickel are better choices as contact materials than palladium and palladium–silver alloys.[180] Hence, in sockets the use of palladium coatings is recommended in combination with a thin gold coating acting as a lubricant.[177]

Rhodium Coatings. Rhodium is an excellent contact material and inferior only to silver, copper, aluminum, and gold in electrical conductivity. Rhodium has a high ionization potential and possesses a good chemical resistance to acids, alkalis, halogens, sulfur-containing compounds, and other agents. Rhodium galvanic coatings are highly hard and wear resistant. Coatings up to 1 μm thick are usually used in low-current contacts. They can act as a diffusion barrier, e.g., between Permalloy and gold in magnetically operated sealed switches; protect silver against sulfidizing, and protect silver and gold against electrical erosion, and other effects. The operation of rhodium coatings can be improved significantly by depositing interlayers of soft ductile metals such as silver, tin, indium, and lead which have structures strongly differing from those of the substrate and coating materials.[181,182]

The wear and corrosion resistance of rhodium-based coatings can be improved with a multilayered Rh–Sn–Rh system with gold flash as an intermediate layer.[181,183] The heat treatment of this alloy resulted in a tin-enrichment amounting to 5–6% in the Rh plating.

Like other metals of the platinum group, rhodium has the tendency to form polymers at the contact surface, especially under friction conditions. Yet this tendency is less pronounced than in the cases of platinum and palladium. The catalytic activity of rhodium can affect the operation of sliding contacts. This drawback can be overcome by protecting the contact surface against environment effects by using a lubricant, since the structure of rhodium coating favors lubrication due to significant surface oil absorption.

Multiplated Coatings. A modern trend in the production of coatings for electrical/electronic contacts is the application of multiple surface systems. Such systems are widely used in separable electrical contacts for different purposes, such as improved conductivity, wear, and corrosion resistance.[184,185] A contact configuration using a noble metal (e.g., soft and/or hard Au or Pd) or a semi-noble alloy (e.g., Pd–Ni) for the surface coating on a Ni layer deposited onto Cu or copper alloy is judiciously combined to fulfill multiple criteria to insure reliability with respect to their intended functions. Although such thin films are typically a micron thick, they still ensure a satisfactory performance of a connection and thus avoid the large scale use of scarce or expensive materials.

Deposition of noble metal films onto the surface of multiplated electrical contacts yields a low contact resistance and plastic deformation and form a ductile nonoxidizing film on the surface that provides resistance to brittle fracture. Nickel coating serves as a hard protective underplate, whereas copper substrate provides a cushion against repeated mechanical loads arising in the contact. These types of contact material configurations are found in large quantities in electronic connectors, slip rings, and switches in low-voltage, low-current circuits in computers, telecommunication devices, and many other applications.

In many circumstances, the determining factor for production cost of these coatings is their ability to operate under conditions of normal repeated dynamic loads as well as under extreme vibration and shocks conditions. Obviously, operating under these conditions the reliability and useful life of these multiplated connections may deteriorate with time. Hence, to verify the robustness of the surface, wear testing has to be carried out.

Examples of multiplated systems comprising different contact materials for connectors are given below[186]:

- Hard Au plated CA654 (0.8-μm of 0.2% Co gold plating/2-μm Ni/CA654)
- DGR-156: (0.3-μm diffuse gold/2-μm R-156 60Pd–40Ag cladding/12.7-μm Ni/CA654)
- Sn plated half hard CA638 flat, and Sn plated C1750 dimple (3 μm electro-plate matte tin)
- Ag plated Cl70 (2.5-μm Ag/4-μm Ni/C170)

The above four materials represent conventional tin-plated copper alloys as well as the more expensive gold plating and gold cladding. A silver plate was added as a less expensive alternative

to gold. Copper substrate composition is as follows: CA654: 95.5%Cu–3.0%S–1.5%Sn–0.1%Cr; CA638: 95%Cu–2.8%Al–1.8%Si–0.4%Co; C1750: 97%Cu–0.5%Be–2.5%Co; C170: 98.1% Cu–1.7%Be–0.2%Co.

Numerous studies have dealt with the mechanical and tribological characteristics of multilayered contact materials, and the interpretation of the results was obtained by Engel.[184,187–189]

Base Metals. It should be noted that along with the development of new types of effective noble metal based coatings, there has been relentless research in the search for new contact materials as replacements for the ones presently used in electronic/electrical applications.[183,190–195] One or two characteristics of the best new materials are usually compared with those of materials on the basis of silver or gold, yet other characteristics such as the contact resistance stability, susceptibility to tarnishing, and life, are most often poorer. For example, according to the results of Waine and McKarthy,[83] the coatings Sn60Pb40 and Sn90Pb10 can compete with gold in the transition resistance, but they have a short life since seizure rapidly occurs in their operation. Moreover, their corrosion resistance is less than that of gold. For this reason they are suitable only for lubricated units which should not meet strict requirements on their reliability and life.

Nickel can be used as a final coating for separable electrical contacts in various applications such as batteries, automotive connectors, and others.[196–198] When using nickel, the main problem is noxious oxidation of the nickel surface which, depending on the atmosphere, can deteriorate its electrical performance. One way to avoid this problem is to protect the nickel surface with an organic layer capable of impeding the oxidation but not interfering with the passage of current.

Titanium Nitride. Today, ceramic coatings are widely used in friction units. The advantages of ceramics are high wear resistance, low friction coefficient, easy-to-perform deposition technology, and high chemical stability. Since almost all ceramics are insulating, their widespread use of ceramics in electrical contacts is restricted. Nevertheless, ceramic material such as titanium nitride TiN has conductivity comparable to that of many metals. Its specific resistance ($30\times 10^8\ \Omega\,m$) is the same as that of, for example, German silver. It was shown[199,200] that titanium nitride and other conductive ceramic materials deposited by the physical vapor deposition and chemical vapor deposition techniques have properties which make them potentially useful in electrical contact applications. These include an excellent wear resistance, a low bulk resistivity, and a high degree of environmental stability. It was found that TiN has a thin passive layer whereby the predominant species are oxynitrides. The composition of this passive layer appears to be process-sensitive and controls the contact resistance. Also, initial data shows that TiN coated samples are relatively stable to accelerated aging compared to current state-of-the-art gold electroplates.

In summary, it should be noted that notwithstanding significant achievements in the science of coating materials for electrical contacts these were developed primarily empirically. To some extent, this is due to fact that the calculation methods for determining the electrical and mechanical characteristics of contacts taking into account the coating properties are still lacking.[201]

4.3 COMPOSITE CONTACT MATERIALS

There are no pure metals or their alloys possessing a combination of properties to satisfy the requirements for the contacts commutating electric current within the whole range of devices from low-current apparatuses intended to commutate small currents ($I = 10^{-6}$ A, $U = 10^{-6}$ V) to power heavy-current high- and low-voltage apparatuses commutating direct and alternating current ($I > 1000$ A, $U > 1000$ V). The processes of erosion, friction, and wear are related to the chemical and physical properties of materials such as hardness, corrosion resistance, electric and thermal conductivity, thermal diffusivity, atomic volume, characteristic parameters of arc, electron work function, temperature and heat of melting and boiling, heat resistance, and others. The

combination of these properties is impossible to achieve in a pure material and hard to obtain in an alloy.

A way of creating a contact with universal properties is to develop heterogeneous systems or composite materials whose components do not form a mixture and provide the required set of properties.

The following sections deal with the main types of composite contact materials used in two fields, differing principally in the operating conditions, such as in arc-breaking and sliding contacts of electrical devices. As pointed out in the preface of this book, the topics covered will deal principally with permanent and sliding and not with make-and-brake (arcing) contacts. The latter is extensively covered in Lindmayer,[202] and in Slade.[203,204] Nevertheless, a brief review of the contact materials for arcing contact is in order.

4.3.1 Composite Materials for Contacts of Commutating Apparatuses

Pseudoalloys. Pseudoalloys are heterogeneous systems containing components which do not intermix either in the solid nor in liquid states and do not form chemical compounds. The results of intensive research and development in this field yielded materials with a combination of properties seemingly incompatible in one material alone. Pseudoalloys are those materials with nonequilibrium compositions and phases that do not interact or interact weakly with each other over a wide temperature range and retain their individual properties in the mix. In pseudoalloys both the properties of each individual component are combined, and their specific features appear.

The heavy-current breaking contacts are made from silver- and copper-based pseudoalloys using the powder metallurgy processes. These alloys include silver–cadmium oxide, silver–copper oxide, silver–nickel, silver–graphite, silver–nickel–graphite, silver–tungsten–nickel, copper–graphite, and copper–tungsten–nickel.[205] The silver or copper phase provides high electrical and thermal conductivities for the contact, whereas the refractory inclusions or frame improve the resistance to mechanical wear, electrical erosion, and welding. Compositions are produced by either the solid-phase sintering of blanks compacted from powders or impregnating preliminarily pressed porous frames from tungsten or tungsten–nickel alloys with silver or copper. Table 4.11 contains the compositions and characteristics of some pseudoalloy contact materials.

Silver-based contacts are widely used for switching power circuits and low-power control and signal circuits. Due to the contact material's low cost, as well as a lower receptivity to pollutants in

TABLE 4.11
Properties of Some Pseudoalloy Contact Materials

Contact Material	Density (kg/m^3)	Hardness, H_B	Electrical Resistivity, μΩm, Not Higher Than	Thermal Conductivity (W/(m°C))
Ag–CdO 85/15	9,700	100	0.028	325
Ag–Ni 70/30	9,600	75	0.030	355
Ag–Ni 60/40	9,500	80	0.035	310
Ag–C 97/3	9,300	50	0.026	—
Ag–C 95/5	8,700	40	0.030	420
Ag–Ni–C 68/29/3	8,900	65	0.035	355
Ag–Ni–C 69/29/2	9,500	95	0.035	—
Ag–Wo–Ni 48/50/2	13,500	160	0.041	275
Ag–Wo–Ni 27/70/3	15,000	210	0.045	230
Cu–C 97/3	7,300	35	0.040	380
Cu–Wo–Ni 48/50/2	12,100	150	0.060	190
Cu–Wo–Ni 27/70/3	13,800	200	0.070	135

the industrial atmosphere, Ag-based materials could in low-power applications replace more expensive noble metals through the careful selection of materials and surface treatments.

AgCd. Ag–CdO is widely used in devices operating at low voltages. In such materials high electrical and thermal conductivities of silver are combined with a hardening of the precipitation provided by the cadmium oxide. During operation of these contacts, the arc is suppressed by the vapors resulting from the endothermic thermal dissociation of CdO. The presence of dispersed cadmium oxide in the silver-based composite materials suppresses the action of plasma jets even at high currents, thus reducing electrical wear. The composition has a low stable contact resistance. Contacts made of silver and cadmium oxide are reliable in operation at high current loads and light contact pressures (1.5–10 N) since no insulating oxide films required for heavy pressure damage appear on their surfaces. They are highly resistant to welding and arcing but inferior to tungsten-containing compositions.

Ag–CuO. The use of fine dispersed Ag–CuO in heavy-current contacts for low-voltage applications increases significantly the wear resistance of contacts, improves the arc suppression capability, and reduces the silver consumption. Contacts made with these compositions have a low and stable contact resistance as well as high resistance to electrical wear and welding. At high current loads their performance is comparable to the AgCd-based contacts.

Ag–SnO_2. Ecological issues concerning the use of CdO in electrical contacts forced manufacturers to search for alternative solutions to CdO. As a result of extensive research and development efforts, Ag–SnO_2 was introduced as contact material for low-voltage applications.[206,207] In Europe and Japan the use of $AgSnO_2$ is mandatory, whereas in the United States, the replacement of AgCdO by $AgSnO_2$ has not proceeded due to different environmental regulations and because of lower costs for AgCdO and the necessary modifications to devices to accommodate $AgSnO_2$. In most cases the basic compositions of $AgSnO_2$ materials contain small amounts (up to 1 wt%) of additives of Bi_2O_3, WO_3, MoO_3, CuO, $FeWO_4$, and some other compounds.

Different manufacturing processes were developed and used to manufacture components with $AgSnO_2$-based contact materials for particular applications. Among the many processes available, the following are probably the most widely used: pressing of single articles, extrusion of preliminarily sintered powder bricks, rolling of powder bricks, cold upsetting from wire, and others. Table 4.12 shows the characteristics of silver–tin oxide compositions with different oxide contents and produced by different processes.

In switching devices operating up to 100 A, $AgSnO_2$ materials have excellent resistance to needle formation and mass transfer as compared to other contact materials such as pure silver and its alloys. $AgSnO_2$ contact materials are currently widely used as contactors, automotive relays, thermostat switches, motor starters, and others.[208,209]

Silver–tin oxide materials are generally more expensive for a given size relative to other contact materials. Their application depends on the need for their superior weld resistance under the specified electrical conditions or the need to maximize the contact life to material weight and/or size ratio. Applications where either of these two conditions exist provide the best opportunities for the use of silver–tin oxide materials (Table 4.13).[210]

AgZnO. The production costs of Ag/ZnO compared to Ag/SnO_2 encouraged the development of doped Ag/ZnO types which was aimed at improving the switching behavior of Ag/ZnO under inrush current load, but without loss of the good performance at resistive and inductive loads. Both investigated additives, silver tungstate and silver molybdate, had a great impact on the switching behavior of silver zinc oxide (with constant total content of metal oxide of 8%) at AC1, P1 and AC15 load. Results showed the performance of Ag/ZnO to be significantly dependent on the amount of additives and their grain size. Depending on the applied load, the optimum Ag/ZnO was found to be equivalent or superior to other silver metal oxides. Best results were achieved with silver zinc oxide doped with 0.25% silver tungstate (Ag/ZnO 8–0.25%) with a switching performance similar to that of the silver tin

TABLE 4.12
Compositions and Characteristics of Silver–Tin Oxide Composites

Content of SnO_2 (wt%)	Fabrication Method	Density (10^3 kg/m^3)	Vickers Hardness H_V (MPa) State[a] "Hard"	Vickers Hardness H_V (MPa) State[a] "Soft"	Strength σ (MPa) "Hard"	Strength σ (MPa) "Soft"	Specific Electrical Resistance (μΩcm)
8	Pressing of single articles, sintering	9.7–9.9	700	450	340	190	2.15–2.27
10		9.6–9.8	770	520	390	230	2.20–2.40
12		9.7–9.6	800	550	400	230	2.44–2.67
8	Extrusion (rolling) of sintered blanks	10.0	1,000	550	400	210	2.03–2.20
10		9.9	1,000	630	450	230	2.05–2.31
12		9.8	1,050	700	470	230	2.25–2.50

[a] Columns "hard" and "soft" contain maximal and minimal values of hardness and strength in these states; range of specific electrical resistance includes real data for "hard" and "soft" states.

oxide type $AgSnO_2$. Therefore, the new silver zinc oxide type is more than just an alternative to Ag/CdO due to its good results at inductive loads.[211]

Ag–Ni. The properties of Ag–Ni pseudoalloys are strongly controlled by the distribution, shape, and grain size of the constituents. Depending on chemical composition and production methods, all known morphological types of structures including the matrix, frame, mixed structures, required dispersity and anisotropy degree can be realized in these pseudoalloys. The solubility of silver in nickel and nickel in silver allows solid-solution strengthening and precipitation-hardening

TABLE 4.13
Compositions and Characteristics of Silver and Silver-Based Contact Materials

Material	Oxide (wt%)	Additives	Hardness	Conductivity (m/Ωmm^2)	Process[a]
Ag			$H_V10 < 30$	60	Melting
Ag/Ni10			$H_V10 < 60$	52–55	PM
Ag/SnO_2	2	Bi_2O_3 CuO	$H_V1 < 50$	58–59	PM based on reaction spray
Ag/SnO_2	2	Bi_2O_3 CuO	$H_V < 50$	58–59	PM based on reaction spray
Ag/SnO_2	8		$H_V1 < 55$	51–52	PM
Ag/SnO_2	10		$H_V1 < 55$	48–49	PM
Ag/SnO_2	12		$H_V1 < 70$	48–49	PM
Ag/ZnO	8	Ag_2WO_4	$H_V3 < 60$	50	PM
Ag/ZnO	12			43	PM

[a] PM, Powder metallurgy.

Source: From Behrens, V., Honig, T., Kraus, A., Michal, R., Saeger, K. E., Schmidberger, R., and Staneff, T., *IEEE Trans. on Components Packaging Manufact. Technol. Part A*, 17(3), 24–31, 1994. With permission.

processes to be used in the production of the materials with desired combinations of the properties required for a particular operation. Contacts made of the Ag–Ni composition are widely used in the low-voltage DC and AC applications at moderate loads. The AgNi contacts have a low and stable contact resistance and have superior resistance to welding and arcing compared to silver but inferior to Ag–CdO and Ag–CuO contacts.

The Ag–Ni compositions containing up to 50% of silver are ductile and easily rolled into wires, tapes, profiles or strips of any dimensions and can be soldered and welded. Contact elements of complex shapes can be fabricated by cold deformation using different forms of this material, thus making it suitable for a variety of applications such as bimetallic contacts, electromechanical relays, control contactors, etc.[212]

Note that when producing silver-containing contact materials on the basis of Ag–Ni, Ag–CdO, Ag–SnO_2, and Ag–CuO by powder metallurgy methods the chemical technique of charge preparation for contact pressing is used most often. It involves the precipitation of oxalates and carbonates of silver and the second metal from solutions of their salts and the subsequent thermal decomposition of the dried sediments. This technique provides uniform distribution of the mixture components and their high dispersity.

The AgMeO (Me = Cd, Sn, Zn) materials can be made using variety of process such as die compacting a chemically precipitated MeO, mixing it with additives, granulating, compacting, sintering and annealing, powder mixing, sintering and extrusion, or can be produced by a reaction spray process.[214]

Ag–C. Contacts made of silver–graphite are very resistant to welding and mechanical wear, have a low contact resistance but demonstrate a high wear under arcing conditions and a low mechanical strength and hardness. The introduction of graphite suppresses the arc ignition in typical 20 V applications.

Ag–Ni–C. The silver–nickel–graphite materials have a high welding resistance and relatively poor arc ignition, yet have a lower electrical wear resistance compared to silver–nickel compositions. These contacts are used for low-voltage applications operating at high current loads and overloads such as automatic switches. Adding fine dispersed silver–nickel improves the wear resistance. The silver–nickel–graphite is used in a combination with the silver–nickel to provide the contact with a high wear resistance.

W–Cu(Ag). The W–Cu(Ag) sintered composite materials have high mechanical characteristics, as the temperature and heat of melting of tungsten are combined with the good electrical and thermal conductivities of silver and copper. Switching contacts made of pseudoalloys demonstrate the ability to absorb excessive heat due to the melting and evaporation of a low-melting (sacrificial) components which are retained in capillaries of the refractory component due to capillary pressure.

Ag–W–Ni. Contacts made of the Ag–W–Ni composition have a high resistance to melting, welding, and wear at high current loads and are efficient as contact materials for air high- and low-current switches. The oxidation of tungsten favors the rise of the contact resistance which at low contact loads become unstable. The additions of nickel (2–3%) soluble in tungsten increase the strength of the material. The contacts include a silver sublayer.

Cu–Graphite. The copper–graphite composition is used for making contacts resistant to welding and capable of switching currents up to 30–100 kA. For this purpose the 10–15% porosity, relatively low hardness, and tensile strength are provided to ensure their separation in the welded contacts. These contacts are intended for a smaller number of operations. In some contacts, an interlayer with 3% of graphite is inserted between the top working layer with 5% of graphite between the copper sublayer. The interlayer decreases the warping of the contact resulting from the sintering of the top layer and copper sublayer brought about by the significant shrinkage differences.

Cu–W. Contacts made of copper–tungsten materials have superior properties such as wear resistance, resistance to welding, melting at high currents and voltages, and similar mechanical characteristics to that of silver–tungsten contacts.[215,216] Due to a strong susceptibility to oxidation,

the copper–tungsten materials are used in contacts operating in oil at high contact pressures such as in high-voltage oil switches. The W–Cu materials with the tungsten content of 40–70 wt% are effective arc-breaking contact materials for high-power contactors with an excellent electric wear resistance of up to 3,00,000–4,00,000 switching operations at currents up to 1000 A.

Cu–Cr. The Cu–Cr material is the major contact material for vacuum interrupter use, in particular for high current, short circuit interruptions.[205,217] The conventional isotropic structure of a powder metallurgy Cu–Cr can be improved by warm and cold extrusion to form long Cr particles perpendicular to the contact surfaces.[218] This structure improves the resistance to welding, the conductivity and the arc erosion resistance over the conventional Cu–Cr material. Cu–Cr can be used instead of WC–Ag for medium-voltage motor switching applications as well.[219]

Layer-Structured Contacts. The layer-structured contacts are widely used to replace the all-metal materials and to avoid the use of precious materials. Such contacts can be made by deposition of noble metals on the substrate base metals by using processes such as galvanic plating, ion-plasma deposition, and electric-spark alloying. The thickness of the working layer is usually less than 50% and in some cases it is 2–50% of the total contact thickness. Typical layered-structure contact materials are Ag–Ni, Ag–C, Ag–CdO, Ag–CuO, Ag–Ni–C, Ag–W(Mo), Cu–Ag–W, etc. The base metal can be copper, copper-based alloys, nickel, and steel. The following deposition methods are commonly used to fabricate the layer-structured materials: rolling; drawing; pressing; but, cold and diffusion welding; friction welding; sputtering; facing; and electroplating. Electroerosion coating deposition is an alternative method.

Pd–Cu. Palladium–copper alloys containing 15 or 40 wt% copper are commonly used as contact materials in telecommunications and automotive engineering because of their good resistance against material transfer. Since palladium and copper are completely miscible by forming superlattices in the solid state, the electrical conductivity of a formed alloy is extremely dependent on the composition of the alloys (Table 4.14). This is manifested by a distinct drop in the conductivity of copper with increasing palladium content in the solid solution. However, the presence of ordered phase in Pd/Cu40 substantially increases electrical conductivity. Five to ten times higher values can be attained if palladium and copper are combined as components in a composite material. Moreover, since no solid solution hardening is present, these composites have excellent ductility that allows for easy fabrication of contact parts like bimetallic rivets.

Palladium–silver–copper alloys are ideal for electrical contact applications due to their high hardness, good conductivity, good tarnish and wear resistance, and relatively low cost as compared with gold. The extreme hardness, although associated with desired properties, makes fabrication very difficult and prohibitively expensive using traditional metallurgy methods. Powder metallurgy offers an economical fabrication route by employing near net shape forming, thus greatly reducing

TABLE 4.14
Electrical Conductivity and Hardness of Cu/Pd Alloys

Composition	Conductivity, m/Ωmm^2 (as extruded)	Conductivity, m/Ωmm^2 (theoretical)	Hardness (H_V)	
			Annealed	Deformed
Cu/Pd 82	19.3	20.3		
Cu/Pd 68	27.2	27.9		
Cu/Pd 51	35.3	36.5	~90	~110
Cu/Pd 28	45.6	46.5		
Pd/Cu 40 (ordered phase)	15	21	120	250

Source: From Claus, H., Kocher, H.-H., and Stockel, D., *Proceedings of 30th IEEE Holm Conference on Electrical Contacts*, Illinois Institute of Technology, Chicago, 455–461, 1984. With permission.

TABLE 4.15
Physical Properties of Several Liquid Metals

	Hg	Hg–In	Na	NaK-78	GaIn-76	BZ
Melting Point (°C)	−38.9	—	97.8	−12.5	15.7	−76.0
Density (kg/m^3)$\times 10^{-3}$	13.6	10.0	0.93	0.85	6.30	1.48
Viscosity (kg/m s)$\times 10^3$	1.2	1.5	0.69	0.47	1.50	0.62
Surface Tension (N/m)	0.48	—	0.195	0.115	—	0.093
Conductivity (mho/m)$\times 10^{-6}$	1.0	1.0	10.0	2.17	3.45	1.41

Source: Johnson, L. J., Mole, C. J., and Arcella, F. G., *Proceedings of 20th Holm Conference on Electrical Contacts*, Illinois, Institute of Technolgoy, Chicago, 201–210, 1973. With permission.

machining expenses. Other methods include canning of the copper clad palladium wire bundle and extruding the arrangement in one step nearly to the final dimensions, as well as the extrusion of a two-sheet wound body without the formation of the solid solution.[58,220]

Liquid-Metal Composite Materials. Liquid-metal composite materials form a specific group of composite contact materials made by impregnation. These materials consist of a porous tungsten frame (rigid powder or elastic wire) impregnated with a low-melting metal or alloy.[87,90,221] Liquid-metal composites combine the advantages of both solid metal and liquid contacts. The solid frame gives mechanical strength to the contact, making its performance characteristics independent of the spatial position, while the liquid metal provides a low transition resistance, allows independence of the contact pressure, and eliminates welding.

Liquid-metal composite materials for power applications with the powder frame are fabricated from the tungsten powder with a certain granularity and materials. The elastic frame is made of a tungsten grid with a regular structure. The grid frame allows the reduction of the volume and porosity of the material at light contact pressures to improve the supply of the liquid metal to the contact surface, thus making the contact characteristics more stable. Gallium or its eutectic alloys being in the liquid state at temperatures above 3°C are an example of liquid metals. The liquid-metal contacts with the elastic frame reduce the impact loads when closing contacts. Properties of commonly used liquid metals are shown in Table 4.15 and Table 4.16.[87,221]

It is reported in the literature that currents of 20,000–300,000 A can be transferred across close-fitting stationary and rotating members through a liquid metal medium because essentially 100% of the surface area is available for electrical contact at the interfaces of the collector members and the

TABLE 4.16
Composition and Melting Points of Some Low-Melting Temperature Alloys

Melting Point (°C)	Ga	In	Sn	Bi	Pb	Cd
10.7	62.5	21.5	16	—	—	—
15.7	75.5	24.5	—	—	—	—
29.75	—	100	—	—	—	—
47	—	19.1	8.3	44.7	22.6	5.3
58	—	21.0	12.0	49.0	18.0	—
60	—	51.0	16.5	32.5	—	—

Source: From Burton R. A. and Burton, R. G., *Proceedings of 34th IEEE Holm Conference on Electrical Contacts*, Institute of Electric and Electronic Engineers, Inc., 187–192, 1988. With permission.

liquid metal, in contrast to micro areas of contact (about 1%) in the case of conventional solid brushes. Consequently, very low contact voltages and low associated electrical power losses occur even when very high currents are collected in liquid metal systems. In addition to providing low contact resistance, liquid metals also possess low bulk resistance, leading to low electrical power loss associated with the conduction of load current through the liquid metal medium. To achieve efficient transfer of electrical current, however, the liquid metal must be confined to the thin ring-shaped volumes or annular channels which comprise the machine's current transfer or collection zones. Successful utilization of liquid metals for this purpose is seriously challenged by an ability to hold the fluid in the annular channels under all operating conditions. This is especially of concern in the case of horizontal shaft machines.

Although the liquid-metal materials are used primarily to make contacts for high-current commutating machines intended for various applications, recently the liquid metals have been used as a flexible nondegrading contact mechanism in MEMS power relay. The basic systematic requirements for the microrelay include large current carrying capacity, high speed, use of control voltages readily available in the given application, and an acceptable hold-off voltage.[222] The benefits of liquid-metal contacts are low contact resistance, no signal bounce, no mechanical contact wear, and contact stability at microscale levels. Another recent application of liquid metal is a micromechanical switch with electrostatically driven liquid-metal droplets. The droplet is driven by a given voltage bias that induces electrostatic force between a grounded liquid metal and an imbedded actuation electrode.[223]

4.3.2 Self-Lubricating Composites for Sliding Contacts

Composite materials used in sliding contacts can be conventionally divided into the following groups: carbon-based materials, metal-based self-lubricating materials, combined (sectional) contact elements, polymer-based materials, and carbon-fiber composites. Detailed descriptions of these materials are given in the following sections.

Carbon-Based Materials. In 1888, the first practical application of carbon materials was made by Thompson Houston Company (which later became General Electric).[224] Since that time, carbon-based materials have played a dominant role in wear applications, including bearings, seals, and electrical brushes. Most carbonaceous materials are related to graphite in that they are made up of hexagonal rings of carbon in a variety of arrangements.[225]

Conventional graphite is well known as a solid lubricant of lamellar structure. Graphite crystallites are highly anisotropic in their physical characteristics. In terms of crystal structure and chemical reactivity, the main features of the graphite crystallites are the basal planes which are the cleavage faces of the crystalline lamellae, constituted by carbon atoms in a hexagonal arrangement; and the edges of the basal planes that are corrugated surfaces resulting from the rupture of the hexagonal lattices. Atoms on the basal plane only have van der Waals attractions available and, therefore, are chemically inactive but favorable to physisorption of nonpolar molecules from their environments. In contrast, the edge surfaces are fairly chemically active because each exposed atom has free chemical bonds which will readily react with oxygen and water molecules in the atmosphere. Polar compounds (water, aliphatic alcohols, and halides) will likely be adsorbed on the edge surfaces. The ratio of basal plane area to edge surface area is important in the surface reactivity of the crystallites and their antifriction and antiwear properties. Unless the crystallites are finely subdivided, the edges of the flaky crystallites will comprise only a small fraction of the total surface area. Much of the effectiveness of graphite in controlling sliding friction and wear is attributed to this structure.[226]

Graphite has a reasonably good conductivity, does not form tarnish films, has good arc-resisting characteristics, and is not subject to welding. Thus graphite, or carbon, contacts have been utilized in many applications requiring these special characteristics. Graphite has another well-known and worthwhile characteristic: its retention of properties at high temperatures.

Synthetic graphite may be formed by the pyrolysis of pitch and coke at temperatures above 2200°C. Thermosetting resins of many types, but notably phenolic, may also be pyrolyzed. They may be reduced to a special form of carbon that is described as glassy or vitreous.[227] Sometimes it has been termed amorphous or mesomorphous; however, it has been suggested that there is, indeed, an allotropic form of carbon identifiable as vitreous carbon.[228] To form the material, liquid polymer is cast and hardened by a catalyst or by heating; it is then dried and allowed to cross link at the elevated temperature, and then slowly pyrolyzed in an inert atmosphere.

Most of carbon-based contact materials are obtained using carbon ceramics or powder metallurgy methods from graphite, coal, black, etc. powders. The properties of the raw carbon materials are described in detail in Ubbelohde and Lewis,[229] and in Shobert.[230]

The widest application field of carbon materials is *electrical machine brushes*.[231–236] Carbon substances like graphite, coal, black, etc. contained in the most kinds of brushes provide a relatively low friction coefficient and good commutation behavior. They are characterized by a high chemical resistance, a low linear thermal expansion coefficient, satisfactory electrical and thermal conductivities, and antifriction properties that ensure high performance of contact materials operating under normal conditions.

Electric brush materials can be divided roughly into four main classes: metal–graphite, carbon–graphite, graphite, and electrographite (see Table 4.17).

Carbon–graphite brushes are made by compacting graphite powders with other carbon materials such as coke and black and binders like tars and pitches followed by heat treatment at a temperature of about 1400°C. They have a high hardness and specific resistance.

Graphite brushes are fabricated from natural graphite without (soft brushes) and with (hard brushes) binders. Soft brushes are not sintered after compacting. They are soft and produce insignificant noise in operation.

Electrographite brushes are produced from powders of graphite and other carbon materials such as coke and black and binders by high-temperature sintering at above 2500°C. In this process impurities are removed and graphitization occurs, such as the formation of electrotechnical polycrystalline dense graphite with a higher crystallite size. These brushes have a high mechanical

TABLE 4.17
Basic Information on the Main Classes of Brush Materials

Class, Primary Application Field	Raw Materials and Production Process
Metal–graphite	Graphite and copper/silver powders with small amount of additives, e.g., tin
Low-voltage generators, slip ring assemblies	Mixing without binders, compacting, sintering at temperatures below 1000°C
Carbon–graphite	Powders of graphite and other carbon materials (technical carbon, coke)
Generators and motors with alleviated commutation conditions and alternating current collector machines	Mixing with binders (pitch, tar), compacting, sintering at temperatures above 1000°C
Graphite	Graphite powder. Mixing with binders (pitch, tar), compacting at temperatures above 1000°C
Generators and motors with alleviated commutation conditions, slip ring assemblies	High-resistance (resin-bonded) type: graphite powder. Mixing with binders (e.g., bakelite), compacting, sintering at temperature about 200°C
Electrographite	The same as graphite or carbon–graphite brushes, but with electrographitization, i.e., heat treatment at 2500–2800°C
Generators and motors with moderate or bad commutation conditions, slip ring assemblies	

strength and resistance to pulse load variations in traction motors. Depending on the composition and treatment regime, they can have different hardness and provide good commutation in high-speed machines.

Metal–graphite brushes can be made by the ordinary powdered metal processes, or by processes using plastic molding techniques. These give another dimension to the applicability of brush materials.

Technology of all types of brushes is quite complicated, including a series of operations. For example, Figure 4.13 shows a schematic of the general technological process for electrographitic brushes.

Systematic observations of the operation of brush-collector units of electrical machines performed over a long time permitted the establishment of general requirements concerning replacement scheduling of the collector and the performance characteristics of carbon brush materials. For example, as the content of black introduced into the brush material increases, the commutating ability of brushes rises, yet their wear resistance decreases. On the contrary, increasing the graphite content at the expense of black reduces the wear while making the commutating characteristics poorer. In the case of metal–graphite brushes, higher speeds suggest greater percentages of graphite while higher current requirements dictate greater volume fractions of metals.

There are many technical characteristics used in the assessment of properties and selection of brush materials: physical–chemical (the specific electrical resistance, density, and ash content); mechanical (the hardness and ultimate strength); collector (the contact voltage drop, friction coefficient, and wear); and performance (the nominal current density, permissible peripheral velocity, nominal pressure, commutating ability). Table 4.18 shows the physical properties of some of the generic types of brush materials.

Since brush articles are important in modern engineering they are produced in many countries and the assortment of brush materials and the range of their properties are very wide. Catalogs of brushes produced by the major companies in the field can be found in the following URLs:

Dow Chemical Company (http://www.dow.com)
Morganite, Inc. (http://www.carbonbrushes.com)

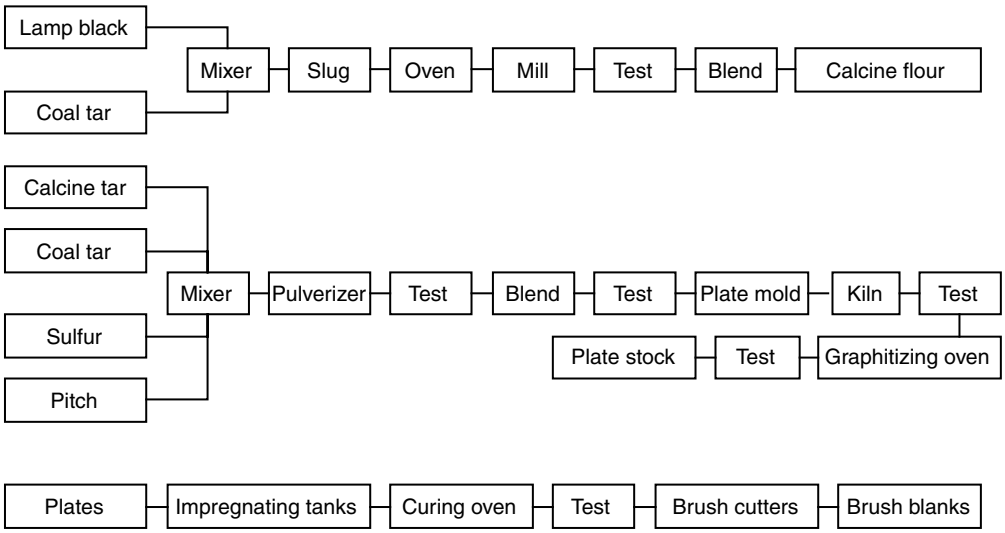

FIGURE 4.13 Typical process for the manufacture of electrographite brushes.

TABLE 4.18
Physical Properties of Some Generic Types of Brush Materials

Type of Brush Material	Contact Hardness (N/mm^2)	Density (g/cm^3)	Resistivity ($\mu\Omega cm$)	Thermal Conductivity ($W/cm°C$)	Heat Capacity ($J/cm^3°C$)
Copper–graphite (40Cu60C)	100	2.75	75	—	1.79
Resin-bonded graphite	260	1.70	100,000	0.088	1.41
Electrographite	290	1.52	2,000	0.3	1.26
Carbon graphite	350	1.72	7,300	0.064	1.43

Source: Based on data from Shobert, E., *Electrical Contacts: Principles and Applications*, Slade, P. G., Ed., Marcel Dekker, New York, 839–872, 1999.

Schunk Graphite Technology LLC (http://www.schunkgraphite.com)
Carbon of America (http://www.carbonebrush.com)
St. Mary's Carbon Company (http://www.stmaryscarbon.com)
Repco, Inc. (http://www.repcoinc.com)

Carbon-based materials have a number of disadvantages, but the most serious is that their contact characteristics are environment-dependent. For example, it was shown that there is a critical water vapor content in the atmosphere below which the catastrophic wear of graphite brushes occurs.[237] A similar phenomenon was also found for electrographite and silver–graphite brushes.[238,239] It should be noted that the satisfactory operation of brushes at high altitudes and in vacuum represents a serious problem, and a solution is a challenging development task. High contact resistance sensitivity of most brush grades to heat and moisture impedes the reliable operation of small electrical motors under poor climatic conditions.

The operating performance (contact resistance, friction, and wear rate) of conventional carbon brushes is known to be dependent on the application requirements (electrical load, speed, and efficiency), the materials of the contacting members, and the nature of the environment. With regard to environmental factors, the pressure and composition of ambient gases, including additives such as water vapor, play an important role in reducing brush friction and wear. High friction and wear occur when sliding contact pairs operate in vacuum or dry gas ambient media.[226,240] Carbon brushes were never considered serious candidates for high currents. However, under special environmental conditions, e.g., in humidified CO_2 gas environments, the permissible current density for carbon and metal–graphite brushes can be increased almost by an order of magnitude.[240]

Taking into account the restricted capabilities of pure carbon materials, a wide variety of composite contact materials has been developed combining a carbon matrix with components made of other materials such as metals, metal oxides, and other functional additives. These materials include brushes of the metal–graphite class like silver–graphite and copper–graphite while excluding grades with a very high metal content. Compared with carbon brush grades, these brushes have a lower specific resistance and contact voltage drop and allow a higher current density (see Table 4.18). For this reason they are primarily used in low-voltage electrical machines operating at relatively high currents.

Increasing the metal content in metal–graphite compositions increases their strength, density, thermal and electrical conductivities, and raises performance characteristics such as the contact

TABLE 4.19
Some Properties of Silver–Graphite Materials

Composition % Ag	Resistivity (10^{-7} Ω m)	Hardness (10^5 N/m^2)	Density (kg/m^3)	Thermal Conductivity (W/m° C)	Coefficient of Friction
60	10	2.96	3,800	35	0.15
70	3	3.05	4,500	115	0.175
75	1.75	3.10	5,200	210	0.19
80	1	3.13	6,000	345	0.20
90	0.32	3.22	7,000	385	0.23
95	0.20	3.26	8,000	410	0.25

Source: Based on data from Kuhlmann-Wilsdorf, D., Makel, D. D., Sondergaard, N. A., and Maribo, D. W., *IEEE Trans. Components Hybrids. Manufact. Technol.* 12(2), 237–245, 1989. With permission.

resistance, friction coefficient, and heating. The pattern of changes in these characteristics of silver–graphite materials is illustrated in Table 4.19.

Problems arising in operation of carbon materials are often solved by impregnating available materials with functional additives, thus varying the material composition.[242,243]

As an alternative to graphite as the lubricant, molybdenum disulfide, niobium diselenide and other dichalcogenides were added to replace graphite for vacuum or other environments where there is insufficient moisture to allow the graphite to form and maintain a lamellar film. Molybdenum disulfide is used as the most effective replacement for graphite.

Vitreous carbon-based materials have unique properties.[227] The material has a yield strength of 100–200 MPa, compressive strength of 100 MPa, Young's modulus of 20,000 MPa, electrical resistivity of 30–80 μΩm, thermal conductivity of 80 W/cm °C, and a coefficient of thermal expansion of 3.2×10^{-6} l/°C. It can be polished to a metallic luster and exhibits a conchoidal fracture pattern similar to that of glass or flint. Vitreous carbon can be made into macroscopic bodies such as sealing rings and brushes. It may constitute the matrix phase of carbon–fiber reinforced structures or carbon/carbon composites as well.

The perspective contact materials can be made by the polymerization and pyrolysis of an organic material to form the vitreous carbon matrix around copper alloy fibers.[228] For the composites, the polymer was formed around copper alloy fibers (30–50 μm in diameter) that, upon pyrolysis, led to the formation of a continuous matrix of vitreous carbon. This is a radically different process from techniques of forming such composites from a powder, or by pressure infusion of the metal into a graphitic body. The resistivity and friction coefficient are shown to be comparable to reported values for typical copper graphite specimens, and the wear is shown to be exceptionally low. Although vitreous carbon is hard, it does not appear to act as an abrasive on a soft material. These results, along with good measured wear behavior, suggest that vitreous carbon merits further study as a component material in current collectors.

Metal-Based Self-Lubricating Materials. Materials intended for operation under extreme conditions including heavy electrical and mechanical loads and high velocities should possess a high mechanical strength, electrical and thermal conductivity, and wear resistance. Composite materials with a metallic matrix and multifunctional filler meet these requirements. The metallic matrix serves as a frame to withstand the mechanical load, and the filler distributed uniformly in frame pores provides a combination of the necessary electrical and thermal characteristics.

Copper- and iron-based matrix contact materials are produced most often by powder metallurgy methods. In copper-based composite materials, Al, Ni, Cr, Cd, Ag, Si, and P having different

solubilities in copper and forming solid solutions can be used as alloying elements. Metals with a low melting point such as Sn and Pb, lamellar-type substances such as graphite, MoS_2, WS, and CuS, and carbon materials like black and coke, are also known to be solid-solution formers.

For light-load contacts and weak-current/low-voltage applications such as micromotors or small capacity current collection brushes, self-lubricating Ag or Ag–Pd alloy composite materials can be used. For example, using the powder metallurgy methods it was possible to obtain Ag–Pd composite material in which graphite, being evenly distributed, is firmly held in the continuous metal structure.[244] Because the developed composite materials are less porous than the sintered ones, the former are softer and provide a lower specific wear rate than the latter.

Copper–graphite and silver–graphite brushes are used in electrical drives, metallurgical and chemical equipment, urban railway and automobile transportation, power equipment, domestic electrical devices, the aircraft industry, and space applications. Monolithic brushes made of metal–graphite compositions with a high metal content are used as current collectors for pulse generators operating at extreme currents and velocities during short periods of time.[67,245,246]

The metals and alloys containing metal dichalcogenides and sulfides and low-melting point metals are promising contact materials for operations under high vacuum conditions.[247–249] For example, brush-slip ring contacts are usually used to transmit power from the rotating solar arrays onto the body of the satellite. The slip rings are commonly made of coin silver, whereas the brush contacts are made of sintered silver, molybdenum disulfide MoS_2, and graphite. The addition of the lubricating MoS_2 is critical since graphite alone does not provide the required lubricating film under vacuum conditions under which the satellite hardware operates.

The metal-based composite materials containing solid lubricants such as WS_2, MoS_2, and graphite have been developed for devices operating under severe working conditions. It was shown that adding Cu, Sn, and Ag significantly reduces the contact, whereas the friction coefficient was in the range of 0.4–0.5.[250–252]

The content of solid lubricants like graphite in a metallic matrix is usually no more than a few percent; otherwise, the number of contacts between metal particles decreases and mechanical strength is reduced. It was shown that a wide variety of solid lubricants can be introduced into the matrix-type by compacting the lubricants into relatively coarse particles (up to 1.0–1.6 mm in size).[253] The optimal proportions between the matrix and lubricant particles are 70:30 and 60:40 with the total lubricant content above 12%. Such materials possess good antifriction properties and are efficient when used as contact slabs for railway current pick-offs and trolley bus pantographs.

Considerable improvements in the friction coefficient, wear rate, and contact voltage drop of the brushes are achieved by compacting the copper-metallized carbon particles followed by sintering.[254,255] Contact materials for transport pick-offs using the metallized graphite impregnated with the Cu–Pb alloy are produced by Ringsdorf-Wrke GMBH (Germany) and Morganite Carbon (U.K.). The graphite volume in the brush may be of 25%.

The use of the precipitation hardened composite material was found to be efficient for current-collecting elements. It contains a copper matrix with evenly distributed nanoparticles of $A1_2O_3$ oxide (20–40 nm in size) and retained carbon.[256,257]

The material is used in combined current pick-offs for high-speed electric trains in Russia and Italy. Such pick-offs are also efficient under severe climatic conditions (i.e., polar regions) where no common pick-off could operate reliably.

Pulse Electric Current Sintering (PECS). This novel fast sintering method attracted increasing interest in the P/M field and has been introduced into the fabrication of many metals and ceramics. It enables powders to be sintered by Joule heat and spark/plasma generated by high pulse electric current through the compact. Compared with conventional sintering, hot pressing and hot isostatic pressing, PECS can consolidate powders to near-full density at a relatively lower temperature and in a much shorter sintering duration, typically a few minutes. Therefore, the grain growth during sintering tends to be hindered. As a consequence, high mechanical properties of sintered compacts could be expected.[258,259]

Brushes with a vibration absorber, i.e., copper–graphite brushes lined with a porous copper, have been developed to reduce vibrations in the brush-collector sliding contact.[255] The brushes are fabricated by the powder metallurgy method and consist of two parts, namely the working part with the required composition and the auxiliary part made of sintered copper with a high (up to 20%) porosity. Such copper is obtained by using a mixture of copper and polymer powders at one of the production process stages. The polymer powder burns in subsequent sintering.

Polymer-Based Contact Materials. Materials produced by hot pressing the thermosetting resins, such as phenol–formaldehyde and phenol–aniline–formaldehyde, are used in modern electrical devices in addition to contact materials obtained by the powder metallurgy and carbon ceramics methods. Fast-polymerized synthetic resins provide the cohesiveness and ductility of the paste being formed and give the required solidity, homogeneity, and strength to the material obtained. Yet they do not form the current-conductive coke lattice in low-temperature sintering that increases the specific resistance of the material to restrict the binder content by a few percent.

In some cases the use of a polymeric binder is the only possibility of ensuring specific performance characteristics to the contact material. This is exemplified by composite variable resistors or potentiometers.[260] This is a carbon–fiber composite consisting of a center core of unidirectional carbon fibers surrounded by a matrix consisting of a thermoplastic resin and randomly placed secondary carbon fibers. The resultant structure overcomes the hysteresis difficulties with the loose carbon–fiber structures.

A contact fabricated from a carbon–fiber composite material provides an interface of flexible compatible materials versus the more rigid metal/conductive plastic design of dissimilar materials. A contact composed of carbon and plastic resin is, therefore, more similar to that of the resistive element than one made from metal. Both have a negative coefficient of expansion and resistance compared to the metal contact, which has positive thermal coefficients. This interface of compatible materials and the multiple points of contact provided by the carbon fibers will provide for lower friction and a smoother sliding action during and after long life operation.

Historically, the materials used to produce sliding contacts were composed of noble metals such as silver, gold, palladium, and platinum, which are characterized by lower oxidation and higher wear resistance. However, as pointed out in Section 4.2, noble metals such as palladium and platinum used in metal sliding contacts act as a catalyst resulting in frictional polymerization[261] and generate insulating friction polymers on the contact surface. The use of the carbon–fiber composite material eliminates the noble metals and retards the growth of these insulating polymers.

The resistive elements are fabricated by mechanical mixing of semiconducting materials, metals, and the binder followed by forming. The advantages of these resistors are the simplicity of the production process, the possibility of making the resistive element of any shape as a bulky body or homogeneous film on a surface of any shape and size, and possibilities to control the electrical characteristics by varying the composition. Disadvantages of these resistors are their voltage-dependent resistance and a relatively high noise level. Moreover, resistors containing organic binders are quite susceptible to moisture and elevated temperatures. Their operating temperatures do not exceed 150°C. The use of inorganic binders, such as glass and ceramics, provides high resistance to moisture and heat. However, these binders make the resistance range narrower and nonlinear and increase the current noise.

Carbon–Fiber-Based Materials. Carbon fibers are formed from polymers by pyrolysis. The fibers show an unusual strength when pyrolyzed under a tensile load. Such fibers may be incorporated into graphitic bodies which may serve as structural materials or current collector materials. They may be incorporated into metallic matrices to improve strength, rigidity, and wear resistance.

In the 1970s when the carbon fiber was transformed from a laboratory curiosity into a practical product, new types of contact materials were developed. The unique properties of carbon fibers were used in the development of electrical brushes capable of satisfying increasing demands. Particularly, fibrous brushes were developed containing carbon or metallized carbon

fibers[71,76,246,262,263] for sliding contacts operating at extremely heavy current loads and sliding velocities, e.g., homopolar machines for pulsed power applications. The fringe fiber brush is an extension of the original all-fiber brush in which a fringe of carbon fibers is fitted to an otherwise standard brush.[264] Note that the development of fibrous brushes involved the latest achievements in tribology and the electrical contact theory.[76]

The fibers which are positioned at the trailing brush edge provide a "paint brush" effect to maintain contact with the rotating surface. This surface contact is provided under all conditions of surface irregularity and vibration. The fiber prevents brush bounce sparking and serves to conduct the current at the trailing edge with the resistance-effect type of commutation. Fiber brushes have demonstrated a remarkable degree of improvement in the contact performance when compared with monolithic brushes.

Recently, carbon–fiber brushes have been manufactured for a DC motor of an automotive fuel pump.[265] It was shown that the wear rate and commutation ability of new brushes are much better than those of carbon brushes in gasoline.

Carbon–fiber composites have been used for polymer resistive position sensors (potentiometers) as well. The two main functional components of the sensors are the carbon-based resistive ink track and the contactor, which slides along that track resulting in a proportional voltage change.[266] Metal contactors of the rake or knuckle configurations are usually applied in such potentiometers. Initially, when life requirements were in the range of one million or less cycles and the currents through the contact were higher, this incompatibility was tolerated. As life requirements increased to the present levels of hundreds of millions of cycles, and currents reduced to the dry circuit range, it became more difficult to penetrate various barriers and transmit a clean noise free signal.

Dietrich[267] first produced contactors from a composite of carbon fiber and a carbon-rich binder. Liu from CTS Corporation[9,268] concluded that carbon–fiber contactors give a significantly improved contact reliability as well as sensor durability. Finally, Stinson and Sarro[260] reported successful performances of a new type of the contact fiber composite.

4.4 NANOSTRUCTURED MATERIALS

In his famous lecture, "There is a Plenty of Room at the Bottom," delivered in 1959, Nobel laureate physicist Richard Feynman envisioned new discoveries if materials and devices could be manufactured at the atomic/molecular scale. For this to happen, he pointed out that a new class of miniaturized instrumentation would be required to manipulate and measure the properties of the "nano" structures. The advent of sophisticated instruments, such as scanning tunneling microscopes, atomic force microscopes, nanoindenters, and many others provided the "eyes" and "fingers" required for nanostructure measurement and manipulation.

As a result, the end of the twentieth and beginning of the twenty-first century has been marked by a rapidly expanding and relentlessly pursued field of nanoscience and engineering knowledge. It is one of the most visible and growing research areas in materials science in its broadest sense. There have been fundamental scientific breakthroughs and technological paradigm changes in the ways materials, devices, and systems are understood and created. Nanotechnology has promoted truly exciting developments in fundamental science and has opened new way of thinking on long-standing issues in physics, chemistry, biological science, materials science, and mechanical engineering. However, while imaginations may be limitless, material and process constraints pose severe limits on the practicality of such ideas.

The recent rapid advances in nanotechnology are due in large part to newly acquired abilities to measure and manipulate individual structures on the nanoscale using the specifically developed and designed tools that permit the study of new phenomena, the creation of new structures and the exploration of new applications. The driving force behind the apparent explosion in research and

development interests in the nanostructured materials stems from different and superior properties that can be achieved within the realms of nanotechnology.

Nanostructured materials include atomic clusters, layered films, filamentary structures, and bulk nanostructured materials. The common feature of these materials is the nanoscale dimensionality, i.e., in the range of about 10^{-9}–10^{-7} m (1–100 nm), where the nanostructured materials properties such as mechanical, optical, electrical, and magnetic are substantially different from those displayed by either atoms or bulk materials. Because of their size, such materials and systems can be rationally designed to exhibit novel and significantly improved physical, chemical and biological properties, phenomena, and processes.

Clearly, the ability offered by nanotechnology to synthesize nanoscale building blocks with precisely controlled size and composition and to assemble them into larger structures with unique properties and functions will revolutionize the way materials and devices will be produced in the future. For example, nanoscale synthesis and assembly methods will result in significant improvements in solar energy conversion; more energy-efficient lighting; stronger, lighter materials with programmable properties with lower failure rates and extended life-cycle; greatly improved chemical and biological sensing; and environmental remediation and restoration.

Realizing the benefits of this new functionality will, in many cases, require the integration of nanomaterials within microscale and macroscale devices and components. For this reason, integration of nanomaterials with the micro and macro worlds is a key scientific and technological challenge. In nanotechnologies, "top–down" and "bottom–up" trends are distinguishable. In the "top–down" technology, the macroscopic objects are refined "down" into the nano-size structure, whereas in the "bottom–up" technology, the nanostructured layers are built "up" into macroscopic through the use of different surface deposition/coating techniques (such as electroplating, PVD, etc.). The result is nanostructured materials with extraordinary improvements in a variety of properties.

It should be pointed out, however, that the properties of matter at the nanoscale level are not necessarily predictable from those observed at larger scale. This is because the important changes in behavior of nanostructured materials are the result of not only continuous modification of characteristics with shrinking size, but also the emergence of totally new phenomena and the predominant effects of interfaces (grain boundaries).

Notwithstanding unprecedented interests and relentless R&D efforts worldwide, often identified as a *new industrial revolution*, or *nanorevolution*, formidable challenges remain in fundamental understanding of the nanoscale systems before the potential of nanoscale materials can be realized. An acceleration of the pace of fundamental research in nanoscale science and engineering will allow for development of the necessary knowledge and technology to control the feature size and shape of nanomaterials, thus enhancing by orders of magnitude material properties and device functionality beyond what is already established. The plethora of the information that can be found on the Internet by simply entering a key word "nano*" is perhaps the best indication of worldwide interest and diversified activities in nanoscience and nanotechnology.

The important areas where improved properties and functionality of the nanostructured materials were observed are primarily related to various mechanical, electrical, and magnetic properties. For example, the hardness and tensile strength of metals are significantly increased when the crystal size is reduced. Also, nanocoating of metallic surfaces improves wear properties of these materials, lowers friction, and enhances corrosion protection.

Electrical and mechanical properties are crucial issues for the long-term properties of electrical contacts. Wear resistance and fretting properties have been found to impact greatly on the long term stability and reliability of electrical contacts. Because of the improved properties of nanostructured materials as compared to normal coarse grained system, the possibilities of using nanostructured materials in electrical contacts could be very advantageous. In the following sections some relevant accomplishments in the field of electrical and mechanical applications of nanostructured materials will be discussed.

4.4.1 "Bulk" Properties Nanomaterials

Polycrystalline materials consist of a large number of small grains characterized by different orientations and separated by grain boundaries that possess higher energy as compared to the grain interior. Due to their inferior physical, mechanical and chemical properties, grain boundaries creating a three-dimensional net throughout the whole material represent the weakest link of the material structure. Nevertheless, because the grain-boundary properties exhibit a strong structural dependence, the distribution of individual types of grain boundaries in a polycrystal will control the material behavior under different loading conditions. For instance, formation of continuous path in the polycrystal comprised of brittle boundaries will cause the material to crack under low stress. On the other hand, a specific arrangement of special grain boundaries can prevent crack propagation along the grain boundaries in polycrystal in such an extent that the material cracking becomes comparable with transgranular fracture.

It was first proposed by Watanabe[269] that by controlling thermo-mechanical processing, the type of boundaries in a polycrystalline material could also be controlled by deliberately incorporating materials into the material boundaries which have particularly low values for properties such as energy, diffusivity, and resistivity. This is how the concept of *grain-boundary engineering* (GBE) was born, which is essentially the manipulation of grain-boundary structure to improve material properties. In other words, grain-boundary engineering allows the production of polycrystalline material whereby the character and distribution of grain boundaries suppress their detrimental effects and enhance their beneficial effects to a maximum extent. These remarkable property enhancements are possible through tailoring the grain-boundary network and promoting the development of grain boundaries with special crystallography and properties. As a result, material properties such as resistance to intergranular corrosion and fracture, creep, and electromigration were greatly improved.[270–272]

As the grain size reduces to nanometer range, where they are nearly equivalent in diameter to the width of the disordered grain-boundary regions between them, the fraction of atoms located on grain boundaries becomes appreciable and the grain-boundary surface area increases dramatically; thus, the role of grain boundaries becomes paramount. The result of a remarkable body of experimental and theoretical studies indicates that there is a structural difference of the boundaries between nanometer-sized crystallites as compared to boundaries in coarse-grained polycrystals.

Clearly, understanding of the properties of nanostructured materials in terms of their atomic arrangements requires a detailed knowledge about the grain-boundary structure. The atomic structure of nanocrystalline materials seems to depend on the nature of the material (chemical bonds) since even relatively small variations may result in severe structural changes. The other important parameters seem to be the grain size and the preparation method. Depending on the preparation procedure and/or the time–temperature history, profound differences in the atomic structure were revealed by measurements of various properties.[272]

4.4.2 Mechanical Properties

Among the various properties studied, the mechanical strength that is yield (flow) stress and hardness has been probably the most extensively studied property of the nanostructured material. In polycrystalline materials the grain size is one of the controlling factors affecting the number of properties. Understanding mechanical properties of polycrystalline solids is important in technology for its direct impact on the material strength.

It is a well known fact that mechanical properties of materials crucially depend on grain size. In the mid 1950s, Hall and Petch[273,274] showed that with grain sizes in the micrometer range, the lower

yield strength is inversely proportional to the square root of the average grain size, that is

$$\sigma_y = \sigma_0 + kd^{-1/2} \tag{4.1}$$

where σ_0 is a friction stress below which dislocations will not move in a single crystal, k is a constant and d is the grain size. A similar expression also holds for hardness. The pile-up of dislocations at grain boundaries was envisioned as a key mechanistic process underlying an enhanced resistance to plastic flow from grain refinement.

Extrapolating this empirical relationship to the nanoscale grain size of about 10 nm would result in extremely high strength and hardness values. To date, however, the experimental hardness and strength data fall well below these extrapolations. As the grain size decreases down to the nanoscale range, this process invariably breaks down and this relationship departs markedly from that seen at coarser grain sizes. With further grain refinement, the hardness and strength peaks in many cases at an average grain size value on the order of 10–20 nm or so. Further decrease in grain size can cause weakening of the metal as manifested by an inverse Hall–Petch relationship.[275,276,282,283] This is illustrated in Figure 4.14a which shows the effect of grain size on hardness of different metals.[275–284]

Despite the great scatter in the results shown in Figure 4.14, it would appear that hardness data follow the classical Hall–Petch relationships down to a few tenths of nanometers with different slopes in the submicron range but maintaining the classical exponent $d^{-1/2}$,where d is the grain size. However, at smaller grain sizes (<20 nm) the results are contradictory since some results indicate a hardness independent of grain size, or even an inverse Hall–Petch relation that is softening,[275,283,284] whereas others confirm an increasing hardness (hardening) with decreasing grain size.[277,278,281] This is clearly depicted in Figure 4.14b, which shows the hardness of Cu, Ni and Pd as a function of grain size.

Although a detailed explanation of the apparent contradictory results is beyond the scope of this work, some plausible explanations put forward by different researchers to account for the observed contradiction are worth mentioning. Basically, there are two types of explanations: sample preparation/microstructure and theoretical arguments. The preparation of artifact-free samples can seriously compromise the measurements of strength properties of nanocrystalline materials since

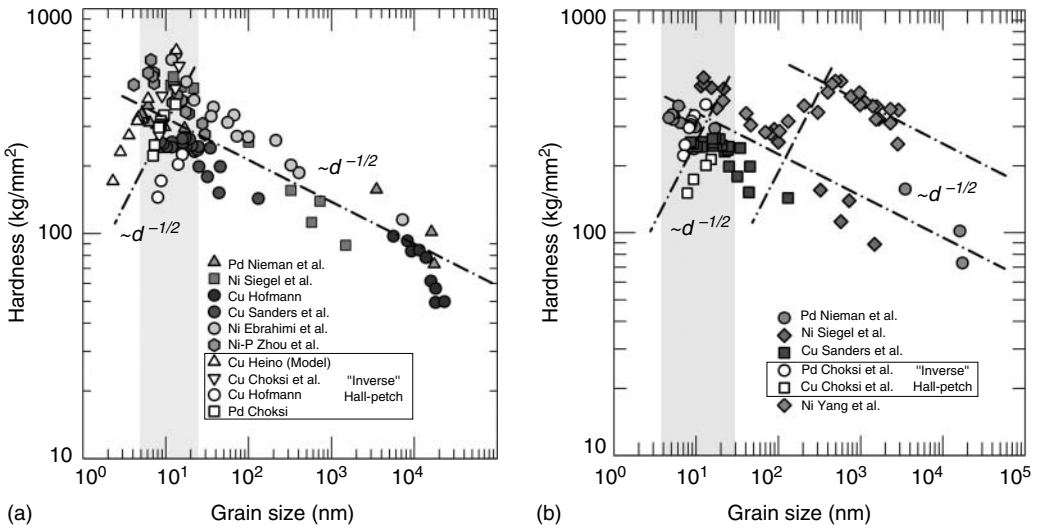

FIGURE 4.14 (a) Effect of grain size on the hardness of different metals. (b) Effect of grain size on the hardness of Cu, Ni, and Pd shoving the classical and "inverse" Hall–Petch relationship.

the presence of porosity, surface defects during sample polishing, and measurement and distribution of grain sizes can lead to misinterpretation of the data.[281]

Equally important is the heat treatment used to produce a range of grain sizes, since the thermal treatment used to obtain grain growth and therefore a range of grain sizes may result in such changes in structure as densification, stress relief, phase transformations, or grain-boundary structure (equilibrium or nonequilibrium). All of these may impact the grain-size dependence of hardness/strength of a nanostructured material.[282]

Another important factor that can impact the interpretation of the data is the measurement techniques used. Indeed, it has been shown that in defect-free Ni samples, four dependencies of nanohardness on grain size were observed.[283,284] The observed results were interpreted in terms of the ratio of indent size to grain size (see Figure 4.14b). Another interesting feature of these results is that when the indent size is smaller than the grain size, direct interaction between indenter-generated dislocations and grain boundaries was observed whereby the pile-up length was within the grain size and the hardness determined by the dislocation density.

On the other hand, since the experimental studies of hardness/deformation of nanocrystalline materials are complicated by material and analytical problems, a number of models for deformation of nanocrystalline materials have been developed to address the inverse Hall–Petch effect. The main theoretical argument is that as the grain size decreases, a point will be reached at which each individual grain will no longer be able support more than one dislocation; at this point the Hall–Petch relationship will no longer hold. Upon further decreases in grain size as it approaches zero, the material essentially becomes amorphous. This is schematically illustrated in Figure 4.15a.

In recent years, considerable progress has been made by computer simulation of the deformation behavior of fcc metals such as Cu and Ni.[281–289] Using the molecular dynamics approach, Schiøtz et al.[285–287] has shown that the flow stress and thus the strength, exhibit a maximum at a grain size of 10–15 nm. This maximum is due to a shift in the microscopic deformation mechanism from dislocation-mediated plasticity in the coarse-grained material to grain-boundary sliding in the nanocrystalline region. Softening is observed at the smallest grain sizes due to the larger number of atoms at grain boundaries. The results of this simulation for Cu with grain sizes from about 7 to 3 nm exhibit the inverse Hall–Petch effect. This is illustrated in Figure 4.15b.

Van Swygenhoven et al.[289] also carried out computer simulations and showed that there is a change from intra-grain dislocation activity to deformation in the grain boundaries as the grain size is reduced. An intermediate grain size range was observed in which deformation is a result of a combination of intra- and inter-grain plasticity and thus the transition between the conventional Hall–Petch behavior and grain-boundary sliding.

From the experimental data and theoretical models, it appears that there is a critical grain size at which the material reaches its maximum strength, followed by a softening mechanism by which the material loses this maximum strength. Typical values for critical grains size (dc) are apparently different for different metals but in general fall within a range of 10–15 nm. It should be pointed out, however, that despite the problems associated with the measurements of the mechanical properties as a function of grain size, as well as the shortcomings of the proposed models, it unambiguously appears that the inverse Hall–Petch (softening) effect is real. However, the nature of the process or a combination of processes responsible for such a behavior (for $d < dc$) are still elusive and a number of mechanisms have been proposed:[275–289]

- Reduction of the effectiveness of dislocation sources under the severe microstructural constraints associated with a very small grain size
- Suppression of dislocation pile-ups due to the presence of a large concentration of grain boundaries
- Dislocation motion through multiple grains, i.e., grain boundaries that are “transparent” to dislocations

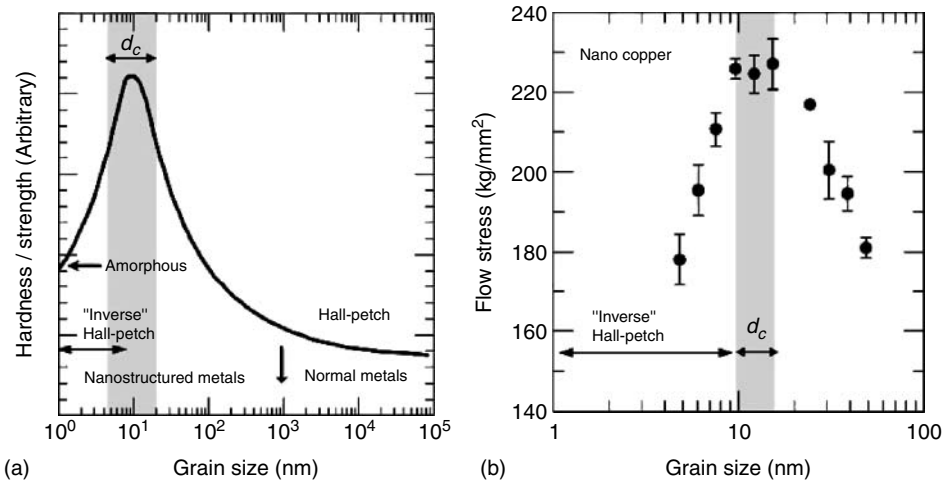

FIGURE 4.15 (a) Schematic illustration of grain-size dependence of mechanical characteristics; (b) simulated grain-size dependence of flow stress of nanocrystalline copper. (From Schiøtz, J., Vegge, T. D., Tolla, F. D., and Jacobsen, K. W., *Phys. Rev.*, B60, 11971–11983, 1999; Schiøtz, J., Tolla, F. D. D., and Jacobsen, K. W., *Nature*, 391(5), 561–563, 1998. With permission.)

- Grain-boundary-sliding induced deformation
- Enhanced diffusional creep (Coble) in the grain boundaries

It should be pointed out, however, that despite the experimental difficulties and limitations of the mathematical simulations, the results obtained are an invaluable source of inspiration for the guidance and understanding of experimental results and the development of new theories. Knowledge of a detailed relation between grain-boundary structure and its mechanical behavior will help in designing better microstructures.

Nanocoatings. The use of nanocoatings enables the alteration of intrinsic properties of materials that cannot be achieved by conventional methods and materials. Among the key applications of nanostructured materials are nanocoatings of metallic surfaces that provide superhardening, low friction, better thermal expansion coefficients and magnetic properties, and enhanced corrosion protection.

Nanometallic coatings are deposited using a number of techniques including electroplating, electroless plating, spraying, chemical vapor deposition (CVD), molecular beam epitaxy (MBE), and ion vapor deposition. For various applications alternative metal deposition methods are being developed which are replacing some of these traditional techniques.[290,291]

Electrodepositon is one coating method that has emerged as a technologically and economically viable means of producing nanostructured metals, alloys, and composite materials. There are a large number of pure metals, alloys, composites and ceramics which can be electrodeposited with grain sizes less than 100 nm, such as nickel, cobalt, palladium, copper, composites like nickel–silicon carbide and ceramics like zirconium oxide, among others. Among the many advantages of electrodepositon are production of grain sizes from the essentially amorphous to nano-scaled materials (5–40 nm) or to larger, micrometer-sized grains; fully dense essentially equiaxed, randomly orientated or textured microstructures; the development of room-temperature technology; and their relative inexpensiveness and ease to scale up.[292]

Atomic Layer Deposition (ALD)[293] is an example of these novel coating techniques. This method allows the placement of conformal, pinhole-free, chemically bonded, and nanoscale-thickness films on individual primary fine particle surfaces. There is no physical mechanism

for deposition, and competing CVD-like homogeneous gas phase reactions are prevented from occurring. ALD is independent of line of sight, and so internal particle surfaces can be coated.

The thickness of the films is determined solely by the number of sequential, self-limiting, half-step reaction cycles carried out.

As pointed out in the previous section, as the grain size is reduced to nanometer range, the fraction of atoms located on the grain boundaries become significantly high, thereby affecting a number of properties such as yield strength and hardness. Hence, nanocoated metals and composites show a remarkable improvement as compared to ordinary polycrystalline materials. This is clearly illustrated in Table 4.20 which summarizes some mechanical properties of nickel-plated materials.[294,295] As can be seen, decreasing the grain size significantly increases hardness and strength properties of nanostructured Ni while at the same time reducing the wear rate and friction coefficient.

The effect of nanocrystalline structure on the wear properties of various nanostructured materials is depicted in Figure 4.16 and Figure 4.17.[296] Figure 4.16 shows the effect of average grain size on hardness and Tabor wear index (a measure of volume loss due to wear) for Ni, whereas Figure 4.17 shows the pin-on-disk volume wear loss for conventional and nanocrystalline materials. From Figure 4.12, it is clear that decreasing the grain size results in a considerable increase in hardness and significant reduction in wear loss. On the other hand, from Figure 4.13 it is evident that the wear resistance of nanocrystalline materials exceeds that of hardfacing materials despite the fact the hardness of hard chromate is higher than that of nanocrystalline materials.

Another example of thin film coatings is the area of amorphous thin film metallic alloys. Amorphous alloys form a structure very different from crystalline alloys, which are characterized by randomly placed atoms in a continuous coating, thus eliminating the presence of grain boundaries. The absence of these defects in amorphous metals leads to the intrinsic properties of amorphous alloys. The lack of dislocations leads to good wear resistance to abrasive particles and metal-to-metal contact and non work-hardening. The absence of dislocations and the lack of boundaries allow for a low friction coefficient, near theoretical strength, and hardness. The lack of boundaries improves the resistance to corrosion and resistance to reactions (such as oxidation and sulfidation) at elevated temperatures. A large variety of two or more component metallic alloys can be deposited at comparatively low cost using the metal coating technique for a wide range of potential applications.[290]

4.4.3 Electrical Properties

The foundations of the modern electron theory of metals were laid at the beginning of the twentieth century when the existence of a gas of free electrons was postulated by Drude to explain the conducting properties of metals. The behavior of the electrons was subsequently analyzed by

TABLE 4.20
Mechanical Properties of Conventional and Nanocrystalline Nickel

Property	Ni	Nano-Ni 100 nm	Nano-Ni, 0 nm	Nano-Ni–Co/Diamond
Yield strength	103		>900	
Ultimate tensile strength	403		>2,000	
Modulus of elasticity	207	690	204	
Vickers hardness	140	1,100	650	850
Wear rate	1,330	214	7.9	2.08
Coefficient of friction	0.9	300	0.5	0.2–0.3

Source: From Robertson, A., Erb, U., and Palumbo, G., *Nanostructured Materials*, 12, 1035–1040; Wang, L., Gao, Y., Liu, H., Xue, Q., and Xu, T., *Surface and Coatings Technology*, 191(1), 1–6, 1999. With permission.

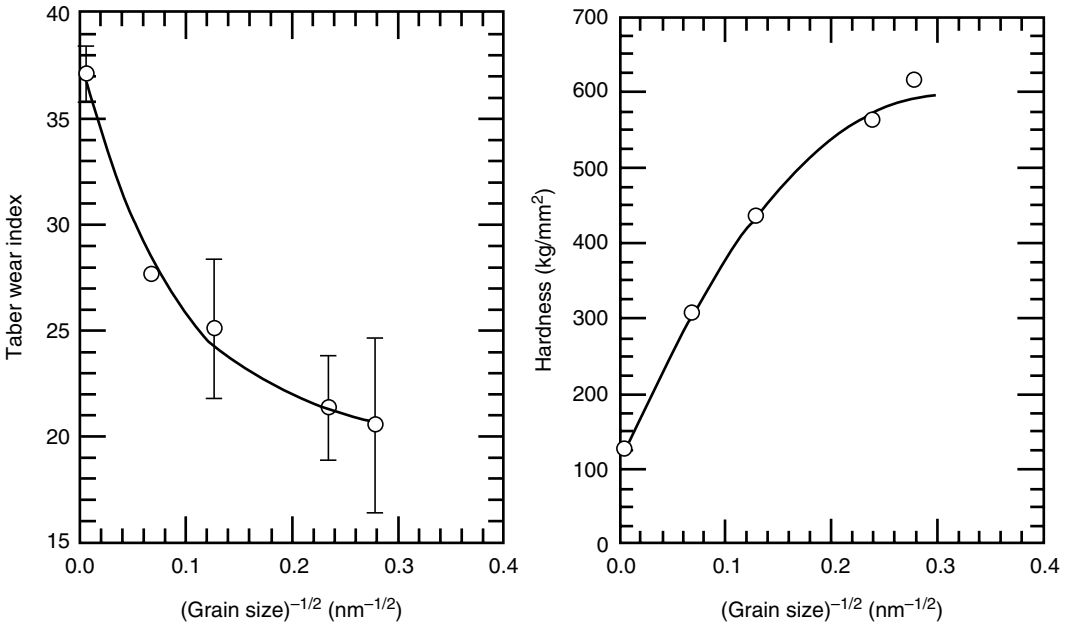

FIGURE 4.16 Effect of grain size on tabor index and hardness of Ni. (From Palumbo, G., Gonzales, F., Tomantschger, K., Erb, U., and Aust, K. T., *Plat. Surf. Finish.*, (February), 36–45, 2003. With permission.)

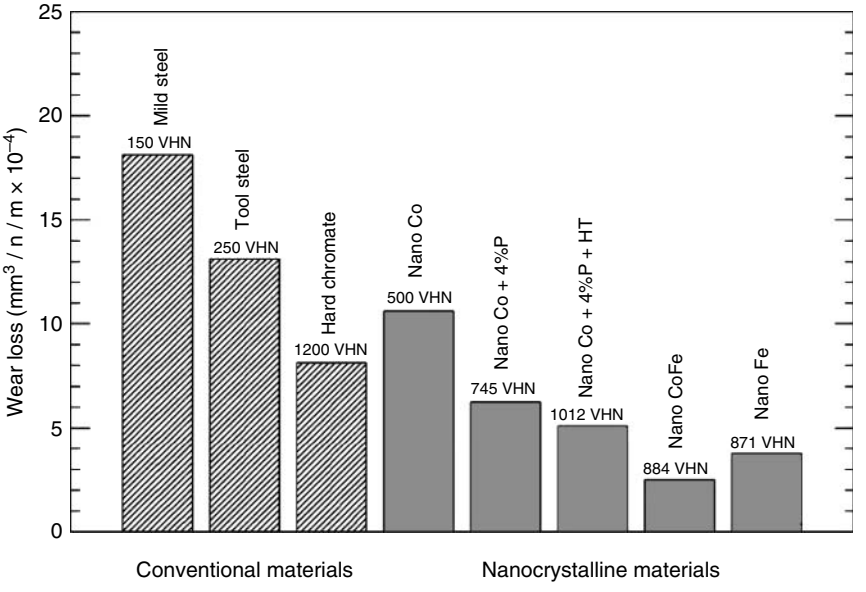

FIGURE 4.17 Pin-on-disk wear loss for different conventional and nanocrystalline materials. (From Palumbo, G., Gonzales, F., Tomantschger, K., Erb, U., and Aust, K. T., *Plat. Surf. Finish.*, (February), 36–45, 2003. With permission.)

Lorentz by means of the dynamic theory of gases. The main successes of this theory were expressing Ohm's law in an analytical form and predicting the Wideman–Frantz law which connects electrical and thermal conductivities. However, later developments revealed an increasing number of difficulties which could not be resolved until the advent of quantum mechanics, when Pauli and Sommerfeld applied the Fermi-Dirac statistics to the free electrons in a metal, showing that in this way most of the contradictions could be reconciled.[297]

The present theories on electron conduction in metals are based on quantum mechanical principles initiated by Bloch. However, with the present state of the theory of metals it is rather difficult to work out a theory which fully takes into account the electronic structure peculiar to a particular metal. Hence, instead of introducing a large number of parameters of doubtful physical significance, the simple Sommerfeld theory of free electrons in metals and their mean free path gives reasonable results as proposed by Sondheimer.[298] The mean free path is defined as the distance an electron moves between scattering events. That is, it scatters by colliding with defects in the lattice or with a quantum of energy of a lattice vibration (phonon). As the temperature is lowered, the vibrations of the lattice and the scattering are reduced and thus the mean free path becomes longer.

When an electrical field is applied to a metal which has free electron distribution given by the Fermi statistics, the whole Fermi distribution is displaced in the direction of the field. Initially, the conduction electrons accelerate, but an equilibrium state resulting in a steady current is quickly reached because of the interaction with lattice vibrations (phonons) and with lattice imperfections.

As far as electrical conductivity is concerned, the results of the Sommerfeld theory can be summarized by the formulas

$$\begin{aligned} n &= \frac{8\pi}{3}\left(\frac{mv_{\mathrm{F}}}{h^3}\right), \\ \sigma &= \frac{ne^2}{m}\tau, \end{aligned} \tag{4.2}$$

in which n is the number of free electrons per unit volume, h is Planck's const, e is the charge of the electron, m is the mass of the electron, v_{F} is the velocity of an electron at the surface of the Fermi distribution, and τ is the relaxation time, i.e., the characteristic time needed to reach a static equilibrium.

The result of a quantum mechanical treatment of electron in a lattice is that the Sommerfeld model remains formally applicable but with the restriction that a new concept must be assigned to the mass of the electron. Namely, since the electrons move in a lattice of positive ions, an effective mass (m^*) should be taken instead of the free electron mass (m) The constancy of the Fermi velocity, found to be of the order of 10^8 cm/s, implies that the relaxation time is directly related to an electron mean free path as follows:

$$l = v_{\mathrm{F}}\tau. \tag{4.3}$$

At low temperatures, most of the mobile electrons are right at the Fermi surface, so $v = v_{\mathrm{F}}$ (Fermi velocity). At these temperatures, one can have mean free paths on the order of ~ 1 cm for very pure crystals. For instance, at 4.2 K copper has $l = 0.3$ cm, whereas at room temperatures, $l = 3\times10^{-6}$ cm. Table 4.21 shows the electron mean free paths for some of the metals.[299]

If the lattice is truly perfect with no imperfections whatsoever, the electrons, or rather electron waves, will propagate through the lattice without any loss of energy, i.e., there is no resistance to the motion of the electrons. However, in practice, the lattice is not perfect and resistance to the electron motion (electron scattering) arises from two main sources:

TABLE 4.21
Electron Mean Free Path for Common Conductor Metals

Metal	Electron Mean Free Path (nm)
Copper	39.3
Aluminum	14.9
Tungsten	14.2
Silver	52.7
Gold	35.5

Source: From Fuchs, K., *Proc. Camb. Philoso. Soc.*, 34, 100–108, 1938. With permission.

- The vibration of the lattice ions due to the thermal energy (phonons) which they gain with increasing temperature
- The presence of chemical or physical imperfections in the lattice, such as foreign atoms, vacancies, dislocations of internal (grain boundaries) and external surfaces

An experimental fact, known for a long time, is that the contributions to the resistivity (defined as 1/conductivity) from these sources of electron scattering are additive. This is known as *Mattheisen's rule*, which may be summarized as:[297]

$$\rho = \rho_T + \rho_R. \tag{4.4}$$

The first part of Equation 4.4 is a temperature-dependent term known variously as the "ideal, the intrinsic, the lattice, or the phonon resistivity." At low temperatures, this part is proportional to T^5, but is a linear function at higher temperatures. The second part of the equation, usually called the *residual* resistivity, arises from the electron scattering by lattice imperfections and is generally independent of temperature, that is, $d\rho/dT$ is temperature independent. Although the rule gives good agreement with experimental data, particularly at higher temperatures, there is increasing evidence that the rule is not strictly valid, and according to Sondheimer,[298] some deviations are to be expected at lower temperatures. Indeed, the accurate experimental studies made of the performance of this rule in dilute alloy systems have shown that $d\rho/dT$ varies systematically with the impurity or other defect present in the lattice concentration and is temperature dependent.[300–302] It has been known for a long time that decreasing physical dimensions of metallic thin films increases electrical resistivity. This is commonly referred to as the size effect.[303] As a result of extensive studies, both theoretical and experimental, significant progress in understanding its underlying mechanism has been made.

Because of the recent rapid advancement in nanostructured materials and the use of copper interconnection technology, the size effect is becoming a subject of considerable practical interest. This is because the size-affected resistivity may be prohibitively high for copper interconnects used in modern microelectronic devices, thus affecting not only their functionality but their functionality as well. It should be pointed out, however, that despite a number of studies dealing with the size effect, detailed mechanisms responsible for this effect are still incomplete partly because of several assumptions that have been employed in the analysis of the results. Although the theories behind the size effect are relatively simple, their application to the analysis of resistivity in realistic copper interconnects poses formidable challenges. Difficulty in preparing nanoscale samples is only a small part of the problem. The bigger challenge is to apply theories to experimental data without losing physical validity. A simple illustration of such a difficulty can be seen in the case of surface

(or interface) scattering. Surface scattering, where a portion of conducting electrons lose their momentum during interaction with the surface, is the most well-studied origin of the size effect and is claimed to be the leading cause of the size effect observed in many experimental studies. Any theory on surface scattering involves four significant parameters: the bulk resistivity (ρ_0), the electron mean-free path (l), the electron specularity (measure of inelastic scattering) at the surface (p), and the physical dimension which is film thickness (t) and/or grain size (d).[303] The increase in resistivity is influenced by the number of electrons inelastically scattered at the internal (grain boundaries) and external surfaces. The effect of the grain boundaries and the interconnections line thickness on the resistivity can be approximated by the expression[296]

$$\rho = \rho_0 \left[1 + \frac{\alpha}{d} + \frac{3l}{8t}(1-p) \right]$$
$$\alpha = \frac{3}{2} l \left(\frac{R}{1-R} \right) \tag{4.5}$$

where p is the probability of reflective scattering by the interconnect wall surfaces, whereas R is the reflection coefficient of grain boundaries. Both p and R assume values between 0 and 1. Hence, for $p = 1$, all electrons are scattered in an elastic way, and no resistivity increase caused by interconnection sidewall scattering occurs, whereas for $R = 0$ there is no grain-boundary scattering. The effects of interconnection thickness and grain size are shown in Figure 4.18.[296,306]

It is important to note that in the above discussion, the effect of impurities/solutes segregated at the surface of grain boundaries were not considered as the possible additional scattering centers for the electrons in these areas. Hence, bearing in mind the fact that the solute/impurity segregation at free surfaces[296,306] and grain boundaries[307,308] exert considerable effect on the mechanical[309] and electrical[269,310–313] properties of conventional polycrystalline materials, it is reasonable to expect that similar effects will also be operative in the nanostructured materials.

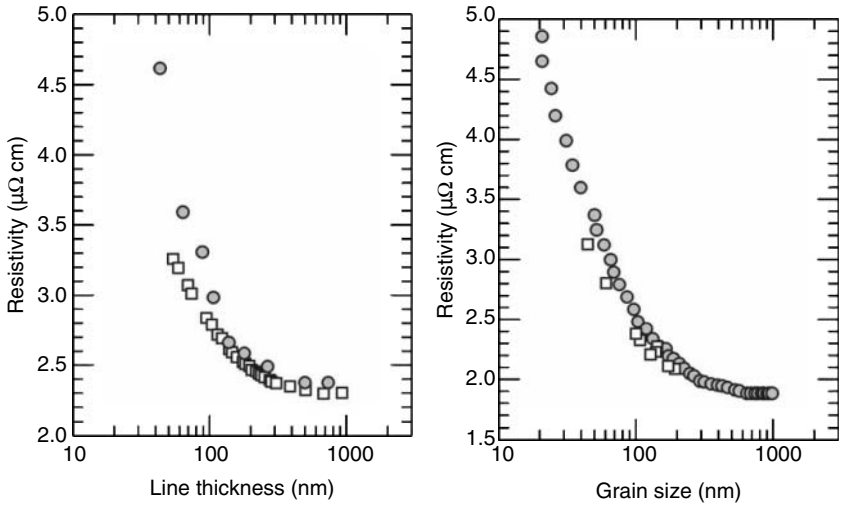

FIGURE 4.18 Effect of interconnection line thickness[304,305] and grain size[296,306] on the resistivity of copper interconnection lines in nanostructured coatings.

4.4.4 Magnetic Properties

During the last several years, magnetic nanostructured materials have been a subject of intense research because their unique magnetic properties make them very appealing from both theoretical and technological points of view. Magnetic nanostructured materials have a number of extraordinary magnetic behaviors when compared to bulk materials, generally due to surface/interface effects. Furthermore, because nanostructured materials can have as much as 50% surface material, they represent surface and interfacial material in bulk quantities; thus, the new magnetism that may develop should be of practical value.

In nanocrystalline materials, as the grain size approaches or decreases below the critical magnetic length scales found in conventional materials such as the domain (Bloch) wall thickness or the ferromagnetic exchange length, considerable changes in the magnetic behavior can occur. The coercive force, H_c, of conventional polycrystalline materials with grain sizes greater than 100 nm is found to be inversely proportional to the grain size. In other words, when the grain size exceeds the domain wall thickness, the grain boundaries effectively pin magnetic domain wall motion as a result of which the materials become magnetically harder.[314]

However, when the crystal size is reduced to the extent that the domain wall thickness is comparable to the average grain diameter, the magnetic structure in relation to the microstructure is not well understood. For a series of nanostructured materials produced by crystallization from amorphous precursors, it was found that the coercivity decreased by several orders of magnitude for grain sizes less than abut 50 nm, following a d^6 relationship, where d is the grain size of nanocrystals.[315] This observation was explained in terms of a random anisotropy model. Although this effect is not observed for all nanocrystalline materials, recent results have demonstrated that materials prepared by electrodepositon show similar trends.[316]

The effect of grain size on coercive force H_c for some nanocrystalline and conventional magnetic materials are shown in Figure 4.19.[315–317] As it can be seen, decreasing the grain size causes substantial decrease in the coercivity of nanocrystalline materials, whereas the opposite tendency is observed in conventional magnetic materials.

However, in the case of saturation magnetization, rather contradictory results are reported. Specifically, Gong et al.[318] reported significant reduction of M_s with grain size, whereas Aus et al.[319] showed practically grain-size independent variation of M_s. Initially, the reduced M_s in consolidated nanocrystalline powders was explained in terms of the structural disorder of the intersects, in which atoms located at the interfaces were estimated to possess only half the magnetic moment of the atoms located within the grains.[320]

Recent detailed calculations on the magnetic properties of grain boundaries[321] revealed that the local magnetic moment in nickel is rather insensitive to the amount of disorder present in the structure, varying at most by 20% for only certain sites in the boundary, thereby agreeing with the measured M_s values from nanocrystalline materials made by electrodeposition.[319]

The magnetic properties of nanostructured materials are probably the most promising for industrial applications for materials in the area of soft magnets for high-efficiency transformers, motors, and others. Considerable development activity has been generated in the area of reducing magnetic crystalline anisotropy and coercivity by reducing the grain size below the mean thickness of a magnetic domain wall in conventional materials. Figure 4.20 summarizes the potential opportunity for nanocrystalline soft magnets, whereby these electrodeposited nanocrystals can possess coercivity without compromise of saturation magnetization.[314]

4.4.4.1 Giant Magnetoresistance (GMR)

The most prominent magnetotransport phenomenon in ferromagnetic materials is the giant magnetoresistance (GMR) effect that relates the electric resistivity dependence on the relative alignment of the magnetizations of adjacent ferromagnetic layers. The effect was first reported in Fe–Cr/Fe

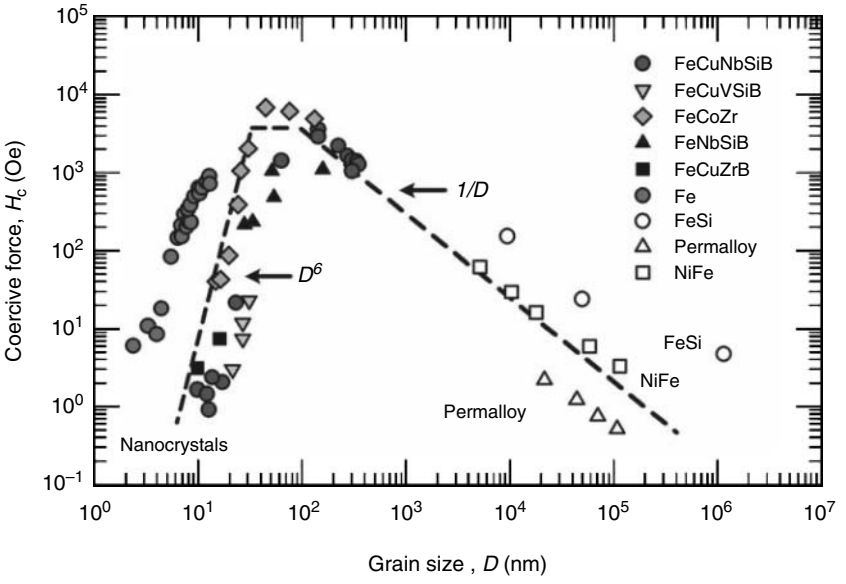

FIGURE 4.19 Effect of grain size on the coercivity of nanocrystalline and conventional magnetic materials. (From Herzer, G., *Magnetic Hysteresis in Novel Magnetic Materials*, Hadjipanayis, G. C., Ed., Kluwer Academic, Boston, MA, 711–730, 1997; Cheung, C., Aus, M. J., Erb, U., McCreas, J. L., and Palumbo, G., *Proceedings 6th International Conference Nanostructured Matter*, 2002; Gangopadhyay, S., Hadjipanaysis, G. C., Dale, B., Sorensen, C. M., and Klabunde, K. J., *Nanostruct. Mater.*, 1, 77–81, 1992. With permission.)

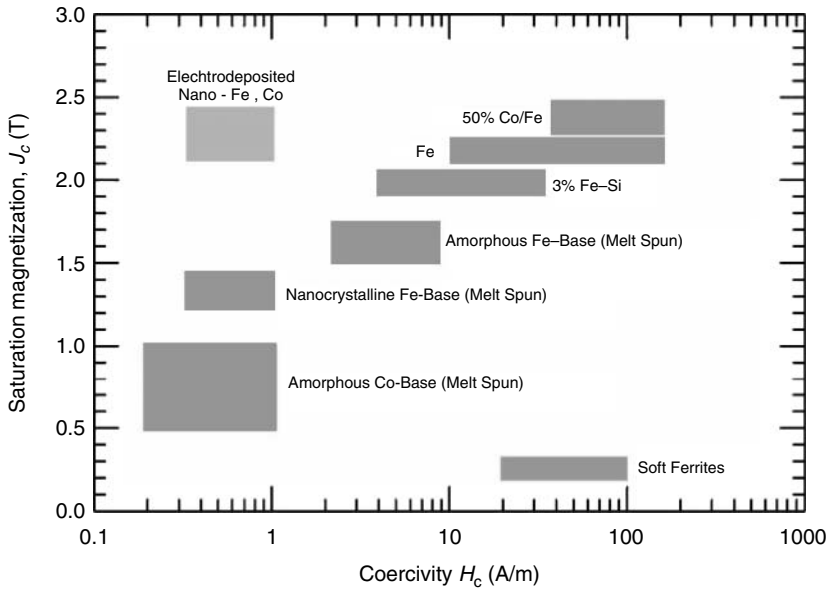

FIGURE 4.20 Typical coercivity (H_c) and saturation magnetization (J_s) ranges for some ferromagnetic materials. (From Palumbo, G., McCrea, K. J., and Erb, U. In *Encyclopedia of Nanoscience and Nanotechnology*, Nalwa, H. S., Ed., vol. 1, 89–99, 2004. With permission.)

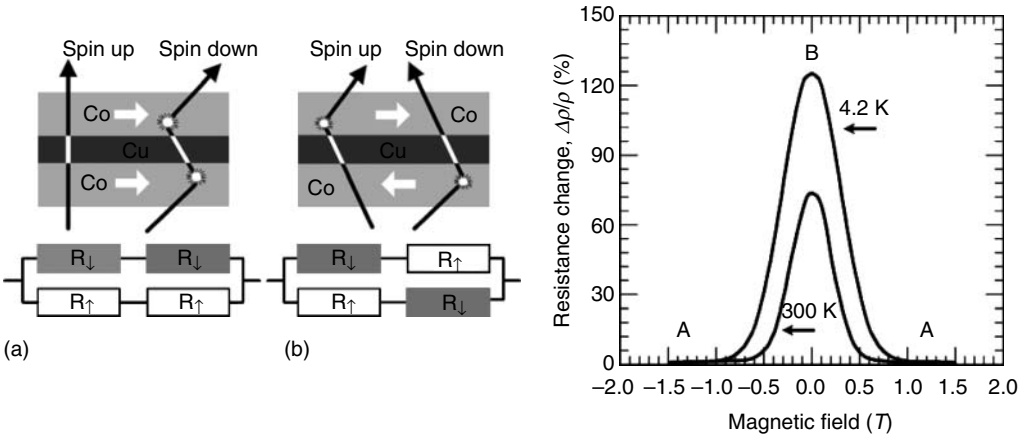

FIGURE 4.21 Schematic of GMR in two Co layers separated by a nonmagnetic Cu layer with parallel (a), and antiparellel magnetization (b).

multilayers by Baibich.[322] For transition metal magnetic materials, the s-d scattering is the major contribution to electrical resistivity of these materials, and the scattering is very much dependent on the relative orientation between the electron spin moment and the 3d atomic moment. When electrons travel in a magnetic metal, the resistivity for the electrons with spins parallel to the magnetization of the metal is different from that of the electrons with spins antiparallel to the magnetization.

The effect is illustrated in Figure 4.21, in which two magnetic layers (Co) are closely separated by a thin antiferromagnetic (Cu) spacer layer a few nm thick. The first magnetic layer allows electrons in only one spin state to pass through easily because the second magnetic layer is aligned with applied magnetizing field. Thus, the spin channel can easily pass through the structure and the resistance is low (Figure 4.21a). However, when the second magnetic layer is antiparallel to the magnetization field, the passage of either spin channels through the structure is impeded and the electrical resistance is high (Figure 4.21a).

Sensors based on the GMR effect led to its widespread applications, including read heads of hard disc drives, avionic compasses, swipe-card readers, wheel rotation sensors in ABS brakes, and current sensors for use in safety power breakers and electricity meters. A detailed and well-balanced introduction to both the underlying physical fundamentals and the technological applications of GMR is given by Hartmann.[323]

4.4.4.2 Ballistic Magnetoresistance (BMR)

Probably the most prominent and intriguing magneto-transport phenomenon is the ballistic magnetoresistance (BMR) manifested by the change in the resistance across a point contact between two ferromagnetic islands under the influence of applied magnetic field. In such a system, the conduction electrons are spin polarized so that the relative orientation of the magnetization of the two islands determines the resistance to current flow across the contact. In other words, if the islands are magnetized opposite to each other, there far less available states in the second electrode that the electrons can occupy, which leads to a much higher resistance than when the islands are magnetized in the same direction. The cause of this phenomenon is explained in terms of domain wall scattering assuming that the domain wall width formed at the contact is of the order of the contact size. If the domain wall is narrow, strong nonadiabatic scattering with spin conservation at both sides of the contact, the BMR can be expressed by the following equation:[324]

$$\text{BMR} = \frac{\pi^2}{4}\left(\frac{\xi^2}{1-\xi^2}\right)F(\xi,\lambda), \tag{4.6}$$

where $F(\zeta, \lambda)$ describes the nonconservation spin and is dependent on ζ and λ (the domain width). The term $(\zeta^2/1-\zeta^2)$ is the ratio of the difference in the density of states between majority and minority spins at the Fermi level in the electrodes at both ends of the contact. The resistance is spin ballistic if the contact is small and the spin mean free path (l) is larger than the contact size. The resistance can be estimated assuming that one atom at the contact provides a conducting channel, and that one atom takes a surface area of approximately 0.1 nm^2 by:

$$R_0 = \left(\frac{ne^2}{h}\right)\frac{1}{10a^2} = \left(\frac{12.9}{10a^2}\right)\frac{\text{k}\Omega}{\text{nm}^2}, \tag{4.7}$$

where 12.9 kΩ is the quantum of resistance, and a is the size of the contact in nm. The above formula is basically Sharvin's formula for ballistic transport.[325] The giant magnetic resistance of Ni and Co as a function of the conductance expressed in quantum units is shown in Figure 4.22. The resistance of the contact is obtained by dividing the quantum of resistance 12.9 kΩ by the number of conducting channels (given in the upper x-axis).

From Figure 4.22, it appears that for 20 channels, corresponding approximately to 2 nm^2 of contact area, the resistance is 600 Ω. This conforms very well with theory, as indicated by the good agreement between the lines (theory) and dots (experiment) in Figure 4.18. However, although this observation may produce very interesting physics from the point of view of theory and experiments, it does not qualify for technological applications because the contacts are unstable and last only a few minutes.[324]

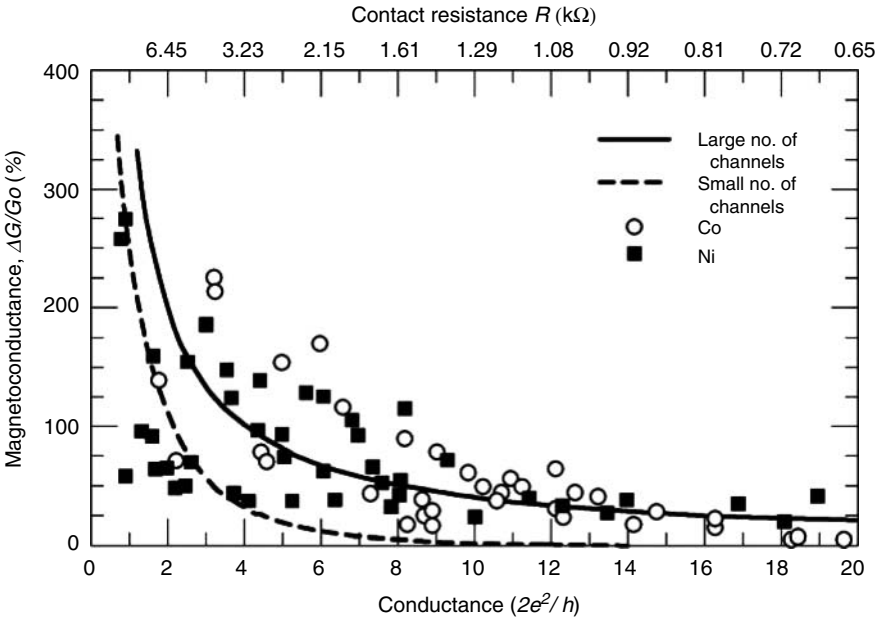

FIGURE 4.22 Magnetoconductance as a function of the contact conductance and the contact resistance for Ni and Co contacts. Full and dashed lines are respectively the theory line approximations in the limits of a large and small number of conducting channels. (From Garcia, N., *Europhys. News*, 34(6), 2003. With permission.)

It is interesting to note that ballistic magnetoresistance over 3000% in electrodeposited Ni nanocontacts was reported by Chopra[326] at room temperature using a T-shaped contact configuration. The observed large values of ballistic magnetoresistance were obtained in switching fields of only a few hundred oersteds. The results are attributed to spin-dependent electron transport across nanometer sharp domain walls within the nanocontacts. These results were subsequently questioned by Egelhoff et al.,[327] who suggested that the observed effect is due to the artifacts or factors unrelated to the quantum effects. It was pointed out that subjecting two Ni wires in T-configuration to the magnetic field causes shortening of the wires which, in turn distorts the cluster of atoms forming the nanoscale contact between wires. The result is a large increase in resistance.

4.4.5 Nanotubes

The carbon nanotubes are a fascinating new class of materials attracting unprecedented attention from both theoretical and applied standpoints. Such an interest is exemplified by an enormous wealth of information available both in print and on the Internet.[323–330] Hence, this section will deal only briefly with some basic features of the nanostructured materials.

The carbon nanotubes are rolled up sheets of sp^2, bonded graphite with no surface broken bonds. The remarkable material properties of carbon nanotubes (CNT) such as strength, stiffness, toughness, chemical robustness, and thermal and electrical conductivity make these materials one of the hottest subjects of both theoretical and experimental studies. Depending on their precise molecular symmetry, carbon nanotubes can exhibit semiconducting or truly metallic conductivity, making them ideal candidates for wires, interconnects and molecular electronic devices. However, despite such remarkable properties, development of nanotubes-based products has been delayed principally due to unavailability of quantities of materials and deficient control of their growth.

Nanotube structure can be mathematically defined in terms of a chiral vector C_h ($C_h = na_1 + ma_2$), which can determine the tube diameter d_t. This vector determines the rolling direction of a graphite sheet (grapheme), in which a lattice point (m,n) is superimposed with an origin defined as (0, 0). Depending on the direction of the carbon–carbon bonds during wrapping of a graphite sheet (grapheme), that is parallel or perpendicular to the tube axis, the nanotubes are conventionally distinguished as zigzag, armchair and chiral. These nanotube structures are shown in Figure 4.23.

The mapping specifies the number of unit vectors required to connect two atoms in the planar hexagonal lattice to form a seamless tube. These numbers specify a vector for the mapping, commonly expressed as (m, n), where m and n are integers. Tubes with carbon–carbon bonds parallel to tube axis are labeled zigzag, whereas those with carbon–carbon bonds perpendicular to the tube axis are called *armchair*. The tubes with $m \neq n$, 0 are called *chiral* and have left and right handed variants.[329]

The properties of tubes of different types are essentially the same. However, due to subtle structural differences, the electrical properties can be profoundly affected. For example, all

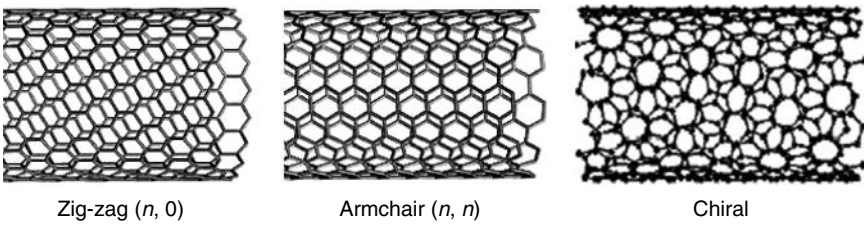

FIGURE 4.23 Typical carbon structures. (http://www.pa.msu.edu/cmp/csc/nanotube.html and http://nanotube.msu.edu.)

armchair tubes where $m = n$ have truly metallic electrical conductivity and transport electrons along the tube axis just as metals do, without a single atom of metal in their structure. In contrast, the other tubes are intrinsically semiconducting, either with a very small band gap of a few meV, or with moderate band gaps on the order of 1 eV. The nanotubes can carry the highest current density of any known materials, as high as 10^7 A/cm^2.[329]

The mechanical properties of the carbon nanotubes exceed that of any known metal. The Young's modulus of 1.4 TPa and elongation of 20–30% were measured. For comparison, the Young modulus of high-strength steel is about 200 GPa; its tensile strength is 1–2 GPa and its elongation is less than 0.2%.[329] Although the high strength of carbon nanotubes makes them promising candidates in reinforcement applications, there are many outstanding problems that must be overcome, including optimization of the properties of the individual tubes, efficient bonding to the material they are reinforcing (the matrix) so that they actually carry the loads, and uniform load distribution within the nanotube itself to ensure that the outermost layer does not shear off.

When two nanotubes were placed in a cross-rod contact configuration, a very interesting contact resistance dependence on the rotation angle was observed in intermolecular junctions.[330] It was found that atomic structures in the contact region exert strong influences on the contact resistance between the tubes. The contact resistance is low when two tubes are in-registry, whereby the atoms from one tube are placed on top of another like A–B stacking of graphite. Hence, an armchair tube crossing a zigzag tube forms an in-registry junction and the contact resistance is low. However, when two perpendicular armchair tubes form an out-of-registry junction, the contact resistance between the tubes is high. In general, different transport properties can be achieved by manipulating these junctions such as rotating or translating one of the tubes with respect to the other. This is depicted in Figure 4.24 which shows the variations of contact resistance with respect to rotation angle between the tubus.

In summary, the unique properties of carbon nanotubes justify the enthusiasm and extensive R&D works in this field of nanotechnology. Although many of these properties are understood, others still remain controversial, thus making them an exciting area of condensed-matter physics. It is equally important to bear in mind, however, that the applications of nanotubes are not as easy as the numerous reports in the literature suggest. A number of possible applications include interconnects for electronic devices (vias), diodes and transistors for computing, capacitors, data storage, field emission materials, conducting and high strength composites, hydrogen storage,

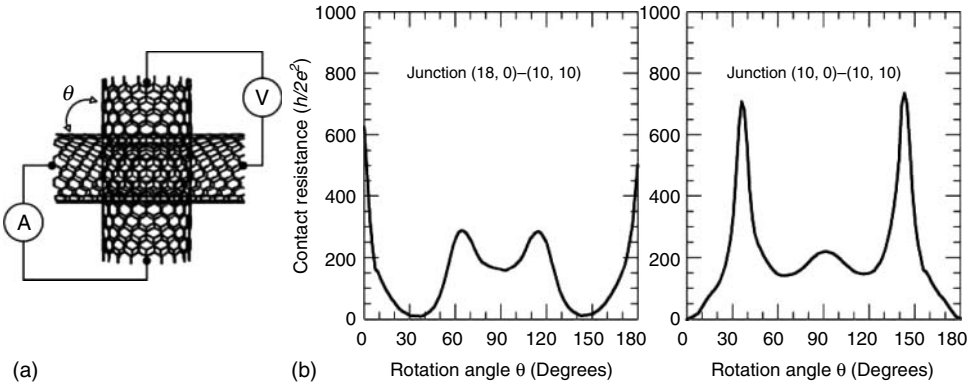

FIGURE 4.24 Schematic of the cross-rod contact configuration of two nanotubes (a) and contact resistance of the (18, 0)–(10, 10) and (10, 10)–(10, 10) junctions as a function of the rotation angle θ (b). (Smoothed data from Buldum, A. and Lu, J.-P., *Phys. Rev.*, B63, 161403–161406, 2001.)

ultrasensitive electromechanical sensors, flat-panel displays, biosensors, molecular gears, motors and actuators, fuel cells, and other applications.

4.4.6 Thermal Stability

The thermal stability of nanocrystalline materials is one of the major concerns for the applications of nanocrystalline materials at elevated temperatures. This is principally due to excess free energy stored at the grain boundaries that results in a large driving force for grain growth that can be considerably greater than that for conventional polycrystalline materials.

The effect of annealing temperature on the hardness[332] and grain growth kinetics[333] in pure Ni and Ni–P alloys is illustrated in Figure 4.25. It is clear that for pure nanocrystalline Ni, the hardness decreased rapidly from about 420 to 150 VHN, whereas the hardness of nanocrystalline Ni–P remained unchanged at ~400 VHN for annealing times greater than 10^6 min.

The grain growth kinetics for a nanocrystalline Ni–1.2 wt%P alloy as evaluated from insitu electron microscopy studies showed that at 473 K, no grain growth was observed and the material was stable as a solid solution. At 673 K, substantial grain growth was observed within the first few minutes of annealing, resulting in a microcrystalline two phase (Ni + Ni3P) structure. However, at 573 and 623 K, the grain size initially increased rapidly by a factor of 2–3 and then became essentially independent of annealing time.[333]

The apparent thermal stability of Ni–P alloys was attributed to combined effects of solute drag effects on the grain boundaries, reduction in grain-boundary energy from solute segregation and Zener drag effects associated with the possible formation of nano-precipitates.[333] A recent theoretical and experimental study on the effect of grain growth on resultant grain-boundary character distributions indicates that the thermal stability of nanocrystalline materials may be further enhanced by the tendency for these ultrafine grained materials to form special low-energy grain boundaries during the early stages of grain growth.[334]

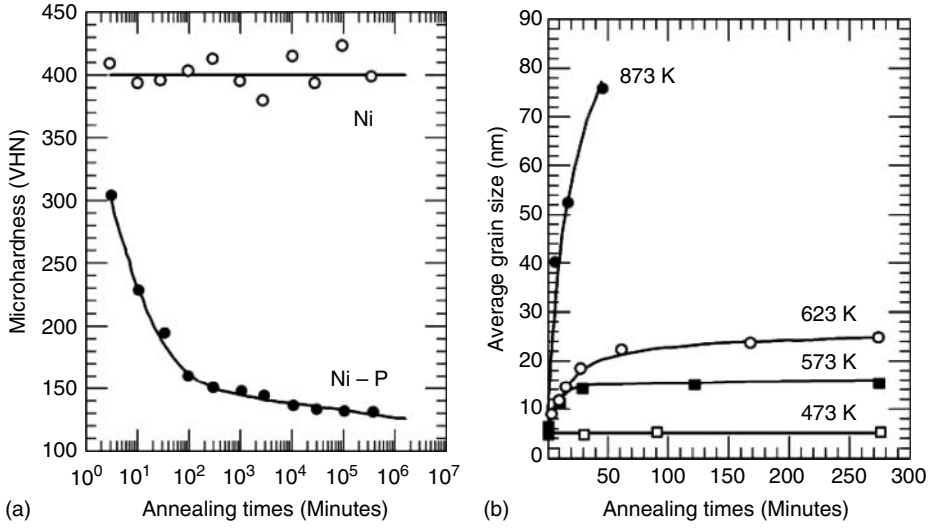

FIGURE 4.25 Effect of annealing temperature on the hardness of (a) pure Ni and Ni–P alloys and (b) grain growth of electrodeposited nanocrystaline Ni–1.2 wt% P. (From Palumbo, G., Gonzales, F., Brennenstuhl, A. M., Erb, U., Shmaydaa, W., and Lichtenberger, P. C., *Nanostruct. Mater.*, 19, 737–746, 1997; Boylan, K., Ostrander, D., Erb, U., Palumbo, G., and Aust, K. T., *Scripta Metallurgica et Materialia*, 25, 2711–2716, 1991.)

4.4.7 Characterization Techniques for Nanostructured Materials

The unprecedented progress in nanotechnology would not have been possible without the useof sophisticated tools to observe, characterize, and control phenomena at the nanometer scale. A whole new generation of analytical instrumentation and nanoscale devices, capable of providing information about nanoscale physical, chemical and mechanical phenomena, has been and are being developed. There is practically an abundance of literature both in print and on the Internet providing detailed descriptions of the tools for the characterization of nanostructured materials and measuring properties at the nanoscale. In this section only a brief description of the most common and widely used characterization techniques and devices will be given.

4.4.7.1 Nanoindentation

Indentation hardness testing has been successfully used for many years to evaluate the mechanical properties of materials.[335,336] Initially, the hardness and elastic modulus were derived from the measurements of the size of the residual plastic imprint. It was shown that for ductile materials the hardness (average contact pressure) is three times the yielding stress of the materials under simple compression.[335] However, difficulties in determining the exact size of the imprint due to the piling-up or sinking-in of material around the indentation prompted development of the depth-sensing indentation (DSI) instrumentation. In the DSI devices, the load and displacements (indenter penetration) are continuously recorded during indentation process and subsequently interpreted to determine the mechanical properties.

The first depth-sensing indentation unit was described by Alekhin et al.[337] and subsequently used by Bulichev et al.[338] to evaluate the Young's modulus. This assumes that, during unloading the material only deforms elastically. An implicit assumption is that the presence of a residual hardness impression does not affect the elastic solution for an initially flat surface. Figure 4.26 depicts a schematic of the indenter penetration and load–displacement curve. The elastic modulus can be determined from the stiffness (S) in the contact between the indenter and the sample, that is, from the slope (dP/dh) of the unloading curve as

$$S = \frac{dP}{dh} = \frac{2}{\sqrt{\pi}} E^* \sqrt{A_c}, \tag{4.8}$$

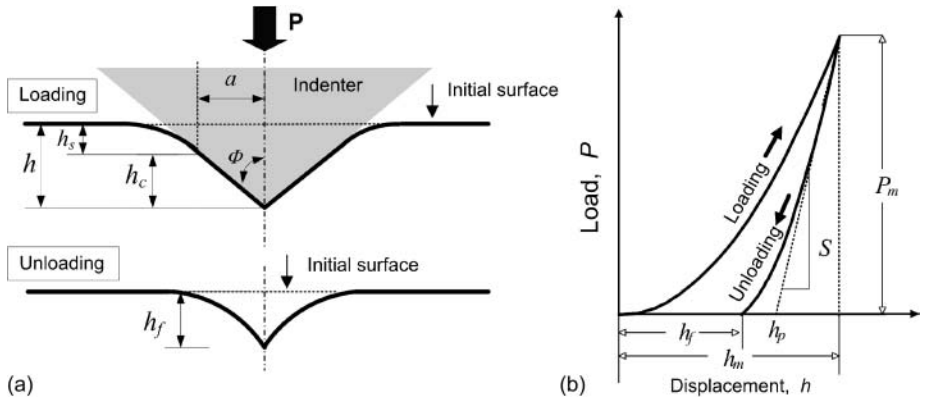

FIGURE 4.26 Schematic of the indentation process and load–displacement curve.

where A_c is the projected area of the elastic contact at the point where the stiffness is determined. E^* is the reduced modulus due to a nonrigid indenter defined as

$$\frac{1}{E^*} = \frac{(1-\upsilon_s^2)}{E_s} + \frac{(1-\upsilon_i^2)}{E_i}, \tag{4.9}$$

where the indices s and i refer to sample and indenter respectively. Although strictly speaking, Equation 4.9 is only rigorous for spherical indenters, Pharr et al.[339] showed that the equation holds for any indenter geometry. Based on these fundamentals the most comprehensive and commonly used analysis methods for depth-sensing indentation experiments were described by Doerner and Nix[340] and Oliver and Pharr.[341]

From the above description of depth-sensing techniques, it is clear that calculating the hardness and elastic modulus from indentation–load displacement requires the accurate measurement of the elastic contact stiffness (S) and the projected area under load (A). The most widely used method for establishing the contact area was developed by Oliver and Pharr[342] by fitting the unloading portion of the load–displacement data to the power-law relation:

$$P = BA(h-h_f)^m, \tag{4.10}$$

where B and m are empirically determined fitting parameters and h_f is the final displacement (penetration) after complete unloading as determined from the curve fit. The contact depth h_c is estimated as

$$h_c = h-\varepsilon(P/S), \tag{4.11}$$

where ε is a constant that depends on the indenter geometry that is 0.75 and 0.72 for spherical and conical indenters respectively. This method has been widely adopted and used in the characterization of mechanical behavior of materials at small scales. The apparent advantages of these methods result largely from the fact that mechanical properties can be determined directly from indentation load and displacement measurements without the need to image the hardness impression. With high-resolution testing equipment, this facilitates the measurement of properties at the micrometer and nanometer scales. The depth-sensing technique was also successfully used to determine the mechanical properties of brittle materials,[343,346] creep[345,346] fracture toughness,[347,348] and stress relaxation.[349]

In summary, it is important to note that despite the unquestionable success of the depth-sensing indentation (nanoindentation) technique in the evaluation of the mechanical properties of small volumes, there are a number of uncertainties that impose certain limitations on the accuracy of the technique. The factors affecting the accuracy of this technique are the indenter tip and shape, friction, surface energy, and thermal drift, to cite just a few. Nevertheless, despite the adverse effects of these factors, they do not prevent acquiring useful information with this technique.

Depth-sensing indentation is one of very few ways in which very small volumes of materials can be deformed in a controlled way to determine mechanical properties. The method proposed by Oliver, Pharr, and Brotzen[339,341] is robust and repeatable and represents a significant improvement in the analysis of depth-sensing indentation data to provide excellent comparative results, as long as all tests are conducted and analyzed in the same way under the same conditions.[350] As testing and analysis methods mature, the accuracy and precision of such methods are expected to improve.

4.4.7.2 Scanning Probe Microscopes

During the past two decades, nanotechnology has benefited from a large number of novel instrumentations capable of studying materials at the nanoscale levels. This in turn has enabled discoveries to be made in nanoscience and engineering, thus providing the basis for the

development of unprecedented new instruments for synthesizing nanostructures as well as for characterizing nanostructures and measuring properties at the nanoscale.

The inventions of the scanning tunneling microscope (STM)[351] and the atomic force microscope (AFM)[352] have generated the development of a variety of new scanning probe microscopes (SPMs) such as the scanning thermal microscope (SThM),[353] magnetic force microscope (MFM),[354] scanning spreading resistance microscope (SSRM) and many others. The SPMs are providing access to and enabling observation of physical, chemical, and biological phenomena at nanometer scales. The web sites of PSIA, Inc. (XE-series) and Veeco Instruments, Inc. provide a wealth of information on a large number of scanning probe microscopes made by these companies intended for a variety of applications.[355,356] In this section only brief descriptions of the SPMs that can be used to study phenomena associated with electrical contacts will be given.

Atomic Force Microscopy. Atomic force microscopy (AFM) is a method of measuring surface topography on a scale from angstroms to 100 microns. The technique involves imaging a sample through the use of a probe, or tip, with a radius of 20 nm. The tip is held several nanometers above the surface using a feedback mechanism that measures surface–tip interactions on the scale of nanoNewtons. Variations in tip height are recorded while the tip is scanned repeatedly across the sample, producing a topographic image of the surface. The AFM can work with the tip touching the sample (contact mode), tapping across the surface (tapping mode), lift mode, and noncontact mode.

AFM's principle of contact relies on the use of a sharp, pyramidal tip positioned at the end of a cantilever which is brought into close proximity to the surface where intermolecular forces acting between the tip and the surface cause the cantilever to bend. As the scanner gently traces the tip across the sample, the contact force causes the cantilever to bend to accommodate changes in topography. A laser beam focused on the top of the cantilever records the cantilever deflections and provides a three-dimensional image of the surface. The topographic data can be generated by operating in one of two modes: constant-force or constant-height mode.[355]

In *constant-force* mode, the deflection of the cantilever can be used as input to a feedback circuit that moves the scanner up and down in the z direction, responding to the topography by keeping the cantilever deflection constant. In this case, the image is generated from the scanner's motion. With the cantilever deflection held constant, the total force applied to the sample is constant. In this mode, the speed of scanning is limited by the response time of the overall feedback circuit, but the total force exerted on the sample by the tip is well controlled. Constant-force mode is preferred for most of applications.[355]

In *constant-height* mode, the z-servo is turned off and a sample is scanned without z-feedback. Instead, the cantilever deflection, error signal, is used directly to generate the topographic data set because the height of the scanner is fixed as it scans. The cantilever deflections and thus variations in applied force are small. Constant-height mode is essential for recording real-time images of changing surfaces, where high scan speed is required.[355] Figure 4.27 shows a schematic diagram of the contact AFM operation.

Other method of detecting cantilever deflection is to fabricate the cantilever from a piezoresistive material, a so-called self-actuating cantilever, that enables electrical detection of the cantilever deflection. In piezoresistive materials, strain from mechanical deformation changes the resistivity of material thus providing a measure of cantilever deflection. For piezoresistive detection, a laser beam and a photodetector are not necessary.[355]

Scanning Tunneling Microscope. Scanning tunneling microscopes measure topography using the tunneling current between the probe tip and a conductive sample surface and thus it cannot image insulating materials. A bias voltage is applied between the tip and the sample. When the tip is brought within about 10 Å of the sample, electrons from the sample begin to tunnel through the 10Å gap into the tip or vice versa, depending upon the sign of the bias voltage. The resulting tunneling current varies with tip-to-sample spacing; both the sample and the tip must be conductors or semiconductors.

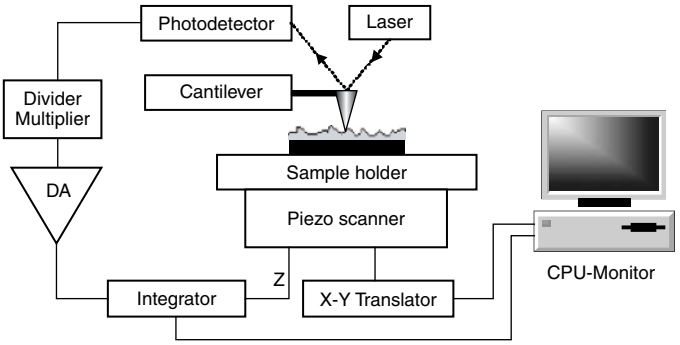

FIGURE 4.27 Schematic diagram of an atomic force microscope (AFM).

The variation in tunneling current as it passes over the atomically uneven surface is recorded, and by repeating this process across the entire sample, a three-dimensional "map" of the surface can be obtained. Since the tunneling current is an exponential function of distance, when the separation between the tip and the sample changes by 10% (on the order of 1 Å), the tunneling current changes by an order of magnitude. STMs can image the surface of the sample with sub-angstrom precision vertically, and atomic resolution laterally. Figure 4.28 illustrates schematically the operation of a scanning tunneling microscope.

STM techniques encompass many methods such as "topographic" (constant-current) imaging, using and comparing different bias voltages and by taking current (constant-height) images at different heights; and ramping the bias voltage with the tip positioned over a feature of interest while recording the tunneling current that is the current–voltage (I–V) curves characteristic of the electronic structure at a specific x–y location on the sample surface. Setting up an STM to collect I–V curves at every point in a data set provides a three-dimensional map of electronic structure. With a lock-in amplifier, $dI/dV - V$ (conductivity) or $dI/dz - V$ (work function), curves can be collected directly.[355]

Scanning Thermal Microscope. The scanning thermal microscope (SThM) maps the thermal properties of the sample surface by using a nanofabricated thermal probe with a resistive element either by measuring the temperature or the thermal conductivity variations on the sample surface. Figure 4.29 depicts the schematic diagram of the PSIA XE-Series SThM system and examples of thermal conductivity and topography images of hydrogen silsesquioxane (HSQ) posts. A "V" shaped resistive element is mounted at the end of a cantilever. While the distance between the probe tip and sample surface is controlled by usual AFM scheme, the thermal probe forms one leg

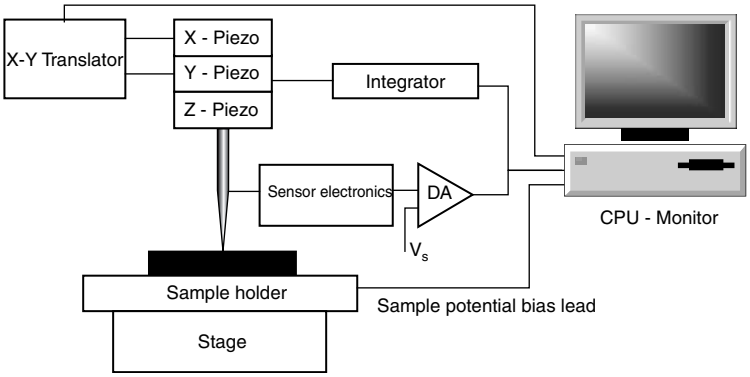

FIGURE 4.28 Schematic diagram of the scanning tunneling microscope (STM).

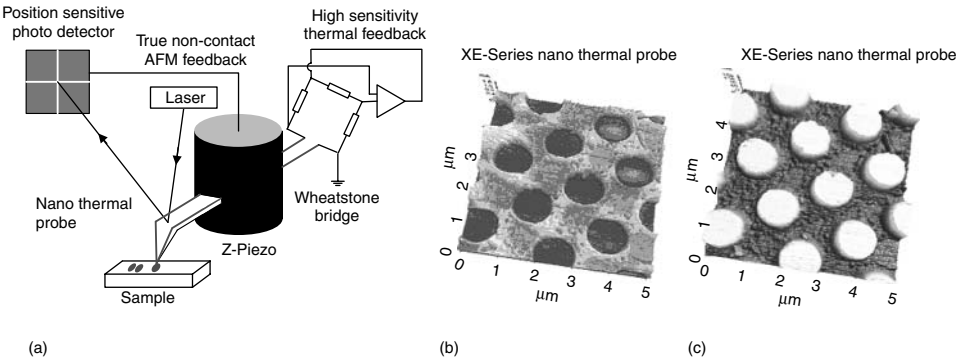

FIGURE 4.29 (a) Schematic diagram of the scanning thermal microscope (SThM); thermal conductivity image (b) and topography image (c) of HSQ posts of 1-mm diameter patterned on a silicon substrate (5 µm×5 µm) using XE-Series nano thermal probe. (From http://www.psiainc.com. With permission.)

of a Wheatstone bridge which feedbacks, adjusts, and balances the bridge voltage to measure the probe's temperature or maintain a constant probe temperature.[355]

A topographical noncontact AFM image can be generated from changes in the cantilever's amplitude of vibration. The advantage of having true noncontact AFM is crucial in achieving the higher spatial and thermal resolution of the SThM since topographic information can be separated from local variations in the sample's thermal properties, thus enabling simultaneous collection of the two types of images. The key part of the SThM is the tip, which serves as a resistance thermometer (or a heater) at the same time as an AFM tip. The thermal element of a cantilever responds differently to changes in thermal conductivity and cause the cantilever to deflect. The XE-Series SThM uses a nanofabricated thermal probe where a resistive element is lithographically patterned on the AFM tip.

Lateral Force Microscope. The principle of lateral force microscopy (LFM) is based on the measurements of the deflection of the cantilever in the horizontal direction. The lateral deflection of the cantilever is a result of the force applied to the cantilever when it moves horizontally across the sample surface, and the magnitude of this deflection is determined by the frictional coefficient, the topography of the sample surface, the direction of the cantilever movement, and the cantilever's lateral spring constant.

LFM of the XE-Series is very useful for studying a sample whose surface consists of heterogeneous compounds. It is also used to enhance contrast at the edge of an abruptly changing slope of a sample surface, or at a boundary between different compounds.

Because the LFM measures the cantilever movement in the horizontal direction as well as the vertical one to quantitatively indicate the surface friction between the probe tip and the sample, it uses a position sensitive photo detector (PSPD) that consists of four domains (quad-cell).[355]

Force Modulation Microscope. Force modulation microscopy (FMM) is used to detect variations in the mechanical properties of the sample surface, such as surface elasticity, adhesion, and friction. In FMM mode, the AFM tip is scanned in contact with the sample surface, and the z feedback loop maintains a constant cantilever deflection as in constant-force mode AFM. The FMM generates a force modulation image, which is a map of the elastic properties of the samples tested, from the changes in the amplitude of cantilever modulation. The frequency of the applied signal is in the order of hundreds of kilohertz, which is faster than the z feedback loop is set up to track. Thus, topographic information can be separated from local variations in the sample's elastic properties, and the two types of images can be collected simultaneously. In addition, a periodic signal known as the *driving signal* is applied to the bimorph piezo and vibrates either the tip or the

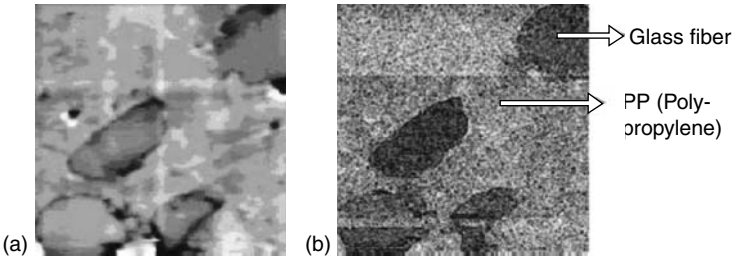

FIGURE 4.30 Topography (a) and FMM image (b) of glass fiber-PP composite (30 μm×30 μm). (From Pharr, G. M., *Mater. Sci. Eng.: A*, 253, 151–159, 1998. With permission.)

sample. The resulting tip motion is converted to an electric signal that is separated into AC and DC components for analysis.

The DC signal represents tip deflection as in contact AFM. The z feedback loop uses this signal to maintain a constant force between the tip and the sample to generate a topographic image. The AC signal contains the tip response due to oscillation. The amplitude of the AC signal (called FMM *amplitude*) is sensitive to the elastic properties of the sample surface. A hard surface will deflect the oscillation, resulting in a large amplitude response. On the other hand, a soft surface will absorb the oscillation, resulting in a small amplitude response.

The FMM image, which is a measure of the elastic properties of a sample, is generated from variations in the FMM amplitude. Figure 4.30 shows the topography and FMM image of a glass fiber-PP (polypropylene) composite. The difference of stiffness between the glass and the PP regions is clearly visible. Furthermore, because the phase shift of the AC signal (FMM phase) differs according to the elastic properties of the sample surface, it can be used to generate an FMM image. This technique is called *phase detection microscopy* (PDM) and is often more sensitive to the elastic properties of the surface than FMM.[355]

Electrostatic Force Microscope. Electrostatic force microscopes (EFM) map electric properties on a sample surface by measuring the electrostatic force between the surface and a biased AFM cantilever. EFM applies a voltage between the tip and the sample while the cantilever hovers above the surface without touching it. The EFM images generated contain information about electric properties such as the surface potential and charge distribution of a sample surface, and the EFM maps show locally charged domains on the sample surface. The magnitude of the deflection, proportional to the charge density, can be measured with the standard beam-bounce system. Thus, EFM can be used to study the spatial variation of the surface charge carrier. For instance, EFM can map the electrostatic fields of an electronic circuit as the device is turned on and off. This technique is known as *voltage probing* and is a valuable tool for testing live microprocessor chips at the sub-micron scale.[355]

In summary, it is clear that the above described techniques and instruments are but a few of the wide selection of available techniques for characterization of nanostructured materials. These techniques and instruments have paved the way for increased understanding of these materials and their associated phenomena. It should be pointed out, however, that despite the huge impact of scanning probe microscopy, there is ever-growing and pressing need for new tools capable of characterizing the structure and generating images with nanoscale resolution and operating in a wide range of temperatures and environments. These new techniques and instruments should be able to provide rapid chemical and physical characterization of nanoparticles as well as automated or quasi-automated systems requiring a minimum of operator attention.

5 Current and Heat Transfer across the Contact Interface

5.1 CONTACT RESISTANCE

As mentioned in previous chapters, the surfaces of solids are always rough. The size of asperities can vary from the length of the sample to the atomic scale. By convention, the surface irregularities are classified into errors in form, waviness, roughness, and subroughness (nanoscale roughness). Those levels of roughness are associated with corresponding types of contact area (apparent, real, and physical area of contact). Study of these areas follows the general trend of mechanics from the macroscopic models up to the current attempts to understand the micro/nano scale processes in the contact of solids. Surface topography affects all the contact characteristics but primarily the mechanical ones. Another important factor affecting the contact behavior is the presence of various films (such as oxides, contaminants, and reaction products).

The current passes through the "*a*-spots" that are smaller than the real contact spots (Figure 5.1). Since the electrical current lines are constricted to allow them to pass through the *a*-spots, the electrical resistance increases. This increase is defined as the constriction resistance. Contaminant films on the mating surfaces increase the resistance of *a*-spots. The total resistance due to constriction and contaminant films is termed the *contact resistance*.

The fundamental monograph of Holm[1] considered most of the contact phenomena important for mechanical and electrical engineers. Timsit's review[4] updated this topic within the framework of a general Holm's approach describing the factors of either electrical or thermal origin affecting the contact resistance. In the following sections, this approach will be followed with the addition of more recent research data.

In the case of isotropic roughness topographies, the *a*-spots are assumed to be circular or noncircular when the roughness has a directional characteristic (e.g., in rolled-metal sheets or extruded rods).

5.1.1 Circular and Noncircular *a*-Spots

A great variety characterizes the shape of *a*-spots. Of all the *a*-spot shapes, the circular ones are most studied. Figure 5.2 illustrates equipotential surfaces and current flow lines near an electrical constriction. The equipotential surfaces in the contact members consist of ellipsoids defined by the equation:

$$\frac{r^2}{a^2+\mu^2}+\frac{z^2}{\mu^2}=1,$$

where μ is a parameter and r and z are cylindrical coordinates. The resistance between the equipotential surface with vertical axis of length μ and the constriction is given as:[1,357]

$$R_\mu = \rho/2\pi \int \mathrm{d}\mu/(a^2+\mu^2) = (\rho/2\pi a)\tan^{-1}(\mu/a), \tag{5.1}$$

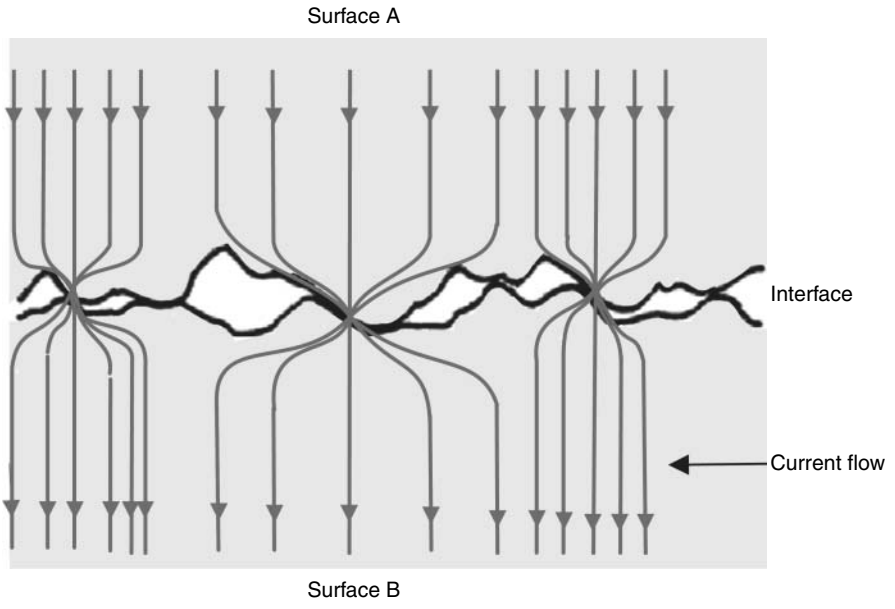

FIGURE 5.1 Electrical constriction resistance. (From Holm, R., *Electrical Contacts*, Springer, New York, 1979.)

where ρ is the resistivity of the conductor. When μ is very large, the spreading resistance is obtained, which is the constriction resistance for each of contact members:

$$R_s = \rho/4a. \tag{5.2}$$

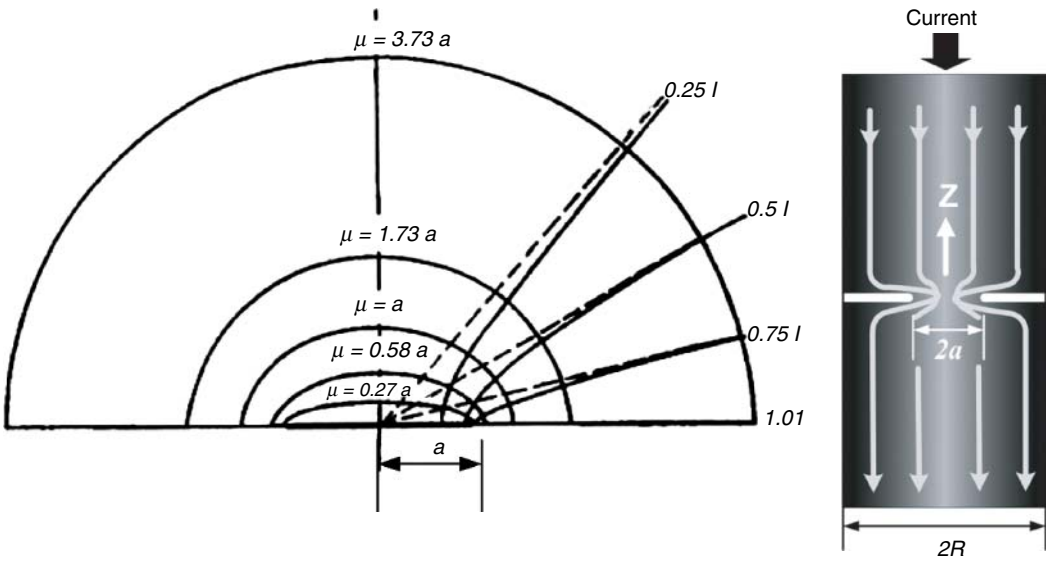

FIGURE 5.2 (a) Equipotential surfaces and current flow lines near an electrical constriction. The parameter μ is the vertical axis of the vertical ellipsoidal surface. The curves corresponding to current flow identify the boundaries enclosing the current fraction indicated. (b) Electrically conducting cylinder of radius R carrying a circular constriction of radius a.

Then the total constriction resistance is

$$R_c = \rho/2a. \tag{5.3}$$

If the upper and lower halves of a contact consist, respectively, of materials with resistivity ρ_1 and ρ_2, the spreading resistance associated with each half of the contact is then $\rho_i/4a$ where $i = 1, 2$. The electrical constriction resistance then becomes

$$R_c = (\rho_1 + \rho_2)/4a. \tag{5.4}$$

It is instructive to evaluate the magnitude of contact resistance as a function of the a-spot radius for a circular constriction in a copper–copper interface ($\rho = 1.75\times10^{-8}$ Ωm). This is illustrated in Table 5.1.

The electrical resistance R_c presented by a circular constriction in a cylindrical conductor of radius R, as illustrated Figure 5.2b, can be calculated from a solution of Laplace's equation using appropriate boundary conditions.[358,359] It may be shown that the electrical contact resistance is accurately given as

$$R_c = (\rho/2a)[l - 1.41581(a/R) + 0.06322(a/R)^2 + 0.15261(a/R)^3 + 0.19998(a/R)^4]. \tag{5.5}$$

Figure 5.3 shows the measured and calculated dependence of R_c on the ratio a/R.[358]

It is shown by Holm[1] that the spreading resistance $R_s(a,b)$ associated with an elliptical a-spot with semi-axes a and b is given as:[4]

$$R_s(a,b) = \rho/2\pi \int_0^\infty d\mu/[(a^2 + \mu^2)(b^2 + \mu^2)]^{1/2},$$

and may be expressed as

$$R_s(a,b) = (\rho/4a)f(\gamma), \tag{5.6}$$

where $\gamma = (a/b)^{1/2}$ is the square root of the aspect ratio of the constriction, the function $f(\gamma)$ is a form factor and the quantity, and a is the radius of a circular spot with area identical to that of the elliptical spot.

The form factor, shown in Figure 5.4[1] decreases from 1 to 0 as the aspect ratio increases from 1 to ∞, subject to the contact-spot elongation. In case of an elliptical a-spot located between semi-infinite solids, the constriction resistance is given as $2R_s$ (a,b). Aichi and Tahara[360] measured

TABLE 5.1
Electrical Resistance of a Circular Constriction in a Copper–Copper Interface

Spot Radius (μm)	Constriction Resistance (Ω)
0.01	0.88
0.1	8.8×10^{-2}
1.0	8.8×10^{-3}
10.0	8.8×10^{-4}

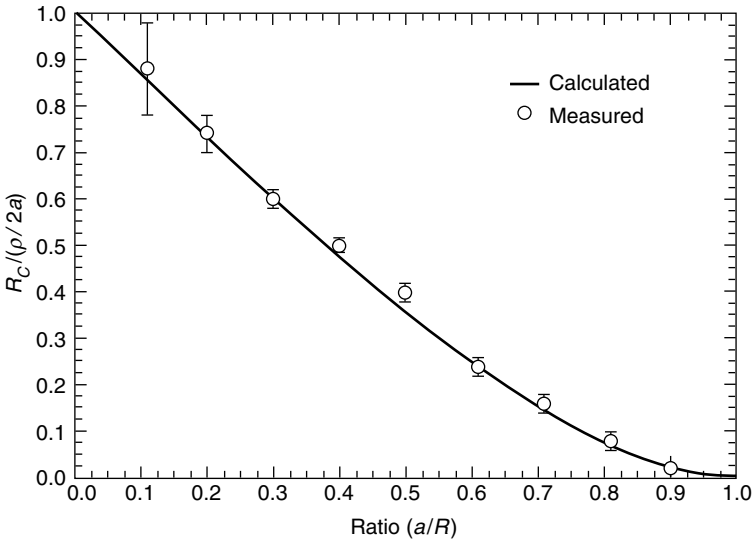

FIGURE 5.3 Measured and calculated (full curve) constriction resistance in a constricted cylinder of radius R, as a function of a/R.

the spreading resistance of rectangular a-spots using an electrolytic bath. Their data, shown in Figure 5.5, indicate that the spreading resistances can be expressed as

$$R_s = (\rho/4L)[(k'/w^{0.26})(w/l)^{0.13}], \tag{5.7}$$

where w and l are, respectively, the width, and length of the constriction. $L = (wl)^{1/2}$ is the width of a square constriction of identical area and $k' = 4k$, where k is a parameter that depends upon

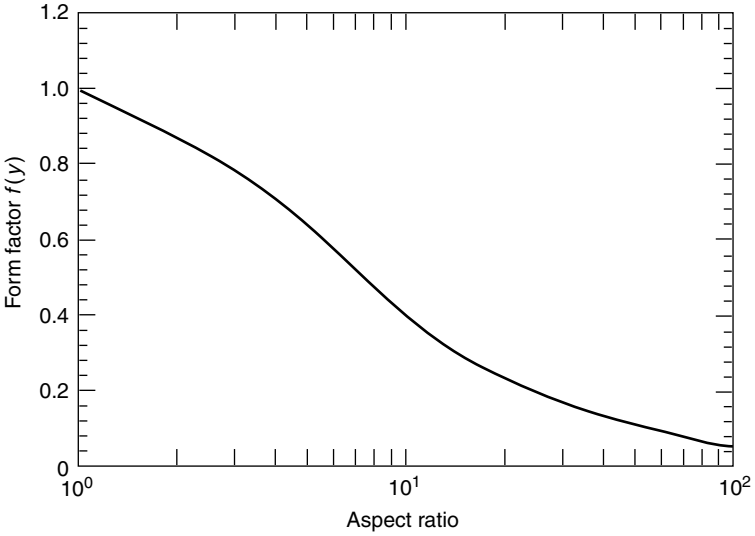

FIGURE 5.4 Dependence of the form factor $f(y)$ on the aspect ratio γ. (From Holm, R., *Electrical Contacts*, Springer, New York, 1979.)

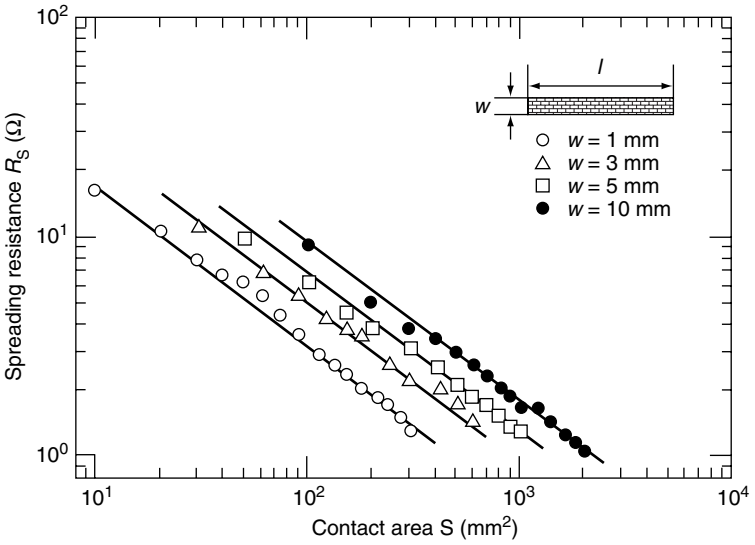

FIGURE 5.5 Dependence of spreading resistance on the area of the rectangular *a*-spot; the area is given as *wl*, where *w* and *l* are the width and length of the spot, respectively. The resistivity of the electrolytic bath is 175 Ωm. (From Aichi, H. and Tahara, N., *Proceedings of 17th International Conference on Electrical Contacts*, Nagoya, Japan, 1–10, 1994.)

the constriction width and varies from 0.36 to approximately 1 as the constriction width increases from 1 to 10 mm. Hence, the spreading resistance of square *a*-spot and of *a*-spot consisting of circular and square rings can be expressed as:[361]

$$R_s = 0.43\rho/L. \tag{5.8}$$

A more general expression for the spreading resistance of circular ring-shaped constriction is given as

$$R_s = R_0/F(\zeta), \tag{5.9}$$

where R_0 is the spreading resistance of the full circular or square spot and $F(\zeta)$ is a conductance form factor. In the case of the circular ring constriction, $\zeta = t/a$, where t and a are the thickness and the outer radius respectively, whereas in the case of the square constriction, $\zeta = t/nL$. The difference between the spreading resistances of circular $R_s/[\rho/4a]$ and square-strip contacts $R_s/[0.434\rho/L]$ is very small, as seen in Figure 5.6.

Cases of rectangular/square contacts are important when surfaces are textured, for example, in the case of power utility connections with pyramidal knurls that penetrate conductors to increase friction force.[4] Ring-shaped constrictions occur when one contacting surface carries a highly conductive cladded layer on a knurled surface. Passage of electrical current occurs largely through the cladding material of the knurls in contact with the mating surface.

The constriction resistance of identical areas (l00 μm^2) but having different shapes in a copper-to-copper interface ($\rho = 1.75\times10^{-8}$ Ω m) is given in Table 5.2. The constriction resistance is significantly affected by constriction shape. The spreading resistances for different shapes of *a*-spots are summarized in Table 5.3.

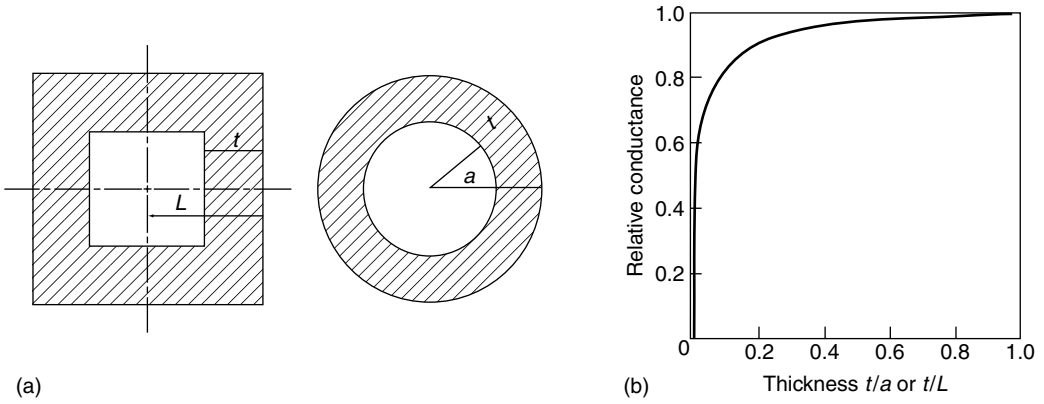

FIGURE 5.6 (a) Square and circular ring constrictions. (b) Form factor $F(f)$ for the ring constrictions shown in (a). The relative spreading conductance is given as $(\rho/4a)/R_s$ for the circular ring, and as $(0.434\rho/L)/R_s$ for the square ring. The difference between the two curves is too small to be seen in the plot.

5.1.2 Effect of Signal Frequency

The basic expression (Equation 5.2) for constriction resistance was derived under the assumption of direct current (DC) passage and based on analytical solution to the Laplace equation. The validity of Equation 5.2 under conditions of alternating current (AC) is considered elsewhere.[361–363]

The major difference between the DC and AC constriction resistance problems stems from the skin-effect that occurs under AC conditions. This effect limits the penetration of the electromagnetic field to a depth of a few times the *electromagnetic penetration depth*, δ, within a conductor defined as

$$\delta = \sqrt{\frac{\rho}{\pi f \mu_0}}, \tag{5.10}$$

where f is the AC excitation frequency, and μ_0 is the magnetic permeability of free space $[4\pi \times 10^{-7}$ H/m]. Constriction resistance for the AC case is different from the DC case because the current is concentrated near the conductor surfaces, particularly at high frequency.

Table 5.4 lists values of penetration depth for typical conductor (e.g., aluminum) at various frequencies.

The constriction resistance for AC for a given conductor deviates from the DC value if the penetration depth becomes smaller than the characteristic dimensions of that conductor. Skin effect

TABLE 5.2
Resistance of Constrictions of the Same Area (100 μm²) and Different Shapes at a Copper–Copper Interface

Constriction Type	Radius (μm)	Length (μm)	Width (μm)	Ring Thickness (μm)	Resistance$\times 10^{-3}$ (Ω)
Circular disk	5.64				1.55
Square		10	10		3.04
Rectangular		50	2		0.43
Ring	16.41			1	0.71

TABLE 5.3
Spreading Resistance for Different *a*-Spots

Nos	*a*-spot	Spreading Resistance, R_s	Expression	Comment
1	Circular	$\rho/4a$	(5.2)	
2	Elliptical	$(\rho/4a)f(\gamma)$	(5.6)	$\gamma=\sqrt{a/b}$ is the square root of the aspect ratio of the constriction, the function $f(\gamma)$ is a form factor and the quantity a_c is the radius of a circular spot with area identical to that of the elliptical *a*-spot
3	Rectangular	$k\rho/S^{0.63}$	(5.8)	S is the area of the rectangular constriction, when the aspect ratio of the constriction is 10 or larger. The quantity κ is a parameter that depends on the constriction width and varies from 0.36 to approximately 1 (when S and ρ are expressed respectively in mm^2 and Ωmm) as the constriction width increases from 1 to 10 mm
4	Square and circular ring-shaped	$R_oF(\zeta)^{-1'}$	(5.9)	R_o is the spreading resistance of the full circular or square *a*-spot, and $F(\zeta)$ is a conductance form factor. In the case of the circular ring constriction, $\zeta = t/a$ where t and a are, respectively, the thickness and the outer radius. In the case of the square constriction, $\zeta = t/L$. The form functions $F(\zeta)$ for the square and circular rings are essentially identical and are shown in Figure 5.6b

causes the current at high frequencies to be concentrated near conductor surfaces and insulating boundaries. If the skin effect dominates, the entire current is confined to a layer not more than five penetration depths. Constriction with radius of several micrometers will be affected by the penetration depth at frequencies larger than 10 MHz, and frequencies of up to 10 kHz will not affect the constriction with radii up to several hundred micrometers. Several authors[361–363] have estimated the effect of frequency by finite element method (FEM).

FEM application to a calculation[363] of resistance at 60 Hz for constriction of radius of 40 μm has agreed well with the analytical formula of Greenwood and Williamson.[364] Thus, the solution for DC constriction can be used at $a/\delta < 0.1$. For high frequency, the calculations have been done for

TABLE 5.4
Variation of Skin Depth with Frequency for a Metal of Resistivity 3×10^{-8} Ω

Frequency (Hz)	Skin Depth, δ (μm)
60	11,254
10^3	2757
10^4	872
10^5	276
10^6	87
10^7	28
10^8	8.7
10^9	2.8

Source: From Lavers, J. D. and Timsit, R. S., *Proceedings of 20th International Conference on Electrical Contacts*, Stockholm, Sweden, 29–30, 2000. With permission.

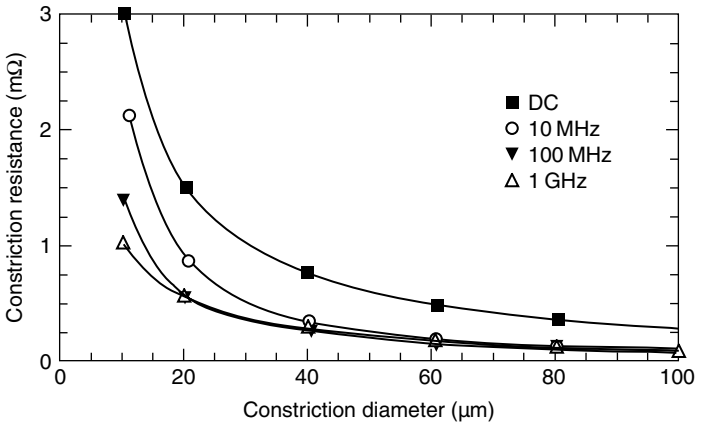

FIGURE 5.7 Dependence of constriction resistance on constriction radius for excitation frequencies ranging from DC to 1 GHz. (From Lavers, J. D. and Timsit, R. S., *Proceedings of 20th International Conference on Electrical Contacts*, Stockholm, Sweden, 29–34, 2000. With permission.)

constriction radii from 5 to 50 μm at frequencies of 10, 100, and 1000 MHz. These data are presented in Figure 5.7. Data presented in the figure show that values of constriction resistance for different frequencies converge as the contact radius becomes large, and there is a critical radius a_c above which frequency is a dominant factor in resistance. This critical radius relates to penetration depth as $a_c/\delta \approx 8$.

The data also show that the constriction resistance decreases with increasing frequency for a certain constriction radius.

Malucci[365] has studied the contact resistance affected by high frequency of AC in experiments with center conductor and coaxial fixture. He has tried also to consider the possible effect of contact capacitance on resistance. Figure 5.8 presents a contact of two similar cylindrical conductors with the spherical tip of the same radius as cylinders. It is assumed that, due to skin effect, the effective

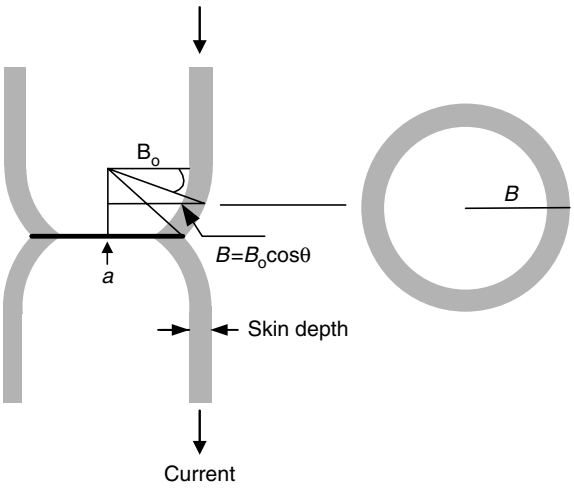

FIGURE 5.8 Skin effect on bulk and constriction resistance. (From Malucci, R. D., *Proceedings of 47th IEEE Holm Conference on Electrical Contacts*, Institute of Electric and Electronic Engineers, Inc., 175–185, 2001.)

current is carried in a thin sheath as defined by the penetration depth. The latter is assumed to be smaller than the contact-spot radius.

When current approaches the contact spot, it passes through a ring that decreases in radius as $B_0 \cos\theta = B$, where θ is the angle from the horizontal. The resistance of the sheath in spherical region is found after integrating the resistance elements as

$$R_t = 2\int \left(\frac{\rho B_0}{2\pi\delta B_0 \cos\theta}\right) d\theta. \tag{5.11}$$

Taking the integral from B_0 to a gives the resistance:

$$R_t = (\rho/\pi\delta)\ln\left[(B_0/a)\left(1+\sqrt{1-(a/B_0)^2}\right)\right]. \tag{5.12}$$

The last equation relates contact-spot radius, geometry, and skin depth to the frequency of the current. In general, this equation shows the growing contact resistance with frequency, which is in some contradiction with the FEM calculations,[363] at least at a frequency range from tens of MHz to GHz. Confirming his calculation by test data obtained for real contact of flat surfaces and coaxial conductors, Malucci also mentioned that further work is needed to understand the behavior of contact resistance at high frequency, taking into account capacitance and inductance of contact.

Brief analysis of the frequency effect on contact resistance shows that this subject is still not adequately studied, especially for contact with multiple spots. Considering the growing importance of high-frequency applications in electrical engineering and electronics, the necessity of further extensive research appears urgent. It is also clear that frequency effects are closely related to the effect of contact size, especially at the nanoscale.

5.1.3 Size Effects, Nanocontacts

A nanocontact is an area between two macroscopic bodies where the dimensions are comparable to the mean free path of the electrons traversing the contact interface. The rapid development of electronic devices having nanometer-scale dimensions imposes very stringent requirements, such as low contact resistance and spatial uniformity at the nanometer-length scale. Therefore, it is of great technological importance to understand the contact-size dependence of constriction resistance. Despite great technological importance, the size-dependence of constriction resistance is not well addressed.

The well-known Holm expression for the contact resistance between the same metals is[1]

$$R_H = \frac{\rho}{2a},$$
$$\rho = \frac{m v_F}{n e^2 l},$$

where ρ is the bulk resistance and $2a$ is the contact diameter of a circular contact, m is the electron mass, v_F is the Fermi velocity, n is the electron density, and e is the electron charge. This expression is only applicable when a contact size is much larger than the mean free path of electrons ($a \gg l$). On the other hand, the *Sharvin resistance*,[325,366] i.e.,

$$R_S = \frac{4\rho l}{3\pi a^2} \tag{5.13}$$

is valid for the opposite limit—when the contact size is much smaller that the electron mean free path.

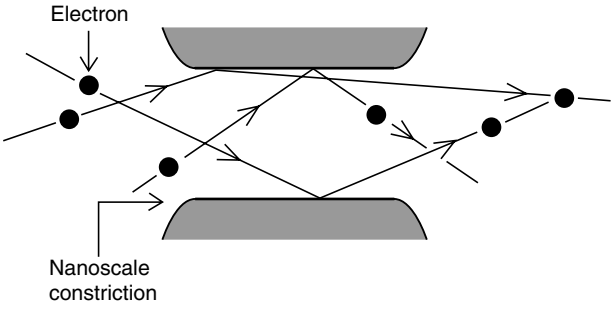

FIGURE 5.9 Ballistic motion of electrons through a small constriction.

Figure 5.9 illustrates the Sharvin mechanism of electron conductivity through the small spots. To find the Sharvin effect scale limit, one can use the Knudsen ratio K ($K = l/a$, where l is the electronic mean free path and a is the radius of the contact spot), which must be much greater than 1 to observe the effect. In this limit, the electrons move in a ballistic way and are scattered deeply inside the bulk of the specimens.

Taking into account the resistance of ballistic motion of electrons, Wexler[367] derived an expression combining classic and ballistic components as

$$R_W = \frac{4\rho}{3\pi a}K + \frac{\rho}{2a}\Gamma(K), \tag{5.14}$$

where $K = l/a$ and $\Gamma(K)$ is a function that takes the value 1 at $K = 0$, and decreases slowly to $9\pi/128$ as K increases to large values.[366] For $K < 1$, Equation 5.14 reduces to the conventional constriction resistance relation; however, for $K > 1$, the quation strongly deviates from it. Because resistivity is inversely proportional to electronic mean free path,[297] the Sharvin component is temperature-independent and represents the resistance of the constriction to effusive electronic flow. It describes an effect analogous to the Knudsen effect in gases, whereby the transport properties of a gas are altered in the neighborhood of a solid boundary.

The effect of this resistance on the relationship between potential drop and contact temperature is not immediately apparent from Equation 5.14 and may be understood qualitatively as follows: Because this resistance originates from boundary scattering and not from the interaction of conduction electrons with the lattice, it is not a source of heat generation within the conducting medium proper. The resistance contributing to Joule heating in a manner consistent with the assumptions of classical contact theory is thus a quantity of order ($R_c - 4\rho K/3\pi a$), where R_c is the "cold" resistance (i.e., the contact resistance at room temperature).[368] Therefore, if this effective resistance is appreciably lower than R_c, as is the case when a is sufficiently small, it generates considerably less heat than anticipated from classical theory on the basis of a measurement of R_c alone. In aluminum with an electronic mean free path of approximately 10 nm, the implications of the Sharvin effect for the predictions of classical electrical contact theory become noticeable at $a \cong 20$ nm. This estimate was consistent with the experimentally observed threshold.[368]

Using a scanning tunneling microscope (STM) inside a transmission electron microscope (TEM), Erts et al.[369] made a direct comparison with the prediction by Holm, Sharvin, and Wexler. The conductance of gold point contacts was determined as a function of contact radius, whereby the contact size varied between a single atom and 20 nm. Using an interpolated Wexler expression between the two limits, a mean free electron path of 4 nm was obtained, which is about ten times shorter than its room-temperature bulk value.

The low values were attributed to an enhanced scattering at a large number of scattering centers created during the contact formation process and not to high temperature in the point. The applied bias voltages of 10 mV used in this experiment resulted in a temperature increase of only 2 K and

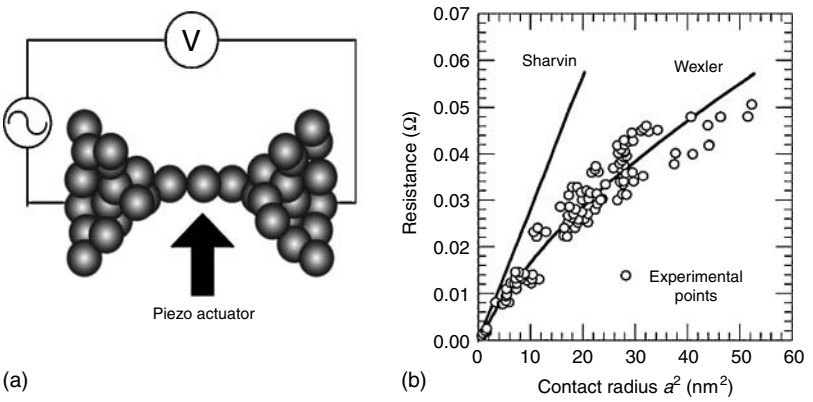

FIGURE 5.10 Schematic of pulling gold nanosized wires inside the TEM (a) and contact resistance as a function of the contact radius squared (a^2) at a bias voltage 10 mV. (b) The Wexler interpolation formula is plotted using a mean free path value of $l = 3.8$ nm and $\Gamma = 0.7$. Sharvin's resistance is added for comparison.

could not be the main reason for the decreased electron mean free path. Figure 5.10 schematically shows the separation of the gold nanowires (a) and the point contact resistance (b) as a function of contact radius squared (a^2). The data were found to fit well with the Wexler interpolation formula using an electron mean free path $l = 3.8$ nm.

To verify whether the temperature may have been responsible for the observed decreased mean electron free path, the current–voltage tests were carried out with a bias voltage up to 140 mV, which corresponds to 540 K. The linear *I–V* relationship was observed, thus confirming that the scattering was mainly due to fixed scattering centers.

In a nanocontact, the quantum-mechanical wave character of the electrons becomes important, thus giving the possibility of observing quantized conductance. Basically, the theory states that, in diamagnetic nanowires as the area of the contact between the wires decreases, the number of conduction channels available to conduct electrons decreases in steps of $2e^2/h$ where the factor 2 represents spin degeneracy. In the case of ferromagnetic nanometals, such as Ni, the exchange energy lifts the spin degeneracy and the conductance is quantized in units of e^2/h.[370]

Conductance measurements have shown clearly the signs of quantized conductance for point nanocontacts.[371,372] Quantum properties of the conductance can be observed when "breaking" a metallic contact: as two metal electrodes in contact with each other are slowly retracted, the contact area undergoes structural rearrangements until it consists in its final stages of only a few bridging atoms.[371,372] Just before the abrupt transition to tunneling occurs, the electrical conductance through a monovalent metal contact is always close to a value of $2e^2/h$.

Mechanical properties and their correlation with the conductance have been studied experimentally,[373–375] whereas theoretically different approaches, ranging from free-electron models to molecular-dynamics simulations, have been used to understand the relation between the geometry and the conductance of the point nanocontacts.[328,375] A typical example of quantized conductance in gold contact measured during breaking of a gold contact at low temperature using mechanically controllable break-junction (MCB) technique is shown in Figure 5.11.[371]

Electronic and quantum effects considered above should be taken into account when discussing the electrical contacts in nanoscale. As shown in Section 5.1.2, the effect of contact size is closely related to frequency effect of current in high-frequency range.

Considering the growing interest in miniature contact systems and the prospects of micro- and nano-electromechanical systems (MEMS and NEMS), the scale factors should be investigated in further detail.

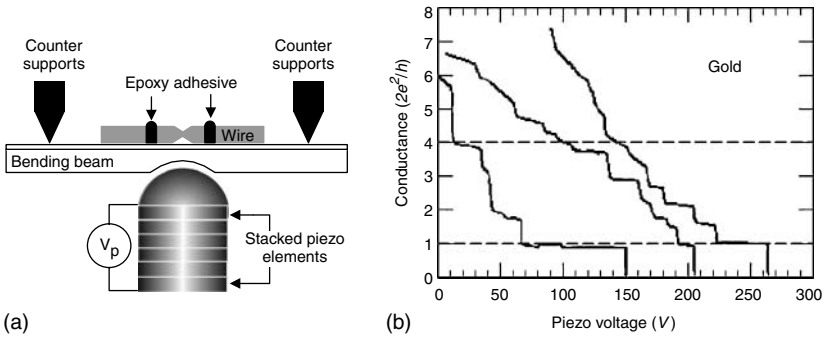

FIGURE 5.11 (a) Schematic of the mechanically controlled break-junction (MCB). (b) Typical recording of the conductance measured in atomic size contacts for gold at 4.2 K. The electrodes were separated by the piezo-voltage whereby the corresponding displacement was about 0.1 nm/25 V. Following each recording in the electrodes are pushed firmly together, and each trace has new structure. (From Van Ruitenbeek, J. M., *Mesoscopic Electron Transport*, Sohn, L. L., Kouwenhoven, L. P., and Schoïn, T. G. Eds., Kluwer Academic, Dordrecht, 549–579, 1997.)

5.1.4 Effect of Surface Films

In the case of a conductive film on one of the mating surfaces, its effect on the constriction resistance of *a*-spot can be positive or negative, depending on the relation of the film and substrate resistivities. Presence of the film can also change the hardness and affect the contact resistance by changing the mode of deformation. If the film is formed as a result of diffusion, high-resistivity intermetallic compounds can be formed, increasing the contact resistance. In case of insulating film formed on the contact surface, the current conduction occurs only when the film is broken, at least partially, and where the metal–metal contacts are made.

Electrically conductive coatings produced by electroplating reduce the contact resistance caused by, among other factors, decrease in hardness, higher conductivity of plating compared to substrate, prevention of insulating film formation, corrosion, and reduction in mechanical wear. Gold plating is often used in case of copper-based connecting members, but even gold-plated contacts can be affected by environmental action if the plating is thin and porous.[376,377]

Since the thick gold coatings are not cost-efficient, alternatives were tried. Palladium was considered to be a good substitute, but its application is disadvantageous due to the formation of tarnish films and friction polymers.[45] Alternative alloys such as palladium–silver, tin–lead, tin–nickel, and cobalt–gold were also considered and evaluated.[378–382] For aluminum-base connectors, the use of tin and nickel plating was evaluated to mitigate the problem of corrosion and surface oxidation.[383]

In case of conductive plating, the electrical resistance depends on the relation between the coating thickness and the *a*-spot diameter as well as on the ratio of conductivities of plating and substrate. If the resistivity of the plating is larger than that of the substrate and the spot radius is close to the film thickness, the electrical current from the spot spreads out more easily into the substrate than into the plating (Figure 5.12a). The potential drop in the vicinity of the *a*-spot in the substrate is negligible in comparison with the potential drop across the film.[1] Hence, the film–metal interface is nearly equipotential and the current density in the film is uniform across the *a*-spot (Figure 5.12a), and the spreading resistance is still nearly described by Equation 5.2.

Since the current passes through the resistive film of area πa^2 with thickness d and resistivity ρ_f, the additional film resistance equals to $\rho_f d/\pi a^2$. To a first approximation when the film is thin, the

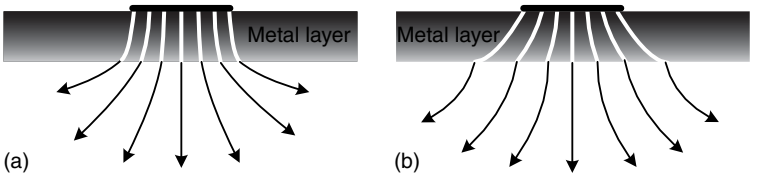

FIGURE 5.12 Current distribution in metal surface film: (a) the film conductivity is smaller than that of the substrate and a-spot radius is of the same size as the film thickness; (b) the film conductivity is higher than that of the substrate and the current lines spread out within the plating easily than within the substrate.

total resistance R_t then becomes

$$R_t = R_s + \rho_f d/\pi\alpha^2. \tag{5.15a}$$

This equation reduces to

$$R_t = (\rho/4a)[1 + (4/\pi)(\rho_f/\rho)(d/a)]. \tag{5.15b}$$

If spot radius and the plating thickness do not differ greatly, the spreading resistance increases approximately linearly with plating thickness. For relatively thick film, the spreading resistance deviates from the above expression and approaches $\rho_f/4a$. Equation 5.15b shows that the effect of constriction resistance is overshadowed by the film resistance if the ratio $(\rho_f/\rho)(d/a)$ is much larger than unity. This conclusion was confirmed through the computer simulation of Nakamura[361] and Minowa.[384]

If the conductivity of the plating material is higher than that of the substrate, the current lines spread out in the plating more easily than they do in the substrate (Figure 5.12b), and the spreading resistance decreases with increasing film thickness. It approaches $\rho_f/4a$, when a-spot is much smaller than the film thickness. If P_f is smaller or larger than the substrate resistivity, the effect of plating on contact resistance can be found as:

$$P_f(d/a,\rho_f,\rho) = (\rho_{eff}/4a)/(\rho/4a) = \rho_{eff}/\rho, \tag{5.16}$$

where $P_f(d/a,\rho_f,\rho)$ is the "plating factor" and ρ_{eff} is the effective resistivity of the plated substrate, where $\rho_{eff} = \rho$ for $d = 0$.

The plating factor may be evaluated using the algorithm described by Williamson and Greenwood.[385] The calculated dependencies of the plating factor on the ratio $d/2a$, respectively, for typical cases for which $\rho_f/\rho > 1$ and $\rho_f/\rho < 1$ are shown in Figure 5.13.

In practice, the effect of surface deformation on contact resistance should be taken into account. If the resistivities of two rough contacting materials (e.g., the plated surface and a measuring probe) are, respectively, ρ and ρ_p, and the effective resistivity of the plated material is ρP_f, then the contact resistance is

$$R_t = [(\rho_p + \rho P_f)/2](\pi\eta H/4F)^{1/2} \tag{5.17}$$

where H is the hardness of the softer metal in the interface.

In the case of a contact with the contaminant film present on the surface, the resistivity (ρ_c) of contaminant materials is generally much larger than that of metals; Equation 5.15a can be used. In this case the film resistance is $\rho_c d_c/\pi a^2$ where d_c is the contaminant film thickness. Since the

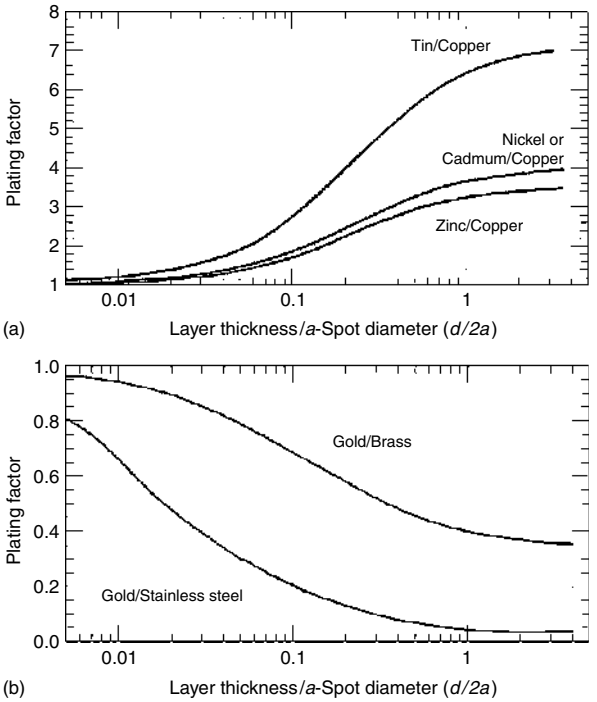

FIGURE 5.13 Dependence of the plating factor on the ratio $d/2a$ for the case of (a) $\rho_f/\rho > 1$ and (b) $\rho_f/\rho < 1$.

contact area is given as F/H (i.e., $\pi a^2 = F/H$), the expression for total contact resistance is

$$R_c = [(\rho_p + \rho P_f)/2](\pi\eta H/4F)^{1/2} + \rho_c d_c H/F. \tag{5.18}$$

This equation is widely used to interpret contact resistance data for plated surfaces. The electrical contact properties of metal coatings for connectors are generally measured by probing the coated surface. Details of the measuring procedure are given in the ASTM Standard Practice.[386]

Data on contact resistance as a function of contact force for gold probes pressed against a gold target are given in Figure 5.14a.[387] Four of the probe tips were shaped as spheres with radii equal to 3.2, 1.6, 1.2 and 0.9 mm; the fifth tip was made as a sharply pointed conical end (60° apex angle) of a gold rod 3.18 mm in diameter. The contact resistance for spherical tips was very close to the values predicted by Equation 5.18 in the absence of a contaminant film (i.e., $d_c = 0$). In the case of a conical tip, the larger resistance stemmed from a larger bulk resistance for the tip.[387] If this factor is taken into account, the data for all the tips are similar, being independent of the gold probe radius and dependent only of the applied force. This finding means that the metal-to-metal contact area is independent of probe geometry and depends only on hardness.

Figure 5.15b shows the results of contact resistance measurements on freshly polished copper using the five gold tips mentioned above. These results are different from those given in Figure 5.14a. The slope of the initial parts of the curves for load less than 20 g is approximately -1, and the contact resistance is generally larger than that obtained from gold-on-gold. The initial inverse proportionality to load (F) suggests that the contact behavior is described by Equation 5.18, where $d_c \neq 0$, i.e., in the presence of a contaminant film of relatively large resistivity such as an oxide film. A good fit to Equation 5.18 was found using a value for $(\rho_c d_c)$ of 2.75×10^{-14} Ωm^2. The curves of Figure 5.11 are also independent of probe geometry as predicted by Equation 5.18.

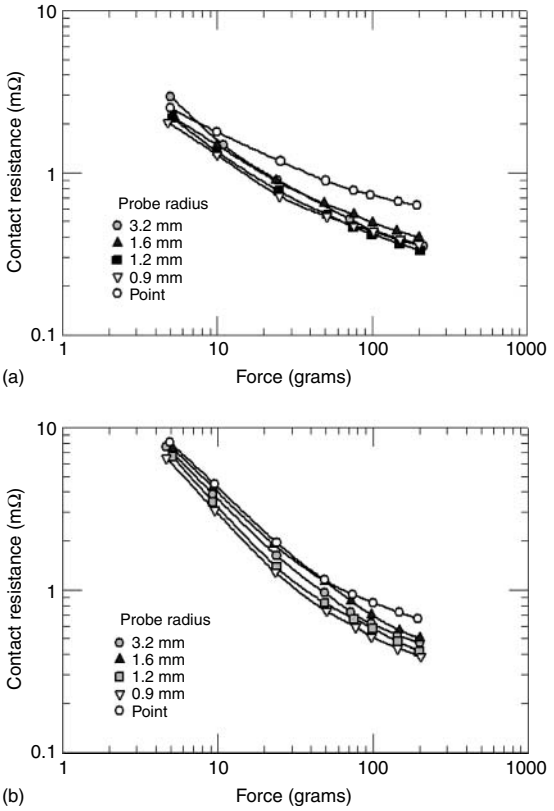

FIGURE 5.14 Contact resistances vs. applied force for gold probes of various tip radius: (a) clean gold-to-gold and (b) clean gold on freshly polished copper.

Data given in Figure 5.14 support the assumption that the area of metal-to-metal contact is determined only by plastic deformation (hardness) of the contact surfaces.

Using an approach based on the Holm hypothesis[1] that there is a possibility of transmitting significant current densities through a contact with tunnel-conductive tarnish films without damaging them, Konchits and Kim[388] carried out an experimental study of electrical conductance of a stainless steel contact with the surface films. Continuous films on stainless steel of approximately uniform 1–1.5 nm thickness with specific resistance of 6×10^{-10}–7×10^{-8} Ωm^2 are a typical example.[84] This phenomenon was studied using a probe-plate contact configuration whereby the plate was stainless steel plate and the probe made of noble metal.[389] The samples studied were polished stainless steel plates, whereas a twisted gold wire piece 0.5 mm in diameter was used as a microprobe to localize the contact zone and to minimize the effect of surface topography.

Prior to resistance measurements the probe tip was shaped by a repeated loading until the maximum possible load (0.6 N) was achieved. The reduced radius of the tip working area produced by plastic deformation was ≈ 20 μm. The preformed probe tip and a fixed position of contacting members in holders yield good run-in conditions required to establish a full contact of the probe with the specimen over the entire working area ($S \approx 1.25\times10^3$ μm^2). Electrical characteristics of the contact were measured by applying a static load of 0.2 N and holding it during the period 2–3 min.

Figure 5.15 illustrates the schematic electrical diagram of the test setup. Voltage U (up to 6 V) was applied to the contact through resistor R_1 from controllable current source I. Current in the measuring circuit was limited by the resistor R_2 and controlled by the voltage drop across resistance

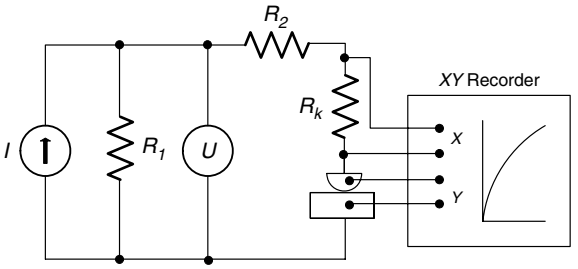

FIGURE 5.15 Electric diagram of tests. I, controllable current source; U, voltage in measuring circuit; R_1, R_2, R_k, resistors.

R_k. An X–Y recorder was used to register the voltage drop across the contact U_c and the applied current, i.e., the current–voltage characteristics (IU_c-characteristics) of the contact junction. The IU_c characteristics (direct in case of voltage U rise and reverse in case of U decrease) and derived R_cU_c-characteristics were used to analyze the mechanism of current passage through the contact. Attention was focused on the surface areas where the initial resistance R_c exceeded (sometimes by the order of magnitude and more) the mean statistical level, thus indicating that a continuous tarnish film exists on the steel. Because the area of real contact is always smaller than that of load bearing resistance of order, say, 40 Ω (Figure 5.12, Section O–A), corresponds to a continuous tarnish film with specific resistance below $5\times10^{-8}\,\Omega m^2$. Using the known formulas for tunnel conductivity,[390,391] the estimated average film thickness h did not exceed an 0.8–0.9-nm value. However, this value is clearly underestimated since under real conditions it may exceed 1 nm because of a probable conductivity contribution from the film material to the contact conductivity.

The initial portion of IU_c-characteristics is nonlinear over the entire area, i.e., R_c decreases as the measuring voltage U, contact potential U_c and current I increase in the contact (Figure 5.16). At some contact voltage U_{cf} of 0.4–0.5 V and current I, apparently 10–50 mA, IU_c-characteristics bend (point A in Figure 5.17), indicating a sharp reduction of contact resistance R_c. At this point the current density $j = 8\times10^{-6}$–$4\times10^{-5}\,A/\mu m^2$ and the contact area $S = 1.25\times10^{3}\,\mu m^2$. A further increase in the measuring voltage increases current I, whereas U_c remains unaffected but fluctuates at a level slightly lower than U_{cf}. At this point, R_c falls rapidly to 1–2 Ω at $I \sim 0.3$ A.

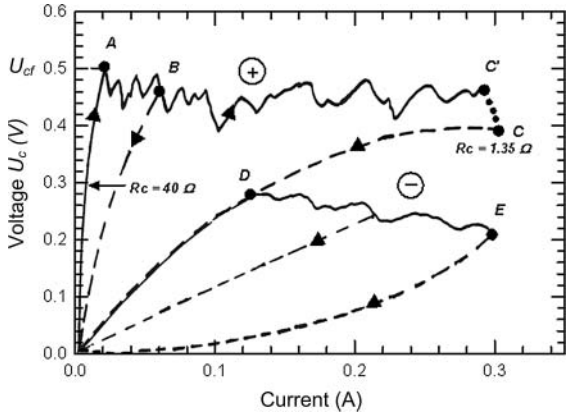

FIGURE 5.16 Direct (full lines) and reverse (dotted lines) IU_c-characteristics of contact between gold probe and steel surface with continuous tarnish film (pathway C′–C, delivery of constant U during 60 s; "+," "−" represent probe polarities).

When the polarity is reversed, the IU_c-characteristic (e.g., from points B or C) shows a different tendency since it does not coincide with the initial one. When U is maintained unchanged during tens of seconds and more of a gradual decrease of R_c occurs (e.g., from point C′ to point C in Figure 5.16). This situation provides clear evidence that irreversible changes occur in the contact when U_{cf} is reached.

The integrity of the obtained data indicates that fritting (low-voltage breakdown of thin insulating films on a metal surface), as described by Holm,[1] takes place at contact potential U_{cf} when the critical field intensity $E_{cr} = U_{cf}/h$ is reached. Assuming $h = 1$–1.5 nm and $U_{cf} = 0.4$–0.5 V, then $E_{cr} = (3\text{–}5)\times 10^8$ V/m. This finding agrees well with the earlier reported data[1,392] for thicker oxide films on copper, nickel, brass, and aluminium alloys. The current-conductive channels (bridges), appearing during fritting, are formed by a mixture of metal and film materials rather than by a pure metal. This is confirmed by the slope of reverse IU_c-characteristics (Section B–O and C–D–O, Figure 5.16) indicating decreasing R_c with voltage, and/or a negative contact resistance temperature coefficient. The IU_c-characteristics after repeated fritting and without changing the probe position and positive polarity (e.g., from point C′ in Figure 5.16) practically coincide (Section C–D–O).

When the polarity of the probe is switched from "+" to "−," the IU_c-characteristics coincidence remains unchanged up to point D. A further increase of U and I induces IU_c-characteristics to bend, and R_c decreases more rapidly. At some current values, bending of the IU_c-characteristics is indicative of the "metallic" nature characterised by a positive temperature coefficient (Section EO).

Requiring a definite time period, formation of the conductivity channels is determined by the electrical field direction in the contact clearance. The R_cU_c-characteristics in Figure 5.17 depict these processes. These characteristics were recorded on the same surface area with initially positive "+" and then switching to negative "−" probe polarity. The recording time for direct and reverse IU_c-characteristics remained below 10 s, and the probe was kept for 120 s at the terminal points (at the maximum current $I = 0.35$ A). All the characteristics have a positive temperature coefficient, thus confirming the predominant metallic conductivity. When the contact is kept under constant current, a noticeable decrease (probe polarity is "+") or rise (the probe polarity is "−") of R_c occurs with good repeatability. The increase in contact resistance during current switching is an unusual effect that is hard to explain.

The plausible explanation for the results obtained is based on the assumption that the appearance of the current-conductive metallic bridges in the film results from the predominant migration of positively charged ions of the probe material under strong electric field and the elevated temperatures generated in the spots by high current density. This process requires time for

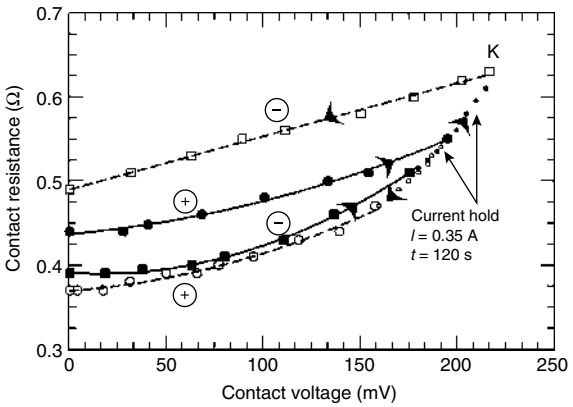

FIGURE 5.17 Direct (full lines) and reverse (dotted lines) R_cU_c-characteristics at positive (+) and negative (−) polarities of gold probe over steel surface area with low R_c.

a bridge to appear. Therefore, R_c reduces when the probe acts as the anode, and bridges are formed because of the action of gold ions. When the polarity is changed, and the contact remains under current carrying conditions, a transition to the bridges from a less-conductive iron is initiated, thus forcing R_c to rise.

5.1.5 Effect of Contact Geometry

In practice, contact between nominally flat surfaces takes place at clusters of *a*-spots (Figure 5.18). It is well known that the real contact area is a set of separated contact spots. The real spots consist of a set of smaller spots formed by nanoscale roughness. This fact has a clear meaning when comparing contact areas bearing the load and those conducting the electric current.[394] Figure 5.18 is an illustration of this concept, depicting the AFM data processing with the extraction of subroughness by median filtration of a digital image.

The positions of the clusters are determined by the large-scale waviness of the contact surfaces and the positions of *a*-spots by the small-scale surface roughness. Contact resistance in this case can be affected by the number and size of the *a*-spots and by the pattern and size of the clusters. Keeping in mind the data on the nonclassic behavior of microscopic contact spots (see Section 5.1.2), the presence and pattern of these spots on the contact interface look very important for their part in contact resistance.

When electrically conductive spots are formed only where the surface insulating layers are fractured and the fracture mode of films may depend on the deformation of the contacting asperities, the number of metal-to-metal spots is difficult to predict. This number should be much smaller than the number of asperities in mechanical contact.

In the simplest case of a large number n of circular *a*-spots situated within a single cluster, it was shown approximately by Greenwood[393] that the contact resistance is given as

$$R_c = \rho(1/2na + 1/2a) = R_1 + R_2, \tag{5.19}$$

where a is the mean *a*-spot radius defined as $\Sigma a_i/n$, a_i is the radius of the ith spot, n is the number of circular *a*-spots (n is taken to be large), and α is the radius of the cluster sometimes defined as the Holm radius: $\alpha^{-1} = (3\pi/16n^2)\sum_{i\neq j}\sum_{i\neq j}(1/s_{ij})$, where s_{ij} are the distances between the spots.

Table 5.5 shows the relative magnitudes of the two terms in Equation 5.19 calculated by Greenwood[393] for the regular array of 76 identical *a*-spots illustrated in Figure 5.19a, as the *a*-spot radius is increased. In the calculation, the spot spacings are taken as 1 and the maximum *a*-spot radius is 0.5. The cluster resistance $1/2\alpha$ exceeds the *a*-spot resistance when the spot radius increases beyond approximately 0.05. This means that the effect of arraying the spots becomes

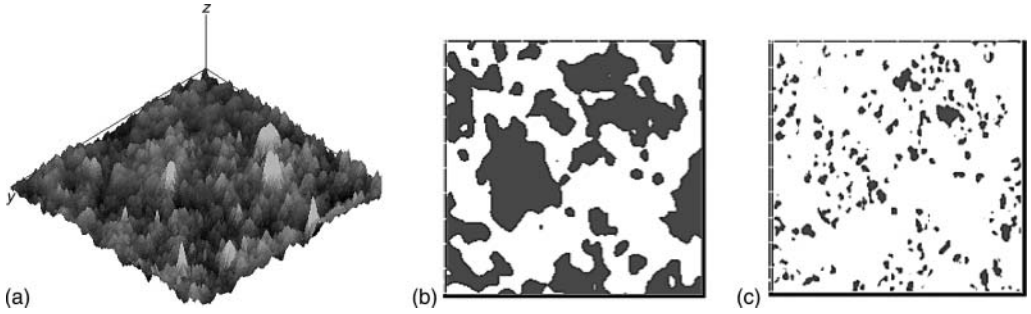

FIGURE 5.18 Visualization of contact spots at various scales when contacting a smooth plane: (a) An AFM image of an analyzed area (scan 15×15 μm^2). (b) Contact spots at microscale. (c) Contact spots at nanoscale (physical contact area, see Section 2.5.2).

TABLE 5.5
Effect of *a*-Spot Radius on Constriction Resistance $1/2na$ and Holm Radius α

a-Spot Radius	*a*-Spot Resistance, $1/2na$	Holm Radius, α	Cluster Resistance, $1/2\alpha$	Radius of Single Spot of Same Resistance
0.02	0.3289	5.34	0.0937	1.18
0.04	0.1645	5.36	0.0932	1.94
0.1	0.0658	5.42	0.0923	3.16
0.2	0.0329	5.50	0.0909	4.04
0.5	0.0132	5.68	0.0880	4.94

more significant when the area of spots is increasing in the contact area. Such an effect is common at the increasing contact load.

The radius of equivalent single contacts and the Holm radius for a variety of *a*-spot distributions, also calculated by Greenwood,[393] are illustrated in Figure 5.19a–d. In each case, the circular area of the Holm radius provides a reasonable representation of the area over which electrical contact occurs. Nakamura and Minowa[362] and Minowa et al.[395] have examined the effect of *a*-spot distribution on electrical resistance using the finite element and Monte Carlo techniques. They found that the Holm radius may be sufficient to estimate contact resistance if films are absent on the contact interface.

Earlier Greenwood's model was tested by Yip and Venart in their model experiments with electrolytic solution when studying the effect of conductive spots array in the apparent contact area.[396] They found the effect of arrangement of contact spots in a cluster of spots as well as clusters in the apparent contact area to be quite significant. So the effect of the clusters grouping in the total

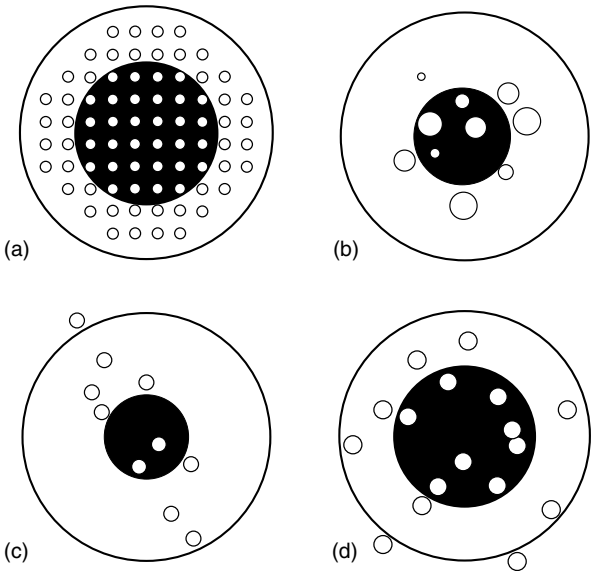

FIGURE 5.19 (a) Regular array of *a*-spots. The shaded area is the single continuous contact with the same resistance; the outer circle is the radius of the cluster given to a reasonable approximation by the Holm radius α. (b), (c), (d) Clusters of *a*-spots with corresponding radius of equivalent single contact (shaded area) and Holm radius (outer radius).

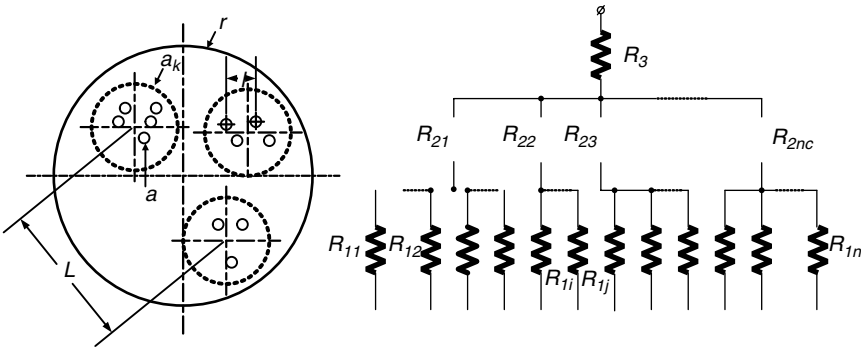

FIGURE 5.20 (a) Cluster structure of contact region and (b) electrical scheme of contact resistance in one of the contacting bodies: R_{2i}, resistance of cluster of the contact spots with total resistance $R_2 = \sum R_{2i}/n_c$, where n_c is number of clusters; R_1, resistance of an elementary contact spot with total resistance of spots $R_1 = \sum R_{1i}/n$.

apparent contact area should be taken into account for contact of rough solids.[2] Equation 5.19 can be added, with the third term taking into account the mutual influence of clusters:

$$R_3 = \frac{16}{3\pi^2 r}. \tag{5.20}$$

Here r can be found by the same technique as Holm radius α but replacing the distances between elementary spots s_{ij} by distances between clusters L_{ij} (Figure 5.20). Upper limit for r is equal to the radius of apparent contact area. Finally the total contact resistance can be found as the following sum:

$$R = R_1 + R_2 + R_3 = \rho(1/2na + 1/2n_c\alpha + 1/2r). \tag{5.21}$$

It is well known in tribology that the number of clusters of contact spots (cluster is considered as elastic Hertzian contact on the waviness) shows no appreciable increase with increasing contact load and that the growth of the real contact area occurs basically as a result of the increasing number of contact spots. Therefore in the overall resistance as expressed by Equation 5.21, it is expected that the second and third terms will show a weaker load dependence than the first term.[2] Therefore, the effect of adding these terms to the overall resistance, although weak for small loads, becomes the governing factor for high loads, when the contact resistance decreases due to increase in the number of contacts spots, but their density and size increase. Table 5.5 shows the dominance of cluster resistance at increasing the elementary spot radius at the constant number of elementary spots.

A simple qualitative estimate also shows that in the real contact of rough surfaces, for example, assuming the clusters of contact spots to be located at the peaks of the surface waves, the contribution of the clusters and their arrangement to the overall contact conductivity may be significant or even dominant. For example, suppose the elementary spot size to be on the order of micrometers and the total number of spots as 100 grouped in 5 equal clusters of 20 spots with Holm radius 20 μm in the apparent contact area of 1 mm radius. One can find R_1 equal to R_2 with R_3 being only 1% of R_1 and R_2. But if the number of spots increases to 1000, with the number of clusters equal to 10 at the same radius of spot and Holm radius increased to 100, all the components R_1, R_2, and R_3 become equal.

In a study of the influence of the surface roughness spectrum on the contact thermal resistance, Thomas[397] also explained the nature of this effect by considering the contribution due to the long-wave components of the surface profile spectrum (waviness).

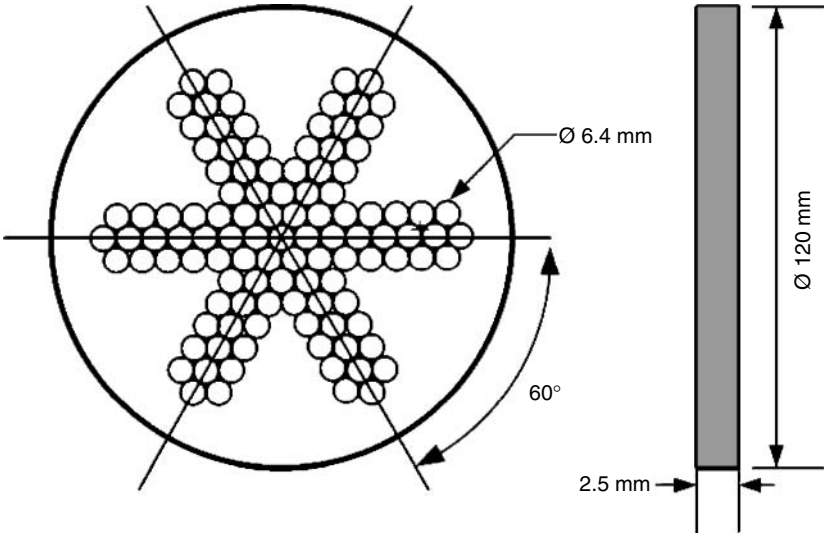

FIGURE 5.21 Schematic of plastic cage retaining the balls between the disc plates and separating them of each other.

The setup shown in Figure 5.21 and Figure 5.22 was used to test the theoretical calculations mentioned above.[398] A plastic cage containing a certain number of standard polished balls of steel AISI 52100, with a diameter of 6.3 mm, is compressed between two steel or copper discs with diameter equal to 130 mm. The plastic cage was fabricated from glass-cloth laminate, having the shape of a disc with diameter equal to 120 mm and thickness 2.5 mm (Figure 5.21). Total of 109 holes with diameters slightly larger than 6.3 mm were drilled in the cage providing the possibility to arrange the balls in the regular groups with different spacing. The distance between the centers of neighboring holes is 7.3 mm, so balls are insulated in the horizontal plane of the cage and are free to move in a normal direction. Contact resistance was measured by a four-wire technique using the electrical circuit presented in Figure 5.22.

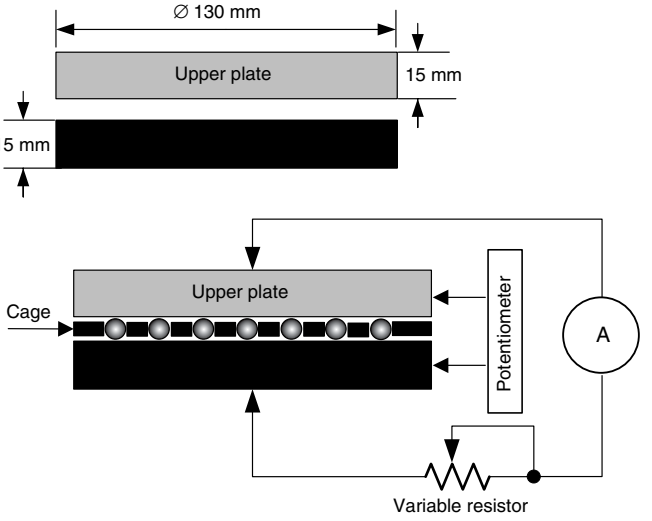

FIGURE 5.22 Schematic of test setup.

Each ball has two contacts with the opposite discs whereby the basic electrical circuit comprises two zones of current constriction in the discs and resistance of the ball itself. The analytical solution of the resistance of a sphere when current passes between the opposing spots is given by the following formula, assuming that the radius of a spot a is much smaller than ball diameter D:

$$R' = \rho_1 \left(\frac{1}{2a} - \frac{1}{\pi D} \right), \tag{5.22}$$

where ρ_1 is the resistivity of the ball material.

Constriction resistance of the contact spots with the size comparatively negligible with the thickness of disc can be calculated in each disc using the Holm expression 5.2 $R = \rho_2/4a$, where ρ_2 is the disc resistivity. Cluster resistance in the discs was found as a second term in the Greenwood formula (Equation 5.19) equal to $\rho_2/2n_c\alpha$, where n_c is a number of clusters.

This analysis gives the final formula for resistance calculation in the form:

$$R_c = \frac{1}{n} \left(\frac{\rho_1}{2a} - \frac{\rho_1}{\pi D} + \frac{\rho_2}{2a} \right) + \frac{\rho_2}{2n_c\alpha} + \frac{\rho_2}{2r}. \tag{5.23a}$$

For a more clear comparison of the effect of cluster arrays, it is possible to use a more simple formula excluding the resistances of ball volumes and assuming R_3 to be negligible because the number of clusters is small, with a symmetrical arrangement in the large apparent contact area:

$$R^* = \frac{1}{n} \left(\frac{\rho_1}{2a} + \frac{\rho_2}{2a} \right) + \frac{\rho_2}{2\alpha} = R_1^* + R_2. \tag{5.23b}$$

The results shown in Table 5.6 illustrate the comparison of the measured contact resistance with that calculated using Equation 5.23a and Equation 5.23b.

Examination of the data presented in Table 5.6 shows a difference between the measured and calculated results. In the case of steel discs, this difference is 19–48% for steel discs and 72–89% for copper discs. The difference is not surprising since the apparent and real contact areas are different due to the roughness of the discs. In the simplest case of six isolated balls placed on the periphery of the steel discs when the interrelation term in constriction resistance is negligible, the difference is 19% only. The real contact area with metal conductivity in that case is about 60% of apparent one. In other cases when the difference is higher, the contribution arising from the array of the spots should be considered. For copper discs, the difference is much higher than for those made from steel and reaches 70% in the best case. This means that only one-tenth of the contact area supporting the load is metallically conductive. Data available in the literature confirm that oxide films on copper are much thicker than on steel and that their fracture is rather difficult.

The analysis of the data in Table 5.6 shows that the test and calculation results describing the changes in the number of balls and their position within the apparent contact area are in good qualitative agreement. A more homogeneous and less dense array of spots under approximately the same contact area results in a lower contact resistance. This trend is more apparent when the number of balls in contact is increased. This trend is expected from the the theoretical predictions made by Holm and Greenwood. These predictions were confirmed by calculation and testing of the real metal specimens with different surface treatment.[392,399]

In the case of copper discs, there is a clear distinction in the mechanical interrelation of the deformed zones under the balls. In other words, the indentation diameters are smaller if the balls have a denser array. The higher increase in contact resistance of copper as compared to the case of steel can be attributed to the combined effect of mechanical and electrical interrelation of spots in their clusters.

It is necessary to mention the complexity of the contact resistance behavior in a real contact when a multilevel pattern of roughness and mixed elastic–plastic mechanism of deformation takes place.

TABLE 5.6
Comparison of the Calculation and Test Data on Contact Resistance

No.	Array of Balls	N (kN)	$2\bar{a}$ (mm)	R_1^* (μΩ)	R_2 (μΩ)	Calculated R_c (μΩ)	Test R_t (μΩ)	R_2/R_1^* (%)	R_c/R_t (%)
Disc—medium-carbon steel 45, average roughness 0.4 μm, hardness 170 HB, polished ball—steel AISI 52100,65HRC									
1	6 Balls at the periphery of disc ($s_{ij} \geq 45$ mm)	150	2.9	17.3	1.2	48.5	60	7	81
2	12 Balls in 6 groups by 2 at the periphery of discs ($s_{ij} \geq 14.6$ mm)	150	2.7	9.3	1.7	27	48	18	56
4	12 Balls in one group in the center ($s_{ij} \geq 7.3$ mm)	150	2.6	9.5	6.0	32	56	63	57
5	18 Balls in 3 groups by 6 at the periphery ($s_{ij} \geq 7.3$ mm)	150	2.1	8.3	3.2	26.5	39	39	68
6	18 Balls in 1 group in the center ($s_{ij} \geq 7.3$ mm)	150	2.0	8.0	5.9	28.1	45	74	63
7	21 Balls in 3 groups by 7 at the periphery ($s_{ij} \geq 7.3$ mm)	150	2.0	7.2	3.6	23.3	38	50	62
8	21 Balls in 1 group in the center	150	2.0	12	5.9	25.9	50	82	52
Disc—copper, average roughness 0.8 μm, hardness 50 HB									
9	9 Balls in the periphery ($s_{ij} \geq 12.5$ mm)	60	3.8	4.6	0.1	15.7	83	3	19
		120	5.0	3.5	0.1	11.5	41	4	28
10	9 Balls in 3 groups by 3 in the middle part of disc ($s_{ij} \geq 7.3$ mm)	60	3.7	4.7	0.2	16.5	191	5	9
		120	4.7	3.8	0.2	12.5	92	7	14
11	9 Balls in 1 group in the center	120	4.3	4.1	0.4	14.1	126	11	11

Coming from a macroscopic scale to micro/nanoscale, it is necessary to consider the combination of factors. For example the original Holm's model of contact area and spots in it should be modified with taking account of micro and nanospots. Somewhere, the limit of further complication of models should be fixed because the natural atomic scale limit is being approached, where the nature of Ohmic resistance should be considered from quantum point of view. Full understanding of the whole combination of factors in play has not been attained. Therefore, the natural method should be to analyze the up-to-date experience and to outline the directions of further urgent studies.

5.1.6 Conductivity of Rough Contact

The determination of the contact conductivity of rough bodies is of great interest for studies in both the field of surface phenomena and a whole series of practical applications. No less interesting is the problem of determining the real area of a contact on the basis of its conductivity. Hence, the use of random fields for describing the electrical contact phenomena is very promising.[14,397] Rather straightforward, such an approach involves three main steps: (1) determination of distribution probability for asperity parameters using measurement or/and theories of roughness (here, it is assumed that the distribution is given); (2) solution of governing equation for electrical resistance of elementary contact spots and their array (see Equation 5.19 and Equation 5.21); and (3) determination of the total contact resistance of rough surfaces.

Let us consider the contact resistance of two cylinders with flat ends contacting each other. In the following analytical model, it is assumed that the asperities on the contact surfaces have ellipsoidal form and are positioned uniformly on the surface. The peak height distributions, asperity curvatures, and their eccentricities with respect to height are described by the expressions.[14,397] The resistance of elementary asperity contact when considering the ellipticity of the contact area can be presented as

$$R_i = \frac{\rho U(m)}{\pi(a+b)}, \quad m = (b-a)/(b+a), \tag{5.24}$$

where $U(m)$ is the elliptic integral of the first kind.

The formulas for calculating the total electrical contact resistance of rough surfaces can be derived using the approach for evaluating the contact thermal conductivity, such as in Tomas.[397] The dependence of the dimensionless contact resistance on normal load N, represented by the parametric function of separation h, is selected as the basic computational equation:

$$R^* = 1 + \frac{2}{l}\alpha^{-\frac{3}{4}}\left(\frac{m_0}{m_2}\right)^{\frac{1}{2}}\overline{R}(h), \tag{5.25}$$

To simplify the calculations and make easier their comparison with the test data for end contact of cylinders of the same material with total length l and contact apparent contact area A_a equal to cylinder cross-section, relative resistance R^* is presented as a ratio of resistance of contacting cylinders R_0+R to the resistance R_0 of the solid cylinder with length l and cross-section equal to appreant contact area A_a:

$$R^* = (R_0 + R)/R_0 \text{ (see further test scheme description).}$$
$$\overline{N} = N/EA_a,$$

where E is the modulus of elasticity; $\alpha = m_0 m_4/m_2^2$ is the bandwidth parameter; m_0, m_2, m_4 are the moments of spectral density of asperity heights (can be obtained with data of surface profile measurements); h is the separation of surfaces. The relative separation of the surfaces h is selected as a common parameter. The dimensionless electrical resistance $\bar{R}(h)$ and load $\bar{N}(h)$ are represented in a form convenient for programming and depend on the roughness parameters and mechanical

properties of the material:

$$\overline{R}(h) = 6\pi\sqrt{3}\left\{\int_h^\infty (\varepsilon - h)^{\frac{1}{2}} p(\varepsilon)\left[\frac{\Re_4(\varepsilon)}{\overline{H}^{\frac{1}{2}}(\varepsilon)} V_1(\xi_1(\varepsilon)) + \frac{\Re_5(\varepsilon)}{\overline{K}^{\frac{1}{4}}(\varepsilon)} V_2(\xi_2(\varepsilon))\right] d\varepsilon\right\}^{-1} \tag{5.26}$$

$$\overline{N}(h) = \frac{1}{6\pi\sqrt{3}} \int_h^\infty (\varepsilon - h) p(\varepsilon)\left[(\alpha m_2^2)^{\frac{1}{4}} \frac{\Re_2(\varepsilon)}{\overline{H}^{\frac{1}{2}}(\varepsilon)} V_1(\xi_1(\varepsilon)) + 2\pi \frac{q_m}{E'} \frac{\Re_3(\varepsilon)}{\overline{K}^{\frac{1}{2}}(\varepsilon)} V_2(\xi_2(\varepsilon))\right] d\varepsilon, \tag{5.27}$$

where $\overline{H}(\varepsilon) = m_4^{1/2} H(\varepsilon)$, $\overline{K}(\varepsilon) = m_4^{-1/4} K(\varepsilon)$; $H(\varepsilon)$ and $K(\varepsilon)$ are the mean and total curvatures of asperities. The expressions for the functions $H(\varepsilon)$ and $K(\varepsilon)$ are presented by Nayak[14] and Konchits et al.[392]

$$\Re_2(\varepsilon) = \frac{2\pi}{3U(e_{el})}\left[\frac{E(e_{el})}{U(e_{el})(1-e_{el}^2)}\right]^{1/2}$$

$$\Re_3(\varepsilon) = \left\{1 + U(e_{pl})\frac{q_m}{E}\left(\frac{1}{R_z\sqrt{m_4}}\right)^{1/2}\left[\frac{2\bar{H}_1(\varepsilon)}{\bar{K}(\varepsilon)}\right]^{1/2}\right\}^{-1}$$

$$\Re_4(\varepsilon) = \frac{\pi\sqrt{2}\left(1 + \sqrt{1-e_{pl}^2}\right)}{U(m)}\left[\frac{E(e_{el})}{U(e_{el})(1-e_{el}^2)}\right]^{1/2}$$

$$\Re_5(\varepsilon) = \frac{\pi\sqrt{2}\left(1 + \sqrt{1-e_{pl}^2}\right)}{U(m)}.$$

$E(x)$ is the elliptic integral of second kind; $V_1(\xi) = 0$ if contact is plastic and $\xi = \varepsilon - h > 0$; $V_2(\xi) = 0$ if contact is elastic and $\xi = \varepsilon - h < 0$; otherwise they are equal to unity; e_{el}, e_{pl} are eccentricities of contact spot at elastic and plastic contacts, E is the modulus of elasticity, q_m is the contact stress relating to onset of plasticity equal to HB/3 for metals where HB is the the Brinell hardness.

Using criteria for transition to plastic deformation,[17] Equation 5.26 and Equation 5.27 become suitable for calculating the elastic–plastic contact. The numerical integration is performed by the cubic spline method. The calculation results show that roughness exerts stronger influence on the contact conductivity (Figure 5.23a) for elastic contact than for plastic contact (Figure 5.23b). The effect of hardness of the contacting material is more significant in the case of plastic contact (Figure 5.23b). Thus, the calculation technique using the random field method is very sensitive to the mode of contact deformation, the hardness of the mated surfaces, and the roughness characteristics. Experimental technique: the silver cylinders of diameter 3 mm and height 10 mm, mounted in isolating holders were used as the contacting members. The end surfaces of the specimens were machined to the required roughness in the holders to ensure their planarity. The roughness characteristics and the distribution of statistical moments were determined with a computerized profilometer. The magnitudes of the parameters are shown in Table 5.7, which also shows the specimen microhardness as determined by indenting the surface with a diamond pyramid with tip angle 136°. The pyramid loads made it possible to limit the indentation depth to 10 μm. The effect of annealing, polishing, and work hardening of the test specimens was also evaluated. In the experiments the average roughness of one of the specimens was approximately an order of magnitude smaller than that of the other so that the less rough surface could be considered as ideally smooth. Figure 5.24 shows the experimental setup.

The load was transmitted through the ball to the specimen holders that were connected to the measurement circuit. The contact resistance was measured using the four-probe measuring arrangement shown in Figure 5.25 and was calculated from the voltage drop between measuring probes by applying the stabilized current of $I_1 = 0.1$ A. The 100-Ω resistor R_L eliminated current oscillations in the circuit. The voltage drop U between the probes was compensated by the counter-emf E of the opposite sign produced by compensation potentiometer and the measurements were made with current $I_2 = 0$ in the measuring circuit. Contact voltage drop value in this case was equal to counter emf value.

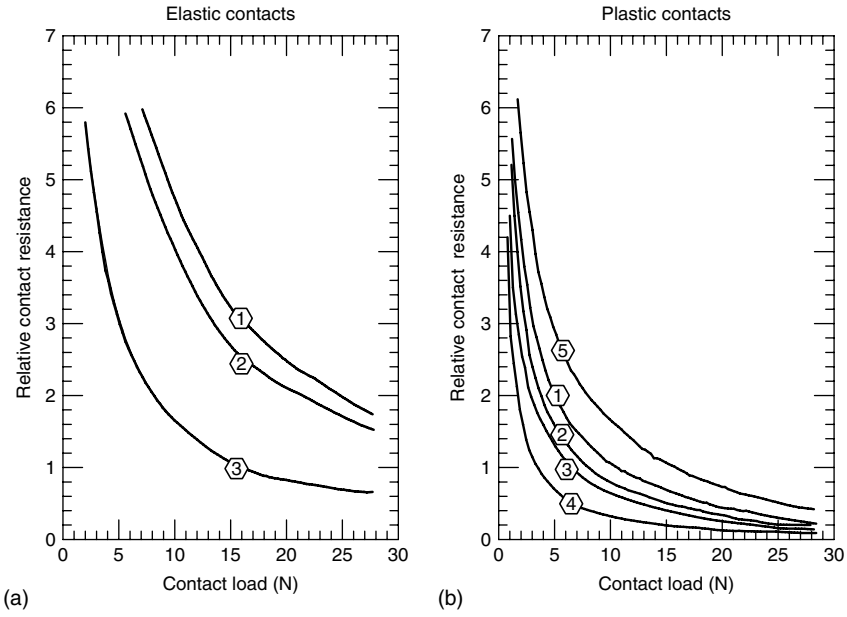

FIGURE 5.23 Calculated relative contact resistance R^* dependence on load for elastic (a) and plastic (b) contacts. The numerals on the curves correspond to the specimen numbers in Table 5.7.

The resistances of the wires and connectors in the measuring circuit did not introduce any error into the experimental results as the current in the measuring circuit was equal zero. The accuracy of measurement circuit was tested by measuring the resistance R_0 of a solid silver cylinder having the same cross-section area A_a as the silver test specimens and length l equal to the distance between the potential probes of measurement circuit. The resistivity of a solid cylinder $\rho = R_0 A_a/l$ calculated with the test data agreed well with the tabulated value for pure silver. This agreement suggests the adequate accuracy of measurements. To increase the accuracy, the data on contact resistance were presented in dimensionless form excluding resistivity and apparent contact area of the specimens. The measurement of resistance of two silver cylinders with total length l, including the contact of end surfaces, gives the

TABLE 5.7
Surface-Roughness Parameters and Mechanical Characteristics of Silver Specimens

Specimen Number	R_a (μm)	R_z (μm)	m_0 (μm^2)	m_2	m_4 (μm^{-4})	α	q_m (MPa)	Specimen Preparation
1	1.5	6.7	3.7	0.023	9.7×10^{-4}	6.8	800	Polishing with abrasive paper
2	1.3	5.9	2.7	0.023	9.2×10^{-4}	4.7	800	The same
3	0.4	2.0	0.29	0.0013	6.1×10^{-5}	10.5	500	Annealing at 973 K in vacuum, polishing with felt and one loading cycle
4	1.5	6.7	3.7	0.023	9.7×10^{-4}	6.8	250	—*
5	1.5	6.7	3.7	0.023	9.7×10^{-4}	6.8	1000	—*
6	1.3	5.9	2.7	0.023	9.2×10^{-4}	4.7	1000	Polishing with abrasive paper and 10 loading cycles

**Note*: For specimens 4 and 5 the calculation was made only for the smallest and largest hardness values.

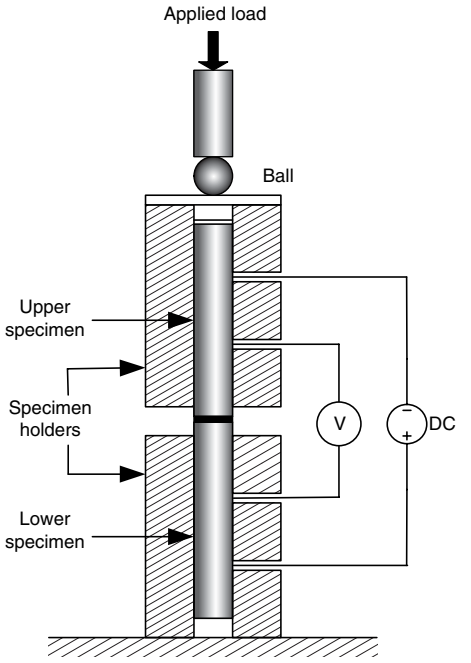

FIGURE 5.24 Schematic of specimen contact assembly for the contact electrical resistance measurement.

value $R_0 + R$, where R is contact resistance. Relating this value to the resistance of the solid cylinder of the same length gives the dimensionless resistance R^*.

$$R^* \cong \frac{R_0 + R}{R_0} = 1 + R/R_0 \tag{5.28}$$

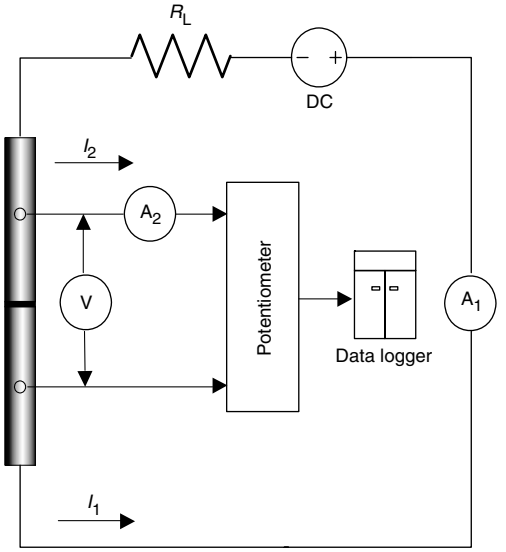

FIGURE 5.25 Electrical schematic of measurements: R_L, load resistance; U, contact voltage drop; I_1, I_2, currents in power, and measurement circuits; A_1 and A_2, ampermeters in power and measurement circuits.

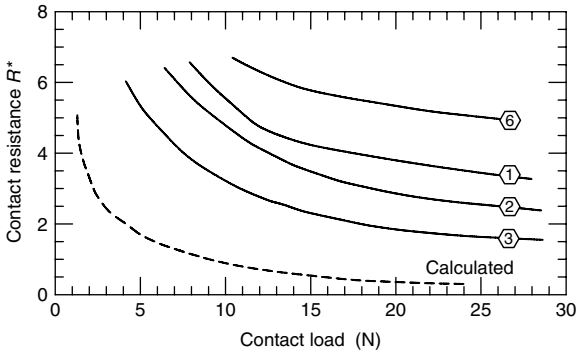

FIGURE 5.26 Experimental contact resistance data and calculation results (dashed line) for silver specimen no. 3. Numerals on the curves correspond to specimen numbers in Table 5.7.

The measurements were made as follows: the applied load to the specimens was successively increased and for each applied load, the corresponding resistances were recorded. This process was followed by a gradual reduction of applied load and continuous measurement of the resistance. Subsequently, one of the specimens was rotated around the axis of load application to generate new contacting areas. Each series of measurements was repeated 15–20 times to ensure the reproducibility of the experimental results and the measurement error was less than 10%. The results of the experiments carried out on silver specimens are shown in Figure 5.26.

Analysis of the theoretical and experimental results obtained for the contact resistance-load dependence allowed identification of the basic factors influencing the contact resistance, such as the deformation mode, specimen pretreatment history, number of loading cycles, surface roughness characteristics, and the effect of nonconductive films.

The least square method was used to conduct a detailed qualitative analysis of the calculated and test data. The most adequate approximating expression was found to be a power function of the form

$$R^* = c\overline{N}^{-d}, \tag{5.29}$$

where c is the auxiliary coefficient and d is the power-function factor.

In case of elastic contact when both the contact-spot area and the number of spots are increasing rapidly with load it is common to accept d to be equal to approximately 2/3.[24] In case of plastic contact when the number of spots is practically not increasing and the area of contact grows mostly due to increase in the contact-spot size d is supposed to be close to 0.5.[23,24]

Analysis of the data of Table 5.8 shows that within the test range of loads for the specimens with a lesser degree of work-hardening (specimen 3), the contact deformation is nearly purely plastic,

TABLE 5.8
Power Factor *d* in the Function Approximating the Calculated and Test Data (Load Range 1–30 N, Correlation Coefficients > 0.95)

Specimen Number	*d*		Contact Mode in Calculation Scheme
	Calculation	Experiment	
1	0.50	0.53	Plastic
2	0.46	0.43	Plastic
3	0.46	0.46	Plastic
6	0.72	0.59	Elastic
	0.46		Plastic

whereas after many work hardening cycles the mode of deformation becomes mixed. For example, in the case of specimen 6, neither purely elastic nor plastic solutions could provide a better agreement between the test and calculated contact resistance data.

Figure 5.26 shows the calculated and test data comparison. Although the contact resistance varies with load in the same manner, the calculated values are substantially lower. Since the hardness of the specimens was taken into account in the calculation and the experiments were done with noble metal, thus excluding the effect of nonconductive films,[23] it is believed that nonuniform distribution of the *a*-spots and their mutual interaction may be responsible for the observed difference.

Another set of test specimens with a much larger apparent contact area made of copper was prepared to make additional experiments clarifying the effect of contact spots on the resistance. After taking into account the effect of films on copper, it was determined to employ special lubricants to remove the films.

The specimens were made of M1 copper (purity: 99.9%Cu) in the form of cylinders with 20 mm diameter and 15 mm height. The end contact surfaces were ground in a special adjustment to provide necessary flatness. Then one of the cylinders was abraded to a certain roughness. The other one was polished to provide two orders of magnitude difference in roughness when one of the specimens can be considered as ideally smooth. Description of the specimens is given in the Table 5.9. The specimens were tested with the same measuring circuit as silver ones, excepting that the loading was made by hydraulic press in the range necessary to provide the same contact stresses as in case of silver cylinders. Dimensionless resistance R^* was found as a function of dimensionless load $N/A_a q_m$. The specimens were treated by solvents and gloss discharge to remove contaminants. Preliminary oxidation to model oxide films was performed at $T = 473$ K during 5 h. Glycerin was used to affect the oxide films as a surface-active agent with specific action to copper oxide (see also Chapter 9, Section 9.3).

The data on the test dependence of dimensionless resistance on dimensionless load in log scale are presented in Figure 5.27 as well as calculation data for copper specimens without account of the contact-spots' array. It is seen that the test dependencies are placed much higher than the calculated ones, especially for oxidized specimens. Application of glycerin moves the dependencies down both for specimens with and without preliminary oxidation, but still the difference between test and calculation is great as in the case of silver specimens.

The natural conclusion from the tests is that the effect of contact-spots' array on the total resistance should be studied more rigorously. To take account of this effect the calculation scheme given above was modified as follows:

TABLE 5.9
Characteristics of Copper Specimens

Specimen Number	R_a (μm)	R_z (μm)	α	q_m (MPa)	Samples Preparation
1	0.82	5	12	1200	Fine turning, end grinding, treatment by emery paper, cleaning by solvent and gloss charge in low vacuum
2	0.51	3	6	1600	Id.
3	0.08	0.2	2	1200	Id. with polishing before cleaning
4	0.51	0.2	2	1200	Id. as for specimen 2 with further oxidation
5	0.08	0.2	2	1200	Id. as for specimen 3 with further oxidation

Note: Specimen 3 was used as a counterbody in all the tests.

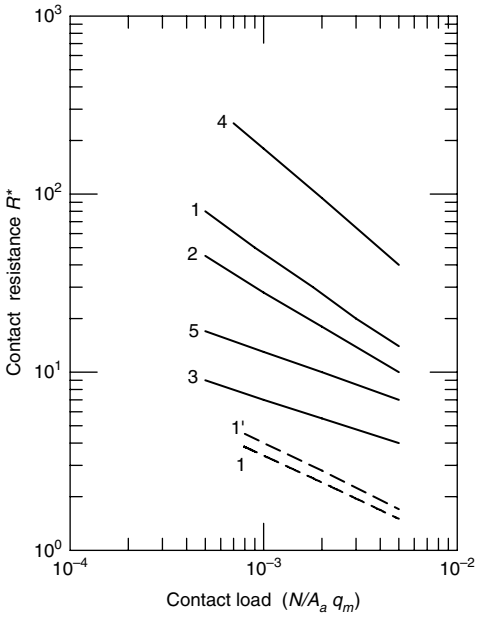

FIGURE 5.27 Contact resistance of copper specimens in load range of 20–2000 H. Solid line: test data; dashed line: calculation results without account of contact-spots array. Numerals on the curves correspond to specimen numbers in Table 5.9. Lines 3 and 5 correspond to contact lubricated with glycerin.

- Clusters are assumed to be placed on the surface waviness simulated by spherical segments deformed elastically.
- Elementary contact spots are arranged in the boundaries of clusters and assumed to be deformed plastically.

The full scheme of calculations is given elsewhere[392] so the simplified one is given below. The radius of cluster can be determined as a radius of Hertzian contact as:

$$a_c = \left(\frac{rR_w N}{4n_c E}\right)^{1/3}, \tag{5.30}$$

where R_w is a wave radius and n_c is a number of waves in the apparent contact area that can be obtained easily with the profile measurement data.

This value gives possibility to obtain the second term in the Equation 5.21. The third term in Equation 5.21 is obtained using the radius of apparent contact area. Finally, the total resistance of the contact with an array of spots combined in clusters as a function of normal load can be written as:

$$R_c = (\rho/\pi n_c {n_c}^{1/3})(4E'/p_a A_a R_w)^{1/3}\left[(4E'/3p_a A_a R_w)^{1/3}\alpha^{-3/4}(m_0/m_2)^{1/2}\bar{R}_{\bar{p}_c} + 16/3\pi {n_c}^{1/3}\right] + 16\rho/3\pi^2 r, \tag{5.31}$$

where,

$$\bar{p}_c = \frac{1}{\pi}\left(\frac{4}{3n_c R_w}\right)^{1/3}\left(\frac{4p_a A_a}{3E'R_w}\right)^{1/3}.$$

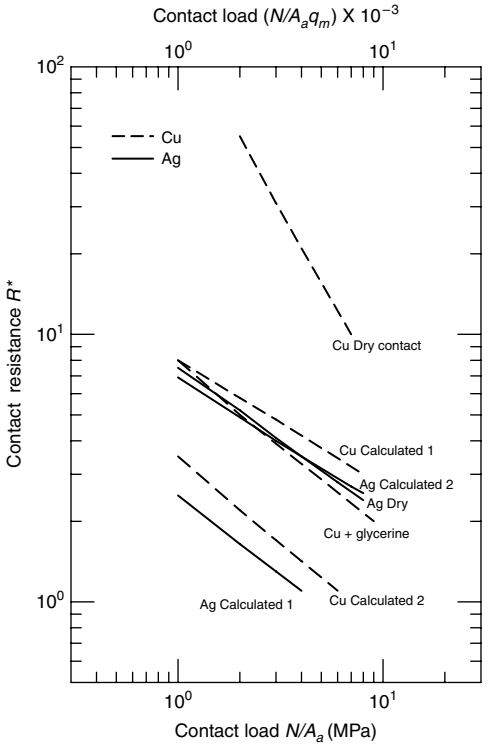

FIGURE 5.28 Data of experimental determination of the contact resistance of specimens of silver (solid lines) and copper (dashed lines) in comparison with the results of calculation (1) without and (2) with accounting for the distribution of the contact spots in the contact area.

Comparison of the calculation and test data is given in Figure 5.28.

It is evident that a good correlation of calculation and test data is present in the case of silver specimens when the distribution of contact spots is taken into account in the range of contact pressures of 0.1–10 MPa. In the case of copper specimens contacted without lubricant, the difference between test and calculation is still significant, but application of glycerin makes this difference much less due to removal of the oxide film on copper.

The application of random field theory to the calculation of contact resistance of rough surfaces looks promising because it can provide the opportunity to take account the arrangement of elementary contact spots in the real area of contact. This gives the opportunity to obtain a good agreement (10–15% difference) between the calculation and test data on contact resistance for noble metal (silver) in the range of contact pressures of 0.1–10 MPa. In the case of oxidized metal (copper), the calculation accuracy also looks reasonable (difference less than 30%) in the same range of contact pressure.

The effect of contact-spots' distribution on the contact resistance dependence on pressure is presented in Figure 5.29, where three terms of Equation 5.21 are presented as functions of contact pressure. The effect of elementary spots' arrangement is quite significant at contact pressure of 0.1 MPa and becomes dominant above 0.5 MPa.

There are some conclusions when resuming the issue of rough contact resistance: (1) the calculation of contact resistance account is taken of elementary contact spots appears feasible when using the random field theory of surface roughness and contact-area calculations substantiated

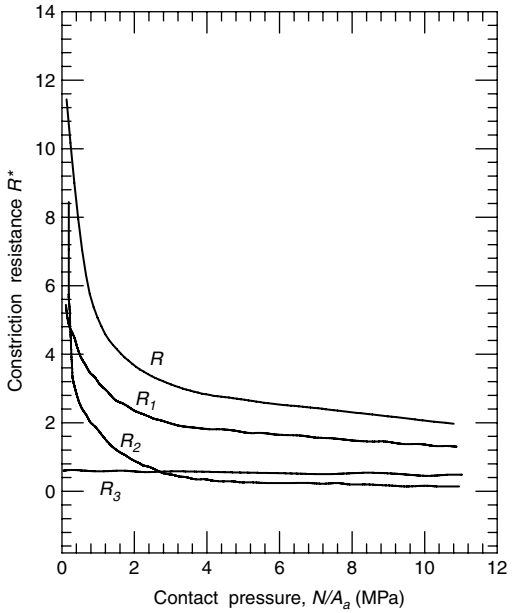

FIGURE 5.29 Calculated dependence of total constriction resistance and its components on the contact pressure.

by this theory; (2) common engineering presentation of rough surface as a combination of waviness and roughness can be easily used in random field calculation techniques, even if the mechanism of surface deformation needs special consideration; (3) the presence of nanoscale elementary spots in the contact of rough surfaces, which is confirmed by AFM data, gives grounds to consider the general contact problem as a multilevel system of conductivity channels with the mechanism of resistance described by such nonlinear effects as Sharvin's and frequency, as well as tunnel conductivity of surface films; (4) all of the above-mentioned considerations give a basis for more extensive research in contact resistance problems if consideration is given to the scale factor (macro-to-nano bridge), frequency effect comprising the impedance of the contact, and quantum effects; and (5) further progress in the miniaturization of contacts, the decreasing of current value, and the increasing of frequency requires further intensive research in the area of the interface phenomena and surface engineering to meet the needs of high-tech electrical engineering.

5.2 INTERFACIAL HEATING

The common feature of all electrical and electronic devices is the passage of current combined with heating. Sliding contacts of heavy-current electrical devices commute currents reaching 10^6 A. High current densities in sliding contacts deform contact elements, alter the friction coefficient, intensify wear, and damage the rubbing surfaces. This may be the result of single or combined effects of various phenomena.[1,392,400–405] Current-induced temperature rise due to generation of the Joule heat in the contact zone is, however, the most common and evident factor that is frequently used to explain the adverse influence of current on friction behavior of contacts.[401–404] Numerous studies on the temperature behavior in electrical contacts were undertaken and described in the literature.[1,234,400–405] In the case of static contacts, however, a number of processes such as creep, stress relaxation, and fretting, are found to exert a strong effect on their performances. This topic is covered in Chapter 6.

These problems are also important when electric current is used to heat the contact.[405–408] Temperature in the contact zone is experimentally determined by measuring the potential drop across the contact (for noble metals),[1,406] or the Joule heat and the contact area.[391,403,407] This method is convenient to investigate surface-layers' response to heating,[406,408] and to estimate temperature stability of the base material[403] or boundary layers, including lubricating films.[392] It can be a useful research tool to model steady and unsteady conditions in the contact spots, which is otherwise difficult to achieve in friction tests. The effectiveness of the method depends strongly upon the possibility of analyzing temperature fields in the vicinity of the contact, which possess sharp gradients both in axial and radial directions when the current passes through even a pure metallic spot.[1] Distortion of the current line arising from heterogeneity of surface films or their breakdown can impede the analysis.

Sliding friction is an additional and important source of heat in electrical contact since friction is a typical dissipative process in which mechanical energy is converted into heat (up to 90–95% according to the available experimental data). The thermal state of friction contact is frequently a decisive factor when evaluating the performance of a friction unit. Determination of temperature fields generated by friction is an independent area of tribology which was pioneered by Blok.[409]

It is commonly believed that heat generation during friction results from deformation of material in the real contact spots. In connection with this, some processes can be related to the transformation of mechanical energy into heat, namely, plastic deformation, hysteresis, dispersion, and viscous flow. The last process is the most typical for hydrodynamic lubrication being in fact a single source of heat.

Another source of heat can be attributed to the processes originating from the destruction of adhesive bonds. These processes are most probably nonequivalent energetically since the energy difference may generate (and in specific situations absorb) heat. Once heat appears in the friction zone, it is distributed between rubbing bodies and the environment. This heat exchange evolves through the heat conduction, convection, and/or radiation. Heat conduction occupies an important place in the triad governing the appearance of the thermal state of rubbing parts.

5.2.1 Principles of Heat Conduction Theory

Heat generated by friction transfers from one part of body to another or from one body to another. Surfaces (lines), each characterized by their own constant temperature, may be identified in the body in which heat propagation occurs; this is termed *isothermal surfaces (lines)*. A combination of the surfaces at any moment of time yields the temperature distribution in the body, i.e., its *temperature field*. Its determination is the basic problem of heat conduction theory. Because two different temperatures cannot exist at a fixed moment of time at the same point, two isothermal surfaces with different temperatures cannot intersect (Figure 5.30).

Heat cannot propagate along the isothermal surfaces, the shortest path being along the normal to the isothermal surface where the temperature drop is maximum. This temperature rise per unit of displacement in the direction of increasing temperature is termed the *temperature gradient* or the *gradient of the temperature field* at a given point. The temperature gradient is a vector defined as a directional derivative of the temperature function $T = T(x,y,z,t)$ with respect to the normal, n:

$$\text{grad } T = n\, \mathrm{d}t/\mathrm{d}n.$$

If the gradient differs from zero, heat transfer should, by necessity, take place; it proceeds in the direction opposite to the gradient. *Heat flow* is the measure of heat transfer defined as an amount of heat per unit of time in the direction of decreasing temperature. Its dimensionality is W or J/s. The heat flow q per unit of section area perpendicular to the flow direction is termed the *specific*

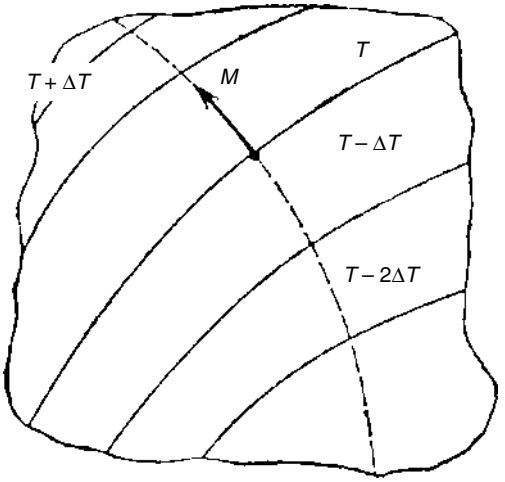

FIGURE 5.30 Isothermic lines of two-dimensional temperature field.

heat flow (W/m^2 or J/(m^2 s)). Numerous experiments have shown that there is a direct proportionality between the specific heat flow and the temperature gradient (Fourier law):

$$q = -\lambda \operatorname{grad} T. \tag{5.32a}$$

The minus sign indicates that the heat flow and temperature gradient are opposite in direction, as noted above. The proportionality factor, λ, is termed the *thermal conductivity* of a material. Numerically, it is equal to the amount of heat passing through a unit of area of the isothermal surface per unit of time at a temperature gradient equal to unity. Its dimensionality is W/(m K).

Thermoinertial properties of material are characterized by the heat diffusivity, which determines the rate of temperature equalization during nonstationary heat conduction. It is numerically equal to the ratio between the thermal conductivity and the specific volumetric heat capacity: $a = \lambda/c\rho$ [m^2/s], where c is the specific heat capacity, and ρ is the density of a material.

The temperature field in a solid is determined by solving a differential equation of heat conduction; its derivation is based on the Fourier law (Equation 5.32a) and on the analysis of the heat balance in an elementary volume of the body in which heat is conducted.

A three-dimensional nonstationary temperature field $T = T(x,y,z,t)$ in Cartesian coordinates is described by a differential equation of the following type:

$$\frac{\mathrm{d}T}{\mathrm{d}t} = a\left(\frac{\mathrm{d}^2T}{\mathrm{d}x^2} + \frac{\mathrm{d}^2T}{\mathrm{d}y^2} + \frac{\mathrm{d}^2T}{\mathrm{d}z^2}\right). \tag{5.32b}$$

Its deduction and a discussion of the methods for its solution are analyzed in a variety of monographs on the theory of heat conduction. Tribological problems are frequently limited to the analysis of the one-dimensional heat flow, $T = T(x,t)$, for which the equation of heat conduction reduces to:

$$\frac{\mathrm{d}T}{\mathrm{d}t} = a\frac{\mathrm{d}^2T}{\mathrm{d}x^2}. \tag{5.33}$$

In cylindrical coordinates (r, φ, z) linked with the Cartesian coordinates by the relations $x = r\cos\varphi$, $y = r\sin\varphi$, $z = z$ $(0 \le r < \infty, 0 \le \varphi < 2\pi, -\infty < z < \infty)$, the equation becomes:

$$\frac{dT}{dt} = a\left(\frac{d^2T}{dr^2} + \frac{1}{r}\frac{dT}{dr} + \frac{1}{r^2}\frac{d^2T}{d\varphi^2} + \frac{d^2T}{d\varphi^2}\right). \tag{5.34}$$

If the body contains a heat source with efficiency Φ (the amount of heat generated or absorbed per unit of time by a unit of volume), the term $\Phi/c\rho$ should be added to the right-hand side of the heat equation. If the stationary temperature field is to be determined, the left-hand side of the heat equation vanishes.

To solve the equation of heat conduction, some initial and boundary conditions should be specified. In particular, the temperature distribution in the body at the initial moment of time should be known. Usually, a uniform temperature distribution is assumed: $T(x, y, z, 0) = T_0 = \text{constant}$. Also, one of the following boundary conditions that governs the heat exchange between the surface and the environment is specified. The temperature distribution over the surface (the condition of the first kind) or the heat flow through it (the condition of the second kind) is given. The heat exchange is assumed to be known, most often in the form of the Newton law (the condition of the third kind).

Finally, in the case of contact between solids, or between a solid and liquid, it is assumed that there is no temperature jump at the interface, i.e., the temperatures of the contacting surfaces are equal (the condition of the fourth kind). In tribology, heat is generated at the interface and thereby the condition that heat flow due to friction should be equal to the sum of the flows into each of contacting bodies should be added.

5.2.2 Simple Problems of Heat Conduction Theory

Some simple problems of heat conduction will be discussed[409–412] that are used for the description of heating electrical contact. First, consider how a point heat source acts on a half-space. This source is an analog of the concentrated force for the elastic half-space in the sense that the temperature field induced by the source distributed over the surface and in time can be determined by the summation of the solutions for point sources. Such solutions present not only theoretical interest, but practical interest as well. Individual asperities are known to be in contact over very small spots and during very short intervals of time, i.e., the spots may be treated as point sources. This fact allows estimation of the temperature fields outside the contact spot and for the time exceeding the contact time of asperities using comparatively simple formulas (discussed below) for point sources.

An instantaneous point source (Figure 5.31) is an idealization relating to the following situation: let a finite amount of heat, Q, be liberated over a small (practically zero) area on the surface of a half-

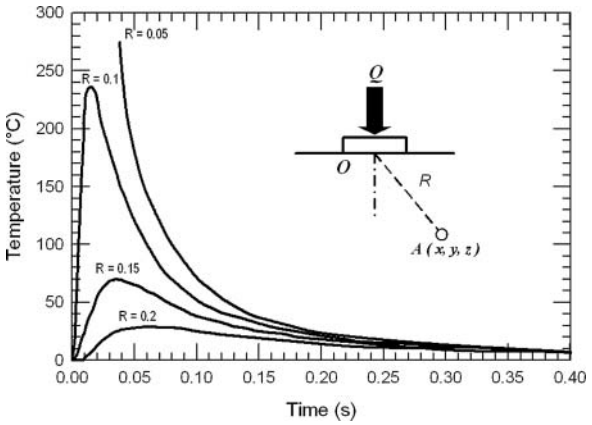

FIGURE 5.31 Instantaneous point source.

space with a constant initial surface temperature, T_0, at some time, assumed as the initial $t = 0$. The temperature field of the half-space is then described by the following equation:

$$T = \frac{Q}{4\rho c(\pi a t)^{3/2}} \exp\left(-\frac{R^2}{4at}\right), \tag{5.35}$$

where R is the distance between the point in question and the origin of coordinates where the source acts.

The solution to Equation 5.35 can be found in practically any manual on the theory of heat conduction. It shows that the temperature at any point of the body increases from zero to the maximum that is reached at a moment of time $t = R^2/6a$, and then diminishes to zero (Figure 5.31). *Continuous point source* (Figure 5.32) simulates a situation when heat at some point is generated with the rate q. If this rate is constant, then $dQ = q\Delta t$ is the heat generated within a short interval of time $(t, t+\Delta t)$ at a point O. According to Equation 5.35, this heat induces the temperature rise:

$$\Delta T = \frac{q\Delta t}{4\rho c(\pi a t)^{3/2}} \exp\left(-\frac{R^2}{4at}\right).$$

Integration of the latter relation yields the temperature field in the half-space (Figure 5.32):

$$T = \frac{q}{2\pi\lambda R} \operatorname{erfc}\left(\frac{R}{\sqrt{4at}}\right), \tag{5.36}$$

where $\operatorname{erfc}(\chi) = 1 - 2/\sqrt{\pi}\int_0^{\chi} e^{-\xi^2} d\xi$ is the complimentary error function. Equation 5.36 shows that at $t \geqq R^2/4a$, a steady state develops with a temperature $T = q/2\pi\lambda R$ near the source.

Continuous moving point source (Figure 5.33): let a point source with the heat rate q move with a speed v over the boundary of the half-space along the x-axis (Figure 5.33a).

The temperature at an arbitrary point $A(x,y,z)$ of the half-space is estimated in the moving coordinates linked with the sources, which in the fixed coordinates (x',y',z') at some moment of time t' locates at a point $B(vt, 0, 0)$. During a short interval of time, dt', it generates $dQ = q\,dt'$ of heat, which after an interval of time $t - t'$ (i.e., at the moment t) causes the temperature to rise at the point A that was determined by Equation 5.35:

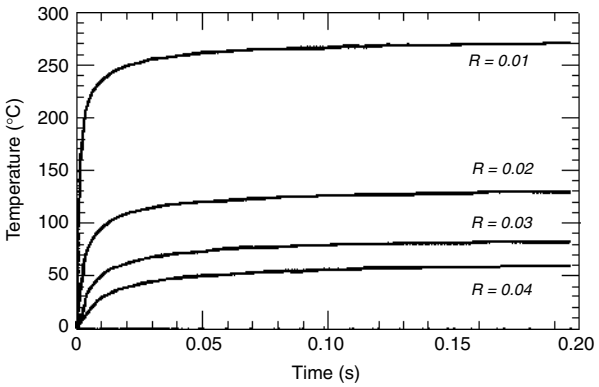

FIGURE 5.32 Continuous point source.

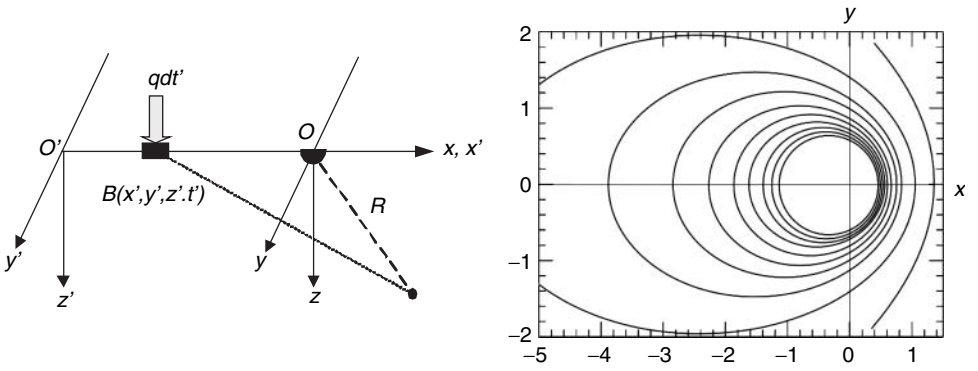

FIGURE 5.33 Continuous moving point source: (a) geometry of contact; (b) temperature field.

$$\Delta T(x', y', z', t) = \frac{q\Delta t'}{4\rho c(\pi a(t-t'))^{3/2}} \exp\left(-\frac{R'^2}{4a(t-t')}\right),$$

where $R'^2 = ((x' - vt')^2 + y^2 + z^2)^{1/2}$. Summation over all intervals of time from 0 to t, transition to the moving coordinates, and integration yield:

$$T = \frac{q}{4\rho c(\pi a)^{3/2}} \int_0^t \exp\left[-\frac{(x'-vt')^2 + y'^2 + z'^2}{4a(t-t')}\right] \frac{\mathrm{d}t'}{(t-t')^{3/2}}$$

$$= \frac{q}{4\pi\lambda R} \exp\left(-\frac{vx}{2a}\right) \left[\exp\left(\frac{Rv}{2a}\right) \operatorname{erfc}\left(\frac{R}{\sqrt{4at}} + \frac{v\sqrt{t}}{\sqrt{4a}}\right) + \exp\left(-\frac{Rv}{2a}\right) \operatorname{erfc}\left(\frac{R}{\sqrt{4at}} - \frac{v\sqrt{t}}{\sqrt{4a}}\right)\right]. \tag{5.37}$$

where $R^2 = (x^2 + y^2 + z^2)^{1/2}$.

When $t \to \infty$, a quasistationary temperature field is reached that is produced by the moving point source:

$$T = \frac{q}{2\pi\lambda R} \exp\left[-\frac{v}{2a}(x + R)\right]. \tag{5.38}$$

This formula indicates that the temperature distribution over the surface of the half-space has the pattern shown in Figure 5.33b. The isotherms typically become denser ahead of the source (i.e., a higher gradient is observed), then they become less dense behind the source.

Distributed heat source: Heat during friction is usually generated over areas with finite dimensions. The temperature field of the body during its heating is determined by the superposition of the solutions for point sources. Thus, for a rectangular source $2b \times 2l$ acting on the surface of the half-space and moving along the x-axis with a speed v, it is obtained that

$$\tilde{T} = \frac{1}{4\sqrt{\pi}} \int_0^{2\sqrt{Fo}} \exp\left(-\frac{\bar{z}^2}{u^2}\right) \left[\operatorname{erf}\left(\frac{\bar{y} + \bar{b}}{u}\right) - \operatorname{erf}\left(\frac{\bar{y} - \bar{b}}{u}\right)\right]$$

$$\times \left[\operatorname{erf}\left(\frac{\bar{x} + 1}{u} + \frac{1}{2}uPe\right) - \operatorname{erf}\left(\frac{\bar{x} - 1}{u} + \frac{1}{2}uPe\right)\right] \mathrm{d}u \tag{5.39}$$

where $\tilde{T} = T/(ql/\lambda)$, $Pe = vl/(2a)$, $Fo = at/l^2$; the bar over symbols designates that the value is normalized by a typical dimension.

The mean surface temperature over the area of the source is determined from the formula

$$\tilde{T}_{\mathrm{m}} = \frac{1}{4\bar{b}} \int_{-\bar{b}}^{\bar{b}} \int_{-1}^{1} \tilde{T}(z=0)\mathrm{d}y\mathrm{d}x.$$

For low sliding velocities, the maximum and mean steady-state temperatures are calculated by the formulas:

$$\tilde{T}_{\max} = 1.122; \quad \tilde{T}_{\mathrm{m}} = 0.946.$$

The case of high velocities is discussed below. Figure 5.34 shows the distribution of the nondimensional surface temperature in the plane of a square source as a function of sliding velocity.

The distribution was calculated by Equation 5.39 with different velocities (Peclet *numbers*). For low velocities, the temperature is distributed almost symmetrically with maximum in the vicinity of the center of contact. As the sliding velocity increases, the maximum shifts in the direction opposite to sliding, and it occurs at the outlet from contact at high velocities.

Another important conclusion made by Jaeger[413] concerns the effect of the heat-source shape on the mean surface temperature. The curves in Figure 5.35 show that the mean surface temperatures generated by the square and rectangular sources are in close agreement for great Peclet numbers. The source shape can vary more essentially, e.g., for simplicity of calculation, if the circular source is widely replaced with a square one.

Thus far, it has been assumed that heat is supplied at a steady rate. Yet, in real situations, this is not the case. Jaeger's calculation has shown that the surface temperature distributions for different heat rates are somewhat different in shape, but their mean and maximum temperatures are very close in magnitude. This fact allows the above equations to be used for the sources with a nonconstant but sufficiently smooth rate.

The presence of a *line heat source* implies that heat with rate q is liberated on the surface of a half-space along the y-axis. Practically the source acts over a strip of width $2l$. The strip is taken to move with velocity v in the plane $z = 0$ along the normal to the strip. Such a situation takes place when bodies are in initial line contact, e.g., contact of spur gears.

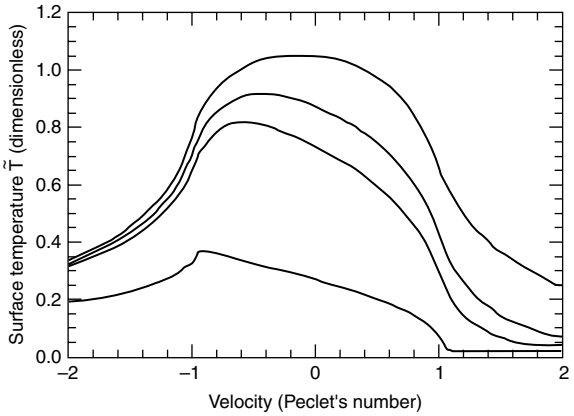

FIGURE 5.34 Effect of velocity (Peclet's number) of square source on the surface temperature distribution.

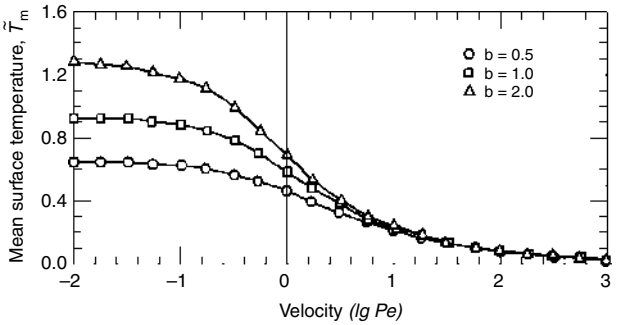

FIGURE 5.35 The mean surface temperature as a function of velocity (Peclet number).

The nondimensional temperature of the half-space over which the strip moves is calculated by:

$$\tilde{T} = \frac{1}{2\sqrt{\pi}} \int_0^{2\sqrt{Fo}} \exp\left(-\frac{\bar{z}^2}{u^2}\right) \times \left[\operatorname{erf}\left(\frac{1+\bar{x}}{u} - \frac{1}{2}uPe\right) + \operatorname{erf}\left(\frac{1-\bar{x}}{u} + \frac{1}{2}uPe\right)\right] du. \tag{5.40}$$

This equation is appropriate for calculating the subsurface temperatures. Such calculations demonstrate that heat propagates into the half-space to a small depth. Because of this, the significant temperature gradient appears across the surface layer and, as a result, the layer can undergo the great thermal stresses affecting its physical–mechanical properties.

If the strip moves over a long period of time ($t \to \infty$), the steady-state temperature is calculated by Equation 5.40, with an infinite upper limit. As in the case of the rectangular heat source, the temperature distribution depends on velocity (Peclet number) and varies from nearly symmetrical with maximum in the center of the strip for small Peclet numbers to asymmetrical. Given this variance, the maximum shifts into the direction opposite to the sliding one, and for the great Peclet numbers it appears on the rear boundary of the source.

As was shown by Jaeger[413] for steady-state temperatures, the maximum temperature is approximated by the equation:

$$\tilde{T}_{\max} = \begin{cases} \dfrac{2}{\sqrt{\pi}} Pe^{-3/2}, & Pe > 5 \\ \dfrac{2}{\pi}(-\ln Pe + 1.116), & Pe < 0.1 \end{cases} \tag{5.41}$$

The following approximate equation is valid for the mean temperature:

$$\tilde{T}_{\mathrm{m}} = \begin{cases} \dfrac{1.064}{\sqrt{Pe}}, & Pe > 5 \\ \dfrac{2}{\pi}(-\ln Pe + 0.923), & Pe < 0.1 \end{cases} \tag{5.42}$$

Here, it should be noted that for high Peclet numbers, the maximum and mean temperatures initiated by the square source are close to those initiated by the linear source and they can be calculated by Equation 5.41 and Equation 5.42.

Finally, it should be recognized that the present literature gives rigorous solutions to problems for heat sources with different shapes, including circular and elliptic ones, and with different profiles of heat flows over the contact spot, as well as with heat exchange with the environment. In addition, modern software allows one to solve the heat problems with very complicated boundary conditions. Here, a compromise should be made between the labor hours expended for the solution and the utility of greater accuracy.

5.2.3 Contact Spots Heated by Electrical Current

The features of thermal effects induced by electric current in contact spots are described in Konchits et al.[388] In this section, the emphasis, however, is placed on analytical and experimental study of simulating the heat conditions in the contact zone by electric current. It can be shown that the method of local heating of the contact zone by electric current can be effective only when the surface films are absent or homogeneous conductive films are present. Experimental studies of the passage of heavy currents through the contacts with oxide films and the formation of conductive channel (bridge) even in extremely thin films were carried out. It was shown that this leads to localisation of the Joule heat predominantly in the vicinity of the formed bridge, which excludes regular heating of the contact area.

5.2.3.1 Film-Free Metal Contact

The mechanism of current passage through metallic contacts without contaminating films and their heating have been investigated by Holm.[1] The contact resistance, R_c, in this case is determined by constriction resistance, R_s, arising from the geometrical effect of current lines' constriction from the specimen bulk to the spot. The current density varies over the contact-spot surface, increasing towards its periphery. Heat is generated in a small region (constriction region) adjacent to the spot with temperature peak Q_m at the interface. Because of the negligible mass of the heated metal volume in the constriction region, a rapid overheating leap (10^{-5}–10^{-3} s, as reported by Hilgarth[414]) occurs there.

The temperature rise at the interface is calculated using Kohlraush's equation:[364]

$$U_c^2 = 8\int_{T_0}^{T_m} z(T)\rho(T)\,dT, \tag{5.43}$$

where the integral is taken over the thermal gradient between the isothermal surfaces at which T_0 is measured and T_m in the contact-spot plane, and where the dependence of all thermophysical properties are taken into account. Kohlraush's equation is based on the classical contact theory with the assumption of thermally isolated boundaries when the Joule heat dissipates only in the conducting medium (contact of conductors) by diffusion into colder parts. Heat dissipation into boundary (electrically nonconductive) regions is ignored.

Different expressions for contact temperature have been derived and are presented in Table 5.10. Equation 5.44 has an apparently limited application and is suitable for approximate calculations only. Application of Equation 5.45 for metals meeting the Viedemann–Franz–Lorenz law may yield a sufficiently good approximation assuming Lorenz's coefficient, $L = 2.4\times10^{-8}$ $(V/K)^2$. Lorenz's coefficient magnitudes can be approximately assumed constant up to the melting point for copper, silver, and gold, and up to 423–473 K for metals of the platinum group and its alloys.[1] Known $g(T)$ and $z(T)$ dependencies for contacting metals are needed to use Equation 5.46 and Equation 5.47.

Kohlraush's equation has been experimentally validated only for large enough spots (from several to hundreds of micrometers in diameter).[408,415,416] As the contact area is reduced, heat

TABLE 5.10
Some Formulas Derived Using Kohlraush's Equation

Formula, Equation Number	Assumptions	Ref.
$Q_m = \frac{U_c}{8 z_0 \rho_0}$ (5.44)	Ignoring the dependencies of electrical and heat conductivity	1
$L(T_m^2 - T_0^2) = \frac{U_c}{4}$, or $L(Q_m + 2T_0)Q_m = U_c^2/4$ (5.45)	Viedemann–Franz–Lorenz law ($z_T \rho_T = LT$) is valid	1
$Q_m + \frac{1}{2} t Q_m = \frac{U_c}{\rho_0 z_0}$ (5.46)	$\rho_T = \rho_0 (1 + tQ)$	388
$U_c^2 = 8\rho_0 z_0 \left[(T_m - T_0) + \frac{1}{2}(c - t)(T_m^2 - T_0^2) + \frac{1}{3}(t_1 + c_1 - tc)(T_m^3 - T_0^3) + \ldots \right]$ (5.47)	$\rho_T = \rho_0(1 + tQ + t_1 Q^2)$ $z_T = z_0(1 + cQ + c_1 Q^2)$	364

dissipation into boundary nonconductive regions (for example, organic or oxide films) may play an even greater role,[417] violating the conventional assumptions. Furthermore, the classic theory ignores the existence of the "Knudsen resistance" that results from electron scattering over the constriction boundaries (see Section 5.1.3). It has been demonstrated[418] that reduction of the spot linear dimensions to the size comparable with the free electron path ($\sim$10 nm for many metals) accentuates the significance of this resistance in comparison with R_s. Therefore, Kohlraush's equation becomes useless when applied to very small spots (up to approximately 0.1 μm), as was experimentally proven.[415]

From the point of view of a heat condition simulation, the current loading necessary to achieve a given overheating of the contact spot seems to be the most essential problem. Because formulas based on Equation 5.43 ignore the possibility of contact-spot growth due to softening when I increases, the current density parameter, j, is a more convenient analytical tool.

Consider a simple case of a round contact spot with diameter a between similar metals. When the Joule heat is negligible and the distance from other contact spots is quite long, the contact resistance can be determined as follows:[1] $R_c = R_s = \rho/2a$. Because $j = I/\pi a^2$, $I = U_c/R_s$; with consideration of Equation 5.45,

$$j = \frac{2U_c}{\pi\rho a} = \frac{4L(T_m^2 - T_0^2)^{\frac{1}{2}}}{\pi\rho a}. \tag{5.48}$$

It is assumed that the current density inducing overheating ($Q_m = 1$ K) of the spot is a threshold, j_{cr}, at which the heating commences. The Table 5.11 lists the parameters j_{cr} for some metals, as determined by Equation 5.48. These parameters correlate in their order of magnitude with the experimental results.[415] For example, contact temperature of the aluminium contact spot with the radius 8.1 μm starts to grow at $I \sim 10$ A, i.e., when current density $j \cong 0.04$ A/μm^2 (estimated magnitude is 0.02 A/μm^2), and the relevant magnitudes are $I \cong 0.1$ A, $j \cong 3$ A/μm^2 when the spot radius is 0.1 μm. It can be seen that the contact-spot heating becomes noticeable at rather high current densities (Table 5.11). On the other hand, the analysis of Equation 5.48 indicates that the contact surface rapidly heats up when j surpasses j_{cr} (Figure 5.36). Current densities should increase approximately 20 times to bring about $T_m \cong 1000$ K. In reality, contact temperature growth with current is much faster because Equation 5.48 does not take into account the full measure increase of g under Joule's heat effect. The rate of overheating variations with j accelerates as T_m increases

TABLE 5.11
Current Density j_{cr} (A/μm²) versus the Contact-Spot Radius a for Some Metals ($L = 2.4\times10^{-7}$ V²/K², $T_0 = 293$ K)

Metal	ρ (10^{-8} Ωm)	$a = 0.1$ (μm)	$a = 1$ (μm)	$a = 10$ (μm)
Copper	1.75	2.73	0.27	0.027
Gold	2.3	2.08	0.21	0.021
Aluminum	2.9	1.68	0.165	0.017
Platinum	11.7	0.41	0.041	0.004
Steel	30	0.16	0.018	0.002

(Figure 5.36). It is especially evident at T_m above 500–600 K. Correspondingly, an accurate setting of j for the specific contact surface overheating is more difficult to attain.

In addition to thermal effects, high electric current can produce other effects as well. For example, an electroplastic effect appears at $j = 10^{-4} - 10^{-2}$ A/μm².[392] Table 5.11 shows that the thermal and electroplastic effects can overlap in many metals, and this fact should always be considered when modelling thermal conditions.

A strong dependence of j_{cr} upon the contact-spot size is a salient feature because the smaller the linear dimensions, the higher the current density required for heating the spot (Table 5.11). Therefore, the thermal effect due to constriction of electric current is evident within a relatively narrow range of high current densities determined by specific conductivity of metal and the contact-spot dimensions. In general, the above data prove that temperature fields for purely metallic contact spots having simple geometry with at least 0.1 μm radius can be easily determined using experimentally recorded parameters of U_c, as well as known $g(T)$ and $z(T)$ for contacting metals.

5.2.3.2 Heating of Contact Spots Having Surface Films

Surface films add a number of features to current passage and consequently to heat generation in the contact. When the film is continuous, contact resistance R_c is the sum of two components of fundamentally different nature, i.e., the resistance of the film R_f. and constriction resistance R_s.

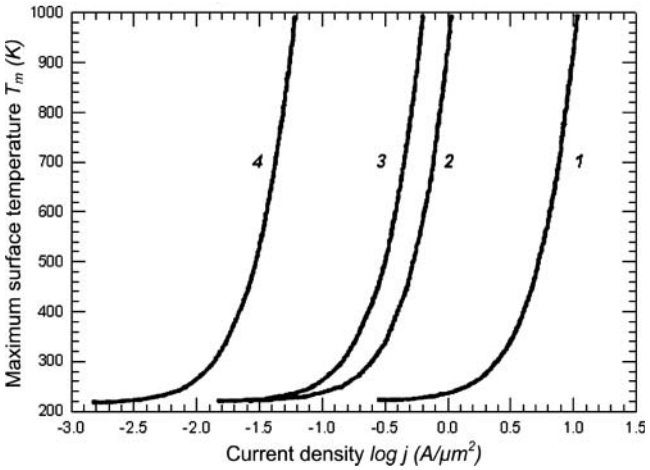

FIGURE 5.36 Maximum surface temperature T_m versus current density j in contact spot with radius a for copper (1,2) and steel (3,4); 1,3: $a = 1$ μm, 2,4: $a = 10$ μm ($L = 2.4\times10^{-7}$ V²/K², $T_0 = 293$ K). T_m is calculated from Equation 5.48.

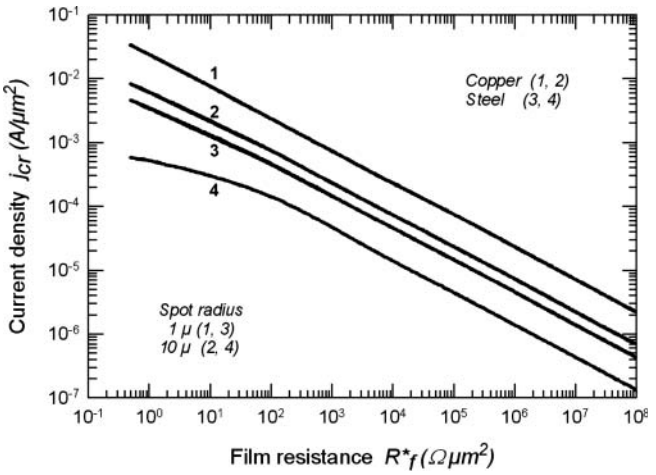

FIGURE 5.37 Current density j_{cr} as a function of specific film resistance R_f^* for copper (1,2) and steel (3,4), for different contact-spot radius, a; (1,3) $a = 1$ μm; (2,4): $a = 10$ μm. ($T_0 = 293$ K); j_{cr} is calculated from Equation 5.52.

The Joule heat is practically fully liberated at the interface (film) when R_f dominates. Therefore the Kohlraush contact theory cannot be used to estimate the temperature produced by the Joule heat. A more general approach developed in tribology based on by Block and Jaeger's fundamental works[409,413] seems more suitable (see Section 5.2.5).

Assuming that a continuous film with specific resistance R_f^* separates the contacting elements the constriction resistance of contacts with films is determined as $2g/\pi a$.[1] Hence

$$R_c = R_s + R_f = \frac{2\rho}{\pi a} + \frac{R_f^*}{S}. \tag{5.49}$$

When current I passes through the contact spot of area $S = \pi a^2$, the following expression is obtained:

$$q_j = \frac{I^2 R_c}{S} = \frac{I^2\left(\frac{2\rho}{\pi a} + \frac{R_f^*}{S}\right)}{S} = j^2(2a\rho + R_f^*). \tag{5.50}$$

Hence,

$$Q_m = \frac{\pi a j^2 (2a\rho + R_f^*)}{8z}. \tag{5.51}$$

An expression for current density can be obtained from Equation 5.49 in the form:

$$j = \frac{2}{\pi}\left[\frac{2Q_m z}{a(2a\rho + R_f^*)}\right]^{\frac{1}{2}}. \tag{5.52}$$

Figure 5.37 shows the values of j_{cr} derived from Equation 5.52 (current density necessary to reach $Q_m = 1$ K) for copper and steel specimens with different a and R_f^*. It is obvious that even for highly conductive films (e.g., adsorption of approximately 0.5-nm thick films can have $R_f^* \cong 0.5\ \Omega\ \mu m^2$)[1] the obtained j_{cr} are much lower than those for purely metallic contacts under

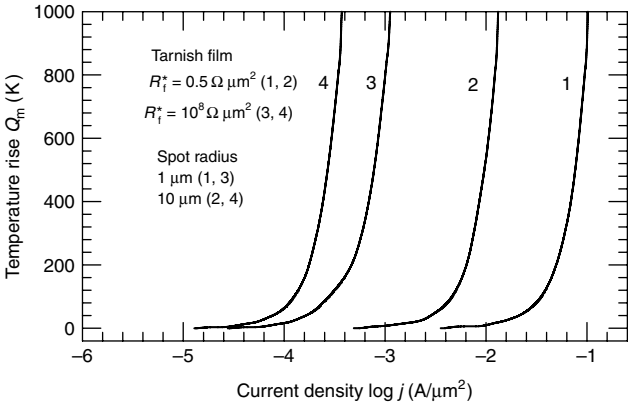

FIGURE 5.38 Temperature rise Q_m in the contact spot with different radius a versus current density j for steel with high conductive ($R_f^* = 0.5\ \Omega\ \mu m^2$) (1,2) and poorly conductive ($R_f^* = 10^8\ \Omega\ \mu m^2$) (3,4) films; (1,3) $a =$ 1 μm, 2,4: $a = 10$ μm. ($T_0 = 293$ K). Origin of the curves corresponds to the critical current density, j_{cr}.

similar conditions (Table 5.11). As R_f^* rises, the magnitudes of j_{cr} rapidly decrease. The heating of contacts with poorly conductive films ($R_f^* = 10^8\ \Omega\ \mu m^2$) begins at current densities 4–5 orders of magnitude less than in film-free contacts. It is clear that the lower current densities needed for heating leave more room for avoiding other effects of electric current, including electroplastic effects. When the threshold is reached, as in metallic contacts, increases in current density lead to faster temperature increases. The dependencies $Q_m(j)$ shown in Figure 5.38 for steel specimens (dependencies of g and z on temperature were ignored in calculations) roughly depicts this situation. When j surpasses j_{cr} by an order of magnitude, Q_m may reach approximately 200 K, but with a further slight increase in current density, Q_m reaches $\sim$1000 K.

The transmission of high currents through thin, intact boundary films has been considered in many publications.[1,234,408] This assumption is probably true for surface films with a relatively high conductivity, e.g., thin sulfide films.[408] However, there are, in fact, no quantitative experimental data confirming the feasibility of creating such a situation for dielectric or poorly conductive films. Relatively high and stable currents through the thin dielectric layers have been attained.[419] For example, stable currents with a density of about 10^{-6} A/μm^2 have been observed through oxide layers produced by thermal oxidation. It has been demonstrated above, however, (Figure 5.37 and Figure 5.38) that the current densities should be several orders of magnitude greater to generate noticeable heating in the contact zone. Therefore, the possibility of high current passage through poorly conductive films on the interface without disintegration requires experimental validation.

From the viewpoint of the contact-zone heating, and based on the experiments described in Section 5.1.2, the above described data call for a closer scrutiny. The amount of Joule heat, q_j, can be expressed as $U_c I/\pi a^2$:

$$Q_m = \frac{U_c I}{4a(z_{Fe} + z_{Au})}. \tag{5.53}$$

From Equation 5.53, it can be seen that the overheating of contact surface Q_m with contact parameters corresponding, for instance, to point A in Figure 5.16, amounts to less than 1 K. Estimates of the initial portions (until the moment of fritting) of other IU_c-characteristics yield similar results. This means that even the maximum possible current at $U_c < U_{cf}$ can cause a rather slight rise of surface temperature. The formation of high-conductive bridge (point A) is accompanied with a contact potential decrease, excluding the emergence of new bridges on other contact

area portions. As a result, the major share of current passes through the appearing channel, the greater part of heat liberates at this channel and the heat source cannot be considered evenly distributed over the contact area.

Probable dimensions and temperature of the current-conductive bridge, for example, corresponding to point K (Figure 5.17), were evaluated in the case of the iron–gold contact. If the conductivity through the intact tarnish film over the remaining portion of the contact area is ignored, then contact resistance is a sum of constriction resistance to the bridge and the resistance of the bridge in sequence, i.e.,

$$R_c = \frac{(\rho_{Fe} + \rho_{Au})}{4i} + \frac{\rho_b h}{\pi i^2}. \tag{5.54}$$

For more precise evaluation, the values ρ_{Fe} and ρ_{Ag} at room temperature and the "cold resistance," R_c, corresponding to contact parameters in the point K are used. The cold resistance is obtained from the reverse IU_c-characteristics (when U rapidly reduces to zero) and amounts to approximately 0.49 Ω (see Figure 5.17). Because the specific resistance of the bridge material (steel, in this case) is somewhat higher than that of the electrode material,[1] it may be assumed that $\rho_b = 10^{-6}$ Ω m. The solution of quadratic Equation 5.54 then yields $i \cong 0.42$ μm. The results of i estimation do not vary significantly if ρ_b is assumed to be one order of magnitude higher. When still higher currents (above 1 A) pass through the contact, the bridge effective radii would exceed 1 μm. It is obvious, however, that its linear dimensions are much smaller than that of the contact area. Current densities through the forming bridges ($I/\pi i^2$) would then amount to 0.2–0.7 A/μm^2 as a function of their dimensions.

An approximate estimate of the Q_m magnitude of the bridge is obtained based on the following considerations: The analysis indicates that the resistance of the bridge with $i > 10$ nm (the second right hand term in Equation 5.54 equals the insignificant fraction of constriction resistance towards the bridge. Because ρ_{Fe} is much higher than g_{Au}, then $R \cong \rho_{Fe}/4i$. From relationship $R_{cT} = R_{c0}(1 + 2tQ_m/3)$[1] expressing the temperature dependence of constriction resistance:

$$Q_m = \frac{3(R_{cT} - R_{c0})}{2tR_{c0}}. \tag{5.55}$$

In the present case, R_{sT} corresponds to the contact resistance in point K, i.e., approximately 0.62 Ω (Figure 5.17), whereas magnitude R_{s0} is the aforementioned "cold" resistance, i.e., approximately 0.49 Ω. The resistance temperature coefficient, t, for steel, determined up to 523 K, is 0.002 K^{-1}. Then, assuming in the first approximation that t is independent of temperature, Q_m is determined as 400 K. This rather approximate estimate illustrates to what extent the zone adjacent to the conductivity channel can be heated. Moreover, in the case of the thicker oxide films, the temperature of the bridge can reach the melting point in one of the electrodes.[1] At the same time, if the power of liberated heat energy corresponding to the point K parameters distributes across the contact area, then according to Equation 5.53, the temperature of the interfaced surfaces would be about 2.4 K.

The experimental data proved that electric current cannot heat—even to a few degrees—the contact spots with poorly conductive films about 1 nm or more thick. Contact potential (field intensity) increases to some critical value causing electric breakdown of the film; liberated heat localizes in the vicinity of the forming bridge.

Interpretation of experimental results relating to thinner films is problematic because R_c is comparable to the constriction resistance of the small (up to 0.1–0.2 μm) metallic microspots, but the employed experimental scheme lacks the film continuity control criterion. The probability of heating the contact spot with tunnel-conductive films without any electrical damage is analyzed

below. Note that the tunnel-conductive junction effects are not perceptible until the field intensity reaches values on the order 10^8 V/m.[1]

5.2.3.3 Field Intensity in the Contact Clearance with Tunnel-Conductive Films

Assuming that a continuous insulating below 1-nm thick film exists on a round contact spot with radius a formed by steel specimens. Conductivity of the spot is determined both by tunnel resistance and constriction resistance in series.[1,391] Taking into account Equation 5.49:

$$q_j = \frac{U_c^2}{R_c S} = \frac{U_c^2}{2\rho a + R_f^*}. \tag{5.56}$$

The contact temperature rise then transforms into:

$$Q_m = \frac{\pi U_c^2 a}{8z(2a\rho + R_f^*)} = \frac{\pi h^2 a}{8z(2a\rho + R_f^*)} E^2. \tag{5.57}$$

The value of R_f^* at a given h necessary for calculations can be obtained from the known formulas of tunnel conductivity.[390] It varies. between 1×10^{-12} and 3×10^{-7} Ωm^2 at h between 0.5 and 1.0 nm.

Figure 5.39 shows that contact spots start heating at very high field intensities even for extremely thin films. Therefore, it is necessary to achieve $E = 1.1\times10^8$ V/m, i.e., close to electric breakdown, to obtain overheating $Q_m = 5$ K at $h = 0.8$ nm. The estimated E rises rapidly when h increases even slightly (0.1 nm). According to Equation 5.57, the higher the thermal and electrical conductivities of a metal, the higher E is required to achieve the necessary overheating Q_m. In other words, copper requires higher field intensities than steel to heat contact spots at identical parameters a and h.

The above estimates have been obtained for an ideal contact with an evenly thick tunnel-conductive film. In practice, thickness and electrical properties of the films are always nonhomogenous,[1,420] which makes field intensities to exceed the average level. Hence, it is highly

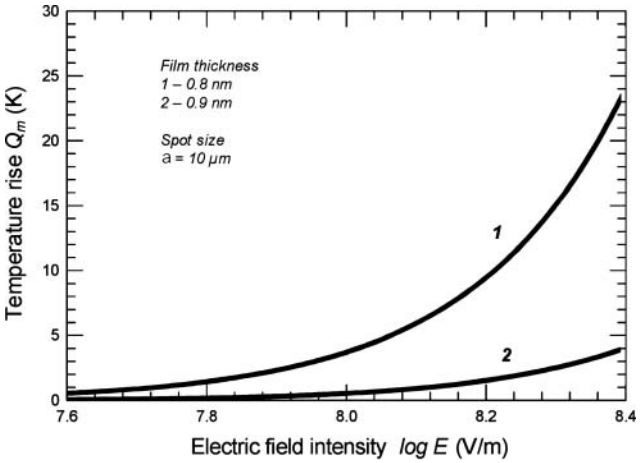

FIGURE 5.39 Relationship between electric field intensity E and temperature rise Q_m on steel contact spot with tunnel conductive film of thickness 0.8 nm (1) and 0.9 nm (2); $a = 10$ μm.

problematic to achieve any noticeable heating of contact spots without electric breakdown and current-conductive channel formation. The above analysis shows that this is the case.

A number of heating factors for metallic electrical contact should be considered, mainly: (1) high current densities at which heating of the contact spot starts; (2) thermal effect within a relatively narrow range of current densities conditioned by contact conductivity and spot dimensions; and (3) reduction in the accuracy of contact temperature estimate as the temperature increases.

Heating with electric current can be effective only when homogeneous conductive films are present. The above-cited features (1) and (2) should also be considered in this case.

In contrast to common knowledge[1] it appears that noticeable heating of the contact zone is impossible for thin tunnel-conductive films. Any effort to increase current density leads to critical field intensities in the film, its electrical damage and formation of a current-conductive bridge. The bridge dimensions are one or two orders of magnitude less than typical dimensions of the contact-spot area.

Application of Block and Jaeger formulas (or their modifications) for the average surface temperature becomes pointless in case when the bridge mechanism is responsible for the passage of current. Analytical expressions are needed for temperature distribution at contact surface as a function of the power source, dimensions, temperature, and location of the bridges.

In contrast to a static contact, the number of the channels may increase during sliding, due to the combination of mechanical and electrical damage of boundary films. The more conductivity channels exist simultaneously, the smoother temperature field will be in the contact and average temperature will tend to equalise with that calculated by the Block–Jaeger formulas.

5.2.4 Formulation of Heat Problem with Friction

Heat generated in the friction zone is distributed between the rubbing bodies and between the bodies and environment. Although conduction, convection, and/or thermal radiation are responsible for the heat transfer, the formation of thermal state of rubbing parts is principally controlled by the conduction.

An exact estimate of heat released during friction is rather difficult. Because of this, it is generally believed that the whole work done by the friction force is converted into heat. In other words, the *heat flow* q (J/(m^2 s)) is defined as

$$q = \mu p v, \tag{5.58}$$

where μ is the friction coefficient, p is the contact pressure, and v is the sliding velocity.

As an example a tribosystem consisting of two bodies is considered (Figure 5.40). In this case one-dimensional heat flow propagates through either of two contacting bodies, and their temperature fields are described by the system:

$$\begin{aligned} \frac{\mathrm{d}T_1}{\mathrm{d}t} &= a_1 \frac{\mathrm{d}^2 T_1}{\mathrm{d}x_1^2}, \\ \frac{\mathrm{d}T_2}{\mathrm{d}t} &= a_2 \frac{\mathrm{d}^2 T_2}{\mathrm{d}x_2^2}. \end{aligned} \tag{5.59}$$

This system can be described by two standard equations of heat conduction. Initial and boundary conditions should be specified. It is generally believed that initially the temperature of

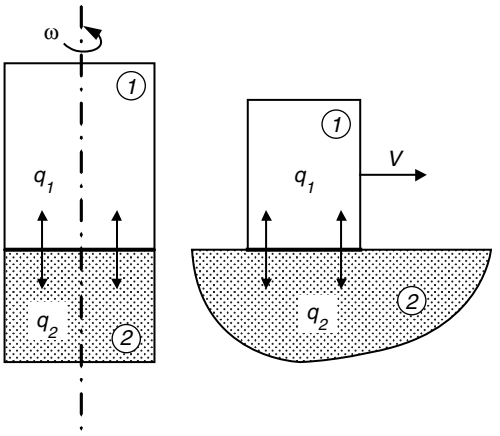

FIGURE 5.40 The simple model of tribocontact with different coefficients of mutual overlapping: (a) $K_{mo} = 1$; (b) $K_{mo} < 1$.

the bodies is constant and equal; therefore, the initial condition may be written in the form:

$$T_1(t = 0) = T_2(t = 0) = T_0. \tag{5.60}$$

where, as a rule, $T_0 = 0$.

The boundary conditions associated with the specific behavior of friction contact are as follows:

- The first boundary condition assumes the absence e of a temperature jump in the contact zone:

$$T_1(x_1 = 0, t) = T_2(x_2 = 0, t). \tag{5.61}$$

- The second boundary condition is most fundamental and is related to the situation when only the total amount of heat generated by friction is considered. The heat flow into each of mating bodies can be determined as a separate solution of the problem. This boundary condition is written as

$$q = q_1 + q_2 \tag{5.62a}$$

or,

$$\lambda_1 \frac{\partial T_1}{\partial x_1} + \lambda_2 \frac{\partial T_2}{\partial x_2} = -fpv. \tag{5.62b}$$

- For infinite bodies, the regularity condition is added to the above conditions. It requires that, at infinity, the temperatures of the bodies remain unchanged:

$$T_1(x_1 \to \infty, t) = T_2(x_2 \to \infty, t) = 0. \tag{5.63}$$

- There is a heat transfer between the boundaries of bodies and the environment of temperature, T_e. The Newton law generally describes it:

$$\lambda_{1,2} \frac{\partial T_{1,2}}{x_{1,2}} = \sigma'_{1,2}(T_{1,2} - T_{окр}) \tag{5.64}$$

where $\sigma'_{1,2}$ is the heat transfer coefficient for bodies 1 and 2.

The heat-transfer conditions are closely related to the *mutual overlapping coefficient* K_o. This term was first coined by Chichinadze.[421] The mutual overlapping coefficient is defined as the ratio of the current contact area to the area of whole friction trace. For example, when two cylinders are rubbed with faces (Figure 5.40a), $K_{mo} = 1$ and the heat transfer can occur only from the end surface. Another limiting case is shown in Figure 5.40b. If body 1 moves linearly over half-space 2, then its friction path area is infinite and $K_{mo} = 0$; the greatest part of released heat is dissipated into the environment. In the general case, the overlapping coefficient varies from zero to unity: $0 \le K_{mo} \le 1$.

Therefore, the solution to a problem of heat in friction is reduced to the system of Equation 5.59 with the initial and boundary conditions of Equation 5.60 through Equation 5.64. Such system may be reduced to the integral equation of Fredholm type. Its numerical solution is obtained only for some specific cases. Thus far, the problem has not been completely treated and the tribological requirements can be addressed using the approximate methods based on the ideas put forward by Blok and Jaeger.[409,413]

In tribology, the system of Equation 5.59 is examined under some additional conditions allowing to simplify its solution and derive relatively straightforward formulas suitable for use in practical calculations. Specifically, the shape of contact spot (heat source), the distribution of heat flow over contact and the partition of heat flow between the rubbing bodies are assumed. The last assumption is most fundamental, because it allows the system described by Equation 5.59 to be treated as two individual problems for each of the bodies in contact. The rectangular or line heat source with uniform or parabolic distribution of heat flow is usually considered. In some situations of practical importance, the shape of source and the heat flow distribution over the contact do not exert essential effect on the final result. Thus, calculations of the contact temperature (especially the mean temperature) for square source can be used as a source of arbitrary shape at high sliding velocity ($Pe = lv/a^2 > 4$). For low velocities ($Pe < 0.2$) the temperature field of moving source approaches that of stationary source which is shape-independent. For example, according to Jaeger, the maximum contact temperatures developed by the square and circular sources with the same size l differ by 12%. As for the heat flow distribution over the contact area, calculations for some simple distributions (uniform, linear, parabolic) showed that the maximum (and mean) temperatures are very close.

It should be pointed out that before solving the heat problem, special attention should be centered on the heat partition factor, which allows determination of the share of heat propagated into each of contacting bodies. Once the heat partition factor has been calculated, the temperature fields in each of mating bodies can be determined relatively simply using the solutions given in the theory of heat conduction.

Frictional contact temperature: Because a real contact is discrete, three types of temperatures can be recognized: (1) volume temperature, T_v, (2) surface temperature, T_s, and (3) the flash temperature, T_f, defined as the highest temperature increases occurring close to the areas of true contact at which the energy is dissipated.[422] The duration of the flash temperature is very short and accounts for 10^{-3}–10^{-9} s. It should be remembered that any asperity experiences repeated collisions with counter-body asperities. In other words, an asperity functions under the conditions of quasi-stationary (intermittent duty) friction.

The time interval, t_*, between two successive contacts is defined as a ratio of the mean distance between asperities and the sliding velocity. The temperature at the end of the $(j-1)$th cycle, T_{j-1}, becomes the initial temperature for the next cycle.

The temperature rise after N cycles is written as the series:

$$T = 2\frac{q}{\lambda}\left(\frac{a}{\pi}\right)^{1/2} \sum_{j=1}^{N} \left(\sqrt{jt_* + t} - \sqrt{jt_* + t - t_c} + \sqrt{t} - \sqrt{t - t_c}\right).$$

Here, t_c is the contact duration, r is the characteristic size (the contact-spot radius), and q is the rate of heat source. As an example, Figure 5.41 demonstrates the nondimensional surface

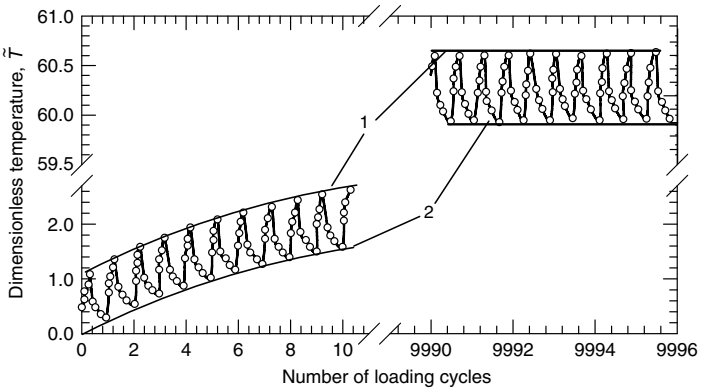

FIGURE 5.41 Dependence of the nondimensional temperature $\bar{T}$ on the number of loading cycles N of a single asperity: (1) envelope of maximum temperature within a cycle; (2) envelope of initial temperature of a cycle.

temperature as a function of number of loading cycles. The temperature is found to oscillate and its envelope increases monotonically. The band within which the surface temperature varies becomes narrower with number of cycles.

5.2.5 Flash Temperature of Electrical Contact

Based on the Blok and Jaeger work,[409,413] the following expression was derived for the flash temperature in the elliptical contact spot:[423]

$$\Delta T_e = \frac{(\pi/4)qr}{\lambda_1/Z_0(v_r)S(v_r) + \lambda_2/S_0}, \tag{5.65}$$

where $v_r = v/v_0 = v/(k_1/r)$ is the relative velocity between two mating surfaces; S is the shape factor; S_0 is the shape factor at zero velocity and up to $v_r = 1$. It should be remembered that

$$q = q_F + q_J,$$

where q_F and q_J are the heat evolutions due to friction and Joule heat.

Here,

$$Z_0(v_r \le 2) = \frac{1}{1 + v_r/3}, \tag{5.66}$$

and

$$Z_0(v_r \ge 2) = \frac{9/8}{v_r^{1/2} + 1/8^{1/2}}. \tag{5.67}$$

The shape factor was approximated as:

$$S(v_r \le 1) = S_0 = \frac{4/3}{\{(1 + e^{3/4}/3)(1 + 1/3e^{3/4})\}^{1/2}},$$

and

$$S(v_r \geq 1) = \frac{e^{1/4} + e^{1/4}/(8v_r)^{1/2}}{1 + e^{3/4}/(8v_r)^{1/2}}, \tag{5.68}$$

where e is the axis ratio of the elliptical load-bearing contact spots.

It should be borne in mind that the Joule heat at the interface exerts an effect on the constriction resistance:

$$R_c = \frac{(\rho_1 + \rho_2)\ln(2e^{1/2})/e^{1/2}}{N_a \pi_i a}, \tag{5.69}$$

where ρ is the electrical resistivity of the sliding materials.

In the general case, the flash temperature can be calculated for arbitrary speeds and elliptical contact spots if (1) heat is evolved at flat interface, (2) mating materials are free of surface films and (3) both materials have the same temperature. For a contact spot moving relative to both surfaces,

$$\Delta T(e, v_r) = f(Z, S)\Delta T_0 = \frac{\Delta T_0}{1/Z(v_r)S(e,v_r) + \lambda_r/S_0(e)}. \tag{5.70}$$

In this case, the velocity function for computing the velocity dependence of the flash temperature can be approximated as:

$$Z(v_r < 2) = \frac{1}{1 + v_r/3}, \tag{5.71a}$$

and

$$Z(v_r \geq 2) = \frac{9/8}{v_r + 1/8^{1/2}}. \tag{5.71b}$$

It should be noted that a comparison of results for circular spots with Jaeger's results for quadratic spots is very good:

$$\frac{\Delta T(\lambda_r = 0, v_r \geq 1)}{\Delta T(\lambda_r = 0, v_r = 0)} = Z(v_r \geq 1) = \frac{9}{8v_r^{1/2}}. \tag{5.72}$$

According to Jaeger, the shape function can be represented as

$$S(e, v_r = 0) = S_0(e) = \frac{4/3}{\{(1 + e^{3/4}/3)(1 + 1/3e^{3/4})\}^{1/2}}, \tag{5.73a}$$

$$S(e, v_r < 1) = S_0(e), \tag{5.73b}$$

and

$$S(e, v_r > 1) = \frac{e^{1/4} + e^{1/4}/(8v_r)^{1/2}}{1 + e^{3/4}/(8v_r)^{1/2}}. \tag{5.73c}$$

The shape function is shown in Figure 5.42. The average temperature of the contact spot above ambient can be written as

$$\Delta T(e,v_{r1},v_{r2}) = \frac{(\pi F)^{1/2} q/4\lambda_1}{1/Z(v_{r1})S(e,v_{r1}) + \lambda_r/Z(v_{r2})S(e,v_{r2})}. \tag{5.74}$$

Figure 5.43 shows an effect of relative velocity on the flash temperature for circular spot at different values of relative thermal conductivity. Similar results were obtained for plastic contact. In this case the relative motion is accompanied by shear, as shown in Figure 5.44.

The flash temperature of circular contact spot at $v = v_0$ is

$$\Delta T_0 = \frac{\Delta T_{ch}}{(1/Y) + (\lambda_r/v_r)}, \tag{5.75}$$

where ΔT_{ch} is the characteristic temperature. Figure 5.45 shows $\Delta T_0/\Delta T_{ch}$ as a function of velocity and thermal conductivity for circular and elliptical contact spots.

5.2.6 Thermal Instability of Friction Contact

Contact temperature exerts a significant effect on friction and wear as well as initiates additional stresses and strains in the contact zone. The sliding contact tends to adapt to new conditions. Such a

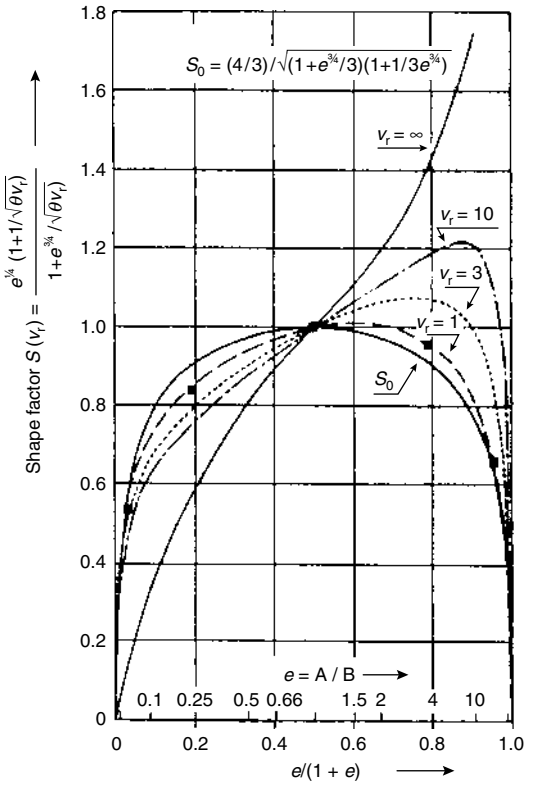

FIGURE 5.42 The shape function $S(e,v_r)$. Points ■ are computed by Jaeger. (From Kuhlmann-Wilsdorf, D., *Wear*, 105, 187–198, 1985. With permission.)

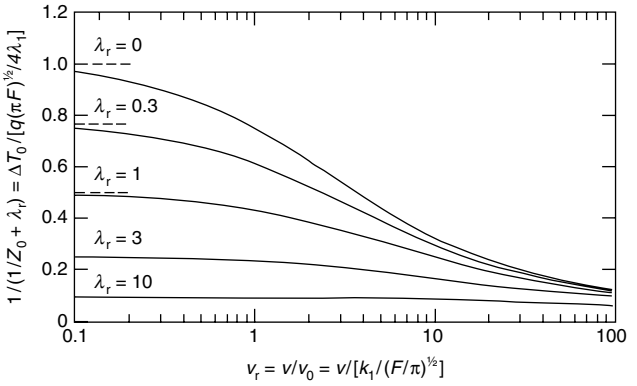

FIGURE 5.43 The flash temperature of a circular contact spot in units of $q(\pi F)^{1/2}/4\lambda_1$ as a function of relative velocity and relative thermal conductivity. (From Kuhlmann-Wilsdorf, D., *Mater. Sci. Eng.*, 93, 119–133, 1987. With permission.)

transition, termed the *thermal instability*, is often accompanied by quasiperiodic fluctuations of friction characteristics.

5.2.6.1 Thermoelastic Instability

Thermoelastic instability can be considered a consequence of interrelated variations in stress and thermal states of sliding contact. This instability occurs with a formation of "hot spots" on the contact area. It is assumed that thermal expansion and wear of material are the main factors that affect the thermoelastic instability.[400] Variation of pressure or current density from nominal values may cause localized friction heating. The greater the pressure and current density, the higher the temperature in the particular regions of the interface ("hot spots"). Thermal expansion of the hot spots exceeds that of the surrounding material, with the result that the contact pressure increases and promotes further elevation of frictional heating. This process continues until wear of the expanded spots begins, and gradually the load is transferred to other spots. Heat flow through

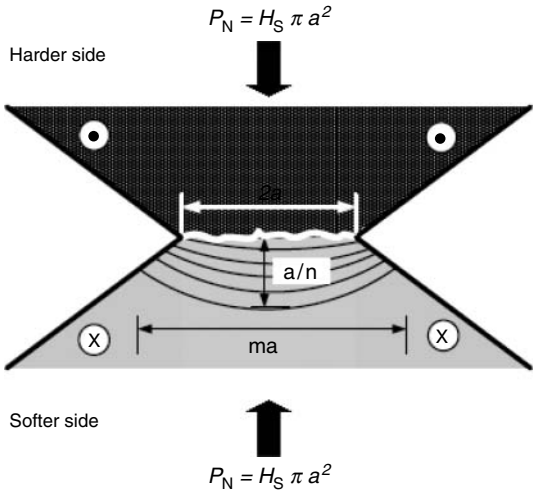

FIGURE 5.44 Model of a circular contact spot. (From Kuhlmann-Wilsdorf, D., *Mater. Sci. Eng.*, 93, 119–133, 1987. With permission.)

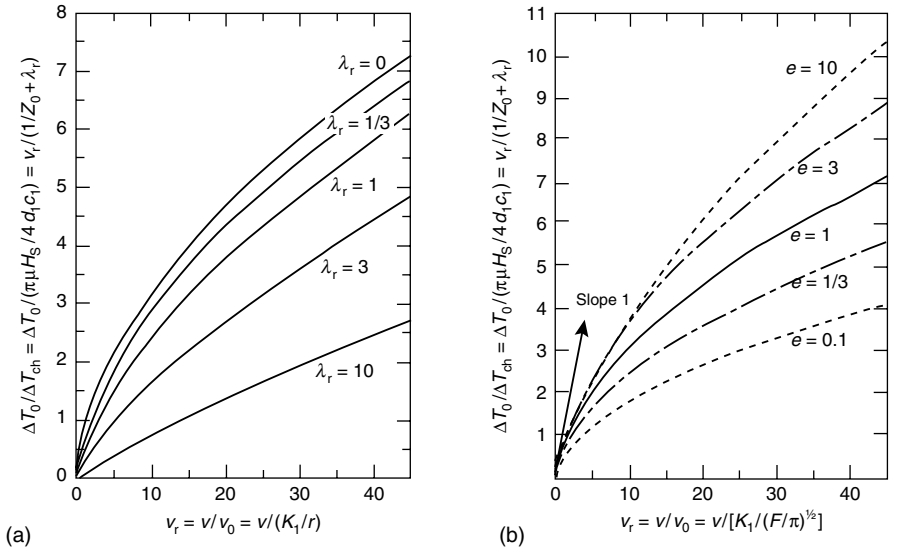

FIGURE 5.45 Flash temperature for (a) circular contact spot; (b) elliptical contact spot. (From Kuhlmann-Wilsdorf, D., *Mater. Sci. Eng.*, 93, 119–133, 1987. With permission.)

the old spots ceases, their material undergoes thermal compression, and depressions of volume equal to the volume of worn material remain in the surface. Here, wear serves to dampen the unstable behavior. Such behavior promotes fatigue wear of sliding contacts. This process can be complicated by heterogeneity of material in mechanical and thermal (electrical) properties. Some features of thermoelastic instability in electric brushes have been discussed elsewhere.[426]

5.2.6.2 Instability Caused by Temperature-Dependent Coefficient of Friction

The coefficient of friction can vary in different patterns with temperature. Contact-temperature increases can typically be accompanied by increases or decreases in friction coefficients. If tangential load is constant, the sliding velocity changes. However, because of a nonlinear dependence of friction on velocity, the rates of change in friction coefficient and velocity are different. Frictionally generated heat flow, μpv, can either increase or decrease, depending on the relationship between these rates. Analysis of this case has shown that variation of friction force with temperature can result in oscillating modes of sliding. Depending on tribosystem parameters, the contact temperature also varies in a quasiperiodic manner.

5.2.6.3 Instability Related to Friction Mode Variation

This mode of instability relates to severe friction when the changeover is expected from dry sliding to boundary or hydrodynamic conditions. Calculations show that the mean surface temperature increases with an increase in sliding velocity (Peclet number) according to a nonlinear law. This fact is caused by both an increase of friction heat generation and a decrease of heat transfer into the material. If the temperature of the layer reaches a critical value, e.g., melting point, and the coefficient of friction decreases sharply to a value typical for hydrodynamic lubrication, a transient process can start. The process is affected by two competing factors. On the one hand, heat generation decreases due to reduction in the friction force. On the other hand, the viscosity of the surface layer and the coefficient of friction increase with decreasing heat flow. Partial removal of the heated layer (wear) can occur in this case.

In conclusion, electric current and friction are the dominant factors controlling the behavior of sliding electrical contacts. Their interrelation is very important, and it can be roughly evaluated considering the energy balance in the contact. Parameters affecting this interrelation are load, velocity, friction coefficient, surface topography, lubricant, and the presence of various films. When designing an efficient electrical contact, an engineer should consider all of the above factors to make a balanced solution providing the optimal combination of mechanical and electrical characteristics.

6 Reliability Issues in Electrical Contacts

6.1 SIGNIFICANCE OF ELECTRICAL CONTACTS RELIABILITY

Electrical contacts are the most important components of electrical machines and electric engineering and telecommunication devices because they provide efficiency. The necessity of developing reliable electrical contact dates the beginning of the nineteenth century, when the first electrical machines were used. B. S. Yakobi developed commutating devices similar to a collector with brushes in 1834. First contacts were made of copper. As electrical engineering evolved, the metal–carbon–graphite material became the most common material presently widely used in sliding contacts such as many types of electric machines and current pick-offs. Progress in engineering, the development of new electronic circuits, and automatics and telecommunication devices prompted extensive applications of separable, breaking, and sliding contacts of new kinds such as relay contacts, low-voltage, and high-voltage electrical apparatuses, rheostats, potentiometers, and electronic circuit joints. Currents and voltages at which the contacts operate can vary by ten or more orders of magnitude, and their operating conditions include space, vacuum, and high temperatures (hundreds of centigrade).

In the twenty-first century, electric energy will remain one of the most basic needs for civilization. A huge number of various electrical contacts will be used in the process of energy production, transmission, distribution, and usage. The trend of the extensive utilization of microprocessor devices, automatic control systems of technological processes, communication equipment, speedy electric-powered transport, and modular telecommunication device design increases the number of contact joints in one device to thousands or tens of thousands. For instance, a motherboard of a PC unit may comprise up to 20,000 contacts.

The appearance of noncontact commutating semiconductor devices did not replace mechanical electrical contacts, as it was expected to do. Electrical contacts have a number of unquestionable advantages such as:

- A low resistance in the closed state and the infinite resistance in the open state
- A wide range of currents (10^{-12}–10^{6} A) and voltages (10^{-12}–10^{5} V)
- The possibility of the commutation of the direct, alternating, and pulse currents
- Withstanding severe (up to 100 times) overloads without catastrophic consequences
- A low heat losses and a small sensitivity to temperature variations and
- A substantial lower cost per unit power being commutated.

Because of some intrinsic problems with electrical contacts, such as noise and constricted current transfer across the contact interface, numerous attempts are being made to use electronic noncontact circuits as an alternative in some electrical/electronic devices. However, the ability of these noncontact replacements may be compromised and their cost prohibitive. Consequently, any

notion that in the future the application field of electrical contacts will become narrower or even obsolete is unjustified.

The variety of types of contacts and operating requirements prompted the use of a great number of conducting materials, from graphite to rhenium. The world consumption of only noble metals used in the fabrication of materials and coatings for contacts is in thousands of tons. On the other hand, not only noble metals, but also common contact material, such as copper, are becoming more and more deficient. Therefore, the replacement of copper with aluminum, which features improved connectability and reliability is an important step towards a wider use of aluminum in electrical devices.

The concern with the problems associated with the electrical contacts is addressed world-wide through a number of national and international and conferences. The most notable are the IEEE Holm Conference of Electrical Contacts, held annually in the U.S. or Canada, and the International Conference on Electrical Contacts (ICEC) held biannually in various countries.

6.2 ELECTRICAL CONTACT REQUIREMENTS

Different types of contacts should satisfy different sets of requirements depending on their stability and reliability. These problems can be addressed and solved by the careful consideration of the application, design, and operating conditions of electrical contacts. Because the main function of an electrical contact is to enable transmission of the electric current from one contacting member to another with a minimal impact on the transmitted signal, the following set of requirements should be met:

- Electrical: low power losses, no signal distortion, no overheating
- Mechanical: stable contact force during closing and opening, high wear resistance
- Ecological: resistance to environmental factors, minimal pollution to the environment under fabricating, operating, and recycling conditions
- Ergonomic: simplicity of design and fabrication, simple maintenance repair and replacement, possibility of combining units
- Economic: minimal content of noble and deficient nonferrous metals.

In view of the above requirements, reliability has become one of the most important characteristics of any electric/electronic device. Hence, as the demands on connectors increase, the development process becomes substantially more complex. These requirements are particularly important in the case of make-and-break contacts. Requirements imposed on these contacts because of the variety of commutating devices from low-current used to commutate low currents ($I = 10^{-6}$ A, $U = 10^{-6}$ V) to power devices commutating high-direct and alternating currents and voltages ($I > 1{,}000$ A, $U > 1{,}000$ V).

The contact materials should meet strict requirements, such as resistance to corrosion to prevent the formation of an insulating film on the contact surface and thus partial or total loss of conductivity, the resistance to electric erosion due to melting, evaporation, sputtering of the material or its transfer from one contact to another resulting from electric discharges and contact spot overheating, resistance to welding, the resistance to compressive and impact loads, wear resistance, high conductivity and good thermal characteristics, ease of fabrication, and running-in ability.

6.3 FACTORS AFFECTING RELIABILITY

One of the most important problems in providing reliability to electrical contact is the discrete nature of the interface. As discussed in Chapter 1, Chapter 3 and Chapter 5, an electrical contact

between solids is formed at discrete areas within the contacting interface and these areas (*a*-spots) are the only current conducting paths.

The formation of the real and conductive contact areas controls the reliability and efficiency of the electrical contact. These processes depend on a great number of independent or interrelated factors. The variety of the factors can be conventionally divided into (1) the performance factors governed by the operating conditions and (2) the design-technological factors determined by the fabrication characteristics of a contact unit. The performance factors (parameters) are divided basically into two groups: internal and external (Figure 6.1).

The internal factors are mechanical (the contact load, the type and characteristics of motion such as slip, the sliding velocity, and reciprocation) and electric (type and strength of current, operating voltages) factors. The external factors include temperature–time variations, humidity, atmospheric pressure, and the effect of aerosols, and these are often uncontrollable. The performance factors affect the properties of contact materials and surface films, the occurrence of physical and chemical processes in the contact zone, wear particle formation thus influencing the state of the interface and, finally, the contact resistance and reliability of electrical contacts.

Figure 6.2 shows schematically the influence of the design-technological factors on the reliability and quality of electrical contacts. The selected kind of contact materials, the contact geometry, the intermediate layers separating the contacting surfaces, the quality of the deposited coatings, and the contact surface microrelief determine the apparent contact area, size, number, and distribution of contact spots. This, in its turn, influences the real and electrical contact areas, the constriction and surface film resistances, and, finally, the electrical contact reliability.

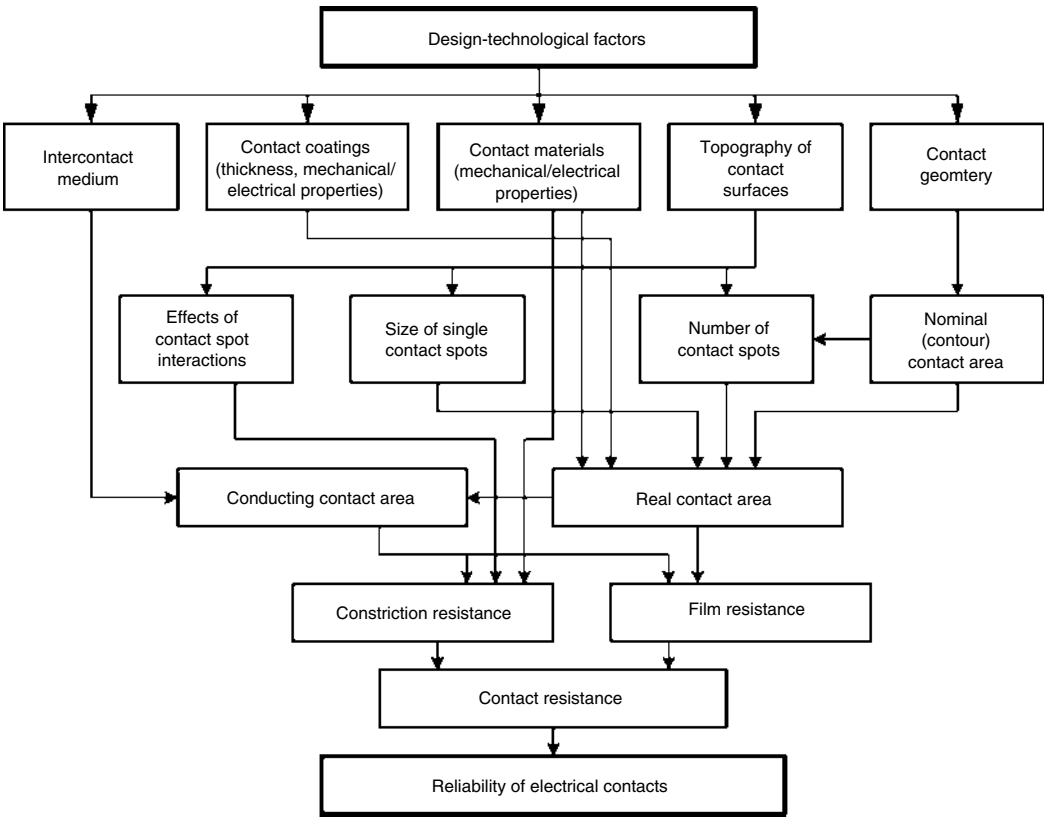

FIGURE 6.1 Effect of performance factors on the reliability of electrical contacts.

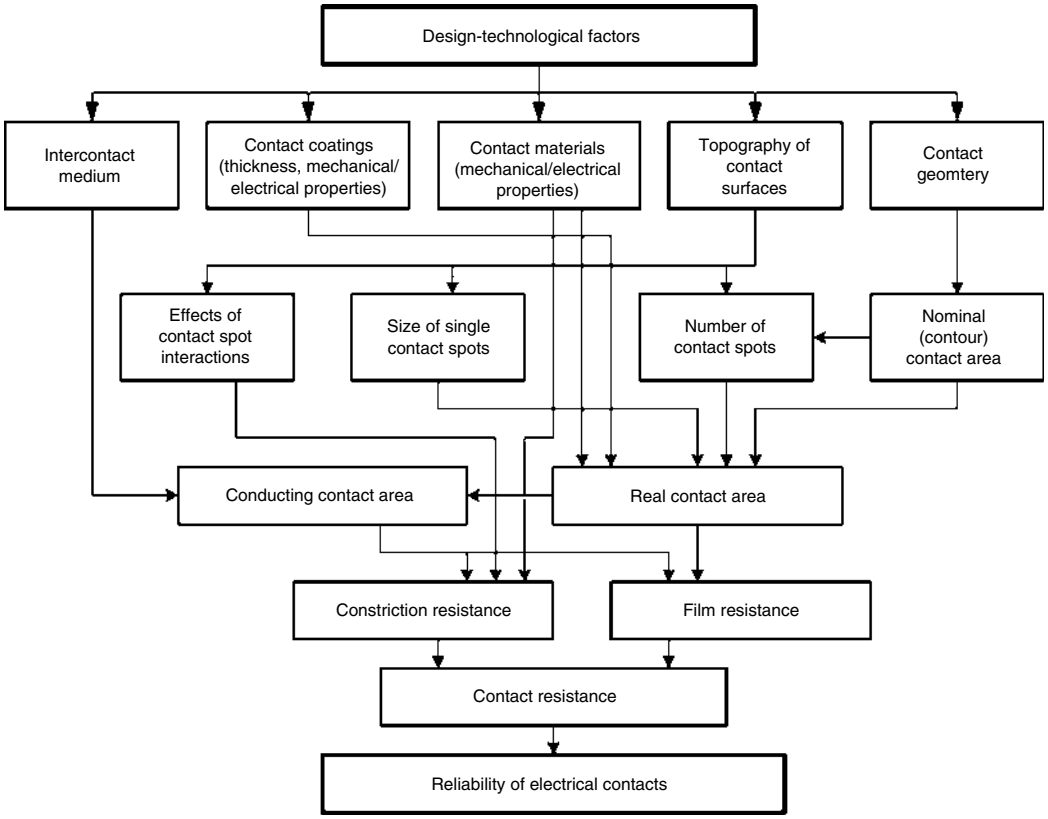

FIGURE 6.2 Effect of design-technological factors on the performance of electrical contacts.

The diagrams shown in Figure 6.1 and Figure 6.2 are not free of simplifications and approximations typical for such formalizations. One should always bear in mind that in addition to the above-mentioned factors uncontrollable (random) conditions may act in contact operation such as impact, vibration, and acceleration. Second, each type of electrical contact is characterized by a specific set of factors governing the contact reliability. It is not always easy to determine the most important factors.

In the following sections, a general description of degradation mechanisms in electrical contacts and their impact on the reliability of electrical contacts will be given. A detailed and exhaustive account of these degradation mechanisms and characteristic examples is provided in Chapters 7 and 8.

6.4 CONNECTION DEGRADATION MECHANISMS

The primary purpose of an electrical connection is to allow the uninterrupted passage of electrical current across the contact interface. This can only be achieved if a good metal-to-metal contact is established. The processes occurring in the contact zone are complex and not fully explained within the limits of present knowledge.

Although the nature of these processes may differ, they are all governed by the same fundamental phenomena, the degradation of the contacting interface and the associated changes in contact resistance, load, temperature, and other parameters of a multipoint contact. However, despite extensive investigations in the past of the effect of different parameters on the contact

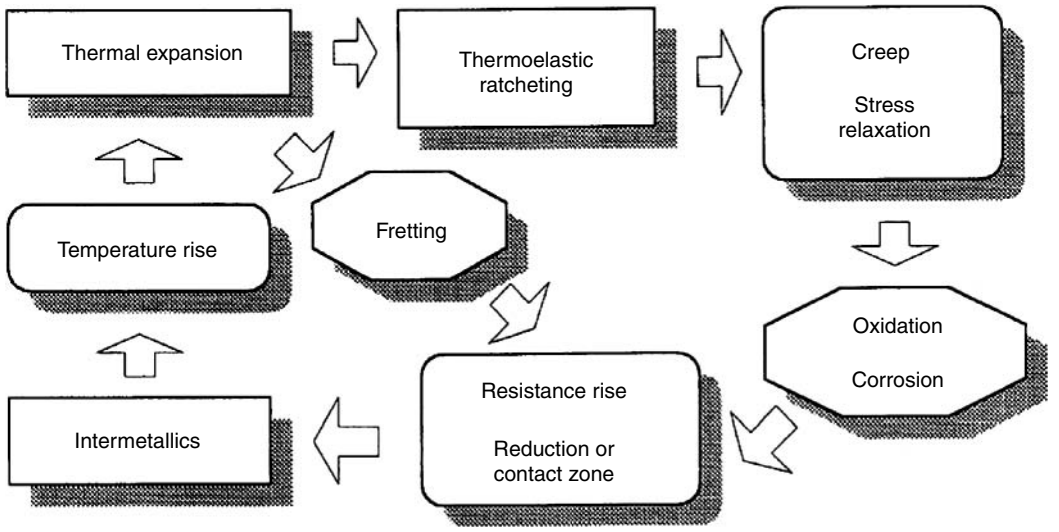

FIGURE 6.3 Schematic of degradation mechanisms in power connections.

behavior, a unified model describing the complex processes occurring in the contact zone is still lacking.

It is convenient at this point to briefly consider the probable causes of failure affecting the reliability of the power connections. *Failure*, in this context, is defined as the point at which the connection is no longer capable of supporting the function for which it was designed. In other words, it is the condition in which the bulk temperature of the joint, under normal current-transfer conditions, rises significantly above the permissible connection operating temperature.

The term *failure mechanism* refers to the actual physical phenomenon behind a failure occurrence. The complexity of failure mechanisms in power connections is best described in the form of a cycle, as shown in Figure 6.3. It is clear that breaking this cycle requires a thorough understanding of the parameters affecting various properties of conductor and contact materials subjected to different load and environmental conditions.

6.4.1 Contact Area

When the current is confined to flow through the conducting spots (*a*-spots), the temperature of the point of contact (T_c) may be higher than that of the bulk (T_b). Hence, the constriction resistance R_c in respect to the resistance that would exist if the metal–metal contact were continuous across the entire contact area $R_c(0)$ can be expressed as

$$R_c = R_c(0)[1 + 2/3\alpha(T_c - T_b)] \tag{6.1}$$

where α is temperature coefficient of resistance, the term $(T_c - T_b)$ is called the supertemperature and is related to the voltage drop across the contact interface (U) as follows[1]:

$$T_c^2 - T_b^2 = U^2/4L \tag{6.2}$$

where L is the Wiedemann-Franz–Lorenz number with the value of 2.45×10^{-8} $(V/K)^2$. It is clear that even a relatively small increase in the contact voltage drop (U) can raise the supertemperature considerably, enough to produce basic metallurgical changes such as softening or even melting of the conducting areas.

Although this argument may have some impact in the case of contacts with a contact load and an *a*-spot diameter that are both small, it is unlikely to have any practical significance in the case of a power connector operating at higher contact stresses and having much larger constriction radii.

In a good connection, the temperature of the interface is only slightly higher than the bulk temperature but in a poor connection, the supertemperature increases the bulk temperature and accelerates deterioration of the contact areas, causing higher resistance. The deterioration is cumulative resulting in increasingly higher temperatures and ultimate failure of the connection. In certain circumstances, such as short-circuit conditions, melting of the contact zones can occur even in well-designed joints, resulting in the formation of bridges of molten metal. As further deterioration occurs, these molten zones coalesce into larger areas in which arcing occurs and the whole joint assembly becomes overheated.

At first sight, it might appear that the creation of welded contacts would improve the connection stability. However, on subsequent cooling, the metal shrinks and cracks because of the internal stresses set up in the process of solidification of these bridges. Oxidation of the contact zones further reduces the number of available electrical conducting paths. Thus, overheating and ultimate mechanical failure of the joint occur.

From the above considerations, it is clear that one of the most important requirements for good connector performance is for the real area of contact to be sufficiently large so that even with initial and long-term deterioration, a reserve of contact area is still available to prevent overheating conditions in the joint. Unfortunately, present knowledge and understanding of various aspects relating to the failure mechanisms of electrical contacts are insufficient to assess with any degree of accuracy just how large the true area of contact should be in any given type of joint.

The deterioration of a connector proceeds slowly at a rate determined by the nature of different processes operating in the contact zone and in the environment. This initial stage persists for a long time without causing any noticeable changes because it is an intrinsic property of clusters of *a*-spots that their overall constriction resistance is not sensitive to small changes in their size. However, when the contact resistance increases sufficiently to raise the local temperature, a self-accelerating deterioration resulting from the interaction of thermal, chemical, mechanical and electrical processes will be triggered, and the contact resistance will rise abruptly. Hence, no deterioration will be noticeable until the final stages of the connector life. This process is clearly illustrated in Figure 6.4.[427]

The size of the contact area is generally determined by the hardness of the contacting members, applied force, and the rated current density. It should be sufficiently large to prevent the rise of the contact interface temperature under normal and emergency conditions. However, the contact

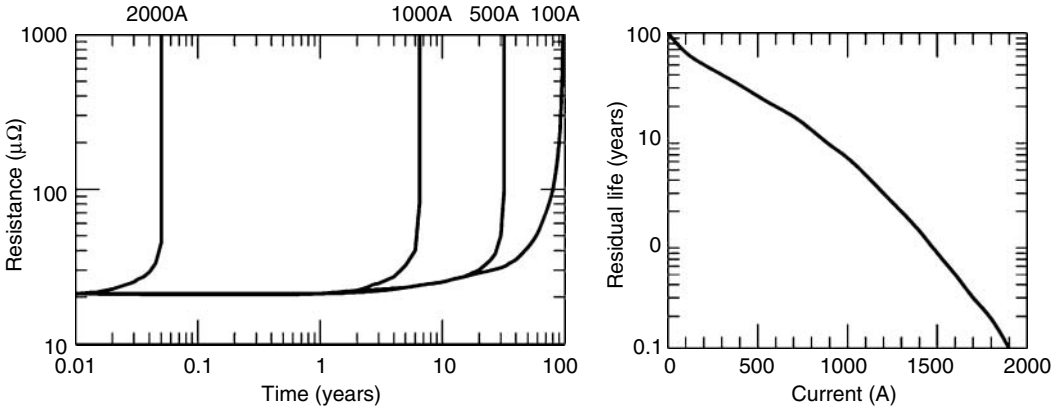

FIGURE 6.4 Variation of the connector resistance with time for different values of the applied current.

temperature itself is not a critical parameter because it is a result rather than a cause of the processes occurring in a joint, being a function of the current density, the geometrical dimensions of the contact, and the voltage drop across the contact.

The contact temperature can exceed that in the bulk of a conductor or connector without causing electrical instability at contact interface. On the other hand, the contact voltage can increase to very high values without causing the contact temperature to exceed that of the conductor or connector bulk temperature.

It is therefore imperative that changes in the contact temperature and voltage with the connector operating time remain very small. These requirements can be met providing the area of real contact is sufficiently large so that, despite initial and long-term deterioration, there is still a reserve of contact spots (*a*-spots) to ensure that the overheating conditions in the joints are not reached. Means of enlarging and maintaining the contact area will be dealt with in Chapter 7, Mitigating Measures.

6.4.2 Oxidation

Oxidation is a chemical process increasing the oxygen content of a base metal, and as a result, base metal or radical looses electrons. Oxidation of the metal–metal contacts within the contact interface is widely accepted as the most serious degradation mechanism occurring in mechanical connectors. In the case of aluminum contacts, it is generally considered a less likely mechanism of degradation because oxide growth is self-limiting and reaches a limiting thickness of about 10 nm within a very short period of time. This is very much less than the diameter of the contact spots, generally considered being much more than 10 nm for rough surfaces. Oxidation kinetics for some common contact materials are shown in Table 6.1.

Aluminum oxide is hard, tenacious, and brittle, with a high resistivity of 10^{24} μΩ cm. It is also transparent so that even the bright and clean appearance of an aluminum conductor does not assure that a low contact resistance can be achieved without appropriate surface preparation. In electrical contacts having one or both contact members of aluminum, the current flow is restricted to the areas where the oxide film is ruptured.

TABLE 6.1
Oxidation Kinetics of Some Common Electrical Contact Materials

Metal	Ambient	Product	Characteristic Features		Thickness (nm) at 10^3 h	Thickness (nm) at 10^5 h
Cu	Air	Cu_2O	Oxide forms immediately	20°C	2.2	4.0
			Temperature-dependent	100°C	15.0	130.0
Sn	Air	SnO	Initially slow growth rate	20°C	4.2	6.1
			Weak temperature-dependence	100°C	25.0	36.0
Ni	Air	NiO	Self-limiting	20°C	1.6	15.0
			Weak temperature-dependence	100°C	3.4	34.0
Al	Air	Al_2O_3	Oxide forms immediately (2 nm in sec)	Self-limiting growth		
			Humidity and temperature-dependent	Very hard and insulating		
Ag	Sulfur	Ag_2S	Depends of sulfur-vapor concentration	Humidity-dependent		
	Ozone	Ag_2O	Remains thin and decomposes at 200°C	No effect on contact		

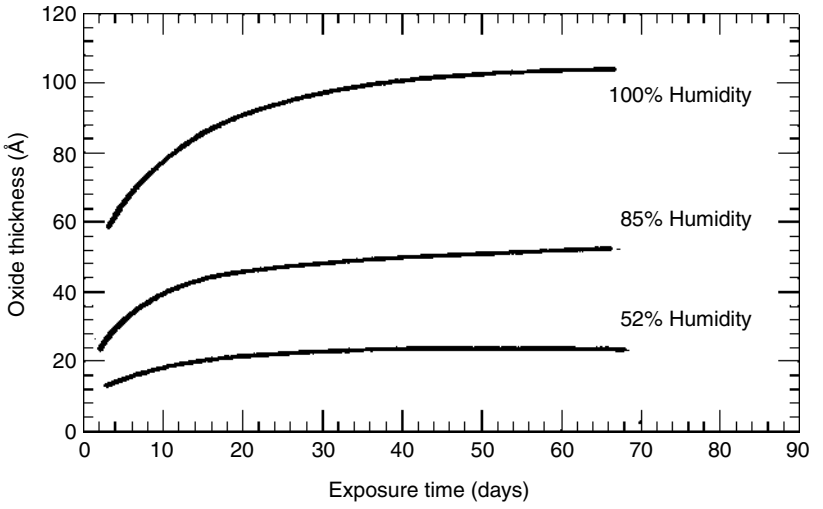

FIGURE 6.5 Effect of humidity on the oxidation of aluminum.

In the case of copper, it was shown that in the presence of oxygen-bearing atmospheres, the continuous oxidation of the metal–metal contacts by oxidation can cause rapid increase in the contact resistance to a high value after remaining relatively low for a considerable length of time. The oxides of copper grow, flake, and spall off from the base metal. Copper oxides are softer as compared to aluminum oxides and more easily disrupted by the applied contact force. They are also semiconducting and copper contacts with an initially high resistance, caused, for instance, by poor surface preparation, can show a steady decrease in contact resistance with time as a result of the growth of semiconducting layer over a large area. The electrical resistivity of Cu_2O is 10^{10} $\mu\Omega$ cm.

In the presence of a sulfur-bearing atmosphere, tarnishing of the copper surface is normally observed because of sulfide formation from hydrogen sulfide in the atmosphere. The growth of tarnished film is strongly dependent on the humidity, which can reduce it if a low sulfide concentration prevails or increase it if sulfide concentration is high. The effect of humidity on the growth of oxide layer in aluminum is shown in Figure 6.5.[428]

6.4.3 Corrosion

Corrosion is a chemical or electrochemical reaction between a metallic component and the surrounding environment causing detectable changes that lead to a deterioration of the component material, its properties and function. It begins at an exposed metal surface altering progressively the geometry of the affected component without changing the chemical composition of the material or its microstructure. Degradation initiates with the formation of a corrosion product layer and continues as long as at least one of the reactants can diffuse through the layer and sustain the reaction. The composition and characteristics of the corrosion product layer can significantly influence the corrosion rate. Among the many forms of general corrosion that could potentially affect the power equipment metallic components atmospheric, localized, crevice, pitting and galvanic are probably the most common.

Atmospheric corrosion is the gradual degradation or alteration of a material by contact with substances such as oxygen, carbon dioxide, water vapor, and sulfur and chloride compounds that are present in the atmosphere. Uniform thinning of component material is probably the most common form of general corrosion. Due to electrolytic nature of corrosion, only a very thin film of water is required to accelerate degradation. Although the rate of atmospheric corrosion is

dependent on the humidity, temperature, and levels of sulfate, chloride, and other atmospheric pollutants, it is usually not constant with time and tends to decrease as the length of exposure increases.

Localized corrosion is similar to general corrosion, except the rate of attack is usually much faster and the size of the affected area is significantly smaller. Damage caused by localized corrosion is often difficult to detect and quantify because visible surface flaws tend to be small and often do not provide a good indication of the extent of damage that has occurred under the surface. Specific forms of localized corrosion include crevice, pitting, and localized biological.

Crevice corrosion is a form of localized attack of metal surface adjacent to an area shielded from full exposure to the environment because of close proximity between the metal and the surface of another material. Narrow openings or spaces between metal-to-metal or nonmetal-to-metal components, cracks, seams, or other surface flaws can serve as sites for corrosion initiation. Humidity and pollution can penetrate into crevices and cavities inside mechanical and compression connectors not filled with contact lubricant. In the bolted connectors, the bolts made of stainless steel are more prone to crevice corrosion than those of carbon steels, particularly in the presence of chlorides.

Pitting corrosion is a localized degradation of a metal surface confined to a point or small area that takes the form of cavities. The cavities are generally irregularly shaped and may or may not become filled with corrosion products. Pitting usually affects metals covered with a very thin coating, with the pits forming at weak spots in the coating and at sites where the coating is damaged mechanically under conditions, in which self-repair will not occur.

Pore corrosion occurs in thin porous plating as result of a galvanic cell formed in the presence of a thin water layer containing ionizable gas. The corrosion products are transported from the reactive base or substrate metal though the hole in the plating to the contact surface. This type of corrosion is usually associated with a synergistic effect between chlorides, oxygen and/or sulfates, and is manifested by the appearance of pockmarks as seen in Figure 6.6.[429] The pores are defects in a coating that exposes underlying metal, underplate, or underplate and substrate.[430]

Creep corrosion can occur when a reactive substrate metal like silver or copper is located next to and in physical contact with a noble metal or a noble alloy inlay of plating. The substrate metal corrosion products creep over the noble metal surface. Creep can also be initiated from the pores in the thin gold plating. This corrosion process is usually associated with copper sulfide and silver sulfide corrosion films.[203]

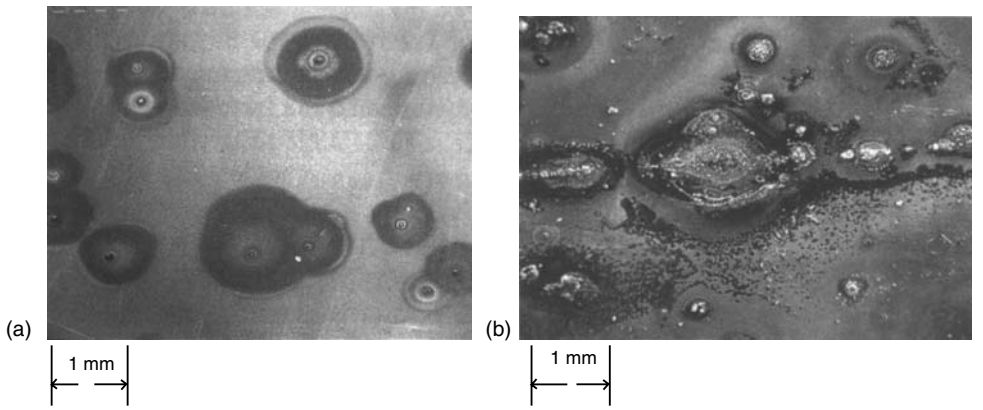

FIGURE 6.6 (a) Pore corrosion and (b) pore and creep corrosion. (From Abbott, W. H., In Electrical Contacts, Slade, P. H., Ed., pp. 113–154, 1999. With permission.)

Galvanic corrosion is accelerated corrosion occurring when a metal or alloy is electrically coupled to a more noble metal in the same electrolyte. In a bimetallic system, this form of corrosion is one of the most serious degradation mechanisms. Whenever dissimilar metals are coupled in the presence of solutions containing ionized salts, galvanic corrosion will occur. The requirements for galvanic corrosion are: (1) materials possessing different surface potentials, (2) common electrolyte, and (3) a common electrical path.

The driving force behind the flow of electrons is the difference in potential between the two metals with the direction of flow depending on which metal is more active. The more active (less noble) metal becomes anodic, and corrosion occurs while the less active metal becomes cathodic.

In the case of aluminum-to-copper connections, aluminum (the anodic component) dissolves and is deposited at the copper cathode in the form of a complex hydrated aluminum oxide, with a simultaneous evolution of hydrogen at the cathode (copper). The process will continue as long as the electrolyte is present or until all the aluminum has been consumed, even though the buildup of corrosion products may limit the rate of corrosion at the surface.

The aluminum-to-copper connection is affected by corrosion in two ways: either the contact area is drastically reduced, causing an electrical failure, or the connector is severely corroded, causing a mechanical failure. In most instances, failure is due to a combination of both effects. The factors that influence the degree or severity of galvanic corrosion are numerous and complex but probably the most important is humidity.

To limit the detrimental effect of galvanic action in corrosive environments and maintain a low contact resistance, various palliative measures such as plating with a metal of intermediate galvanic potential, contact aid-compounds, and transition washers have been employed. Figure 6.7a illustrates schematically galvanic corrosion in aluminum-to-copper joints whereas Figure 6.7b shows typical corrosion damage in aluminum-to-copper compression connector.

Dust corrosion occurs because of the presence of water-soluble salts in the dust. Such solutions form electrolyte and cause metal to corrode. This problem has been extensively studied in China by Zhang and his associates,[431,432] who have shown that the relative humidity and, in particular, the pH factor were two of the most important parameters affecting dust corrosion. It appears that the corrosion of dust particles increases almost linearly with relative humidity as seen in Figure 6.8, whereas the typical appearance of corrosion product around the dust particle is shown in Figure 6.9.

Stress corrosion cracking is the cracking induced from the combined influence of tensile stress and a corrosive environment. The required tensile stresses may be in the form of directly applied stresses or in the form of residual stresses such as cold deformation and forming, welding, heat treatment, machining and grinding. The magnitude and importance of such stresses is often underestimated. The residual stresses set up as a result of welding operations tend to approach the yield strength. Also, the build-up of corrosion products in confined spaces can generate significant stresses and should not be overlooked. Due to the difficulties in detecting fine cracks and predicting the incipient damage, stress corrosion cracking is classified as a catastrophic form of corrosion. A disastrous failure may occur unexpectedly, with minimal overall material loss.

6.4.4 Fretting

The process is defined as accelerated surface damage occurring at the interface of contacting materials subjected to small oscillatory movements. Two basic conditions necessary for fretting to occur are relative movement or slip and amplitude of motion sufficient to cause the damage. Experimental evidence shows that amplitudes of the order of 10^{-8} cm (<100 nm) are sufficient to produce fretting.[433] Thus, from a practical standpoint, there appears to be no minimum surface slip amplitude below which fretting will not occur.

Although there may be an argument as to the upper limit, which may still qualify the process as fretting, there is no doubt that in situations where microslip prevails, i.e., where slip occurs over only part of the contacting surface, the movement is entirely characteristic of fretting. This problem

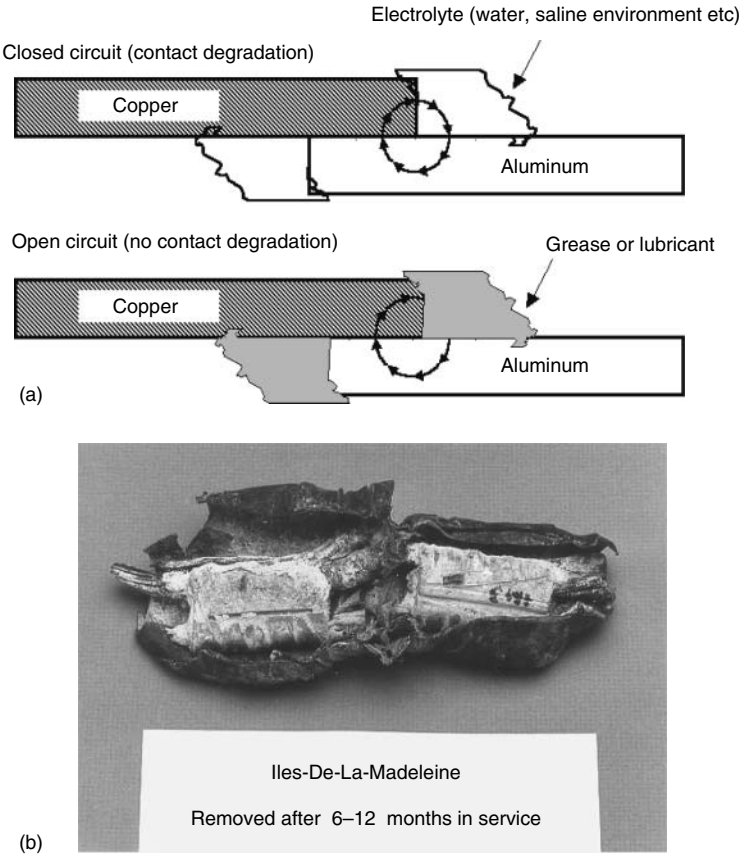

FIGURE 6.7 Schematic of galvanic corrosion in aluminum-to-copper joints (a) and example of corrosion damage in aluminum-to-copper compression connector (b).

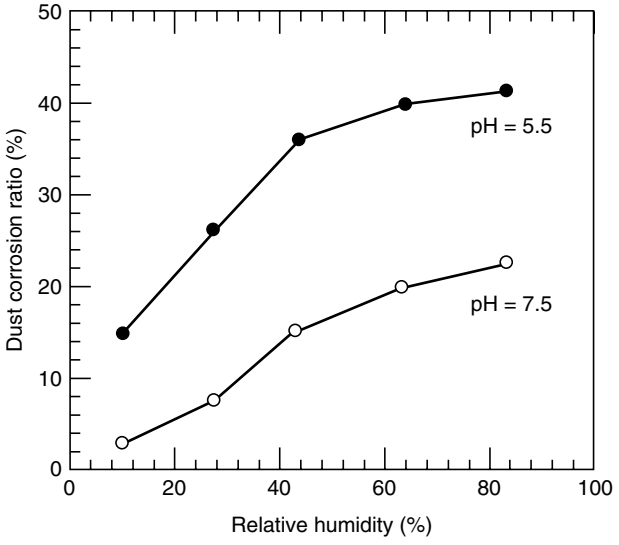

FIGURE 6.8 Corrosion ratios of dust particles with different pH as a function relative humidity.

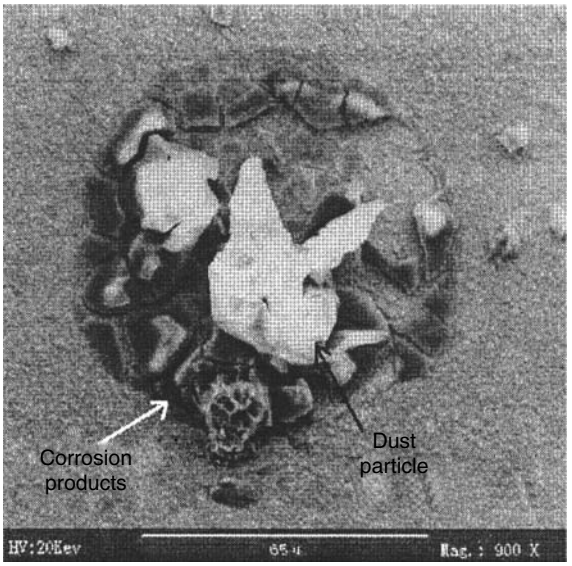

FIGURE 6.9 SEM images of the corrosion product around dust particle.

has been studied by Mindlin,[434] who has shown that the minimum slip amplitude for fretting to occur is given by

$$\delta = \frac{[3(2-\upsilon)(1+\upsilon)]}{8Ea}\mu P\left[1-\left(1-\frac{T}{\mu P}\right)^{2/3}\right], \tag{6.3}$$

where a is the diameter of the contact outer radius, E is the Young modulus, ν is Poisson's ratio, P is the normal force, μ is the static coefficient of friction between the contact surfaces and T is the tangential force ($T < \mu P$).

Figure 6.10 illustrates a classical example of microslip occurring between a steel ball and flat, where the ball experiences an oscillating tangential force. It is generally agreed that fretting damage

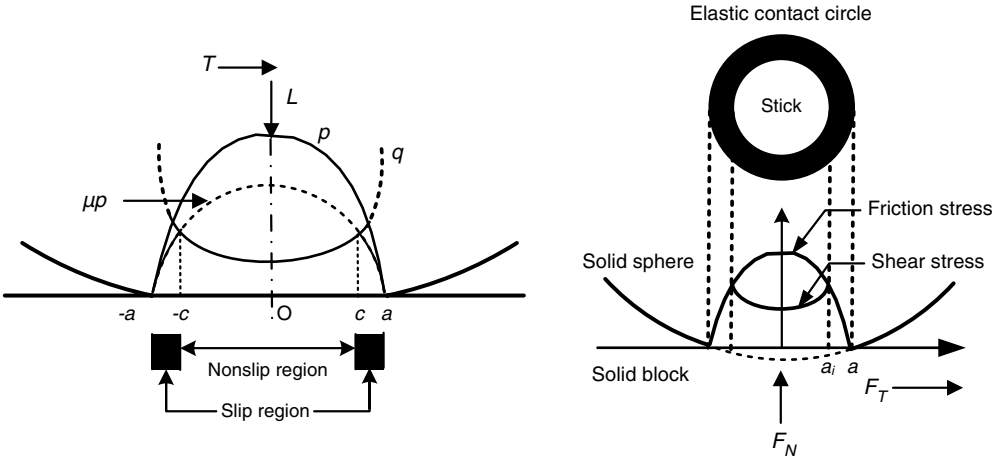

FIGURE 6.10 Microslip occurring between a steel ball and flat, where the ball experiences oscillating tangential force.

increases with increasing amplitude and that the mechanical properties of the contacting materials significantly affect the threshold value for fretting to occur.[434]

6.4.4.1 Mechanisms of Fretting

A study of the literature shows complex physicomechanical processes occur during fretting in the contact zone and that a single mechanism is unlikely to be responsible for the observed surface damage. It is therefore of interest to briefly review the principal theories regarding the mechanisms of fretting.

Although the adverse effects of fretting were observed as early as 1911,[435] at the contact surfaces closely fitting machine elements subjected to vibration and correctly diagnosed as mechanical in origin, the phenomenon was given little attention until 1927, when Tomlinson[436] coined the term "fretting corrosion" to cover this form of surface damage. This term describes phenomena including fretting wear, fretting fatigue, and fretting corrosion. Distinctions between these three fretting classifications are dictated more by the nature of a specific problem or objective of a particular study than by any fundamental difference in the processes taking place at the contacting surfaces.

Tomlinson suggested that fretting corrosion is caused by molecular attrition. The cohesion between atoms and molecules, which arises as they approach, causes them to detach from the surfaces and subsequently become oxidized. Tomlinson argued that fretting corrosion is not influenced by the normal load because, according to him, molecular attrition is independent of external forces.

Godfrey[437] proposed that fretting damage occurs as a result of adhesion between the surfaces. The wear debris is extruded from the contact area and reacts with the environment. However, good adhesion between two oxide-covered surfaces is questionable.

Feng and Rightmire[438] stated that fretting begins with adhesive wear followed by a transition period in which accumulation of the trapped wear particles gradually contributes to abrasive action. Eventually the damage is entirely caused by abrasion. The occurrence of loose wear particles is attributed to plastic deformation at the contacting high spots. Uhlig[439] proposed that chemical and mechanical factors are responsible for fretting corrosion.

An asperity rubbing on a metal surface produces a track of clean metal, which immediately oxidizes or upon which gas molecules rapidly adsorb. The following asperity wipes off the oxide or initiates the reaction of metal with adsorbed gas to form oxide. This is the chemical factor of fretting. In addition, asperities penetrate below the surface to cause wear by a welding or shearing action by which metal particles are dislodged. This is the mechanical factor of fretting. Uhlig has also derived an expression for wear at different values of load, frequency, and amplitude on the basis of the above model.

Stowers and Rabinowicz[440] identified two different regimes of fretting as a function of amplitude. In the low-amplitude regime, the volumetric wear per cycle is a function of the amplitude squared, whereas in the high-amplitude regime, it is directly proportional to the amplitude. They suggested that material loss resembles that produced by unidirectional adhesive wear much more closely than that produced by other modes of wear. Accordingly, the amount of wear can be computed using Archard's adhesion model for wear,[30] which postulates that when asperities come into contact and adhere strongly to each other, the subsequent separation occurs in the bulk of the weaker asperity in a single action. This process is assumed to create a particle from the softer surface, which adheres to the harder surface. When these transferred particles become free, loose wear particles are formed and wear, observed as weight loss, is assumed to occur.

Oding and Ivanova[441] stated that fretting is associated with a thermoelectric effect that causes electro-erosive action at the contacting surfaces. Material from one surface, anodic in respect to the

other, is removed by atoms torn from the surface by the direction of the electric field. Atoms moving in to fill the vacant sites at the surface result in vacancy diffusion into the region below the surface. The concentration of vacancies increases until a critical concentration is reached. When this concentration occurs, they coalesce as micropores and microcracks. This implies that only one of the surfaces undergoes damage. By passing the counter-current or by choosing suitable pairs of metals for the contact, this could be reversed. Although attractive, this theory cannot explain why surface damage arises between two similar metals, unless the thermoelectric effect of an oxide film is invoked.

Suh[35] proposed a delamination mechanism of wear which involves the initiation of subsurface cracks that propagate parallel to the surface and lead to detachment of flakes 0.1–20 μm thick. These cracks are thought to begin at voids and vacancies developing from dislocation pile-ups bellow the surface layer, and at a critical length, the cracks shear to the surface. A wear equation based on the theory was also developed. The delamination theory of wear as it stands is applicable only to the case of low-speed sliding, where the temperature rise at the contacting surface is so low that diffusion and phase transformation are not involved in the wear process.

The delamination mechanism of wear was used by Waterhouse and Taylor[442] to explain the formation of loose-wear particles and the propagation of subsurface cracks in the fretting surfaces. The end result of this process is the detachment of oxide-coated plates of metal about 1.3–3.5 μm thick. The continuing fretting action grinds the initial wear particles down to particles of smaller size with higher oxide content. They also divided the fretting corrosion process into two stages. Adhesion occurs in the early stage of fretting, and it is more significant with noble metals or in an inert environment. When this stage is passed, the surfaces become smooth, and removal of material from the surfaces occurs by delamination. The transition from adhesion to delamination is a function of the material and the nature of the environment.

Sproles et al.[443] concluded from the observed mode of metallic material removal that fretting wear by a delamination mechanism is predominant, rather than an abrasive wear mechanism or a welding and material transfer mechanism. Oxide debris is formed by the oxidation of metallic debris or by the formation and subsequent scraping away of a thin oxide film from the metallic surfaces.

Godet[444] proposed a third-body concept and a velocity accommodation mechanism. The debris formed in the contact remains in the interface for several cycles, and fretting has to be considered as a three-body contact. This approach focuses on the role of the third-body material, which separates the two first bodies rubbing through its load-carrying capacity. Directly transposed from the lubrication theory, this concept emphasizes notions of third-body flow and velocity accommodation. A contact can usually be broken down into five basic elements: two solids rubbing against each other, the first bodies, the interface or third-body bulk, and the two thin layers separating that bulk from the first bodies. The difference in velocity between the two points of each first body is thus accommodated through five sites following four modes, which have been shown to be the elastic, rupture, shear and roll modes.

Despite the significant progress made in our understanding of the fretting phenomena in general, and electrical contacts in particular, there is still no complete unanimity on the mechanisms of fretting, specifically with regard to the relative importance of the processes involved. Nevertheless, based on the existing knowledge of the phenomenon, it can be safely assumed that the following processes are present: (1) disruption of oxide film on the surface by the mechanical action exposes clean and strained metal which will react with the environment and rapidly oxidize, (2) the removal of material from the surfaces by adhesion wear, delamination or by shearing the microwelds formed between the asperities of the contacting surfaces when the contact was made, (3) oxidation of the wear debris and formation of hard abrasive particles that will continue to damage the surfaces by plowing, (4) formation of a thick insulating layer of oxides and wear debris (a third body) between the contacting surfaces.

6.4.4.2 Factors Affecting Fretting

The nature of fretting depends on a large number of variables. Many theories have been proposed to account for the effects observed, but no unified model for the process has yet emerged, and no one theory has yet been established as correct to the exclusion of any other. Detailed accounts of fretting and fretting corrosion have been given by Waterhouse[445] and Hurricks.[446] Factors known to affect fretting may be divided into three broad categories, namely: (1) contact conditions, (2) environmental conditions, and (3) material properties and behavior.

As indicated in Figure 6.11, these factors may interact with one another and influence both the nature and the extent of fretting damage. For example, under certain conditions, the effects of environment may be excluded from the contact area and, hence, will have no strong influence on fretting. On the other hand, under different contact conditions, the same environment may have ready access to the contact zone and have a strong influence.

It is clear that adequate simulation of any practical fretting wear problem, contact conditions, fretting load levels and amplitudes, materials, and environmental conditions must be considered. The fretting process is too complex to enable extrapolation with confidence from one set of conditions to another very different set of conditions.

In the sections that follow, factors affecting the fretting in electrical contact will be discussed, whereas the practical examples of the effects of fretting in electrical and electronic connections will be given in Chapters 7 and 8.

6.4.4.3 Fretting in Electrical Contacts

Although contact resistance was used to monitor the development of fretting damage in steel specimens as long ago as 1956,[447] it was only eight years later that Fairweather et al.[448] demonstrated how fretting can cause considerable instability and serious degradation of telephone relays and switches. Its effect, however, was not widely recognized as a serious factor in the degradation of electrical connections until 1974, when Bock and Whitley[449] clearly demonstrated its importance. Since then, systematic studies of electronic[450–461] and automotive[174,462–464] connector systems and reports on in-service failures[383,465–467] have established fretting as one of the major contact deterioration mechanisms in dry connections. A number of models were proposed the effects of fretting on contact resistance.[468–472]

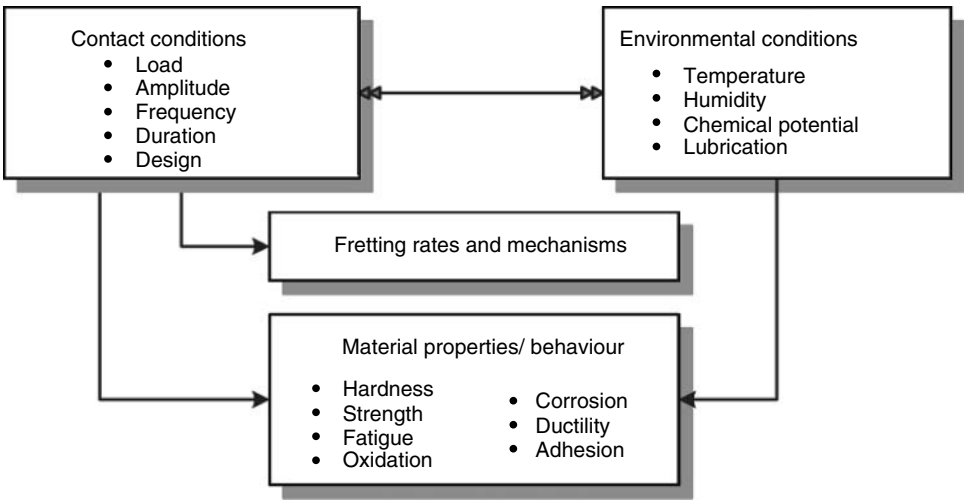

FIGURE 6.11 Schematic representation of the factors affecting fretting.

In the case of power connectors, however, very little published information of failures due to fretting is available. There are two main reasons for this lack. First is the general lack of awareness of fretting as it affects power connections. This is not surprising because fretting is a time-related process causing an appreciable effect only after a long period of time as a result of the accumulation of wear debris and oxides in the contact zone. Second, the effects of fretting, particularly in the early stages, are not readily recognizable because failure of a power connection is usually associated with destruction of the contact zone by arcing and melting. This destruction makes identification of the fretting products, namely wear debris and oxides accumulated at the interface between contacting members, quite difficult. The problem of fretting in power connections was extensively studied by Braunović.[144,146,472,473]

The required oscillatory movement of the contacting members can be produced by mechanical vibrations, differential thermal expansion of the contacting metals, load relaxation, and by junction heating as the power is switched on and off. It is generally accepted that fretting is concerned with slip amplitudes not greater than 125 μm. Because this movement is of limited amplitude, it is ineffective in cleaning away the wear debris and accumulating oxides, and a highly localized, thick insulating layer is formed in the contact zone, leading to a dramatic increase in contact resistance and, subsequently, to virtual open circuits.

The sequence of events depicting the initiation and spreading of fretting damage of electrical contacts and the SEM image of the fretting damage in contact zone of tin-plated contact are shown in Figure 6.12. The effect of fretting on the contact resistance of different contact materials is shown in Figure 6.13.[146,475]

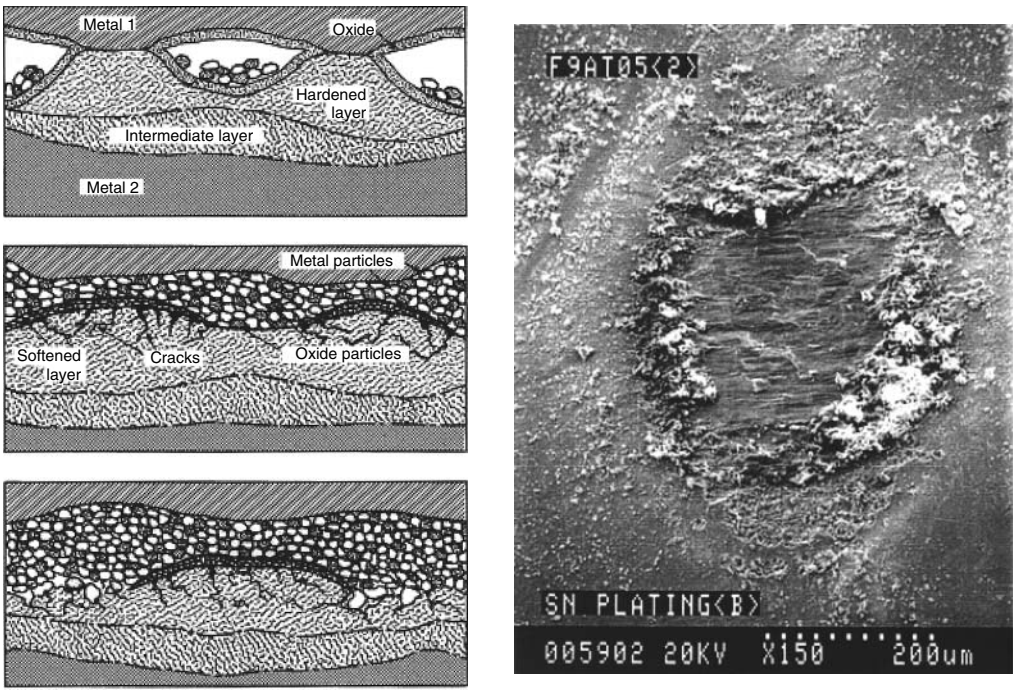

FIGURE 6.12 Schematic of evolution of fretting damage in electrical contacts and a SEM image of a typical fretting wear damage of the contact zone.

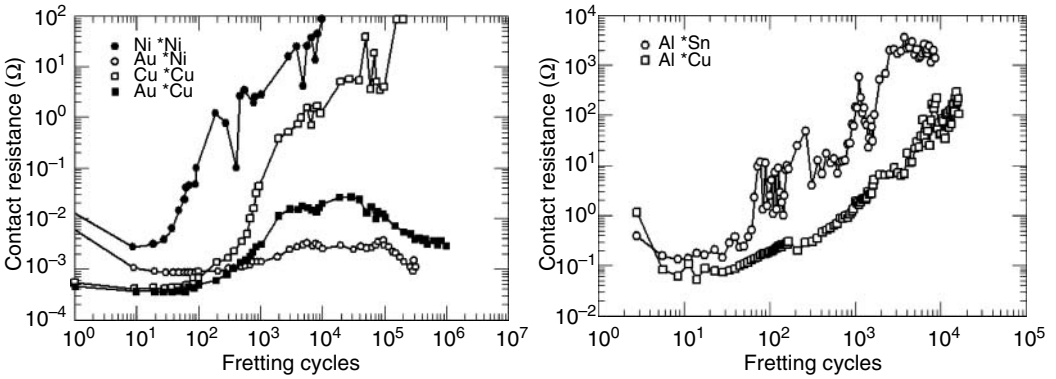

FIGURE 6.13 Effect of fretting on the contact resistance of different contact plating materials and aluminum–tin-plated-copper and aluminum–copper. (From Antler, M. and Sproles, E. S., *IEEE Trans. CHMT*, 5(1), 158–166, 1982; Braunović, M., *IEEE Trans. CHMT*, 15, 204–214, 1992. With permission.)

6.4.4.4 Contact Load

Contact load exerts significant influence on the contact resistance under fretting conditions. The effect is manifested by significant suppression of the deleterious effect of fretting with increasing load.[26,476,477] Figure 6.14 illustrates the contact resistance behavior of aluminum fretting against tin-plated copper at 1-N and 10-N contact loads.[476] As it can be seen, over the entire range of fretting time (cycling) the contact resistance at 10 N is practically unaffected by the fretting action whereas the contact resistance at 1 N is characterized by large fluctuations and eventually an open circuit. The beneficial effect of applying higher contact loads can be rationalized by invoking a basic model of the processes occurring during fretting action.

At low contact loads (1 N), when a contact is made, surface asperities of a harder material penetrate the natural oxide films, thereby establishing localized metallic contacts and, thus, conducting paths. Displacement of the contact interface during fretting shear these metallic

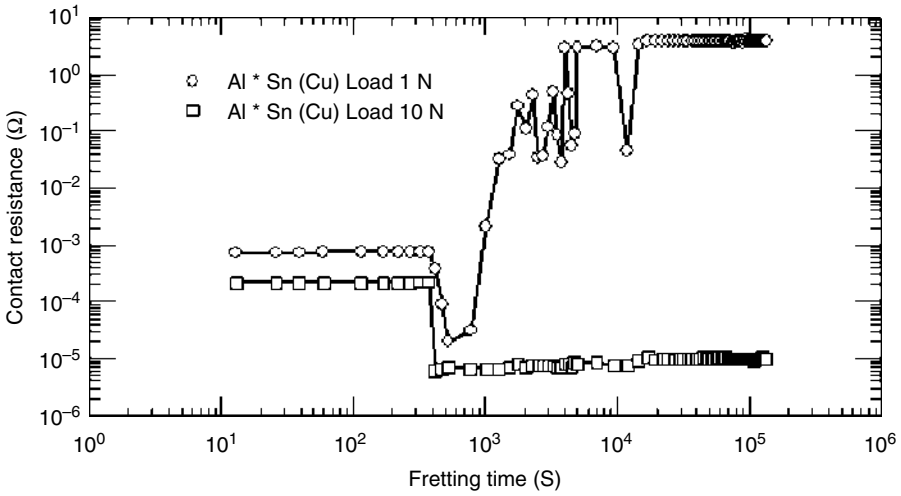

FIGURE 6.14 Effect of contact load on the contact resistance behavior of aluminum fretting against tin-plated copper. (From Braunović, M., *Proceedings of 19th ICEC*, Nuremberg, 283–287, 1998. With permission.)

bridges, resulting in the formation of the first wear products, a fraction of which will oxidize with the greater portion remaining as metallic particles (burnishing effect), thus, a good metallic contact between contacting surfaces is established as manifested by decreasing contact resistance. Prolonged exposure to the fatigue–oxidation process, metallic layers in the contact zones soften and progressively separate. The contact zone now consists of a thick insulating layer containing oxides and wear debris, and any remaining metallic contact is lost, causing a sharp increase in the contact resistance.

The cyclic nature of the latter is caused by the temporary rupture of the insulating layer and the appearance of localized metallic contacts and conducting paths. Subsequent wiping and accelerated oxidation due to the high current density will rapidly eliminate these conducting spots and the contact resistance will rise sharply. The sequence of events depicting the development of fretting damage in the contact zone at 1-N contact load is illustrated in Figure 6.15a.

At higher contact loads, however, the model no longer applies because the contact resistance remains relatively stable and fluctuation-free and gradually increases as the fretting action

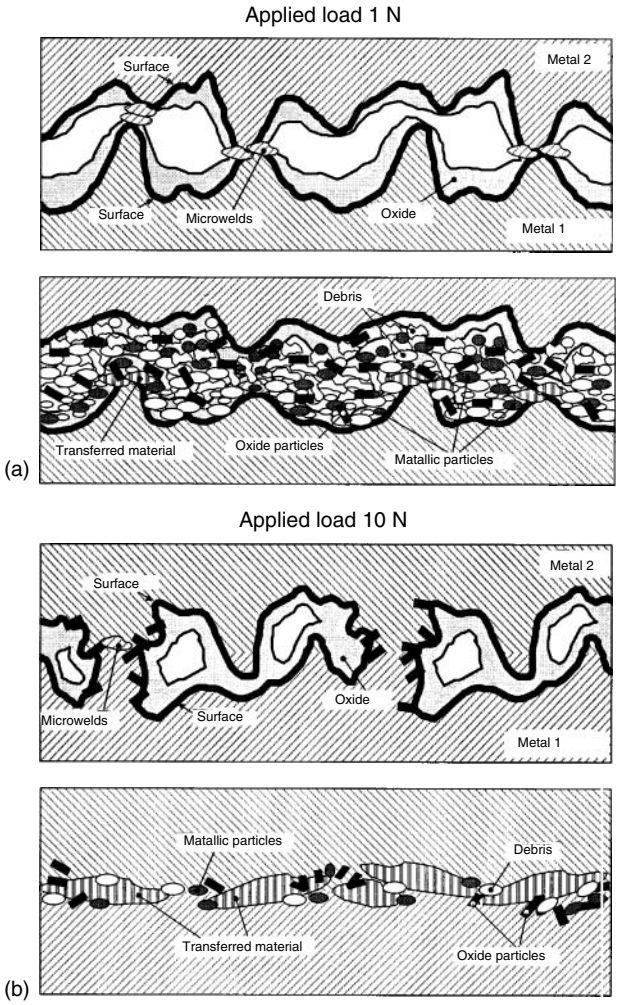

FIGURE 6.15 The sequence of events depicting development of fretting damage in the contact zone of a connection between two different conductor and/or contact materials at 1 and 10 N load.

proceeds. The observed difference in the contact resistance behavior at 1 and 10 N loads can be explained by invoking the following mechanism. When a contact is made, the asperities rupture the oxide and become practically embedded in the contacting surfaces under high contact pressure, thus forming a large number of strong adhesive bonds (microwelds). The ruptured oxide film is trapped in the surface pits and virtually seals off the contact zone. When fretting motion is initiated, these bonds are broken and primary wear products, composed almost entirely of metallic particles, will be formed. Because the contact zones are practically sealed-off from the environment, oxidation of these wear products is minimal. The sequence of events depicting the development of fretting damage in the contact zones of aluminum-to-copper connections at 10 N contact load is shown in Figure 6.15b.

It should be pointed out, however, that the higher loads only delay the onset of fretting damage because the prolonged fretting action eventually causes fretting fatigue and fracture of the surface layers. Subsequent formation of thick insulating layer that higher contact loads would not be able to break through results in a sharp increase of the contact resistance. This is shown in Figure 6.16. Data for this figure were derived from papers by Antler[26] and Lee.[477] The observed linear relationship between the number of fretting cycles required to attain the stated contact resistance values is fortuitous and in no way implies that for different loads and different contact configuration this relationship would hold.

6.4.4.5 Frequency of Motion

Because fretting is a rate-dependent phenomenon, the contact resistance will be affected by the frequency of oscillations. The results in Figure 6.17 show the variation of the number of fretting cycles required to attain a predetermined contact resistance value as a function of the oscillating frequency. The data shown are for copper vs. copper[26] and aluminum vs. tin-plated copper[478] contact combinations. It is clear that the lower the frequency, the shorter the time to reach a given level of elevated contact resistance. The observed effect of frequency can be explained in terms of oxidation factor of fretting. Because oxidation is time dependent, at lower frequencies for a longer time the contact zone will be exposed by fretting to oxidation as a result of which an

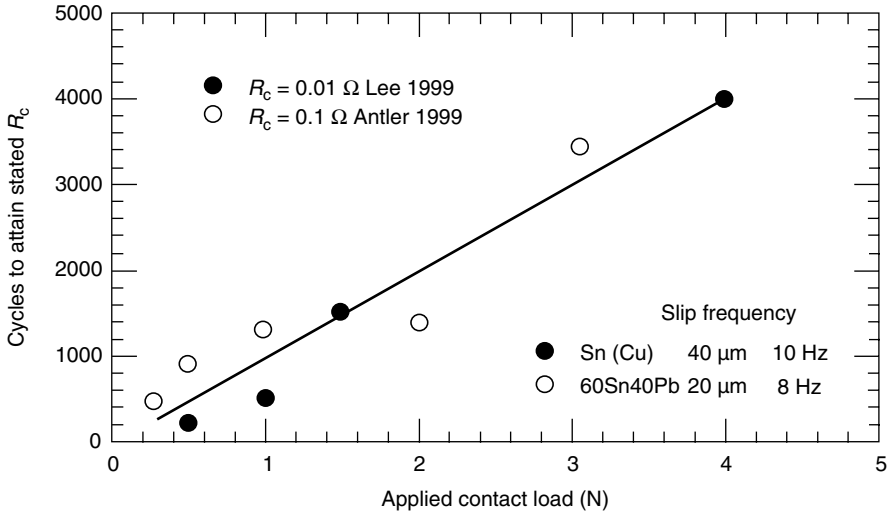

FIGURE 6.16 Number of fretting cycles in tin-plated copper and 60Sn40Pb vs. 60Sn40Pb contacts required to attain 0.01 and 0.1 Ω respectively, as a function of contact load.

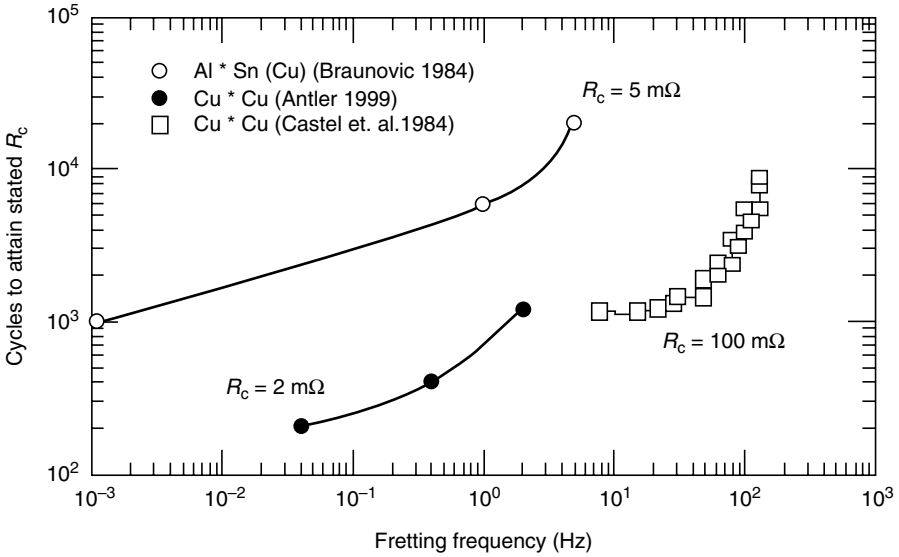

FIGURE 6.17 Number of fretting cycles in copper–copper[26,478] and aluminum–tin-plated-copper[479] contacts required to attain a predetermined level of contact resistance as a function of fretting frequency.

increasing number of conducting spots in the contact zone will be closed, thus increasing the contact resistance.

It is rather interesting to note that Castel[478] pointed out that below 50 Hz the frequency has little effect on the contact resistance behavior. This finding is in a clear disagreement with the results of Antler,[26] who has shown that frequencies as low as 0.04 Hz can produce significant contact degradation in copper-to-copper contacts.

6.4.4.6 Slip Amplitude

The effects of fretting slip amplitude at different frequencies and for different contact material combinations are shown in Figure 6.18. The data shown are derived from[453,455,459,479] as the number of fretting cycles required to attain a predetermined contact resistance levels as a function of fretting slip amplitude. It is clear that for all contact material combinations the longer the slip amplitude the shorter is the time to attain a given increase in the contact resistance.

The observed effect can be rationalized in terms of kinetics of debris removal and also the formation and closure of the conducting spots in the contact area. In other words, the shorter slip amplitude, the lower the number of contact spots exposed to oxidation, which, in turn, delays the onset of contact resistance degradation. On the other hand, longer slip amplitudes facilitate the exposure of the contact zone to oxidation, thus reducing the number of conducting contact spots and thus shortening the time to onset of the increases of contact resistance.

6.4.4.7 Relative Humidity

Relatively humidity (RH) has a significant and complex effect on the fretting behavior of electrical contacts because it involves interaction between chemical reaction rates, the effect of moisture on the physical characteristics of the debris, and possibly effects of moisture on the surface mechanical properties of the contacting materials. Fretting wear is consistently lower in saturated air than in dry air.[445]

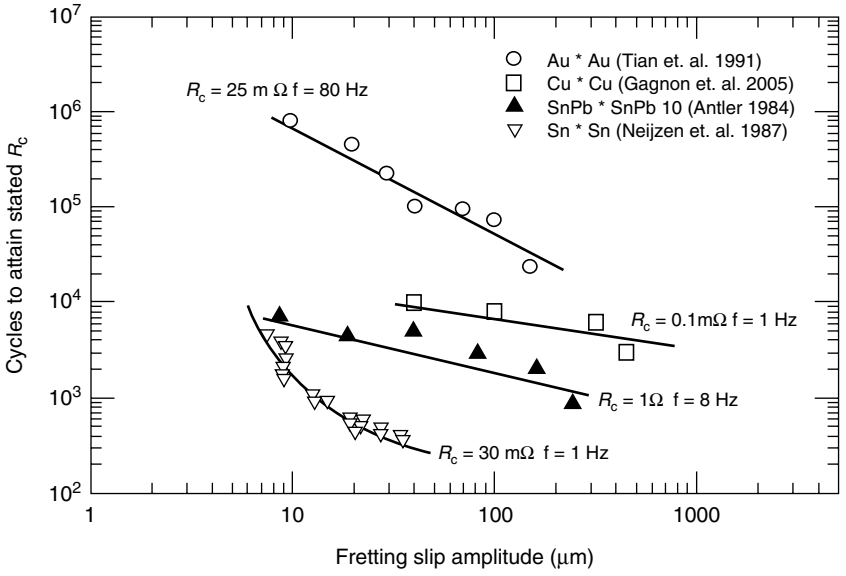

FIGURE 6.18 Number of fretting cycles required to attain predetermined contact resistance level as a function of fretting slip amplitude.

Introduction of an aqueous solution into a fretting zone may influence the fretting process in one or both of two distinct ways. Firstly, the liquid can serve as a lubricant, thus separating the metal surfaces and reducing adhesion, friction and wear rates. Secondly, a liquid may induce an anodic corrosion reaction within the fretting scar, causing the corrosion products to be trapped in the scars and thus increasing the rate of wear. The effect of relative humidity on contact resistance of copper-to-copper pair fretting under different relative humidity is shown in Figure 6.19.[480]

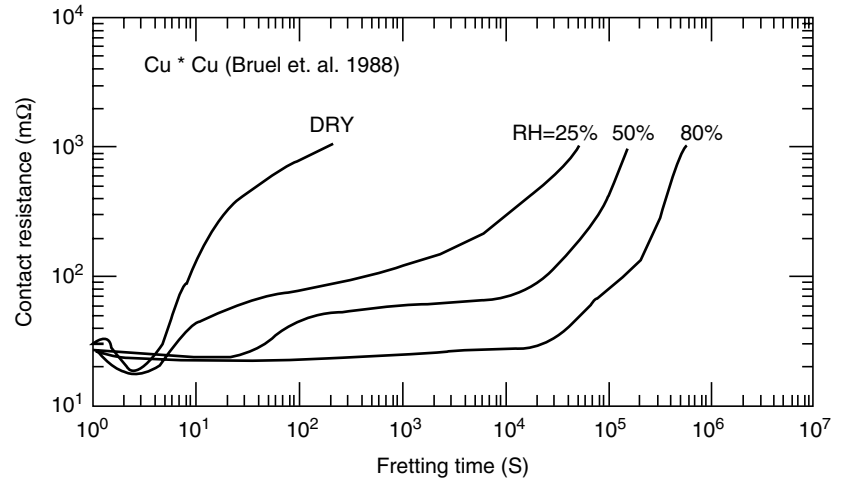

FIGURE 6.19 Effect of relative humidity on the evolution of contact resistance under fretting condition. (From Bruel, J. F., Smirou, P., and Caraballeria, A., *Proceedings of 14th ICEC*, Paris, 219–223, 1988.)

The effect of relative humidity is apparently negligible in the case of nickel-, bold- and silver-based contacts.[480,481]

6.4.4.8 Temperature

The effect of temperature on the fretting process is manifested in two ways: changing the rate of oxidation or corrosion with temperature and affecting the mechanical properties of the materials. The effect of temperature on the contact resistance of tin-plated copper alloy under fretting conditions at elevated temperatures was investigated by Lee et al.[482] The tests were carried out at 35, 60, 85, and 110°C in a specially designed fretting assembly whereby the coupons tested were heated by a steady flow of hot fluid through a reservoir inside the assembly. The fluid was supplied by a heater-circulator that maintained the fluid temperature to within 0.1°C. The results shown in Figure 6.20 indicate that up 60°C, the number of cycles to failure decreased whereas at higher temperature the trend was reversed. Oxidation of tin at temperatures bellow 60°C was the main cause for the increased susceptibility of tin-plated samples to fail. At temperatures above 60°C, softening of tin plating occurs, thus enlarging the contact area and thus reducing of the effective track length and lowering the rate of degradation.

It should be pointed out that although the elevated temperatures can bring some improvement to the performance of tin plated samples, other base metals with higher softening temperature may not have the same tendency. Furthermore, higher temperatures will definitely provoke the formation of intermetallic compounds at the tin–copper interfaces, as it will be discussed in the sections that follow.

6.4.4.9 Effect of Current

The passage of current across the contact interface may affect surface film formation, interface topography and provoke interface heating, structural changes in near-surface regions and

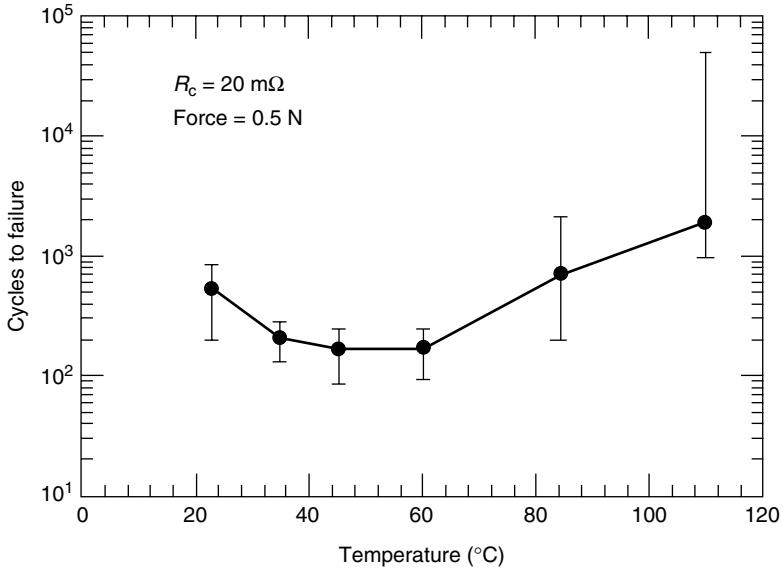

FIGURE 6.20 Cycle to failure as a function of temperature as derived from the fretting corrosion characteristics for contact force 0.5 N. Failure is defined by the contact resistance attaining 20 mΩ for the first time. (From Lee, A., Mao, A. and Mamrick, M. S., *Proceedings of 34th IEEE Holm Conference on Electrical Contacts*, 87–91, 1988. With permission.)

microarcing. As a result, the profound changes in the contact resistance would occur. Bowden and Williamson[406] have shown that for any given current there is a certain critical degree of constriction through which it will just pass without causing a permanent change in the contact region. In other words, if the current flows through a contact area that presents a constriction resistance greater than this critical value, then the heat generated will be sufficient to cause the yield pressure of the metal near the interface to fall, and the area of contact will increase accordingly. The critical constriction resistance associated with any current has been found to be inversely proportional to the magnitude of the current.

In light of these statements, it is rather surprising, however, that the effect of current on the contact resistance behavior of samples undergoing fretting was not given wider attention. Braunović[483] examined the effect of electrical load (10–500 mA) on the contact resistance behavior under fretting conditions of aluminum wire in combination with different plating materials (Ag, Cd, Ni, Sn, and Zn). It was shown that the onset and large fluctuations of contact resistance were delayed by higher currents. The effect of electrical load was attributed to fritting, that is, the breakdown of the insulating layer by high electrical fields. Bearing in mind that the true area of metallic contact is much smaller than the area of mechanical contact, it is conceivable that at higher current levels, localized high-current densities are generated capable of rupturing the layer of oxides and wear debris formed during fretting.

Subsequently, the effect of current on the contact resistance behavior of tin-plated copper contacts under fretting corrosion conditions was investigated in detail by Lee and Mamrick.[462] The results shown in Figure 6.21 depict the contact resistance (a) and contact voltage (b) as a function fretting cycles and the electrical current. The results indicate that the contact resistance behavior was characterized by the presence of fluctuating resistance plateaus delaying further resistance rise. Lower and longer resistance plateaus were the result of higher currents and applied voltages.

These resistance plateaus are consistent with the physical picture so that the current through the contact constriction causes the contact spots to thermally runaway until melting of tin occurs (the first plateau). With further corrosion giving higher resistance and more heating, the temperature can rise further to the melting, sublimation, and decomposition of the oxides, and even up to the vaporization of tin collectively forming the second contact resistance or voltage plateau.

The effect of current on fretting degradation of hot-dipped tin contact was recently evaluated by Alamarguy et al.[484] The tests were carried out at currents ranging from 10 mA to 1 A. The presence of plateaus in the contact voltage dependence on the fretting cycles was observed. Apparently, the applied current determined the occurrence of plateau, that is, the higher the applied current, the lower the number of cycles at which this plateau is reached. For the tests at 10 and 100 mA the voltage strongly fluctuates over a few μm while for tests at higher currents the local values of the voltage are fairly constant around a same level. The average value of the plateau of V_{av} is about 0.5 V. Although the effect of contact heating was considered as a possible explanation for the observed effect, the limiting effect of voltage occurring during fretting could not. Electrostatic effects in granular oxide interface were considered as an alternative explanation for the observed effect of current.

More recently, Gagnon and Braunović[485] investigated the effect of fretting in copper-to-copper contacts under AC (60 Hz) and DC current conditions. The fretting frequency was 1 Hz, slip amplitude 100 μm and current 50 mA. The results showed that the overall contact resistance behavior of copper-to-copper wire-plate couples under AC and DC current was practically the same as illustrated in Figure 6.22. The characteristic feature of the samples under AC current conditions is a pronounced distortion of the contact voltage (Figure 6.23a), and the presence of large amounts of flake-like fretting debris widely scattered around the contact zone (Figure 6.23b). However, fretting debris in the samples fretted under DC conditions are compacted and without the flake-like debris.

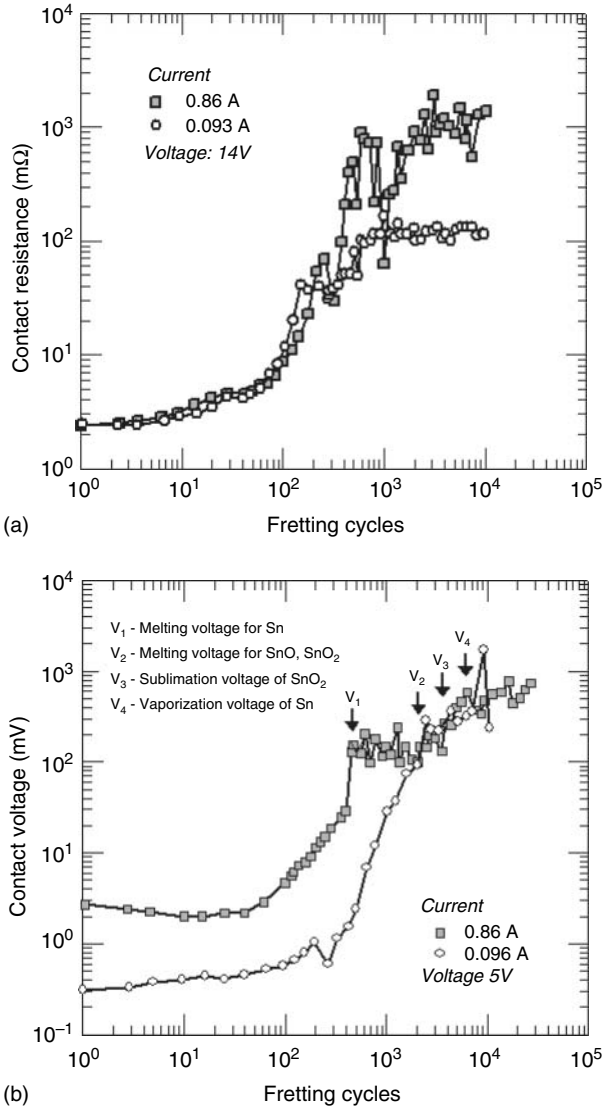

FIGURE 6.21 Contact resistance (a) and contact voltage (b) as a function of fretting cycles at two different current levels: 0.86 and 0.096 A. (From Lee, A., Mao, A., and Mamrick, M. S., *Proceedings of 34th IEEE Holm Conference on Electrical Contacts*, San Francisco, 87–91, 1988. With permission.)

6.4.4.10 Surface Finish

It is a general observation that the higher the degree of surface finish, the more serious is the fretting damage. Rough surfaces have a higher plasticity index than smooth surfaces so that some plastic deformation will occur at the tips of the asperities but work hardening is likely to prevent them being completely flattened, allowing the sharper asperities on a rough surface to take up more of the tangential movement by elastic deformation. Also on a rough surface there is more possibility of debris being able to escape from areas of contact and settling in adjacent hollows in the surface.

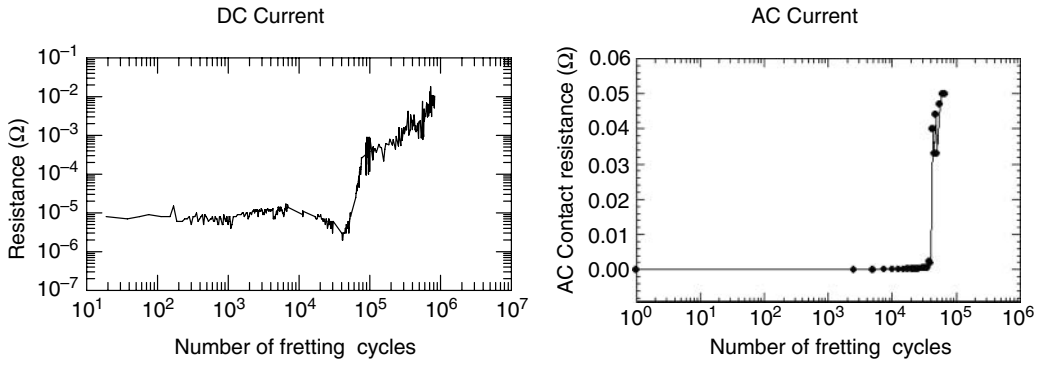

FIGURE 6.22 Effect of fretting on the DC and AC contact resistance of copper-to-copper wire-plate contacts. Fretting conditions: contact load 400 grf, fretting frequency 1 Hz, slip amplitude 100 μm; current 50 mA. (From Gagnon, D. and Braunović, M., *IEEE Trans. CPT*, 24, 378–383, 2001.)

6.4.4.11 Hardness

Hardness can influence fretting behavior in two ways. Higher hardness implies higher ultimate tensile strength and higher fatigue strength. In so far as fretting damage involves breakdown of the surface by local high-stress fatigue processes, a decrease in damage is to be expected with an increase in surface hardness. Secondly, the abrasive action of oxide debris is a factor in fretting corrosion, and, therefore, the harder the surface, the higher the abrasion resistance, and the less the damage. In particular, the relative hardness of the debris and the surface would seem to be an important factor.

The effect of hardness of the contacting metals is inseparable from the hardness and strength of bonding of the oxide film. Combinations of similar metals with different hardnesses and surface finishes will have the best resistance to fretting. It is likely that combinations of metals showing poor alloying tendencies will be more resistant to fretting than those that alloy readily. Surface treatments that increase the hardness would be expected to reduce fretting wear and delay the onset of contact resistance degradation.

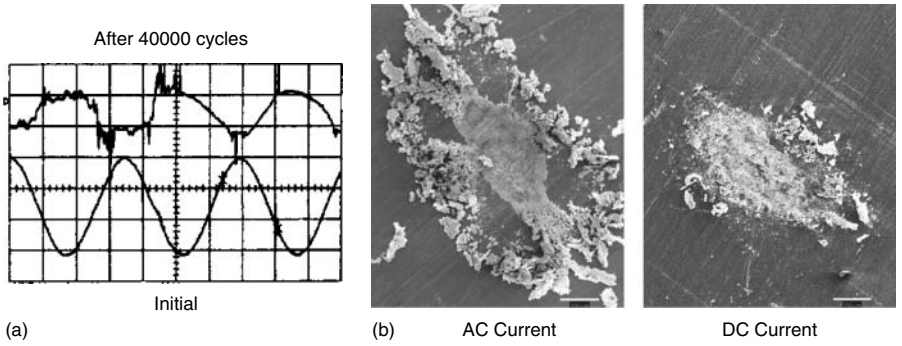

FIGURE 6.23 (a) Contact voltage wave forms initial and after 40,000 fretting cycles. (b) SEM images of the contact zones after 40,000 fretting cycles under AC and DC current conditions. (From Gagnon, D. and Braunović, M., *IEEE Trans. CPT*, 24, 378–383, 2001.)

6.4.4.12 Metal Oxide

The properties of the metal oxide formed during fretting significantly affect the extent and the kinetics of fretting damage. The oxide debris produced by fretting action will increase the coefficient of friction and act as an abrasive to increase the surface damage. Bowden and Tabor[23] have shown that the relative hardness of the underlying metal plays the primary role in determining the wear rate. In other words, a hard metal producing a soft oxide will resist fretting wear, whereas a soft metal producing a hard oxide may result in a severe wear. The effect of metal oxide is further complicated by the variation in the strength of the metal-oxide bond.

In the case of fretting with identical original contact materials, both surfaces become oxidized. Because oxides are much less plastic than their underlying parent metals, when mated materials differ in harness, the harder material partially supports the softer materials and inhibits cracking of the oxide. Oxide fracture is a necessary requirement for metal contact and low contact resistance, but when the metals have similar hardnesses, there is more extensive fracture of the oxide film. Furthermore, there is a higher degree of superposition of the cracks, which facilitates establishment of the bridges extruding through them.[486] This hypothesis was supported by an experiment that showed that there was a significantly higher contact resistance of a gold contact thinly coated with tin–lead, mated without wipe to heavily oxidized tin–lead compared with that of a contact with thick tin–lead plating joined to the same oxidized tin–lead specimens.[455]

6.4.4.13 Coefficient of Friction

If the length of the slip amplitude is short, it may be possible to prevent a slip by raising the coefficient of friction because, for the slip to occur, the product of the normal force and the coefficient of friction must be exceeded by the tangential force. High friction will, however, cause severe plastic deformation and fatigue failure of the contacts. Wear particles, generated by the accumulation of plastic strain and the interface failure, will result in plowing, thus increasing the friction and accelerating damage to the contacting surfaces.

On the other hand, if a slip is unavoidable, a low coefficient of friction is desirable because a low friction causes no plastic deformation of the contact surface and may result in elastic sliding. Nevertheless, the plastic deformation of the contacting surfaces is inevitable even for very low friction because a contact is in the elastic–plastic regime whenever a friction force exists, but the magnitude of plastic strain and the extent of plastically deformed region may be reduced by decreasing friction.

6.4.4.14 Electrochemical Factor

An extensive amount of work by Russian authors[487] suggests that fretting wear damage in steel decreases as the electrode potential of the opposing member becomes more negative with respect to steel. In other words, materials such as Zn and Cd that have electrode potential more negative than steel would provide a better protection from fretting wear because these would wearoff more intensively than steel. On the other hand, when steel is in contact with Pb, Sn, or Ag, the steel would wear more than its counterpart.

6.4.5 Intermetallic Compounds

Bimetallic welds, particularly, aluminum-to-copper are increasingly being used in a variety of electrical applications. Such joints, made by friction welding, pressure welding, diffusion and roll bonding, flash welding and explosion welding, are characterized by a relatively stable joint interface and negligible intermetallic formation. In service, however, frequent current surges on the network may generate favorable conditions for interdiffusion to occur and, thus, nucleation and growth of intermetallics at or near the initial interface. This, in turn, can seriously impair the overall

electrical stability and mechanical integrity of bimetallic joints because intermetallic phases have much higher electrical resistance and lower mechanical strength.

Some authors found that tensile strength, ductility, impact resistance and electrical resistance of flash-welded aluminum-to-copper joints are practically unaffected by thermal treatment from two years at 149°C to 5 min at 371°C.[488] However, more recent investigations of roll-bonded,[489–492] hot-pressed[493] and flash-welded[169,493,494] aluminum-to-copper joints showed that the mechanical and electrical properties are significantly affected by the formation and growth of intermetallics at the joint interface. It was shown that, when the total width of intermetallic phases exceeds 2–5 μm, the aluminum-to-copper joint rapidly loses its mechanical integrity.[489,490] The formation and deleterious effects of intermetallics in electronic (soldered) connections and integrated circuit devices, principally copper–tin based alloys, will be discussed in Chapter 7.

The deleterious effect of intermetallic phases is reflected in the greater brittleness of the contact interface and significantly higher resistance. Figure 6.24a depicts the intermetallic phases formed at the interface of an aluminum–copper contact while Figure 6.24b illustrates the brittleness of the intermetallic phases formed at the Al–Cu interface in samples diffusion annealed by an electric current. The composition and characteristics of intermetallic phases formed in the aluminum-to-copper joints are shown in Table 6.2. Data for resistivity, diffusion rate constants, and activation energy were taken from Rayne and Bauer,[494] whereas the hardness data were experimentally determined at 0.4 N (40 g).[165]

To illustrate the importance of interdiffusion and the formation of intermetallic compounds, let us use the following example. The process of diffusion is controlled by the following expression:

$$D = D_0 \exp(-Q/RT), \tag{6.4}$$

where D_0 is a constant, Q is the activation energy for diffusion and R is the universal gas constant. In the case of aluminum–copper, the activation energy for diffusion of aluminum is of the order $Q = 40$ kcal/mol. Hence the diffusion rates at temperatures T_1 and T_2 ($T_2 = T_1 + \Delta T$) will be

$$\begin{aligned} D_1 &= D_0 \exp(-Q/RT_1) \\ D_2 &= D_0 \exp(-Q/RT_2) \\ D_2/D_1 &= \exp[Q/R(1/T_1 - 1/T_2)] \end{aligned} \tag{6.5}$$

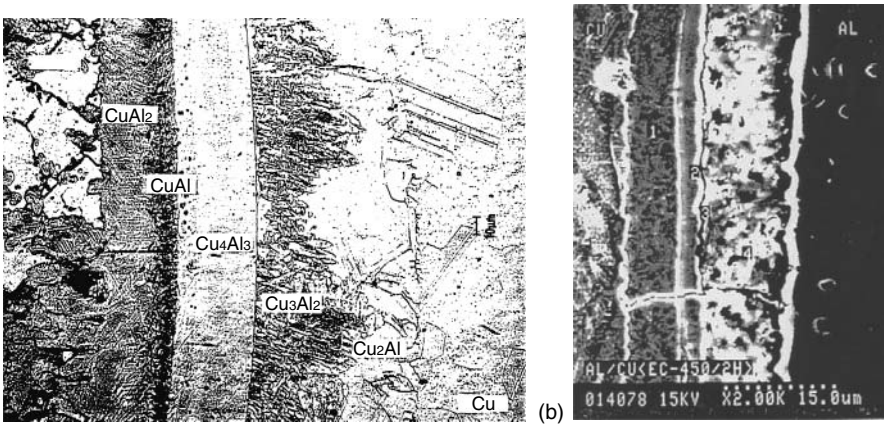

FIGURE 6.24 (a) Microstructure of the intermetallic phases formed at the interface of Al–Cu contact under the influence of thermal gradient. (b) Cracks formed in the Al–Cu bimetallic layers illustrate the fragility of intermetallics.

TABLE 6.2
Important Characteristics of Phases Formed in the Bimetallic Aluminum-to-Copper Systems

Private phase	Symbol	Compsn	Cu (wt%)	Al (wt%)	Hardness (kg/mm^2)	Resistivity (μΩ cm)	D_0 (cm^2/s)	Q (kcal/mol)
Phase 1	γ_2	Cu_2Al	80	20	35	14.2	3.2×10^{-2}	31.6
Phase 2	δ	Cu_3Al_2	78	22	180	13.4	2.6×10^{-1}	33.5
Phase 3	ζ_2	Cu_4Al_3	75	25	624	12.2	2.7×10^{6}	61.2
Phase 4	η_2	CuAl	70	30	648	11.4	1.7×10^{-6}	19.6
Phase 5	θ	$CuAl_2$	55	45	413	8.0	9.1×10^{-3}	29.3

Note: Data for the resistivity, diffusion rate constant D_0 and activation energy Q were taken from Gjosten,[495] whereas hardness was measured at 0.4 N (40 g).[165], The hardnesses of aluminum and copper were 38 and 42 kg/mm^2, respectively.

Using Equation 6.3, one can determine that the temperature rise required to double the diffusion rate $D_2/D_1 = 2$ at $T_1 = 60°C$ is calculated to be $\Delta T = 4°C$. Because of the current constriction, the *a*-spot may develop a higher temperature; the diffusion rates at the *a*-spot can be considerably higher than in the bulk. To prove this point, let us assume that the *a*-spot is at $T_2 = 300°C$ and the bulk at $T_1 = 60°C$. Then the calculated diffusion rate at the *a*-spot will be 10^{12} faster than that in the bulk. Under these conditions, the formation of intermetallics is very likely to occur.

It is now a well established fact that accelerated diffusion can occur via some short-circuit diffusing paths rather than through the lattice. Such paths, called "pipe diffusion," can be dislocations, grain boundaries, and subgrain boundaries. Diffusion along these paths is found to be considerably faster (a few orders of magnitude) than diffusion of the same species through the lattice.[495]

The formation and growth of intermetallic phase aluminum–brass and zinc-, indium- and tin-plated brass systems has been extensively studied by Timsit.[496] It was shown that intermetallic growth could not generally be described satisfactorily by a single activation energy over the entire temperature ranges used but rather by considering the data from the temperature ranges 150–300 and 350–450°C separately. For temperatures 150–300°C, the activation energies were in the range 16.8–23.4 kcal/mol whereas for the temperatures 250–450°C, the activation energies were in the range 31.5–50.7 kcal/mol. Considerably smaller activation energies for temperatures below 300°C were associated with the short-circuit diffusion mechanism such as grain boundary or dissociated dislocation diffusion.

6.4.5.1 Effect of Electrical Current

In view of the strong influence that electric current exerts on the mass flow in conductor and contacts, it is rather surprising that the effect of electrical current on diffusion in dissimilar metal junctions and the formation of intermetallic phases have not been investigated. Nevertheless, the problem has been treated both theoretically and experimentally by Gusak[497] and Pimenov,[498] who have shown that the current exert a considerable effect not only on the diffusion but also on the kinetics of nucleation and formation of intermetallic phase in bimetallic systems.

The effect of electrical current on the morphology and kinetics of formation of intermetallic phases in friction-welded aluminum-to-copper joints was studied by Braunović and Alexandrov.[165] The formation and growth of intermetallic phases by heating the aluminum–copper joints with an AC current of different intensities (400–100 A) maintaining the temperature range of 200–500°C and also in a temperature gradient in the range 250–515°C.

Following diffusion annealing, the contact resistance across the aluminum–copper interface was measured using the high-precision microohmmeter with a resolution of 0.01 μΩ operating on current pulses of 10 A and 17 ms duration. A simplified schema used for resistance measurements is

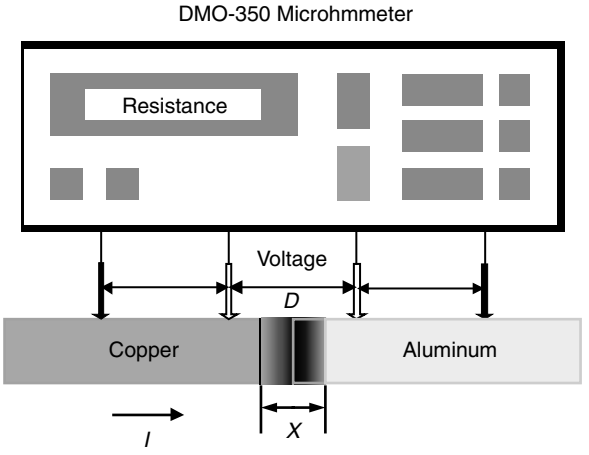

FIGURE 6.25 Simplified schematic of the assembly used to measure resistance of aluminum–copper bimetallic contacts.

shown in Figure 6.25. The separation between the potential probes was approximately 3 mm. The resistance changes due to the formation of intermetallic phases at the aluminum–copper interface were sufficiently large to be measured between the potential probes.

The resistance rise resulting was determined by averaging ten resistance measurements made across this interface after selected time intervals at each of the diffusion annealing temperatures. The results are shown in Figure 6.26. Within the scatter of experimental data, the rate of resistance

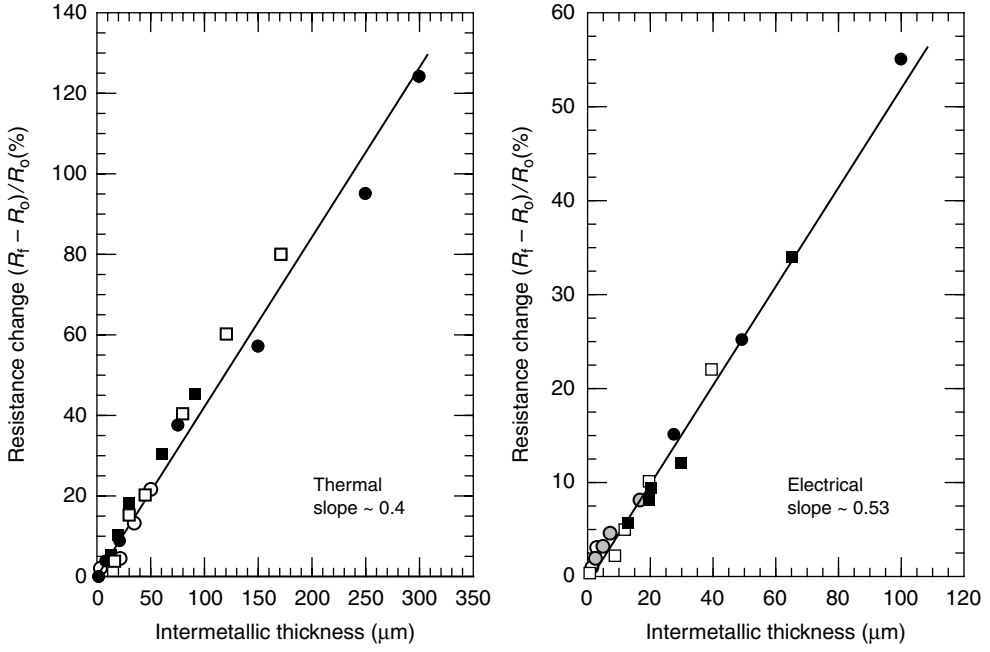

FIGURE 6.26 Growth of contact resistance with thickness of the intermetallic phases formed at the Al–Cu bimetallic joints after heat treatment by thermal gradient and an electrical current at different times and temperatures.

rise across the Al–Cu interface and thickness (x) of the intermetallic layers formed can be approximated by a linear relationship

$$(R_f - R_0)/R_0 = Ax \tag{6.6}$$

where R_0 and R_f are the resistances measured across the Al–Cu interface before and after diffusion treatment; A is the proportionality constant with the value of 0.4 for samples diffusion annealed in thermal gradient and 0.5 for the samples diffusion annealed by electrical current. From the resistance days it can be inferred that the rate of formation of intermetallic phase under the influence of electrical current is much faster than under thermal gradient.

The resistivity of the intermetallic layers in the aluminum-to-copper bimetallic joints can be calculated from weighted averages of resistors in series by the following expression

$$R = (1/A) \ni \rho i x i \tag{6.7}$$

where A is the cross-sectional area of the bimetallic joint; ρ_i and x_i are the resistivity and the thickness of each of the component. The resistivity of the total intermetallic layer in aluminum-to-copper bimetallic joints can be expressed as

$$\rho_t = (1/x_t)[RA - (d/2)(\rho_{Al} + \rho_{Cu})] \tag{6.8}$$

where x_t is the thickness of the total intermetallic layer (microns); $\rho_{Al} = 2.4$ μΩ cm and $\rho_{Cu} = 2.0$ μΩ cm are the resistivities of aluminum and copper, respectively; $d = (D - x_t)$; $D = 0.3$ cm is the spacing between the potential probes. The calculated value of the resistivity of the total intermetallic layer in Al–Cu heat-treated solid-phase joints is $\rho_t = 18.5$ μΩ cm.

The values of resistivity for the individual phases range between 8 and 14.2 μΩ cm (Table 6.2). Hence, the observed difference is beyond the experimental error, indicating that there are additional contributions to the total resistivity attributed to porosity, cracking, grain size changes and increased dislocation density in the diffusion zone. These defects constrict the current flow across the interface and considerably reduce the effective contact area (A) thus, as a result, increasing the resistivity of the total intermetallic layer.

From the results presented, it is clear that complex structural processes occur at the contact interface during the action of the electrical current, as a result of which the mode and kinetics of formation and growth of the intermetallics are significantly altered.

One possibility is that the observed effect might be associated with the materials transport by electromigration.[499] It is now well established that in electromigration the material transport occurs via interaction between the atoms of a conductor and a high density current of the order of 10^3–10^5 A/cm^2. On the other hand, electromigration is not expected under the low-current densities or AC conditions. Therefore, because AC current of comparatively low density ($< 10^3$ A/cm^2) was used in the present work, electromigration alone is unlikely to be the operating mechanism responsible for the observed accelerated formation of the intermetallic phases in electrically heat-treated Al–Cu bimetallic joints.

An alternative is that accelerated formation of the intermetallic phases is a result of an enhanced diffusion of some species, most probably copper. The enhancement may result from the concentration of vacancies and interstitials exceeding their respective equilibrium values, thus increasing proportionally the contributions from the vacancies and interstitials to the diffusion rates. Indeed, an extensive experimental and theoretical work in the general area of the behavior of irradiated materials showed that the atomic mobilities can be increased under ion irradiation by many orders of magnitude. This, although being a rather attractive possibility, is unlikely because it is inconceivable that a relatively low density current can produce marked changes in the vacancy and interstitial concentrations as in the case of irradiated materials.

Another possible mechanism is that accelerated diffusion occurs via some short-circuit diffusing paths rather than through the lattice. Such short diffusion paths, called "pipe diffusion" can be dislocations, or grain and subgrain boundaries. Diffusion along these paths is found to be considerably faster (several orders of magnitude) than diffusion of the same species through the lattice.[495]

If the "pipe diffusion" is the operating mechanism, then the kinetics of the intermetallic phase formation and growth leads to the conclusion that the mobility of diffusing species, probably copper, is much greater in the presence of an electric field than in the temperature gradient. Hence, it is believed that interaction between the applied electric field and lattice defects notably dislocations and grain boundaries, enhance the migration of the diffusing species along the short-circuit diffusion paths and thus accelerate the formation of the intermetallics. The effect of electrical current on the formation and growth of intermetallic phases deserves more attention because the electrical connections are constantly under the action of electric current.

Another important feature of the effect of electrical current on the formation of intermetallics in Al–Cu bimetallic joints is the absence of certain phases as seen in Figure 6.24b. In other words, the growth of these phases from their critical nuclei is apparently suppressed by diffusion interaction with the critical nuclei of neighboring phases having greater diffusion permeability.[497] This finding agrees well with the results of the study dealing with the effect of electrical current on the formation and growth of intermetallic phases in Al–Au system.[496] These results demonstrated that electrical current can accelerate or suppress the growth of certain phases.

As in the case of aluminum–brass system, the activation energy for the growth of the intermetallics in aluminum–copper systems heat treated either in thermal gradient or by an electrical current, could not be described by a single activation energy over the entire temperature range but rather by considering two separate regions, i.e., 200–350 and 360–525°C, as shown in Figure 6.27.

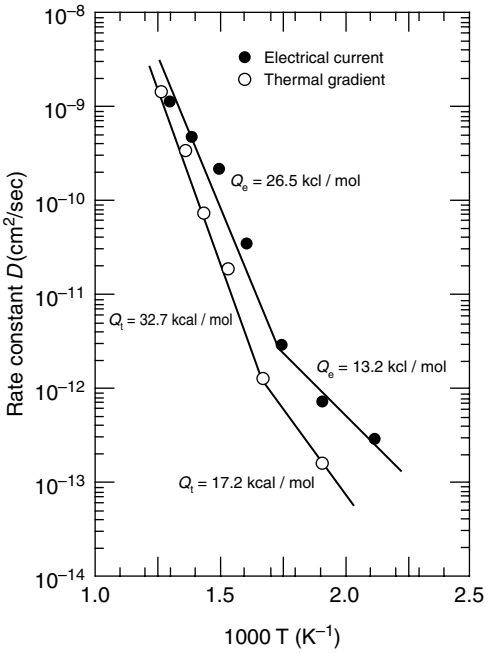

FIGURE 6.27 Arrhenius plot of the rate constant D for growth of the diffusion layers in Al–Cu bimetallic samples diffusion annealed by thermal gradient (furnace) and by an electrical current. Q_e and Q_t indicate the activation energies for samples treated by an electrical current and by thermal gradient.

The activation energy characterizing the growth of intermetallic phases in Al–Cu interfaces was determined based on the relationship between the thickness of the intermetallic layers formed (x) and the time (t) at a given temperature as expressed by

$$x^2 = Dt, \tag{6.9}$$

where D is the interdiffusion rate constant at the selected temperature and expressed by Equation 6.4.

For the samples diffusion annealed by an electrical current, the activation energy corresponding to temperatures below approximately 350°C is considerably lower $Q_e = 13.2$ kcal/mol than that obtained for higher temperatures $Q_e = 20.5$ kcal/mol. For the same temperature range, these values are significantly lower than those obtained for the samples diffusion annealed in a temperature gradient, i.e, $Q_t = 17.2$ kcal/mol and $Q_t = 32.2$ kcal/mol.

From the above described results, it can be inferred that both the rate and the total diffusion bandwidth of the intermetallic phases formed under the influence of electrical current are higher than in samples diffusion annealed under thermal gradient. These results are in contrast with those obtained in the case of roll-bonded aluminum-to-brass because no effect of electrical current on the intermetallic growth was found.[430]

A plausible explanation for the apparent disaccord concerning the effect of electrical current on the formation and growth of intermetallics is that in[430] electromigration was considered as the only possible driving mechanisms for the intermetallic growth. However, as pointed in the preceding discussion, electromigration was not considered as a driving mechanism but rather an accelerated short-circuit diffusion of most likely copper via grain grain-boundaries or dislocations.

Further support for the electrical current enhanced intermetallic formation and growth stems from the work of Silveira et al.[500] The tests were carried out under the influence of an electrical current of 10 A/mm^2 sufficient to raise the conductor temperature to 100°C and thermal gradient at 100°C in both cycling and continuous modes. Electrical current exerts a significant effect on the kinetic of intermetallic phase formation in the Cu–Sn/Pb coating on aluminum wire as manifested by much faster formation of phase Cu_3Sn under the influence of electric current as compared with that under the thermal gradient at 100°C. This phenomenon is illustrated in Figure 6.28.

The most important feature of the results shown in Figure 6.28 is the kinetics of formation of Cu_3Sn and Cu_6Sn_5 phases in the coating. It is evident that that under the thermal gradient, the phase Cu_6Sn_5 forms at the later stages of heat treatment, whereas under the electric current conditions, this phase is formed much faster, as seen in Figure 6.28. The observed enhanced formation kinetics of the Cu_6Sn_5 intermetallic phase under the effect of electric field were associated with the short-circuit diffusion ("pipe diffusion"), most likely of copper, along the grain boundaries and dislocations.

Most recent studies of the effects of electrical currents in the range of 500–1000 A/cm^2 in Sn/Ag, Sn/Ni, and Al/Ni have clearly shown that the passage of electric current[501–503] can enhance or retard the growth of the reaction layers in these systems. For instance, in the case of AlNi, the thickness of the intermetallic layer was 15 μm after annealing for 336 h, but with identical annealing time and the passage of electric current of 1000 A/cm^2, the thickness of the intermetallic layer was 45 μm. The intermetallic phases formed in both cases were the same Al_3Ni and Al_3Ni_2. It was suggested that the electric current enhances the nucleation rate of the Al_3Ni_2 phases and thus the growth rate of the intermetallic layers. Furthermore, it was also shown that the effect of electromigration becomes more significant with higher current densities but decreases with increasing temperature.[503]

Further studies are needed to elucidate the exact nature of the observed effect of an electric current on the kinetics of formation and growth of intermetallic phases in bimetallic joints. This is of particular interest because there is mounting evidence indicating that mechanical properties such

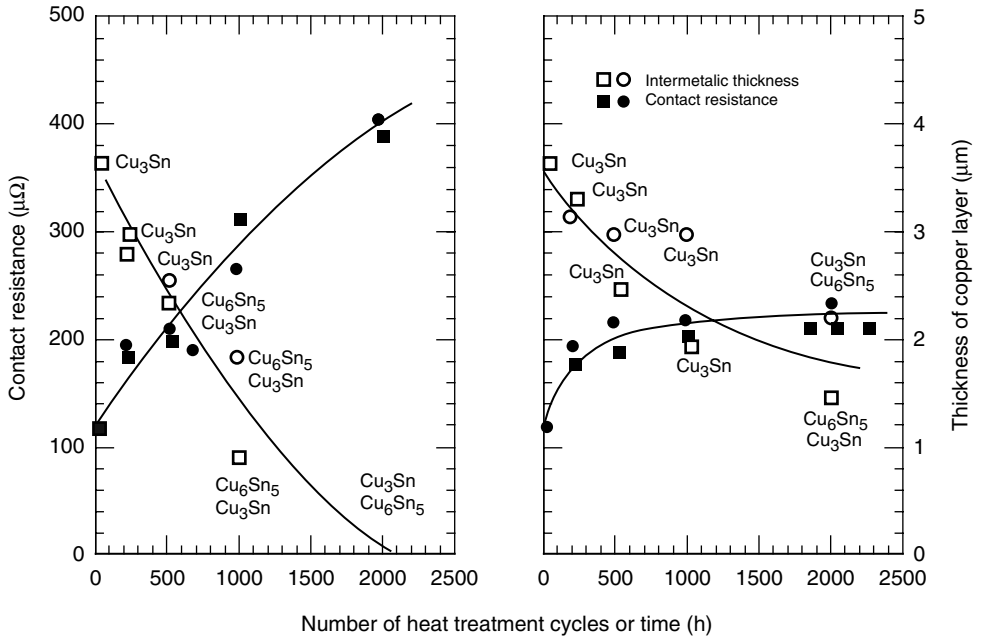

FIGURE 6.28 Contact resistance and thickness of intermetallic phases formed in the Cu–Sn/Pb coating on aluminum wire under the influence of electrical current and thermal gradient. The presence of the intermetallic phases Cu_6Sn_5 and Cu_3Sn are also indicated.

as creep, stress relaxation, flow stress, and also recrystallization, recovery and grain growth can be significantly altered and the structure changed by the action of electrical current (see Section 6.4.7).

6.4.6 Electromigration

Electromigration is defined as the forced motion of metal ions under the influence of an electric field. It is one of the most deleterious failure mechanisms in interconnects of large scale integrated microelectronic devices.[504] The migration occurs predominantly via grain boundaries leading, eventually, to voids and extrusions near grain boundary triple points and to a failure of an entire device. The atomic flux (J) can be expressed as

$$J = \frac{D}{kT} j\rho e Z^* \tag{6.10}$$

$$D = D_0 \mathrm{e}^{-Q/kT}$$

where D is the diffusion coefficient, j is the current density, ρ is the electrical resistivity and eZ^* is the effective charge, k is the Boltzmann constant, T is the absolute temperature, D_0 and Q are the diffusivity constant and activation energy for diffusion, respectively. The atomic drift velocity v_e is usually expressed as

$$v_e = \frac{j\rho D e Z^*}{kT}. \tag{6.11}$$

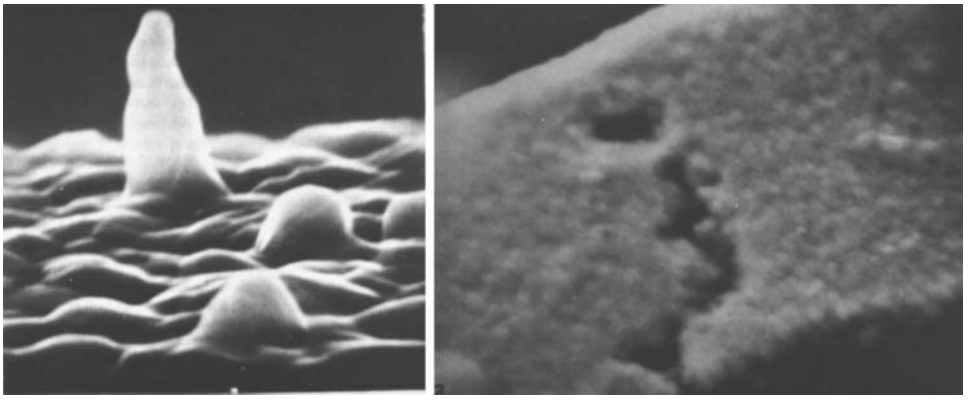

FIGURE 6.29 SEM images of the hillocks and void formation in aluminum thin-film interconnection lines. (From Hummel, R. E., *International Materials Reviews*, 39, 97–111, 1994. With permission.)

As a result of electromigration, hillocks or voids would form that eventually coalesce and grow leading to a failure. Voids and hillocks are preferentially formed whenever a gradient in temperature, grain size, geometric features, current density, crystal orientation of the grains etc. occurs.[505] The formation of voids and hillocks is illustrated in Figure 6.29.[506]

Despite the use of different mitigating measures such as alloy additions to Al, multiple layer interconnects, alternate deposition techniques, or different base metals such as Au or Cu, a complete elimination of all electromigration-induced failures, has not been found. Furthermore, a steadily increasing number of devices being accommodated on a single chip aggravates the situation even further. As a consequence, the active elements on a chip become smaller, and the connecting stripes are made narrower, which causes an increase in current density and thus a greater potential for electromigration-induced failure.[504] A comprehensive review of the electromigration in thin-film interconnection lines has been given by Scorzioni et al.[506]

Although in bulk electrical contacts electromigration has not previously been associated with the deterioration of contact spots, the current density in the *a*-spots of a practical contact can be substantial, thus creating favorable conditions for the electromigration to occur. Hence, electromigration should be considered as one of the important parameters affecting the reliability and degradation of bulk electric contacts.

Electromigration deterioration of *a*-spots in aluminum contacts has been extensively studied by Runde et al.[507,508] in Al–Al and Al–AlZn alloys using both AC and DC currents. Mass transport by electromigration appears to influence both the mechanical and the electrical properties of a contact spot. In aluminum contacts, the atoms tend to migrate toward the anode, and hence an accumulation of vacancies occurs a short distance inside the cathode contact member. The high vacancy concentration causes considerably lower mechanical strength and higher electrical resistivity in these areas.

More recently Ruppert and Runde[509] investigated thermally induced mechanical degradation of contact spots in aluminum interfaces under DC and AC current conditions. The results showed that in both cases ageing and deterioration lead to contact spot fracture of increasing size, whereby the cracks appeared some distance inside the contact members as shown in Figure 6.30. The cracks severely reduced the electrical conductivity of the area, forcing the current to take new paths, thus increasing the contact spot size without lowering the resistance of the contact.

It was pointed out, however, that the physical mechanisms creating the cracks are apparently not the same. Under DC conditions, the very high current densities found in the contact spots were causing a net mass transport by electromigration parallel to the electron flow.[508] Atoms migrated

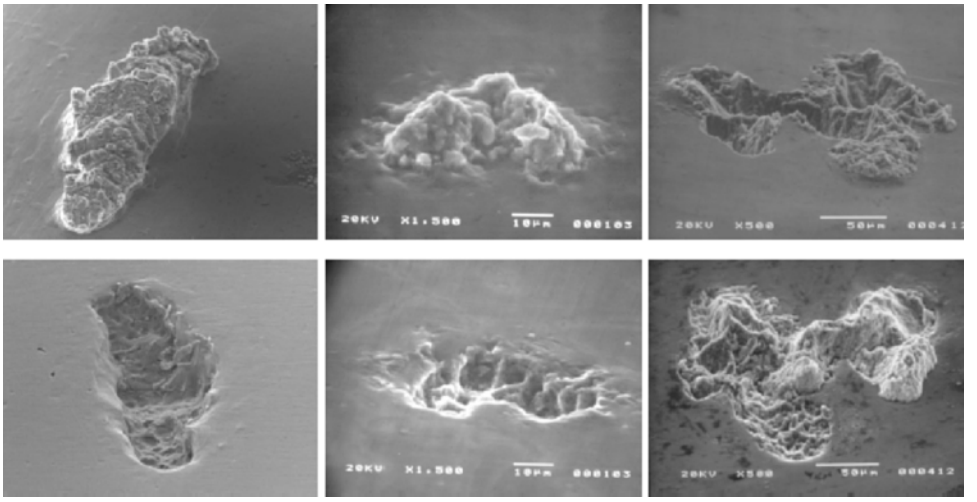

FIGURE 6.30 SEM images of corresponding contact spot fractures from DC (left), rectified AC (center) and AC (right) experiments. (From Ruppert, C. and Runde, M., *Proceedings of 22nd ICEC*, Seattle, 494–501, 2004.)

out of the cathode and into the anode, leaving behind vacancies and voids that clustered to crevices and cracks. When separating the contact members, the interface always broke some distance inside the cathode, yielding an asymmetric fracture characteristic.

Under AC current, where the conditions in all respects are symmetric and cracks are found inside both electrodes, the observed fracture features were attributed to the cyclic mechanical stress and strain induced by thermal expansion and contraction in the contact spot region. This assumption is supported by the fact that samples subjected to DC current appeared to be considerably more stable, in terms of having a lower and more constant voltage drop, compared to the AC or rectified AC contacts. Also, under DC conditions, the temperature increased locally in the contact spot region, but the associated thermal expansion exerted merely a constant mechanical tension. The strong effect of AC on the deterioration and cracking of a material under AC conditions was attributed to thermal fatigue. This process can only occur if the contact voltage is very high. Hence, in practical connectors, it may occur only in already severely aged connectors, or under short-circuit conditions.

The effect of AC and DC electromigration in aluminum under the identical conditions was also investigated by Aronstein.[510,511] The specimens tested were two-dimensional models of asperity contact junctions, made of solid metal configured to avoid experimental scatter due to many of the variables inevitably encountered in experiments utilizing actual contact interfaces. To obtain the most reproducible and meaningful results, the actual metallic current-carrying area of the *a*-spot constriction was carefully controlled.

The experimental results demonstrated electromigration failure with AC as well as DC. No significance was attached to the observed difference in median time-to-failure because the sample size for each condition tested was relatively small. Electromigration in AC applications is expected in aluminum connections when current density through the *a*-spots is high. With AC, the aluminum atoms in *a*-spots at the contact interface may be considered to have double the number of available paths (relative to DC) by which to move out of the high-current–density region, but only half the current-application time in each direction. Conceptually, all other factors being equal, AC electromigration deterioration of an *a*-spot should therefore be about the same as DC.

6.4.7 Stress Relaxation and Creep

One of the most serious drawbacks when using aluminum conductors is their tendency to move toward creep and stress relaxation. Creep, or cold flow, occurs when aluminum is subjected to a constant external force over a period of time. The rate of creep depends on stress and temperature and is higher for aluminum than for copper. Stress relaxation also depends on time, temperature, and stress but, unlike creep, is not accompanied by dimensional changes. It occurs at high stress levels and is evidenced by a reduction in the contact pressure due to changes in metallurgical structure. The change from elastic to plastic strain has the effect of significantly reducing the residual contact pressure in the joints, resulting in increased contact resistance, possibly to the point of failure.

The loss of initial contact pressure can be further accelerated at elevated temperatures, causing a loss of contact area in a relatively short time. Hence, excessive conductor deformation and high stresses produced by certain connector systems having no means of providing residual mechanical loading to the contact interface cause accelerated stress relaxation and eventual failure of a joint.

The effect of the metallurgical state and temperature on the stress relaxation of aluminum and copper was investigated by Naybour et al.[512] and Atermo et al.[513] It was shown that, for electrical grade aluminum (EC-1350 grade), increasing the temperature and the amount of hardening augmented the rate of stress relaxation. It was also shown that stress relaxation in hard-drawn EC-grade aluminum conductors was anisotropic, being much faster to transverse than in longitudinal direction, and much faster in hard-drawn than annealed wire. This is shown in Figure 6.31.

Mounting evidence indicates that mechanical properties such as creep,[514–516] stress relaxation,[516–519] and flow stress,[520–523] can be significantly affected by the action of electric current. This so-called electroplasticity manifests itself in a dramatic increase in the ductility of a material. It is generally believed that the effect is a result of the interaction between electrons and dislocations, although some controversy still exists regarding the exact nature of this electron–dislocation interaction. A comprehensive overview of the electroplastic effect in metals was given by Sprecher et al.[522] In view of these remarks, it is warranted to briefly review the nature of the effect of electric current on and provide some examples of this effect on stress relaxation and creep of some metals.

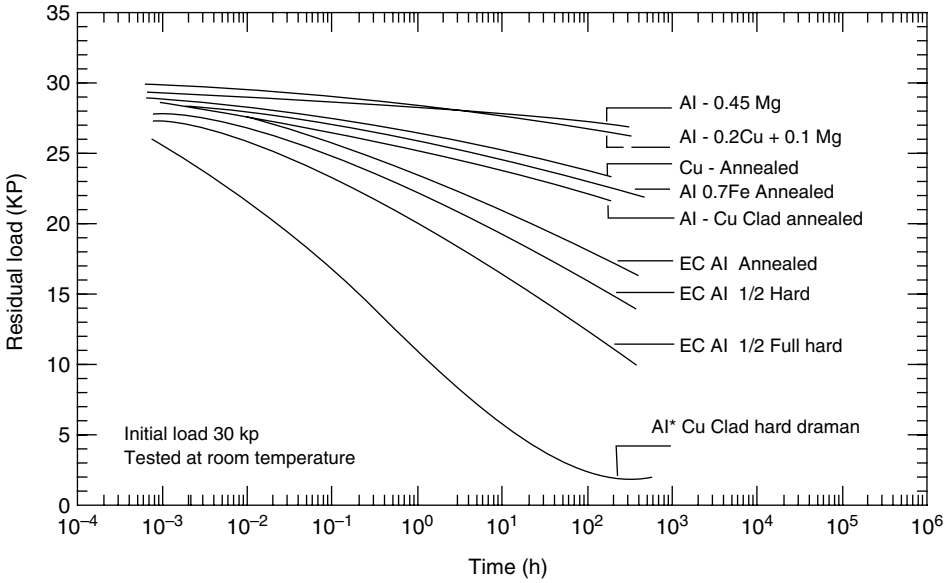

FIGURE 6.31 Effect of metallurgical state on the stress relaxation of aluminum.

6.4.7.1 Nature of the Effect of Electric Current

It is now well established that the electrons in a metal can exert a drag on dislocations, especially those moving at high speed at very low temperatures.[524–526] The electron drag, coefficient B_e is given by

$$(f/l) = \tau b = B_e V_d \tag{6.12}$$

where (f/l) is the force per unit length acting on the dislocation, τ is the resolved shear stress, b is the Burgers vector, and V_d is the dislocation velocity. The electron drag coefficient B_e has been determined for metals by a number of methods, including ultrasonic attenuation, dislocation velocity and the decrease in flow stress associated with the normal-to-superconducting transition and values in the range of 10^{-6} to 10^{-3} dyne s/cm^2 have been reported. However, more recent considerations[525,526] suggest that B_e is of the order of 10^{-5} dyne/cm^2.

The idea that drift electrons in a metal may assist dislocations in overcoming obstacles to their motion, thus, exert a push or "wind" on dislocations, in contrast to a drag was first reported by Troitskii and Lichtman in 1963.[527] They found during electron irradiation of Zn single crystals undergoing plastic deformation that a significant decrease occurred in the flow stress and noted an improvement in ductility when the electron beam was directed along the (001) slip plane compared to when it was normal to the plane. The interaction of moving electrons with the dislocations led these authors to conclude that drift electrons can exert a force ("electron wind") on dislocations and, therefore, that such a force should occur during the passage of an electric current through a metal when plastically deformed.

This finding prompted Russian scientists to conduct an extensive series of investigations into the influence of direct current pulses of the order of 10^3 A/mm^2 for approximately 50 μs duration on the mechanical properties of metals, including the flow stress, stress relaxation, creep, brittle fracture, fatigue and metalworking. High current densities were employed to enhance the effect of the drift electrons for short times to avoid Joule heating. A comprehensive review of the extensive work of Russian scientists on the electroplastic effect is given by Spitsyn and Troitskii.[528]

Theoretical considerations of the force exerted by drift electrons on dislocations are given in the papers by Kravchenko[529] and, more recently Roschupkin et al.[531] The force is considered to be proportional to the difference between the drift electron velocity v_e, and the dislocation velocity v_d thus indicating that the electron wind force (f_{ew}/l) is proportional to the current density

$$\tau_{ew} b = K_{ew} J \tag{6.13}$$

where τ_{ew} is the stress acting on the dislocation due to an electron wind, b the Burgers vector, K_{ew} is the electron force coefficient and J is the current density. These theories give a different magnitude of the constant K_{ew} which, in turn, is reflected in the value of the electron drag coefficient B_{ew} given by

$$B_{ew} = \tau_{ew} b / v_e = K_{ew} e n \tag{6.14}$$

where e is the electron charge and n is the electron density. The values of B_{ew} predicted by Kravchenko for metals are on the order of 10^{-6} dyne s/cm^2, those by Klimov et al. are 10^{-6} to 10^{-4} dyne s/cm^2 and those by Roschupkin et al. are 10^{-5} to 10^{-3} dyne/cm^2. These values are all within the range of those measured experimentally for B_{ew} although the theory of Klimov et al. gives the values in best accord with those most generally accepted.[524–526]

The electroplastic effect has been widely studied in the U.S. by Conrad and co-workers,[522,523,532–536] who have carried out a series of investigations into the effects of single high-density DC pulses ($\sim 10^3$ A/mm^2 for $\sim$60-μs duration) on the flow stress of a number of

polycrystalline metals (Cu, Pb, Sn, Fe, and Ti), representing a range of crystal structures and valences. This group was to determine the magnitude of the drift electron–dislocation interaction, which occurs with the application of a current pulse during plastic flow and the physical basis of this interaction.

To determine the magnitude of the electron–dislocation interaction, special attention was given to separating the side effects of the current, such as Joule heating, pinch, skin, and magnetostrictive effects. This was an indispensable first step because there was considerable scepticism[537,538] as to whether the electroplastic effect is, indeed, a result of the electron–dislocation interaction. It has been argued that the observed changes in the mechanical properties such as flow stress, creep, etc., are caused by side effect of current such as Joule heating and pinch effect. However, Cao and Okazaki[539] have clearly shown that the observed changes in the mechanical properties cannot be explained in terms of the current side effects but rather are the consequence of the electron–dislocation interaction.

6.4.7.2 Effect of Electric Current on Stress Relaxation

Troitskii and coworkers[540] have used stress relaxation to study the electroplastic effect in a number of metals such as zinc, lead, and cadmium under the influence of high-density (10^4 A/cm^2) current pulses. The frequency of the pulsing current was 100 Hz and the pulse duration 65 μs. They found that the application of current increases the rate of stress relaxation and significantly affects its onset. Figure 6.32a depicts stress relaxation dependence on time with and without current. Figure 6.32b illustrates the rate of stress relaxation with and without current as a function of applied stress. Note that the onset of stress relaxation with and without electric current is different: it is significantly lower for the samples under the influence of electric current.

The mechanical properties of metals may also be influenced by low-density electric current as reported by Silveira et al.[541,542] They have shown that the rate of stress relaxation of polycrystalline Al and Cu near 0.5 T_m can be increased with the application of a small (1.6 A/mm^2 continuous AC or DC) current, the effect being greater for the DC current. The effect decreased with the number of times the relaxation was carried out, as seen in Figure 6.33. Also, they found that the DC current altered the dislocation arrangement in the Cu specimens; partial destruction of the cell structure occurred after the eighth relaxation cycle (Figure 6.34).

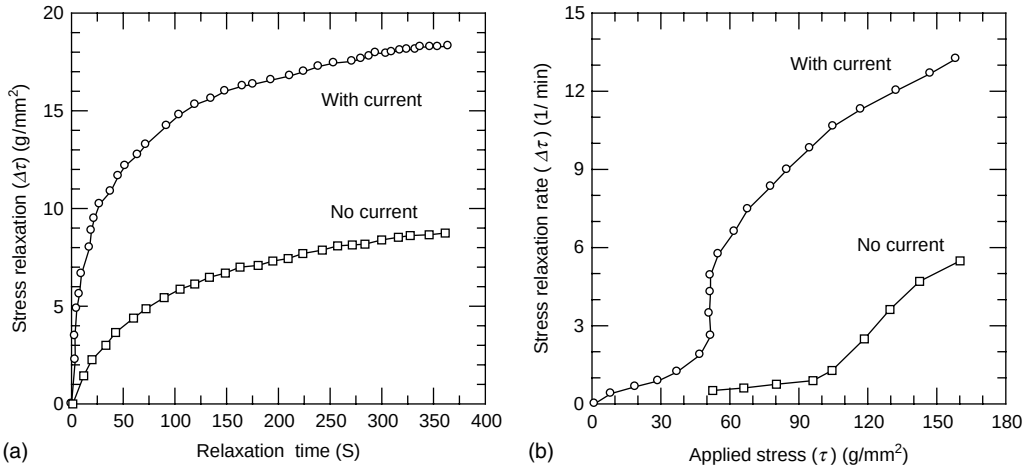

FIGURE 6.32 (a) Variation of stress relaxation with time with and without current. (b) Variation of the rate of stress relaxation with applied stress for samples with and without current.

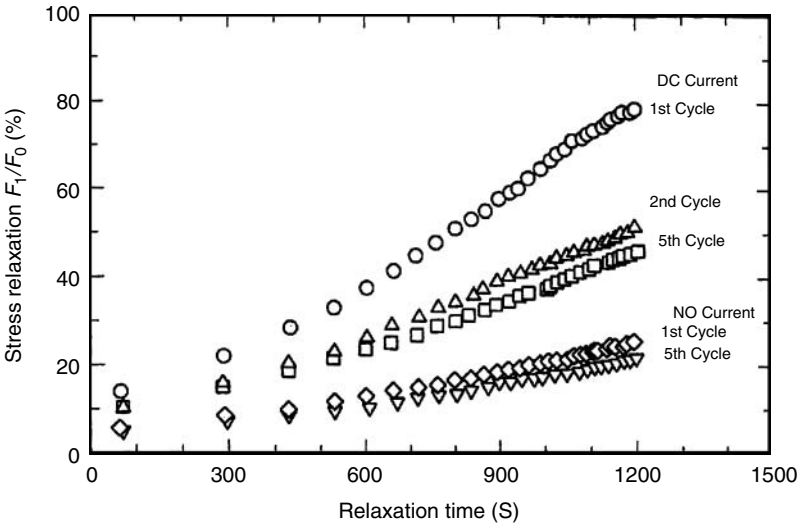

FIGURE 6.33 Effect of DC electric current on stress relaxation of copper. (From Silveira, V. L., Porto, M. F. S., and Mannheimer, W. A., *Scripta Met.*, 15, 945–949, 1981.)

Braunović[543] compared the stress relaxation of an aluminum conductor wire at room temperature and low initial stress (20 N) under the influence of a low-density electric current (3 A/mm^2) with that of a wire relaxing at higher temperature (150°C) and higher initial contact stress (260 N). The results are shown in Figure 6.35 as relative force changes (F_i/F_0) versus time, where F_i is the contact force at the instant i and F_0 is the initial contact force.

It is clear that the stress relaxation of an aluminum wire conductor at elevated temperature (150°C) and under current cycling conditions is similar. In other words, the initial contact force ($F_i = 20$ N) of a wire subjected to current cycling decreases at virtually the same rate as a wire subjected to stress relaxation at 150°C and higher initial stress $F_0 = 260$ N. The observed effect of current cycling on stress relaxation cannot be rationalized in terms of the temperature effect alone because the temperature rise produced by the passage of a low-density current through the wire conductor is merely 2–3°C.

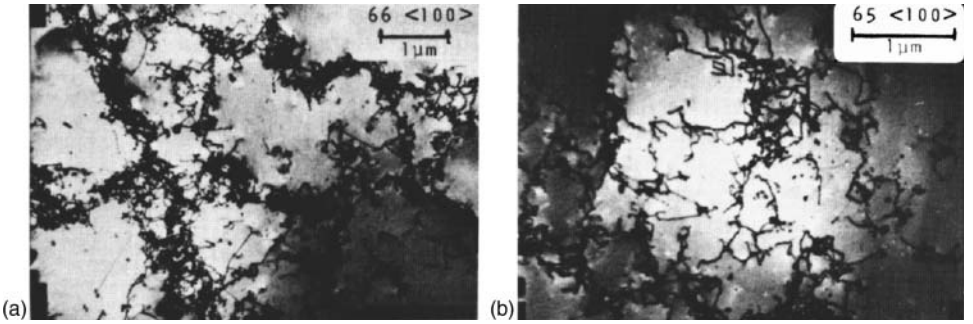

FIGURE 6.34 Dislocation structure of polycrystalline copper after eight stress relaxation cycles: (a) without current; (b) with DC current. Note the disappearance of the cell structure and the presence of increased dislocation distribution within the cells. (From Silveira, V. L., Fortes, R. A. F. O., and Mannheimer, W. A., *Beitr. Elektronenemikroskp. Direktabb. Oberfl.*, 15, 217–219, 1982.)

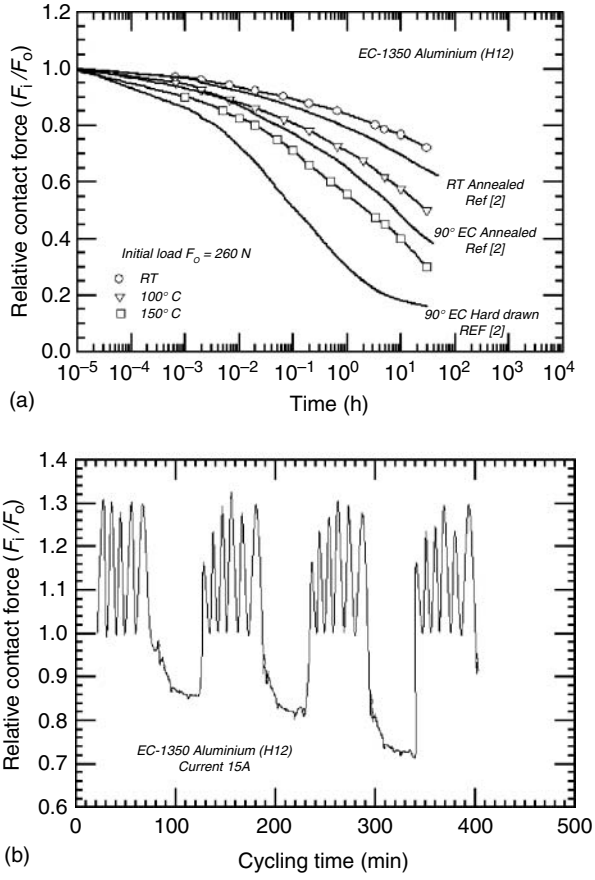

FIGURE 6.35 Stress relaxation of aluminum wire conductor: (a) at room temperature (RT), 100 and 150°C and 260 N initial load; (b) at room temperature under current cycling conditions and 20 N initial load.

Possible explanations for the observed effect of electric current on stress relaxation include thermal fatigue of aluminum, work-hardening of contact brought about by thermal expansion, and electroplasticity. There are many possibilities put forward to account for the observed electroplasticity effect in metals. Hence a brief discussion of the plausible ones is warranted.

One possibility is that the observed effect of currentcycling can be best explained in terms of the thermal stresses generated in the contact zone during cycling tests. When a wire conductor is compressed and then subjected to current cycling, the contact area will experience the combined action of thermal and mechanical stresses. The total strain in the contact is then the sum of these strains

$$\varepsilon = \varepsilon_m + \varepsilon_t \tag{6.15}$$

where ε_m and ε_t are respectively mechanical and thermal stresses defined as

$$\begin{aligned} \varepsilon_m &= \sigma/E = F/EA \\ \varepsilon_t &= \alpha_t(T - T_0), \end{aligned} \tag{6.16}$$

where σ is the mechanical stress, F is the applied contact load, E is the elastic constant, A is the apparent

contact area, α_t is the coefficient of linear thermal expansion, T_0 and T are the initial and final temperature, respectively. Hence the total strain imposed on a wire by thermal and mechanical stresses is:

$$\varepsilon_d = s/E + \alpha_t(T - T_0). \tag{6.17}$$

In the case of static tests, however, the total strain imposed on a wire will comprise only the mechanical stress. This is because these tests were carried out at some elevated temperature when the wire was first stabilized at that temperature for a period of time before the load was applied.

From the results presented, it is apparent that thermal stresses generated by current-cycling can be of considerable magnitude. According to the data shown in Figure 6.35 the increase in the contact load brought about by current-induced thermal stresses can be as high as 30% above the initial mechanical stresses.

Hence, the combined action of thermal and mechanical stresses during current cycling causes thermal fatigue in aluminum wires, which in turn reduces the overall strength of the material and thus increases the rate of stress relaxation. The magnitude of the thermal strains thus induced in the wire will depend on the temperature rise involved and the coefficient of thermal expansion of the material.

The magnitude of corresponding thermal stress set up by the thermal strains is influenced by the reduction of both elastic modulus and yield strength with temperature and also structural changes such as polygonization, recrystallization, recovery, grain growth, precipitation and intergranular segregation that can affect ductility and resistance to repeated thermal shock. However, the maximum temperature rise in the wire resulting from the passage of 15 A is on the order of 10°C, which is unlikely to significantly change the properties and the structure of the material (wire). Another possibility is that during cycling, the contact zone, which is under compression, work-hardens as a result of an increased contact stresses brought about by the thermal expansion of the wire. This, in turn, can augment the rate of stress relaxation because work hardening increases the rate of relaxation.[513] Work hardening of the contact zone may occur because the stresses generated by thermal expansion of the wire are sufficient to cause localized yielding.

An alternative is that the observed effect of electrical current on stress relaxation is associated with the electroplasticity. As mentioned in the Introduction, a number of investigators have clearly established that mechanical properties such as flow stress, creep, and stress relaxation undergo significant changes under the influence of electrical field.

It is important to emphasize that whatever the detailed mechanism for the observed effect of electric current on stress relaxation, the effect is most likely associated with the interaction of the electric field with the structural defects, notably dislocations. In view of these remarks and also the dynamic nature of the current-cycling, a rather simplified model for the observed effect of current-cycling on stress relaxation is proposed.

The stress relaxation of a metal is generally associated with arrangement, density, and motion of dislocations and their interactions with other structural defects such as grain and subgrain boundaries, impurities, solutes, and precipitates. Hence, when the electrical current passes through the wire, it will cause not only heating and thus expansion of the wire, but also will weaken the binding forces between dislocations and obstacles impeding dislocation motion that otherwise cannot be overcome by thermal activation alone. As a result, nucleation and multiplication of dislocations will be alleviated that in turn will increase the density of mobile dislocations and alter their arrangement in the material.

Repeated passage (current cycling) of the electrical current through the wire will free more and more dislocations from the pinning defects, enhance mobility and reduce density of dislocations in the material that will be reflected as an increased rate of stress relaxation.

It should be pointed out, however, that the proposed model does not exclude the effect of temperature on the processes involved. Rather, because of the relatively low heating generated by the passing current, the thermal activation alone is insufficient to significantly affect the dynamics of dislocation motion and their arrangements in the material.

In the case of creep, the elementary processes of plastic deformation can be described by the phenomena related to the dislocation dynamics and viscous diffusion flow. The latter takes place at temperatures close to melting point. At medium temperatures and low applied stresses the creep rate gradually diminishes and vanishes, as described by the logarithmic law

$$\varepsilon = \varepsilon_0 + \alpha \ln(\beta t + 1), \tag{6.18}$$

where α and β are constants and ε_0 is the initial deformation.

The logarithmic law of creep is valid for metals and alloys with different types of crystal lattice at temperatures below (0.2–0.3) T_m, and can be used to study the mechanisms responsible for the rate of plastic deformation of a metal. At low temperatures, creep is dominated by the dislocation mechanism which reflects the combined action of thermal fluctuations and applied stress, resulting in an unimpeded motion of dislocations throughout the lattice.

The effect of electric current on creep in different metals has been studied extensively by Klypin[515,544] at a low-density DC current, (0.25 A/mm^2) and different temperatures. The creep rate is significantly affected by the action of the electric current, the more so at lower creep rates and higher current densities (see Table 6.3). Increasing the number of current applications (cycles) was found to reduce the effect of electric current.

A typical creep curve for copper tested at 400°C and a stress $\sigma = 6$ kgf/mm^2 is shown in Figure 6.36. It is clear that when the current is applied, the creep rate sharply increases. The results of Klypin's work on different metals are given in Table 6.3 showing average creep rates before and after application of DC current.[515] Although no definite conclusions can be drawn from this data, as to the relative susceptibility to creep of the materials tested under the influence of

TABLE 6.3
Effect of DC Current (0.15 A/mm^2) on the Creep of Different Materials

Material	Temperature (°C)	Stress (kgf/mm^2)	Creep Rate (%/h)		Creep Strain Polarity +	Creep Strain Polarity −
			Current OFF	Current ON		
Copper	400	6.0	0.55	1.8	0.5	0.2
	400	4.0	0.20	1.2	0.2	0.05
	600	2.0	0.30	1.0	0.2	0.0
	800	0.2	0.10	1.0	0.2	0.15
Nickel	800	5.0	1.00	—	—	—
	800	3.0	0.06	0.3	0.3	0.25
Cobalt	500	20.0	0.06	2.20	0.9	0.12
	700	10.0	0.50	0.80	0.9	0.2
	700	6.00	0.30	1.00	0.25	0.16
	700	0.12	0.05	0.36	0.08	0.08
	800	5.00	0.60	1.20	0.25	0.12
Titanium	600	6.00	0.15	1.2	0.45	0.0
Aluminum	300	2.0	0.03	1.5	0.3	0.16
Steel	500	20.0	0.5	3.6	0.5	—
	500	8.0	0.2	1.7	0.3	0.2
	600	5.0	0.3	1.8	0.45	0.4

Source: Klypin, A. A., *Strengh of Materials*, 9, 35–39, 1972

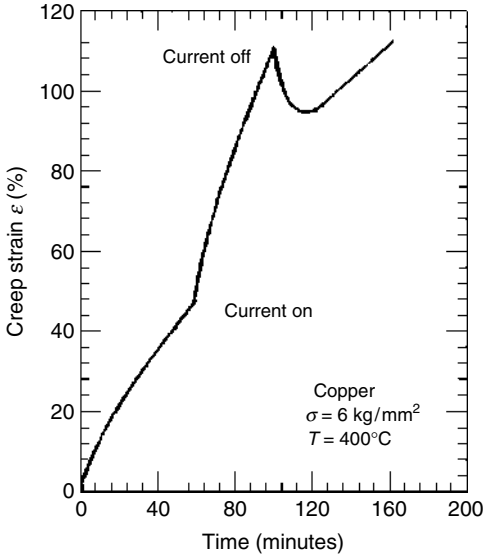

FIGURE 6.36 Effect of current on the creep of copper at 400°C and stress $\sigma = 6$ kg/mm^2. Note the change in creep rate when current was switched ON and OFF.

electric current, it is clear that the creep rate of practically all the materials tested is affected to a degree by the electric current.

Stashenko et al.[545] investigated the effect of current on the creep of zinc crystals using a high-density current pulses (10^4 A/mm^2) of short duration (10^{-2}S). They found that the pulse action of electric current results in a considerable increase in the creep rate and a discontinuous plastic deformation. The extent to which the creep rate is affected is determined by the mode and basic parameters of the current pulse, the degree of deformation, and the initial state of the metal. Observed changes in the creep rate can be best explained in terms of a combined action of thermoplastic and electroplastic effects.

The importance of the effect of electric current on the mechanical behavior of conductors and connectors is very difficult to assess because of the scarcity of published data. On the other hand, if the effect of electric current is operative and its influence on the mechanical integrity of electrical conductors and connectors, notably creep and stress relaxation, is as pronounced as initial results suggests, it could have extremely important practical implications.

The effect of current cycling on the mechanical response of aluminum conductors deserves more attention and further studies because the conductors during a normal service lifetime are constantly subjected to one form or the other of current cycling. It is therefore of considerable importance to investigate further the observed effects to elucidate the exact nature and importance of the electric field in general and current cycling in particular on the mechanical properties of aluminum conductors.

6.4.8 Thermal Expansion

The difference in the coefficients of thermal expansion of aluminum and copper is another important factor in the degradation mechanisms of aluminum-to-copper connections. Aluminum expands at a greater rate than copper when exposed to an increase in temperature. As a result, either large lateral movements occur in the contact zone shearing the metal-contact bridges, thus reducing the contact area, or plastic deformation occurs in a region adjacent to the contact interface. This loss increases the contact resistance which, in turn, causes the connection temperature to rise.

At higher temperatures, the stresses may be relieved by recovery in the matrix. On cooling, however, the thermal stresses build up again and further interfacial shearing and/or plastic deformation occurs because, at lower temperatures, there will be very little recovery in the matrix and thus little stress relief. When the process is repeated many times, considerable plastic deformation in the contact zone will take place if the thermal stresses generated are greater than the yield stress of the aluminum. The end result is a cascading effect that accelerates the degradation of the connection until failure.

In the case of aluminum-to-copper connections, a simple estimate of the magnitude of the maximum elastic stresses generated at the peak temperature in a thermal cycle can be calculated by assuming that the thermal stresses generated in the aluminum are negligible because the sample is effectively annealed. On cooling, both aluminum and copper will contract by the amount Δd given by

$$\Delta d = \varepsilon_t \Delta T, \tag{6.19}$$

where ε_t is the coefficient of thermal expansion and ΔT is the temperature change. The differential strain due to the constraint is then

$$\Delta d\varepsilon = \Delta T[\varepsilon_t(\mathrm{Al}) - \varepsilon_t(\mathrm{Cu})] \tag{6.20}$$

Because for aluminum $\varepsilon_t = 24.0\times10^{-6}$ (1/°C) and for copper $\varepsilon_t = 17.2\times10^{-6}$ (1/°C), the corresponding differential strains for aluminum–copper contacts at 100, 150, and 200°C are, respectively, 6.8, 10.2, and 13.6×10^{-4} (1/°C). The tensile yield strength of aluminum is 55 MN/m^2 and the elastic modulus 70 GN/m^2 hence the yield strain is 7.8×10^{-4} (1/°C). Comparison with the calculated differential strain values above indicates that the aluminum will yield during cooling of the contact.

Another result of the greater thermal expansion of aluminum is thermoelastic ratcheting. In a bolted aluminum-to-copper joint where a steel bolt is used, excessive tightening of the bolt can plastically deform the aluminum and copper conductors during the heating cycle that cannot regain their original dimensions during the cooling cycle. Repeated heating and cooling cycles can thus cause loosening of the joint that, in turn, will increase the joint temperature and contact resistance.

6.5 IMPACT OF CONNECTION DEGRADATION

Electrical connections are designed to last a long time. They age, however, and their life span and optimum life cycle managements are affected by a number of factors, such as original design criteria, manufacturing process, operation conditions, maintenance procedure and safety consideration. Hence, the accumulated damage can be measured, their history analyzed, and an expected remaining life calculated. The remaining life is the period of time after which the probability of failure becomes unacceptably high. A common feature in usefulness and life expectancy of any component is expresses by the well-known “bathtub” reliability curve, shown in Figure 6.37.

As can be seen, there is a high probability of failure during the first few hours or weeks of operation—the break-in (start-up) period—usually caused by manufacturing or installation problems. Following this initial period, the probability of failure is relatively low for an extended period (normal life) until it increases sharply with elapsed time or hours of operation (wear-out period). The sum of operating time and the most probable expected remaining life may or may not equal the original design life. Hence, the expected remaining life, while still a range or probability distribution, will probably be more precise.

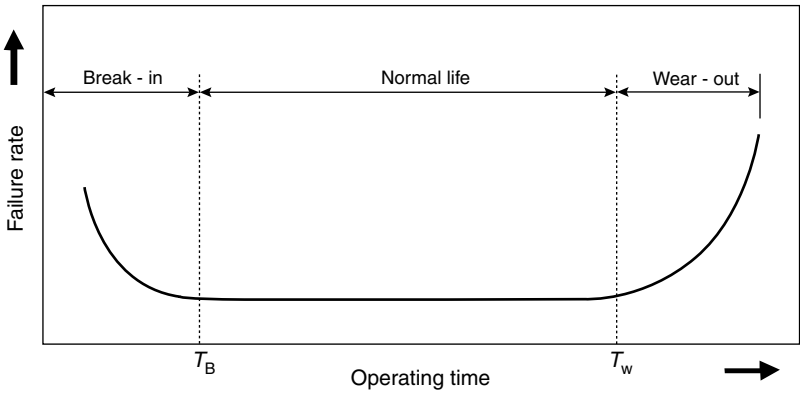

FIGURE 6.37 Failure probability ("bathtub") curve.

Every component of an electrical system can reach the failure situation, which will probably occur as the operating time approaches the end of its life span. The life span is the end of life determined by the ageing and the deterioration mechanisms as discussed in the preceding section.

The useful life of an electrical component or a device is determined by design and manufacture and is affected by a series of service conditions considered as normal. Clearly, if during the life of a component the operating conditions are or become severe than expected, the useful life will be shortened at a higher rate.

The useful life of an electrical connection or any piece of equipment is determined basically in terms of the reliability of the component in performing its intended function. However, the reliability of an electrical component cannot be predicted with certainty. Thus, a probability approach has been introduced to reflect the uncertainty of the component reliability.

Generally speaking, reliability can be defined as the probability of a component to perform its designed function over the period of time under the operating conditions. The reliability is defined as

$$R(t) = 1 - F(t) = \mathrm{e}^{-\lambda t}, \tag{6.21}$$

where λ is the failure rate and t is the operating time. The function $F(t)$ is called the probability of failure and is defined as

$$F(t) = 1 - \mathrm{e}^{-\lambda t} \tag{6.22}$$

The probability density function, providing the random variable is time to failure, is defined as:

$$f(t) = \mathrm{d}R(t)/\mathrm{d}t. \tag{6.23}$$

Identifying, understanding, and modeling material failure and damage mechanisms are essential in characterizing component aging and predicting remaining service life. Obviously, quantifying aging and predicting remaining life cannot be realized unless the failure and damage mechanisms are known. Information from design, operating experience, and failure analysis is used to select the most likely failure and damage mechanism.

The application of accurate life assessment methods is essential for life- extension decisions concerning the increase of the operational reliability and optimization of the resource allocation. Accurate predictions of remaining life provide guidance for scheduling the repair, replacement, or

removal of key components during planned shutdowns, avoiding costly unplanned outages caused by component failures.

Calculating expected remaining life generally involves identifying four areas: (1) part(s) of the equipment that will limit its continued service; (2) damage mechanism(s) that will cause the part(s) to fail; (3) inspection techniques that will locate damage and characterize the extent of damage; and (4) mathematical model(s) of the equipment or its structure that can use the equipment history and existing condition to calculate its expected remaining life.

The information from this assessment can be used to determine whether a connection will survive for its intended application life, or whether it can be used to redesign the connection for increased strength against the dominant failure mechanisms. Key to extending the useful life of an electrical connections or device is the capability to extract information from the operational experience of the connection or device to produce reliable diagnostics and prognostics about its state and remaining useful life.

6.5.1 Prognostic Model for Contact Remaining Life

From the perspective of its reliability implications, prognostic modeling of a contact's remaining life is the mathematical representation of a failure mechanism in terms of a set of algebraic or differential equations. *Modeling* is a means of determining and understanding the different variables or factors responsible for initiating and accelerating a failure mechanism. Modeling a failure mechanism and quantifying how it is affected by various environmental factors allow development of appropriate reliability assessment of field failure rates and prediction of the onset of the failures. Among the advantages of predicting reliability include advance warning signs of failure and the reduction of life cycle costs by reducing inspection and unscheduled maintenance. However, predictions can be inaccurate if they do not account for the actual environments that the product is subjected to in its life cycle.

It has to be pointed out, however, that regardless of the fidelity of a prognostic model or the quantity and quality of the seeded fault or run-to-failure data, modeling should be adaptable based on the operating and environmental conditions to which a connection or a device is subjected to. The inherent uncertainties and variability in material capacity and localized environmental conditions, as well as the realization that the complex nature of deterioration mechanisms will always possess some uncertainty, all contribute to the stochastic nature of prognostic modeling. However, accuracy can be improved by creating a prognostic architecture with the ability to account for unexpected damage events, blend with diagnostic results, and statistically calibrate predictions based on inspection information and real-time features.

It is well known that in closed electrical contacts, the contact resistance increases with time.[427] Takano and Mano[546] used diffusion model for oxidation to determine the lifetime of electrical contacts. Bron et al.[547] proposed a model based on the assumption that the rate of diminution of the radius of conducting metallic spot is proportional to the growth rate of the oxide forming at the free surface while the number of contact spots remains constant.

It should be pointed out, however, that these assumptions are not based on the physical mechanisms of the deterioration processes occurring in the contact zone. Izmailov[548] has proposed that the contact resistance of a single-point contact increases as a result of surface diffusion of oxidizing agent (not necessarily oxygen) and subsequent growth of surface oxide layer. Furthermore, it was also proposed that the oxide layer grows across the whole contact spot area and that its thickness increases from the center towards the periphery of the *a*-spot. This approach is in agreement with the model proposed by Boyer et al.[549] Similar models to account for the growth of oxide layer were put forward.[550,551]

Recently, Ming et al.[552] proposed a model based on the assumption that the oxide layer grows from the exterior to the center of the contact spot, which remains nonoxidized (metallic). It was

assumed that oxidation occurs as a result of ion migration through the circular zone of oxidized contact.

The results of studies of electrical contacts under fretting conditions show that the contact resistance deteriorates in the same manner as that of the closed contacts subjected to oxidation. The only difference is that in the latter case the variable is a time whereas in the former case the variable is a number of fretting cycles.

Malucci[553] carried out a detailed surface analysis of the contact zones subjected to fretting conditions and showed that the cause of contact deterioration is the growth of oxide film and fretting debris in the contact zone. In the case of closed contact, oxide growth at the surface is a dominant mechanism.[553] It is evident that micromotions activate the deterioration of contact spots. Hence, it is reasonable to assume that the mechanisms for the oxidation-driven deterioration of closed contacts may be extended to the contacts under fretting conditions. Such an assumption is justifiable because in both cases (closed contacts with and without micromotion) the deterioration mechanism is the same, namely diffusion of the oxidizing agent into contact gap.

Oxidation of a contact spot can be considered as an analogous process to oxidation along grain boundaries in metals. It is well known that oxidation along grain boundaries occurs much faster and proceeds deeper than that in the bulk of metal due to an intensive diffusion of oxidizing agent ions along the grain boundary. It should be pointed out, however, that it is generally accepted that the oxidation of metals is a result of diffusion of metallic ions to the surface through the oxide.[554]

The contact interfaces of similar and especially dissimilar metals, as well as grain boundaries, are favorable sites for ions migration. Therefore, it is reasonable to assume that diffusion of the oxidizing agent within the contact area is one of the oxidation mechanisms of a contact spot. In other words, the thickness of the oxide film formed within the contact spot area is proportional to the concentration C of the oxidizing species. Based on these assumptions, Braunović et al. proposed a model for evaluating the life time closed electrical contacts[555] whereby the thickness of the oxide film was described by an expression

$$\delta = \delta_{\mathrm{m}}\left[1 - 2\sum_{1}^{\infty}\frac{1}{\alpha_n}\frac{J_0(\alpha_n r/a)}{J_1(\alpha_n)}\exp\left(\frac{D\alpha_n^2 t}{a^2}\right)\right], \tag{6.24}$$

where a is the contact spot radius, r is the instantaneous contact radius ($0 \le r \le a$), $J_0(x)$ and $J_1(x)$ are the Bessel's functions of the zero and first order, α_n are roots of the equation $J_0(\alpha_n a) = 0$; D is the diffusion coefficient along the contact interface, t is the time. From Equation 6.24, it follows that the surface film grows across the whole contact area with nonuniform thickness: for $r = a$ it is thickest and, and it is the thinnest for $r = 0$. As the time progresses the film thickness becomes more uniform.

It is well known that thin films exert very little effect on the current flow. For film thickness δ less than some critical value δ_{c} the contact can be considered as a quasimetallic because the film resistance is lower than the constriction resistance. As the film grows, the contact resistance increases rapidly, and the film can be considered as practically nonconducting when $\delta > \delta_{\mathrm{c}}$.

Figure 6.38 provides a clearer explanation of the proposed model. The interior of the circular contact with diameter $2r$ and $\delta < \delta_{\mathrm{c}}$ is considered as a quasimetallic (conducting) region of the contact whereas the region outside the contact circle as nonconducting.

With the use of software such as *MathCAD*, Equation 6.24 was solved for values of $\delta_{\mathrm{c}}/\delta_{\mathrm{m}} = 0.01$–$0.1$, which are of interest for practical purposes. The solution was carried out taking into account ten roots α_n of the Bessel's function ($n = 10$). Figure 6.38 shows the dimensionless radius of quasimetallic contact spot r/a as a function of dimensionless time Dt/a^2 for different values of $\delta/\delta_{\mathrm{m}}$.

For practical purposes, the numerical solution of Equation 6.24 is inconvenient. Therefore the *Table Curve* software was used to derive an approximate expression in agreement with the

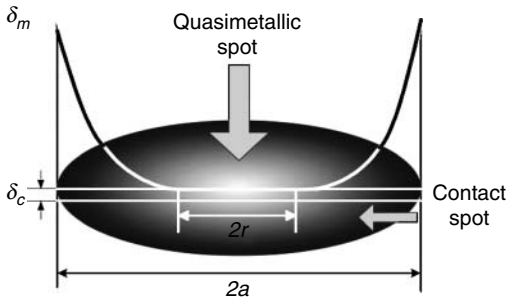

FIGURE 6.38 Schematic view of the contact spot with a nonuniform thickness distribution of the surface film.

numerical solution (the greatest values of correlation coefficients)

$$\frac{r}{a} = \left[1 - K_\delta^{1/2}\left(\frac{Dt}{a^2}\right)^{1/2}\right]\left[1 + K_\delta\left(\frac{Dt}{a^2}\right)\right], \tag{6.25}$$

where $K_\delta = [2.2 - 4\ln(\delta_c/\delta_m)]$ is the coefficient of approximation less than 30%.

Following Holm[1] and assuming that the contact conductivity is basically determined by the conductivity of the quasimetallic region, the time-dependence expression for the contact resistance was obtained as

$$R = \frac{\rho}{2r(t)} = \frac{R_0}{\left[1 - K_\delta^{1/2}\left(\frac{Dt}{a^2}\right)^{1/2}\right]\left[1 + K_\delta\left(\frac{Dt}{a^2}\right)\right]}. \tag{6.26}$$

where $R_0 = \rho/2a$ is the initial contact resistance of a single contact. Hence, when $t \to 1/(K_\delta\, D/a^2)$ the contact resistance tends to infinity, which, in real situations, is not the case. After a very long time, the contact spot is covered with a film having a very high resistance value but not that of infinity. Also, at certain contact voltages, fritting of a surface film takes place. However in this case it has no significance because under these conditions the contact is considered as failed.

Equation 6.26 describes the increase of contact resistance of a single contact spot with time. For multispots contact the following expression can be used:[1]

$$R = \frac{\rho}{2n(t)r(t)},$$

where $r(t)$ is the average value of the contact spot radius, $n(t)$ is the number of contact spots. To derive the expression for the average contact spot radius $r(t)$ as a function of time, the following assumptions were made:

- Time-dependence of each quasimetallic contact spot radius follows Equation 6.25.
- The function describing the distribution of contact spot radii is not time-dependent, i.e., the ratio between average and maximum values for contact spot radius remains constant.

Based on these assumptions, the average contact spot radius can be expressed as

$$r(t) = a\left[1 - K_\delta^{1/2}\left(\frac{Dt}{a_m^2}\right)^{1/2}\right]\left[1 + K_\delta\left(\frac{Dt}{a_m^2}\right)\right], \tag{6.27}$$

where a is the initial value of the average radius and a_m is the initial value of the maximal contact

spot radius. Because the small-sized contact spots will disappear as the oxidation proceeds, the number of conducting spots decreases with time. After a certain time t, the contact spots with the initial radius $a < a_c = (K_\delta\, Dt)^{1/2}$ will disappear. The number of contact spots is then

$$n(t) = n_0\left(1 - \int_0^{x_c} f(x)\mathrm{d}x\right), \tag{6.28}$$

where $f(x)$ is a function describing the contact spot radius distribution with $x = a/a_m$, $x_c = a_c/a_m$.

Example 6.1. If the distribution function $f(x) = 1$ (uniform distribution), then

$$R = \frac{R_0}{\left[1 - K_\delta^{1/2}\left(\frac{Dt}{a_m^2}\right)^{1/2}\right]^2\left[1 + K_\delta\left(\frac{Dt}{a_m^2}\right)\right]}. \tag{6.29}$$

Example 6.2. For $f(x) = 6x(1-x)$ (beta distribution)

$$R = \frac{R_0}{\left[1 - K_\delta^{1/2}\left(\frac{Dt}{a_m^2}\right)^{1/2}\right]^3\left[1 + 2K_\delta^{1/2}\left(\frac{Dt}{a_m^2}\right)^{1/2}\right]\left(1 + K_\delta\frac{Dt}{a_m^2}\right)}. \tag{6.30}$$

Figure 6.41 shows the relationships between the dimensionless contact resistance increments $k = R/R_0$ and dimensionless time t/t_m ($t_m = a^2/K_\delta D$) for different distribution of the contact spots.

It is apparent that contact resistance with uniform and beta distributions of contact spot radii (Equation 6.29) increases much faster than that of a single-point contact (Equation 6.26). This is because the smaller spots disappear much faster. Similarly, the resistance of a contact with the uniform distribution of contact spot radii initially increases much faster than that with the beta-distribution because, in the latter, the number of smaller contact-spots' radii is significantly lower.

From Equation 6.26, Equation 6.29 and Equation 6.30, it is clear that the resistance of a single-point contact $R \to \infty$ when $t \to (K_\delta\, D/a^2)^{-1}$ and thus $t_m = a^2/(K_\delta\, D)$ is the maximal lifetime for a single-point contact. In reality, the contact is considered to be failing much sooner.

The failure criterion is usually defined as the incremental increase of contact resistance in respect to its initial value, that is, $k = R/R_0$. In this case, the numerical solutions of Equation 6.26, Equation 6.29 and Equation 6.30, in respect to time for a given value of k, can be used to calculate the contact lifetime. Through the use of *Maple 7* software, the numerical solutions of these equations in respect to time t for given values of k were obtained. The results of numerical solutions for the contact lifetime as a function of the allowable contact resistance increment k for a single- and multipoint contact with uniform and beta-distribution of contact spots are shown in Figure 6.39.

For practical purposes, it is convenient to have analytical expressions for the contact lifetime t_l as a function of dimensionless contact resistance increment $k = R/R_0$. Because these expressions cannot be derived analytically, the problem is circumvented by approximating the solutions using *Table Curve* software. The approximate numerical solutions of Equation 6.26, Equation 6.29 and Equation 6.30 for the contact lifetime were obtained as a function of parameter k in the range of $k = 1$–100. These expressions ensure minimal deviations of the approximate values from the precise ones and are as follows:

For a single-point contact,

$$t_l = 0.96t_m\left(1 - \frac{1}{k^{1.5}}\right)^2. \tag{6.31}$$

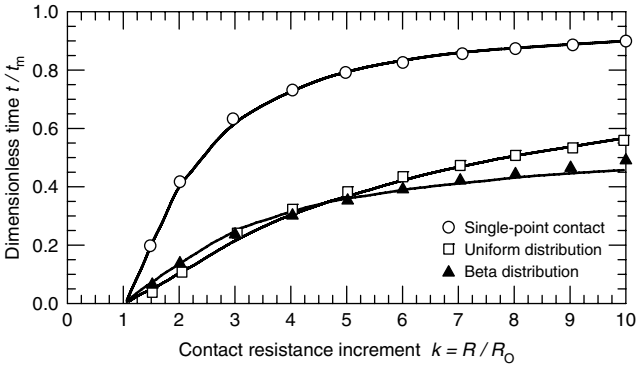

FIGURE 6.39 Dimensionless contact resistance increment, $k = R/R_0$, as a function of dimensionless time, t/t_m; (points: exact solution; lines: approximations).

For a multipoint contact with uniform distribution of contact spot radii:

$$t_l = 1.2t_m\left(1-\frac{1}{k^{0.5}}\right)^2. \tag{6.32}$$

For a multipoint contact with beta distribution of contact spot radii

$$t_l = 0.56t_m\left(1-\frac{1}{k}\right)^2, \tag{6.33}$$

where $t_m = a^2/(K_\delta D)$. The above expressions for dimensionless contact lifetime (t_i/t_m) as a function of allowable dimensionless contact resistance k are shown as continuous lines in Figure 6.39.

The error of approximation in Equation 6.31 does not exceed 5% in the range of $k = 1$–100, whereas in Equation 6.32 and Equation 6.33, this error is less than 7% in the range $k = 1$–10 and less than 25% in the range of $k = 10$–100.

The time-dependence of contact resistance, as expressed by Equation 6.26, Equation 6.29 and Equation 6.30 have been observed in different contact materials under different operating conditions by many authors.[491,546,552,556] The most detailed description of such dependence is given by Timsit,[491] and by Takano and Mano,[546] who made estimates of the actual contact spot size.

The analytical expressions in Equation 6.29 and Equation 6.30 were compared with the experimentally determined contact resistance time-dependence for various contact configurations as reported in the literature.[551,552,556] The results are shown in Figure 6.40. Theoretical curves were obtained by fitting the experimental data to Equation 6.29 and Equation 6.30 that made possible to determine t_m.

From the results shown in Figure 6.40 it can be inferred that there is good agreement between the experimental data as reported by different authors in the literature and those described by the Equation 6.29 and Equation 6.30. Therefore, these expressions can be used to determine the limiting value of contact lifetime.

The results in Figure 6.41 illustrate the variation of the dimensionless contact spot radius r/a with dimensionless time t/t_m as determined by the Equation 6.27 (continuous line) and that obtained experimentally (points)[491] at practically constant contact temperature. The experimental data were fitted to Equation 6.27 as it was done for the contact resistance. The results shown indicate this expression can be used to describe accurately the experimentally obtained time-dependence of the contact spot radius.

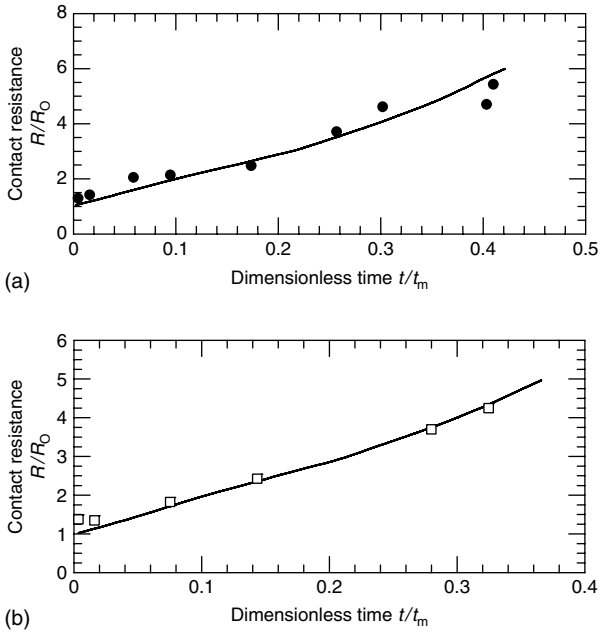

FIGURE 6.40 Contact resistance increment, R/R_0, as a function of the dimensionless time, t/t_m, for uniform distribution of contact spots: (a) $t/t_m = 9.5\times10^7$ s[551]; (b) $t_m = 2.4\times10^7$ s.[556]

From the practical point of view it should be pointed out that the limiting value of contact lifetime is determined by $t = a^2/(K_\delta D)$. In other words, the contact lifetime can be increased by a smaller number of contact spots having larger initial radius because the contact resistance behavior is determined by the size of the contact spot. On the other hand, the larger contact radius a, the lower is the initial contact resistance.

According to Holm,[1] the contact spot radius a can be expressed in terms of the initial contact resistance R_0 as $a = \rho/(2nR_0)$ and consequently the contact lifetime $t_m \propto (1/R_0^2)$. Hence, the higher is the initial contact resistance, the shorter is contact lifetime. Consequently, contacts with higher initial resistance will have unstable contact resistance behavior.

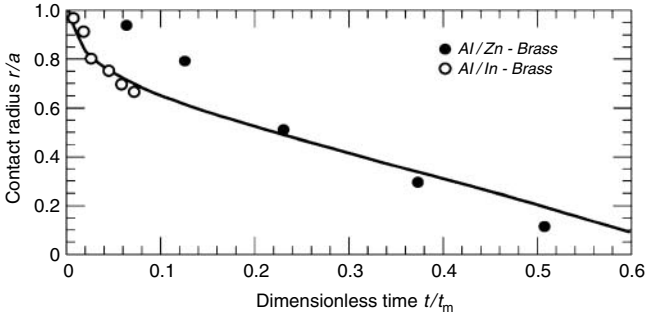

FIGURE 6.41 Contact radius r/a as a function of dimensionless time t/t_m, $t_m = 0.16$–1.1×10^7 s. (From Rabkin, D. M., Ryabov, V. R., Lozovskaya, A. V., and Dovzhenko, V. A., *Soviet Powder Metallurgy and Metal Ceramics*, (8), 695–701, 1970. With permission.)

6.5.2 Economical Consequences of Contact Deterioration

Electrical connections are designed conservatively and are expected to operate over a long period of time. The properties of the materials used in the connections may deteriorate because of the in-service aging or under the influence of deterioration mechanisms that can reduce their useful life and/or reduce their operating safety margin. Extending the use of older connections beyond their originally anticipated life can provide major economic benefits. To extend their operating life, however, their remaining useful life must be assessed to ensure that safety and structural integrity are maintained during the extended operating period.

Failure of an electrical connection is not always due to intrinsic deterioration mechanisms but can be caused by an inadvertent over-stress event after installation; latent damage during storage, handling or installation, selection of an inadequate or wrong component for use in the system by either the installer or designer. Variable stress environments can also impact the predicting of the field failures. Managing and extending the life of critical power equipment require reliable and continuous monitoring as the validity of any action taken affects the life of a component. Once a fault has been detected and its evolution is monitored, the severity of the fault can be assessed and decisions made about what actions should be taken. Potential damages will be restricted when incipient faults are detected and timely actions implemented. Early detection limits the amount of adjacent damages and confines the area requiring repair and maintenance.

The early detection of incipient faults will greatly reduce unplanned power outages and improve the reliability of the power and service supplied. Furthermore, because fault conditions often lead to catastrophic failures, their early detection will limit these events and thus ensure the safety of the substation personnel. Monitoring a fast developing fault and evaluating its progress provide the necessary information to apply all the essential resources to react on time and reduce the overall damages.

The deleterious consequences of connector degradation affect not only performance, but also economics, in terms of the cost of energy loss. To illustrate the effect of increase of resistance on the cost of energy loss (C), the following expression was used[557]

$$C = (\mathrm{d}r/\mathrm{d}t)I^2ft^2(h/2000)G, \tag{6.34}$$

where $\mathrm{d}R/\mathrm{d}t$ is the average rate of resistance increase per year (μΩ/year), I is maximum carrying current, f is the load factor (0.4), h is the total hours per year (8760) and G is the generation cost per kWh (0.05 U.S.$/kWh).

This expression was used to calculate the cost energy loss in three types of power connectors, compression, bolted and fire-wedge, subjected to 1030 days of exposure under severe saline environment.[558] All connectors used in this tests were supplied with an original corrosion inhibitor in place as supplied by the manufacturers. No modifications of any type were made to the inhibitor. For each connector type, a single connector size was selected for compatibility with strand bare aluminum or copper conductor.

The resistance rise due to the environmental exposure was $\mathrm{d}R/\mathrm{d}t = 24$, 234, and 325 μΩ/year respectively for the fired wedge, bolted, and compression connectors. The results of calculations of cost of energy loss due to an increase in resistance and carrying current of 400 A are shown in Figure 6.42. These results indicate clearly that the cost of energy loss due to average resistance increase per *single connector* is the highest in the compression and lowest in the fired wedge connector.

The superior performance of the fired wedge connectors over that of compression and bolted connectors is also illustrated in Figure 6.43 which depicts changes in the average resistance from the three connector populations with the exposure time. The average resistance was obtained as an arithmetic mean of the resistance values of all the samples tested including those that failed in the course of the test.

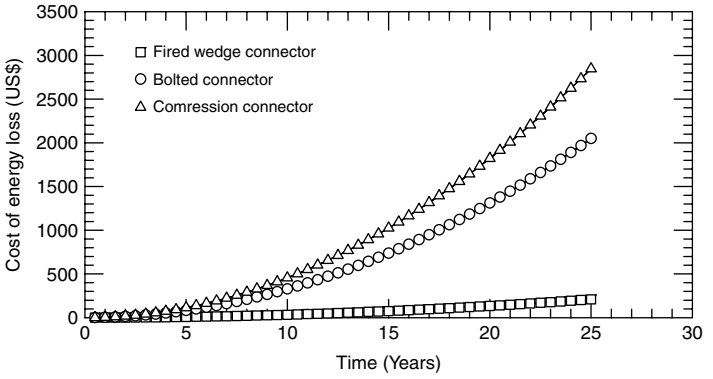

FIGURE 6.42 Cost of energy loss per connector due to resistance increase for the three connector populations.

The results of this study showed that differences in design, installation procedure, and corrosion inhibitor usage of power connectors have a major effect on the connector performance in a harsh marine environment. All observed connector failures were caused by galvanic corrosion that provoked severe degradation of the copper conductor–connector interfaces. The effect of the inhibitor in mitigating corrosion was rather limited in all cases.

From these results, it can be inferred that connector life was probably determined largely by connector design and that loss of mechanical contact load at conductor–connector interfaces, due to corrosion and corrosion product buildup, was a major factor controlling connector life. The superior long-term performance of fired wedge connectors is due to the "spring-action" of the connector C-member that resists loss of mechanical contact load and maintains the uniform stress distribution over the contact interfaces and the large area of metal-to-metal contact.[559] In contrast, engineering designs of compression- and bolted-type connectors lack these properties and thus these connectors performed less well in the long-term exposure test.

It should be emphasized, however, that the results of this study did not imply that all compression- or bolted-type connectors will fail in service or will have unacceptable failure rates in all environments. Rather, it accentuated the effect of engineering design on connector robustness of fired wedge connector in a harsh environment.

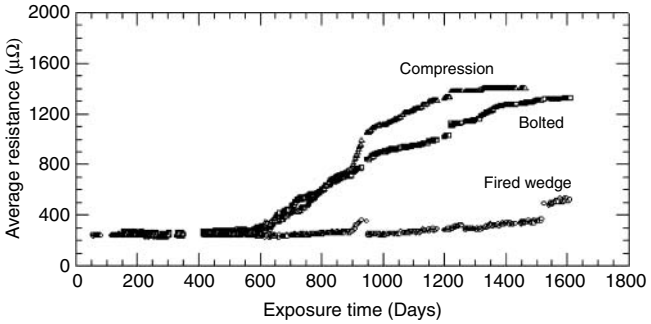

FIGURE 6.43 Typical variations of the average resistance across connectors from the three connector populations as a function of exposure time.

6.5.3 Power Quality

In recent years, power quality has become an important issue and is receiving increasing attention by utility companies, equipment manufacturers and end-users. Present equipment setups and devices used in commercial and industrial facilities, such as digital computers, power electronic devices, and automated equipment, are sensitive to power quality problems, which can slowly damage or destroy these devices.

Power quality is defined as the interaction of electrical power with electrical equipment. Correct and reliable operation of electrical equipment without being damaged or stressed qualifies the electrical power as of good quality. On the other hand, if the electrical equipment malfunctions, is unreliable, or is damaged during normal usage, the power quality is poor. Generally speaking, any deviation from normal voltage source (either DC or AC) can be classified as a power quality issue such as an electrical disturbance, a cause of the disturbance, contributing factors and the effect of the electrical disturbance on an appliance.

Most power quality problems are chain reactions. An incipient event causes an electrical disturbance, which is conducted by electrical system and eventually reaching an electronic appliance, which can be upset or even damaged, depending upon the energy level of the disturbance and the tolerance level of the appliance.

Disturbances refer to power quality variations that occur at random intervals but are not associated with the steady-state characteristics of the voltage. The most common power quality issues are as follows:[560]

- Transients, also called *surges* and *spikes*, are distortions of electricity caused by lightning, large motors starting, routine utility activities and other appliances.
- Harmonic distortion is deviation from a perfect sine wave represented by sinusoidal components having a frequency that is an integral multiple of the fundamental frequency caused by the power supplies of certain electronic appliances, including televisions, fax machines, and especially, personal computers. Harmonic distortion can overheat building transformers, building wiring, wiring in modular office panels, motors, and components in some appliances. This results in an increase in power consumption. The immediate effects of harmonic distortion are an increases in peak voltage, malfunctioning of control and/or regulation circuits, false switching of electrotechnical and electronic equipment and interfere with the neighboring telecommunication lines.
- A sag is a short (less than a second) decrease in the normal voltage level caused by faults on distribution and transmission circuits. Sags do not damage equipment, but can cause computers to restart or lock up and other appliances to lose memory. Even though the effects of these disturbances can be the same as long-duration outages, voltage sags can be more important because they occur much more frequently.
- A swell is a short (less than a second) increase in the normal voltage level. Mostly caused by motors stopping, swells generally do not upset or damage appliances but can initiate the failure of a stressed component in an electronic appliance.
- Interruption is defined as a momentary power outage that can last anywhere from fractions of a second to hours. Caused by lightning, downed power lines, tripped circuit breakers and blown fuses, interruptions disrupt computer processes, clocks and the memories of unprotected electronic devices.

Figure 6.44 shows the most common electrical disturbances found in the electrical system.

Power disturbances arising within end-user facilities have increased significantly due to the increasing use of energy efficient equipment. Characterization of disturbances requires a comprehensive monitoring and data capturing system that to understand power quality problems. Monitoring will provide us with valuable data. However the data needs to be interpreted and

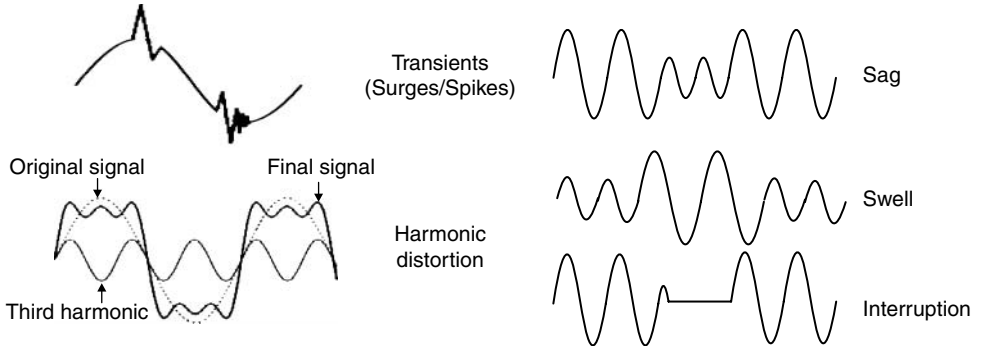

FIGURE 6.44 Most common electrical disturbances found in the electrical system.

applied to the type of equipment being powered. Power quality measures a wide range of power-supply characteristics that also can influence the performance of equipment and processes. In other words, the reliability of end-use processes is dependent on both the reliability and quality of the electric service. It is important to note that many power quality characteristics are a function of both the supply system and end-user system and equipment characteristics.

A good understanding of electrical power quality and its impact on the performance of power systems is a critical part of developing the best design for equipment specifications and for facility protection. In general, equipment should be designed to withstand the normal steady-state power quality variations expected as part of the normal operation of the power system. Although it is unrealistic, however, to expect the equipment to handle all disturbances that may occur, understanding the expected disturbances and the frequency of their occurrence is essential for optimization of the investments in equipment protection.

7 Power Connections

7.1 TYPES OF POWER CONNECTORS

To meet the mechanical and electrical requirements and also assure reliable performance of a connector during its expected service life, various designs have been developed and used in the field with varying degree of success. The generic connector designs commonly used on distribution network are illustrated in Figure 7.1.

The field experience has shown that a wide variety of connector designs have served well over several years, but the factors contributing to their success and to their failure elsewhere could not be determined with any degree of certainty. However, the ever-increasing demand for electricity in recent years increased electrical loading on power transmission and distribution lines by many utilities, which, in turn, raised the average operating temperature of conductor lines—up to 130°C during times of peak power transmission.[561] Consequently, these operating conditions may expose connectors to temperatures exceeding the operating range for which many connecting devices were initially designed,[562,563] thus imposing new performance demands on electrical connectors. In other words, connectors are now expected to operate reliably at relatively elevated temperatures.

The types of connectors can be generally classified as: compression, mechanical, wedge, make and brake (disconnect), and fusion. Compression connections use engineered tooling to crimp the connector to the conductor with high force, creating a permanent electrical joint. Mechanical connections employ hardware or similar mechanical means to create a contact between two metals and to maintain its integrity. Wedge connectors are made by driving the wedge between two conductors into the "C." Fusion connections are made primarily by welding, soldering or brazing. A classification of connectors according to their design and functional operation is given below.

Although it is generally accepted that a good mechanical joint is also a good electric joint (and this is indeed true in many cases), in some instances, this may not be so due to the intrinsic nature of current transfer across the contacting members, and also design features of a particular connection and deterioration mechanisms that may impact the connection performance. Hence, it is important to review the basic design features of the most common types of power connections and the factors that impact their performance; only with the proper attention to these factors can a good electric connection be made consistently.

7.2 DESIGN FEATURES AND DEGRADATION MECHANISMS

7.2.1 Bolted Connectors

Bolted type connection is a widely used method of joining aluminum and copper conductors. In properly prepared conductor (busbar) surfaces, the contact resistance of a joint is determined by the resistivity of the contact members, the contact area, and distribution of the conducting spots in the interface between the contact members. The area and distribution of the conducting spots are generally determined by the surface finish and the magnitude of the applied force, and the manner in which it is applied.

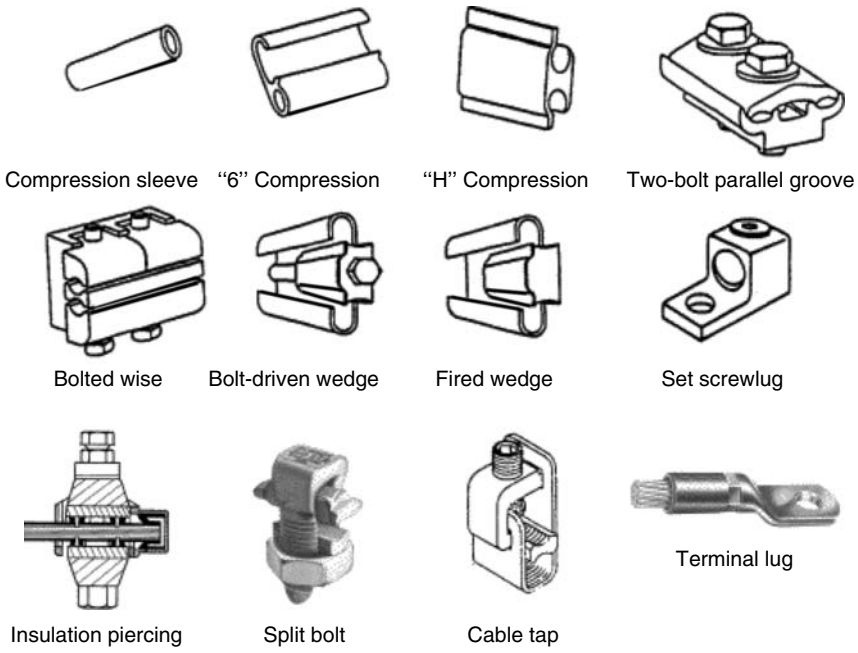

FIGURE 7.1 The generic connector designs commonly used on power network.

When a joint is made, the metal yields plastically under the increasing pressure at the local projections. The brittle film on the contact surface fractures, since it cannot follow the deformation, and fissures formed in the film provide the true metal contact (a-spots) where current passes the interface without any transition resistance. The a-spots are surrounded by areas of insulating films (oxides, sulfides) that have not been fractured and where no passage of current occurs. As shown in Equation 1.5, the total contact resistance (R) of a joint between two contacting metallic surfaces consists of the constriction resistance (R_c) and the resistance of the film (R_f), that is,

$$R = R_c + R_f = (\rho_1 + \rho_2)/2a + \sigma/\pi a^2, \tag{7.1}$$

where ρ_1 and ρ_2 are the resistivities of the contacting metals and σ is the resistance per area of the film.

It has been shown that in a bolted joint that current lines are distorted at the joints, and as a result, the resistance of even a perfectly made overlapping joint (no interface resistance) is higher than that of a bar of the same length as the joint.[564] This is known as "streamline effect" and is determined by the ratio between the overlap and busbar thickness. Figure 7.2 shows the action of current flowing through overlapping busbars of uniform width (w), and thickness (t).

Thus, the strip is shaped like a lapped joint but is void of contact surfaces along AB, except through the art of its length AB where the thickness is $2t$. A current (I), is passed through the busbar from end to end. The voltage drop is measured between A and B, and between B and C, whereby distance AB = BC. Hence,

$$V_{AB} = RI \text{ and } V_{BC} = R_B I$$
$$e = V_{AB}/V_{BC} = R/R_B \tag{7.2}$$

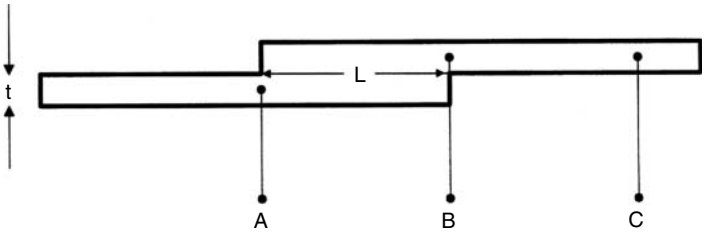

FIGURE 7.2 Schematic of an overlap joint without contact interface.

where e is the streamline effect, R is the total resistance of a joint and R_B is resistance of equal length of a busbar and is given as

$$R_B = \rho(L/wt). \tag{7.3}$$

Hence, the streamline effect e becomes a function of the ratio L/t, i.e.,

$$e = R\left(\frac{w}{\rho}\right)\left(\frac{1}{L/t}\right). \tag{7.4}$$

Melsom and Booth[564] have tested a number of different busbar combinations and obtained the results shown in Figure 7.3, which allows calculating the resistance caused by the streamline effect of a perfectly made overlap in relation to the resistance of an equal length of a single busbar.

From this figure, it appears that the streamline effect rapidly decreases until the overlap/thickness ratio reaches a value of two when its decrease is slowed down and practically stabilized upon passing a value of 6. In other words, upon reaching this value, the current distortion is minimized and the current lines become parallels. Consequently, the optimal overlap length in a bolted joint should be 5–7 times the busbar thickness. However, to meet all requirements, and for the sake of convenience, it is common practice to make overlaps equal to the width of the busbar.

Although this procedure is usually satisfactory for busbars of ordinary dimensions, it may not provide sufficient joint contact area on busbars that have a high thickness-to-width ratio. Hence, as

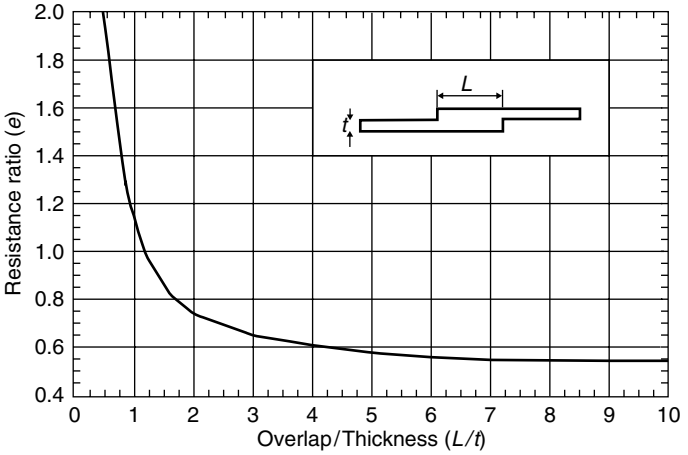

FIGURE 7.3 Effect of current distortion (streamline effect) on the contact resistance of an overlapping joint.

a rule of thumb, the minimum overlap should be from 8 to 10 times the bar thickness. Furthermore, since the actual area of contact is much less than the total area of overlap, the determination of overlap on the basis of the width alone is a reasonably safe practice only if the current density in the contact surface does not exceed one-third to one-fourth of the current density in the busbar cross-section.

It is interesting to note that Donatti[565] has shown that in a bolted joint, unless it is produced in a perfect way, it is not possible to have a uniform distribution of the current on the contact surface. Furthermore, he has also shown that the current tends to traverse the contact surface at the end points of the joint while the intermediate region only sees little use in the passage of current. This feature was exploited in the edge-shaped transition washer as seen in Figure 7.4.[566]

In a bolted connection, the relationship between the contact resistance (R_c) and the applied force (F) can be described by the following expression,

$$R_c = C/F^n \tag{7.5}$$

where C is the proportionality constant and n is the exponent. The values of the constants C and n depend on the joint configuration, type of lubricant and coating used. The values of n for bare, coated, and lubricated aluminum-to-aluminum and aluminum-to-copper connections were found to vary between 0.1 and 1.0.[146,567]

It should be emphasized, however, that the use of contact force as an indicator of a satisfactory joint assembly is impractical. Instead, tightening torque is used almost exclusively in practical situations. An empirical relationship commonly used to relate the tightening torque with the applied force generated by the bolt in a joint is given as:

$$T = KDF, \tag{7.6}$$

where T is the tightening torque (Nm), K is a constant ("nut factor," dimensionless), D is the bolt diameter (mm), and F is the contact force (N).

The "nut factor," K, is greatly dependent on the coefficient of friction, finish and lubrication of the threads, and other bearing surfaces. Even for specified conditions of finish and lubrication there

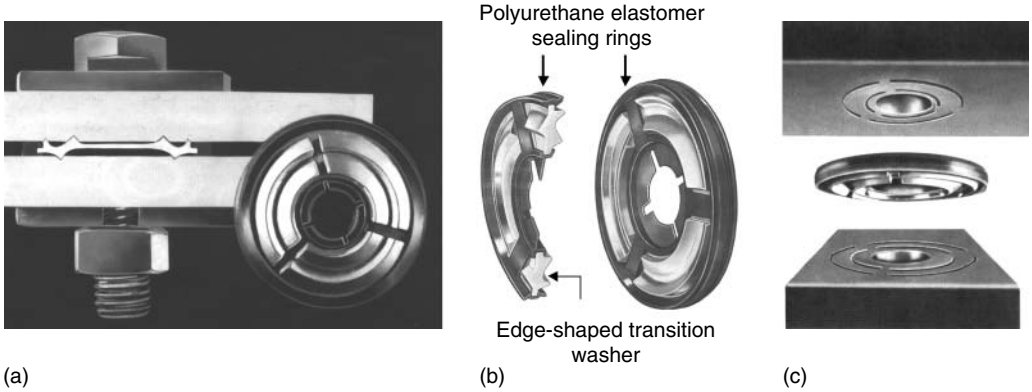

FIGURE 7.4 Pfisterer transition washer (Elast contact disk) (a) Cross-section of the busbars with the transitions washer showing the contact points; (b) cross-section of a transition washer; (c) busbar contact surface showing the impressions left by the sharp edges of transition washer. (From *Pfisterer Technical Notes: Station fittings* 5, 14–16, 1987.)

is considerable variation in this relationship. Furthermore, not only must the tightening torque be specified, but the rate of tightening must be controlled as well.

The rate of relaxation from cold flow of aluminum conductor is quite large under the pressures encountered in most bolted connectors. Hence, a slow rate of application of torque will result in more relaxation being taken up before the final installation torque is reached. Although continuous torque application produces more rapid failure, a stepped application of torque was selected as the standard of tests. Continuous torque application was considered impractical for a standard procedure since multibolt connectors must be installed by tightening each bolt in turn by steps.

Tightening torques depend upon the contact pressure required for the particular busbar application. The amount of pressure for a given torque value varies over a wide range, depending upon if threads are dry, lubricated, hot galvanized, or otherwise treated. From the standpoint of the strength of the bolts, a maximum tightening torque equal to 95% of the yield strength of bolt is recommended. Hence, it is essential to maintain the tightening torque within this limit, since upon exceeding it the busbar will undergo plastic deformation, which in turn, will increase the stress relaxation and creep and thus cause loosening of a joint. The end result is an increased contact resistance and temperature, eventually causing the joint to fail.

A review of the tightening torques specified by different manufacturers for bolting different power equipment reveals a great diversity in the recommended torque values. For instance, the range of tightening torque for a 12.7-mm (1/2-in.) diameter bolt is 50–80 Nm (35–60 lb ft). Hence, the forces generated by these torques may exceed the yield strength of certain bolt material.

To illustrate the importance of tightening torque and the nut factor K, the stresses generated by the torque range 50–80 Nm (35–60 lb ft) in 12.7 mm diameter (1/2–13 in.) bolts made of silicon bronze and stainless steel 304 and 316 were calculated and the results are shown in Table 7.1. From this table, it can be inferred that for lower values of nut factor K ($K = 0.15$), certain bolt materials cannot sustain the forces generated by the applied tightening torque and will deform plastically. The lower values of the nut factor K ($K = 0.15$) are generally attributed to the effect of lubrication on the coefficient of friction. Hence, it appears that same tightening torque may induce much higher forces in the lubricated than in nonlubricated bolts.

This is very important, since it may be argued that the use of contact aid compounds may adversely affect the mechanical integrity of a bolted joint by exceeding the permissible force limits in the bolts. It was shown, however, that the use of common contact aid compounds did not produce any significant increase in the contact forces in neither the bolts nor the joint.[567]

On the other hand, when boundary lubricant, such as Mo_2S ($K = 0.15$) was used, much higher forces were generated in the bolt. Table 7.2 shows the range of the nut factor when jointing was made with dry bolts and also when lubricated with the contact aid compounds and boundary type lubricant. It appears that there is a very small difference between the values of the nut factor K for dry bolts and those lubricated with the contact aid compounds.

The effect of lubrication that is the nut factor K on the contact force generated in bolted joints is shown in Figure 7.5. It is clear that the same tightening torque generates much higher contact forces in a joint when assembled with the bolts lubricated with the Mo_2S lubricant than when assembled with the bolts lubricated with the contact aid compounds. Furthermore, at higher tightening torques the permissible limits of certain bolt materials will be exceeded and thus the mechanical integrity of a bolted joint will be adversely affected.

In a properly assembled bolted joint, the stresses developed increase very rapidly with increase in bolt diameter and also with the yield strength of the bolt material. Therefore, the use of bolts of too small a diameter is insufficient to provide adequate contact area that will lead to unsatisfactory joint performance. Furthermore, the stress distribution required to create areas of low resistance (a-spots) are developed only in the zone immediately under the bolt head or flat washer (when used), and thus are very local. Since these zones are located immediately under

TABLE 7.1
Characteristics of Bolt Materials and Calculated Forces in Bolts Generated by Tightening Torques for Different Values of "Nut Factor," K

Bolt	σ_y[a] MPa (KSI)	A_b,[b] mm^2 (in.^{2})	F_{max}[c] (95% σ_y) kN (lb)	Torque, Nm (lb ft)	Calculated Force in Bolt, kN (lb)		
					$K = 0.3$	$K = 0.2$	$K = 0.15$
Silicon	365 (53)	91.5 (0.142)	31.7 (7 144)	50 (35)	12.4 (2 800)	18.7 (4 200)	24.8 (5 600)
Bronze	365 (53)	91.5 (0.142)	31.7 (7 144)	60 (45)	16.0 (3 600)	23.9 (5 400)	31.8 (7 200)
C651000	365 (53)	91.5 (0.142)	31.7 (7 144)	70 (50)	17.8 (4 000)	26.5 (6 000)	35.5 (8 000)
ASTM	365 (53)	91.5 (0.142)	31.7 (7 144)	80 (60)	21.3 (4 800)	31.8 (7 200)	42.5 (9 600)
468-93							
Stainless	207 (30)	91.5(0.142)	17.9 (4 044)	50 (35)	12.4 (2 800)	18.7 (4 200)	24.8 (5 600)
Steel 304	207 (30)	91.5 (0.142)	17.9 (4 044)	60 (45)	16.0 (3 600)	23.9 (5 400)	31.8 (7 200)
ASTM	207 (30	91.5 (0.142)	17.9 (4 044)	70 (50)	17.8 (4 000)	26.5 (6 000)	35.5 (8 000)
593	207 (30)	91.5 (0.142)	17.9 (4 044)	80 (60)	21.3 (4 800)	31.8 (7 200)	42.5 (9 600)
Stainless	414 (60)	91.5 (0.142)	35.8 (8 088)	50 (35)	12.4 (2 800)	18.7 (4 200)	24.8 (5 600)
Steel 316	414 (60)	91.5 (0.142)	35.8 (8 088)	60 (45)	16.0 (3 600)	23.9 (5 400)	31.8 (7 200)
Cold	414 (60)	91.5 (0.142)	35.8 (8 088)	70 (50)	17.8 (4 000)	26.5 (6 000)	35.5 (8 000)
Worked	414 (60)	91.5 (0.142)	35.8 (8 088)	80 (60)	21.3 (4 800)	31.8 (7 200)	42.5 (9 600)
ASTM							
593							

[a] σ_y, yield stress.
[b] A_b, bolt cross-section.
[c] F_{max}, maximum force supported by the bolt.

those bolt heads or flat washers and increase rapidly in area with increasing bolt/washer size, this should be taken into account when deciding the number and the size of the bolts to be used in a connection.

Thus, the use of high-strength bolts and distributing stress as uniformly as possible will yield many more *a*-spots and a lower contact resistance. Another advantage of using the high-strength bolts is the situations when the projected area is limited by external factors, or by a particular design. On the other hand, bearing in mind that the true area of contact developed by a given bolt loading is proportional to the elastic limit of the bar material, it is clear that a lower total clamping pressure would be required for aluminum than for copper bars. The size and the number of the bolts depend on the projected contact area. Bolts should be tightened evenly and the use of a torque wrench is helpful in this respect.

Further improvement in the stress distribution and also an increased size of the contact area can be achieved using the rigid flat washers under the bolt heads and nuts. These washers may be of

TABLE 7.2
Values of "Nut Factor" When Dry and Lubricated Bolts Were Used for Assembling the Bolted Busbar Joints

Nut Factor	Dry Bolts	Contact Aid Compounds	Boundary Lubricants
K	0.20–0.22	0.19–0.21	0.15–0.16

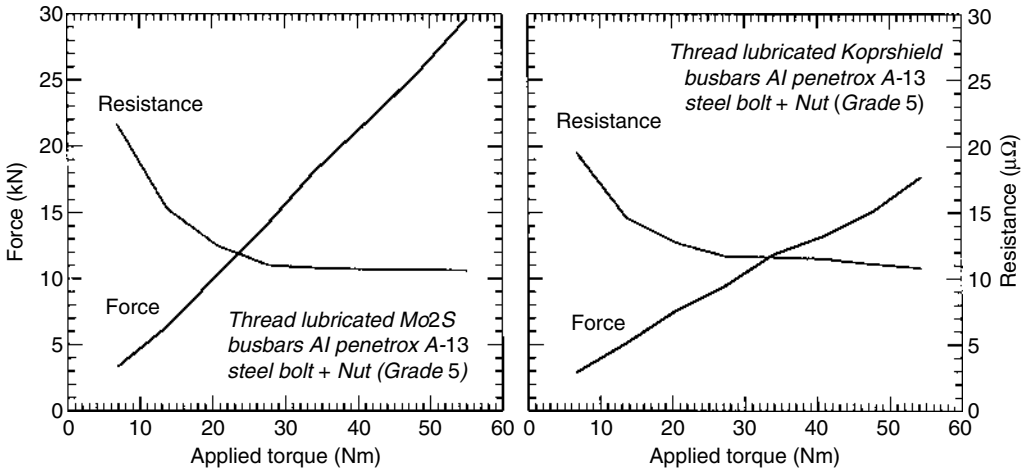

FIGURE 7.5 Effect of the "nut factor" on the contact force generated in bolted joints.

steel, cast iron, aluminum alloy or bronze and should have a larger diameter. Detailed descriptions of the various mitigating measures required to assure satisfactory performance of bolted joint is given in Section 7.3.

Although the bolt joint configuration assures reliable and trouble-free performance, the bolted joints are not impervious to the deleterious effects of different degradation mechanisms. Some examples of deterioration mechanisms in bolted joints follow.

7.2.1.1 Fretting in Bolted Connectors

It is generally accepted that the reliability of bolted joints is attributed to high contact forces and large apparent contact areas with virtually no relative displacement between the contacting members. Although this may hold for copper–copper joints, it is certainly not the case for aluminum–copper connections. This is because the coefficient of thermal expansion of aluminum is 1.36 times that of copper and when a bolted aluminum–copper joint is heated by the passage of current, aluminum will tend to expand relative to copper, causing displacement of the contact interface. The shearing forces generated by differential thermal expansion will rupture the metallic bonds at the contact interface and cause significant degradation of the joint. Published experimental evidence and reports of trouble in service show that bolted joints may not be as impervious to degradation and failure.

The effect of relative motion in aluminum–copper bolted joints has been investigated in the laboratory by Bond,[568] Naybour,[569] Jackson,[140] and Roullier.[570] They have shown that the relative displacement induced by differential thermal expansion forces is one of the major degradation mechanisms of aluminum–copper joints. However, despite the seriousness of this problem, there is very little published information linking field failures with the degradation effects of relative motion (fretting) in bolted joints.

Fretting damage in real life tin-plated aluminum and copper connectors, commonly used for distribution transformers, has been reported by Braunović.[571] The connectors examined had been removed from the service after 7–10 years of service due to either overheating, as revealed by routine thermographic inspection, or unstable performance on the network under normal operating conditions. The connectors were bolt-type tin-plated aluminum or copper busbars jointed with either tin-plated or bare aluminum cable terminals. A typical example of the connectors with signs of severe fretting damage as evidenced by a characteristic band of accumulated fretting debris and oxides is shown in Figure 7.6.

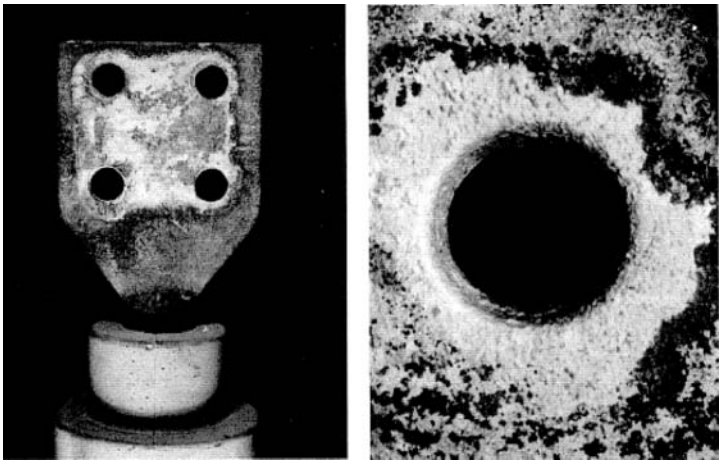

FIGURE 7.6 Typical example of a tin-plated connector removed from service with signs of severe fretting damage as evidenced by a characteristic band of accumulated fretting debris and oxides.

A detailed examination of these areas reveals the presence of four distinct forms of fretting damage: electrical erosion by melting/arcing, accumulation fretting debris, delamination, and abrasion. These forms of fretting damage are shown in Figure 7.7.

The results of contact resistance measurements across the contact zone of a tin-plated copper connector are shown in Figure 7.8. The most important feature is that the contact resistances of the

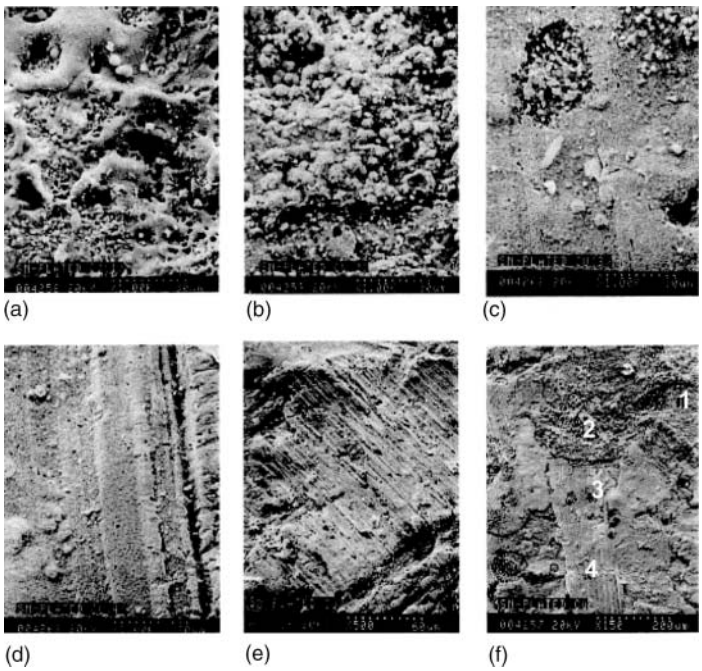

FIGURE 7.7 SEM surface analysis of typical fretting damage in aluminum-to-tin-plated copper connection: (Z) contact zone damaged by fretting; (a) electrical erosion (region 1); (b) accumulation of fretting debris and oxides (region 2); (c) delamination wear (region 3); (d) abrasion (region 4); (e) combined delamination–abrasion.

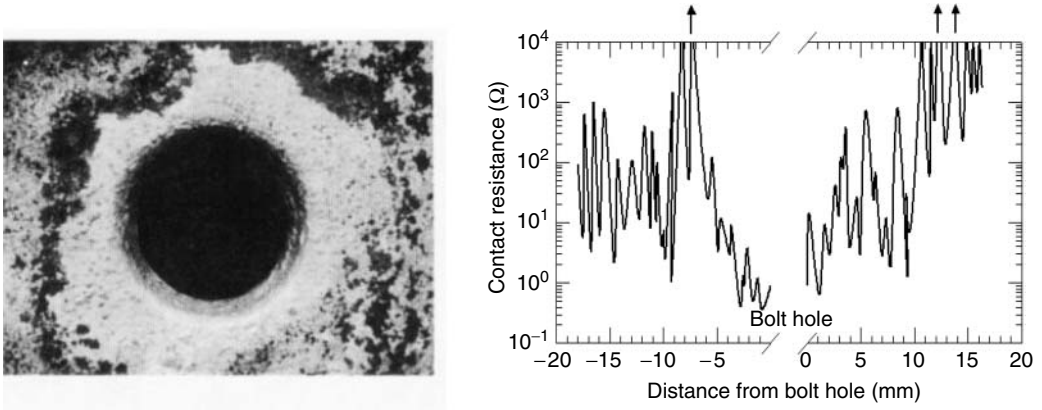

FIGURE 7.8 Contact resistance variations with the distance from the bolt hole in the contact zone of a tin-plated copper connector.

zones severely damaged by fretting increases rapidly to very high values, and in some locations, open-circuit conditions develop. The cyclic nature of the contact resistance, manifested by sharp fluctuations from one site to another, indicates that the fretting debris formed on the connector surface is not a continuous layer but rather, porous, since the transition from high- to low-conducting current paths occurs over relatively short distances.

The presence of a region around the bolt with very low contact resistance values can be associated with the formation of good metallic contact in the load-bearing area under the flat washer where the contact pressure is highest. Detailed SEM examination of these zones shows no evidence of severe fretting damage or accumulation of fretting debris. Rather, the granular texture of the tin-plating was heavily deformed and compacted, as revealed by the presence of areas with smooth surfaces with clearly visible scars of mild abrasion.

The results of x-ray diffraction analysis of the fretting debris removed from the damaged contact zones of tin-plated aluminum connectors showed that the fretting debris was composed mainly of tin, but the presence of $Al(OH)_3$ was also detected, indicating that corrosion products of aluminum were also prominent constituents. This finding suggests that fretting was not the only mechanism responsible for the observed degradation of tin-plated connectors and that corrosion also played a very important part.

The presence of corrosion products in the contact zones indicates that the introduction of an aqueous solution to a fretting environment may influence the fretting process in one or both of two distinct ways. First, the liquid can serve as a lubricant, thus separating the metal surfaces and reducing adhesion, friction, and wear rate. Second, a liquid may induce an anodic corrosion reaction within the fretting scar, trapping the corrosion products inside the fretting scars and thus increasing the rate of wear.

7.2.1.2 Fretting in Aluminum Connections

The deleterious effects of fretting are of particular interest in aluminum connections since aluminum exposed to the atmosphere rapidly oxidizes, forming an oxide film within a very short time. Hence, under fretting conditions, accumulated wear debris and oxides cannot be effectively removed from the contact zone and a highly localized, thick insulating layer is formed, leading to a rapid increase in contact resistance and, subsequently, to virtually open circuits.

The performance of aluminum conductors in contact with different plating and base metals under fretting conditions has been extensively studied by Braunović[474,571–574] who has shown that

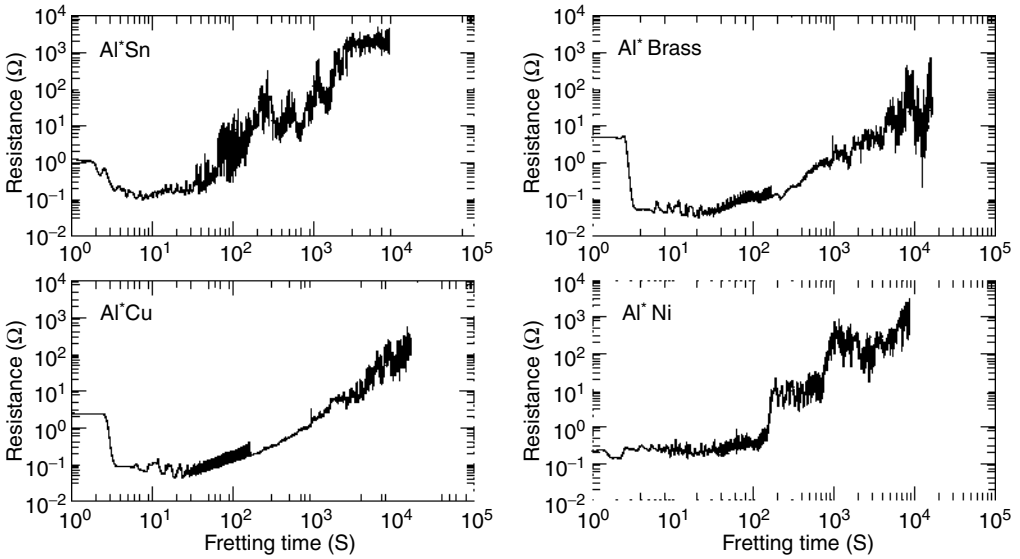

FIGURE 7.9 Contact resistance behavior of aluminum in contact with common contact materials under fretting conditions: slip amplitude 25 μm contact load 2 N; frequency 0.005 Hz.

fretting adversely affects the contact behavior of aluminum in contact with practically all common contact materials. Some typical examples of such behavior are shown in Figure 7.9.

Another important finding of the work on aluminum connections is that fretting causes an extensive exchange of materials in the contact zones. Some representative examples of the scanning electron microscope (SEM) and energy dispersive x-ray analyses (x-ray mapping) of material transfer in the aluminum-to-tin plated brass connections are shown in Figure 7.10.

The deleterious effects of fretting can be greatly reduced by applying higher contact loads and/or lubricants to the contact zones. When higher load are applied, the onset of the thermal run-away condition can be delayed since much higher contact resistance is needed to reach the contact voltage or spot temperature required for this to occur (see Chapter 6, Section 4.4 and Chapter 7, Section 3).

7.2.1.3 Intermetallics

Flexible connectors often referred to as expansion joints, jumpers, braids, braided shunts are widely used in power generating stations and substations. Their main function is to establish continuous current transfer, for instance, between rigid busbars, tubular conductors, or current-carrying parts of other electrical equipment such a power meters, disconnect switches, etc. Flexible connectors are made by compressing the copper or tinned copper ferrules with inserted ends of stacks of copper or tinned copper laminates or bundles of braided wires. In order to maintain mechanical and electrical uniformity, the sides of ferrule are often soldered.

In flexible connectors made of bare copper wires or laminates, an increase in temperature accelerates the rate of oxidation of wires or laminates,[575] while in the tinned copper flexible connectors it accelerates the rate of formation of intermetallic phases at the tin–copper interfaces. In both cases the end results is the same—reduction of the current-carrying cross-section area, overheating and connector failure.

The formation of intermetallics in flexible tinned-copper connectors, or jumpers (Figure 7.11), removed from the generating station duct-busbar assemblies after different periods of service as a result of overheating (revealed by routine thermographic inspection), was investigated by Braunović.[576] The bolt-type jumper connections with tin-plated copper laminates were subjected to a

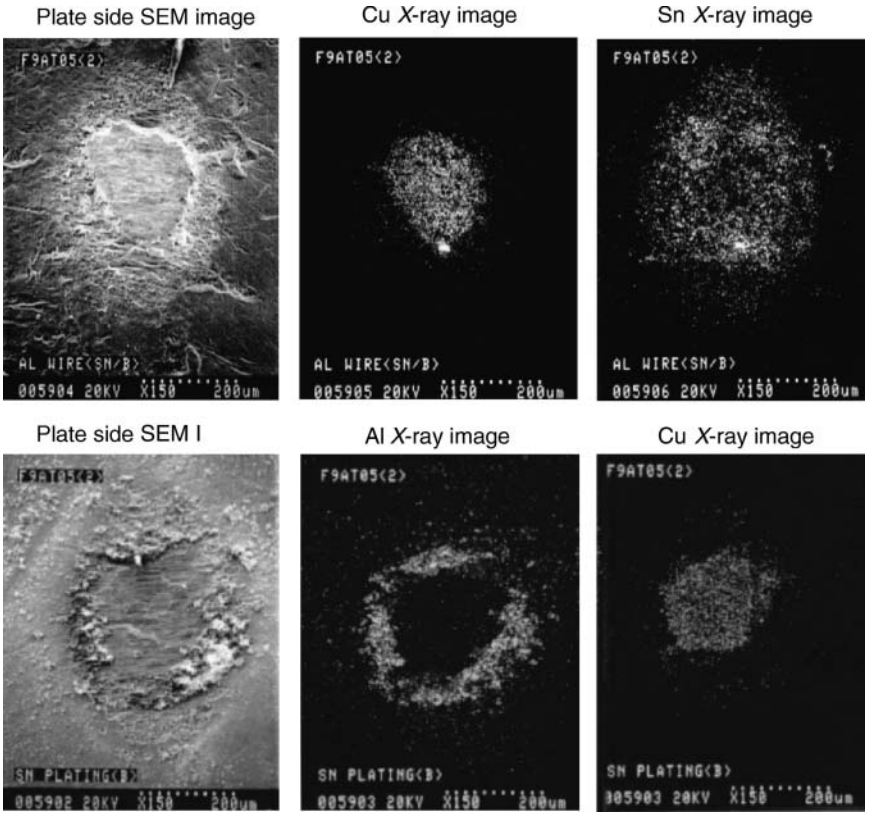

FIGURE 7.10 SEM micrographs of fretting damage in contact zones of an aluminum conductor in contact with tin-plated connections. The x-ray images of Al, Cu, and Sn exemplify the transfer of materials in both directions.

detailed metallographic analysis including microhardness, contact resistance measurements, optical, and SEM examinations of selected zones of connector pads. For contact resistance and microhardness measurements, thin cross-sectioned slabs were cut from the connector pads, metallographically polished, and lightly etched to reveal the microstructures of the tin–copper interfaces and copper laminates.

Contact resistance measurements in the selected zones were made using a precision DMO 350 microohmmeter with a specially designed four-point probe, replacing the diamond indenter in a hardness tester. Figure 7.12a shows an optical micrograph of the flexible connector cross-section with some of the locations for the four-point probe resistance measurements. The resistance

FIGURE 7.11 Typical examples of flexible tinned copper connectors: intact and failed connector.

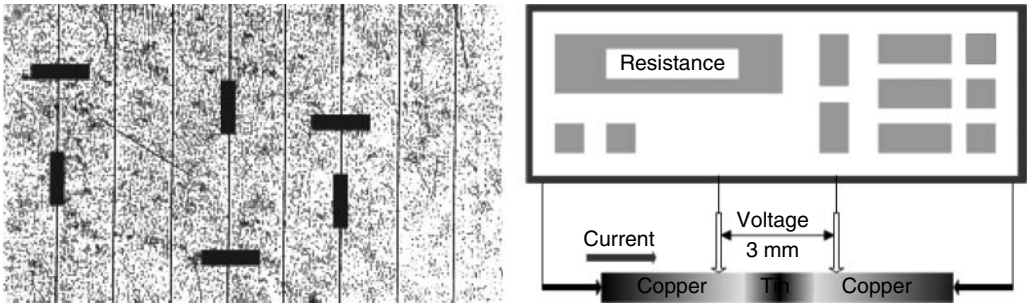

FIGURE 7.12 (a) Optical micrograph of flexible connector pad cross-section showing the positioning of the four-point resistance probe (not to scale); (b) simplified schematic of the assembly used to measure the resistance across and inside tin–copper interfaces and bulk of flexible connector laminations.

changes in the selected zones were sufficiently large to be measured between the potential probe points. This method allowed measurement of the resistance across and inside the copper–tin interfaces as well as in the bulk of copper laminates. Figure 7.12b shows a simplified schema for resistance measurements.

The advantage of the four-probe resistance measuring technique lies in its ability to detect minute structural change in the bulk of the material within a very small volume penetrated by current. The size of the current penetration is determined by the probe spacing. Typically, current penetration is limited to 1.5 times the probe spacing.[577] This technique has been successfully used for studying semiconductor materials as well as in monitoring the case-, precipitation-, and strain-hardening processes in metallic systems.[577]

The results of resistance measurements made on the cross-sectioned intact and damaged flexible connectors are presented in Table 7.3, clearly showing that the resistance of intermetallic phases formed at the copper–tin interfaces is much higher than the bulk resistance of copper laminates. Hence, the presence of high resistive intermetallic phases will significantly increase the contact resistance of connector pads and consequently temperature of the bolted joint.

The difference in resistance measured across the Cu–Sn–Cu interface and inside Cu–Sn intermetallic bands of intact and damaged connectors can be attributed to the presence of different amounts of fractured intermetallics and porosity in these zones. Higher concentrations of fractured intermetallics and porosity will reduce the effective conducting area and hence increase the bulk

TABLE 7.3
Resistance Measured in the Bulk of Connector Laminates across Cu–Sn Interface and Inside of Cu–Sn Intermetallic Phases and Microhardness Measured in Copper Connector Laminates within Tin Plating and Inside Cu–Sn Intermetallic Phases

Resistance Data				Microhardness Data			
Sample	Laminate Bulk (μΩ)	Cu–Sn–Cu Interface (μΩ)	Inside Cu–Sn Band (μΩ)	Sample	Laminate Bulk (kg/mm^2)	Tin Plating (kg/mm^2)	Inside Intermetallics (kg/mm^2)
Intact	3.00	9.35	16.78	Intact	100	6	345
Damaged	2.20	15.25	25.65	Damaged	70	—	266

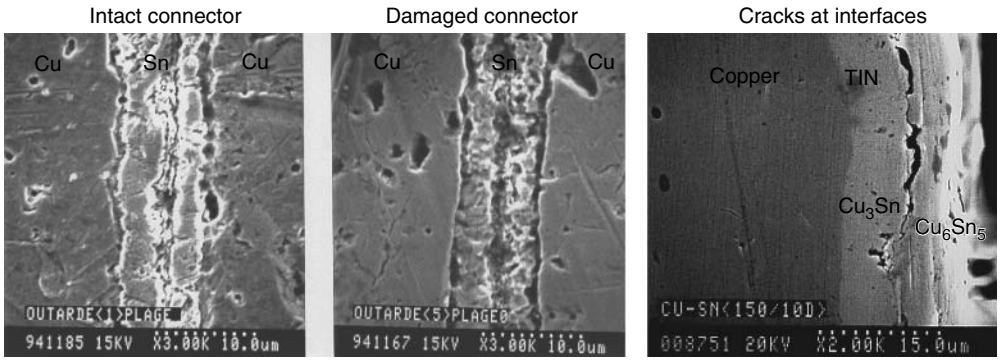

FIGURE 7.13 SEM micrographs of the intermetallic phases formed in (a) intact; (b) damaged flexible tinned copper connectors; (c) Cracks formed at the interface of intermetallic phases Cu_3Sn and Cu_6Sn_5.

resistance. Lower bulk resistance of damaged connectors is a result of annealing of cold drawn copper laminates as the connector overheats.

The results of microhardness measurements, shown in Table 7.3, clearly indicate that the microhardness of the intermetallic phases is considerably higher than that of copper laminates (70–100 kg/mm^2) and tin plating (6 kg/mm^2). In addition, the microhardness of intermetallic phases formed in intact connectors is higher than that in a damaged one. The observed difference is associated with the morphology of the phases present in these samples.

The results of SEM surface analysis (Figure 7.13a and b) show that the intermetallic phases at the copper–tin interface formed not only in the damaged, but also the intact flexible connector during the hot-dip tinning process. Detailed examination of the intermetallic phases reveals considerable cracking at the copper–tin and tin–tin interfaces, which is a clear indication of their low mechanical strength, hence their brittle nature. The brittleness of these phases is illustrated by the presence of cracks at these interfaces (see Figure 7.13c) and also by their substantially higher microhardness values (see Table 7.3).

7.2.1.4 Creep and Stress Relaxation

The mechanisms that may be responsible for creep are due to dislocation climb, viscous dislocation glide and climb, grain boundary sliding, and a general reordering of dislocations to a more stable configuration.[578] Although there is a great deal of published data treating the problem of creep and stress relaxation in different materials, there are rather limited data on the effect of creep and stress relaxation in electrical contacts.

As pointed out in Section 6.4.7, due to the intrinsic properties of aluminum, stress relaxation, and creep are probably the most deleterious degradation mechanisms in aluminum-based connections. Although alloying aluminum with different elements was found to produce a considerable improvement in reducing the effects of stress relaxation and creep, their adverse effect on the mechanical and thus electrical integrities of aluminum-based joints could not be completely suppressed.[513] To mitigate this problem, different mechanical contact-aid devices (hardware) have to be used; their effects on the performance of bolted joints are discussed in Section 7.3.

The effect of creep on the performance of aluminum-to-aluminum busbar joints was investigated by Grossman et al.,[579] Kindersberger et al.,[580] and Schoft.[581] These authors have clearly shown that creep exerts strong influence on the performance and thus reliability of bolted power

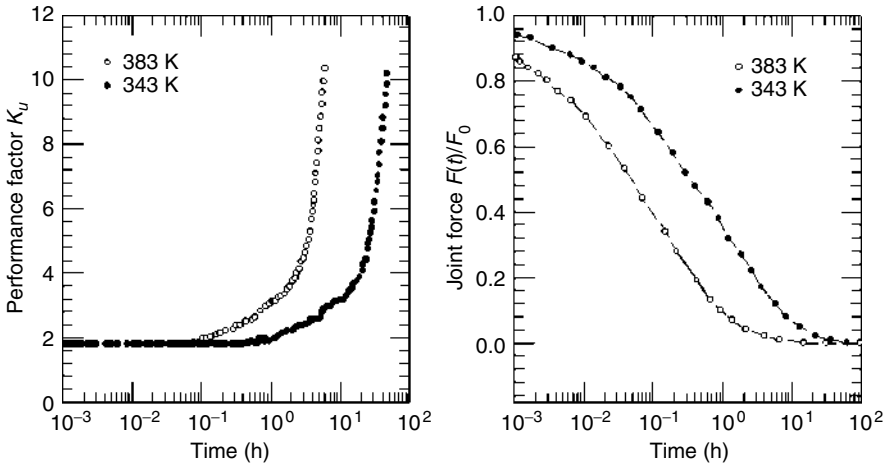

FIGURE 7.14 Effect of creep on the performance factor $k_u = R(t)/R_0$ and relative joint force $F(t)/F_0$ where $R(t)$ and $F(t)$ are the values of contact resistance and force after time t and R_0 and F_0 are the initial values of the contact resistance and force. (Data derived from Kindersberger, J., Lobl, J., and Schoft, S., *Proceedings of 20th International Conference on Electrical Contacts*, Stockholm, Sweden 367–372, 2000. With permission.)

connectors when relatively pure aluminum conductors (type EC-1350 grade) are used. The effect of creep was manifested by significant loss of contact force, causing equally significant augmentation of contact resistance leading to a run-away situation. The effect of creep on the performance factor, (basically contact resistance) and contact force is illustrated in Figure 7.14.[579]

The effect of stress relaxation on the contact resistance and force in bolted connections with EC-1350 grade aluminum busbar conductors under static (low current) and dynamic (current cycling) conditions was also investigated by Braunović.[582] Both static and dynamic tests were conducted using different mechanical contact aid devices (hardware). Braunović showed that although the deleterious effect of stress relaxation could not be prevented, the use of adequate hardware (joint configuration) can significantly improve the mechanical and electrical stabilities of the bolted joints and thus minimize loosening of the joint during stress relaxation and exposure to the current-cycling conditions.

The effects of different hardware and joint configurations on the performance of bolted joints is depicted on Figure 7.15. The use of disc-spring (Belleville) washers combined with thick flat washers assured the most satisfactory mechanical and electrical stability of a bolted joint.

7.2.2 Bus-Stab Contacts

Field experience with separable power contacts involving aluminum busbars has indicated failures in certain industrial locations. These were evidenced by mechanical erosion and electrical burning of metal at the contact areas, resulting ultimately in an open-circuit condition. Johnson and Moberly[583] have investigated the effect of fretting on the performance of bus-stab contacts with tin- and silver-plated aluminum busbars under normal operating conditions.

It is now recognized that bus-stab contacts are subjected to three modes of mechanical motions, illustrated in Figure 7.16. The first mode occurs when the busbars are subjected to variations in electrical load, changing their lengths due to thermal expansion. This results in slow slide motions with respect to the stab contact (direction A–A, Figure 7.16) that, in turn, causes elongation of the stab contact area along the busbar. This was confirmed by the burnished track on an actual

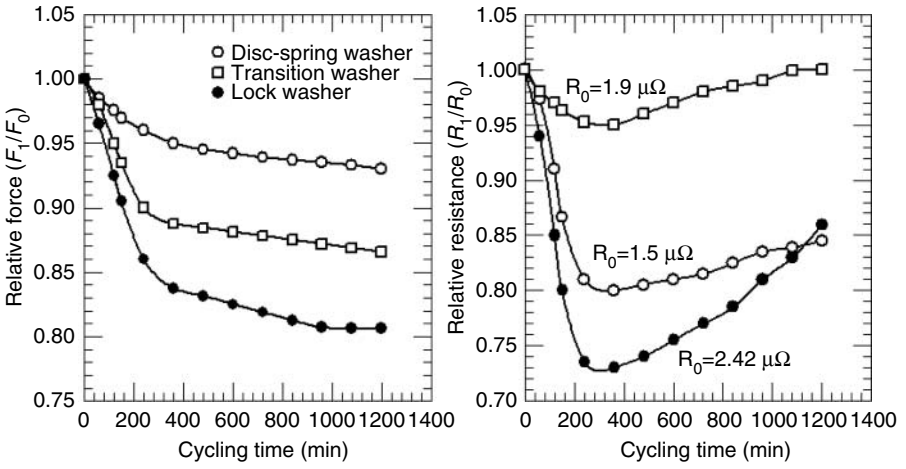

FIGURE 7.15 Effect of stress relaxation under current-cycling conditions on the contact force and resistance of bolted joints with different joint configurations.

aluminum bar. These relatively slow induced motions are a function of bus-run length and temperature changes, and consequently, will be relatively short in many applications.

The second mode of motion (direction B–B, Figure 7.16a) is attributed to electromagnetically induced vibrations. The driving force for these motions is created by currents flowing in adjacent bus members. In common busway configurations, the forces between busbars can be as large as 100 Nm of busbar length under rated current conditions. Such forces can cause busbars displacement of the order 20 μm perpendicular to those induced by thermal expansion.

The third mode of bus-stab contact motion is transverse displacement perpendicular to both thermal and electromagnetically induced motions (direction C–C, Figure 7.16a). It is due to rigid stab mounting and the vibratory motions discussed above. An illustration of how such "transverse" motions are generated is shown in Figure 7.16b. As the busbar vibrates to the right of its resting or neutral position, due to the motion shown as B–B in Figure 7.16a, the stab's two contacts are constrained to move in a transverse direction. One contact moves upward and the other downward along the bar, as they follow their respective arc lines. Busbar vibration to the left results in reverse transverse motion of the stab contacts. The frequency of these rubbing transverse movements is identical to that of the electromagnetically induced vibratory motions, 120 Hz, from which they are generated.

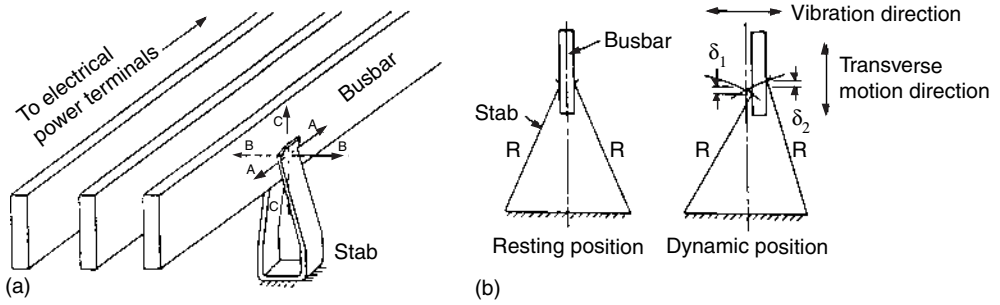

FIGURE 7.16 (a) Direction of mechanical motion acting on bus-stab contacts; (b) transverse motion of stab contact along busbar width.

TABLE 7.4
Bus-Stab Electrical Contact Performance Characteristics[a]

Part	Stab Plate	Bar Motion[b] (mm)	Contact Voltage (mV)		Contact Bulk Temperature (°C)		Contact Distress (%)
			Pulse	Steady	Pulse	Steady	
1	Sn	12	>270	>290	52	>156	95
	Ag	12	31	12	31	41	15
2	none[c]	8	134[d]	—	30	—	75
	Sn	8	42[d]	38	26	32	20
	Ag	8	13[d]	7	24	25	2
	Sn	5	7[d]	3	24	25	8
3	Sn	5	42	15	31	36	11
	Ag	5	33	13	29	41	—
4	None[e]	"Static"	174	180	70	168	90
	None	"Static"	35	15	33	44	1
	Sn	"Static"	43	17	29	36	2
	Ag	"Static"	29	11	30	41	1
5	Ag[f]	8	112	162	52	108	90

[a] Conditions: busbar (Ag-plated aluminum busbar); electrical load: 1000 A (RMS), 46 h, 400 A (RMS), 4 h; stab: copper–cadmium alloy; contact load: 70 N (7 kg).
[b] 120 Hz double-amplitude motion frequency.
[c] 3 h run.
[d] Electrical load: 250 A (RMS), 46 h; 100 A (RMS), 4 h.
[e] Aluminum busbar unplated.
[f] Aluminum busbar tin-plated.

Based on the physical dimensions of a typical 400 A stab, and under normal electrical load conditions, the relative displacement of bus-stab contacts due to transverse motions is expected to be less than 25 μm. Although such motion displacements are small, significant fretting wear of the bus or the plating may occur because of increasing number of slides. The resulting degradation of protective platings would lead to the formation of high-resistance films, surface damage, and arcing, which, in turn, favors more chemical attack, burning, and failure of the contact metals.

The results of this study are summarized in Table 7.4. Contact area distresses of 95 and 15% was observed following tests of tin-plated and silver-plated stabs, respectively. Distress percentages were assigned by the authors and they represent judgments based on the preliminary contact failures being 100%. An indication of contact distress related to the bus-stab interface contact materials may be obtained from the micrographs in Figure 7.17. Contact distress becomes very small when transverse sliding motions of the stab are reduced to 5 μm. It is most likely that, at this level of motion, inherent resiliency of the stab actually prevents relative slide thus reducing abrasive rolling or rocking motion.

Direct correlation with the above observations of distress is found in the contact voltage and bulk temperature values shown in Table 7.4. When a tin-plated stab was combined with the silver-plated aluminum bar, contact voltages greater than 270 mV were measured. However, in the case of silver-plated bus-stab contacts subjected to pulsed and steady electrical loads of 1000 and 400 A, relatively low contact voltage values of 31 and 12 mV, respectively, were measured.

The best performance is obtained when the contact members are plated with silver, rather than tin, and mechanically held together with forces of at least 70 N. Nevertheless, when the contact members are subjected to 120 Hz, relative slide motions with amplitudes greater than 5 μm the time

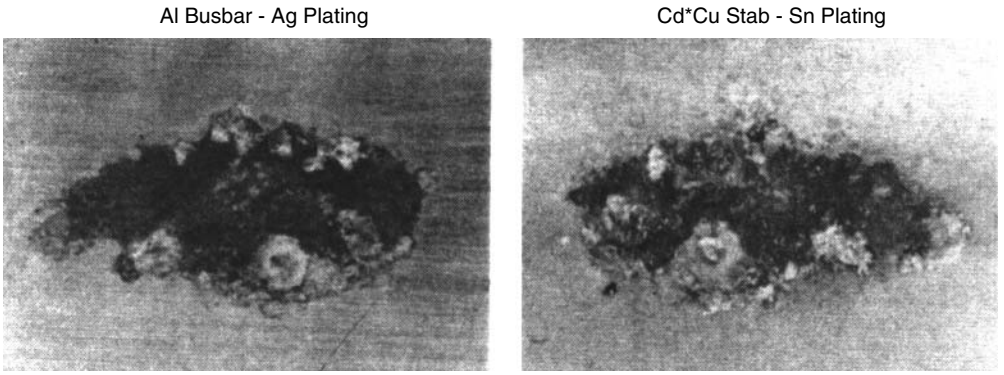

FIGURE 7.17 Contact zone after distress caused by transverse sliding motion of bus-stab interface, Contact load 25 N, slip amplitude 25 μm and frequency 120 Hz. (From Johnson, J. L. and Moberly, L. E., *Electric Contacts-1975*, IIT, Chicago, 53–59, 1975.)

to failure is greatly shortened. Hence, unless transverse motions can be minimized below the critical amplitude level, bus-stab protective metal platings will wear at appreciable rates and eventually be worn out, resulting in higher contact resistance and temperature, and final "burn" failure.

7.2.3 Compression Connectors

Compression connectors are made using a variety of crimping techniques. There is a number of different types of compression connector designs such H-type, stepped-deep indentation, compression sleeve, and set-screw (see Figure 7.1). The characteristic feature of the compression type connectors is that the contact between conductor and connector is made by compression realized either by special crimping tools, such as hydraulic presses, or by torque action of screw or bolt.

Stepped deep-indentation connectors use a specially designed crimping technique to attach a conductor permanently to the connector. The crimp, made on one side of the barrel carrying the conductor, is carried out using a cylindrical or oblong punch with two cone steps and a die that fully encloses the connector. Full enclosure of the connector is necessary to control the deformation of both the connector and conductor. The small inner indentation maximizes compaction of the conductor strands to decrease interstrand electrical resistance.

Owing to the deformation of the connector and conductor, all the metal displaced by the punch is subjected to compressive and shearing forces that generate significant cold welding between the deformed connector walls and the displaced conductor strands. This increases the shear strength of the connector/conductor interface and thus increases the mechanical holding force on the conductor.[584] Figure 7.18 depicts the schematics of typical hexagonal compression sleeve and stepped deep indentation connectors.

One of the main features of stepped deep indentation connectors is that all the conductor strands participate in current conduction, thus yielding exceptionally low contact resistance. Since the walls of the smaller deep indentation can only be deformed in compression, the two cone steps generate a deformation geometry that resists metal flow in the connector after crimping. Thus the electrical interfaces do not degrade due to creep flow or stress relaxation in the connector.

It is interesting to note that under current cycling conditions, carried out in accordance with the ANSI[562] and CSA[563] standards, the stepped deep indentation connectors showed more stable contact resistance performance than the hexagonal compression connectors.[585]

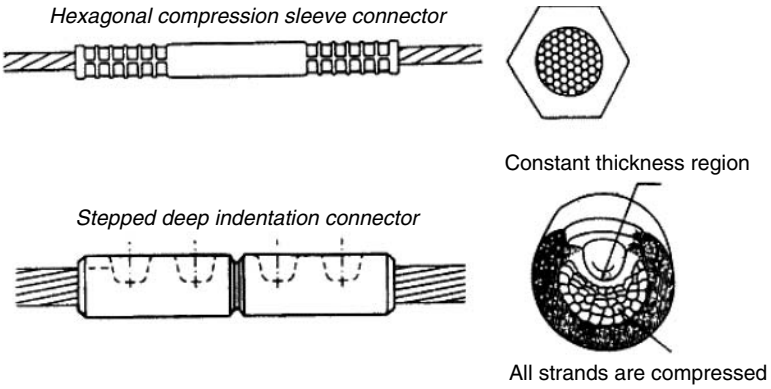

FIGURE 7.18 Schematic of typical hexagonal compression sleeve and stepped deep indentation connectors.

In a compression-type connector, the force required to bring two or more conductors into contact and maintain this contact is provided through the deformation of a portion of the connector. This portion, usually referred to as the barrel or sleeve, is deformed in a predetermined shape and to a predetermined extent by a special tool, which may be a simple hand-actuated tool or a fully automatic power-operated machine. The deformation of the connector barrel is permanent so that the clamping force is maintained.

The degree of compression is determined by considering several factors. Mechanically, the compression force has to be sufficient to meet the mechanical requirement for the connection. Electrically, the resistance of the connection has to be low enough so that the joint complies with the electrical requirements. At the same time, the deformation of the connector sleeve has to be sufficient to maintain the required compression force permanently. The force required to accomplish this operation has to be within the capabilities of the installation tool, leaving a sufficient margin of safety.[586]

The electrical and mechanical characteristics of a compression connector (or any power connector in general) are equally important aspects that determine its reliability. Hence, to obtain a satisfactory electrical and mechanical connection, both characteristics have to be considered. Unlike electrical resistance which reaches a practically steady state with progressive deformation, the mechanical strength of a connection gradually decreases with increasing deformation which, in turn, will increase the rate of stress relaxation and creep of a connector.

Closely related to this is the effect when dissimilar metals are used for the conductor and in the connector. Heating the joint by passing current through it creates a difference in the relative coefficient of expansion which may reduce the contact pressure, particularly if the conductor has a higher coefficient of expansion than the connector.

There are, however, other factors that can cause loss of mechanical load on the contacts. In a compression joint, a stranded conductor may not align itself perfectly during assembly and any subsequent realignment will cause serious reductions in mechanical load. Furthermore, since aluminum is susceptible to creep, some parts will be under much greater stress than others and some stressed far beyond the yield point, thus creating the conditions for extrusion to occur. Temperature will affect the rate of creep, and if increased far enough, will reduce the mechanical strength of a joint by annealing.

An important parameter that can also impact on the reliable performance of compression connectors is the conductor hardness and the degree of mechanical created during assembly.[587] It has been shown that reliable connections between soft (annealed) aluminum conductors require

connectors that mechanically deform the strands so heavily that the strand hardness becomes comparable with hard-drawn conductors. The conductor hardness is therefore a parameter that has to be considered when the compression joints are made.

Regardless of these drawbacks, however, experience has shown that a properly designed compression connector can exhibit very good performance under heat cycling conditions. This is due to the mechanical restraint provided by the structural shape of the connector and almost complete enclosure of the conductor, which partially seals the contact area from adverse effects of the environment.3

One of the advantages of compression-type power connectors is the removal of the human element during installation with the use of recommended tools and/or dies. Consistent and repeatable forces are imparted with each and every crimp. Due to their geometry, these connectors are considerably easier to insulate or tape than mechanical connectors. However, despite the lower cost of these connectors as compared to the alternative types, the selection of proper installation tooling from the multitude of tools available involves a rather expensive capital investment. Advantages and disadvantages of compression connectors are illustrated in Table 7.5.

7.2.3.1 Degradation Mechanisms in Compression Connectors

When properly installed, the compression type connectors will provide reliable performance over a long period of time. Nevertheless, under the operating and environmental conditions they are susceptible to degradation. The rate of degradation determines how long the connector can be usefully and safely operated. It depends on the connector quality, that is, its metallurgical state,

TABLE 7.5
Summary of Advantages and Disadvantages of Compression Connectors

Advantages	Disadvantages
Low cost, relatively reliable performance, use of recommended tools and/or dies removes the human element during installation.	Proper installation tooling for a compression system program involves potentially high capital investments due to a large variety of different types of compression tooling to select from.
Connector construction provides better conductor encirclement while retained oxide inhibiting compound protects the contact area from the atmosphere, thus assuring a maintenance free connection.	Accurate die and tool selection is essential for proper installation of a compression connection.
High localized and consistent forces imparted by the installation tool break down the oxides and establish contact points (*a*-spots) for reduced contact resistance, thus providing electrically and mechanically sound connection.	Due to the need for specific tools and dies to install a compression connection, installers must be trained how to use the proper techniques and maintain these tools.
The softness of compression connector material relative to the conductor prevents spring back and contact separation.	In some compression connections, manually operated tools require greater physical exertion to install, thus when installing numerous connections, installers can become fatigued and possibly not complete the specified number of crimps.
Due to their geometry, compression connectors are considerably easier to insulate or tape than mechanical connectors.	
These connectors are most suitable in areas of wind, vibration, ice build-up, and other stress-associated tension applications.	

the installation methods used for assembling the connectors, and operating and environmental conditions. Perhaps the most frequently observed types of degradation in compression-type connectors are corrosion (most notably galvanic corrosion), fretting, and stress relaxation (creep). Deleterious effects of these degradation mechanisms are enhanced when dissimilar metals, such as copper and aluminum, are in contact.

Although corrosion is identified as the principal cause of deterioration of power connectors and their reliability and security, other degradation mechanism can also contribute to the detriment of these connections. These are fretting and stress relaxation, which are manifested as the loss of mechanical and electrical integrity that eventually may lead to the point of failure. Hence, detecting and monitoring fretting and stress relaxation in power connections is equally as important as corrosion. However, due to the strong interfering effects of corrosion, on-site detection and monitoring of fretting and stress relaxation in power connectors is a difficult but challenging technological task.

7.2.3.2 Corrosion

Many power connectors in service are subjected to relatively severe outdoor environments. As a result, corrosion is recognized as one of the most significant reliability concerns. The corrosion problem is particularly severe in some areas, since connections must often be made between dissimilar metals and in particular, aluminum to copper.

In recognition of the long-term effects of a marine/coastal, subtropical environment on the performance of power connector systems, a program aimed at comparative evaluation of compression, bolted, and fired wedge connector systems was conducted by Tyco in cooperation with Battelle.[558] The test samples included compression, bolted, and fired wedge types of overhead power connectors. These connectors are schematically illustrated in Figure 7.19. The sample size was 50 connectors of each type.

The connectors were installed at the site using the tools and practices recommended by the respective manufacturers. Prior to the assembly of each connector, the surfaces of all conductors were wire brushed. Separate wire brushes were used for the copper and aluminum conductors. After brushing, the connections were typically made within a period of 3–5 min. Specimens corresponding to a given connector type were connected in series on a single line, so that three separate lines were assembled and connected in a continuous series loop.

A connector was deemed to have failed when the resistance between the two corresponding equalizers increased by 1000 μΩ above its initial value. This represents 4–5 times the typical initial resistance value across the connectors. This criterion represented a threshold beyond which connector failure was typically rapid and catastrophic, for all connector types.

The results in Figure 7.19 show the cumulative failures measured over the entire period of 1600 days of exposure. The data indicate that a considerable number of compression and bolted connectors were failing after 900 days of exposure, whereas only one fired wedge connector showed signs of deterioration. After 1200 days of exposure, all compression connectors had failed while only 3 bolted connectors remained intact until the end of the test, that is, 1600 days of exposure. In sharp contrast to the compression and bolted connectors, the fire wedge showed remarkable stability throughout the entire exposure test, as evidenced by only 4 failed samples.

As pointed out in Section 6.5.2, the differences in design, installation procedure, and corrosion inhibitor usage of power connectors, can have a major effect on the connector performance in a harsh marine environment. Degradation of the copper conductor–connector interfaces was caused by the action of galvanic corrosion and build-up of corrosion products leading to the loss of the mechanical integrity at the conductor–connector interface and ultimately, failure of a joint.

Corrosion behavior of different material combinations in power connectors and recommended mitigating measures required to suppress deleterious effect of corrosion are summarized in Table 7.6.

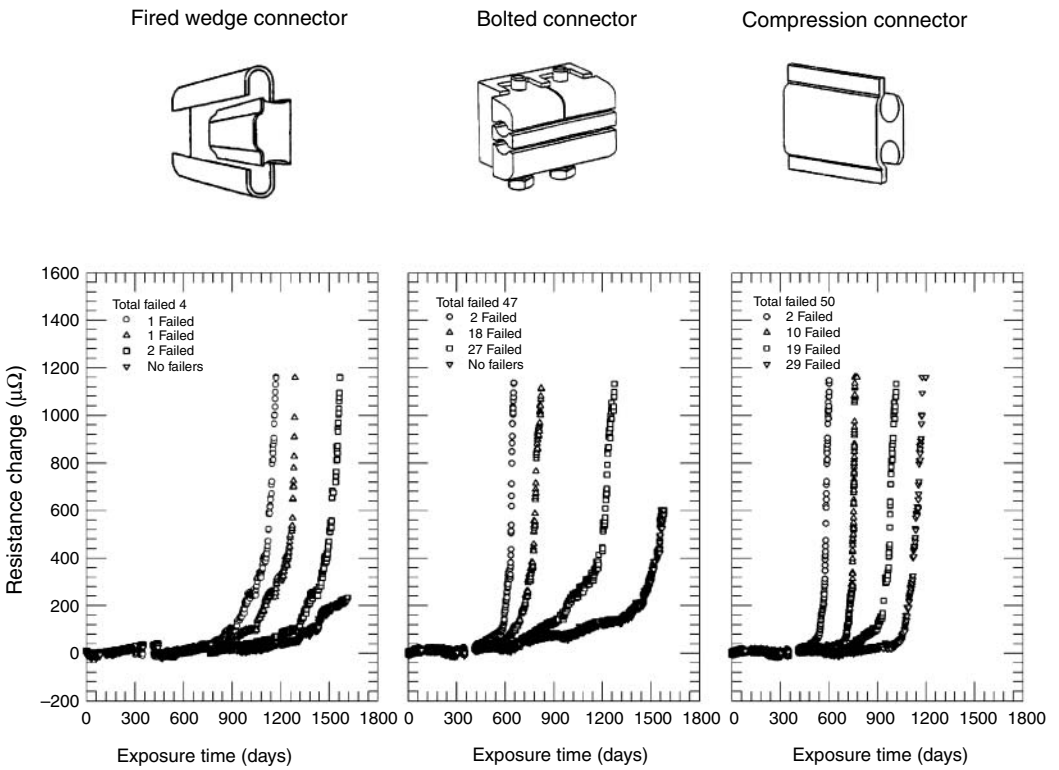

FIGURE 7.19 Types of the overhead power connectors used in the exposure stud. Typical variations of electrical resistance across connectors from the three connector populations. Note a relatively rapid connector failure with the appearance of first signs of deterioration.

7.2.3.3 Fretting in Compression Connectors

In the compression connectors, such as those shown in Figure 7.20, when two dissimilar metals are pressed against each other, surface asperities will penetrate the natural oxide films, providing a good metallic contact. In addition, because of the highly localized contact stresses, the asperities will be severely deformed and there will be mechanical seizure of the contacting metallic surfaces.

In the case of unprotected (nonlubricated) aluminum over unprotected copper (Figure 7.20a), an increase in temperature causes the outer aluminum portion of the connection to expand at a rate greater than that of the copper, thus generating fretting motion at the contact interface and shearing the metallic bridges. This, in turn, will cause a loss of contact surface area. Exposed to the atmosphere, aluminum oxidizes, resulting in further reduction of the contact area when the connection returns to the initial temperature.[588]

With unprotected copper over unprotected aluminum (Figure 7.20b), the latter expands in the axial direction since the residual stress in the copper and its lower rate of thermal expansion restrict the wire to expand circumferentially. If the axial stress exceeds the elastic limit of aluminum, a permanent deformation results, and the wire will not return to its original compressed position contact. Indeed, detailed metallographic examination of the aluminum cable splices subjected to accelerate current cycling tests have shown[585] that fretting and thermomechanical movements resulting from current cycling were the most probable causes for the degradation and overheating of these connectors.

TABLE 7.6
Corrosion Behaviors of Different Contact-Material Combinations and Mitigating Measures Required to Suppress the Effect of Corrosion

Material Combination	Corrosion Behavior	Mitigating Measures
Aluminum/copper (alloy)	Severe corrosion of aluminum surfaces in saline environment	Lubrication and use of Al transition washers.
Aluminum/tin-plated copper (alloy)	Plating thickness < 10 μm, severe corrosion	Lubrication.
	Plating thickness > 10 μm, no severe corrosion	
Aluminum/silver-plated copper (alloy)	Plating thickness > 5 μm No severe corrosion of the contact zone	Not required. In current-carrying contact-pairing should be avoided due to formation of intermetallics.
Tin-plated aluminum/copper (alloy)	In industrial environment corrosion of tin and its peeling intensifies corrosion of aluminum	Remove tin and lubricate. Use lubricated Al transition washers.
Tin-plated aluminum/tin-plated copper (alloy)	Plating thickness < 10 μm no severe corrosion of aluminum surface	Remove tin and lubricate. Use lubricated Al transition washers.
Nickel-plated aluminum/copper (alloy)	If not protected corrosion at nickel–aluminum interface in saline environment can occur	Lubrication.
Nickel-plated aluminum/nickel-plated copper	If not protected corrosion at nickel–aluminum interface in saline environment can occur	Lubrication.

7.2.4 Mechanical Connectors

Mechanical connectors are installed using basic tools, i.e., socket or open-end wrenches, screwdrivers, etc. These connectors are simple to use and often require minimal training to install

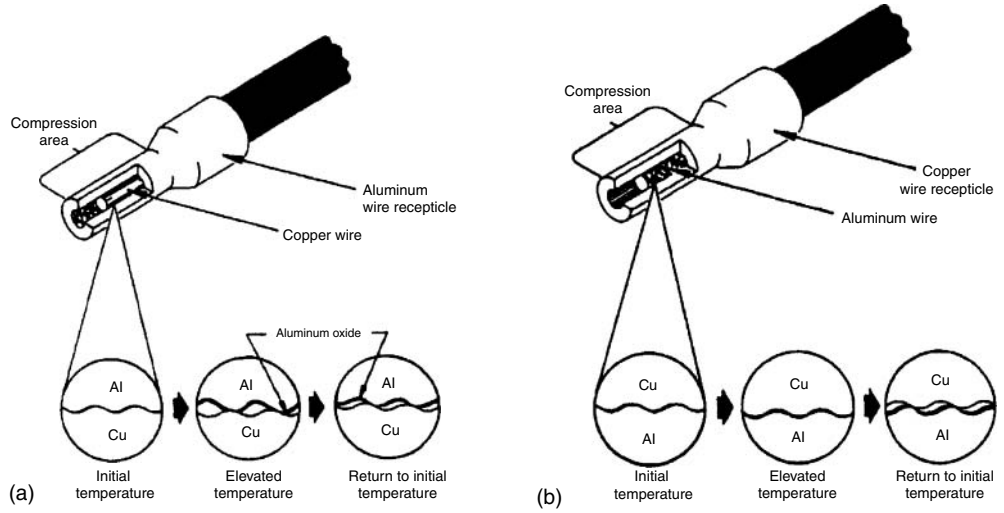

FIGURE 7.20 Compression connection between (a) aluminum terminal and copper conductor; (b) copper terminal and aluminum conductor.

properly. Their main advantage is in the degree of inherent resilience of the connector components, which permits follow-up of creep and reduces the stresses due to thermal expansion that tend to cause excessive creep. The removable feature of mechanical connectors offers an additional advantage allowing reuse if in good condition. If required, mechanical connectors can be disassembled without damage to the connection components.

7.2.4.1 Binding-Head Screw Connectors

A binding-head screw receptacle is a widely used type of terminal connector in North America for branch-circuit wiring. The connection is made by wrapping aluminum or copper conductors around a screw in a clockwise direction for the quarter of a complete loop and tightening the screw. The contact plates are usually made of brass or bronze; although binding-screws are generally made of brass or bronze, steel screws are also used. Hence, when different metals are present in the connection, differences in thermal expansion of the metals used may provoke the fretting action when the power is turned ON and OFF (see Chapter 6, Section 6.4.7). This problem was investigated by Braunović[589] in cases when steel and brass screws were used to terminate aluminum or copper conductors. The schematics of typical binding-head screw connector and wire termination under the binding-head screw are shown in Figure 7.21.

As shown in Section 6.4.4, the minimum slip amplitude for fretting to occur at the interface between two contacting bodies is given as:

$$\delta = \frac{[3(2-\nu)(1+\nu)]}{8Ea}\mu P\left[1-\left(1-\frac{T}{\mu P}\right)^{2/3}\right], \tag{7.7}$$

where E is the Young modulus, ν is Poisson's ratio, P is the normal force, μ is the static coefficient of friction between the contact surfaces, and T is the tangential force ($T<\mu P$). The a term is the radius of the contact area given as:

$$\begin{aligned} a &= \left(\frac{3PR_0}{4E_0}\right)^{1/3} \\ \frac{1}{R_0} &= \frac{1}{R_1}+\frac{1}{R_2}, \\ \frac{1}{E_0} &= \frac{(1-\nu^2)}{E_1}+\frac{(1-\nu^2)}{E_2}, \end{aligned} \tag{7.8}$$

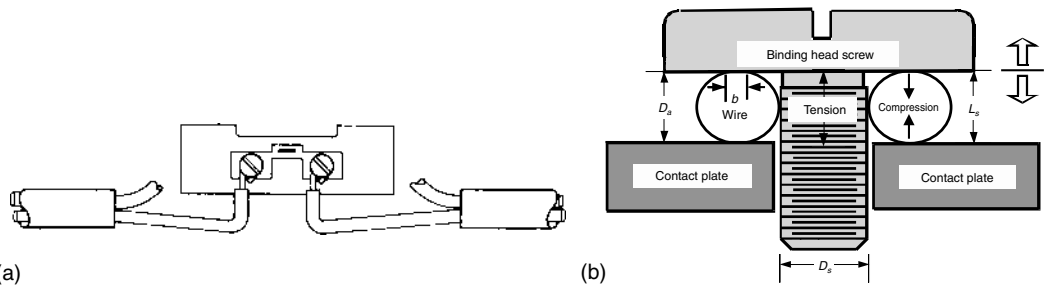

FIGURE 7.21 (a) Schematic of a typical binding-head screw connectors; (b) Schematic of a wire terminated under the binding-head screw. The applied normal load causes compression in the wire and tension in the screw shank.

where E_1, E_2, R_1, and R_2 are, respectively, elastic moduli and radii of the contacting bodies. Inserting Equation 7.8 into Equation 7.7, the following expression for the critical displacement is obtained:

$$\delta = \left(\frac{3P}{E_0}\right)\frac{\mu[(2-\nu)(1-\nu)][1-(1-T/\mu P)^{2/3}]}{(8R_0)^{1/3}}. \tag{7.9}$$

In the case of a wire terminated under the binding head screw, the wire can be considered as a cylinder of radius R_w and length L compressed between two flat rigid plates. The width of the contact zone (flattened area), b, given as:[590]

$$b = 2\left(\frac{P_L R_w}{\pi E_0}\right)^{1/2}, \tag{7.10}$$

where $P_L = P/L$ is the normal force per unit length of cylinder, and E_w and E_S are, respectively, elastic moduli of wire materials (aluminum or copper) and screws. Therefore, the critical displacement required for fretting to occur in a compressed cylinder (wire) is obtained as:

$$\begin{aligned} \delta_W &= \frac{C_W}{\mu(P)^{1/2}}\left[1-\left(1-\frac{T}{\mu P}\right)^{2/3}\right], \\ C_W &= \left(\frac{3\sqrt{\pi}}{16}\right)\left[\frac{(2-\nu^2)(1+\nu^2)}{(E_0 R_0 L)^{1/2}}\right]. \end{aligned} \tag{7.11}$$

Differential thermal expansion of a wire resulting from the heating by passing current is one of the most common causes of motion in electrical contacts. Hence, changes in the applied contact load due to heating of a wire will determine the critical slip occurring in a contact, considering a uniform distribution of applied load P over a flattened area A_w. This situation is illustrated in Figure 7.21b where b is the width of the flattened area given by Equation 7.10. The area of the contact zone (flattened area) of the wire is given as:

$$\begin{aligned} A_w &= bL, \\ A_W &= \frac{P}{3\sigma_Y}, \end{aligned} \tag{7.12}$$

where σ_y is the wire yield strength and L is the length of the wire taken as 3/4 loop around the screw of radius R_S that is

$$L = \frac{3}{2\pi}(R_W + R_S). \tag{7.13}$$

For mechanical equilibrium, the following condition holds:

$$L_S + \Delta L_S = D_w + \Delta D_w, \tag{7.14}$$

where L_S and D_W are, respectively, the initial length of the screw and diameter of the wire ($L_S = D_a$); ΔL_S and ΔD_W are, respectively, the corresponding strains produced by the normal force prior to heating by a current. From the contact theory it follows that:[591]

$$\Delta L_S = \left(\frac{L_S P_0}{A_S E_S}\right),$$

$$\Delta D_{\mathrm{W}} = \frac{4P_0}{\pi L E_{\mathrm{W}}}\left(\frac{1}{3} - \ln\frac{2D_{\mathrm{W}}}{b}\right), \tag{7.15}$$

where $A_{\mathrm{S}} = \pi D_{\mathrm{S}}^2/4$ is the cross-sectional area of the screw shank; therefore,

$$L_{\mathrm{S}} + \frac{L_{\mathrm{S}}P_0}{A_{\mathrm{S}}E_{\mathrm{S}}} = D_{\mathrm{W}} - (1-\nu^2)\left(\frac{4P_0}{\pi L E_{\mathrm{W}}}\right)\left(\frac{1}{3} + \ln\frac{2D_{\mathrm{W}}}{b}\right). \tag{7.16}$$

When the current is passed through the wire its temperature will increase to $T+\Delta T$, thereby causing the wire to expand and thus increase the contact load to P_1 and thus thermal and mechanical equilibrium will be

$$L_{\mathrm{S}}(1 + \alpha_{\mathrm{S}}\Delta T) + \frac{A_{\mathrm{S}}P_1}{A_{\mathrm{S}}E_{\mathrm{S}}} = D_{\mathrm{W}}(1 + \alpha_{\mathrm{W}}\Delta T) - (1-\nu^2)\left(\frac{4P_1}{\pi L E_{\mathrm{W}}}\right)\left(\frac{1}{3} + \ln\frac{2D_{\mathrm{W}}}{b}\right), \tag{7.17}$$

where α_{w} and α_{s} are the linear coefficients of thermal expansion of the wire and the screw, respectively. By subtracting and rearranging the above equations,

$$L_{\mathrm{S}}\alpha_{\mathrm{S}}\Delta T + \frac{L_{\mathrm{S}}\Delta P}{A_{\mathrm{S}}E_{\mathrm{S}}} = D_{\mathrm{W}}\alpha_{\mathrm{W}}\Delta T - (1-\nu^2)\left(\frac{4\Delta P}{L E_{\mathrm{W}}}\right)\left(\frac{1}{3} + \ln\frac{2D_{\mathrm{W}}}{b}\right), \tag{7.18}$$

where $\Delta P = P_1 - P_0$ is the increase in the contact load caused by thermal expansion of the wire. Because $L_{\mathrm{S}} = D_{\mathrm{W}}$, the following expression for P is obtained:

$$\begin{gathered}\Delta P = C_{\mathrm{n}}\Delta T, \\ C_{\mathrm{n}} = \frac{\frac{\pi}{4}(\alpha_{\mathrm{W}} - \alpha_{\mathrm{S}})}{\frac{1}{D_{\mathrm{S}}^2 E_{\mathrm{S}}} + \pi L E_{\mathrm{W}}(1-\nu^2)\left(\frac{1}{3} + \ln\frac{2D_{\mathrm{W}}}{b}\right)}.\end{gathered} \tag{7.19}$$

Therefore, the slip in electrical contact between the wire and binding head screw can be approximated by the following expression:

$$\delta_{\mathrm{t}} = C_{\mathrm{t}}\mu\sqrt{\Delta T}\left[1 - \left(1 - \frac{T}{\mu P}\right)^{2/3}\right], \tag{7.20}$$

where $C_{\mathrm{t}} = C_{\mathrm{W}}C_{\mathrm{n}}$.

For pure metals on themselves, unlubricated and prepared "grease free" in air, the coefficient of static friction is of the order of $\mu = 1-1.5$.[590] For different metals on one another, the friction is somewhat less than that observed with similar metals. If there is appreciable transfer from one metal to the other, the frictional behavior soon becomes characteristic of similar metals. However, under kinetic conditions, such as fretting, the kinetic friction is generally lower than the static friction.[23]

Passage of an electrical current through the contact will reduce even further the coefficient of friction.[404] This is because the current will intensify the oxidation of the fretting surfaces and thus reduce the number of metal–metal contacts so that the contacting metals will slide mainly over the wear debris. Therefore, for simplicity, the coefficient of friction is arbitrarily selected as $\mu = 0.25$. The initial normal load P was selected on the basis of torque–force measurements made on the wire looped around a strain-gauged 6.35-mm diameter bolt. The load of $P = 600$ N corresponded to a torque of 1.35 N m (12 lb in.) and was used in the calculations as the applied load. By inserting the values for the friction coefficient ($\mu = 0.25$), contact load and other appropriate values for the constants in Equation 7.11 and Equation 7.20, the critical slip amplitudes as

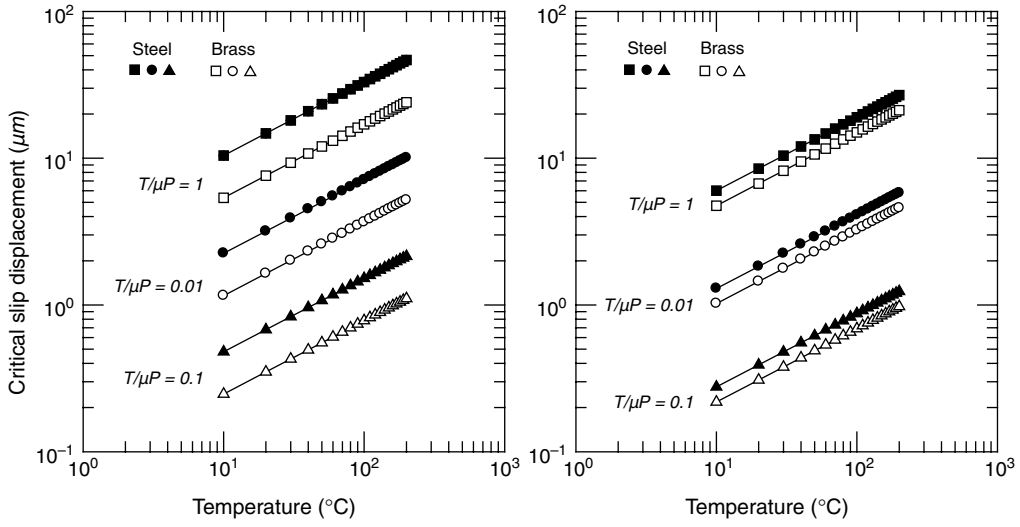

FIGURE 7.22 Calculated values for critical slip amplitude for aluminum and copper wire copper wire conductors in combination with brass and steel screw for different values of ratio $T/\mu P$.

a function of temperature are obtained and shown in Figure 7.22 for the values of $T/\mu P = 1$; 0.1 and 0.01.

The results of calculations show that the temperature rise in the binding-head screw connection generated by passage of current sets up the required conditions for initialization of the fretting motion at the contact interface. The critical slip amplitude increases not only with the temperature but also with the difference in the thermal expansion coefficient of the contacting members. The larger the difference, the larger is the slip amplitude generated by the temperature. From Figure 7.22, it is apparent that the same temperature rise generates larger slip amplitudes in the joints assembled with aluminum than with copper wire conductors.

It should be pointed out that the above calculations are made assuming a simple stick–slip process neglecting other parameters such as environment, stress relaxation, formation of intermetallic compounds and galvanic corrosion that are in practical applications present and exert significant influence on the performance of a connection. Nevertheless, despite some shortcomings of the approach used in these calculations, it is clear that this type of connection is susceptible to the deleterious effects of fretting.

Among the mitigating measures for the deleterious effect of fretting in the binding-head screw terminations, the following are the most obvious:

- Reducing the effect of differential thermal expansion, i.e., use of dissimilar metals having largely different coefficient of thermal expansion
- Reducing the slip amplitude as much as possible
- Lowering the contact pressure, P
- Lowering the coefficient of friction

Clearly, these means cannot be simultaneously applied since some of them are contradictory. However, reducing the contact pressure and coefficient of friction as well avoiding the use of dissimilar metals are the probably the most practical palliative measures.

7.2.4.2 Insulation Piercing Connectors

Insulation piercing connectors are mechanical connectors designed for indoor and outdoor nontension tap and splice applications on insulated secondary distribution lines for use on combinations of insulated copper and aluminum conductors (see Figure 7.1). Their design allows hermetical-sealing of electrical contact zone to prevent moisture ingress. The incorporated contact teeth penetrate conductor insulation and make electrical contact while pre-filled oxide inhibiting compound fills voids where contamination may enter.

Installation requires no special tooling since the connection is made with a wrench. After installation, the perforated insulator on the conductor presses on the sides of connector teeth with sufficient force to prevent ingress of harmful environmental contaminants through the perforations. The shape and number of teeth on the jaw are designed to optimize the grip on the conductors.

This type of mechanical connector has also some disadvantages such as limited scope of application (600 V and lower), can be used only on insulated conductors and nontension applications and may not be suitable for the conductors with very thin, very thick, or very hard insulation material.

In summary, despite versatility and ease of installation, mechanical connectors have some drawbacks, such as those outlined in Table 7.7.

7.2.4.3 Wedge Connectors

The wedge connector incorporates a wedge component and a tapered, C-shaped spring body (or C-body). Installation is made by driving the wedge between two conductors into the C-member, deforming it plastically and generating the force that secure the installed wedge and conductors in place. The mechanical properties of the C-member are the most important to the reliable mechanical function of wedge connector.

The C-body is characterized by an elastic compliance capable of compensating for cable compaction and is thus responsible for maintaining nearly constant mechanical load on conductors during the life of the connectors. In addition, the relatively small mechanical stresses

TABLE 7.7
Advantages and Disadvantages of Mechanical Connectors

Advantages	Disadvantages
Inherent resilience of the connector components permits follow-up of creep and reduces the stresses due to thermal expansion that tend to cause excessive creep.	Specific torque requirements must be followed to provide the proper clamping force needed for a sound electrical connection.
Ease of installation (sockets, wrenches, screwdrivers, etc.) and removal, simple to use, require minimal training to install properly.	Inconsistency of forces applied over identical mechanical installations is not generally repeatable due to use of uncalibrated torque wrenches.
Can be disassembled without damage to the connection components and may be reusable if in good condition.	Because of relatively low mechanical holding strength, these connectors can not be used as full tension connections and in areas of high vibration; more maintenance and periodic inspection may be required.
Electrical performance of mechanical connectors meets or exceeds the industry requirements for which they are designed, thus, performance is not compromised when using mechanical connectors in tested applications.	Owing to their geometry, installing mechanical connectors on insulated conductors is usually difficult and awkward.

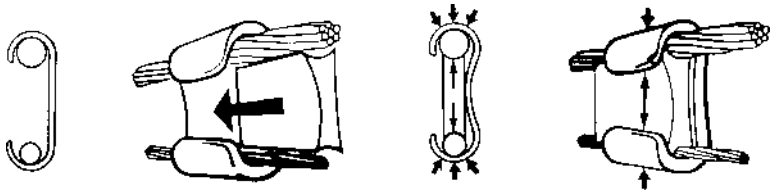

FIGURE 7.23 Schematic of the wedge connector assembling.

generated in the electrical contact interfaces prevent significant conductor creep and assure the reliable performance of the wedge connector under severe operating and environmental conditions.[558]

Driving action is produced either by firing a cartridge to propel the wedge at high velocity (powder actuated) or by tightening a mechanically driven bolt which drives the wedge between the conductors. As a result, the electrical interfaces are formed by the shearing of rough sliding interfaces in which the large mechanical stresses at the contacting surface asperities generate the conditions favorable to the abrasion and dispersal of oxide and other contaminant films. Metallographic examination of the contact interfaces shows that metal-to-metal contact area is increased greatly.[558] Figure 7.23 depicts schematically assembling of the wedge connector and the forces generated in the joint. Table 7.8 summarizes the advantages and disadvantages of wedge-connectors.

7.2.5 Welded Connectors

Welding is a highly satisfactory method for making connections in all types of aluminum and copper conductors. It produces highly efficient electrical connections which are permanent,

TABLE 7.8
Advantages and Disadvantages of Wedge Connectors

Advantages	Disadvantages
Powder actuation provides consistent, uniform performance and requires low physical exertion from an operator to complete a connection.	Dedicated nature of powder actuation requires full support from the user in terms of training, maintenance and service.
Rapid mechanical wiping action as the wedge is driven between the conductors breaks down surface oxides and generates superior contact points thus reducing overall contact resistance.	To ensure a safe and proper installation, precautions are and specially trained and qualified installers are required for installing wedge connections.
Installation is accelerated with the use of lightweight, portable tooling with simplified loading and engaging mechanisms.	Mechanical wedge connectors are installed with wrenches, require more physical exertion for installation, and show more inconsistent performance due to discrepancies caused by contaminants on the hardware and wide tolerances of shear-off bolts.
The spring effect of the "C" body maintains constant pressure for reliable performance under severe load and climatic conditions whereas a large connector mass provides better heat dissipation.	Mechanical wedge spring bodies are typically manufactured by casting which produces much less spring action to maintain the connection.
Electrical performance of fired-on wedge connectors are excellent due to the low contact resistance developed during installation.	Wedge connectors are restricted to nontension, outdoor applications and suited only for a limited range of conductors; due to their geometry, full insulation of wedge connector is difficult.

economical, have good appearance, and particularly suitable for joining two members of different cross-sections. A properly welded joint is the most reliable joint from the electrical standpoint since there is an essentially homogeneous union with no contact resistance to generate heat from high currents. There is a large number of welding processes that can be used for joining aluminum and copper, but only those most commonly used for welding power connections and conductors will be described. A detailed description of different welding processes can be found in *ASM Handbook Volume 6: Welding, Brazing and Soldering*.[592] Out of a large number of welding processes used to make the power connections, the following two methods are probably the most widely used.

Thermite (*Exothermic*) welding is a fusion welding process in which an electrical connection is formed when superheated, molten copper alloy is poured on and around the conductors to be joined (Table 7.9). This process requires no external source of heat or current and is completed within few seconds in a semi-permanent graphite mold in which the molten copper alloys causes the conductors to melt. The result of a reaction between a metal oxide and aluminum is liquid metal that acts as the filler metal and flows around the conductors making a molecular weld. The alumino-thermic reaction that occurs in the welding of copper conductors is:

$$3Cu_2O + 2Al \rightarrow 6Cu + Al_2O_3 + \text{Heat (1,060 kJ)} \tag{7.21}$$

The total amount of heat applied to the conductors or surfaces is considerably less than that employed in brazing or welding. The thermite welding is extensively used for making grounding connections between copper conductors. The advantages of this process are excellent current-carrying capacity equal to or greater than that of the conductors, high stability during repeated short-circuit current pulses, excellent corrosion resistance, and mechanical strength. Disadvantages of this process are cost, lack of repeatability, numerous mold requirements, potential downtime caused by inclement weather or wet conditions, and safety risks to personnel and equipment. Figure 7.24 shows a typical crucible-mold setup for welding copper conductors.

Friction welding is a solid-state welding process in which the heat for welding is produced by direct conversion of mechanical energy to thermal energy at the contact interface without the application of external electrical energy or heat from other sources. Friction welds are made by holding a nonrotating workpiece in a contact with a rotating workpiece under constant or gradually increasing pressure until the interface reaches welding temperature and then the rotation is interrupted to complete the weld. The frictional heat developed at the interface rapidly raises the temperature of the workpieces, over a very short axial distance, values approaching but below

TABLE 7.9
Advantages and Disadvantages of Exothermic (Thermite) Connections

Advantages	Disadvantages
Excellent current-carrying capacity equal to or greater than that of the conductors, high stability during repeated short-circuit current pulses, excellent corrosion resistance and mechanical strength.	Cost, lack of repeatability, numerous mold requirements, potential down-time caused by inclement weather or wet conditions, safety risks to personnel and equipment. The intense heat damages both the conductor and its insulation anneals the conductor so that exothermic connections can not be used in tension applications. The resultant weld material exhibits lower conductivity and physical properties than the conductor, being similar to cast copper.

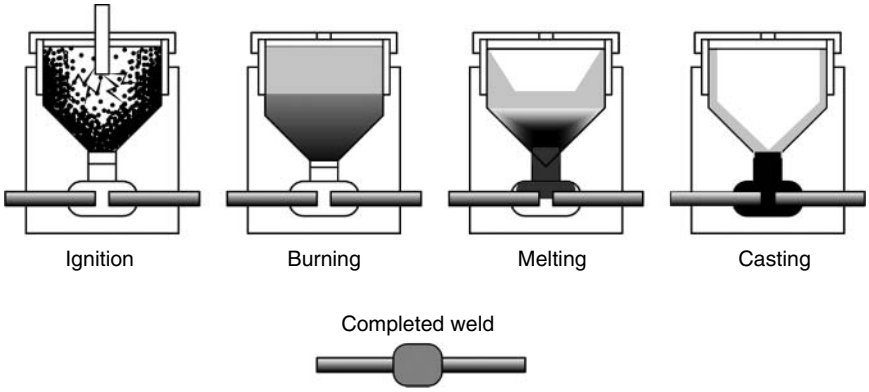

FIGURE 7.24 Typical crucible-mould set-up for thermite welding of copper conductors.

the melting range. During the last stage of welding process, atomic diffusion occurs while the interfaces are in contact, allowing a metallurgical bond to form between the two materials.

This welding process is used to make bimetallic aluminum-to-copper terminals and thus avoid direct contact between aluminum and copper. These terminals are usually copper flat plates or tubes friction welded to compression-type aluminum connectors. When installed, the friction welded terminals convert the aluminum-to-copper joint into an aluminum–aluminum and copper–copper joint. This type of connector is widely used in Europe. Figure 7.25 illustrates typical friction-welded terminals.

7.3 MITIGATING MEASURES

The uninterrupted passage of current across the contact interface is determined by many parameters such as the size and condition of the contact surface, pressure (torque) and contact resistance, and protection against adverse environmental effects. Various palliative measures are used to assure the uninterrupted passage of current, and these will be reviewed in the following sections.

7.3.1 Contact Area–Connector Design

The size of the contact area is generally determined by the hardness of the contacting members, applied force, and the rated current density. It should be sufficiently large to prevent the rise of the contact interface temperature under normal and emergency conditions. However, the contact temperature itself is not a critical parameter since it is a result rather than a cause of the processes

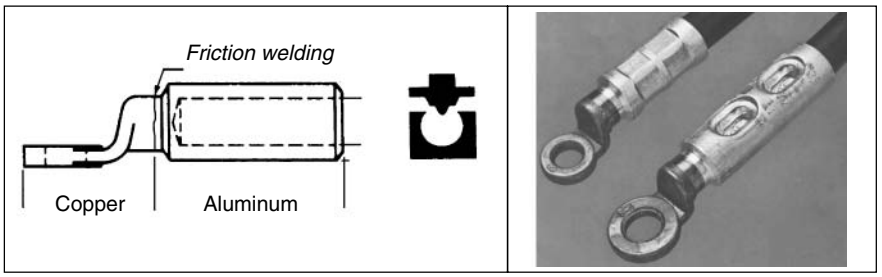

FIGURE 7.25 Typical friction-welded terminals.

occurring in a joint, being a function of the current density, the geometrical dimensions of the contact, and the voltage drop across the contact.

The contact temperature can exceed that in the bulk of a conductor or connector without causing electrical instability at contact interface. On the other hand, the contact voltage can increase to very high values without causing the contact temperature to exceed that of the conductor or connector bulk temperature.

It is therefore imperative that changes in the contact temperature and voltage with the connector operating time remain very small. These requirements can be met, providing the area of real contact is sufficiently large so that despite initial and long-term deterioration, there is still a reserve of contact spots (a-spots) to ensure that the overheating conditions in the joints are not reached.

In the case of bolted connections, it was shown that the contact area can be increased by changing the busbar design.[593] In other words, cutting the slots in the busbar in a manner as shown in Figure 7.26, the actual surface area of a joint can be increased by 1.5–1.7 times that of a joint without slots. The contact resistance of a joint configuration with slots (b) is 30–40% lower than that of (a) and is mechanically and electrically more stable when subjected to current cycling test (Figure 7.26). The beneficial effect of sectioning the busbar is attributed to a uniform contact pressure distribution under the bolt which, in turn, creates a larger contact area.

This idea has been explored by Braunović[594] in the case of high voltage (>700 kV) power connectors used for connecting stranded 4000-MCM conductors to a variety of power equipment at the substation site. The connectors used were with intact current-carrying pads (no slots) and with pads modified by cutting slots seen in Figure 7.27. The contact resistance was derived from the voltage drop measured between the potential leads positioned on the connector pads and busbars as shown in Figure 7.27. Although this figure depicts only the positioning of the voltage drop leads for the connectors with slots, the same arrangement was used for the connectors without slots.

Contact resistance measurements were carried out on the connector-pad/busbar combinations whose contacting surfaces were given a different surface finish; as received, brushed, brushed and lubricated, machined, and machined and lubricated. The results of the contact resistance measurement are also summarized in Table 7.10 showing the joint contact resistance of connectors with four and sixbolt joint configuration with and without slots and different surface finish.

The results in Table 7.11 show the calculated composite radius of a-spot (a_c) and composite contact area (A_c). Both composite radius and contact area were derived to estimate the size of the contact zone where conduction takes place; this zone can be envisaged as a large circular composite area comprising several discrete small areas (a-spots) with composite electrical resistance R_c given as

$$R_c = \rho/2a_c, \tag{7.22}$$

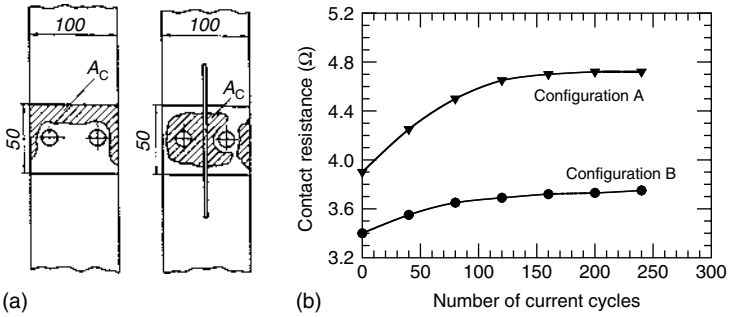

FIGURE 7.26 Effect of current-cycling on contact resistance of bolted joints with and without slots. The contact area of a joint with slots (b) is 1.5–1.7 times larger than without slots (a).

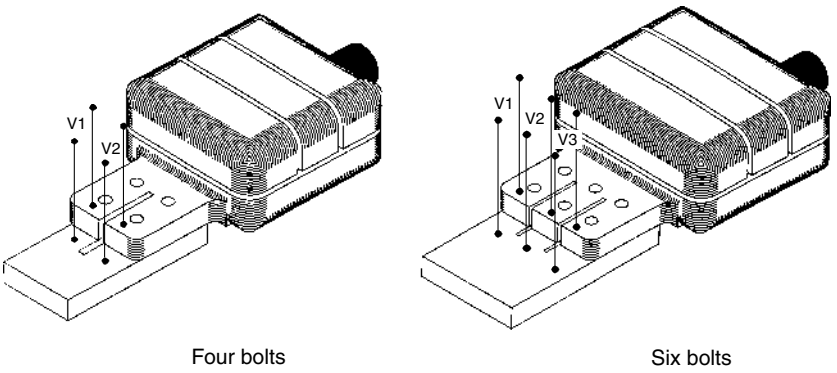

FIGURE 7.27 Schematic of the bolted joint configurations and positioning of the voltage probe leads for the contact resistance measurements.

where ρ is the bulk resistivity of connector aluminum alloy and a_c is the composite radius. Hence, using the resistivity value $\rho = 50$ nΩ m—typical for the aluminum commonly used for this type of connectors—the composite radius a_c and real conducting area A_c, was calculated from:

$$\begin{aligned} a_c &= \rho/2R_c, \\ A_c &= a_c^2\pi. \end{aligned} \tag{7.23}$$

From the results shown in Table 7.11, it is clear that sectioning the overlapping bolted joints combined with machining and lubricating the contact surface assured very pronounced enlargement of the actual conducting area and thus the lowest contact resistance. On the other hand, connectors whose current-carrying parts (pads) were not given any surface treatment nor sectioned, had extremely small conducting area and thus, the highest contact resistance.

7.3.2 Contact Pressure

A well-designed connector should have adequate mechanical strength to maintain its mechanical integrity under normal and overload conductor operating conditions. It should also have sufficient

TABLE 7.10
Mean Values of Joint Contact Resistance of Connectors with Four- and Six-Bolt Configuration

Condition	No Slots	With Slots	R_s/R_{ns}
Four-bolt configuration			
As-received	9.19	6.7	0.73
Brushed	5.48	3.97	0.72
Brushed/lubricated	0.39	0.27	0.69
Six-bolt configuration			
As-received	22.52	15.2	0.68
Machined	2.74	1.55	0.56
Machined/lubricated	0.32	0.18	0.56

R_s, contact resistance of contacting members with slots.
R_{ns}, contact resistance of contacting members without slots.

TABLE 7.11
Calculated Values for Composite Radius (a_c) of Composite Contact Area (A_c)

Surface Finish	No Slots		With Slots	
	a_c	A_c	a_c	A_c
Four-bolt configuration				
As received	0.27	0.23	0.37	0.43
Brushed	0.46	0.66	0.63	1.25
Brushed/lubricated	6.29	124.21	8.85	245.92
Six-bolt configuration				
As received	0.11	0.04	0.16	0.08
Machined	0.91	2.6	1.61	8.14
Machined/lubricated	7.72	187.14	13.89	605.81

contact pressure to maintain an ample contact area, thus allowing uninterrupted passage of current across the contacting interfaces. However, this pressure should never exceed elastic limits of the joint components since plastic deformation can increase stress relaxation and creep of the contacting members, leading to eventual loss of a contact.

The effect of contact load on the contact resistance of closed current-carrying copper contacts was investigated by Bron et al.[595] The evolution of contact resistance of spherical copper contacts under 50- and 100-N contact forces and a current of 1000 A was measured as a function of time. The results, shown in Figure 7.28, demonstrate clearly that increasing the contact load from 50 to 100 N extended the onset of the contact resistance increase, i.e., the contact lifetime, by 5 times. Furthermore, it was also shown that by increasing the applied contact force, the permissible temperature of electrical contacts can also be increased.

In the case of compression-type connectors, used for splicing aluminum or copper conductors or terminating these at particular electrical equipment, such as transformers, disconnect switches, etc., the force required to bring two or more conductors into contact and maintain this contact is provided through the deformation of a portion of the connector. This portion, usually referred to as the barrel or sleeve, is deformed in a predetermined shape and to a predetermined extent by a special tool, which may be a simple hand-actuated tool or a fully automatic power-operated

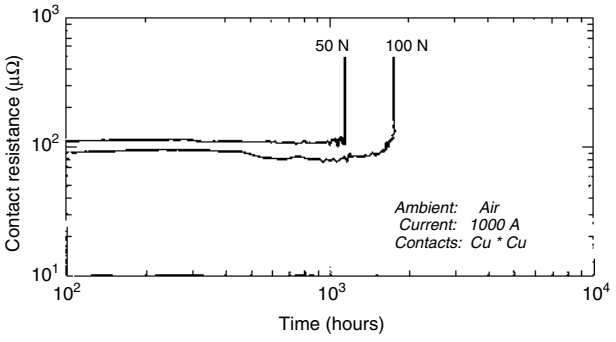

FIGURE 7.28 Evolution of contact resistance with time of spherical copper contacts at 50 and 100 N contact force. (Derived from Bron, O. B., Myasnikova, M. G., Miroschnikov, I. P., and Fyodorov, V. N., *Proceedings of 10th ICEC*, Budapest, 71–75, 1980.)

machine. The deformation of the connector barrel is permanent so that the clamping force is maintained.

The degree of compression is determined by considering several factors. Mechanically, the compression force has to be sufficient to meet the mechanical requirement for the connection. Electrically, the resistance of the connection has to be low enough so that the joint complies with the electrical requirements. At the same time, the deformation of the connector sleeve has to be sufficient to maintain the required compression force permanently. The force required to accomplish this operation has to be within the capabilities of the installation tool, leaving a sufficient margin of safety.

The electrical and mechanical characteristics of a connector are equally important aspects that determine its reliability. Hence, to obtain a satisfactory electrical and mechanical connection, both characteristics have to be considered. Unlike electrical resistance, which reaches a practically steady state with progressive deformation, the mechanical strength of a connection gradually decreases with increasing deformation which, in turn, will increase the rate of stress relaxation and creep of a connector.

Closely related to this is the effect when dissimilar metals are used for the conductor and in the connector. Heating the joint by passing current through it creates a difference in the relative coefficient of expansion, which may reduce the contact pressure, particularly if the conductor has a higher coefficient of expansion than the connector.

There are, however, other factors that can cause loss of mechanical load on the contacts. In a compression joint, a stranded conductor may not align itself perfectly during assembly and any subsequent realignment will cause serious reductions in mechanical load. Furthermore, since aluminum is susceptible to creep, some parts will be under much greater stress than others and some stressed far beyond the yield point, thus creating the conditions for extrusion to occur. Temperature will affect the rate of creep and if increased far enough, will reduce the mechanical strength of a joint by annealing.

7.3.3 Surface Preparation

The surface finish and the magnitude of the applied force and manner in which it is applied, generally determines the size of the contact area and distribution of the conducting spots in the contact zone and thus, the connector electrical efficiency.

Practice and published experimental evidence have shown that mechanical abrasion (brushing) is the simplest and most effective method of obtaining a large number of contact points. The effect of surface preparation on the performance of bolted connections was investigated by Jackson,[596] Oberg et al.[597] It was shown that surface treatment of aluminum-based joints is very important for maintaining low contact resistance and that its effectiveness depends on the type of techniques applied. A significant difference between the preparation methods was observed. The most effective technique was sand blasting, whereas steel brushing, a commonly used method for installing bolted joints in the field, was found to be ineffective in ensuring low and stable contact resistance. It is also important to note that copper joints were found to be relatively insensitive to differences in surface preparation, although the use of joints as-received, without any surface preparation, is not recommended.[597]

In the case of bolted connections, the holes in the connector pads are made by cutting, punching or drilling; burs and other mechanical defects are formed on the pad surfaces. Their presence may adversely affect both electrical and mechanical integrities of a bolted joint. It is therefore very important to machine the pad surfaces with the aid of a suitable tool not only to remove burs and other mechanical defects, but more so to generate a surface finish that assures a larger contact area for current transfer and a lower contact resistance.

Although it is a common practice to machine only the contact surfaces of cast connectors and not those made from wrought alloys, it is equally essential to machine the pad contact surfaces

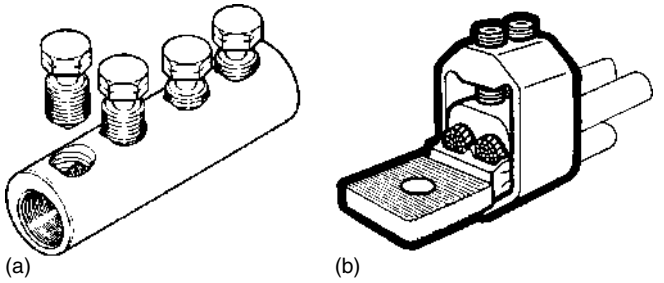

FIGURE 7.29 Examples of the serrated contact surfaces (a) AMP/Simel splice; (b) Pfisterer terminal lug. (From Braunović, M., *CEA Report No. 188, D 335*, Montreal 1986. With permission.)

irrespective of the material that the connector is made of. When preparing the contact surface, care also must be taken to ensure that the flatness of the pad contact surfaces is not damaged. The misalignment between the two connector pads when assembled should not exceed 0.5 mm (1/64 in.) across the entire contact surfaces and in any direction. Direct consequence when this misalignment limit is exceeded is the reduction of the actual contact area where the current transfer occurs and increase in the contact resistance and joint temperature.

Further enhancement of the connector electrical efficiency can be achieved by making the serrations in the contact surface as shown in Figure 7.29. The presence of a distinct distribution of the serrations having uniform height and width ensures that a more controllable load-bearing and current-conducting area is obtained. Furthermore, this type of surface finish eliminates the problem of misalignment between the contacting members.

7.3.4 Mechanical Contact Devices

Although a bolted type connection is widely used method of joining aluminum and copper conductors, there are doubts concerning its reliability under the operating conditions, owing primarily to the fact that when two dissimilar metals are used, the difference in their physical, mechanical and metallurgical properties results in difficulties to make a satisfactory joint. In order to reduce this problem, various palliative measures in the design and joint configuration were considered. One of these is the use of suitable mechanical contact devices combined with appropriate tightening of a joint, thus ensuring that all members of a joint remain within their elastic limits under all expected operating conditions.

To illustrate the importance of these mechanical contact devices, let us examine the stresses generated in a bolted joint with no current passing through the joint. The joint configuration consists of two aluminum or copper busbars measuring $38 \times 12.7 \times 250$ mm^3, two 38-mm diameter flat washers, and a 12.7-mm diameter steel or bronze bolt. During assembly, the bolt is subjected to a simple tension while the busbars are subjected to compression. The nut factor used for calculating the forces generated in the bolt by applied torque was $K = 0.2$. The stress distribution in the busbars under the washer was assumed to be uniform. The results of calculation are shown in Table 7.12.

If the busbars were made of aluminum EC-0, the stresses generated by tightening torque of 60 Nm (45 lb ft) would exceed their yield strength, which is 28 MPa (4000 psi). It should be pointed out, that the above calculations were made assuming a uniform stress distribution in the contact zone under the washers. However, since the real contact area is much smaller than the apparent contact area, the stresses generated at the *a*-spots, where the actual contact is made, will be much higher.

TABLE 7.12
Stresses Generated in the Bolt and Busbar Conductors

Torque, Nm (lb ft)	A_b,[a] mm^2 (in.^{2})	A_w,[b] mm^2 (in.^{2})	Contact Force, kN (lb)	Bolt Stress, MPa (psi)	Busbar Stress, MPa (psi)
50 (35)	91.5 (0.142)	824 (1.276)	18.7 (4 200)	204 (29 577)	23 (3 290)
60 (45)	91.5 (0.142)	824 (1.276)	23.9 (5 400)	260 (38 028)	29 (4 230)
70 (50)	91.5 (0.142)	824 (1.276)	26.5 (6 000)	290 (42 253)	32 (4 700)
80 (60)	91.5 (0.142)	824 (1.276)	31.8 (7 200)	348 (50 704)	39 (5 650)

[a] A_b, bolt cross-section.
[b] A_w, apparent contact area under washer.

The heating and cooling of a bus joint as the result of normal changes in electrical load cause corresponding increases and diminutions in the thickness of the bolted joint, varying in magnitude with the thermal expansion coefficient of the material. Moreover, the bolts are usually not heated by the current in the conductors to the same extent as the conductor itself. The result may be a temperature differential of 10°C or more between the bolt and the conductor, which tends to narrow over a period of time.

During the hot portion of the load cycle, the differential expansion of the bus conductor and the bolts add additional stresses to the original stresses in the conductor and the bolt. The increase in the stresses in the busbar conductors (F_{sup}) and the bolt is proportional to the temperature rise (T) and is given as:[82]

$$F_{sup} = k_1 T,$$
$$k_1 = \frac{(\alpha_a - \alpha_b) A_b E_b}{1 + \frac{t}{a}\left(1 + \frac{A_b}{A_w}\right) + \frac{A_b E_b}{A_a E_a}}, \tag{7.24}$$

where α_a is the coefficient of thermal expansion of the busbar conductor, α_b is the coefficient of thermal expansion of the bolt, A_b is the bolt cross-section, E_b is the elastic modulus of the bolt, E_a is the elastic modulus of the busbar conductor, t is the thickness of the washer, a is the thickness of the busbar conductor, A_w is the apparent area under the washer, and A_a is the apparent contact area of overlapping joint.

For the joint assembled initially at 55 Nm (40 lb ft), i.e., contact force of 22 kN (4800 lb), the calculated additional force, generated in the busbars and the bolt when the joint temperature increased to 120°C is given in Table 7.12. The coefficients of thermal expansion used to calculate the additional force in the joints were: steel—11, aluminum—23.6, and copper—16.5 ($°C^{-1} \times 10^{-6}$). The results shown in Table 7.13 clearly show that the stresses and the resulting

TABLE 7.13
Increase in Stresses in the Bolt and the Busbar Conductors due to Temperature Rise of 120°C

Bolt	Busbars	F_{sup}, kN (lb)	F_{tot}, kN (lb)	Bolt Stress, MPa (psi)	Busbar Stress, MPa (psi)
Steel	Aluminum	19.0 (4 327)	41.0 (9 127)	443.0 (64 319)	40.0 (5 810)
Steel	Copper	6.7 (1 510)	28.0 (6 310)	306.0 (44 487)	28.0 (4 017)
Bronze	Aluminum	8.0 (1 794)	30.0 (6 594)	320.0 (46 469)	29.0 (4 197)

deformation are much greater for aluminum than for copper busbar conductor for the same temperature rise. This illustrates the importance of maintaining reasonably constant pressure in bolted joints during the heating and cooling cycles of operation. Hence, the higher yield strength and better creep characteristics of busbar conductors and the use of suitable mechanical contact device are very important to obtain stable electric joints.

The effect of different types of mechanical contact devices on the performance of bolted aluminum-to-aluminum joints under current cycling and stress relaxation conditions was investigated by Braunović.[582] It was shown that the mechanical integrity of the connector is strongly affected by the joint configuration, which differs according to the mechanical device used. Combination of a disc-spring (Belleville) and thick flat washers assured the most satisfactory mechanical and electrical integrity of bolted joints under current-cycling and stress relaxation conditions.

One of the most important characteristics of disc-spring washers is their ability to elastically absorb deformation caused by an outside load. To comply with the space limitations imposed by the geometry of a bolted joint, disc-spring washers have to be as small as possible and made from materials having a high tensile strength and high elastic limit. These materials should also have high dynamic fatigue resistance, and sufficient plastic deformation ability exceeding the elastic limit to allow fabrication of cold worked springs, as well as minimizing failure of springs under sudden and sharp load changes.

Disc-spring washers are generally made of spring steel such as high-carbon, chrome–vanadium, chrome–vanadium–molybdenum, tungsten–chrome–vanadium and stainless steels. However, other resilient materials, such as silicon and phosphor bronze, beryllium copper, inconel and nimonic can also be employed.

The effect of disc-spring (Belleville) washer on the performance of a bolted joint with steel bolts can be evaluated using the expression Equation 7.24 in which the constant k_1 is given as

$$k_1 = \frac{(\alpha_a - \alpha_b)A_b E_b}{1 + \frac{h}{a} + \frac{t}{a}\left(1 + \frac{A_b}{A_w}\right) + \frac{A_b E_b}{A_a E_a} + \frac{A_b E_b}{aK}}, \tag{7.25}$$

where h is the overall height and K is the spring constant of the disc-spring washer. The calculations were made using the spring constant of $K = 50$ kN/m (290,000 lb/in.). The results, shown in Table 7.14, clearly show that the use of disc-spring washers reduces the adverse effect of differential thermal expansion in bolted joints assembled with the steel bolts by a factor of 10.

Figure 7.30 illustrates the preferred joint configurations for jointing aluminum or copper busbar conductors. In all cases, to have a more uniform stress distribution in the busbars under the washer and avoid its buckling, it is recommended to use flat washers at least 3–4-mm thick. When steel bolts are used, it is recommended to use disc spring washers with a high spring constant and flat

TABLE 7.14
Forces Generated in the Busbar Conductors without and with the Disc-Spring (Belleville) Washers

Bolt	Busbars	Force in Busbars without Disc-Spring Washer, kN (lb)	Force in Busbar with Disc-Spring Washer, kN (lb)
Steel	Aluminum	19.0 (4,327)	1.2 (276)
Steel	Copper	6.7 (1,510)	0.4 (95)
Bronze	Aluminum	8.0 (1,794)	0.8 (173)

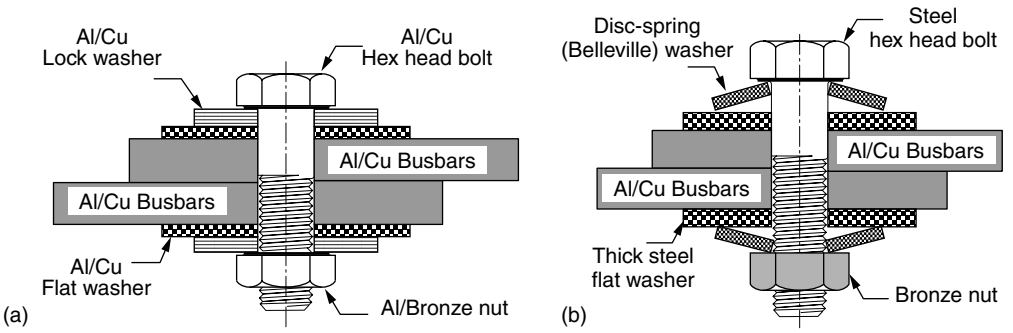

FIGURE 7.30 Recommended bolted joint configurations for aluminum and copper busbar conductors.

washers with thickness at least twice that of the disc-spring washer. Furthermore, the disc spring has to have a very high spring constant to provide the required elasticity of a joint during temperature excursions caused by joint overheating, short circuit conditions, and other causes impacting on the mechanical integrity of a bolted joint.

One method of avoiding failures due to differential thermal expansion consists of using the bolting hardware of the same material as that of conductor. For instance, when the conductors and hardware are made of aluminum, the coefficient of their thermal expansion is essentially the same and thus a high contact pressure is maintained during both heating and cooling cycles. The same principle applies to all copper bolted joints.

Because the compressive stress in a bolted joint is concentrated under the head and nut of the bolt, bolts made of high strength aluminum alloys such as 7075 T-72 alloy, are recommended. Aluminum bolts are usually anodized and covered with a thin layer of a lanoline lubricant. Equally, for jointing the copper busbars, bolts made of a high-strength bronze (Everdur) are preferable over those of steel. Bronze bolts should be assembled dry. Aluminum alloy and bronze bolts are nonmagnetic and therefore not subject to heating from hysteresis losses in AC fields, as is the case with steel bolts.

7.3.4.1 Retightening

As pointed out in Section 7.2.1, stress relaxation and creep are the major parameters impacting on the performance of power connections. One of the simplest and most widely used methods of maintaining the contact force in a bolted joint is retightening. The results in Figure 7.31 depict the effect of retightening on the contact force and resistance of bolted aluminum-to-aluminum joints with two different joint configurations subjected to current-cycling conditions.[596]

It is clear that retightening has a very beneficial effect on the overall performance of bolted joints as manifested by a considerable stabilization of the contact force and resistance. The effect is more pronounced in the joints assembled with a combination of a spring lock (Grower) and thin flat washers. The initial pronounced loss of the contact force in this joint configuration is substantially reduced by subsequent retightening.

In a joint with a combination of disc-spring (Belleville) washer and thick flat washers, the initial contact loss of contact force is considerably lower due to the beneficial action of the Belleville washer. Nevertheless, retightening improves even further the integrity of this joint. Since the creep and stress relaxation are responsible for the loss of contact force, from these results it can be inferred that retightening lowers the rates of creep and stress relaxation in bolted joints.[580] It should be pointed out, however, that despite the beneficial effect of retightening on the mechanical and electrical stabilities of bolted joints, this method of mitigating the loss of contact force in bolted joints is rather impractical.

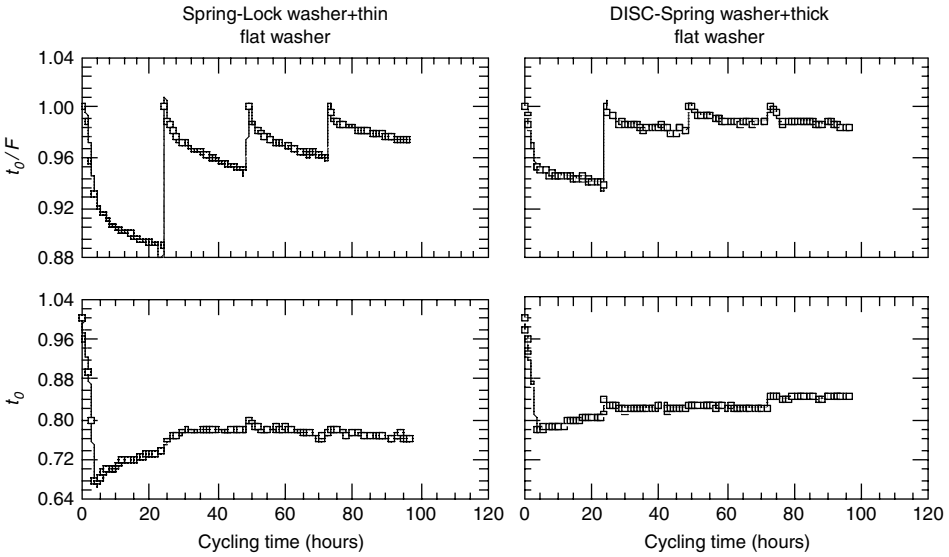

FIGURE 7.31 Effect of retightening on the relative contact force F_0/F_t and relative contact resistance R_0/R_t of the joints with two different joint configurations. F_0 and R_0 are the initial values of contact force and resistance whereas F_t and R_t are their values after time t.

7.3.4.2 Bimetallic Inserts

Another method of circumventing the incompatibility between aluminum and copper is the use of bimetallic aluminum–copper transition contact plates. These bimetallic inserts are copper and aluminum plates joined together by roll-bonding or other jointing methods which assure a continuous interface and good transition bond between those two metals. The bimetallic plates are primarily intended for the busbar type connectors and require the use of contact-aid compound (grease) to prevent the galvanic corrosion at the copper–aluminum interface.

It should be pointed out, however, that although the bimetallic contact plates reduce the risk of gross corrosion, the problem of jointing aluminum to copper still remains, since the two new interfaces (aluminum–aluminum and copper–copper) created in the contact zone, may introduce an additional impediment to the passage of the current across the joint. Also, these new contact surfaces have to be treated in the same manner as in the case of aluminum-to-aluminum and copper-to-copper connections that are to be brushed and greased.

7.3.4.3 Transition Washers

An alternative method of joining aluminum-to-copper is the use of a transition washer inserted between the contacting aluminum and copper surfaces. This method of joining is recommended for situations where plating is inconvenient, or where improvements are required for existing installations. The material used for transition washers is either 60/40 brass or high-strength Al–Mg–Si alloy. The sharp surface profile of these washers ruptures the oxide films without need for further cleaning and establishes substantially larger contact area that is more resistant to aging then direct surface contact. Figure 7.32 shows examples of transition washers commonly used in Germany (Figure 7.32a) and Great Britain, France, and Canada (Figure 7.32b).

Although these washers do not require surface preparation of the busbar conductors, the use of contact aid compounds is essential. Furthermore, in the case of brass transition washers, there is always a danger of formation of intermetallics at the contact interface since, if not properly

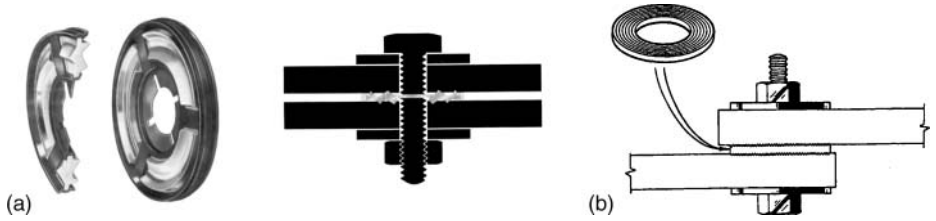

FIGURE 7.32 Transition washers made of (a) Al–Mg–Si alloy, used in Germany, and (b) brass, used in the U.K., France and Canada.

installed, the washer/conductor interface temperature may rise high enough to provoke the formation of intermetallics.

7.3.4.4 Multilam Contact Elements

Another type of transition washers that is gaining popularity and widespread use not only in the power industry but also in electronic and medical applications is based on the multilam contact elements that are torsion spring louvers made of copper–beryllium alloys, allowing a large number of defined contact points to be made. Each louver forms an independent current bridge thus creating a multitude of the current paths that substantially reduce the overall contact resistance. The advantages of multilam contacts are high-current transmission in hermetically sealed chambers, thus eliminating the need for plating, cleaning, or lubricating of busbars, ease of installation, modular design, substantially prolonged service life, cost effectiveness, and high operating reliability. Figure 7.33 shows the application of the multilam contacts in the busbar joints.[601]

7.3.4.5 Shape-Memory Alloy Mechanical Devices

The shape-memory alloys (SMA) have high sensitivity to deformation over a narrow temperature range, which makes them ideal as disc-spring washers.[602] Furthermore, these alloys have the ability

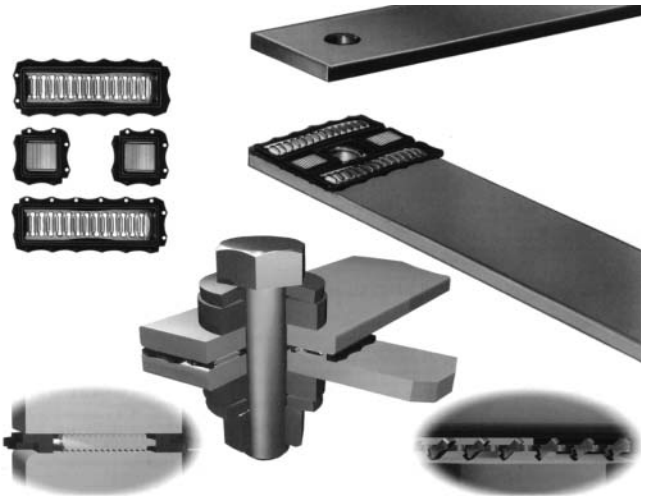

FIGURE 7.33 Typical application of the multilam contacts in busbar connection. (From *Multi-contact Tech. Catalog*.)

to change the shape of the load–deflection curve which can be advantageous in many applications. This feature of SMA washer was used by Oberg and Nilsson[603] to demonstrate that even in improperly installed bolted joints (low contact force), the heat developed by the joint looseness can be used to lower and stabilize the contact resistance in a bolted joint.

The effect of shape-memory (SMA) disc-spring (Belleville) washers on the performance of aluminum-to-aluminum bolted joints under current-cycling conditions has been investigated by Braunović et al.[604] and Labrecque et al.[605] It was shown that the use of SMA disc-spring washers produced significant improvements in electrical and mechanical stabilities of bolted joints during current-cycling conditions.

The beneficial effect of SMA disc-spring washers is emphasized by the fact that even with a low initial contact force (faulty installation), the heating caused by the reduced contact force generates an additional stress in the joint, thereby preventing the joint from failing. This is of significant practical importance, since field experience show that very often, joint failures are linked to poor or inadequate installation.

The high sensitivity of shape-memory alloys over a narrow temperature range makes them ideal as Belleville washers. Figure 7.34 illustrates the force–deflection dependence of NiTi shape-memory Belleville washers at 20 and 65°C.[50] Because the material at 20°C is fully martensitic, the force–deflection curve is nonlinear, whereas at 65°C it is essentially linear, indicating that the materials are fully austenitic. This ability of an SMA washer to vary the shape of the force–deflection curve can be advantageous in many contact applications.

7.3.4.6 Self-Repairing Joints

Recently, a very inventive and interesting solution for controlling the mechanical integrity of bolted joints is described. This solution involves the use of piezoelectric (PZT) and shape-memory alloy (SMA) elements. The impedance-based health monitoring technique, employing the electromechanical coupling property of piezoelectric materials, is used to assess the conditions of joints. When the joint loses it mechanical integrity due to stress relaxation, creep, or other extraneous effects, the shape-memory washers automatically regains lost contact force. The SMA actuator is a cylindrical Nitinol (Ni–Ti alloy) washer that expands axially when heated. The stress generated by the axial strain compresses the joint members and creates a force, generating a preload and restoring lost contact force.[606]

It is important to point out, however, that there is a number of problem areas such as low mechanical strength of SMA alloys, susceptibility to fatigue and loss of shape-memory effect, fabrication procedure, and cost that have to be solved before SMA-based mechanical contact

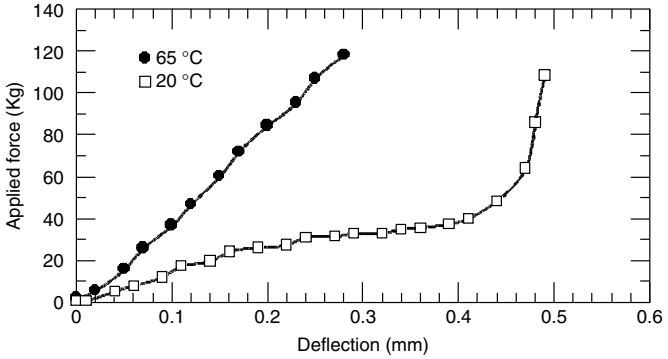

FIGURE 7.34 Effect of SMA Belleville washer on the force–deflection dependence of SMA Belleville washer. (Derived from Waram, T., *Raychem Tech. Doc.*)

devices can be safely used in practical applications. A review of the basic features of shape-memory alloys and their applications in power connections is given in.[567]

7.3.5 Lubrication: Contact Aid Compounds

It has been known for some time that the use of suitable lubricant (contact aid compound) improves the performance of an electric contact. When the contact is made, the lubricant is squeezed away from the points of highest pressure and hence the metallic conduction through the contact is not disturbed. As a result, the oxidation of clean metal surfaces is virtually prevented and a high area of metallic contact, hence, low contact resistance, and protection of the contact zone from adverse environmental effects are maintained.

It is a common practice that for both aluminum and copper busbar connections, the contact surfaces should be abraded through the suitable contact aid compound with a wire brush or abrasive cloth. Due to a more rapid formation of initial oxide film on aluminum, this procedure is more important for aluminum conductors than for copper. Tests have shown that small variations in bolt pressures after initial application, have little effect on the performance of this type of joint.[596]

However, when electrical equipment is supplied with either silver- or tin-plated terminals, the plated contact surfaces should not be scratched or brushed. Only the contact surfaces of the aluminum or copper bus that are to be bolted to these surfaces should be prepared. It is recommended that such plated surfaces, before being bolted to aluminum or copper bus, be cleaned with cotton waste and then coated with a suitable compound to serve only as a sealer (see Section 7.4).

The beneficial effect of contact load, surface preparation, and lubrication on the contact resistance of bolted connections is illustrated in Figure 7.35. It is apparent that both surface preparation (machining and brushing) combined with lubrication considerably reduces the contact resistance of bolted joints.[567]

Another example of the beneficial effect of lubrication is depicted in Figure 7.36.[607] The contact voltage of nonlubricated and lubricated aluminum–copper contact under fretting conditions was shown as function of two complete fretting cycles. The results shown were obtained after approximately 10^6 s of fretting at 2-N contact load and 25-μm slip amplitude. The data were obtained by continuously recording the contact voltage variations with time.

From Figure 7.36, it is clear that in the case of the nonlubricated aluminum–copper coupling, the contact voltage fluctuates from a few millivolts to more than 2 V along the wear track. The high contact voltages correspond to the situation where a thick layer of fretting debris is encountered by the contacting surface that greatly impedes the current passage. The magnitudes of these voltages exceed the softening and melting voltages of both aluminum and copper, indicating that very high temperatures are attained in these regions of a contact. The regions of high contact

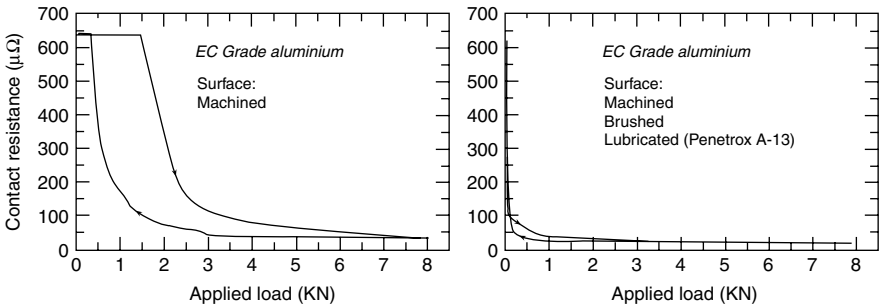

FIGURE 7.35 Effect of contact load and surface finish on the contact resistance of aluminum.

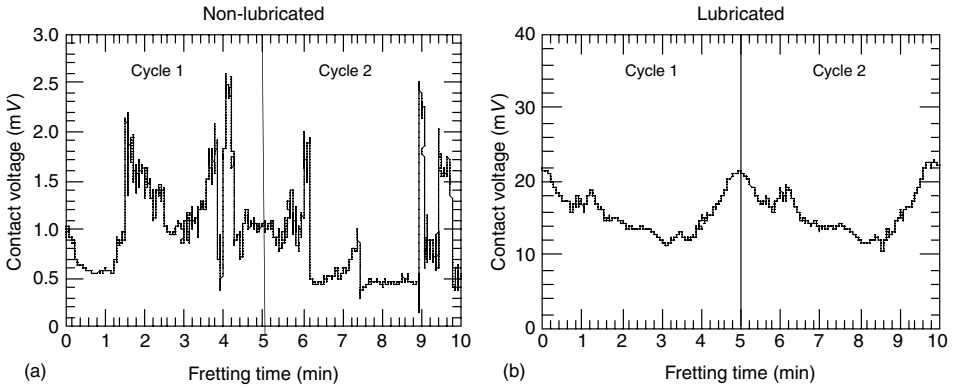

FIGURE 7.36 Effect of lubrication on the contact voltages of (a) nonlubricated and (b) lubricated aluminum–copper couples along the wear track as a function of fretting time.

voltages are apparently not stationary since the subsequent wipe they shift along the wear track indicates the dynamic nature of the processes involved. On the other hand, the low contact voltages correspond to the situation when the metallic contact has been regained between the contacting members.

Figure 7.36b depicts the contact voltage variation along the wear track of a lubricated contact. As it can be seen, lubrication significantly reduced the contact voltage fluctuations and maintained relatively stable contact voltages along the wear track.

Over the years, various contact aid compounds have been used for ensuring reliable performance of aluminum and copper connections. Although many such compounds are commercially available, very little published information relevant to their performance and efficiency under accepted utility service conditions can be found in the literature.

Braunović[146,567,608] evaluated the contact aid compounds commonly used for aluminum-to-aluminum and aluminum-to-copper connections. The evaluation was based on their effect on the performance and stability of a bolted joint under current cycling and fretting conditions, contact resistance force relationships, stability to thermal degradation, spreading tendency, and ability to protect the contact against corrosion in saline and industrial pollution environments.

The results, summarized in Table 7.15, provide an overall assessment of the various compounds and a quantitative method of comparison. The INDEX is defined as an average of the numerical values assigned to the performance of joints under different laboratory and environmental conditions. The lower the INDEX number, the more efficient the compound. Therefore, the compounds rendering a low initial contact resistance and having the performance INDEX less than 1.0 enhance the stable performance of these connections.

In the case of all-copper connections, it is generally accepted practice not to use any contact aid compound. However, copper connections are also susceptible to degradation during their service life although their deterioration can proceed for a long time without any appreciable changes in their performance. This engenders a false sense of security, since experience has shown that the deterioration of copper connections occurs rather abruptly triggered by accelerated interaction of chemical, thermal, mechanical, and electrical processes at the contact interface. Hence, to prolong the useful service life of copper connections, the use of contact aid compounds such as Nikkei or Koprshield or the equivalent having the performance INDEX 1.0 is strongly recommended.

It is important to emphasize, however, that the ranking of the contact aid compounds was determined under controlled laboratory conditions using laboratory equipment. Hence, the significance of different effects exerted by these compounds on the properties of aluminum and copper

TABLE 7.15
Summary of Comparative Evaluation of Different Contact-Aid Compounds for Aluminum-to-Aluminum and Aluminum-to-Copper Connections

Contact-Aid Compound	Index
Aluminum-to-aluminum	
Penetrox A-13	0.7
Silicon Vacuum Grease	0.7
Penetrox A	0.8
Aluma Shield	1.2
Fargolene GF-138	1.2
Contactal HPG	1.3
Petroleum Jelly	1.3
ZLN 100	1.5
Alcan Jointing Compound	1.8
AMP Inhibitor	2.5
Kearnalex	2.5
Non-lubricated	2.6
Aluminum-to-copper	
Nikkei S-200	0.7
Koprshield CP-8	1
Penetrox A-13	1
Pefco	1
No-Oxid-A	1.3
Fargolene GF-158	1.4
Silicone Vacuum Grease	1.5
Non-lubricated	1.6
Contactal HPG	1.8
Petroleum Jelly	1.9

connections under different operating and environmental conditions is yet to be determined since the field service variables such as water, sand, dirt, dust, acid rain, extreme ambient temperatures, pollutants, etc., can be very important parameters. Nonetheless, it is clear that contact aid compounds play a key role in the search for reliable electrical connections.

In summing up, it has to be pointed out that despite the protective benefits derived from the use of contact aid compounds, in some cases, the effectiveness of these compounds may be limited due to inadequate or improper application of the compound, loss of compound as a result of excessive operating temperatures, and weathering characteristics of the compound.

7.4 INSTALLATION PROCEDURES

To ensure proper function of a joint, certain measures must be taken during installation. The most important items for proper bus connections include the correct selection of connecting hardware, surface preparation and applying the adequate contact force. For low-resistance connections, the surface preparation of the connection is as important as—if not more important than—the selection of the proper joint compound. The measures to be taken to prevent the adverse effect of environment on the functioning of the joint depend upon the busbar material and the environment in which the busbars are installed. The procedures are given in Table 7.16.

TABLE 7.16
Typical Installation Procedures for Assembling the Bolted Busbar Joints

Busbar Contact Material	Environment	
	Indoors—Dry Places—Oil	**Corrosive—Damp Indoors—Outdoors**
Bare aluminum, aluminum alloys, aluminum-to-copper, aluminum-to-tin-plated surfaces	Remove dirt and grease with white spirit, alcohol, solvent cleaner or the like. Abrade aluminum and copper surfaces only with a wire brush or a rough file. Do not abrade plated surfaces. Apply immediately a thin layer of contact-aid compound (inhibitor) to the contact surfaces. Bolt the joint.	Remove dirt and grease with white spirit, alcohol, solvent cleaner or the like. Abrade the aluminum and copper surfaces only with a wire brush or a rough file. Do not abrade plated surfaces. Apply immediately a thin layer of contact-aid compound (inhibitor) to the contact surfaces. Bolt the joint.
Bare copper, copper alloys, copper-to-tin plated surfaces.	Remove dirt and grease with white spirit, alcohol, solvent cleaner or the like. Abrade copper surfaces only with a wire brush or a rough file soaked in with a contact-aid compound (inhibitor). Bolt the joint.	Remove dirt and grease with white spirit, alcohol, solvent cleaner or the like. Abrade the copper surfaces only with a wire brush or a rough file soaked in with a contact-aid compound (inhibitor). Bolt the joint.
Tin-plated surfaces.	Remove dirt and grease with white spirit, alcohol, solvent cleaner or the like. Bolt the joint.	Remove dirt and grease with white spirit, alcohol, solvent cleaner or the like. Apply a thin layer of contact-aid compound (inhibitor) to the contact surfaces. Bolt the joint.
Nickel-plated surfaces.	Remove dirt and grease with white spirit, alcohol, solvent cleaner or the like. Bolt the joint.	Remove dirt and grease with white spirit, alcohol, solvent cleaner or the like. Apply a thin layer of contact-aid compound (inhibitor) to the contact surfaces. Bolt the joint.
Silver-plated surfaces	Remove dirt and grease with white spirit, alcohol, solvent cleaner or the like. Bolt the joint.	Remove dirt and grease with white spirit, alcohol, solvent cleaner or the like. Apply a thin layer of contact-aid compound (inhibitor) to the contact surfaces. Bolt the joint.

The contact force required in bolted joints is attained with one or more bolts. By tightening the nuts to a given torque, the bolts are pre-tensioned and the required contact force is obtained in the joint. Maintaining certain pre-tension force is important not only for keeping the contact resistance low but also for preventing the nut and thus the joint from loosening when subjected to vibrations. If the bolts are tightened to less than the prescribed values, this will loosen the joint that will heat

due to poor electrical contact. If the bolts are overtightened, however, the connection will be subjected to stress relaxation and creep, and eventually will fail. The process by which stress relaxation and creep cause failure is explained in Chapter 4, Section 1.7.

Contact resistance is lowest near the bolts where the clamping force is highest. The majority of the current passes through these points of low contact resistance; if the contact zone is small, current density will increase that will generate heat at the contact interface. If the heat is not dissipated by radiation, a hot spot develops. The hot metal creeps toward the bolt holes at these high temperature and high pressure points. This gradual metal flow from the hot spots leads to a reduction in total clamping force over several heating–cooling cycles. A slight loss of clamping force can increase the joint resistance. The end result is a slow but progressive failure. To overcome this problem and ensure stable and low resistance operation, thick and large diameter flat washers are recommended.

In summary, it can be stated that despite deleterious effects of different degradation mechanisms to which the power connections are subjected under operating conditions, their reliable performance can be obtained and maintained providing the mitigating measures are applied and the installation procedures strictly followed.

8 Electronic Connections

8.1 TYPES OF ELECTRONIC CONNECTIONS

The advent of semiconductor and integrated circuits in the mid-twentieth century signaled a revolution in the electronic industry. As this industry began to explode, the need for miniaturization and interconnection reliability, increased device functionality, and higher-speed circuits resulted in the development of different manufacturing technologies aimed at packing more functionality into smaller spaces. To keep up with continuous reduction of the size of transistors and to support an explosion of new products and capabilities with ever-increasing complexity, the packaging became a very important issue in the manufacturing technology.

The increased functionality and complexity of microelectronic systems in less space and the need for more reliability at lower cost have led to the evolution of several types of area array packages like dual-in-line packages (DIP), plastic leadless chip carrier (PLCC), ceramic pin grid array (CPGA), ball grid array (BGA), and most recently, chip scale packages (CSP). The important characteristic of these devices is not only their smaller size, but also the capability to provide environmental protection and reliable electrical performance for use in harsh environments such as automotive, military, and space applications. This goal can only be achieved when the connector degradation mechanisms are well defined and various mitigating measures have been identified. In recent years, great attention has been devoted to improving IC packaging technology because, in many cases, the performance of the IC is determined by the IC package.

Presently, there is practically a myriad of different types and sizes of electronic connectors used in a huge variety of electronic devices and applications. Nevertheless, despite such a vast diversity of devices and applications, electronic connectors can generally be classified as the power connectors: compression (crimp), mechanical (pin) and socket, and welded (soldered). Typical electronic connection configurations are shown in Figure 8.1.

8.2 MATERIALS FOR ELECTRONIC CONNECTIONS

Electronic connections are one of the most critical links of the interconnection system and essential elements in providing the electronic signal path. Although over the past 10 years the electronic systems have experienced radical changes, the basics of connector technology have remained essentially unchanged. This is because the design criteria essential for defining the parameters that ensure reliable performance of an electrical connection are established by the laws of contact physics developed over many years.

The performance of an electronic connection is dependent on both the bulk resistance of the contact and the interface resistance. For optimal electrical performance, the electrical path should comprise the material with the highest electrical conductivity, largest cross-section, and shortest conductive path. In the past, a very low contact resistance and resistance to adverse effects of environment (corrosion) were ensured by plating the whole contact, often with a noble metal such as gold. With the increasing price of gold, selectively plating gold only in the mating area became an absolute necessity. To further reduce the cost of gold plating, the manufacturers of

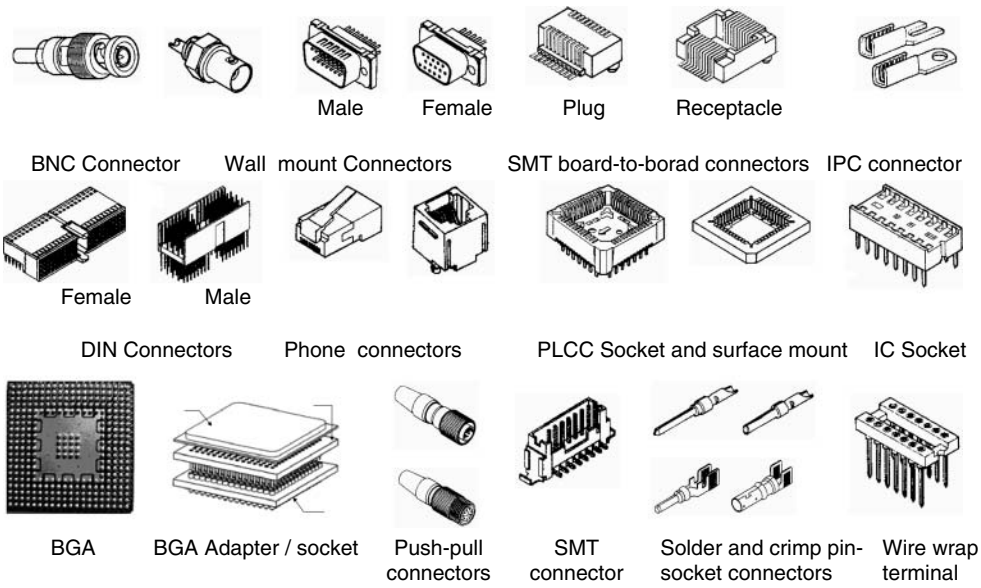

FIGURE 8.1 The generic electronic connector design and configurations used in different electronic system and devices.

electronic components are steadily decreasing the thickness of gold finishes, thus potentially creating porosity problems that can adversely affect the quality of the component.

Coating (plating) is of particular importance in electronic connections because its use enables one to alter the intrinsic properties of materials that otherwise cannot be altered by conventional methods. In other words, coating can significantly improve properties of a connection such as mechanical (hardness, toughness, and strength), thermal (expansion, conductivity), electrical (resistivity), wear (abrasion and erosion resistance), and chemical (resistance to oxidation, corrosion, tarnishing). Because the coating materials for electrical/electronic contacts are covered extensively in Chapter 4, Section 2, only a comprehensive review of the solder materials used for electronic connections will be given in the following section.

8.2.1 Solder Materials

Evolution of modern electronic equipment towards small-scaled and high-density components prompted development of various connecting methods. However, despite numerous novel jointing techniques, soldering remains the most widely used method of jointing electronic connections. Such a wide use is demonstrated by extensive coverage in the literature.[609–612] Although the history of soldering goes back some 5000 years, the fundamental soldering has always been based on the Sn–Pb alloys.

Some two millennia later, soldering remains the widely used method of joining metal surfaces in one of the most advanced technological areas of the modern era—the fabrication and assembly of microelectronics. Indeed, for the last 50 years, Sn–Pb solders have been used extensively as interconnection materials in the electronics industry for attaching components to printed circuit boards (PCBs) and other microcircuit devices. Such solders are inexpensive, perform reliably under a variety of operating conditions, and possess unique characteristics (e.g., low melting point, high ductility, and high fatigue resistance) that are well suited to electronics applications.

It is rather surprising, however, that despite the long history and the widespread use of Sn–Pb soldering practices, the fundamental physics of the processes are still not well understood. This is mainly due to the fact that soldering involves complex interactions between materials affecting physical, chemical, metallurgical, and mechanical properties of solders, such as phase changes, reaction and product formation, dissolution and diffusion, creep and stress relaxation, and wetting. The situation is further complicated by the nonequilibrium nature and the simultaneous occurrence of many interactions during soldering that makes the process very difficult to fundamentally understand. Consequently, the lack of detailed characterization of the realistic solder joint microstructure and its evolution under service operating conditions represents a major hurdle in achieving an optimal service performance that is essential for engineering and introduction into manufacturing settings.

The relentless reduction of electronic packages resulted in a reduction of several orders of magnitudes in their characteristic macroscopic dimensions. The trend to reduce the size of electronic packages and demand for increasingly sophisticated electronic devices with more, higher-density inputs/outputs (I/Os) prompted development of new technologies such as CSP, FC, BGA, WLP, etc. The changes in interconnect technology demanded changes in processes and in the dispensing technologies required for their application. For these technologies, solder is the electrical and mechanical bond and thus its reliability is one of the most critical issues in the development of these technologies.

Considerable attention and efforts have been focused on reliability aspects of soldering, specifically on understanding the material behavior of solidified solder joints under different operating and environmental conditions. It has been established that the solder-joint reliability is highly dependent on solder-joint geometry, as well as on solder material properties; as a consequence, predicting solder performance became a critical issue for the electronic community.

During the short but spectacular evolution of microelectronics, the Sn–Pb system has been used almost exclusively in widely differing interconnect technologies. However, in recent years, these materials are now coming under close scrutiny due to concerns over lead contamination and pollution in groundwater, and higher-temperature applications in the automobile industry. It is now recognized that the use of lead-based alloys is as an environmental and health problem.

As a result of environmental concerns and anxiety over the presence of lead in microelectronics, lead-free soldering is no longer an esoteric concept but rather an issue of utmost importance. In Europe, the Waste Electronic and Electrical Equipment (WEEE) and the Restriction of Hazardous Substances (RoHS) Directives[613,614] stipulated that consumer electronic equipment must be lead-free by July 1, 2006. In Asia, the Japanese Ministry of Industry and Trade Institute (MITI) has enacted new environmental legislation calling for a complete elimination of the use of lead by December 31, 2005.[615]

In the U.S., however, there is no pending legislation to ban lead-bearing alloys. The microelectronics industry responded rather reluctantly because the essential requirement would require the need to abandon the Sn–Pb system for which a considerable empirical knowledge base had been accrued over the years. Although a considerable amount of information on lead-free solders has been published in the last few years, the database on these new materials is still at an infant stage compared to that of lead-containing solders. Nevertheless, the search for the lead-free alternatives has been given considerable attention as demonstrated by the development work on lead-free solders that has been initiated by a number of organizations and institutions.

Another equally important issue in lead-free development is the trend toward continued densification in electronic packages, and even tighter pitches. This, in turn, requires finer-line circuitry solders with the mechanical properties capable of withstanding the increasingly severe mechanical demands compared to the eutectic Pb–Sn solder. As a result of concentrated efforts, alternates to lead-bearing solder alloy with significantly better strength and fatigue life performances than eutectic Pb–Sn have been identified and extensively researched.[616–620]

8.2.2 Lead-Free Solders

Research into lead-free materials resulted in the development of large numbers of solders with lower and higher melting points and improved mechanical (creep, stress relaxation, and fatigue) properties. In view of the widespread use and importance of lead-free materials in electronics, a comprehensive review of the characteristic features of these materials is warranted and given below.

8.2.2.1 Tin

Owing to its ability to wet and spread on a wide range of substrates using mild fluxes, tin has become the principal component of most solder alloys used for electronic applications. Tin exists in two different forms with two different crystal structures: white tin with a body-centered tetragonal crystal structure and gray tin with a diamond cubic crystal structure.

Thermodynamically, white tin is stable at room temperature, whereas gray tin is thermodynamically stable below 13°C. The transformation of white to gray tin, also called "tin pest," takes place when the temperature falls below 13°C, and results in a large increase in volume that can induce cracking in the tin structure. Consequently, tin pest can be a problem for applications that operate at extremely low temperatures. Tin is also prone to whisker growth. Whiskers can be defined as a single-crystal growth resembling fine wire that can extend up to 0.64 mm high (see Section 8.3.8).

8.2.2.2 Tin–Silver

The eutectic composition for the Sn–Ag binary system (Sn–3.5Ag) has a higher melting point than Sn–Pb, e.g., it melts at 221°C and, as such, is suitable for higher-temperature applications. The microstructure consists of Sn and the intermetallic Ag_3Sn in the form of thin platelets. The solidified microstructure of the binary eutectic Sn–3.5%Ag consists of a β-Sn phase with dendritic globules and interdendritic regions with a eutectic dispersion of Ag_3Sn precipitates within a β-Sn matrix.

The addition of 1% Zn has been shown to improve the solidification microstructure of this alloy by eliminating the large β-Sn dendritic globules and introducing a finer, more uniform, two-phase distribution throughout the alloy. The Sn–Ag alloys have improved wetting and joint strengths and exhibit superior resistance to thermal fatigue. However, the high level of tin, combined with elevated reflow temperatures, can accelerate the diffusion of copper into the joint, leading to brittleness. The Sn–Ag solders solder may likely be prone to whisker growth due to its high tin content.[621]

Compared to Sn–63Pb alloys, the wetting of Sn–3.5Ag is quite poor due to high interfacial tension between solder and flux that is probably related to the high surface tension of Ag. The Sn–Ag alloys have shear strengths comparable to eutectic Sn–Pb and ultimate tensile strengths comparable with or slightly higher than Sn–Pb. At high shear strain rates, the room-temperature isothermal fatigue behavior of Sn–Ag alloys are substantially superior to Sn–63Pb at high shear strain amplitudes, but far inferior at low strain amplitudes.

The thickness of intermetallic layers has been found to increase despite the fact that no microstructure coarsening was observed. Cracks propagated at the solder/intermetallic interface and through the solder. However, no complete failures were observed after 70 cycles. The superior overall property of Sn–3.5Ag makes this alloy suitable for solder interconnects in thick film automotive electronics packages when used with a mixed bonded Ag conductor.[621]

Due to a limited solid solubility of Ag in Sn, this alloy is resistant to coarsening and thus has a more stable, uniform microstructure and is more reliable. Although the Sn–3.5Ag alloy itself exhibits good microstructural stability, when soldered to copper base metal, the combination of a higher Sn content (96.5Sn compared to 63Sn) and higher reflow temperature environments

accelerates the diffusion rates for copper base metal in Sn. Upon reaching the composition corresponding to Cu_6Sn_5, the nucleation and growth of brittle intermetallic compound occurs. The use of alternative surface finishes, such as immersion gold (Au over Ni over Cu), slows the diffusion rate and thereby decreases the growth kinetics. Diffusion of Cu into the solder and formation of the brittle Cu_6Sn_5 intermetallic compound can be limited using Ni in the immersion gold coating as a diffusion barrier. Other surface finishes such as immersion silver (Ag over Cu) and immersion palladium (Pd over Cu) do not contain a Ni barrier layer.[622]

8.2.2.3 Tin–Silver–Bismuth

Addition of Bi to Sn–3.5Ag improved wetting/spreading performance on Cu; a minimum contact angle of $31 \pm 4°$ was observed with 4.83 wt% Bi addition. Increasing the Bi content of the ternary alloy raised the Cu/solder/Cu solder joint shear strength to 81 MPa as determined by the ring-and-plug tests. Transmission electron microscopy (TEM) analysis of the Sn–3.33Ag–4.83Bi composition indicated that the strength improvement was due to solid solution and precipitation strengthening effects by the Bi addition residing in the Sn-rich phase. Microhardness of the Sn–Ag–Bi alloy, as a function of Bi content, reached maximum values of 30 (Knoop, 50 g) and 110 (Knoop, 5 g) for Bi contents greater than approximately 4–5 wt%.[623]

A differential scanning calorimetry (DSC) evaluation of the Sn–3.33Ag–4.83Bi composition suggested the appearance of metastable, short-range order in the atomic structure as a result of low temperature and thermal aging. TEM analysis of this alloy indicated that solid-solution and precipitation strengthening mechanisms were a likely consequence of the Bi additions. Solid-state aging studies on Sn–3.33Ag–4.83Bi/Cu couples showed the growth of an intermetallic compound layer at the solder/substrate interface comprised of Cu_3Sn and the Cu_6Sn_5 sublayers. Although Bi was not detected within the intermetallic compound layer, however, a small concentration of Bi was observed at the ahead of the growing intermetallic compound layer. The growth kinetics of this solder was not significantly different from those of the Sn–3.5Ag alloy.[623]

8.2.2.4 Tin–Silver–Copper

In the Sn–Ag–Cu system, metallurgical reactions between Sn and the minor elements (Ag and Cu) are primary factors in determining the application temperature and solidification mechanism as well as mechanical properties.[624] Due to thermodynamically favorable interaction of Ag or Cu with Sn, Ag_3Sn or Cu_6Sn_5 intermetallic compounds are formed in the Sn-matrix phase.

The presence of relatively hard Ag_3Sn and Cu_6Sn_5 particles in the Sn-matrix of Sn–Ag–Cu ternary alloys can effectively strengthen the alloy by building a long-range internal stress and acting as the most effective blocks for fatigue crack propagation. Formation of Ag_3Sn and Cu_6Sn_5 particles could partition finer Sn-matrix grains. The finer the Ag_3Sn and Cu_6Sn_5 particles are, the more effectively they partition Sn-matrix grains, resulting in an overall finer microstructure. This facilitates grain boundary gliding mechanisms, accounting for the extended fatigue lifetime under elevated temperatures.[624] In the Sn–Ag–Cu ternary system, Cu at 1.5% (3–3.1% Ag) most efficiently generates the proper amount of Cu_6Sn_5 particles with the finest microstructure size, contributing to the highest fatigue life, strength and plasticity. The compositions with 3.0–4.7% Ag and 0.5–1.7% Cu generally possess a higher tensile strength than Sn–37Pb alloy. The melting temperature of Sn–3.1Ag–1.5Cu is 216–217°C (nearly eutectic), which is about 4°C lower than eutectic Sn–3.5Ag.

The melting temperatures of Sn–Ag–Cu solders make them ideal in high operating temperatures up to 175°C. Although the Sn–Ag–Cu solders do not wet Cu as well as Sn–Pb, improved wetting can be achieved using high-temperature fluxes. Soldering in nitrogen atmosphere also improves wettability.[622]

The Sn–Ag–Cu system containing 0.5–1.5% Cu and 3.0–3.1% Ag have reasonably good physical and mechanical properties. In comparison, Sn–3.1Ag–1.5Cu costs less than those compositions bearing a higher Ag content, such as Sn–4.1Ag–0.5Cu and Sn–4.7Ag–1.7Cu. In some cases, the higher Ag content may degrade some properties.[623]

The optimal composition in the Sn–Ag–Cu system is Sn–3.1Ag–1.5Cu, which has good strength, fatigue resistance, and plasticity. It should be noted, however, that the lowest melting temperature that can be achieved in the Sn–Ag–Cu system is 216–219°C, which is still too high to fit a broad range of applications under the current surface mount technology (SMT) infrastructure for which a melting temperature below 215°C is considered as a practical criterion.[624]

8.2.2.5 Tin–Silver–Copper–Antimony

The alloy Sn–2.5Ag–0.8Cu–Sb–0.5 (CASTIN) has the lowest liquidus temperature with the melting point of 216°C. One of the characteristic features of this alloy is a relatively lower rate of intermetallic growth. The microstructure of this alloy has a consistent, leafy, dendritic structure regardless of the cooling rates used. Due to its good fatigue resistance and joint strength it can be used in flip-chip attachments, component tinning, bare board coating, surface mount assemblies, and wave soldering. It is almost a drop-in substitution for the Sn–Pb alloy in most soldering applications.[625]

8.2.2.6 Tin–Silver–Antimony

The melting point of this alloy, commonly known as *Motorola J* alloy (Sn–25Ag–10Sb), is a relatively high-temperature alloy (232–340°C) but with a good creep resistance. Most notably, this alloy is currently used as a replacement for Au–Si die attaches material. The high strength of this alloy may occasionally break the die. This behavior can be explained in terms of the alloy microstructure and resulting properties. With this relatively high amount of antimony, a large amount of the hard SbSn phase is likely present. These SbSn cubes can act as crack initiation sites and eventually lead to failures. Therefore, the high strength that the high antimony content imparts may prove to be too stiff for microelectronics applications where compliance to shear stresses is a requirement.[622]

The presence of large amounts of Sb may also be responsible for the very poor wetting behavior of this alloy. The poor wetting behavior was associated with a higher content of Ag ($>4\%$) causing a decreased fluidity. This observation can be attributed to the formation of a substantial amount of the needle-like Ag_3Sn phase that remains solid until 480°C. A large number of solid Ag_3Sn particles could inhibit solder wetting and spreading. It is likely that both the high Sb and Ag levels that are present in this alloy contribute to its poor wetting behavior. The needle-like Ag_3Sn phase may also act as a crack nucleation site, affecting fatigue behavior. From an electronics manufacturing standpoint, this alloy is too strong, wets poorly, and is too expensive with 25% Ag.[622]

8.2.2.7 Tin–Bismuth

The eutectic Sn–Bi alloy (42Sn–58Bi) alloys have a lower melting point (138°C) and are suitable for use with heat sensitive components while still showing high strength when solid. Due to very low solubility of Sn in Bi at the eutectic solidification temperature of 130°C, the Bi phase is primarily pure Bi. Under moderate cooling conditions, the microstructure of eutectic Sn–Bi is lamellar with degenerate material at the boundaries of the eutectic grains. In slow cooled eutectic Sn–Bi alloys cracks and formation of large grains were observed. Tin precipitated from the solder matrix along the boundaries of the large grains through which cracking occurred. Cracking was not observed during rapid cooling. In general, conventional solders, when Sn is replaced with Bi, are less prone to intermetallics formation.[621]

Compared with Sn–Pb, the wetting of eutectic Sn–Bi is not as good, but is acceptable; this, in turn, restricts the allowed concentration of foreign elements. Consequently, the presence of 0.0002% phosphorus would cause wetting to degrade, implying a potential problem on electroless Ni containing some phosphorus. Under thermal cycling conditions, the eutectic Sn–Bi alloys outperform Sn–Pb alloys. Due to the presence of high bismuth content, the Sn–Bi alloy is susceptible to a rapid oxidation when exposed to air and thus the use of adequately activated fluxes is required. Owing to its high Bi content, this alloy displays little elasticity.[621]

Thermal cycling between -40 and $+100$°C showed the appearance of very early failure and extensive porosity is observed, probably a result of local melting during cycling. The shear strength and life in creep rupture tests at 50–80°C decreased relative to joints made on plain Cu. When the alloy has an equiaxed grain structure, it can be quite ductile and may exhibit superplastic behavior.[621]

The mechanical properties of this alloy (ultimate tensile and shear strengths) between 20 and 60°C are comparable to that of eutectic Sn–Pb alloy, whereas at 100°C this alloy is much weaker than eutectic Sn–Pb. One of the disadvantages of this high bismuth-containing alloy is its susceptibility to a rapid oxidation when exposed to air. This requires the use of adequately activated fluxes. Owing to its high Bi content, this alloy displays little elasticity.

8.2.2.8 Tin–Copper

The Sn–Cu binary alloy has a eutectic composition at Sn–0.7Cu. The solidification reaction consists of Cu precipitated in the form of hollow rods of the intermetallic Cu_6Sn_5. Because of the high concentration of tin in this alloy, it may be prone to whisker growth or transformation to gray tin may occur.

The eutectic alloy Sn–0.7Cu with a melting temperature of 227°C is similar to Sn–37Pb for surface-mount use. However, owing to melting temperature that is 10°C higher than tin/silver/copper, this alloy is undesirable for reflow applications. In wave-soldering applications, the temperatures that the boards and components reach are much lower than in reflow soldering. Because this alloy does not contain silver or bismuth, it is one of the cheapest lead-free solder alloys available and thus its use in wave soldering is advantageous as a low-cost alternative to tin-lead solder in wave-soldering applications. The alloy apparently works well in high-temperature applications, such as those required by the automotive industry.

8.2.2.9 Tin–Indium

The indium-based solder, with the composition of 52In–48Sn, is the one with the lowest melting point of 118°C and commonly used in low temperature applications, such as SMT. The microstructure of this alloy is characterized with the lamellar features. The Sn-rich phase is composed of equiaxed grains whereas the In-rich phase contains Sn precipitates. Wetting of this alloy is fair to acceptable, but only with a relatively active flux. Wetting on Cu, Ni–Sn, and pretinned Kovar (53Fe–17Co–29Ni) can be acceptable at 215°C, but wetting on Au is sluggish and poor.[621] Creep behavior of this alloy is characterized by rapid and extensive deformation leading to early failure. There is no microstructural change like coarsening and recrystallization that occur in Sn–Pb. This stability is due to rapid recovery of deformation. Although the isothermal fatigue behavior and fatigue life in temperature cycling tests of this alloy are poorer than that of eutectic Sn–Pb, tendency to crack propagation is slower. This behavior may contribute to the better fatigue performance of In alloys at low cyclic strain rates versus that of high Sn alloys.[621]

Indium-based alloys are more compatible with gold than tin, and the dissolution therein of gold is considerably slower. This alloy displays good oxidation resistance, but is susceptible to corrosion in a humid environment. It is also a very soft metal and has a tendency to cold weld. Due to its low

melting point, this alloy has a rather poor high-temperature fatigue behavior. The high indium content limits the widespread use of this alloy due to cost and availability constraints.[622]

This alloy is relatively ductile as manifested by higher elongation due to superplastic behavior in creep under shear loading at temperatures above 0.8 T_m of their melting point (T_m). The superplastic microstructure generally has a longer isothermal fatigue life than the nonsuperplastic microstructure. Pb–Sn forms a recrystallized band of material along a region of concentrated shear deformation. This microstructural changes does not occur in 52In–48Sn samples.[621]

Shear strength of this alloys between 20 and 60°C is much weaker than eutectic Sn–Pb and is attributed to the fact that the homologous temperature at which the testing was carried out was much higher for eutectic Sn–In (121°C) than for Sn63 (183°C). The shear strength of this alloy on Ni is almost 50% lower than for samples on Cu. This may be due to the dissolved Cu in In–Sn; the Cu takes the alloy away from eutectic composition and may harden it as well.[621]

8.2.2.10 Tin–Indium–Silver

In general, the physical properties of Sn–20.0In–2.8Ag are fairly comparable to those of Sn–37Pb. In addition, this alloy has higher tensile and shear strengths and greater elongation than Sn–37Pb. The adequate ductility of this alloy allows to be fabricated into various physical forms, such as wires, ribbons, preforms, etc. Overall, the data indicate that in bulk form, this alloy exhibits superior mechanical properties than Sn–37Pb, as manifested by the steady creep rate about two and half orders of magnitude lower than that of 63Sn–37Pb. This superior creep resistance behavior suggests an improved solder joint reliability of this alloy.

Melting of this alloy occurs between 174.7 and 186.5°C. Regardless of the small temperature difference at the onset of the melting process, the softening point of this alloy is found to be almost identical to that of Sn–37Pb. This result strongly suggests that the upper limit of the service temperature of both solders should be very comparable.[621]

Wetting of Sn–20.0In–2.8Ag is somewhat slower than the conventional Sn–37Pb; however, the difference in the wetting time is fairly insignificant when compared with the soldering time typically employed by the assembly process. Hence, it can be concluded that, in a practical sense, the wetting behavior of this alloy is comparable to that of Sn–37Pb solder. Evaluation results based on surface mount assembly and temperature cycling tests indicate that this Sn–In–Ag solder is a very viable candidate as substitute for Sn63.[621]

8.2.2.11 Tin–Zinc

The Sn–9 wt% Zn appears to be an attractive alternative to eutectic tin–lead with a relatively close melting temperature of 198°C. The solidified microstructure exhibits large grains with a fine, uniform, two-phase eutectic colony. The microstructure of this high Sn alloy, essentially comprising a small volume fraction of intermetallics distributed throughout a Sn-rich solid solution, differs significantly from the microstructure of eutectic Sn–Pb solders.

Because of its corrosion potential, zinc poses a concern. Solder paste incorporating this alloy would have a poor shelf life due to attack on the metal spheres by the organic acids or bases present in the flux vehicle.[621] One of the major concerns regarding the Sn–Zn solder is its oxidation and corrosion resistances. Silver and aluminum are among the alloying elements considered to promote improvement in the oxidation resistance.

8.2.2.12 Tin–Zinc–Silver

The Sn–(8.73–9)Zn–(0–3)Ag is attractive because of its eutectic temperature of 198°C, which is 20°C lower than that of the Sn–Ag–Cu system. However, the poor oxidation resistance and embrittlement behavior of this system represent a serious problem that must be resolved. The oxidation resistance has been improved by alloying with Ag.[626]

The Sn–Zn–Ag solders, based on the eutectic Sn–Zn matrix, form Ag–Zn compounds in the matrix. Increasing the level of Ag decreases the Sn–Zn eutectic structure. The melting of the solder containing up to 3% of Ag results in a formation of a two-phase zone whose liquidus temperature increases with increasing Ag level. This solder exhibits a eutectic behavior at the Ag level of 0.5% and less. The eutectic phase is Sn–9Zn. The Ag tends to form Ag_5Zn_8 and $AgZn_3$ intermetallic compounds. The formation of these compounds gradually diminishes the eutectic structure when the Ag level increases. The liquidus temperature increases from 206.0 to 215.5°C with an increase in the Ag level from 1.0 to 3.0%.[626]

8.2.2.13 Tin–Zinc–Silver–Aluminum–Gallium

This alloy, consisting of a Sn–Zn–Ag–Al–Ga combination exhibits a eutectic temperature of around 196°C. The thermogravimetric analysis (TGA) study shows that it attains much better oxidation resistance than the eutectic Sn–Pb solder at 250°C. This alloy has greater tensile strength and higher ductility than the eutectic Sn–Pb solder when the Ga level is 0.25–0.5%. Gallium tends to enhance wettability of the solder, although the wetting behavior mainly results from the interaction between Cu and Zn. Silver and zinc form Ag–Zn intermetallic compounds that become visible on XRD analysis when the Ag level is about 0.5%. The cost of this solder was also estimated and was found to be comparable with the Sn–Pb solder. The oxidation resistance of this five-element solder alloy is also superior to eutectic Sn–Pb.

In summary, despite relentless R&D in the field of lead-free alloys, there is no direct replacement for Sn–Pb solders without some form of compromise. In general, all the lead-free solder alternatives investigated show some shortcomings, such as price, physical, metallurgical, or mechanical properties. For instance, Sn–In systems are promising in terms of solder mechanical properties and soldering performance, but the price of In is the factor that negatively impacts wide application of these solder alloys. However, excluding elements on the grounds of cost should not necessarily be a barrier to widespread adoption because the costs of solder content of assembly represent a relatively small percentage.

The alloys based on the eutectic Sn–Ag doped with Zn, Cu, or Sb exhibit good mechanical strength and creep resistance, due to refined microstructure. The Bi–Sn systems doped with other elements may be used in the low temperature soldering field but their widespread has to be ruled out due to the future availability of Bi. Owing to a good fatigue resistance, eutectic Sn–Cu alloys are also potentially viable candidates for wider applications. The mechanical properties of eutectic Sn–Zn systems modified with In and/or Ag qualify these alloys as promising candidates. Clearly, finding a lead-free alternative for high-temperature solders as direct replacement of Sn–Pb presents the biggest challenge to the electronic industry.

Some fundamental properties of the most studied and reported Pb-free alloys in the literature are listed in Table 8.1 along with some properties of Sn–37Pb alloy. The advantages and disadvantages of the most common lead-free alloys are given in Table 8.2.

8.3 DEGRADATION MECHANISMS IN ELECTRONIC CONNECTIONS

Individual physical and mechanical properties of the constituents of electronic connections and their behavior under different operating and environmental conditions affect their overall reliability. As in the case of power connections (see Chapter 7), the electronic connections are susceptible to more or less the same degradation mechanisms. Bearing in mind the intrinsic characteristics of electronic connections such as size, combinations of different materials, performance requirements, etc., the influence of deterioration mechanisms on the reliability of electronic connections becomes of considerable importance. In the following sections, the characteristic features of common deterioration mechanisms in electronic connections will be discussed.

TABLE 8.1
Characteristic Properties of Common Lead-Base and Lead-Free Alloys

Composition	T_m (°C)	Density (g/cm^3)	ρ(μΩ cm)	CTE (10^{-6}/K)	TC (W/m K)	E (GPa)	Hardness VHN	σ_y (0.2%) (MPa)	Wetting Angle
Sn–37Pb	183	8.40	14.5	25	50.0	35.0	15	30.2	18
Bi–33In	109	8.81							
Bi–42Sn	138	8.56	30.0–34.4			43.0		41	42
In–3Ag	143	7.38		20	73				
In–32.5Bi–16.5Sn	60	7.88							
In–48Sn	118	7.30	14.7	20		19.5			
Sn–3.5Ag	221	7.36	12.3	22	33	56	13.5	48	35
Sn–4Ag–0.5Cu	216	7.39	12.42		57.3	51.0	16	33.5	32
Sn–2.5Ag–0.8Cu–0.5Sb	215	7.30	8.25		57.26	51.2		33.5	45
Sn–3.4Ag–4.8Bi	211							46.3	30
Sn–0.7Cu	227	7.4	13.0	13.3	64		10.5		
Sn–30In	120					17		10	
Sn–42In	118	7.30							
Sn–20In–2.8Ag	175	7.25							
Sn–10In–10Bi	153								
Sn–10In–9.5Bi–0.5Ag	179								
Sn–9Zn	199							51.6	
Sn–9Zn–1Ag	206								
Sn–8.55Zn–0.45Al–0.5Ag–2Ga	193							105.5	
Sn–8Zn–5In–0.1Ag	175								

Source: From Miric, A. Z. and Grusd, A., *Solder. Surf. M. Tech.*, 10(1), 19–25, 1998. With permission.

TABLE 8.2
Advantages and Disadvantages of Some Lead-Free Alloys

Composition	Advantages	Disadvantages
Sn–37Pb	Overall good properties; inexpressive	Structural coarsening; melting point high; creep susceptibility
Bi–33In		Poor wetting
Bi–42Sn	Good fluidity	Strain rate sensitive; poor wetting
In–3Ag		Poor wetting; expressive
In–32.5Bi–16.5Sn		
In–48Sn	Au soldering	MP low; poor fatigue and mechanical properties; expensive
Sn–3.5Ag	Good strength and creep resistance; good wetting	Poor isothermal fatigue at low strains; MP slightly higher
Sn–4Ag–0.5Cu		
Sn–2.5Ag–0.8Cu–0.5Sb	Improved thermal fatigue; Sb refines grain structure and lowers MP	MP slightly higher; Sb trioxide may exhibit toxicity at higher temperatures
Sn–25Ag–10Sb	High strength	MP very high; expensive
Sn–3.5Ag–1Zn	Good mechanical strength	MP slightly high
Sn–3.5Ag–1Zn–0.5Cu	Good ductility	MP slightly high
Sn–0.7Cu	Fatigue resistance	
Sn–4Cu–0.5Ag		Very high and wide melting range
Sn–3Cu–1Sb–0.5Ag		MP too high
Sn–30In		Poor creep
Sn–20In–2.8Ag	Good ductility, strength, and creep resistance; virtual drop-in replacement; low dross	Slightly expensive; large plastic range
Sn–8In–2Bi	High strength	MP too high
Sn–10In– 9.5Bi–0.5Ag	Creep and fatigue resistant	Slightly expensive
Sn–5Sb	Creep resistant; good temperature shear; mechanically strong	MP too high
Sn–9Zn	Good strength; abundant	Poor corrosion resistance and wetting; high drossing
Sn–8Zn–5In		Poor wetting; eutectic 52In–46Sn–2Zn (106°C) a concern
Sn–8.55Zn–0.45Al–0.5Ag–2Ga		

Note: MP = melting point.
Source: From Miric, A. Z. and Grusd, A., *Solder. Surf. M. Tech.*, 10(1), 19–25, 1998. With permission.

8.3.1 Porosity

Porosity of electrical contacts, defined as the degree of microscopic exposure of the metal to the environment, is considered as one of the major failure mechanisms in electrical connectors specifically for gold or precious metal electroplated surfaces. The characteristic feature of porosity is the presence of voids extending from substrate to surface. Porosity is not confined only to the initial state or as-prepared surfaces ("intrinsic porosity"),[103] but is also applied to inlays,[628] deformed, heat-treated, worn, or any other electroless prepared surfaces.[82,105,244,629–637]

Owing to its inherent resistance to corrosion and low electrical and contact resistance, gold plating has been more or less standard in the electronic contact field. It is also relatively easy to deposit in a pore-free condition on a variety of substrate metals practically impervious to the

build-up of insulation films in the presence of organic vapors (e.g., oil vapor) as do platinum group metals.

In view of the widespread use of gold electrodeposits in high-reliability electronic systems, there are a number of interrelated physical properties of gold electrodeposits that ultimately determine the useful life of contacts; these properties include appearance, co-deposited metallic impurities, metallic hardening agents, hardness, porosity, thickness, solderability, adhesion, resistivity, wearer resistance, and ductility applicability.

The porosity of a gold deposit is considered one of the most important characteristics in view of its ultimate effect on the long-term degradation of contacts. Ideally, a noble metal such as gold should be pore-free because any pores are potential sites for the generation of tarnish films or corrosion products on the underlying basis metal. With the trend toward miniaturized components and contacts, even minute quantities of tarnish films or corrosion products can cause contact failures.

The relationship between porosity and contact behavior originates in the chemical reactions between atmospheric corrodants and the base metal through the pores. All of the commonly used contact and underplate materials (including nickel, silver, and the copper alloys) are attacked by atmospheric pollutants, particularly those containing sulfur. The most common and pervasive corrodant in the majority of urban and industrial environments is sulfur dioxide, whereas hydrogen sulfide is often present in significant concentrations in the vicinity of many electronic installations.[103]

The widespread use of gold as plating material in electronic connections prompted extensive investigations of the effect of porosity on the reliability of gold-plated contacts. The deleterious effect of porosity has been thoroughly investigated by Antler,[82,103,629,630] Abbott,[631–634] and Zhang.[637] It was found that the porosity of electrodeposited gold was inversely related to its thickness (see Figure 4.4). This dependence was particularly sensitive for thicknesses below 1–2 μm.[629]

The porosity in gold plate was found to be dependent on substrate roughness and the condition of the substrate surface and underplates. Figure 8.2 illustrates some typical data on the effect of roughness on the porosity and percentage of satisfactory contacts (contact area). The increase in porosity with substrate surface roughness at constant plate thickness can be clearly seen.

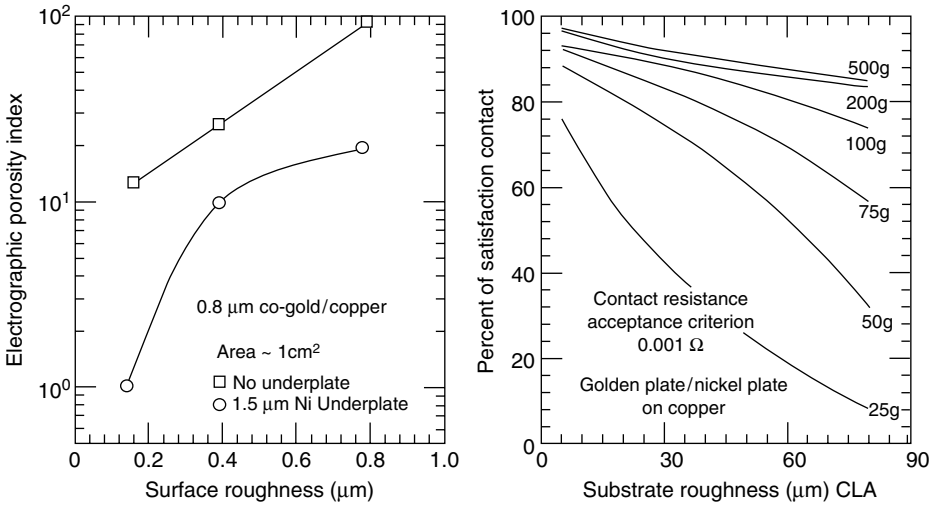

FIGURE 8.2 Effect of roughness on the porosity and the contact area of gold deposits. (Derived from Antler, M., *Electric Contacts-1969*, 111–118, 1969.)

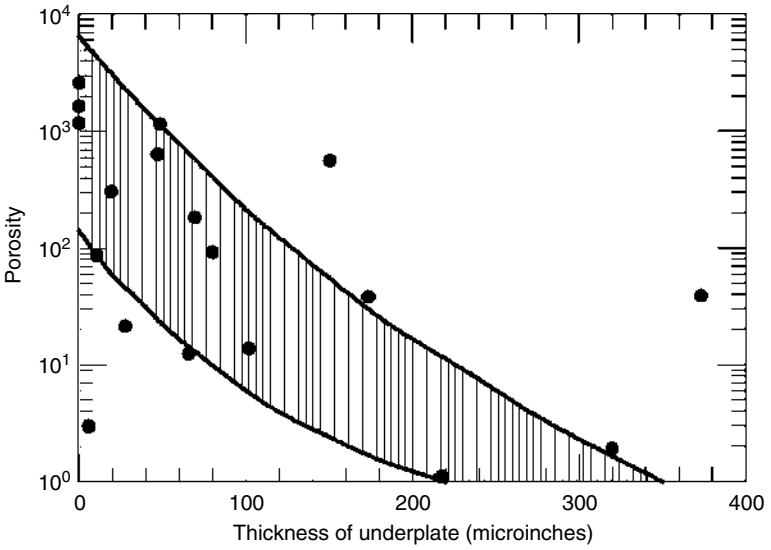

FIGURE 8.3 Effect of copper underplate thickness on the porosity of gold plate. (Derived from Antler, M., Garte, S. M., and Krumbein, S. J., *Electrical Contacts-1967*, 79–92, 1967.)

Reduction in gold thickness does not by itself explain the increase in porosity. The origin of most pores lies in the inability of the plate to deposit on specific spots on the substrate.[103]

The intrinsic porosity of gold plate can be reduced by some underplates. Figure 8.3 graphically illustrates the results for the soft gold; the hard gold responded in the same way. It is evident that increasing the thickness of the copper underplate increases the probability of bridging gaps in it, thus reducing the porosity of the gold plate. A combination of a nickel underplate and copper subplate also showed a marked reduction in the porosity of the gold plate compared to the system of gold directly on the copper substrate. Nickel underplate is often used with gold plate to keep the substrate elements from diffusing through the gold to the surface where they will produce insulating films.[103]

Another contributing factor to the porosity problem in gold plated contact is dust contamination. It has been shown experimentally that if the surface to be plated was not thoroughly cleaned, this would lead to the formation of pores during gold plating process. It appears that the pores created by dust contamination were formed even if the thickness of gold was increased to 2.5 μm.[637] Although it is generally accepted that increasing the surface roughness increases the contact area, the agglomeration of dust particles in the valleys between the surface asperities will interfere with the gold plating process and thus reduce the conducting contact area.

Practice has shown that although porosity is almost impossible to circumvent, there are various palliative measure that can be used to mitigate the deleterious effect of porosity. From the above discussion it appears that reducing the surface roughness by chemical or electrochemical polishing can significantly suppress the effect of roughness. Nevertheless, variations in the surface condition of the basis metal, the electrodeposit thickness, and the plating conditions usually result in the presence of some porosity. Hence, the amount of porosity that can be safely tolerated is usually determined by engineering judgment and whatever long-term test data may exist for the particular system in question.[631]

The importance of porosity on the reliability of electronic connections is now recognized and covered by the American Society for Testing and Materials (ASTM), which specifies the standard methods of test for porosity in gold coatings on metal substrates.[638]

8.3.2 Corrosion/Contamination

Practice has shown that contact degradation of electronic connections resulting from the reaction with chemical agents in the atmosphere is unlikely to occur. However, certain environments, specifically sulfur-bearing atmospheres, can be very detrimental to the reliability of electronic connections. Basically, there are three types of corrosion/contamination processes that can seriously impact the reliability of electronic contacts: pore corrosion, corrosion creep, and tarnishing.

8.3.2.1 Pore Corrosion

Pore corrosion is defined as chemical or electrochemical reactions between atmospheric corrodants and the base metal through pores and other breaks in the plating, and is probably most detrimental to the electric contact because it makes the coating and substrate susceptible to corrosion. The formation of insulating films and corrosion products leads to instability, accelerated wear, increased contact resistance, and ultimately to failure of a connection. Figure 8.4 illustrates schematically the mechanism of pore corrosion with battery analog.[635]

When porous gold plating on copper substrate is subjected to a humid SO_2-bearing atmosphere, gold—a thermodynamically more stable metal—is now in direct contact with less noble copper. As a result, a low conductivity electrolytic path between the two metals is created through the pores. This situation is schematically illustrated in Figure 8.4. In addition, because the cathodic portion (the porous gold plate) has a much larger area than the minute points at the bottoms of the pores, the corrosive attack of these anodic points is accelerated, leading to formation and growth of insulating corrosion products in the pores and their expulsion onto the gold surface.[635] As the exposure time increases, the films increase in thickness and spread over the surface. In severe cases, the plate is also undercut by corrosion, which could lead to its spalling from the contact. The corrosion products will appear at the surface in the form of large etch pits (stains) such as seen in Figure 8.5.[639]

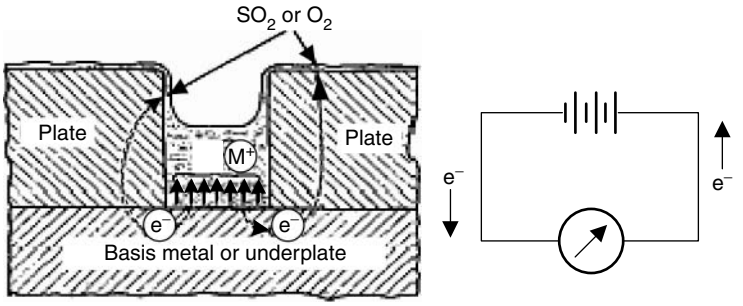

FIGURE 8.4 Schematic of pore corrosion mechanism and battery analog.

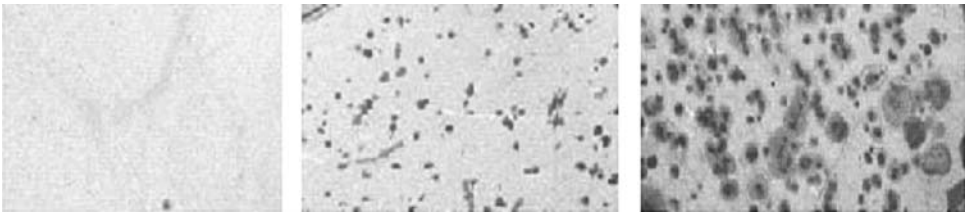

FIGURE 8.5 Pore corrosion stains formed on gold-plated surface. (From Malucci, R. D., Private communication. With permission.)

It is interesting to note that the primary controlling factors in constant-temperature corrosion through porous plates are the relative humidity of the environment and the porosity of the plate and not the quantity of the corrodants. Although the presence of some minimum quantity of SO_2, may be necessary, its actual concentration is of secondary importance in its effect on the properties of the exposed surface.[103]

In view of considerable interest to control the effects of corrosion on the performance of electronic connectors and to minimize the use of costly noble metals such as gold, palladium, and their alloys without sacrifice in reliability, various palliative methods have been proposed. These methods include barrier coatings such as polyphenylether microcrystalline wax (PPE-MCW) and microcrystalline wax with alkyl sarcosines or sarcosinates mixtures that restrict access of air to the contact. The use of post-plating protective coatings gives a thin residual surface film that does not degrade contact resistance, yet protects against many aggressive environments. Many of these coatings also are good contact lubricants. Other treatments that may have some value are based on chromates, benzotriazole and its derivatives, and mercaptans. It was found that gold finishes, even as thin as 0.1 μm, when treated with suitable coatings can approach the corrosion performance of much thicker platings.[629,635,640,641]

8.3.2.2 Creep Corrosion

Creep corrosion is defined as a process occurring when a reactive base metal, such as copper, is located adjacent to a noble plating or inlay such as gold. The process is manifested by an extensive creep of base material corrosion product over the gold surface. Because the gold is resistant to the formation of oxides and other films, it offers little resistance to the creep of some corrosion products such as sulfite- and sulfide-based films. These films spread over the gold surface in liquid form and become immobilized when they are slowly hydrolyzed and oxidized to insoluble sulfates.[64,642–644]

Creep corrosion rates of several different electroplates and inlay stripes coupled to the Cu–Ni–Sn alloy were investigated by Abbott and the results are shown in Figure 8.6.[642] It was found that gold was the material most susceptible to creep corrosion as manifested by the significantly higher

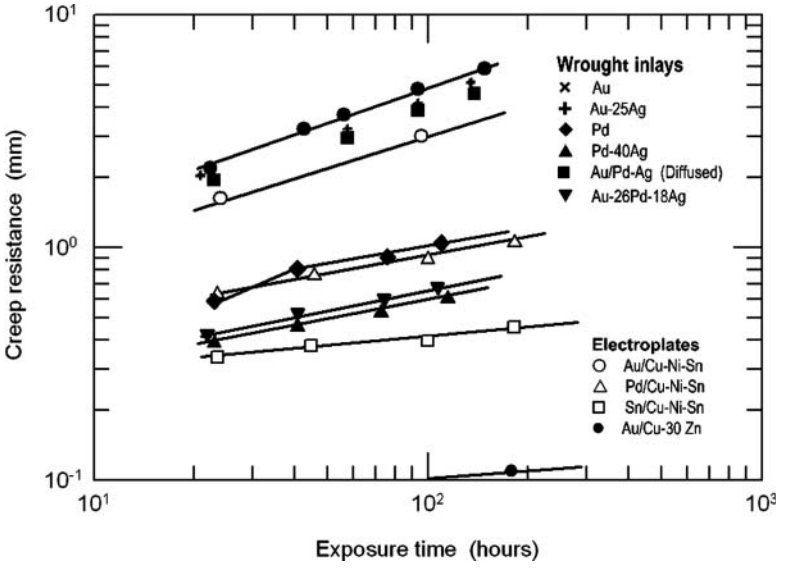

FIGURE 8.6 Effect of contact materials on creep corrosion in H_2S–NO_2–Cl_2 atmosphere. (From Abbott, W. H., *Electrical Contacts-1984*, 47–52, 1984.)

rate of creep for the 24 K gold inlay in comparison to the Au–0.1Co electroplate. It was suggested that such behavior is an indication of inhibition by a thin oxide film and/or residual surface contaminants on the electroplated surface. Comparative results for Pd and Sn surfaces show the strong materials dependency. Rates over palladium were reduced by a factor of about 3–1, whereas tin effected a reduction of about a factor of 10 compared to gold.[642]

The observed large differences among creep rates for the precious metal inlay surfaces were attributed to an inverse correlation between nobility and creep susceptibility. Despite the complexity of the observed differences among the contact material surfaces, all showed a significant degree of creep when coupled to the Cu–Ni–Sn alloy. Furthermore, it was also shown that the thicker the natural (oxide) film on the precious metal, the lower the creep corrosion rate. Considerably greater effects were produced by variations in the copper alloy chemistry, as exemplified by the data for brass in which creep was barely measurable. The ability of brass to inhibit creep was attributed to its relatively low susceptibility to Cu_2S formation that, in turn, is probably due to the stability of the zinc–oxide surface film even in the presence of chlorides.[642]

Although the differences among the contact finishes studied are large, they were overshadowed by the greater effects produced by changes in the base metal alloy. The observed differences among various copper alloys coupled to gold can be partially correlated with the tendency of these materials to form stable oxides films, the stability of these films in the presence of a reactive chloride, and the tendency of the base metals to form Cu_2S. Nickel corrosion products do not creep at significant rates across precious-metal surfaces. Although it is shown that thick nickel barriers can be effective for inhibiting the migration of copper corrosion products onto gold, this approach was only effective for a masked and plated surface configuration. A minimum width of approximately 125 μm would be required to effectively inhibit the creep corrosion process.[642]

8.3.2.3 Tarnishing

Tarnishing occurs as a result of diffusion of reactive sulfur species in the gas phase across a boundary layer to react at the surface of those metals that form sulfides preferentially over oxides. Although most metals have tendency to tarnish, copper and silver are especially susceptible to tarnishing due to their respective oxidative potentials. In the presence of even relatively low concentrations of hydrogen sulfide (H_2S) and under normal exposure times, silver and copper form the respective sulfide (Ag_2S and Cu_2S) preferentially over the respective oxide (Ag_2O and Cu_2O).

The formation of these sulfides renders a major drawback when utilizing these metals. The tarnishing rate of silver, copper, and their respective alloys is accelerated with increasing humidity, an increased concentration of sulfur compounds, the presence of ammonia in the environment, the volumetric flow rate around the specimen, and the temperature. The deleterious effects of tarnishing on the performance of electrical/electronic contacts has been extensively investigated by Abbott,[64,123,645,646] Antler,[647,648] and others.[51,649–655]

Figure 8.7 depicts the rate of tarnishing of silver (a) and copper (b) and their alloys with gold and palladium in sulfur-bearing environments.[64,645] From the data shown it can be inferred that in the case of silver the rate of tarnish kinetics appears to be a nearly a linear in all environments containing free sulfur with Ag_2S as a major reaction product. The linear rate of Ag_2S was interpreted in terms of gas phase diffusion as the rate controlling process.

In the case of copper, however, (Figure 8.7b), the tarnish process is highly dependent on the environment because the tarnish kinetics ranged from a linear to cubic (Figure 8.8a).[645] The low rates of film growth were attributed to a rate controlling mechanism of ionic transport of copper through Cu_2O and CuO films which formed during the early stages (<50 Å) of film growth. Diffusion through Cu_2S alone appeared to be sufficiently rapid to support a linear tarnish rate.

The tarnish kinetics of Ag–Au and Ag–Pd alloys was found to be characterized by a two-stage process: an initial linear rate equivalent to that of pure silver and transition corresponding to a lower (secondary) rate at minimum Ag_2S thickness (transition thickness). For alloys containing up to 50%

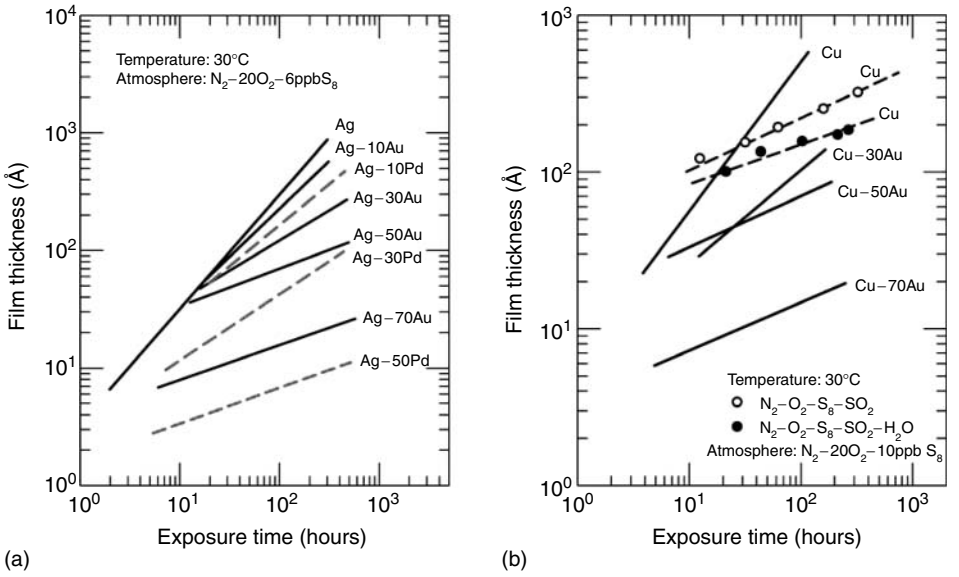

FIGURE 8.7 Tarnish rate of (a) silver, silver–gold, silver–palladium alloys and (b) copper and copper–gold alloys in sulfur bearing environments. (Derived from Abbott, W. H., *Electrical Contacts-1969*, 1–5, 1969.)

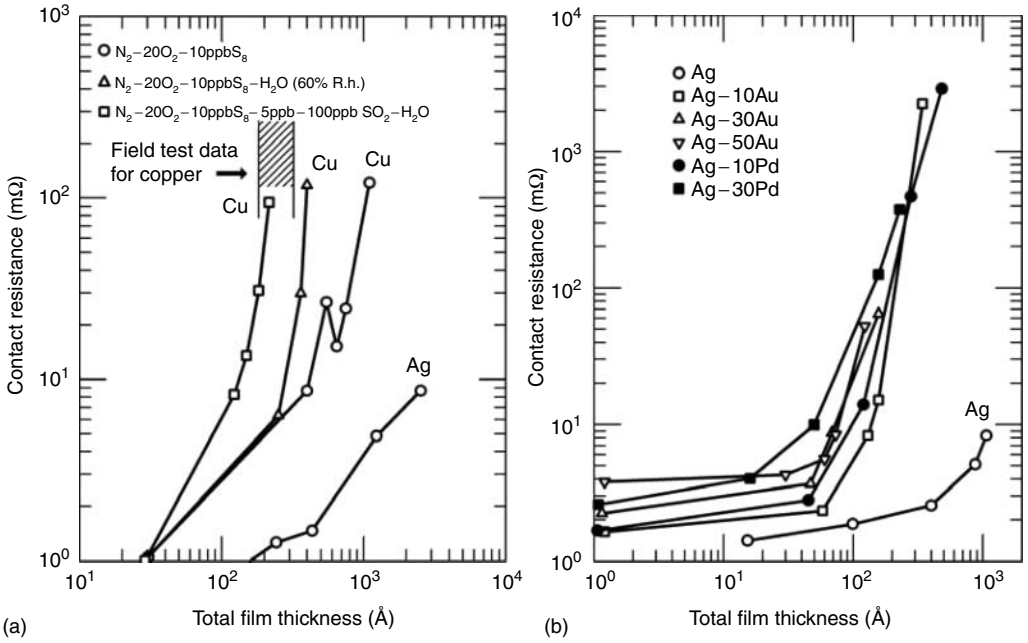

FIGURE 8.8 Effect of tarnishing on the contact resistance of (a) copper and silver in different environments and (b) silver and silver alloys. (Derived from Abbott, W. H., *Electrical Contacts-1970*, 21–25, 1970.)

of Ag the transition thickness increased with silver content. Although the sulfur concentration was found to affect the transition point, it had no effect on the secondary (cubic) rate of tarnishing.

From data shown in Figure 8.7 it is clear that palladium was much more effective than gold in inhibiting the tarnish of silver. Such an effect was associated with the lower transition thickness rather than lower secondary rates. For alloys containing higher concentration of Pd the transition thickness was exceedingly low (<5 Å), thus limiting the accurate determination of the tarnishing kinetics.

In an attempt to explain the transition from linear to cubic tarnish kinetics, as indicated by a distinct change in the rate controlling mechanism at low temperatures, Abbott[64] proposed that the observed change is a result of a transition from gas phase diffusion to solid state diffusion control. Accordingly, "short-circuit" diffusion via dislocations and/or grain boundaries was proposed as the most probable mechanism of transport of reactive species to the alloy-film interface.

The results shown in Figure 8.8b depict the contact resistance variation with the thickness of tarnished film formed on the surface of silver alloys. The most important characteristic feature of these results is a pronounced increase in the contact resistance beyond 100–200-Å thick films. Further increase in the tarnish film thickness increased even more the divergence between silver and the alloys.[645]

The high contact resistance shown by sulfide films on the alloys is attributed to differences in mechanical rather than electrical properties, that is, by facilitated film breakdown by microasperity plastic deformation of a soft substrate.[656] Although this may partially account for the increasing film resistance with decreasing silver content (increasing hardness), the observed contact resistance rise cannot be attributed entirely to substrate properties. Abbott[645] concluded that the use of materials based on either the Au–Ag or Pd–Ag system presents an obvious trade off among long-term kinetics, cost, and reliability. Because all compositions containing silver will tarnish to some degree, only binary alloys of Au–Ag containing less than 50% Ag and Pd–Ag containing less than 60% Ag could be expected to perform reliably for periods in excess of several years.

In a search for reliable Ag–Pd alloys with reduced Pd content, Harmsen[652] has shown that the contact properties of this system can be maintained by adding different metals such as In, Sn, Cu, and Ni. Similarly, Simmon et al.[653] have shown that the thickness of Ag_2S film decreases with increasing content of palladium. However, it was also shown that the concentration Pd has to reach the level of 15–20% to effectively limit the Ag_2S film formation.

It is interesting to note that Kassman et al.[654] have shown that despite high resistivity of corrosion films on silver (primarily Ag_2S) their presence is not always the cause of high contact resistance in high current applications. Initially the contact resistance was high (higher the thicker the corrosion film), but it rapidly falls and levels out on low values (for some parameters even lower than on noncorroded surfaces). These low values were attributed to the increase in conducting area partly generated by creep of the corrosion film as a result of the mechanical pressure, and possibly softening of the silver coating. An additional mechanism significantly affecting the contact performance was associated with the silver ion transport through the corrosion film. It was suggested that the Ag_2S corrosion film provided the electrolyte (in solid phase) required for transfer of silver ions from the silver-coated anode to the silver-coated cathode. Furthermore, it was also shown that the tarnishing films on silver contacts act as a lubricant, thus reducing tendency to contact welding.

As the ever-increasing demands are placed on the contact interface, determination of electronic connector performance in a variety of ever-increasing applications has become a critical task. As a result a number of testing methods have been developed aimed at reproducing in the laboratory the conditions approximating those to which the electronic connections are subjected to in the field.[105,657–662] A comprehensive review of the accelerated environmental testing designed to simulate the kinetics and degradation mechanisms of electronic connectors found in indoor environments was given by Abbott.[660] In the same review a new method, known as flowing mixed gas (FMG), was proposed. The method incorporates three-component mixtures based upon low levels of H_2S, NO_2, and Cl_2 that can be used to satisfy simulation of all reactive environmental classes.

Three tests of this type have been developed to achieve realistic simulation through the synergistic effects of (1) low concentrations of the relevant pollutants, (2) humidity, and (3) temperature. These studies have demonstrated the extreme importance of incorporating the sulfide–chloride synergisms into all of the environments to simulate the observed corrosion response. It has further been found that by adjusting these variables, large differences can be found in materials reaction rates, corrosion mechanisms, and chemistries. To be successful, the FMG method requires analysis of the environment actually existing in the test chamber and verification by reactivity monitoring. For the latter, copper and porous–gold electroplated coatings are useful and strongly recommended.

However, although the FMG procedures introduced a significant advance in the art of environmental aging by simulating realistic degradation mechanisms and chemistries for a wide range of materials, they must be used with some caution. These procedures are specifically designed to examine long-term corrosion from natural environmental influences and not, for example, influences such as infant mortality due to surface contamination, organic contamination, fretting, etc. Neither can they be considered as "quick look" corrosion tests applied to small sample sizes, particularly in component evaluation. Because the FMG procedures cannot be regarded as all-inclusive of all potential failure mechanisms, the interpretation of data from such tests must be accompanied by good engineering judgment.[660]

8.3.3 Fretting

As pointed out in Chapter 6, Section 6.4, fretting is now recognized as a serious factor in the degradation of electric/electronic connector systems. Because the parameters affecting fretting such as contact load, frequency, slip amplitude, etc., were discussed in detail in Chapter 6, Section 6.4, the aim of this section is to cover the salient features of this degradation mechanism in electronic connections and the advances made in our understanding of the fretting phenomenon. The problem of fretting damage in electronic connections has been extensively investigated by Antler,[454,456,475,664] Auckland,[665–667] Malucci,[553,668] Swingler,[669–671] and others.[672–674]

From a connector perspective, nonnoble materials such as copper- and lead-free-base materials, tin- and palladium–alloy plating systems, as well as nickel underplating, are especially susceptible to fretting corrosion. It is generally believed that due to its nobility, gold is not susceptible to deleterious effects of fretting. However, when fretting motion wears off gold plating, significant areas of nickel, underplate, or base metal are exposed to the detrimental effects of fretting. Depending on the thickness of the gold, its use on both mating surfaces can extend the time before the effects of fretting become perceptible. The practice has shown that the use of gold in "flash" plated contacts has significantly increased the incidence of fretting, thus seriously affecting the connection reliability.

In view of the primary role that gold electrodeposits play in determining the long-term reliability of low force, low voltage contacts, evaluation of the gold deposit becomes of considerable importance. Improperly plated gold can and does seriously compromise the satisfactory performance of electronic systems because the manufacturing, shipping, and storage environments to which these systems are exposed even before their useful life begins are seldom as benign as many of the usage environments.

Based on the results of extensive studies of electronic connections, Antler has concluded[456,663] that the contact resistance behavior during fretting between dissimilar metals is determined by the composition changes occurring at the interface due to metal transfer, wear, and film formation. In general, the direction of net metal movement is from soft to hard surfaces. Gold mated to a harder material, such as palladium, becomes all-gold and contact resistance tends to remain low. Gold alloys which are harder than palladium, such as 75Au25Cu, experience transfer of palladium, and the contact becomes all-palladium with consequent rise of contact resistance.

In case when gold is fretting against tin or tin–lead solder, contact resistance may degrade even more rapidly than tin–tin or solder–solder contacts due to a greater difficulty which asperities of these dissimilar metal systems have in fracturing oxide to reestablish clean metal contact. A thin layer of a contact metal may wear out due to fretting, especially in the absence of lubricant, and contact resistance changes to that characteristic of the underlying metal.

From a fretting point of view, the worst combination of the contacting materials is gold mating tin. Under fretting conditions, the softer tin will transfer into the contact area and cover the harder gold. The transferred material is a combination of tin oxide and debris, which is not easily displaced during the fretting process. As the fretting process continues, the transfer process continues, thus increasing the thickness of transferred coating and provoking significant surface degradation which, in turn, impacts the electrical stability of the contact system. This process is illustrated in Figure 8.9a.[663]

The durability of thin plating in sliding over long tracks is affected by the composite hardness of the system. Hence, it is advantageous to incorporate hard nickel plating ($\sim$450 kg/mm^2) between the gold deposit and a substrate that is considerably softer, such as copper (ca. 120 kg/mm^2). The same consideration applies to fretting wear as exemplified in Figure 8.9b showing improvement in contact resistance for 70Au30Ag versus 0.05 μm cobalt–gold plated copper by using a nickel underplate.[454]

When the underplate is not used, wear-out of the gold occurs quickly, and fretting corrosion ensues whereas with a nickel underplate, the contact resistance remains stable for about 100 times more fretting cycles because 70Au–30Ag does not transfer to nickel as readily as does solid gold.[454] Hence, following wear-out of the 0.05 μm cobalt–gold beyond 10^5 fretting cycles, nickel was probably responsible for the insulating materials at the interface which caused the contact resistance to rise.

It is interesting to note that from the susceptibility to fretting point of view the experimental evidence indicates that silver plated contacts are less susceptible to fretting than generally accepted and preferred gold platings. This is clearly illustrated in Figure 8.10a and Figure 8.10b, which depict the contact resistance behavior of solid palladium fretting against palladium and

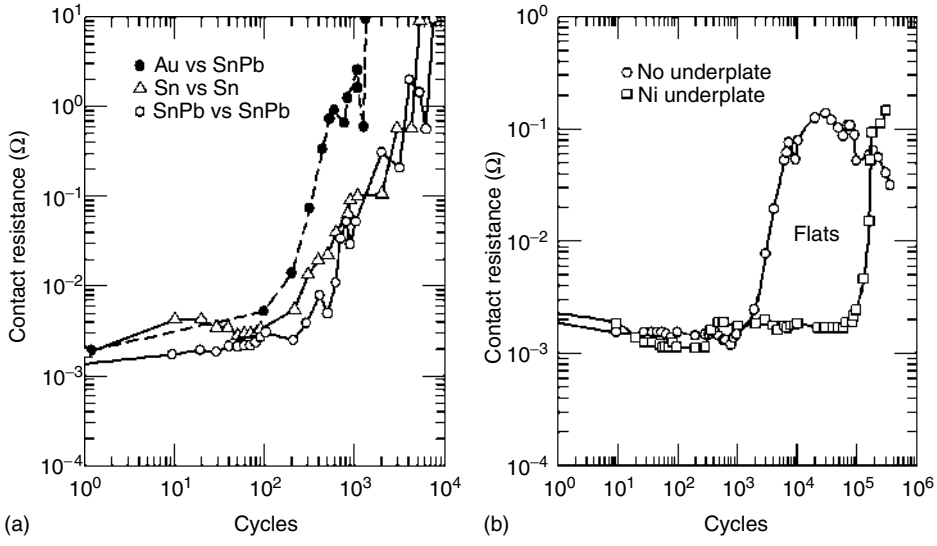

FIGURE 8.9 Contact resistance of (a) gold fretting against tin and solders and (b) solid 70Au–30Ag alloy fretting against 0.05 μm cobalt–gold-plated copper with and without 2.5 μm nickel underplate. Fretting conditions: 50 g load, slip amplitude 20 μm.

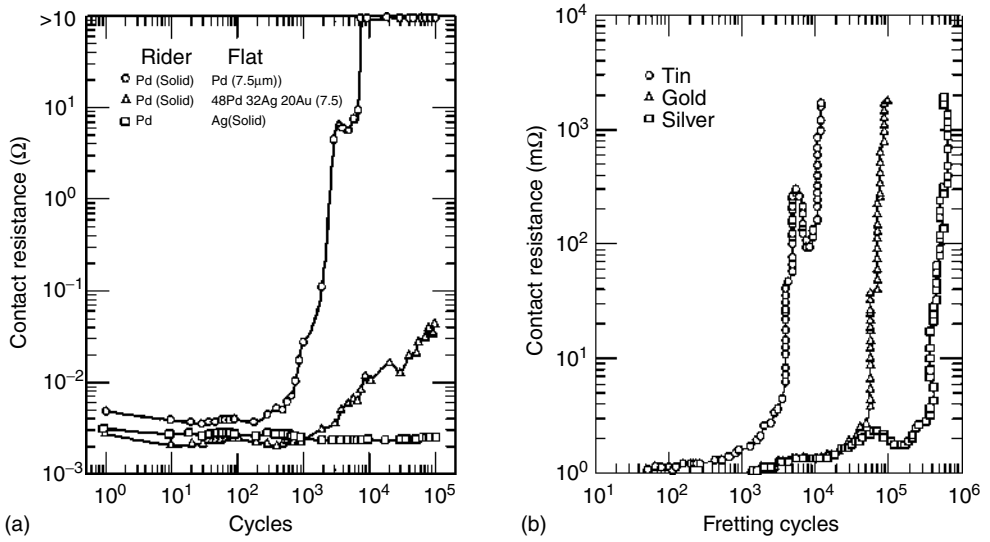

FIGURE 8.10 Contact resistance behavior of (a) solid palladium fretting against palladium- and PdAgAu-plating and solid silver and (b) tin-plated spherical pin (rider) fretting against tin-, gold-, and silver-plated flats. (From Antler, M., *IEEE Trans. CHMT*, 18, 87–104, 1985; Queffelec, J. L., Ben Jemaa, N., Travers, D., and Pethieu, G., *Proceedings of 15th ICEC*, Montreal, 225–231, 1990.)

42Pd32Ag20Au platings and solid silver,[663] and tin-, gold-, and silver-plated flat contacts fretting against tin-plated pins.[673] Unfortunately, silver is prone to tarnishing in atmospheres containing certain sulfur or chlorine compounds, which limits its application in electronic connectors. It has, however, been used successfully as a finish on aluminum busbar contacts.[583]

In recent years considerable attention was devoted to the lead-free materials as an alternative contact finish for electronic devices. As a result, numerous studies were conducted into the mechanical, electrical and thermal properties of these materials.[616,622–627,675–678] It is rather surprising, however, bearing in mind the susceptibility of tin and tin alloys to fretting and its deleterious effect on the integrity of electronic joints, that this problem has not been investigated thoroughly in the literature as extensively as creep, formation of intermetallics, and thermal fatigue.

The first publication dealing with the problem of fretting in lead-free alloy plated contacts was probably reported by Wu and Pecht.[679] The alloys investigated were SnAgCu and SnCu, and their behavior under fretting conditions was compared to that of Sn–Pb alloy. The tests were carried out at different temperatures and slip amplitudes using pin-on-flat configurations. Both pin and flat samples were prepared by hot dipping in a solder pot. The coating thickness for the flat was about 10 μm whereas for the tip of the hemispherical pin it was about 5 μm. The results shown in Figure 8.11 depict the effect of temperature and fretting slip amplitude on the mean time to failure defined as the number of fretting cycles needed for the contact resistance to increase to 100 mΩ.

From the results shown it can be inferred that fretting damage is greatly accelerated at higher temperatures different temperatures due to the accelerated oxidation of the metal at the contact interfaces. At room temperature, SnAgCu alloy coatings show better performance under fretting conditions than the Sn–Pb alloy coating. As temperature rises, however, the time to failure of the SnAgCu alloy coating becomes closer to that of the Sn–Pb alloy coating. At 80°C, both materials have very similar time to failure. On the other hand, the SnCu alloy showed very similar performance to the Sn–Pb alloy coating at all the temperatures tested.[679]

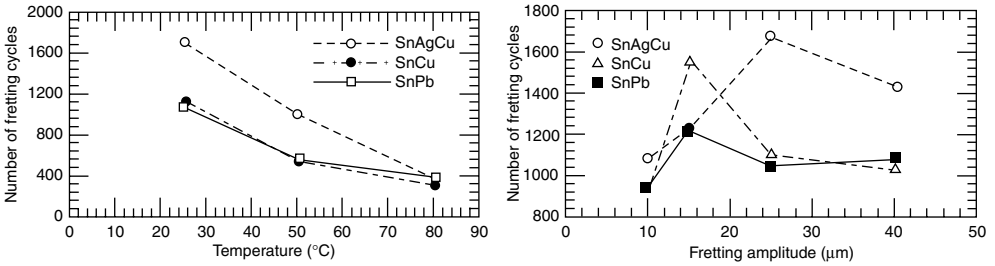

FIGURE 8.11 Effect of temperature and fretting slip amplitude on the mean time to failure of lead-free and tin–lead alloys. (From Wu, J. and Pecht, M., *Proceedings of 4th Electronics Packaging Tech. Conf.*, Singapore, 20–22, 2002.)

The results of the effect of slip amplitude showed that for the two lead-free alloys, the times to failure had better or as good resistance to fretting as the eutectic tin–lead alloy coating. The increase in contact resistance was attributed to the irregularity of the fretted contact interface and the accumulation of the metal oxides in the fretted region. Figure 8.12 shows the SEM image of the fretted contact zone and the energy dispersive x-ray (EDX) elemental line scans of oxygen, tin, silver, and copper across the fretted area. The presence of extensive oxygen content implies that the fretting debris is mainly composed of the metal oxides.

More recently, Gagnon and Braunović[680] investigated the effect of fretting on the performance of four commercially available lead-free solder alloys: Sn–Ag2.5–Cu.8–Sb.5, Sn–Ag3.8/4/Cu0.5/0.7, Sn99.3–Cu.7, and Sn42–Bi58. Table 8.1 shows some of the properties of the selected alloys. The alloys were obtained from a commercial manufacturer and came as spools of 12-AWG-gage wires. For the fretting tests, coatings were made on ETP grade copper flats (2.5×1.25 cm^2) cut from as-rolled sheets. Prior to coating, the copper coupons were cleaned with a commercial degreaser/

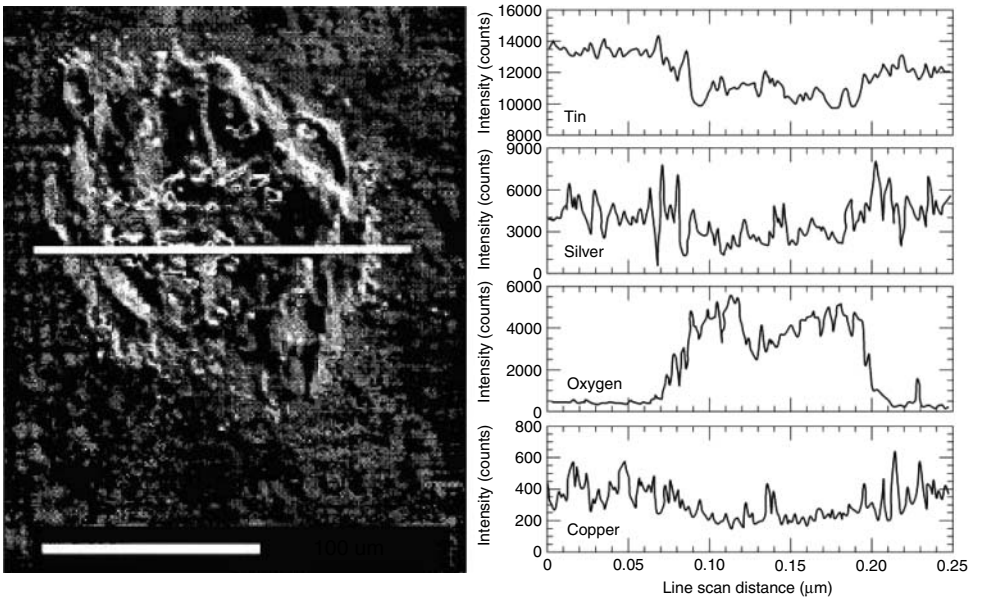

FIGURE 8.12 SEM image and EDX elemental line scan across the fretted contact zone of SnAgCu lead-free coating.

defluxer solvent, dried, and then dipped in RMA-2002 commercial liquid flux followed by dipping in the molten alloy bath for 30 sec and cooling down to room temperature. Because each alloy has a slightly different melting point, the molten bath and the coupons at a temperature were kept at 50°C above the alloy melting point as recommended by the manufacturers. The nominal thickness for the coatings on the copper flats varied from 50 to 60 μm.

The effect of fretting on the contact resistance was evaluated in a specially constructed fretting apparatus[572] comprising 10 independent stations, all of which have the same fretting motion amplitude. Each station uses a fixed rider on a movable flat specimen configuration, which permits variation in both the systems operating conditions and contact materials. A simplified schematic of the fretting assembly and data acquisition equipment is shown in Figure 8.13.

The U-shaped lead-free alloy wire rider was deadweight loaded against a movable lead-free alloy coated contact plate inserted in a holder on the moving stage. Bias springs at each end of the moving stage ensured the precise positioning of the samples. Displacement of the moving stage was measured using a high-precision DC LVDT (linear variable displacement transducer), sensitive enough to detect displacements of a fraction of a micrometer. Data acquisition and motion control was managed by a PC computer.

The fretting tests were carried out at frequency 0.5 Hz, constant slip amplitude of 100 μm and different loads. All tests were carried out on dry contact surfaces as no lubricant of any kind was used. The fretting motion was generated with a high precision linear motor-screw driven

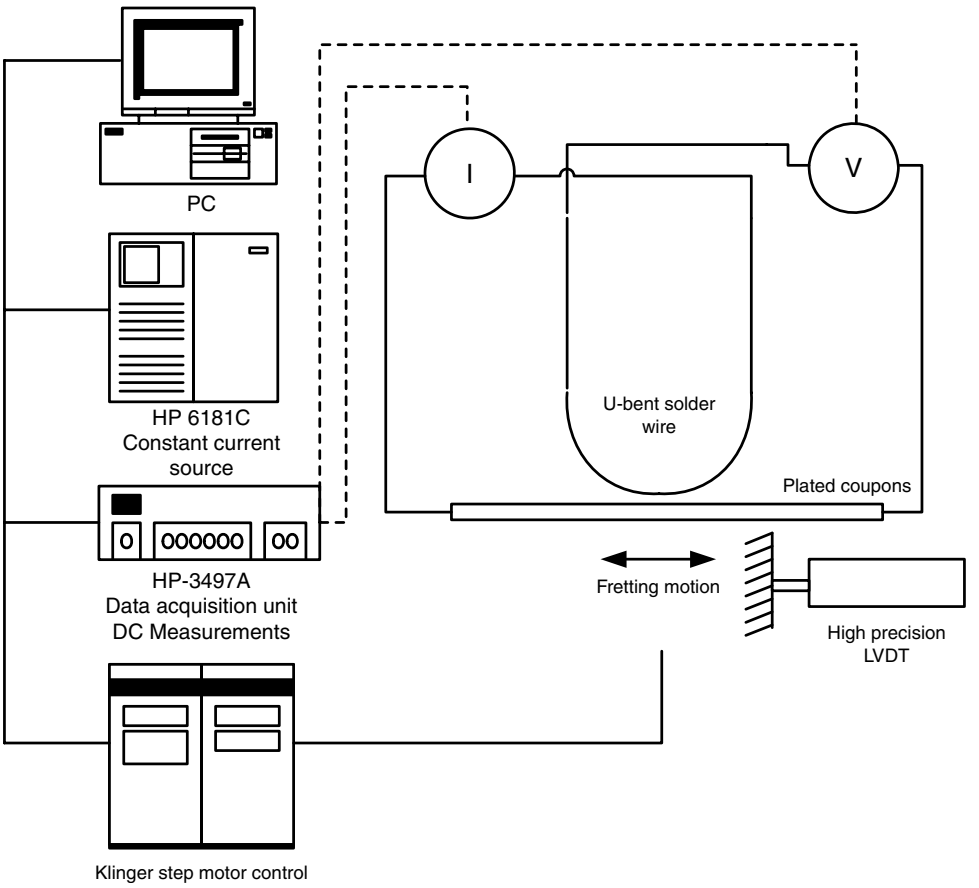

FIGURE 8.13 Schematic of experimental fretting assembly.

transmission and lever arm assembly. A continuous feedback loop was introduced into the displacement control system to maintain constant amplitude movement thorough the tests.

The contact resistance was derived from the contact voltages measured between the solder wires and the flat copper plated coupons using a cross-rod four-terminal technique which eliminated the bulk effect on the contact resistance. The open-circuit voltage was 10 V and a 50 mA DC current was applied and maintained through each contact from a constant current power supply. For each sample, a contact potential value is measured and recorded at 30-s intervals using a data logger whose output was transferred to a computer for data processing. The tests were carried out until the contact voltage reached an open circuit situation.

The recording of dynamic rather than static contact voltages was selected as representing a much closer approximation of the actual situation in the contact because the contact resistance has been shown to differ by orders of magnitude within one fretting cycle.[474,475] Typical contact resistance data for the lead-free alloys studied as function of fretting time are shown in Figure 8.14.[680]

The most important feature of these results is that the contact resistance of all wire-plate combinations is significantly affected by the fretting action. This is manifested by a rapid worsening of the contact resistance stability as the fretting progresses. For all wire-plate combinations, the contact resistance behavior seems to be characterized by three distinct stages. In the first stage, which represents 10^3 s or 500 cycles of fretting, the contact resistance is stable and practically fluctuation free.

In the second stage, apparently between 10^3 and 10^4 s of fretting, the contact resistance of all wire-plate combinations increases by 3–4 orders of magnitude but still in the mΩ to hundreds of mΩ range and relatively fluctuation free. In the third stage after 10^4 s of fretting the contact resistance increases sharply and is very unstable as characterized by large fluctuations 3–4 orders of magnitude and an open circuit situation. The contact resistance in this stage is the range of several hundreds of ohms. The open circuit situation was apparently dependent on the applied load, that is, as the contact load increase the threshold of the open circuit is delayed to the later stages of

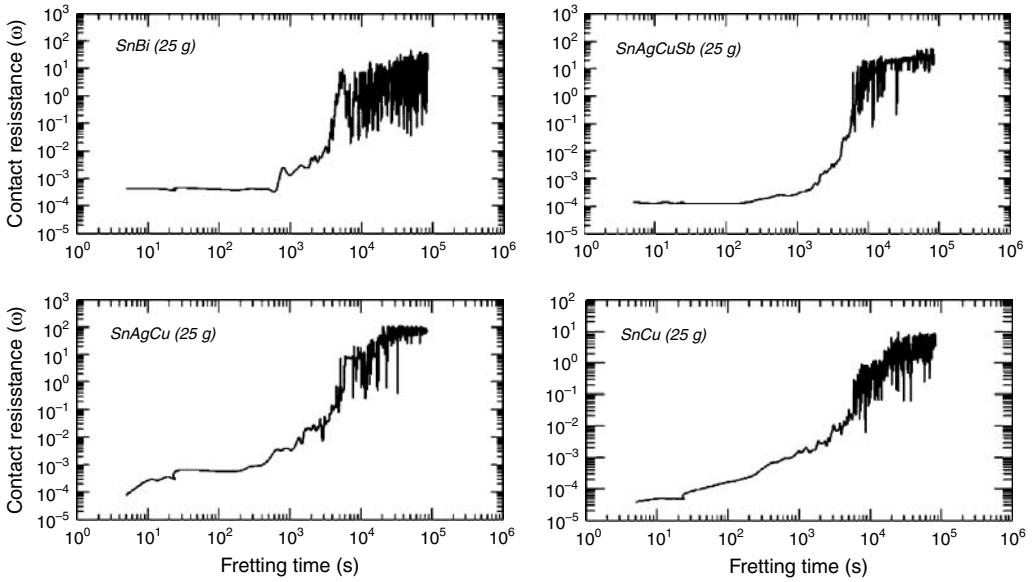

FIGURE 8.14 Contact resistance of lead-free alloy wire-plate combinations as a function fretting time at 100 μm slip amplitude and frequency of 0.5 Hz.

fretting. From the results shown in Figure 8.14 it would appear that SnAgCuSb solders show relatively the most stable contact resistance behavior.

Representative examples of the SEM examination of the fretting damage in contact zones of dry lead-free plated copper plates are shown in Figure 8.15. It is clear that fretting causes serious damage in these zones, typical damage being severe abrasion, delamination in the center, and accumulation of the wear debris at the edges of the wear track.

From the above discussions and detailed studies of fretting by Antler,[454,456,475,663,664] a variety of processes occurring during fretting can be summarized as follows:

1. When nonfilm-forming metals, such as gold, are fretting against themselves, they are particularly prone to transfer and back transfer of metal. Due to work hardening of transferred metal and generation of loose wear particles, the contact resistance remains relatively stable during fretting and may even fall as the contact area grows.
2. When then the same base metals such as tin–lead or lead-free solders are fretting against themselves, two characteristic processes may occur.

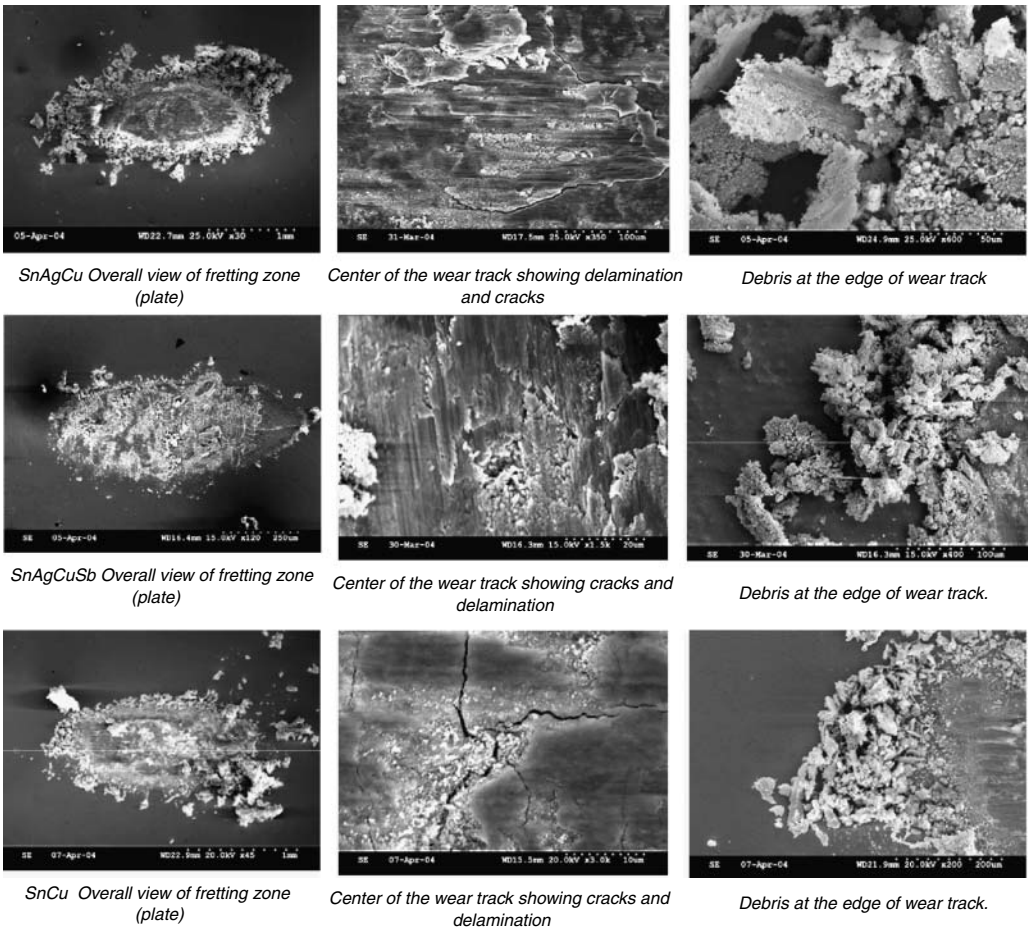

FIGURE 8.15 Representative SEM micrographs of the fretting damage produced in dry lead-free contact. Note the presence of cracks and delamination wear features in the center of the fretting zone.

   a. Metal transfer and back transfer between the surfaces with work-hardening and the generation of occasional particles that then oxidize
   b. Preliminary oxidation of the metal surface, followed by the removal of oxide to expose the original surface which then oxidizes in a repeating process
   In both situations the contact resistance rises (Figure 8.14) as a result of accumulation of loose oxides and facilitated build-up of fretting debris by the small amplitudes of movement (Figure 8.15)
3. When dissimilar metals are subjected to fretting whereby one is film-forming, two processes can occur:
   a. The nonfilm-former is significantly softer (e.g., gold versus palladium), which then results in the base surface becoming covered with the noble one, thus converting the system to (a).
   b. The film-former is softer (e.g., tin–lead solder versus gold) which, due to metal transfer, results in an all-base metal system like (b).
   The mechanics of oxide film fracture may be less favorable with dissimilar contact metals than when both surfaces are initially identical.
4. Contact material wear-out and transfer occur with contact resistance determined by the metal originally at the surface, such as gold-flashed palladium, followed by the appearance of underlying material with changing contact resistance.
5. Delamination wear is a process of metal removal which occurs after prolonged fretting in which thin layers are lost by the surface to become loose debris. Delamination originates as a result of crack nucleation below the surface due to dislocation pile-ups. Detailed descriptions of this process are given in Section 3.2 and Section 6.4.4. Delamination and adhesive transfer and wear are mutually exclusive, but delamination may follow adhesive wear when its rate becomes small.

8.3.4 Frictional Polymerization

The phenomenon of frictional polymer formation refers to the build-up of organic polymer deposits in and around the contact area as a result of exposure to relatively low levels of simple organic vapors under operating conditions The phenomenon was first reported by Hermance and Egan[45] who have shown that in the presence of even minute amounts of organic vapors the Pd, Pt, Ru, Rh, Au, and their alloys become susceptible to the formation of complex solid, insulating polymeric compounds at the sliding interfaces. The compounds are of high molecular weight and adhere to the surface. Although their accumulation inhibits the wear, it causes the contact resistance to increase, leading ultimately to contact failure.

An example of the contact zones following the friction polymerization effect on palladium–palladium contacts subjected to fretting motions is shown in Figure 8.16a. The debris consists of a mixture of palladium wear particles and frictional polymers. Figure 8.16b depicts the contact resistance changes with fretting cycles of palladium–palladium contact as a result of the formation of a frictional polymer in the contact zone. Although lightly loaded contacts, such as instrument slip rings which operate under light loads (2–10 gf) are particularly prone to this type of degradation, heavily loaded (50–300 gf) separable connector contacts can be even more unreliable when coated with catalytically active metals.[663]

In view of deleterious effect of frictional polymerization on the reliability of palladium-based contact materials, it is rather surprising that the mechanisms of frictional polymerization remained unknown and structural characterizations extremely limited. Nevertheless, several hypotheses were proposed to account for polymer formation such as an electron-induced polymerization resulting from the combined effects of catalysis and stimulated electron emission from the sliding metal surfaces,[261] the formation of organometallic polymers to account for the presence of metal in these

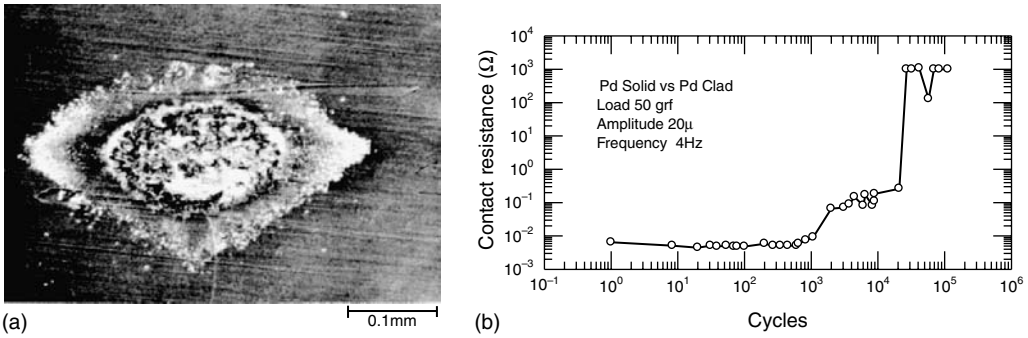

FIGURE 8.16 (a) SEM image of the contact zone following the fretting showing the presence of debris consisting of palladium wear particles and friction polymer; (b) effect of the formation of a frictional polymer on the contact resistance of palladium–palladium contact.

deposits,[681] and the existence of an induction period for the formation of frictional polymers.[56,682] Using the techniques of Fourier Transform IR Spectroscopy and Pyrolysis-K/MS, Reagor and Seibles[683] have shown that all polymers were extensively oxygenated, as evidenced by the presence of aryl and unsaturated ester linkages.

Despite considerable speculation, the hypothesis advanced by Hermance and Egan[45] is as plausible as any because it is in accord with most observations of the process and of the composition and physical properties of the polymeric materials.

It has been suggested that the conditions necessary for frictional polymerization to occur are as follows:

- The presence of polymer precursor adsorbed on the sliding surfaces that can be virtually any organic compound containing more than one carbon atom.
- The contact material must be a "catalytically active metal"; platinum group metals are particularly vulnerable.
- Although wipe was cited as an essential requirement to scrape the surface, thereby re-exposing active sites, Abbott[94] has shown that identical effects could be obtained on metal surfaces mated repeatedly with pure normal contact, i.e., without measurable wipe.

The experimental evidence indicates that deleterious effect of frictional polymerization can be mitigated, but not eliminated, by alloying and lubrication. Crossland and Murphy[684] have shown that addition of 36% and more of silver significantly reduced the effects of frictional polymerization because silver is not a catalytically active transition metal and does not form friction polymer.

Antler[46] has shown that lubricants are able to stabilize the contact resistance of metals susceptible to degradation by frictional polymerization. The effectiveness of lubricants is found to be strongly dependent on the thickness of the lubricant layer, as shown in Figure 8.17. Lubricant coatings were obtained by immersing and withdrawing the flat contact in solutions of the lubricants having different concentrations in a volatile solvent or by placing a drop of lubricant on the mated contacts. The stabilization of contact resistance was attributed to dispersal of friction polymer by excess unreacted lubricant. Hence, lubricants with frictional polymer-causing metals should have low volatility and migration tendencies to assure that they are always present on the contact surfaces. One of the common lubricants, polyphonylether, was found to produce coatings that are highly effective, particularly when they are thick.

Antler has concluded that although most laboratory work has been conducted with artificial atmospheres containing high levels of pollutants, virtually any real environment contains enough

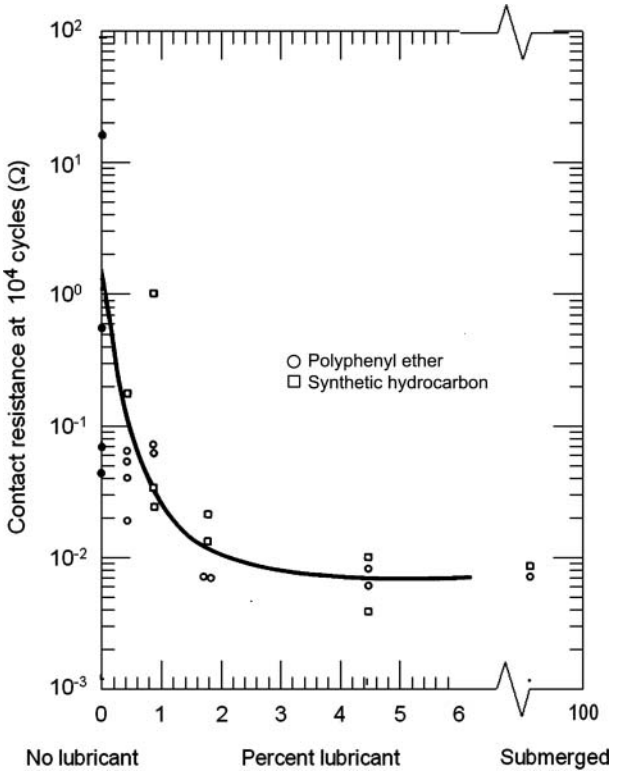

FIGURE 8.17 Contact resistance after 10^4 cycles of fretting of Pd–Pd contacts as a function of the amount of lubricant on the surface.

organic material for frictional polymers to form in sufficient quantity to cause electrical contact problems with palladium–palladium contacts at some conditions. Practically, all plastic materials used for electronic connections, printed wiring boards, etc., represent a major source of organic material contamination in the contact environment.

8.3.5 Intermetallic Compounds

The ever-increasing demands for improved performance and the growing complexity of the electronic devices and their microminiaturization have imposed severe service requirements on the constituent materials and focused the attention on the ability of electronic interconnections to provide structural and electrical integrity of electronic packages.

During the last 20 years or so, the relentless developments in electronics and demands on the materials involved such as the miniaturization requirements, faster switching, and emergence of surface mount technology, in which joints must provide a structural as well as electrical functionality, have imposed stringent requirements for reliability and longevity of the products, but have also revealed some universal problems.

Formation and growth of intermetallics is one of the most important problems in the search for reliable electronic and electrical connections. The use of different materials as connector finishes and a prolonged exposure to higher temperatures result in the continuous growth of a brittle intermetallic layer that is prone to facture leading to mechanical and electrical failure of a joint. The intermetallic compounds formed at the contacting interfaces continue to grow over time as a result of a solid-state reaction driven by energy differential. Due to the exothermic nature of the

formation, the intermetallic compounds that are formed have a lower energy content than the reacting metals by themselves.

Over the years, gold plating has been used almost exclusively as the normal contact finish in electronic connections. However, in recent years, the escalating price of gold forced the electronic industry to search for an economical alternative coating material. Tin was accepted as a suitable alternative because its cost is substantially lower than that of gold and within certain limits of operating conditions, its properties are comparable with gold. As a result, tin and its alloys are increasingly used as a replacement for gold plating on electrical connectors in low voltage–low current operations either as solders or as electroplated or hot-dipped coatings mainly on copper-base alloys for the purpose of retaining solderability of components and ensuring a low contact resistance in a vast variety of electronic connections, devices, and packages.

The widespread use of tin as a connector finish is mainly due to its intrinsic properties such as hardness, stability of thin oxide layer, and good corrosion resistance. When making a connection, the softness of tin oxide and wiping action allow displacement of its oxide layer. At the same time, however, this material is susceptible to adhesive wear, formation of debris and fretting which, in turn, affects the contact resistance and integrity of a joint. Furthermore, there is also a long-term reliability concern due to tendency of tin to form intermetallics with other materials generally used in these connections, such as copper and nickel. The intermetallics formed are brittle and may compromise the mechanical integrity of a joint thus leading to failure at low mechanical stresses, such as those applied during shipping, handling, or mild mechanical shock.

Intermetallic compound formation between tin or tin-based alloys and copper, nickel, and other elements has been studied extensively at low and high temperatures.[169,171,685–692] It is now well established that the growth of the intermetallic layer obeys Fick's Law relating the thickness of the intermetallic layers x to the time t and diffusion coefficient D as

$$\begin{aligned} x &= (Dt)^{1/2} \\ D &= D_0 \exp(-E_a/kT) \end{aligned} \tag{8.1}$$

where D_0 is a constant, E_a is the activation energy, k is the Boltzman constant, and T is the absolute temperature.

In the case of tin-plated copper systems, the interdiffusion between tin coating and a copper alloy substrate results in the formation of Cu_3Sn intermetallic compound at the copper/intermetallic interface and C_6Sn_5 at the tin/intermetallic interface. Figure 8.18a shows the SEM image of these phases formed at the interfaces of tin-coated copper while Figure 8.18b shows the elemental x-ray line scan of Sn across the tin coating.[690]

The results of numerous studies showed that the mechanical properties of copper–tin are strongly affected by the presence of the intermetallics when their thicknesses at the interface exceeds the critical value of 2 μm. At this thickness, the interface between the two metals in contact becomes brittle, thus making the interface highly porous and more susceptible to adverse environmental effects due to the generation of numerous fissures in the interdiffusion layer.[169,171,689–692]

The evolution of the intermetallic phases at the lead-free-copper interface is schematically illustrated in Figure 8.19a[693] whereas Figure 8.19b[694] depicts the SEM images of the cross section of the copper–tin interface at different stages of diffusion annealing. In addition to the embrittling effect of the interfacial intermetallic compounds, the formation of Kirkendall voids often leads to reduced mechanical strength of the solder joint at the interface. Kirkendall voids occur as a result of the difference in the diffusing rates of two or more elements in the joint. In other words, when diffusion rate of one element is higher than the others, vacancies are formed in the material with the higher diffusion rate. The end result is the accumulation of vacancies forming a line of voids and severely diminished mechanical stability (see Figure 8.19c).

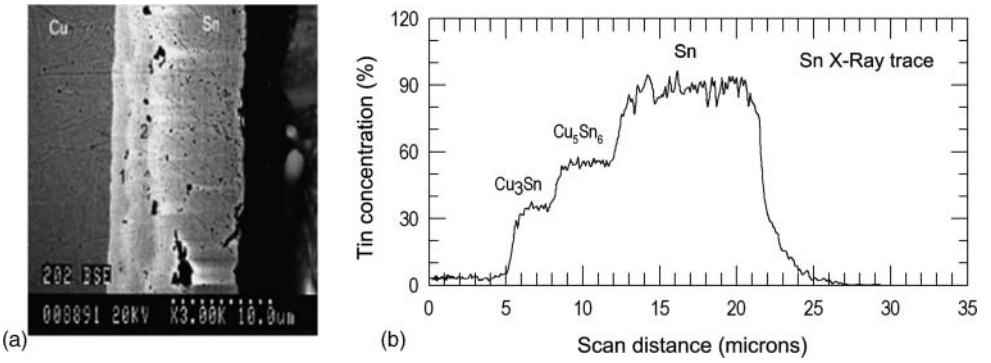

FIGURE 8.18 (a) SEM micrograph of the intermetallic phases formed at the copper–tin interface in tin-plated copper wires. Note the presence of two distinct phases: (1) Cu_3Sn and (2) Cu_6Sn_5; (b) tin x-ray scan across the copper–tin interface of tin-plated copper wires showing the phases Cu_3Sn and Cu_6Sn_5.

The formation of the intermetallic phases and their effects on the electrical properties (contact resistance and resistivity) of lead-free alloys was investigated by Braunović and Gagnon.[693] The alloys studied and some of their properties are listed in Table 8.3. For this purpose bimetallic couples were formed between commercially available lead-free alloys and copper busbars by hot-dipping were subjected to diffusion annealing using thermal gradients and heating by electrical current.

Diffusion annealing in thermal gradient was realized in an environmental chamber at 100 and 150°C. Diffusion annealing by an electrical current was realized by passing a DC current across coated bus-bars assembled in a cross-rod configuration. A calibrated shunt mounted in the

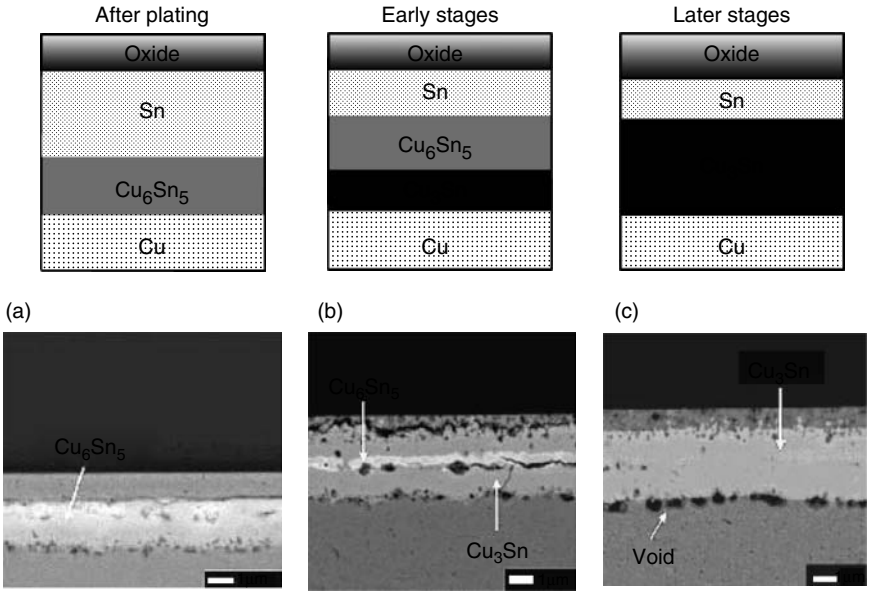

FIGURE 8.19 Schematic and the SEM images of the intermetallic phase formed at the lead-free-copper interface after plating and in the early and later stages of diffusion annealing. Note the cracking at the Cu_6Sn_5 and Cu_3Sn interface (B). (From Braunović, *Proceedings of 22nd ICEC*, Seattle, 267–273, 2004; Lee, S.-H., Roh, H.-R., Chen, Z. G., and Kim, Y.-H., *J. Electron Mater.*, 34, 1446–1451, 2005.)

TABLE 8.3
Selected Properties of the Lead-Free Alloys Used

Alloy	Melting Point (°C)	Microhardness HV (10 grf)	Electrical Resistivity (μΩ cm)
Sn–Ag2.5–Cu8–Sb0.5	217	17.6	13.8
Sn–Ag3.8/4–Cu0.5/0.7	217	15.2	12.4
Sn–Cu0.7	227	12.9	11.4
Sn48–Bi58	138	17.2	30

Source: From Lau, J. H., *Solder Joint Reliability: Theory and Applications*, McGraw-Hill, NY, USA, 1995. With permission.

circuit loop monitored the current level required to bring the joint temperature to pre-set values at 100 and 150°C.

Following diffusion annealing by electrical current and thermal gradient after 25 days, a four-point probe DMO 350 microohmmeter, with a precision of 0.01 μΩ, was used to measure the resistance changes developed between the plating and the copper base within the volume sampled by current penetration. The probe spacing was 1 mm. The microohmmeter operates on current pulses of 10 A and 17 ms duration.

The advantage of the four-probe resistance measuring technique lies in its ability to correctly measure the resistance of the sample without any interference from the contact resistance at the probe contacts. This is because no current flows through the inner pair of contacts, thus no voltage drop is generated at the probe contacts. The resistance changes in the selected zones were sufficiently large to be measured between the potential probe points. Simplified schematics of the setup used for the diffusion annealing by electrical current and that of four-probe resistance measurements are shown in Figure 8.20.

The results of four-point probe resistance measurements are shown in Figure 8.21. The resistance data were obtained by averaging the readings from ten different measurements made on the plated surfaces at random locations. For the reproducibility and accuracy of the four-point probe measurement technique, the resistance on nonplated sections of the busbars and some other

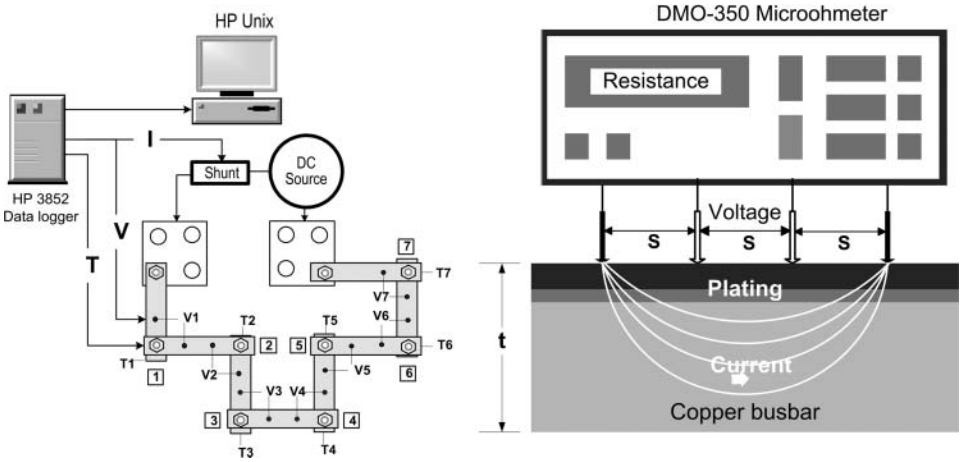

FIGURE 8.20 Schematics of the setup used for diffusion annealing by an electrical current (a) and four-probe resistance measurements assembly (b).

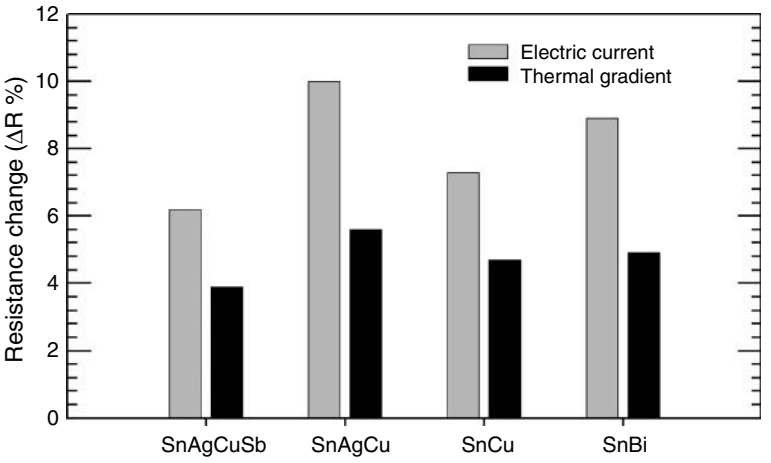

FIGURE 8.21 Resistance increments of samples diffusion annealed by electric current and thermal gradient.

materials such aluminum alloy 6061, nickel, and silver were measured and are listed in Table 8.4. The resistivity values for these materials derived from these measurements agree with the ones generally attributed to these types of materials.

The characteristic feature of the resistance data is that the formation of intermetallic phases under the influence of electric current and thermal gradient exerts an appreciable effect on the interface resistance. This is manifested by significant increase in the interface resistance. The diffusion annealed samples, plated with SnAgCu, showed the highest increase in the resistance while those plated with SnAgCuSb and SnCu showed the least. Another very important feature of these results is that the increase in resistance of samples subjected to diffusion annealing by electrical current is higher than that of diffusion annealed ones in the thermal gradient. It would appear that the structural changes produced by diffusion annealing with electrical current in the intermetallic phases formed at the copper-solder interface are more detrimental to the interface resistivity than those caused by thermal gradient.

To calculate the resistivity of the intermetallics formed at the lead-free-copper interface, a simple model can be invoked. Because the resistance measurement of the microohmmeter is based on the current penetration into the material,[577,695] a rectangular "conductor," such as that shown in Figure 8.22, can be envisaged as a volume of the material sampled by the microohmmeter probes.

The cross-sectional area $A = ab$ ($b = 1.5S$) of such a conductor can be derived from the resistance, R, measured on a copper sample using the known resistivity value for hard-drawn copper

TABLE 8.4
Reference Resistivity Measurements

Reference Materials	Cu ETP	Ni	Al-6061	Ag
Measured resistance (μΩ)	2.55	9.09	5.07	2.18
Calculated resistivity (μΩ cm)	1.97	7.0	3.9	1.68

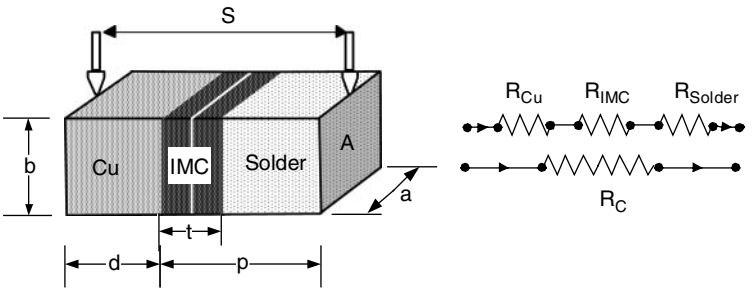

FIGURE 8.22 Schematic illustration of the "conductor" sampled by the microohmmeter probes.

$\rho_{Cu} = 1.80$ μΩ cm and the probe spacing $S = 0.1$ cm.

$$\begin{aligned} R &= (1/A)\rho_{Cu}S \\ A &= \rho_{Cu}S/R. \end{aligned} \tag{8.2}$$

The total resistance of the conductor sampled by the potential probes of the microohmmeter measured across the intermetallic layer is comprised of resistors in series and given as

$$\begin{aligned} R_c &= (1/A)\sum \rho_n x_n \\ \rho_{imc} &= (1/t)[R_c A - \rho_{Cu}(S-p) - \rho_{Solder}(p-t)] \end{aligned} \tag{8.3}$$

where t is the thickness of the intermetallic layers, A is the cross-sectional area of the conductor, and ρ_n and x_n are the resistivity and the thickness of each of the components. The SEM images of the copper-solder interface showed that the thickness of the intermetallic phases formed were within 4–6 μm, so the value of 5 μm was used in these calculations. Figure 8.23 exemplifies the typical morphology of the intermetallic phases formed at the interface between copper and solder plating. Phase 1 corresponds to Cu_3Sn while phase 2 corresponds to Cu_6Sn_5. The results of the calculations are shown in Table 8.5. The obtained values for the resistivities of the intermetallic phases formed under the influence of thermal gradient are within the values generally found in the literature for the Cu_3Sn and C_6Sn_5 phases. However, the resistivities of samples diffusion annealed by electrical current are significantly higher than those treated by temperature gradient. Therefore, if the assumptions used to make these calculations are correct, then the obtained results are very intriguing.

One possibility is that the observed difference is an indication of different stresses generated during diffusion annealing. It is now well established that as a result of rapid interstitial and grain

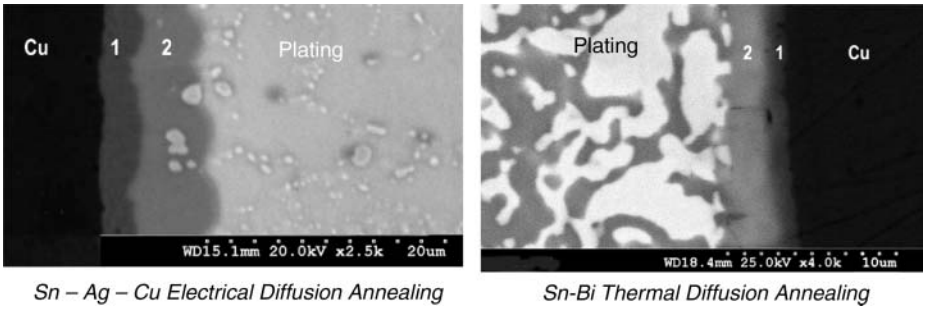

Sn – Ag – Cu Electrical Diffusion Annealing *Sn-Bi Thermal Diffusion Annealing*

FIGURE 8.23 Typical morphology of the intermetallic phases formed at the interface between copper and plating. Phase 1 corresponds to Cu_3Sn and phase 2 corresponds to Cu_6Sn_5.

TABLE 8.5
Calculated Resistivity Values for the Intermetallic Layers Formed at the Lead-Free-Copper Interface after Diffusion Annealing by Thermal Gradient and Electrical Current

	SnAgCuSb	SnAgCu	SnCu	SnBi
Plating thickness (μm)	50	40	50	60
Total intermetallic thickness (μm)	5	5	5	5
Initial solder resistivity (μΩ cm)	12.1	13.5	11.7	10.7
Resistivity of Cu–solder interface after diffusion annealing by thermal gradient ρ_{imc} (μΩ cm)	14.8	14.6	19.9	30.5
Resistivity of Cu–solder interface after diffusion annealing by electric current ρ_{imc} (μΩ cm)	24.1	22.3	27.7	47.5

boundary diffusion, significant mechanical stresses can be developed in the intermetallic layers that impair mechanical integrity of the layered contact interface.[169,696] Indeed, the microhardness of the phases formed is much harder than that of copper and lead-free plating and are very brittle.[697,698] Therefore, it would appear that under the influence of electrical current, higher mechanical stresses are generated, leading to crack formation at the intermetallic interfaces. Indeed, as seen in Figure 8.24, cracks were observed in the samples subjected to diffusion annealing by electrical current.

In addition, because an electric current was used to generate the intermetallic growth, it may be argued that the observed acceleration might be associated with the materials transported by electromigration.[499] In electromigration, the material transport occurs via interaction between the atoms of a conductor and a high density current of the order of 10^4–10^5 A/cm^2. However, electromigration is not expected under the low current densities or AC conditions. The AC current densities used in this work ($< 10^3$ A/cm^2) were lower than the levels used to generate the material transport. Therefore, electromigration alone is unlikely to be the operating mechanism responsible for the initial rapid increase in the contact resistance with intermetallic thickness.

It is clear that although a detailed mechanism responsible for the formation of intermetallic phases could not be clearly determined, the results presented are sufficiently consistent to conclude that electrical current exerts a pronounced effect on the morphology of the lead-free plated solid-phase joints, as clearly demonstrated in the case of Al–Cu bimetallic contacts.[165] Hence, in view of ever-increasing use of lead-free alloys in a variety of electronic applications, it is evident that the effect of electrical current has significant importance in the search for reliable electronic connections.

In the modern electronic packaging there are a large number of microelectronic assemblies. Among the variety of these assemblies, flip-chip and BGA solder interconnections are probably the

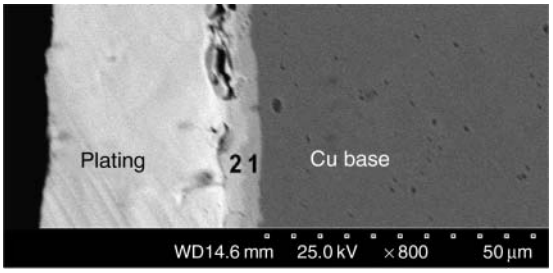

FIGURE 8.24 Cracks at the intermetallic boundaries in diffusion annealed SnCu by electrical current.

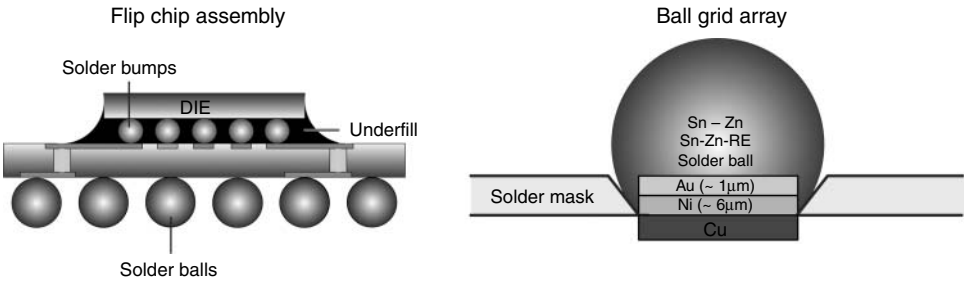

FIGURE 8.25 Flip-chip and Ball grid array (BGA) packaging interconnections.

most widely used technologies in the microelectronic packaging industry. Figure 8.25 illustrates schematically these configurations.

Flip chip interconnection assembly is the direct electrical connection of face-down electronic components onto substrates, circuit boards, or carriers, by means of conductive bumps on the chip bond pads. BGA is a surface mount chip package that uses a grid of solder balls to ensure both the electrical and mechanical connection between the bond pads on the package substrate to those on the board.

The balls serve several functions in these assemblies. Electrically, the balls provide the conductive path from chip to substrate and thermally by carrying the heat from the chip to substrate. In addition, the balls provide part of the mechanical mounting of the die to the substrate and as spacers, preventing electrical contact between the chip and substrate conductors, thus acting as a short lead to relieve mechanical strain between board and substrate.

In the electronic packaging, the intermetallic compounds (IMC) are formed as a result of interaction between solder and metallization. Owing to their attractive concoction of physical and mechanical properties, the IMC are extensively used in microelectronic packages. Because these joints provide mechanical and electrical contacts between the components, their reliability is essential in determining the performance of the microelectronic devices. Furthermore, due to the trend in modern electronics towards miniaturization, faster switching requirements, and emergence of surface mount technology (SMT), in which joints must play a structural as well as electrical role, the formation of intermetallic phase at the contact interfaces of electronic connections is of considerable importance to the reliability of the microelectronic packages.

The formation and growth kinetics of the IMC between solders (lead-free or lead-based) and Cu substrate is of considerable importance for the reliability of the solder joints.[342,699–704] During the soldering process, diffusion of the copper into the molten solder occurs, resulting in the formation of an IMC layer which is regarded as part of the chemical bonding mechanism controlling the solder joint strength. However, due to the brittle nature of the IMCs and the thermal mismatch between the solder and the printed circuit board (PCB), the presence of an excessively thick intermetallic layer may compromise the mechanical integrity of a joint leading to failure at unacceptably low mechanical stresses, such as those potentially applied during shipping, handling, or mild mechanical shock.

To suppress rapid formation of intermetallic phases in copper–tin systems, a nickel layer of 5–10 μm thick is used as a diffusion barrier between tin coating and copper base. Experience has shown, however, that intermetallic phases are also formed between nickel and tin.[699–703] The diffusion rate of nickel into tin is slower than that of copper resulting in the formation of thin nickel–tin (Ni_3Sn_4) intermetallic layer after a normal soldering process. Although the Ni–Sn intermetallic compound tends to be more brittle than Sn–Cu compounds, the fracture of the solder usually occurs within the solder in a region adjacent to the IMC layer.[700] Furthermore, because nickel tends to form a passivating layer that affects the solderability, coating 0.1–1.0 μm of gold,

silver or palladium are used to alleviate this problem. Some of these materials, however, can interact with solder by forming compounds and infiltrating into the solder joint.

The formation of Ni–Sn intermetallic compounds in lead–tin solder subjected to a long-term aging at 160°C is exemplified in Figure 8.26 showing the SEM images of the cross-sections of the interface between the copper substrate having an electrodeposited Au/Ni surface finish and the PbSn solder ball after 500 and 4000 h of aging at 160°C.[700] Note the presence of a continuous, dense layer of $(Au_{1-x}Ni_x)Sn_4$ after 500 h of aging and disappearance of Cu layer after 4000 h of aging.

The composition and physical and mechanical characteristics of intermetallic phases formed in the tin–copper and tin–nickel systems are shown in Table 8.6.[105]

Using the nanoindenation technique and the method developed by Pharr,[342] Jang et al.[704] have determined the nanohardness and elastic modulii of intermetallic phases C_6Sn_5, Cu_3Sn, and Ni_3Sn_4 in Sn–3.5Ag and Sn–37Pb solder joints. These joints were prepared by placing the Sn–3.5Ag and Sn–37Pb solder pastes on a Cu/Ti/Si substrate and Ni foil followed by annealing at 240°C. The thickness of intermetallic layers formed after annealing was 8 and 6 μm, respectively, for the intermetallic phases formed at the copper–solder nickel–solder interfaces. Thus the size of the intermetallic phases formed was sufficient to carry out the nanoindenation measurements. Typical load-depth profiles for the intermetallic phases formed are shown in Figure 8.27. Table 8.7 shows hardness and elastic modulus values for these intermetallics as determined by Jang et al. and other investigators.[691,705]

From the results shown in Table 8.5 it can be inferred that the magnitude of hardness measured by nanoindenation was in the order $Ni_3Sn_4 > Cu_6Sn_5 > Cu_3Sn$. The elastic modulus of Cu_6Sn_5, Cu_3Sn, and Ni_3Sn_4 IMCs in Sn–3.5Ag joints was 125, 136, and 143 GPa, respectively. The elastic modulus of the Cu_6Sn_5 intermetallic compound in the Sn–37Pb joint was similar to that for the bulk specimen but less than that in the Sn–3.5Ag joint. This might be attributed to the dissolved Ag atoms in the intermetallic compound that enhance the elastic modulus of the Cu_6Sn_5 in the Sn–3.5Ag/Cu joint.

The lower hardness and elastic modulus values as determined from the microindentation (Vickers) measurements can be interpreted in terms of the "indentation size effect" as proposed by Atkinson.[706] It was shown that the size effect in low-load indentation of a metal is due to changing proportions of perimeter deformation zone in relation to the broader indentation-accommodating strain field. The magnitude of the effect is governed by the indentation geometry, friction and the strain-hardening propensity of the indented metal.

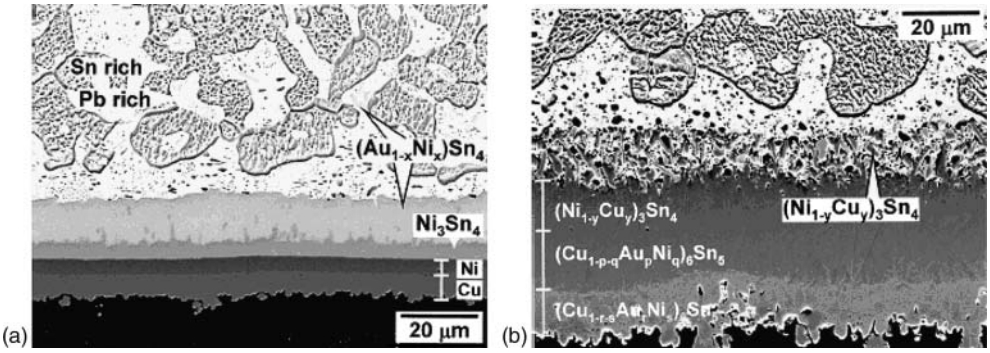

FIGURE 8.26 Formation of intermetallic phases between copper substrate and electrodeposited Au/Ni surface finish and the PbSn solder. (From Ho, C. E., Chen, W. T., and Kao, C. R., *J. Electron. Mater.*, 30, 379–385, 2001.)

TABLE 8.6
Room Temperature Properties of Intermetallic Compounds

	Cu_6Sn_5	Cu_3Sn	Ni_3Sn_4
Hardness VHN (kg/mm^2)	378.0	343.0	365.0
Toughness (MPa $m^{1/2}$)	1.4	1.7	1.2
Young modulus (GPa)	85.56	108.3	133.3
Poisson ratio	0.309	0.299	0.330
Thermal expansion (PPM/°C)	16.3	19.0	13.7
Thermal diffusivity (cm^2/s)	0.145	0.240	0.083
Heat capacity (J/g/°C)	0.286	0.326	0.272
Resistivity (μΩ cm)	17.5	8.93	28.5
Density (g/cm^3)	8.28	8.90	8.65
Thermal conductivity (W/cm° C)	0.341	0.704	0.169

Source: From Fields, R. J. and Low, S. R., NIST Publication, www.metallurgy.nist.gov

It is interesting to note that despite the fact that the intermetallic layer formed at the solder/metallized electronic component and solder/substrate interfaces are hard and brittle, the actual fracture in Sn–Ag-based solders occurs within the soldered region adjacent to the solder/substrate interface intermetallic layer as shown in Figure 8.28.[678] The only requirement for this to occur is that a sufficient amount of solder remains within the joint after the interface intermetallic layer forms and grows during thermal aging.

The formation of intermetallic compounds strongly affects the solderability of lead-free and lead-based components and substrates. As the intermetallic layer grows and consumes the fusible layer, it may penetrate the surface, thus exposing the intermetallic surface to a rapid oxidation that does not wet easily. The time needed for the intermetallic to overcome the surface finish is dependent on the thickness of the coating and the storage atmosphere.

"*Purple plague.*" Although the formation of intermetallic compounds is prevalent in the copper–tin, lead-based, and lead-free electronic systems, it also occurs in the interconnections

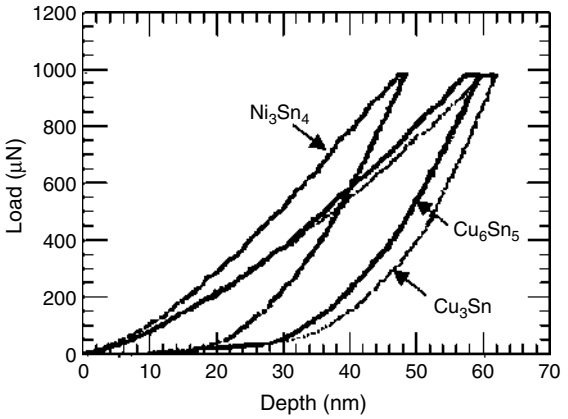

FIGURE 8.27 Load-depth curves for the Ni_3Sn_4 intermetallic compounds in the Sn–3.5Ag/Ni joint annealed for 24 h and also for Cu_6Sn_5, and Cu_3Sn intermetallic compounds in the Sn–3.5Ag/Cu joint annealed for 2 h. (From Jang, G.-Y., Lee, J.-W., and Du, J.-Q., *J. Electron. Mater.*, 33, 1103–1110, 2004.)

TABLE 8.7
Hardness and Elastic Modulus of Cu_6Sn_5, Cu_3Sn, and Ni_3Sn_4 Intermetallic Compounds

		Cu_6Sn_5		Cu_3Sn		Ni_3Sn_4	
	Method	***H* (GPa)**	***E* (GPa)**	***H* (GPa)**	***E* (GPa)**	***H* (GPa)**	***E* (GPa)**
Sn–3.5Ag joint annealed at 240°C	Nano	6.10	125.0	5.69	135.7	8.12	142.7
Sn–37Pb/Cu joint annealed at 240°C	Nano	5.62	116.3	—	—	8.9	138.0
Bulk specimen casting	Nano	6.27	114.9	5.72	121.7	—	—
Bulks specimens hot isostatic pressed[691]	Vickers	3.71	85.6	3.36	108.3	3.58	133.3
Solid state aging of diffusion couple[705]	Nano	6.50	119.0	6.2	143.0	—	—

Note: *H*, hardness; *E*, elastic modulus.

such as wire bonding for which aluminum and gold are extensively used. The term *purple plague* is associated with the purple color of the intermetallic compound $AuAl_2$ formed between aluminum pad and gold wire. It forms at high temperatures and can be prevented by bonding processes that avoid high temperatures such as ultrasonic welding, or by using aluminum-to-aluminum or gold-to-gold junctions instead of the aluminum-to-gold ones.

Deleterious effects of Au–Al intermetallics are manifested by the formation of Kirkendahl voids at the interfaces between the intermetallic zone and the Au side of the joint that will initially give rise to an increase in electrical resistance. Prolonged diffusion reaction between Al and Au results ultimately in electrical or physical failure of the joint. The intermetallic phases formed between Au and Al are neither electrically resistive nor mechanically weak. However, as a result of the reduced strength due to the formation of a Kirkendahl void zone at the interface between the intermetallics and the Au-rich side of the joint, the failure occurs.

The formation and effect of intermetallic compounds on the interface resistance of Al–Au wire-bond was investigated by Maiocco et al.[707] The tests were carried out using thermosonic gold ball bonds on aluminum metallization films. Isothermal annealing was performed at temperatures in the range 77–277°C for different times. After heat treatments at temperatures of 107°C or above, a peripheral ring of intermetallic was observed around the base of the bond as shown in Figure 8.29a. Coincident with the growth of this ring, depletion of aluminum around the base of

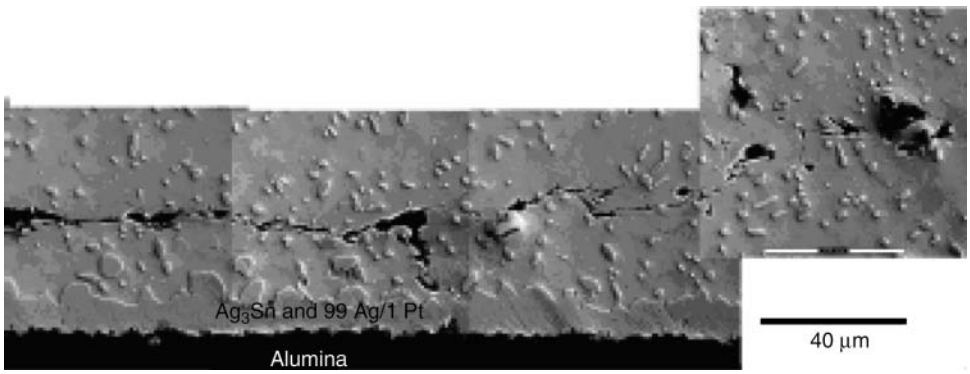

FIGURE 8.28 SEM micrograph showing fracture in solder region adjacent to the solder/substrate interfacial intermetallic layer. (From Subramanian, K. N. and Lee, J. G., *J. Mater.*, 55, 26–32, 2003.)

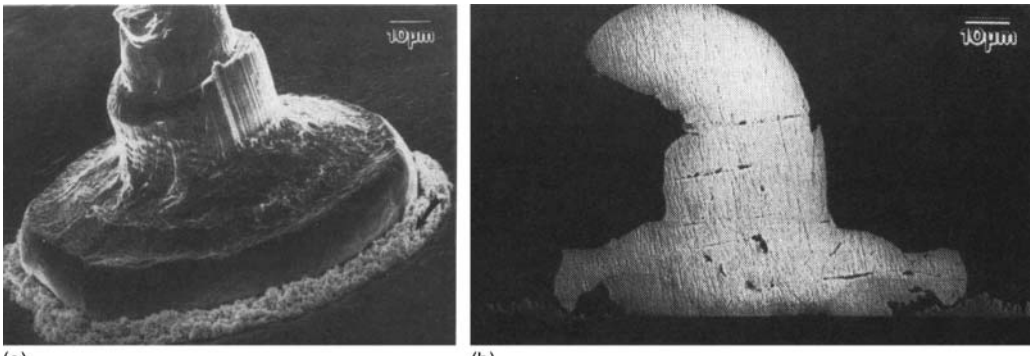

FIGURE 8.29 (a) SEM image of a ring of intermetallic compound formed at the edge of a bond. Pure Al metallization sample was annealed at 277°C for 24 h; (b) SEM image of a cross-sectioned bond showing the final stage of edge voiding. Pure Al metallization sample after annealing at 277°C for 500 h. (From Maiocco, L., Smyers, D., Munroe, R., and Baker, I., *IEEE Trans. CHMT*, 13, 592–599, 1999.)

the bond was observed, indicating that peripheral ring formation was assisted by aluminum diffusing to the bond from the surrounding film.

Depending on the heat treatment the voids of different sizes were observed. At the lowest annealing temperatures, 77 and 107°C, voids as large as 1.1 μm in diameter were observed at the Al/Au_2Al interface. Following initial void formation and growth, the voids decreased in size upon further annealing. At higher temperatures, Kirkendahl voiding was observed within the Au_4Al and at the Au_5A_2Au interface. At temperatures above 150°C, voiding was observed at the bond edge and progressed through distinctive stages. In the earlier stages, small voids (less than 0.2 μm in diameter) were observed to grow in from the bond edge and to coalesce into lines and large voids (2–8 μm in diameter) after a longer annealing time, causing complete separation of the bond from the surrounding intermetallic ring as seen in Figure 8.29b.

Microstructural examination of the bond appearance showed the presence of all five intermetallic phases as predicted by the equilibrium phase diagram with the more Al-rich intermetallic phases present at the outer bond edge and the Au-rich phases present in the central bond region. The most Au-rich intermetallic phases exhibited the highest resistivities, as given in Table 8.8. For all annealing performed at 77 and 107°C, and for short annealing times at 150°C, Au_2Al was the prevalent intermetallic phase formed in the pure A1 metallization samples. For the longest annealing times at 150°C (1000 h), only the most resistive intermetallics (Au_5A1_2 and Au_4A1) were observed. For the pure A1 samples above 150°C at all temperatures and times, the phases Au_5A1_2 and Au_4Al were predominant.

The results of the resistance measurements shown in Figure 8.30a indicated that in the temperature range 77–223°C the resistance increases linearly with time t following the empirical law of the form $\Delta R = c(t)^n$ with of $n = 0.4$. When the effect of temperature was taken into account, the

TABLE 8.8
Resistivities of the Intermetallic Phases Formed at the Au–Al Interface

	Al	$AuAl_2$	AuAl	Au_2Al	Au_5Al_2	Au_4Al	Au
Resistivity (μΩ cm)	3.2	7.9	12.4	13.1	25.5	37.5	2.3

Source: From Kashiwabara, M. and Hattori, S., *Rev. Elec. Comm. Lab.*, 17, 1001–1007, 1969.

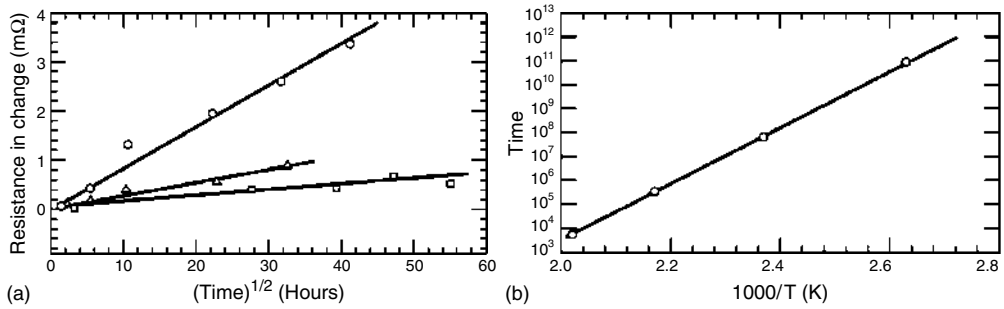

FIGURE 8.30 (a) Variation of interface resistance with square root of time; (b) Arrhenius plot of ln (t) as a function of $1/T$ in the temperature range 77–223°C.

empirical relationship up to 8 mΩ for the ΔR followed the expression

$$\Delta R = C \exp(-E_a/kT)t^n \tag{8.4}$$

where ΔR is the resistance increase ΔR in respect to the nonannealed samples, C is a constant, E_a is the activation energy and k is the Boltzman constant. The resistance increase of less than 8 mΩ was attributed to the growth of intermetallic ring around the bond and depletion of aluminum metallization around the peripheral ring. The activation energy was determined from the ln t as a function of $1/T$, where t is the time required at each temperature to reach $\Delta R = 4$ mΩ. The results shown in Figure 8.30b indicated that the activation energy $E_a = 0.40$ eV (9.22 kcal/mol) with $C = 10\ \Omega/h^t$.

The calculated value of the activation energy of 0.40 eV/atom (9.22 kcal/mol) is significantly lower in comparison with the activation energy of intermetallic growth in gold–aluminum couples as reported in the literature.[709] Nevertheless, Chen[710] has also reported low activation energy for diffusion in gold–aluminum wire-pad configuration, i.e., 12.8 kcal/mol (0.55 eV/atom).

The apparently low activation energy can be attributed to the combined effect of volume (vacancy), grain boundary and surface diffusion. Indeed, it has been shown that accelerated diffusion can occur via some short-circuit diffusing paths rather than through the lattice. Such short diffusion paths, called *pipe diffusion*, can be dislocations, grain and subgrain boundaries. Diffusion along these paths is found to be considerably faster (several orders of magnitude) than diffusion of the same species through the lattice.[495]

In summing up, it can be stated that despite significant advancements in the contact physics and plating metallurgy made so far by contemporary design of electronic connectors, the exact nature of the process involved in the formation and growth of intermetallic interface layers in microelectronic packages is still elusive and needs further elucidation of the diffusion mechanisms involved. Undoubtedly, a clear understanding of these processes in electronic connections will enable one to control their influence on joint properties and the reliability of an electronic package as a whole.

8.3.6 Creep and Stress Relaxation

As in the case of power connections, creep and stress relaxation play very important roles in electronic connections, particularly in modern electronic packages because of the continuing miniaturization of electronic components which, in turn, places ever-increasing demands upon soldered joints to provide reliable structural integrity. As a result of the reduced joint dimensions and the requirements for more arduous service performance, the individual components of the joint

are subjected to higher stress and strain levels. The most frequent failures during the operation of electronic connections occur in soldered joints as a result of thermal cycling, which causes thermo-mechanical fatigue, flexural bending, and impact loading (shocks).

The soldered joints comprise the materials with very different coefficients of thermal expansion. Hence, temperature variations, resulting from the power switching or the external environment, generate fluctuating thermal strains within the joint that lead to the initiation and growth of a crack and ultimately failure of a joint. Furthermore, the service cycles are rarely uniform and continuous but rather, comprise temperature excursions interspersed between hold or dwell periods of fairly constant temperature. Damage may thus arise from two sources as a result of thermal cycling or stress relaxation during the hold period.

The rate at which the damage accumulates in solder joints during operation is determined by their microstructural properties and variables such as time, stress, and temperature. Consequently, to understand, predict and even control the reliability of solder joints, it is essential to characterize deformation behavior of solder joints and identify the degradation mechanisms.

Under normal operating conditions, solder joints in microelectronic packages operate at temperatures in the range between 25 and 100°C, which corresponds to a high homologous temperature (0.6–0.8T_m, where T_m is the melting point). In this temperature range, the solder is subjected to thermal cycling and also stress relaxation during dwell periods at the temperatures extremes. Therefore, determination of the reliability characteristics of solder joints and evaluation, modeling and prediction of the joint lifetime require the knowledge and understanding of the creep or stress relaxation properties of solders.

Although the mechanical properties and fatigue behavior of lead-free and lead-based solders have been extensively studied,[711–716] the existing data are still limited and serve largely to reveal the complexity of the processes involved and wide scattering of the experimental results. There are many causes for such discrepancies in the results such as the variability of the solder microstructures, the difference in testing procedures used ranging from ball shear and large bulk material tensile tests to highly sophisticated bending tests as well as the specimen sizes varying from centimeters to the dimension of a solder joint of a single BGA. Furthermore, in many cases the available data are incomplete, contradictory, or of questionable relevance to electrical/electronic assemblies. Nevertheless, despite these shortcomings, the available data, albeit inconsistent, can still provide an insight into the complex nature of the processes involved. Hence, in this section only the most characteristic creep-related data for the lead-free solder alloys will be reviewed. Detailed accounts of the creep and stress relaxation behavior can be found elsewhere.[711,712]

The most indicative characteristic of creep is variation of strain with time that is generally divided into primary, steady-state, and tertiary stages and encountered sequentially. The rate of steady-state creep is not only reproducible to be used in a constitutive equation, but it is also the most pertinent to solder fatigue because it dominates cyclic deformation during creep fatigue.[715] The Dorn power-law constitutive equation is most commonly used to describe the steady-state creep rate

$$E = A(1/d)^p \exp(-Q/RT)\sigma^n \tag{8.5}$$

where A is a pre-exponent factor, p is the grain size exponent, Q is the activation energy, and n is the stress exponent. The values of p, Q, and n change with the materials and the creep mechanisms while the pre-exponential factor A changes with the microstructure.

Because solder joints are used at high homologous temperatures (up to $T/T_m = 0.9$) and stresses σ ($10^{-5} < \sigma/E < 10^{-4}$, where E is Young's modulus) dislocation creep is frequently invoked as the dominant mechanism of the deformation kinetics. However, Igoshev and Kleiman[714] have argued that a scatter in experimental data could not be explained by the dislocation creep mechanism only,

even if the data was corrected for Young's modulus temperature dependence. An analysis of the data implied that possible origin of such a scatter was nucleation, accumulation and further growth of such internal defects as pores and microcracks during creep. It was shown that these processes may affect the measured steady-state creep rates, and may be one of the major reasons for the observed scatter in experimental data.

Igoshev and Kleiman proposed that at homologous temperatures higher than about $0.4T_m$, grain boundaries represent a system of glide planes which generally becomes active simultaneously with crystallographic glide systems within the grains. Thus, under the action of applied stress, grain boundary sliding takes place and this naturally would contribute to the plastic strain. The grain boundary sliding causes extreme heterogeneity of plastic deformation at temperatures where it takes place because it can lead to reduction in the polycrystal compatibility by formation of voids at grain boundaries if the grain boundary sliding is not accommodated by bulk deformation inside the grains either due to dislocation glide or by stress directed diffusion of vacancies, i.e., due to diffusion creep.

When the polycrystal integrity is affected, the nucleation, and especially, the growth of grain boundary voids as cavities or cracks naturally contribute to the measured strain. Under certain external conditions, this contribution can be quite significant or even dominant. The nucleation and growth of intergranular cavities finally leads to intergranular fracture typical of creep, though in some cases transgranular creep fracture is observed not differing significantly from ductile fracture at low homologous temperatures.

Indeed, Homa[716] has shown that severe intergranular cracking and cavitation occurred in solder joints as a result of mismatch of thermal expansion coefficients between the solder and the substrate. The stresses generated during a thermal excursion from room temperature to 100°C were reduced by grain boundary sliding. Subsequent repeated cycling resulted in the formation of voids that eventually grew into large cracks as seen in Figure 8.31.

Based on the experimental data available in the literature, Igoshev and Kleiman proposed that the overall plastic strain generally consists of several components

$$\varepsilon = \varepsilon_{dg} + \varepsilon_n + \varepsilon_{gb} + \varepsilon_d + \varepsilon_v \tag{8.6}$$

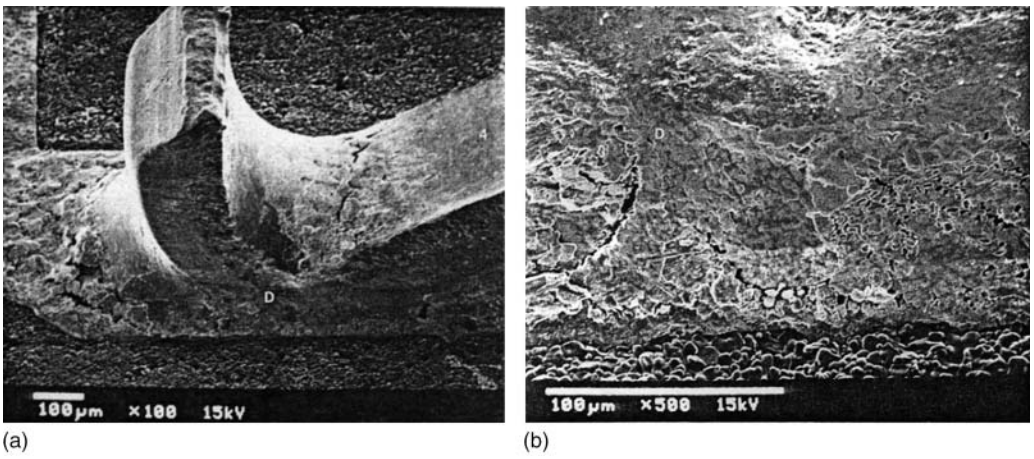

FIGURE 8.31 (a) SEM micrographs of the damage caused by grain boundary sliding in electronic packaging due to creep-fatigue and (b) a close-up of the damaged zone D. Note the presence of extensive damage characterized by cracks at grain boundaries and voids. (From Homa, T. R., *Electronic Packaging and Corrosion in Microelectronics*, ASM International, 209–215, 1987. With permission.)

where and ε_{dg}, ε_n, ε_{gb}, ε_d, and ε_v are the strains caused by dislocation glide, nonconservative motion of dislocations, grain boundary sliding, stress directed diffusion of vacancies and by intercrystalline void nucleation, and growth, respectively. It is clear that not all of the above operating processes are independent of each other, as frequently assumed.

When the steady-state stage on the creep curve is well developed and is considerably longer then the transient and the tertiary stages, as depicted in Figure 8.32a, one of the processes mentioned above (dislocation or diffusive creep in particular) may be considered as a lifetime-controlling process. Otherwise, processes relevant to the tertiary stage may affect the data obtained for the steady-state stage. It may be quite difficult to identify the secondary creep stage as illustrated in Figure 8.32b and c.[717,718] The behavior of the curve in Figure 8.32c is typical for a delayed fracture, during initiation and growth of a subcritical crack.[714]

Igoshev and Kleiman concluded that the large scatter in activation energy values as reported in the literature cannot be rationalized in terms of existing theories. Fracture processes and the associated nucleation, accumulation, and propagation of pores and/or microcracks may play a significant role during creep deformation of lead-free solder joints at appropriate testing conditions and in "real life," and therefore will affect the creep rates. The values of activation energy should contain corrections for the true temperature dependence of creep because, in most published works, this temperature dependence has not been taken into account; this has mostly likely led to the observed scatter in experimental results.

Huang et al.[715] arrived at the same conclusion while investigating the microstructure–creep property relationship of three precipitation strengthened tin-based lead-free solder alloys Sn–0.7Cu, Sn–3.5Ag and Sn–3.8Ag–0.7Cu. The creep behavior of these alloys was compared with that of Sn–37Pb alloy that was used the reference. The microstructure of the three as-solidified Pb-free solder alloys consists of the β–Sn matrix and IMCs. The IMC phase dispersed regions are separated by regions of dendritic β–Sn, giving the microstructure a network-like appearance, as shown in Figure 8.33.

Huang et al.[715] have also shown that, generally, the three Pb-free solder alloys and Sn–37Pb, exhibited typical creep curves with stages of primary, steady-state, and tertiary creep. The data shown in Figure 8.34 exemplifies the typical creep curves of Sn–0.7Cu, Sn–3.5Ag, and Sn–3.8Ag–0.7Cu solder alloys under 17.5 MPa and at 348 K and the steady-state creep rates of these alloys at different temperatures.

From the results presented it Huang et al. concluded that the precipitation-strengthened Sn-based Pb-free solder alloys studied had that the steady-state creep rates in bulk samples

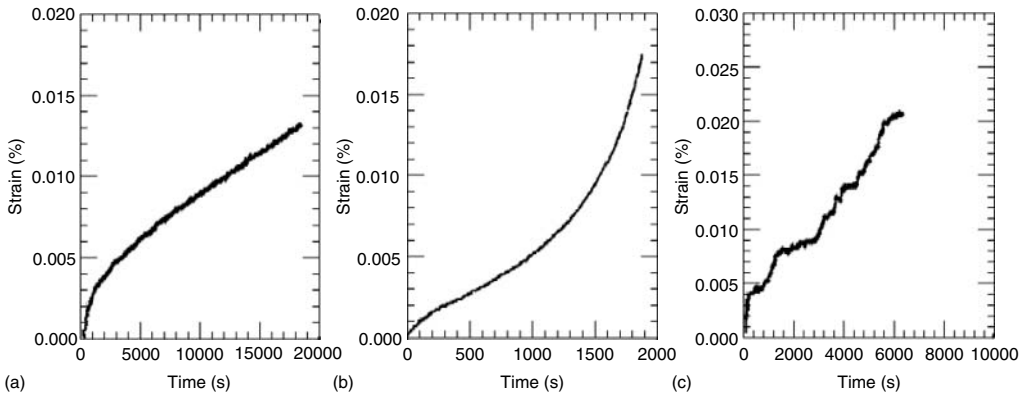

FIGURE 8.32 Typical creep curves of Sn–58Bi solder joints at different temperatures and applied stress (a) $T = 20°C$, $\sigma = 10$ MPa, (b) $T = 20°C$, $\sigma = 21$ MPa, (c) $T = 65°C$, $\sigma = 10$ MPa. (From Igoshev, V. I. and Kleiman, J. I., *J. Electron. Mater.*, 29, 244–251, 2000.)

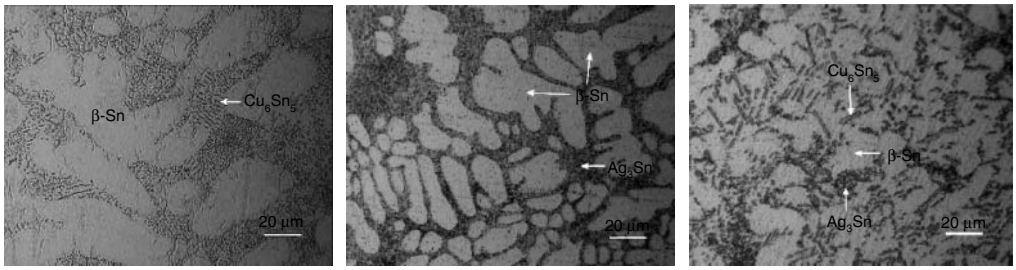

FIGURE 8.33 Optical micrographs of as-solidified state of three precipitation-strengthened Sn-based Pb-free solder alloys: (a) Sn–0.7Cu, (b) Sn–3.5Ag, and (c) Sn–3.8Ag–0.7Cu, showing finely dispersed IMC phase Cu_6Sn_5 or Ag_3Sn in β–Sn matrix. (From Huang, M. J., Wu, C. M. L., and Wang, *J. Electron. Mater.*, 34(11), 1373–1380, 2005.)

lower than that of eutectic Sn–37Pb. These rates decreased with increasing volume fraction of the precipitate phases. The apparent stress exponents ($n_a \sim 7.3$–17), which was higher than that of pure Sn, attained higher values with increasing volume fraction of precipitate phases at the constant temperature, and with the decreasing temperature for the same solder alloy. The threshold stress associated with the particle bypass mechanism was considered to account for high values of stress exponent of Sn-based Pb-free solders. It also explains why the stress exponent attains higher values with the increasing particle volume fraction at constant temperature. The steady-state creep rate of Sn–3.8Ag–0.7Cu is only slightly lower than that of Sn–3.5Ag. This may be attributable to the minimal strengthening effect of Cu_6Sn_5 phase as its size becomes large.

With decreasing size of microelectronic devices, the intermetallics comprise a larger volume of the entire package. The morphologies of these phases are different from that observed in the lead-based solders. Hence, extensive knowledge and understanding of the mechanical behavior of the lead-free solders and the intermetallics is required to satisfy the demands of structural reliability of microelectronic packages and enable predictions of the mechanical behavior of an overall joint more straightforward.

As shown in Section 8.3.5 nanoindenation has been successfully used as a useful probe of the mechanical properties of intermetallics in solder joints with lead-free solder.[691,704,705]

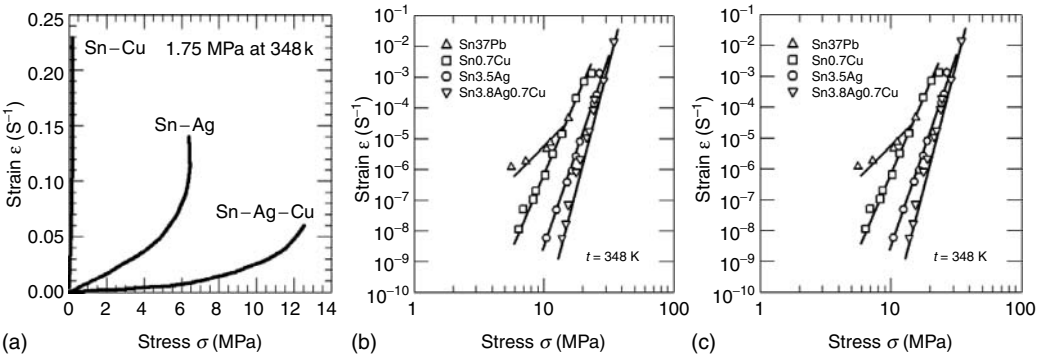

FIGURE 8.34 (a) Typical creep curves of Sn–0.7Cu, Sn–3.5Ag and Sn–3.8Ag–0.7Cu solder alloys at 17.5 MPa and 348 K; Comparison of steady-state creep rates of Sn–0.7Cu, Sn–3.5Ag, Sn–3.8Ag–0.7Cu, and Sn–37Pb at (b) 393 K and (c) 348 K. (From Huang, M. J., Wu, C. M. L., and Wang, *J. Electron. Mater.*, 34(11), 1373–1380, 2005.)

Nanoindenation tests carried out on Sn–Ag–Cu solder revealed that intermetallics deform by both elastic and plastic mechanisms, while the solder is primarily plastic. Hardness data indicates that Cu–Sn intermetallics have the potential for brittle behavior, while the Ag_3Sn compound was found to be more soft and ductile. These results are consistent with the failure mechanisms observed in real solder joints, but also reveal that, at small stresses and small scales of deformation, all of the intermetallics studied exhibit plasticity.[705]

In summing up, it is evident that the data available in the literature on the creep and stress relaxation of soldered contacts is lacking and that additional work is still needed to elucidate the complexity of their mechanical behavior.

8.3.7 Electromigration

As pointed out in Section 8.3.7 electromigration is defined as atomic diffusion driven by high electric current flow. The process is diffusion controlled and thus highly temperature dependent. The driving force for electromigration is the momentum exchange between electrons and ions whereby the direction of atomic mass transport is the same as that of electron flow. This failure mechanism has been given the greatest scrutiny because of the trend toward higher complexity, higher circuit element density and smaller dimensions for all elements of microelectronic packages, including the line width of metallization runs.

Owing to increased microminiaturization, the current densities generated in these interconnects can reach the levels of 10^6 A/cm^2. The resulting atomic transport will lead to depletion/void formation at cathode and extrusion/hillock formation at the anode, where mass flux divergence exists (see Figure 6.18). The growth of these holes leads eventually to circuit failure due to the interruption of the continuity of conducting lines, opening or cracks in the lines or short circuits with neighboring metal areas occurs. Hence, electromigration appears to be the degradation mechanism of considerable importance to the reliability of integrated circuits.

It is interesting to note that although the volume electromigration was investigated by Gerardin[717] in 1861, the phenomenon was not given a wider attention until late 1960 with the rapid advent with microelectronics. The primary objective in studying electromigration in microelectronic circuits stemmed from the deleterious effect associated with the integrated circuitry that was failing with a rather short lifetime due to the electromigration-induced voids. As a result, electromigration became and remains a serious detriment to the reliability of microelectronic interconnections, as evidenced by a considerable attention devoted to this problem.[718–722]

Due to its low electrical resistivity, good adherence to the substrate and the formation of ohmic contacts with silicon, aluminum is used almost exclusively for metallization in integrated circuits. Electromigration damage in Al lines was discovered in the 1960s and was soon recognized to occur by grain boundary diffusion. The recognition has led to two major trends in the study of electromigration in Al: the effect of solute and the effect of microstructure.[721]

The effect of solute was investigated by Shien and d'Heurle[723] who have shown that the lifetime of aluminum lines can be increased by a factor of 50 by alloying with 2–4% of copper. This is exemplified in Figure 8.35a, showing the electromigration-induced changes in the resistance ratio $\Delta R/R$ for various aluminum–copper alloys as a function of time at 210°C and current density of 4×10^6 A/cm^2.

The beneficial effect of copper additions and thus greater increase in the lifetime of aluminum–copper lines was attributed to the grain boundary segregation of copper that ostensibly retards the aluminum grain boundary diffusion. Because grain boundary diffusion is the predominantly flux-driven mechanism, local boundary structure will influence and may determine the failure process. Hence, decreasing the grain size will reduce lifetime due to a larger number of boundaries and triple points in the conductor of given width. It has been shown that that the effect of grain size on the lifetime can be incorporated by considering the line width/grain size ratio (L/d) as seen in Figure 8.35b.[724]

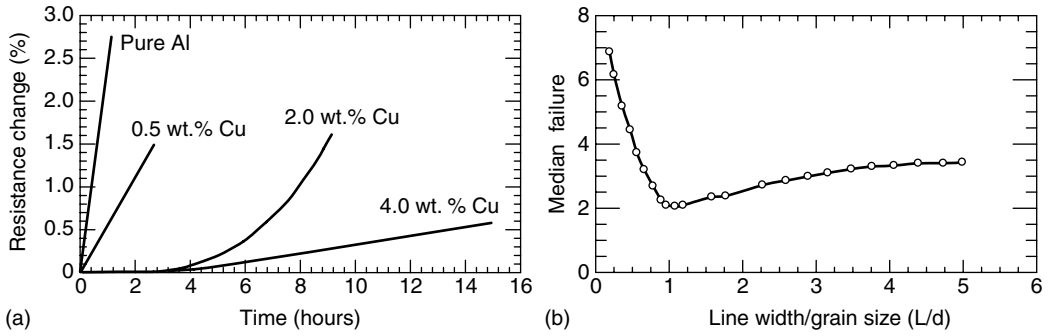

FIGURE 8.35 (a) Effect of copper addition on the time dependence change of resistance of pure aluminum and aluminum–copper lines; current flow 4×10^6 A/cm^2; (b) effect of line width/grain size ratio on the electromigration median failure time. Note rapid increase in the lifetime as conductor microstructure becomes "bamboo," $L/d \sim 1$. (From Shine, M. C. and d'Heurle, F. M., *J. Res. Dev.*, 15, 378–386, 1971; Cho, J. and Thompson, C. V., Appl. Phys. Lett., 54(25), 1577–1582, 1989.)

From the practical point of view, Black[725] has introduced a characteristic time t_{50} at which 50% of a large number of identical devices fails. This characteristic time defines the median time to failure (MTF) and is expressed as

$$t_{50} = A(1/j^n) \exp(Q/kT), \tag{8.7}$$

where A is a materials constant that depends on the geometry, microstructure, and composition of the line, j is the current density in metallic lines, n is a numerical constant called the current exponent having values between 1 and 3 or sometimes higher, Q is an activation energy, k is the Boltzman constant, and T is the absolute temperature.

Although the Al–Cu alloy has performed well as an interconnect conductor for a long time, the trend of miniaturization has recently demanded a change due to, among other reasons, electromigration. Because copper has much better electromigration resistance than the conventional aluminum, it is being extensively used in the integrated circuits (IC) applications. Park and Vook[726] have shown that further improvement in the electromigration resistance of copper can be obtained by addition of Pd. Figure 8.36a and Figure 8.36b depict the effect of Pd on the electrical resistivity of Cu and activation energy for electromigration damage (EMD).

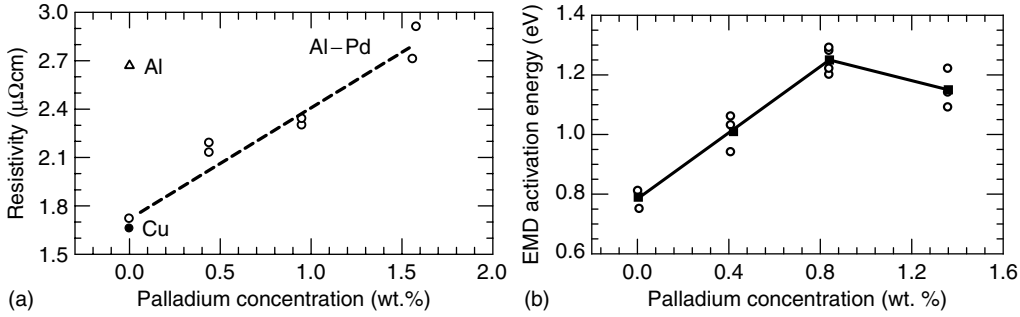

FIGURE 8.36 Effect of Pd on (a) the resistivity of copper and (b) the activation energy for electromigration damage. (From Park, C. W. and Vook, R. W., *Thin Solid Films*, 226, 238–246, 1993.)

Scanning electron microscopy showed that electromigration was characterized by voids and hillocks, the latter being concentrated in the anode region. Many of the hillocks that formed had crystalline facets. Because Cu was the main diffusing atom in Cu–Pd alloys during electromigration stressing, the presence of Pd in the grain boundaries may reduce the rate of grain boundary diffusion, thereby tending to favor surface diffusion in the later stage of electromigration damage. The maximum decrease in grain boundary diffusion was observed at 1 wt% Pd and thus also the highest resistance to electromigration damage (Figure 8.36b). Film thinning and voiding were also observed, the former being more prominent in the alloy films than in pure Cu. X-ray energy spectroscopy showed that the hillocks on the Cu–Pd alloy films had a measurably lower Pd concentration than the hillock-free areas. Hence, it would appear that Cu diffuses faster than Pd when electromigration takes place.[726]

In recent years, to achieve smaller size, higher reliability, and perfect performance the past decade, area array technologies, for example, BGA and flip chip interconnections, have been attracting ever-increasing applications in electronic packaging. However, with trends towards higher integration and further miniaturization of area array structure, electromigration becomes a new reliability concern for the solder joint due to high current density.

It has been found that electromigration significantly affects intermetallic compound growth in microelectronic systems. Growth rates of the intermetallic compounds are either enhanced or retarded depending upon the diffusion directions of the primary moving species and those of the applied electric currents. Chen et al.[727,728] investigated the effect of electric current on the formation of intermetallic phases in Sn/Ag and Sn/Ni systems at different temperatures and at current density of 500 A/cm^2. Figure 8.37 depicts a schematic of the experimental setup with the passage of current (a) and the reaction couple (b) whereas Figure 8.38 exemplifies the effect of electric current on the growth of intermetallics in Sn/Ag and Sn/Ni systems.[727]

From the results shown it can be inferred that the passage of electric current does not change the kind of compound formed at the interface and only the growth rates of the intermetallic compounds are affected. The growth rates of the compounds are enhanced when the flowing direction of the electrons is the same as the diffusion direction of the primary moving species, but retarded when the two directions are different. However, disparate results have been found for Sn/Cu, Zn/Ni, Bi/N, Al/Ni, and Al/Au systems. For the Sn/Cu and Zn/Ni systems at 200°C, the passage of 500 and 300 A/cm^2 electric currents, respectively, does not have any noticeable effects upon both the phase formation and the growth rates. For the Bi/Ni which system reacted at 150 and 170°C with the passage of a 300 A/cm^2 electric current and the Al/Ni at 400°C with 1000 A/cm^2 electric current, the layers at both sides of the interfaces in the sandwich-type couples are thicker than those in the couples without the passage of electric currents.[727]

Gan et al.[729] investigated the effect of electromigration in flip-chip joints and has shown that the effect differs from that in aluminum or copper interconnects. It was shown that while electromigration in aluminum interconnects occurs by grain boundary diffusion, and in copper interconnects by surface diffusion, it occurs by lattice diffusion in solder joints. Electromigration was found to enhance the growth of IMC at the anode side and inhibits the growth at the cathode side when compared with the no-current case.

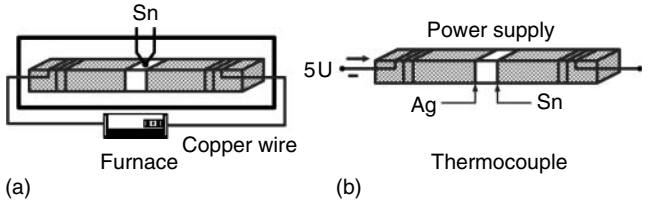

FIGURE 8.37 Schematic of the experimental setup with the passage of current (a) and the reaction couple (b). (From Gan, H., Choi, W. J., Xu, G., and Tu, K. N., *J. Mater.*, 54, 34–40, 2002.)

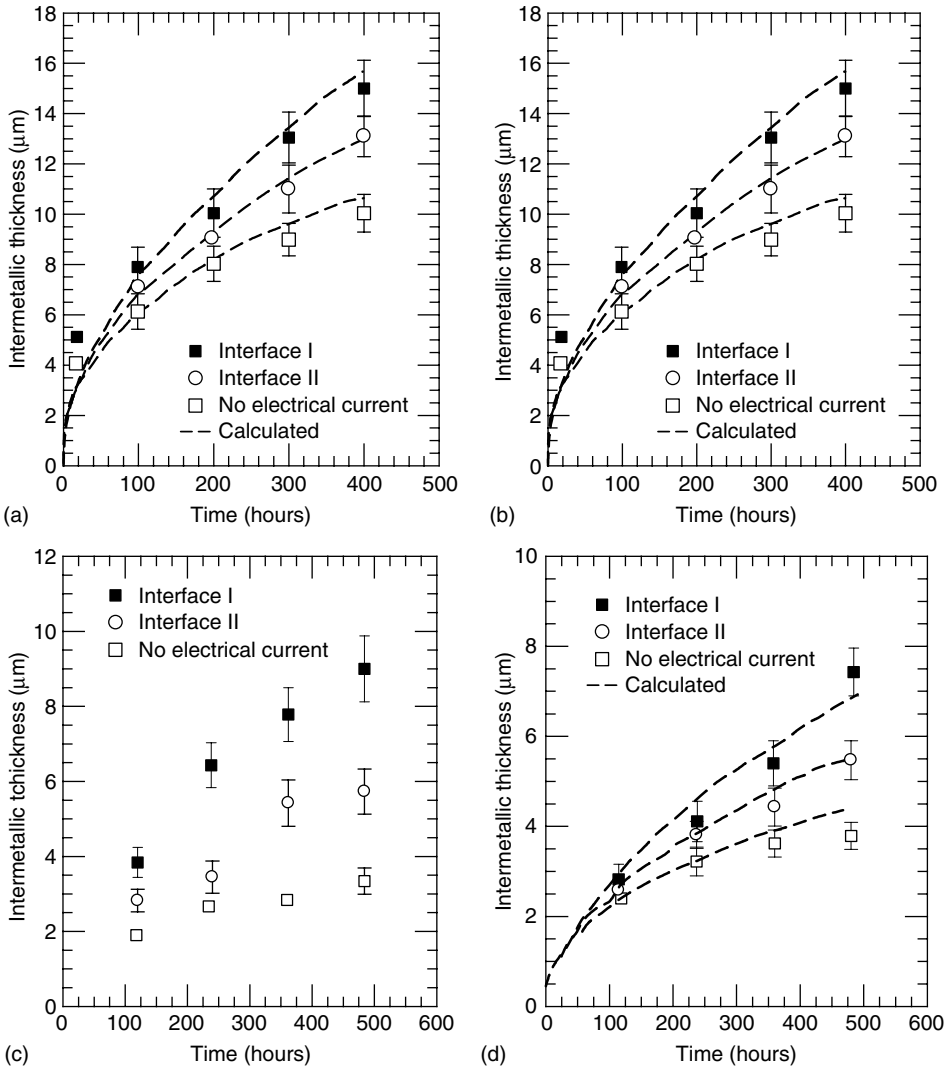

FIGURE 8.38 Formation of intermetallics in Sn/Ag, Sn/Ni, and Sn–0.7Cu/Ni systems: (a) Sn/Ag at 140°C, (b) Sn/Ni at 200°, (c) Sn–0.7Cu/Ni at 180°C, and (d) Sn–3.5%Ag/Ni at 200°C. (Derived from Gan, H., Choi, W. J., Xu, G., and Tu, K. N., *J. Mater.*, 54, 34-40, 2002.)

From the results shown in Figure 8.39a and Figure 8.39b, it can be seen that for the sample stressed with current density of 3.2×10^4 A/cm^2 at 180°C, both Cu_6Sn_5 and Cu_3Sn layers kept growing with stressing time at the anode side. The total thickness approaches 9 μm after 87 h, comparable with that of thermal annealing or solid-state aging for 200 h at the same temperature without current stressing. At the cathode side, as shown in Figure 8.39c and Figure 8.39d, IMC grew much slower, or shrank, compared to that the anode side. Voids started to appear in the solder part just in front of the older/IMC interface at the cathode after 21 h and grew larger after 87 h.[729]

Deleterious effects of electrical current on the mechanical integrity of solder joints was observed in flip-chip solders subjected to current stressing. Using the nanoindenation measuring technique, Ye et al.[730] have shown that mechanical properties, e.g., Young's modulus of flip-chip solder joints, degrade in the localized area where voids are nucleated during current stressing. It was

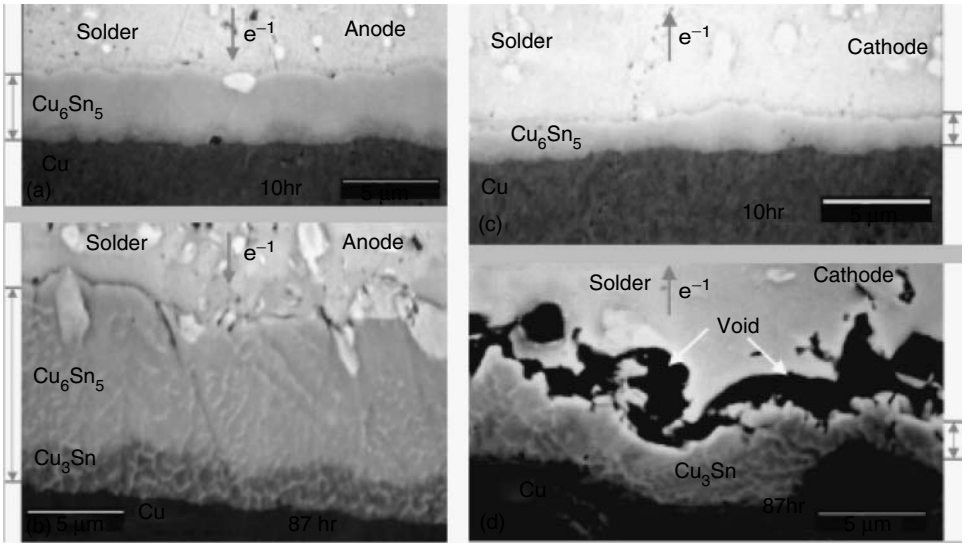

FIGURE 8.39 SEM micrographs of the intermetallic thickness growth at the anode and cathode caused by current stressing of 3.2×10^4 A/cm^2 at 180°C for (a) 10 h (anode), (b) 87 h (anode), (c) 10 h (cathode), and (d) 87 h (cathode). (From Gan, H., Choi, W. J., Xu, G., and Tu, K. N., *J. Mater*., 54, 34–40, 2002.)

also shown that thermomigration due to the thermal gradient within the solder joint caused by joule heating is significant during current stressing.

In summary, it should be pointed out that despite the significant progress made in our understanding of electromigration and its deleterious effects on the reliability of electronic systems, a real breakthrough, that is, a complete elimination of all electromigration-induced failures, has not (yet) been found. This is aggravated by the ever-increasing the number of individual devices that are accommodated on a single chip. Hence, as the active elements on a chip become smaller and the connecting lines are made narrower, the density of current increases, thus generating a greater potential for failure. Although electromigration effects upon interfacial reactions are important and challenging research topics, there is not enough understanding of the phenomena at this time. Extensive further investigation is needed to elucidate the exact nature and the effects of electromigration.

8.3.8 Whiskers

In the search for an alternative coating material, tin was used as substitute plating in many applications. However, it became apparent that in addition to susceptibility to fretting, the additional problem when using tin is its propensity to whisker formation. A whisker is a typically a single crystal, mechanically strong, metallic filaments that can spontaneously nucleate and grow protruding from the surface of a metal. Tin whiskers are of considerable reliability concern as they can grow to a length capable of shorting device leads. The phenomenon of whisker formation was first discovered in 1940s[731] and because then has become the topic of considerable academic and industrial interest. However, in spite of a considerable wealth of published information, basic understanding of the mechanisms that control whisker growth and ultimately its prevention remains elusive. This is because of a significant number of conflicting and sometimes contradictory published results leading to diametrically opposed conclusions.

An annotated tin whisker bibliography and anthology was given by Gaylon[732] whereas Osenbach et al.[733] provided a comprehensive review of the overall phenomenological theory

of tin whiskers. The physical metallurgy of whiskers formation and role of internal stresses was reviewed by Gaylon.[734,735]

Despite the conflicting data and lack of agreement on the detailed mechanisms responsible for the tin whisker formation and growth, it is widely believed that compressive stress within the tin finish influences tin whisker growth. Stresses within the finish can arise from:[736]

- Intermetallic compound formation between the plating material and substrate, resulting in compressive stress within the plating.
- Mismatches in coefficient of thermal expansion of the tin-based plating material and substrate, or underlayer.
- Presence of residual stress from the electroplating process itself.
- Extrinsic compressive stress, such as mechanical bending and forming.

The prevailing but not universal point of view is that the intrinsic stress exerts the dominant effect on matte-tin finishes. The intrinsic stress is due to the formation of Cu_6Sn_5 intermetallic layer between the tin and copper at low temperatures (70–125°C). Because the intermetallic has a smaller volume than tin, it is generally nonplanar at the lower growth temperatures. The volume difference is increased further by excess tin at the interface due to the Kirkendahl diffusion effect. In the case of bright-tin, the high contamination level and its grain structure are believed to be the main reasons for its increased susceptibility to whisker formation relative to matter-tin.[733]

The complexity of the whisker growth mechanism is illustrated in Figure 8.40,[737] whereas some typical micrographs of tin whiskers are shown in Figure 8.41.

According to Gaylon et al.[735] there are several intervening factors that impact on the formation and the growth tin whiskers:

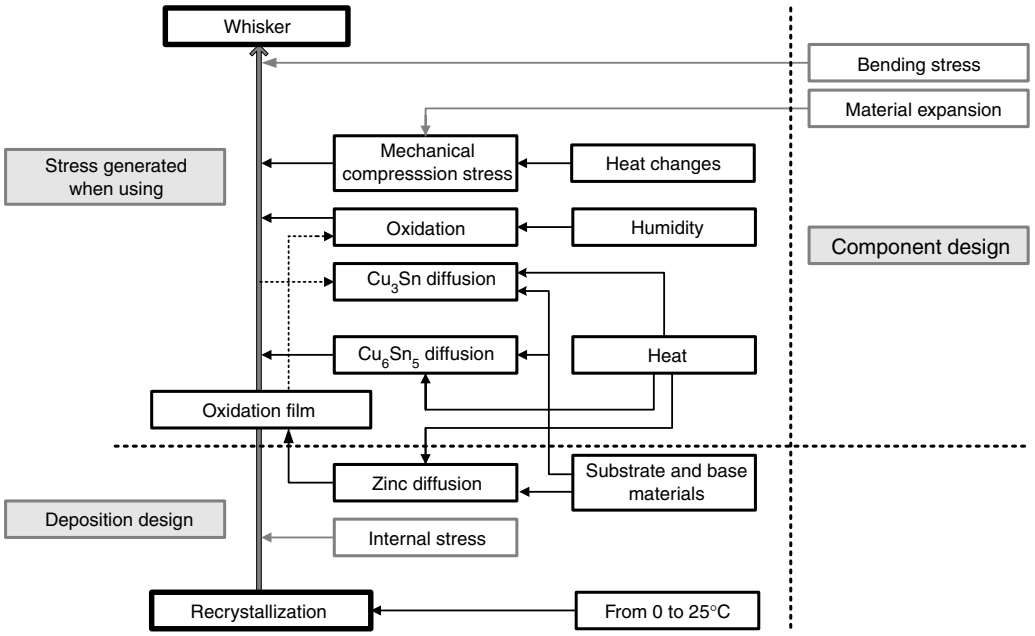

FIGURE 8.40 Whisker growth mechanism. (From Sakamoto, I., *IEEE Trans. Electron. Packag. Manuf.*, 28, 10–17, 2005.)

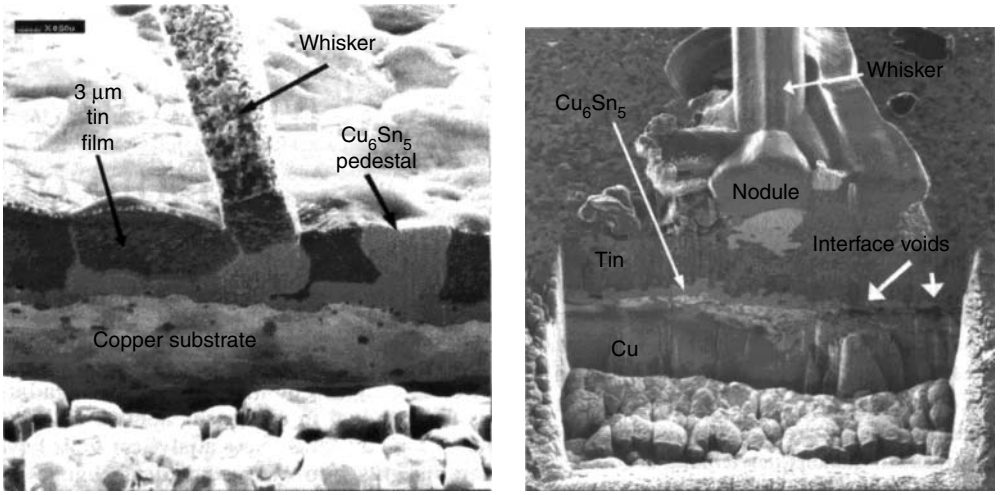

FIGURE 8.41 Focus ion beam (FIB) micrographs of (a) matte tin whisker (b) bright Sn/Cu whiskers showing voids at the Sn/Cu interface. (From Gaylon, G. T. and Palmer, L., *IEEE Trans. Electron. Packag. Manuf.*, 28, 17–22, 2005.)

- *Stress*. Although it is generally believed that compressive stress is the primary driving force for all tin whisker formation, the microstresses within the grain structure and not any overall stress (macro stress) or stress gradient state are also cited as possible causes. In tin films, stress levels may be caused by intermetallic growth, thermally induced stresses (such as thermal cycling), diffusion effects, or mechanically induced stresses. A detailed understanding of the stress and stress gradients generated within the film is still lacking.
- *Impurities.* It generally is recognized that film impurities affect stress states. Some impurities, notably copper additions to tin, make overall stress levels more compressive, which usually leads to increased whisker growth. Other impurities, such as lead in tin, appear to reduce overall stress levels and mitigate whisker growth. Impurities are also thought to play a role in the pinning of grain boundaries, which is generally considered to be a necessary condition for whisker growth.
- *Diffusion*. Because whisker formation requires movement of material within the Sn film, it is generally believed that diffusion is the mechanism responsible for the net mass transfer of material necessary for whisker growth. Grain boundary diffusion is generally accepted as the dominant diffusion mechanism in whisker formation and growth; however, experimental results point to surface diffusion as the operative diffusion mechanism. It is possible that the diffusion is a combination of surface diffusion and grain boundary diffusion.
- *Dislocation mechanisms*. Although some approaches insist that there must be some kind of dislocation mechanism to move material from the whisker grain grain-boundary to the base of the whisker, some theoretical approaches discount the need to have any dislocation mechanisms involved in whisker growth. As yet, there are no direct experimental data that confirms the existence of any dislocation structures within the whisker grain. It is general opinion that dislocations are not a necessary part of a whisker growth mechanism and the available data seem to support that position. However, the evidence is not conclusive and the question remains open.

- *Recrystallization*. There is general agreement that whiskers do not grow from an as-plated grain structure but rather grow out of grains that are "different" than the bulk of the as-plated grain structure. Some theorists conclude that these "different" grains are the result of a recrystallization event. There is general agreement that recrystallization events appear to be the rule for bright tin nodule/whisker growth, but the case is not so clear for matte tin whisker growth.
- *Substrate material*. The effect of substrate materials is not clear because the results to date could not establish as to whether the different coefficients of expansion of the substrate materials, surface topography effects on the growth of intermetallic compounds or some other mechanism are responsible for the whisker formation and growth.
- *Grain orientation*. Some recent data indicates that the film grain orientation spectra of the Sn film affect whisker growth. It appears, however, that the specific dominant preferred orientation index is not critical but rather the angular relationships between the dominant grain orientations. To date, there are no published data that contradict this observation.

Although the formation and growth of whiskers in tin-based systems is well documented in the literature,[738] the phenomenon was also observed in silver-based connections as reported by Chudnovski.[739] The whiskers were observed in power circuit-breakers operating over an extended period of time in the H_2S environment. The surface of the silver whiskers was contaminated with silver sulfide at different degrees, and amount of this contamination possibly depends on how long these whiskers have been exposed to atmospheric H_2S.

The temperature seems to be the major accelerating factor of the growth. The silvery whiskers could grow much faster in the hotter areas of the breaker and be exposed to H_2S for a shorter period of time than the identically sized whiskers, which grew slower in cooler locations.

The most important conclusion is that because silver whiskers are metallic formations, they are highly conductive. Taking into consideration the rate of the growth, the size, and amount of the whiskers developing practically everywhere, but mostly on corners and edges of conductive parts, including moving and stationary contacts and finger cluster, it is obvious that the consequences of the phenomenon are extremely dangerous. Typical examples of the silver whiskers detected on the circuit breakers contacts are shown in Figure 8.42.

In summary, given all the possible variables and difficulty of obtaining data, it is very difficult to establish mechanisms of whisker growth with certainty. One conclusion is the need for samples built in the laboratory under controlled conditions so that some of these variables can be isolated.

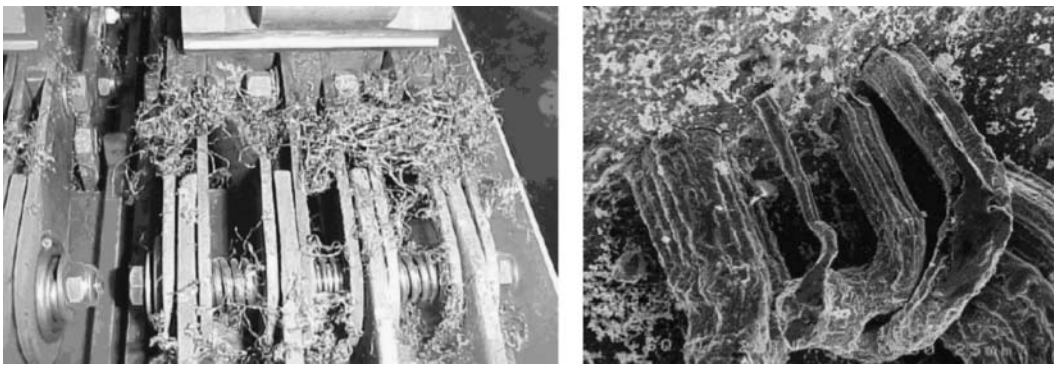

FIGURE 8.42 Examples of silver whiskers observed on power contacts of circuit breaker. (From Chudnovski, B. H., *Proceedings of 48th IEEE Holm Conference on Electrical Contacts*, Orlando, 140–150, 2002.)

Even so, availability of sophisticated tools required to see what is happening in the grain structure may limit the evaluations.[735]

8.4 MITIGATING MEASURES

Significant advancements in the contact physics and plating metallurgy made by contemporary design of electronic connectors enabled the prediction of their basic electrical and mechanical performance. As the drive toward miniaturization of electronic devices continues unabated, increasing demands are placed on the contact interface, including higher current loads without exceeding temperature limits. Hence, many of the reliability issues affecting electronic connections or contact as a whole can be traced to the contact interface.

To design robust, reliable connectors and sockets, the effects and interactions of design parameters on the reliability of the contact interface must be examined, especially in the limited design space as required by the ever-increasing density of contacts in microelectronic packages. To achieve this goal, various mitigating methods are being used to assure the reliability of a large variety of microelectronic applications. The following sections will deal with some of these methods.

8.4.1 Effect of Coating

The demand for longer life of electronic connections and devices under increasingly severe service conditions, the realization of the materials cost, and the recognition of importance of saving metallic resources emphasize the need for assuring and maintaining the reliable performance within the expected lifetime of the connections. Precious metals such as gold, palladium, and their alloys are preferred contact materials for electronic connectors and are used primarily as electrodeposits and clad coatings. However, tin and tin alloys (solders) are also being used due to their intrinsic properties such as forming an oxide that can easily be displaced when making a connection. Because the subject of coating for electrical/electronic contact is extensively covered in Chapter 4, Section 4.2, this section deals with only the salient features of some of the most widely used coating materials for electronic connections.

8.4.1.1 Gold Coatings

Generally, gold coatings can be divided into those which are soft (<90 KHN_{25}) and those which are hard (>90 KHN_{25}). Soft gold is used mostly in applications where resistance to wear is not a primary concern.[105] For some applications in benign environments, the gold thickness can be less than 25 nm. In most applications, however, a gold thickness of 0.1–0.8 μm is needed to meet performance requirements. Hard gold coatings, usually alloys containing cobalt or nickel have been the preferred contact finishes for the contacts of separable electronic connectors. This is due to their unique combination of properties: nobility, durability, resistance to fretting corrosion, and ease of plating.[740]

The contact resistance of a pure gold finish (soft gold) is less than that of gold–cobalt alloy because the greater deformability of the softer gold tends to increase asperity contact, thereby reducing any effect on contact resistance by insulating contaminants. Pure gold is a better conductor than cobalt-hardened gold, which also contributes to its smaller contact resistance.

Pinnel and Bennet[741] have shown that when thin electroplated gold on copper substrates is exposed to temperatures below 250°C, mass diffusion of copper can occur resulting in a substantial degradation of an electrical connection. The effect was rationalized in terms of in an enhanced diffusion along the lattice defects, notably grain boundaries and dislocation pipes. This is clearly illustrated in Figure 8.43a showing the Arrhenius type dependence of diffusion coefficient on temperature. The activation energy at low temperatures is apparently half of that at high

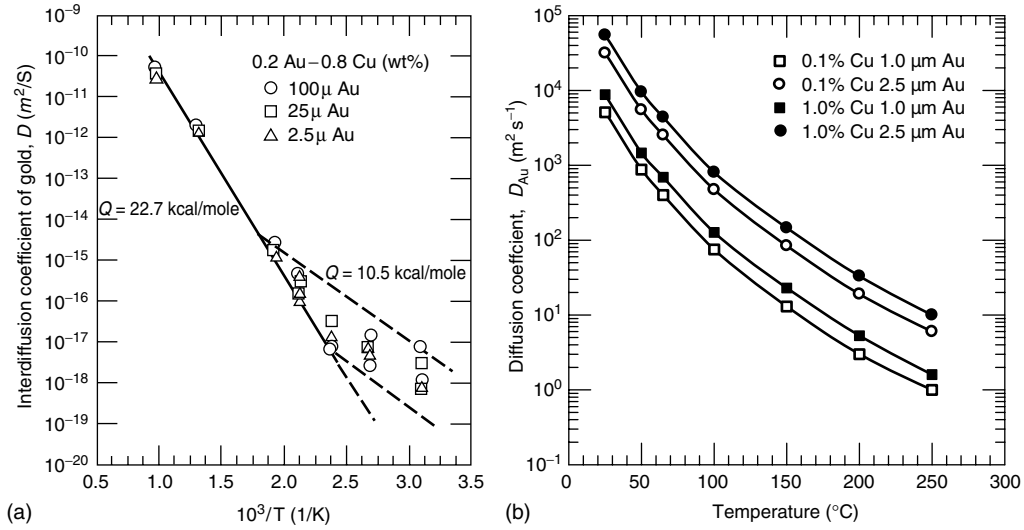

FIGURE 8.43 (a) Arrhenius plot of the interdiffusion coefficient vs. $1/T$ at 20 wt% Au; (b) failure based on time to attain 0.1 and 1.0 at% Cu at the surface.

temperatures. Using the diffusion obtained data this study, Pinnel and Bennet estimated the times at various temperatures required to degrade an electroplated gold surface by mass diffusion of the base copper. The results are shown in Figure 8.43b.

To prevent diffusion of copper the use of ductile nickel underplate for hard golds that are less than 5 μm thick is nearly universal. The nickel thickness usually is between 1.25 and 2.5 μm. Among the advantages of nickel underplate are its enhancement of (1) the adhesive and abrasive sliding wear resistance of the gold, (2) gold durability during fretting, and (3) nobility of the contact if the gold is porous and sulfur, hydrogen sulfide, and some other pollutants are present (although nickel may be severely corroded by sulfur dioxide at pore sites).[740]

In addition, thin gold deposits may be less porous when some nickel electroplating processes are used. Another advantage of nickel is its effectiveness as a barrier to the thermal diffusion through the gold of copper, zinc, and other metals. The nickel diffuses at a slower rate than most metals, although relative rates of diffusion are temperature dependent. Thus, in elevated temperature service, nickel apparently stabilizes the contact resistance of gold plated contacts which eventually would increase due to the appearance and subsequent oxidation at the surface of diffused metals to nonconductive compounds. Thin nickel–gold finishes (0.5 μm) may be acceptable for contacts in connectors at 150°C, and even to 200°C, depending on the intended duration of service.[740] In addition, as shown in Section 8.3.3, a nickel underplate enhances the durability of a thin gold deposit against fretting damage.[454]

8.4.1.2 Palladium and Palladium Alloys

Palladium is a noble metal considered as a possible replacement for gold in electronic connections. It is available like gold in wrought, clad, and electrodeposit forms and is noticeably less expensive at the same thickness. Unfortunately, however, palladium is susceptible to frictional polymerization resulting from small oscillatory motion (fretting) leading to the formation of insulating polymers.[742] The oscillatory movements can also wear out thin palladium coatings and subsequently expose the underlying base metal to oxidation or corrosion which may, in turn, cause contact resistance to become unstable.[454,475,664] Deleterious effects of fretting on the performance

of palladium contacts can be mitigated by increasing the contact load and lubrication (see Section 8.4.2).

Another possibility of improving the reliability of palladium contacts is mating of hard palladium to soft gold and silver counterparts. The gold and gold–silver versus palladium contact systems were initially found to be satisfactory[742] in practical applications, in contrast to all-palladium contacts which produce frictional polymers. This is because transfer takes place primarily to the palladium surface, so that the system becomes all-gold or all-gold alloy or all-silver.

A rather intriguing connection method using palladium dendrite was described by Schultz.[743] This method uses palladium dendrites plated on circuit or contact pads providing high-density connections with improved electrical performance. Palladium dendrites grown on copper contact pads can provide a direct-contact connection to a mating circuit pad plated with gold or tin/lead solder with as little as 30 g of pressure. Connect/disconnect testing to 5000 cycles has shown no wear or destruction to the dendrites and negligible wear on the mating gold surface.

The connector technology based on the uncontrolled growth of dendrites was originally developed by IBM under the trade name DendriPlate to meet the need for a connector exhibiting superior electrical performance, including the elimination of noise and resistance in the electrical connection. The dendrites on the contact pad vary in size with a maximum spike height at 50 mm. There are approximately 100 dendrites per 0.64-mm diameter pad. Figure 8.44 shows random dendrite growth patterns.

Owing to the unique shape and randomness of the dendrites, contact with relatively low pressure can be applied to the backside of the contact pads. As a pressure or pressfit connection, there are two methods to make contact between mating surfaces-dendrites on dendrites or dendrites on a flat pad.

Contact resistance with dendrites on dendrites is slightly higher than dendrites on a pad. The dendrites on dendrites method makes contact by sliding the upright, elongated shapes against each other side by side, making contact as well as pressing the longer points into the valleys between the dendrites on the mating pad.

The dendrites on a flat pad method make contact by dendrites being pressed against a flat gold or tin/lead-plated surface. With a gold mating surface, the electrical connection is made by point contact, whereby a constant contact with the gold surface is achieved by applying pressure as low as 30 g, with a thin, high-compliancy elastomer on the opposite side of the dendrite-plated pad. The dendrite tips press tightly against the surface of the gold, making slight indentations at the contact points.

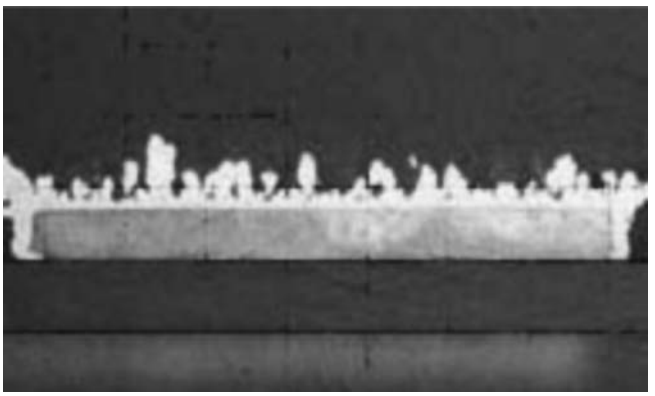

FIGURE 8.44 Cross-section of an individual contact pad with the needle-like palladium dendrites. (From Schultz, D., *Connector Specifier*, February, 2001.)

Contact to a plated tin/lead solder finish actually penetrates the surface, sinking the dendrites into the solder. By penetrating the surface finish, contact is made on the tips and sides of the dendrites, which can provide a gastight connection across the pad.

Another attribute assuring a highly reliable electrical connection is the self-wiping action of the dendrite-plated surface. When the contact between needle-like dendrite tips and the gold pad is made, the dendrite spike actually pierces the gold, making a good electrical connection. This mating action self-wipes, or cleans off, debris and dust that in traditional pin connections can affect the integrity of the connection.

8.4.1.3 Tin Coatings

Tin and tin alloys have been used extensively in a variety of electronic applications, particularly to confer solderability to the substrate. With the escalating price of gold, tin, and its alloys was considered as a possible alternative to gold plating in a number of connector applications.

The utility of tin as a contact finish derives from the disparate hardness of the surface tin oxide and the underlying tin metal. Tin oxides are thin, very hard, and brittle whereas tin itself is very soft. The composite finish then is a thin, hard, and brittle surface over a soft and ductile layer. When a load is applied to such a composite, the surface oxide cracks and the load transfers to the soft and ductile tin, which flows readily leading to widening of the cracks in the oxide. Tin extrudes through the cracks and establishing the desired metallic contact interface. This process is greatly enhanced by the sliding/wiping action that occurs on connector mating. However, because tin is thermodynamically driven to oxidize, the problem arises when is exposed to the environment during the wiping action (fretting).[744]

As shown in Section 6.4.4 and Section 8.3.3, the susceptibility of tin and tin-based alloys to fretting is one of the major problems in assuring the reliable performance of electronic connections. However, deleterious effect of fretting in tin-based systems can be limited but not eliminated by preventing the fretting motion and lubrication (see Section 8.4.2).

Tin and tin alloys are generally recommended for electronic applications working in benign environments and moderate ambient temperatures where the number of make-or-break operations is small, life requirements are relatively short, and reliability requirements modest.

8.4.1.4 Nickel and Nickel-Base Alloys

As shown in Sections 4.2.3 and 4.2.4, nickel and its alloys are widely used in power connections. Electroplated Ni–In was considered as a promising, less expensive alternative to gold as shown by Ross et al.[745] It was shown that both wear resistance and contact resistance are greatly improved by addition of In to nickel, as seen in Figure 8.45 that shows the friction coefficient and contact resistance as a function of In content of the deposit.

8.4.2 Effect of Lubrication

Lubrication is one of the most effective means of improving and maintaining the reliable performance of electronic connections, and for that matter, any electrical connection. The beneficial effect of lubrication is manifested in reduced coefficient of friction, and thus wear, and fretting between mating surfaces. Lubricants with additives provide protection against corrosion by inhibiting the ingress of the corrosive environments into the contact zone. It also protects against substrate corrosion by sealing the pores in the thin precious metal (usually gold) plating, thus preventing the oxidation of substrate which can eventually exude through the pores, build up on the noble metal surface, and lead to high contact resistance. An additional advantage of lubrication

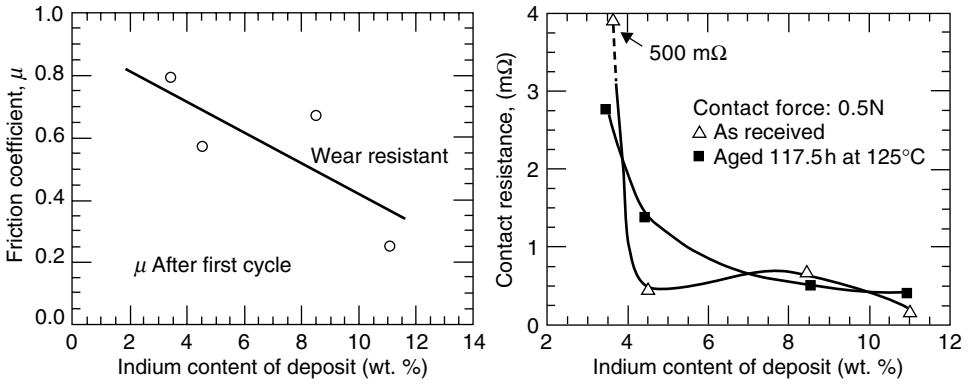

FIGURE 8.45 Effect of indium on the coefficient of friction and contact resistance of Ni–In alloy. (From Roos, J. R., Celis, J. P., and Vancoille, E., *Plating Surf. Finish.*, February, 60–67, 1990.)

is the possibility of using thinner plating without compromising the reliability of a connection. The main characteristics of lubricants for electronic/electrical connections include:

- Thermal stability
- Spreading tendency
- Resistance to oxidation
- Resistance to UV radiation
- Ability to protect the contact zone
- Reactivity with ambient vapors
- Dispensability for dust and wear particles
- Applicability
- Stability to polymerization
- Viscosity
- Corrosion inhibition
- Volatility
- Solvency for adjacent insulating materials

It is clear, however, that no one lubricant can satisfy all these requirements and be used for all types electronic/electrical connections. It is the end use that ultimately determines the type and the properties that are essential for a particular application.

The effect of lubrication on the performance of electronic connections has been investigated by many authors, but most notably by Antler[46,454,640,746,747] and Noel et al.[196,748,749] In view of the importance of lubricants in the reliability of electronic connections, only salient features of these works will be discussed.

A five-ring polyphenylether (5-PPE) fluid has been a widely accepted contact lubricant for many years. It is usually applied by immersing the contacts in a 0.5-wt% solution in a volatile solvent. The 5-PPE is effective for many noble contact materials and, being nonwetting, does not migrate. However, it has been observed to volatilize from heated surfaces, which suggests that it may be short-lived at elevated temperatures.[746] Assuming a product life of 20 years, the maximum service temperature to which contacts with a coating from a 0.5-wt% solution of the 5-PPE in a volatile solvent, such as 1,1,1-trichloroethane, may be continuously subjected is about 30–50°C, whereas a 2.0-wt% coating of a six-ring polyphenylether (6-PPE) fluid has an estimated maximum service temperature of 85–110°C under the same conditions.

It is recommended that a 2.0-wt% coating of 6-PPE be used when a connector contact lubricant having a broad service temperature range is required. The 5-PPE is not an ideal lubricant for long-lived applications much above room temperature but is effective within its lower maximum operating temperature limits.

Figure 8.46 exemplifies the beneficial effect of lubrication on the contact resistance of palladium contacts subjected to fretting.[475]

The effect of lubrication on the friction, wear, and electrical contacts of hot-dipped tin coatings on bronze-base separable contacts can be improved using the fluorinated lubricants.[748] It has been shown that different lubricants exert different effect on the contact's resistance, friction, and wear characteristics of tin-plated contacts. The friction and fretting tests were carried out at room and high temperatures using pertluorinated polyethers (PFPE) with viscosities $v = 1800$ cSt and $v = 250$ cSt, a linear PFPE with OH end groups, and viscosity of $v = 73$ cSt and stamping oil. Solutions of 20% (v/v) concentration were made from dilution in the proper solvent. The results shown in Figure 8.47 illustrate the effect of lubrication on the friction coefficient and contact resistance as a number of friction and fretting cycles before and after heat treatment at 150°C.

From these results it can be inferred that both coefficient of friction and contact resistance are greatly affected by the type of lubricant used, and also temperature. It appears that viscosity of the lubricant exerts considerable influence on the friction and contact resistance behaviors either prior to or after heat treatment. In other words, Noel et al.[749] have shown that if the viscosity is too high, severe degradation is observed, which leads to the accumulation of the tin and tin oxide particles in the contact zone, thus raising the contact resistance values. The effect of a low viscosity and low tension energy fluid is to postpone wear and lead to very thin powder-like particles.

It is also interesting to note that there are greases containing soaps, silicas, or clays that are created by mixing a solid thickening agent with oil. Upon application to the contact surface, the solvent evaporates, leaving a thin, protective lubricating film with excellent stability against oxidation or aging.

In summary, it is clear that lubricants can stabilize contact resistance by retarding the rate of wear of thin noble metals on film-forming substrates, by dispersing frictional polymers and with base metals by protecting the surfaces and wear debris from the environment, thereby reducing the

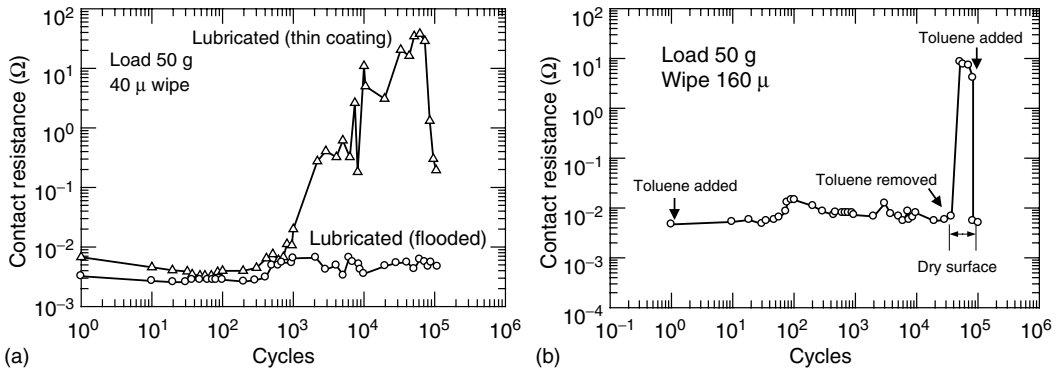

FIGURE 8.46 (a) Effect of lubrication on the fretting of solid palladium riders rubbing against clad palladium lubricated flooded or with a thin coating obtained by retraction from a 0.5% solution in 1,1,1-trichloroethane; (b) contact resistance of solid palladium rider fretting against clad palladium flat with and without the presence of toluene. (From Antler, M. and Sproles, E. E., *IEEE Trans. CHMT*, 5, 158–166, 1982.)

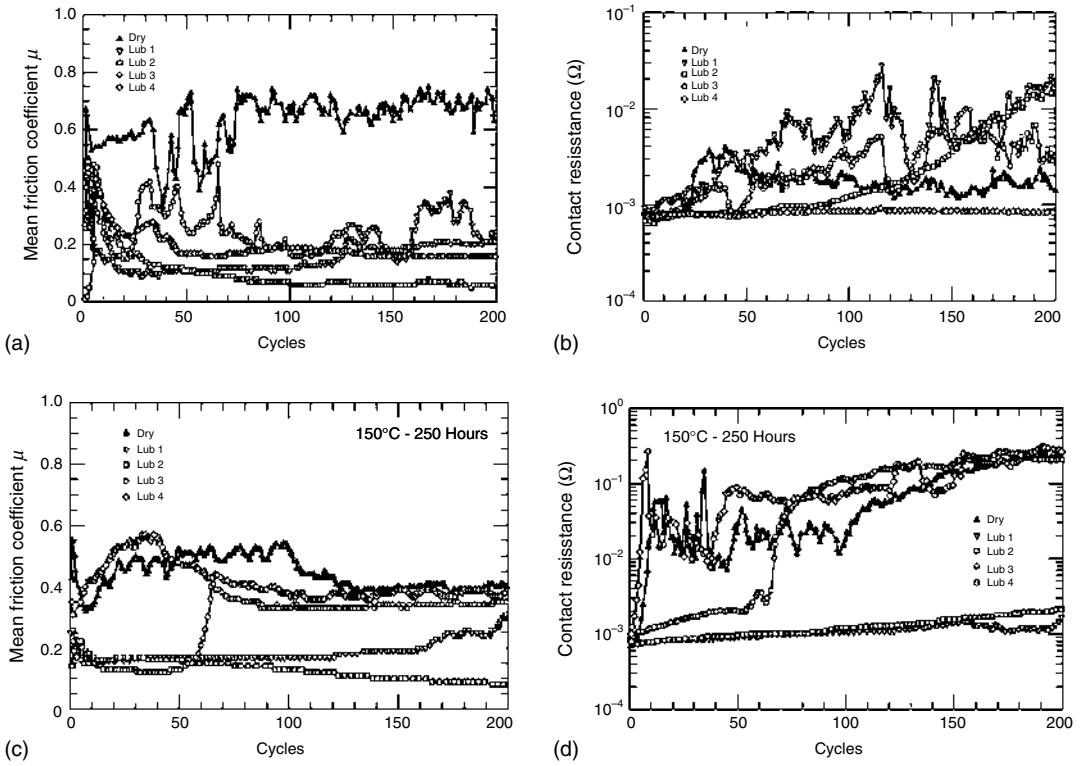

FIGURE 8.47 The effect of lubrication and temperature on the coefficient of friction (a and c) and contact resistance (b and d) of hot-dipped tin separable contacts. (From Noel, S., Lecaude, N., Almarguy, D., and Tristani, L., *Proceedings of 47th IEEE Holm Conference on Electrical Contacts*, Montreal, Canada, 197–202, 2001.)

oxidation rate. Lubricants are used commercially to alleviate fretting corrosion problems with tin and solder coated connectors. It is equally important to note, however, that despite the significant improvement in the stability and performance of electrical and electronic connections brought about by lubrication, there are also some shortcomings when lubricants are used.

9 Sliding Contacts

9.1 TRIBOLOGY OF ELECTRICAL CONTACTS

All electrical contacts, excluding welded and soldered contacts, can be considered friction units. When analyzing the operation of different types of contacts, they can be considered as current-passing tribosystems for which friction, wear, and lubrication problems are essential.[750]

In Figure 1.1 (see Chapter 1) the moving electrical contacts whose performance is greatly governed by friction and wear are shaded. Yet it should be noted that the tribological aspects are important not only for sliding and separable contacts but also for nominally stationary contacts, such as bolted joints. Even assuming that these contacts are totally stationary, one should realize the necessity of applying the tribological approach to the problem of improving the contact quality and reliability since electric current passes through the discrete contact spots. For example, in clamped contacts it is important to attain the maximal area of the mechanical contact without the formation of insulating, e.g., oxide, films in contact operation. At the same time, the formation of the contact area between rough surfaces under load have always attracted the attention of tribologists thinking of using the contact resistance measurement as a tool of contact monitoring.

Another significant issue for nominally stationary contacts is their normal and tangential micromotion in operation which causes a number of tribological problems.[3,751] The micromotion induces the deformation and wear of the contact surfaces leading to surface activation, corrosion, formation of wear particles and contaminations on contact spots, and finally, current passage breakdown (see Figure 9.1).

When designing separable contacts, one should take into account the applied contact force, wear resistance, and durability. Since in most electronic and electrical devices a large amount of nonferrous and noble metals is used for separable electrical c ontacts by the manufacturers, the tribological assessment of their reliability is crucial. The most complex problem in such a contact is to ensure a combination of minimal wear and minimal contact resistance. Clearly, since these characteristics are strongly dependent on the contact pressure and surface state, optimization should be performed.

A specific feature of sliding electrical contacts (SC) is their wear under operation conditions. Two basic wear modes are typical: mechanical wear caused by friction and electrical wear resulting from the effect of electric current on the contact materials. The mechanical wear appears in sliding electrical contacts in a similar manner as in common friction pairs (see Chapter 3). Depending on the current passage mechanism and the combination of contact materials, the electrical wear may be caused mainly by the transfer of ions of one material to another as well as oxide film fritting. This factor can increase molecular attraction between the juvenile metals and induce seizure with deep tearing-off, sparking, and arcing. Heat generated in the contact gap and evaporation of metal into the gap makes the mechanical wear more severe.

The processes of friction transfer and the formation of intermediate films on friction surfaces are of primary importance for sliding electrical contacts of all types. For example, the formation of the film called “patina” or “collector film” is characteristic for brush contacts and is, in addition to other factors, strongly controlled by the direction of current.[234,404] In low-current contacts the films appear due to friction even on such noble metals as platinum due to the effect of frictional polymerization. This process should be taken into account when developing and selecting contact materials.[26]

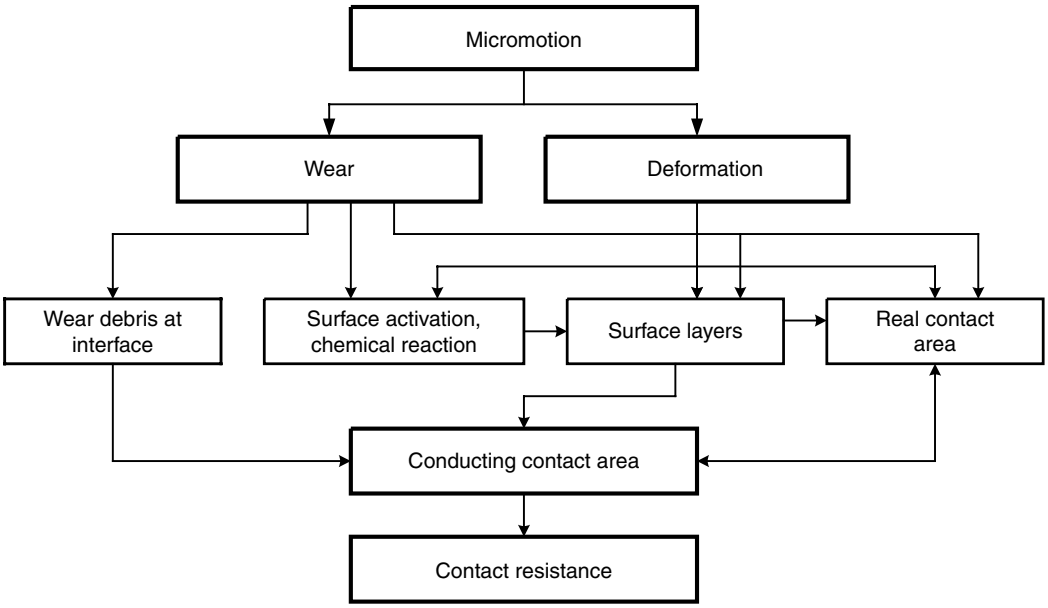

FIGURE 9.1 Influence of micromotion on nominally stationary electrical contact reliability.

As a rule, low-current sliding contacts should combine high wear resistance and low friction with high stability of the contact voltage drop. To meet these requirements contacts with good oxidation and wear resistances made of gold, platinum, rhodium, and palladium alloys are widely used. In addition to high cost of these components, they are not always suitable to meet the service requirements such as vibration stability, impact resistance, and reliability under severe weather and extreme conditions (for example, low-current sliding contacts of ships and airplanes). Therefore, designers of low-current sliding contacts should solve the problem by improving the operation characteristics of the contacts with high reliability of light-current commutation.

9.1.1 Interrelation of Friction and Electrical Processes

Inevitable interrelation of friction and current in operation is an important feature of moving electrical contacts. This specific feature is taken into account as the essential requirement for contact materials, coatings, lubricants, and contact design. The contact areas in moving electrical contacts, through which the current passes, coincide, at least partially with deformation spots. Therefore, the interrelation of the friction and electrical processes is governed by the state of the interface and by behavior of boundary films.

The analysis of the combination of the mechanical and physical–chemical factors acting on the sliding electrical contact can be described by a flow chart, as shown in Figure 9.2. The basic tribological and electromechanical characteristics of the contact are load p, velocity of relative motion of the contact surfaces v, current density j, and voltage in the circuit U. The environment can be characterized by pressure p_0 and chemical activity μ, with temperature T an additional factor. The contact comprises two solids and in a general case, the third body consists of a boundary lubricant film and other films on the contact surfaces. The output characteristics include wear rate I_h governing the contact life, friction coefficient f characterizing mechanical losses, contact voltage drop U_c corresponding to electrical losses, and failure rate λ.

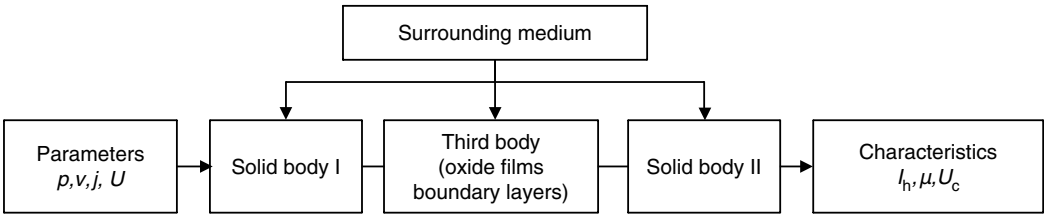

FIGURE 9.2 Diagram of factors influencing sliding electrical contact.

9.1.2 Role of Boundary Films

The effect of boundary films can also be divided into groups which define positive and negative factors influencing the performance of sliding contacts (see Figure 9.3). Positive factors reduce the mechanical and electrical losses and improve contact life and reliability, while negative factors may cause the contact to break down. The effect of many factors within a broad range of operation conditions implies the existence of an optimal combination of boundary film characteristics. From the analysis of available data, it can be concluded that there is a substantial amount of evidence on the effective use of boundary lubrication for improving wear resistance and reliability of many types of electrical contacts.

9.1.3 Main Means of Improving Reliability of Sliding Contacts

The effect of different modes of motion on the interface is generally considered as the most important factor determining the sliding contact performance. Therefore, the application of tribological experience is one of the main ways of increasing its efficiency. The analysis shows that the improvement of sliding contacts includes the following three basic directions: development of new contact materials, coatings, and lubricants; special techniques affecting structure and state of the interface; and contact design improvements (see Figure 9.4).

Formation of thin transfer films on contact surfaces, which do not strongly affect the current passage but reduce essentially the probability of seizure, welding, and severe wear, is a generally used method of improving the performance of sliding contacts. For these purposes composite materials containing conductive solid lubricants are commonly used. This method, implemented first in carbon–graphite contact materials for electrical machine brushes,[234] is currently widely used

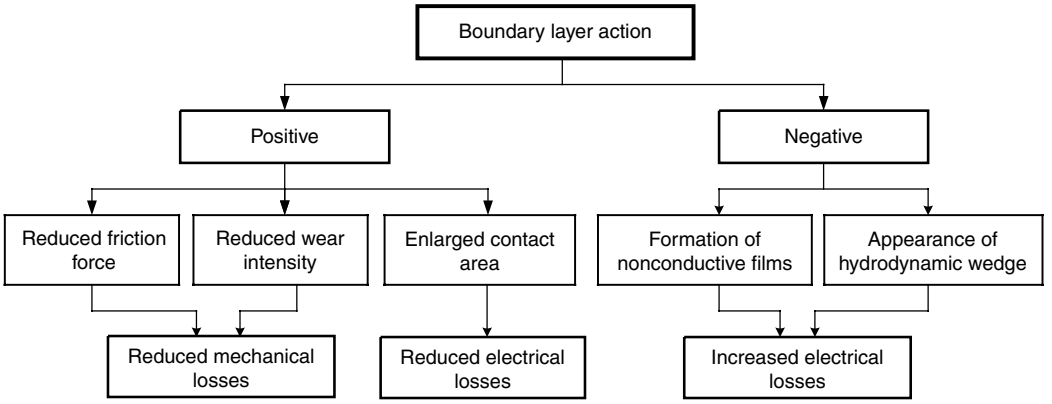

FIGURE 9.3 Boundary layer influence on performance of sliding electrical contact.

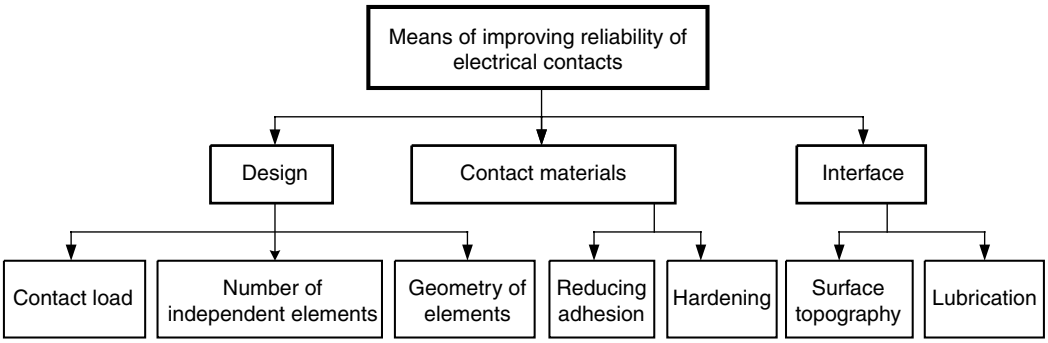

FIGURE 9.4 Main means of improving reliability of sliding contacts.

in designing different types of sliding and breaking contacts. Recommendations are also given on the application of conductive solid lubricants in some low-current contacts.

Development of new electric contact materials and lubricants involves a considerable amount of research in tribology and surface engineering. For example, ion implantation of steel surfaces is a well-known tribological method of hardening the surface and reducing friction and wear. It was also successfully used to modify surfaces of soft noble metals, including gold, platinum, and silver alloys applied as thin coatings in connectors.[118,119]

In recent years the use of special contact lubricants for high-current pick-offs and low-current electronic contacts have become a standard design feature. The first lubricants for electrical contacts had limited applications and were used effectively only for low-speed metallic contact pairs operating at relatively low current densities.[46] Lately, a great number of efficient lubricants for electrical contacts of different types have been developed and produced commercially (Castrol, Nye, Electrolub, etc.).

Formation of the interface structure is one of the most important means of improving the efficiency of contacts. The data relating the contact conductivity to topography are essential for making the recommendations for contact design. For example, it was shown that the use of regular texture of contact surfaces can greatly improve their efficiency.[752,753]

When base metal contacts are subjected to fretting, the generation of wear debris by the oscillating motion is one of the main contributing factors to high contact resistance. Wear debris can accumulate at the contact interface and oxidize, thus separating the surfaces electrically and increasing the contact resistance. The modulated contact surface, which had cavities for trapping the oxide wear debris (see Figure 9.5), has shown low contact resistance under fretting motion. This result suggests that nonnoble metals with modulated surfaces could be used as substitutes for noble metals.

The modulated contact surface used for trapping the wear particles can also be used to reduce friction. It has been shown that the friction coefficient could be maintained at about 0.2 during steady sliding.[752]

The reliability of sliding contacts can also be improved by designs that provide parallel operation of several single contact pairs to reduce the probability of failure. This method is based on the well-known feature of electrical contacts that increasing the number of contact spots at the interface improves the contact resistance stability. This approach of improving the contact efficiency has been applied to many types of contact designs and configurations. For example, using split or combined brushes considerably improves the performance of electrical machines. The method was used in potentiometers, thus increasing the number of fingers sliding over the resistive element.[9]

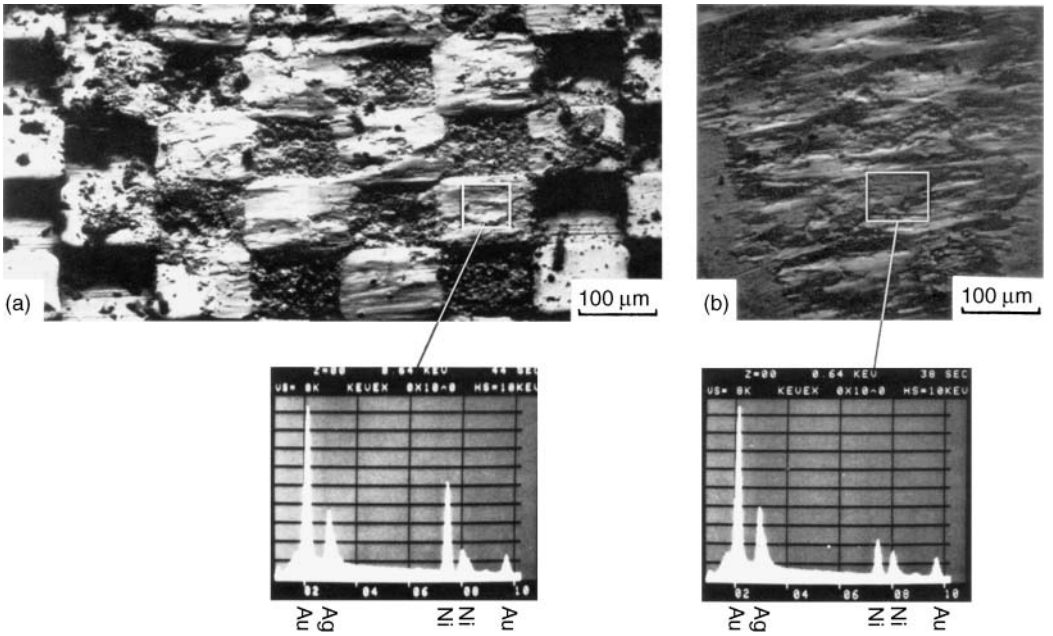

FIGURE 9.5 Scanning electron micrographs of (a) the modulated surface and (b) the pin after 105 fretting cycles. The wear debris trapped in the cavities should be noted. (From Saka, N., Llou, M. G., and Suh, N. P., *Wear*, 100, 77–105, 1984. With permission.)

The development of fiber brushes for high-current pick-offs, however, is the most outstanding result in this field.[70] Materials and constructions of fiber brushes are presented in Chapter 4 Section 3.2. Solving the brush wear problem by increasing the number of elastic contact spots is interesting from a tribological point of view. Unlubricated metal-fiber brushes can operate in the microwear transition region through a very large number of contact spots. Calculations and experimental data of Kuhlmann-Wilsdorf[70,76,79] have shown that uniform distribution of the contact force among many fiber elements results in lightly loaded (elastic) contact spots. Very low wear rates and friction coefficient are associated with elastic contact spots (see Figure 9.6). By contrast, monolithic graphite or metal–graphite brushes attain similarly low wear rates with plastic contact spots, such that the relative motion between brush and substrate is largely accommodated via extensive shearing of graphite particles parallel to the basal plane.

9.1.4 Tribophysical Aspects in the Development of Sliding Contacts

The materials for SC should combine acceptable electrical (low contact resistance) with perfect antifrictional (low friction coefficient and high wear resistance) characteristics. The required contact characteristics and physical–mechanical properties are given in Table 9.1. Note that hardness and oxidation rates are given both positive and negative characteristics in the table.

In homogeneous materials, a desirable correlation of physical–mechanical properties is in most cases impossible to attain. This problem can be solved by separating the conductivity and self-lubrication characteristics of the composite material components. Such materials may include conducting matrix with antifriction fillers, like graphite, sulfides, halogenides, metal selenides, and fusible additives.

When designing or electing contact materials, it should be borne in mind that performance, design, or technological factors of SC and mechanical tribosystems, e.g., plain bearings,

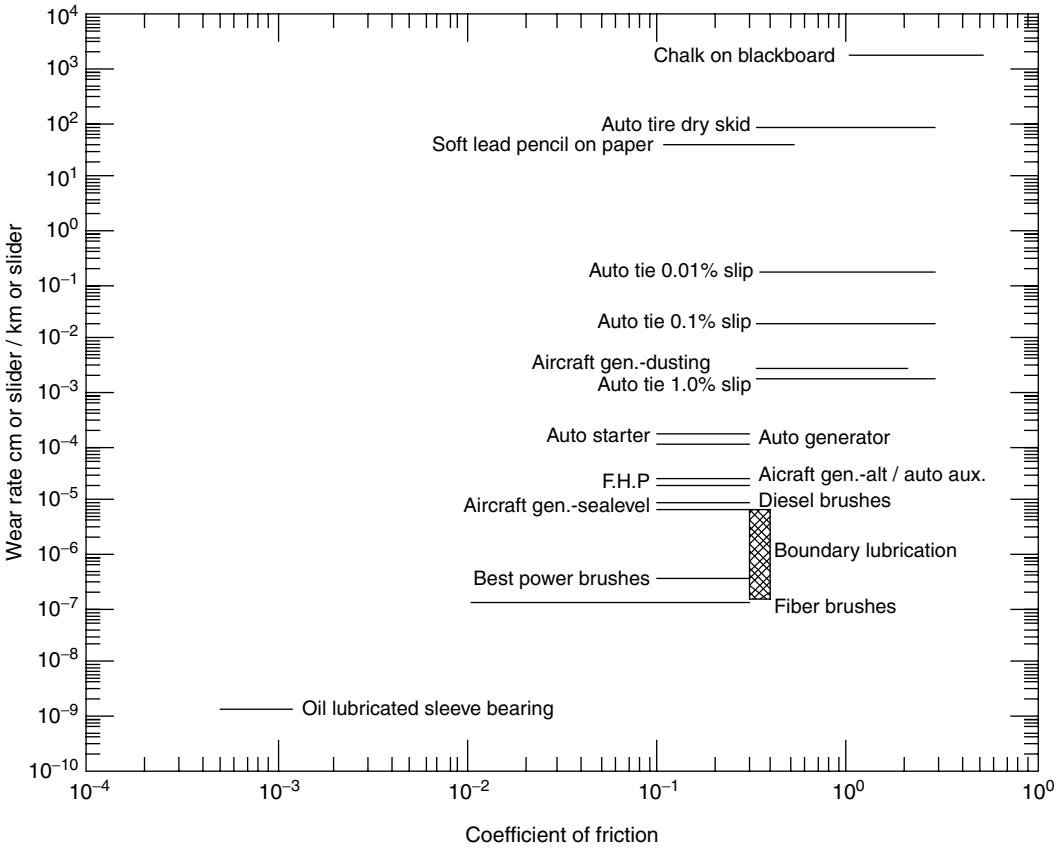

FIGURE 9.6 Dimensionless wear rates and friction coefficients of a wide range of monolithic and fiber brushes plus several other sliding situations. (From Kuhlmann-Wilsdorf, D., *Electrical Contacts: Principles and Applications*, Slade, P. G. Ed., Marcel Dekker, New York, pp. 943–1017, 1999. With permission.)

TABLE 9.1
Interrelation between Contact Material Properties and Sliding Contact Characteristics

Contact Characteristics	Properties of Contact Materials	
Electrical contact resistance [−]	ρ [−] Resistivity	μ [−] Poisson's ratio
	H [−] Hardness	Oxidation rate [−]
	E [−] Young modulus	Surface film strength [−]
Mechanical wear [−]	σ [+] Tensile strength	Oxidation rate [+]
	H [+] Hardness	E [+] Young modulus
Electrical wear [−]	T_m [+] Melting point	q [+] Specific heat of fusion
	σ [−] Tensile strength	H [+] Hardness
	λ [+] Thermal conductivity	
Contact overheating [−]	Oxidation rate [−]	Surface film strength [−]

Note: [+] property desirable to be as high as possible; [−] property desirable to be as low as possible.

TABLE 9.2
Factors Affecting the Performance of Plain Bearing and Electrical Sliding Contact

Factors	Plain Bearing	Sliding Electrical Contact
Mechanical load	Should be as low as possible	Requires a certain minimum force
Sliding velocity	Higher values are preferable	Lower values are preferable
Contact surface geometry	Should be as smooth as possible	Requires a certain roughness of the mating surface
Coefficient of friction	Should be as low as possible	Rather higher values are to be preferred
Resistance to shear, surface hardening	As high as possible	Lower values are preferable
Lubricating layers	Preferable	Can deteriorate the current passage

differ considerably under operating conditions. Table 9.2 lists some of the factors and requirements for contact materials of lubricated plain bearing and electrical sliding contacts.

It is evident that the influencing factors shown in Table 9.2 are contradictory. For example, from a mechanical point of view, *load* should be as low as possible, whereas in electrical contacts a certain minimum force is required to penetrate the surface (tarnish) films. Low *coefficient of friction* is desired for any mechanical tribosystem while high values are preferred for electrical systems. High *sliding velocity* is useful in many lubricated tribosystems, but in electrical contacts lower values are preferable. *Lubrication* is very efficient in mechanical systems, but it can have a deleterious effect on the passage of current in electrical contacts. *Wear* is to be avoided by all means, as it affects both mechanical and electrical stability. *Seizure tendency* is to be avoided by all means in a sliding bearing. However, in electrical contacts formation of welding bridges cannot always be avoided. *Resistance to high temperature*, *thermal conductivity*, *and resistance to chemicals* should be as high as possible in mechanical and electrical contacts. If properly used, the effects of *surface anisotropy and texture* could be very advantageous.

Table 9.3 shows the relations between a number of selected materials' properties and crystal structural defects. Such data may help to understand some features of materials' behavior affecting their mechanical and electrical performances. Few remarks concerning the selection of the mating materials deserve attention. Recent tribological findings indicate that the mating materials for sliding contacts should not have any mutual structural affinity, thereby reducing the tendency to bonding.

Barber and Rabinowicz[179] argued that incompatible metals (those that form immiscible phases when in a molten state) may be preferred in contact applications. Compared to combinations of compatible metals (which have a high degree of solid solubility), such pairs should ensure low friction and wear. A compatibility chart for noble metals is given in Table 9.4. According to compatibility theory, it is reasoned that gold would be highly desirable as one of the contact metals because of its nobility and should be used as the ring in a slip-on-ring assembly. Owing to their hardness, iridium, rhodium, and ruthenium would be preferred for brush materials.

However, these recommendations were not confirmed in practice. A test of compatibility theory can be seen in Antler's experiments where the sliding of rhodium on gold without lubrication was examined.[157] It was found that adhesion of the members was so great that gold prows were immediately formed (see Figure 9.7). Wear and coefficient of friction were actually the same as for gold sliding on gold. A later study showed that there is pronounced adhesion of gold to all platinum group metals.

At the same time detailed studies[26,157] of numerous noble metals, e.g., gold electrodeposits have shown that that the ductility of the metal is the key to determining whether high wear by prow

TABLE 9.3
Mutual Relation between the Crystal Structure Faults and Material Characteristics

	Adjoining Causes			
May Effect the Following Characteristics	**Point Faults (Vacancies, Interstitial Atoms, Substitution Atoms)**	**Line Faults (Dislocations)**	**Area Faults (Stacking Faults, Boundaries, Segregations)**	**Volume Faults (Precipitations, Segregations)**
General				
Anisotropic effects	□	▥	▥	▣
Diffusion effects	■	▣	▣	▥
Resistance to chemicals	▥	▥	▥	▣
Mechanical				
Hardness, yield point	▥	■	■	■
Elongation at rupture	□	■	■	■
Linear modulus of elasticity	□	▥	▥	▥
Impact strength	□	▥	▥	■
Machinability	▣	■	■	■
Magnetic				
Initial permeability	▣	▣	■	■
Remanence	▣	▣	■	■
Saturation	▣	□	▣	▣
Coercitivity	▣	■	■	■
Electrical				
Electrical conductibility	■	▥	▥	▥
Thermal				
Melting point	▥	▥	▥	▣
Dilatation	▣	▥	▥	▥
Thermal conductibility	□	□	□	▥

Note: □, no influence; ▥, influence possible, but weak; ▣, appreciable influence; ■, strong and distinctive influence.

formation will occur. Ductile wrought metals, such as inlays, are prone to adhesive wear, but this tendency can be reduced if they are hard and if contact lubricants are used. The relationship between ductility and adhesive wear lies in the junction growth which permits the area of contact to grow during sliding, and in turn permits large transfer prows and coarse wear debris to form later. Thus, in many cases special studies are necessary for the selection of optimal materials for sliding electrical contacts.

9.2 DRY METAL CONTACTS

9.2.1 Low-Current Contacts

It is well known that in the absence of lubricants, sliding contact of metals occurs only at relatively low contact loads because of the lubricating action provided only by oxide and adsorbed films. As a rule, light-current sliding contacts should combine high wear resistance and low friction with highly stable contact voltage drop. To meet these requirements, contacts with good oxidation and wear resistances made of gold, platinum, rhodium, and palladium alloys are widely used. In addition to high cost these materials are not always suitable to meet the performance requirements such as vibration stability, impact resistance, and reliability under severe weather and extreme conditions.

TABLE 9.4
Compatibility of Noble Metals

	Os	Ir	Re	Ru	Rh	Pl	Pd	Au	Ag
Ag	●	●	●	●	●	◘	◘	◘	○
Au	●	●	●	●	●	◘	◘	○	
Pd	⊡	◘	◘	⊡	◘	◘	○		
Pl	◘	⊡	◘	◘	◘	○			
Rh	◘	◘	◘	◘	○				
Ru	◘	◘	◘	○					
Re	◘	◘	○						
Ir	◘	○							
Os	○								

Note: ○, identical; ◘, compatible; ⊡, partially compatible; ●, incompatible.

Source: From Barber, S. A. and Rabinovich, E., *Proceedings of 26th IEEE Holm Conference on Electrical Contacts*, Illinois Institute of Technology, Chicago, 33–40, 1980. With permission.

Therefore, combining the improved mechanical characteristic of contacts with reliability of current commutation is one of the design solutions for low-current sliding contacts.

9.2.1.1 Effects of Low Current and Electrical Field on Friction

The passage of electrical current through the contact of sliding metals even with low current intensity (0.1–100 mA) increases wear, intensifies oxidation of surfaces, accelerates formation of chemisorption films, and generally degrades the electromechanical characteristics of the sliding contact.[392]

The effect of weak currents and electrical fields is not a crucial factor for low-current sliding contacts. The influence of sliding-induced physical processes in the contact turns out to be more important. The level and stability of the contact resistance may be strongly influenced by sliding generating or braking *a*-spots, altering the real contact area, generation of wear debris, friction transfer, modification of surface layers, hardening, formation of chemisorbed layers on the contact surfaces, and so on.[6,26,157,641,754] Hence, it is of interest to consider the most important friction factors influencing the contact resistance.

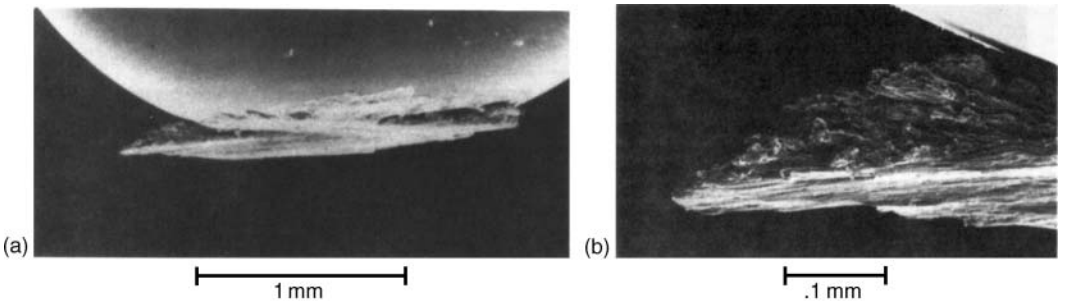

FIGURE 9.7 Gold rider with adherent prow after unlubricated sliding against solid flat. Note layered structure of prow. Conditions: 300 g, 500 passes, reciprocation. (From Antler, M., In *Electrical Contacts: Principles and Applications*, Slade, P. G. Ed., Marcel Dekker, New York, pp. 309–402, 1999. With permission.)

9.2.1.2 Effect of Interfacial Shear

It is known that sliding, even at the microscale levels, causes considerable deformation and wear but also has a strong cleaning effect.[751] It is often referred to as wiping rather than sliding.[6] Wiping may also refer to a single pass of contact members. Repeated wiping leads to fretting wear and is detrimental to contact reliability. Occasional wipes, however, may lead to lower contact resistance. Mechanical wipe lowers electrical contact resistance through the separate or combined actions of the following factors: flattening and smearing of surface asperities to increase the average *a*-spot dimensions, damage of electrically insulating films, and contaminants.[4]

With further miniaturization of connectors, lower normal forces are required. To establish low contact resistance at low normal force, increased contact pressure and wipe at the contact interface are sometimes necessary. Therefore, the optimal wipe lengths and normal force/geometry interactions are needed to establish low and stable contact resistance.

In the case of noble metals or coatings, contact wiping is intended to displace surface contaminants. For common metals wiping action is necessary to remove films, usually oxides, which are present on such surfaces in addition to environmental contaminants. The effectiveness of wiping action is dependent on normal load, geometry and materials of the contact surfaces, nature of surface contamination, and distance of wiping. It is generally known from field experience that even gold-plated contacts need wiping in order to be reliable.

Wiping action on clean, lubricated, and severely contaminated surfaces in precious metal-plated contacts was studied in detail by Brockman et al.[755] The effects of load, geometry, and wiping distance on contact resistance for cylindrical and hemispherical contacts were evaluated. Lubrication and dust conditions were simulated in order to provide severe conditions for wiping action.

It was found that wiping distance of the order of 0.25 mm or less in the range of 0.5 N was sufficient to achieve contact of lubricated and dusted surfaces. At the same time, clean surfaces present no barrier to establishing metal-to-metal interface and wiping action was not necessary. The value of contact resistance can increase or decrease as wiping begins. There are a number of possible mechanisms, which could result in change in contact area, and therefore contact resistance, as wiping, begins. First, the contact area could increase due to tangential stresses introduced as motion begins. This mechanism would result in a decrease in contact resistance. Second, the contact area could decrease at wiping if the film fragments can be trapped in the interface. In this case an increase in contact resistance can be observed. Both effects were observed[755] depending on contact geometry and normal force.

Martens and Pecht[756] examined the effects of wipe and normal force on corroded nickel contact finishes. The phosphorus bronze test coupons plated with 1.25 μm of nickel were exposed to the Battelle class II mixed flowing gas environment for 1 and 2 days to produce an aged contact surface. Experimental results show a significant decrease in the contact resistance with 0.125 mm of wipe, but little decrease in resistance if the wipe continues. Of particular note is the beneficial effect of the back-wipe on the corroded nickel coupons. As is generally accepted, normal force was shown to be the most significant individual variable in decreasing contact resistance, with a combination of high contact pressure and wipe producing the best results in terms of a low contact resistance.

Abbott[757] has presented data on the effects of wipe on cylindrical oxidized copper contacts. The studies were carried out in an environmental chamber in which oxide (C_2O) films were formed to thicknesses ranging from 50 to 200 A. It was shown that wipe can cause further degradation in performance if the wipe distance was shorter than about 0.025 mm. However, at wipe distances >0.025 mm the contact performance was improved. Specific examples of the effectiveness of contact wipe for soft and hard copper are shown in Figure 9.8 and Figure 9.9. It is seen that small amounts of wipe/motion may produce exactly the reverse effect and contact failure. These conclusions are particularly important when the contact normal forces are less than 100 g.

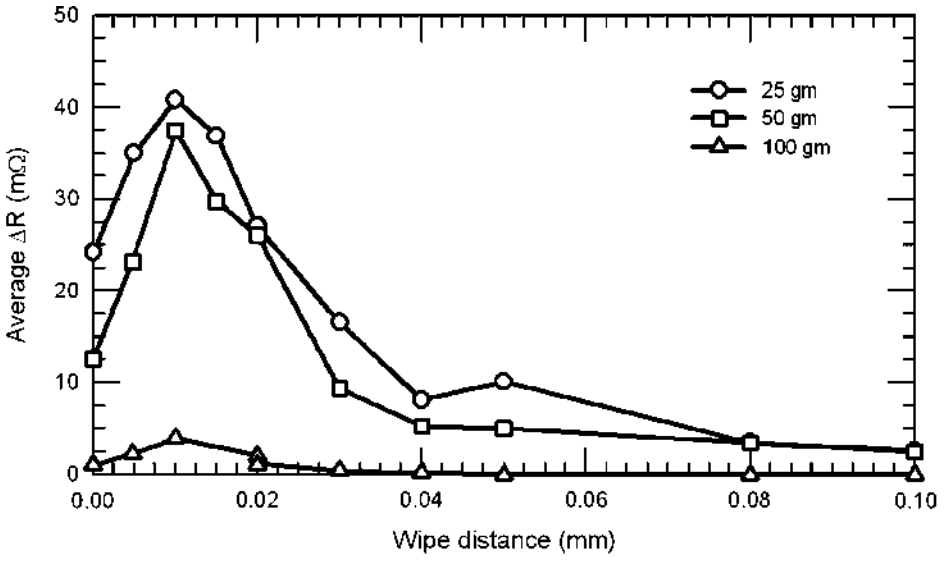

FIGURE 9.8 Contact resistance vs. wipe; effects of force; 3.2 mm soft copper. (From Abbott, W. H., *Proceedings of 38th IEEE Holm Conference on Electrical Contacts*, Institute of Electric and Electronic Engineers, Inc., 219–235, 1992. With permission.)

Fortunately, the results also show that the minimum amount of wipe necessary to achieve low-contact resistance may be relatively low compared to common design practice.

It is generally believed that wiping is helpful in removing films formed on real contact surfaces. For example, investigations by Timsit et al.[758] indicate that wiping is very effective in disrupting

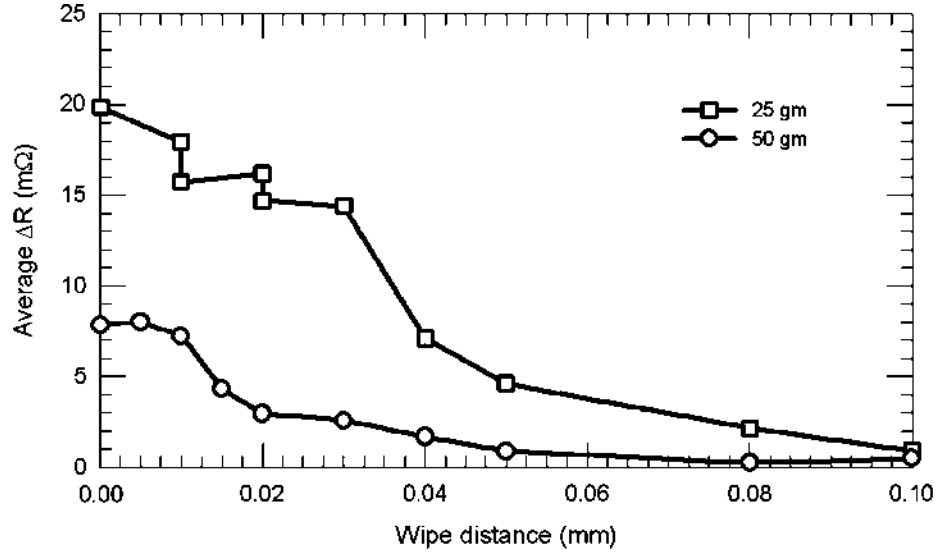

FIGURE 9.9 Contact resistance vs. wipe; effects of force; 3.2-mm hard copper. (From Abbott, W. H., *Proceedings of 38th IEEE Holm Conference on Electrical Contacts*, Institute of Electric and Electronic Engineers, Inc., 219–235, 1992. With permission.)

oxide films in aluminum–aluminum contacts. It is also known that small disturbances or wiping across contaminated regions can degrade electrical performance.

Probe measurements were made by Malucci[759] on corroded test samples to show the effect of wiping on contact resistance. Data are provided for two types of films: oxidized copper and corrosion on porous gold due to flowing mixed gas tests. The results in both cases show contact resistance is reduced by nearly two orders of magnitude for 0.25 mm wipe. Figure 9.10a shows the results of 100 random measurements after environmental corrosion of gold samples. A large difference is seen between the wipe and no wipe conditions. It would appear that the no wipe results exhibit the presence of a significant film at the interface.

Using a developed model of degradation, the Monte Carlo analysis was conducted for the gold (see Figure 9.10b). In this case the film thickness was estimated by comparing the gold no wipe data to the copper results at the 50 percentile point. The Monte Carlo analysis produced results that agreed reasonably well with observation.

It may be pointed that in many investigations on contact materials, the contact resistance is measured without applying a wiping motion which makes the data not completely adequate to real situations.

9.2.1.3 Adhesion, Transfer, Wear Debris Formation, and Surface Transformation

Noble metals and alloys are most frequently used as electrical contact materials, particularly in devices functioning in dry and hydrocarbon-free inert atmospheres. Sliding wear is a key determinant of the sliding contact performance with metal transfer, friction, and electrical noise affecting contact behavior. A number of factors affect the wear and electrical behavior of such materials.[6,26,148,159,760,761] For pin-on-flat type sliding contacts, the wear process of unlubricated

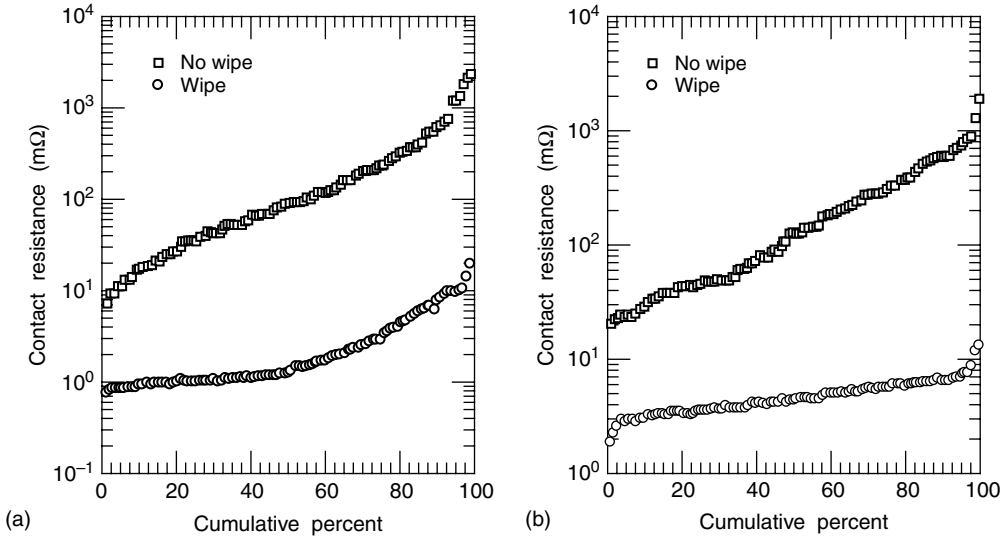

FIGURE 9.10 (a) Results of 100 random measurements of contact resistance for the wipe and no wipe cases after environmental corrosion of gold samples (samples: plated with of 0.5 μm hard gold over 0.75 μm nickel over brass base material; contact probe: 3/8 in. copper wire plated with 2.5 μm gold over 2.5 μm nickel; constant load of 100 g; 2 days exposure to the class-II FMG environment); (b) Monte Carlo analysis for the gold samples (experimental conditions: similar to (a). (From Malucci, R. D., *Proceedings of 40th IEEE Holm Conference on Electrical Contacts*, Institute of Electric and Electronic Engineers, Inc., Chicago, 131–144, 1994. With permission.)

soft, ductile metals (Au, Ag, Pd, Sn, and solders) is typically of adhesion mode.[59,157,761] It occurs in mild or severe regimes depending on load, and differs significantly in surface damage.

For pure gold, the following stages of wear were found:

1. Prow formation on the pin
2. Intermediate stage of roughening and work hardening
3. Transition to rider wear

The gold alloy in the age-hardened condition is significantly harder than pure gold; however, it also wears by adhesion mechanism. For a palladium-alloy pin sliding on a gold-alloy plate, the above-mentioned three stages of wear were also identified.[761] Initially, a prow consisting of plate material is formed on the pin, and as the prow grows, the track widens. Debris is back transferred from the prow to the plate, and frequently the debris is reincorporated into the track. When sliding occurs repeatedly over the same track, there is a transition to a process called rider wear in which in the severe regime only the smaller member loses metal by transfer. This transition depends on the material, load, track length, and surface roughness, usually coming within the expected lifetime of components.

Both the surface and the near-surface material can be important in wear mechanisms of noble metals. For some wear couples, delamination theory adequately explains the wear process, where crack nucleation in the near-surface material occurs due to accumulation of plastic deformation and subsequent crack extension leads to debris formation.[762] Other experiments have shown that characteristic subsurface regions are formed during wear tests.[763] The results of a wear experiment can be altered by the test apparatus or by the specimen stiffness and the geometry of the specimen and counterface materials.[764]

Segregation of elements to wear tracks during sliding of a gold base and palladium base alloys has been observed and is believed to affect wear behavior.[114,765–767] The wear experiments with an oscillating pin simulating an electrical contact switch were conducted in switch atmospheres of dry He, dry CO_2 and dry air. The analyses using scanning Auger microscopy combined with Ar-ion beam sputtering revealed that the wear tracks formed in all three atmospheres contained an approximately 6-nm thick surface film consisting of S, Ag, Cu, C, O, and Pd; the Pd was transferred from the pin as small debris particles. The sulfur in this thin surface film may be present as Ag and/or Cu sulfides. The observed increase in the contact resistance and decrease in the coefficient of kinetic friction are attributed to the growth of thin sulfide layers on the wear track surfaces.

Segregation of sulfur to the wear track was also observed for gold and palladium alloys by Pope and Peebles.[766] Experiments were made with an in situ, pin-on-flat device inside the scanning Auger analytical system. Sulfur segregation occurred after as few as ten wear cycles in the 700-torr 0.05% oxygen in nitrogen ambient for both as-received and clean wear track surfaces. The source of the sulfur was the bulk (or near-surface) material rather than gaseous contaminants. No sulfur segregation was observed in the 10^{-7}-torr nitrogen or the 10^{-6}-torr oxygen ambient.

Wear mechanism depends strongly on hardness and structure of contact materials. Four types of wear were found by Liljestrand et al.[148] for electroplated nickel-hardened gold (0.2–2.5 wt% Ni): severe, mild, adhesive brittle, and brittle (Figure 9.11). The occurrence of these wear types is governed by nickel content (hardness) and plating current density (internal stress). Adhesive brittle wear caused by adhesion in combination with a high internal stress for gold with medium high Ni is characterized by low coefficient of friction and high wear rate. The large flat wear particles following this type of wear are formed with the aid of weak zones forming the banded structure seen in most electroplated deposits. Severe wear dominated at low nickel contents similar to soft gold. Mild wear and low coefficient of friction occurred at high nickel contents. Hard gold with the highest nickel content wore by brittle damage (Figure 9.11).

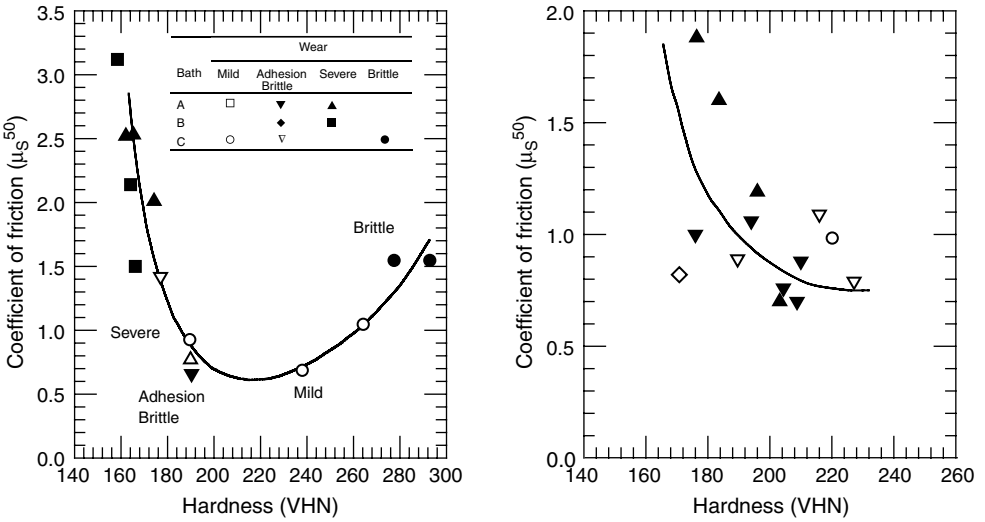

FIGURE 9.11 Dependence of the coefficient of friction on the hardness of nickel hardened gold when wear tested against springs with clad gold and Au–25Ag–5Cu. (From Liljestrand, L-G., Sjogren, L., Revay, L., and Asthner, B., *Proceedings of 30th IEEE Holm Conference on Electrical Contacts*, Illinois Institute of Technology, Chicago, 53–60, 1984. With permission.)

According to Antler,[157] the ductility of the metal is the key in determining whether high wear by prow formation will occur. Brittle gold, such as that containing cobalt which has an elongation below about 0.4%, is preferred to more ductile deposits. Ductile hard and soft pure or alloyed gold platings, with or without co-deposited organic polymer, are prone to adhesion wear. Thus, either deposit hardness or its polymer content is not a reliable guide to the selection of electrodeposited gold for low adhesion wear. Ductile wrought metals, such as inlays, are also prone to adhesion wear, but this tendency can be reduced if they are hard and if lubricants are used. The relationship between ductility and adhesion wear lies in junction growth which permits the area of contact to grow to a large size during sliding, and in turn permits large transfer prows and coarse wear debris to form later.

The mechanism of electrical contact resistance between light-loaded sliding surfaces of nonnoble metal (Sn–Pb) contacts was investigated by Saka et al.[752] It was found that the increase in contact resistance of nonnoble or base metal contacts results from oxidation of metal wear debris entrapped in sliding contact. Wear debris generated by sliding may accumulate at the contact interface and oxidize, thus separating the surfaces electrically and increasing the contact resistance. It was shown that the modulated contact surface (see Figure 9.12) that had cavities for trapping the oxide wear debris showed low contact resistance under sliding, particularly under fretting motion. This result suggests that nonnoble metals with modulated surfaces could be used as substitutes for noble metals. The modulated contact surface used for trapping the wear particles can also be used to reduce friction. The friction coefficient of the modulated surfaces will be lower than that of a flat surface because the wear particles are entrapped in the cavities (see Figure 9.13).

An important aspect of sliding wear of tin and tin–lead alloys is the effect of intermetallic compounds on their coefficient of friction and contact resistance. The intermetallic layer, such as Cu_6Sn_5 and Cu_3Sn for a copper-based substrate, is hard and has lower electrical conductivity than tin.

It has been found by Hammam[173,768] that there are three stages in wear, described as plowing of tin, which is actually adhesion wear (stage I), sliding over the intermetallic compound (stage II), and penetration of the intermetallic compound with sliding over the substrate (stage III).

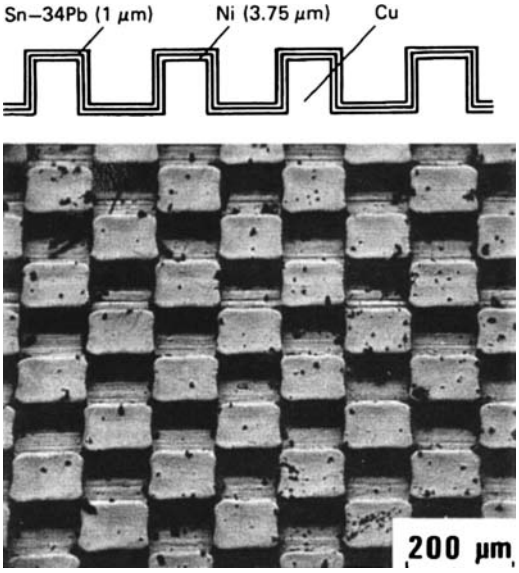

FIGURE 9.12 Scanning electron micrograph of the modulated surface. (From Saka, N., Llou, M. G., and Suh, N. P., *Wear*, 100, 77–105, 1984. With permission.)

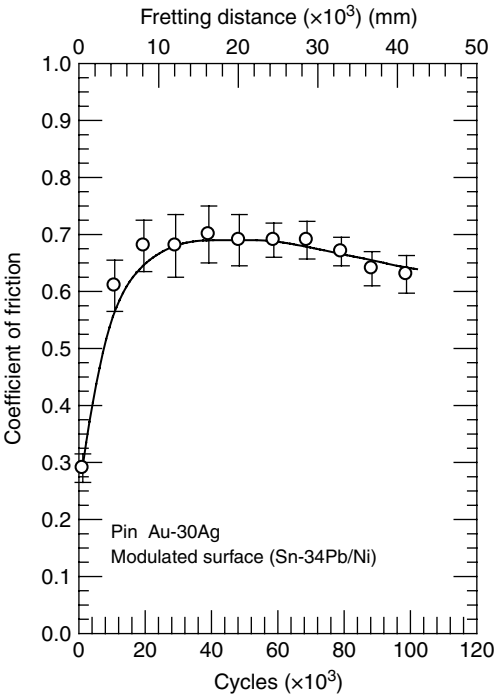

FIGURE 9.13 Friction coefficient of modulated surface (Sn–34Pb/Ni/Cu) and Au–30Ag pin combination. (From Saka, N., Llou, M. G., and Suh, N. P., *Wear*, 100, 77–105, 1984. With permission.)

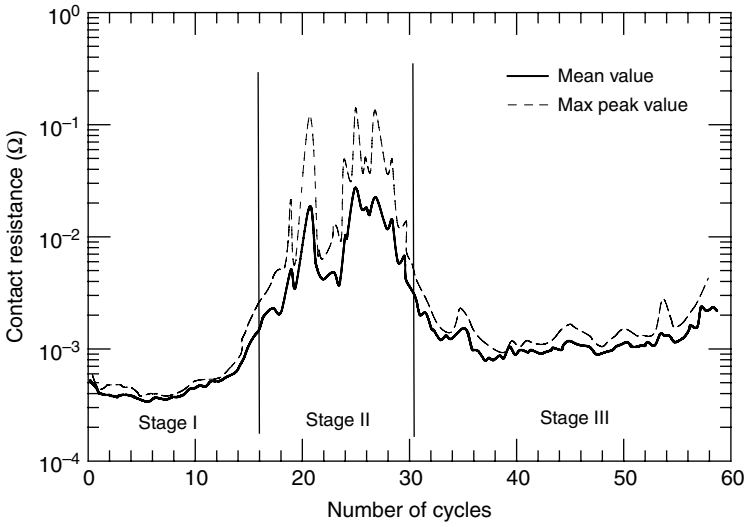

FIGURE 9.14 The variation in contact resistance during a test sequence for ELD (10 μm) with a normal force of 10 N. (From Hammam, T., *Proceedings of 42nd IEEE Holm Conference on Electrical Contacts*, Institute of Electric and Electronic Engineers, Inc., CHMT, Chicago, 321–330, 1996. With permission.)

The differences between the stages regarding friction, wear, and electrical properties were significant. Figure 9.14 shows the contact resistance corresponding to each stage; the mean value and max peak value for every half cycle are illustrated. The termination of stage 1 marks the end of the most efficient operation of a tin-plated contact. The sliding of tin and tin–lead should be considered as a successive generation of interfacial materials which changes the characteristics of the contact as they appear due to wear. It is proposed[768] that differences between the tin coating techniques regarding friction, wear, and electric properties are mainly correlated to differences in thickness of the pure residual tin layer as well as differences in thickness of the intermetallic compound.

The sliding wear processes described above affect strongly the mechanism of current conduction in the interface. Each factor directly affects the tangential forces (friction) developed in the contact and simultaneously the electrical resistance between the contact members. Possible correlations between wear and contact resistance are discussed in detail by many authors.[6,26,752,760,761]

The *rider hardening* does not reduce friction because the latter is dependent on the softer material of the contact pair. Deformation and work hardening of the rider, however, will cause an increase in the resistivity of most contact metals. This factor results in a relatively slight but steady increase in the contact resistance.[760] Furthermore, Pope and Peebles[761] showed that work-hardening in the plate tracks does not affect significantly the contact resistance.

Adhesion is the principal component of friction force in the beginning of sliding. As the tangential load is first applied to the static contact, it is the growth of junctions and their simultaneous fracture that produces high static friction compared to more random formation and fracture of dynamic junctions. Contact resistance during the adhesion periods (stick) is low because of the large load-bearing area and metal-to-metal contact. At the instant of shear, and during the subsequent contact motion (slip) the resistance becomes very high while the friction falls to an instantaneous low level as a result of the low dynamic contact force. In severe conditions a complete electrical breakdown can happen (see Figure 9.15). Contact resistance variation (noise) is most severe in the periods of stick–slip.

The *growth of a wedge* produces a small increase in resistance. Its loss usually causes a corresponding drop following an instantaneous high resistance noise while the prow particle

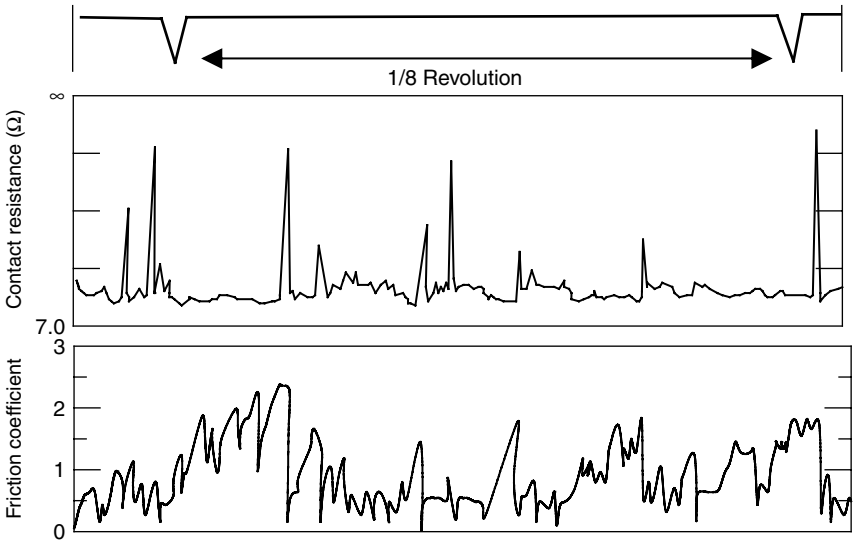

FIGURE 9.15 Stick–slip and electrical opens. Gold reader on gold flat; 0.1 cm/s, 0.1 N. Recorder time constants: 0.003 s. Severe sticks produce contact separation. (From Antler, M., *ASLE Transactions*, 11(Mar), 240–260, 1962. With permission.)

rolls under the rider. Friction simultaneously decreases drastically during the rolling of the prow. The cutting and plowing action of the hard prow on the softer flat produces high frictional forces, but since the contact is quite intimate the resistance is low during the cutting action.

After *loose wear particles*, regardless of origin, get into the wear track, both friction and noise become erratic. The particles create the resistance, which is the sum of two constriction resistances and the bulk resistance of the particle, each of which is inversely proportional to the diameter of the particle. Therefore, as the particles become finer or smaller in size, their effect on contact resistance increases considerably. In addition, particles may tend to agglomerate, causing still further increases in resistance when contacted by the rider. They can accumulate on the rider; loosely attached compared to the prow, transfer back to the ring at any discontinuity of motion (impact reversal, etc.), and produce debris piles of high electrical resistance in subsequent passes of the rider. Embedment of individual particles or adhering particles will cause increased resistance, both because of their resistance and their mechanical effect on the contact stability. Some examples of topography of wear tracks formed at dry friction of precious metals are shown in Figure 9.16.

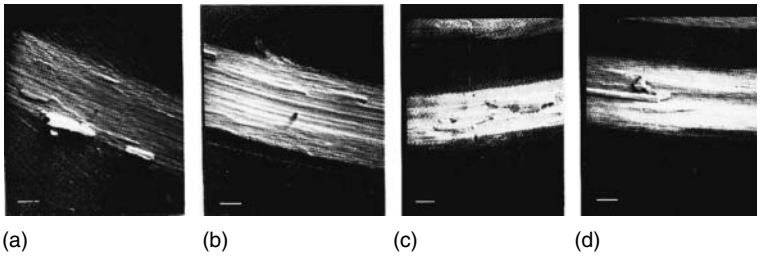

FIGURE 9.16 Topography of wear tracks on gold alloy plate (ASTM B540) formed by palladium alloy pin (ASTM B540) after (a) 1000 cycles in 4.3×10^5 Pa nitrogen, (b) same track as (a) except 5000 cycles, (c) 10,000 cycles in 9.3×10^4 Pa, 5% oxygen in nitrogen, and (d) same track as (c) except a different location (bar equals 100 μm). (From Pope, L. E. and Peebles, D. E., *Tribology Transactions*, 31(2), 202–213, 1988. With permission.)

In general, it has been found[157,760,766,767] that increase in wear rate is accompanied by increase in friction and decrease in contact resistance and noise. There is an inverse relationship between friction coefficient and contact resistance (see Figure 9.17).[766] When friction coefficient increases, there is a decrease in contact resistance. Conversely, an increase in contact resistance and noise often signals a decrease in wear rate and friction. Accumulation of wear debris, on the other hand, tends to reduce friction and increase the noise.

The increase in contact resistance is concomitant with the transition to the third stage of wear when rider wear occurred. It is suggested[761] that two factors explain the increased contact resistance for Pd (rider)–Au (plane) systems with the transition to rider wear. First, after the ridges were formed in the plane track, the pin subsequently would make contact with one or more ridges continuously rather than the track; therefore, the contact area was greatly reduced. Second, the greater reactivity of the palladium relative to gold probably explains the increased contamination on the ridges and on the pin scar. These contaminants could be expected to form a higher resistance interface between the pin and plate. Partial breakup and reformation of the ridges could explain the variability in contact resistance after rider wear initiated.

9.2.2 High-Current Contacts

9.2.2.1 Effects of Electrical Current on Tribological Behavior

Physical–mechanical properties of contact surfaces vary under high currents in unlubricated contacts, giving rise to such processes as creep, seizure, oxidation, and transfer in addition to severe wear.[401,769–771] The friction coefficient often rises as the current density grows,[772] though for certain material combinations it may stay invariable or even decrease.[771,773]

The change in frictional characteristics of the contacts without lubrication in the presence of high alternating currents and light mechanical loading was investigated by Brailford[401] in aluminum, copper, brass, and tin interfaces. Passage of current through the interface was found to gives rise to very high temperature at the contact regions. Although the temperature of these regions rises

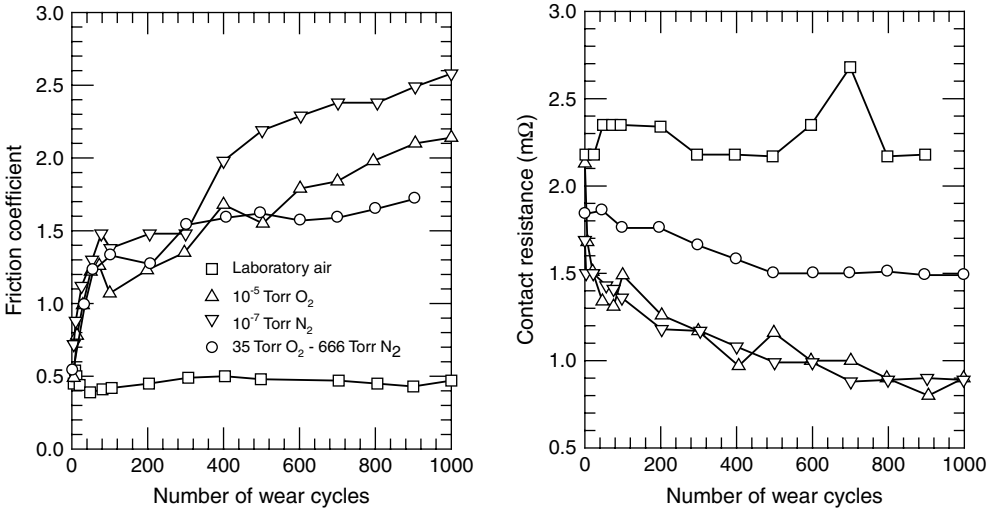

FIGURE 9.17 Representative values for coefficient of friction and contact resistance as a function of wear cycles in ambient of laboratory air, 10^{-7} torr nitrogen, 10^{-6} torr oxygen, and 700-torr 0.05 oxygen in nitrogen. (From Pope, L. E. and Peebles, D. E., *IEEE Transactions on Components, Hybrids and Manufacturing Technology*, 10(1), 47–55, 1987. With permission.)

above the softening point of metal and contact growth might be expected, leading to increased force of friction this is counterbalanced by the following factors:

- Reduction of the shear strength as the contact spot temperature rises
- Keeping of bulk temperature of material below the softening point, whereas the contact spot temperature is increased to the level of softening and even melting

Both these factors will tend to inhibit the growth in contact area, and so the effect of the current on friction will be determined by the dominating process. It was shown that in the case of aluminum mated to aluminum, brass, copper, or tin, the passage of 50 Hz AC current raises the temperature of the contacts spots above 200°C and exerts a profound effect on the mechanical performance of these contacts.

In the case of copper-to-copper interfaces, the effect of current was not apparent because the contact temperature was limited to values well bellow the melting point. For brass-to-brass surfaces, a tendency towards increased friction with increasing contact temperature was observed. Tinned surfaces mated together showed a large increase in friction up to the melting point of the tin and appeared to be the best for power connection applications. The performance of aluminum power connectors which rely on frictional forces to maintain mechanical integrity may be affected during fault current conditions. The effect of contact spot temperature on the friction coefficient of the test contact pairs is shown in Figure 9.18.

Electrical current density is the most important factor influencing tribological behavior in high power pantograph-wire systems. Experiments of Zhang et al.[772] simulating the behavior of such systems (dry sliding of a copper pin specimen against copper–chromium) show that wear rate and friction coefficient increase greatly (see Figure 9.19). Moreover, electrical current and tribological parameters have combined effects on both electrical conductivity and tribological properties. It was

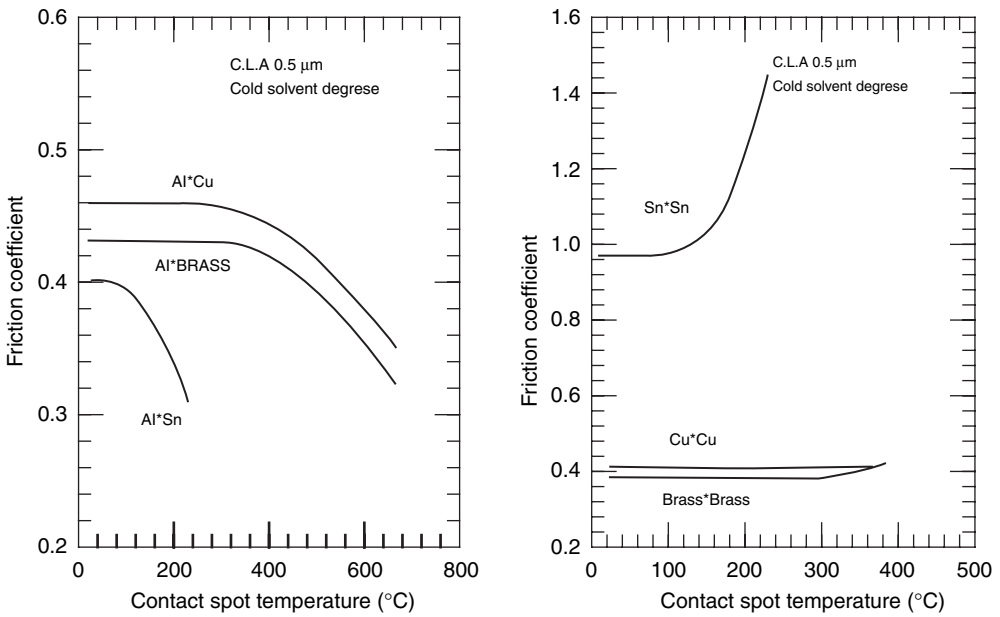

FIGURE 9.18 Friction coefficient of dissimilar and similar surfaces as a function of increasing contact spot temperature. (From Brailford, J. B., *Wear*, 25(1), 85–97, 1973. With permission.)

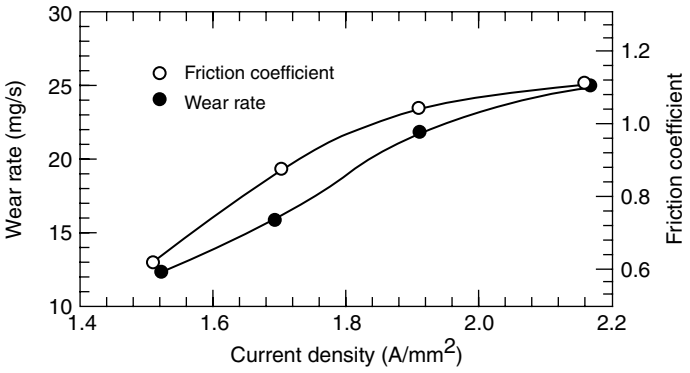

FIGURE 9.19 Effect of current density on tribological properties of dry sliding pair copper (pin)—copper–chromium Cu–Cr alloy (Cr 0.5 wt%) disk. (From Zhang, Y., Sun, I., Chen, Y., and Shangguan, B., *Proceedings of the 4th China International Symposium on Tribology*, Xiàn, China, 35–40, 2004. With permission.)

shown (Figure 9.20) that there is an instantaneous relation between the fluctuation of friction coefficient and electrical current in sliding. When the friction coefficient gets to its peak value, the electrical current also reaches its peak value.

Severe plastic deformation takes place on the contact surfaces due to effects of normal and friction forces, frictional heating and contact resistance, and electrical arc (see Figure 9.21). At sliding with current density higher than 2 MA/m^2, microstructural fibers in the subsurface layer of copper bend in the friction direction, deformation thickness is about 50–100 μm; the deformation degree is much less if electrical current is absent at sliding. Considerable deformation indicates that the material near the sliding surface is softened; which helps friction surfaces to contact closely and causes the friction coefficient to grow.

Rather unusual results were obtained in experiments with deformation-processed composites (composite material whose morphology is produced at heavy deformation processing), e.g., Cu–Nb composites.[773,774] This composite is considered as a promising material for electrical contacts in heavy-current devices. Liu et al.[774] studied friction and wear behavior of Cu–Nb composites when an electrical current passed between the components of the sliding couple. The wear rate and the

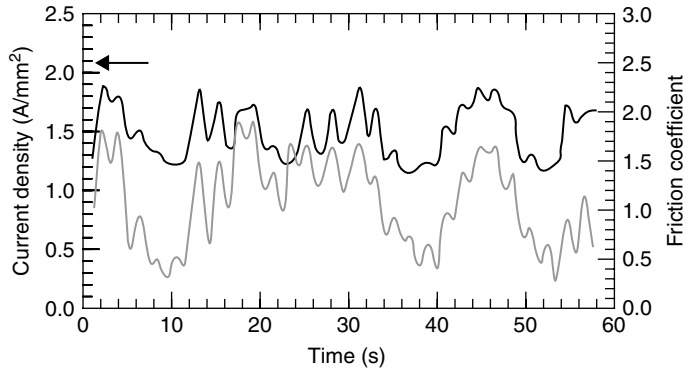

FIGURE 9.20 Instantaneous relation between current density and friction coefficient. Dry sliding between copper (pin) and copper–chromium Cu Cr alloy (Cr 0.5 wt%) disk.[772] (From Zhang, Y., Sun, I., Chen, Y., and Shangguan, B., *Proceedings of the 4th China International Symposium on Tribology*, Xiàn, China, 35–40, 2004. With permission.)

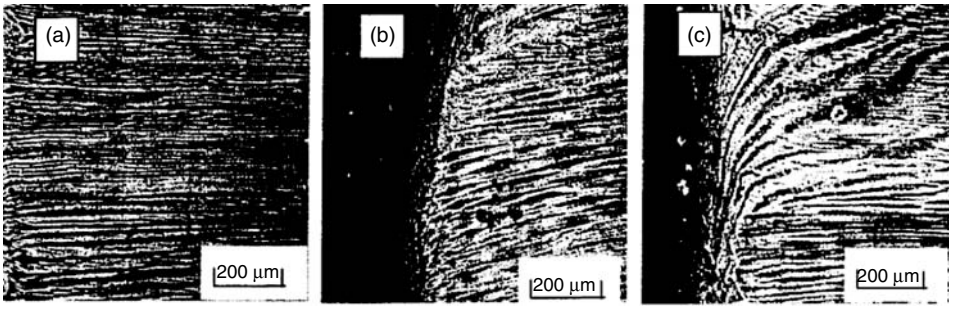

FIGURE 9.21 SEM morphologies of the pin specimen: (a) original morphology, (b) morphology after sliding without current; (c) morphology after sliding with current density 2.158 A mm^{-2} (Observation of the specimen perpendicular to the sliding surface). (From Zhang, Y., Sun, I., Chen, Y., and Shangguan, B., *Proceedings of the 4th China International Symposium on Tribology*, Xiàn, China, 35–40, 2004. With permission.)

coefficient of friction both increased initially with the increase in current density of 0.287 MA/m^2 (see Figure 9.22), but then decreased with further increase in current density. The initial increase in the wear rate and coefficient of friction with the application of electrical current may result from the microwelding of asperities on the contacting surfaces. As the current density increased, both temperature and oxidation rates increased. This resulted in a thicker oxide film on the surfaces which, in turn, caused considerable reduction of adhesion. Thus, frictional shear occurred at the interface, as opposed to the bulk material in the earlier case. Consequently, both wear rate and the coefficient of friction decreased with the higher current density.

The tribological behavior of Cu–15 vol% Cr composite in situ under dry sliding against steel was studied by Chen et al.[773] Within the studied range of electrical current (up to 50 A), normal pressure (up to 0.56 MPa) and sliding speed (up to 5.83 m/s), coefficient of friction and wear rate decreased with increasing electrical current (see Figure 9.23), whereas the bulk temperature increased. A hardened surface layer, consisting of a refined structure, oxides; wear debris, back transferred steel, and arc-eroded droplets, was observed after sliding. The thickness of the subsurface deformation layer decreased with increasing electrical current (see Figure 9.24). The hardened surface layer accounted for wear rate reduction as electrical current was applied.

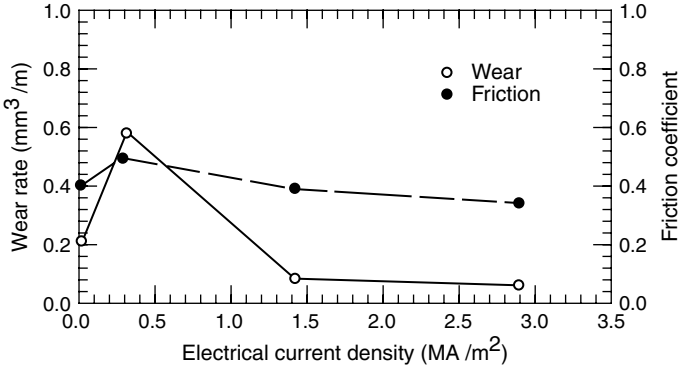

FIGURE 9.22 Variation of friction and wear with electrical current density for Cu–20%Nb in situ sheet composite, sliding against tool steel at a sliding speed of 0.25 m/s, and a normal pressure 0.68 MPa. (From Liu, P., Bahadur, S., and Verhoeven, J. D., *IEEE Transactions on Components, Packaging and Manufacturing Technology, Part A*, 17, 616–623, 1994. With permission.)

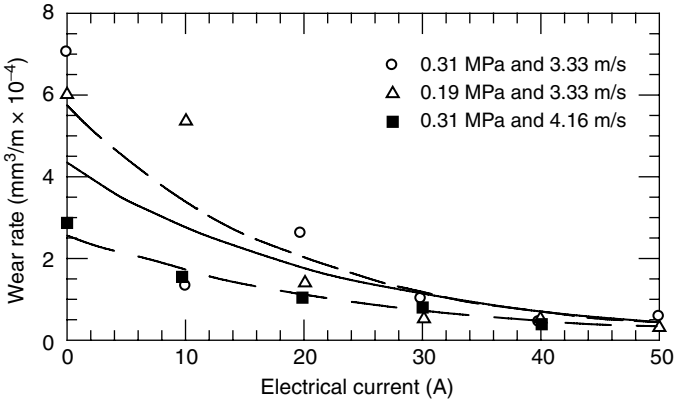

FIGURE 9.23 Variation of wear rate with electrical current for Cu–15 vol% Cr sliding against a hardened AISI 53100 steel disk under three testing conditions. (From Chen, Z., Liu, P., Verhoeven, J. D., and Gibson, E. D., *Wear*, 203–204, 28–35, 1997. With permission.)

The mechanism of a strong effect of heavy electrical current on the tribological behavior was proposed by Chen et al.[773] According to the proposed mechanism, when electrical current is applied to the sliding interface, arc erosion occurs and the temperature increases drastically. As a result, both the composite and steel specimens are softened, which results in a lower coefficient of friction and thinner subsurface deformation layer. Due to electric arc, the steel disk is severely eroded and a significant number of steel particles are transferred back to the composite pin during sliding. Hence, as a result of hardened layer formed, the wear rate of the composite decreases with increasing electrical current whereas the characteristic features of the steel disk surface are deep cuts in the sliding track.

9.2.2.2 Influence of Electric Fields

Detailed study of high-current copper (wire)/steel (disk) contacts[770,771,775] has shown that an electric field and its direction play an important role in friction and wear. Wear is directly affected

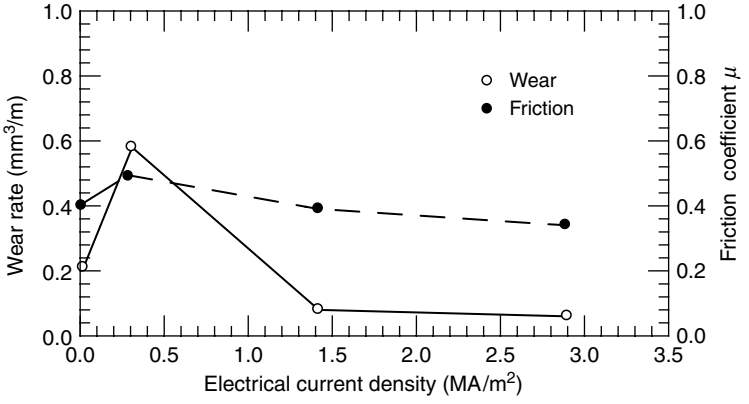

FIGURE 9.24 Variation of subsurface deformation thickness with electrical current for Cu–15 vol% Cr electrically sliding under a normal pressure of 0.31 MPa and at a speed of 4.16 m/s. (From Chen, Z., Liu, P., Verhoeven, J. D., and Gibson, E. D., *Wear*, 203–204, 28–35, 1997. With permission.)

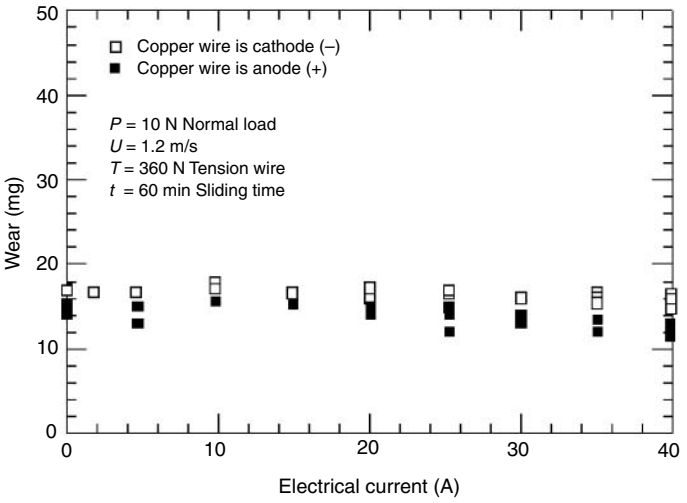

FIGURE 9.25 Effects of electric current and its polarity on the wear of copper wire. (From Bouchoucha, A., Zaidi, H., Kadiri, E. K., and Paulmier, D., *Wear*, 2003–2004, 434–441, 1997. With permission.)

by the presence of an electric current and its polarity (Figure 9.25). This effect was confirmed when the sliding speed (see Figure 9.26) and the normal load were varied.

The passage of electric current favors oxidation by increasing the surface temperature and modifies the mechanical properties of the oxides and substrate. The nature of the oxides that develop at the rubbing surfaces determines the behavior of friction and wear.

At high electric fields oxidation is activated and the oxide layer grows on the wire friction track (copper). Upon reaching a critical depth, the oxide layer is broken by the ploughing action of hard asperities of the disc or hard wear debris. The removed oxide is mixed with the transferred copper in the interface and thus the contact between the oxide layer and a mixture of transferred copper and other oxides on the disc reduces wear. As a result, this layer protects the copper from wear, but contact resistance starts to increase and fluctuate (see Figure 9.27).

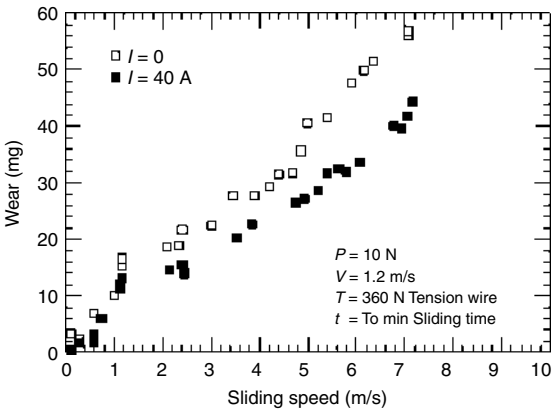

FIGURE 9.26 Effects of an electric current on wear in a copper/chromium steel sliding contact in various environments. (From Bouchoucha, A., Zaidi, H., Kadiri, E. K., and Paulmier, D., *Wear*, 2003–2004, 434–441, 1997. With permission.)

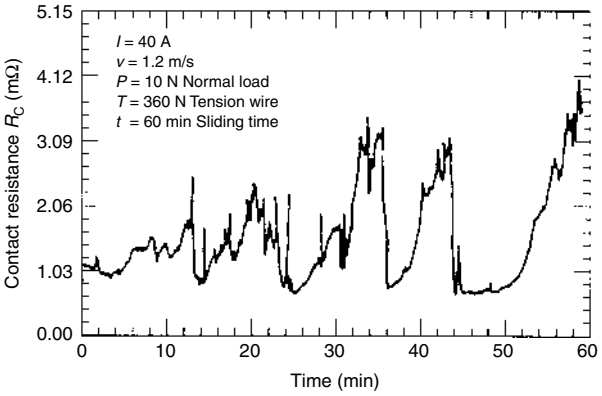

FIGURE 9.27 Evolution of electrical contact resistance with time when the wire is the anode. $I^+ = 40$ A. (From Bouchoucha, A., Zaidi, H., Kadiri, E. K., and Paulmier, D., *Wear*, 2003–2004, 434–441, 1997. With permission.)

The electric field direction increases the oxide layer growth on the wire friction track when it is the anode. However, if the wire is cathode, iron oxide and hard abrasive chromium oxide particles form at the interface. This leads to high friction and severe wear, especially when the electric field intensity is high. In the absence of oxidation, the electric field has no significant influence on friction and wear. This result is confirmed by their behavior in an inert argon atmosphere. The analysis[775] has shown that the quantity of iron transferred to the copper increases with the electric field intensity, especially if the copper is the anode.

9.2.2.3 Effect of Velocity

The results of the above-mentioned experiments[772,775] suggest that the working conditions of the high-current contacts are more severe under high sliding speed (see Figure 9.26), partly due to more severe wear and partly due to the relatively higher friction coefficient, which increases the friction heating and finally weakens material near the sliding surface. In the presence and absence of electrical current, the differences in wear rates and friction coefficients increase with augmenting the sliding velocity, as seen in Figure 9.28. Hence, it is apparent that the passage of electrical current alters the relation between wear rate, friction coefficient, and sliding speed. Under the same current, the increase in sliding velocity not only enlarges the current fluctuation, but also decreases

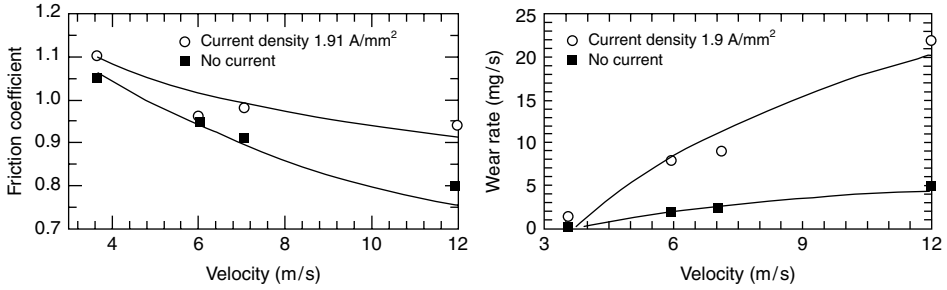

FIGURE 9.28 Effects of velocity on tribological behaviors of copper under dry sliding against copper–chromium alloys. (From Zhang, Y., Sun, I., Chen, Y., and Shangguan, B., *Proceedings of the 4th China International Symposium on Tribology*, Xiàn, China, 35–40, 2004. With permission.)

the real current passing through the contact surfaces. That is, the electrical conductivity of the sliding pairs decreases with the increase in sliding velocity.

In addition, it is worthwhile to mention that other factors control the performance of sliding contacts under high velocities, such as oxidation, which exerts a contradictory effect on the service characteristics. In order to control friction-generated heat, the materials should possess a low friction coefficient. The existence of surface film increases the contact resistance, but helps to decrease the friction coefficient. On the other hand, the film formed by oxidation might lead to a high wear rate. The close contact and large contact area help to obtain lower contact resistance, but, in turn they can also contribute to the growth of the friction coefficient.

Problems may appear when selecting pick-off materials for a high-speed railroad transport. The limitation in tribological properties of pantograph-wire system has gradually become clearer. High sliding velocity and current density impair both the tribological behavior and electrical conductivity in such sliding systems. One problem is the severe wear, and another is decrease in current conductivity due to deterioration of the contact surfaces.[776–779]

9.2.2.4 Effect of Material Combination of Contacting Members

The electric current effect on the interfacial processes involving metal transfer, oxidation, wear debris, and subsurface layer formation is dependent on the contact element materials. For instance, the composition is important for multiwire brush sliding on contact ring. Chen and Vook[780] found the asymmetry of the contact resistance with respect to whether Cu was sliding on Al or vice versa. The contact resistance of the Al brush–Cu slip ring system is always higher than when the metals are reversed, as shown in Figure 9.29. This result appears to result from the formation of Al–Cu alloys in the interface region. A similar phenomenon was not observed in the Cu brush–Al slip ring case. Examination of the slip ring surface topography and wear debris has shown that the slip ring surface became rough and the wear particles became larger after several thousand rotations. These phenomena explain why the contact resistance of the Al brush–Cu slip ring system becomes unstable. In the Cu brush–Al slip ring system, however, a low and stable resistance is maintained because in this case aluminum transfers to copper.

Heating of contact spots by electric current and temperature distribution in the contact zone are conditioned by the current passage mechanism in the sliding contact and compatibility of the properties of the elements in contact. Some specific effects of the electric current heating on the metal contact spots are contrasted to those of frictional heating described in Section 5.2. In general,

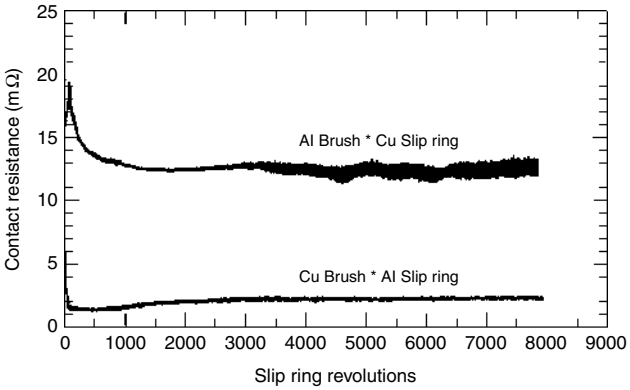

FIGURE 9.29 Contact resistance vs. slip-ring revolutions using 10-A current. (From Chen, J. C. and Vook, R. W., *Proceedings of 31st IEEE Holm Conference on Electrical Contacts*, Illinois Institute of Technology, Chicago, 101–106, 1985. With permission.)

the significance of the current-generated heat effect on the heavy-current metal sliding contacts evokes no doubts. Moreover, along with the heat and electroerosive effects, some other factors on the effect of current on the friction processes can also be envisaged.

9.2.2.5 Electroplastic Effect in Sliding Contact

In a theoretical study of free electrons drifting through the metal lattice, it was shown that flow of electrons can alleviate motion of dislocations in the electron drift direction.[529] This implies that the mechanical properties of metals could be affected by the flow of free electrons. The effect is called electroplasticity and manifests itself in a dramatic increase in material ductility. Overview of the electroplastic effect in metals is given by Troitskii[540] and Specher et al.[522] It is generally believed that the effect is a result of the interaction between electrons and dislocations, although some controversy still exists regarding the exact nature of this electron–dislocation interaction. The electroplastic effect is discussed in detail in Chapter 6. In this section, attention will be placed on the possible effect of electrical current on the frictional characteristic of metals.

The effect of electrical current on friction of different metals under sliding conditions was examined by Konchits.[781] Slow sliding was used to estimate the plastic deformation and heating in the friction zone when avoiding the electric erosion. For this purpose, microtribometer was used to study the friction behavior of steel ball (ball bearing steel, analog of AISI 52100) of radius $r = 0.5$ mm sliding over a plate of another metal (lead, tin, copper, and silver) at low velocity ($v = 2.25$ μm/s) and load ($N = 0.05$–0.4 N). The deformation component of friction coefficient, μ_d, was determined by the friction track width, d, using the Spurr formula $\mu_d = 2d/3\pi r$.[782] The adhesion component of friction coefficient, μ_a was determined by subtracting μ_d from the total friction coefficient μ. Preliminary investigations and computations for the test materials have shown that the constriction resistance is small compared to the total contact resistance R_c at any current; i.e., R_c is comprised almost entirely of the resistance of the tarnish film on the steel ball and partially of the resistance of the film on the samples. In this case, the use of the modified Bock formula for temperature rise due to the passage of current in the friction zone is justified.

$$\Delta T = (fvN + U_c I)/[\rho(\lambda_1 + \lambda_2)a], \tag{9.1}$$

where I is the current; U_c is the contact voltage drop; λ_1 and λ_2 are the thermal conductivities of the contact bodies; a is the contact zone radius. The effect of electrical current on the friction force and voltage drop is depicted in Figure 9.30, whereas Table 9.5 and Table 9.6 provide the results of numerical calculations.

Sliding over soft metals (see Figure 9.30a), e.g., tin or lead, is characterized by stick–slip behavior. Therefore, the maximal points, F_{st} in the figure, characterize the static friction and the minima stand for the dynamic behavior. As the electric current passes through the contact, F_{st} increases, the stick period of the surfaces becomes longer, and the real contact spot corresponding to stick enlarges too. These variations are especially evident when the current density is $j \cong 10^4$ A/cm^2 and becomes intensified with further increase of j. It should be emphasized that when the current initiates changes in the frictional behavior of the system, both volume and surface temperature of the samples remain essentially lower than the softening temperature.

In copper and silver tests the friction forces are relatively stable and the stick–slip behavior is not observed (see Figure 9.30b). As shown in Table 9.6, variations in the friction parameters are negligible when the current density in the contact spot is below 10^4–10^5 A/cm^2. Low U_c and high heat conductivity of metals make the temperature rise slightly (up to 10 K) in the friction zone under a given current. Further increase of the current results in the broadening of friction track and a fall in friction force. This cannot be attributed to softening of the contact materials by the Joule heat only. It appears that the current alleviates plastic deformation of the metal by exerting a peculiar softening effect on the subsurface layer. It is believed that the softening effect of current can be

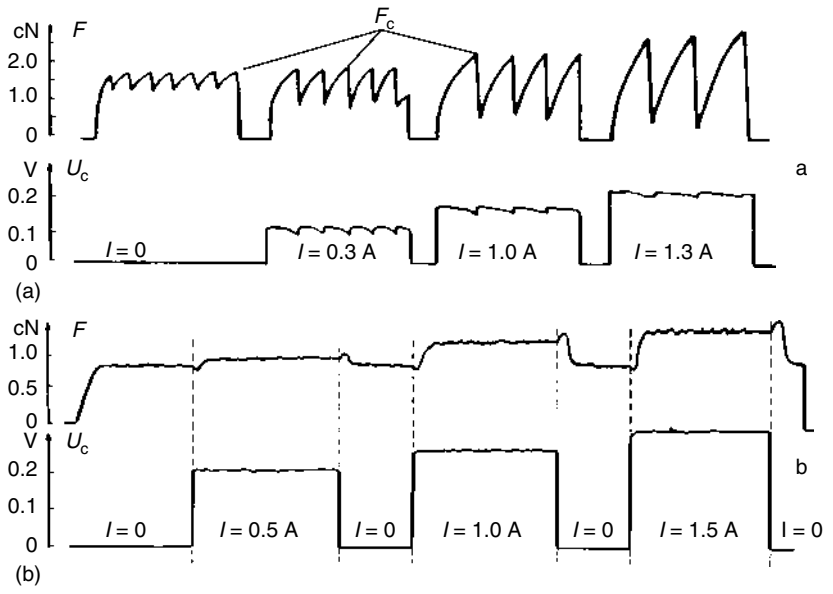

FIGURE 9.30 Friction force F and contact voltage drop U_c as a function of current magnitude in sliding of steel indenter against tin (a) and copper (b): (a) load $N = 0.1$ N; (b) $N = 0.15$ N.

attributed to the enhanced mobility of dislocations under the influence of electron flow in the subsurface layer.

The full extent of the effect of electrical current on the softening of contact spots becomes appreciable only in the range 10^4–10^6 A/cm^2 and is determined by the physical characteristics of the contact metals. The current densities of this magnitude can easily be reached in the real high-current sliding contacts. Although the heat generated by the current within this range is not a dominant factor, it affects the friction process. The temperature rise in the friction zone and adjacent microvolumes favors enlargement of the contact area and, as a result the friction coefficient increases. However, since the temperature rise lowers the specific friction force ψ, the friction coefficient μ decreases. Both factors become apparent during current switching (see Figure 9.30). The temperature in the friction zone increases instantaneously when the current is switched on, thus lowering both ψ and μ. Softening provoked by current and generated heat enlarges the contact area,

TABLE 9.5
Influence of Electrical Current on Parameters of Steel Indenter Friction against Tin ($N = 0$, 1 N)

Current, I (A)	Force of Static Friction, F_{st} (10^{-2} H)	Diameter of Contact Spot, d (μm)	Contact Area, S (10^{-6} cm^2)	Contact Voltage Drop, U_c (V)	Surface Temperature Rise, ΔT (K)	Current Density, j (10^5 A/cm^2)
0	1.6	45.3	16.0	0	0.1	0
0.1	1.65	46.0	16.5	0.06	0.8	0.06
0.3	1.8	49.0	18.7	0.08	2.8	0.16
0.6	2.2	53.2	22.1	0.12	7.8	0.27
1.0	2.4	58.5	26.7	0.16	15.8	0.38
1.3	2.7	63.0	30.9	0.21	25	0.42

TABLE 9.6
Influence of Electrical Current on Parameters of Steel Indenter Friction against Copper ($N = 0$, 15 N)

Current, I (A)	Contact Voltage Drop, U_c (V)	Friction Track Width, d (μm)	Contact Area, S (10^{-6} cm^2)	Friction Coefficient, μ	Deformation Fraction of Friction Coefficient, μ_d	Adhesive Fraction of Friction Coefficient, μ_a	Surface Temperature Rise, ΔT (K)	Current Density, j (10^5 A/cm^2)
0	0	21.0	3.4	0.062	0.009	0.053	0.1	0
0.1	0.08	21.0	3.4	0.062	0.009	0.053	0.6	0.3
0.5	0.20	21.4	3.6	0.067	0.009	0.058	7	1.4
1.0	0.26	22.5	4.0	0.080	0.009	0.071	17	2.5
1.5	0.32	23.9	4.5	0.085	0.010	0.075	30	3.3
2.0	0.38	25.8	5.2	0.090	0.011	0.079	44	3.8

thus alleviating the augmentation of friction coefficient. When the current is switched off, the temperature drops which causes both friction coefficient μ and force ψ to increase.

When the current density reaches 10^6–10^7 A/cm^2, the current-generated heat intensifies and becomes the dominant factor, causing softening of the surface layers and eventually their seizure. However, when the current density in the metal contact spots is less than 10^3 A/cm^2, the effects of both softening and heating are negligible. It should be pointed out that although such low current densities exert no appreciable effect on the friction characteristics, they greatly affect the oxidation of low-current contacts.[392,783]

9.2.2.6 Friction and Current Transfer in Metal Fiber Brush Contacts

The use of fiber brushes for high-current pick-off made significant progress in the efficient operation of sliding contact.[70] Monolithic carbon–graphite composites are unsuitable for pick-offs of high-power electrical machines and transport machines since they require contact pairs capable of passing currents with densities of hundreds of A/cm^2 at sliding velocities more than 100 m/s.[263] The current density is less than 50 A/cm^2 at sliding velocities of 10–20 m/s in monolithic carbon brushes and 120 A/cm^2 at 40–50 m/s in metal–graphite brushes.

In order to meet these strict requirements for current density and sliding velocities with low friction and wear, brush design similar to those used in the nineteenth century (brush made of copper wires) has been proposed for high-current pick-offs. Modern brushes of this type are made of small diameter metallic or metallized carbon fibers with good tribological characteristics at high current densities. Potentially superior properties of metal fiber brushes, in particular low resistance, low noise, and high speed, and current density capabilities, have been demonstrated in numerous investigations.[76–79,263] For example, Figure 9.31 shows the difference in noise level and voltage drop at the same current density for the best available monolithic brushes run under optimum conditions as contrasted to gold-fiber brushes. The absence of electrical noise in fiber brushes is clearly a significant advantage, since the noise would otherwise interfere with signal reception and suppressing it would be rather difficult. In Canada, the noise level for hand-held tools is limited by law.

In addition to numerous design solutions, a number of technological methods have been developed to improve the performance of metal fiber brushes. For example, Kuhlmann-Wilsdorf and Makel[74,784] described a method of improving the performance of high-current sliding contacts

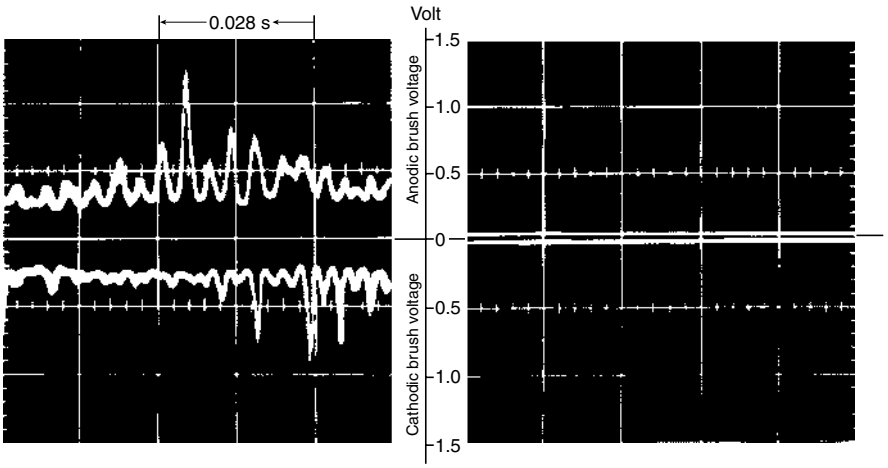

FIGURE 9.31 Oscillograms of optimally run brush pairs of monolithic 75 wt% Ag–C brushes (left) and gold fiber brushes (right) both at 35 m/s speed and 310 Am^{-2} in a protective atmosphere. Note the much lower voltage drop and virtual absence of electrical noise of the fiber brushes, as also that not only the electrical but also the mechanical loss is much lower for the fiber brushes. (From Kuhlmann-Wilsdorf, D., In: *Electrical Contacts: Principles and Applications*, Slade, P. G., Ed., Marcel Dekker, New York, pp. 943–1017, 1999. With permission.)

with fiber brushes by using atomized water and CO_2 protective atmospheres for lubrication and cooling.

To ensure long-lasting, slow-wearing sliding metal–metal contacts, it is essential to make the contact operate in the elastic deformation mode. In old-fashioned metal wire brushes, pressure at the contact spots caused deformation; i.e., contact spots were plastic. This plastic flow, which takes place mainly on the softer side, increases the contact spot area and hardens the material until the resistance to indentation (hardness H) balances the applied load. Therefore, under normal force, P, the load-bearing and current-conducting, area of brushes with plastic contact spots is $A_c \cong P/H$. Due to tangential shear in sliding, H tends to increase to a saturation value and A_c decreases. Finally, it impairs the operation of high-current contacts.

As shown by Kuhlmann-Wilsdorf,[40] wear rate decreases to much lower levels when contact spots are elastic. Unlubricated metal-fiber brushes can operate with mild wear due to a very large number of contact spots and hence low contact pressure. As seen from Figure 9.32, below the transition brush pressure P_{trans} (for elastic contact spots), the dimensionless wear rate is roughly proportional to $P^{4.6}$, i.e., it falls off very steeply at low pressure. With little doubt this is the microwear regime with $\Delta l/L < 10^{-10}$. Elastic vs. plastic contact spots have the additional benefit of increased load bearing area at the same load and hence reduced contact resistance.

In general, the electrical resistance of brushes R_b consists of three parts, being the sum of the resistance of the brush body R_0, surface film resistance R_f, and constriction resistance R_c. For monolithic brushes, e.g., graphite brushes, all three are significant, while for metal fiber brushes, R_0 and R_c are typically negligible, so that for them $R_b \sim R_f$. This is obvious for the case of R_0 on account of the much smaller resistivity of metal compared to graphite or metal–graphite. The constriction resistance R_c, results from the fact that all of the current has to pass through the contact spots, so the current flow lines have to constrict as they pass through the contact spots. For monolithic brushes the number of contact spots can vary between one and perhaps as much as one hundred, but typically it is $n \cong 10$.[70] This rather small number of constrictions causes more significant constriction resistance. Moreover, in graphite brushes specific resistivity p is relatively high. As a result their constriction resistance tends to provide in the order of one third of R_b.

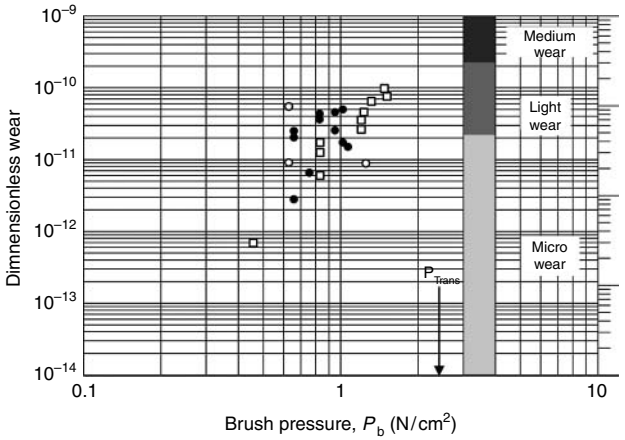

FIGURE 9.32 Dimensionless wear rates, $\Delta l/L$, of bundles of 50-μm thick copper fibers (running painter's brush style on polished copper at $v = 14$ m/s in a protective atmosphere of moist CO_2), as a function of "brush pressure," p_b, i.e., average macroscopic pressure applied to the bundles. The transition brush pressure, p_{trans}, at which contact spots become elastic is indicated. A simultaneously applied current of 50 A/cm^2 of brush area had no measurable effect on the wear rate. (From Kuhlmann-Wilsdorf, D., *Wear*, 200, 8–29, 1996. With permission.)

By contrast, due to large n and small p, for metal fiber brushes R_c is negligible even if their running surface, A_b, should be quite small. For example, for $A_b = 0.1$ cm^2, with $d = 50$ μm fibers occupying $f = 10\%$ of the volume, $n \cong 500$. Thus, with both R_0 and R_c negligibly small, the film resistance, R_f, is dominant.

Therefore, it is clearly advantageous to try and make the real specific resistivity of the film separating the contact spots, σ_f, as small as possible. But film resistance cannot be avoided altogether. Some nonmetallic film is necessary to prevent cold-welding and catastrophic wear. The current conduction through the thin films takes place by electron tunneling. As a result the dependence of σ_f on film thickness is indeed very steep as shown in Holm[1], but it is independent of the chemical nature of the film. Moreover, unlike the case for graphite brushes, the voltage dependence of σ_f is also negligible for fiber brushes since they will be operated with voltage drops of less than 0.2 V across the contact spots.

In metal-fiber brushes the presence of oxides and hard insulating surfaces creates a serious problem.[70] The presence of moisture film ($\sim$5 A) at contact spots is extremely valuable for metal-fiber brush operation, since it is the thinnest conceivable surface film shield which prevents cold-welding and permits almost wearless sliding at modest friction. While a single molecular layer would exhibit a still much smaller electrical resistance, it could not accommodate relative motion in sliding. Therefore, specific resistivity of surface film at contact spots of $\sigma_f \cong 10^{-12}\ \Omega\ m^2$ may be assumed as the optimal value of film resistivity for metal-fiber brushes.

The formation of insulating solid surface films poses a basic problem for using commercial metal fiber brushes in the open atmosphere. Two problems exist with the use of fluid contact lubricants. First, over long sliding distances they do not protect well enough against oxidation. Second, being much more viscous than water, they form rather thick layers and thereby raise the film resistivity substantially. Furthermore, nontarnishing metals such as aluminum, stainless steel, chromium and nickel are not useful for low-resistance fiber brushes. They are protected by an oxide film of 30-Å thickness or more, with correspondingly high film resistivity, and their oxidation rates can vary greatly. Clearly, the best base candidate metals for fiber-brushes have yet to be discovered. Certainly, good metal fiber brush materials are Ag, Au, Cu, Pd, or Pt.

So far the best solution for overcoming the problem of insulating surface films on commercial metals and alloys is the use of graphite. While graphite does not squeeze out from contact spots and thus leaves a relatively thick film, it is sufficiently conductive and also protects against oxidation.

There are other factors affecting performance of fiber brushes.[70] An important aspect of current transfer in contact of metal fiber brushes is tunneling around contact spots ("annular tunneling"). The load-bearing part of a Hertzian contact spot is surrounded by an annular gap within which the separation between two sides gradually increases. Current conduction is therefore not strictly limited to the load-bearing area but also occurs with rapidly diminishing intensity via tunneling through the zone adjacent to contact. In first approximation it may extend to a distance at which the gap width s has increased to $s \cong 5$ A.[73]

According to geometrical argument,[70,73] peripheral tunneling about elastic contact spots increases the apparent contact spot area by the factor:

$$K^2 = 1 + \left(\frac{s}{d}\right)\left(\frac{2fE}{p_b}\right)^{2/3}, \tag{9.2}$$

where d is diameter of fibers, E is Young's modulus, f is the "packing fraction" of wire brush that is occupied by solid, and p_b is the macroscopic pressure on brush. It is shown by Kuhlmann-Wilsdorf,[70] that including $s = 5$ A, and giving d in microns, Equation 9.2 can be simplified, i.e., specifically for copper, to

$$K^2 \cong \frac{1 + 7_{[\mu m]}}{\beta^{2/3} d}, \tag{9.3}$$

where $\beta = p_b/p_{trans}$. Then numerically, for $\beta = ½$ one obtains for $d = 50$ μm and $d = 20$ μm fibers, $K^2 \cong 1.22$ and 1.56, respectively, while for $d = 3$ μm with $\beta = 0.05$, $K^2 \cong 18$. Hence, for fiber sizes and brush pressures at the upper end of usability, peripheral tunneling is a small effect, but it can theoretically become quite large at small pressure and very fine fiber diameters.

Fiber-brush resistances are speed dependent. Specifically, with rising speed an increasing number of excess water molecules are trapped between the two monolayers. The fractional extra layer of water molecules between the contact spot sides causes a mild decrease of friction but a disproportionately large increase in σ_f on account of the sensitive dependence of tunnel resistance with the gap.[1] At otherwise identical conditions, the concentration of trapped molecules decreases slowly with contact spot size and more rapidly with increasing contact spot pressure, i.e., increasing β. On this account, therefore, when high speeds are to be attained one should use larger rather than smaller contact spots and as high pressure as may be tolerable. At high speeds, therefore, thicker fibers and harder metals are advantageous.

These conditions, however, counteract peripheral tunneling, i.e., decrease K^2 towards unity. According to Kuhlmann-Wilsdorf,[70] this is the most important effect preventing use of extreme conditions of peripheral tunneling. Specifically, the conditions required for truly large K^2 values would give rise to an intolerably high concentration of the trapped molecules, and thus prohibitively large values of σ_f, even at zero speed. Combining these considerations with the theoretical model developed by Kuhlmann-Wilsdorf[70] will give guidance for selecting optimum fiber sizes and pressures for any one desired combination of speed and current density; however, practical experience in this important area of concern is still very scanty.

Elastic contact spots are prevalent during fiber-brush sliding. However, spots can be at least at some time plastic through overloading, but short of macroscopic crushing. That may be deduced from pads at the fiber ends of brushes tested in some operating conditions (see Figure 9.33). Increase of the fiber end diameters through the pad leads to increasing contact spot sizes. Experimental observations[70,73] suggest another effect influencing the fiber-brush performance: brushes

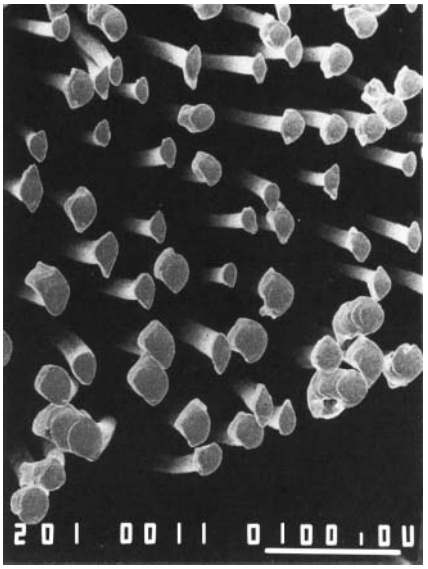

FIGURE 9.33 "Pads" at fiber ends of a gold fiber brush which was mechanically overloaded during testing to $\beta \approx 1$. In this condition the fiber end diameter is large than d.

may polish the rotor and themselves be polished. This effect should be more thoroughly investigated and exploited, especially if it should give rise to lower wear rates.

Fiber brushes were initially invented in order to provide current collection for homopolar motors. They need to provide current density of $j = 310$ A/cm^2 at velocity $v = 40$ m/s with a maximum total loss of $L_T = 0.25$ W A^{-1} and to be operated in a protective atmosphere of moist CO_2.[77,78,263] Further investigations[70] have shown that fiber brushes may displace monolithic brushes everywhere. Due to low heat loss and voltage drops of about 0.1 V and less, extremely low noise, and very high current density, metal fiber brushes should spread to all types of brush motors as costs come down and reliability is established. They will be irreplaceable whenever very high current density is needed, even in short pulses. For example, brushes are currently being developed for magnetically levitated trains, planned to run at up to 300 mph, or approximately 150 m/s.

Carbon nanotube brushes may still be a scientific hypothesis, but there is no any reason to try them as a potential current-collecting component.[48]

9.2.3 Stability of the Contact Resistance. Electrical Noise

Contact resistance has a statistical nature since the real contact occurs on the finite number of conducting spots in the real contact area. Consequently, the contact resistance, R_c, of both stationary and sliding contacts will undergo certain fluctuations. The frequency and amplitude ranges of the fluctuations (contact noise) are very broad. The nature of contact electrical noise is rather specific since it differs from the electrical noise in a continuous conducting media (heat noise) being also different in the closed and movable contacts.

9.2.3.1 Contact Noise in Closed Connections

In nonsliding contacts, the voltage across the contact fluctuates when a constant current is passed through it. The spectral density of the contact electrical noise is in a number of cases inversely proportional to frequency, i.e., this type of noise can be considered as $1/f$ noise.[785–787]

The relative voltage and resistance fluctuations are related as $(\Delta U/U)^2 = (\Delta R/R)^2 = C(\Delta f/f)$, where C is the relative $1/f$ noise measured through the filter with a bandwidth $\Delta f = 1$ Hz at $f = 1$ Hz. C is denoted often as the normalized noise of a resistor; C is a measure of the $1/f$ noise, independent of the applied voltage across the resistor.

The noise generated by fluctuations, as a function of the charge carriers' concentration in the vicinity of the contact area, was treated in detail by Vandamme and Tioburg.[785,786] This is, however, only a single example. Among other mechanisms that affect noise characteristics, we can mention diffusion on the contact surface, oxidation and fritting of surface films, variations in the conducting spot dimensions due to creep, and other mechanisms.[785,787,788] Most of the researchers have come to the opinion that l/*f* noise has a broad relaxation time spectrum embracing a few orders of magnitude. Formulas for contact noise calculation were deduced for different situations in static contact, in particular for single constriction dominated contacts, film dominated contacts, and multispot dominated contacts. For homogeneous samples subjected to uniform fields, the normalized noise is given by an empirical relation of the form.[787]

$$C = \alpha N = \alpha/nV \tag{9.4}$$

where N is the total number of free charge carriers equal to the product of the sample volume V and the free charge carries concentration n, α is a dimensionless constant of about 2×10^{-3}. By measuring the noise and the contact resistance of multispot contacts, the effective contact area can be calculated. It was shown that for the effective contact area the following expression holds:

$$n\pi a^2 = \left(\frac{\alpha\rho}{20nCR}\right)^{1/2}. \tag{9.5}$$

For example, Figure 9.34 represents the experimental dependence of noise C as a function of contact resistance R_c for smooth and rough brass rods. This dependence is typical of metal crossed rod contacts. The dots represent smooth crossed rod contacts. Triangles denote the results of sandblasted rods. Squares were obtained after using shearing and normal forces which acted together in the contact. For high resistances the proportionality $C = R^3$ is applied, suggesting the existence of

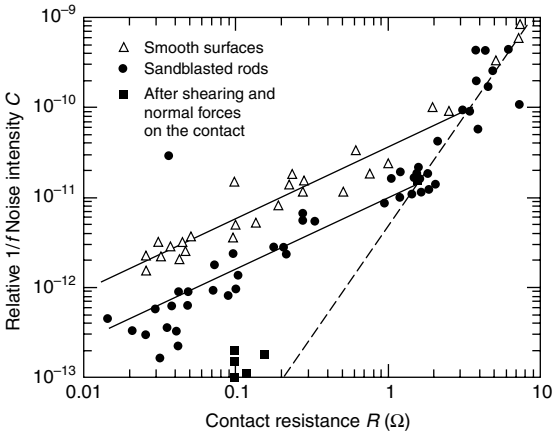

FIGURE 9.34 The experimental C vs. contact resistance plots for smooth and rough brass (●, smooth surfaces; △, sandblasted rods; ■, after using shearing and normal forces on the contact. The broken line represents the single constriction). (From Vandamme, L. K. J., *Proceedings of International Conference on Electrical Contact Phenomena*, VDE-Verlag GMBH, Berlin, Offenbach, 60–63, 1982. With permission.)

single contacts with areas several orders smaller than the load-bearing area. For low R values, $C \infty R$, suggesting multispot dominated contacts.

The initial contact resistance plays a significant role in reducing the intensity of contact noise in infinitely closed electrical contacts. The lower the initial resistance, the lesser is the noise level. Just like in any other physical system, fluctuations in the contact resistance of closed contacts exert more pronounced effect on the contact quality under elevated temperatures, whereas cooling of the contact leads to a lower contact noise level.

One of the verified means of decreasing contact noise is the use of a designed multipoint contact. According to a well-proven physics theorem on fluctuations of the additive physical value (including conductivity), the relative fluctuation (relative standard deviation) in a system incorporating N subsystems is $N^{1/2}$ times less than in an individual subsystem. Hence, in a three-point contact the relative fluctuation is to be 1.7 times less in contrast to a single-point one.

9.2.3.2 Electrical Noise in Sliding Contacts

During sliding, changes in resistance can result from work hardening and also due to changes in the composition of material at the sliding interface. As in any contact interface, a random set of actual contact spots is present in the sliding contact. In a stationary regime of sliding, the real contact area can be considered as constant. For a multipoint contact consisting of n spots operating in parallel, the following equality is true:

$$\frac{1}{R_c} = \sum \frac{2}{\rho} a_i = \frac{2}{\rho} = \sum a_i = \frac{2n}{\rho} \frac{\sum a_i}{n} = \frac{2na_{av}}{\rho} \tag{9.6}$$

where a_{av} is the mean radius of the contact spots which, as any other mean value, changes and consequently, causes the contact resistance to vary as well. When the number of contact spots is $n = A_r/\pi(a^2)_{av}$, where $(a^2)_{av}$ is the mean squared radius of the contact spots, then the contact resistance is given as:

$$R_c = \frac{\rho}{2a_{av}} \frac{\pi(a^2)_{av}}{A_r} = \frac{\pi\rho}{2A_r} \frac{(a^2)_{av}}{a_{av}} = \frac{\pi}{2} \frac{\rho a_v}{A_r} \frac{(a^2)av}{(a_{av})^2}, \tag{9.7}$$

$$A_r = \pi(a_i)^2 = \pi \sum (a_i)^2 = \pi n \frac{\sum (a_i)^2}{n} = \pi n (a^2)_{av}. \tag{9.8}$$

Because the changes of the real contact spot are negligibly small (A_r is statistically a very stable value), the variations R_c are in fact fully dependent on the changes of the mean contact spot radius a_{av}. It should be pointed out that each distribution function, $(a^2)_{av}/(a_{av})^2$ has its specific importance. Hence, the changes in the contact resistance correspond to the changes in the contact spot radii.

Sliding contact noise was extensively discussed in a number of publications.[789–794] It was shown that for sliding contacts, dynamic nature of the spots is the main cause for noise that can be affected by load, velocity, stick–slip phenomena, debris formation, oxidation, fritting, etc.

Increasing the contact load either in elastic or plastic mode decreases the noise[790] as shown in Figure 9.35. It is well known that low contact loads are one of the major issues in the reliability of contacts. Low contact force in combination with surface contamination greatly increases the contact noise.[792]

According to data of Taniguchi et al.,[793] the noise in sliding contacts increases proportionally with the sliding velocity, as seen in Figure 9.36.

The effects of stick–slip phenomena on contact resistance stability are discussed by Gao et al.[27,28] Stick–slip, in which two sliding surfaces cycle between relative rest and motion, is a

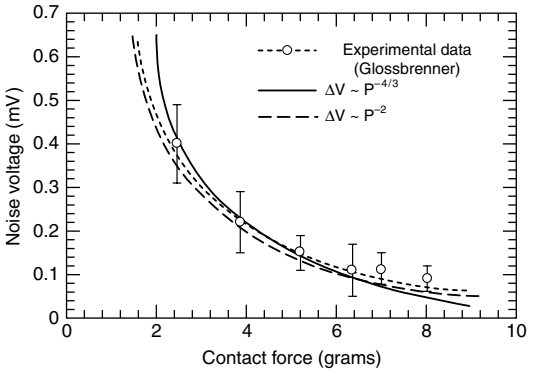

FIGURE 9.35 Relation between noise voltage and contact force. (From Mano, K. and Oguma, T., *Proceedings of 5th International Research Symposium on Electrical Contact Phenomena*, VDE-Verlag GMBH, Berlin, Vol. 1, 297–300, 1970. With permission.)

widely observed phenomenon, ranging from the atomic to macroscopic scale (see Chapter 3, Section 3.1.7). Such type of motion has a number of very important consequences for both mechanical systems, e.g., static friction (stiction) in magnetic information storage systems; jerking of brakes; and electrical systems, e.g., severe wear or seizing of different materials of electric contacts.[795]

The most widely accepted cause for stick–slip in metal contacts is that static friction exceeds kinetic friction or, more rigorously, that the friction coefficient drops rapidly at low speeds.[27] It has long been recognized that interfacial adsorbed water films and their effects on adhesion play a critical role in this phenomena. Therefore, Gao, Kuhlmann-Wilsdorf, and Makel[27,28] studied meniscus formation, molecular ordering and fluid drainage for the case of adsorbed water films and their influence on stick–slip and electrical noise. The coefficient of friction and the electrical resistance were measured simultaneously in the hoop apparatus[40,796] (also described in Section 10.3), using fiber sliders on a gold-plated copper substrate. The sliding surfaces were gold plated to minimize complications from oxidization, and a metal fiber slider was used to eliminate the effect of electric constriction resistance as well as fluctuations in the number and

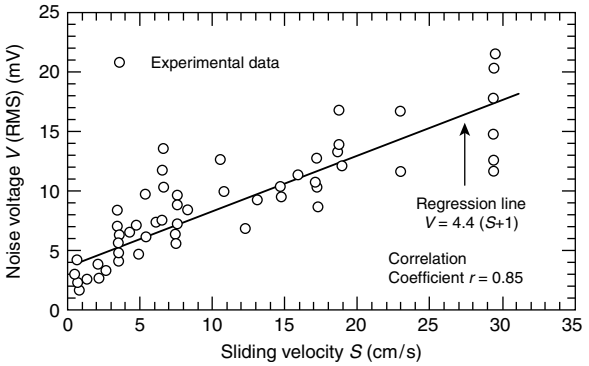

FIGURE 9.36 Relationship between contact noise voltage and sliding velocity sliding contact is phosphorus bronze wire (diameter of 0.5 mm) plated with Ag of 10-μm thickness; fixed contact is coated with carbon ink on a board of resin. (From Taniguchi, M., Inoue, T., and Mano, K., *Proceedings of 30th IEEE Holm Conference on Electrical Contacts*, Illinois Institute of Technology, Chicago, 491–498, 1984. With permission.)

size of the contact spots.[73] In this case, the measured contact resistance is proportional to resistance of the adsorbed film at the contact spots.

It was shown that in the low velocity range, the properties of the adsorbed films determine the slip mode, i.e., smooth sliding vs. oscillatory sliding and stick–slip. Specifically, stick–slip was common at low speeds and high humidity but practically absent at low humidity and high speeds. Electrical noise is correlated with sliding mode, being the highest in stick slip. It is seen from Figure 9.37, which shows the electrical noise ($\Delta R/R$, where ΔR is the difference between the average extrema in $R(t)$ curves from the average value), as a function of both humidity and hoop surface velocity.

Figure 9.38 illustrates the stick–slip mode in terms of position-time and resistance-time tracings. A striking result shown in Figure 9.38 is that the film resistance spikes whenever the stick phase breaks to slip. Plotting the resistance and sliding speed on the same graph, as shown in Figure 9.39a, reveals that the resistance peaks at the beginning of the slip, not at the maximum slip speed as one might think, and that the higher resistance persists as long as the sample slides. The symmetric shape of the speed peak demonstrates that the slider motion in the slip episode is nearly that of a harmonic oscillator, indicating that the speed dependence of kinetic friction is very weak.

Furthermore, a plot of the film resistance as a function of the surface speed (see Figure 9.39b) shows that the resistance has a hysteresis effect. The arrows in the figure indicate the time progression, and the dark vertical root at zero speed results from the resistance decreasing with stick time. This is interpreted as evidence that menisci form around the contact spots during stick episodes, thereby increasing the local pressure through surface tension and the Laplace pressure. This in turn causes (1) the drainage of molecules in excess of the two monolayers trapped during the previous slip episodes, and (2) increased ordering of the two layers. At the breaking point, the sample slips over the meniscus and thus temporarily more molecules than twice the layer film are buried under the contact spots. This results in the resistance spikes and the symmetry of the meniscus breaks down, as shown in Figure 9.38.

It is tentatively concluded that this effect occurs because of tiny wedges of trapped moisture or other adsorbed molecules at the leading edges of the contact spots. By implication, normal electrical noise is due to tiny fluctuations in the average thickness of adsorption films in the path of the

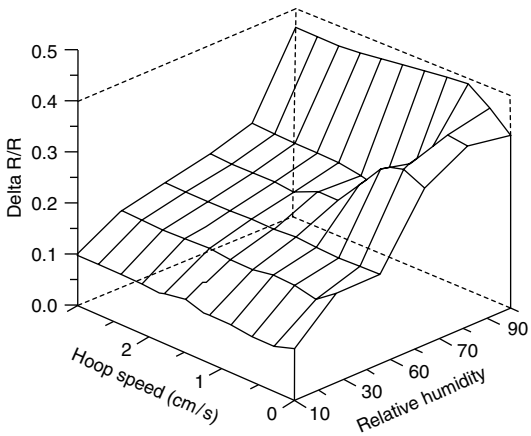

FIGURE 9.37 Electrical noise, $\Delta R/R$, of three similar bundles of 2800 each gold-plated 50-μm copper fibers sliding end-on gold-plate as a function of hoop surface speed (v) and relative humidity (H, in percent). Normal force between sample and substrate: $P = 0.45$ N; ambient laboratory air at normal pressure. (From Gao, C. and Kuhlmann-Wilsdorf, D., *Proceedings of 36th IEEE Holm Conference on Electrical Contacts*, Institute of Electric and Electronic Engineers, Inc., 292–300, 1990. With permission.)

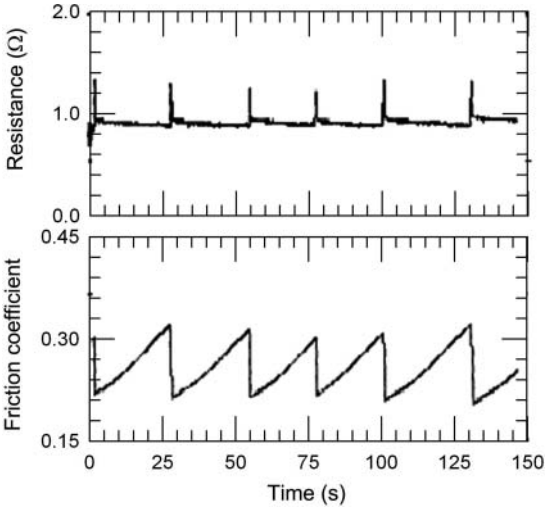

FIGURE 9.38 Coefficient of friction (as derived from the momentary slider position) as a function of time in stick–slip (lower curve) for the same fiber bundles as in Figure 9.37, and correlated momentary values of the contact resistance (upper curve). Humidity $H = 60\%$, $v_H = 0.05$ cm/s, laboratory air at 1 atm. (From Gao, C. and Kuhlmann-Wilsdorf, D., *Proceedings of 36th IEEE Holm Conference on Electrical Contacts*, Institute of Electric and Electronic Engineers, Inc., 292–300, 1990. With permission.)

contact spots. With fewer spots on monolithic samples as compared to fiber bundles, the noise is correspondingly larger for the former.

When the severity of stick–slip becomes very great, the contact may actually spring apart due to surface roughness and reader inertia.[795] Contact separation is pictured in Figure 9.40, in which the rough spot is a transfer particle on the flat. Severe stick–slip is shown as well in Figure 9.15, which is taken from actual recorder records.[795]

The variation of instantaneous contact resistance and friction is also related to details of the production of loose particles. This is most evident when loss of prow by rider occurs with the

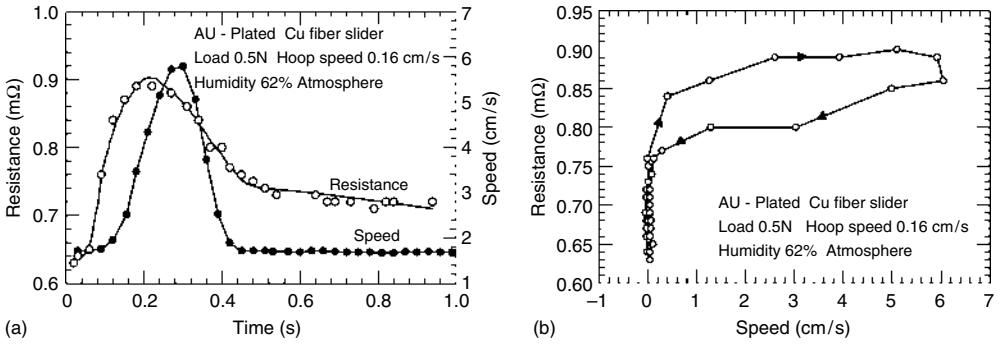

FIGURE 9.39 (a) Interfacial electrical resistance and surface speed of a fiber slider as a function of time. The load, hoop speed and relative humidity were 0.5 N, 0.16 cm/s and 62%, respectively. (b) The same interfacial resistance as in (a) but as a function of surface speed. The arrows show the time progression and the dark root is due to the resistance reduction in the stick phase. (From Gao, C., Kuhlmann-Wilsdorf, D., and Makel, D. D., *Wear*, 162–164, 1139–1149, 1993. With permission.)

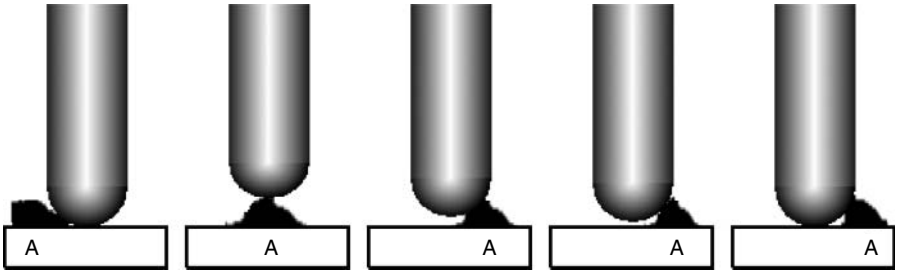

FIGURE 9.40 Contact separation caused by surface high spot. (From Antler, M., *ASLE Transactions*, 5(2), 297–307, 1962. With permission.)

formation of a roller-shaped particle.[795] As expected, friction falls sharply and contact resistance increases. Figure 9.41 is a record associated with roller debris formation.

The action of roller debris causes electrical noise, since a three-body system involves two constriction resistances in series, plus added bulk resistance due to a work-hardened particle. It was shown[795] that palladium contacts produce more electrical noise than gold because palladium generates more rollers. Palladium wear particles are smaller, but due to their larger number the volume wear rate is slightly greater than that of gold.

Wear particles, surface roughness, and noise due to fluctuations of contact resistance arising from sliding were analyzed in details by Tsuchiya and Tamai[791] from the viewpoint of adhesive wear. A reciprocating sliding device in which a slider reciprocates relative to a reader (see Figure 9.42) was used. Similar metal specimens were subjected to reciprocating motion (amplitude of 50 mm) under contact loads of 2 g and 20 g at a sliding speed of one cycle/second to prevent the contact surface from being affected by thermal action and complicated vibration due to high speed and high load.

It was shown that metals undergoing the oscillating dry sliding conditions can be classified into two groups. In the first group (Ag, Cu, Pt, Mo, W), the noise shows no significant changes when the

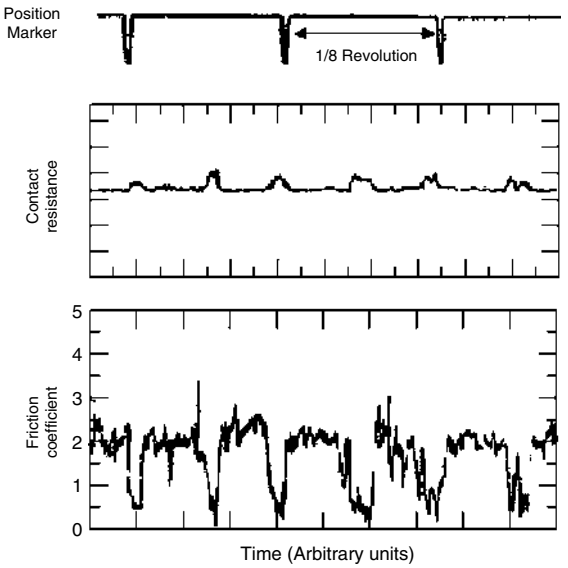

FIGURE 9.41 Roller-shaped wear particles between rider and flat cause low friction and increased contact resistance. Gold rider on gold flat, 0.2 cm/s, 30 g. Recorder time constants: contact resistance, 0.003 s; friction, 0.01 s. (From Antler, M., *ASLE Transactions*, 5(2), 297–307, 1962. With permission.)

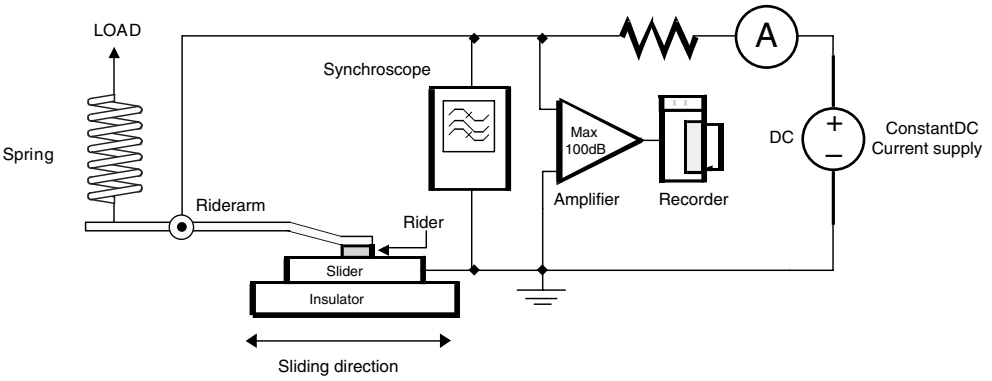

FIGURE 9.42 Reciprocating sliding device for study fluctuations of contact resistance in sliding contact. (From Tsuchiya, K. and Tamai, T., *Wear*, 16, 337–349, 1970. With permission.)

sliding motion is initiated but then increases when the mating surfaces become rough and wear particles are formed, as seen in Figure 9.43. In the second group (Zn, Sn, Al, Pb), the noise is higher at the beginning of sliding, but it tends to decrease as sliding motion proceeds, as seen in Figure 9.44.

Size of wear particles and surface roughness arising from sliding have characteristic values for each metal. Consequently, there may be a relation between the size of wear particles and noise voltage. Analysis of the experimental data[791] (see Figure 9.45) gives the relationship between the diameter of the wear particles d and noise voltage peak-to-peak V_n as:

$$V_n = 2 \times 10^{10} d^{-3.77}. \tag{9.9}$$

This expression indicates that, when a metal forms larger wear particles, the noise level is lower. The relationship between surface roughness and noise, shown in Figure 9.46, follows the expression:

$$V_n = 5.91 \times 10^3 H^{-3.77} \tag{9.10}$$

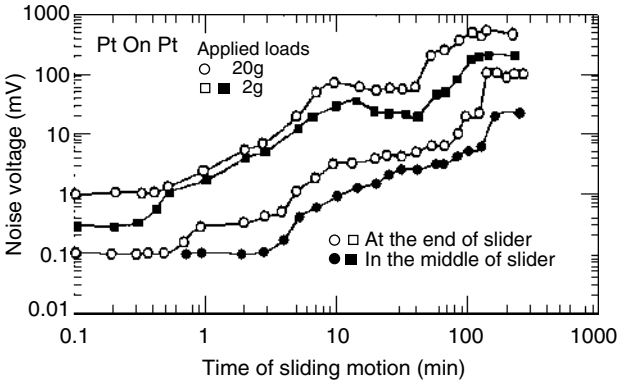

FIGURE 9.43 Change in noise voltage due to fluctuations of contact resistance against the time of sliding motion for Pt specimen. (From Tsuchiya, K. and Tamai, T., *Wear*, 16, 337–349, 1970. With permission.)

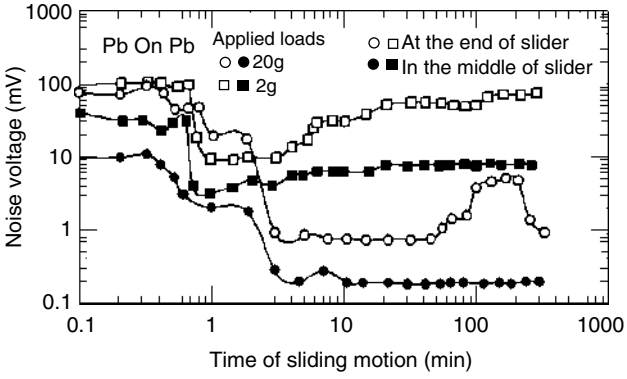

FIGURE 9.44 Change in noise voltage due to fluctuations of contact resistance against the time of sliding motion for Pb specimen. (From Tsuchiya, K. and Tamai, T., *Wear*, 16, 337–349, 1970. With permission.)

where H is surface roughness. Hence, from this expression it appears that as the value of apparent surface roughness increases, the noise voltage decreases.

Friction force as well as contact resistance is a random value. We can find a correlation between friction force and resistance in some cases.[157,792] In metallic contacts an inverse relationship can often be seen between friction coefficient and electrical contact noise.[792]

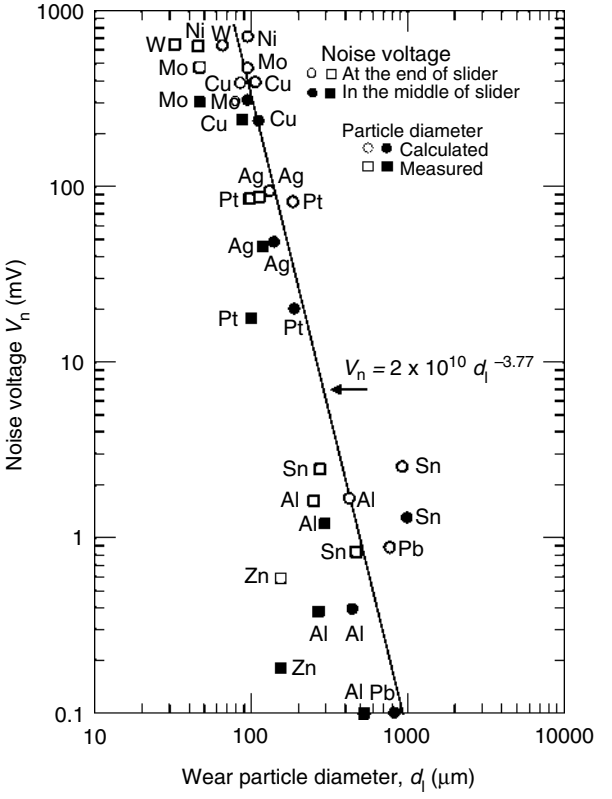

FIGURE 9.45 Noise voltage as function of wear particle diameter for similar metals reciprocated at low load and velocity. (From Tsuchiya, K. and Tamai, T., *Wear*, 16, 337–349, 1970. With permission.)

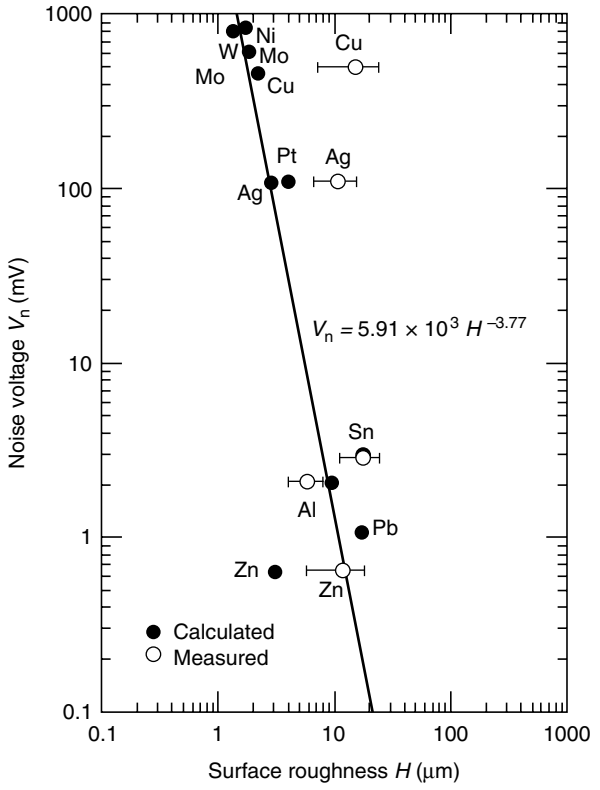

FIGURE 9.46 Noise voltage as function of surface roughness for similar metals reciprocated at low load and velocity. (From Tsuchiya, K. and Tamai, T., *Wear*, 16, 337–349, 1970. With permission.)

Calculations and observations concerning sliding noise spectrum were carried out by many researchers.[1,790,793,797] Mano and Oguma[790] presented relationships between sliding contact noise, contact force, contact resistance and sliding velocity. The theoretical calculations of the power spectrum of electrical sliding contact noise and test results were obtained in cases of precious metal contact with the aid of observations of the frequency characteristics. The contact resistance was assumed to be a random step function. In this case where the variation of contact resistance R_c follows the Poisson distribution, the power spectrum can be obtained as follows:[790]

$$\frac{G(f)}{2a\bar{R}_c} = \frac{l}{v}\left(\frac{\sin(\pi fl/v)}{\pi fl/v}\right), \tag{9.11}$$

where $G(f)$ is the power spectrum, R_c is the mean value of variation, l and a are constants, and v is the sliding velocity.

On the other hand, if the variation of contact resistance, R_c, is the Gaussian distribution, the power spectrum can be obtained as follows:[790]

$$\frac{G(f)}{4\alpha^2 l^2 \bar{R}_{c0}^2} = \frac{v}{l}\left(\frac{\sin(\pi fl/v)}{\pi fl/v}\right)^2, \tag{9.12}$$

where α is constant, and R_{c0} is the variation value of contact resistance unrelated to the sliding velocity, v.

In calculations,[790] the model waveform of sliding contact noise does not match to the real waveform. The actual power spectrum of sliding contact noise was studied by Taniguchi et al.[793] Experiments were made on a test sample which was used as a digital encoder. It consists of a fixed contact coated with carbon ink on a board of resin and sliding contact as the phosphorus bronze wires plated with Ag (the number is fifteen in parallel). The analysis was expressed as follows: (1) computation of amplitude, maximum value, minimum value and square mean value; (2) analysis of power spectrum and power regression; (3) computation of autocorrelation coefficient and amplitude; (4) determination of the parameters of quadratic autocorrelation process.

The experimental results of the relationship between the contact noise voltage and sliding velocity are shown in Figure 9.47. A regression line is calculated $V = 4.4$ ($S = 1$) with correlation coefficient about 0.85. The contact noise voltage rises in proportion to the increase of sliding velocity.

Some experimental results of power spectrum analysis of sliding contact noise are shown in Figure 9.48. The power regression line is calculated as $G(f) = 0.3f^{-1.93}$. From these experimental results, the whole power spectrum is found to be of higher level and wider band with an increase of sliding velocity. It is shown that the characteristics of autocorrelation coefficient decrease rapidly with the increase of sliding (see Figure 9.49). Besides, the time variation of the autocorrelation coefficient of the sliding contact noise increases proportionally to sliding velocity.

It is proposed that the noise waveform is modeled by the auto-regression. The waveform analysis allows linear prediction coefficients to be found from the real noise waveform. The waveform model gives a good agreement with the real noise waveform, power spectrum, power regression line, and autocorrelation coefficients.

The studies of the electrical noise of carbon slip-rings brush contacts indicted that the noise spectra characteristics vary as $f^{-1.1}$. The noise spectrum of sliding metal contacts, however, varies for different metals.[798] By analyzing the frequency spectrum of the noise of commercially pure In, Sn, Al, Zn, Ni, Cu, Pd, Au, Ag, Mo, and W, it was found[797] that there are three types of noise spectra depending on the properties of the metal surfaces. The first is characterized by a power spectrum with an $f^{-1/2}$ shape, the second by those of an f^{-1} shape, and the third by an f^{-2} shape.

The noise frequency component V^2 generated in Au, Ag, Cu, Zn, and Ni decreases with the frequency f (see Figure 9.50). This relation can be expressed by an inversely proportional formula $V^2 = kf^{-1}$, where k is a constant. The noise voltage waveforms for this group were different from the others, and the difference was found to be due to stick–slip.

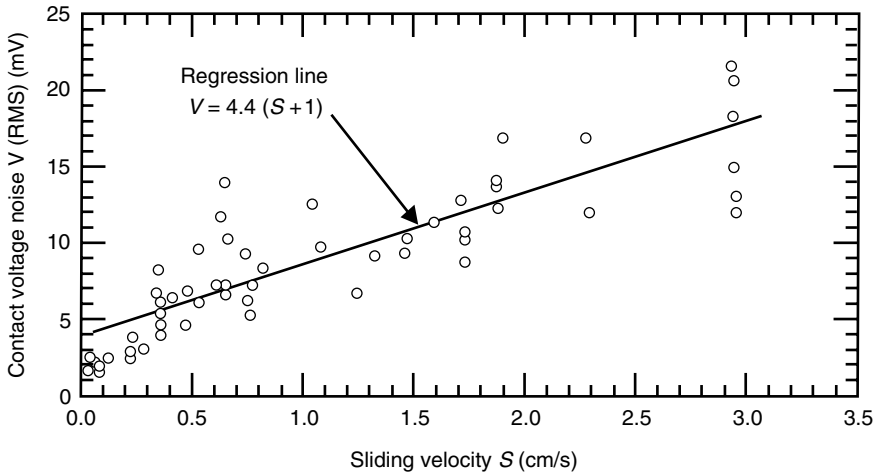

FIGURE 9.47 Relationship between contact noise voltage and sliding velocity. (From Taniguchi, M., Inoue, T., and Mano, K., *Proceedings of 30th IEEE Holm Conference on Electrical Contacts*, Illinois Institute of Technology, Chicago, 491–498, 1984. With permission.)

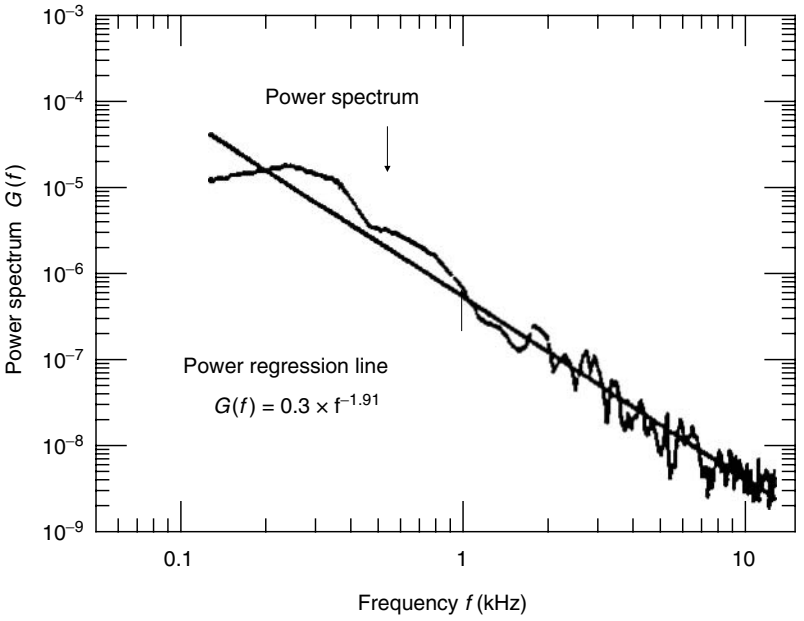

FIGURE 9.48 Power spectrum of real contact noise when sliding velocity is 2.96 cm/s. (From Taniguchi, M., Inoue, T., and Mano, K., *Proceedings of 30th IEEE Holm Conference on Electrical Contacts*, Illinois Institute of Technology, Chicago, 491–498, 1984. With permission.)

Since the study was made under sliding conditions where adhesive wear occurs (polished and ultrasonically cleaned specimens of pure metals were used), the fluctuations of contact resistance during sliding motion depend on the size of the adhesive junction at the interface which is proportional to the ratio W/P (W is surface energy, P is hardness of metal). Therefore, it may be considered that the main frequency component of the noise is a pulse which has time proportional to W/P, since successive repetition of growing and breaking of the adhesive junction causes fluctuations of contact resistance.

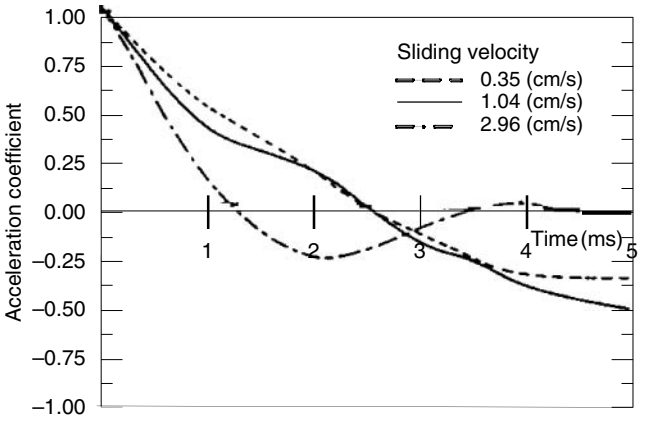

FIGURE 9.49 Autocorrelation coefficient of real sliding contact noise. (From Taniguchi, M., Inoue, T., and Mano, K., *Proceedings of 30th IEEE Holm Conference on Electrical Contacts*, Illinois Institute of Technology, Chicago, 491–498, 1984. With permission.)

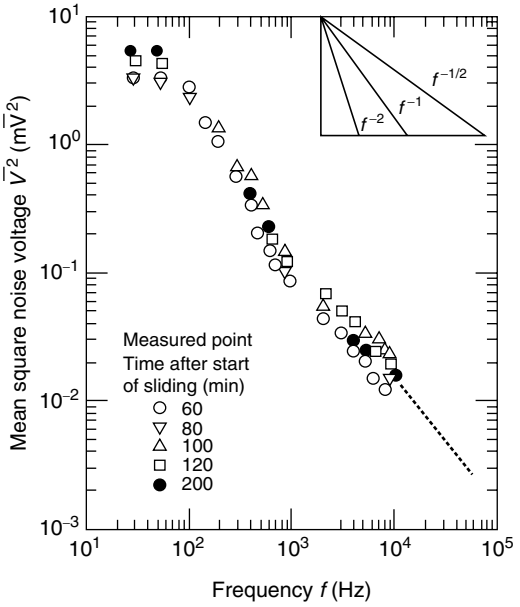

FIGURE 9.50 Noise spectrum for Ag specimen. (From Tsuchiya, K. and Tamai, T., *Wear*, 19, 245–258, 1972. With permission.)

It is well known that by obtaining the amplitude of each term of the Fourier expansion of the pulse wave, the spectrum of the pulse wave has an f^{-1} characteristic, in which the low frequency components are at constant level depending on the pulse width. Thus, the noise accruing from sliding motion with adhesive wear may have a spectrum with an f^{-1} characteristic. In the case of Au, Ag, Cu, Zn, and Ni, the oxide films hardly grow on the metal surface, or are easily broken mechanically. Consequently, metallic contact results in stick–slip, and only adhesive wear influences the noise generation.

The formation of contaminant films and the generation of wear particles differ with different metals and differ the effect on the noise. Therefore, it is necessary to add the characteristic of the noise due to adhesive wear to the f^{-1}.

Tin and other metals with large *W*/*P* ratios and large contact junctions give a low level of noise, and the noise spectrum has $f^{-1/2}$ characteristic (see Figure 9.51). Even if adherent films grow at their surfaces, metallic contact immediately occurs during sliding because of the low hardness of the basic metal. The noise voltage, however, varies because the surface becomes roughened easily by breaking of the surface layer and the generation of wear particles due to the softness of this metal.

Metals such as W, Mo, and Al form strong and adherent films with high electrical resistance. W and Mo films are difficult to break under sliding motion because of their high hardness. For Al, even if the film breaks mechanically, a film with high electrical resistance reforms immediately. Therefore, these metals give rise to noise containing higher-level components in the low-frequency range with f^{-2} characteristic (see Figure 9.52).

As spectral analysis shows, the most efficient way to reduce contact noise is to provide a larger area of contact or increasing the number of contact spots. It is not easy to control these parameters by load or initial surface roughness. The most efficient way can be the use of a multipoint contact instead of a single-point one. In practice it was done in the case of metal wire brushes.[79] (See Figure 9.32 and Section 9.2.2.)

Another way to decrease the contact noise is the application of special lubricants (see Section 9.3).

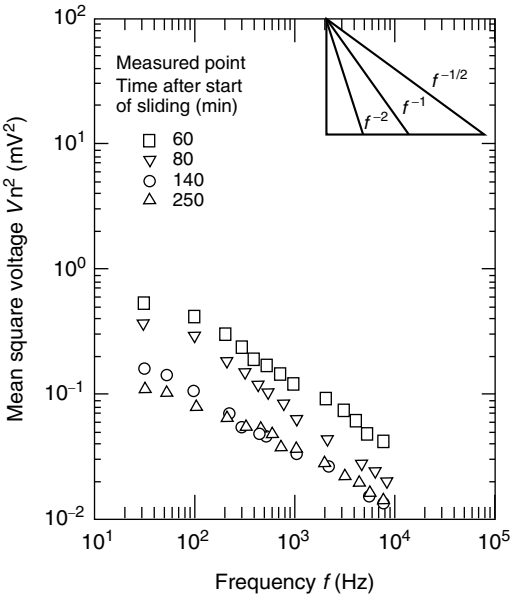

FIGURE 9.51 Noise spectrum for Sn specimen. (From Tsuchiya, K. and Tamai, T., *Wear*, 19, 245–258, 1972. With permission.)

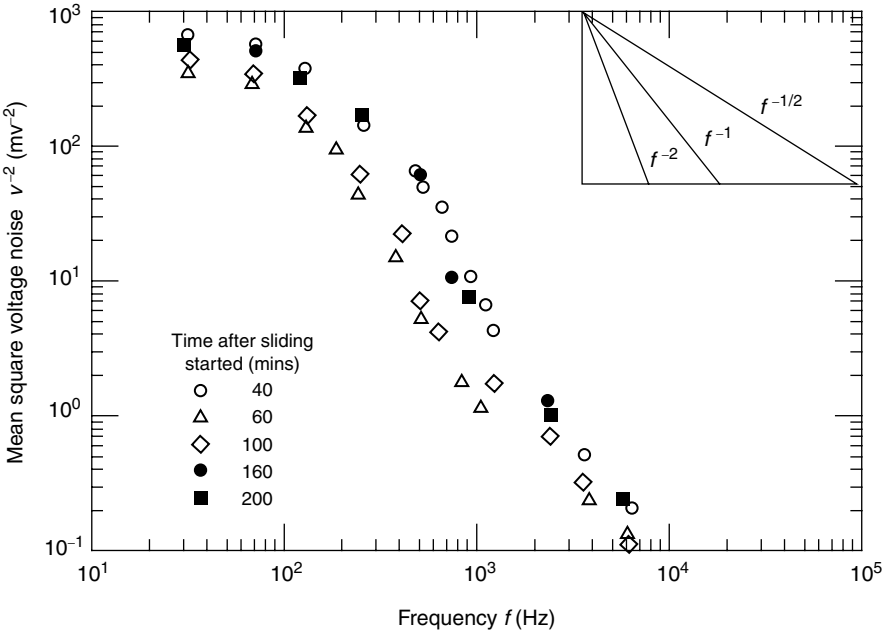

FIGURE 9.52 Noise spectrum for W specimen. (From Tsuchiya, K. and Tamai, T., *Wear*, 19, 245–258, 1972. With permission.)

9.3 LUBRICATED METAL CONTACTS

9.3.1 Introduction. Lubrication Factors

The first studies in the field of lubrication of electrical contacts were described by Aronstein in his review.[799] Campbell and Aronstein[800] showed the possibility of improving wear resistance and providing reliable contact when using lubricants. The properly selected lubricant plays several useful roles: it reduces wear, damps vibrations, and protects the contact surfaces against environmental effects.

The applications of lubricants in electrical contacts are steadily increasing. Currently almost all types of light-duty sliding contacts operating at low velocities without arcing and electrical erosion are lubricated. Lubricants have also been used in heavy-duty sliding contacts. The application of a proper contact lubricant can reduce sliding wear by several orders of magnitude.[746] In some contact pairs the application of lubricants improves vibration stability and spark-proofing of sliding contacts.[801]

In order to examine the role of lubrication, it is necessary to evaluate its influence on both frictional and electrical characteristics of the contact; this influence may evidently be ambiguous. In a general case, the effects of lubricants can be both positive and negative (see Figure 9.53). Along with positive effects, leading to reductions of mechanical and electrical losses and improvement of the service life and operating reliability of the contact, negative effects are also possible. The negative effects are characterized by the necessity of complicated design and prevention of irreversible changes in lubricant composition, and also prevention of hydrodynamic lubrication conditions which lead to sparking and electrical erosion of the contact.

The existence of multifactor actions in a wide range of conditions leads to the necessity of providing an optimal combination of lubricant properties to ensure fulfilling the conflicting requirements of the contact friction and electromechanical characteristics. The search for such a combination can be made on the basis of an integrated study of the electrical properties of lubricating boundary layers, the influence of lubricant on friction and current passage in the contact, and changes in structure and composition of lubricant layer and surface layers of the rubbing bodies.

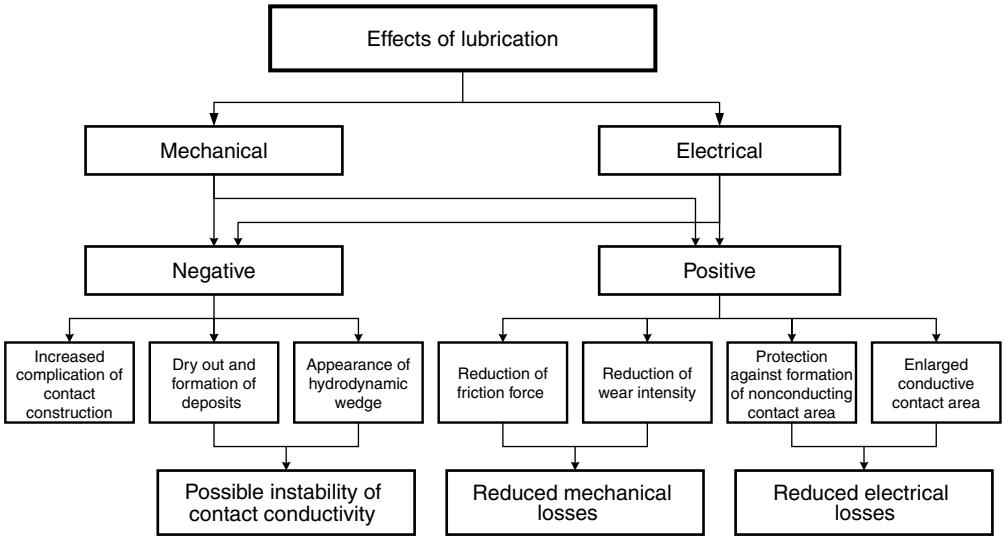

FIGURE 9.53 Factors affecting electrical contacts at lubrication.

9.3.2 Electrical Properties of Lubricating Boundary Layers

Materials that are used as lubricants (mineral and synthetic oils, esters and ethers, and so on) are dielectrics with electric strength about 10^6–10^7 V/m and with volume resistivity in the range 10^5–10^{13} Ωm, i.e., 12–20 orders of magnitude higher than resistivity of the commercial metals. Hence, the formation of a continuous lubricating film on the contact should lead to complete breakdown of the contact conductivity. However, experience has shown that the conductivity of lubricated contacts is not degraded but rather improved when compared to that of nonlubricated contacts. The contradiction may be explained by invoking the following two factors. First, lubricants in thin boundary layers (10^{-6}–10^{-7} m) behave not as insulators but rather as semiconductors. Second, the lubricants do not form continuous boundary films, and in the contact zone there are always metallic spots or spots that are covered only by a thin layer of molecules with the tunnel-type conductivity. Hence, the initial line of thought was that the boundary lubricant layer may provide an additional conductive channel between the rough surfaces. On the other hand, some authors have suggested that in this case the lubricant film has to be thinner than the height of asperities.

Investigations of conductivity of thin lubricant layers are of significant importance for such applications as electrical methods of monitoring friction (thickness of lubricant layer, load-bearing capacity, structure of boundary layers, etc.). A well-known method of monitoring friction in lubricated units is based on the measurement of contact resistance.[798,802,803] This method assumes that a very high resistance of relatively thick lubricant film (micrometer range) becomes conductive only when a metallic contact is established. Obviously, this method relies on the lubricant electrical properties and assumes that the electric strength and specific volume resistance of the lubricant in a thin layer are low; thus, the low values of contact resistance may not correspond to metal conductivity.

Early studies on the electric properties of thin layers have shown that there is a significant disagreement concerning the nature of thin layer conductivity. It must be noted that test methods used in these studies had serious disadvantages, such as the use of plain electrodes that can introduce significant errors when adjusting the gap. Other authors used indirect methods to measure the lubricant conductivity.

Myshkin et al.[804] used a direct method to measure lubricant layer conductivity. Layers with thicknesses of 3–300 μm have been tested between a plate and steel sphere of 3 mm diameter. The gap has been adjusted by a micrometric mechanism. Layers with thickness of 0.05–3 μm have been tested with a special device (see Figure 9.54). The lubricant film (1) was placed in the gap between plate (2) and needle electrode (3) supported by pivot of profilometer (4). The gap was adjusted by micrometric mechanism (5), steel cylinder (6), and pin (7). Correct adjustments were produced by heating of the cylinder (6), causing its slow and linear heat expansion in the micrometer range. Measurement of the gap was carried out by an electronic scheme of profilometer (8). Maximal accuracy of the gap measurement was around 0.01 μm.

The resistance of the layer was determined by a voltage drop at the standard resistor R_3. Under dynamic conditions (i.e., breaking of electrodes), the output of the profilometer (8) was connected with the abscissa input of an oscillograph (9) and voltage drop with the ordinate input of the oscillograph. Gold and steel cone needles with radius of curvature of 30–50 microns were used. The heights of asperities on their surface have not exceeded 0.01 μm. The geometry of the gap made it possible to calculate specific bulk resistance of the lubricant using total resistance data. According to electrostatic theory the capacitance of sphere-to-plane gap is given as:

$$C = 4\pi\varepsilon R_0 sh\mu \sum_{n=0}^{\infty} \frac{1}{sh(n+1)\mu}, \tag{9.13}$$

where $\mu = \mathrm{Arch}[(R_0 + d)/R_0]$.

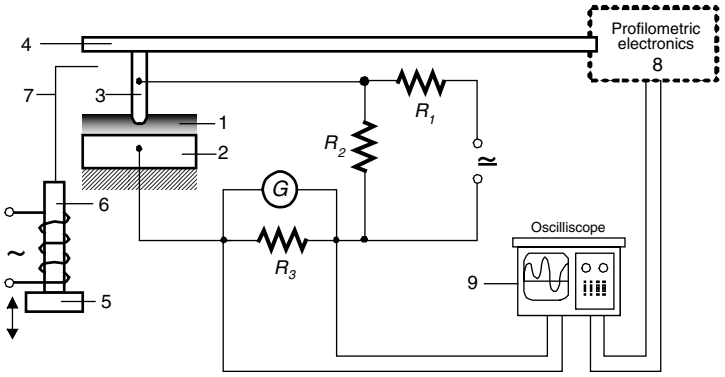

FIGURE 9.54 The scheme of device for investigation of electrical properties of lubricants.

Using electrostatic analogy between capacitance and conductivity, in this case we may assume that

$$G = \frac{1}{R} = 4\frac{\pi R_0 sh\mu}{\rho}\sum_{n=0}^{\infty}\frac{1}{sh(n=1)\mu}.$$

After transformation and integration, it follows that

$$\rho = 4\pi R_0 R\frac{sh\mu}{\mu}\left(-\ln th\frac{\mu}{2}\right). \tag{9.14}$$

Maximum field intensity may be found as

$$E_{\max} = (U_0/d)f_1 \tag{9.15}$$

where $f_1 \to 1$ at $d/R_0 \to 0$.

Some hydrocarbons and commercial oils differing in bulk electric conductivity, surface active properties, viscosity, and dielectric permeability (Vaseline oil, glycerin, oleic acid, alkylsulphonate, and commercial oils) were tested between oxidizing (copper, aluminum, and steel) and nonoxidizing (gold and platinum) electrodes.

Experimental observations have shown that at low voltage, applied conductivity drops drastically at the moment of the breaking of the electrodes (see Figure 9.55).

Specific resistances of the test substances do not change, or at best slightly increase, when the thickness of layer decreases (see Figure 9.56). Calculated values of bulk resistance, ρ, are in good agreement with the values obtained using standard cells.

These values are dependent on admixtures and applied voltages (see Figure 9.57). Increasing the applied voltage does not sufficiently reduce values of ρ, and there was no evidence for the existence of critical value of voltage reducing ρ significantly.

Data presented in Figure 9.57 show the effect of applied voltage on the resistance of glycerin film in the contact zone (gap). Studies have shown that electrical strength of the film falls in the range (0.5–2.2) 10^8 V/m and is independent of the material of electrode and its polarity. Clearly, the initial stage of breakdown is independent of the lubricant, since an electronic autoemission begins at field intensity 10^8–10^9 V/m. Furthermore, these studies have also shown that the resistivity and electrical strength of boundary layers are not affected by the pure lubricants as long as the film thicknesses are greater than the zone of influence of the tunnel effect ($\sim$3 nm).

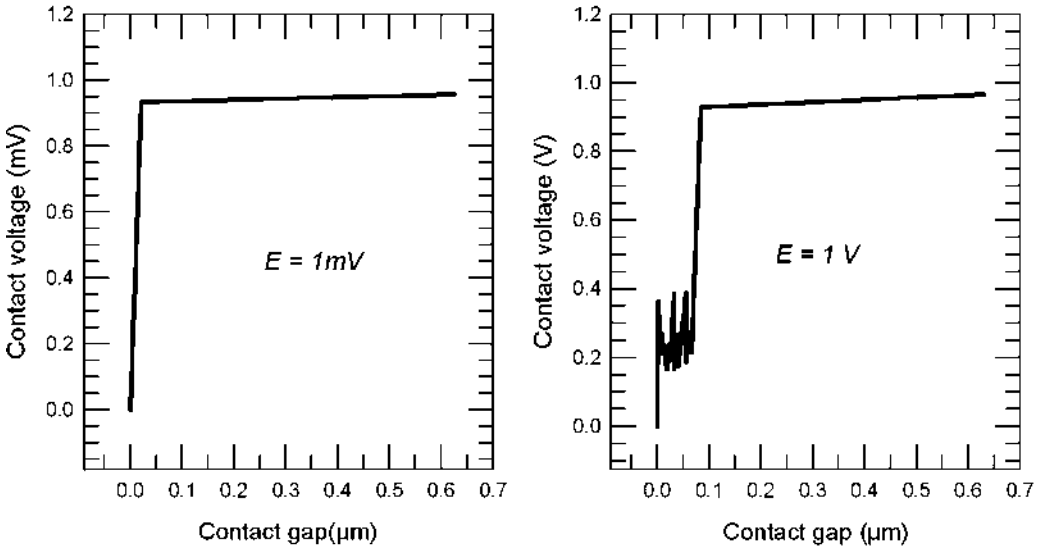

FIGURE 9.55 Contact voltage drop vs. gap between gold needle (tip radius of 50 μm) and platinum plate for (a) low and (b) high applied voltage.

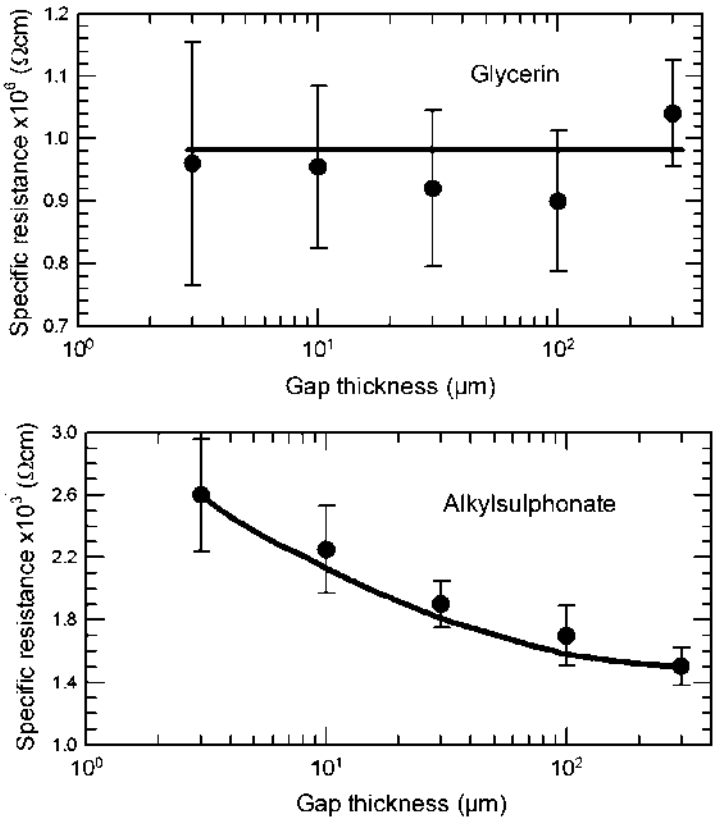

FIGURE 9.56 Bulk specific resistance of glycerin and alkylsulphonate vs. thickness of gap between electrodes (steel sphere-silver plate, applied voltage is 40 mV).

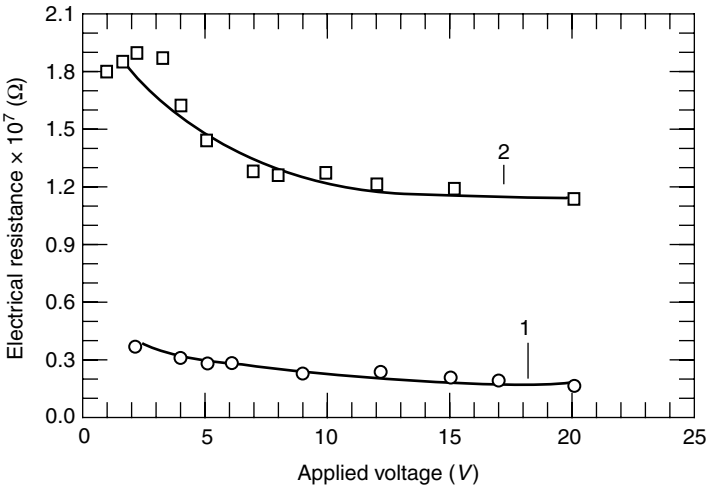

FIGURE 9.57 Dependence of electrical resistance of a normal (1) and waterless glycerin (2) on applied voltage (steel needle and silver plain electrode, thickness of layer is 2.5 μm).

Experimental verification of the theory of tunnel conductivity has given valuable information on electrical properties of the thin lubricating layers (below 10 nm).[805] In these experiments, the monolayers of fatty acids, i.e., classical additives to lubricants, were used to form dielectric layers of a required thickness between the metal electrodes. Using the Langmuir–Blodgett method, the monolayers of fatty acids of different chain lengths (25.8–30.9 Å) as well as multimolecular layers of these acids were deposited on aluminum. Mercury was used as a second electrode. Since the molecules of fatty acids are arranged perpendicularly to the electrode surface, their length complies with the gap size. In addition to verifying the exponential dependence of tunnel conductivity on the layer thickness, these studies nave also shown that the intrinsic conductivity of the lubricating layer within 2–10 nm thickness is extremely low (specific electrical resistance exceeds 10^{13} Ω m).

Very high electrical resistance of organic monolayers and multilayers (fatty acids and its salts), sandwiched between metal electrodes were obtained by other authors[806–808] as well. In these studies 1–10 monolayer thick films (approximately 2–25 nm) were investigated.

Recently, electrical and mechanical characteristics of gold surfaces covered with self-assembled monolayers (SAM) of an alkanethiolates were studied by Alamarguy et al.[809] They used a conducting probe Atomic Force Microscope which, during loading and unloading, allows simultaneous recording of the mechanical and electrical interactions of the tip with the nanocontact surface. The characteristics of the SAM were determined as a function of applied load and layer thickness. It was shown that during loading, the resistance of the layers sampled by the microscope tip is very high. Since the detection of the tunneling current is possible only for the short-length absorbed molecules, the presence of long-chained molecules requires higher loads to be applied. As a result, the layers are deformed and damaged irreversibly after several loading/unloading cycles.

Therefore, measurements of the electrical properties of thin lubricant films indicate that the boundary layers have very high electric strength and that the semiconducting effects are absent. The results also point out that a pure lubricant in boundary layers shows no sudden loss of volume resistivity and electric strength, at least for thicknesses greater than the values corresponding to the onset of the tunnel effect. This is not particularly surprising since the ordering of liquid molecules in boundary layers under the action of the solid-phase field exerts no appreciable effects on its conductivity. Furthermore, since the mobility of carriers in the boundary layers is limited by the action of the solid phase, the probability of formation of a conduction channel is greatly reduced.

These data are of fundamental importance in the search for a solution to several problems. For example, in the case of a low-current sliding contact, the conductivity becomes negligible when the metallic contact spots break down. This is in agreement with the test data of Furey,[803] where the resistance of low-voltage contacts sliding at high speed varied from values close to zero up to infinity. On the other hand, due to low conductivity of thin layers of liquid dielectrics, the measurements of the electrical resistance of oil films during friction enables detection of the metal-to-metal contacts between the mating parts.

9.3.3 Conductivity of Lubricated Contacts

9.3.3.1 Effect of Lubricant on Conductivity near the Contact Spots

The above-mentioned data (Section 9.3.1) make it possible to use the bulk electric properties of lubricants for calculating their effect on the conductivity of contact of rough metal surfaces. The model of contacting asperities is presented in Figure 9.58 by a cone with small lateral angle, φ. Each contact spot has metal conductivity, and it is surrounded by the conical gap. Conductivity of metal contact is $G_m = 2\pi\sigma_m$, where σ_m is the specific conductivity of the metal. This equation was obtained by Holm,[1] and it assumes that all the current lines cross the contact spot only. Assuming that these lines go through the contact gap, we may present unit current tubes as parts of thin concentric cylinders with small φ In such a case the unit tube conductivity is:

$$G_i = \sigma_l(S_i/l_i),$$

where σ_l is specific conductivity of lubricant; S and l are the cross-section and length, respectively, of the field force tube, $l_i = \delta + (x_i - a)\varphi$, where δ is the critical value of gap depending on tunneling and a is contact sport radius. Total conductivity of a lubricant layer is:

$$G_L = \sigma_L \int_0^{\gamma} \frac{2\pi x}{\delta + (x-a)\varphi} dx.$$

Usually the real area of contact, A_r, is much smaller than apparent contact area, A_a, and $a \leq (10^{-2}$–$10^{-1})r$. The critical gap, δ, depends only on tunnel effects, and this is approximately 30-Å thick. A typical contact spot radius is about 10^{-6} m. For these conditions,

$$G_m/G_L = (10^{-4} - 10^{-3})(\sigma_m/\sigma_L).$$

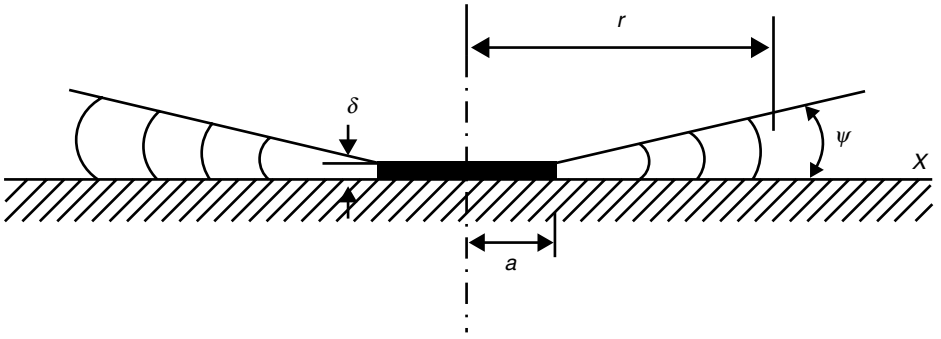

FIGURE 9.58 Asperity contact model.

Because the σ_m value is about 10^3–$10^4\ \Omega^{-1}\ m^{-1}$ and the resistances of metal contact and lubricant film are connected in parallel, the effect of lubricant conductivity will be significant if $\sigma_L = 10^{-1}$–$10^{-2}\ \Omega^{-1}\ m^{-1}$. These values correspond only to strong electrolytes, which are usually not used as lubricants. Although the above described model is an approximation, the conclusion is nevertheless correct. Assuming a minimum value for the contact gap δ and $A = n\pi a^2$ (n—number of contact spots), the relation may be written as:

$$\frac{G_n}{G_L} \approx \frac{\sigma_n}{\sigma_L}\frac{na\sigma}{A_a - A_r} = \frac{\sigma_n}{\sigma_L}\frac{A_r}{A_a - A_r}\frac{\delta}{a}. \tag{9.16}$$

Typically, $A_r/(A_a - A_r) \leq 10^{-1}$–$10^{-2}$ and $\delta/a \leq 10^{-3}$; therefore, the qualitative character of conclusion is not changed. It can also be mentioned that this model and the conclusions made above are valid in the case of real engineering surfaces when the contact spot size is of the order of micrometers. In the case of very smooth surfaces with very small contact spots, the situation can be different and the conductivity of tunnel zone can be more significant.[79]

9.3.3.2 Effect of Lubricant on Conductivity of Contact Spots

The boundary lubrication regime is characterized quite often by high conductivity similar to that of dry metal contacts. A question arises: does the low R_c (e.g., 0.1 Ω) mean a complete breakdown of the boundary lubricating layer and formation of metal spots, or can the conductivity level also be ensured by maintaining a lubricating layer between the surfaces? If such a layer is formed, how thick can it be in reality? In many cases the explanation is based on the assumption that only the existence of metal contact spots can provide low values of R_c.[800] The role of the lubricant is considered only as a factor affecting the size of these spots. Hypotheses were formulated on the possibility of high conductivity in the presence of continuous tunnel-conducting lubricating films on the contact spots.[798] Holm[1] argues that good conductivity cannot be considered as the fact supporting or denying the existence of film on the contact spots.

Calculation of electric conductivity of lubricated point contact. The evaluation of conducting mechanism in boundary lubrication is simpler for a point contact of noble metals. Let a nominally fixed point contact be formed by the pressing of two lubricated cylindrical rods of the same diameter (crossed cylinders). The rods are made of the same noble metal with the surfaces free of oxides or contaminating films. Three types of interfaces can be formed, and they are of interest from the conductivity viewpoint (see Figure 9.59 and Figure 9.60).

In the simplest case of interface of A-type, the lubricants are completely squeezed out of the contact gap; the apparent, real, and electrically conducting areas coincide. It is not difficult to calculate the conductivity of such a contact, using Holm's formula (1.4) for constriction resistance $R_s(a)$. The specific constriction resistance (unit area resistance found as the product of R_c and the conducting contact area) can be determined in this case as follows:

$$R_{\otimes s}(a) = \pi\rho a/2 \tag{9.17}$$

According to Equation 1.4[1] and Equation 9.17, the values of $R_s(a)$ fall within 10^{-2}–$10^{-4}\ \Omega$, and those of $R_{\otimes s}(a)$ fall within 10^{-14}–$10^{-12}\ \Omega\ m^2$ for highly conductive noble metals (Ag and Au) when the contact spot radius, a, varies from 1 to 100 μm (see Figure 9.59).

An interface of B-type includes an apparent bearing area of radius a including randomly placed metallic spots of radius i (cluster of conducting spots), whereas the remaining contact area is covered with a lubricating film. With a few metal spots, n, distributed at distances greater than their linear dimension (each spot has a long constriction region and the current channels of the neighboring spots do not interfere), the following expressions are valid:[1]

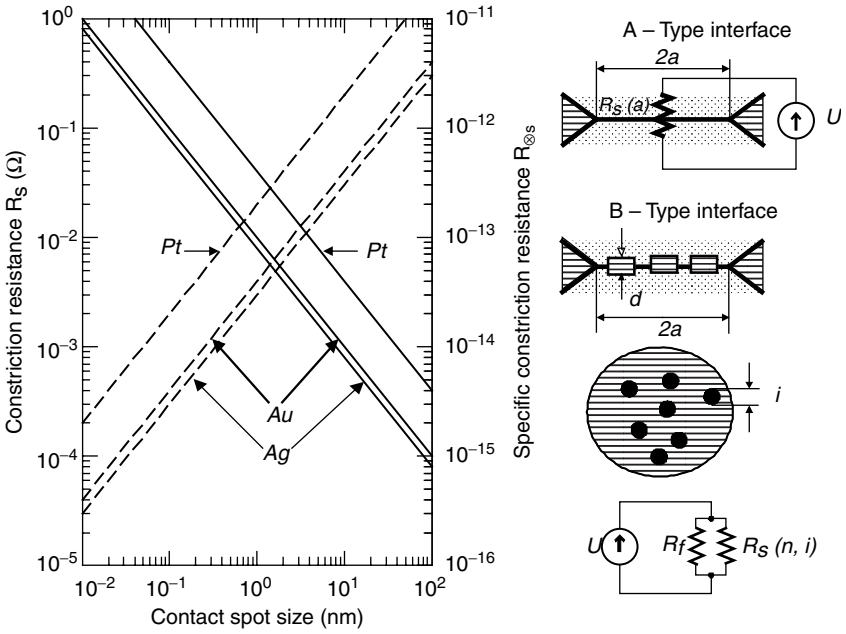

FIGURE 9.59 Interface models for lubricated point contacts of noble metals; dependence of constriction resistance R_s (a) and specific resistance $R_{⊗s}$ (a) on contact area radius.

$$R_s(n, i) = \rho/(2ni) \tag{9.18}$$

$$R_{⊗s}(n, i) = \pi\rho\alpha/2 \tag{9.19}$$

It is essential that $R_{⊗s}(n, i)$ does not depend on n but on the linear dimensions of the spots. The result is that with similar conductive areas within the contour region, $R_s(n, i)$ will be the lower; the smaller are metal spots.

For this model the relation between resistance of the n contact spots inside the known bearing area and constriction resistance of the bearing area assuming complete conductivity is of importance. It is stated by Barkan and Tuohy[810] that this relation can be expressed as

$$R_s(a)/R_s(n, i) = 1 - \exp(-\delta a/i), \tag{9.20}$$

where $\delta = n(i/\alpha)^2$ is the relation between the conductive area and the total bearing area.

Equation 9.20 indicates that a small portion of the bearing area can provide high conductivity, approaching that of the whole apparent area (maximum). For instance, from the calculations made by Barkan and Tuohy,[810] for $a/i = 100$, $R_s(n, i)$ exceeds $R_s(a)$ by 10% only, for the situation where 2.3% of the bearing area has metal conductivity. Greenwood[393] came to a similar conclusion and provided the numerical illustration. Barkan and Tuohy[810] stated that (1) a large number of conductive spots $R_s(n, i)$ depend primarily on the bearing area containing conductive spots; (2) R_c measurements cannot give the true conductive area; and (3) the most effective is the contact geometry with the bearing area containing the smallest isolated spots.

Figure 9.61 shows that for a given contour area a, there exist various combinations of n, and i/a at which $R_s(n, i)$ considerably exceeds $R_s(a)$. Several scientists have used $R_s(n, i)$ approaching the theoretical minimum $R_s(a)$ to explain the data on contact conductivity under boundary lubrication conditions. Campbell and Aronstein[800] described a lubricated contact model containing numerous metal spots within the loaded contact area and explained the combination of low R_c, low friction,

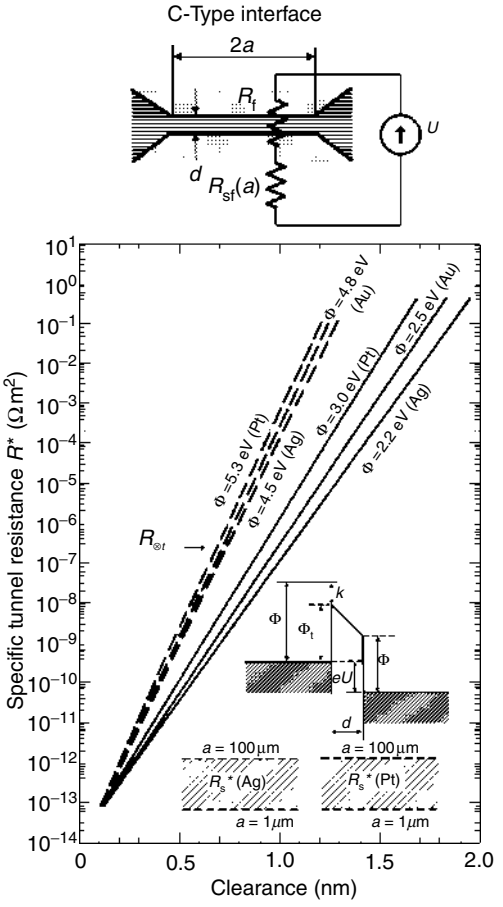

FIGURE 9.60 Interface type C: specific tunnel resistance $R_{\otimes t}$ vs. gap size d between Ag, Au and Pt surfaces if gap was filled up with lubricant (solid lines) and without lubricant (dashed lines); specific constriction resistance $R_{\otimes s}$ for Ag and Pt contacts (shaded areas) if contact radius was $a = 1$–100 μm.

and wear rate observed in practice. These theories considered that no current passage occurs through the thin lubricating layers of the main part of the bearing contact area.

In the case of interface of C-type (see Figure 9.60), a continuous thin lubricating layer of thickness d is formed on the contact spot. If there is a current passage through this gap, then

$$R_c = R_{sf}(a) + R_f. \tag{9.21}$$

The film changes the current channels distribution near the interface, leading to the constriction resistance to be somewhat higher than that of pure metal contacts (between $\rho/2a$ and $2\rho/(\pi\alpha)$).[1] With $R_f > R_{sf}$ for a limiting case,

$$R_{sf}(a) = 2\rho/(\pi a). \tag{9.22}$$

When a low voltage ($U < 50$–100 mV) is applied across the metal electrodes, the thin, separating lubricant layer can be considered as a potential barrier with the effective work function φ and the effective width being equal to the gap, d (see Figure 9.60). For a general case, the current can pass through the lubricating film by the *tunnel mechanism* (quantum–mechanical effect of transfer of electrons having energy below φ, i.e., inside the forbidden zone), *thermal electron emission*

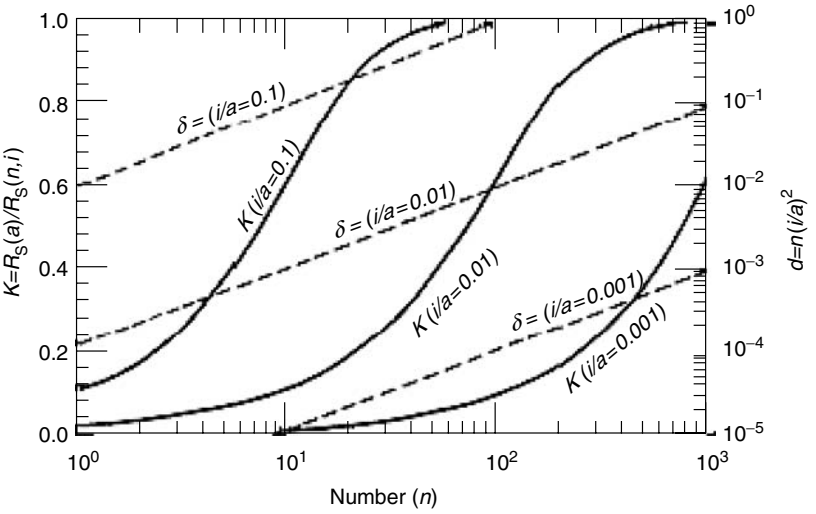

FIGURE 9.61 Relation K between $R_s(n, i)$ and R_s (A), as well as ratio of metal spots area to contour area (δ) depending on the number (n) and relative dimension (i/a) of metal spots.

(electron energy is above φ; transfer takes place inside the conduction band), and the *intrinsic conductivity* of the lubricant.

The quantum-mechanical tunnel theory first applied to the metal–dielectric–metal system[811] was further developed by several researchers,[1,390,812] resulting in a series of equations for tunnel conductivity of the whole range of voltages applied across the electrodes. For very low voltage, an expression is used[811] that is applied to idealized potential barrier of thickness d (see Figure 9.60):

$$\sigma_{\otimes t} = \frac{e^2(2m\varphi)^2}{h^2 d}\exp\left[-\frac{4\pi d}{h}(2m\varphi)^{1/2}\right], \tag{9.23}$$

where $\sigma_{\otimes t}$ is the specific (related to surface unit) tunnel conductivity; e and m are the charge and mass, respectively, of the electron; h is Planck's constant; φ is electron work function from metal to insulator. For two similar metals, $\varphi = \Phi - K$ (Φ is the work function from metal to vacuum and K is the electron affinity of the insulator).

Using Equation 9.23, another equation can be derived for specific tunnel resistance (d and K are in nanometers and electron volts, respectively):

$$R_{\otimes t}(\Omega\ \mathrm{m}^2) = \frac{1}{\sigma_t} = 3.18 \times 10^{-14}\frac{d}{\varphi^{1/2}}\exp[10.24\varphi^{1/2}d]. \tag{9.24}$$

For real contacts, it is difficult to estimate the effective work function, φ, from metal to film. For lubricating films, this task is not so difficult when using the available data[805,806] that shows the existence of prevailing tunneling conductivity through the monolayer of fatty acids at cryogenic and room temperatures by measuring the electron affinity for fatty acid monolayer ($K = 2.3$ eV). The effective work function for gold, silver, and platinum in vacuum at 4.8, 4.5, and 5.3 eV were found to be $\varphi_{Au} = 2.5$ eV, $\varphi_{Ag} = 2.2$ eV and $\varphi_{Pt} = 3.0$ eV.

Using the above data for φ, the resistances $R_{\otimes s}(d)$ for Au, Ag, and Pt derived from Equation 9.24 are plotted in Figure 9.56. For the same metals, $R_{\otimes s}(d)$ (broken lines) was plotted for unlubricated gaps ($\varphi = \Phi$). Figure 9.60 shows the extreme sensitivity of the tunnel conductivity to

variations in d even by 0.1 nm. At the bottom, the values of specific constriction resistance are given for the bearing area of radius 1–100 μm.

From Equation 9.24 the tunnel resistance depending on d can be expressed as:

$$R_t(\Omega) = 10^{-14}\frac{d}{a^2\varphi^{1/2}}\exp(10.24\varphi^{1/2}d). \tag{9.25}$$

It should be noted that $K \cong 2.3$ eV for the lubricant film with an approximate thickness of 1.5 nm or more.[805] However, for $d < 1.5$ nm K was found to be dependent on thickness, and approaches zero at minimal values of d.[813] Assuming K to be gradually reducing from 2.3 eV to 0 and d reducing from 1.5 to 0.5 nm, we have $K = 2.3(d - 0.5)$.

The *thermal electronic contact conductivity* at low voltages can be found as follows:[812]

$$\sigma_{\otimes T} = AT^2\frac{e}{kT}\exp\left(-\frac{\varphi}{kT}\right)\exp\left(\frac{e^2\ln 2}{kT\varepsilon d}\right), \tag{9.26}$$

where $\sigma_{\otimes T}$ is specific surface thermoelectronic conductivity; A is Richardson's constant; T is temperature; k is Boltzmann's constant; ε is the dielectric constant.

It was found[806] that the dielectric constant ε for monolayers of different fatty acids is 2.5–3.0. Assuming $\varepsilon \approx 3$ and taking φ in eV and d in nm, Equation 9.26 can be expressed in the form:

$$R_{\otimes T}(\Omega\ \mathrm{m}^2) = 7.1 \times 10^{-11}\frac{1}{T}\exp\left(\frac{11,600\varphi}{T}\right)\exp\left(\frac{-3,857}{dT}\right). \tag{9.27}$$

The calculations performed by using Equation 9.27 show that, at room temperatures ($d = 0.5$–3 nm; $\varphi = 2$–4 eV), values of $R_{\otimes T}$ are so high that the thermoelectron component in the total conductivity of the gap is negligible.

The lubricant in the gap, like any other insulator, has its own specific volume resistance ρ_v, which is independent of d. Special experiments conducted by Mann et al.[805] gave typical values $\rho_v \cong 10^{12}$–10^{13} Ω m for multimolecular fatty acid layers of 10-nm thickness. The specific resistance of gap (see Figure 9.60) resulting from the intrinsic lubricant conductivity can be calculated as follows:

$$R_{\otimes v} = \rho_v d \tag{9.28}$$

Then, at $d \cong 10$ nm and less (until ρ_v has physical meaning), $R_{\otimes v}$ has values of 10^7–10^9 Ω m^2 for the boundary layers formed by lubricants containing reagents such as fatty acids.

It follows from the above analysis that the conductivity of the C-type interface at d varying from a minimum to 2.0–2.5 nm depends mainly on the tunnel effect. As d increases further, the gap in fact becomes an insulator. If the size of bearing area is known, Equation 9.15 can be used in practice to evaluate the film resistance of lubricated point contacts with C-type interface. For example, for a gold–platinum point contact with reduced radius of approximately 20 μm, it was shown that at minimal possible thickness of continuous lubricant film $d = 0.5$ nm, $R_f \approx 0.6$ Ω. When the gap was increased, R_t grew rapidly, reaching approximately 10^4 Ω at $d = 1.0$ nm, and 3.8×10^6 Ω at $d = 1.5$ nm.[389]

Relations between the components of contact resistance. The above equations along with Figure 9.59 and Figure 9.60 can be used to estimate quantitative relations between the components of contact resistance for point contacts of the known bearing areas and different interface types. A hypothetical lubricated contact of silver cylinders having circular bearing area of radius $a = 100$ μm was considered (see Table 9.7) for the three types of interface mentioned above (Figure 9.55 and Figure 9.56) with different combinations of n, α and d.[391] When a contact with

TABLE 9.7
Example of Numerical Calculation of Contact Resistance and Its Components for Circular Contour Area at Different Combinations of *n*, *a* and *d*

Interface Type	Serial Number	*n*	*i* (μm)	*δ*	*d* (nm)	R_s (*a*) (Ω)	R_s (*n*, *i*) (Ω)	R_t (Ω)	R_c (Ω)
A-type (Figure 9.59)	1	—	—	1	—	0.8×10^{-4}	—	—	0.8×10^{-4}
B-type (Figure 9.59)	2	10	1	0.001	0.5	1×10^{-4}	8.2×10^{-4}	6.8×10^{-4}	4.7×10^{-4}
	3	100	1	0.01	0.5	1×10^{-4}	1.3×10^{-4}	6.8×10^{-4}	2.1×10^{-4}
	4	10	1	0.001	1	1×10^{-4}	8.2×10^{-4}	2.7	9.2×10^{-4}
C-type (Figure 9.60)	5	—	—	—	0.5	$1\times\times10^{-4}$	—	6.8×10^{-4}	7.8×10^{-4}
	6	—	—	—	1	1×10^{-4}	—	2.7	2.7
	7	—	—	—	1.5	$1.\times10^{-4}$	—	8×10^{3}	8×10^{-3}
	8	—	—	—	2	1×10^{-4}	—	2.1×10^{7}	2.1×10^{-7}

Note: Contact material: silver, $\rho = 1.65\times10^{-8}$ Ω m; $\varphi = 2.2$ eV; $a = 100$ μm.

a continuous lubricating film 2 nm thick (C-type, number 8 in Table 9.7) was changed to a pure metallic contact (A-type), R_c varied by more than 11 orders of magnitude. Narrower gaps with a continuous lubricating film caused a rapid decrease in R_t, while absolute values for R_c remained quite high up to $d = 0.8$–1 nm. In this situation a single small metallic spot can determine the conductivity of the whole contact.

With further gap narrowing, the situation is quite different. It is well known that long-chain carbon molecules of lubricants, fatty acids included, have a cross-section approaching a circle of diameter about 0.5 nm. This value can be taken as the lower gap thickness, assuming that there is a densely packed lubricant monolayer with ideal chain arrangement parallel to the electrode surfaces. If the monolayer is assumed to cover the whole bearing surface, a very low tunnel resistance (1.0 m Ω, Table 9.7, number 5) can be obtained. Hence, even with dozens of metal spots (radius $i = 1$ μm) formed within the bearing area, the tunnel conductivity of the remaining part of the contact surface is important or at least comparable with $R_s(n, i)$ (see Table 9.7, numbers 2 and 3). For $d = 0.5$ nm, the tunnel resistance, R_t, exceeds the maximum possible constriction resistance ($R_s(a)$), but only by a few times.

We can come to conclusion that the tunnel conductivity adds significantly to the total conductivity of the lubricated noble metals since the high contact conductivity can result from the tunnel effect alone. If metal spot clusters are formed (B-type interface), then this possibility can easily be illustrated by Figure 9.60 and Figure 9.61.

When the metal part δ of the contact area is small, the resistances R_t and $R_s(n, i)$ can be balanced as follows:

$$R_{\otimes t}/R_{\otimes s} = S_t/S_{me} = 1/\delta, \tag{9.29}$$

where S_t and S_{me} are contact areas with tunnel and metallic conductivity. It can be seen in Figure 9.60 that low d (0.5–1 nm) gives low value for $R_{\otimes t}/R_{\otimes s}$, *e.g.*, 10^2–10^4. However, Figure 9.61 shows a great number of combinations of n and i/a for clustering, when $\delta = 10^{-4}$–10^{-2}; therefore, Equation 9.29 will be valid.

It is evident that the role of tunnel conductivity becomes more important with narrower contact gaps. The approach depends not only on the lubricant properties but on the microgeometry of the contact surfaces as well. Hence, under equal conditions, the tunnel conductivity will be higher for smoother contact surfaces. From the above discussion the following conclusions can be made:

- High conductivity of lubricated noble metal contacts does not imply that metal spots are present on the surfaces, except in situations where the contact resistance, R_c, approaches the lower limit ($R_s(a)$). Low R_c can be obtained for three types of interfaces; see Figure 9.59 and Figure 9.60.
- With a continuous lubricating layer in the contact gap, a high enough conductivity can be provided with the gap thickness below 1 nm. This is only possible when the boundary lubricating layer consists of chain molecules arranged parallel to the contact surfaces. The existence of even a monomolecular lubricating layer (e.g., fatty acids), in which molecules are arranged normal to the surface, prevents the passage of current.
- For high conductivity contacts (the exception being when $R_c \rightarrow R_s(a)$), it is difficult to define the type of the interface (B or C), and the prevailing mechanism of contact conductivity (metallic or tunnel) can be estimated by measurements of R_c. To clarify the conductivity mechanism, additional information on the contact behavior is required, e.g., dependence of R_c on temperature and voltage between the electrodes, data on the electrical noise, and friction in the contact.

9.3.3.3 Experimental Studies of Electric Conductivity of Lubricated Contacts

Low-speed microtribometers and probe devices with geometrically regular specimens have been used in numerous experimental studies related to electric conductivity of lubricated contacts. Such devices allow tests to be conducted under static conditions ($R_c(N)$ dependences) or in dynamics when recording tribological parameters and electric conductivity simultaneously.

$R_c(N)$ *dependence* for specimens with point contact has been widely used in the estimation of relative efficiency of contact materials; study of surface films, different ambient-medium effects on metal surface, and for some other purposes.[1,66,810] This dependence can give important information on the effect of the lubricant on the contact conductivity, strength of boundary lubricating layers, and the ability to separate surfaces.

In a number of studies of lubricated point contacts of crossed cylinders or sphere-on-plane contacts,[391,810] dependences $R_c(N)$ during smooth contact loading were obtained (see Figure 9.62). The dependencies are characterized by a sharp bend at a certain critical load N_{cr} which depends on the type of lubricating medium. The calculations indicate that for many liquid lubricants, N_{cr} corresponds to the onset of formation of the metallic conducting spots within the bearing area.

It was found in experiments with noble metals[391] that even with metallic spots formed at loads that exceed the critical value under conditions of elastic–plastic contact, the lubricant would not be completely squeezed out of the contact gap. Contact resistance measured at these loads can indicate the ability of lubricant molecules to prevent surface contact after the boundary layer was destroyed. It was revealed that $R_c(N)$ relationships recorded during smooth contact loading can provide information on the strength of lubricant monolayers, namely, on critical pressure damaging monolayer structure, and also on the ability of lubricant molecules to separate surfaces at loads exceeding the critical values. When selecting or developing lubricants for joints operating at high contact pressure, it is not necessary to have $R_c(N)$ dependences over the whole load range. Information on the protective effect of boundary monolayer molecules can be obtained when R_c is determined at values $N > N_{cr}$.

Figure 9.63 presents comparative data[814] on such protective effects of different lubricants (oils, greases with soap, organic and inorganic thickeners), obtained for a stationary contact between a silver sphere and platinum plane under normal load in the range of $N > N_{cr}$. The contact resistance

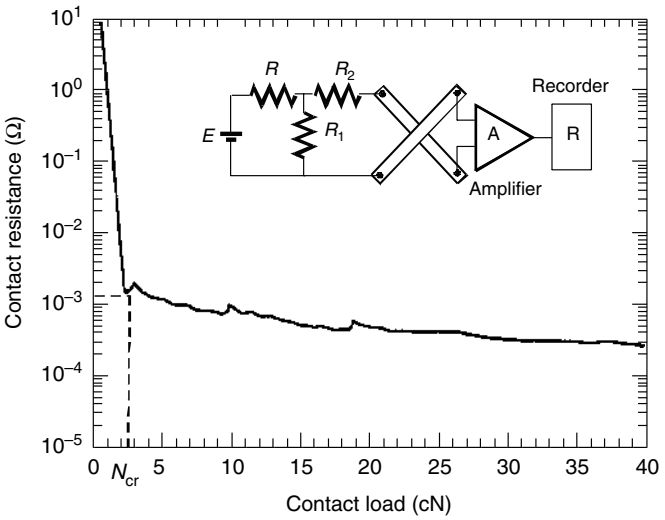

FIGURE 9.62 Diagram for measuring contact resistance R_c (E: stabilized power source; R, R_1, R_2: resistors; A: wide-band amplifier; R: recording device) and typical dependence for R_c (N) for lubricated contact.

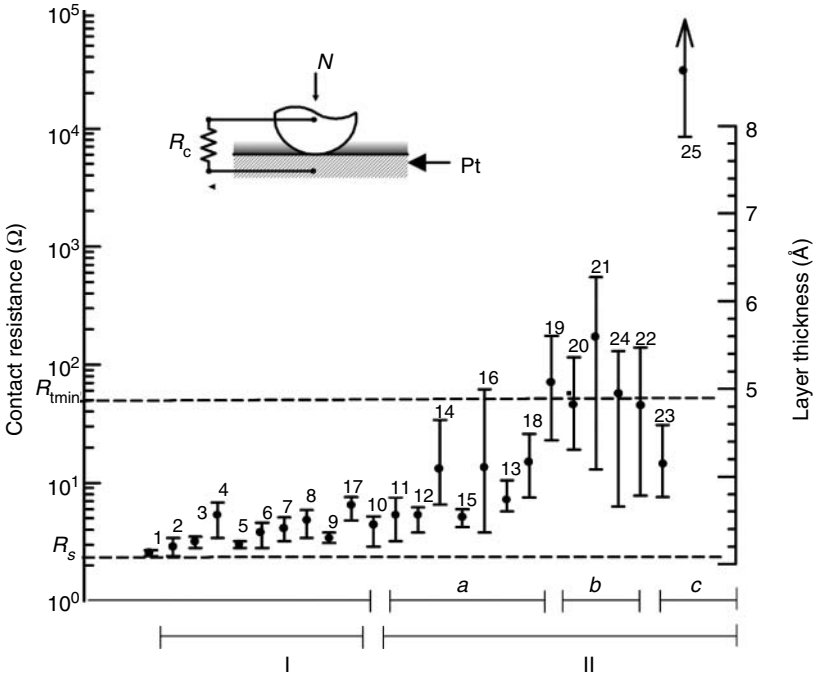

FIGURE 9.63 Contact resistance for silver probe (sphere of 20-mm curvature) on platinum plate covered with (I) liquid lubricants and (II) greases containing thickeners: (a) soap, (b) organic, and (c) inorganic (Load $N =$ 1 N, R_{tmin} is the tunnel resistance for lubricant layer of 0.5-nm thickness). The lubricants used were: (1) no lubricant; (2) Vaseline oil (VO); (3) oleic acid (OA); (4) VO + OA (2%); (5) silicon fluid; (6) dioctilsebazinate (DOS); (7) diproxamine (D157); (8) pentaerythritol ester (PET); (9) polyglycol ester. Soap greases: (10) silicon fluid + seresin; (11) PET + lithium hydroxystearate (12OHLiSt) + additives; (12) DOS–D157 + LiSt + additives; (13) DOS–D157 + lithium oxystearate (LiOSt); (14) DOS + 12OHLiSt + additives; (15) DOS–D157 + LiSt + additives; (16) fluid 132-24 + Ca-soap + additives; (17) PET + LiSt. Organic greases: (18) DOS–D157 + polyurea (P); (19) PET + P; (20) VO + P; (21) VO + polyethylene. Inorganic grease: (22) DOS + alkil petroleum oil + LiSt + Benton; (23) DOS–D157 + Benton; (24) DOS–D157 + silica gel; and (25) DOS–D157 + ammelin.

below $R_{tmin} = 50$ m Ω indicates the presence of metallic spots, whereas with a higher level of R_c, metallic contact is hardly possible, and the contact conductivity depends mostly on the lubricating film thickness d.

In case of greases and some viscous oils, the $R_c(N)$ dependencies often demonstrate that the lubricating film is 1.5–2 nm thick at N_{cr} and that there are no metallic spots (see Figure 9.64, numbers 6–8).[389] Hence, N_{cr} indicates a critical stress at which the multimolecular boundary layer becomes damaged. This stress can be useful in evaluating the mechanical properties of the multimolecular boundary layer.

The data obtained from analysis of $R_c(N)$ dependencies have led to some conclusions on the mechanical properties of boundary lubricating layers in the contact gaps of nanometer thickness.[389] It is a matter of common knowledge that monomolecular layers of surfactants adsorbed on a metal surface are much stronger than multimolecular layers, e.g., it is believed[1,23] that even plastic strain of asperities may take place without the failure of monolayers. Some experimental observations support the validity of this assumption. First of all, it is clear that lubricant films of thickness down to 2 nm can contain continuity at loads $N > N_{cr.}$. From the relations $R_c(N)$ implying the presence of shelves (see Figure 9.64, numbers 8 and 9) it is obvious that the loads at which the monolayer fails

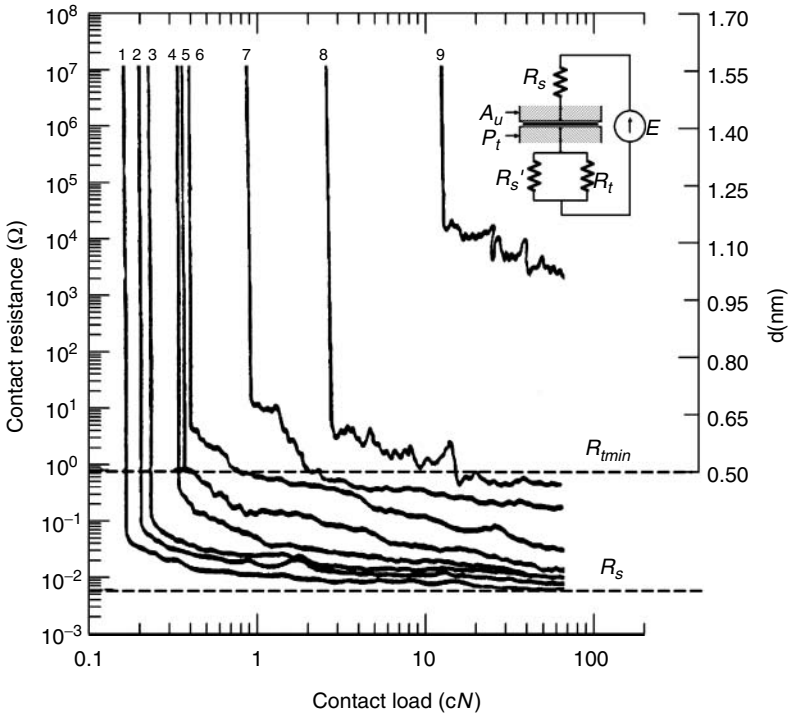

FIGURE 9.64 Substitution schematic diagram and typical dependences of R_c (N) at normal loading when gold probe was loaded over platinum: (1) unlubricated; (2) lubricated by Vaseline oil; (3) oleic acid; (4) Vaseline oil + 1% oleic acid; (5) polyglycol diproxamine D157; (6) Epilamen (fluororganic film); lubricants thickened by (7) lithium stearate, (8) lithium oxystearate, and (9) lithium 12 hydroxystearate. R_s and R_{tmin} are calculated constriction resistance and tunnel resistance, respectively, for lubricant layer of 0.5-nm thickness.

exceed N_{cr} by an order of magnitude or even more. Monolayers appear to survive under average contact pressures of about 0.5 GPa, which is comparable with the microhardnesses of several metals.

The data obtained experimentally, together with the analytical results presented above, lead to some general conclusions on the current flow through the point contacts under conditions of boundary lubrication:

1. In terms of conductivity of a lubricated contact, boundary lubricating films may be conditionally divided into two types:
   a. "Thick" (over 1 nm) monomolecular and multimolecular films ensuring excellent antifriction characteristics of the contact and excluding its high electric conductivity;
   b. "Thin" (less than 1 nm) continuous (or containing few breaks) films characterized by high contact conductivity. In practice, pairs with the point contact geometry in a fixed position as well as in sliding can create conditions when two types of boundary lubricating films are possible. In order to form a thin film, a critical pressure p_{cr} should be reached which is characteristic of the given lubricant and the substrate metal and leads to boundary layer structure decomposition. This is in agreement with data on noble metals with adsorbed lubricant monolayers that show a transition from low to high contact conductivity upon exceeding a critical load.[23]

2. It is also possible that under conditions when a continuous lubricating interlayer between metal surfaces is maintained, high contact conductivity occurs due to the tunneling effect.[798] The calculations do not exclude such a possibility for smooth noble metallic surfaces. However, the analysis of experimental data showed that in boundary lubrication, a model of B-type interface is most probable for real metals, e.g., low-speed sliding contacts, where the tunnel conductivity coexists with the metallic conductivity. For the C-model, the extremely high sensitivity of R_t to the gap thickness should lead to an extremely unstable R_c even at negligible variations in d-values which is unavoidable under sliding conditions.
3. The combination of different conductivity types found in lubricated friction units makes it impossible to determine the threshold contact resistance which would indicate formation of the contact metallic spots based on R_c values. For the same reason, estimating the real contact area basing on R_c data is not possible. Nevertheless, for the lubricated noble metallic pairs, where the bearing contact area is known, it is possible to estimate R_c peak values; this is helpful in classifying the three types of interfaces discussed above (see Figure 9.59 and Figure 9.60).

9.3.3.4 Contact Resistance between Very Smooth Lubricated Surfaces

In most of the studies on electrical contact resistance of lubricated contacts, the Hertzian-type of contact was used, whereas very few studies dealt with smooth plane surfaces at low contact pressure of around 1 MPa. Contact problems concerning very smooth lubricated surfaces, however, are becoming important because increasing of applications of fine polished plane surfaces of nanometer roughness, such as magnetic disks and sliders, semiconductor wafers, and different MEMS devices. In many cases, the contact surfaces are plain and larger than the Hertzian contact area. The thickness of the oil film is comparable with the roughness height, but it can support pressure to some degree without any hydrodynamic effect.[815] This means that solid surfaces can be kept apart, and wear by solid–solid contact does not occur if the oil film covers sufficient surface area.

Contact resistance between a Ni plate with roughness 1–3 nm coated with perfluoropolyester (PFPE) and an uncoated plate was evaluated under different apparent contact pressures by Hiraoka[816] to estimate the isolation ability of PFPE. Precision test equipment included conical pin (R_a: 3 nm) on top of parallel leaf springs pressed into a polished Ni plate (R_a: 1 nm) with PFPE coating of 4–6 nm thickness.

Two types of relationships between load and R_c under static loading were observed (see Figure 9.65). The specimen surface of first type (cases 4 and 5) was estimated to be uniformly covered by an oil film, and the second type (case 3) was estimated to be covered by a patchy oil film. The oil-coated specimens (cases 4 and 5) exhibit a much larger resistance than the uncoated specimens under lower loads, and nearly the same or even smaller resistance and slope under higher loads.

The analysis of R_c slope and friction test results have shown that in the cases 4 and 5, the uniformly coated oil film (corresponds to C-type interface, see Figure 9.60) supports the load in statics and prevents solid–solid contact. The electric current flows through the oil film by a tunnel effect that leads to a steep resistance slope related to load. For larger loads (about 2–3 MPa of apparent contact pressure), the oil film breaks down, changing the slopes of resistance to those of cases 1–3 (A- and B-types of interface; see Figure 9.59). Under large loads, when the oil film has been broken, the specimens of cases 4 and 5 can exhibit a smaller resistance than the uncoated specimens. As the resistance of solid–solid contact is sensitive to any oxide layer or contaminant on the surface, this smaller resistance may be due to variation in the surface characteristics of nickel.

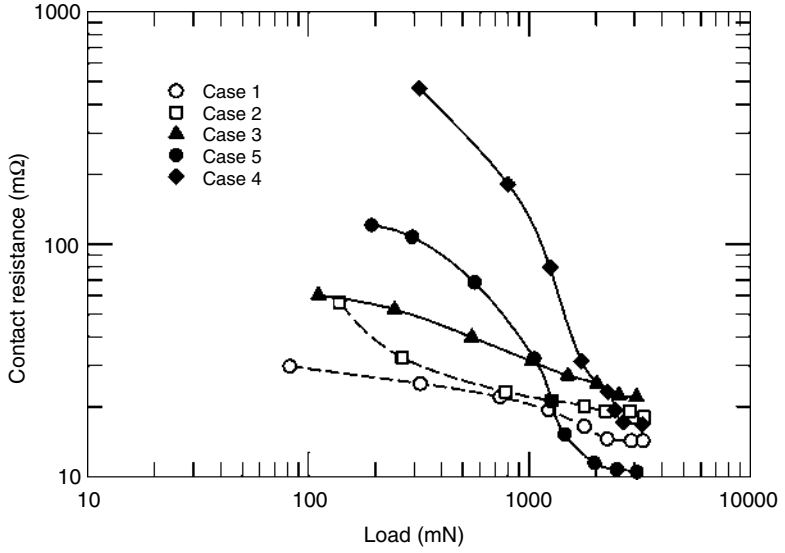

FIGURE 9.65 Relationships between contact force F and electrical contact resistance R_c for polished nickel plates with PFPE coating. Cases 1 and 2 are uncoated specimens; case 3 has patchy coating of the oil film; cases 4 and 5 have uniform coating of the oil film. (From Hiraoka, N., *Tribology International*, 33, 99–105, 2000. With permission.)

9.3.3.5 Temperature Dependencies of Contact Conductivity

It is obvious that the temperature variation of the interface state exerts an influence on the contact conductivity. Correct interpretation of the results, however, may be hindered because all types of contact conductivities are temperature-dependent. Thus, the observed changes of R_c with temperature can be reversible and may not result from the boundary layer transformation. In addition, the contribution of different types of conductivity to the total contact conductivity can vary with temperature. Therefore, consideration of the temperature dependencies of the main types of contact conductivities is necessary.

Metal conductivity. The electrical resistance of metal is known to increase with temperature. Therefore, if there are no metal phase transformations, the temperature dependence of contact resistance R_c is almost linear. A positive temperature coefficient of resistance within the range 0.002–0.005°C^{-1} and low absolute R_c displays dominating metallic conductivity. The difference in the absolute R_c of two contacts when their $R_c(T)$ are linear shows that metallic conductivity varies with the respective areas of metal microcontacts.

Tunnel conductivity. Equation 9.24 was obtained for absolute zero temperature. Simmons[817] has shown that the following relation between specific tunnel resistance at temperature T and that at absolute zero for the units mentioned (d (nm), φ (eV)), is valid:

$$R_{\otimes t}(T) = R_{\otimes t}(0)/(1 + 3 \times 10^{-7} d^2 T^2/\varphi). \tag{9.30}$$

Analysis of Equation 9.30 shows that the temperature dependence of tunnel conductivity is quite weak over a wide temperature range, thus Equation 9.24 and Equation 9.25 can be used at low and room temperatures. This statement has been confirmed experimentally by Polymeropoulos,[806] who has found that the tunnel resistance of fatty acid monolayers changes only slightly within the range 293–373 K.

On the other hand, Holm[813] has shown that up to a critical temperature T_{cr}, the decrease of tunnel resistance is insignificant and determined by the following expression:

$$T_{cr} = C\varphi^{1/2}/d, \tag{9.31}$$

($C = 1130$, if d in (nm) and (in (eV)).

At $T = T_{cr}/3$, $R_{\otimes t}$ decreases by no more than 5%; at $T = T_{cr}$ it decreases twofold; and with a further increase in temperature, $R_{\otimes t}$ decreases sharply. Table 9.8 shows T_{cr} values for contact gap for films of different types and thicknesses. For technical metals, Φ cannot be lower than 4 eV; hence, at $d < 2$ nm ($\varphi \sim \Phi$), T_{cr} exceeds 1000 K independently of the nature of the substance in the contact gap. At $d > 3.5$ nm and $K = 2.0$–2.3 eV for lubricating films, tunnel conductivity remains independent of temperature only up to -450 to 550 K, i.e., inflections of the dependences $R_{\otimes t}(T)$ can be within a realistic temperature range. The absolute values of tunnel resistance, however, are excessively high for such a film thickness, and the use of the contact resistance method makes no sense.

With gaps of 2–3.5 nm, values of φ are hardly likely to be less than 3 eV. Thus, T_{cr} can be between 600 and 800 K, i.e., much higher than the temperature of the lubricant in use.

Thermoelectronic conductivity. The analysis[818] shows that $R_{\otimes T}$ decreases quickly with T, but it is much higher than $R_{\otimes t}$ over a wide temperature range (see Figure 9.66). In particular, for dielectric films with $\varepsilon = 3$–10 and $d_Q < 2$ nm, thermoelectronic conductivity becomes dominant only at $T = 1000$ K. Thus, thermoelectronic emission plays an insignificant role in contact conductivity, especially for thin films.[812,813]

Intrinsic conductivity. Typical values of ρ_v are approximately 10^{12}–10^{13} Ω m for thin lubricant layers were obtained in special experiments.[805] Hence, for boundary layers formed by lubricants with such components, according to Equation 9.28, $R_{\otimes v}$ could be between 10^7 and 10^9 Ω m^2, which is many orders of magnitude higher than $R_{\otimes t}$ (see Figure 9.66). A thermally activated component of conductivity resulting from the impurities and film imperfections appears even at room temperature. On the other hand, high contact pressure in the gap (usually about 10^7–10^9 Pa), decreases the impurities' mobility. This fact, with excessively high $R_{\otimes v}$ values in comparison with $R_{\otimes t}$, confirms that intrinsic conductivity is not a dominant factor at real temperatures in lubricated contacts.

Thus, in thermal tests under boundary lubrication, the thermoelectronic and intrinsic conductivities may be neglected in many cases, especially for lubricating film thicker than 2–3 nm.

TABLE 9.8
Critical Temperature T_{cr} (K) for Tunnel Conductivity of Lubricant Films of Different Nature and Thickness

	Thickness of Layer, d (nm)								
φ (eV)	1	1.5	2	2.5	3	3.5	4	4.5	5
1	1130	753	565	452	377	323	282	251	226
1.5	1384	923	692	554	461	395	346	308	277
2	1598	1065	800	639	533	456	400	355	320
2.5	1787	1191	893	714	596	510	447	397	357
3	1957	1305	978	782	652	559	489	435	391
3.5	2114	1409	1957	846	705	604	529	470	423
4	2260	1507	1030	904	753	645	565	502	452
4.5	2397	1598	1198	956	800	685	600	503	479
5	2526	1685	1263	1011	842	722	632	562	505

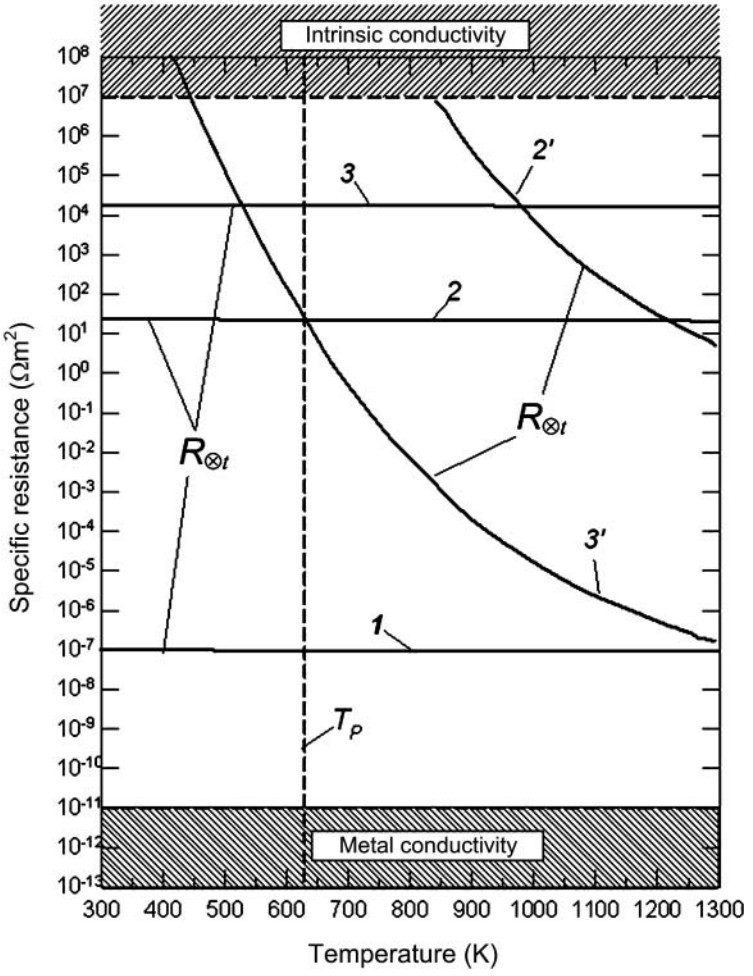

FIGURE 9.66 Temperature dependences of main types of contact conductivity with a lubricating film ($\varepsilon = 3$, $\Phi = 4.1$ eV, $K = 2.3$ eV). (1) $d = 1$ nm; (2, 2′) $d = 2$ nm; (3, 3′) $d = 3.5$ nm. T_p: conventional temperature limit of lubricant use in practice.

In situations when electrical methods are especially sensitive to changes in the interface state (clusters of metal spots within the contour area, or a continuous lubricating film with a thickness of approximately 3 nm), tunnel conductivity theory and constriction theory may be used to analyze experimental data. Thus, Equation 9.24 and Equation 9.25 may be used without taking account of the temperature effects.

9.3.4 Lubrication Factors in Sliding Contacts

The primary purpose of lubricant application in industry is to lower friction and prevent wear. In design of a bearing, the objective is therefore to keep the surfaces completely separated so that they will not rub against each other. Since most commercial lubricants are insulators, this means that metallic contact is prevented entirely and contact resistance between the sliding surfaces is very high.

In contrast, the primary purpose in developing lubricants for electrical contacts is to maximize and maintain a high area of metallic (quasimetallic) contact, so as to maintain minimum contact resistance. Thus, the antiwear additives of a good commercial lubricant are almost inapplicable.[819] For instance, soap formation through the use of fatty acids as additives is unacceptable for gold and other inert noble metals. Examples of such noneffectiveness were demonstrated by Antler[820] for gold lubricated by dilute mineral-oil solutions of lauric acid, tricresyl phosphate, and carbon tetrachloride.

Nevertheless, oils and greases have been developed which do not significantly change the contact resistance of static contacts but have a remarkable ability to lower friction by as much as a factor of 10 and to reduce wear by many orders of magnitude.[26,819] The explanation for these effects is given elsewhere.[800]

9.3.4.1 Effect of Lubricant Origin

The sliding lubricated contacts operate largely in the elastohydrodynamic region,[819] where both boundary effects and bulk properties control lubricating behavior.

In the 1960s, it was shown that the use of mineral oil for sliding contact is detrimental to conductivity due to the formation of tar, especially at elevated temperatures.[821] Silicon oils are not susceptible to lacquer formation and chemically stable, but they have a poor lubricity. In switching contacts, under arcing conditions an insulating film of silicon dioxide SiO_2 is formed that can completely cover the contacting surfaces.

Various fluids were tested as lubricants for gold and other contact materials by Antler.[26,640,746,747,820] These range from pure materials to complex mixtures incorporating antioxidants, viscosity index improvers, detergents, and other additives used for mechanical devices. In an early study on the lubrication for gold, Antler[640] determined sliding characteristics for a number of fluids including dimethylpolysiloxanes, phenylmethylpolysiloxanes, silicate esters, polychlorotrifluoroethylenes, diesters, fluorinated esters, polyalkylene glycols, chlorinated hydrocarbons, phosphate esters, polyphenyl ether, petroleum oils, and several metalorganics dissolved in mineral oil. The study was continued[747,820] at slightly different test conditions with additional materials, including other polyphenyl ethers, perfluoroalkyl polyethers, and poly-alpha-olefins.

The investigation initially involved a determination of the coefficient of sliding friction, wear rate, and contact resistance using solid gold specimens in a rider-flat bench apparatus. Contacts were submerged in fluids. It was found that the effectiveness of the lubricant depended on its chemical structure and viscosity.

The friction data are summarized in Figure 9.67, which also shows data on contact resistance.[822] The salient findings are that:

- Halogen-containing fluids are better lubricants than those which incorporate silicon. Oxygen-containing lubricants and hydrocarbons have intermediate behavior.
- Electrical noise can occur during sliding with fluids having either low or high viscosity; low-viscosity fluids are poor lubricants. High-viscosity fluids promote hydrodynamic separation of the contacts. The viscosities where these effects occur depend on contact normal load, sliding velocity, and other factors.

The shapes of the curves in Figure 9.67 are remarkably similar. The coefficient of friction was low and wear was negligible during sliding with several classes of fluids having a viscosity in the range of 100–1000 centistokes at 25°C. Reasons for differences in the effectiveness of lubricants according to chemical class at low viscosities are unknown. Antler proposed that more effective fluids are adsorbed more strongly on gold surfaces than the less effective ones.

Antler's studies also included an evaluation of thin-film sliding with several of the better lubricants. The films were obtained by immersion and withdrawal of specimens from 0.5% to

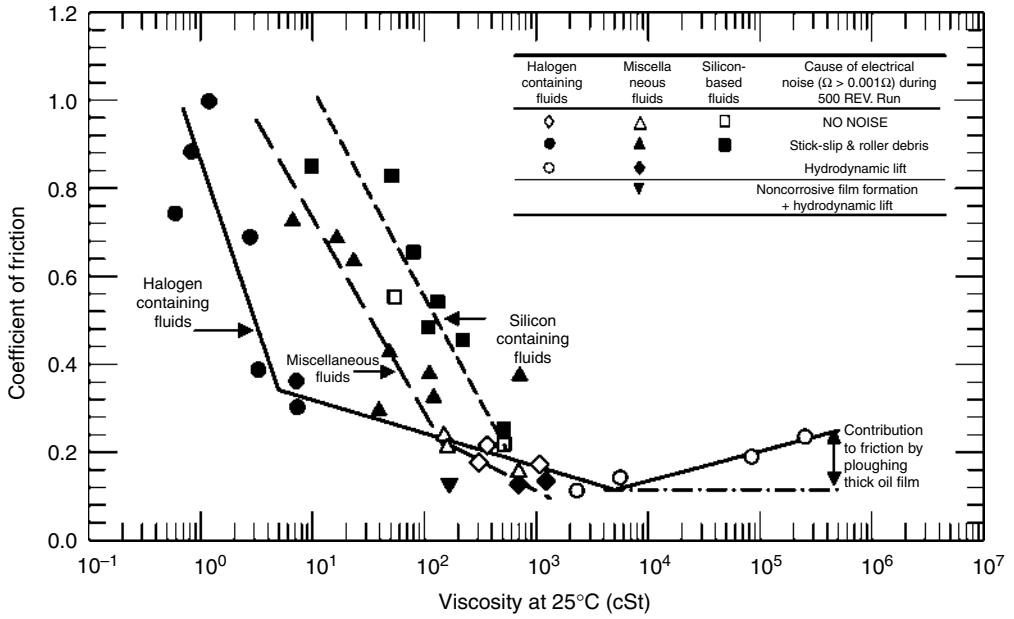

FIGURE 9.67 Coefficient of friction vs. viscosity for fluid lubricants. Friction determined near end of 500 rev runs at 100 g and 1 cm/s on 2.5-cm circular track using solid gold contacts. Friction is related both to fluid type and to its viscosity. Electrical noise with poor lubricants is due to hydrodynamic lift or sliding-generated insulating solids which adhere to surface.

1.0% solutions in volatile solvents. The results of the study with submerged contacts were confirmed, and additional details of lubricant wear-out were obtained.[26]

Capp and Williams[159] studied friction and wear of lubricated palladium alloy inlays. It was shown that lubrication is essential in order to achieve a low and repeatable coefficient of friction whether using inlay or electroplated material. Polyphenyl ether was the most effective in preventing adhesive wear. Mineral oil and polyolester also reduced the coefficient of friction, but were not as effective, probably due to their lower viscosity.

9.3.4.2 Lubricant Durability

In many electric contacts, lubricant films are thin and consequently have limited lifetimes. Data on sliding with different fluid films can be found elsewhere;[26,159,819] the quantity, not only type of lubricant, are important. Experiments in which thickness of the lubricant film was varied by diluting the lubricant with a solvent have shown that very little lubricant is required to achieve low friction. Except for the case of 0.1% mineral oil, the samples maintained a low and consistent friction (<0.25) for at least 1000 cycles (see Figure 9.68).

For thermally and oxidation stable materials, the causes of lubricant wear-out are related to depletion by evaporation, creep, and mechanical removal with debris.[26] When chemical effects occur, such as oxidation of lubricants at high temperatures, viscosity changes, sludge formation, and contact corrosion, they are considered as the wear-out mechanisms.

The wear-out causes an increase in friction during repeated sliding at a rate which reflects the combined rates of the several processes of lubricant depletion. This is shown schematically in Figure 9.69. A very thick initial film (curve C in the figure) does not wear out. Antler[640] has shown that in such a case, the coefficient of friction and contact resistance are low and stable and the wear

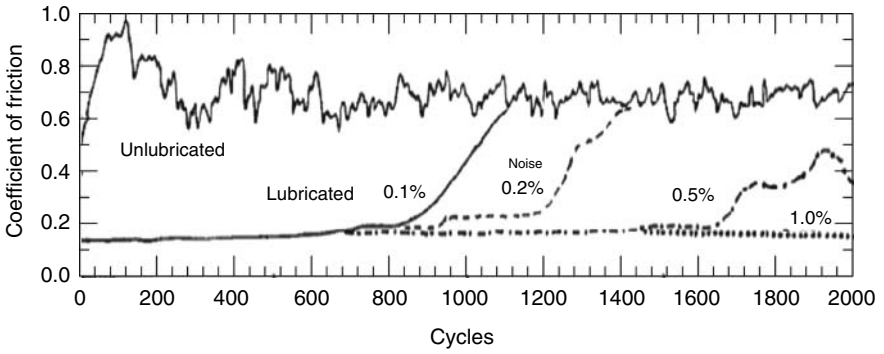

FIGURE 9.68 Coefficient of friction as a function of quantity of lubricant (mineral oil, 25 N, brass electroplated with Au vs. diffused gold 60Pd40Ag).

rate of the contact material is negligible in the long run. Lubricant films of small initial thickness results in sliding with a rising coefficient of friction until the transition between mild and severe wear occurs (see Figure 9.69, curve A). Lubricant films having an intermediate initial thickness display a rising coefficient of friction, but at a smaller slope (Figure 9.69, curve B). The criterion of failure of the system could be the value of the coefficient of friction relating to transition between mild to severe wear.

Based on numerous tests conducted on a rider-flat apparatus for cobalt–gold-plated riders vs. DG R-156 clad flats, Antler[746] recommended the use of concentration of 1–2 wt% of common

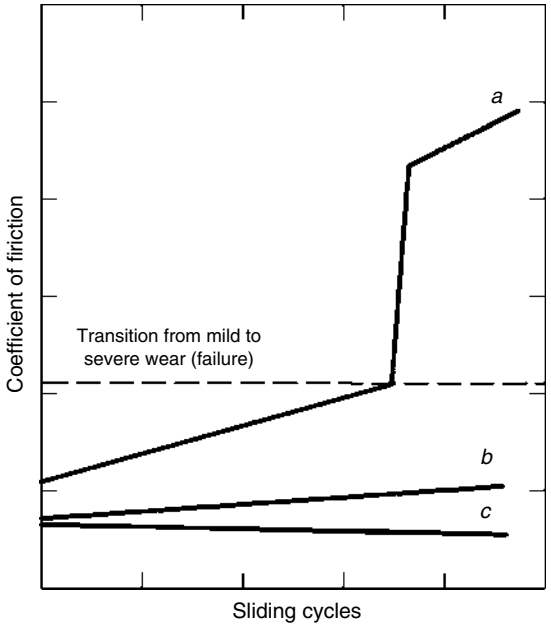

FIGURE 9.69 Relationship between coefficient of friction and cycles of sliding for postulated wear-out mechanisms of contact lubricants as function of their thickness (schematic). Initial thickness $a < b < c$. As lubricant is depleted by evaporation, migration, or physical removal, such as by wear debris produced during sliding, coefficient of friction rises. If transition from mild to severe wear occurs during intended lifetime of connector, lubricant has failed.

lubricants in appropriate solvent solutions for practical applications in wiping and sliding contacts. Thicker lubricant films are not deleterious, and neat fluids as droplets or smears of greases, have been used with good results.

In general, when applying a lubricant to a contact, the maximum amount which can be maintained in the contact zone should be used, especially when a base metal is involved.[819] Too little lubricant is commonly added for fear that dust will be attracted. This is not the case, because the area exposed to particle impact is the same for thin and thick films. The thin film is less protective to oxidation and tarnish, much poorer at dispersing particles which enter the contact zone, and very prone to oxidation and gumming.

An example of the action of too little lubricant is shown in curve *a* of Figure 9.70 for phosphorus bronze sliding on brass. The lubricant was petrolatum, which is basically a natural dispersion of wax in heavy oil. The rise in contact resistance is much faster than for curve, *b*, for a thick film of petrolatum. At point, *A*, on curve, *a*, the surfaces were thoroughly washed with solvent, with the result of a very rapid increase in contact resistance leading to an open circuit. This indicates that a thin, gummy-oxide film still remains on the contact surface. The descending portion of the curve *a* presents the frictional removal of the lubricating film as manifested by a sharp drop in the resistance. When the friction is at its minimum, the resistance is at maximum.

Various lubricants (both liquids and greases), once applied as a quite thick layer, are able to maintain light-current sliding contact operation under boundary lubrication conditions during 10^5 cycles and more. The service life of the component in this case depends often not on the wear of the contact elements, but on the contact resistance which can exceed the limiting value. This was demonstrated in the case of lubricated sliding contacts of electromechanical switches subjected to a long-term operation.[823] The tests were carried out on a cylinder-on-flat contact configuration with 2–3 μm thick silver coating and friction, wear, and a contact conductivity recorded as functions of sliding cycles.

Lubrication of contacts is shown to stabilize friction, and most of the lubricants used (polyglycol esters, epilamen, fluorinated liquids, polyethylsiloxane liquids, greases on its base) maintain the boundary lubrication condition even after 150,000 sliding cycles. However, contact resistance is

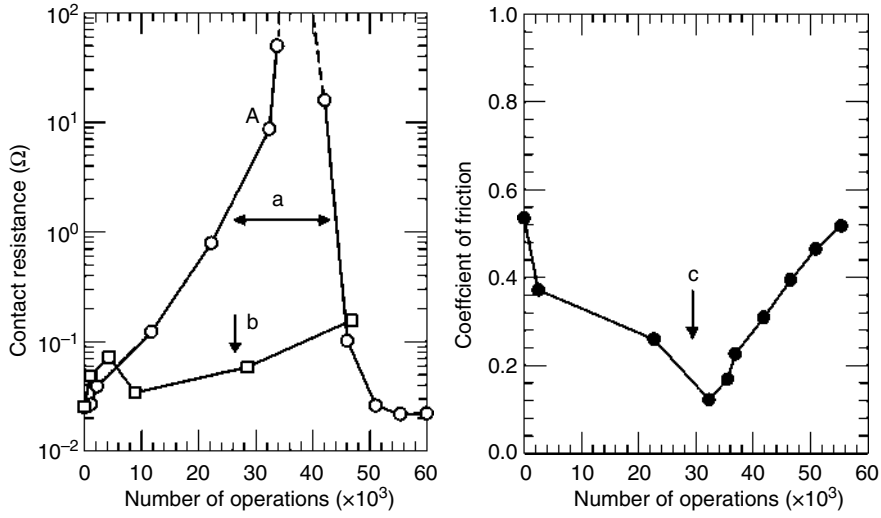

FIGURE 9.70 Effect of lubricant-film thickness on rate of increase in contact resistance. (a) Thin film of petrolatum, removed by solvent at point A; (b) thick film of petrolatum; (c) coefficient of friction corresponding to curve (a).

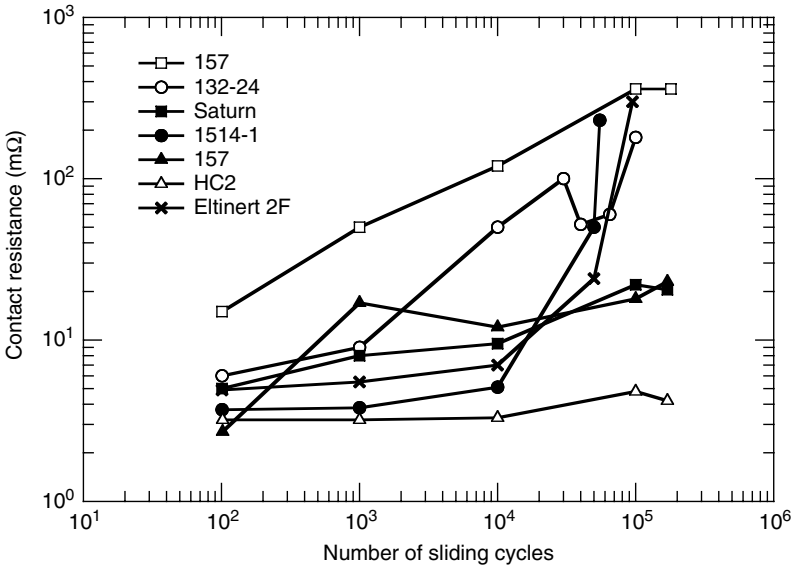

FIGURE 9.71 Contact resistance R_c vs. number of sliding cycles with different lubricants ($N = 0.6$ N; $v = 30$ mm/s). 1: calcium grease based on PES (analog to MIL-G-7421B); 2: polyethylsiloxane liquid 132-24 (PES); 3: polyglycol ester PE (HC2); 4: lithium grease based on PE; 5: mixture dioctylsebacinate:poliglycol-diproxamine; 6: Saturn (lithium grease based on dioctylsebacinate); 7: Eltinert 2F (grease based on fluorinated liquid).

found to increase with time (see Figure 9.71), and its instability leads to a significant distortion of the transmitted signal. The studies of boundary lubricating layer behavior showed that under multiple reciprocating motions, polymer-like substances are formed. Such modification of the lubricating layer increases the load-carrying capacity, provides a more reliable protection of the surfaces, and simultaneously impairs contact conductivity. The origin of these effects and means of their prevention are peculiar for every lubricant and require special investigations. From a tribological point of view of sliding contact, some liquids (esters, polyglycols) are equal or even better than liquid-based greases despite their strong tendency to increase R_c in operation.

9.3.4.3 Tribochemical Aspects of Lubrication

Studies of conductivity of lubricated contacts showed that contact conductivity can be enhanced either indirectly by adsorption-induced impairment of metal strength or by the interactions with poorly conducting films present on the surface.[392]

To determine the effect of different environmental factors, contact resistance of silver and copper samples used earlier (see Chapter 5, Section 5.1.2) has been measured in the presence of various media: air, inactive Vaseline oil, castor oil, ethylene glycol, and glycerin (relative dielectric constants $\varepsilon = 2–60\varepsilon_0$). Prior to the contact resistance measurements, a part of the copper samples was subjected to thermal oxidation at 473 K for 30 min. (Roughness and hardness parameters for samples are presented in Table 5.7). The computation of probable contribution of the media to the contact conductivity was based on the random field theory that defines the conditions for the tunnel conductivity within a gap of 30 Å. It is assumed that the tunnel conductivity zone encompasses each metal contact spot in the contact area. An equivalent specific resistance of the tunnel-type conductivity in a gap is introduced in accordance with Holm's approach.[1]

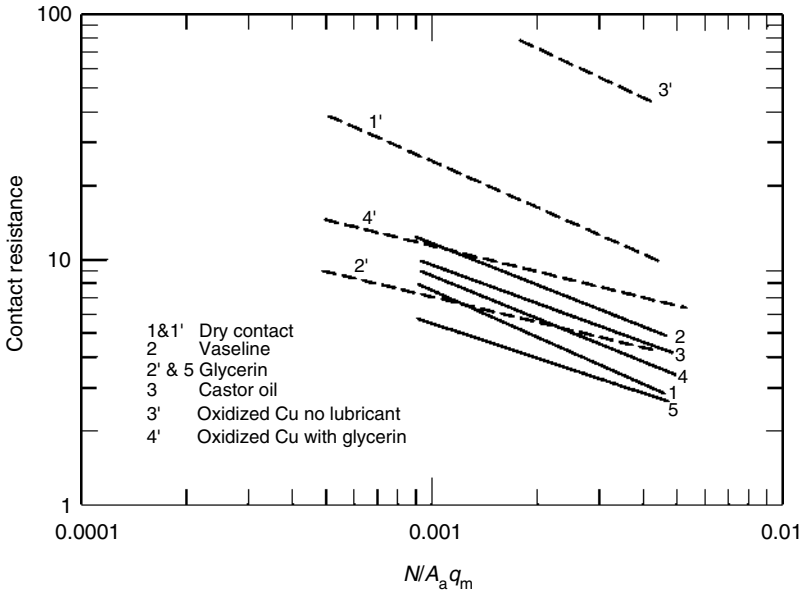

FIGURE 9.72 Experimental data on conductivity in contact of silver (solid lines) and copper (dashed lines) samples: 1, 1′: dry contact; 2: Vaseline oil; 2′, 5: glycerin; 3: castor oil; 3′: oxidized copper without lubricant; 4′: oxidized copper lubricated with glycerin.

The experimental and computation data for silver samples, which actually do not have nonconducting films on the surface, are presented in Figure 9.72. The calculated contact resistances of dry contacts with an additional tunnel zone merges practically with contacts in which the effect of tunnel conductivity was absent. This is a clear indication of a negligible effect of tunnel conductivity on the contact resistance of metallic spots. Hence, the $R(N)$ dependence is not affected even in cases when the high values for dielectric constants are considered ($\varepsilon \cong 50$–60). The experimental data for silver samples with and without lubrication differ slightly even in the presence of most polar media, e.g., glycerin.

Experimentally observed load dependencies of contact resistance for metal contacts with the oxidized surface in various media show considerable qualitative differences. The evidence shows that the lubricating media with different surface activity towards metal affect differently the static contact conductivity. For instance, glycerin, which has surface-active and reducing effects on copper oxides, turns out to be most efficient in attaining high contact conductivity for copper samples. Based on above discussion, the experimental data showing the positive effect of lubricating media on the electrical contact characteristics can be explained in terms of the softening and failure of nonconducting films rather than by the direct action of the lubricant having additional conductivity channels.

Special device was used to identify the role of the lubricant under dynamic conditions, experimental studies[2,824] (see Figure 9.73). A gold needle with tip radius of 50 μm was slided over the surface of platinum, silver, copper, and aluminum plates, and the contact voltage drop was continuously recorded. The load on the needle was 10^{-2}–10^{-4} N, and the sliding speed was 1–10^3 μm/s. Drops of the lubricants were applied to the surface of the plates and the instant when the needle traversed from the dry segments to the lubricated segments of the contact zone was observed with an optical microscope.

It was established (see Figure 9.74a) that when the noble metal contact pairs are used, the presence of lubricant has relatively little influence on the level and stability of the contact resistance. No essential changes in the integral contact conductivity were observed when the indenter

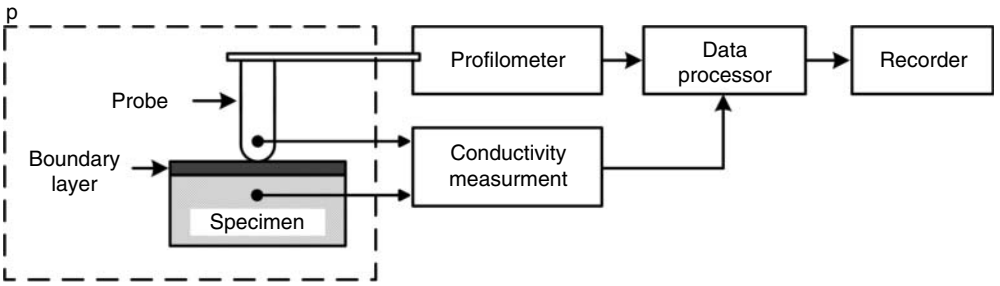

FIGURE 9.73 Diagram of automatic probing device.

traversed from a dry surface to the area covered by a thin lubricant layer, irrespective of the voltage and type of lubricant. Current–voltage characteristics recorded in the stationary state remain linear on both dry and lubricated surfaces. With copper and aluminum samples, most of the test media exerted no significant effect on the contact conductivity either. The only exception is the copper–glycerin combination, for which the contact voltage drop was reduced and stabilized (see Figure 9.74b). This phenomenon cannot be attributed to any mechanical phenomena, e.g., damping frictional oscillations by glycerin, since no stabilizing effect of glycerin was observed for other metals.

The results of additional experiments, carried out on copper samples oxidized in air ($T = 453$ K, $\tau = 30$ min) and under high applied voltages (~ 5 V), showed that in a contact with dry surface, there is practically no conduction (see Figure 9.74c). As soon as the indenter enters the area with the glycerin layer, the situation changes and a frequent fritting is observed due to thinning of the oxide film. Absence of conduction when the voltage is lowered down to 0.5 V is an indication of the oxide film thinning rather than indenter-induced mechanical failure. Consequently, in the absence of hydrodynamic effects, the lubricant may influence the conducting area via chemical interactions with poor conducting layers on the friction surface.

Chemical reactivity of the lubricant can be a key descriptive parameter for the compatibility of lubricants with electrical contact materials. A good example of this is the surface reactivity of stearic acid boundary films on aluminum.[825] Stearic acid is an excellent lubricant for aluminum–aluminum sliding interfaces. This lubricant action stems from attachment of the acid to the native oxide layer on aluminum via the functional polar group. However, the reactivity of stearic acid with aluminum metal leads to a large increase in contact resistance as compared to that measured on dry interfaces. The contact resistance increase is particularly severe during sliding. This increase is a result of the oxide formation on the contact interface when the protective surface oxide film is fractured and the virgin aluminum is exposed to the stearic acid during mating.[826] Thus, stearic acid is an unacceptable lubricant for aluminum–aluminum electrical contacts despite its effectiveness in lubricating the aluminum interfaces. It was suggested that the screening of lubricants for application in electrical contacts can be greatly facilitated by an evaluation of the chemical reactivity of active molecular groups in the lubricant species with the contact materials.

Another important example of lubricant surface activity for noble contact materials is the effect of higher mercaptanes, which are reported to improve the sliding characteristics of silver contacts.[827] It was found that mercaptan layers on silver surfaces are very persistent and are retained by a rather strong chemical force. The same layers on pure electrodeposited gold are only bonded by physical adsorption. Due to environmental effects and likely by evaporation, the observed lubrication effect is diminished.

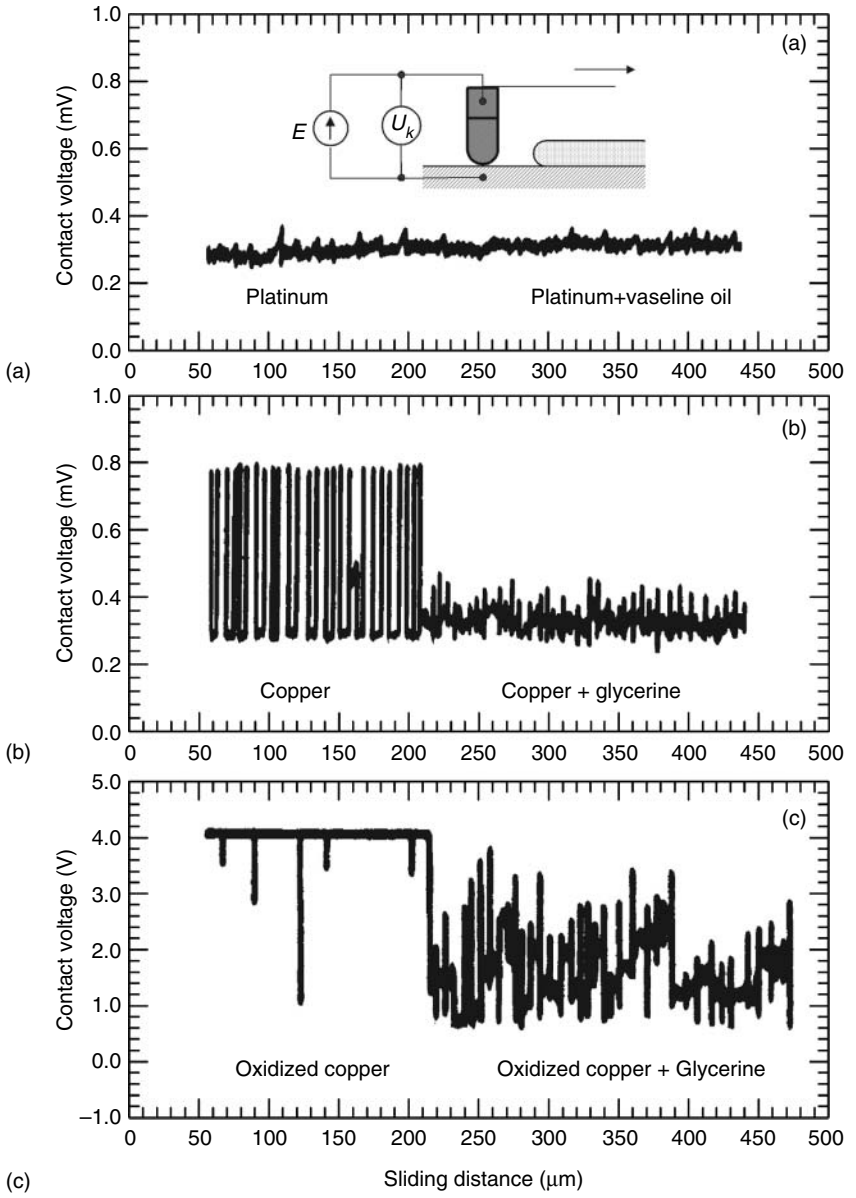

FIGURE 9.74 Variation of contact voltage drop in sliding of gold needle over a plate with transition from dry segment to lubricated segment.

9.3.4.4 Effect of Velocity in Light-Current Contacts

With increasing sliding velocity, the probability of separating contact surfaces by a continuous lubricating layer whose thickness surpasses that of the tunnel conductivity area is increased. As soon as the contacting asperities separate to a distance exceeding the tunnel conductivity zone, the passage of current through these conduction bridges ceases. This is visualized in experiments simulating breakage of metal contact spots under a few millivolts voltage (see

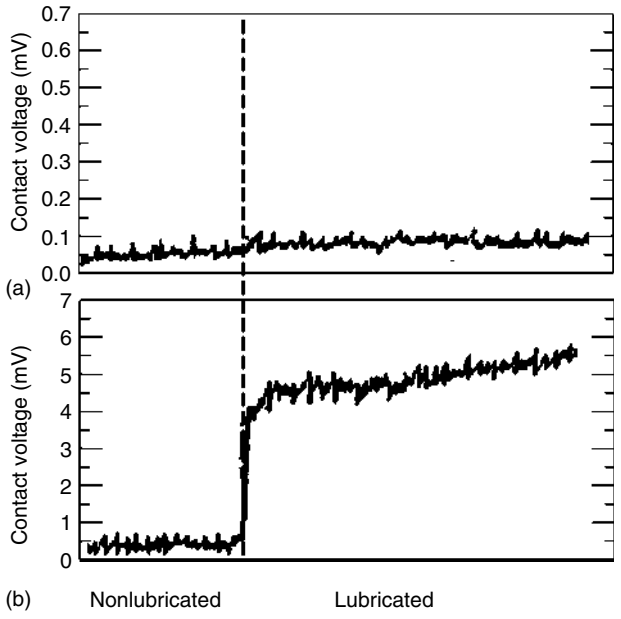

FIGURE 9.75 Effect of introduction of a drop of oil into the contact zone on the contact voltage of contact pair copper–steel: (a) sliding velocity: 0.1 m/s; (b) 2 m/s (contact load $p = 0.1$ MPa, contact voltage $E = 10$ mV).

Figure 9.75a). Therefore, we may anticipate that conductivity in low-voltage sliding contact will be absent when metal contacts disappear. This supposition corroborates with oscillographic tests conducted by Furey.[803] He showed that under relatively high sliding velocity and low voltage in the lubricated contact, the instants of low contact resistance alternate with those when R_c is infinitely large.

Introduction of a lubricant into a high-velocity low-current contact results in abrupt growth of the mean value of the contact voltage drop U_c (see Figure 9.75). According to Furey, the mean contact voltage drop recorded by high-inertia instruments (e.g., potentiometers) characterizes the frequency of formation or disappearance of metal contact spots. Consequently, high contact voltage U_c means that under relatively high sliding velocity, low-current contact conductivity is absent for a prolonged time interval. At the moments when metal contact spots are formed, electric current passes in the form of pulses. Therefore, lubrication of this type of contacts requires thorough consideration of the load-velocity modes, contact geometry, and the probability of emergence of the hydrodynamic wedge.

9.3.4.5 Effects of Lubricant Contact Properties

Based on the behavior of lubricants in the zone of closest approach (ZCA), two modes of lubrication—*anaerobic and aerobic*—have been defined by Glossbrenner.[6] The zone of closest approach (ZCA) is defined as an area between the two sliding contact members which at any instant in time contains all interacting asperities, all load-bearing areas, and load supporting films. Anaerobic lubrication exists when the zone of closest approach is surrounded by a film or meniscus of lubricant, and aerobic exists when the lubricant meniscus is not totally intact. It has been suggested that there may be a transitional condition.

Principal characteristics of anaerobic lubrication are:

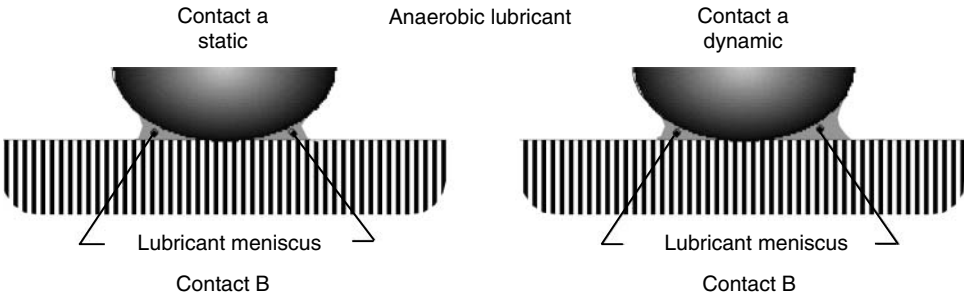

FIGURE 9.76 Illustration of an anaerobic lubricated contact region. A meniscus of lubricant surrounds the ZCA while static and particularly during sliding motion, precluding access by air or vapors to the load-bearing areas.

- Contact ZCA is surrounded and sealed by lubricant meniscus
- Meniscus reduces gas and vapor access to *a*-spots
- Contact properties depend on force and lubricant quality
- Access of surface-active species is retarded
- Lubricant recoats *a*-spots and particles, as formed
- Lubricant suspends wear debris
- Loss of lubricant leads ultimately to an aerobic condition

Figure 9.76 shows the anaerobic case. Most deliberately lubricated contacts start out as anaerobic. The life of sliding contacts in the desired operating mode depends, as an approximation, on the length of time the anaerobic condition can be maintained. Even static connection manufacturers recognize the desirability of a lubricant seal around contacts, as illustrated by the frequently recommended practice of coating the members with petroleum jelly or grease to increase the environmental protection of the interface.

A low surface tension lubricant tends to reduce the creep of surface-active species back into the *a*-spot vicinity and to prevent gaseous species from coating the contact surface. The maintenance of a meniscus may be difficult if both the viscosity of the lubricant and the surface energy are low, as it may migrate to adjacent surfaces.

While in the anaerobic condition, the lubricant controls the mechanisms at the *a*-spot; therefore, the lubricant must be optimum for the surface materials. Atmospheric contaminants can only reach the *a*-spot by absorption and diffusion through the lubricant.[828] This is particularly true if the lubricant is not miscible with these gases and vapors. The contact behavior depends on force expelling the lubricant from asperities in the zone of closest approach and formation of metallic *a*-spots. This requires the proper lubricant viscosity at the operation temperatures. The lubricant also helps to remove particles from the vicinity of the contact by partial suspension of debris.

The above effects are all time-related: rate of absorption of contaminants into the lubricant, their diffusion rates through the lubricant to the nascent α-spot, and the rates of reaction of the contaminant at the surface.

Lubricant will be lost from the meniscus area by evaporation, reaction, spreading to nearby surface, and absorption around wear debris and other particles. Thus, the quantity is reduced and the lubrication condition eventually changes to aerobic. Only if the contact assembly is totally submerged and sealed in the contact lubricant is such a change not possible. The lifetime can be extended by use of lubricant reservoirs contained within the housing of the slip-ring assembly. This technique has been effective for use in vacuum conditions.

The characteristics of *aerobic lubrication* are:

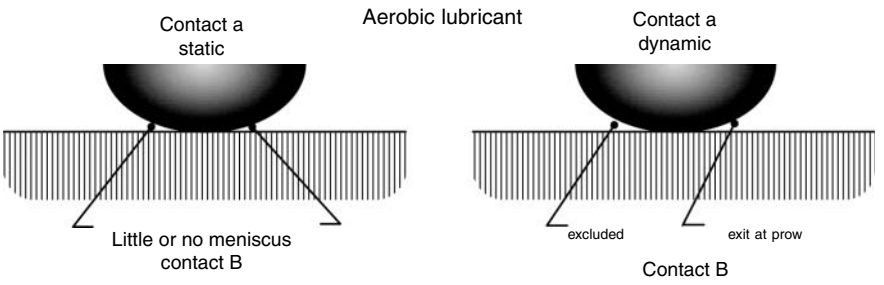

FIGURE 9.77 Illustration of an aerobic lubricated contact region. There is no meniscus surrounding the load-bearing areas, allowing easy access by gases and vapors.

- Absence of lubricant meniscus seal around contact ZCA
- Adsorption and reactions from reactive gases at *a*-spots
- Condensation and polymerization from organic vapors
- Contact behavior controlled by cyclic rate vs. condensation and reflow times
- Ultimate state of most contact surfaces

Figure 9.77 shows a diagram of *aerobic lubrication* around a contact. There may be lubricant, but the meniscus is not contiguous and therefore atmospheric gases and vapors can reach the nascent α-spots. Even if there is no deliberate application of lubricant, there is almost always an adventitious lubricant which finds its way to the contact surface, providing an aerobic lubricant behavior to the α-spots.

In this case the determining factors in the behavior are the cyclic activity of the contact, the nature of vapors which can get to the nascent *a*-spot, the quantity which can be adsorbed in the period between successive encounters for the *a*-spot, and the reactions of vapors on the *a*-spot. If the principal reactive gas arriving is oxygen and the surface is oxidizable, the result will be a fretting corrosion of the surface. On the other hand, when the surface is platinum, palladium, or a similar material, and polymerizable organic vapors are present, the result will be the formation of a so-called *friction polymer* that provides lubrication, but leads ultimately to high contact resistance and noise.

If the cycle time is longer than the time for the gases or fluids to recoat the nascent α-spot, then the properties and effects of the film formed control the behavior of the contact. If the cycle time is shorter than the film reformation time, the contact will operate as if unlubricated and severe wear will occur.

9.3.4.6 Current Passage and Friction in High-Current Lubricated Contacts

Low-velocity sliding contacts. Lubrication does not commonly impede the formation of metal and tunnel-conducting contact spots in low-velocity sliding contacts. This is why the main share of the current passes through these spots, whereas the lubricating layers whose thickness exceeds the tunnel conductivity zone do not almost participate in the current transfer. As a result, spark discharge and electroerosion of the surface can be eliminated. Hence, we may presume that, in general, frictional interaction in low-velocity sliding contacts is affected by the current, as in the case of nonlubricated metal pairs.

In order to evaluate the influence of the contact current density on the lubricant behavior, experiments were performed[407] with a spherical steel indenter sliding over a lubricated metallic plate. The same materials and methods were employed as for the dry metal contact studies (see Section 9.2.2). In contrast to dry friction, sliding of the indenter over a sample surface covered by a

TABLE 9.9
Influence of Electrical Current on Friction Characteristics of System Consisting of Steel Indenter—Lithium Grease (Analog of MIL-G-7711A)—Copper Plate ($N = 0.1$ N, $v = 2.25$ μm/s, $T = 293$ K)

Current, I (A)	Contact Voltage, U_c (V)	Current Density, j (10^5A/cm^2)	Friction Track Width, d (μm)	Contour Area of Contact, A_c (10^{-6} cm^2)	Temperature Rise in Friction Zone, ΔT (K)	Temperature in Friction Zone, T_f (K)	Temperature of Bulk Specimen, T_b (K)	Specific Friction Force, ψ (kN/cm^2)
0	—	—	21.0	3.4	—	293	293	2.5
0.2	0.15	0.6	21.0	3.4	2.2	295.2	293	2.3
0.6	0.29	1.7	21.2	3.5	12.3	305.3	296	2.4
1.0	0.35	2.8	21.6	3.6	24.3	317.3	299	2.3
1.4	0.40	3.7	22	3.8	38	331	305	2.3
1.6	0.50	4.1	22.4	3.9	53.5	346.5	310	2.4
1.8	0.62	4.4	23.0	4.1	72.8	365.8	316	2.3
2.0	0.75	4.5	24	4.5	83.7	376.7	323	3.0

grease or oil is characterized by a more stable and low coefficient of friction μ, and a wider friction path due to the Rebinder effect. Passage of electric current (up to 10^3 A/cm^2) through the friction zone has no appreciable effect on the frictional characteristics as seen in Table 9.9. The current density of 10^4–10^5 A/cm^2 results in growing friction coefficient, friction path and contact area under insignificant temperature rise in the friction zone. This means that just like in the case of dry metal contacts, electric current alleviates the process of plastic deformation of the surface. The softening proceeds as a result of the heat-induced action of the current. Switching of the current reduces friction force for a short time, which is connected with variations in specific friction force under instantaneous temperature variations on the real contact area. This reduction is more evident in lubricated contacts than in nonlubricated ones.

A characteristic feature of the lubricated contact behavior during friction is the presence of some critical current depending on the lubricant nature at which the specific friction force leaps up (see Table 9.9) and sliding becomes jerky. As the calculations show, average temperature in the friction zone under critical current reaches the magnitude corresponding to the loss of lubricity of the medium. Based on this observation, a method of determining temperature resistance of the boundary lubricating layers has been proposed.[407] The method will be discussed in detail in Chapter 10, Section 10.3.4.

The experiments described above clearly illustrate the fact that at low sliding speeds, the passage of current does not significantly degrade the lubrication while markedly reducing the friction coefficient in comparison with the dry contact. Very high current densities in the contact spot can be achieved without overheating the contact zone.

Effect of velocity in high-current contacts. The conditions of current passage in high-current sliding contacts change abruptly as the velocity of contact surfaces increases and the probability of the hydrodynamic wedge appears. Testing of contact rings with traditional lubricants and oils shows that a multiple high-velocity sliding contact is characterized by *IU*-characteristic with clear nonlinearity. It was underlined by Brix[829] that the *IU*-characteristic of lubricated metal contacts acquired a curvilinear and straight portion under high sliding velocities. In this case the straight section goes parallel to the *IU*-characteristic recorded for a stationary state of the given pair, and the distance between them is independent of the current but increases as the load lowers or the sliding

velocity grows. Hence, it is accepted that this distance expresses the voltage drop across the lubricating film, U_d, and its value is proportional to the film thickness d. The U_d ratio to d has been estimated in additional experiments using a device with two parallel disc electrodes. Based on U_d (d) measurements, Brix concluded that under boundary lubrication, the lubricant layer thickness varies within 2.5–25 μm, and conductivity is provided by the electric discharge. Analogous results are cited elsewhere.[830]

Computations of strength of lubricating boundary layers based on the results presented in[829] give electric strength $E_f = 10^3$–10^4 V/m, which is much less than E_f for thin boundary layers,[804] and electric strength of the oil (10^5–10^7 V/m). Low U_d and high d are, presumably, conditioned by the method used. Electric discharges through the lubricating layer in sliding contact take place on instantaneously forming and continuously varying spots. U_d has been calibrated vs. d in experiments, but by using immovable electrodes. In these conditions, electric breakdown can be accompanied by the formation of stable current-conducting bridges able to short-circuit the gap and lower voltage drop. This justifies the conclusion on the absence of metal contact spots under boundary lubrication conditions and discharge-driven conduction through a relatively thick lubricating layer with reduced electric strength as reported by Brix,[829] and by Siripongese, Rogers, and Cameron.[830]

Simulation of the contact spot breakup (see Figure 9.55b) under relatively high voltage has shown that conductivity does not disappear at once in the instant of breakage. As the contact moves apart until a gap d_{cr} reaches a value of about 0.01–0.1 (m, the oscillograph registers fluctuations of the contact voltage drop U_c. This value depends on the voltage applied, circuit parameters, electrode material, the lubricant, and some other factors. Evidently, electric discharges through the lubricating medium, generated as the contact elements separate, are accompanied with the formation of erosion products that short-circuit the gap. Each following discharge involves the bridge formed during the preceding discharges. Therefore, we may assume that in high-current sliding contacts where hydrodynamic effects are present, conductivity is ensured by the breakdown of the lubricating layer in the areas between the surface asperities where the field voltage reaches E_f values, and in the bridges consisting of erosion products. Increasing the applied voltage augments the number of areas subjected to breakdown and reduction of R_c. As the voltage reaches the level when the areas with a typical film thickness undergo breakdown, the point of saturation is attained as shown by bending of the IU-characteristic.

To estimate the effect of lubricants on friction in high-velocity contacts, lubricants were tested using a brush–ring pair under conditions whereby this effect can be observed in a pure form.[824] In other words, the loads were low and the short testing times used eliminated the probable effects of accumulation of the conducting debris from the broken surface in the gap. The efficiency of wear-resistance of the lubricants was estimated by the period that precedes an abrupt friction coefficient increase which corresponds to termination of the efficient lubricating action, formation of scuffs, and severe wear. The results obtained are summarized in Table 9.10.

TABLE 9.10
Effect of Electric Current on the Friction Behavior of Lubricated Contacts

	Time Before Seizure (min) at the Following Currents			Contact Voltage Drop (mV)	
Lubricant	$I = 0$	$I = 1$ A	$I = 3$ A	At an External e.m.f. of 15 mV	$I = 3$ A
Lithium-soap grease (analog of MIL-G-7711A)	300–350	50–60	30	10–13	200–500
Vaseline oil	120–160	10–15	8	8–12	300–1000

Note: Copper brush–stainless steel ring ($R_a = 0.25$ μm), $p = 0.1$ MPa, $v = 2$ m/s, $A_a = 0.25$ cm^2.

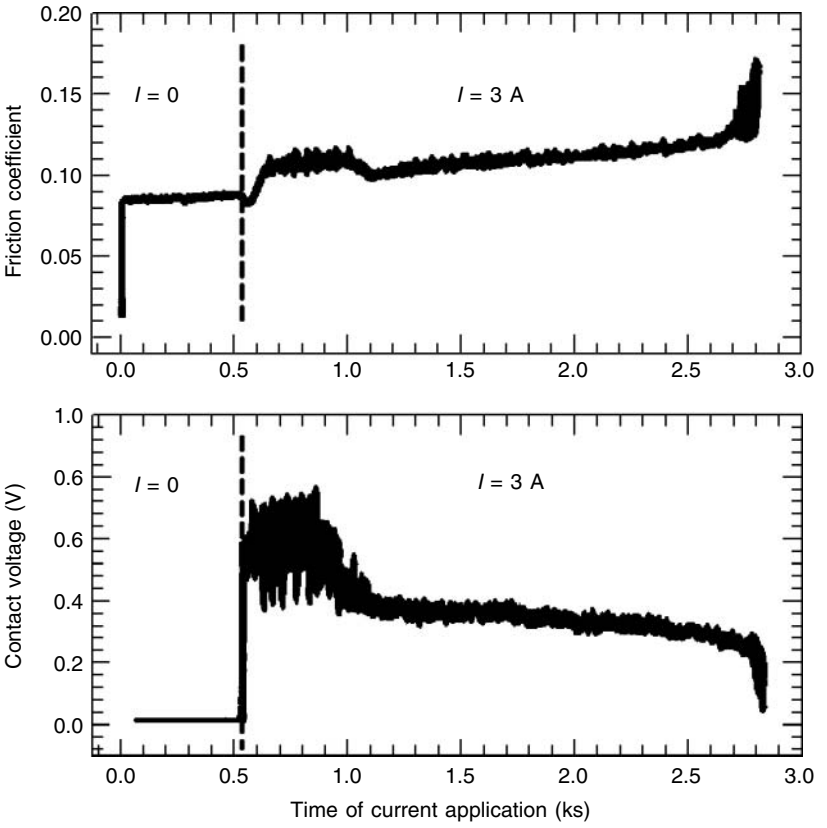

FIGURE 9.78 Typical dependence of the frictional force F and the contact voltage drop U_c on time in the presence of an electric current for ball-bearing steel (analog of steel AISI 52100) rubbing on pure copper lubricated with grease (analog of MIL-G-7711A).

The above-described tests have shown that current passing through the contact drastically impairs its frictional characteristics. After application of current, the friction force increases rapidly due to its instability (see Figure 9.78). The operation time of the sliding contact without seizure is greatly reduced. Initially, after switching the current, severe sparking and fluctuation of the contact voltage drop U_c was observed. One-time application of a viscous lubricant extinguishes the sparking and somewhat stabilizes U_c, whereas the friction force remains unstable and gradually augments. As a rule, sparking with the oils does not stop until the seizure occurs.

Frictional behavior of the pair is also affected by polarity. In case of a negative polarity of the brush, the friction track on the ring is quickly stripped of the lubricant, which leads to seizure. The positive polarity regime is characterized by formation of a lasting lubricant film on the ring that elevates mean U_c values. In general, a single application of the lubricant at positive brush polarity prolongs the period until seizure.

It is important to note that in the unit with the one-time applied lubricant, switching off the current after operating for a period of time neither reduces nor stabilizes the friction force. However, if the lubricant is replenished after the current is switched-off, the friction force stabilizes, and attains the values characteristic of the operation in de-energized state.

These experiments confirm that the adverse effect of electric current on the performance of lubricated sliding contacts is due primarily to electric erosion causing irreversible changes in the

lubricant composition, loss of lubricity and, finally, seizure of the friction joint. This can be explained in terms of generation of a high-intensity field between the asperities at separation of metal contact spots at comparatively high sliding velocity and partially liquid lubrication regime. For the high-current contacts operating under typical voltages of 0.1–1 V in a gap 0.1–1 μm, the field intensity is about 10^6–10^7 V/m. This is quite sufficient to provoke the electric breakdown and discharge that are accompanied by failure of the lubricant and surfaces. Under the same conditions, the apparent higher efficiency of the viscous lubricant is attributed to the formation of a thick liquid oil layer separating the contacting surfaces and to a lubricant chain skeleton capable of lowering the field intensity required for breakdown to occur and and to soften discharge conditions.

From the above discussion it follows that the maintenance of continuous current flow via metallic and tunnel-conducting spots or bridges is an essential prerequisite for avoiding discharge in the lubricant and ensuring high wear resistance. The materials of the conducting bridges can be fine-dispersed (below mean asperity size), conducting particles in the gap between rough contacting surfaces.

The *IU*-characteristics of the brush–ring contact in a pure and powder copper-filled model media are presented in Figure 9.79. It is evident that there is no clear sharp bend in the region of low current, which is characteristic for pure lubricants. It should be pointed out that the conducting fillers in lubricants do not always lower the voltage drop when compared to the dry contact. Nevertheless, they ensure by far better electrical and frictional characteristics of the sliding contact than nonfilled media. This is especially evident in high-current contacts at comparatively low sliding velocities. This is probably due to improved conditions of current flow in the presence of auxiliary conductivity channels through the lubricating layer and improved lubricity of the medium composed of the plastically deformed particles forming on the contacting surfaces films with low shear resistance.

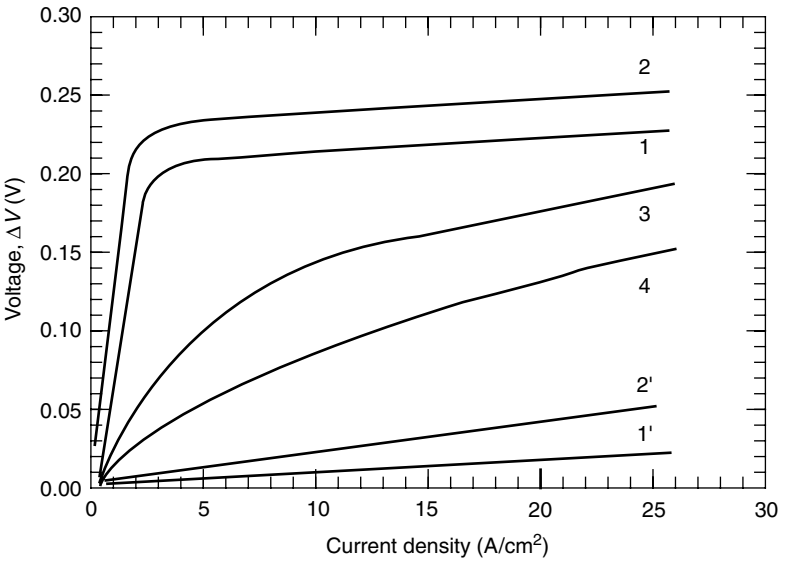

FIGURE 9.79 IU-characteristics of brush (pure copper) vs. ring (analog of AISI 52100) sliding contact with the use of various lubricants: 1-vaseline oil; 2-lithium grease (analog of MIL-G-7711A); 3-lithium grease + 10% copper powder; 4-dry (ring diameter 40 mm, $v = 2$ m/s, $\rho = 0.1$ MPa, $S_b = 0.25$ cm^2). Curves $1'$ and $2'$ are for corresponding media in the static contact.

High currents impair the electrical and mechanical characteristics of sliding contacts operating at high sliding velocities in particle-filled media. As in the case with unfilled lubricants, current flow leads to instability, elevated friction coefficient, and fluctuations in the contact voltage drop. In the contacts with one-time lubrication, the time to seizure is also shortened. De-energizing after some period of operation does not lower the friction coefficient to its initial value. In case of replenishing with a fresh metal-containing lubricant, the friction coefficient and contact voltage decreases at the same time. It follows that current flow in high-velocity, high-current contacts with metal-filled lubricants takes place, at least partially, via electric discharge through the lubricating medium; this is similar to the case with unfilled lubricants and oils. In contrast to pure lubricating media, discharges are transferred by the filler particles, thus decreasing the effective thickness of the broken layers and alleviating discharge conditions. In spite of more favorable conditions for the current flow, it alters the structure and worsens lubricity of the filled medium. This means that continuous lubricant replenishing is an essential requirement for stable operation of the sliding contact.

Fine-dispersed conducting particles in the lubricating medium turn out to be an important factor in reducing electric erosion and improving wear resistance of lubricated high-current contacts. The test results proved that application of metal-containing lubricants may be efficient for both low-velocity and high-velocity high-current sliding contacts. One should remember that the lubricant with impregnated dispersed particles presents a heterogeneous system, and thus its behavior may be strongly affected by structures formed in the gap and the influence of electric field.

It should be noted that passage of electric current through the lubricated contact of rubbing bodies can take place not only in electrical contacts, but in some other tribosystems. The research in the area of tribology in electrical environment was reviewed recently by Prashad.[831] In short, his monograph covers original contributions of the author establishing the behavior of different bearings and lubricants under the influence of an electric current. It presents the assessment of the flow of current through the rolling-element bearings, theoretical evaluation of corrugation pattern, resistivity in the lubricants, a theory that explains causation, morphology and rate of the formation of electric current damage, and damage by unforeseen causes.

9.3.5 Lubricants for Electrical Contacts

Ideal properties of a good sliding-contact lubricant were formulated by Glossbrenner[6] as follows:

- Operates best if retained on the contact surface by chemical adsorption or strong physical adsorption
- Must not chemically degrade metals of the contact surfaces
- Must not chemically react with insulation of the contact assembly
- Must not chemically react with gases of the operating environment
- Must have low volatility at the operating temperature and pressure
- Must have proper viscosity at given velocity, temperature, and contact force
- Must not form friction polymer of sufficient viscosity to separate contacts
- Should have low surface energy to wet the contact surfaces

These are tough criteria and somewhat contradictory for any lubricant. Both liquid lubricants and greases are used in sliding contacts. Some organic fluids such as esters and polyglycols provide better antifriction and antiwear properties for sliding contacts than the organic greases.[823] Among the positive effects, we note one which is achieved only by the application of liquid lubricants. If a liquid lubricant wets the contact surface well, i.e., the wetting angle is close to zero, the lubricant removes (extrudes) other fluids, e.g., water, from the surface and forms a thin protective film. Contact surfaces treated by sputtering with the fluid or immersed into it are less susceptible to external effects.[832]

As mentioned above, the halogen-containing liquid lubricants are effective for application in sliding electrical contacts whereas the silicon fluids are the poorest lubricants.[747] Oxygen-containing and hydrocarbon fluids take an intermediate position. Excellent results were obtained when using ethylene glycol as a lubricant for sliding electrical contacts.[833] The life of such contacts was prolonged 5–10 times in comparison with the dry contact. Mass-produced perfluorinated polyalkylether (PFPE) fluids are widely used. They also serve as a base for developing filled lubricants for application in certain contact pairs, for example made of gold.[834]

Greases are quite often used in sliding contacts, e.g., greases based on the polyphenyl esters possess a combination of good lubricating and electrical properties.[747,835]

Graphite, dichalcogenides of metals (Mo, W, Nb, Ta), and metal powders are used as fillers to greases. The bulk electrical characteristics of lubricants with the conductive filler vary slightly, yet the conductivity of thin films (from a few to hundreds microns) increases significantly. High filler concentration can deteriorate the grease lubricity. For this reason the optimal content of the conductive filler has to be determined experimentally for each application. Lubricants applied to different electrical contacts must provide dependable operation under a variety of operating conditions.

9.3.5.1 Lubricants for Sliding Electric Switch Contacts

Lubricants for both high and low current applications must enhance switching performance and reliability. In particular, the ability of grease to prevent wear in switches is critical. Wear particles create two problems. They can inhibit current flow when the contact is closed, increasing contact voltage drop. When the contact is open, conductive wear debris can cause open circuit resistance problems. The viscosity of the base oil should complement the contact force of the switch. Light-current/low contact force applications require lighter base oils. High-current/high contact force applications benefit from more viscous base oils.

Lubricants for arcing contacts. The temperatures in an electric arc can reach thousands of degrees, far beyond the thermal degradation temperatures of any known functional fluid even polyphenul esters or fluorinated ethers. In the path of the arc, lubricant molecules are blasted apart into smaller fragments. Silicones become sand and fluoroethers transform into toxic gases. There is no material with the capacity to suppress arc formation. Thus, the tendency of a lubricant to burn cleanly is a definite advantage. Traditionally, cleanly burning glycols were used to minimize carbon build-up. A new approach to eliminating problems associated with oxidation is to use nonburning perfluoropolyether-based greases. Dispersed in a nonflammable, ozone-safe, fluorinated solvent, these greases leave a thin film of lubricant which is ideal for low load/low current applications. An additional benefit is that this thin film does not attract dust and debris. Lubricants for switch contacts are produced by NYE, Ltd. (see Table 9.11). For example, NyoGel 782 is an electric-contact grease prepared for switches operating in the temperature range $-10°F$ to $+200°F$ when arcing is unavoidable. The base oil is a polyether, and precautions have to be taken with a few plastics and elastomers.

Lubricants for distribution switchgear, which may remain inactivated for long periods, have protective as well as lubricating roles. They should be oxidation-stable, water-resistant and nonmigrating. Because high temperatures may be induced by high current or high-temperature conditions, wide temperature operation range can be important.

In high-current sliding contacts, lubricants are used more rarely and they can be divided into two groups. The first group includes the compositions whose properties are similar to those of mass-produced lubricants for light-current contacts, i.e., they do not contain conducting particles.[754,823] The second group comprises greases with fine conductive fillers. For example, graphite suspensions in oil are used to lubricate contacts of welding machines. The slider of railway and urban transport pantographs and current pick-offs can be made of hard-drawn copper lubricated with a graphite paste.

TABLE 9.11
NYE Lubricants for Sliding Electric Switch Contacts

General Purpose Lubricants

Lubricant	Temperature Range (°C)	Recommended Contract Force (g)[a]	Low Current, < 1 A	Medium Current, 1–10 A	High Current, >10 A	Salt Water Resistance	Plastic Compatible
Rheolube737S	−60 to 120	20	●			●	●
Rheolube716A[b]	−4 to 150	20	●	●			
Instrument Greasse732C[b]	−54 to 150	20	●	●		●	
Rheolube362HT	−54 to 125	50	●	●			●
Rheolube789DM[b]	−40 to 150	80					
Rheolube798[b]	−40 to 150	120		●	●		
Rheolube368	−40 to 125	150			●		●

Lubricants for Arcing Contacts

Lubricants	Temperature Range (°C)	Low Contact Force (<100 g)	High Contact Force (>250 g)	Plastic Compatible
NyoGel782G[b]	−40 to 100	●		
Rheolube748LT	−40 to 100		●	●
Rheolube731	−15 to 100		●	
UniFlor™ 8512	−50 to 225	●	●	

Nonburning Switch Lubricants

Lubricants	Temperature Range (°C)	Characteristics
NyeTsct570H-10	−30 to 225	Nonburning grease dispersion for all contacts where mV drop and open circuit resistance can be a problem
NyeTact571H-10	−54 to 225	Lower-temp version of NyeTact570Y-10
UniFlor™ 8923	−54 to 250	Extreme-environment, nonburming grease for medium-to-low current switches

Lubricants for Distribution Switch Gear

Lubricants	Temperature Range (°C)	High Contact Force >250 g	Salt Water Resistance	Plastic Compatible
Rheolube368	−40 to 125			●
NyoGel760D	−40 to 125		●	●
Rheolube786D[b]	−30 to 150	●		

[a] Minimum contact force (g) that must be available for serviceability at −40°C.
[b] Use with caution around polycarbonate, a-b-s-resins, Buna N and other ester-vulnerable plastics and elastomers.

9.3.5.2 Lubricants for Sliding Contacts of Sensors

Many sensors, e.g., potentiometers and variable resistors, have moving contact parts in a form of wiper on track. The wiper is likely to be a noble metal alloy and the track can be any of the conductive materials, from a metal wire to a conductive plastic or ceramic composition.

TABLE 9.12
NYE Gels for Potentiometers, Variable Resistors, Sensors and Related Devices

Gel	Base Oil	Performance Temperature (°C)	Characteristic
Nye Fluorocarbon gel 813 and 813S (soft)	Halogenated silicone	−70 to 200	Widely used for low and high temperature extremes and for its proven noise reduction properties in a broad variety of designs
Nyosil	Halogenated silicone	−70 to 200	A traditional solution for wide temperature wirewound designs
Nye Nyogel 781A	Halogenated silicone	−70 to 175	An alternative to the fluorocarbon-gelled 813 series using a different gelling agent. Recommended where noise reduction is of special concern
NYE Rheolube 716A	Complex polyol ester	−50 to 150	For lowest friction and good electrical noise reduction over a wide temperature range. Use with caution around ester-vulnerable plastics
NYE Fluoroether grease 833B	Fluorinated ether	−40 to 150	A soft, solvent resistant grease for applications involving hostile chemical or fuel vapor exposure
NYE Fluoroether grease 842	Fluorinated ether	−40 to 225	Intended for "dimmer switch" type applications where high resistive loads create exceptionally high temperatures on the conductive track
NYE Fluoroether grease 899	Linear fluoroether	−65 to 250	Exceptional wide temperature capability. Lowest shear resistance for delicate low temperature applications

Voltages and currents are low; arcing is not normally an issue. Lubrication of the sliding electrical contact inherently used in these devices can reduce electrical noise and wear and increase effective operating life. The most successful lubricants are soft gels of complex silicone fluids or esters with wide temperature operation range.

NYE lubricants for potentiometers and variable resistors are presented in Table 9.12. Among effective lubricants for this contacts are Nye Fluorocarbon Gel 813 and Nye Fluoroether Grease 833B. Nye Fluorocarbon Gel 813 is a silicone-based grease with extreme wide temperature capability which works well in a broad spectrum of wiper/track combinations. Where resistance to hydrocarbon fuels is needed, the alternative is Nye Fluoroether Grease 833B.

For high-temperature electrical contacts, NYE, Inc. recommends very soft, inorganically thickened grease NYE UNIFLOR™ 8923 based on medium viscosity perfluorinated ether oil and fortified with special additives to reduce friction and wear. Recommended temperature range is from −54°C to +250°C.

The UniFlor 8900 Series is recommended for delicate precision sensors, potentiometers, and actuators where ultra low temperature and low torque are critical design parameters (see Table 9.13).

ELECTROLUBE, Ltd. provides a broad spectrum of oils and greases specifically designed to meet production and maintenance requirements in electrical contacts. Among them two product groups manufactured since the 1970s should be pointed out (see Table 9.14):

- 2 GROUP contact lubricants are suitable for heavy-duty, wide operating temperature applications where certain thermoplastics are not involved.
- 2X GROUP contact lubricants are suitable for light-duty applications in equipment less subjected to severe environmental conditions; they are safe for use with virtually all known plastics, paints, and rubbers.

TABLE 9.13
NYE Contact Lubricants (UniFlor 8900 Series) for Ultra-Low-Temperature Performance

Product Number	Temperature Range (°C)	Base Oil Viscosity 40°C (cSt)	Pour Point (°C)	Viscosity Index	Vapor Pressure, torr @ 250°C
Greases					
8951	−90 to 200	18	−90	317	10^{-8}
8961	−80 to 200	33	−85	336	10^{-9}
8961R	−80 to 200	33	−85	336	10^{-9}
8971	−75 to 225	90	−80	320	10^{-9}
8971R	−75 to 225	90	−67	320	10^{-10}
8981	−65 to 250	140	−67	345	10^{-10}
8981R	−65 to 250	140	−67	345	10^{-10}
8981S	−65 to 250	140	−67	345	10^{-10}
Oils					
8950	−90 to 200	18	−90	317	10^{-9}
8970	−75 to 250	90	−80	320	10^{-9}
8980	−65 to 250	140	−66	345	10^{-10}
8990	−65 to 250	335	−63	365	10^{-10}

Note: R, rust inhibitor; S, NLGI Grade 1 soft grease.

TABLE 9.14
Electrolube, Ltd. Specialized Contact Lubricants

Lubricants	Temperature Range (°C)	Viscosity 20°C (cSt)	Melting Point (°C)	Characteristic
2 Group 2 oil	−40 to 240	118−126		For heavy-duty, low or high contact force applications where long-life lubrication is vital and where oil will not migrate. Reduces arcing. Excellent electro-mechanical lubricant
2G grease	−55 to 250		−51	Will not migrate from vertical surfaces. Resists the severest atmospheric conditions and suitable for heavily arcing contacts. Nonmelting grease with exceptionally wide temperature range characteristics. Excellent electro-mechanical lubricant
2X Group 2X oil	−40 to 200	640	−29	For medium- and light-duty, low or high contact force applications, where oil will not migrate, and particularly suitable for use in equipment operating in mild atmospheric conditions or involving thermoplastics, paints or rubbers. Excellent electro-mechanical lubricant
2GX grease	−29 to 200			Nonmelting grease for use on vertical arcing contacts in equipment where certain thermoplastics, paints or rubbers preclude the use of 2G. Excellent electro-mechanical lubricant

9.3.5.3 Selection of Contact Lubricants

Both greases and oils are used in sliding contacts. With very light contact forces and in a benign environment, oil can be used. However, grease, which is base oil immobilized by a thickener, is often preferred. Unlike oil, grease is less susceptible to migration.

Several base oil chemistries have been used and successfully applied in contact lubricants (see Table 9.15 and Table 9.16). Selecting the proper lubricant starts with the choice between synthetic and petroleum-based products. For continuous performance, ambient temperatures sometimes mandate a synthetic lubricant. Petroleum products begin to degrade at or before 100°C, and become virtually intractable at sub-zero temperatures; some synthetic lubricants still function well at −70°C to beyond 200°C. Synthetic lubricants may cost more than petroleum-based lubricants, but they generally can be used in smaller quantities.

In selecting a base oil, it is important to consider is if it is able to withstand the temperature range in which the electrical contact must operate. At elevated temperatures, oil is subjected to evaporation or thermal degradation. At low temperatures, it can become intractable. When selecting grease, it is the temperature range of the oil, not the thickener, that defines the greases temperature limits.

Material compatibility should be considered as well. While lubricants do not affect most thermoplastics, esters (diesters and polyolesters) are noted for their incompatibility with polycarbonate, polyvinyl chloride, polystyrene and acrylonitrile–buta-diene–styrene copolymer resins. Material reactivity and additives, such as flame retardants, can also have an effect on compatibility. Only the fluoroethers (PFPEs) are inert enough to be safe with almost all polymers. Compatibility charts are available from many manufacturers, but testing is the only way to guarantee a successful match between lubricant and contact material.

For water resistance, grease should be specified. Even though oil is generally not water-soluble, it is easily displaced by moisture. Grease water resistance is determined by the thickener. Lithium soap grease has good fresh-water resistance but poor salt-water resistance. Silica can be hydrophobic or hydrophilic. Clay and PTFE generally perform well in wet environments.

9.4 COMPOSITE CONTACTS

In many contact devices only one of the components is made of metal. Four types of self-lubricating carbon-based composites are used as materials mating the metal component: metal–graphite, graphite, carbon–graphite, and electrographite ones (see Section 4.3.2).

In the case of metal–composite contact, the formation of an intermediate layer (third body) is a necessity in providing low friction and wear, as well as low contact resistance. Therefore, the

TABLE 9.15
Characteristics of Synthetic Lubricants

Property	Fluoroethers (Perfluoroether)	Synthetic Hydro-Carbons (Polyolpha-olefin)	Polyglycols (Panther)	Polyesters	Silicones
Usable range (°C)	−70/−40 to 250	−60 to 125	−40 to 110	−60 to 150	−70/−40 to 200
Viscosity index	100 to 350	125 to 145	160 to 220	120 to 150	300 to 400
Lubricity	Excellent	Excellent	Excellent	Excellent	Fair
Volatility	Excellent	Good	Fair	Excellent	Excellent

TABLE 9.16
Lubricant Application in Electrical Connectors and Sliding Electrical Contacts

Application	Lubricant Alternatives	Special Characteristics
Electrical connectors (automotive, telecommunications, computer or PC Board connectors; backplanes; instrumentation accessories)	Synthetic hydrocarbon and ester based lubricants	Provides thin protective film on tin-lead connectors, reducing corrosion and contact forces while making a weather resistant seal
	Fluorinated ether based lubricants	Long life without generating lubricant decomposition products
	Polyphenyl ether based lubricants	Traditional for gold on gold
Electrical sliding contacts (automotive instrumentation; rotary, toggle, ignition, and sliding switches; appliance controls; distribution switch gear)	Synthetic hydrocarbon greases	Water resistant; good plastic compatibility
	Synthetic hydrocarbon gels	Nan-melting; water-resistant; oxidation stability; low volatility
	Synthetic polyether greases	Suitable for high temperature, arcing conditions
	Polyol ester greases	High lubricity; salt water-resistant; wide temperature fluidity
Potentiometers (wire wound and conductive plastic potentiometers; trimmers; automotive sensors; aerospace controls)	Hologenated silicone oils and gels	Temperatures from −70 to 200°C; good noise reduction
	Polyol ester greases	High temperatures stability; good noise reduction; low thin-film volatility
	Fluorinated ether greases	Resists aggressive chemicals and all except fluorinated solvents; temps from −65 to 225°C

properties of the intermediate layers, nature of their influence on the current passage, and resulting contact electrical characteristics have been studied extensively.

9.4.1 Effect of Intermediate Layers on Electrical Characteristics

The character of current passage in composite sliding contacts governs both its electrical characteristics and frictional behavior. In a general case, the current can pass the SC through three parallel channels: the zone of physical contact between the members, the dust zone (wear particles arising and moving chaotically in the friction zone), and the breakdown zone (spark and arc in air gap between the surfaces).

The intermediate film appearing on the metallic counterface in this case determines some features of the behavior of the SC:[1,7,392]

- Usually no correlation is found between the physical–mechanical (modulus of elasticity), electrical properties of the self-lubricating contact material (electrical conductivity), and the contact electrical characteristics.
- As a rule, *IU*-characteristics of the contact are nonlinear.
- Direction of current passage noticeably influences the contact voltage drop.

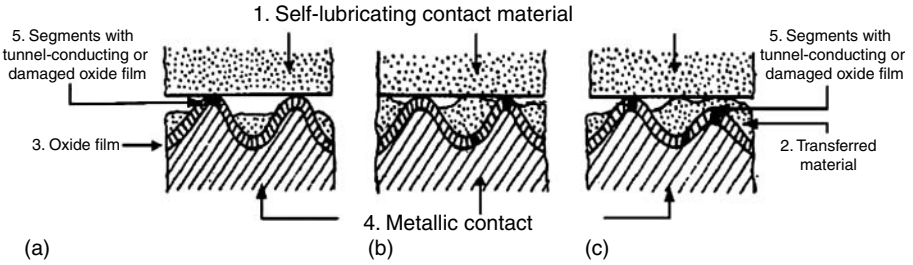

FIGURE 9.80 Models of intermediate layer on the surface of an oxidizing metal in operation with a self-lubricating contact material: (1) self-lubricating contact material; (2) transferred material; (3) oxide film; (4) metal; (5) segments with tunnel-conducting or damaged oxide film.

9.4.1.1 Structure and Electrical Properties of Intermediate Films

The films which are formed on sliding contacts operating in air result from a combination of chemical reactions, gas and vapor adsorption, and material transfer. In the classical case of carbon brushes in contact with a copper ring, for instance, the film on the ring consists of cuprous oxide, water vapor, and carbon.[7] The color of the film (orange to blue) indicates that the oxide thickness is a few dozen nanometers.

When studying and explaining the behavior of the conventional graphite brushes on copper collectors, Holm and his followers used the model of the surface layer (see Figure 9.80a) in which the transferred brush material filled up valleys of the collector surface and asperity summits remained uncovered.[1,7,836] It is believed that another structure of the intermediate layer is more likely to appear (see Figure 9.80b) in which the thickness of the transfer film is comparable with the height of counterface asperities. The film is broken only on the summits of the highest asperities and brush contacts with the collector on these sites through the copper oxide film. The formation of the collector film of such kind is apparently possible on very smooth surfaces without abrasive wear.

Different probe devices were used in early investigations of collector films. Shobert[838] was one of the first to study the conductivity of the collector films formed by electrographite brushes by using a gold probe shaped as a bent wire moving over the test surface. It was found that the film was completely insulating at low voltages ($\sim$0.01 V). Yet, single conductive sites were detected whose number grew with increasing current. E. Holm[839] used gold or carbon probes, which were arranged on the film covering the collector ring normally to the ring axis.

Konchits et al.[392] developed the probe device (EP1) based on a stylus profilograph (see Figure 9.73). In this instrument the specimen and stylus are the elements of the circuit. Voltage drop in the stylus-specimen contact, current in the circuit, and surface profile trace are simultaneously recorded. Conductive tips made of gold or stainless steel with radius of 30–50 μm were used instead of a standard diamond stylus. The tip pressure on the surface does not exceed 2×10^{-4} N. Electric circuits used in tests and the simultaneous recording of the surface profile and microscopic examination made it possible to determine the contact resistance, IU-characteristic, and fritting voltage at any given point of the surface.

Electroconductive properties of friction transfer films were studied[392] for electric brush materials sliding on silver collector rings (in which the oxide component of the intermediate film is eliminated). It was shown that in the absence of oxide films on the metallic counterface, the friction transfer films favors the contact resistance increase, leading to intensified heat generation in the contact zone and polarity effects (see Figure 9.81). When the stationary brush contacts the freshly cleaned ring surface, the *IU* characteristic is almost linear and the contact resistance R_c is low. As the transferred material film appears on the ring surface in sliding, R_c increases and the

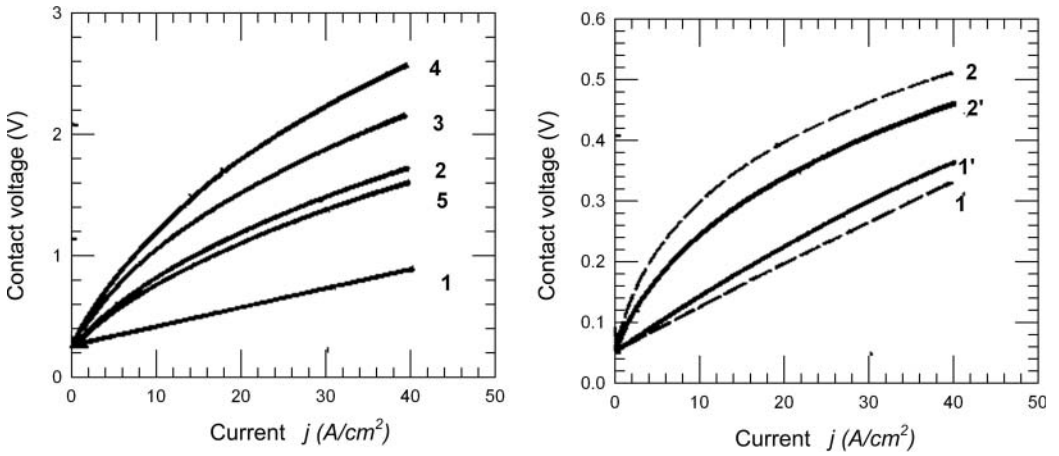

FIGURE 9.81 *IU*-characteristics of electric brushes in pair with silver contact ring (diameter 40 mm, $p =$ 30 kPa, $v = 1.5$ m/s): (a) experimental metal–graphite brushes (1: freshly cleaned stationary ring; 2, 3, 4: after 5s, 300s, 5.4 ks after beginning of operation; 5: stationary ring after operation during 5.4 ks); (b) copper–graphite brushes MGS-7 (hot-pressed copper–graphite brush with addition of 7 mass% of lead, resistivity less than 1 mcOhm m, hardness 110–130 MPa) (1, 1′) and electrographite brushes EG-2A (resistivity 11–28 mcOhm m, hardness 70–220 MPa, analog of Morganite EG3) (2, 2′) with anode (1′, 2′) and cathode (1, 2) polarities.

IU-characteristics shift upwards (see Figure 9.81, curves 2–4). The *IU*-characteristic of the stationary contact with the film covering the ring surface (curve 5) lies higher than the characteristic for the uncovered ring (curve 1). It is significant that when the transfer film appears between the surfaces in the contact, the *IU*-characteristic becomes nonlinear and the contact resistance depends on the direction of current passage (see Figure 9.81b).

If the gold tip was located outside the friction track on the ring or on the sites of the friction surface free of the transfer film of the brush material, the *IU*-characteristic was linear and the contact resistance was low (<0.1 Ω). If the tip passed the transfer material, the contact resistance varied within the 1–100-Ω range.

High resistance of friction transfer films is apparently caused by their extreme heterogeneity. In addition, it should be kept in mind that graphite flakes can orient along the slip plane in the film formed by graphite-containing materials on the metallic counterface, as some authors pointed out.[840] Yet, it is known that graphite shows metallic conductivity along the slip planes while it behaves as a semiconductor with a high resistance in the perpendicular direction.

Effect of brush material on properties of intermediate films on base metals. The films formed by graphite, copper–graphite, silver–graphite, and experimental brushes containing silver foil on copper contact rings were studied under normal operation conditions.[392,841] The studies carried out using the probe device (see Figure 9.73) have shown no conductivity on most sites of the films with clearly seen traces of friction transfer formed by graphite and copper–graphite brushes at voltage excluding fritting ($E' = 10$ mV) (see Figure 9.82a). This proves the presence of an insulating layer of copper oxide between the transfer material and the ring metal. At $E' = 1$ V the field strength on some sites of the copper oxide film exceeds the film electric strength ($\sim 10^8$ V/m,[1] and fritting (see Section 9.4.1.2) occurs as single peaks of a high conductivity on contact voltage records (see Figure 9.82b). Stable conductivity at $E' = 10$ mV and abrupt oscillations of U_c at $E' = 1$ V are typical for those film sites on which the friction transfer layers are less noticeable (see Figure 9.82c). Points at which fritting and total insulation occur alternate within a length of only a few micrometers.

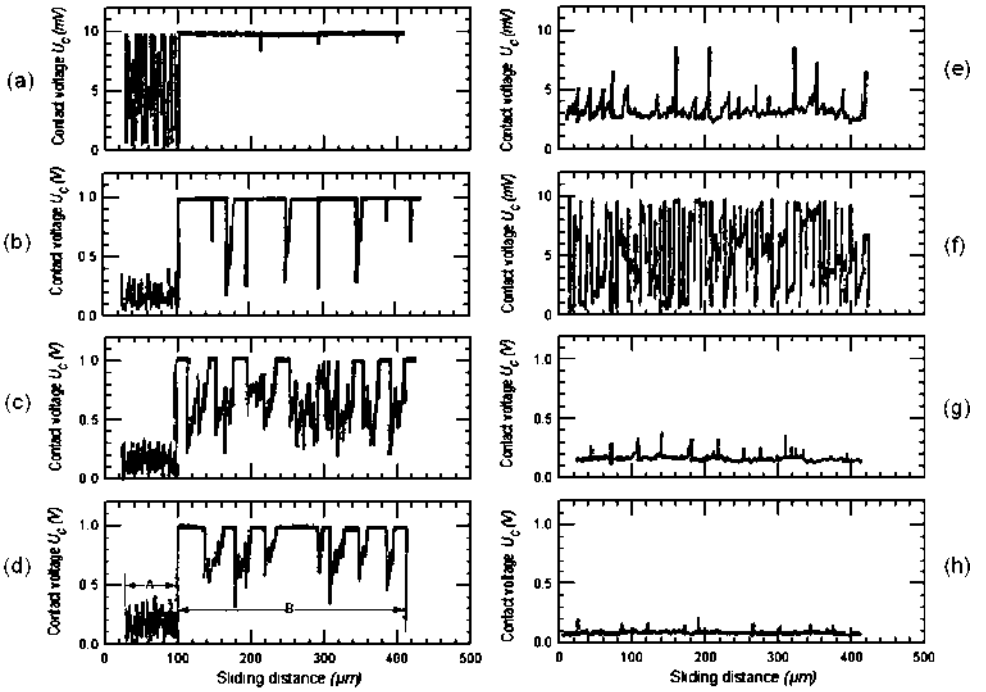

FIGURE 9.82 Typical contact voltage records in sliding of tip over the friction track on copper ring surface after operation in pair with different types of brushes: (a, b) brushes BT-3 (soft graphite brush with addition of MoS_2, resistivity 30–65 mcOhm m, hardness 70–190 MPa); (c, d) brushes MGS-7; (f, h) brushes SG-3 (silver–graphite brush made by powder metallurgy with 3 mass% of graphite); (e, g) experimental brushes containing silver foil and binder filled with colloid silver; (a, e, f) $E' = 10$ mV; (b, c, d, g, h) $E' = 1$ V; (A) nontrack part of ring surface; (B) friction track.

When examining the films at single points with the stationary tip the *IU*-characteristics showed a high initial resistance (10^4–10^6 Ω) and fritting at some critical voltage U_f (see Figure 9.83b and Figure 9.83e). The film sites covered with the transferred brush material have the following feature: the *IU*-curves recorded at points close to a spot of fritting (15–20 μm) are usually characterized by relatively low contact resistance R_c (10–10^3 Ω). This proves that electrons pass through the conductive bridge formed earlier.

It follows from these results that the structure of the intermediate film formed on the ring surface in operation of graphite and copper–graphite brushes agrees with the models presented in Figure 9.80a and Figure 9.80b. Indeed, when obtaining the *IU*-characteristics on the slopes of asperities of the graphite brush BT-3, fritting occurs even at points being 2–3 μm apart one from another. The pattern of the U_c diagram at $E' = 1$ V (see Figure 9.82b) also proves the absence of conductive film connecting the conductive bridge formed earlier and the closest film site. So, in this case the intermediate film structure can be described by the model presented in Figure 9.80a.

The test results for the films formed by the copper–graphite brushes MGS-7 on the counterface can be explained by assuming that the structure of the films corresponds to the model shown in Figure 9.80b. In this case relatively high conductivity within small spots 5–20 μm in size (see Figure 9.82d) and the pattern of *IU*-characteristics obtained at different surface points can correspond to the passage of the tip over the surface valleys filled up with the conductive material and insulated from each other.

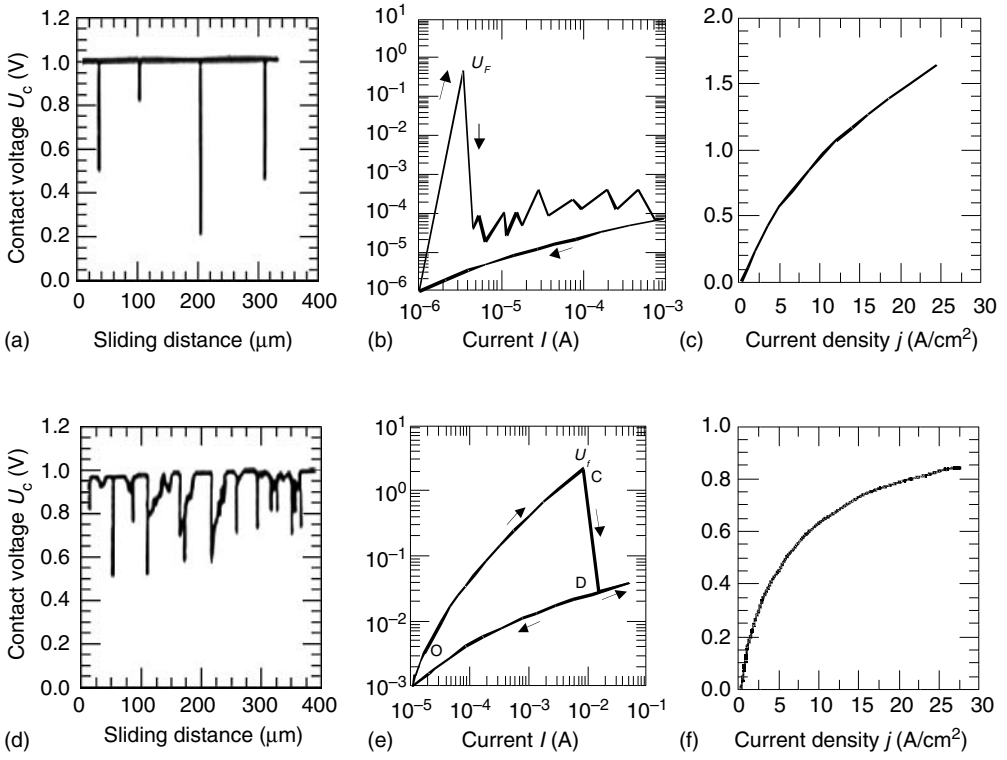

FIGURE 9.83 Typical contact voltage records in sliding of gold tip ($v = 3.3$ μm/s, $N = 2\times10^{-4}$ N, $r_0 =$ 50 μm) over copper ring surface after operation in pair with brush EG-74 (hard electrographite, resistivity 35–75 mcΩ m, hardness 150–500 MPa, analog of Morganite EG63) (a) and copper–graphite MGS-7 brushes (d) at e.m.f. of source equal to 1 V; *IU*-characteristics recorded at points of contact between tip and film formed on ring surface by brushes ЭГ-74 (b) and MGS-7 (e); typical *IU*-characteristics of brushes EG-74 (c) and MGS-7 (f) in pair with copper ring.

Yet, the results of studies of the films formed by silver-containing brushes could not be explained by the models presented in Figure 9.80a and Figure 9.80b. When the tip slides over the ring friction surface, a high conductivity is recorded at most points, including the sites covered with clearly visible friction transfer films irrespective of voltage. Only single spots show a high electric resistance (see Figure 9.82e through Figure 9.82h). This fact, along with the linear pattern of the corresponding *IU*-characteristics, proves the absence of the continuous insulating copper oxide film on the ring working surface. The transferred conductive material directly contacts the ring metal. The formation of the intermediate film of this type (see Figure 9.80c) can be described as follows. The brush material can be transferred onto both the ring surface sites covered with a relatively thick oxide film and the sites being juvenile (due to microcutting, plastic deformation, etc.) or covered with a thin (tunnel-conductive) oxide film. The transferred film of the corrosion-resistant brush material with a high silver content prevents these sites against further oxidation, thus retaining the stable electrical contact between the film and copper matrix for a long time.

The electrical properties and structure of the intermediate film can change significantly if the operation conditions (load, sliding velocity, current density and direction, environment) are varied. For example, Figure 9.84 illustrates the typical contact voltage records for the films formed by the graphite brushes BT-3 in air (a) and in vacuum (b). It is apparent that in the absence of an oxidative environment, the copper oxide layer in the collector film fails, resulting in the formation of the

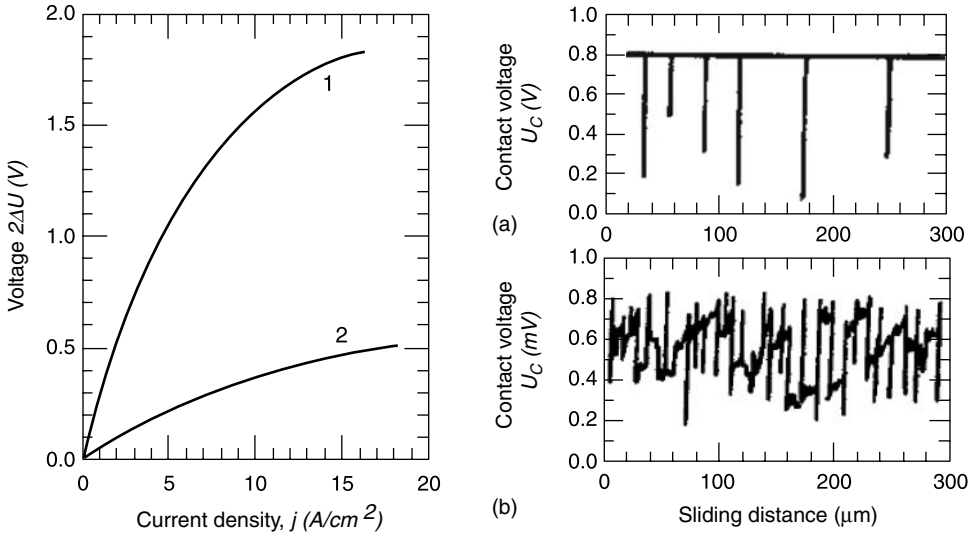

FIGURE 9.84 Voltage–current characteristics of graphite brushes BT-3 in sliding over copper contact ring (diameter 8.5 mm, $p = 70$ kPa, $\omega = 200\pi$ rad/s) in air (1) and in vacuum 6.65×10^{-3} Pa (2); contact voltage records obtained in sliding of gold probe ($v = 3.3$ μm/s, $N = 2 \times 10^{-4}$ N, $r_0 = 50$ μm) over the surface of ring operated in air (a) and in vacuum (b).

intermediate layer with the stable electrical contact between the transferred material and base metal (see Figure 9.80c).

However, numerous studies have shown that the collector films produced by the brushes of the same type are similar under normal operating regimes of electrical machines. For example, the brushes of the electrographite type form a light-brown film without great deposits of the transferred material but with a continuous copper oxide layer. The structure and resistivity of these films do not principally change when varying the brush pressure within the 10–100 kPa range, sliding velocity up to 5 m/s, and current density up to 25 A/cm^2.

Hence, each group of the brush materials operating under normal conditions is characterized by a certain structure and resistivity of the intermediate film on the counterface. The structure and properties of the film can vary greatly depending on the brush type. For this reason it is natural to expect that the pattern of current passage through the composite-metal SC can depend strongly on the type of the composite and properties of the intermediate film.

9.4.1.2 Mechanism of Current Passage through the Contact with Intermediate Films

Several mechanisms of current passage through the brush–collector contact have been proposed. The authors holding the viewpoint that an intermediate film covers the collector surface (see Figure 9.80a) believe that the copper oxide layer on asperity summits of the surface plays a decisive role in current passage, while the transfer material filling up surface valleys is of secondary importance. Contact spots of the following types can appear:[1,7] α-spots of the contact between the brush surface and melted copper, α-spots formed in the contact between the brush and solid copper, and b-spots of the contact between the brush and copper oxide.

Fritting mechanism. According to the Holm theory,[1] the great share of the current passes through the contact spots belonging to the first two types resulted from the *fritting* of the oxide film. Holm has mentioned[1] that real *fritting* is the breakdown of bonds in dielectric. This breakdown results in the formation of channels in the film or in a simple case, the failure of film around the

existing metallic α-spot. It is assumed that the first stage of high resistivity film breakdown is the injection of electrons into the film by field emission. The strong field makes the boundary barrier steeper and consequently thinner, so that electrons can tunnel through the barrier. The injection will surely happen at a certain point of the film, never being uniform. The injected electrons produce a strongly enhanced current flow within a narrow path, and the material within the path is strongly heated. Thereby, the cohesion of the film material is diminished with the result that a channel through the film is produced. If copper melts and metallic bridge appears in the Cu_2O film at the breakdown site, an α-spot is formed. If breakdown does not produce an elevated temperature sufficient for melting of copper, an *a*-spot appears.

The breakdown was called regular *A*-fritting.[1] Observations on *A*-fritting of base metals have been conducted by many researchers.[1,392,838,842,843] Crossed rods and sphere-plane schemes were used in most of the experiments. Contact pressure has played a great role in the mechanical breakdown of the film. Therefore, electrical breakdown data obtained with liquid metal probes are more reliable.

As an example of typical *A*-fritting, let us consider the recent results of Liu and McCarthy[842] (see Figure 9.85a). The voltage across the contact between a gallium drop and the oxidized copper was recorded with a delay time of 5 s. The contact resistance was then plotted against the voltage. As seen, the *A*-fritting occurred at 1.8 V (point A) when the voltage suddenly dropped, indicating an electric breakdown, or creation of a conducting channel. It may be further noted that the formation of the channel was not a one-time process before the metallic *a*-spot was produced. At point *B*, the breakdown process was halted until the current further increased and the fritting process started again before it proceeded to the stage D.

Figure 9.85b presents a typical result from the same sample but with the delay time being 60 ms. It can be seen that there are more sudden voltage drops (region A) as the current increases in

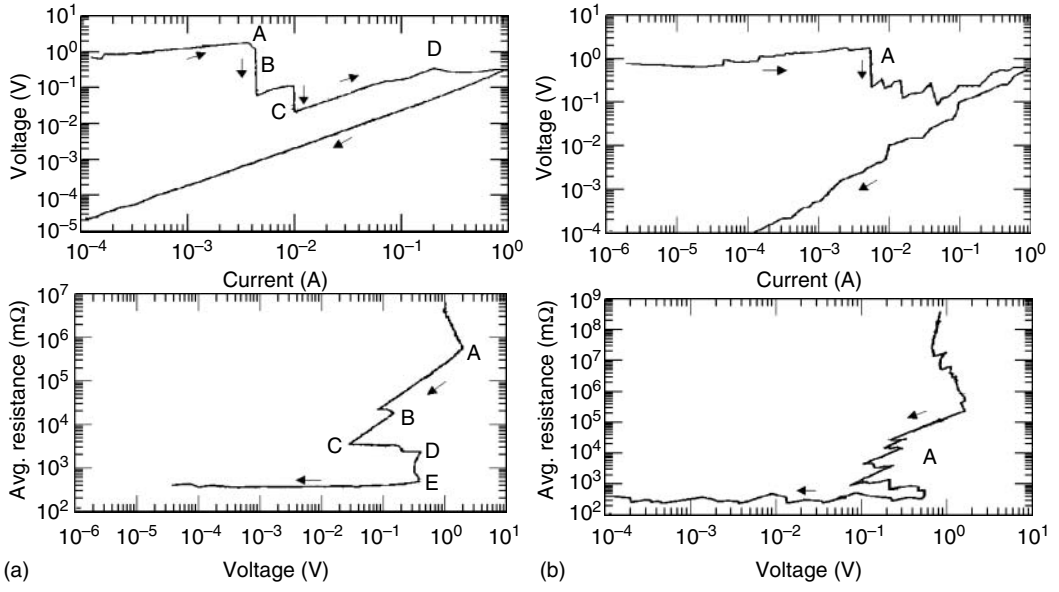

FIGURE 9.85 Typical *IU*-curves (a) and *RU*-curves (b) for oxidized samples of copper (heating to 150°C for 125 h, film thickness of 55 nm) contacted with gallium drop. (a) Delay time of 5 s; (b) delay time of 60 ms. (From Liu, D. R. and McCarthy, S., *Proceedings of 46th IEEE Holm Conference on Electrical Contacts*, Institute of Electric and Electronic Engineers, Inc., 183–190, 2000. With permission.)

the 0.005–0.1 A range. There could be more steep steps in the fritting process (region A). Holm called this process *B-fritting*.

It is customary to speak of *B*-fritting when the fritting starts from an existing *a*-spot, and constitutes the adaptation of this spot to increasing currents through widening of the conducting area. The widening can involve, for example, plastic yielding. Figure 9.86 shows the *B*-fritting of a collector film on copper as probed with a gold wire. The test results in Figure 9.86 were taken in insulating and conducting regions of a carbon brush track with a gold wire. It is typical that *B*-fritting voltage is more or less constant when current is increased in the region of conductivity.

The metallic spots severely oxidize when they exit the brush contact due to their high chemical activity. As the Cu_2O film becomes thicker, the oxidized spots undergo fritting again. Of course, the abrasion and microcutting of the collector surface also favor the appearance of juvenile copper surface sites. Thus, the dynamic equilibrium is attained among the processes of fritting, wear, and oxidation occurring on the contact spots. It follows that the thickness of the copper oxide film on asperity summits of the collector surface is the main factor influencing the contact resistance. The more severe the contact spots oxidize, the higher is the breakdown voltage and the contact resistance.

The fritting mechanism provides a qualitative explanation of the polarity effect on the black grade brushes, nonlinear *IU*-characteristics, and some other phenomena. At the same time, this mechanism fails to explain some other facts, e.g., polarity differences of the metal-containing brushes.

The analysis of the experimental data[392] shows that there is an interrelation between the structure, mechanism of current passage, and contact electrical characteristics (see Figure 9.82 through Figure 9.84).

In a film (see Figure 9.80a) containing continuous copper oxide layer and transfer material (hard electrographite brushes), the current can pass mainly through the contact spots at asperity summits of the collector contacting the brush. When the average thickness of the Cu_2O layer on the contact spots is $h \cong 10^{-8}$ m, the specific resistance of copper oxide is $\rho \cong 200\ \Omega$ m,[1] the contact spot radius is $a \cong 10^{-6}$ m, and the number of the spots is $n \cong 10^2$, the resistance of a single contact spot (*b*-spot) is $R_c = h/(\pi a^2) \cong 10^6$–$10^7\ \Omega$, and the resistance of n paralleled *b*-spots is 10^4–$10^5\ \Omega$. Because of light loads used in sliding contacts, the size and number of the *b*-spots can be less than those assumed in calculation (about 10 according to Kuhlmann–Wilsdorf),[241] and contact resistance can be still higher. At the usually registered voltage drop in the brush contact ($\Delta U \cong 1$ V),

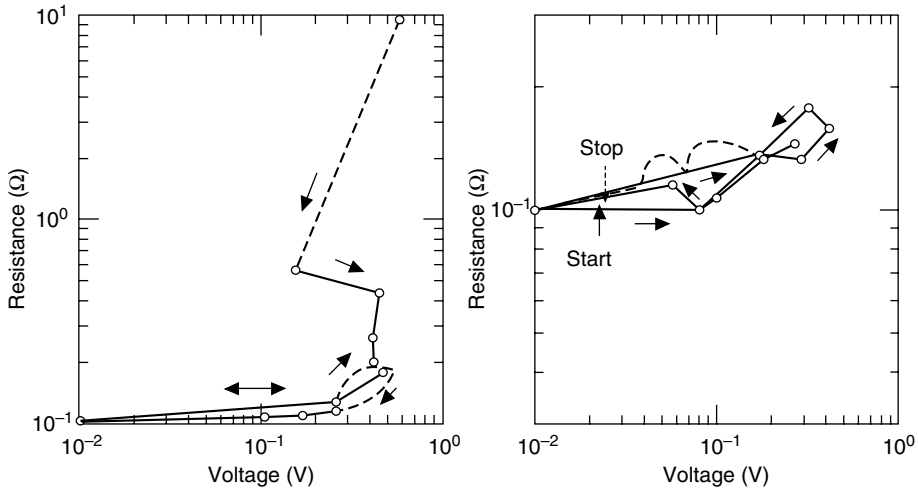

FIGURE 9.86 B-fritting of copper oxide: (a) insulating spot on the ring; (b) conducting spot on the ring. (From Shobert, E. I., *Transactions of the AIEE: Part III*, B(13), 788–798, 1954. With permission.)

the current which can pass through the contact spots with the intact Cu_2O film does not exceed 0.01–0.1 mA. Therefore, if there are no ways for current passage except the *b*-spots, the electric strength of the oxide is already reached ($\sim 10^8$ V/m) at light currents, and fritting results in the appearance of α- or *a*-spots.[1] In this case the current via *b*-spots can be neglected and copper oxide in the collector film can be considered as a dielectric. It was confirmed experimentally by simulating electric current passage from a single brush asperity to the collector (see Figure 9.82b). The brushes forming this type of the collector film have a high voltage drop and nonlinear *IU*-characteristics (see Figure 9.82c).

The role of transferred material in the collector film. If the thickness of the transferred material in the collector film (see Figure 9.80b) is comparable with the asperity height (soft graphite and copper–graphite brushes), large portions of the collector surface covered with the Cu_2O film are in the electric contact with the brush through the transferred material. It is apparent that only part of this material is involved in current passage due to high heterogeneity of the material. Dimensions of these regions were found based on the size of conductivity sites recorded after fritting (see Figure 9.82d). The size of the conductivity spots of the transfer film covering the ring reaches 10–50 μm across the sliding direction and several hundred micrometers along it. Therefore, the area of the conductivity spots *S* can be 10^{-8}–10^{-9} m^2. The resistance of the copper oxide layer ($h \cong 10^{-8}$ m, $\rho \cong 200\ \Omega$ m, $S \cong 10^{-8}$–$10-^{9}$ m^2) in this case should be below 200 Ω.

Therefore, the total resistance to current passage from a single brush asperity to the collector through the transfer film and the underlying layer can amount to 10^2–10^3 Ω, that is by 3 or 4 orders of magnitude less than the resistance of the *b*-spot. If we assume the number of the transfer film sites involved in current passage to be 10, the total resistance of the brush contact can vary within the 10–10^2 Ω range. It is apparent that for the collector film shown in Figure 9.80b, a great share of the current can pass through the film and the underlying oxide film and no fritting can occur at low current density. In this case copper oxide in the collector film should be considered as a semiconductor rather than a dielectric.

The *IU*-characteristics obtained have low initial resistance when the tip is located on a site of the collector film with the transferred material ($R_c \cong 10^3\ \Omega$), which decreases exponentially with increasing the applied voltage (see Figure 9.82e). Fritting occurs at the same U_f as in the above case (Figure 9.82b) but at current of 2 or 3 orders of magnitude higher. After fritting, the residual contact resistance is high ($R_c = 10$–$100\ \Omega$) and rather stable.

The features of current passage via the intermediate layers with a friction transfer film allow one to explain the nonlinear pattern of the *IU*-characteristics for many kinds of brushes (see Figure 9.82f). At low densities the current can pass without fritting through the transfer film and the underlying Cu_2O film; this factor results in a high contact resistance. The beginning of the sharp inflection of the *IU*-characteristic at current density of 3–8 A/cm^2 is apparently caused by fritting and formation of the current-conducting bridges in the Cu_2O film and *b*-spots that drastically reduces the value of R_c.

The higher the current in the brush contact, the higher the electrical conductivity of the collector films. The current-conducting channels formed in the oxide film under the transferred brush material can last for some time after current turn-off. It can be confirmed by comparing the *IU*-characteristics for the same contact working at various pre-operation currents[844] (see Figure 9.87). As is seen, when a pre-operation current density in brush contact is high, a contact voltage drop is lower.

In case of the intermediate layers with the stable electrical contact between the transferred material and metal (see Figure 9.80c), the largest share of the current passes through the transfer film. Low initial resistance is registered when obtaining the *IU*-characteristics at any site of such films (see the lower branch of the curve in Figure 9.82e). Under these conditions the ΔU of the brush–collector contact and the *IU*-characteristic should be governed by the properties of the friction transfer film, either continuous or islet, rather than the oxide component of the collector film.

For example, when sliding occurs in an oxygen-free, humidified atmosphere that precludes normal chemical reactions, the films consist of an extremely thin adsorbed water layer (1.5–3.0 nm

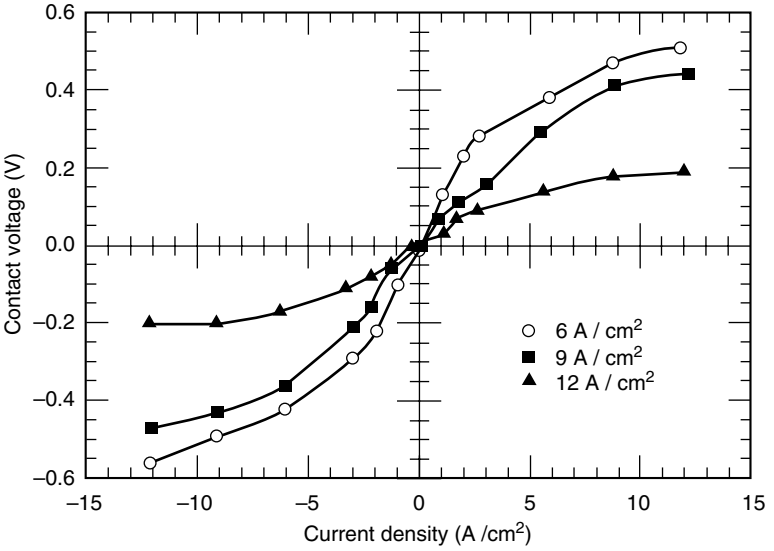

FIGURE 9.87 IU-characteristics of metal–graphite brushes ($\rho = 100$ μm, $H = 16$ Hs) for various pre-operation current (in the air, preoperation time: 20 h). (From Ueno, T. and Sawa, K., *Proceedings of 45th IEEE Holm Conference on Electrical Contacts*, Institute of Electric and Electronic Engineers, Inc., 169–174, 1999. With permission.)

thick) and a mixture of transferred brush material and slip ring material. Schreurs et al.[845] analyzed the formation of thick films (10–100 μm thick) on copper rings sliding against the silver–graphite brushes (0.75 mass fraction of silver) in a humidified carbon dioxide atmosphere. After run-in the original copper surface is no longer exists and the brush slides over the deposited brush material. No oxides of appreciable thickness are formed, as shown by Auger spectrometry. The metal-to-metal weld provides thick film formation on the slip ring surface. The atmosphere is maintaining a thin film of adsorbed molecules on the graphite and the freshly exposed metal. The film provides lubrication and limits the number of metal-to-metal welds.

Contact model for this case is presented in Figure 9.88. In the steady state, the metal–graphite brush slides over a thick film very similar in composition to the brush material. Because of the discrete patchy nature of the thick film, two interfaces and a bulk volume have to be considered in modeling the contact interface. These components are: (1) the brush–film interface, (2) the film–slip ring interface, and (3) the film volume which connects both interfaces.

Influence of operating conditions. As mentioned above, the structure of the intermediate layer formed by certain type of brush material is influenced by electrical and mechanical factors, such as current density and polarity, sliding speed, contact pressure, materials of brush and collector (slip ring), and geometry of contact surfaces. Other factors are: temperature, humidity, atmospheric pressure, and composition of atmosphere. In some cases these factors can greatly change the intermediate layer structure and current passage mechanism. For example, monolithic electrical brushes made of silver–graphite materials, and in particular 75 wt% Ag, exhibit two distinctly different modes of operation.[241,846] Transition from low temperature (mode I) to high temperature (mode II) behavior have been interpreted as resulting from a change in the interfacial film, such that in mode I the film underneath the contact spots contains layers of graphite which cause the film resistance to be comparatively high and the friction coefficient low, whereas in mode II the silver layer is continuous in the films, causing lower film resistivity but higher friction.

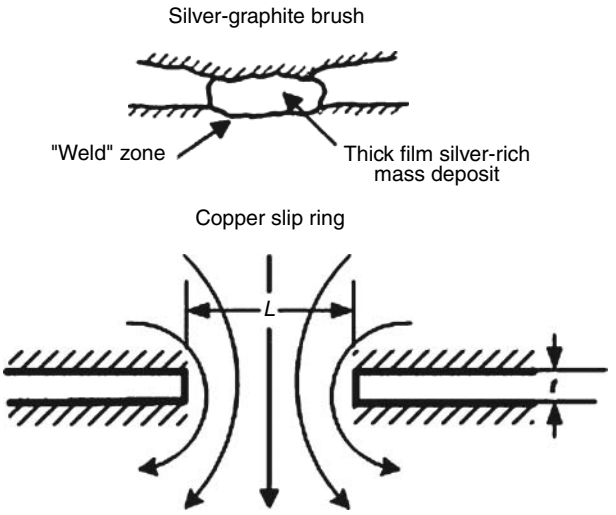

FIGURE 9.88 Thick film contact mode: cross-section (top) and constricted current path. (From Schreurs, J., Johnson, L., and McNab, I. R., *IEEE Transactions on Componenets, Hybrids and Manufacturing Technology*, 4(1), 30–35, 1981. With permission.)

The analysis[241] indicates that the seemingly unbroken wear particles are the pads at contact spots which separate the silver–graphite material from the solid metal substrate (interface similar to that shown in Figure 9.82 is formed). These pads determine the film resistivity as well as the contact spot size. Two types of pads may be distinguished: (1) pads apparently formed through the prow or wedge mechanism, having a lamellar structure of parallel graphite and silver layers bonded over their respective close packed planes; (2) pads of compacted silver fragments which are welded together due to contact pressure and flash temperature, and containing some embedded graphite fragments. The lamellar pads depend on bonding between the lattice planes of graphite and silver mediated by adsorbed water vapor and ceasing at about 160–180°C when water vapor is desorbed.

The sliding test of the metal–graphite brush and copper slip ring was conducted at low atmospheric pressure by Ueno and Sawa.[844] Figure 9.89 shows the contact voltage drop characteristics of the brush depending on atmospheric pressure. A contact voltage drop is high in air, and the *IU*-characteristics are nonlinear near normal atmospheric pressure. When atmospheric pressure decreases, the contact voltage drop tends to decrease. Furthermore, *IU*-characteristics become almost linear in 0.02 Pa. The life of the test brushes, depending on the brush grade, was many times larger than those in air. Based on the results obtained, it was concluded that at low atmospheric pressure, the oxidized film scarcely grew on the slip ring surface, so the contact resistance is thought to be generated mainly by the current constriction and the resistance of the transferred film.

Ueno and Sawa[847] studied the sliding contact phenomena in natural graphite brushes and surface film formation at low oxygen atmospheres. The test brush and slip ring were placed in a vacuum chamber and then a mixture of oxygen and nitrogen was introduced into the chamber to atmosphere pressure. For zero oxygen content, the oxide film with lubricating effect is not formed on the sliding surface. In addition, the surface roughness grows, and contact voltage drop rises (see Figure 9.90) due to small *a*-spots and an increased brush wear.

On the other hand, the oxide film forms on the sliding surface even at low oxygen content (2%). As a result, both the contact voltage drop and the brush wear decrease. However, there is no smooth film formation on the slip-ring surface and the copper of the ring material has been partially exposed. When the oxygen content is increased to 20%, sliding surface becomes smooth.

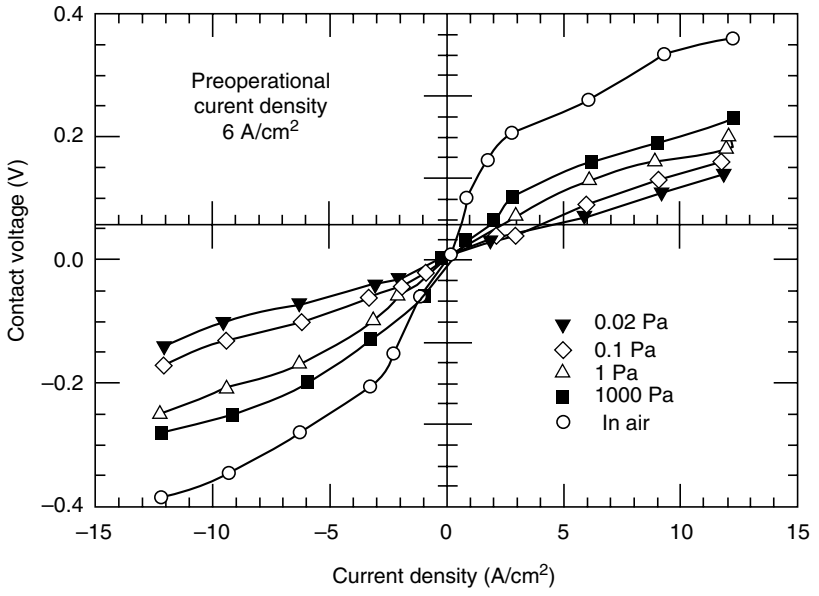

FIGURE 9.89 IU-characteristics of metal–graphite brushes ($\rho = 100$ μΩ cm, $H = 16$ Hs) for various atmospheric pressure. (From Ueno, T. and Sawa, K., *Proceedings of 45th IEEE Holm Conference on Electrical Contacts*, Institute of Electric and Electronic Engineers, Inc., 169–174, 1999. With permission.)

The contact voltage drop showed characteristics almost similar to those observed under atmospheric condition (see Figure 9.90). It was suggested[847] that the contact voltage drop decrease is due to the lubricating effect of the oxide film formed on the slip ring surface resulting in a smooth sliding surface and reduced brush wear.

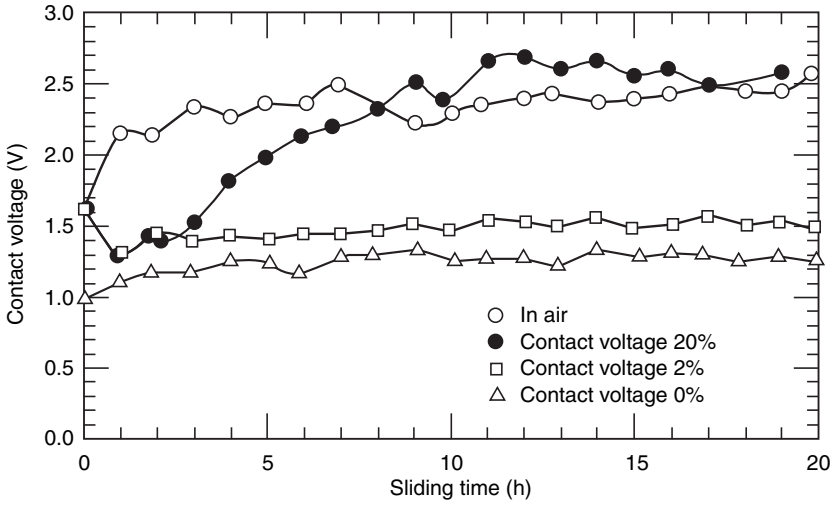

FIGURE 9.90 Relation between contact voltage drop and sliding time for natural graphite brush ($\rho = 700$ μΩ cm, $H = 25$ Hs) on copper slipring. (From Ueno, T. and Sawa, K., *Proceedings of 20th International Conference on Electrical Contacts*, Institute of Electric and Electronic Engineers, Inc., 209–214, 2000. With permission.)

It would appear, therefore, that the structure of the intermediate layer covering the metal member of SC controls the current passage and contact electrical characteristics. If the intermediate layer is a result of formation of continuous oxide film and loose transferred film, the current will pass through the contact predominantly by the fritting of the oxide on counterface asperity.[1] If the thickness of the transferred film is comparable with the asperity height of the counterface, a great share of current can pass without fritting through the film and underlying oxide film. If the friction transfer film directly contacts the counterface metal, most of the current passes through the transfer film and its conductivity governs the electrical characteristics of the contact.

9.4.1.3 Influence of Polarity on Conductivity in Composite–Metal Contact

A specific feature of the composite–metal sliding contacts is the dependence of their electrical characteristics on the direction of current passage (see Figure 9.81). Contact voltage drop under the anode (ΔU_+) and cathode (ΔU_-) brushes can deviate sometimes 2–3 times.[234] As a rule, for metal-containing brushes (copper–graphite and silver–graphite) $\Delta U_+ > \Delta U_-$ and for black types of brushes which do not contain metallic components, the inequality has the reverse sign. Changes in external factors differently influence ΔU_+ and ΔU_-. For example, water vapor reduces ΔU_+ and increases ΔU_-[239] For black types of brushes, ΔU_+ always grows with increasing current density while ΔU_- varies little at high j, and sometimes it can decrease.

According to the fritting mechanism, a high thickness of the copper oxide layer in the collector film under the cathode brush causes the inequality $\Delta U_- > \Delta U_+$ which is true for carbon brushes. It is mentioned[836] that the thickness of the Cu_2O film on asperity summits of the collector surface is of vital importance. Electric field affects ion motion only at the moment when a contact spot appears. Therefore, if brush polarity is positive, the field hampers ion motion and oxide film growth on contact spots, while at negative polarity it favors these processes. It is believed that the oxidation of contact spots under the effect of the field runs rapidly. To prove this, Shobert[234] carried out the experiment in which the value of ΔU for the electrographite brush was recorded when reversing the current direction (see Figure 9.91). Changing brush polarity from "+" to "−" resulted in almost immediate rise of ΔU for less than 0.2 s. After 1 s, polarity was changed oppositely and ΔU decreased also sharply for a still shorter period.

It is concluded[843] that the inequality $\Delta U_- > \Delta U_+$ which is typical for carbon brushes is caused by different mechanisms of fritting in addition to different oxidation rates. If the brush has negative polarity, metallic bridges appear in fritting due to ions moving and agglomerating in the film. The bridges oxidize very rapidly and undergo fritting again. The fluctuations of ΔU_- typical for cathode brushes result from the repeated fritting of the oxidizing bridges. Fritting under the anode brush relates to the breakdown of the film at the field strength of approximately 10^8 V/m. A film having tunnel conductivity is retained on contact spots which prevents further rapid oxidation. As a result, the value of ΔU_+ is lower and more stable.

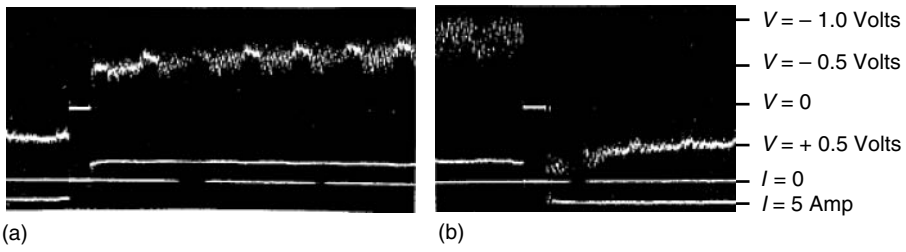

FIGURE 9.91 Oscillograms of brush voltage drop on reversing current: (a) brush anode to cathode; (b) brush cathode to anode. (From Shobert, E. I., *Carbon Brushes—The Physics and Chemistry of Sliding Contacts*, Chemical Publishing Co., New York, 1965. With permission.)

Proceeding from the fact that the collector film contains a lot of copper oxide as a p-type semiconductor, some researchers dealing with polar effects have considered the brush contact using an analogy with a copper-oxide rectifier. It is believed that the copper-oxide film plays the role of an insulating surface for the cathode brush. However, copper and zinc demonstrate similar polar effects even though their oxides are p- and n-type semiconductors, respectively.

To determine the factors causing the inequality of the intermediate voltage drop under the metal-containing brushes of different polarity contacting the copper slip-ring, the effect of polarity on the resistance of the main conductivity channels in the brush contact was studied.[848] As shown above, in a general case, the current passes through the brush contact via α- and a-spots and transfer material layer. Let us introduce the following types of conductivity: via α- or a-spots (a-conductivity), via the sites with the damaged Cu_2O film where the contact between copper and the transferred brush material occurs (c-conductivity), and via the sites with the intact copper oxide film under the transfer material (d-conductivity).

If the gold probe is placed at the sites of the copper slip-ring surface free of the transferred material, change in the probe polarity after the fritting of the oxide film (see Figure 9.92a) (i.e., when α- or a-spot have appeared) has practically no effect on the variation of the contact voltage drop U_c. Therefore, under static conditions a-conductivity is independent of the current direction.

Figure 9.92b illustrates the features of current passage through the sites of the slip-ring surface covered with the brush material. The line *OBCD* represents the voltage–current characteristics obtained on the EP-1 instrument for the intermediate films formed by a metal–graphite brush (MGS-7) at the anodic polarity of the probe. A sharp drop of U_c at the point B indicates the fritting of the copper oxide film lying under the transfer material. Fritting does not occur in repeated recording of the voltage–current characteristic at the given site (line *OCD*). Changing the probe polarity from positive to negative at a voltage below the fritting voltage (e.g., point d on the branch *OB*) results in a sharp rise of U_c (from d to d'). The similar probe polarity variation after fritting (point c on the branch *OD*) gives the opposite situation when U_c sharply drops from c to c'.

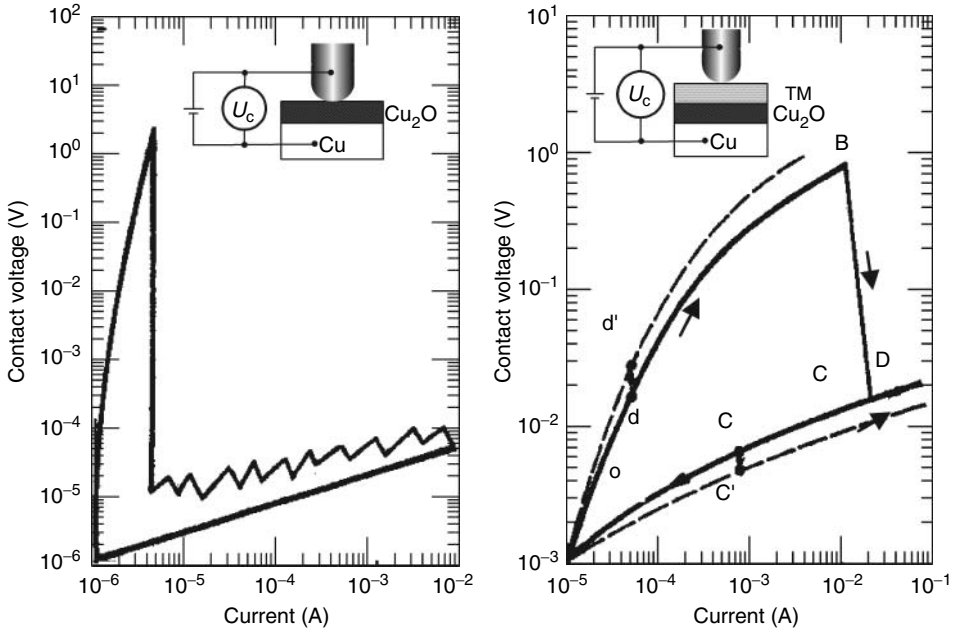

FIGURE 9.92 IU-characteristics recorded when gold probe locates on copper slip-ring surface with poor (a) and noticeable (b) friction transfer layer.

Accordingly, the *IU*-characteristics recorded at the probe cathode polarity (dashed lines) before fritting appear to be positioned higher than the characteristics obtained at the anode polarity. Furthermore, in the case when the characteristics show no fritting (similar to curve *OD* in Figure 9.82b), the contact voltage drop U_c is higher at the positive polarity than at the negative polarity irrespective of the applied voltage.

The obtained results imply that the rectifying effect can occur in the sliding contact of metal-containing brushes if a great share of the current passes through the transfer material. The presence of the continuous copper oxide film under the transfer material leads to the inequality $\Delta U_- > \Delta U_+$ and, if the oxide film is damaged, the inequality has the reversed sign.

The above-mentioned difference in the amount of the transfer material under the brushes of different polarity sliding over the separate friction tracks can also be a factor resulting in the inequality between ΔU_- and ΔU_+. The role of the transferred material is obvious when the electrical and tribological characteristics of the brush–ring contact are simultaneously recorded after changing the brush polarity (see Figure 9.93). Sharp change in ΔU at the moment of changing the polarity is apparently caused by the rectifying behavior of the collector film. Fast increase or decrease in the friction coefficient after the polarity has been changed means that depending on polarity, a film of the brush material with a low shear resistance is formed on the ring surface, or removed from it. It follows from Figure 9.93 that with increasing the amount of the brush material in the collector film, the voltage drop rises. On the contrary, if the ring surface is cleaned, ΔU decreases. Therefore, when the brushes slide over the separate tracks, the inequality $\Delta U_+ > \Delta U_-$ becomes more pronounced due to the different amount of the brush material in the collector film under the brushes having different polarities.

The causes of polarity effect on the sliding contacts of the metal-containing brushes can be explained by introducing an equivalent circuit, as seen in Figure 9.94. The electric current passes through two parallel branches, via α- or a-spots having the resistance R and via the transfer material layer (TM) in the collector film. In the latter case, the resistances within constriction spots R_s and in

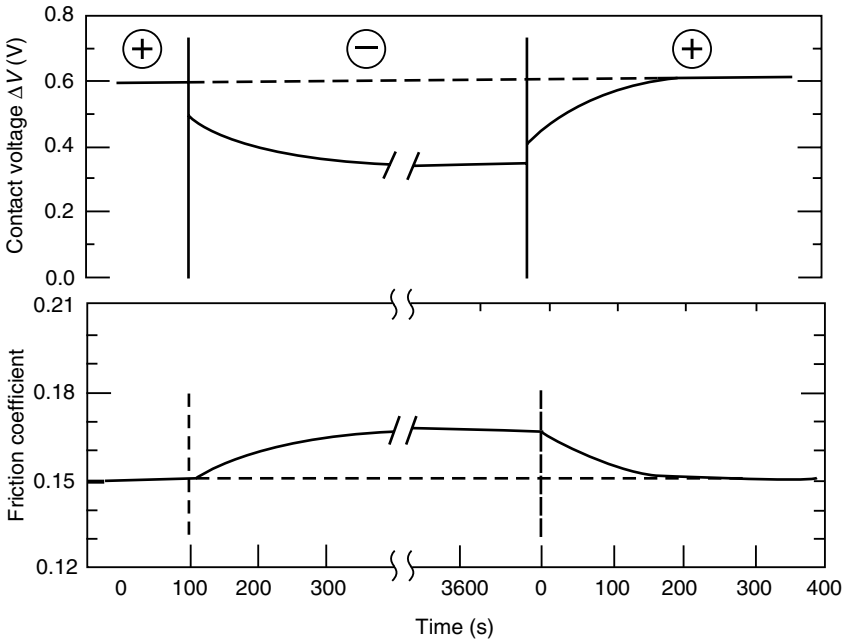

FIGURE 9.93 Contact voltage drop ΔU and friction coefficient f at different polarities of metal–graphite brush MGS-7 sliding over copper ring surface ($j = 20$ A/cm^2).

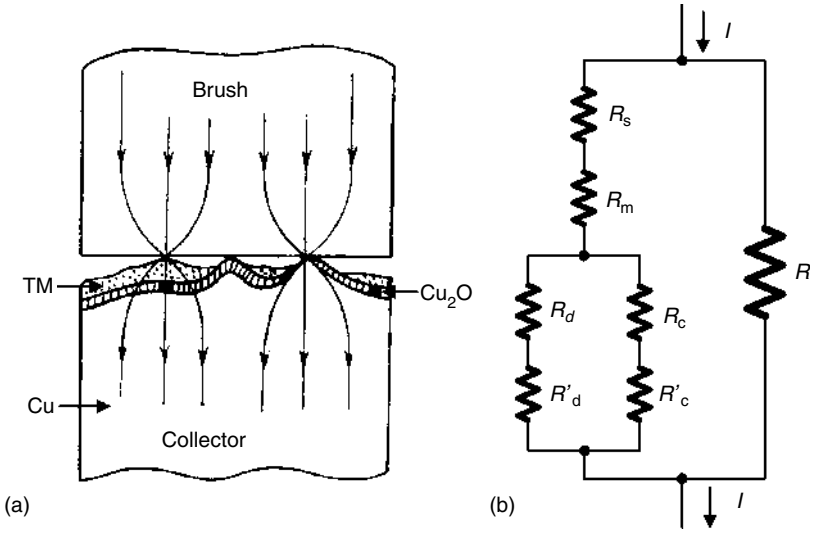

FIGURE 9.94 Model (a) and equivalent circuit (b) of contact metal-containing brush–copper collector.

the brush material layer R_m, increase. Then the current can pass through the copper oxide layer with the resistance R_d or cavities in the oxide film with the resistance R_c. Depending on the brush polarity, the interfaces copper oxide–copper and the transfer material–copper have the rectifier resistances R'_d and R'_c. The additional resistance R'_d operates when the current passes from the collector to the brush (cathode polarity) and the resistance R'_c operates when the current passes in the opposite direction.

With a similar structure of the intermediate layer under the brushes with different polarities, for example when the brushes slide over the same track on the collector surface, the relation between ΔU_+ and ΔU_- is governed by the mode of conductivity via the transferred material. At low current density when the layer underlying the transferred material is not damaged (*d*-conductivity prevails), the additional resistance R'_d operates under the cathode brush; because of this, ΔU_- exceeds ΔU_+. Increase in the current causes the fritting of the oxide film and *c*-conductivity becomes the predominant conductivity mode. As a result, the additional resistance R'_c under the anode brush appears and the relation between ΔU_- and ΔU_+ changes.

The inequality $\Delta U_+ > \Delta U_-$ obtained in practice for metal-containing brushes means that under operation conditions of electric machines, a large share of the current passes through the contact due to *c*-conductivity. The magnitude of the difference between ΔU_+ and ΔU_- depends on the operation regime of the contact and on the properties of the brush material. The adhesive properties and corrosion resistance of the brush material influence the collector film structure, and its electrical properties govern the rectifying coefficient of the barrier layer on the interface of the transfer material with copper.

When the brushes slide over the separate tracks, the different structures of the collector films under the brushes with different polarities result in dissimilar conductivity modes. In the case of a cathode brush, current passes mainly through the spots of the physical contact between the brush and collector (*a*-conductivity). The anode brush contacts the collector mainly through the intermediate layer of the transferred brush material. If the number of spots of the direct contact between the brush and collector decreases, ΔU rises. As is seen in Figure 9.93, the difference of the transfer material amount on the ring surface can be a more significant factor, causing the inequality $\Delta U_+ > \Delta U_-$ in comparison with the rectifying action of the collector film.

9.4.2 The "Lubricating" Effect of Electrical Current

9.4.2.1 Effect of Current on Friction Characteristics

In most cases the passage of an electric current through the contact of metal and self-lubricating composite material is accompanied by significant change in friction behavior. For contact self--lubricating materials, an increase in the current density often results in reduced noise ("chattering") and friction coefficient.[1,849] In electrical machine operation, these changes are so significant that in many cases they speak of the lubricating action of electric current or current lubrication.

Decrease in the friction coefficient with increasing current density is most typical for carbon materials irrespective of the nature of the metal counterbody.[234,840,849,850] For example, this phenomenon was observed in operation of electrographite and copper–graphite brushes paired with copper, aluminum, and steel (see Figure 9.95).[849]

Passage of electric current through the sliding contacts leads to fast decrease in the friction coefficient (see Figure 9.96). This decrease depends on the direction of current. In addition, the polarity in the contact affects contact resistance and also damage mechanism.[840] Houkponou et al.[850] observed a similar behavior of graphite–graphite sliding contact: friction coefficient decreases with increase in electric current. Moreover, friction coefficient drop increases with rise in electric contact potential and generated thermal effect.

It is important to note that lubricating action of electric current is observed not only for a classical couple carbon brush–metal collector (slip), but for inverse couples. For example, in electrical motors such as small uniphase ones, they use the sliding contact of steel on carbon collectors. Paulmier and Mansori, et al.[851,852] have investigated the effects of electric current and/or magnetic field on the frictional behavior of steel/graphite couple. Experimental results have shown that both magnetic field and electric current reduce and stabilize the mean value of friction coefficient. The drop in friction coefficient depends on the current intensity and polarity (see Figure 9.97).

Metal–graphite brushes, especially brushes with a high metal content, demonstrate a less pronounced descending dependence of friction coefficient on current density which sometimes is not observed at all at moderate current densities (up to 30 A/cm^2).[251,252,853] This dependence is not

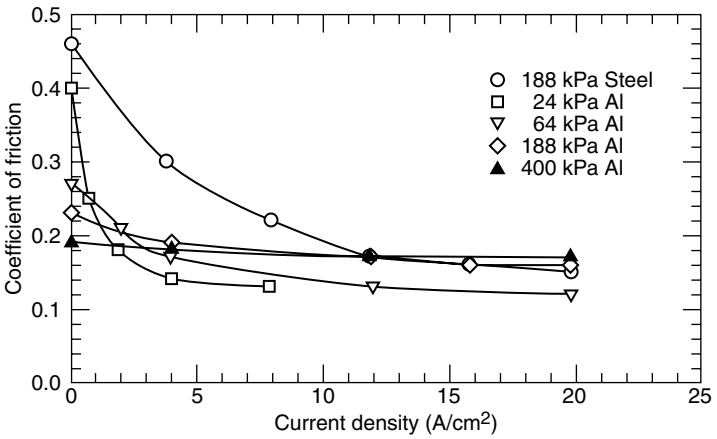

FIGURE 9.95 Dependence of friction coefficient, f, on current density, j, for electrographite sliding over stainless steel at load $p = 188$ kPa (1) and over aluminum at $p = 24$ kPa (2); 64 (3); 188 kPa (4); $p = 400$ kPa (5). (Data from Fisher, J., Campbell, K. J., and Quinn, T. F. J., *ASLE Transactions* 15(3), 192–200, 1972. With permission.)

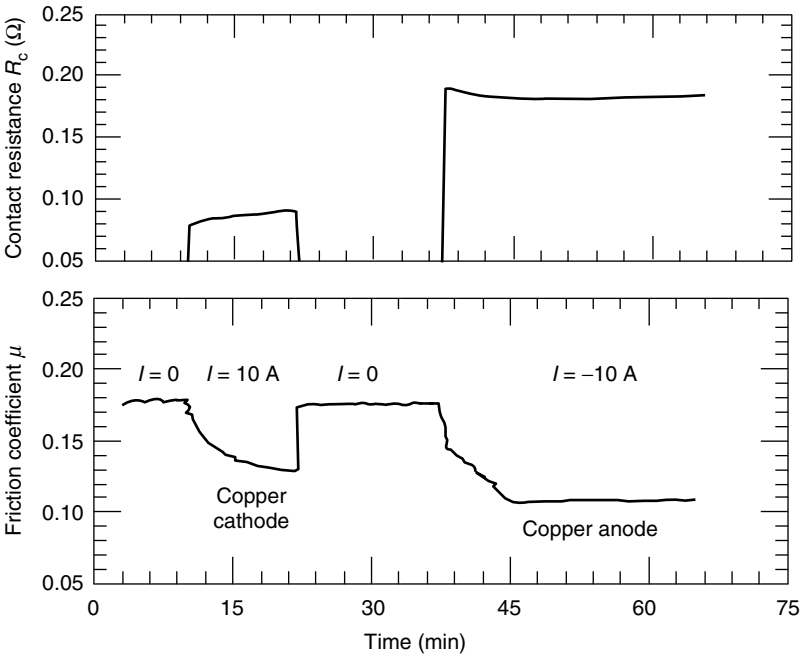

FIGURE 9.96 Evolution of the friction coefficient and the electric contact resistance against time with and without electric current, $N = 20$ N; $v = 2$ m/s. (From Senouci, A., Frene, J., and Zaidi, H., *Wear*, 225–229, 949–953, 1999. With permission.)

typical for some types of brush materials and for metallic contacts;[401] therefore, we cannot assert that the lubricating effect of the electric current is universal.

Experiments[404] have shown that, in the range of the current densities up to 50 A/cm^2 , often used in the sliding contact of electrical machines, three basic forms of the dependence $f(j)$ are possible (see Figure 9.98). A smooth reduction in friction with an increase in the current

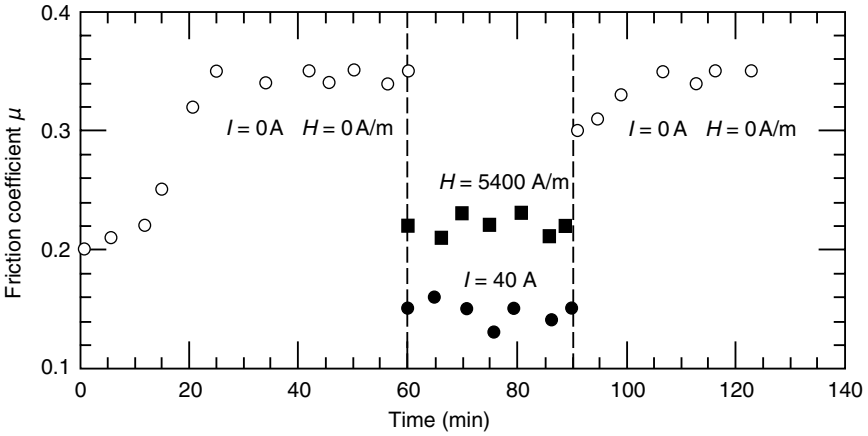

FIGURE 9.97 Influence of an electrical current or a magnetic field on the friction coefficient of a sliding contact of steel XC48 pin/graphite disc (normal load $N = 5$ N; sliding speed $v = 1$ m/s; in ambient atmosphere environment). (From Paulmier, D., Mansori, M., and Zaidi, H., *Wear*, 2003–2004, 148–184, 1997. With permission.)

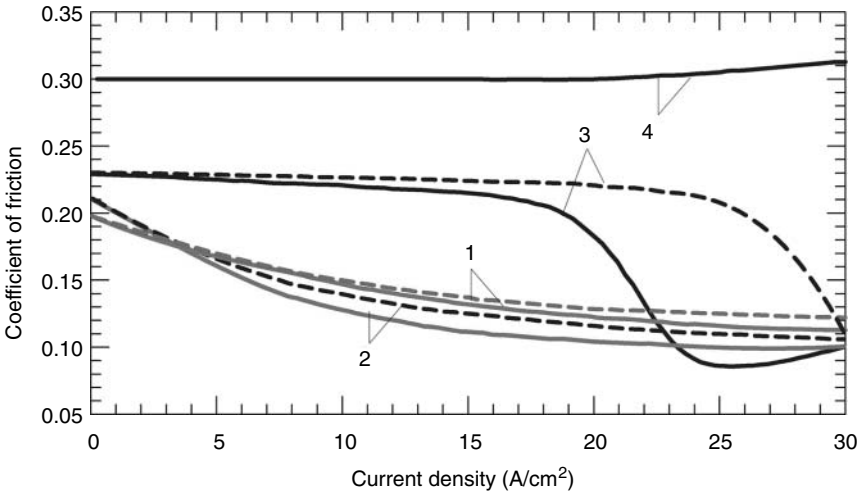

FIGURE 9.98 Dependence of friction coefficient on the current density for different brushes; 1: EG-2A electrographite brush; 2: MGS-7 copper–graphite brush; 3: brush with a high non-carbonized polymer binder content (25 wt%); 4: brush with a very high copper content (94 wt%); solid lines: curves for an anode-polarized brush; dashed lines: curves for a cathode-polarized brush.

("lubrication") is characteristic for brushes of the graphite, electrographite and carbon–graphite classes, and also for metal–graphite brushes when they contain limited amounts of the metallic components and binder (see Figure 9.98, curves 1 and 2). With a high noncarbonized binder content (20–30 wt%) in the brushes, formed by the hot-pressing method, friction is reduced to a lesser degree, but there is a marked reduction when achieving the critical current density (curve 3). For the composites with a high metallic content (over 90 wt%) the lubrication effect is not generally observed; instead, at high current density, there is a tendency towards an increase in friction coefficient (curve 4).

A change in friction coefficient of the brush–collector (slip ring) sliding contact with current is associated in most cases with additional heating of the friction zone because of the Joule heat and changes in the collector film state. However, unsuccessful attempts to explain experiments by the action of only two factors indicate the complexity of the effect.

9.4.2.2 Mechanism of the "Lubricating" Action of the Electric Current

Although the causes of reduced friction due to increasing the current in brush–collector contact have been studied by several researchers; no common viewpoint has yet emerged. According to E. Holm,[854] who studied the operation of graphite brushes, surface temperature increase at current passage leads to reduction in the energy of the bond between the oriented graphite flakes in the collector film on the brush surface, thereby facilitating sliding. Lancaster and Stanley[403] have reported that there is no direct influence of the electric current on the molecular interaction and suggest that the current results in the irreversible change (oxidation) of material in the brush surface layer, leading to reduction of the real contact area.

Hypothesis has also been proposed[855] that current lubrication may result from softening of the collector material on the contact spots and tearing out of the weld bridges. It leads to increase in the amount of wear products in the contact zone, transformation of sliding into rolling friction, and to heating, softening, and fracture of the wear debris between the rubbing surfaces.

The brittleness and relatively low elastic modulus and elastic limit of the brush materials for which the effect of lubrication by the electric current is observed suggest that the work of friction is spent in overcoming molecular interaction on the segments of elastic contact and destruction of the surface layer by microcutting.[856,857]

Paulmier and Mansori, et al.[851,852,858] pointed out two factors of current influence on friction of steel/graphite couples: (1) passage of current through the contact tends to orient the hexagonal planes of the graphite crystallites perpendicular to the sliding surface. As the graphite conductivity is about 8×10^4 times better in a direction parallel to the planes than perpendicular to them, this increases contact conductivity and leads to reduction of friction coefficient; (2) oxide layer growth on the steel track is enhanced by a magnetic field that favors carbon transfer to the steel, so the steel/graphite contact becomes a partially carbon/graphite one, and the friction coefficient decreases.

Summarizing the results, Paulmier[851] and Mansori[852,858] noted that the frictional characteristics of the steel/graphite couples are basically determined by the action of the electromagnetic field on the metal surface and by the mechanical effect of the normal load on the graphite surface. The reversible reduction in the real contact area at the Joule heating reduces the work of the frictional forces, leading to the effect of lubrication by the current. The simultaneous effect of electromagnetic field leads to the oxidation in steel, also leading to a reduction of the real contact area and to carbon transfer on steel.

The brittleness and relatively low elastic modulus and elastic limit of the brush materials for which the effect of lubrication is observed[856,857] suggest that the friction work in the brush–collector contact is expended at overcoming molecular interactions on sites of elastic contact and damage of the brush by microcutting. With these results in mind[856,857] model experiments were carried out by Myshkin and Konchits[392,404] dealing with the effect of electric current on friction of carbon materials under mostly elastic contact or dominant microcutting.

In the first case, the run-in face of the cylindrical rod (1 mm in diameter) made of electrographite rubbed under law speed over a copper flat specimen, and the contact occurred always on the fresh surface. To implement mainly elastic contact, the copper counterface with a low roughness ($R_a = 0.05$ μm) was used at low pressure (10 kPa). It was found that the friction coefficient is independent of the current, even at densities exceeding 100 A/cm^2 (see Figure 9.99, curve 1) while

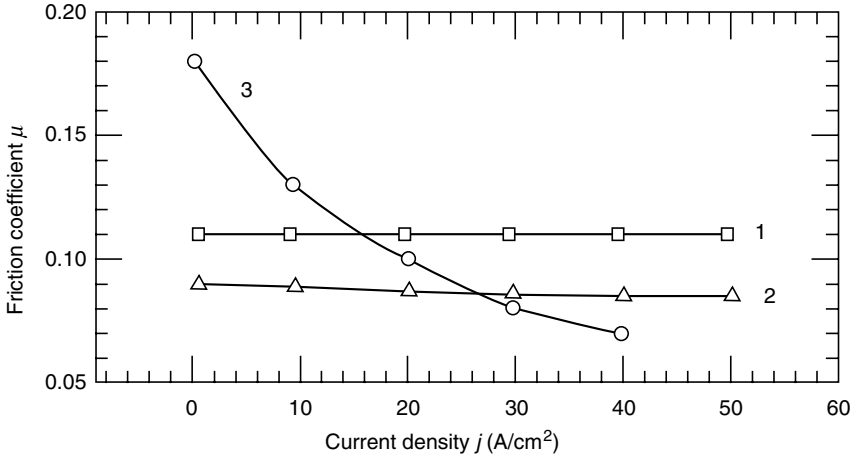

FIGURE 9.99 Friction coefficient f as a function of current density; for anode-polarized electrographite EG-2A sliding over a copper ring (curve 3) (diameter, 40 mm; $p = 10$ kPa; $\varpi = 20\pi$ rad/s) and over a flat copper specimen with a friction transfer film (curve 2) and without a film (curve 1) ($p = 10$ kPa; $v = 17$ μm/s).

for multiple electrographite brush–ring contacts f starts to decrease at $j = 5$ A/cm^2 (see Figure 9.99, curve 3). The polarity also does not influence the friction coefficient. A marked decrease in f is observed only at high densities ($> 10^3$ A/cm^2) which are not usual for contact materials of this type. When the cylinder slid over the copper covered with the friction transferred film, the friction coefficient decreased slightly with increasing current density (see Figure 9.99, curve 2).

The results mean that at unchanged metal counterface and elastic contact, one cannot expect noticeable friction reduction, as it takes place in the real brush–ring contact (see Figure 9.99, curve 3).

At the same time, the reversible influence of electric current on the wear resistance of composite materials was also observed in the microcutting regime (see Figure 9.100). The effect of the electric current on strength of the surface layers of brush materials was studied by scratching the brush with a steel sphere. The conventional ultimate stress σ being the ratio of the tangential force F required to form a scratch to its cross-section area ($\sigma = 12Fr_0/d^3$, where d is the scratch width and r_0 is the radius of the steel sphere) served as the strength characteristic of the surface layer. As seen in Figure 9.100, the ultimate stress σ rapidly drops with increasing the current density and the friction track width rises, and the contact temperature increases simultaneously. In the range of current densities of 10^4–10^5 A/cm^2, typical for contact spots,[234] these effects are very significant. The calculated temperature rise in the contact zone may exceed 500 K for carbon materials. This allows one to attribute variation in the friction coefficient to increasing current, which decreases work spent on damaging the contact material due to microcutting.

Experiments[392,404] carried out with and without current loads on test specimens sliding along the same friction track on a slip ring showed that the counterbody surface changes may lead to either decrease or increase of the friction coefficient, depending on the operation conditions (specimen polarity, load, vibration, etc.). Figure 9.101, A illustrates the dependencies obtained for two identical electro–graphite brushes operating in pair with the slip ring under the same load (30 kPa). When a brush with measured fiction coefficient was energized, the friction coefficient dropped rapidly within 2–5 s and then continued to decrease to a stable value during 10^2–10^3 s. When the current was switched off, the opposite situation occurred.

If the test brush was currentless and the additional brush was energized, the friction coefficient decreased gradually, but there was no rapid change in the magnitude of the test brush friction coefficient upon activation or deactivation of the current (Figure 9.101b). Since in the latter case, the friction coefficient of the test brush serves as an indicator of the state of the ring working surface,[32] then it means that changes in the counterface due to current passage through the contact favors the lubricating effect. However, it was found that for the same contact pair, the effect of counterface changes on friction characteristics depends on the operating conditions, and in some

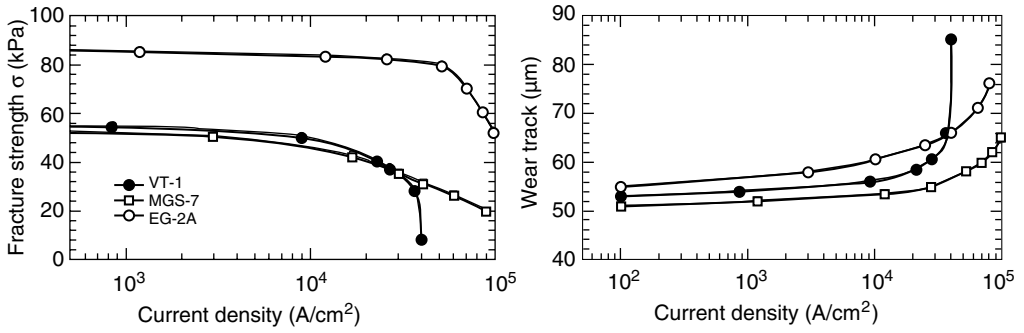

FIGURE 9.100 Conditional ultimate stress σ and friction track width d vs. contact current density y for brushes VT-3, MGS-7, and EG-2A.

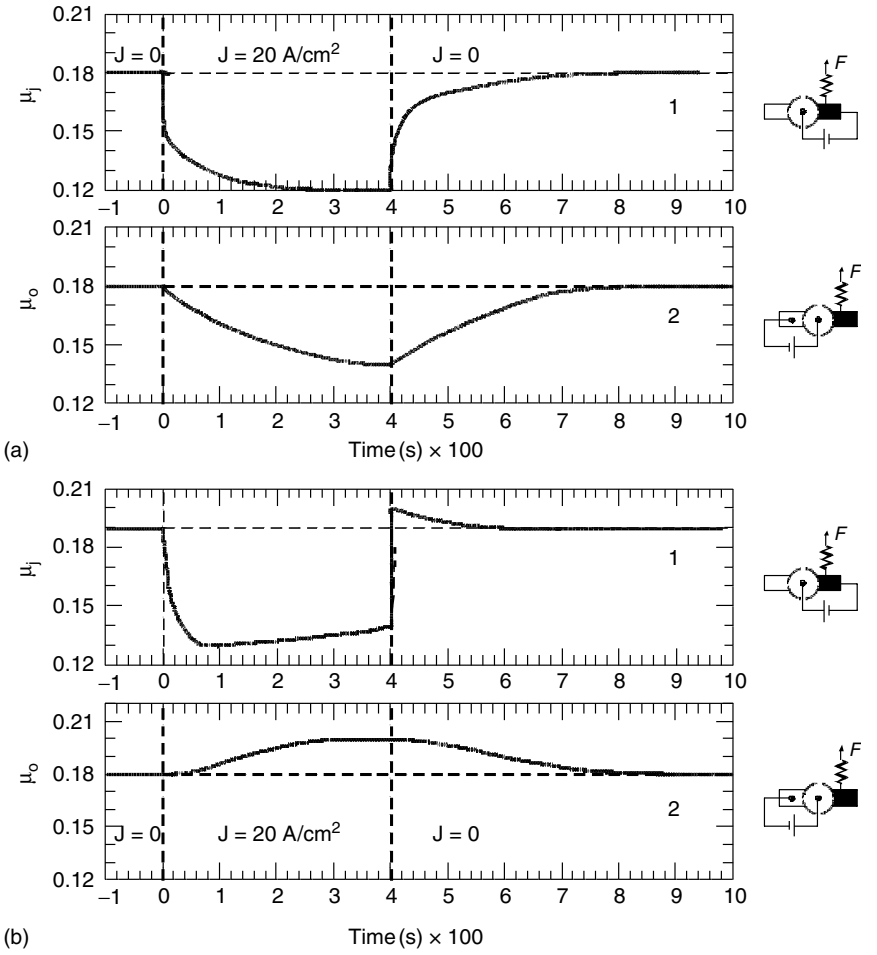

FIGURE 9.101 Friction coefficient of a EG-2A test brush (shown in black on the diagram) sliding over the same friction track with an identical additional brush for additional brush loads of (a) 30 kPa and (b) 150 kPa: curves 1, test brush energized, additional brush without current; curves 2, test brush without current, additional brush energized; I, III: $j = 0$; II: $j = +20$ A/cm^2.

cases these changes make the lubricating effect weaker (see Figure 9.101b). Therefore, changes in the state of the ring (collector) surface influence the dependence of the tribological characteristics on the current density in a complex way and cannot be considered as the main cause of friction reduction with increasing j.

Thus, the primary factor leading to the lubrication effect for carbon materials is the thermal action of the electric current. It leads to reversible weakening of material structure in the microvolumes adjacent to the contact spots and to reduction in the work of the friction on the part of the contact spots where microcutting is realized. At the same time the magnitude of the ultimate stress necessary for microcutting decreases. As a result, together with the reduction of friction in the brush–collector SC, another well-known effect appears: an increase in the intensity of brush wear with increase in current density.[1,234] The influence of the operation regime on the state of the transfer layers leads to a situation in which there is no unique relationship between the thermal power released by current and friction.

9.4.2.3 Effect of Brush Material on Friction Behavior with Electric Current

Studies of modeling the influence of electric current on friction[404] have shown that for each brush material there is a critical current density for the contact spots (see Figure 9.100). Upon reaching this density, the friction track width increases markedly, friction becomes unstable, and σ decreases by one to two orders of magnitude. It is clear that in this case the Joule heat release leads to destruction of the binding skeleton of the brush material in the region adjacent to the contact spot.

Having in mind the data of Section 5.2, we shall examine the factors determining the critical current density j_{cr} on the contact spot. In the case of a single circular contact sliding at low speed, the surface temperature increase due to current passage can be estimated from the simplified formula (friction heat is negligible):

$$\theta = \frac{U_c I}{\pi(\lambda_1 + \lambda_2)a} \tag{9.32}$$

where, λ_1 λ_2—heat transfer coefficients of contacting materials, a—contact spot radius. Considering that $I = \pi d^2 j/4$, $a = d/2$, $U_c = IR_c$, we have

$$j = \frac{2\theta(\lambda_1 + \lambda_2)}{U_c d} \quad \text{or} \quad j_{cr} = \left(\frac{2(T_{cr} - T_0)(\lambda_1 + \lambda_2)}{R_c d^3}\right)^{1/2} \tag{9.33}$$

here, θ is contact surface temperature rise, T_0 is volume temperature, T_{cr} is critical temperature characterizing the material thermal stabilities. Consequently, for constant spot dimensions, j_{cr} will be lower for lower thermal conductivities and lower thermal stabilities of the brush material and for higher contact resistances.

As was shown above for commercial brush materials, the surface changes due to current heating are reversible, i.e., the contact spot temperature does not reach the critical value. However, with reduced thermal stability or the thermal and electrical conductivity of the brush material, the critical value of the temperature at the contact spots will be reached at lower current densities in accordance with Equation 9.33. Tests with microtribometer confirmed that for the hot-pressed brush materials with a binder of the same type, value of j_{cr} is lower for larger content of the binder, i.e., for lower thermal and electrical conductivities. With high noncarbonized binder content (above 20 wt%) in the brush, the values of j_{cr} on the contact spots decrease so significantly that they may be reached even with the currents actually used in electrical machines.

It is precisely this circumstance that leads to anomalies in the behavior of friction and electrical characteristics of contacts and reduction in the allowable current density for brush materials with a high content of noncarbonized thermoset binders. Such materials are serviceable only at relatively low current densities of 2–6 A/cm^2.[243] At increase in current we observe instability of operation of the contact, deterioration of commutation, and accelerated brush wear. Model experiments[392] relating to the brush–collector contact confirmed that j_{cr} depends on the resistivity of material and contact voltage drop (see Figure 9.102). At the same time it was shown in experiments with energized and currentless brushes sliding over the same friction track that the change in the counterbody surface abrasiveness for $j > j_{cr}$ is not the primary cause of the change in the wear rate.

Summarizing the results, it can be concluded that at current densities above the critical value ($j > j_{cr}$), the temperature at most of the contact spots reaches values sufficient for intensive destruction of the binder. This destruction in surface layer adjacent to the contact spots leads to weakening of the bond between the filler particles and to their easy removal, which explains the intensification of the wear. The reduction in shear strength of material in the surface layer is the cause of the marked reduction in friction coefficient.

Thus, for composite materials with a low thermal stability and low electrical conductivity, the Lancaster and Stanley concepts[403] are applicable and the friction behavior of the sliding contacts is

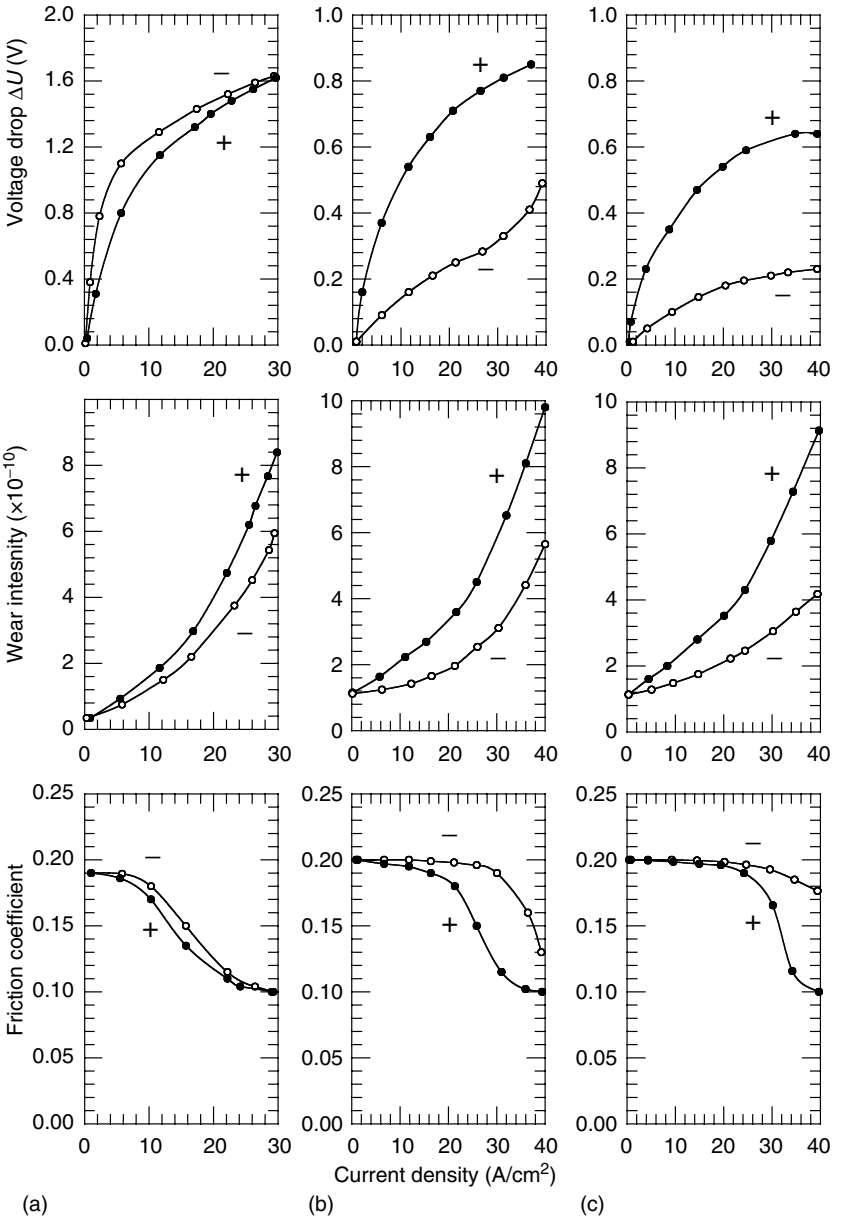

FIGURE 9.102 Dependence of contact voltage drop ΔU, wear rate I_h, and friction coefficient f on current density in contact j for anode (+) and cathode (−) model composite brushes in operation of separate tracks on copper ring ($\phi = 40$ mm, $p = 70$ kPa, $v = 2$ m/s). (a) brush on base phenol resin (20 wt%) filled with graphite, (b) brush on base graphite and colloid silver, graphite, (c) the same as (b) with adding of silver foil.

determined by the intensity of destruction of the binder in the material surface layer under the action of the Joule heat.

High metal-containing brush materials. As noted above that the frictional behavior of brushes with a high metal content differs from the behavior of the carbon materials; the decreasing

dependence of friction coefficient on current density does not show up in practice, and at high currents friction increases in many cases. It should be noted that coefficient of friction is quite high in this case, reaching 0.4–0.5.[251] Typically, the surface layers formed by such brushes on the counterbody surface have only a slight amount of transferred brush material. Consequently, the probability of formation of contact spots of metal–metal type during sliding is high. It is obvious that in this case most of the current is transmitted through the metal or quasi-metal contact spots, and the nature of friction on these spots determines the frictional behavior of the multiple contact as a whole.

It was shown[781] that for metallic sliding contacts, there is a range of contact current densities (10^4–10^6 A/cm^2) within which the influence of the current on friction facilitates plastic deformation of surfaces, leading to an increased real contact area and friction coefficient (see Section 9.2.2). Upon further increase in the current density ($>10^6$ A/cm^2), the thermal action of the electric current intensifies and becomes dominant, leading to softening of the surface layers, increased real contact area, and scuffing. With current densities less than 10^3 A/cm^2, both the plasticity and thermal actions of current are not significant. The influence of the electric field in the clearance on the kinetics of the oxidative processes can be more significant, as noted repeatedly in studies of low-current sliding contacts.[392,783]

9.4.3 Electrical Wear

9.4.3.1 Wear of Currentless Contacts

Most contact self-lubricating materials are based on carbon (graphite, soot, coke, etc.) and the friction and wear of pure carbon materials (graphite, soot, coke, etc.). Friction and wear of pure carbon materials (brushes of graphite, carbon–graphite, and electrographite) against copper were studied most extensively. Lancaster, Hirst, Carriage, and Stanley[32,403,856,857,859] have shown that the brittleness and low elastic limit of these materials cause two modes of contact in the currentless state. They are microcutting dominating at run-in and elastic deformation in the steady state when wear debris fills up counterface valleys. In the latter case, wear results from the contact fatigue. The fatigue wear mode was confirmed for the main types of carbon contact materials.[32,859]

Shobert[7,234] did not deny the occurrence of fatigue wear, but he believed that microcutting and grinding of carbon materials by metal asperities and abrasive wear debris are dominant during a steady-state wear. He considered the role of the abrasive particles to be especially important. This point of view is supported by the following facts. The clearance between the members of the composite-metal SC is always filled up with wear debris whose shape, size, and number depend mainly on the operation conditions and type of composite. Mechanical wear particles are, as a rule, of irregular shape. If the brush is current-loaded, the wear particles are more rounded and small. Their size can vary within a broad range (from fractions to hundreds of micrometers).

The analysis of the granularity of the wear debris collected in electric machines has shown that about 90% of particles are 15–100 μm and the rest are 0.1–3 μm in size. For typical porosity of the electric brush material is 25% and its linear wear rate is approximately 2 mm/1000 h of operation; the volume of the material removed from 1 cm^2 of the contact surface per second is $\sim 0.4\times10^{-4}$ mm^3. If spherical wear particles are 5 μm in diameter, more than 600 particles appear in the contact every second. Therefore, wear debris play an important role in both current passage and mechanical effect on the brush surface. Small particles (0.5–1.5 μm) can separate asperities in contact, and if the particles are 20–50 μm in size, they can even lift the brush slightly and roll under it. The particles are deformed and fail, and the hardest ones penetrate the brush surface.

The presence of graphite or other carbon-containing substances in brush materials leads to high sensitivity of the wear characteristics to adsorbed moisture and gas films. It is evident now that these films play a critical role in operation of brushes containing graphite. Such brushes operate reliably in pair with like materials or metals, provided that adsorbed gases, moisture or organic

molecules are present in the zones of real contact.[7,238,241,846,847,860–862] If there are no such films in the contact zones (when operating in waterless gases and vacuum or at temperatures above 300°C), graphite and graphite-based materials lose their lubricity and wear out rapidly.

This problem appeared during World War II when at high altitudes, aircraft lost electric power when the brushes wore rapidly or dusted. The problem was solved by adding metal halides (PbI and BaF) to the brushes.[863] But there was a drawback requiring extensive run-in at sea level to develop a protecting film. Dihalcogenides MoS_2, WS_2 etc., helped to overcome this drawback under severe conditions in aerospace applications.[249,252,864]

The thickness, composition, and mechanism of thin film adsorption on copper slip rings were studied by Schreurs et al.[860] Figure 9.103 is a schematic view of a hypothetical structure of the film. Such structure should provide low friction, since water molecules are weakly bound (dashed lines) and can shear easily. At the same time they should exhibit the compressibility of a liquid layer. The water film separates metal in the brush from the copper ring in areas where elastic contact is formed, while at the same time providing low shear resistance. When load becomes high enough to cause plastic deformation of metals, the water film breaks down, thereby providing the microscopic brush–ring welds, and material transfer with subsequent wear due to adhesion. In principle, the careful control of load, gas and vapor environment, and surface roughness should enable friction and wear to be minimized while maintaining good electric contact.

In most electrical sliding systems, graphite brushes run on copper or copper-plated surfaces. However, in a few instances steel, nickel, or noble metals have been used.[240,865] Therefore, compatibility effects were studied by Rabinowicz and Ross.[865] It was found that when carbon and the metal of the counterbody are incompatible (low solid solubility), the wear tends to be low, whereas when compatible, the reverse situation occurs (see Figure 9.104). When silver–graphite brushes were used, it was found that the lowest wear was obtained when metal of the counterbody had poor compatibility against both carbon and silver. Gold and copper were the metals giving least wear against graphite, while rhodium and iridium were the best against silver–graphite. It must be noted as well that in the case of friction and electrical resistance, there is no clear correlation with compatibility.

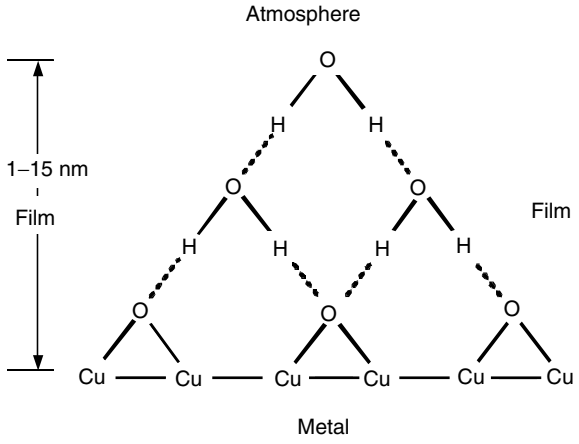

FIGURE 9.103 Schematic view of Cu_2O H_2O complex formed on copper surfaces exposed to humid environments. When two surfaces, each carrying a film of about 1 nm to 1.5 nm, meet the metal atoms they are separated by a film about 2- to 3-nm wide. (From Schreurs, J., Johnson, J. L., and McNab, R., *IEEE Transactions on Components, Hybrids and Manufacturing Technology*, 3(1), 83–88, 1980. With permission.)

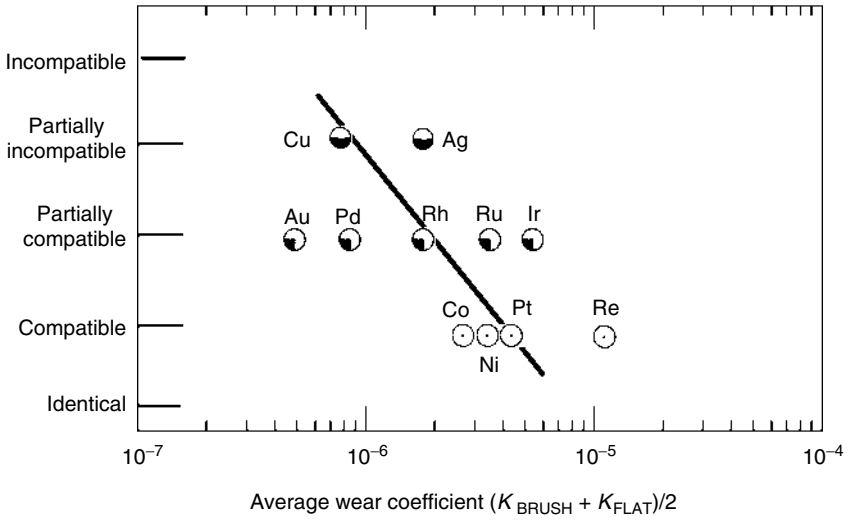

FIGURE 9.104 A plot of the average wear coefficient vs. the compatibility of the flat materials against graphite for pure graphite brush tests. (From Rabinowicz, E. and Ross, A. Z., *Proceedings of 30th IEEE Holm Conference on Electrical Contacts*, Illinois Institute of Technology, Chicago, 499–506, 1984. With permission.)

9.4.3.2 Effect of Current on Wear

The passage of electric current significantly complicates wear of the contact elements. In general, intensity of brush wear rapidly increases with the increase in the current density, independently of the material of collector (slip-ring).[1,7,866] Test data by Rabinowicz and Ross[865] shown in Figure 9.105 are typical and indicate that in certain current range (between 50 and 75 A), there

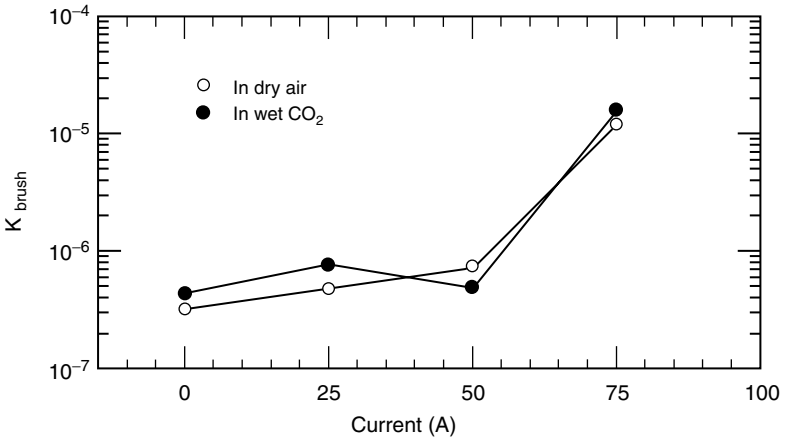

FIGURE 9.105 A plot of the brush wear coefficient vs. current for a silver graphite brush sliding on an iridium flat. (From Rabinowicz, E. and Ross, A. Z., *Proceedings of 30th IEEE Holm Conference on Electrical Contacts*, Illinois Institute of Technology, Chicago, 499–506, 1984. With permission.)

is an increase in wear by about two orders of magnitude, but below that point the influence of current is smaller. Other studies have led to the same conclusion.[867]

The additional wear of contact elements is termed "electrical" wear. This term is introduced without accounting for the fact that the actual causes of the additional wear may be both electrical (electric erosion with sparking or arcing) and mechanical in nature (change in roughness and mechanical properties of contact elements).[1,868]

The proportion of electric and mechanical wear depends significantly on contact load N.[392] The mechanical instability of contact at low load induces electric erosion and high wear due to the "electric" component. With increasing N the wear decreases and reaches its minimum and then rises as N continues to increase because the contribution of the mechanical wear grows. For this reason, for example in electrical machines, the wear of brushes as a function of load is illustrated by the U-type curve (see Figure 9.106). The optimal pressure is different for various types of brushes and ranges from 15 to 100 kPa.

A specific feature of the sliding contacts with dissimilar contact members is the dependence of the tribological characteristics on the polarity of the members. So, when electric brushes of black type operate in pair with copper or steel collectors and rings, the inequalities $J_{h-} > J_{h+}$ and $f_- > f_+$ are most common (J_{h-} and J_{h+} are wear rates of cathode brush and anode one, respectively).[392,849] Such effects may be significant even at relatively small current densities (see Figure 9.107).

For metal-containing brushes, the relation between I_{h-} and I_{h+} has the opposite sign and the relation between f_- and f_+ can be different depending on the operation conditions and composition of the brush material. When the brushes slide over the common track on the collector, polar differences are less marked in comparison with sliding over the different tracks.

The tribological behavior of the composite–metal sliding contacts at extremely high current densities (10^3 A cm^{-2} and more) and sliding velocities (300 m/s and higher) is of special interest. Such conditions can arise in starters, powerful turbo-generators, linear electromagnetic nuclear accelerators, homopolar generators, railway current collectors, and other modern electrical devices.[246,243,777,869–871] Metal–graphite brushes are used predominantly for such conditions.

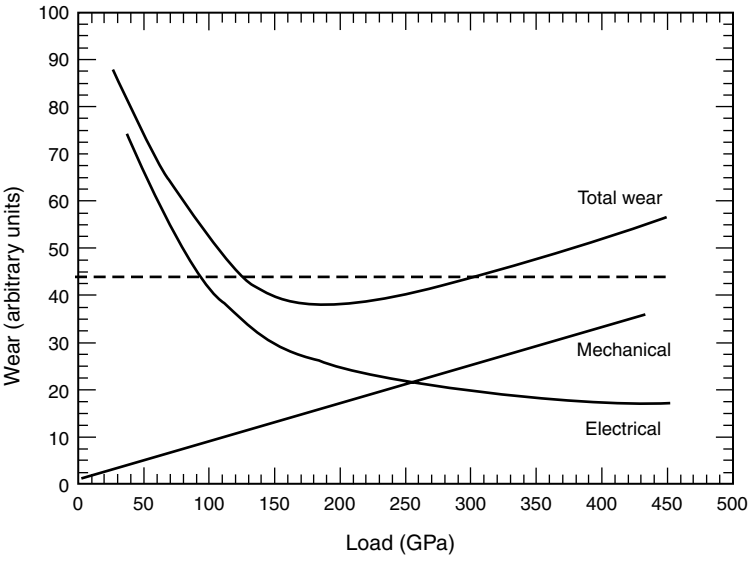

FIGURE 9.106 Typical dependence of wear of electric machine brushes on load.

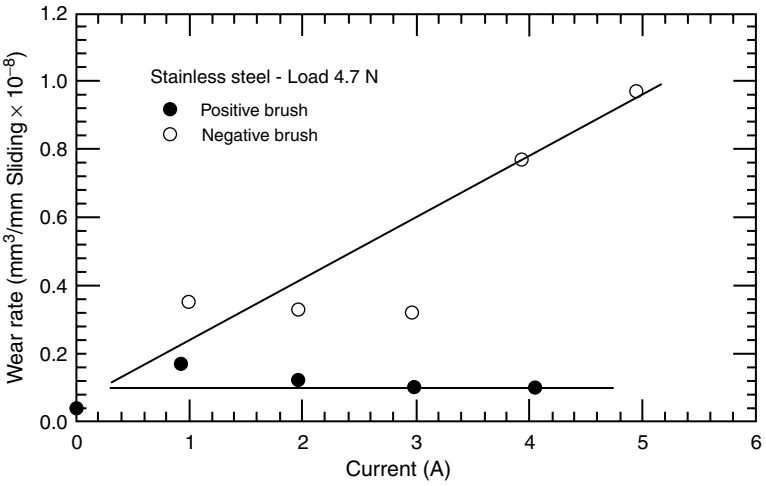

FIGURE 9.107 Variation in wear rate of electrographite brushes sliding on stainless steel with current ($N =$ 4.7 N, $v = 9$ m/s). (From Fisher, J., Campbell, K. J., and Quinn, T. F. J., *ASLE Transactions* 15(3), 192–200, 1972. With permission.)

The tests of metal-containing brushes at extremely high j have shown that tribological behavior typical for brushes under normal operation conditions remains the same. It was found that friction coefficient of the silver–graphite brushes (75 wt% Ag) decreases with increasing j at current densities up to 600 A/cm^2,[245] the wear rate rises approximately proportionally to the current density, polar differences arise at any sliding velocity, and the inequalities $J_{h+} > J_{h-}$ and $R_{c+} > R_{c-}$ are correct (see Figure 9.108). Casstevens et al.[869] reported that for metal-containing brushes SMIS (81.5% Cu, 4.5% Sn, 2% Pb, and 11% of graphite), an increase in j also leads to decrease in f, a higher I_h and the inequality $I_{h+} > I_{h-}$ remains correct at current densities up to 870 A/cm^2 and sliding velocity $v = 160$ m s^{-1} when periods of current passage last 65 s.

According to Marshall[872] the simplest form of expression describing the wear of brushes under extremely high currents is

$$W = kvIt \tag{9.34}$$

where W is the amount worn from a brush which runs on a collector at velocity v and carries a current I for time t; and k is a constant which depends on rotor and brush material. Any wear which occurs when current is not flowing is negligible compared with that when current is flowing. Experience with homopolar machines has shown this to be the case.[872]

It was shown that at high current densities, the slip-ring systems containing noble metals produce less wear than the slip-ring systems which contain oxide-forming metals regardless of the compatibility.[865] This effect is especially marked for tests involving silver–graphite brushes.

9.4.3.3 Factors Leading to Electrical Wear in the Absence of Sparking

In the presence of electric current wear, mechanisms become much more intricate. It is impossible to predict wear rate under variable sliding conditions based on the experiments carried out under fixed conditions even for brushes of the same type.[856] This results from a variety of factors governing wear, and the effect of each factor is not described by a simple law.

Effect on metal surface. In the first studies of friction in the contact of carbon brush with copper collectors, the primary causes of the negative effect of current on brush wear were considered to be

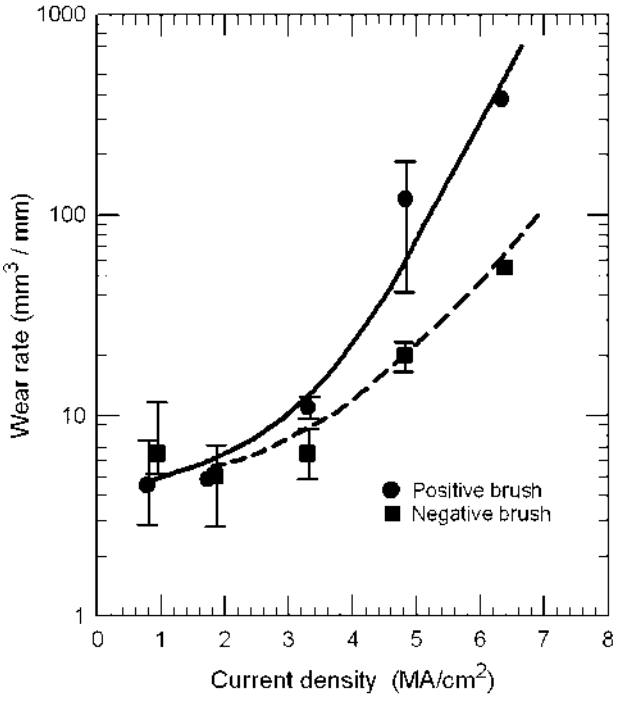

FIGURE 9.108 Volume wear rate, I_v, of silver–graphite brushes in humid carbon dioxide as a function of current density, j (copper ring: $\varnothing = 83$ mm, $v = 12.7$ m/s, $p = 115$ kPa; humidity: dew point 20°C). (From Johnson, J. L. and Schreurs, J., *Wear*, 78, 219–232, 1982. With permission.)

the increase in roughness and abrasive properties of the metal counterbody.[873] This viewpoint was later confirmed in several studies.[1,7,874]

High temperature, deformation of copper crystal lattice during friction, electrolyte decomposition of the adsorbed moisture in the friction zone, and displacement of ions in electric field lead to significant oxidation of the wear track on the collector. Current passage is accompanied by continuous fritting of the oxide films with formation of the α- and a-spots[1] and their repeated oxidation. These processes result in roughening of the collector surface and the appearance of hard oxidized particles intensifying the abrasive wear.

The above-mentioned factors play the governing roles for brittle carbon brushes which are strongly affected by the metal counterface.[875] It was found as follows:

- For current-loaded and currentless brushes, sliding over the same friction track wear of the energized brush is almost completely determined by current density as well as nature and polarity of the brush.[876]
- For metals that are characterized by high oxidation rate and abrasivity of the oxides (e.g., $A1_2O_3$ on aluminum), wear intensity is considerably higher than for copper and steel.[843,849]
- Wear of the cathode carbon brushes sliding over the metal rings is higher than that of the anode brushes. In the former case the ring surface under the brush is rougher and oxidized more severe.[1,876]

However, there are several facts indicating that abrasive wear often does not play the governing role, particularly for metal-containing brushes. For example, increase in wear intensity or increase in current density is observed under conditions when oxidation of metal surface is eliminated, such as brushes sliding on gold or silver collectors and slip rings in a carbon dioxide atmosphere and in vacuum.[226]

Effect on adhesion on contact spots. According to Lancaster,[877] wear fragment separation from the brush surface is a result of weakening of the material in surface layer due to deformation and adhesion. It is shown that adhesion of carbon materials to copper oxides is considerably weaker than to pure copper. Current passage causes breakdown of the oxide film and increase in adhesion of brush with copper, and therefore an increase in the tangential stress at the interface and reduction in the number of deformation cycles causing wear.

Growth in contact adhesion may also take place because of electrolytic dissociation of adsorbed and chemisorbed water or organic substances.[245,877] Microcontact welding and brush material transfer to the counterbody may take place.[245] When increasing the current, a transition from mild to severe wear with formation of plenty of wear debris can be observed. For example, carbon begins to dust when the local contact temperatures reach 150–180°C. At these temperatures, the ratio of the local partial pressure of water to the saturation vapor pressure falls below the critical value necessary to prevent dusting.

The effect of current on the adsorbed water film is the cause of alternative modes of operation of silver–graphite brushes.[241,846] When the current density grows beyond some critical value, the contact resistance drops and unstable performance is established. Brush performance is associated with two different surface films. In the first case, copper is covered with a lubricating layer, composed of finely dispersed layered particles of silver and graphite, as in Figure 9.109. It would give rise to the relatively high resistance (film resistivity in the range of $0.5–6\times10^{-11}$ Ω m^2) and low friction (coefficient of friction between 0.15 and 0.2) of mode I. The second type of film is a debris layer of sintered silver with graphite inclusions, as in Figure 9.110, formed at dusting under high temperature. It would give rise to the relatively low resistance/high friction of mode II.

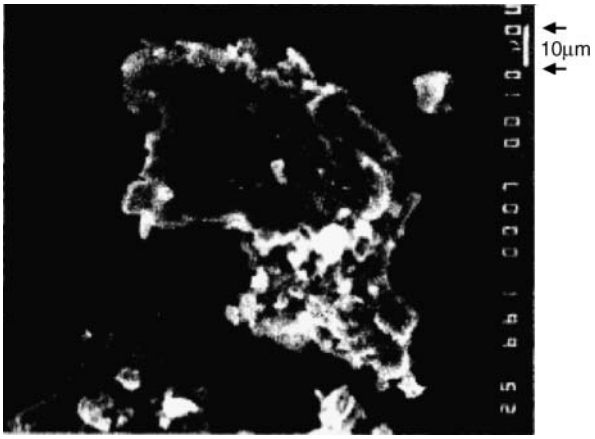

FIGURE 9.109 SEM micrograph of a "primary" wear particle collected in an oven experiment at 125°C from 95 wt% Ag–C material, together with small "tertiary" particles believed to have broken off larger ones. The layering of the particle together with the striations in the long direction suggests that it was formed by the wedge mechanism. (From Kuhlmann–Wilsdorf, D., Makel, D. D., Sondergaard, N. A. and Maribo, D. W., *IEEE Transactions on Components, Hybrids and Manufacturing Technology*, 12(2), 237–245, 1989. With permission.)

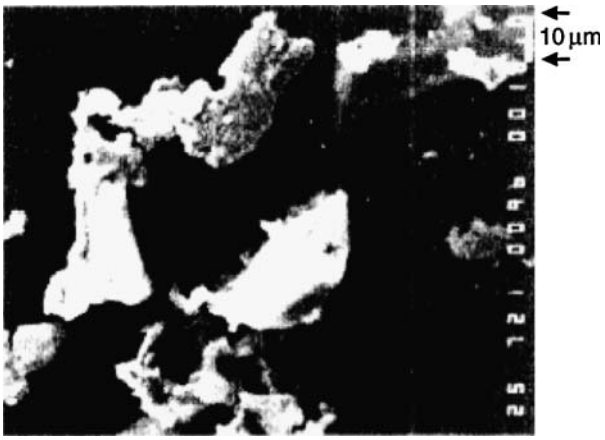

FIGURE 9.110 SEM micrograph of wear particles collected from 70 w/o Ag–C material in an experiment at 225°C. (From Kuhlmann–Wilsdorf, D., Makel, D. D., Sondergaard, N. A. and Maribo, D. W., *IEEE Transactions on Components, Hybrids and Manufacturing Technology*, 12(2), 237–245, 1989. With permission.)

Oxidation of brush material. Baker and Hewitt,[878] in explaining the effect of the high wear of carbon brushes in an oxygen medium compared to a hydrogen medium, suggested that electrical wear is caused by weakening of the brush surface layer due to oxidation. Such explanation was later confirmed by Lancaster and Stanley.[403,877] Current passage causes marked increase in contact temperature which may exceed the limit at which the brush material noticeably oxidizes. The diffusion of atmospheric oxygen into the pores of the brush contributes to this process. As a rule the brush binder, having the lowest critical temperature, will most probably oxidize. Oxidation of the binder weakens the bond between the grains in the brush surface layer, thereby contributing to spalling of the grains in sliding.

The data presented in Section 9.4.2 have shown that the intensity of thermal oxidation of the nongraphitized binder governs the friction behavior of composites with low heat stability and electrical conductivity. At current densities higher than the critical value, this effect becomes dominant in brush wear.[392] Figure 9.111 is an illustration of this case and shows the wear and electrical performances of copper–graphite brushes with phenol–formaldehyde binder. The difference between wear of the anode and cathode brushes when rubbing along the same wear track illustrates the fact that the surface of the ring in this case has little effect. The wear rate is clearly related to value of ΔU controlling the contact heating and hence thermal oxidation of the brush binder. The anode polarity can result in more intensive oxidation of the brush due to oxygen transport under the effect of electric field.

McKee et al.[879] have shown that at high temperature, high current density or high sliding velocity direct oxidation can be an important factor influencing wear of carbon materials. A correlation between the wear rate of carbon brushes and their oxidation temperature at operation temperatures of 460–473 K was obtained (Figure 9.112). It was shown that a sufficiently high temperature for oxidation of the carbon material can be created by the current passing through the high resistant contact. The copper oxide particles migrating within the brush act as catalyst, reducing the temperature at which intensive oxidation begins. Thus, the current determines the oxidation rate and the migration of the copper catalyst.

The occurrence of chemical oxidation at elevated temperatures is indirectly confirmed by the following facts:[879] (1) correlation between the easy oxidation of the carbon brushes in the presence of copper oxide and their wear at elevated temperatures; (2) migration of metallic particles into the

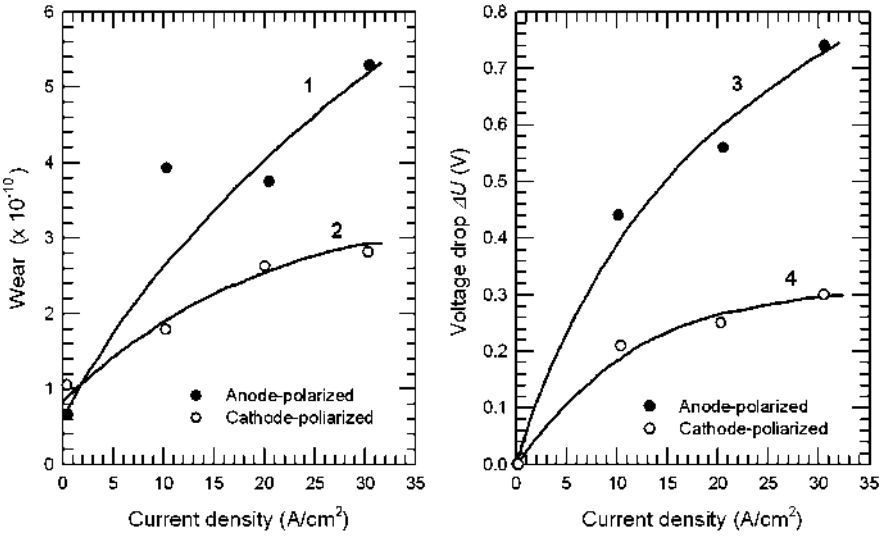

FIGURE 9.111 Contact voltage drop ΔU and wear rate J_h of copper–graphite brushes (MGS-7) as functions of current density, j, when rubbing along the same track on the copper contact ring. 1, 3: brush is anode-polarized; 2, 4: brush is cathode-polarized (ring diameter $\varnothing = 40$ mm; $v = 1.5$ m/s; $p = 10$ kPa).

brush followed by catalytic effect on oxidation; (3) presence of substances which can act as oxidation catalysts intensifying wear as well as oxidation inhibitors (ZnO, phosphor-containing compounds) producing the opposite effect; (4) presence of adsorbed water film reducing brush oxidation and wear.

Weakening of the brush material. It was shown[226,392] that in a wide range of contact current density (10^3–10^5 A/cm^2), there is a reduction in strength of material in the microvolumes adjacent to the contact (see Section 9.4.2). As a result the fraction of contact spots where microcutting is

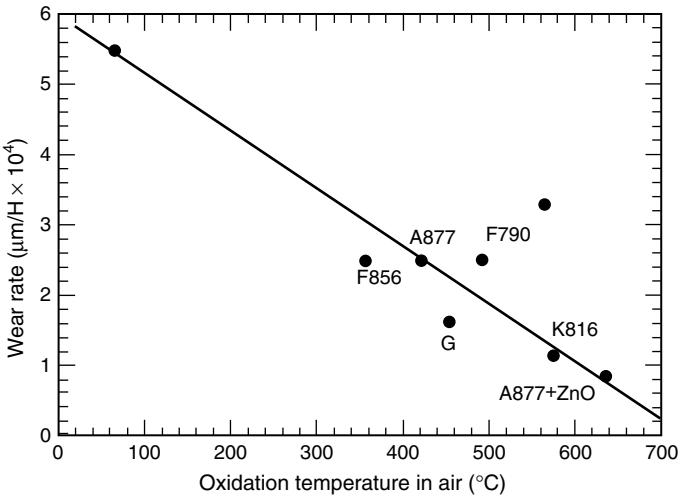

FIGURE 9.112 Wear rate of carbon brushes as a function of temperature of oxidation in air in the presence of 0.5 wt% CuO. (From McKee, D. W., Savage, R. H., and Gunnoc, G., *Wear*, 22(2), 193–214, 1972. With permission.)

occurs can increase. Moreover, with reduction in strength, deformation of the surface layer can take place as a result of combined normal and tangential loading.

Thermal shocks. It was found that thermal shocks, arising as a result of the Joule contact heating,[405] are the factor leading to severe wear of the contact elements. The considerable heating during a short time (microseconds) leads to high temperature gradients and mechanical stresses because of thermal expansion. This applies in particular to materials with components having significantly different thermal expansion coefficients, e.g., copper–graphite brushes (the coefficients of thermal expansion for copper, graphite and Bakelite binder are respectively $17\times10^{-6}\,K^{-1}$, $7.8\times10^{-6}\,K^{-1}$ and $22\times10^{-6}\,K^{-1}$).

The appearance of mechanical stresses may lead to formation of microcracks at the interface of the components. The combination of thermal and mechanical shocks creates conditions for the crack propagation and surface damage. In addition to the difference in thermal expansion of the components, another condition for thermal shock is the heterogeneity of material heat conductivity that causes local heat release. This applies, for example, to the carbon electrical brushes with pitch as the binder.

It was shown[872,880–882] that at high currents (>1000 A/brush), another mechanism of surface damage called *thermal mounding* or *thermoelastic instability* can be observed. It is caused by the Joule heating and consequent expansion of the brush material near the contact spot. Intensive heat generation due to heavy current and high speed can result in very high contact temperatures (1000–3000°C). At the same time, material close to the contact will expand; this expansion can separate the brush and ring surfaces and disconnect less dominant conducting spots. As a result, higher electrical and mechanical loads must be carried by the remaining spots, which are heated more intensively. The result is a brush that contacts the ring via very few spots loaded by all mechanical load and current.[882,883]

It should be noted that almost all the explanations of electrical wear in the brush–collector SC in the absence of sparking and arcing postulate the Joule heat released in the contact as the most important factor (see Figure 9.113). Depending on the operation conditions and material nature, this heat results in the mechanical weakening of the composite surface layer or in intensification adhesion on contact spots, or in a roughening of the metal surface, or in the direct loss of the composite material due to chemical erosion (see Figure 9.113). It is important that the nature of heat release due to current passage and due to friction is not equivalent.

In the case of clean metallic contact spots, the maximum temperature due to the Joule heat is observed at the interface.[1] Quite a different case is found when current passes through the contact of metal and carbon-base material with much lower thermal and electrical conductivities. In this case, the magnitudes of R_c and of the Joule heat are determined by the brush material, whereas the metal acts as an ideal conductor and heat absorber. The most heated region lies within the brush at a distance of the order of the mean radius of the conducting spot (see Figure 9.114). Calculations[1] show that the maximum temperature may exceed the surface one by several times. This facilitates electrical wear. For example, oxidation of the binder and chemical erosion or thermal stresses will be realized at some depth, leading to the formation of cracks and particles weakly bonded with the substrate, and finally to mechanical weakening of the composite surface layer and its severe wear.

These processes can be intensified because for graphite-based materials, the heat conductivity λ and resistivity ρ depend on temperature. After initial reduction, ρ remains the same or increases with increase in temperature, while λ usually decreases with increase in T.[405] When increasing the current the heat generation is increased, but the heat dissipation does not accelerate to the same degree. As was shown,[405] this leads to the existence of a critical current, namely I_{cr}, above which thermal equilibrium is not possible. For $I>I_{cr}$ the increase in the spot surface temperature is limited only by the destruction temperature of the material.

The formation of friction transfer film on the collector surface has a dual influence on brush wear. On the one hand, the friction and intermolecular interaction between contact materials decrease, which leads to reduction in wear intensity. On the other hand, there is an additional

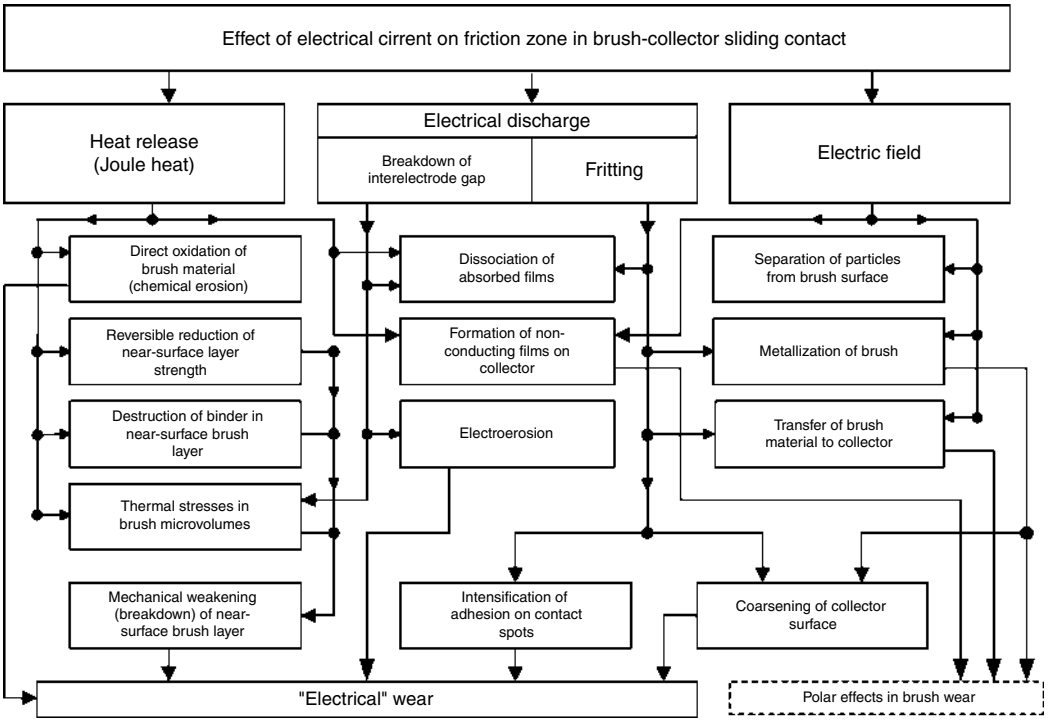

FIGURE 9.113 Factors leading to electric wear in composite-metal sliding contact.

resistance of the brush contact covered by transfer film. Consequently, the critical magnitude of current that leads to disruption of thermal equilibrium can be decreased by a factor of more than 2 for such contact spots.[405] Intensification of thermal action on the surface of the composite inevitably leads to increase in wear intensity.

The size of the near-surface brush zones that are subjected to thermal action is important for wear induced by electric current. In the current-free state, the maximal tangential stresses at sliding arise at a definite depth h, comparable with the size of contact spots (see Figure 9.115), and h defines the thickness of the weakened layer and the size of wear debris.

Only some part of the real contact area conducting current is subjected to the additional heating, so the process shown in Figure 9.113 takes place in brush microvolumes much smaller than the deformed microvolumes. This is shown schematically in Figure 9.115. It is evident that the size of wear debris formed due to the current action will be smaller than the size of mechanical wear debris. This fact is confirmed in practice.

9.4.3.4 Influence of the Electric Field in the Clearance

The influence of the electric field on surface layer of SC, and primarily on the oxidation and mass transfer, is obvious. The oxidation of several metals (copper and its alloys, steel and nickel) is a diffusion process, in which the metal ions migrate through the oxide film to the surface, where they interact with atmospheric oxygen. The oxidation rate is in general determined by the average surface temperature. However, potential gradient on the metal surface segments adjacent to the current-carrying areas may contribute to or prevent motion of ions through the film, thus influencing the oxidation of copper as been confirmed under laboratory conditions and shown in practice.[884] For example, the cathode-polarized carbon brushes form a light-brown film, consisting

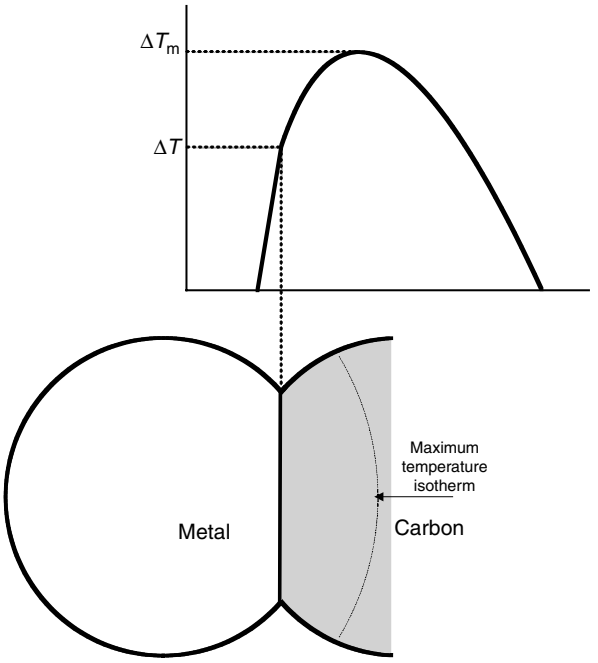

FIGURE 9.114 Temperature increase in metal, *M*, vs. carbon, *C*, constriction region. *I* is the maximal temperature isotherm.

basically of copper oxide, on the copper collector, while the anode-polarized brush forms a dark film with a low Cu_2O content and higher transferred material content.

This fact also reflects the influence of the electric field on the transfer of the brush material to metal surface. Thus, in normal operation of electrical machines, much more material is always transferred from the anode brush to the collector than from the cathode brush. A significant part of the brush material deposited on the collector by the anode brush is transferred to the surface of the cathode brush[885] (see Figure 9.116). Conversely, the transfer of material from the cathode brush to the collector surface is slight, and there is almost no transfer from the collector to the anode brush. It

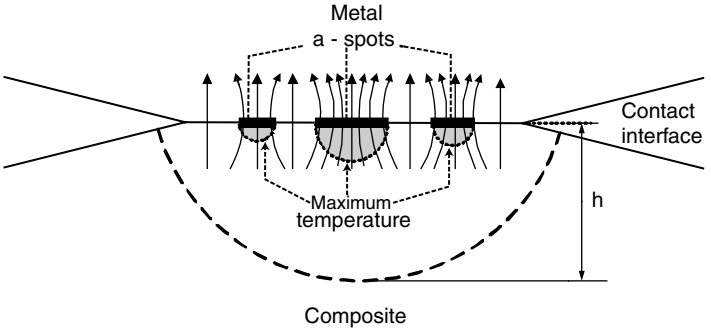

FIGURE 9.115 Schematic diagram or electric current passage through a contact spot experiencing a mechanical load.

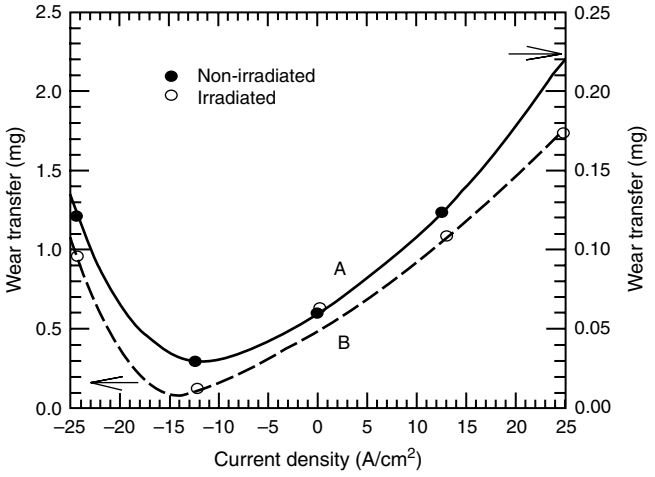

FIGURE 9.116 Dependence of mass m of radioactive brush material transferred to collector A and from collector on inactive brush A on current direction and density. (From Wagner, K., Lenz, R., Britschin, F., and Scheerbarth, H., *Elekrtie*, 8, 248–252, 1964. With permission.)

is typical that more intensive transfer under the anode brush is observed regardless of the counterbody material, ambient medium, and load-velocity parameters.

Electric field influences the mechanism of current passage for brushes of different polarities, especially in case of their operation along the separate friction tracks.[392,848] In case of cathode brush, current passage is realized basically through the physical contact of the brush and ring while, in case of anode polarization, current passage takes place primarily through the intermediate layer of transferred brush material. For the metal-containing brushes this leads to relation $\Delta U_+ > \Delta U_-$ and consequently more intensive heat release under the anode brush. It is evident that this leads to intensification of the electrical wear of the anode brush (in accordance with Figure 9.111) and shows up the relation of wear rates $J_{h-} > J_{h+}$.

Metal transfer to the brush surface may also be realized by passage of metal ions from the anode due to injection of molten metal, vaporization of metal, and its transfer to the brush.[879] Metallization of the brush causes roughening of the counterbody surface, which is one of the causes of the relation of wear rates $J_{h-} > J_{h+}$, typical for carbon brushes. Dissimilar mechanical conditions may cause more intensive sparking under the cathode brush, which also contributes to manifestation of the inequality between J_{h-} and J_{h+}.

Senouci et al.[840] proposed additional factor to account for the effect of electrical field on wear of graphite–copper contact. During friction without electrical current, the graphite basal planes in transferred layer are oriented in sliding direction (see Figure 9.117b). When the current is turned on, electrical field rotates the graphite basal planes trying to increase the electrical conductivity, as was shown by atomic force microscopy. The graphite planes are oriented perpendicularly to the sliding interface when the current exceeds a critical value, creating the effective electrical field in the contact (Figure 9.117d). The action of the electric current is opposite to the effect of sliding, thus resulting the abrasive wear and damage of sliding surfaces.

9.4.3.5 Wear with Sparking and Arcing

The effect of current on wear was considered without visual observation of arcing and sparking. In practice, however, one cannot totally eliminate electric discharges in sliding contacts. Sparking can

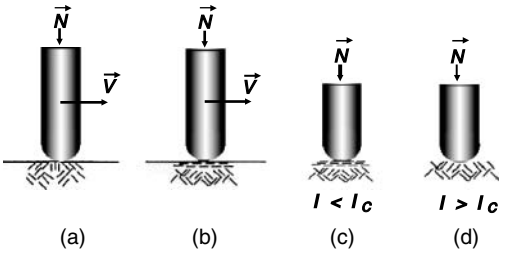

FIGURE 9.117 Orientation of polycrystalline graphite crystallite in sliding electrical contact: (a) crystallites orientation at starting time; (b) high orientation in sliding direction after sliding time in ambient atmosphere plane without electrical current; (c) crystallites orientation with electrical current below a critical intensity/$_c$; (d) disorientation of crystallites by electrical current above the critical intensity. (From Senouci, A., Frene, J., and Zaidi, H., *Wear*, 225–229, 949–953, 1999. With permission.)

result from poor commutation and mechanical instability, insulating films, and any other causes inhibiting current passage through the contact.

Maintenance practice and tests have shown that the occurrence of sparking or arcing in the SC always leads to an additional wear.[1,868,886] R. Holm[1] arrived at the conclusion that the wear of carbon brushes increases in sparking due to two factors: erosion caused by the arc thermal effect and mechanical wear rise due to higher metal surface roughness. These two wear components are believed to be proportional to the arc energy and mechanical load, respectively. The erosion component was determined in tests with separation of the surfaces, and the coefficient of the additional mechanical wear was calculated based on wear measurement in the absence of sparking. Considering these data, Holm proposed the following formula for the brush wear W with sparking:

$$W = N[W_0 + W_1 I + gQ^{1/2}] + \omega Q \quad [\text{cm}^3/\text{km}] \tag{9.35}$$

where N is mechanical load, W_0 is the coefficient for wear without current, W_1 is the coefficient for wear with current $I = 10$ A without sparking, g is the constant of the material characterizing its additional wear due to roughness increase, Q is the charge transported by arc during 1 km of sliding,ω is the constant of the material characterizing its arc resistance. The terms within the bracket represent the following components of brush wear: $NW_0 =$ wear without current, $NW_1 I =$ wear due to surface roughness by the flashing, = wear because of the surface roughness by arcing. The product ωQ is the volume evaporated from the brush under the influence of the arcs.

Lancaster[868] measured directly the contributions of erosion and mechanical wear in sparking. Two brushes slid over the same track on the copper disc surface with an insulating insert. One brush experienced periodical sparking and the other one was insulated and used to determine the influence of surface roughness appearing on the copper surface in sparking. The obtained dependencies between the charge scattered in the arc and the erosion and mechanical wear components (see Figure 9.118) confirmed the Holm's results.

As Lancaster believed,[877] electric discharges cause the dissipation of energy over the small spots on the brush surface. For this reason temperature in microvolumes adjacent to the spots rises to the values at which the oxidation rate is comparable with the rate of brush material loss due to other factors. The removal of gaseous oxidation products is not the only cause of the brush material losses. Predominant binder oxidation can weaken the structure of the brush surface layers to facilitate mechanical wear. For this reason the characteristics of brush material oxidation can play an important role in determining the wear rate in sparking.

Lawson and Dow[886] have shown that at high current density, the increased wear with sparking operation can be related to the material properties of the brush. High wear rates occur for materials

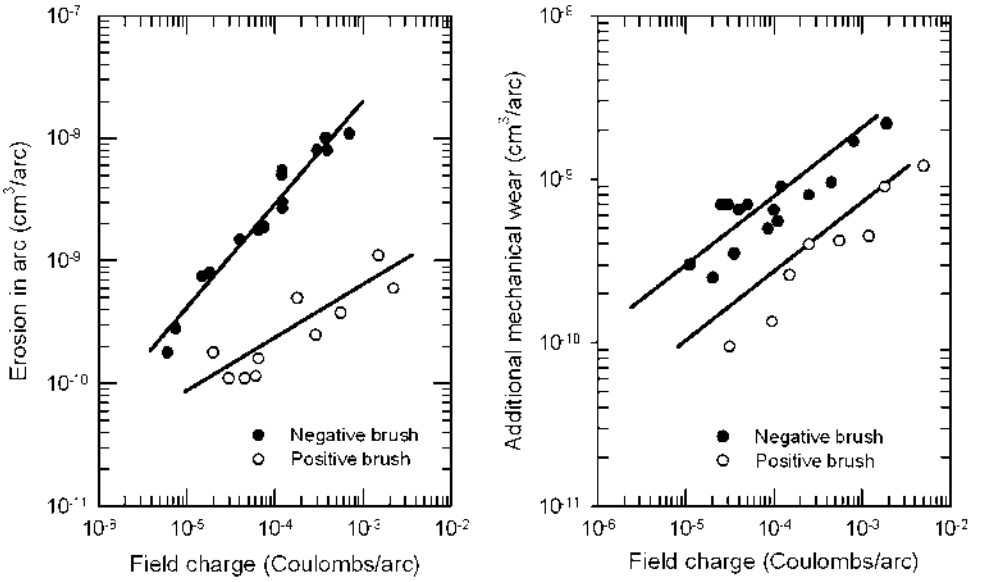

FIGURE 9.118 Additional electroerosion (a) and additional mechanical (b) wear of electrographite brushes EG-11 as a function of charge dissipation in sparking (copper disc, $I = 10$ A, $v = 18$ m/s). (From Lancaster, J. K., *Wear*, 6, 341–352, 1963. With permission.)

having high electrical resistivity and low thermal conductivity. Brushes having such compositions are subjected to extensive Joule heating and do not have the ability to remove heat from the contact region. Thus, materials which dissipate large amounts of power in the electrical contact demonstrate extremely high temperatures and wear. The metal–graphite composites containing easily melted lead ant tin have low electroerosion resistance. The heat being generated over a local spot is sufficient for reaching the boiling point of these metals.

In addition to direct effects on the contact members, sparks and arcs can induce air dissociation in the clearance and the appearance of reactive substances such as atomic nitrogen, oxygen, and ozone which intensify the chemical erosion of the composite materials. The dissociation of water films by electric discharges can result in metal oxidation in the case of anode polarization and the reduction of oxide films on the metallic surface which is cathode-polarized.

9.4.3.6 Some Ways to Reduce Electrical Wear

Electrical wear in composite-metal sliding contacts results from many factors which often influence each other and whose contributions are difficult to separate (see Figure 9.113). However, if the principal factors re determined and the mechanism of wear under the action of current is explained, it becomes possible to select the optimal combination of contact elements and formulate the requirements to mechanical, electrical, and other properties of the contact materials. It can also help in development of contact materials and optimal design of sliding contact and its elements.

It follows from the data presented that the action of several electrical wear factors is facilitated by the presence of oxygen in the ambient medium. Oxygen accelerates the formation of nonconductive films followed by fritting, chemical erosion, selective oxidation of the binder, etc. The search for ways to reduce the harmful influence of oxygen has shown that inert gaseous atmosphere (carbon dioxide, nitrogen, helium, argon, etc.) with controlled moisture can significantly increase the wear resistance and improve electrical characteristics of carbon and metal–graphite contact materials[7,226,887] and that new types of composite contact materials produced by traditional

technology on the base of common materials can operate with much higher current density and sliding velocity than previously assumed. An example is a new type of sintered copper–graphite composite material with improved self-lubrication for railway current collectors.[777] These materials use the concept of a network structure of copper matrix for the electrical conduction and self-lubrication which is provided by graphite and MoS_2 powders stored in the pores. The unique microstructure of the material, which is composed of a graphite islands in a copper matrix achieves the solid lubrication function with very little effect on electrical conduction during sliding. A special electrical conductive mechanism—specifically *network conduction*—plays a major role in maintaining the low resistivity of the material.

An increase in contact current is limited not only by the resistance of the brush material to thermal effects but also by the dynamic stability of the contact system and its ability to avoid intensive sparking with increase in current and velocity. The dynamic stability is determined by velocity, mechanical properties of contact materials, the frequencies of contact elements, and by intensity of contact vibrations. An increase in load applied to brush, the use of many parallel brushes or fiber brushes, good alignment of the machine elements and proper damping characteristics of current collection system minimize the dynamic instability.[70,246,264,888,889]

One prospective way to improve both dynamic stability and brush wear is a usage of wavy metal rotors.[753,890] It was shown that the wear rate of the brush–rotor sliding system can be minimized by prescribing a small amount of surface waviness of a certain mode on the rotor, and then sliding the brush over the rotor at speeds such that the frequency at which a certain waviness mode passes beneath the brush is close to the brush–spring–rotor resonant frequency. Surface waves on the rotor can excite brush vibrations and reduce the wear rate without disconnecting the contact circuit. Such an approach is based on an earlier proposed idea[752,891] that surface undulations in certain forms can improve wear rate and contact resistance of sliding contacts.

Summarizing the data presented in this section, we can note that friction and wear of the composite (brush)–metal sliding contacts are basically determined by the action of electric current on the brush surface layer, and this action is different for various brush materials. The reversible reduction in strength of the surface layer of carbon brushes during the Joule heating reduces microcutting and causes "lubrication" by the electric current. Irreversible changes in the surface layer of brushes with high content of noncarbonized polymer binder at certain critical magnitude of contact current lead to sharp reduction in friction and increase in wear intensity of these materials. Development of plastic deformation leading to increase in the contact area explains the frictional behavior of brush materials with high content of metal. The changes in the collector surface layer and intermediate films during current passage influences the frictional characteristics to a lesser degree. As was shown (Section 9.4.1) films on the collector surface determine predominantly the current passage mechanism and electrical characteristics of the contact.

In the absence of sparking, the basic cause of brush wear intensification under the action of electrical current is the Joule heating in the friction contact. Depending on the operation conditions and type of contact materials, the additional heat release resulting from current passage may lead to mechanical weakening of the brush surface layer, roughening of the collector surface, intensification of adhesion on contact spots, reversible reduction in the brush material strength near the contact spots, mechanical stresses because of thermal expansion, etc. The action of one or several factors leads to occurrence of so-called electrical wear in the brush contact. The electric field in the contact area can be additional factor affecting wear rate due to oxidation, mass transfer, and debris formation.

10 Electrical Methods in Tribology

Measurements of contact resistance can be an efficient tool in various engineering applications. These measurements can be applied in many areas, including failure analysis, condition monitoring, and predictive maintenance of machines and apparatuses. Surface characterization is one of the most informative areas when using the electrical methods. In particular, the probe method of evaluating the surface electrical conductivity is widely used.[386,838,892–894]

Electrical methods are used extensively in tribology. Historically, the development of electrical methods began in connection with the problem of evaluating lubrication conditions. Thus, Vieweg and Lunn made an early attempt to evaluate boundary-lubrication conditions from the behavior of conductivity in contacts between solids.[802,895] Later, many studies were carried out on exoemission and emission of high-energy electrons in friction, thermoelectric phenomena, electroplastic and electroacoustic effects, electrochemical processes, and magnetic phenomena.[896]

Many methods involve the use of signals from external current or voltage sources and subsequent evaluation of contact resistance and its frequency characteristics. These techniques produce estimates of the real contact area[392,399] thickness of lubricant film,[389,897–899] or the probability of breaks in its continuity and, consequently, the probability of scuffing.[900] The level of frictional work-hardening can be estimated from measurements of the electric resistance of this layer.[901,902]

A number of electrical methods used in tribology estimate the properties of materials and lubricants used in friction units of machines. The methods of estimating the lubricating properties of oils based on their conductivities, determination of heat stability of lubricants, etc.[407,903–906] are discussed here.

The list of electrical methods used in surface science, tribology, and mechanical engineering can be continued by novel techniques involving nanotechnologies and nano-based instruments. Basically, scanning tunnel microscopy is based on conductivity of nanoscale gap between conducting bodies. In the following section, a brief review of electrical methods used in tribology will be given. The emphasis will be placed on the trend towards more precise microscale- and nanoscale-based instrumentations.

10.1 SURFACE CHARACTERIZATION

Savage and Flom[907] first introduced the method of diagnosis of the state of a metal surface on the basis of its surface electrical conductivity. They used a setup with a probe in the form of a fine gold wire loop, pressed against the surface by a small load. The parameter characterizing the electrical conductivity of the surface and degree of its contamination was the contact resistance, R_c, measured discretely at the points of probe-to-surface contact. To avoid electrical or mechanical damage of the surface films, the measurements were made with contact a voltage about 1 mV under a contact load of about 10^{-5} N.

The probe method of evaluating the surface electrical conductivity was later improved by many researchers.[798,838,884,908] At the present time, many research organizations have various probe systems operating on the principle described above. The surface-probing method has been used

with success in studies of the oxide films,[798,894] changes in the state of metal surfaces under the influence of the ambient medium, electrical fields, and high temperature,[387,740,892,909] and study of the intermediate layers that appear on the friction surfaces in electrical contacts.[838,884,910,911]

In the general case, the contact resistance, R_c, in the probe-surface contact depends on the probe material, shape, dimension, and the measurement method.[387,892] ASTM Subcommittee B-4.04 on Materials for Electrical Contacts standardized the surface-probe method with the stationary probe position. The standard specifies the setup design, the probe material and shape, and the measurement technique[386,892,893] (Figure 10.1). The method makes it possible to determine the probability distribution for a given load, N, the dependence $R_c = \phi(N)$ with standard deviations, and the dependence of the failure percentage (R_c exceeding the specified level) on the load.

The preferred probe is made of solid pure gold and has a smooth spherical end with a radius of curvature equal to 1.6 mm. The probe contact material, its shape, and its dimensions have been found to insignificantly affect contact resistance, and solid gold uniquely satisfied the requirements of a readily available inert reference material having well-known properties. The preferred shape and size has minimal influence on the surface of the material being probed. The ASTM B667 standard gives a practical, reproducible method of surface study by measuring R_c.

No work has yet been done on standardization of the method with sliding of the probe. Here, the modern trends in instrumentation include the use of sensitive, low-voltage, commercial four-wire milliohmmeter circuits, automatic indexing of specimens, machine control of instrument functions, and data acquisition systems with computerized data processing.[893,912–914]

Studies of materials by probing are often combined with surface analysis methods, such as Auger, ESCA, SIMMS, and cathodic reduction. For example, a method correlating surface resistance and elemental composition of a reed contact is described elsewhere.[913] Special software was used to compare the surface resistance distribution function and the distribution function of the elemental composition of the same surface segments obtained with the aid of Auger spectroscopy.

The apparatus for measuring the distribution of the surface resistance consists of a AuNi tip-shaped electrode with a radius of curvature of 100 μm and the contact force of 10^{-2} N. Two stepping motors provide the movement of the electrode in the x- and y-directions along the

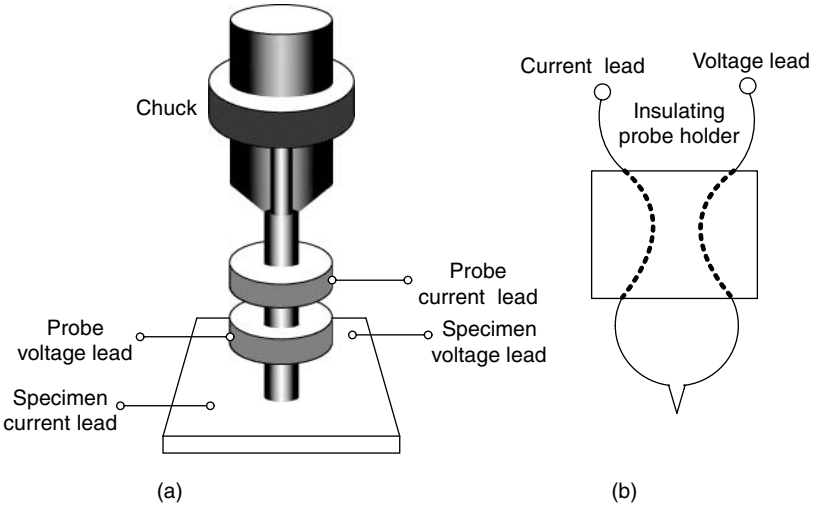

FIGURE 10.1 Arrangement of current and voltage leads to probe and to specimen (typical): (a) Rod probe with hemispherical end having the voltage lead occurred as close as possible to the point of contact. (b) Wire probe. (Adapted from Antler, M., *Proceedings of 10th International Conference on Electrical Contacts*, Budapest, Hungary, Vol. 1, 13–21, 1980.)

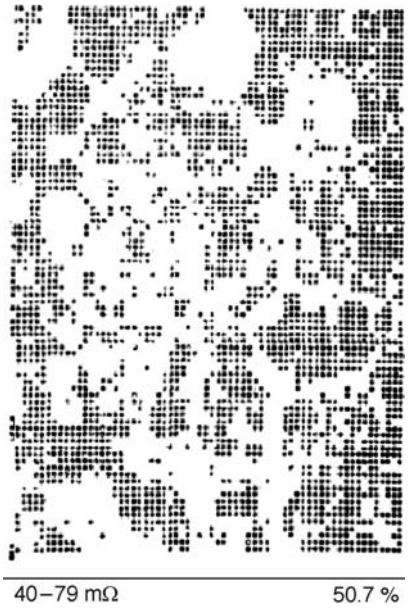

FIGURE 10.2 Distribution of measuring points with a surface resistance between 40–79 mΩ. The total surface area scanned is $450 \times 600\ \mu m^2$. (From Voostrom, A., Augustus, L., Steinmentz, A., and Berg, G., *Proceedings of 24th Holm Conference on Electrical Contacts*, Illinois Institute of Technology, Chicago, IL, 1978, 521–526. With permission.)

surface. The minimum distance between two points is 2.5 μm. Values of surface resistance can be used to obtain maps of surface resistance. Figure 10.2 shows the distribution of points with a surface resistance between 40 and 79 mΩ in the particular case of a ruthenium contact. About half the number of measuring points had a resistance in this range.

After completion of the resistance measurement, the reed contact is mounted in a vacuum system for scanning Auger analysis. If necessary, in-depth profiling by combined sputter-etching and Auger analysis was used to determine the composition of the near-surface layer, particularly in defect regions. It was shown that a direct correlation is observed between surface resistance and the amount of contamination. Areas with a low surface resistance correspond to clean ruthenium; slightly higher values are found in carbon-contaminated regions. Local areas of even higher surface resistance are correlated with the presence of metal oxide impurities. Such areas are further analyzed by in-depth profiling.

It is evident that the combination of methods significantly expands the capabilities in studies of surface structures. A probe system that makes it possible to combine measurement of the surface conductivity with the surface topography parameters is described by Konchits and Markova.[915] As mentioned in Chapter 9, Section 3 (Figure 9.28), an EP-1 probe setup was used. The setup is based on electromechanical profilograph with point contact with small contact load (10^{-4}–10^{-3} N) and displacement of contacting elements at low relative velocity. By replacing the standard diamond needle by a probe made of an electroconductive material (gold, steel) and sliding it over the test specimen, it was possible to simultaneously record surface profile and contact resistance.

This technique is based on the use of spectral correlation analysis. The essence of the technique consists of obtaining the spectral power autocorrelation functions of the signals characterizing the distribution of surface conductance and surface profile signals with respect to the spatial frequencies. The degree of interconnection of the studied signals is evaluated with the aid of the coherence function that makes it possible to determine that part of the spectrum in which the signals are coherent, i.e., the frequency range in which the studied signals are correlated.

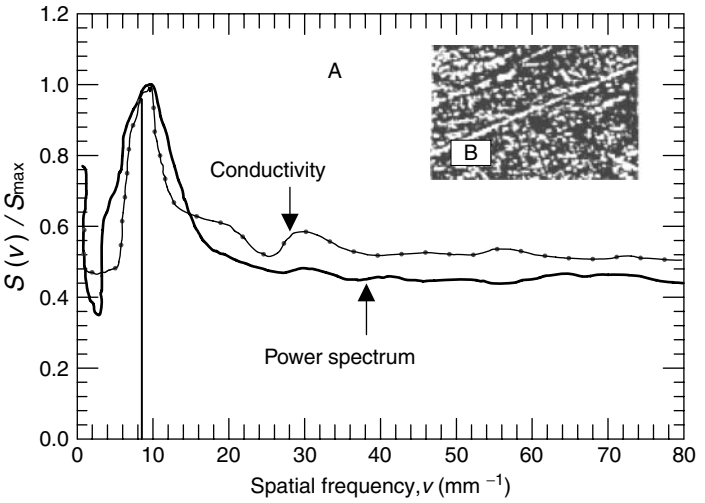

FIGURE 10.3 Power spectra (A) of profile and conductivity of surface of friction track of Ag–Pd20 specimen and its photomicrograph (B).

An example of the setup is presented in Figure 10.3.[915] A nonuniform transferred layer of the brush material was formed on the surface of Ag–Pd20 alloy during operation for 2 h against copper–graphite brush ($p = 700$ hPa, $v = 2$ m/sec). Studies of the friction track with the probe setup based on the power spectra (Figure 10.3) showed that there is significant correlation in the spatial frequency range 5–10 mm^{-1}. This means that the asperities with spacing $\lambda = 100$–200 μm have a conductivity that is much lower than the conductivity of the primary material. This result agrees with the friction-surface photomicrograph, where flakes of the transferred brush material (dark segments) with size of 100–200 μm are observed.

Recently, considerable progress in the development of probe methods was made at Laboratoire de Genie Electrique de Paris, UMR CNRS 0127. The new method is based on the resistance measurements over a surface using an AFM with a conducting probe.[809,916] This technique enables one to simultaneously obtain a map of surface roughness and the local conductance within a given microscopic area of a sample with nanometer-scale resolution.

The experimental setup is schematically presented in Figure 10.4. Both tip and cantilever are made of conducting materials. When the probe is brought into contact with the sample, the square-shaped explored surface (usually a few μm^2) is scanned line by line (e.g., 512 scan lines). The forces involved typically reach a few 10^{-9} to a few 10^{-8} N. A bias voltage is applied between the probe and the sample (about a few 10^{-2} V to a few 10^{-1} V). Then the resulting current at the input of the logarithmic current amplifier reflects the local contact resistance. By synchronously recording the amplifier output voltage and the height values along each scan line, topographical and electrical maps of the studied area can be obtained simultaneously. The logarithmic amplifier allows a wide range of contact resistance values to be explored (from about 10 kΩ up to a few 10^8 Ω). An additional protective resistance R_o (5 kΩ) prevents the current flowing through the contact from reaching values that are excessively high.

N-doped monocrystalline silicon and metal-coated silicon nitride can be used as probe materials. Although the elaboration of suitable probes remains an open problem, some convincing images of different metal surfaces have been obtained (Figure 10.5), occasionally revealing surprising features.

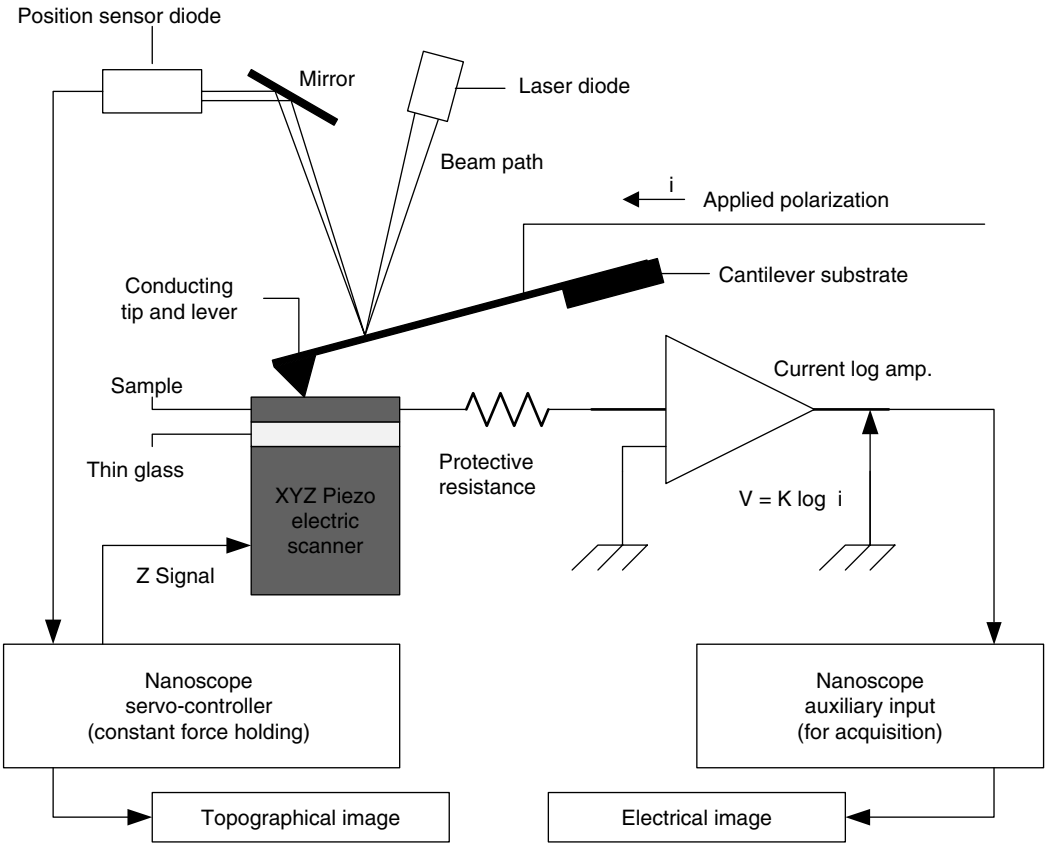

FIGURE 10.4 Schematic view of the AFM with a conducting probe. (From Schneegans, O., Houze, A., Meyer, R., and Bayer, L., *Proceedings of 42nd IEEE Holm Conference on Electrical Contacts*, Institute of Electric and Electronic Engineers, Inc., Chicago, 205–211, 1996. With permission.)

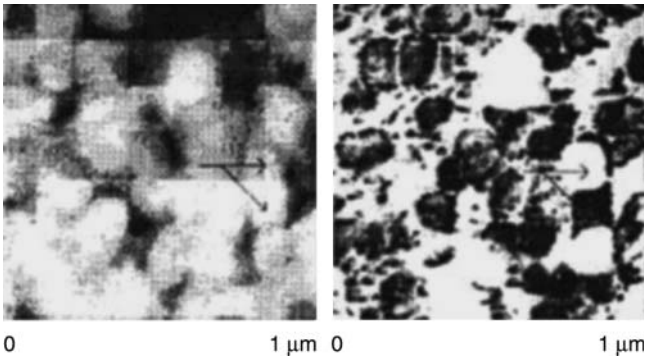

FIGURE 10.5 Topographical and electrical images of a tungsten film obtained with a tungsten-coated silicon nitride tip. (From Schneegans, O., Houze, A., Meyer, R., and Bayer, L., *Proceedings of 42nd IEEE Holm Conference on Electrical Contacts*, Institute of Electric and Electronic Engineers, Inc., Chicago, 205–211, 1996. With permission.)

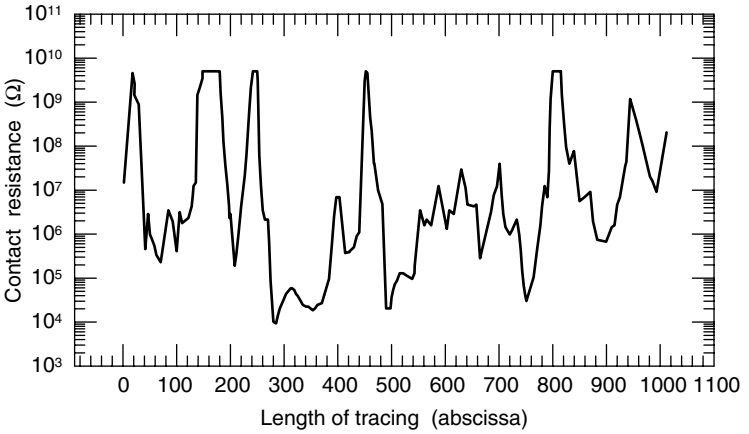

FIGURE 10.6 Example of a local resistance profile, performed in the middle of the electrical image of Figure 10.5. (From Schneegans, O., Houze, A., Meyer, R., and Bayer, L., *Proceedings of 42nd IEEE Holm Conference on Electrical Contacts*, Institute of Electric and Electronic Engineers, Inc., Chicago, 205–211, 1996. With permission.)

One of the possibilities of the developed software consists of performing the one-dimensional resistance profiles along a scan line. An example of such a profile is shown in Figure 10.6. It can be observed, for instance, that the local resistance can vary by several orders of magnitude between two adjacent grains. Calculations performed from the measurements allow one to clarify the mechanism of the tip/surface nanocontact and, consequently, to determine the most probable transport process according to the range of contact resistances.

It was shown[809] that a conducting probe of AFM is a convenient tool in studying the electrical and mechanical properties of thin films, e.g., self-assembled monolayers. Measurement of current flowing between the tip and the surface as a function of the applied force (force–current curves) or sample displacement (force–displacement curves) is used in this case.

Currently, there are many types of contact-resistance probes developed to study contact degradation mechanisms, such as growth of oxide films, pore corrosion, stress relaxation, and other phenomena. Some of them are designed to solve specific problems in different fields, e.g., study of wiping action,[755] probing on a solder bump on electrodes of computer LSIs,[914] probing of aluminum under low contact force,[894] etc. Some of them, however, are universally applicable.

An example of a universal probe device is the *automated contact resistance probe* (ACRP) developed by the CALCE Electronic Products and Systems Center (point of contact: pecht@calce.umd.edu). The ACRP ensures accurate measurement by using a computer-controlled loading system designed to apply a vibration-free normal force to the contact surface. This loading system has an adjustable loading speed and has a range of 0–2,200 g, with a resolution of less than 2 g. Contact resistance is measured using a computer-controlled, high-resolution power supply and measurement unit, which can deliver 1 nA to 1 A of current at a voltage varying between 0.1 mV and 110 V. If contact measurements are required at a higher current, an appropriate source unit can be added to the existing setup.

The ACRP conducts resistance measurements in real time, enables measurement using actual contact geometries, and can simulate the repeated cycles experienced in separable connectors. This "wipe" motion is accomplished through the automatic x–y positioning. This computer-controlled displacement has a 0.2-mm resolution and allows for multiple measurements of a single point (cyclic loading) or over an entire contact surface (automatic multipoint contact). The use of a mixed flowing gas chamber enables accelerated assessment of contact failure mechanisms in corrosive environments.

10.2 DIAGNOSIS OF CONTACT AREA AND FRICTION REGIMES

10.2.1 Formation of Contact Area

Vieweg[895] was the first to perform such an analysis, using conductivity measurements made on a lubricated contact to determine lubrication regimes and the structures of boundary-lubricant films. A diagram of Vieweg's setup appears in Figure 10.7. The shaft-bushing rubbing pair with lubricant on the contact surface is connected into an alternating-current circuit across resistance R. The rectified part of the alternating current was measured with galvanometer G. The current in the circuit amounted to 25 mA, the frequency was 10 kHz, and the capacitance C was equal to 160 μF.

The results performed with this setup (Figure 10.8) indicate that the type of lubricant determines the level of the current rectified by the lubricated contact and the sliding-speed and load ranges in which this effect appears. The rectifier action of the lubricant film was attributed to orientation of the lubricant molecules.[895] The authors believed that it was possible to determine transitions from dry to boundary friction and then to hydrodynamic friction as the sliding speed of the rubbing surfaces was increased.

The idea of using the electrical contact resistance as a mean to characterize frictional behavior was explored by Lunn,[802] who investigated boundary lubrication by measuring the conductivity of the oil film and recording the appearance of metal-to-metal contact spots (Figure 10.9).

Lunn assumed that the average voltage drop, which was registered automatically (Figure 10.10), was proportional to the area of direct metal-to-metal contact. Therefore, the area S referred to the total area under the live $V = \text{const} = 20$ mV after a given sliding time was taken as a characteristic of the lubricating ability of the oil in the particular rubbing pair. The smaller this area, the more rapidly the boundary oil layer separates the surfaces, and the more effective is the particular lubricant.

These descriptions of the Vieweg method on the one hand and Lunn's method on the other indicate that they use two different approaches to provide an electrical diagnosis of rubbing surfaces. The former procedure is based on the ability of the boundary layer to change the nature of an electrical signal passing through it. The latter method is based on integration of elementary events of current passage through the contact to obtain a picture of the contacting process (area ratio of metal-to-metal and lubricated contacts, etc.).

Several experimental procedures based on the electrical conductivity measurements of lubricant films to diagnose friction regimes have been proposed.[901,918] In recent years, this method did not evolve further due to the fact that no specific electrical properties of thin lubricated layers was found (see Chapter 9, Section 3.1). In this context, the second approach, embodying a number of

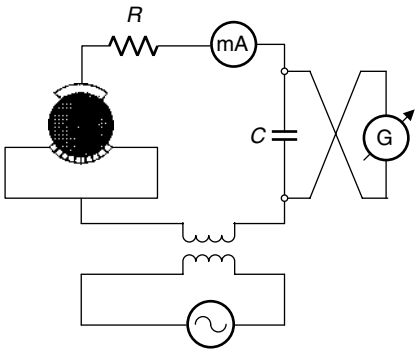

FIGURE 10.7 Diagram of setup used to study the rectifier effect in a boundary lubricant film. (Adapted from Vieweg, V., *Technikal Mechanik und Thermodynamik*, 1(3), 102–108, 1930.)

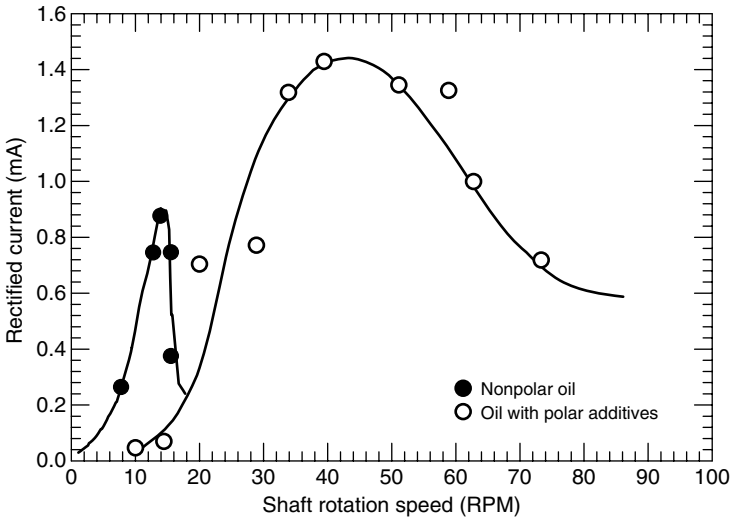

FIGURE 10.8 Rectified current vs. shaft rpm. (Adapted from Vieweg, V., *Technikal Mechanik und Thermodynamik*, 1(3), 102–108, 1930.)

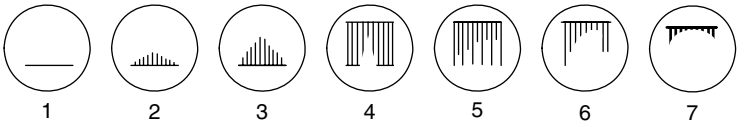

FIGURE 10.9 Metallic contact spots recorded on oscilloscope screen in a study of friction using Lunn's setup. (Adapted from Lunn, B., *VDI-Berichte*, 20, 41–46, 1957.)

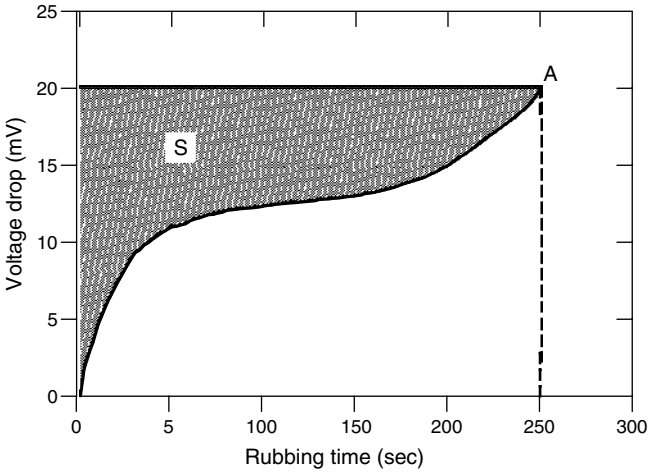

FIGURE 10.10 Voltage drop in oil film as a function of rubbing time. (Adapted from Lunn, B., *VDI-Berichte*, 20, 41–46, 1957.)

procedures, including an electric-pulse diagnosis technique,[803,903] lubrication condition monitoring of piston ring and cylinder,[919] microindentor scanning of lubricated contacts,[392] etc., was more informative.

To illustrate these procedures, the method proposed by Furey for lubricated-contact diagnosis is of interest to examine (Figure 10.11).[803] In this setup, a ball-and-cylinder contact is connected to a DC circuit from an e.m.f. source via a liquid-metal current pickup. The contact resistance is registered with an oscilloscope and automatic recorder. The oscilloscope registers the instantaneous pattern of the voltage drop across the contact, and the recorder the average value of the resistance. The use of small applied voltages (<15 mV) makes it possible to relate the characteristic pulse pattern to the appearance and disappearance of metal-to-metal contacts in the voltage drop makes it possible to estimate the fractions of the friction-contact area that correspond to metal-to-metal contacts and lubricant film. The diagnostic procedure described has been found useful in evaluating the lubricating abilities of various oils and additives.

Combining zero-lag registration of contact resistance with statistical methods to process signals from newly formed microcontacts across lubricant films has been very successful. This approach, developed in several studies,[900,920,921] has made it possible to solve some friction-regime diagnosis problems. Owing to the importance of these approaches, a detailed discussion follows.

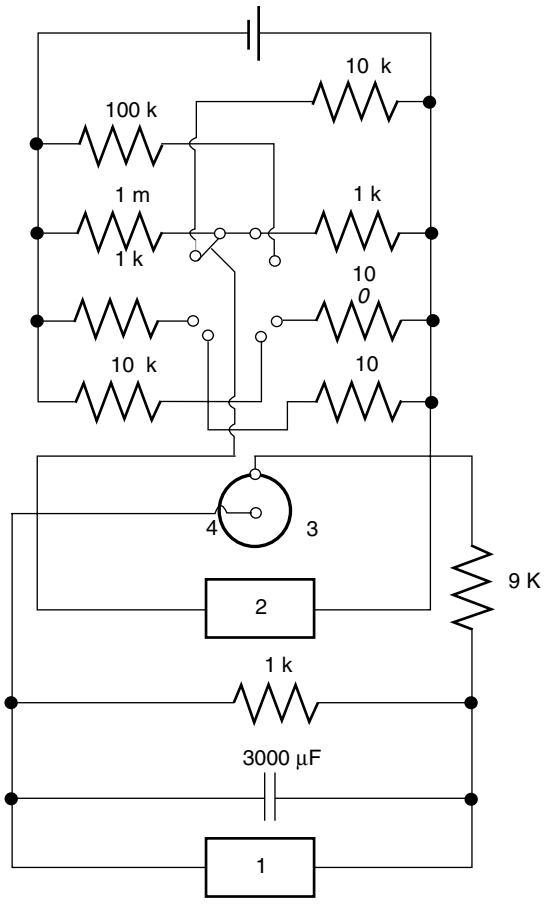

FIGURE 10.11 Measurement scheme used in Furey's experiments: (1) automatic recorder, (2) oscilloscope, (3) cylinder, (4) ball. The dashes line encloses the resistance box. (Adapted from Furey, M. J., *ASLE Trans.*, 4(1), 1–11, 1961.)

Figure 10.12 shows the setup for evaluating properties of tribosystem using statistical properties of electrical conductivity.[921] The properties were characterized by $H = S_m/A_c$, i.e., the ratio of the area of metal-to-metal contact, S_m, to the contour area, A_c. It is assumed that there is a linear relation between the area of metallic contact and the frictional force and, consequently, the wear rate as well. Introducing statistical properties of contact conduction, the authors obtain:

$$\xi = b \int_{n_{max}}^{n_{min}} \Pi f_1(\Pi) \mathrm{d}\Pi = b \int_{R_{max}}^{R_{min}} \frac{1}{R} f(R) \mathrm{d}R,$$

or, in discrete form,

$$\xi = \frac{b}{\Delta T} \sum_j \frac{\Sigma \Delta t_{ij}}{R_j} = \sum_j \sum_i \Delta t_{ij} = \Delta T.$$

Here, ξ is the rate of wear; R, R_{min}, and R_{max} are the resistance of the contact and its minimum and maximum value; $\Pi = 1/R$; ΔT is the time base for evaluation of the average conduction properties of the regime, Δt_i; is the time for which resistance is above a certain level, b is a coefficient; and $f_1(\Pi)$, $f(R)$ are the distribution densities of resistance and conductance.

The setup used in this procedure (Figure 10.12) incorporated the test pair 1, the 20 mV voltage across which was amplified after amplitude selector 2 by preamplifier 3. The resulting signal is converted by the pulse–amplitude modulator 4 to a series of discrete pulses with a frequency of 10 kHz by reference-pulse generator 5. The envelope of these pulses reflects the variation of the instantaneous values of the signal. The pulse–amplitude distribution is analyzed by multichannel analyzer 6 and recorded by recorder 7.

It was concluded that this procedure based on the statistical evaluation of electrical conduction characteristics can be used to solve several tribological problems, including estimation of the properties of tribosystem, kinetics of running-in and specification of optimum lubrication regimes.[921] The procedure has been used, for example, to evaluate film-starvation effects in lubricated contacts. One version of the setup is shown in Figure 10.13. The use of a specimen assembled as a packet of conductive plates separated by insulating spacers enabled the authors to detect nonuniformity of lubricant distribution on the contact surface and to estimate the probability of film starvation.

The statistical approach to the electrical conductivity of a contact was later used in combination with a similar approach to its acoustic properties for running-in study.[920] Korndorf and Podmasteiyev[922] have shown the expediency of a simultaneous use of two parameters which characterize the state of a lubricating film in friction zones—the normalized integral time of the electrical contact of parts and the averaged resistance. The possibility to estimate the averaged thickness of the lubricated film, the character of its thickness fluctuations, and the probability of film destruction in operation of units with lubricants were illustrated by test examples.

Thus improvements in the research equipment and the possibility of connecting amplitude and spectrum analyzers with computers, as well as the use of external electrical sources enables to develop practical diagnostic procedures. However, there is one factor that may limit the value of these methods: the fact that the relation between the real contact area and its electrical conductivity is not linear, since it is not reduced to the sum of the conductivities of the individual contact spots over a broad range of pressures owing to correlations between the conductivities of the spots and their groups. However, this fact can still be taken into consideration because the relation between resistance and RCA was determined using random-field theory to describe the surface roughness.[399]

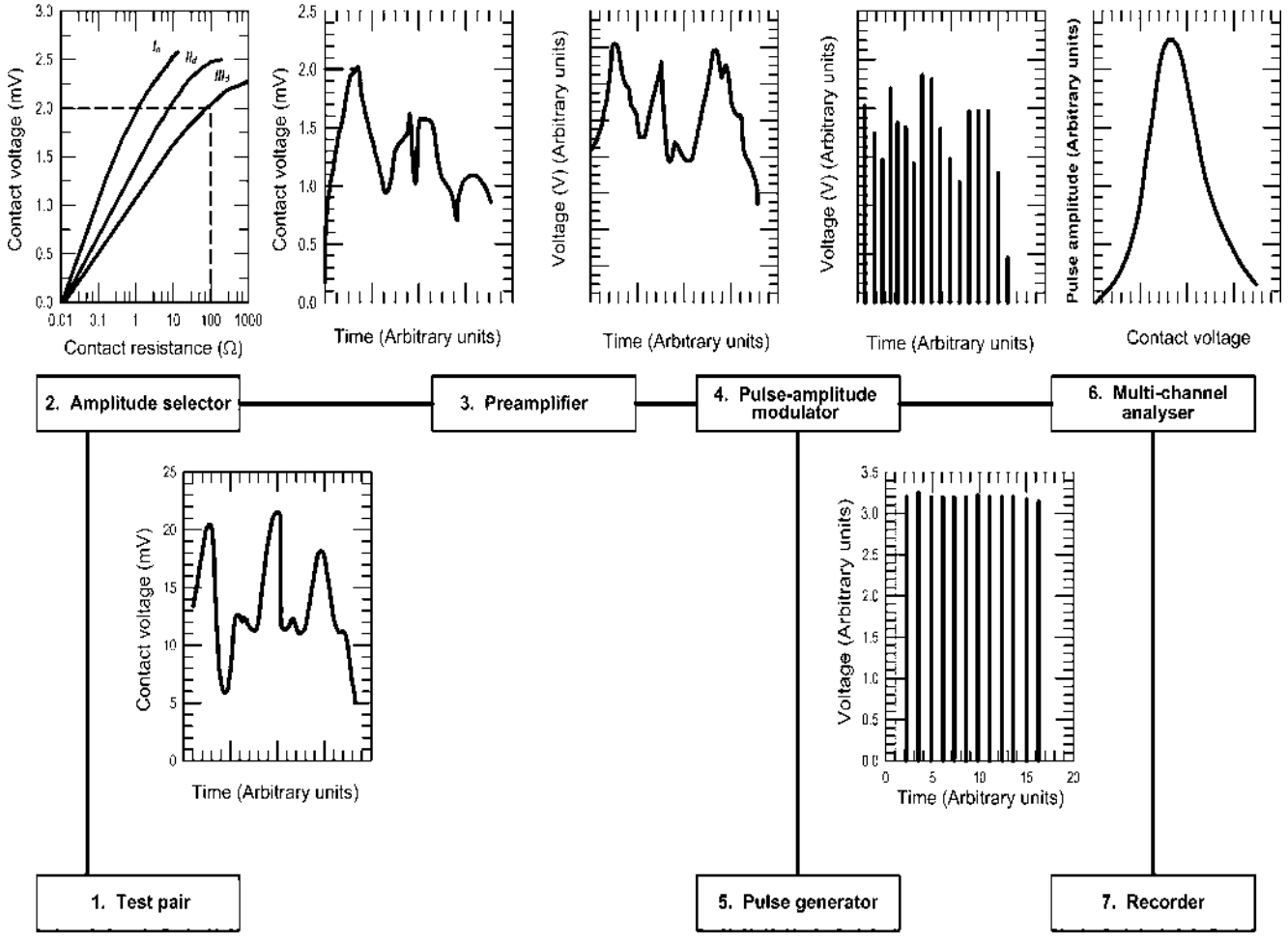

FIGURE 10.12 Setup for estimating the tribosystem loading by electrical conduction statistics: I, II, III—dividers. (From Karasik, I. I. and Kukol, N. P., *Sov. J. Friction Wear*, 2(3), 451–458, 1981. With permission.)

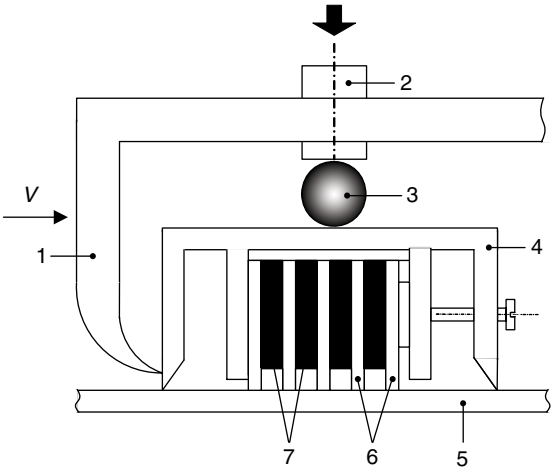

FIGURE 10.13 Friction assembly of setup for study of film-starvation effect: (1) housing, (2) loader, (3) ball, (4) holder, (5) counterspecimen, (6) plates, and (7) insulating spacers.

10.2.2 Control of Sliding Contact with the Presence of Oxide Films

Contact resistance measurements between sliding metals can provide information on the development of surface films, e.g., oxides. Wilson[798] has shown that, under a light load, metal surfaces may exhibit a contact resistance of some milliohms, whereas oxide-coated metal surfaces give larger values, depending on the nature of the oxide, its effective electrical conductivity, thickness, temperature distribution, and the number and size of the real contact areas. Therefore, contact resistance information, in combination with friction data, may be used in evaluation of wear mechanisms and stages.

Evaluation of contact deformation and surface-film damage under conditions of preliminary displacement and sliding is described elsewhere.[923–925]

Stott et al.[926] studied tribological and electrical behavior of sliding contact, when thick, mechanically stable, wear-protective oxides were formed on metal surfaces. A study has been made of two gas-turbine Fe–12%Cr alloys and an electrodeposited cobalt composite coating during reciprocating sliding in air at temperature up to 800°C.

A device for measuring contact resistance (Figure 10.14) was used in resistance range of $1–10^6\ \Omega$, with a maximum applied voltage of 10 mV, a frequency response of 0–10 kHz, and current range of 10^{-8}–10 A. The resistance due to oxide surfaces in sliding contact may be comprised of three components: (1) resistance associated with the alloy/oxide interface; (2) resistance associated with the bulk oxide; and (3) resistance associated with the points of real contact between the sliding specimens. Therefore, contact resistance measurements can only be interpreted qualitatively or quantitatively when the relative importance of these three components is known. According to authors' analysis, the constriction resistance associated with the points of real contact between the oxide surfaces makes a greater contribution to the measured contact resistance than the resistance of the bulk oxide itself.

It was found that contact resistance between the oxide-covered surfaces decreased considerably with increasing temperature from 300 to 600°C during sliding in air, giving a linear relationship between $\ln R_c$ and $1/T$. At a given temperature, sliding speed had only a small effect on contact resistance, particularly at the higher temperature. The contact resistance between the oxide-covered sliding surfaces was very sensitive to applied normal load (N), giving a reasonably linear

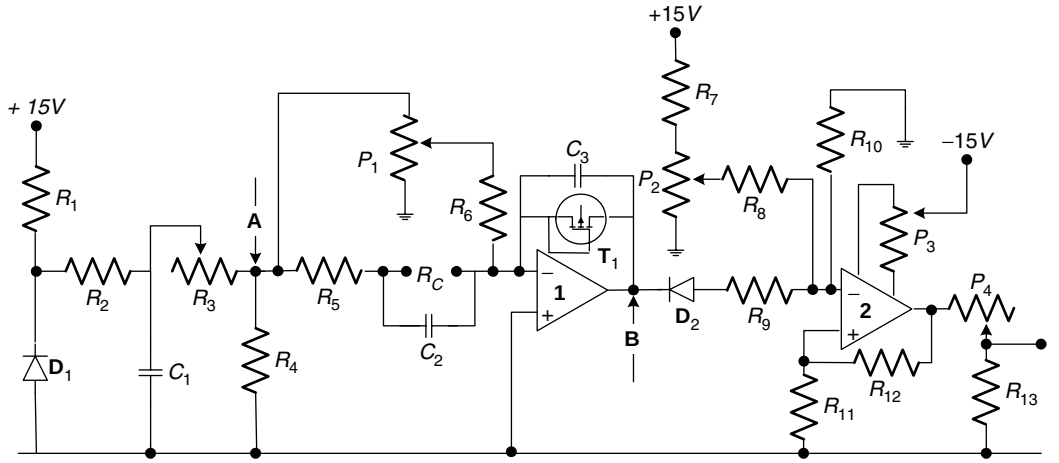

FIGURE 10.14 Schematic diagram of contact resistance measurement device. $R_1 = 330\ \Omega$, $R_2 = 220\ \Omega$, $R_3 = 390\ \Omega$, $R_4 = 1\ \Omega$, $R_5 = 10\ \Omega$, $R_6 = 470\ \text{k}\Omega$, $R_7 = 2.2\ \text{k}\Omega$, $R_8 = 2.2\ \text{k}\Omega$. $R_9 = 2.2\ \text{k}\Omega$, $R_{10} = 22\ \text{k}\Omega$, $R_{11} = 2.2\ \text{k}\Omega$, $R_{12} = 22\ \text{k}\Omega$, $R_{13} = 100\ \Omega$. Amplifier 1: 308 A; amplifier 2: 741 A; transitor T_1, BC109; diode D_1, BYZ 88 (5.6 V); diode D_2, signal diode; $C_1 = 100\ \mu\text{F}$, $C_2 = 0.1\ \mu\text{F}$, $C_3 = 0.1\ \mu\text{F}$; $P_1 = 100\ \Omega$, $P_2 = 220\ \Omega$, $P_3 = 10\ \text{k}\Omega$, $P_4 = 1\ \text{k}\Omega$. (From Stott, F. H., Glascott, J., and Wood, G. S., *J. Phys. D: Appl. Phys*., 18, 541–556, 1985. With permission.)

relationship between R_c and l/N, particularly at the higher temperature. Generally, the contact resistance tended towards zero at infinite loads.

Based on the data obtained, it was concluded that contact resistance measurements can provide useful information on the development of stable wear-protective oxides, on the characteristics of the contacting oxide–oxide junctions, and on surface temperature.

10.2.3 Experimental Study of Metallic Contact Spots Formation

It was shown[389,391] that the dependences of contact resistance on load $R_c(N)$ recorded under normal load of lubricated point contact are characterized by the critical load range at which the boundary layer structure fails and the formation of metallic microcontacts begins (see Chapter 9, Section 3.2, Figure 9.17 and Figure 9.19). The analysis of contact conductivity parameters at loads lower than critical one helps to estimate strength properties of continuous boundary layers of nanometer thickness[389] and those at loads above critical one defines the load-bearing capacity of lubricants.[814]

The work[927] extends the method of electrical probing in detecting the instant of forming the first metallic contact spots at normal loading and to evaluate their number and size for noble and oxidized metals. In this connection, the transition range of critical loads was studied in detail.

The possible behavior of electrical conductivity during formation of a circular contour area when the lubricated point contact is continuously loaded was considered (Figure 10.15). The lubricating layer preserves its continuity at the first stage of loading and actually prevents the electrical current passage. The polymolecular boundary layers with thickness more than 0.1 μm fail during this stage and are squeezed from the contact gap within the pressure range 10^6–10^7 Pa, while the layers with thicknesses of a few molecular diameters fail at pressure within 10^8–10^9 Pa.[391] When the lubricant layer thickness decreases down to 2–3 nm, tunnel conductivity emerges.

It is natural that due to the real surface roughness, tunnel conductivity emerges on the portions of the surfaces, but not on the whole contour area simultaneously. The total contact resistance R_c in such a case is the sum of tunnel resistance on these portions, given by $R_t = R_{\otimes t}/\pi a^2$ (where $R_{\otimes t}$ is

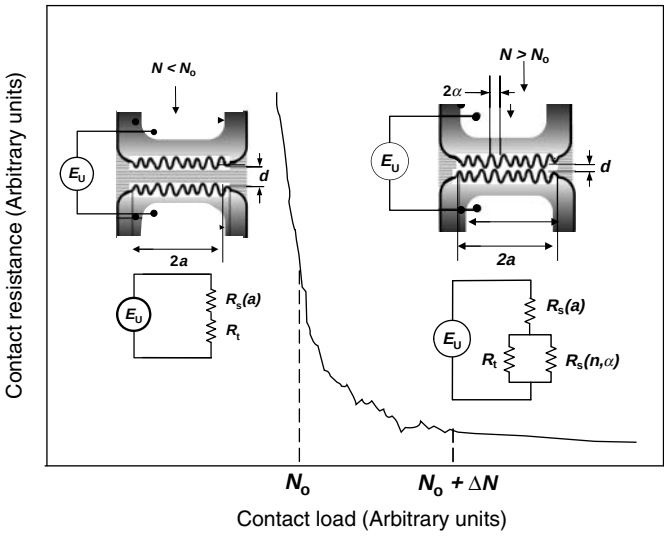

FIGURE 10.15 Basic mechanism of conductivity variation in the nominal point contact of noble metals at normal loading.

the specific tunnel resistance, and a is the radius of the contour area), and constriction resistance $R_s(a) = 2\rho/\pi a$ acting subsequently with R_t. It should be noted that $R_t \gg R_s(a)$ in most real situations.

Decrease of R_c with the load rise results from the growth of number and size of tunnel-conducting areas within the contour area. The decreasing rate of R_t can be rather high because d depends exponentially on R_c. However, R_c will remain a monotonic function of d at this stage (at loads $N < N_c$) and its recording will not be accompanied by the high-frequency fluctuations.

The formation of the first and the following metallic microcontacts at $N_c > N_0$ (Figure 10.15) results in a new parallel path of conductance of a basically different type (metallic one). Constriction resistance $R_s(n, \alpha)$ of n metal microcontact spots with the radius α (denoted by "α-spot") is $\rho/2\alpha n$, whereas specific constriction resistance $R_{\otimes S}(\alpha)$ is $\pi\rho\alpha/2$.[1]

When α is varied within 0.1–1 μm, values of $R_{\otimes S}(\alpha)$ are in the range 2.5×10^{-15} to $2.5\times10^{-14}\ \Omega\ m^2$. At the same time, specific tunnel resistance $R_{\otimes t}$ calculated by Equation 9.14 for the continuous lubricating layer only 0.5 nm thick is equal to about $5\times10^{-12}\ \Omega$ m and increases by an order of magnitude at each 0.1-nm increment. Therefore, at the instant of α-spots formation additional pulses of conduction corresponding to a new high-conducting path formation should emerge on the background of the total conductivity increase. So amplitudes, intervals and the number of experimentally recorded pulses can give information on the number and size of α-spots forming within the contour area. Simultaneous recording of both the total contact conductivity (resistance) and the rate of its change are required for such evaluation.

The tribometer which permits one to obtain $R_c(N)$ dependences during continuous loading of crossed cylinders was used to experimentally verify the possibility of detecting α-spots formation by the method mentioned above. The measurements of contact conductivity and its variations were performed using a modified four-point circuit (Figure 10.16) at applied voltage of 50 mV. The contact voltage drop is fed to two channels, the total voltage U_c carrying information on the total value of R_c is amplified by the first channel (amplifier of constant and alternating voltage Al) and the voltage variable dU_c is the information on the conductivity variation is amplified by the second channel (amplifier of alternating voltage A2). Output signals of the channels and that of the loading strain gauge are simultaneously fed into a computer using an analog-to-digital converter. During

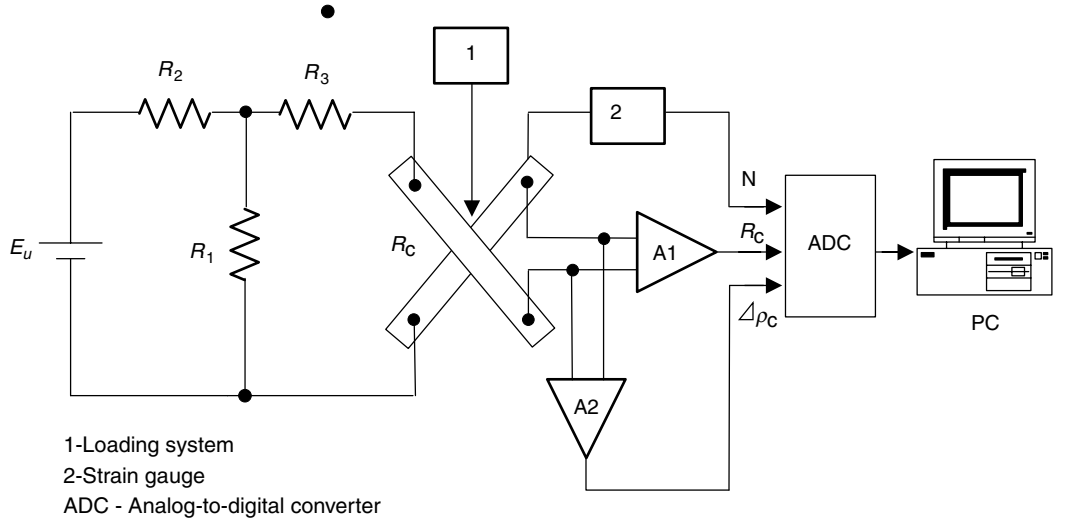

FIGURE 10.16 The scheme for measuring contact resistance, R_c, contact conductivity variation, d_o, and load, N. E_u, power source; R_1, R_2, R_3, resistors; Al, amplifier of constant and alternating voltage; A2, amplifier of alternating voltage.

continuous loading, 10^4 readings of signal with sampling increment 9 and 0.43 ms were taken. Typical results for silver and steel cylinders with liquid media of different origins are presented in Figure 10.17.

The analysis of the results shows that the method could indicate the moment of the first *a*- or *b*-spot formation at a surface's approach more precisely than the traditional methods based on registration of $R_c(N)$ dependence. The method allows one to study kinetics of metallic or quasi-metallic microcontacts generation during contour area formation and to evaluate their number and size. The data are sensitive to the presence of oxides, lubricant and other foreign substances on the metal surface and to their screening capacity.

10.3 EVALUATION OF TRIBOLOGICAL PERFORMANCE OF MATERIALS AND LUBRICANTS

Evaluation of performance of materials and lubricants in friction is one of the most important objectives of tribology. A system of standard reference data was based on the procedures used in these estimates and various types of test equipment were developed for them. Electrical methods occupy a prominent position in this area of tribology.

10.3.1 Evaluation of Load-Bearing Capacity and Lubricity of Surface Films

The electrical resistance method is quite simple both in principle and in arrangements, and it can be readily applied to an actual machine. With this method, it is easy to check whether metallic contact exists or not because very thin film can be detected.

Standard test methods to determine the anti-wear and extreme pressure (EP) performance of lubricants, e.g., in gears, are used widely to determine "load-carrying capacity" or scuffing resistance.[906] The machine elements operating under line or point contact are selected usually as the

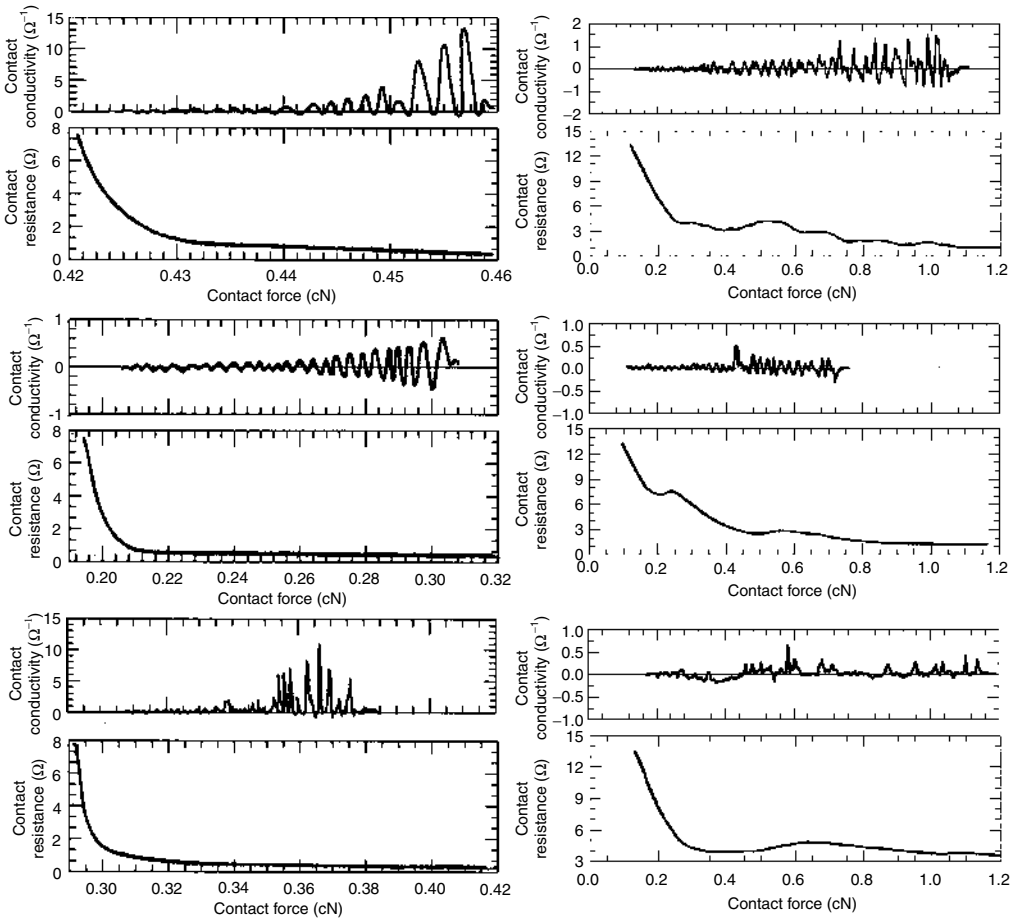

FIGURE 10.17 Contact resistance, R_c, and contact conductivity variation versus load tin under normal loading of silver cylinders (I) and steel cylinders (II): (a) dry; (b) oleic acid; (c) "Electrolub-ZX."

object to measure a state of the oil film. In these cases, the electrical resistance method would be useful because the oil film is very thin.

One popular version of such device is the Cameron–Plint TE77 high-frequency friction machine (Figure 10.18). A sample, in this case a ball, is loaded and reciprocated against the lower flat specimen through an eccentrical drive. The lower specimen is restrained by a force transducer and is held in an electrically heated oil bath. In this way, conditions of load, frequency, amplitude, and temperature can be precisely controlled. The machine is described in more detail elsewhere.[928]

The parameters recorded and used for making assessments of lubricant performance are friction force and contact potential during test and wear at the end of test. The measurement of the contact potential was found to be crucial in lubrication studies. Variations in contact potential give a qualitative assessment of the reduction in metallic contact due to the presence of either hydrodynamic or boundary lubricant films. The instantaneous recordings give information on the lubrication regime and the mean values can be used to assess the effectiveness of anti-wear and extreme pressure lubricants in forming protective reaction layers.

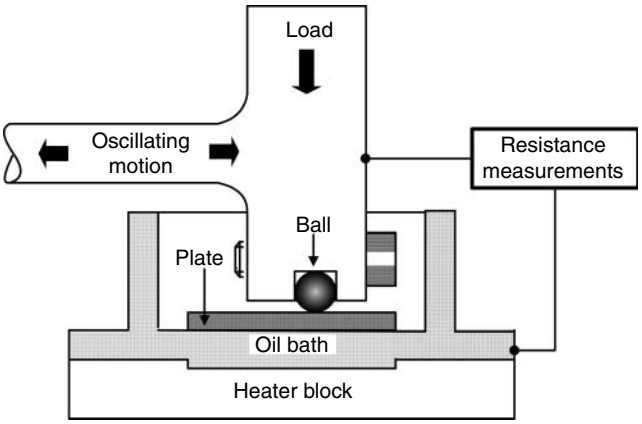

FIGURE 10.18 Schematic view of Cameron–Plint machine. (Adapted from Alliston-Greiner, A. F., *Proc. Inst. Mech. Eng*., 205, 89–101, 1991.)

The behavior of individual additives in refined base stocks was evaluated with the reciprocating machines. Figure 10.19 shows some data of Cann et al.[929] for zinc dialkyldithiophosphate. There is a very clear temperature at which the additive starts to form a film and then later a temperature at which this film fails. The failure in terms of loss of contact potential is accompanied by a dramatic rise in friction force which indicates that this was indeed a "failure" in lubrication. It should be noted; however, when such additives are mixed in commercial base stocks, the picture becomes

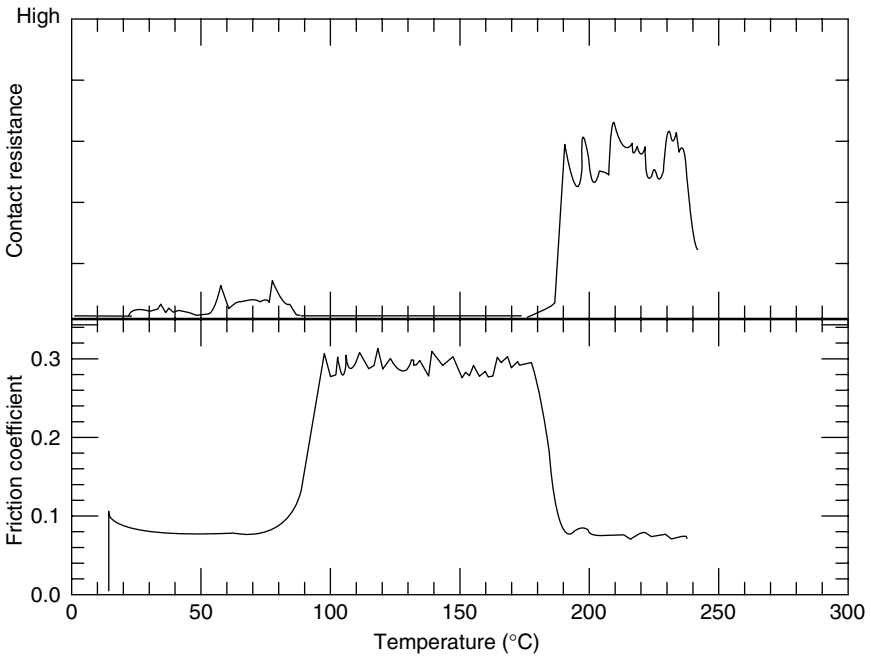

FIGURE 10.19 Friction and contact potential evolution for a typical ZDDP. (Adapted from Cann, P., Spikes, H. A., and Cameron, A., *ASLE Trans*., 26, 48–52, 1983.)

blurred due to the effect of boundary lubricating species in the base stock.[930] Further, when additives are formulated in mineral, semi-synthetic and fully synthetic base stocks for commercial applications the picture is far from clear.

Nevertheless, in such cases the reciprocating type machines provide an empirical method of assessing the performance of the complete additive packages including antagonistic/synergetic interactions, the role of the base stock, and the effect of additive depletion. By studying the lubricant at different temperatures, a complete picture can be built up of the expected performance and the anticipated problems.

The static contact conductivity measurements are also applicable to studying friction properties of lubricants. For example, Marui and Endo[905] used the contact resistance measurements to predict friction behavior of different lubricants for machine tool slides. The mean contact pressure of a machine tool slide is relatively low, and its velocity is also low. Many surfaces in such a contact are in a boundary lubrication state, and it is important to clarify the characteristics of the lubricant film on the metal surface.

In the above-mentioned paper, the contact resistance between smooth model surfaces under boundary lubrication is precisely measured. The result is compared with the static friction measured on real rough surfaces lubricated by various lubricants. It is shown that contact resistance and static friction correlate strongly, and that the boundary lubrication ability of lubricants (the oiliness) is predicted by the contact resistance between smooth model surfaces. The results yield interesting data that are useful for the comprehensive understanding of boundary lubrication as well.

Electrical probing of lubricating layers was discussed in a number of works[389,391,814] describing the point contact devices (see also Chapter 9, Section 3.2). It was shown that when the effects of temperature, chemical and hydrodynamic factors are excluded the equations of tunnel conductivity theory and constriction theory can be used to analyze experimental values of R_c. Moreover, some conclusions on thickness and continuity of intermediate nanometer-scale films can be derived, taking into account the extreme sensitivity of R_c to contact clearance.

Real metal surfaces may be used in conditions of high smoothness and contact zone localization to minimize influence of surface roughness. Distribution of film thickness due to the presence of small-scale surface roughness certainly exists. Therefore, rather approximate estimation of "effective" thickness of the film can be made in such experiments. Nevertheless, investigation of averaging effects can still give important information on the film properties and its transformation under the action of various factors. In particular, analysis of contact conductivity dependencies on load enables one to evaluate mechanical properties of nanometer scale films.[389]

Electrical probing can be a helpful tool to study not only the behavior of physically adsorbed lubricant layers, but also that of a chemisorbed layer of organic deposits characterized primarily by lubricant oxidation and degradation products.[911,931] In particular, the model experiments on measuring the friction and electrical characteristics in static and dynamic point contacts have shown that the layers of polymer-like deposits produced by chemically active additives, such as dithiophosphate, retain sufficiently high load-carrying capacity and lubricity at elevated temperatures (up to 200°C). Their formation reduces the friction coefficient and protects metallic surfaces against direct contact and wear.

The analysis of the temperature dependences of main types of contact conductivity of lubricated contact show that the contact resistance method is promising in studies of thermal tests of boundary films.[932] At static contact conditions it may be useful for evaluation of lubricant bearing capacity at high loads and for study of thin lubricant layers squeezing from the contact clearance during heating.

Figure 10.20 shows some results of work on boundary lubricating film behavior in response to temperature variation.[932] The $R_c(N)$ dependencies for both lithium grease and stearic acid show high mechanical strength of boundary films at room temperature (continuous residual layers presence in contact clearance at load of 1 N). It was expected that boundary film would collapse when squeezed out from the contact zone at some characteristic temperature. The effect would be

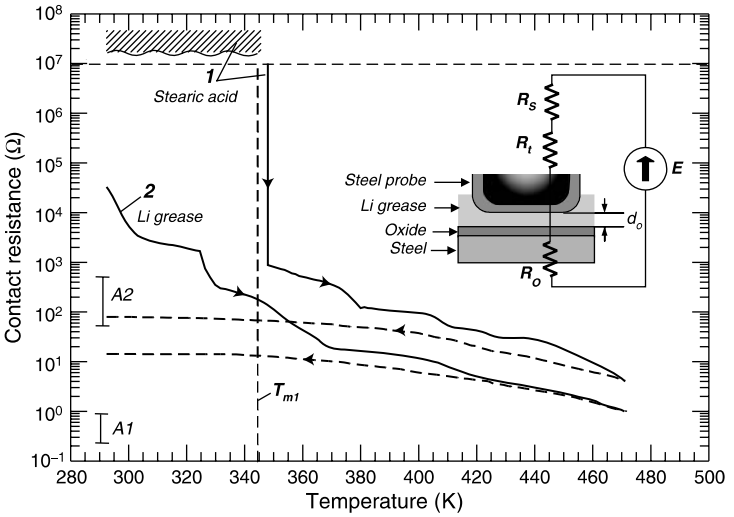

FIGURE 10.20 Analogous circuit of lubricated steel sphere–steel plane surface contact (R_s, R_t, R_o: resistances of the constriction, tunnel, and oxide, respectively) and typical records of $R_c(T)$ dependencies (sphere of 2 mm radius, $N = 1$ N). Lubricants: (1) stearic acid; (2) lithium grease (analog to MIL-G-7711A). A1, A2: R_c ranges for the sphere relocated outside of contact area after temperature tests with stearic acid and lithium grease. Lubricants washed away before A1, A2 measurements. T_{ml} is fatty acid melting point.

useful in the search for a correlation between conductivity of static contact and lubricant transition temperatures at sliding.

Indeed, irreversible decrease of R_c with temperature (Figure 10.20) was observed for lithium grease, evidencing lubricating film bearing capacity decrease and its squeezing out from the contact clearance. However, there was no sharp drop of R_c, it decreased to the minimal level over a quite wide temperature range. Moreover, $R_c(T)$ curves have sections of fast and smooth decrease and even constant R_c. In contrast, the boundary film of stearic acid shows much higher mechanical strength at room temperature, and it collapses at being heated sharply (contact resistance decreases to values typical for unlubricated surfaces). The temperature of boundary film collapse initiation is well correlated with the fatty acid melting point (345 K), it exceeds the melting point by 2–5 K. So, temperature dependencies $R_c(T)$ are informative in evaluation of boundary film strength and thickness at temperature increase.

10.3.2 Estimation of Lubricant Interlayer Shear Strength under Imperfect Lubrication

The existence of an interrelation between contact conductance behavior and the type of interface in boundary lubrication (see Chapter 9, Section 3.2) is the basis for creating new methods of experimental investigation. This approach was considered[933] in studies in the field of molecular tribology, e.g., for evaluation of molecular friction.

The molecular component of the friction force for solids under boundary lubrication is determined by the shear strength, τ_s, in the lubricant film, which depends on the lubricant nature, and the operating mode of the friction pair. It was established[934,935] that the binomial law of friction is valid in this case, provided that wear and plastic deformation of the surfaces are absent and that a continuous lubricating film is maintained:

$$\tau_s = \tau_0 + \alpha p. \tag{10.1}$$

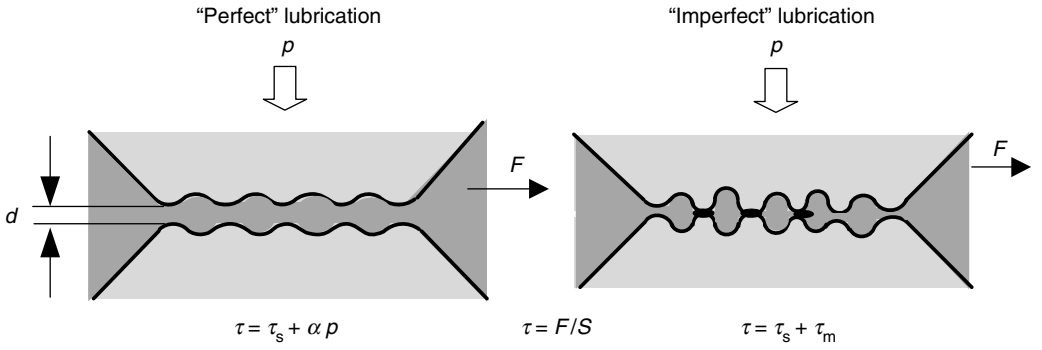

FIGURE 10.21 Models of interface under "perfect" and "imperfect" modes of boundary lubrication.

The shear strength at zero load, τ_0, is a measure of the surfaces molecular interaction in the presence of a lubricating film, and depends on its thickness, d (Figure 10.21). Piezocoefficient α, characterizing the growth of τ_s with increasing contact pressure p, is essentially controlled by the size, shape, and configuration of the lubricant molecules in the gap; it varies within the range 0.05–0.1 for a wide range of materials.[934]

In general, parameters τ_s, τ_0, and α define the tribosystem: solid 1–lubricating film–solid 2. Evaluated under identical conditions they may fully specify the lubricity of various media. However, their experimental determination should meet the following strict requirements: (1) the exact evaluation of the area of molecular contact S over which shear occurs; (2) continuity of the lubricating film and its thickness during sliding; (3) elastic contact of smooth surfaces, avoiding any friction force deformation; and (4) absence of wear debris in the contact zone generated by surface damage.

The operating mode of the lubricated contact when the above conditions are met was defined as "perfect" boundary lubrication. This can be fully realized only by using precision equipment for studying interface forces between optically transparent, molecularly smooth samples, viz. those made of mica.[935] Evaluation of τ_s using traditional tribometers for lubricated commercial metals meets the problem of monitoring and maintaining a given value of the contact clearance, in nanometer thickness range. The shear strength $\tau = F/S$ (where, F is friction force) experimentally determined in such conditions usually includes two components which are difficult to separate: τ_s and shear strength at the metallic contact points, τ_{me}. Nevertheless, the investigations[933] have shown the feasibility of estimating τ_s and its components not only under perfect conditions, but also under imperfect lubrication conditions.

Experiments were conducted in traditional microtribometer with crossed cylinders. The polished steel cylinders of radius 0.5 mm slides with low velocity (50 μm/s) at continuously increased load ($N = 0.5$–50 cN) that guaranteed elastic deformation of the contact. This allowed calculation of the radius and the area of the contour surface, mean contact pressure and constriction resistance for any N using common formulas.[391] The contact parameters for the loads were, accordingly: $a = 2.4$–10.7 μm; $S = (2.1\text{–}36.5)\times 10^{-11}$ m^2; $p = 240$–1,370 MPa; $R_s = 15.9$–67.0 mΩ. Electrical conductivity across the molecular film of the lubricant or adsorption films at ambient temperature basically occurs through tunneling (see Chapter 9 Section 3.2). This allows estimation of the interface state; in particular, the continuity and thickness of lubricating films using the respective relations from the theories of tunneling conductivity and constriction.

Figure 10.22 depicts a typical pattern of parallel monitoring of the friction force, load, and contact resistance. Analysis of the test results[391,814] made it clear that, for a given contact pair, an R_c magnitude below 10^2 Ω indicates the existence of quasimetallic (across the thin tunneling oxide

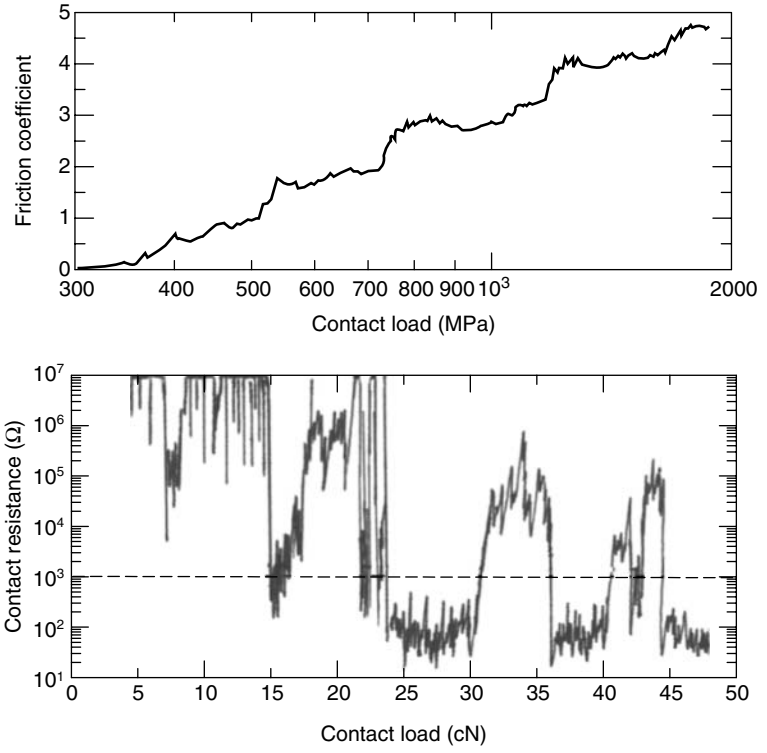

FIGURE 10.22 Typical friction force, F, and contact resistance, R_c, for lubricated steel cylinders ($v = 50$ μm/s) under increasing load N; (lubricant: lithium grease containing 10% by mass of lithium 12-oxystearate as the thickener.)

films) contact points in the contour area. At $R_c > 10^3\ \Omega$, quasimetallic contact is unlikely and the contact surfaces are separated by a continuous dielectric interlayer, e.g., a "perfect" mode of boundary lubrication is realized. The thickness, d, for typical lubricants depends on the size of the contour area, and amounts to 0.8–1.0 nm for $R_c \cong 10^3\ \Omega$ and 1.5–1.8 nm for $R_c \cong 10^6\ \Omega$.

Analysis has shown that the binomial law of friction is true for those areas of sliding track that exhibit perfect boundary lubrication ($R_c > 10^3\ \Omega$). Thus, the experimental data from the respective portions can be used to evaluate τ_s and its components. The results obtained open up wide possibilities for evaluating the friction parameters for the point metal contacts in experiments where a perfect lubrication regime is not maintained. It is sufficient that the regime is realized on separate parts of the sliding track, and they are identified by simultaneously conducted independent measurements of contact conductivity. Moreover, it is possible, using the experimental data corresponding to the chosen R_c range, to evaluate τ_s for the lubricating film or to investigate the data's dependence on d, from the contact clearance d and contact resistance, R_c, previously determined.

10.3.3 Evaluation of Thermal Stability of Materials and Lubricants by Electrical Methods

The standard method of determining the temperature stability of boundary lubricant films by volume heating of the lubricant film in the friction zone with point or line contact between the specimens is widely used.[936] The basic criterion of temperature stability for lubricant layers is the

critical temperature, T_{cr}, at which the coefficient of friction rises sharply with accompanying stick-slip and increased wear of the specimens.

Volume heating makes it possible to determine T_{cr} with high accuracy, but in some cases limits possibilities for modeling of lubricant-service conditions in the friction zone. In reality, there is usually a temperature gradient from the surface of the specimen into its interior, with the bulk temperature remaining far below the temperature in the friction zone. When the specimens are of materials that contain low-melting inclusions, e.g., tin or lead, strong bulk heating results in changes in hardness, load-bearing ability, and contact area. As a result, the friction characteristics may change due to the change in the properties of the contacting specimens rather than loss of lubricant service properties.

These shortcomings are eliminated to some degree when electric current is used to heat the lubricant film locally in the friction zone.[407,937] By this method lubricating materials can be tested using microtribometers where the sliding point contact is realized between the slider having the regular geometrical shape (e.g., a sphere) and a plane. At low speeds (10^{-2}–10^{-1} mm/s) and loads (0.01–1 N) the temperature increment in the contact zone due to frictional heating is negligible. Thus, the temperature in the contact zone can be estimated by registering the contact voltage drop and current as the indenter slides and determining the size of the contact patch. Equation 9.1, for example, can be used.

It was shown that a characteristic feature of the lubricated contact behavior in such a case is the presence of some critical current depending on lubricant nature at which the specific friction force leaps up (Figure 10.23) and sliding becomes jerky. As the calculations show, average temperature in the friction zone under critical current values reaches the magnitude corresponding to the loss of lubricity of the medium. Based on this observation a method of determining temperature resistance of the boundary lubricating layers was proposed.[937]

The method consists of passing electric current through the lubricated contact, during which the temperature in the friction zone is defined at each current stage by the generated Joule's heat. Simultaneously, variations in frictional characteristics are recorded. The temperature at which the friction coefficient augments abruptly and sliding acquires a jerky character is taken as a

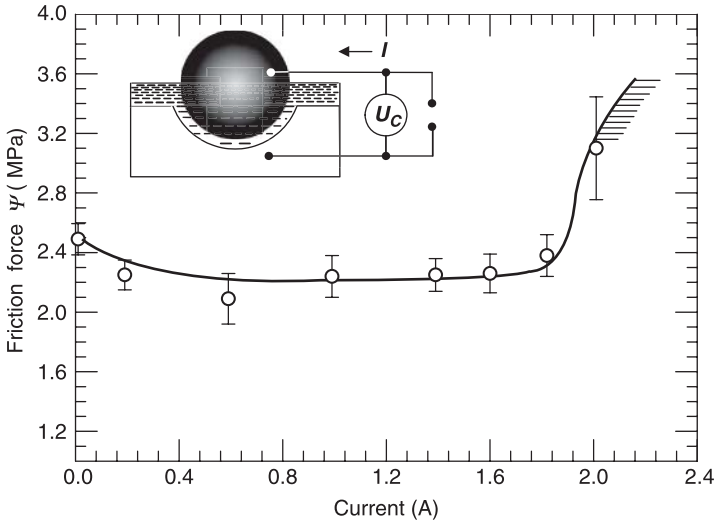

FIGURE 10.23 Schematic of measuring assembly in microtribometer and dependence of specific friction force on current.

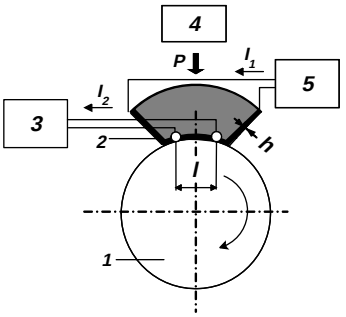

FIGURE 10.24 Diagram of device for evaluation of lubricant and coating temperature stability. (1) Shaft, (2) metal-foil measuring element, (3) temperature-measuring circuit, (4) loading device, and (5) current source.

temperature resistance criterion of the lubricating layers. As opposed to standard methods the proposed procedure uses test conditions that approach most closely the real ones. The procedure makes it possible to test lubricating materials without any essential rise of the volume temperature in the samples, which expands its field of application, and improves accuracy, especially for metals and alloys with low melting points.

An improvement on the contact-heating procedure determines the temperature stability of the materials and lubricants by modeling real-contact conditions.[937] This method can be used in rubbing pairs with nonconductive elements and arbitrary contact configurations. Its distinctive feature is the introduction of a thin conductive element (ribbon, coating, or wire) into the contact zone so that its resistivity variations can be used to estimate the temperature of the rubbing surface. The resistance of a segment of this element (whose ends should be far enough from the boundaries of the contact to prevent edge effects) will depend on temperature in accordance with a certain law, from which it is easy to determine the temperature of the element from its resistance. The origin of the heat sources at the contact makes no difference, since the method determines the total change in resistance by comparison with the value at the start of the test. It is also possible to use the measuring element itself as an additional heat source while a current of adequate density is passed through it.

Figure 10.24 shows the application of the method on a shaft-and-partial-insert friction machine. Any metal can be used to make the measuring element. To improve the measurement accuracy, however, it is desirable that the temperature coefficient of resistivity of the metal be quite high. This coefficient lies in the range $(4–8)\times10^{-3}$°C for many metals, and even on a 10°C temperature change, the change in total resistance exceeds 5% of the initial value. The procedure for temperature stability testing is the same in the new method as the procedures currently in use. The severity of the tribotest conditions is increased by increasing load, speed, or temperature in the contact to the point at which a change in the state of the system begins, for example, a sharp rise in the coefficient of friction. The temperature that corresponds to this change is taken as the temperature-stability limit of the material or lubricant being tested. The methods described above can be applied on various types of friction-testing setups. The measurement scheme for evaluation of critical temperatures is quite simple, and its accuracy can be improved significantly by using a compensation circuit.

10.3.4 Control of Surface Coatings and Films

To analyze performance of coatings on steel, e.g., the friction-seizure test procedure is proposed by Hivart et al.[904] The test involves a rotating cylindrical specimen on which a semi-cylindrical slider exerts localized pressure (Figure 10.25a). The specimen and slider are both insulated from holders

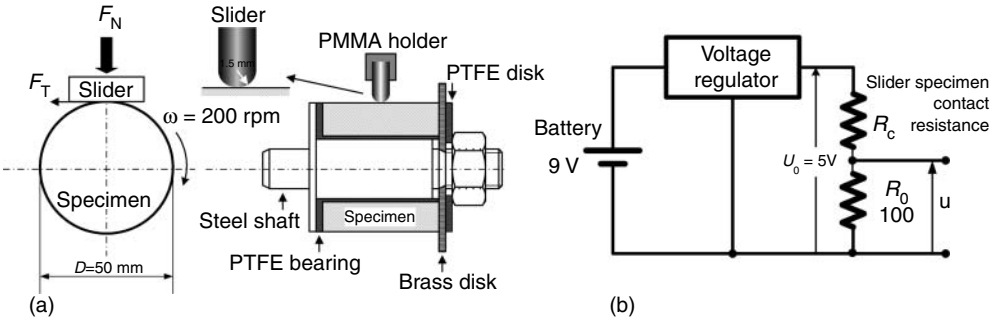

FIGURE 10.25 Friction seizure test, specimen, and slider holders (a) and electrical circuit (b) for coating conductivity measurement. (Adapted from Hivart, P., Bricout L. P., and Oudim, J., *Lubr. Eng*., 49(11), 833–837, 1993. With permission.)

and are connected to a direct current generator (Figure 10.25b). A constant load is applied on a semi-cylindrical tungsten carbide slider in contact with the specimen, and the tangential force is recorded throughout the rotation time. A constant applied voltage $U_0 = 5$ V is used and the contact resistance R_c is equal to R_0 $(U_0/U - 1)$, with R_0 being the serial gauged resistor.

It was shown that two significant curves can be plotted, the direct current voltage curve related to coating conductivity, and the friction torque curve related to coating mechanical behavior (Figure 10.26). The number of revolutions for the beginning of mixed lubrication at the slider-specimen contact surface is obtained from DC voltage measurements, and the number of revolutions at seizure onset from friction torque values.

Typical evolution of the contact between the slider and the coated specimen is presented in Figure 10.27. The virgin specimen coating, shown in Figure 10.27a, is made of three basic layers, a zinc phosphate layer deposited on the parent steel specimen surface, a zinc stearate layer firmly

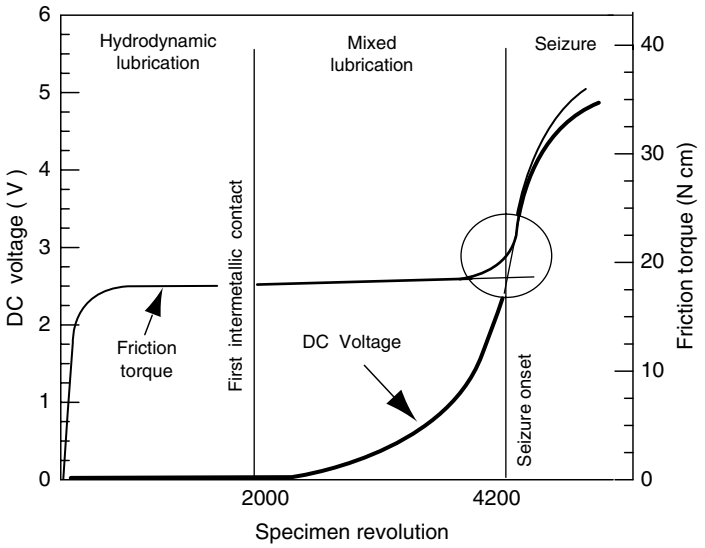

FIGURE 10.26 Friction seizure test of coated steel specimen: direct current voltage and friction torque vs. revolutions.

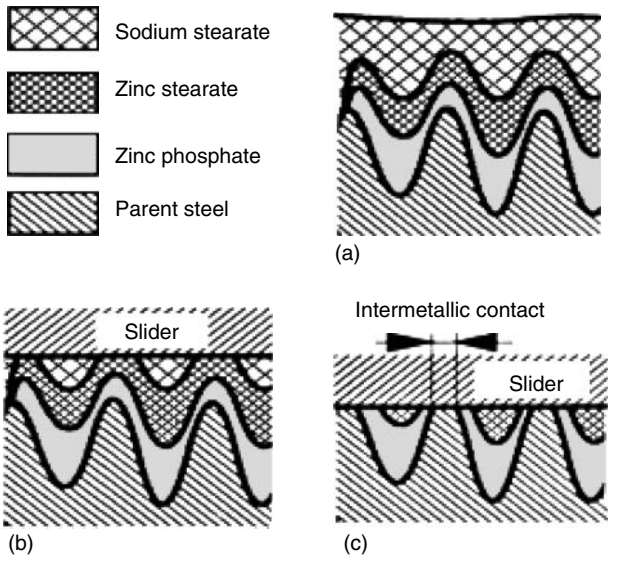

FIGURE 10.27 Typical evolution of the contact between the slider and the phosphated/soaped specimen. (a) Virgin coating, (b) hydrodynamic lubrication, (c) mixed lubrication.

bonded to zinc phosphate, and an unconverted sodium stearate layer. As the slider presses the three layers first, a part of the unconverted sodium stearate is trapped in the cavities. This is related to quasi constant friction torque and zero direct current voltage; hydrodynamic lubrication is then effective.

With the increase of velocity, the zinc stearate and the zinc phosphate layers are progressively worn away. The friction torque and the direct current voltage increase, with the gradient of the last one being higher; thus, mixed lubrication now takes place, as shown in Figure 10.27c. As the test goes on, the contact surface between the slider and specimen grows and the friction torque and the direct current voltage strongly increase, relating to unlubricated contact area increase and seizure onset.

10.3.5 Novel Systems for Measuring and Analysis of Contact Characteristics

It is evident now that tribological research can be greatly aided by the simultaneous observation of friction and electrical contact resistance, especially since the latter permits determination of the real contact area as well as revealing much about the nature of the surface films at interface. Many tribometers are equipped with special systems for contact resistance measuring.[794,938–941]

Among them, a very effective "hoop apparatus" was developed,[796] the construction of which is outlined in Figure 10.28. By means of the hoop apparatus, one may simultaneously monitor (with about 100 Hz sampling frequency) friction coefficient f and R_c of metal samples sliding within a metal hoop rotating at uniform speed. At constant friction coefficient and in the absence of inertial effects, the equilibrium position of a sample in the hoop is at the point at which the tangent of the surface inclination equals the coefficient of friction, and one would expect to find the sample there. As a rule, the sample executes more or less irregular stuck–slip motions, or else it may gently rock about an equilibrium position. By mathematically analyzing the data, the momentary values of the friction force and friction coefficient as well as its dependence on speed and other parameters can be deduced.

Through systematic measurements of friction and electrical resistance in the hoop apparatus, as a function of applied normal force, average sliding speed and ambient atmosphere, a wealth of

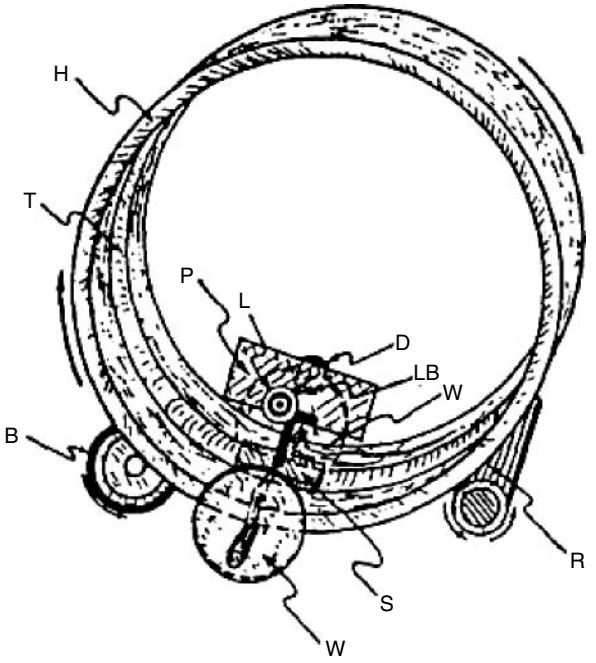

FIGURE 10.28 Schematic of the hoop apparatus. The sample (S, typically in the form of a painter's style vertical fiber bundle), slides in the inside track (T) of the vertical hoop (H). The hoop rotates at a constant speed in clockwise direction about its horizontal axis, as it rests on the one side on a vertical ball-bearing (B) and on its other side on a rotating, rubber-covered shaft (R). The load on the sample, in addition to its own weight and that of the sample holder including the polaroid (P) at its top, is varied by means of disk-shaped weights (W) slipped onto light horizontal axles. These are constructed such that the center of gravity of the whole sample assembly lies just barely below the sliding interface between sample and hoop, thereby avoiding incidental oscillations. The momentary position of the sample is monitored via a horizontal beam of polarized light (LB) which passes from a lamp (L) through the polaroid to a photo diode (D). Its output is monitored at a frequency of about 100 Hz while simultaneously the electrical contact resistance between sample and hoop is monitored in a bridge circuit. The: very light and flexible connecting leads are not shown. The apparatus is housed under a bell jar so as to permit testing in various atmospheres as well as under reduced pressures. (From Bredel, L. J., Johnson, L. B., and Kuhlmann-Wilsdorf, D., *Wear*, 120, 161–173, 1987. With permission.)

detailed information regarding the contact spots could be obtained. Herein, the favored samples were bundles of fine, flexible parallel wires. They were carefully shaped such that the fiber ends defined a cylindrical surface closely matching the hoop, and they were slid painter's brush style in it. Thus, the majority of the fiber ends touch the hoop and by this stratagem one knows the number and average size of the contact spots, which normally are vexing unknowns. Further, through the large number of contact spots the otherwise very disturbing statistical fluctuations of single contact spots are removed. The hoop apparatus is also widely used in solving different problems in the field of electrical contacts and tribology.[28,40]

Using modern electronics and hardware, more sophisticated measurements and data processing are becoming available to study the tribological and electrical phenomena of contact surfaces. Many computerized testing systems are developed which makes possible fast and fully automatic measurements of contact resistance in contact systems of different types.[942–944] The most interesting among them are the digital image measuring systems.

To clarify the relationship between the contact resistance and the damage of an electrical sliding contact surface, a digital image measuring system (DIMS) was developed by Taniguchi

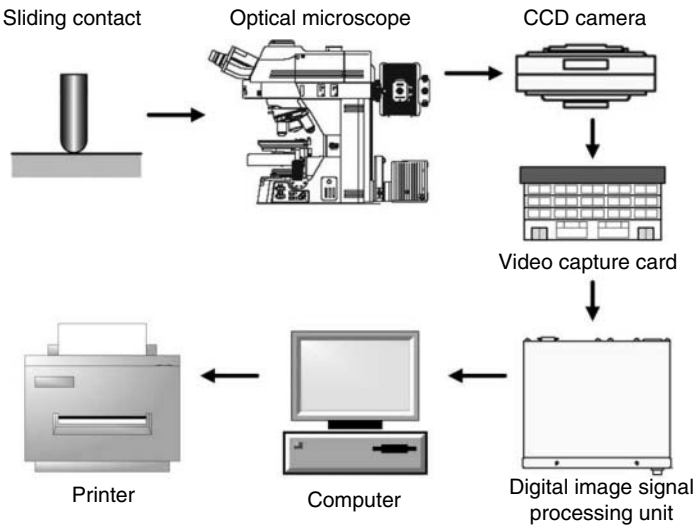

FIGURE 10.29 Schematic diagram of digital image measuring system.

and Takagi.[944] To measure damage width on the sliding contact surface, the shadow image processing technique (SIPT) was applied.

As a test sample of the sliding contact, a round copper disk was used, and two U-type electrodes of copper or nickel (curvature: 0.5 mm) were used as the static contacts. The DIMS (Figure 10.29) primarily consists of the combination of an optical system to record the contact surface image, a digital image signal processing unit, and a personal computer. The contact surface image is recorded with a CCD camera and the DISP carries out the digital processing of the image signal. To record repeatedly the image of the same portion on the sliding contact surface, a trigger signal was periodically applied with a counter unit.

In the Shadow image processing technique (SIPT), the brightness distribution on the sliding contact is calculated by a personal computer, which not only calculates the histogram of brightness in the entire image, but also displays the 3D graphic image on the CRT.

Figure 10.30 shows the example of the measured damage width when the contact was continuously slid. The relationship between the contact resistance and the contact surface damage can be investigated using the SIPT.

10.3.5.1 Method of "Triboscopy"

A technique of easy-to-interpret presentation of physical parameters (friction coefficient and electrical contact resistance) recorded in the course of friction tests is proposed by Myshkin et al.[945,946] The technique is based on construction of digital "triboscopic images" as a 3D map. The map includes space and time (or number of cycles) coordinates; the third coordinate is brightness (grey level) reflecting the value of a given parameter. The map gives evident information on surface wear uniformity, transfer process, wear particles formation and their displacement in the contact zone, scratch formation, etc.

Background of the method. The majority of tribotests is carried out at cyclically variable relative positions of rubbing surfaces. A single sliding cycle can be identified as a single revolution in the system with unidirectional displacement or a single passage along the friction track during reciprocation. At continuous registration of the contact parameters P_x (friction force, contact resistance, etc.) their variations can be recorded within a sliding cycle. In case of a nominal point contact, e.g., sphere–plain, the parameters provides a specific probing of the friction track; incidentally, the

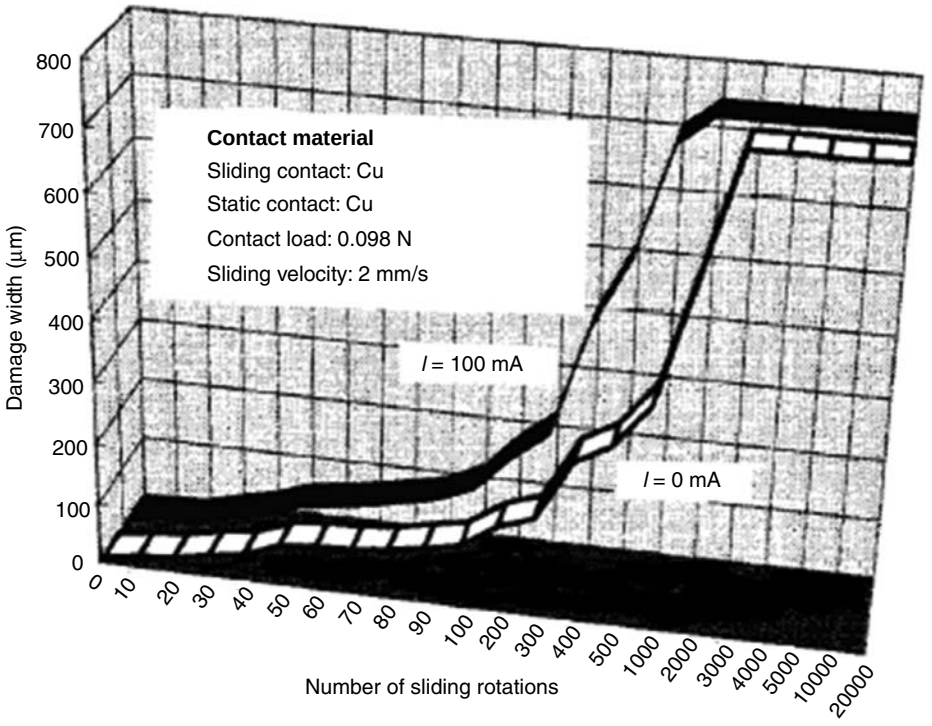

FIGURE 10.30 Measurement of damage width on the sliding contact surface (static contact material: Cu). (Adapted from Taniguchi, M. and Takagi, T., *Proceedings of 19th International Conference on Electrical Contacts*, VDE-Verlag GMBH, Berlin, Offenbach, 111–115, 1998. With permission.)

contour site acts as a probe. In principle, the probe dimensions can be at the microlevel or nanolevel.

When the route is scanned consecutively (cycle by cycle), variations of the signal P_x in position x characterize the change in time of one or both friction surfaces in this position. Consequently, it is possible to observe the evolution of the interface state both as a function of relative position of specimens (x) and time (t) or the number (N) of cycles.

Three-Dimensional Presentation. If a PC-compatible tribometer is equipped with a registration system of specimen positions, a three-dimensional presentation of the experimental data is possible in which the dimensional coordinate of the specimen's relative position extends along x-axis, the number of cycles N along y-axis, while the recorded parameter value along z-axis (Figure 10.31). Such presentation can be obtained using the software in the course of experiment or after its completion by the data file processing.

Combination of the three-dimensional data presentation with the statistically processed data for each cycle (mean, maximum and minimum values, dispersion, etc.) allows one to obtain additional information on microwear processes while retaining the information on the general tendencies of the processes in the macrosystem.

Notwithstanding a number of advantages, three-dimensional data presentation fails in a number of cases to provide visual information on variations of parameters at a given site of friction track and the parameters are sometimes difficult to analyze. Yet, computers have the potential to use digital images instead of three-dimensional data presentation when contrast (grey level) of the pixel indicates variations of the registered parameter and it serves instead of the linear z-axis. Original such images were made in the early 1990s;[947,948] the method was termed *triboscopy* and was used

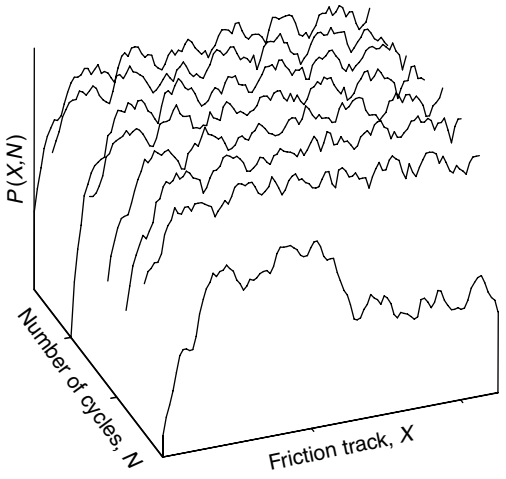

FIGURE 10.31 Typical three-dimensional data presentation for contact parameters, P_x, at reciprocated sliding.

for digital (triboscopic) imaging based on data registered by a reciprocating tribometer (sphere-on-plane contact).

The method combined the tribometer and the numerical image processor. Like the three-dimensional data presentation, the relative position of contacting bodies is plotted along the x-axis and the number N of sliding cycles along the y-axis (Figure 10.32). The grey level of the pixel corresponds to the value of the registered parameter at each point with coordinates (x,N) in the xy plane. Thus, the triboscopic imaging is a two-dimensional presentation of the physical value $P(t)$ fluctuations during the tribotest. Such presentation allows registering concurrently the variations P_i along the route and from cycle to cycle; it allows the conversion of time-dependent data into an (x,N)-dependent diagram (Figure 10.32).

Implementation of the above approach and expansion of its potential enabled elimination of rigid restrictions imposed by the number of sliding cycles and the number of readings per cycle.[945,946] Figure 10.33 shows the schematic diagram of triboscopic image formation. A micro-tribometer that ensures simultaneous registration of friction force and contact resistance during reciprocation between a spherical and plane specimen has been used. The initial and final points of the friction track to be analyzed were registered with an optronic couple capable to "tie up" to one and the same portions of the track.

A computer with special software controls the experiment and processes data. The technique includes a set of the studied sliding distances, quantization steps, and cycle number over which

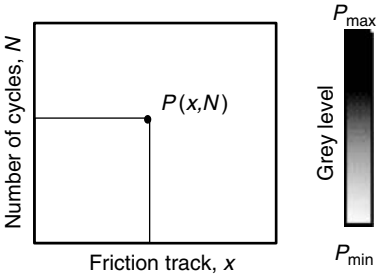

FIGURE 10.32 Parameter $P(x,N)$ presentation as a triboscopic image. (From Belin, M., *Wear*, 168, 7–12, 1993. With permission.)

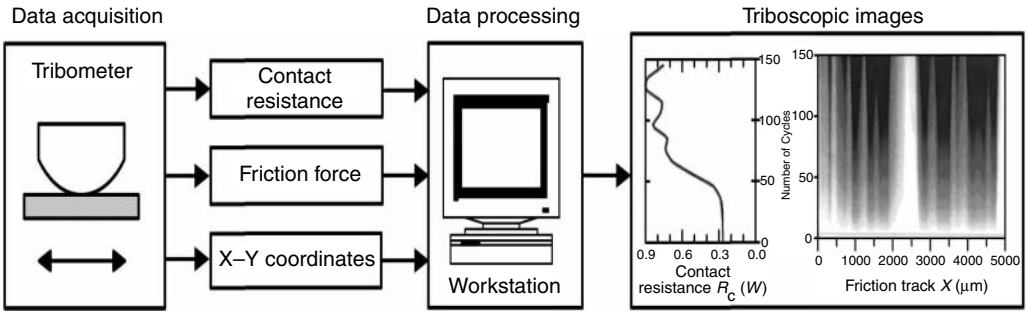

FIGURE 10.33 The scheme of triboscopic images formation.

the momentary values of F and R_c are stored. After the optronic couple actuates, the signals from the friction force and contact resistance sensors are converted by the analog-to-digital converter and stored on the PC. Stored samples served to create two-dimensional matrices of triboscopic images P_i (x_1,…,x_n, N_1,…,N_m) that are displayed or printed out. Synthesized triboscopic images can be processed by standard methods elaborated for real images.

Digital images reflect the evolution of the contact parameter as a function of specimen relative position and the number of sliding cycles. It can be asserted a priori that appearance of flat sample defects (for example, adhesion of wear debris) would produce vertical specific strips on the image of the corresponding width. On the contrary, short-time change of the slider surface (adhesion of particles) would produce a horizontal strip. If free wear debris emerges in the contact zone, horizontal short marks would appear (within one cycle). Comparison of the friction force and contact conductivity images can yield essential additional information. Therefore, it becomes possible to investigate interface local phenomena and their kinetics.

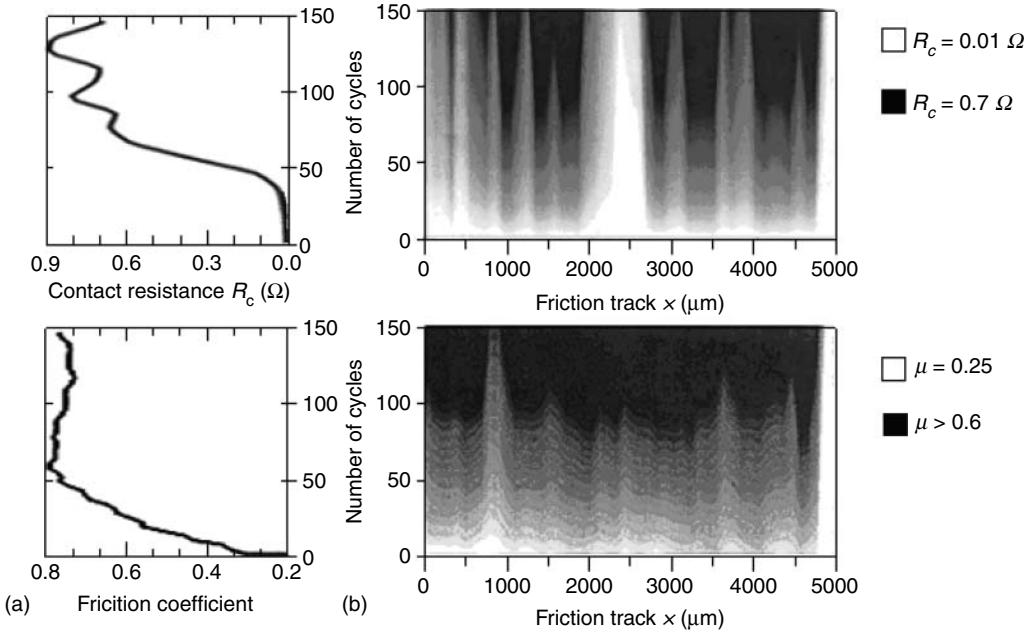

FIGURE 10.34 Mean values per cycle and triboscopic images of contact resistance R_c (a) and friction coefficient f (b) at sliding of platinum sphere on steel plane.

Figure 10.34 shows the triboscopic images reflecting typical processes in the unlubricated soft slider-on-rigid plane system. In the original state, the noble metal (platinum) contacts the steel with thin tunnel-conducting tarnish film. The surfaces are separated by a physically adsorbed layer having poor adhesion to the surfaces. The layer effects insignificantly conductivity, but it reduces friction. As a result, the friction coefficient is relatively low ($\mu \cong 0.25$), which is typical for boundary friction, whereas the contact conductivity is rather high during the first several sliding cycles (as long as the adsorbed layer and the tarnish film exist). At further sliding ($N > 10$), the adsorbed layer and possible tarnish film over separate portions are worn. Adhesion between the surfaces over individual portions becomes stronger, leading to seizure, appearance of wear debris, and friction increase. It has been shown[795] that such processes also increase contact resistance.

The exemplified triboscopic images show that the above processes are intensified as the number of cycles adds up. Vertical expanding strips of higher electrical resistance indicate transfer and gradual conglomeration of debris on the plane, which is supported by microscopic studies. At the same time, absence of distinctive strips in the horizontal direction prove the absence of foreign particles on the slider. Free particles in the friction zone apparently do not affect contact surfaces in any decisive manner. By the end of the tests, the overwhelming portion of the steel friction surface is covered with the transferred layer of conglomerated debris and adhesive wear becomes dominating which is confirmed by a very high friction level.

The new approach is highly promising for tribological studies of heterogeneous materials and materials with thin coatings. The latter is specifically essential when considering expanding application of low loaded couples with multilayered coatings (magnetic memory systems, micromechanical systems) in which wear should tend to zero.

11 Monitoring Technologies

Aging is defined as the continuous time dependent degradation of materials due to normal service conditions, which include normal operation and transient conditions. All electrical/electronic connections undergo aging and lose, partially or totally, their designed functions. If not effectively monitored and controlled, aging degradation of these components may impair their performance characteristics and lead to a reduction in reliability of associated systems. To maintain adequate performance of an electrical/electronic system, it is essential to monitor and predict component and system performance to take appropriate preventive actions.

Effective control of aging degradation of electrical components requires timely detection and mitigation of the degradation. To meet these requirements, different programs have been developed to prevent, detect, correct, and mitigate failures of electrical/electronic components from any cause, including the effects of aging degradation. These include testing, surveillance, preventive maintenance programs, significant event reporting systems, and operational, maintenance and design changes initiated on the basis of detected component failures or deficiencies.

Because of ever-increasing demands, electrical systems and equipment must perform at levels thought impossible a decade ago. The operations, product quality; and equipment reliability, availability, and maintainability are now pushed to unprecedented levels while staying within budgetary constraints. This is also coupled with a demand to reduce operational and support costs and to eliminate or minimize new capital investments in plant equipment because of lengthy returns on investments that impact short-term capital recovery. In short, new measures have to be invoked to ensure network performance while minimizing costs and extending the operational life of new and aging equipment.

For these reasons, the reliability-centered maintenance (RCM) approach is gaining ever-increasing popularity. This approach relies on component condition and criticality, in lieu of routine scheduling for inspection and overhauling. Those components identified as critical are replaced on a conservative time scheduled basis, while others are replaced on a conditional time basis.

Predictive maintenance. Predictive maintenance is defined as maintenance initiated on the basis of observed present and projected future component conditions. The objective of predictive maintenance is to predict component performance so that repairs can be planned and completed before the projected failure occurs. Implementation of the predictive maintenance program requires storing and analysis of relevant data, determining the trends of and the extent of degradation to decide the kind and timing of preventive action to be undertaken.[949]

To understand potential damage mechanisms, design criteria, fail-safe features and structural maintenance philosophy, it is essential to assess the effectiveness of sensor-based systems to monitor the reliability of power connectors and disconnect switches in terms of their life cycle degradation. Therefore, monitoring and diagnostic techniques should be able to:

- Detect deterioration or damage affecting structural integrity of power equipment
- Determine and characterize the extent and severity of deterioration

- Assess the deleterious effect of deterioration on the performance of the power equipment
- Initiate mitigating or corrective actions to restore the operational capabilities of the power equipment

Deterioration is evaluated by continuous or periodic measurement, sensing, recording, and interpretation of physical parameters related to the operation of the equipment. The data obtained are related to either the fraction of degradation or the remaining life of the equipment. Deterioration can be assessed in terms of physical, electrical or performance degradation, such as a deviation of operating parameters from the expected values.

In the case of power connections and power equipment in general, a reduction of failures enhances the network reliability. This task can be realized through predictive maintenance using advanced monitoring and diagnostic techniques, particularly through more accurate online monitoring. The end result of applications of these measures is the improved reliability of power system reliability and the prevention of power outages. This in turn provides economical benefits in terms of cost savings since extending the usable life of power equipment beyond their design lifetimes delays the capital expenditure for replacing aged equipment.

Condition monitoring. Condition monitoring is a continuous or periodic observation and assessment of the functional capability/operational readiness of an electrical component or a system as a whole. It provides information in terms of measurements, periodic tests, or inspections designed to produce consistent, repeatable results, in which current performance or condition is determined.

Effective monitoring of aging degradation requires knowledge of one or more condition indicators which provide information on the physical state of the components at the time of observation. It can identify aging mechanisms that may not have been adequately addressed during original qualification and identify incipient failures. An acceptable indicator for condition monitoring must provide an early warning of impending functional degradation that may not yet be apparent and thus must have a change that is detectable before component failure.

Ideally, monitoring a single condition indicator should show the functional capability of power components within existing criteria, thus allowing the user to select whether to continue operating without change, to perform maintenance, to repair the component, or to replace the component. From a practical point of view, monitoring techniques have to be nondestructive or essentially nondestructive.

Online condition monitoring of equipment is becoming more attractive since accurate condition assessment and the subsequent management of in-service make the network more economically viable and performance reliable. It should be pointed out, however, that broader development of a condition monitoring program is generally weakened by the lack of adequate understanding of the degradation mechanisms which in turn makes identification and development of appropriate condition indicators and monitoring methods rather difficult.

In any power delivery system, electrical contacts are weak links and thus the most frequently found problem on a network. Hence, to monitor the conditions of a variety of power equipments, many sensors and inspection systems are being developed whose primary function is to identify the location, type, and magnitude of the degradation of power components.

To illustrate the importance of condition monitoring of power equipment, Table 11.1 shows itemized power components susceptible to aging degradation and different modes of connection deterioration, as well as the potential impact of connection deterioration on the performance and the ensuing costs.

11.1 THERMAL MEASUREMENTS

Temperature is one of the first observable parameters that can indicate the condition of operating electrical equipment. Over time the components and contact surfaces will begin to deteriorate, resulting in an increased resistance and thus heat; this leads to the eventual failure of power

TABLE 11.1
Itemized Power Equipment/Components Susceptible to Aging and Different Modes of Deterioration; Identifies the Cause and Indicates Potential Impact and Cost

Application	Cause	Impact
Power distribution Circuit breakers Conductors Splices, disconnect switches	Loose/corroded/improper connections and splices Poor breaker connections Overheating, overloading Conductor strands broken	Overheating, arcing, burning, fire Conductor strands broken—overhead line could come down Expensive repair and replacement Safety considerations
Miscellaneous power components Switches Breakers	Loose or corroded connections Poor contacts Overloading Overheating	Arcing, short-circuiting, burning, fire 25% of all power equipment failures are caused by loose electrical connections Cost of repair and replacement very expensive Safety considerations
Transformers	Loose/deteriorated connections Overheated bushings Poor contacts (tap changer) Overloading	Arcing, short-circuiting, burning, fires Expensive rewinding and replacement

components. Fluctuating and high loads, vibration, metal fatigue, age, and specific operational environments such as extreme ambient temperatures, wind, chemicals or dirt in the atmosphere, will increase the rate of degradation and the number of faults in electrical systems.

Temperature monitoring is the most frequently used type of environmental monitoring. The technologies available to monitor the condition of electrical/electronic systems and components are abundant. Temperature measurement can be divided into two categories: contact and noncontact.

Contact sensors, comprising thermocouples, resistance temperature detectors (RTDs), and thermometers are the most prevalent in temperature measurement applications. Since they measure their own temperature, these sensors are in contact with the component. They are relatively slow responding and inexpensive. Due to extensive wiring required to bring the temperature data to the acquisition center for processing, they are not a favorite choice for condition monitoring.

Other contact type sensors include thermal paint/stickers and shape-memory alloy (SMA) temperature indicators. These sensors are permanently mounted or attached to the components or devices and are activated when the temperature of the component reaches a characteristic temperature at which these sensors change either the color (stickers) or the shape (SMA indicators).

Noncontact temperature sensors measure infrared (IR) energy emitted by the target, have quick responses, and are commonly used to measure temperature of power components that are inaccessible due to hostile environments, geometry limitations, or safety hazards. The most common noncontact temperature sensors are IR thermometers, pyrometers, IR image scanners, and fiber optic thermometers.

The use of appropriate sensors at key locations requires an understanding of the system and the characteristics of the devices being monitored. Hence, selecting the characteristics and the appropriate data collection systems and software to track equipment degradation over time is critical to the success of a monitoring program.

11.1.1 Infrared Thermography

Infrared condition monitoring is the technique capable of revealing the presence of thermal distribution produced on the surface of the defective component. The presence of the defect alters the thermal signature of the surface due to the change in the amount of heat generated and in the heat transfer properties of the component. Therefore, infrared thermography enables the remote gathering of thermal information for monitoring the condition of the electrical components of an entire power system.

Under normal operating conditions, each component is characterized with a certain acceptable resistance. It is the deviation of the resistance from this state that signals the heating up of the component that requires intervention. Overheating of components can be caused by any of the failure mechanisms as discussed in Section 6.4, such as loss of contact load, stress relaxation, creep, corrosion, etc. Continuous deterioration of the components results in temperature increases until the melting point of the material is reached, causing a complete failure.

Infrared thermography is presently widely used by electric utilities and industrial sectors. Such growth is not only the result of the benefits offered by this noncontact, nondestructive method but also the sophistication of data acquisition, simplicity of operation, and high performance.

It should be pointed out, however, that despite limitations of infrared systems due to the fact that these can only measure the temperature of exposed surfaces, they are very effective in detecting the presence of slow-evolving faults. This enables the user to follow the evolution of the faults to mitigate and lessen the effect of a failure. For these reasons, IR thermography has become an essential part of the predictive and preventive maintenance programs of electrical utilities and a wide range of industries.

11.1.2 Basic Features of Infrared Thermography

Infrared radiation was discovered in 1800 by William Hershel, who used a prism to refract the sunlight onto thermometers placed just pass the red end of the visible spectrum generated by the prism. He found that this area had the highest temperature of all, contained the most heat, and therefore contained a form of light beyond red light. Herschel's experiment was important not only because it led to the discovery of infrared light, but because it was the first experiment that showed there were forms of light not visible to the human eye.

Infrared radiation is energy radiated by the motion of atoms and molecules on the surface of a body having a temperature above absolute zero degrees Kelvin (-273°C). The emitted energy is a form of electromagnetic radiation which is the same as radio waves, microwaves, ultraviolet rays, visible light, x-rays, and gamma rays. These types of electromagnetic radiation form an electromagnetic spectrum whereby each of these "radiation bands" is characterized by its own wavelength correlated to the amount of energy the waves carry. The wavelength of the infrared radiation falls in the region of 0.78–1000 μm and is longer than the wavelength of visible light but shorter than radio waves. A spectrum of electromagnetic radiations is shown in Figure 11.1.

The thermal energy radiated by an object is expressed in terms of its emissivity, which is defined as the ratio of the radiation intensity of a nonblack body to the radiation intensity of a black body. The emissivity characterizes radiation or absorption quality of nonblack bodies. This ratio is always less than one or just equal to one.

$$\varepsilon = W_o/W_{bb}, \tag{11.1}$$

where W_o is the total radiant energy emitted by a body at a given temperature, T and W_{bb} is the total radiant energy emitted by a blackbody at the same temperature.

The intensity of the energy emitted is a function of the temperature of the material; the higher the temperature, the greater the intensity of emitted infrared energy. In a blackbody, all energy that

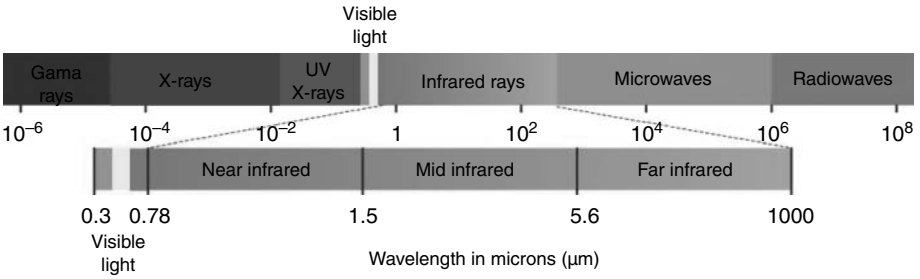

FIGURE 11.1 A spectrum of electromagnetic and infrared radiations.

falls upon it will be absorbed and at a steady temperature emitted in each part of the electromagnetic spectrum. However, in practical situations the real objects do not behave like this since the radiant energy striking an object will be dissipated.

The rate at which a blackbody radiates energy is given by the *Stefan–Boltzmann law*:

$$W = \varepsilon\sigma T^4, \tag{11.2}$$

where W is expressed in W/m, σ is the Stefan–Boltzmann constant, 5.67×10^{-12} (J/m^2 K), and T is absolute temperature. This equation assumes that the body receiving the radiation is at absolute zero. In practical cases, the receiving body is at a temperature T_R and radiates to the blackbody at a rate

$$W = \varepsilon\sigma T_R^4, \tag{11.3}$$

per unit area of the receptor. Thus, the net energy reaching the receptor is

$$W = \varepsilon\sigma\left(T^4 - T_R^4\right). \tag{11.4}$$

These equations give the radiation from all wavelengths in the entire spectrum. However, for more practical uses, in which the receiving object responds significantly only to the short wavelength portion of the spectrum, the Wien–Planck and Wien laws are more useful.

The *Wien–Planck law* expresses the radiation emitted per unit area of a blackbody as a function of wavelength, λ, and temperature, T.

$$W_\lambda = C_1\lambda^{-5}(e^{C_2/\lambda T} - 1)^{-1} \tag{11.5}$$

As temperature increases, the total amount of energy emitted increases and the radiation maximum shifts to shorter wavelengths, as seen in Figure 11.2. *Wien's displacement law* gives the value of the wavelength of maximum radiation per unit area:

$$\lambda_m T = b, \tag{11.6}$$

where λ_m is the wavelength of maximum radiation in μm, T is absolute temperature, and b is equal to 2897.8 μm K.

The dashed line in Figure 11.2 defines this expression and locates the maximum radiation values for each temperature at a specific wavelength. As seen, maximum radiance is associated with higher temperatures and lower wavelengths.

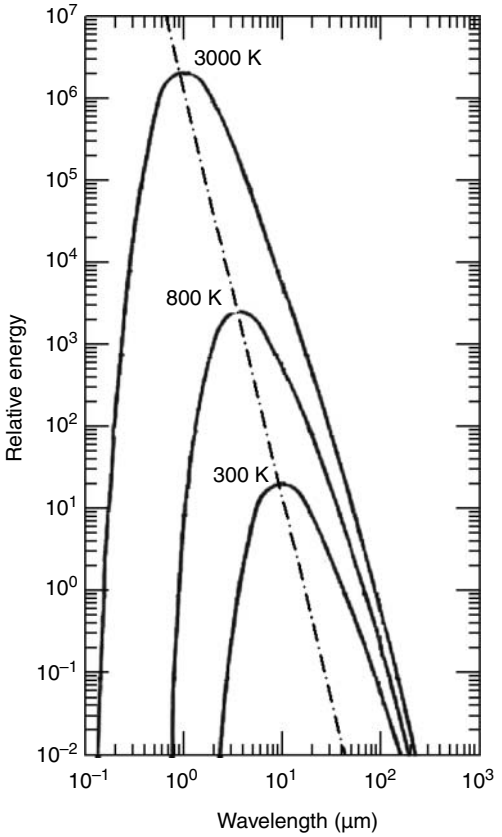

FIGURE 11.2 Radiation intensity as a function of wavelength and temperature (Planck's law).

11.1.3 Types of Infrared Thermal Systems

Infrared camera technology has advanced significantly since the early 1960s when the Swedish company AGA introduced the first commercially available infrared imaging instrument. These early instruments were heavy and bulky, required liquid nitrogen to operate, provided fuzzy black and white images, and offered only relative temperature measurement that required the use of long and complex formulas.

Today there is an abundance of IR thermal measuring systems. These systems are practically hand held computers with incorporated software which enables practically instantaneous data analysis. Basically, there are two general types of infrared instruments that can be used by utilities for condition monitoring: IR thermometers and IR focal plane area (FPA) cameras.

Infrared thermometers. Infrared thermometers or spot radiometers are designed to provide the actual surface temperature at a single, relatively small point on a surface. This is one of the limitations of infrared thermometers because the temperature represents a single point on the body.

Basically, an IR thermometer comprises an optical system to collect the energy emitted by the target; a detector to convert this energy to an electrical signal, an emittivity adjustment to match the thermometer calibration to the specific emitting characteristics of the target, and an ambient temperature compensation circuit to ensure that temperature variations inside the thermometer due to ambient conditions do not affect accuracy. Radiation thermometer sensitivity varies inversely proportionally with wavelength.

The most sophisticated IR thermometers incorporate microprocessor-based electronics with complex algorithms providing real time linearization and compensation of the detector output for higher precision of measured target temperature and instantaneous measurements display of several variables on integral LCD screens. IR thermometers can be broadly classified as

- Broadband radiation thermometers
- Narrow band radiation thermometers
- Ratio radiation thermometers

Broadband IR thermometers are the least expensive simplest devices, with a response from 0.3 microns wavelength to an upper limit of 2.5–20 microns and are capable of measuring a significant fraction of the thermal radiation emitted by the object in normal-use temperature ranges. Broadband thermometers are dependent on the total emittance of the surface being measured. The path to the target must be unobstructed since the presence of water vapor, dust, smoke, steam and radiation, and absorption of the least expensive gases in the atmosphere can attenuate emitted radiation from the target and cause the thermometer to read low. The optical system must be kept clean, and the sighting window protected against any corrosives in the environment. Standard ranges include 0–1000°C. Typical accuracy is 0.5–1% full scale.

Narrow-band IR thermometers operate over a narrow range of wavelengths achieved with the use of selective filtering to restrict response to a selected wavelength, thus obtaining higher measurement accuracy. Common selective spectral responses are 8–14 microns, which avoids interference from atmospheric moisture over long paths. Ranges of narrow band IR thermometers span from simple hand-held devices to sophisticated portables with simultaneous viewing of target and temperature, memory and printout capability of being viewed online, and fixed mounted sensors with remote electronics control. Standard temperature range of interest to utilities is up to 200°C. Typical accuracy is 0.25–2% of full scale.

Two-color (ratio) IR thermometers measure the radiated energy of an object between two narrow wavelength bands and calculate the ratio of the two energies, which is a function of the temperature of the object. The temperature measurement is dependent on the ratio of the two energies measured and not their absolute values. The ratio technique may eliminate or reduce errors in temperature measurement caused by changes in emissivity, surface finish, and energy absorbing materials, such as water vapor between the thermometer and the target.

Two color or multiwavelength thermometers should be seriously considered for applications where accuracy, and not just repeatability, is critical, or if the target object is undergoing a physical or chemical change. Ratio thermometers cover wide temperature ranges, mainly higher temperatures up to 3700°C. These IR thermometers are unlikely to be used for condition monitoring of power equipment. Typical accuracy is 0.5% of reading on narrow spans, to 2% of full scale. Typical IR thermometers—handheld (a, b) and fixed (c)—are shown in Figure 11.3 and Figure 11.4.

The field of view of a radiation thermometer is one of the most important characteristics of IR thermometers, since it essentially defines the size of the target at a specified distance from the instrument. Telescopic eyepieces on some designs can magnify the radiant energy to enable viewing of smaller targets at greater distances. Targets as small as 1.5 mm in diameter can be measured using the correct thermometer design.

The angle of viewing also affects the target size and shape. High-performance IR thermometers are equipped with telescopic attachments that can extend the distance to a target size ratio to 100:1. These thermometers can also have laser-aiming attachments for a precise location of the target. Advantages and disadvantages of IR thermometers are given in Table 11.2.

IR focal plane area cameras. The introduction of focal plane array (FPA) imagers during the early 1990s revolutionized infrared imaging by providing high-resolution imaging systems while greatly reducing size and weight. These high-resolution infrared imaging systems have allowed

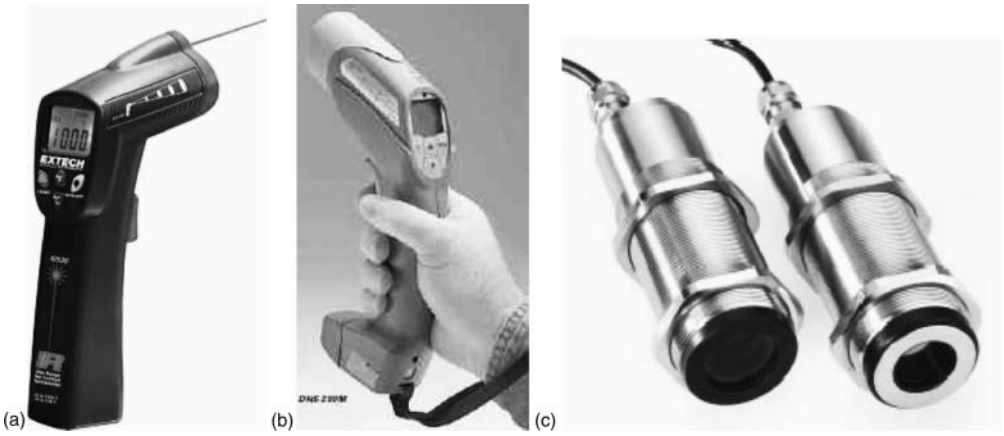

FIGURE 11.3 (a) and (b) Hand-held and (c) Fixed-type IR thermometers.

thermography to be applied to more applications than ever before. Infrared thermography can detect unseen problems such as loose or deteriorated electrical connections.

The infrared focal plane array (FPA) uses a high-density mosaic of small detector elements which are aimed at the target. Each element sees a single infrared pixel of the target, and no mechanically scanned optics are required. The size of the array ranges from a matrix of horizontal/vertical elements 128×128 to one containing 512×512 elements.

The greatest single benefit of an FPA is its ability to generate high-quality images. In mechanically scanned single-element detectors, 14,000–26,000 picture elements make up the field of view. An FPA covering the same field of view will comprise 65,000–262,000 pixels. This means the FPA will have 3–10 times more image detail. An image with higher resolution allows problems to be identified without the camera operator having to change lenses, enhances analysis procedures, and provides an image that is easier to read and understand.

Although the FPA detector represents a significant breakthrough in technology, it is clear that without advancements in optics, electronics, and microprocessor technologies, it would not have been possible to achieve the sophistication and availability of these cameras. Most of these imaging systems function much like a video camera, whereby the thermal emission profile of a wide area is visible in the same way as looking through the instrument's optics. It is expected that the technology will continue to develop, particularly in the area of improved detector performance and reduced noise, equivalent temperature difference, and electronics.

FIGURE 11.4 Typical top of the line IR cameras equipped with high-speed digital interface and report generation software.

TABLE 11.2
Advantages and Disadvantages of IR Thermometers

IR Thermometer Type	Advantages	Disadvantages
Broadband	Economy	Lower sensitivity
	Wide temperature spans	Susceptible to absorption errors due to sight path conditions
	Simple	
Narrowband	High accuracy even when emissivity unknown or varying, if short wavelength units chosen	Narrow temperature spans
	Measurements carried out in the open	Difficult to select optimum unit to meet all criteria
	Selected wave-bands for looking at or through glass, plastics and flames	
Ratio (two-color)	Less sensitive to varying target size or intermittent blockage of sight path by smoke, particles, etc.	Expensive
	Unaffected by emissivity change for gray targets	Ratio of emissivity in the two wavebands of measurement required
	Unaffected by small oscillating target within field of view	Sensitive to changes in ratio of emissivity

There is a movement now into a new semiconductor-based FPA detector technology, known as a Quantum Well Infrared Photo detector. The interest in this technology is that it promises major advances for infrared focal plane arrays by offering:

- Excellent pixel uniformity, imaging, and sensitivity performance
- Large pixel format capability, up to 640×480
- Tunability and responsiveness in the range 3–25 microns
- Relatively low cost and in large quantities

There is a variety of thermal imaging systems on the market ranging from relatively inexpensive black and white scanners, to full color microprocessor-based systems. The typical cost for black and white scanners is less than $1,000. A more sophisticated IR imaging systems will have a price range between $8,000 for a black and white scanner without storage capability to over $60,000 for a microprocessor-based, color imaging system. While advances in technology continue to improve the performance and capabilities of thermal imaging systems, proper use of infrared imaging equipment and interpretation of data requires extensive training and experience.

The performance and capabilities of IR systems depend on the type of detector and lens materials used in the construction of the system. While it is possible to buy filters and accessories, some IR systems may not be suited for certain applications due to their spectral response. Spectral response for commercial imagers generally falls into two categories: 2–5 microns (near infrared) and 8–14 microns (far infrared).

Sophisticated infrared equipment in vans or helicopters is now widely used throughout the electric power industry for rapid scanning of substation and switchyard bus and equipment, as well as transmission lines. Available equipment can survey an average-sized switchyard in about 30 min. Table 11.3 provides advantages and disadvantages of IR thermographic imaging systems. Figure 11.4 shows some top-of-the-line IR imaging systems.

IR images of overhead power components. Continued electrical efficiency depends on low contact resistance. If the quality of the connection degrades, it becomes, in effect, an energy dissipating device as its electrical resistance increases. The heated electrical components appear

TABLE 11.3
Advantages and Disadvantages of IR Imaging Systems

Advantages	Disadvantages
Fast inspection rate	Difficulty in obtaining a quick, uniform and highly energetic thermal stimulation over a large surface
No contact	Effects of thermal losses (convection, radiation) inducing spurious contrasts affecting the reliability of the data
Security of personnel	Cost of the equipment
Results are relatively easy to interpret since they are (often)	Capability of detecting only defects resulting in a measurable change of the thermal properties
Obtained in image format, furthermore images can be processed to extract more information	Inability to inspect a limited thickness of material under the surface (thermography is a boundary' technique)
Wide span of applications	Emissivity problems
Unique inspection tool for some inspection tasks	

as bright spots on a thermogram of the components. Some examples of overheating of power components are shown in Figure 11.5.[954]

11.1.4 SME Temperature Indicators

The shape-memory effect (SME) refers to the ability of certain materials to remember a shape, even after severe deformation. When a material with shape-memory ability is cooled below its

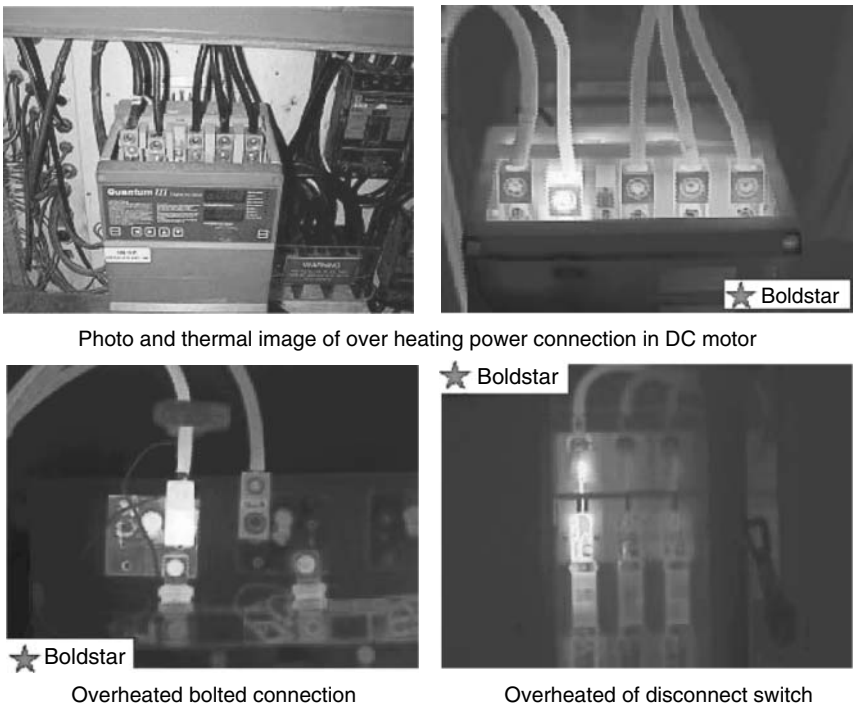

FIGURE 11.5 Examples of overheated power components. (Courtesy of Boldstar Infrared services, http://www.boldstarinfrared.com. With permission.)

transformation temperature (martensite phase), it has a very low yield strength and can be deformed quite easily into a new shape. When it is heated above its transformation temperature, it undergoes a change in crystal structure which causes it to return spontaneously to its original shape (austenite phase). During this isotropic transformation process, as the atoms shift back to their original positions, a substantial amount of energy is released. One square centimeter of SME alloy can exert enough force to move an object weighing 4650 kg!

Although the SME was observed as long ago as 1938, it was not widely recognized until 1962 when the nickel–titanium alloy was discovered and the first important application of this alloy was made. The SME is unique to two groups of alloys: nickel–titanium (Ni–Ti) and copper-based alloys (Cu–Zn–Al and Cu–Ni–Al) whose transition temperature is highly sensitive to the alloy composition and thermo-mechanical treatment. In the case of Ni–Ti, the temperature can be varied from −200°C to +100°C, whereas with copper-based alloys it can range from −105°C to +200°C.

Shape-memory alloys are basically functional devices in that they are more important for what they can do (action) than for what they are (property). The practical applications of shape-memory alloys are numerous: they have been used successfully as thermal and electrical actuators, thermo-mechanical energy converters, electrical connectors, circuit breakers, and mechanical couplers, as well as in robotic applications, medicine, and other areas.

A very simple temperature indicator for monitoring excessive heating of bolted joints is shown in Figure 11.6a.[955] It is a flat 5×40 mm×0.2 mm thick strip of a Cu-based shape-memory alloy (SMA) that has been trained in such a way as to recover its original (austenitic) shape in the temperature range 95–105°C. When in its martensite state (low temperature), the indicator, bent at 90° (position 1), is placed under the flat washer and the joint is bolted. When the temperature of a bolted joint exceeds its transformation temperature (95–105°C), the indicator takes its austenitic shape, i.e., it flattens (position 2), thus providing a visible indication of excessive heating. It is interesting to note that this type of temperature indicator has been successfully used on power systems in Russia and Ukraine, where approximately 100,000 units are currently installed.

A similar temperature indicator[956] is shown in Figure 11.6b. It is a short 0.1–1 mm thick SMAattached to a flat washer. When the bolt is assembled (low temperature), the wire is bent round the bolt head. As soon as the joint wire temperature exceeds the transformation temperature, usually above 100°C, the wire takes its straight (austenitic) shape, providing a visual signal of joint overheating.

The same operating principle has been used to monitor overheating in electric power cables.[957] This is an SMA strip with a flag which is bent round the cable at low temperature (martensitic state).

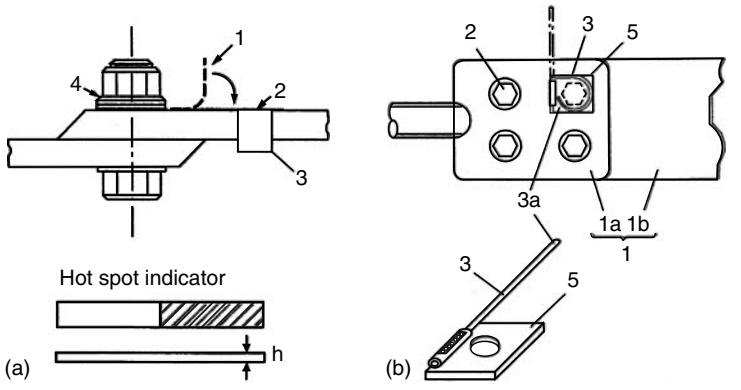

FIGURE 11.6 Simple shape-memory temperature indicator and Furukawa shape-memory over-temperature indicator. (From Lischina, private communication; Furukawa Electric Co., Japanese Patent 2-70218, 1990. With permission.)

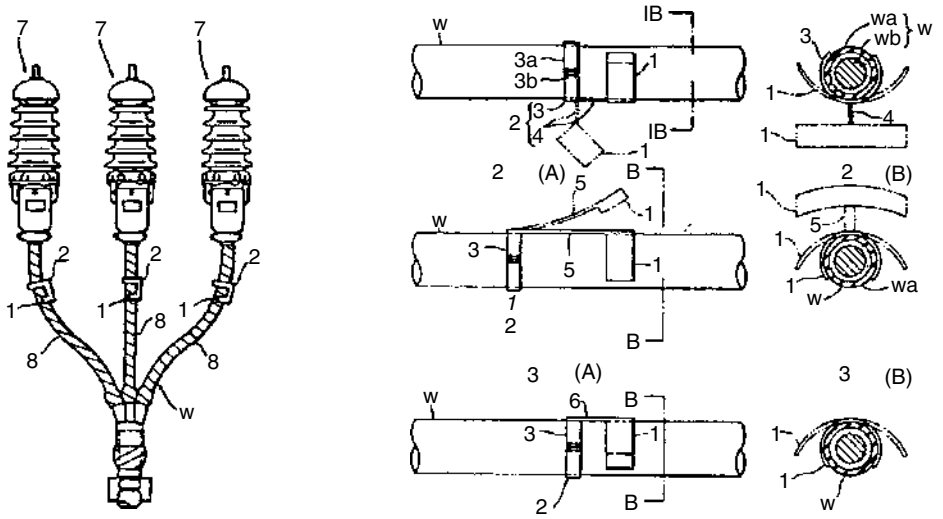

FIGURE 11.7 The Fujikura over-temperature SMA indicator of cable temperature. (From Shape-memory temperature indicator to monitor overheating of electric power cables, Tohoku Deneyoku KK-Fujikura Ltd., Japanese Patent 3-201313, 1991. With permission.)

When the cable reaches the transformation temperature of the SMA element, it expands and the flag pops up to signal cable overheating (see Figure 11.7).

The advantage of this type of temperature indicator over infrared (thermographic) detection is the possibility of continuous supervision of the condition of the joints, electrical contacts of different units of power system equipment and devices, etc. The use of SMA temperature indicators with different transition temperatures offers a more detailed assessment of the state of various devices and contact junctions on the power system.

Another more sophisticated SMA-based temperature indicator is based on monitoring of resistivity changes associated with the martensite–austenite transformation, or using the shape-memory effect itself. These indicators are based on resistivity changes of an SMA element (wire) undergoing sudden reduction (10–20%) in resistivity during martensite–austenite transformation provoked by the temperature increase. This type of detector is effective when large installations or electrical cables are to be protected to avoid overheating. The wire can be laid along lengths of 10–50 m, along electrical cables, or around any other device or equipment to monitor the temperature of the different parts. The alarm signal can be produced if only 1–2% of the installed wire length is heated.

Figure 11.8 shows such a monitoring device that can be used for fire warning or cable overheating.[958] The temperature sensor is an SMA wire (15) coupled to a Wheatstone bridge (9) responsive to the rate of resistance change. When the bridge is out of balance, the difference is amplified by the operational amplifiers (4, 12) which activate a relay (13). The feedback (20) comprising a clock-pulse generator (5), an up-down counter (6), and a digital-to-analog converter (7), ensures that the circuit will react only to a sudden drop in resistance as a result of exceeding the transformation temperature range, and not a gradual decrease in resistance outside the transformation zone.

11.1.5 Temperature Stickers (Labels)

Temperature stickers (labels) are contact-type temperature indicators that change their color gradually once the indicated temperature is reached. The accuracy of temperature indicated is ± 1°C.

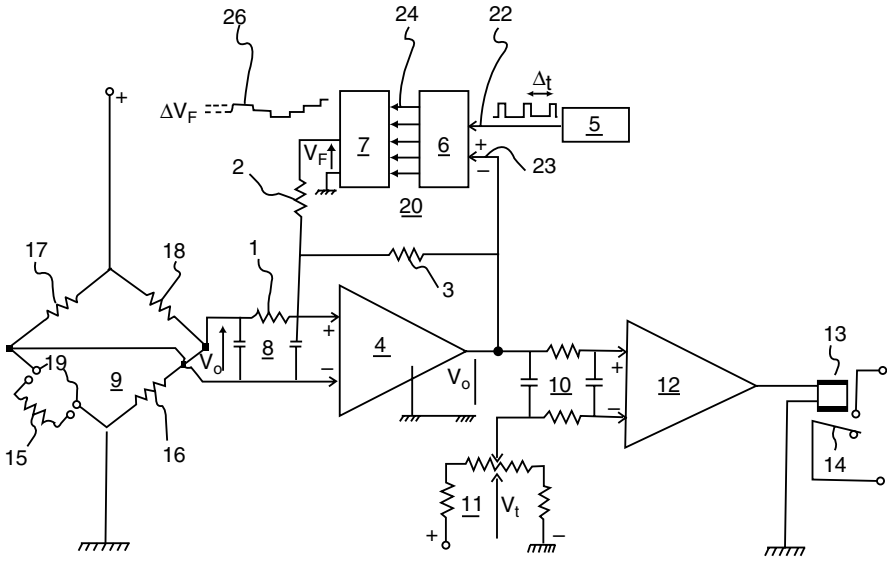

FIGURE 11.8 A circuit diagram of the device for fire warning or cable overheating. (From Vardorpe, J., Shape-memory fire and temperature device. European Patent 0-128-601, 1984. With permission.)

There are two types of these indicators: reversible and irreversible. In the reversible type, the temperature change will be indicated every time the temperature exceeds the indicated value. The irreversible type can be used only one time; once the temperature is exceeded, the color phase change remains as a permanent indication. Figure 11.9 shows some typical temperature stickers.

Temperature stickers are made of polymeric materials such as polyimide, polyesters, and acrylic polymers. The temperature range covered by these indicators is from −30°C to +290°C (Kapton) and usually cover rather limited ranges of temperatures in intervals of 5–6°C. For instance, typical ranges are: 40–71°C, 77–127°C (as seen in Figure 6.10), 132–182°C, and 188–249°C.

11.1.6 Remote Temperature Sensors

Elwood Co., in Wisconsin, has developed a very interesting and practical remote temperature sensor. The sensor, called PhoneDucer, is a simple device that can measure temperature, pressure, and low currents. By connecting it to the point of measurement in the manner of any typical transducer and plugging it into a phone line, this transducer becomes operational.

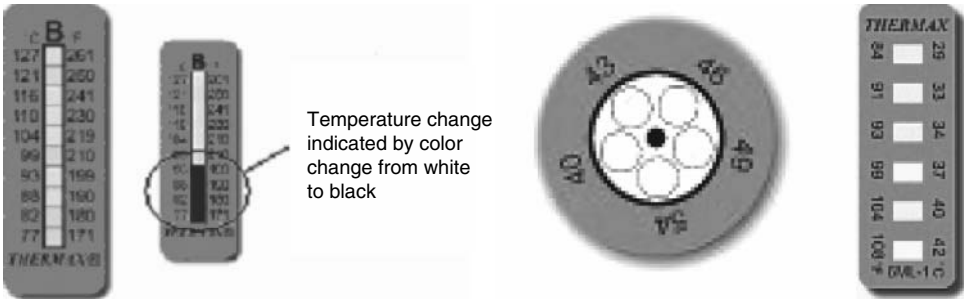

FIGURE 11.9 Typical temperature stickers (labels).

FIGURE 11.10 PhoneDucer. (From PhoneDucer, http://www.elwoodcorp.com. With permission.)

PhoneDucer can send accurate formatted data over standard phone lines by converting the raw analog or digital information obtained from its sensor to a modulated data form that is transmitted over telephone lines via a built-in modem. By programming a personal computer, multiple PhoneDucers in different remote locations can be accessed.

Once the information is in the computer, historical and periodic reports can be generated and conditions of the component under surveillance can be monitored. When PhoneDucer is called by a modem, the unit responds on the first ring and reports the current value of the monitored parameter. PhoneDucer will continue to issue updated readings every ten seconds until the dialing modem hangs up. The transmitted data is in ASCII, 8 bit, no parity.

Using data acquisition software and a computer with Windows, the information from multiple remote locations can be linked or pasted into a spreadsheet or other user-generated software. The remote interrogation ability of this transducer allows centralization of data acquisition for applications, ranging from remote locations within a facility to locations anywhere in the world. This transducer can be a very useful asset for monitoring power components in a switchyard which are very difficult to access and/or extremely remote. It is basically a thermocouple with incorporated telephone line connection. Temperature range covered by this transducer is -40 to $+460$°C. Figure 11.10 shows such a device.

11.2 RESISTANCE MEASUREMENTS

The principal function of an electrical connection is to carry effectively the electrical load over its entire service life. The electrical load, however, can have daily fluctuations, from no load to full loads, and frequently to very heavy overloads, thus causing wide fluctuations of operating temperatures. In addition, all power components are susceptible to aging and progressive deterioration that can partially or totally impair their designed function. The combined effect of heat cycling and aging on a poorly designed or improperly installed connection can lead to ultimate failure of the connection or associated equipment.

Contact resistance is one of the most important characteristics of power connectors and disconnect switches. It is the key element in providing early warning of electrical anomalies and is the most reliable indication of their deterioration and performance. Contact resistance stability is the most effective test for assessing reliability and predicting early failures of most types of power connections, including connectors and disconnect switches.

Properly implemented and maintained, contact resistance monitoring can assist in determining equipment and maintenance priorities, enhance operational safety, and contribute to a more reliable performance of the network as a whole. Resistance measurement data, collected during field inspections, can be used to develop and refine algorithms to facilitate proactive lifecycle and maintenance activities.

The technique most commonly used by utilities to monitor the conditions of power components is resistance measurement with a microohmeter. A microohmmeter uses a four-wire Kelvin

configuration, which eliminates the effect of leads and includes thermal emf and temperature compensations. Both AC and DC voltages and ambient temperature can be measured.

Most high-precision microohmmeters are equipped with the RS232/IEEE interface that enables stored data in the instrument memory to be downloaded to a computer or external printer. Depending on the manufacturer and the meter model, typical resistance range covered by the microohmmeters spans from 1 μΩ to 50 kΩ with a resolution of 0.1 μΩ.

Portability of some microohmmeters is enhanced with an optional battery-powered computer and printer housed in the lid of the instrument, making the whole system ideal for on-site calibration reports and certificates. The built-in data storage and interface to a computer or external printer enhances microohmmeter suitability for a wide range of on-site measurement and performance testing. Microohmmeters are used to measure contact resistances in high-voltage breakers, disconnecting switches, knife-contact fuses, bus joints, line joints, etc. Typical portable units suitable for the resistance monitoring are shown in Figure 11.11.

The high resolution of microohmmeters enables not only the measurement of very low resistance in power connections, but also allows them to be used as quality control tools. This is the case with aluminothermically welded connections such as ground connectors. The common practice for verifying the quality of these joints was only visual inspection; however, experience has shown that despite satisfying visual appearance, this method is ineffective to detect the presence of pores formed inside the weld due to variety of causes including incomplete fusion, trapped air or moisture, etc.

Figure 11.12 shows a microohmeter specifically designed to test the quality of the exothermic (aluminothermic) welded joints. This device uses specifically designed four-point probes to measure the voltage drop across the potential points. The microohmeter is also equipped with a microprocessor that eliminates offsets and parasite voltages. The unique filtering system allows measurements to be taken in the presence of intense magnetic fields.

Current and voltage contacts are spring-loaded gold plated probes with very sharp points that enable the establishment of good electrical contact by piercing the oxide on the part subjected to measurement. The worn-out probes points can easily be replaced. Figure 11.12 illustrates the ohmmeter (a), probes for resistance measurements on welded joints (b), and the measuring procedure (c).

The ohmmeter is also equipped with a split probe (Figure 11.12a) comprised of two holds, each one supporting a current and a voltage contact, so that the measuring distance may vary up to 1.2 m

Tinsley 5898 portable 200A precision micro-ohmmeter

Megger DLRO10X digital low resistance ohmmeter

FIGURE 11.11 Typical portable units suitable for the resistance monitoring.

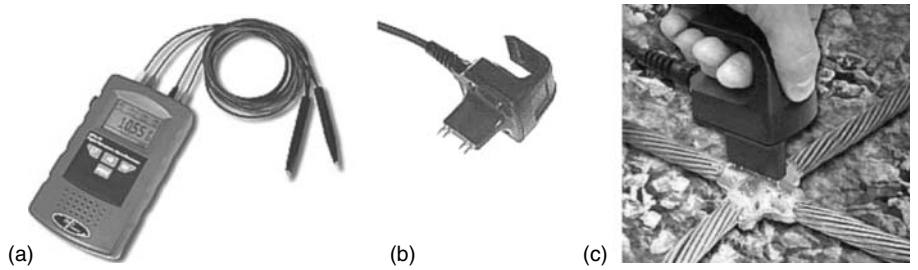

FIGURE 11.12 Microohmmeter DRM-40, probe and a close-up of resistance measurement of the welded joint. (From ndb Technologies, http://www.ndb.qc.ca. With permission.)

(48 in.). By pressing both holds against the piece tested, the current starts to flow and the measurement is displayed automatically on the LCD screen.

The advantage of this probe is that neither the distance between the measuring points nor the shape of the contact surface limits its use. In addition, the small spacing between the contact pins on the same probe eliminates the problem of current and voltage contact positioning during manipulations.

Although the resistance measurement method for monitoring the health of the power components has proven itself as one of the most valuable monitoring and diagnostic techniques for evaluating the component deterioration, its main disadvantage is that the measurements can only be taken on the nonenergized components.

This problem appears to have been solved by a new type of microohmeter, Ohmstik, introduced by the company Sensorlink.[961] Using the AC current in the line, this device enables measurements of resistance and current at any level of line loading above 5 A and on energized lines up to 500 kV. This live line device is a microohmeter mounted on a hotstick that is capable of measuring the resistance in the microohm ranges of connectors, splices, or switching devices carrying current. The instrument is pressed against the splice or connector in such a manner that the connection under test is between the two electrodes. After removing the unit from the line, the resistance and current readings are displayed on the LCD within 10 sec.

The Ohmstik calculates resistance by measuring the AC current in the line and the voltage drop due to the resistance of the line segment under test. This method of using the AC current in the line itself insures that realistic current distributions through the connection are being measured. No changes in the resistance measurement are seen with line currents ranging from 2 to 1400 A.

The advantage of this technique over infrared thermography is that emissivity, weather, current loading, background, and other infrared errors do not affect the measurements. This device can be used to assess the condition of almost any power connection in utilities, either after installation or after many years of service. Switches, fused disconnects, and normally open switches that have been open for long periods can be measured just after closing.

If the correct resistance of connection is not readily known, the Ohmstik can measure the resistance of a nearby line and then compare the resistance of connections to this line measurement. Connections are designed to have new resistance of 30–70% of the line they connect. The instrument can be programmed to indicate "good" or "bad" depending on this ratio and eliminate the need for linemen to know resistance values.

The Ohmstik comes in four different models. Two of these models make comparative readings of current and microohm resistance. The other two models offer the ability to measure current and micro-ohm in multiple locations and save the readings for future review. Standard and wide jaw sizes of the sensor opening are available for both styles. Figure 11.13 illustrates this device.

Based on the same detection principle, Sensorlink developed a device called QualstikPlus (see Figure 11.13) that is specifically intended to measure true RMS current, the power factor, total

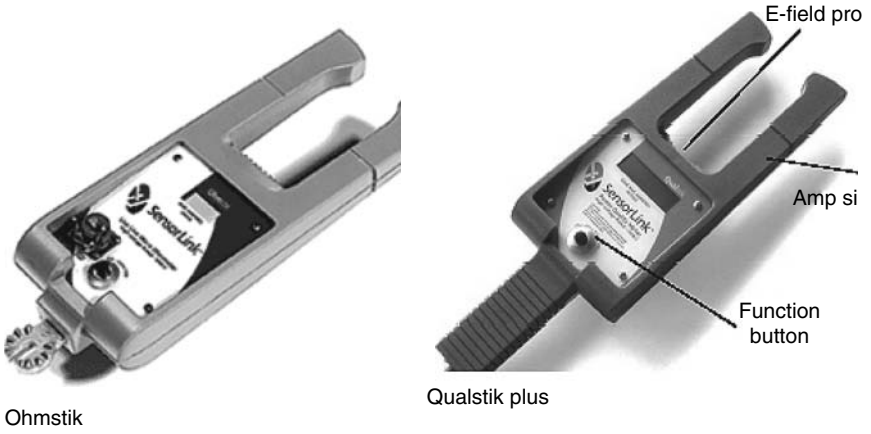

FIGURE 11.13 Ohmstik and Qualstik devices. (Courtesy of Sensorlink Corp., http://www.sensorlink.com.)

current harmonic distortion (THD), and current flow direction. The current is measured by a patented current sensor based on magnetic field induction pickup.

The Qualstik design uses a special air core inductor configuration which simulates the required closure. A large U-shaped inductor provides the primary magnetic field sensing, and small inductors near the opening of the sensor provide detection of the magnetic field moving in or out of the open part of the sensor and compensate for this leakage. Power factor sensing requires two sensors.

The voltage is measured by the electric field sensor, which is directly coupled to the line being measured, and is located in the bottom of the current sensor. The magnitude of the voltage is unknown, but the waveform is precise. By comparing the current and voltage waveforms, an accurate power factor can be calculated. The Total Harmonic Distortion (THD A) of current is a measurement of the percentage of non-sixty/fifty cycle current as compared to the total current and is shown on the meter display as a number from 0% to 100%.

The direction of current flow is determined by measuring the relative phase angle of voltage and current. Since this instrument has no moving parts and does not require clamping onto the wire, it can be used remotely with any hotstick and universal chuck adapter. Direct connections to a bare conductor are required to ensure power factor measurement accuracy.

Figure 11.14 shows several examples how the Ohmstik was used to measure the resistance of each half-joint in mid-span splices.[962]

The advantages and superiority of resistance measurements over IR thermography in detecting the signs of early deterioration in connections is clearly shown in Table 11.4, which is based on the results reported by Snell and Renowden.[962]

11.3 MONITORING CONTACT LOAD (PRESSURE)

Establishing and maintaining required contact load is essential for reliable performance of an electrical connection. Hence, online monitoring of contact loads would provide a possibility to survey the behavior of power connections under normal and overload operating conditions. Unfortunately, monitoring of contact loads can only be applied to bolted-type connections and not to the other types such as compression or insulation piercing connectors.

Figure 11.15 shows instrumented bolts with a foil type bonded strain gauges inserted in a hole drilled inside the bolt to measure the force in the bolt and thus of the joint. This technique consists of the installation of foil type strain gauges inside a small hole drilled along the longitudinal neutral axis of the stud. The hole depth is confined to the shank of the bolt, and the hole diameter is

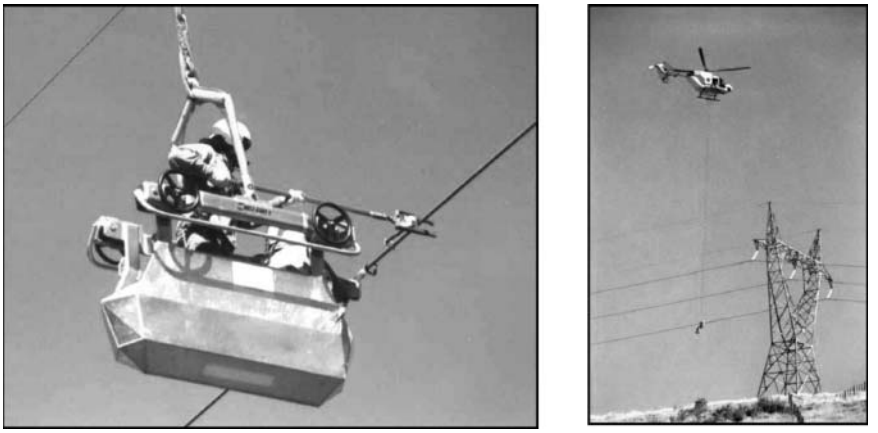

FIGURE 11.14 In-field measurement of joint resistance using Ohmstik. (Courtesy of NZ Transpower; Snell, J. and Renowden, J., Improving results of thermographic inspections of electrical transmission and distribution lines. Paper presented at *IEEE ESMO 2000*, Montreal, Canada, 2000.)

controlled so that the bolt cross-section through the threads is smaller than the section through the shank with the gauge hole. This allows the gauge installation to withstand and accurately indicate loads in high strength bolts.

The force changes are monitored and recorded with a strain-gauge data logger. These fasteners provide a means for accurate, independent inspection of an assembled bolt and thus enhance the structural integrity and reliability of both the bolt and the assembly. However, the drawback of this monitoring technique is that extensive wiring has to be used to connect the instrumented bolts to the data acquisition systems. Therefore, this method is suitable for monitoring the bolted joints in generating stations where vibration and other strenuous influences may provoke loosening of the joints.

11.4 ULTRASONIC MEASUREMENTS

Ultrasonic detectors provide a method of detecting sounds greater than 20 kHz. Loose electrical connections emit characteristic sounds that are beyond the range of the human ear. The ultrasonic detector provides a method of converting inaudible sounds to sounds and tones that match our hearing capabilities. Flashovers across an insulator make crackling sounds that are detectable even when there are no visible signs of arcing.

The basic operation of the ultrasonic detector is relatively simple, as illustrated schematically in Figure 11.16. A transducer, generally equipped with some type of mechanical sound focusing aid, collects the sound energy and passes it to the amplifier, which feeds the modulator section where the collected sound is mixed with a signal from the oscillator section. The mixing of the two signals in the modulator produces a sum frequency, f_1+f_2, and a difference frequency, f_1-f_2. The difference frequency is sent to the output amplifier that provides the audible signal so that arcing and corona discharge can be heard as a buzzing sound on the speaker/headset. The closer the transducer is to the source, the more intense the signal.

A typical use for the ultrasonic detector is detection of loose or arcing connections inside an enclosed cabinet or panel board. Ultrasonic energy resulting from a loose electrical connection should be in the range of 40–50 kHz. Mixing a 40 kHz signal from the detector oscillator section produces a difference signal in a range up to 10 kHz that can be heard from the speaker (or headphone) on the detector unit. Ultrasonic detection equipment can determine incipient

TABLE 11.4
Actions Required Based on the Resistance Ratio and Likelihood of an Infrared Survey Indication in the Various Categories Where the Resistance Ratio Shows Required Action to Be Taken for Deteriorated Connection

Category	Resistance Ratio R/R_c[a]	Condition of Power Connection	Action Needed Based on Resistance Ratio	Likelihood of Infrared Detection
1	0.3–1.0	*Normal connection*—new connections are expected to be in the 0.3–0.8 range	None	*None*—connection will be cooled than conductor
2	1.01–1.2	*Serviceable, shows deterioration*—overloads and faults may deteriorate the connection	Reinspect in one year or after next fault	*None*—connection will appear to be cooler than conductor
3	1.21–1.5	*Serviceable, poor*—overloads and faults may deteriorate the connection	Reinspect in 6 months or after next fault	*Unlikely*—connection may appear to be cooler than conductor
4	1.51–2.0	*Serviceable, very poor*—high loads, overloads or faults may deteriorate the connection	Schedule replacement in less than 3 months	*Unlikely*—connection may appear to be cooler than conductor
5	2.01–3.0	*Bad, deterioration is increasing*—high loads, overloads or faults mail fail the connection. High tension from cold weather of wind may initiate failure under normal loading	Schedule replacement very soon	*Possible*—connection may be close to or the same as conductor
6	>3.0	*Failing*—Normal loads, overloads or faults may fail the connection. High tensions from cold weather or wind are likely to initiate failure under normal loading	Replace as soon as possible (ASAP)	*Somewhat likely*—connection may still be masked at this load level

*Note*1: Estimates of likelihood of detection by IR thermography are based on IEEE ESMO 2000 paper 28C-TPC 17 by Snell J. and Renowden J.[14]

*Note*2: Conductor 795 ACSR 26/7 has 25% of rated load current. Wind in 5 km/h (daytime air is rarely this slow) cooling the connection more than the conductor due to its larger surface area and thereby further masking the connection. Emissivity of conductor and connection is set at 0.7. The connection emissivity can be lower than the conductor, further masking the connection.

[a] R/R_c, Resistance ratio between the connection and conductor.

connection failure that thermography (infrared) could miss since connections often do not produce enough heat to be detected, or the surrounding heat source would mask the problem. This technique can be utilized to measure stress relaxation in bolting (Figure 11.17).

Recent advancements in ultrasound detection include dynamic memory capacity, digital data processing, the use of true RMS technology for enhanced repeatability, and two-way data transfer between the instrument and the computer. If while scanning from the ground, the signal intensity is

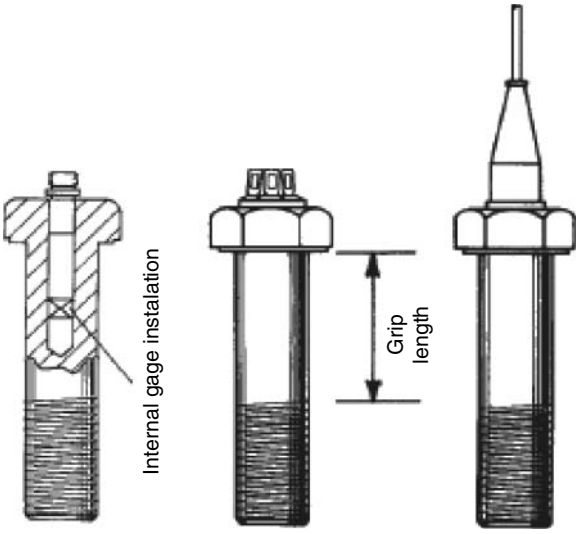

FIGURE 11.15 Schematic of strainsert instrumented bolts.

insufficient to detect an incipient problem with power components, an ultrasonic waveform concentrator (a parabolic reflector) can be used to double the detection distance of the system and provide pinpoint detection.

11.5 WIRELESS MONITORING

One of the most notable trends in utilities and industry as a whole is the desire to integrate real-time operating and equipment status data from field devices and measurement and control systems with enterprise-wide systems controlling overall network reliability and asset management. However, one of the most serious barriers in achieving this goal is the inability to easily integrate information from the field measurement and control systems with maintenance management systems.

Accurate knowledge of the sources affecting the in-service performance of electrical/electronic components and means of reducing or eliminating these can lead to substantial improvement in the system reliability within the allowable operating limits. To achieve these objectives, it is imperative to identify and acquire the knowledge of diagnostic tools available for monitoring, control and evaluating the service performance of power components.

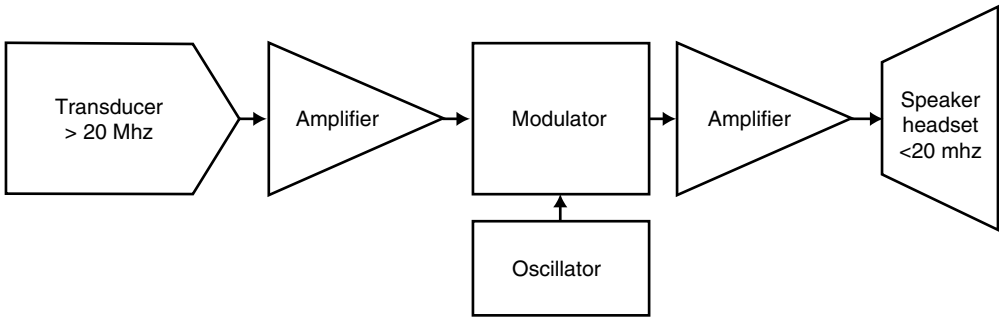

FIGURE 11.16 Schematic of an ultrasonic detector.

These goals can be attained through the use of wireless technology which simplifies the deployment and extends the functionality of these systems by embedding radio technology in a wide variety of inexpensive battery-powered sensors. Unconstrained by wiring that can be very expensive, this emerging technology has the potential to save industry vast amounts of lost productivity. Furthermore, without the necessity to connect cabling to specific locations and high costs, wireless networks allow for the speedy deployment of new systems, saving considerable time and associated cabling costs.

In recent years, wireless technology is experiencing unprecedented growth due to its practically unlimited potential applications in power, agriculture, medicine, transportation, meteorology, etc. The use of wireless sensors can help to avoid the costly failures of power and electronic devices or components by providing an early warning of impending critical situation.

The advantages and disadvantages of wireless technology are listed in Table 11.5.

In the rest of this section, a brief description of the most pertinent wireless devices presently available on the market and systems for monitoring the actual condition of power devices, systems, and components will be given.

The Power-Donut2™ is an engineering instrumentation platform whose functions include data acquisition, data monitoring, and logging of the parameters of high-voltage overhead conductors.[15] The Power-Donut2™ is completely self-contained, allowing for hot-stick installation with no required outage. It measures current, voltage, MW, MVars, conductor temperature, and conductor sag angle stores data on board. The acquired data is transmitted in real time using spread spectrum wireless technology or on demand using a GSM wireless cell phone.

The Power-Donut2 needs no supporting infrastructure. It can be installed onto a live conductor by means of a hot stick without taking an outage. A fitted hub assembly attaches the Donut to the customer's conductor; hubs are available for the entire range of transmission conductor sizes including bundled conductor configurations. The Donut is powered by magnetic flux coupling from the conductor and operates on all voltage level systems up to 500 kV.

TABLE 11.5
Advantages and Disadvantages of Wireless Technology

Advantages	Disadvantages
Reliable remote data acquisition and transmission	Signal attenuation
Improved data accuracy and faster decision making	Need for repeaters
Cost effective	Miniaturization of electronic circuitry, such as MEMS, still in development phase Limited battery life
Possibility of two-way operation from one central base	Limited radio band operation
Remote monitoring, control and assessment of the state of the operating systems	Packaging of wireless devices requires further improvements
Reduced inefficiencies in the maintenance process	
Electronic data collection eliminates limitations of paper-based systems	
Operation in hazardous and difficult-to-reach environments	
Reliability; security; flexibility; and scalability	
Possibility of self-power operation	
Ability to eliminate unscheduled downtimes	
Ease of operation and elimination of process problems	
Compatibility with existing products, components, systems	
Determine operational status of energized equipment	
Evaluate current physical condition of equipment	
Initiate actions preventing upcoming failure	
Schedule condition based equipment maintenance	

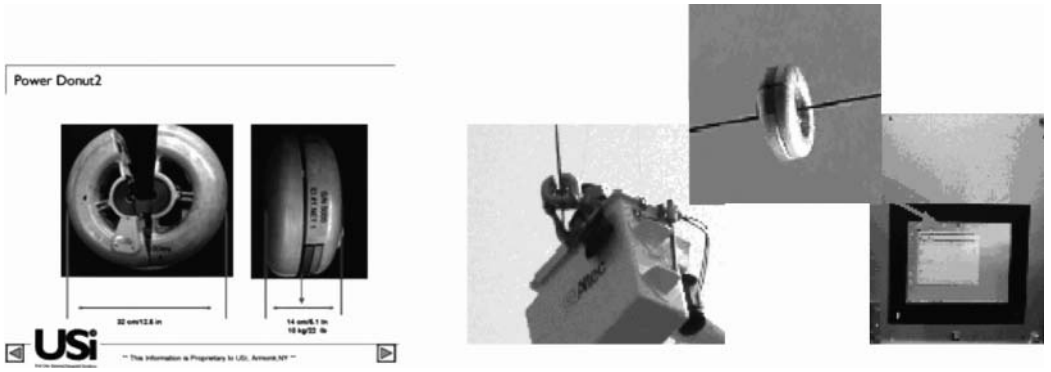

FIGURE 11.17 General view and installation of USi power donut2. (Courtesy of USi, USi power donut2, http://www.usi-power.com.)

The Power-Donut2's built-in radio modem is capable of communicating with ground receivers several kilometers away. U.S.-approved 900 MHz and European-approved 2.4 GHz radios are available. The Donut may be used in real-time, Wide Area Management Systems, in SCADA and Energy Management Systems, and has on board flash memory for analog and event data logging. Users retrieve alarms and data from the Donut using proprietary USi/Nitech software.

The Power-Donut2 includes expansion I/O, expansion memory and has the onboard computational power to implement custom applications. The Power-Donut2's built-in GSM Cell Phone Modem is capable of receiving calls from a remote communications controller,\ and will automatically phone home on pre-set alarm conditions.

SQUARE D wireless temperature monitoring system. Because temperature rise is one of the principal indications of overheating of power units, components or devices, continuous monitoring or alarm reporting when temperature limits are exceeded is of great importance to the reliability of the power system. Figure 11.18a illustrates the schematic of the Square D wireless temperature sensor arrangement, whereas the actual location in a power plant is depicted in Figure 11.18b.[964] Receiving distance is 100 feet (30 m).

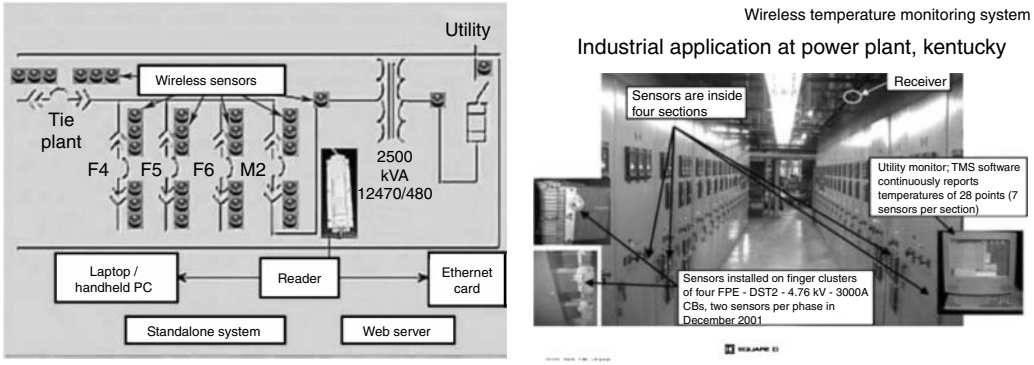

FIGURE 11.18 (a) Schematic of wireless temperature monitoring system; (b) physical positioning of the temperature monitoring sensors. (Courtesy of Square D, Square D wireless temperature monitoring systems, http://www.squared.com.)

This system provides continuous online wireless temperature monitoring by simultaneously measuring temperature of multiple points, thus providing timely detection of abnormal thermal conditions within the cells and monitoring temperature of the points to which visual access is impossible such as behind metallic and insulation barriers. This system does not interfere with dielectric performance of the equipment nor affects electrical and mechanical performance.

Owing to its small size (diameter = 40 mm and height = 25 mm), the system can be installed in very limited spaces. Installation requires no additional testing of performance integrity. It has widespread applications such as in connectors, circuit breakers, switchgear, capacitor banks, transformers, motors, busways, cables, and HV and EHV electrical equipment. This system operates in direct contact with the surface. Enclosure is dielectric and it is waterproofed for humid, corrosive and high-temperature environments. The life of the battery is a minimum of 5 years, with a typical life of 7–10 years, and is easily changeable.

Omega long distance telemetry systems. Another example of wireless temperature monitoring is shown in Figure 11.19. This shows OMEGA's LDTX20 Series long distance wireless data transmitters which are suitable for applications where long distance wireless communication is required.[965] The transmitting range is 3.2 km. The transmitters are powered by a 12 volt internal supply (chargeable) for continuous, uninterrupted measurements. Their small size and light weight enable most measurements to be made without cumbersome transmitter installations. The system operates on UHF at carrier frequency of 450–470 MHz and transmits strain gauge, voltage, and thermocouple signals.

The LDRX20 receiver is also small in size and easy to use. It features a built-in speaker, 110 V AC operation and front-panel zero and span adjustments. The receiver's antenna is conveniently packaged in a remote box, which enables the antenna to be mounted in close proximity to the receiver. The antenna assembly and the base receiver unit are attached with a supplied BNC interface cable.

MTM CdTe temperature sensor/transmitter. Another telemetry temperature system is shown in Figure 11.20. The system was developed at the University of Belgrade's Institute for Microelectronic Technologies and Single Crystals.[966] The system is based on the CdTe optical sensor, thus eliminating the adverse effects of electromagnetic interferences. It can safely be used in the presence of inflammable fluid or explosives (intrinsic safety).

Digital processing is realized using microprocessor-based transmitters, digital calibration, and linearization. It has multichannel transmitters, in which several temperature sensors share the same transmitter. Since it is a nonmetallic type of sensor, there is no need for electrical insulation. Figure 11.20 depicts the schematic diagram of the system and possible system configurations.

In summary, it can be said that the above examples are but a few representative examples of the remarkable potential offered by wireless technologies. Such technologies indeed represent a giant

FIGURE 11.19 Omega telemetry system. (Courtesy of Omega, Omega long range telemetry system, http://www.omega.com.)

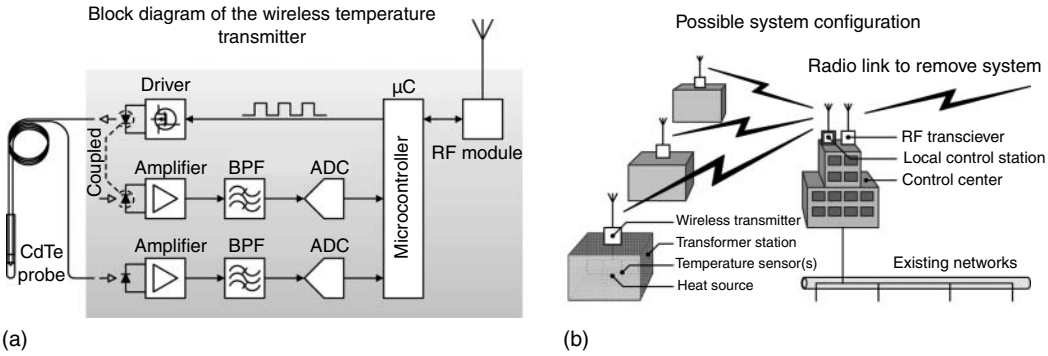

FIGURE 11.20 (a) MTM wireless temperature transmitter and (b) Possible system configurations for wireless transmitter system. (From Djuric, Z. and Frantlovic, M., Wireless CdTe-based temperature transmitter system. Private communication. With permission.)

step forward in the fields of condition-based monitoring (CBM) as well as predictive and preventive maintenance. Wireless technology is undoubtedly going to have a lasting impact on many industries since it provides benefits that directly satisfy their needs in terms of reliability, monitoring, maintenance, security, and quality while meeting goals such as cost savings and streamlined processes.

11.6 COST BENEFITS OF MONITORING AND DIAGNOSTIC TECHNIQUES

Failures of power components often have economical consequences that extend beyond the cost of replacing or repairing the damaged components. In some cases, the cost of the component is not necessarily the main expense because power delivery downtime can offset the cost of replacing the equipment or component. If examples of what has actually happened are not provided, then making a case for what can happen is rather difficult. Hence, it is essential to have the historical data to provide a bridge from the theoretical to the real world.

For a utility embarking on tracking the cost/benefits of its monitoring and diagnostic programs, it is essential to follow and systematically record the cost to fix problems before versus after failure. This in turn will produce an estimate of savings for the utility. Hence, setting up a comprehensive predictive maintenance program with good maintenance follow-up procedures will reduce the extreme examples of potential loss.

One of the most important advantages of using a substation monitoring system is the ability to help mitigate the effects of a catastrophic failure of substation equipment. Monitoring systems enable the detection of faults evolving over a shorter period and thus increase the ability of a utility to minimize the probability and effects of a costly failure. By comparing the costs of parts and labor before versus after failure, a desirable cost savings ratio should be 1:4. From a return on investment perspective, monitoring and diagnostic programs should be able to assure that for every $1 spent on electrical inspections using these programs, a $4 return on investment should be realized for materials and labor from fixing the problems before it fails.

Formal cost-benefit analysis often demands costly and sometimes disputed expertise and data. If completed carefully, information provided will contribute to the decision process. However, if poorly made or taken out of context, the results can create a false sense of clarity and security.

Wurzbach[967] has described a web-based method enabling a universal generic cost benefit calculator that can be accessed from the Internet. The calculator prompts the user for information about the industry, equipment type and predictive maintenance costs that is then used to form a database.

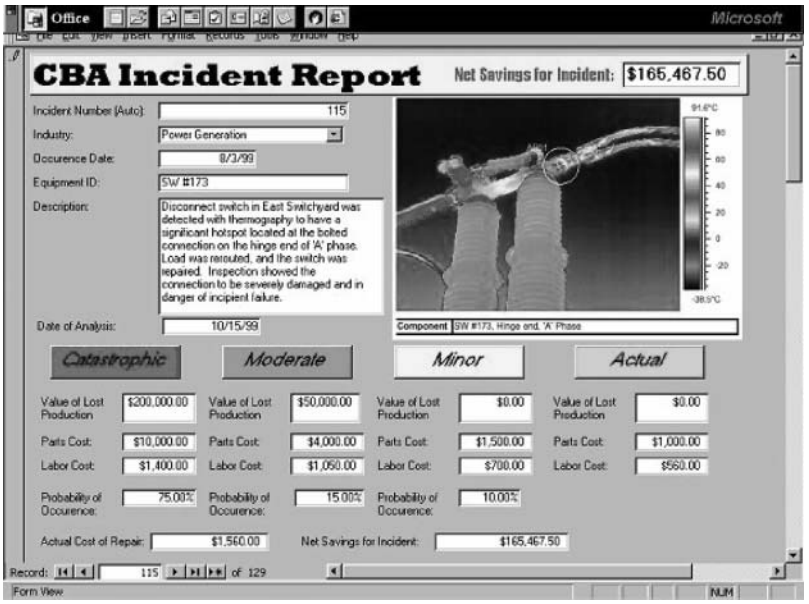

FIGURE 11.21 Typical cost benefits analysis report provided by the web-based method developed by the Maintenance Reliability Group (MRG). (From Wurzbach, R. N., A web-based cost benefit analysis method for predictive maintenance, http://www.mrgcorp.com. With permission.)

The database provides statistical means for the given industry and equipment types and allows the user to make modifications. The calculator also prompts the user for a number of scenarios for the identified anomaly and requires that they be rated as a percentage of probability of occurrence.

The calculator then performs the cost benefits analysis and gives statistical information about how this analysis falls among the statistical distribution of analyses specific to equipment type. The calculator does not query the user for identifying information such as the company's or individual's name. The input data is used for statistical analysis only, thus preserving the confidential nature of company information.

Figure 11.21 illustrates the combination of the supplied and calculated data, with an infrared image providing an immediate impact of potential faults occurring on disconnect switches. The image is directly related to the incident, and supplies with a single picture the story of a latent anomaly that could have led to a significant equipment failure and plant shutdown. Hence, it can be concluded that one of the most important advantages of using a substation monitoring system is its ability to help mitigate the effects of a catastrophic failure of the substation equipment.

A monitoring system allows for the detection of faults that evolve over shorter periods. It is clear, however, that although there will always be a probability that some faults will occur instantaneously and without warning that no type of monitoring can detect, an intelligent monitoring system would provide the utility with the ability to lessen the effects of a failure. Even though a failure can be costly, the probability of a catastrophic failure can be minimized.

The total cost of failure of practically any component of a power system is difficult to fully realize since the impact is usually far-reaching. Although lost revenue, repair costs, repairing, replacing and/or refurbishing, and other direct external damages can be quantified, the costs of property damage claims alone can be significant in comparison to the costs of re-tooling and re-designing to eliminate future failures.

References

1. Holm, R., *Electrical Contacts*, Springer, New York, 1979.
2. Myshkin, N. K., Tribology of electrical contacts, In *Tribology in the U.S.A. and Former Soviet Union*, Belyi, V. A., Ludema, K., and Myshkin, N. K., Eds., Allerton Press, New York, pp. 341–364, 1994.
3. Braunović, M., Power connections, In *Electrical Contacts: Principles and Applications*, Slade, P. G., Ed., Marcel Dekker, New York, pp. 155–270, 1999.
4. Timsit, R. S., Electrical contact resistance: Fundamental principles, In *Electrical Contacts: Principles and Applications*, Slade, P. G., Ed., Marcel Dekker, New York, pp. 1–88, 1999.
5. Antler, M., Materials, coatings, and platings, In *Electrical Contacts: Principles and Applications*, Slade, P. G., Ed., Marcel Dekker, New York, pp. 403–433, 1999.
6. Glossbrenner, E. W., Sliding contact for instrumentation and control, In *Electrical Contacts: Principles and Applications*, Slade, P. G., Ed., Marcel Dekker, New York, pp. 885–941, 1999.
7. Shobert, E., Sliding electrical contacts (graphite type lubrication), In *Electrical Contacts: Principles and Applications*, Slade, P. G., Ed., Marcel Dekker, New York, pp. 839–872, 1999.
8. Cacic, M., Performance improvement for sliding contacts utilizing tip polishing, *Proceedings of 47th IEEE Holm Conference on Electrical Contacts*, Montreal, Canada, September, 25–27, pp. 288–292, 2001.
9. Liu, S., Carbon fiber contactor in polymer resistive position sensors, *Proceedings of 47th IEEE Holm Conference on Electrical Contacts*, Montreal, Canada, September, 25–27, pp. 282–287, 2001.
10. Buckley, D. H., *Surface Effects in Adhesion, Friction, Wear, and Lubrication*, Oxford/Elsevier, Amsterdam/New York, 1981.
11. Thomas, T. R., *Rough Surfaces*, Imperial College Press, London, 1999.
12. Myshkin, N. K., Petrokovets, M. I., and Chizhik, S. A., Wear measurements and monitoring at macro- and microlevel, In *Fundamentals of Tribology and Bridging the Gap Between the Macro- and Micro/Nanoscales*, Bhushan, B., Ed., Kluwer Academic Publishers, Dordrecht, pp. 423–438, 2001.
13. Johnson, K. L., *Contact Mechanics*, Cambridge University Press, Cambridge, 1985.
14. Nayak, P. R., Random process model of rough surfaces, *ASME Journal of Lubrication Technology*, 93, 398–407, 1971.
15. Hutchings, I. M., *Tribology: Friction and Wear of Engineering Materials*, Edward Arnold, London, 1992.
16. Timoshenko, S. P. and Goodier, J. N., *Theory of Elasticity*, McGraw-Hill, New York, 1951.
17. Greenwood, J. A. and Williamson, J. B. R., Contact of nominally flat surfaces, *Proceedings of the Royal Society*, A295, 300–319, 1966.
18. Greenwood, J. A. and Tripp, J. H., The elastic contact of rough spheres, *ASME Journal of Applied Mechanics*, 34, 153–159, 1967.
19. Sayles, R. S. and Thomas, T. R., Surface topography as a non-stationary random process, *Nature*, 271(5644), 431–434, 1978.
20. Myshkin, N. K., Petrokovets, M. I., and Chizhik, S. A., Basic problems in contact characterization at nanolevel, *Tribology International*, 32(7), 379–385, 1999.

21. Myshkin, N. K., Petrokovets, M. I., and Kovalev, A. V., AFM applications for contact and wear simulation, In *Applied Scanning Probe Methods III*, Bhushan, B. and Fuchs, H., Eds., Chapter 9, Springer, New York, pp. 305–332, 2005.
22. Archard, J. F., Elastic deformation and the laws of friction, *Proceedings of the Royal Society A*, A243, 190–205, 1957.
23. Bowden, F. P. and Tabor, D., *Friction and Lubrication of Solids*, Clarendon Press, Oxford, 1986.
24. Kragelskii, I. V., *Friction and Wear*, Pergamon Press, Elmsford, 1982.
25. Dowson, D., *History of Tribology*, Longman Group, London, 1979.
26. Antler, M., Tribology of electronic connectors: Contact sliding wear, fretting, and lubrication, In *Electrical Contacts: Principles and Applications*, Slade, P. G., Ed., Marcel Dekker, New York, pp. 309–402, 1999.
27. Gao, C. and Kuhlmann-Wilsdorf, D., Adsorption films, humidity, stick–slip and resistance of sliding contacts, *Proceedings of 36th IEEE Holm Conference on Electrical Contacts*, Montreal, Canada, August 20–24, pp. 292–300, 1990.
28. Gao, C., Kuhlmann-Wilsdorf, D., and Makel, D. D., Fundamentals of stick–slip, *Wear*, 162–164, 1139–1149, 1993.
29. American Society for Metals (ASM), *Friction, Lubrication, and Wear Technology ASM Handbook*, Vol. 18, ASM International Materials Park, Ohio, 1992.
30. Archard, J. F., Contact and rubbing of flat surfaces, *Journal of Applied Physics*, 24, 981–990, 1953.
31. Khruschov, M. M., Resistance of metals to wear by abrasion, as related to hardness, *Proceedings of Conference on Lubrication and Wear*, London, pp. 655–659, 1957.
32. Clark, W. T. and Lancaster, J. K., Breakdown and surface fatigue of carbon during repeated sliding, *Wear*, 6(6), 467–482, 1963.
33. Welsh, N. C., The dry wear of tool steel, *Philosophical Transactions of the Royal Society of London*, 257, 31–70, 1965.
34. Fagerstrom, W. B. and Nicotera, E. T., Fretting corrosion in connectors, *Proceedings of the Connectors and Interconnections Symposium*, Philadelphia, Electronic Connector Study Group, pp. 303–312, 1981.
35. Suh, N. P., The delamination theory of wear, *Wear*, 25, 111–124, 1973.
36. Suh, N. P., Jahanmir, S., Abrahamson, E. P., and Turner, A. P. L., Further investigation of the delamination theory of wear, *Journal of Lubrication Technology*, 96 (4), (Oct), 631–637, 1974.
37. Jahanmir, S., Suh, N. P., and Abrahamson, E. P., The delamination theory of wear and the wear of a composite surface, *Wear*, 32, 33–49, 1975.
38. Marcinkowski, M. J., A surface dislocation model of wear, *Journal of Materials Science*, 19, 1296–1306, 1984.
39. Bednar, M. S. and Kuhlmann-Wilsdorf, D., Amorphous and alloy film formation in sliding of silver on copper, *Wear*, 181–183, 922–937, 1995.
40. Kuhlmann-Wilsdorf, D., What role for contact spots and dislocations in friction and wear?, *Wear*, 200, 8–29, 1996.
41. Bates, T. R. and Ludema, K. C., Comments on "The delamination theory of wear." 1974, *Wear*, 28, 141–142, 1974.
42. Rigney, D. A., The role of hardness in the sliding behaviour of materials, *Wear*, 175, 63–69, 1994.
43. Rigney, D. A., Physical aspects of friction and wear, In *Tribology in the U.S.A. and Former Soviet Union*, Belyi, V. A., Ludema, K., and Myshkin, N. K., Eds., Chapter 2.3, Allerton Press, New York, pp. 53–65, 1994.
44. Alexeev, N. M. and Dobychin, M. N., Wear models, In *Tribology in the U.S.A. and Former Soviet Union*, Belyi, V. A., Ludema, K., and Myshkin, N. K., Eds., Chapter 2.4, Allerton Press, New York, pp. 67–88, 1994.
45. Hermance, H. W. and Egan, T. F., Organic depositions on precious metal contacts, *Bell System Technical Journal*, 37, 739–777, 1958.
46. Antler, M., Effect of lubricants on friction polymerization and the contact resistance of palladium, *Proceedings of International Conference on Electrical Contact Phenomena,* West Berlin, Germany, June 7–11, pp. 148–152, 1982.

47. Karasawa, K., Chen, Z.-K., and Sawa, K., Effect of impact and wipe action on contact resistance increase in pd material, *Proceedings of 41st IEEE Holm Conference on Electrical Contacts,* Montreal, Canada, October 2–4, pp. 282–288, 1995.
48. Bhushan, B., *Handbook of Micro/Nanotribology*, CRC Press, Boca Raton, 1995.
49. Abbott, W. H., Mechanism of tarnishing of silver and copper, *Proceedings of 14th IEEE Holm Seminar*, Chicago, USA, pp. 53–54, 1968.
50. Abbott, W. H., Effect of industrial air pollutants on electrical contact materials, *Proceedings of 19th IEEE Holm Seminar,* Chicago, USA, pp. 94–99, 1973.
51. Campbel, W. K., Reduction of the rate of film formation on silver and brass by purification of the Atmospheres, *Proceedings of 6th International Conference on Electrical Contact Phenomena,* Chicago, USA, pp. 185–194, 1972.
52. Hirakawa, R., Suzuki, S., Matsuda, A., and Shibata, N., Cd-free silver alloy for sliding contact, *Proceedings of 38th IEEE Holm Conference on Electrical Contacts*, Philadelphia, USA, October 18–21, pp. 119–124, 1992.
53. Potinecke, J., Behavior of contact surfaces consisting of Ag- and Pd-alloys in H_2S-NO_2-SO_2 atmospheres, *Proceedings of 21th IEEE Holm Seminar,* Illinois Institute of Technology, Chicago, USA, pp. 139–144, 1975.
54. Crossland, W. A., Knight, E., and Wright, C. R., The exelerated tarnish testing of contacts and connector employing silver alloy contacts, *Proceedings of 19th IEEE Holm Seminar,* Chicago, USA, pp. 265–270, 1973.
55. Campbel, W. K. and Lee, R. E., Polymer formation on sliding metals in air saturated with organic vapors, *ASLE Transactions*, 5(1), 91–104, 1962.
56. Abbott, W. H. and Campbel, W. K., Friction polymer formation on precious metals. Experimental observation, *Proceedings of 9th International Conference on Electrical Contact Phenomena,* Chicago, USA, pp. 359–363, 1978.
57. Todoraki, T. and Shida, S., Wear of silver–copper alloy sliding contacts, *Proceedings of 8th International Conference on Electrical Contact Phenomena,* Tokyo, Japan, pp. 375–380, 1976.
58. Claus, H., Kocher, H.-H., and Stockel, D., Properties and applications of copper/palladium composite materials for electrical contacts, *Proceedings of 30th IEEE Holm Conference on Electrical Contacts*, Illinois Institute of Technology, Chicago, pp. 455–461, 1984.
59. Antler, M., Wear of electroplated gold, *ASLE Transactions*, 11, 240–260, 1962.
60. Antler, M., Tribological properties of gold for electrical contacts, *IEEE Transactions on Parts, Hybrids and Packaging*, 9(1), 4–14, 1973.
61. Horn, G. and Merl, W., Friction and wear of electrodeposited hard gold deposits for connectors, *Proceedings of 6th International Conference on Electrical Contact Phenomena,* Chicago, USA, pp. 65–72, 1972.
62. Baker, R. G. and Palumbo, T. A., The case for end-point requirements in gold plating specifications in electronic equipment, *Plating*, 58(8), 791–800, 1971.
63. Harmsen, N., Spring-hard precious metal alloys with good tarnishing behavior for electrical contacts, *Proceedings of 8th International Conference on Electrical Contact Phenomena,* Tokyo, Japan, pp. 69–74, 1976.
64. Abbott, W. H., Mechanism of tarnishing of precious metal contact alloys, *Proceedings of 15th IEEE Holm Seminar,* Chicago, USA, pp. 1–6, 1969.
65. Yamazaki, S., Naysuema, T., Kishimato, Y., and Kanno, N., Investigation of contact resistance of open contacts covered by ammonium sulphates films, *Proceedings of 8th International Conference on Electrical Contact Phenomena,* Tokyo, Japan, pp. 281–286, 1976.
66. Solos, L. P., Organic adsorption on precious metals and its effect on static contact resistance, *Proceedings of 16th IEEE Holm Seminar,* Chicago, USA, pp. 27–36, 1970.
67. Taylor, O. S. and Hannan, W. F., Solid brush system evaluation for pulsed high current applications, *Wear*, 78, 151–162, 1982.
68. Challita, A. and Bauer, D., Solid copper commutation brushes for seawater use, *Proceedings of 39th IEEE Holm Conference on Electrical Contacts,* Pittsburg, USA, September 27–29, pp. 135–140, 1993.
69. Walls, W. A., High-speed high-current copper finger brushes for pulsed homopolar generator service, *IEEE Transactions on Components, Hybrids and Manufacturing Technology*, 9(1), 117–123, 1986.

70. Kuhlmann-Wilsdorf, D., Metal fiber brushes, In *Electrical Contacts: Principles and Applications*, Slade, P. G., Ed., Marcel Dekker, New York, pp. 943–1017, 1999.
71. Lupton, W. H. and Riechner, P., Ultrahigh speed fiber brush design and tests, *Wear*, 78, 139–150, 1982.
72. Kuhlmann-Wilsdorf, D. and Alley, D. M., Commutation with metal fiber brushes, *IEEE Transactions on Components, Hybrids and Manufacturing Technology*, 12(2), 246–253, 1989.
73. Adkins, C. M. and Kuhlmann-Wilsdorf, D., Development of high-performance metal fiber brushes. I. background and manufacture, *Proceedings of 25th Holm Conference on Electrical Contacts,* Chicago, USA, pp. 165–170, 1979.
74. Kuhlmann-Wilsdorf, D., A versatile electric fiber brush and method of making, U.S. Patent 4,358,699, filed Nov. 9, 1982.
75. Kuhlmann-Wilsdorf, D., Adkins III, C. M., and Wilsdorf, D., An electric brush and method of making, U.S. Patent 4,415,635, filed Nov. 15, 1983.
76. Kuhlmann-Wilsdorf, D., Awardees' address: uses of theory in the design of sliding electrical contacts, *Proceedings of 37th IEEE Holm Conference on Electrical Contacts*, Institute of Electric and Electronic Engineers, Inc. *CHMT*, Chicago, USA, October 6–9, pp. 1–24, 1991.
77. Reichner, P., High current tests of metal fiber brushes, *IEEE Transactions on Components, Hybrids and Manufacturing Technology*, 4(1), 2–5, 1981.
78. Bouer, L., Chabrerie, J. P., and Saint-Michel, J., Low wear metallic fiber brushes, *Wear*, 78, 59–68, 1982.
79. Kuhlmann-Wilsdorf, D., Electrical fiber brushes—theory and observations, *IEEE Transactions on Components, Hybrids and Manufacturing Technology*, 19(3), 360–375, 1996.
80. Kuptsov, Yu. E., Methodological aspects of studying wear and improving serviceability of contact wire, *Journal of Friction and Wear*, 16(1), 134–139, 1995.
81. American metal market, silver section. March, p. 10, 1977.
82. Antler, M., Gold connector contact: Developments in the search for alternate materials, *IEEE Transactions on Parts, Hybrids, and Packaging*, 11(Sept), 116–220, 1975.
83. Waine, C. A. and McKarthy, R. A., Comparison of gold and alternative low cost finishes for connector contacts, *Proceedings of 9th International Conference on Electrical Contact Phenomena,* Chicago, USA, pp. 159–172, 1978.
84. Klaudy, V. P., Eigenschaften und anwendungsmoglichkeiten von flussigkeitskontakten, *Elektrotechnishe Zeitschrift-A,*, 76(15), 1–8, 1955.
85. Klaudy, V. P., Liquid sliding contact, *Proceedings of International Symposium on Electrical Contact Phenomena,* University of Maine, pp. 49–55, 1961.
86. Spear, W. E., Lanyos, H. P. D., and Mort, J., Some applications of mercury wetted contact relays, *Journal of Scientific Instruments*, 39, 81, 1962.
87. Burton, R. A. and Burton, R. G., Properties and performance of gallium alloys in sliding contacts, *Proceedings of 34th IEEE Holm Conference on Electrical Contacts,* Institute of Electric and Electronic Engineers, Inc. CHMT, San Francisco, USA, September 26–29, pp. 187–192, 1988.
88. Izmailov, V. V. and Mityurev, A. A., Tribological behavior of liquid metals in electrical contacts, *Journal of Friction and Wear*, 16(6), 100–107, 1995.
89. Cannel, M. J. and Stevens, H. O., *Acyclic superconducting generator development, 400 Horsepower generator design*. DTNSRDC Report No. PAS-81/14, 1982.
90. Maribo, D. W. and Sondergaard N. A., Further studies of a low melting point alloy used in a liquid metal current collector, *Proceedings of 32nd IEEE Holm Conference on Electrical Contacts*, Institute of Electric and Electronic Engineers, Inc. CHMT, Boston, USA, October 27–29. pp. 91–94, 1986.
91. Buresch, I., Kaspar, F., and Ganz, J., A new contact layer system for connectors in high temperature applications, *Proceedings of 21st International Conference on Electrical Contacts,* Zurich, Switzerland, September 9–12, pp. 174–178, 2002.
92. Hardy, E. G. and Kenosha, W., Process of treating tin bronze, *U.S. Patent 2,804,408*, August 27, 1957.
93. Steeb, J. and Stuer, H., New developments in the field of copper-base spring alloys, *Proceedings of 11th International Conference on Electrical Contact Phenomena,* West Berlin, Germany, June 7–11, pp. 261–263, 1982.
94. Tautzenberger, P. and Stockel, D., The use of shape memory alloys in switchgear technology, *Proceedings of 30th Holm Conference on Electrical Contacts,* Chicago, pp. 449–454, 1984.

95. Flot, R. F., Kent, H. B., and McGaffigan, T. H., Shape-memory effect alloys as an interconnection technology for IC packages and PC boards, *Proceedings of 34th IEEE Electronic Components Conference,* pp. 394–401, 1984.
96. Fuse, K., Iwai, H., and Tachibana, H., New connecting systems with shape memory alloy fastener for fine pitch connector with excellent high temperature reliability, *Proceedings of 3rd International SAMPE Electronics Conference,* pp. 259–269, 1989.
97. Borden, T., Shape-memory alloys: Forming a tight fit, *Mechanical Engineering*, 13 (10), 67–72, 1991.
98. Oberg, A. and Isberg, J., Simulations of transient thermal and electrical behavior of contact spots, *Proceedings of 45th IEEE Holm Conference on Electrical Contacts,* Pittsburg, USA, October 4–9, pp. 141–145, 1999.
99. Kulisic, I., Gray, G. L., and Mohney, S. E., Shape memory alloy coil-shaped clamp for enhanced normal force in electrical connectors, *Proceedings of 44th IEEE Holm Conference on Electrical Contacts,* Arlington, USA, October 26–28, pp. 20–25, 1998.
100. Schetky, L., *The present status of industrial applications for shape-memory alloys*, EPRI TR-105072:41, 1995.
101. Braunović, M. Use of shape-memory materials in distribution power systems, Canadian electricity association. *CEA Report SD-294A*, 1994.
102. Garts, S. M., Porosity of gold electro-deposits; effect of substrate surface structure, *Plating*, 55, 941–946, 1968.
103. Antler, M., Garte, S. M., and Krumbein, S. J., Recent studies of the contact properties of gold plate, *Proceedings of 13th Holm Seminar on Electrical Contacts,* Illinois Institute of Technology, Chicago, pp. 79–92, 1967.
104. Zhou, Y. L., Lin, X. Y., and Zhang, J. G., Electric contact behavior of various plating after long term indoor air exposure, *Proceedings of 20th International Conference on Electrical Contacts,* Stockholm, Sweden, June 19–23, pp. 313–318, 2000.
105. Baker, R. G., Evaluation of gold deposits for use in dry circuit applications, *Proceedings of 6th International Conference on Electrical Contact Phenomena,* Chicago, USA, pp. 179–183, 1972.
106. Paunovic, M., *Fundamentals of Electrochemical Deposition*, Wiley, New York, 1998.
107. Vook, R. W., Singh, B., Knabbe, E. A., Bhavsar, B. V., and Ho, J. H., Elemental Surface Composition of Slip Ring Copper as a Function of Temperature, *Proceedings of the 24th Annual Holm Conference on Electrical Contacts*, Illinois Institute of Technology, Chicago, IL, pp. 17–21, 1979.
108. Aust, K. T. and Westbrook, J. H., Solute hardening at interfaces in high purity lead-II: Free surfaces, *Acta Metallurgica*, 19, 521–541, 1971.
109. Haque, C. A., Investigations of surface segregation on Pd–Ag 40 at.% and Pd–Au 70 at.% contact metal alloys, *Proceedings of 17th Holm Seminar on Electrical Contacts,* pp. 41–49, 1971.
110. Ferrante, J., An Auger electron spectroscopy and LEED study of equilibrium surface segregation in copper–aluminum alloys, *Acta Metallurgica*, 19, 743–748, 1971.
111. Wayman, M. L. and Gray, J. T., *Acta Metallurgica*, 22, 349, 1974.
112. Braunović, M., Pomathiod, L., and Bailon, J.-P., The effect of surface segregation of mg on the contact resistance of Al–0.5% Mg alloy, *IEEE Transactions on Parts, Hybrids and Packaging*, 13(3), 31–35, 1977.
113. Ruoff, A. L. and Balluvffi, R. W., On strain-enhanced diffusion in metals: Dislocation and grain boundaries short-circuiting models, 34, 1848–1853, 1963.
114. Vook, R. W., Pope, L. E., and Rhode, R. W., The surface segregation of sulfur during oscillatory pin-on plate wear studies of precious metal electrical contact alloys–I, friction and electrical contact resistance, *Proceedings of 30th IEEE Holm Conference on Electrical Contacts,* Chicago, USA, September 17–21, pp. 507–511, 1984.
115. Kothari, R. and Vook, R. W., Enhanced sulphur segregation in plastically deformed OFHC Cu and the effect of surface segregated sulphur on electric contact resistance, *IEEE Transactions on Components, Packaging and Manufacturing Technology*, 17, 121–127, 1994.
116. Dearnley, G. and Hartley, E. W., Ion implantation into metals and carbrides, *Thin Solid Films*, 54, 215–220, 1978.
117. Saritas, S., et al. The effect of ion implantation on the friction and wear behaviour of a phosphor bronze, *Wear*, 82, 233–238, 1982.

118. Antler, M., Preece, C. M., and Kaufmann, E. N., The effect of boron implantation on the sliding wear and contact resistance of palladium, 60Pd40Ag, and a CuNiSn alloy, *IEEE Transactions on Components, Hybrids and Manufacturing Technology*, 5(1), 81–85, 1982.
119. Leech P. W., The effect of nitrogen implantation on the tribological properties of gold based alloys electroplated palladium, *Proceedings of 33rd IEEE Holm Conference on Electrical Contacts*, Institute of Electric and Electronic Engineers, Inc. CHMT, Chicago, USA, September 21–23, pp. 53–61, 1987.
120. Braunovic M. and Trudeau, M. L., Effect of ion-implantation on the contact resistance of copper and silver-copper electrical contacts under fretting conditions. *Proceedings of 40th IEEE Holm Conference on Electrical Contacts*, Institute of Electric and Electronic Engineers, Inc. CPMT, Chicago, USA, October 17–19, pp. 195–210, 1994.
121. Sun, M., Rong, M., Wang, Q., and Chen, D., Modification of Ag-plated contacts by nitrogen ion implantation, *Proceedings of 42nd IEEE Holm Conference on Electrical Contacts,* Chicago, USA, September 16–20, pp. 467–471, 1996.
122. Russel, R. J., Properties of precious metal inlays, *Proceedings of 5th Symposium American Electroplaters Society,* New York, pp. 169–175, 1975.
123. Abbott, W. H., Recent studies of tarnish film creep, *Proceedings of 9th International Conference on Electrical Contact Phenomena,* Chicago, USA, pp. 117–122, 1978.
124. Herklotz, G., Bolmerg, K., Eligehausen, H., Gehlert, B., and Witting, K., Application of sputtered layers in contact technology, *Proceedings of 36th IEEE Holm Conference on Electrical Contacts,* Montreal, Canada, August 20–24, pp. 182–192, 1990.
125. Mock, J. A., Sputtered coatings aim for new uses, *Materials Engineering*, 71(8), 44–47, 1970.
126. Reichelt, W., Vapour deposition of gold alloys. Development of radiofrequency sputtering of electrical contact surfaces, *Gold Bulletin*, 5(3), 55–57, 1972.
127. Varga, J. E. and Bailey, W. A., Evaporation, sputtering and ion-plating, *Solid State Technology*, 12, 79–86, 1973.
128. Swaroop, B. and Adler, I., Ion-plated copper–steel granted interface, *Journal of Vacuum Science and Technology*, 10(4), 503–505, 1973.
129. Antler, M. and Drozdowicz, M. H., Wear of gold electrodeposits; effect of substrate and of nickel underplate, *Bell System Technology Journal*, 58(2), 323–349, 1979.
130. Russ, G. J. and Chesseri, R. J., Contact finish design experiments: Contact resistance of gold plated copper and nickel substates exposed to tarnishing environments, *Proceedings of 9th International Conference on Electrical Contact Phenomena*, Chicago, USA, 227–234.
131. Sauer, H., *Modern Relay Technology*, 2nd ed., Huethig Verlag, Heidelberg, 1986.
132. Johler, W., Switching contacts for low level applications, *Proceedings of 21st International Conference on Electrical Contacts*, Zurich, SEV Schweizerischer Elektrotechnischer Verein, Fehraltorf, Switzerland, September 9–12, pp. 87–100, 2002.
133. Freudenberger, R., Ganz, J., Kaspar, F., Marka, E., and Michal, R., Contact and connection properties of autocatalytically increased gold-deposits, *Proceedings of 42nd IEEE Holm Conference on Electrical Contacts,* Chicago, USA, September 16–20, pp. 461–466, 1996.
134. Bonwitt, W. F., An experimental investigation of the electrical performance of bolted aluminum-to-copper connections, *AIEE Transactions*, 67, 1208–1214, 1948.
135. Hubbard, D. C., Kunkle, R. W., and Chance, A. B., Evaluation of test data in determining minimum design requirements for aluminium–copper connectors, *AIEE Transactions*, 73, 616–623, 1954.
136. Bond, N. and McGeary, F. L., Nickel plating for improved electrical contact to aluminum, *IEEE Transactions*, IA-9, 326–334, 1973.
137. Nguyên-Duy, P., Boisvert, S. P., Lanouette, C., and Blanchette, Y. Optimisation des plages de contact de l'ensemble marteau-mâchoire des sectionneurs GEC Alsthom type BCVB 735 kV 4000A2. Technical Report IREQ 96-013, 1996.
138. Kassman Rudolphi, A. Tribology of Electrical Contacts—Deterioration of Silver Coated Copper, Upsala University, Sweden, 1996.
139. Farahat, M. A., Gockenbach, E., El-Alaily, A. A., and Abdel Aziz, M. M., Effect of coating materials on the electrical performance of copper joints, *Proceedings of 42nd IEEE Holm Conference on Electrical Contacts,* Chicago, USA, September 16–20, pp. 472–478, 1996.
140. Jackson, R. L., Electrical performance of aluminum/copper bolted joints, *IEEE Proceedings, Part C*, 129(4), 77–85, 1982.

141. Lefebre, J., Galand, J., and Marsolais, R. M., Electrical contacts on nickel plated aluminum: the state of the art, *Proceedings of 36th IEEE Holm Conference on Electrical Contacts,* Montreal, Canada, August 20–24, pp. 454–460, 1990.
142. Aronstein, J., Evaluation of a plated aluminum wire for branch circuit applications, *Proceedings of 33rd IEEE Holm Conference on Electrical Contacts,* Chicago, USA, September 21–23, pp. 107–112, 1987.
143. Hare, T. K., Investigation of nickel-plated aluminium wire using analytical electron microscope, *Proceedings of 33rd IEEE Holm Conference on Electrical Contacts,* pp. 113–120, 1987.
144. Braunović, M., Fretting in nickel-coated aluminum conductors, *Proceedings of 36th IEEE Holm Conference on Electrical Contacts,* Montreal, Canada, August 20–24, pp. 461–471, 1990.
145. Bruel, J. F. and Carballeira, A., Durabilité des contacts électriques en aluminum, *Proceedings of SEE*, (December), 139–145, 1986.
146. Braunović, M., Evaluation of different contact aid compounds for aluminum-to-copper connections, *IEEE Transactions on Components, Hybrids and Manufacturing Technology*, 15(2), 216–224, 1992.
147. Gehlert, B., Herklotz, G., and Witting, K., Schaltverhalten von optimierten PVD-Schichten auf Au-Basis für moderne Telekommunikationsanwendungen, *VDEFachbericht*, 40, 51–60, 1989.
148. Liljestrand, L. -G., Sjogren, L., Revay, L., and Asthner, B., Wear resistance of electroplated nickel-hardened gold, *Proceedings of 30th IEEE Holm Conference on Electrical Contacts*, Illinois Institute of Technology, Chicago, USA, September 17–21. pp. 53–60, 1984.
149. Antler, M., Wear of gold plate: Effect of surface films and polymer codeposits, *IEEE Transactions on Parts, Hybrids and Packaging*, 10, 11–17, 1974.
150. Keil, A., Merl, W. A., and Vinaricky, E., *Elektrische Kontakte und ihre Werkstoffe*, Springer, Berlin, 1984.
151. Antler, M., Wear and contact resistance, In *Properties of Electrodeposits. Their Measurements and Significance*, Sard, R., Leidheiser, H., and Ogburn, F., Eds., Princeton University Press, Princeton, NJ, pp. 353–373, 1975.
152. Willcox, P. S. Metallurgical aspects of electrodeposited gold, Ph.D. diss., University of Southern California, 1974.
153. Holden, C. A., Opila, R. L., Law, H. H., and G, R., Wear resistance of nickel and nickel phosphorus alloy electrodeposits, *Proceedings of 34th IEEE Holm Conference on Electrical Contacts,* San Francisco, USA, September 26–29, pp. 101–107, 1988.
154. Herrmann, J., TRIBOR—An Innovative coating system for electrical contacts and connectors, *Proceedings of 19th International Conference on Electrical Contacts,* Nurenberg, Germany, September 21–23, pp. 173–179, 1998.
155. Herrmann, J. and Braun, H. A., An innovative coating system for electrical contacts and connectors, *Proceedings of 20th International Conference on Electrical Contacts,* Stockholm, Sweden, June 19–23, pp. 403–408, 2000.
156. Antler, M. and Ratliff, E. T., Sliding wear of inlay clad metals and electrodeposited cobalt–gold, *IEEE Transaction on Components, Hybrids and Manufacturing Technology*, 6(1), 3–7, 1983.
157. Antler, M., Sliding wear of metallic contacts, *IEEE Transactions on Parts, Hybrids and Packaging*, 4(1), 15–29, 1981.
158. Cheng, Y.-T., Gillispie, B., Simko, S. J., Militello, M. C., Waldo, C. A., and Wong, R. A., Vapor deposited thin gold coatings for high temperature electrical contacts, *Proceedings of 42nd IEEE Holm Conference on Electrical Contacts,* pp. 404–413, 1996.
159. Capp, P. O. and Williams, D. W. M., Evaluation of friction and wear of new palladium alloy inlays and other electrical contact surfaces, *Proceedings of 30th IEEE Holm Conference on Electrical Contacts,* pp. 409–416, 1984.
160. Schröder, K.-H., Werkstoffe für elektrische Kontakte und ihre Anwendung, Expert Verlag, 2nd ed., p. 344, 1997.
161. Sauter, E. A. and Weik, G., Wear of palladium plated surfaces with a thin gold layer for connecto contacts, *Proceedings of International Conference on Electrical Contact Phenomena,* West Berlin, Germany, June 7–11, pp. 121–123, 1982.
162. Antler, M., The application of palladium in electronic connectors, *Platinum Metals Review*, 26(3), 106–117, 1982b.

163. Imrell, T., The importance of the thickness of silver coating in the corrosion behaviour of copper contacts, *Proceedings of 37th IEEE Holm Conference on Electrical Contacts,* Chicago, USA, October 6–9, pp. 237–243, 1991.
164. Buresch, I., Contact resistance measurements at coatings on copper alloys after long-term exposure, *Proceedings of 19th International Conference on Electrical Contacts,* Nurenburg, Germany, September 21–23, pp. 163–168, 1998.
165. Braunović, M. and Aleksandrov, N., Intermetallic Compounds at Aluminium to Copper and Copper to Tin Electrical Interface, *Proceedings of 38th IEEE Holm Conference on Electrical Contacts,* Philadelphia, USA, October 18–21, pp. 25–34, 1992.
166. Larsson, A. K. Crystal structures of tin intermetallics: Honeycomb nets superstructures and Edshammar polyhedra, Ph.D. diss., University of Lund, Sweden, 1994.
167. Hammam, T. and Sundberg, R., Heat-treatment of tin-coated copper base alloy and the subsequent effect on friction, wear and electric properties, *Proceedings of 20th International Conference on Electrical Contacts,* Stockholm, Sweden, June 19–23, pp. 291–296, 2000.
168. Timsit, R. S., Interdiffusion at bimetallic interfaces, *IEEE Transactions on Components, Hybrids and Manufacturing Technology*, 9(1), 106–116, 1986.
169. Bauer, C. L. and Lessmann, G. G., Metal-joining methods, *Annual Review of Materials Science*, 6, 361–387, 1976.
170. Zakraysek, L., Intermetallic growth in tin-rich solders. *Welding Research Supplement*, (November), 537–542, 1972.
171. Lindborg, U., Asthner, B., Lind, L., and Revay, L., Intermetallic growth and contact resistance of tin contacts after aging, *Proceedings of 21st Holm Conference on Electrical Contacts,* Chicago, USA, pp. 25–31, 1975.
172. So, A. C. K., Yan, C., Chan, Y. C., and Lai, J. K. L., Aging studies of Cu–Sn intermetallic compounds in annealed surface mount solder joints, *IEEE Transactions on Components, Packaging and Manufacturing Technology, B*, 20, 161–166, 1997.
173. Hammam, T., Friction, wear and electric properties of tin-coated tin bronze for separable electric connectors, *Proceedings of 42nd IEEE Holm Conference on Electrical Contacts*, Institute of Electric and Electronic Engineers, Inc. CPMT, Chicago, USA, September 16–20, pp. 321–330, 1996.
174. Buresch, I., Advanced hot dip tinned coatings for automotive connectors, *Proceedings of 21st International Conference on Electrical Contacts,* Zurich, Switzerland, September 9–12, pp. 185–188, 2002.
175. Beattie, R. W., Palladium plating on telephone plugs and sockets, *Platinum Metals Review*, 6(2), 52–56, 1962.
176. Antler, M., Wear and friction of platinum metals, *Platinum Metals Review*, 10(1), 2–8, 1966.
177. Sato, T., Matsui, Y., Okado, M., Muracawa, K., and Henmi, Z., Palladium with a thin gold layer as a sliding contact material, *IEEE Transactions on Components, Hybrids and Manufacturing Technology*, 4(1), 10–14, 1981.
178. Becker, H., AES and SIMS Studies of turnishing layers on precious metal contacts materials, *Proceedings of 10th International Conference on Electric Contact Phenomena*, Vol. 2, Budapest, Hungary, August 25–29, pp. 1015–1021, 1980.
179. Barber, S. A. and Rabinovich, E., Material selection for noble metal slip rings, *Proceedings of 26th IEEE Holm Conference on Electrical Contacts,* Illinois Institute of Technology, Chicago, USA, pp. 33–40, 1980.
180. Antler, M. and Drozdowicz, M. H., Connector contact materials: Effect of environment on clad palladium, palladium–silver alloys, and gold electrodeposits, *IEEE Transactions on Components, Hybrids and Manufacturing Technology*, CHMT, 4(4), 482–491, 1981.
181. Hara, T., Baba, H., Hayashi, Y., and Kasai, H., Flatly eroded multi-layers diffused contacts (Rh–Sn–Rh) for dry reed switch, *Proceedings of 24th Holm Conference on Electrical Contacts,* Chicago, USA, pp. 533–539, 1978.
182. Hayashi, G. and Baba, H., Study on bridge phenomena of Sn–Rh and Rh–Sn–Rh contact for dry reed switch, *Proceedings of 9th International Conference on Electrical Contact Phenomena,* Chicago, USA, pp. 541–548, 1978.
183. Matsumoto, K., Nakajima, M., Kuwabara, K., Ishimatsu, M., and Mori, T., Application of the silver–tin plated and diffused contact of sliding contacts, *Proceedings of 8th International Research Symposium on Electrical Contact Phenomena,* Tokyo, Japan, October 21–23, pp. 381–386, 1976.

184. Engel, P. A., Hsue, E. Y., and Bayer, R. G., Hardness, friction and wear of multiplated electrical contacts, *Wear*, 162–164, 538–551, 1993.
185. Yang, Q., Zhao, Z., Engel, P. A., and Constable, J. H., Impact wear of multiplated connectors in the presence of electrical current, *Proceedings of 41st IEEE Holm Conference on Electrical Contacts,* Montreal, Canada, October 2–4, pp. 135–146, 1995.
186. Leung, C. H. and Lee, A., Thermal cycling induced wiping wear of connector contacts at 150 celsius, *Proceedings of 43rd IEEE Holm Conference on Electrical Contacts,* Philadelphia, USA, October 20–22, pp. 132–137, 1997.
187. Engel, P. A., Vickers micro hardness evaluation of multilayer platings for electrical contacts, *Proceedings of 37th IEEE Holm Conference on Electrical Contacts,* Chicago, USA, October 6–9, pp. 66–72, 1991.
188. Engel, P. A. and Yang, Q., Impact wear of multiplated electrical contacts, *Wear*, 181–183, 730–742, 1995.
189. Engel, P. A., Chitsaz, A. R., and Hsue, E. Y., Interpretation of superficial hardness for multilayer platings, *Thin Solid Films*, 207, 144–152, 1992.
190. Caule, E. J. and Gyurina, D., Studies toward the replacement of noble metal contacts by copper alloys, *Proceedings of 9th International Conference on Electrical Contact Phenomena,* Chicago, USA, pp. 173–180, 1978.
191. Galand, J. and Carballeira, A., New contact material for low level relays in controlled atmosphere, *Proceedings of 10th International Conference on Electric Contact Phenomena,* Budapest, Hungary, January 13, pp. 659–668, 1980.
192. Horn, G., Electrical contacts in automotive relays, *Proceedings of 32th IEEE Holm Conference on Electrical Contacts,* Budapest, Hungary, January 13, pp. 125–126, 1986.
193. Niney, C. and Caullian, A., New high conductivity copper alloys for electromechanical applications and as support materials for electrical contacts, *Proceedings of 10th International Conference on Electric Contact Phenomena,* Budapest, Hungary, January 13, pp. 659–668, 1980.
194. Souter, J. W., Adhesive wear properties of electrodeposited coating for sliding Contacts, *Proceedings of 9th International Conference on Electrical Contact Phenomena,* Chicago, USA, pp. 143–144, 1978.
195. Kovacs, G. and Toth, K., Investigation of alternative to gold contact finishes for telecom connector applications, *Proceedings of 36th IEEE Holm Conference on Electrical Contacts,* Chicago, USA, August 20–24, pp. 326–341, 1990.
196. Noel, S., Boyer, L., Houz, F., Boissel, C. J., Bourin, J. M., and Zindine, E. M., Electrical and tribological properties of lubricated nickel coatings for low level connectors, *Proceedings of 16th International Conference on Electrical Contacts,* Loughborough, pp. 73–77, 1992.
197. Holden, C. A., Law, H. H., and Crane, G. R., Effect of surface structure on the contact resistance measurements of electrodeposits, *Proceedings of 34th IEEE Holm Conference on Electrical Contacts,* San Francisco, USA, September 26–29, pp. 93–99, 1988.
198. Law, H. H., Sapjeta, J., Chidsey, C. E. D., and Putvinski, T. M., Protective treatments for nickel based contact materials, *Journal of the Electrochemical Society*, 141(7), 1977–1982, 1994.
199. Ernsberger, C., Miller, A. E., and Moulder, J., Titanium nitride: A potential ceramic low energy contact material, *Proceedings of 30th IEEE Holm Conference on Electrical Contacts,* Chicago, USA, September 17–21, pp. 587–597, 1984.
200. Benhenda, S., Ben Jemaa, N., Travers, D., Perrin, C., and Simon, D., Tin coating in electrical contact applications, *Proceedings of 16th International Conference on Electrical Contacts,* Loughborough, pp. 181–184, 1992.
201. Izmailov, V. V., Effect of coating on mechanical and electrical contact of rough solids, *Journal of Friction and Wear*, 16(6), 20–36, 1995.
202. Lindmayer, M., Medium to high current switching, In *Electrical Contacts: Principles and Applications*, Slade, P. G., Ed., Marcel Dekker, New York, pp. 627–680, 1999.
203. Slade, P. G., Introduction to contact tarnishing and corrosion, In *Electrical Contacts: Principles and Applications*, Slade, P. G., Ed., Marcel Dekker, New York, pp. 89–112, 1999.
204. Slade, P. G., The consequence of arcing, In *Electrical Contacts: Principles and Applications*, Slade, P. G., Ed., Marcel Dekker, New York, pp. 487–533, 1999.
205. Slade, P. G., High Current Contacts: A review and tutorial, *Proceedings of 21st International Conference on Electrical Contacts,* Zurich, Switzerland, September 9–12, pp. 413–424, 2002.

206. Hauner, F., Jeannot, D., McNeilly, K., and Pinard, J., Advanced Ag-SnO_2 contact materials for the replacement of Ag-CdO in high current contactors, *Proceedings of 46th IEEE Holm Conference on Electrical Contacts,* Chicago, USA, September 25–27, pp. 225–230, 2000.
207. Rieder, W. and Weichsler, V., Make erosion mechanism of Ag/Cdo and Ag/SnO_2 contacts, *Proceedings of 37th IEEE Holm Conference on Electrical Contacts,* Chicago, USA, October 6–9, pp. 25–32, 1991.
208. Behrens, V., Honig, T., Kraus, A., and Lutz, O., Switching behaviour of silver based contact materials in 42 V DC applications, *Proceedings of the International Conference on Electric Contacts,* Zurich, pp. 69–75, 2002.
209. Michal, R. and Saeger, K. E., Metallurgical aspects of silver-based contact materials for air-break switching devices for power engineering, *IEEE Transactions on Components, Hybrids and Manufacturing Technology*, CHMT, 12(March), 77–81, 1989.
210. Wingert, P. C. and Leung, C., The development of silver-based cadmium-free contact materials, *IEEE Transactions on Components, Hybrids and Manufacturing Technology*, CHMT, 12(3), 16–20, 1989.
211. Schoepf, T. J., Behrens, V., Honig, T., and Kraus, A., Development of silver zinc oxide for general-purpose relays, *Proceedings of the International Conference on Electric Contacts,* Stockholm, pp. 187–193, 2000.
212. Bizjak, M. and Koller, L., Electrical characteristics of contact coated with protective layers, *Proceedings of 20th International Conference on Electrical Contacts,* Stockholm, Sweden, June 19–23, pp. 67–72, 2000.
213. Behrens, V., Honig, T., Kraus, A., Michal, R., Saeger, K. E., Schmidberger, R., and Staneff, T., An advanced silver/tin oxide contact material, *IEEE Transactions on Components, Packaging and Manufacturing Technology, A*, CPMTA, 17(3), 24–31, 1994.
214. Nilsson, O., Hauner, F., and Jeannot, D., Replacement of AgCdO by AgSnO2 in DC contactors, *Proceedings of 50th IEEE Holm Conference on Electrical Contacts,* Montreal, Canada, pp. 70–74, 2004.
215. Behrens, V., Honig, T., and Kraus, A., Comparisons of different contact materials for low voltage vacuum applications, *Proceedings of 19th International Conference on Electrical Contacts,* Nurenburg, Germany, September 21–23, pp. 247–251, 1998.
216. Behrens, V., Honig, T., and Kraus, A., Tungsten and tungsten carbide based contact materials used in low voltage vacuum contactors, *Proceedings of 45th IEEE Holm Conference on Electrical Contacts,* Pittsburg, USA, October 4–6, pp. 105–110, 1999.
217. Temborius, S., Lindmayer, M., and Gentsch, D., Switching behavior of different contact materials for vacuum interrupters under load switching conditions, *Proceedings of 19th International Symposium on Discharges and Insulation in Vacuum,* Xi'an, China, September, pp. 519–523, 2000.
218. Rolle, S., Lietz, A., Amft, D., and Hauner, F., Cr–Cu contact material for low voltage vacuum contactors, *Proceedings of 20th ICED,* Stockholm, Sweden, June, pp. 179–186, 2000.
219. Chaly, A. M., Chalaya, A. T., Poluyanov, V. N., and Poluyanova, I. N., The Peculiarities of interruption of the medium voltage motors by VCB and Cu–Cr Contacts, *Proceedings of 18th International Symposium on Discharges and Insulation in Vaccum,* Eindhoven, Holland, August, pp. 439–442, 1998.
220. Bourguignon, L. L. and Agarwal, D. P., Powder metallurgy fabrication of palladium contact alloys, *Proceedings of 34th IEEE Holm Conference on Electrical Contacts,* San Francisco, USA, September 26–29, pp. 259–265, 1988.
221. Johnson, L. J., Mole, C. J., and Arcella, F. G., Important problems in applying liquid metal current collectors, *Proceedings of 20th Holm Conference on Electrical Contacts,* Illinois Institute of Technology, Chicago, USA, pp. 201–210, 1973.
222. Gutierrez, A. O., Aceto, S. C., Woo, J. T., and Cormeau, C. Microelectromechanical liquid metal current carrying system, apparatus and method, *US Patent 6,373,356 B1, H01H 29/00*, April 16, 2002.
223. Kim, J., Shen, W., Latorre, L., and Kim, C-J. , A micromechanical switch with electrostatically driven liquid-metal droplet, *Sensors and Actuators A: Physics*, 97–98(April), 672–679, 2002.
224. Duthie, F.W., Professor George Forbes, inventor of the carbon brush, *Proceedings of the 3rd International Current Collector Conference*, Office of Naval Research, OCNR 13187-2, Annapolis, MD, December, 1–5, 1986.

225. Brown, A. R. G. and Watt, W., The preparation of high temperature pyrolytic carbon, *Industrial Carbon and Graphite*, Society of the Chemical Industry, London, pp. 97–102, 1958.
226. Lee, P. K. and Johnson, J. L., High-current brushes. Part II: Effect of gases and hydrocarbon vapors, *IEEE Transactions on Components, Hybrids and Manufacturing Technology*, CHMT, 1(1), 40–45, 1978.
227. Cowlard, F. C. and Lewis, J. C., Vitreous carbon—a new form of carbon, *Journal of Materials Science*, 2, 507–512, 1967.
228. Burton, R. A. and Burton, R. G., Vitreous carbon matrix for low wear carbon/metal current collectors, *Proceedings of 34th IEEE Holm Conference on Electrical Contacts,* San Francisco, USA, September 26–29, pp. 223–228, 1988.
229. Ubbelohde, A. R. and Lewis, F. A., Graphite and its crystal compounds, Clarendon Press, Oxford, 1960.
230. Shobert, E. I., Carbon, graphite and contacts, *IEEE Transactions on Parts, Hybrids and Packaging*, PHP, 12(1), 62–74, 1976.
231. Neukirhen, J., *Curbon Brushes*, E. I. Shobert II, Trans., Telegraph Press, Harrisburg, 1937.
232. Kalb, W. C., Ed., Carbon, graphite and metal–graphite brushes, National Carbon Co., London, 1946.
233. Beech, R. N. and Price, M. S. T., *Copper–Graphite Materials. Industrial Carbon and Graphite*, Society of the Chemical Industry, London, 1958.
234. Shobert, E. I., *Carbon Brushes—The Physics and Chemistry of Sliding Contacts*, Chemical Publishing Co., New York, 1965.
235. Shobert, E., Sliding electrical contacts, *Proceedings of 39th IEEE Holm Conference on Electrical Contacts,* Pittsburg, USA, September 27–29, pp. 123–134, 1993.
236. Livshits, P. S., *Handbook on Electric Machine Brushes*, Energoatomizdat, Moscow, 1983.
237. Millet, Y., Behavior of carbon brushes in dry and wet atmosphere, *Proceedings of 4th Conference on Carbon,* New York, pp. 719–725, 1960.
238. Johnson, J. L. and Moberly, L. E., Brush life and commutation in atmospheres of air, SF_6 and CO_2, *Proceedings of International Conference on Electrical Contact Phenomena,* Chicago, USA, pp. 109–116, 1967.
239. Pardee, R. R., Moisture dependence of silver–graphite brushes in air, nitrogen, helium, and carbon dioxide, *IEEE Transactions on Power Apparatus and Systems*, 86(5), 615–625, 1967.
240. Johnson, J. L. and Moderly, L. E., High-current brushes. Part I: Effect of brush and ring materials, *IEEE Transaction on Components, Hybrids and Manufacturing Technology*, CHMT, 1(1), 36–40, 1978.
241. Kuhlmann-Wilsdorf, D., Makel, D. D., Sondergaard, N. A., and Maribo, D. W., On the two modes of operation of monolithic Ag-C brushes, *IEEE Transactions on Components, Hybrids and Manufacturing Technology*, CHMT, 12(2), 237–245, 1989.
242. Cook, T. H., Trends in brush development, *Proceedings of the First Carbon Brush Conference*, Morganite Carbon, London, pp. 76–91, 1961.
243. Paxton, R. R., Carbon and graphite materials for seals, bearings and brushes, *Electrochemical Technology*, 5(5–6), 174–182, 1967.
244. Okada, K. and Yoshida, M., Contact voltage drop and wear of self-lubricating Ag-Pd alloy base composite materials, *Proceedings of 33rd IEEE Holm Conference on Electrical Contacts,* Chicago, USA, September 21–23, pp. 169–261, 1987.
245. Johnson, J. L. and Schreurs, J., High current brushes. Part VIII: Effect of electrical load, *Wear*, 78, 219–232, 1982.
246. McNab, J. R., Pulsed high-power brush research, *IEEE Transactions on Components, Hybrids and Manufacturing Technology*, CHMT, 1(1), 30–35, 1978.
247. Clauss, F. J., Lubrication under space/vacuum conditions, *Scientific Lubrication*, 15(3), 180–202, 1963.
248. Clauss, F. J., Sliding electrical contact for ultrahigh vacuum, *Research Scientific Instruments*, 36(8), 1251–1253, 1965.
249. Dorsey, G. and Hayes, R., The effects of apparent contact area on thermal and electrical properties of Ag-MoS_2-$C_{graphite}$ brushes in contact with coin-silver slip rings, *Proceedings of 43rd IEEE Holm Conference on Electrical Contacts,* Philadelphia, USA, October 20–21, pp. 272–280, 1997.

250. Kobayashi, M., Matsumoto, M., Oshita, T., Takatsu, S., and Tsuya, Y., Self-lubricating composite material (new SL-alloy) for severe conditions, *Bulletin of the Japan Institute of Metals*, 27(5), 391–393, 1988.
251. Watanabe, Y., Sliding contact characteristics between self-lubricating composite materials and copper, *Proceedings of 38th IEEE Holm Conference on Electrical Contacts,* Philadelphia, USA, October 18–21, pp. 135–142, 1992.
252. Watanabe, Y., Low-speed sliding test characteristic of sliding contact containing solid lubricants for use under severe application conditions, *Proceedings of 47th IEEE Holm Conference on Electrical Contacts,* Montreal, Canada, September 25–27, pp. 293–300, 2001.
253. Berent, V. Y., Aleshina, A. V., and Katrus, O. A., Composite copper based current collector members used in rolling stock, *Journal of Friction and Wear*, 16(1), 41–46, 1995.
254. Baba, S., Sakai, K., and Gotoh, K., Mesh-shaped brushes boost performance of miniature motors, *Journal of Electronic Engineering*, 25(7), 74–75, 1988.
255. Okada, K. and Yoshida, M., Copper–graphite brushes lined with porous metals, *Proceedings of 37th IEEE Holm Conference on Electrical Contacts,* Chicago, USA, October 6–9, pp. 149–152, 1991.
256. Shalunov, E. P., Jangg, G., Walther, H., and Matrosov, A., Kupferwerkstoff fur elektrish leitende Verschleissteile. OP 400.580. OA 1341/93 von 08.07.1993, 1993.
257. Shalunov, E. P., Dovydenkov, V. A., and Simonov, V. S., Anwendung der hocheffizienten dispersionsgeharteten werkstoffe auf pulverkupferbasis in den teilen von motoren und kraftanlagen der transportmittel, *Proceedings of the 15th International Plansee Seminar: "Powder Metallurgical High Performance Materials,"* Reutte, Tirol, May 28, pp. 126–149, 2001.
258. Lenel, F. V., Resistance sintering under pressure, *Journal of Metals*, 7(1), 158–167, 1955.
259. Owen, K. C., Wang, M. J., Persad, C., and Eliezer, Z., Preparation and tribological evaluation of copper–graphite composites by high energy high rate powder consolidation, *Wear*, 120, 117–121, 1981.
260. Stinson, R. S. and Sarro, L. A., The use of carbon fiber composites in sliding contacts, *Proceedings of 48th IEEE Holm Conference on Electrical Contacts,* Orlando, USA, October 21–23, pp. 175–183, 2002.
261. Chaikin, S. W., On frictional polymer, *Wear*, 10, 49–60, 1967.
262. McNab, J. R. and Wikin, G. A., Carbon fiber brushes for superconducting machines, *Electronics and Power*, (1), 8–12, 1972.
263. McNab, J. R., Recent advances in electrical current collection, *Wear*, 59(1), 259–276, 1980.
264. Marcus, A., Operating experience with the fringe fiber brush, *Wear*, 78, 93–107, 1982.
265. Takaoka, M., Aso, T., and Sawa, K., A Commutation Performance and Wear of Carbon–Fiber Brush in Gasoline, *Proceedings of 47th IEEE Holm Conference on Electrical Contacts,* Canada, September 25–27, pp. 44–49, 2001.
266. Leach, S., Performance testing of a low current sliding contactor system, *Proceedings of 38th IEEE Holm Conference on Electrical Contacts,* Philadelphia, USA, October 18–21, pp. 125–133, 1992.
267. Dietrich, F., Use of a contact element for transmitting electric voltage in a potentiometer. German Patent DE 44 42 617 C2, 1996.
268. Liu, S., Carbon fiber contacting position sensor, *U.S. Patent 6,140,907, H01C 10/30*, October 31, 2000.
269. Watanabe, T., An approach to grain boundary design for strong and ductile polycrystals, *Res. Mech.*, 11, 47–84, 1984.
270. Palumbo, G., Lehockey, E. M., and Lin, P., Applications for grain boundary engineered materials, *Journal of Materials*, 2, 40–43, 1998.
271. Lin, P., Palumbo, G., Erb, U., and Aust, K. T., Influence of grain boundary character distribution on sensitization and intergranular corrosion of alloy 600, *Scripta Metallurgica et Materialia*, 33, 1387–1392, 1995.
272. Gleiter, H., Nanocrystalline materials, *Progress in Materials Science*, 33(4), 223–315, 1989.
273. Hall, E. O., The deformation and ageing of mild steel: III Discussion of results, *Proceedings of the Physical Society of London, Section B*, 64, pp. 747–753, 1951.
274. Petch, N. J., The cleavage strength of polycrystals, *Journal of the Iron and Steel Institute*, 174, 25–28, 1953.
275. Chokshi, A. H., Rosen, A., Karch, J., and Gleiter, H., On the validity of the Hall-Petch relationship in nanocrystalline materials, *Scripta Metallurgica et Materialia*, 23, 1679–1684, 1989.

276. Koch, C. C. and Narayan, J., The inverse Hall-Petch effect: Fact or artifact?, *Materials Research Society Symposium Proceedings*, 634, B51.1, 2001.
277. Nieman, G. W., Weertman, J. R., and Siegel, R. W., Mechanical behavior of nanocrystalline Cu and Pd, *Journal of Materials Research*, 6, 1012–1027, 1991.
278. Siegel, R. W. and Fougere, G. E., Mechanical properties of nanophase materials, In *Nanophase Materials: Synthesis—Properties—Applications*, Hadjipanayis, G. C. and Siege, R. W., Eds.. Vol. 260 of NATO-ASI Series E: Applied Sciences, pp. 233–261, 1994.
279. Weertman, J. R., Hall-Petch strengthening in nanocrystalline metals, *Materials Science and Engineering: A*, 166, 161–167, 1993.
280. Zhou, Y., Erb, U., Aust, K.T., and Palumbo, G., Young modulus and hardness at grain sizes bellow 30 nm in nanostructured NiP. Poster presented at TNT2005, Oviedo, Spain, 2005.
281. Sanders, P. G., Youngdahl, C. J., and Weertman, J. R., The strength of nanocrystalline metals with and without flaws, *Materials Science and Engineering: A*, 234–236, 77–82, 1997.
282. Conrad, H., Grain-size dependence of the flow stress of cu from millimeters to nanometers, *Metallurgical and Materials Transactions A*, 35A, 2681–2685, 2004.
283. Jang, B. and Vehoff, H., The effect of grain size on the mechanical properties of nanonickle examined by nanoindentation, *Zeitschrift Metallkunde*, 95(6), 1–6, 2004.
284. Jang, B. and Vehoff, H., Grain size effects on the mechanical properties of nanonickel examined by nanoindentation, *Materials Science and Engineering: A*, 400–401, 467–470, 2005.
285. Schiøtz, J. and Jacobsen, K. W., A maximum in the strength of nanocrystalline copper, *Science*, 301(5), 1357–1359, 2003.
286. Schiøtz, J., Vegge, T. D., Tolla, F. D., and Jacobsen, K. W., Atomic-scale simulations of nanocrystalline metals, *Physical Review*, B60, 11971–11983, 1999.
287. Schiøtz, J., Tolla, F. D. D., and Jacobsen, K. W., Softening of nanocrystalline metals at very small grain sizes, *Nature*, 391(5), 561–563, 1998.
288. Heino, P., Strength of Nanoscale Copper Connection Under Shear, *International Conference on Modeling & Simulation of Microsystems*, 67–70, 2000.
289. Van Swygenhoven, H. and Caro, A., Plastic behavior of nanophase Ni: A molecular dynamics computer simulation, *Applied Physics Letters*, 72, 1652–1654, 1997.
290. Koch, C. C., *Nanostructured Materials—Processing, Properties and Applications*, Noyes Publications, Norwich, NY, 2002.
291. Watanabe, T., *Nano Plating—Microstructure Formation Theory of Plated Films and a Database of Plated Films*, Elsevier, Amsterdam, 2004.
292. Erb, U., El-Sherik, A. M., Palumbo, G., and Aust, K. T., Synthesis, structure and properties of electroplated nanocrystalline materials, *Nanostructured Materials*, 2, 383–390, 1993.
293. Weimer, A. W., Particle coating by atomic layer deposition (ALD). Keynote Lecture presented at PARTEC, 2004.
294. Robertson, A., Erb, U., and Palumbo, G., Practical applications for electrodeposited nanostructured materials, *Nanostructured Materials*, 12, 1035–1040, 1999.
295. Wang, L., Gao, Y., Liu, H., Xue, Q., and Xu, T., Effect of Co-ion on the co-deposition of Ni and nanodiamond particles, *Surface and Coatings Technology*, 191(1), 1–6, 2005.
296. Palumbo, G., Gonzales, K., Tomantschger, K., Erb, U., and Aust, K. T., Nanotechnology opportunities for electroplating industries, *Plating and Surface Finishing*, February 36–45, 2003.
297. Meadin, G. T., *Electrical Resistance of Metals*, Wiley, 1966.
298. Sondheimer, E. H., The mean free path of electrons in metals, *Advances in Physics*, 1, 1–42, 1952.
299. Fuchs, K., The conductivity of thin metallic films according to the electron theory of metals, *Proceedings of the Cambridge Philosophical Society*, 34, 100–108, 1938.
300. Endo, T. and Kino, T., Deviations from Matthiessen's rule of the electrical resistivity due to dislocations in gold, *Journal of the Physical Society of Japan*, 46(5), 1515–1521, 1979.
301. Schafler, E. and Sachslehner, F., The electrical dislocation resistivity and the deviation from Matthiessen's rule of deformed high-purity aluminum, *Journal of Physics: Condensed Matter*, 12(50), 1049–1051, 2000.
302. Ramaswamy, G., Raychaudhuri, A. K., Goswami, J., and Shivashankar, S. A., Large deviation from Matthiessen's rule in chemical vapour deposited copper films and its correlation with nanostructure, *Journal of Physics D: Applied Physics*, 30, 5–9, 1997.

303. Mayadas, A. F. and Shatzkes, M., Electrical-resistivity model for polycrystalline films: The case of arbitrary reflection at external surfaces, *Physical Review B: Condensed Matter*, 1(4), 1382–1389, 1970.
304. Steinhoegl, W., Schindler, G., Steinlesberger, G., Traving, M., and Engelhardt, M., Comprehensive study of copper wires with lateral dimensions of 100 nm and smaller, *Journal of Applied Physics*, 97, 023706–023711, 2005.
305. Steinlesberger, G., Engekhardt, M., Schindler, G., Steinhogel, W., von Glasgow, A., Mosig, K., and Bertannolli, E., Electrical assessment of copper damascene interconnects down to sub 50 nm feature sizes, *Microelectronic Engineering*, 64(1), 409–441, 2002.
306. Riedel, S., Rober, J., and Gessner, T., Electrical properties of copper films produced my MOCVD, *Microelectronic Engineering*, 33, 165–172, 1997.
307. Seah, M. P., Grain boundary segregation, *Journal of Physics F: Meal. Physics*, 10, 1043–1064, 1980.
308. Watanabe, T., Kitamura, S., and Karashima, S., Grain boundary hardening and segregation in alpha iron-tin alloy, *Acta Metallurgica*, 28, 455–463, 1980.
309. McMahon, C. J., *Interfacial Segregation and Embrittlement* 2002. ASM.
310. Braunović, M., Effect of grain boundaries on electrical resistance if iron wires in DC and AC electrical fields, In *Grain Boundaries in Engineering Materials*, Walter, J. L., Westbook, J. H., and Woodford, D. A., Eds., Claitors Publishing, pp. 193–200, 1975.
311. Braunović, M., Effect of surface segregation of impurities on the contact resistance and microhardness of aluminum and its alloys, *Proceedings of 7th International Conference on Electrical Contacts,* Paris, pp. 400–405, 1974.
312. Kasen, M. B., Solute segregation and boundary structural change during grain growth, *Acta Metallurgica*, 31, 489–497, 1983.
313. Tuller, H. L., Ionic conduction in nanocrystalline materials, *Solid State Ionics*, 131, 143–157, 2000.
314. Palumbo, G., McCrea, J. L., and Erb, U., In *Applications of electrodeposited nanostructures*, Nalwa, H. S., Ed. *Encyclopedia of Nanoscience and Nanotechnology,* American Scientific Publisher, Vol. 1, pp. 89–99, 2004.
315. Herzer, G., Amorphous and nanocrystalline soft magnets, In *Magnetic Hysteresis in Novel Magnetic Materials*, Hadjipanayis, G. C., Ed., Kluwer Academic Publishing, Dordrecht, pp. 711–730, 1997.
316. Cheung, C., Aus, M. J., Erb, U., McCreas, J. L., and Palumbo, G., In *Proceedings 6th International Conference Nanostructured Matter*. (NANO2002), Orlando, 2002.
317. Gangopadhyay, S., Hadjipanaysis, G. C., Dale, B., Sorensen, C. M., and Klabunde, K. J., Magnetism of ultrafine particles, *Nanostructured Materials*, 1, 77–81, 1992.
318. Gong, W., Li, H., Zhao, Z., and Chen, J., Magnetic properties of ultrafine nickel particles, *Journal of Applied Physics*, 70, 5903–5905, 1991.
319. Aus, M. J., Szpunar, B., Erb, U., El-Sherik, A. M., Palumbo, G., and Aust, K. T., *Scripta Metallurgica et Materialia*, 27, 1639–1645, 1991.
320. Schaefer, H. E., Kisker, H., Kronmuller, H., and Wurschum, R., Magnetic properties of nanocrystalline nickel, *Nanostructured Materials*, 1, 523–529, 1992.
321. Szpunar, B., Erb, U., Palumbo, G., Aust, K. T., and Lewis, L. J., *Physical Review B*, 53, 5547–5556, 1996.
322. Baibich, M. N., Broto, J. M., Fert, A., Nguyen Van Dau, F., Petroff, F., Etienne, P., Creuzet, G., Friederich, A., and Chazelas, J., *Physical Review Letters*, 61, 247–2475, 1988.
323. Hartmann, U., *Magnetic Multilayers and Giant Magnetoresistance, Fundamentals and Industrial Applications* 2000. Springer Verlag
324. Garcia, N., Magnetoresistance and magnetostriction in magnetic contacts, *Europhysics News*, 34(6), 2003.
325. Sharvin, Y. V., A possible method for studying Fermi surfaces, *Soviet Physics JETR*, 21, 655–660, 1965.
326. Chopra, H. D. and Hua, S. Z., Ballistic magnetoresistance over 3000% in Ni nanocontacts at room temperature, *Physical Review B*, 66, 020403–020406, 2002.
327. Egelhoff, W. F., Stiles, M. D., Moffat, T. P., Mallett, J., McMichael, R. D., Ettedugi, H., Shapiro, A. J., Powell, C. J., Svedberg, and E. B., Artifacts in ballistic magnetoresistance measurements. In *Proceedings of the 50th AVS International Symposium*, November 2–7, Paper No. MI0MoA8, 2003.
328. Dresselhaus, M. S., Dresselhaus, G., and Eklund, P. C., *Science of Fullerenes and Carbon Nanotubes*, Academic Press, New York, 1996.

329. http://www.pa.msu.edu/cmp/csc/nanotube.html and http://nanotube.msu.edu
330. http://www.cnanotech.com
331. Buldum, A. and Lu, J-P., Contact resistance between nanotubes, *Physical Review B*, 63, 161403–161406, 2001.
332. Palumbo, G., Gonzales, F., Brennenstuhl, A. M., Erb, U., Shmaydaa, W., and Lichtenberger, P. C., In-situ nuclear stream generator repair using electrodeposited nanocrystalline nickel, *Nanostructured Materials*, 19, 737–746, 1997.
333. Boylan, K., Ostrander, D., Erb, U., Palumbo, G., and Aust, K. T., An in-situ tem study of the thermal stability of nanocrystalline Ni-P, *Scripta Metallurgica et Materialia*, 25, 2711–2716, 1991.
334. Erb, U., Aust, K. T., and Palumbo, G., Electrodeposited nanocrystalline materials, In *Nanostructured Materials*, Koch, C. C., Ed., Nanostructured Materials, pp. 179–222, 2002.
335. Tabor, D., *Hardness of Metals*, Clarendon Press, Oxford, UK, 1951.
336. Mott, B. W., *Micro-indentation Testing*, Butterworths, London, 1956.
337. Alekhin, V. P., Berlin, G. S., Isaev, A. V., Kalei, G. N., Merkulov, V. A., Skvortsov, V. N., Ternovski, A. P., Krushchov, M. M., Shnyrev, G. D., and Shorshorov, M. Kh., Micromechanical testing of materials by microimpression, *Industrial Laboratyory*, 38, 619–621, 1972.
338. Bulychev, S. I., Alekhin, V. P., Shorshorov, M. Kh., Ternovskii, A. P., and Shnyrev, G. D., Determining Young's modulus from the indenter penetration diagram, *Industrial Laboratory*, 41(9), 1137–1140, 1975.
339. Pharr, G. M., Oliver, W. C., and Brotzen, F. R., On the generality of the relationship among the contacts stiffness, contact area and elastic modulus during indentation, *Journal of Materials Research*, 7, 613–617, 1992.
340. Doerner, M. F. and Nix, W. D., A method for interpreting the data from depth-sensing indentation instruments, *Journal of Materials Research*, 11, 601–609, 1986.
341. Oliver, W. S. and Pharr, G. M., Measurement of hardness and elastic modulus by instrumented indentation: Advances in understanding and refinements to methodology, *Journal of Materials Research*, 19, 3–20, 2004.
342. Oliver, W. S. and Pharr, G. M., An improved technique for determining hardness and elastic modulus using load-displacement sensing indentation experiments, *Journal of Materials Research*, 7, 1564–1583, 1992.
343. Soderlunbd, E. and Rowcliffe, D., Analysis of penetration curves produced by depth-sensing indentation systems, *Journal of Hard Materials*, 5, 149–177, 1994.
344. Ternovski, A. P., Alekhin, V. P., Shorshorov, M. Kh., Khrushchov, M. M., and Skortsov, V. N., Micromechanical testing of materials by depression, *Industrial Laboratory*, 39(10), 1242–1247, 1972.
345. Raman, V. and Berriche, R., Creep behavior of sputtered films using indentation testing, *Materials Research Society Symposium Proceedings*, 188, 171–176, 1990.
346. Lucas, B. N. and Oliver, W. C., Indentation power-law creep of high-purity indium, *Metallurgical and Materials Transactions: A*, 30, 601–610, 1999.
347. Pharr, G. M., Harding, D. S., and Oliver, W. C., Measurement of fracture toughness in thin films and small volumes using nanoindentation methods, *Mechanical Properties and Deformation Behavior of Materials having Ultra-Fine Microstructure*, Kluwer Academic Publishers, Dordrecht, 1993. pp. 449–461.
348. Pharr, G. M., Measurement of mechanical properties by ultra-low load indenation, *Materials Science and Engineering: A*, 253, 151–159, 1998.
349. Korhonen, M. A., LaFontaine, W. R., Pazkiet, C. A., Black, R. D., and Che-Yu, Li, Measurement of stress relaxation in thin aluminum metallization by continuous indentation and x-ray techniques, *Materials Research Society Symposium Proceedings*, 188, 159–164, 1990.
350. Baker, S. P., The analysis of depth-sensing indentation data, *Materials Research Society Symposium Proceedings*, 308, 209–216, 1993.
351. Binnig, G., Quate, C. F., and Gerber, C., Atomic force microscope, *Physical Review Letters*, 56(9), 930–933, 1986.
352. Binnig, G., Rohrer, H., Gerber, C., and Heibel, E., Tunneling through a controllable vacuum gap, *Applied Physics Letters*, 40(2), 178–180, 1982.
353. Majumdar, A., Carrejo, J. P., and Lai, J., Thermal imaging using the atomic force microscope, *Applied Physics Letters*, 62, 2501–2503, 1993.

354. Hobbs, P. C. D., Abraham, D. W., and Wickramasinghe, H. K., Magnetic force microscopy with 25 nm resolution, *Applied Physics Letters*, 55, 2357–2359, 1989.
355. http://www.psiainc.com
356. http://www.veeco.com
357. Smythe, W. R., *Static and Dynamic Electricity*, McGraw-Hill, New York, 1968.
358. Timsit, R. S., The potential distribution in a constricted cylinder, *Proceedings of 14th International Conference on Electrical Contacts,* Paris, pp. 21–25, 1988.
359. Rosenfeld, A. M. and Timsit, R. S., The potential distribution in a constricted cylinder: An exact solution, *Quarterly of Applied Mathematics*, 39, 405, 1981.
360. Aichi, H. Tahara, N. Analysis on the constriction resistance of the electric contact by the contact model using the electrolyte bath, *Proceedings of 20th International Conference on Electrical Contacts*, pp. 1–10, 1994; Aichi, H. Tahara, N. Analysis on the constriction resistance of the electric contact by the contact model using the electrolyte bath, *Proceedings of 7th International Conference on Electrical Contacts*, Nagoya, Japan, pp. 1–10, 1994;
361. Nakamura, M., Constriction resistance of conducting spots by the boundary element method, *IEEE Transactions on Components, Hybrids and Manufacturing Technology,* CHMT, 16, 339–344, 1993.
362. Nakamura, M. and Minowa, I., Computer simulation for the conductance of a contact interface, *IEEE Transaction on Components, Hybrids and Manufacturing Technology,* CHMT, 9, 150–155, 1986.
363. Lavers, J. D. and Timsit, R. S., Effect of signal frequency on constriction resistance, *Proceedings of 20th International Conference on Electrical Contacts,* Stockholm, Sweden, June 19–23, pp. 29–34, 2000.
364. Greenwood, J. A. and Williamson, J. B. P., Electrical conduction in solids. II. Theory of temperature-dependent conductors, *Proceedings of the Royal Society of London*, A246, 13–31, 1958.
365. Malucci, R. D., High frequency considerations for multi-point contact interfaces, *Proceedings of 47th IEEE Holm Conference on Electrical Contacts,* Montreal, Canada, September 25–27, pp. 175–185, 2001.
366. Timsit, R. S., Electrical conduction through small contact spots, *Proceedings of 50th IEEE Holm Conference on Electrical Contacts,* Montreal, Canada, pp. 184–190, 2004.
367. Wexler, G., The size effect and the non-local Boltzmann transport equation in orifice and disk geometry, *Proceedings of the Physical Society*, 89, 927–941, 1966.
368. Timsit, R. S., Electrical contact resistance: Properties of stationary interfaces, *IEEE Transactions on Components and Packaging Technology*, 22, 85–98, 1999.
369. Erts, D., Olin, H., Ryen, L., Olsson, E., and Thoelen, A., Maxwell and Sharvin conductance in gold point contacts investigated using TEM–STM, *Physical Review B*, 61, 12725–12727, 2000.
370. Zhuravlev, M. Y., Tsymbal, E. Y., Vedyayev, A. V., Jaswal, S. S., and Dieny, B., Spin blockade in ferromagnetic nanocontacts, *Applied Physical Letters*, 83, 3534–3536, 2003.
371. Van Ruitenbeek, J. M., Quantum point contacts between metals, In *Mesoscopic Electron Transport*, Sohn, L. L., Kouwenhoven, L. P., and Schön, Eds., Kluwer Academic, Dordrecht, pp. 549–579, 1997.
372. Agraït, N., Rubio, G., and Vieira, S., Plastic deformation of nanometer-scale gold connective necks, *Physical Review Letters*, 74, 3995–3998, 1995.
373. Stalder, A. and Dürig, U., Study of yielding mechanics in nanometer-sized Au contacts, *Applied Physics Letters*, 68, 637–639, 1996.
374. Bloom, S., Olin, H., Costa-Kramer, J. L., Garcia, N., Jonson, M., Serena, P. A., and Shekhter, R. I., Free-electron model for mesoscopic force fluctuations in nanowires, *Physical Review B*, 57, 8830–8833, 1998.
375. Brandbyger, M., Jacobsen, K. W., and Norskov, J. K., Scattering and conductance quantization in three-dimensional metal nanocontacts, *Physical Review B*, 55, 2637–2650, 1997.
376. Preston, P. F., An industrial atmosphere corrosion test for electrical contacts and connections, *Transactions of the Institute of Metal Finishing*, 50, 125–130, 1972.
377. Baker, R. G., Studies of static low voltage contacts at the bell telephone laboratories, *Proceedings of 2nd International Symposium on Electric Contact Phenomena,* Graz, Austria, pp. 545–553, 1964.
378. Antler, M., Feder, M., Hornig, C. F., and Bohland, J., The corrosion behaviour of single and multi-phase tin-nickel alloy electrodeposits, *Plating and Surface Finishing*, 63, 30–39, 1976.
379. Long, T. R. and Bradford, K. F., Contact resistance behavior of the 60pd40ag alloy in tarnishing environments, *Proceedings of Holm Seminar on Electrical Contacts,* Illinois Institute of Technology, Chicago, IL, pp. 145–154, 1975.

380. Antler, M., Drozdowicz, M. H., and Hornig, C. F., The corrosion resistance of worn tin-nickel and gold-coated tin-nickel alloy electrodeposits, *Journal of the Electrochemical Society*, 124, 1069–1078, 1977.
381. Antler, M., Contact resistance of tin-nickel electrodeposits, *Journal of the Electrochemical Society*, 125, 420–428, 1978.
382. Antler, M., Drozdowicz, M. H., and Haque, C. A., Connector contact materials: Effect of environmenton clad palladium, palladium-silver alloys, and gold electrodeposits, *IEEE Transactions on Components, Hybrids and Manufacturing Technology*, 4, 482–492, 1981.
383. Braunović, M., Fretting damage in tin-plated aluminum and copper connections, *Proceedings of 34th IEEE Holm Conference on Electrical Contacts,* San Francisco, USA, September 26–29, pp. 179–186, 1988.
384. Nakamura, M. and Minowa, I., Film resistance and constriction effect of current in a contact interface, *IEEE Transactions on Components, Hybrids and Manufacturing Technology*, 12, 109–114, 1989.
385. Williamson, J. B. P. and Greenwood, J. A., The constriction resistance between electroplated Surfaces, *Proceedings of International Conference on Electrical Contacts and Electromechanical Components, Appendix,* Beijing, China, Pergamon Press, Oxford, 1989.
386. ASTM B667-80, American Society for Testing Materials, 1916 Grace St, Philadelphia, PA 19103.
387. Pinnell, R. M. and Bradford, K., Influence of some geometric factors on contact resistance probe measurements, *IEEE Transactions on Components, Hybrids and Manufacturing Technology*, 3(1), 159–165, 1980.
388. Konchits, V. V. and Kim, C. K., Electric current passage and interface heating, *Wear*, 232, 31–40, 1999.
389. Konchits, V. V. and Korotkevich, S. V., Investigation of lubricant film strength in molecular scale boundary layers, *Journal of Friction and Wear*, 13(6), 1010–1020, 1992.
390. Simmons, J. G., Electric tunnel effect, *Journal of Applied Physics*, 34(6), 1793–1801, 1963.
391. Myshkin, N. K. and Konchits, V. V., Evaluation of the interface using the measurement of electric conductivity, *Wear*, 172(6), 29–40, 1994.
392. Konchits, V. V., Meshkov, V. V., and Myshkin, N. K., *Tribology of Electrical Contacts*, Nauka i Tekhnika, Minsk, 1986.
393. Greenwood, J. A., Constriction resistance and the real area of contact, *British Journal of Applied Physics*, 17, 1621–1631, 1966.
394. Myskin, N. K., Petrokovets, M. I., and Chizhik, S. A., Simulation of real contact in tribology, *Tribology International*, 31(1–3), 79–86, 1998.
395. Minowa, I., Nakamura, M., and Kanno, M., Conductance of a contact interface depending on the location and distribution of conducting spots, *Proceedings of Electrical Conference on Contacts, Electromechanical Components and Their Applications,* pp. 19–25, 1986.
396. Yip, F. and Venart, Y. E. S., Surface topography effects in estimation of thermal and electrical contact resistance, *Proceedings of IME*, 182, pt 3k: 81–93, 1968.
397. Tomas, T. R., Defining the microtopography of surface in thermal contact, *Wear*, 79(1), 73–82, 1982.
398. Myshkin, N. K. and Kim, C. K., Influence of relative position and size of metal contact spots on conductivity, *Journal of Friction and Wear*, 15(4), 54–58, 1994.
399. Myshkin, N. K., Petrokovets, M. I., Chizhik, S. A., Konchits, V. V., and Sviridenok, A. I., Contact of rough bodies and its conductivity, *Soviet Journal of Friction and Wear*, 4(5), 845–853, 1983.
400. Chen, P. and Burton, R. A., Thermoelastic effects in brushes with high current and high sliding speeds, *Proceedings of 24th Holm Conference on Electrical Contacts,* Chicago, USA pp. 571–575, 1978.
401. Brailford, J. B., Influence of electrical current on static friction of metal surface in air, *Wear*, 25(1), 85–97, 1973.
402. Jordan, R. S., Electrotransport in solid metal systems, *Contemporary Physics*, 15(4), 375–400, 1974.
403. Lancaster, J. K. and Stanley, I. W., The effect of current on the friction of carbon brush materials, *British Journal of Applied Physics*, 15, 29–41, 1964.
404. Myshkin, N. K. and Konchits, V. V., Friction and wear of metal-composite electrical contacts, *Wear*, 158, 119–140, 1992.
405. Williamson, J. B. P. and Allen, N., Thermal stability in graphite contacts, *Wear*, 78, 39–48, 1982.

406. Bowden, F. P. and Williamson, J. B. P., Influence of the passage of current on the contact between solids, *Proceedings of the Royal Society of London, Series A*, 246(1), pp. 1–11, 1958.
407. Belyi, V. A., Myshkin, N. K., and Konchits, V. V., Estimation of surface temperatures results in disorientation of boundary lubricating films, *ASLE Transactions*, 25(3), 346–348, 1982.
408. Tamai, T. and Tsuchiya, K., Direct observation for the effect of electric current on contact interface, *IEEE Transactions on Components, Hybrids and Manufacturing Technology*, 2(1), 76–80, 1979.
409. Blok, H., Theoretical study of temperature rise at surfaces of actual contact under oilness lubricating conditions, *Proceedings of the Institute of Mechanical Engineering (London)*, 2, pp. 222–235, 1937.
410. Carslaw, H. S. and Jaeger, J. C., *The Conduction of Heat in Solids,* Oxford, Clarendon, 1959.
411. Johnson, K. L., *Contact Mechanics*, Cambridge University Press, Cambridge, 1987.
412. Ling, F. F., *Surface Mechanics*, Wiley, New York, 1973.
413. Jaeger, J. S., Moving sources of heat and the temperature at sliding surfaces, *Proceedings of the Royal Society of New South Wales*, (56), pp. 203–224, 1942.
414. Hilgarth, G., Zusammenhang zwischen Kontactspannung Kontacteilen Temperatur beikurzeitig belasteten Starkstromkontakten, *ETZ-A*,13 464–467, 1958.
415. Timsit, R. S., On the evaluation of contact temperature from potential drop measurements, *IEEE Transactions on Components, Hybrids and Manufacturing Technology*, 6(1), 115–121, 1983.
416. Kongsjorden, H., Kulsetas, J., and Sletbak, J., Direct detection of A-Spots in current carrying contact by means of IR-microscopy, *Proceedings of 24th Holm Conference on Electrical Contacts,* Chicago, USA, pp. 477–482, 1978.
417. Cuthrell, R. E. and Jones, L. K., Surface contaminant characterization using potential-current curves, *Proceedings of 23rd Holm Conference on Electrical Contacts,* Chicago, USA, pp. 157–162, 1977.
418. Jansen, A. S., Mueller, F. M., and Wyder, P., Normal metallic point contacts, *Science*, (199), 1037–1040, 1978.
419. Meyerhofer, D. and Ochs, S. A., Current flow in very thin films of Al_2O_3 and BeO, *Journal of Applied Physics*, 34(9), 2535–2543, 1963.
420. Chow, C. K., Effect of insulating-film-thickness nonuniformity on tunnel characteristics, *Journal of Applied Physics*, 34(9), 2599–2602, 1963.
421. Chichinadze, A. V. and Braun, E. D., Friction devices, In *Tribology—Lubrication, Friction, and Wear*, Kragelsky, I. V. and Alisin, V. V., Eds., London and Bury St Edmunds, U.K.: Prof. Eng. Publ. Lim., pp. 744–776.
422. Archard, J. F., The temperature of rubbing surfaces, *Wear*, 2, 438–455, 1959.
423. Kuhlmann-Wilsdorf, D., Flash temperatures due to friction and Joule heat at asperities contacts, *Wear*, 105, 187–198, 1985.
424. Kuhlmann-Wilsdorf, D., Demystifying flash temperatures. I. Analytical expressions based on a simple model, *Materials Science and Engineering*, 93, 107–117, 1987.
425. Kuhlmann-Wilsdorf, D., Demystifying flash temperatures. II. First-order approximation for plastic contact spots, *Materials Science and Engineering*, 93, 119–133, 1987.
426. Burton, R. A. and Burton, R. G., Experiments and analysis of the thermoelastic behavior of a brush on a slip ring, *Proceedings of 35th IEEE Holm Conference on Electrical Contacts,* Chicago, USA, September 15–20, pp. 25–30, 1989.
427. Williamson, J. B. P., Deterioration processes in electrical connections, *Proceedings of 5th International Research Symposium on Electrical Contact Phenomena,* The University of Swansea, July, pp. 30–34, 1968.
428. Jackson, R. L., The preparation and performance of bolted joints using grade 1350 aluminium busbar, *CERL Research Report RD/L//R* 2010, 1980.
429. Abbott, W. H., Contact corrosion, In *Electrical Contacts: Principles and Applications*, Slade, P. G., Ed., Marcel Dekker, New York, pp. 113–154, 1999.
430. Garte, S. M., Porosity, In *Gold Plating Technology*, Read, F. H. and Goldie, W., Eds., Electrochemical Publications, Ayr, Scotland, pp. 295, pp. 345–359, 1974.
431. Lin, X.-Y. and Zhang, J.-G., Dust corrosion, *Proceedings of 22nd International Conference on Electrical Contacts,* Seattle, pp. 255–262, 2004.
432. Wan, J. W., Gao, J. C., Lin, X. Y., and Zhang, J. G., Water soluble salts and their effect of electrical contact surfaces, *Proceedings of International Conference on Electric Contacts, Electrical Components and their Applications,* Nagoya, Japan, July 19–24, pp. 37–41, 1999.

433. Mason, W. P. and White, S. D., New techniques for measuring forces and wear in telephone switching apparatus, *Bell Labs Technical Journal*, 31, 469–473, 1952.
434. Mindlin, R. D., Compliance of elastic bodies in contact, *Journal of Applied Mechanics*, 16, 259–263, 1949.
435. Eden, E. M., Rose, W. N., and Cunningham, F. L., The endurance of metals, *Proceedings of the Institute of Mechanical Engineering*, 4, pp. 875–881, 1911.
436. Tomlison, A., Rusting of steel surfaces in contact, *Proceedings of the Royal Society of London, Series A*, 115, 472–476, 1927.
437. Godfrey, D., *Investigation of Fretting Corrosion by Microscopic Observation*, NACA Technical Note No. 2039, 1950.
438. Feng, I. M. and Rightmire, B. G., The mechanism of fretting, *Lubrication Engineering*, 9, 134–139, 1953.
439. Uhlig, H. H., Mechanism of fretting corrosion, *Journal of Applied Mechanics*, 21, 401–405, 1954.
440. Stowers, L. F. and Rabinowicz, E., The mechanism of fretting wear, *Journal of Lubrication Technology*, 95, 65–70, 1973.
441. Oding, A. and Ivanova, V. S., Thermoelectric effects in fretting wear, *Proceedings of International Conference on Fatigue of Metals,* pp. 408–413, 1956.
442. Waterhouse, R. B. and Taylor, D. E., Fretting debris and delamination theory of wear, *Wear*, 29, 337–443, 1977.
443. Sproles, E. S., Gaul, D. J., and Duquette, D. J., A new interpretation of the mechanism of fretting and fretting corrosion damage, In *Fundamentals of Tribology*, Suh, N. P. and Saka, N., Eds., MIT Press, Cambridge, MA, pp. 585–594, 1978.
444. Godet, M., The third body approach: A mechanical view of wear, *Wear*, 100, 437–452, 1994.
445. Waterhouse, R. B., *Fretting corrosion*, Pergamon Press, Oxford, 1972.
446. Hurricks, P. L., The mechanism of fretting—a review, *Wear*, 15, 389–409, 1970.
447. Fenner, A. J., Wright, K. H., and Mann, J. Y., Fretting corrosion and its influence on fatigue failure, *Proceedings of International Conference on Fatigue of Metals, Institute of Mechanical Engineering* London, pp. 11–17, 1956.
448. Fairweather, A., Lazenby, F., and Parker, A., Development of resistance and microphone noise at a disturbed contact, *Proceedings of 2nd International Research Symposium on Electrical Contact Phenomena,* Graz, May 4–6, Technische Hochschule, Graz, pp. 316–319, 1964.
449. Bock, E. M. and Whitley, J. H., Fretting corrosion in electric contacts, *Proceedings of 20th Holm Conference on Electrical Contacts,* Chicago, pp. 128–138, 1974.
450. Krumbein, S. J., Contact properties of tin plates, *Proceedings of 20th Holm Conference on Electrical Contacts,* Chicago, pp. 38–49, 1974.
451. Antler, M., Graddick, W. F., and Tompkins, H. G., Base metal contacts: an exploratory study of separable connection to tin–lead, *Proceedings of 21st Holm Conference on Electrical Contacts,* Chicago, pp. 25–37, 1975.
452. Kongsjorden, H., Kulsetas, J., and Sletbak, J., Degradation of electrical contacts caused by oscillatory micromotion between the contact members, *Proceedings of 24th Holm Conference on Electrical Contacts,* Chicago, pp. 87–92, 1978.
453. Neijzen, J. H. M. and Glashorster, J. H. A., Fretting corrosion of tin-coated electrical contacts, *IEEE Transactions on Components, Hybrids and Manufacturing Technology*, 10, 68–72, 1978.
454. Antler, M. and Drozdowicz, E. S., Fretting corrosion of gold-plated connector contacts, *Wear*, 74, 27–50, 1981–1982.
455. Antler, M., Fretting corrosion of solder-coated electrical contacts, *IEEE Transactions on Components, Hybrids and Manufacturing Technology*, 7, 129–138, 1984.
456. Antler, M., Electrical effects of fretting connector contact materials: A review, *Wear*, 106, 5–33, 1985.
457. Souter, J. W. and Staunton, W., The fretting wear of electrodeposited contact coatings, *Transactions of the Institute of Metal Finishing*, 66(1), 8–13, 1988.
458. Tian, H., Saka, N., and Rabininovicz, E., Friction and failure of electroplated sliding contacts, *Wear*, 142, 57–65, 1991.
459. Tian, H., Saka, N., and Rabininovicz, E., Fretting failure of electroplated gold contacts, *Wear*, 42, 265–274, 1991.

460. Murata, H., Imada, Y., Honda, F., and Nakajima, K., Effect of fretting on electroplated Pd–Ni contacts, *Wear*, 162–164, 339–346, 1993.
461. Kassman, A., Imrell, T., and Jacobson, S., Fretting of powered silver plated connectors in a corrosive environment, *Proceedings of 17th International Conference on Electrical Contacts,* Nagoya, pp. 327–333, 1994.
462. Lee, A. and Mamrick, M., Fretting corrosion of tin-plated copper alloy, *IEEE Transaction on Components, Hybrids and Manufacturing Technology*, 10, 63–67, 1987.
463. Schneegans, O., Houze, F., Chretien, P., Noel, S., Bodin, C., Boyer, L., Tristani, L., and Zindine, E. M., Fretting degradation of tin-plated contacts studied by means of new electrical cartography technique based on the atomic force microscopy, *Proceedings of 19th International Conference on Electrical Contacts,* Nuremburg, pp. 187–193, 1998.
464. Swingler, J. and McBride, J. W., The synergistic relationship of stresses in the automotive connector, *Proceedings of 19th International Conference on Electrical Contacts,* Nuremburg, pp. 141–145, 1998.
465. Klungtvedt, K. and Braunović, M., Effect of intergranular cohesion on the intermittency of automotive headlamp switch contacts, *Proceedings of 47th IEEE Holm Conference on Electrical Contacts,* Montreal, Canada, September 25–27, pp. 56–72, 2001.
466. Motine, J. J. and Reagor, B. T., Investigation of fretting corrosion at dissimilar metal interfaces on socketed IC device applications, *Proceedings of 29th IEEE Holm Conference on Electrical Contacts,* Chicago, pp. 61–71, 1983.
467. Braunović, M. and Gervais, P., Fretting problems in electrical industry, *Proceedings of 17th Inter-Ram,* Hershey, pp. 356–365, 1990.
468. Brayant, M. D., Assessment of fretting failure models of electrical connectors, *Proceedings of 40th IEEE Holm Conference on Electrical Contacts,* Chicago, USA, October 17–19, pp. 167–175, 1994.
469. Boyer, L. and Tristani, L., A model for the contact resistance evolution during a fretting test, *Proceedings of 20th International Conference on Electrical Contacts,* Stockholm, Sweden, June 19–23, pp. 457–466, 2000.
470. Tristani, L., Zindine, E. M., Boyer, L., and Klimek, G., Mechanical modelling of fretting cycles of electrical contacts, *Proceedings of 44th IEEE Holm Conference on Electrical Contacts,* Arlington USA, October 26–28, pp. 44–52, 1998.
471. Mallucci, R. D., Dynamic Model of stationary contacts based on random variations of surface features, *Proceedings of 37th IEEE Holm Conference on Electrical Contacts,* Chicago, USA, October 6–9, pp. 90–101, 1991.
472. Malucci, B., Fretting corrosion degradation, threshold behaviour and contact instability, *Proceedings of 49th IEEE Holm Conference on Electrical Contacts,* Washington, USA, September 8–9, pp. 1–15, 2003.
473. Braunović, M., Fretting corrosion between aluminum and different contact materials, *Proceedings of 22nd Holm Conference on Electrical Contacts,* Chicago, USA, pp. 223–231, 1977.
474. Braunović, M., Degradation of Al–Al and Al–Cu connections due to fretting, *Wear*, 125, 53–66, 1988.
475. Antler, M. and Sproles, E. S., Effect of fretting on the contact resistance of palladium, *IEEE Transactions on Components, Hybrids and Manufacturing Technology*, 5(1), 158–166, 1982.
476. Braunović, M., Effect of contact load on the contact resistance behaviour of different conductor and contact materials under fretting conditions, *Proceedings of 19th International Conference on Electrical Contacts,* Nurenbery, Germany, September 21–23, pp. 283–287, 1998.
477. Lee, A., Low power commercial automotive and appliance connections, In *Electrical Contacts: Principles and Applications*, Slade, P. G., Ed., Marcel Dekker, Inc., New York, pp. 279–307, 1999.
478. Castel, P., Monet, A., and Caraballeira, A., Fretting corrosion in low level electrical contacts: A quantitative analysis of the significant variables, *Proceedings of 12th International Conference on Electrical Contacts,* Chicago, pp. 75–81, 1984.
479. Gagnon, D., Braunović, M., and Masounave, J., Effect of fretting slip amplitude on the friction behaviour of electrical contact materials, *Proceedings of 51st IEEE Holm Conference on Electrical Contacts,* Chicago, pp. 186–195, 2005.
480. Bruel, J. F., Smirou, P., and Caraballeira, A., Gas environment effect on the fretting corrosion behavior of contact materials, *Proceedings of 14th International Conference on Electrical Contacts,* Paris, France, pp. 219–223, 1988.

481. Van Dijk, P., Kassman-Rudolphi, A., and Klaffke, D., Investigations on electrical contacts subjected to fretting motion, *Proceedings of 21st International Conference on Electrical Contacts,* Zurich, Switzerland, September 9–12, pp. 189–195, 2002.
482. Lee, A., Mao, A., and Mamrick, M. S., Fretting corrosion of tin at elevated temperatures, *Proceedings of 34th IEEE Holm Conference on Electrical Contacts,* San Francisco, USA, September 26–29, pp. 87–91, 1988.
483. Braunović, M., Effect of fretting on the contact resistance of aluminum with different contact materials, *IEEE Transactions on Components, Hybrids and Manufacturing Technology*, 2, 25–31, 1979.
484. Alamarguy, D., Lecaude, N., Chretien, P., Noel, S., and Teste, P., Current effect on fretting degradation of hot dipped tin contacts, *Proceedings of 21st International Conference on Electrical Contacts,* Zurich, Switzerland, September 9–12, pp. 179–184, 2002.
485. Gagnon, D. and Braunović, M., Fretting in copper-to-copper contacts under AC and DC current conditions, *IEEE Transactions on Components and Packaging Technologies*, 24, 378–383, 2001.
486. Williamson, J. B. P., The microworld of the contact spot, *Proceedings of 27th IEEE Holm Conference on Electrical Contacts,* Chicago, USA, pp. 1–20, 1981.
487. Golego, N. L., Alyabev, A. Y., and Shevelya, V. V., *Fretting corrosion in metals*, Tekhika, Kiev, 1974.
488. Dixon, C. R. and Nelson, F. G., The effect of elevated temperature on flash-welded aluminum–copper joints, *Transactions of the AIEE, Part II*, 78, 491–495, 1960.
489. Wallach, E. R. and Davis, G. J., Joint resistance and current paths in heat-treated aluminum/copper solid-state welds, *Metals Science*, (March), 97–103, 1977.
490. Wallach, E. R. and Davis, G. J., Mechanical properties of aluminum–copper solid-phase welds, *Metals Technology*, April, 183–189, 1977.
491. Timsit, R., Electrical instabilities in stationary electrical contacts: Al-plated-brass junctions, *IEEE Transactions on Components, Hybrids and Manufacturing Technology*, 11(1), 43–45, 1988.
492. Rabkin, D. M., Ryabov, V. R., Lozovskaya, A. V., and Dovzhenko, V. A., Preparation and properties of copper–aluminum intermetallic compounds, *Soviet Powder Metallurgy and Metals Ceramics*, (8), 695–701, 1970.
493. Nakamura, M. M., Yonezawa, Y., Nakanishi, T., and Kondo, K., Durability of Al–Cu hot-pressure welding joints, *Wire Journal International,* (April), 71–75, 1977.
494. Rayne, J. A. and Bauer, C. L., Effect of intermetallic phase formation on electrical and mechanical properties of flash-welded Al–Cu couples, *Proceedings of 5th Bolton Landing Conference on Weldments,* pp. 353–360, 1979.
495. Gjosten, N. A., Diffusion, ASM, 1973.
496. Timsit, R. S., Intermetallic growth at Al/-brass interfaces, *Acta Metallurgica*, 33, 97–103, 1985.
497. Gusak, A. M. and Gurov, K. P., Kinetics of phase transformations in a diffusion zone during interdiffusion phase formation, *Physics of Metals and Metallography*, 53(5), 12–16, 1982.
498. Pimenov, V. N., Gurov, K. P., Khudyakov, K. I., Dol'nikov, S. S., Milievskii, R. A., Khlomov, V. S., and Miller, Y. G., Effect of electrical current on the phase formation in the diffusion layer, *Fizika i Khimiya Obrabotki Materialov*, (1), 107–112, 1978.
499. Huntington, H. B., Electromigration in metals, In *Diffusion in Solids: Recent Developments*, Nowick, A. S. and Burton, J. J, Eds., Academic Press, New York, Chapter 6, p. 303, 1974.
500. Silveria, V. L. A., Mannheimer, W. A., and Braunović, M., Degradation of Cu–Sn/Pb surface layers on aluminium conductor by the action of an electric current, *Proceedings of 12th International Conference on Electrical Contacts,* Montreal, pp. 117–127, 1984.
501. Liu, W. C., Chen, S. W., and Chen, C. M., The Al/Ni interfacial reactions under the influence of electric current, *Journal of Electronic Materials*, 27, 5–8, 1998.
502. Chen, C. M. and Chen, S. W., Electric current effects on Sn/Ag interfacial reactions, *Journal of Electronic Materials*, 38, 902–906, 1999.
503. Chen, C. M. and Chen, S. W., Electromigration effect upon the Sn/Ag and Sn/Ni interfacial reactions at various temperatures, *Acta Materialia*, 50, 2461–2469, 2002.
504. Hummel, R. E., Electromigration and related failure mechanisms in integrated circuit interconnections, *International Materials Review*, 39, 97–111, 1994.
505. Berenbaum, L. and Rosenberg, R., Surface topology changes during electromigration in metallic thin film stripes, *Thin Solid Films*, 4, 187–204, 1969.

506. Scorzoni, A., Neri, B., Caprile, C., and Fantini, F., Electromigration in thin-film interconnection lines: Models, methods and results, *Materials Science Report*, 7, 143–220, 1991.
507. Runde, M., Hodne, E., and Totdal, B., Experimental study of the conducting spots in aluminum contact interface, *IEEE Transactions on Components, Hybrids and Manufacturing Technology*, 13, 1068–1073, 1990.
508. Runde, M., Mass transport in stationary contact points, *IEEE Transactions on Components, Hybrids and Manufacturing Technology*, 10, 89–99, 1987.
509. Ruppert, C. and Runde, M., Thermally induce mechanical degradation of contact spots in aluminum interfaces, *Proceedings of 22nd International Conference on Electrical Contacts,* pp. 494–501, 2004.
510. Aronstein, J., Electromigration failure of aluminum contact junctions, *Proceedings of 41st IEEE Holm Conference on Electrical Contacts,* Montreal, Canada, October 2–4, pp. 10–16, 1995.
511. Aronstein, J., AC and DC electromigration in aluminum contact junctions, *Proceedings of 42nd IEEE Holm Conference on Electrical Contacts,* Chicago, USA, pp. 311–320, 1996.
512. Naybour, R. D. and Farrell, T., Degradation mechanisms of mechanical connectors on aluminum conductors, *Proceedings of the IEEE*, 120(2), pp. 273–280, 1973.
513. Atermo, R., A method for testing compressive relaxation in aluminum wire conductors, *Wire Journal International*, (September), 127–131, 1973.
514. Troitsky, O. A. and Rozno, A. G., Electroplastic effect in metals, *Soviet Physics of the Solid State*, 12, 161, 1970.
515. Klypin, A. A., Creep of metals under the influence of electric current, *Problemy Prochnosti*, (9) 35–39, 1972 (in Russian).
516. Stashenko, V. I., Troitskii, O. A., and Spitsyn, V. I., Action of current pulses on zinc single crystals during creep, *Physica Status Solidi A*, 79, 549, 1983.
517. Troitskii, O. A. and Spitsyn, V. I., Investigation of the electroplastic deformation of a metal by the method of stress relaxation and creep, *Soviet Physics Doklady*, 21(2), 111, 1976.
518. Troitskii, O. A. and Stashenko, V. I., Stress relaxation investigation of the electroplastic deformation of a metal, *Physics of Metals and Metallography*, 47, 149–159, 1979.
519. Troitskii, O. A., Spitsyn, V. I., and Stashenko, V. I., The effect of an electric current on the relaxation of stresses in crystals of zinc, cadmium and lead, *Soviet Physics Doklady*, 23(7), 509, 1978.
520. Lebedev, V. P. and Hotkevich, V. I., Effect of electric current pulses on the low-temperature deformation of aluminum, *Physics of Metals and Metallography*, 54(2), 353–360, 1982.
521. Varma, S. K. and Cornwell, L. R., The electroplastic effect in aluminum, *Scripta Metallurgica*, 13, 733–738, 1979.
522. Sprecher, A. F., Mannan, S. L., and Conrad, H., On the mechanisms for the electroplastic effect in metals, *Acta Metallurgica*, 34(7), 1145–1151, 1986.
523. Conrad, H. and Sprecher, A. F., The electroplastic effect in metals, In *Dislocations in Solids*, Nabarr, F. R. N., Ed., Vol. 8, Elsevier, Amsterdam, pp. 498–505, 1989.
524. Galligan, J. M., Dislocation drag mechanisms in normal state metals, *Scripta Metallurgica*, 18, 653–656, 1984.
525. Elbaum, C., Dislocation drag determination by ultrasonic methods, *Scripta Metallurgica*, 18, 657–662, 1984.
526. Granato, A. V., Viscosity effects in plastic flow and internal friction, *Scripta Metallurgica*, 18, 663–667, 1984.
527. Troitskii, O. A. and Likhtman, V. I., Anisotropy of electron and -radiation on the deformation of brittle zinc single crystals, *Soviet Physics Doklady*, 148, 332, 1963.
528. Spitsyn, V. I. and Troitskiy, O. A., *Electroplastic Deformation of Metals*, Nauka, Moscow, 1985 (in Russian).
529. Kravchenko, V. Y., Effect of directed electron beam on moving dislocations, *Soviet Physics JETP.*, 51, 1135, 1966.
530. Klimov, K. M., Shnyrev, V. D., and Novikov, N. I., The electroplasticity of metals, *Soviet Physics Doklady*, 19, 787, 1975.
531. Roschupkin, A. M., Troitskii, O. A., and Spitsyn, V. I., Development of the concept of the effect of current with high density on the plastic deformation of metals, *Soviet Physics Doklady*, 286(3), 633–636, 1986.

532. Okazaki, K., Kagawa, H., and Conrad, H., A study of the electroplastic effect in metals, *Scripta Metallurgica*, 12, 1063, 1978.
533. Okazaki, K., Kagawa, M., and Conrad, H., Additional results on the electroplastic effect in metals, *Scripta Metallurgica*, 13, 277–280, 1979.
534. Okazaki, K., Kagawa, M., and Conrad, H., An evaluation of the contribution of skin, pinch and heating effects to the electroplastic effect in titanium, *Materials Science and Engineering*, 45, 109–114, 1980.
535. Conrad, H., White, J., Cao, W. D., Lu, X. P., and Sprecher, A. F., Effect of electric current pulses on fatigue characteristics of polycrystalline copper, *Materials Science and Engineering: A*, 145, 1–9, 1991.
536. Conrad, H., Sprecher, A. F., Cao, W. D., and Lu, X. P., Electroplasticity—the effect of electricity on the mechanical properties of metals, *Journal of Materials*, (September), 28–32, 1990.
537. Goldman, P., Motowidlo, D., and Galligan, J. M., The absence of an electroplastic effect in lead at 4.2 K, *Scripta Metallurgica*, 15, 353–358, 1981.
538. Timsit, R. S., Remarks on recent experimental observations of the electroplastic effect, *Scripta Metallurgica*, 15, 461–467, 1981.
539. Cao, W. D., Sprecher, A. F., and Conrad, H., Measurement of the electroplastic effect in Nb, *Journal of Physics E: Scientific Instruments*, 22, 1026–1031, 1989.
540. Troitskii, O. A., Pressure shaping by the application of high energy, *Materials Science and Engineering*, 75, 37–50, 1985.
541. Silveira, V. L., Porto, M. F. S., and Mannheimer, W. A., Electroplastic effect in copper subjected to low-density electric current, *Scripta Metallurgica*, 15, 945–951, 1981.
542. Silveira, V. L., Fortes, R. A. F. O., and Mannheimer, W. A., Modification of the dislocation substructure in copper during electroplastic treatment, *Beitr. Elektronenmikroskp. Direktabb. Oberfl.*, 15, 217–221, 1982.
543. Braunović, M., Effect of electrical current on stress relaxation of aluminum wire conductors, *Proceedings of 20th International Conference on Electrical Contacts,* Stockholm, Sweden, June 19–23, pp. 355–360, 2000.
544. Klypin, A. A. and Solov'ev, E. S., Relationship between electronic emission and creep of metallic materials, *Strength of Materials*, (11), 45–49, 1975.
545. Stashenko, V. I. and Troitskiy, O. A., Influence of pulsating current frequency and external mechanical stress on the creep rate of crystals, *Physics of Metals and Metallography*, 53(1), 180–184, 1982.
546. Takano, E. and Mano, K., The failure mode and lifetime of static contacts, *IEEE Transactions on Parts, Materials and Packaging*, 1, 51–55, 1968.
547. Bron, O. B., Fridman, B. E., Evseev, E., Evaluation of long-term behavior of closed contacts in different environments, *Electrotechnical Engineering*, (in Russian), (2), 5–7, 1978.
548. Izmailov, V. V., Conductivity of long-term closed electrical contacts, *Proceedings of 10th International Conference on Electric Contact Phenomena,* Budapest, Hungery, January 13–21, pp. 93–104, 1980.
549. Boyer, L., Houze, F., Klimek, G., and Noel, S., Electrical and physical modeling of contact defects due to fretting, *IEEE Transactions on Components, Packaging and Manufacturing Technology, Part A*, 17(1), 134–140, 1994.
550. Bryant, M. D., Time-wise increases in contact resistance due to surface roughness and corrosion, *IEEE Transactions on Components, Hybrids and Manufacturing Technology*, 14(1), 79–89, 1991.
551. Bergmann, R., Löbl, H., Böhme, H., and Großmann, S., Model to assess the reliability of electrical joints, *Proceedings of 42nd IEEE Holm Conference on Electrical Contacts,* Chicago, USA, September 16–20, pp. 180–188, 1996.
552. Sun, M., Pecht, M. G., Natishan, M. A. E., and Martens, R. I., Lifetime resistance model of bare metal electrical contacts, *IEEE Transactions on Advanced Packaging*, 22(1), 60–67, 1999.
553. Malucci, R. D., Impact of fretting parameters on contact degradation, *Proceedings of 42nd IEEE Holm Conference on Electrical Contacts,* Chicago, USA, September 16–20, pp. 395–403, 1996.
554. Kubaschevski, O. and Hopkins, B. E., *Oxidation of Metals and Alloys*, Butterworths, London, 1962.
555. Braunović, M., Izmailov, V. V., and Novoselova, M. V., A model for lifetime evaluation of closed electrical contacts, *Proceedings of 51th IEEE Holm Conference on Electrical Contacts,* Chicago, pp. 217–223, 2005.

556. Silveira, V. L. A., Teixeira, R. R. G., and Mannheimer, W. A., On the behavior of tin-plated electrical connectors during heat cycling tests, *Proceedings of 29th IEEE Holm Conference on Electrical Contacts,* Chicago, USA, pp. 105–110, 1983.
557. Johnson, B. and Braunović, M., Performance of utility power connectors in a saline environment, Paper presented at IEEE/PES, October 28–November 2, Atlanta, Georgia, 2001.
558. King, R., Timsit, S., and Abbott, W. H., Environmental degradation of utility power connectors in a harsh environment, *IEEE Transactions on Components, Packaging Technology*, 23, 261–268, 2000.
559. Schindler, J. J., Axon, R. T., and Timsit, R. S., Mechanical and electrical contact properties of wedge-connectors, *IEEE Transactions on Components, Packaging and Manufacturing Technology, Part A*, 19, 287–294, 1996.
560. Power Smart BC Hydro Tech, http://www.bchydro.com
561. Sprecher, J. and Royse, B., Higher loads demand new tap-connector practices, *Electrical World*, 208, 48–55, 1994.
562. Connectors for use between aluminum-to-aluminum or aluminum-to-copper bare overhead conductors, July, ANSI C119.4-1991, 1991.
563. Electric power connectors for use in overhead line conductors, CSA C57- 1966, 1966.
564. Melsom, S. W. and Booth, H. C., The efficiency of overlapping joints in copper and aluminum busbar conductors, *Journal IEEE*, 60, 312, 1922.
565. Donatti, E., Overlapping joints in electrical furnace circuits, *L'Energia Elettrica*, 12, 433–440, 1935.
566. Al elast contact disks, Pfisterer Technical Notes: Station fittings, 5th ed., pp. 14–16, 1987.
567. Braunović, M., Evaluation of different types of contact aid compounds for aluminum-to-aluminum connectors and conductors, *IEEE Transaction on Components, Hybrids and Manufacturing Technology*, 8(3), 313–320, 1985.
568. Bond, N., Aluminum contact surfaces in electrical transition interfaces, *IEEE Transactions PMP*, 5(2), 104–109, 1969.
569. Naybour, R. D. and Farrell, T., Connectors for aluminum cables: A study of the degradation mechanisms and design criteria for reliable connectors, *IEEE Transactions on Parts, Hybrids and Packaging*, 9(1), 30–36, 1973.
570. Roullier, L., Contact interfaces in aluminum mechanical joints, *Proceedings of 2nd International Research Symposium on Electrical Contact Phenomena,* Graz, Austria, Technische Hokhschule, pp. 503–518, 1964.
571. Braunović, M., Fretting damage in tin-plated aluminum and copper connectors, *IEEE Transactions on Components, Hybrids and Manufacturing Technology*, 12, 215–223, 1989.
572. Braunović, M., Effect of fretting in aluminum-to-tin connections, *IEEE Transactions on Components, Hybrids and Manufacturing Technology*, 13(3), 579–586, 1990.
573. Braunović, M., Evaluation of different platings for aluminum-to-copper connections, *IEEE Transactions on Components, Hybrids and Manufacturing Technology*, 15(2), 204–215, 1992.
574. Braunović, M., Deleterious effect of fretting in aluminum-to-brass electrical connections, *Proceedings of International Conference on Electrical Contacts & Electromechanical Components,* Beijing May 9–21, pp. 57–68, 1989.
575. Cabrera, N. and Mott, N. F., Theory of oxidation of metals, *Progress in Physics*, 12, 163–175, 1948/49.
576. Braunović, M., Overheating of flexible tinned copper connectors, *IEEE Transactions CPT*, 24, 384–395, 2001.
577. Hain, W., Monitoring of material property transformations with electrical resistivity, *Materials Evaluation*, 47(June), 619–629, 1989.
578. Frost, H. J. and Ashby, M. F., *Deformation-Mechanism Maps*, Pergamon Press, Oxford, 1982.
579. Grossman, S., Kindersberger, J., Lobl, J., and Schoft, Creep ageing of bolted electrical busbar joints, *Proceedings of 19th International Conference on Electrical Contacts,* Nurembery, Germany, September 21–23, pp. 269–279, 1998.
580. Kindersberger, J., Lobl, J., and Schoft, Plastic deformation and loss of joint force by creep in high current joints, *Proceedings of 20th International Conference on Electrical Contacts,* Stockholm, Sweden, June 19–23, pp. 367–372, 2000.
581. Schoft, S., Measurement and calculation of the decreasing joint force in high current aluminum joints, *Proceedings of 22nd International Conference on Electrical Contacts,* Seattle, pp. 511–519, 2005.

582. Braunović, M., Effect of different types of mechanical contact devices on the performance of bolted aluminum joints under current cycling and stress relaxation conditions, *Proceedings of 32nd IEEE Holm Conference on Electrical Contacts,* Boston, USA, October 27–29, pp. 133–141, 1986.
583. Johnson, J. L. and Moberly, L. E., Separable electric power contacts involving aluminum bus-bars, *Proceedings of 21st Holm Conference on Electrical Contacts,* Chicago, USA, pp. 53–59, 1975.
584. Mainier, L., A connection technique for aluminum conductors in lv and mv power distribution systems, *Proceedings of 36th IEEE Holm Conference on Electrical Contacts,* Canada, August 20–24, pp. 487–492, 1990.
585. Dang, D. and Braunović, M., Metallurgical and contact resistance studies of sleeve connectors in aluminum cable splices, *IEEE Transactions on Components, Hybrids and Manufacturing Technology*, 13, 74–80, 1990.
586. Bonwitt, W. P. and Dupre, H. P., Designing reliability into electrical connectors, *Proceedings of 3rd EIA Conference on Reliable Electrical Connections,* Dallas, Texas, December 2–4, pp. 30–37, 1958.
587. Jensvold, H., Runde, M., and Tveite, G. I., The effect of conductor hardness on aluminum compression joints, *Proceedings of 17th International Conference on Electrical Contacts,* Nagoya, pp. 497–505, 1994.
588. Sosinski, C. W., Methods for overcoming aluminum/copper termination incompatibilities, *Insulation/Circuits*, (March), 51–55, 1975.
589. Braunović, M., Critical slip amplitude required for initialization of fretting motion in a binding-head screw termination, *Proceedings of 20th International Conference on Electrical Contacts,* Stockholm, Sweden, June 19–23, pp. 355–360, 2000.
590. Flugge, W., *Handbook of Engineering Materials*, McGraw-Hill, p. 42, 1962.
591. Roark, R. J. and Young, W. C., *Formulas for Stress and Strain*, McGraw-Hill, p. 517, 1975.
592. American Society for Metals (ASM), *ASM Handbook: Welding, Brazing and Soldering*, Vol. 6, 10th ed., ASM International, 1993.
593. Boychenko, V. I. and Dzektser, N. N., *Busbar Connections*, Energiya, Leningrad, (In Russian) 1978.
594. Braunović, M., Effect of connector design on the contact resistance of high-power overlapping bolted joints, *IEEE Transactions on Components, Packaging and Manufacgturing Technology*, 25, 642–650, 2002.
595. Bron, O. B., Myasnikova, M. G., Miroschnikov, I. P., and Fyodorov, V. N., Permissible temperatures for electric contacts, *Proceedings of 10th International Conference on Electric Contact Phenomena,* Budapest, Hungery, January 13–21, pp. 71–75, 1980.
596. Jackson, R. L., Significance of surface preparation for bolted aluminum joints, *IEEE Proceedings, Part C*, 128(2), 45–49, 1981.
597. Oberg, A., Bohlin, A., and Olson, K.-E., The influence of contact surface preparation on the performance of copper and aluminum connectors, *Proceedings of 16th International Conference on Electrical Contacts,* Loughborough, pp. 407–413, 1992.
598. AMP-Simel Tech., *Mechanical Connectors*, Publication B8, TycoElectronics, Markhum, Ontorio, Canada, p. 7.
599. Station Fittings, *Pfisterer Technology Publication*, 5th ed., Pfisterer, Sttutgart, Germany, p. 8, 1987.
600. Braunović, M., *Mechanical Contact Devices for Aluminum-to-Aluminum and Aluminum-to-Alloy Connections* 1986. CEA Report No. 188, D 335.
601. The multi-lam principles, Multi-contact Tech., Catalog Multi-Contanst USA, Santa Rosa, California.
602. Waram, T., Design consideration for shape-memory Belleville washers, Raychem Tech. Doc.
603. Oberg, A. and Nilsson, S., Shape-memory alloys for power connector applications, *Proceedings of 39th IEEE Holm Conference on Electrical Contacts,* Pittsburg, USA, September 27–29, pp. 225–228, 1993.
604. Braunović, M. and Labrecque, C., Shape-memory alloy mechanical contact devices, *Proceedings of 41th IEEE Holm Conference on Electrical Contacts,* Chicago, USA, October 17–19, pp. 21–32, 1995.
605. Labrecque, C., Braunović, M., Trochu, F., Brailovski, V., Quian, Y. Y., Terriault, P., and Schetky, L. M., Experimental and theoretical evaluation of the behaviour of a shape-memory alloy belleville washer under different operating conditions, *Proceedings of 41st IEEE Holm Conference on Electrical Contacts,* Montreal, Canada, October 2–4, pp. 195–204, 1996.
606. Park, G., Muntges, D. E., and Inman, D. J., Self-repairing joints employing shape-memory alloy actuators, *Journal of the Minerals, Metals and Materials Society*, 55(11), 33–38, 2003.

607. Braunović, M., Fretting in aluminum-to-copper connections, *Proceedings of 14th International Conference on Electrical Contacts,* Paris, France, pp. 213–218, 1988.
608. Braunović, M., Effect of contact-aid compounds on the performance of bolted aluminum-to-aluminum joints under current-cycling conditions, *IEEE Transactions on Components, Hybrids and Manufacturing Technology*, 9, 59–70, 1986.
609. Manko, H. H., *Solders and Soldering*, McGraw-Hill, New York, 2001.
610. Lau, J. H., *Solder Joint Reliability: Theory and Applications*, McGraw-Hill, New York, 1995.
611. Frear, D. R., *Mechanics of Solder Alloy Interconnects (Electrical Engineering)*, Chapman & Hall, New York, 1994.
612. Hwang, J. S., *Modern Solder Technology for Competitive Electronics Manufacturing*, McGraw-Hill, New York, 1996.
613. Directive 2002/95/EC of the European Parliament and of the Council of Jan. 27, 2003, *Official Journal of the EU*, 13.2.2003, L 37/19–23.
614. Directive 2002/96/EC of the European Parliament and of the Council of Jan. 27, 2003, *Official Journal of the EU*, 13.2.2003, L 37/24–38.
615. 2002 Lead-Free Roadmap, Japan Electronics and Information Technology Industries Association (JEITA), 2002 http://www.jeite.org
616. Puttlitz, J. K., *Handbook of Lead-Free Solder Technology for Microelectronic Assemblies*, Marcel Dekker, Inc., New York, 2004.
617. Ganesan, S., *Lead-Free Electronics*, Willey Interscience, NY, 2006.
618. Suganuma, K., *Lead-Free Soldering in Electronics: Science, Technology, and Environmental Impact*, Marcel Dekker, Inc., NY, 2003.
619. AIM lead-free soldering guide, 2003. http://www.aimsolder.com.
620. (2002). NIST database for solder properties with emphasis on new lead-free solders 2002. http://www.boulder.nist.gov.
621. Lee, N.-C., Getting ready for lead free solders. http://www.indium.com/pbfree/techpapers.
622. Miric, A. Z. and Grusd, A., Lead-free alloys, *Soldering & Surface Mount Technology*, 10(1), 19–25, 1998.
623. Vianco, P. T. and Rejent, J. A., Properties of ternary Sn–Ag–Bi alloys: Part I. Thermal properties and microstructural analysis, *Journal of Electronic Materials*, 28, 1127, 1999.
623a. Vianco, P. T. and Rejent, J. A., Properties of ternary Sn–Ag–Bi alloys: Part II. Wettability and mechanical properties analyses, *Journal of Electronic Materials*, 28, 1138, 1999.
624. Hwang, J. S., Lead-free solders: The Sn–Ag–Cu system, *Surface Mount Technology*, July, 2000.
625. Seeling, K., A comparison of leading lead-free alloys, *AIM Tech, Publication*, 1(1), 1998.
626. Lin, K.-L. and Shih, C.-L., Microstructure and thermal behavior of Sn–Zn–Ag solders, *Journal of Electronic Materials*, 32, 1496–1501, 2003.
627. Lin, K.-L., Chen, K.-I., and Sni, P.-C., A potential drop-in replacement for eutectic Sn–Pb solder: The Sn–Zn–Ag–Al–Ga solder, *Journal of Electronic Materials*, 32, 1490–1497, 2003.
628. Lee, F. F. M., Clad metal inlays for connector springs, *Proceedings of 21st Holm Conference on Electrical Contacts,* Chicago, USA, pp. 67–75, 1975.
629. Antler, M. and Drozdowicz, M. N., Wear and porosity of electrodeposited gold contacts: The effect of laser glazing the substrate metals, *Proceedings of 35th IEEE Holm Conference on Electrical Contacts,* Chicago, USA, September 18–20, pp. 105–109, 1989.
630. Antler, M. and Dunbar, J. J., Environmental tests for connectors and contact materials: An evaluation of method involving sulfur dioxide, *Proceedings of 23rd Holm Conference on Electrical Contacts,* Chicago, USA, pp. 19–42, 1977.
631. Abbott, W. H., Materials, environment, motion and electrical contact failure mechanisms, *Proceedings of 35th IEEE Holm Conference on Electrical Contacts,* Chicago, USA, September 18–20, pp. 3–11, 1989.
632. Abbott, W. H., The role of electroplates in contact reliability, *Proceedings of 48th IEEE Holm Conference on Electrical Contacts,* Orlando, USA, October 21–23, pp. 163–164, 2002.
633. Abbott, W. H., The corrosion of porous gold platings, *Proceedings of 13th International Conference on Electrical Contacts,* Lausanne, Switzerland, September 15–19, pp. 343–348, 1986.
634. Abbott, W. H. and Antler, M., Connector contacts: Corrosion inhibiting surface treatments for gold-plated finishes, *Proceedings of 41st IEEE Holm Conference on Electrical Contacts*, Montreal, Canada, October 2–4, pp. 97–123, 1995.

635. Krumbein, S. J. and Antler, M., Corrosion inhibition and wear protection of gold plated connector contacts, *IEEE Trans. PMP*, 4(1), 3–9, 1968.
636. Garte, S. M., Effect of substrate roughness on the porosity of gold electrodeposits, *Plating*, 53, 1335–1341, 1966.
637. Zhang, J.-G., Zhou, K.-D., and Du, C.-Z., The porosity of gold plating by dust contamination, *Proceedings of 34th IEEE Holm Conference on Electrical Contacts,* San Francisco, USA, September 26–29, pp. 301–309, 1988.
638. ASTM, Standard methods of test for porosity in gold coatings on metal substrates, ASTM B583-73, Annual ASTM Standards, Part 8, ASTM International, West Conshohocken, Pennsylvania, USA, 1973.
639. Malucci, R. D., Private communication.
640. Antler, M., The lubrication of gold, *Wear*, 6, 44–50, 1963.
641. Chiarenzelli, R. V. and Henry, B. C., Lubricating of separable electric contacts and tarnish prevention, *Lubrication Engineering*, 22, 174–180, 1966.
642. Abbott, W. H., The effects of test environment on the creep of surface films over gold, *Proceedings of 30th IEEE Holm Conference on Electrical Contacts,* Chicago, USA, September 17–21, pp. 47–52, 1984.
643. Kulwanoski, G., Gaynes, M., Smith, A., and Darrow, B., Electrical failure mechanisms relevant to electronic packages, *Proceedings of 37th IEEE Holm Conference on Electrical Contacts,* Chicago, USA, October 6–9, pp. 184–192, 1991.
644. Williams, D. W. M., The effect of test environment on the creep of base metal surface film over precious petal inlays, *IEEE Transactions on Components, Hybrids and Manufacturing Technology*, 11(1), 36–43, 1988.
645. Abbott, W. H., The effects of substrate on the contact resistance of tarnish films, *Proceedings of 16th Holm Seminar on Electrical Contacts,* Chicago, pp. 21–25, 1970.
646. Abbott, W. H., The effect of tests atmosphere conditions on the contact resistance of surface films on silver, *Proceedings of 11th International Conference on Electrical Contact Phenomena,* West Berlin, Germany, June 7–11, pp. 294–296, 1982.
647. Antler, M., Current topics in the surface chemistry of electric contacts, *IEEE Transactions PMP*, 2, 59–68, 1966.
648. Antler, M., Connector contact materials: Effect of environment on clad palladium, palladium–silver alloys and gold electrodeposits, *IEEE Transactions on Components, Hybrids and Manufacturing Technology*, 4(4), 482–492, 1981.
649. Hara, T. and Mano, K., Tarnish-resistance contact material, *IEEE Transactions PMP*, 5, 133–139, 1969.
650. Chiarenzelli, R. V., Tarnishing studies on contact materials, *IEEE Transactions PMP*, 3, 89–96, 1967.
651. Crossland, W. A. and Knight, E., The tarnishing of silver–palladium surfaces and its effect on contact resistance in low-energy circuits, *Proceedings of 19th Holm Conference on Electrical Contact,* Chicago, USA, pp. 248–264, 1973.
652. Harmsen, N. and Schiff, K-L. , The basic properties and contact properties of silver-rich Ag–Pd alloys with base metal additions, *Proceedings of 23rd Holm Conference on Electrical Contacts,* Chicago, USA, pp. 93–97, 1977.
653. Simmon, D., Perrin, C., Mollimard, D., Bajard, M. T., and Bardolle, J., Study of contamination of contact materials silver and silver–palladium alloys in air containing hydrogen sulphide and nitrogen dioxide, *Proceedings of 13th International Conference on Electrical Contacts,* Lausanne, Switzerland, September, 15–19, pp. 333–335, 1986.
654. Kassman-Rudolphi, A., Bjorkman, C., Imrell, T., and Jacobson, S., Conduction through corrosion films on silver-plated copper in power contacts, *Proceedings of 41st IEEE Holm Conference on Electrical Contacts,* Montreal, Canada, October 2–4, pp. 124–134, 1995.
655. Schiff, K.-L., Harmsen, N., and Schnabl, R., The tarnishing behavior of gold-base alloys in corrosive atmospheres, *Proceedings of 21th Holm Conference on Electrical Contacts,* Chicago, USA, pp. 37–45, 1975.
656. Zhang, J.-G., Lin, X. Y., and Sugimura, K., Characteristics and electric contact behavior of tarnished film covered silver plated surface formed by indoor air exposure, *Proceedings of 42nd IEEE Holm Conference on Electrical Contacts,* Chicago, USA, September 16–20, pp. 429–437, 1996.

657. Tripp, J. H. and Williamson, J. B. P., Model for mechanical breakup of films on conductors, *Proceedings of the 3rd International Research Symposium on Electrical Contact Phenomena,* Orono, Japan, pp. 73–76, 1966.
658. Mano, K., Studies of environmental test methods of electrical contact in japan, *Proceedings of 19th Holm Conference on Electrical Contacts,* Chicago, USA, pp. 87–93, 1973.
659. Sharma, S. P., Development of a gentle accelerated corrosion test, *Journal of Electrochemical Society*, 125(12), 2002, 1978.
660. Abbott, W. H., The development and performance characteristics of mixed flowing gas test environment, *IEEE Transactions on Components, Hybrids and Manufacturing Technology*, 11(11), 22–34, 1988.
661. Abbott, W. H., Neer, J. H., and Healey, H. J., Effects of test procedure and sequences on the performance of tin-plated connectors, *Proceedings of 39th IEEE Holm Conference on Electrical Contacts,* Pittsburg, USA, September 27–29, pp. 191–204, 1993.
662. Emmons, W., Abbott, W. H., Sharrar, R., Wutka, T., and Stackhouse, H., Connector stability test for small system connectors, *Proceedings of 36th IEEE Holm Conference on Electrical Contacts,* Montreal, Canada, August 20–24, pp. 342–357, 1990.
663. Antler, M., Survey of contact fretting in electrical connectors, *IEEE Transactions on Components, Hybrids and Manufacturing Technology*, 18, 87–93, 1985.
664. Antler, M., Effect of fretting on the contact resistance of palladium electroplate having a gold flash, cobalt gold electroplate and DGR 156, *IEEE Transactions on Components, Hybrids and Manufacturing Technology*, 17, 363–369, 1984.
665. Aukland, N., Leslie, I., and Hardee, H., A statistical comparison of a clad material and gold flashed palladium nickel under various fretting conditions, *Proceedings of 41st IEEE Holm Conference on Electrical Contacts,* Montreal, Canada, October 2–4, pp. 52–63, 1995.
666. Aukland, N., Hardee, H., Wehr, A., Brennan, S., and Lees, P., An examination of the metallic bonding of a clad material and two gold plating systems under constant force fretting conditions, *Proceedings of 43rd IEEE Holm Conference on Electrical Contacts,* Philadelphia, USA, October 20–22, pp. 7–19, 1997.
667. Morse, S. A., Aukland, N., and Hardee, H., A statistical comparison of gold plating systems under specific fretting parameters, *Proceedings of 41st IEEE Holm Conference on Electrical Contacts,* Montreal, Canada, October 2–4, pp. 33–51, 1995.
668. Malucci, R. D., Characteristics of films developed in fretting experiments on tin plated contacts, *Proceedings of 45th IEEE Holm Conference on Electrical Contacts,* Pittsburg, USA, October 4–6, pp. 175–185, 1999.
669. Swingler, J. and McBride, J. W., Fretting corrosion studies of an extrinsic conducting polymer and tin interface, *Proceedings of 47th IEEE Holm Conference on Electrical Contacts,* Montreal, Canada, September 25–27, pp. 215–219, 2001.
670. Swingler, J., McBride, J. H., and Maul, C., Degradation of road tested automotive connectors, *IEEE Transactions on Components and Packaging Technologies*, 23(1), 157–164, 2000.
671. Swingler, J., The automotive connector: The influence of powering and lubricating a fretting contact interface, *Proceedings of the Institute of Mechanical Engineers, Part D*, 214, 615–621, 2000.
672. Lees, P., Fretting behavior of gold flashed palladium, palladium nickel and palladium silver contact materials, *Proceedings of 39th IEEE Holm Conference on Electrical Contacts,* Pittsburg, USA, September, 27–29, pp. 211–217, 1993.
673. Queffelec, J. L., Ben Jemaa, N., Travers, D., and Pethieu, G., Materials and contact shape studies for automobile connector development, *Proceedings of 15th International Conference on Electrical Contacts,* Montreal, Canada, pp. 225–229, 1990.
674. Flowers, G. T., Xie, F., Bozack, M., Hai, X., Ricket, B. I., and Malucci, R. D., A study of the physical characteristics of vibration-induced fretting corrosion, *Proceedings of 22nd International Conference on Electrical Contacts,* Seattle, USA, pp. 312–316, 2004.
675. Kang, S. K., Lauro, P. A., Shih, D.-Y., Henderson, D. W., and Putlitz, K. J., Microstructure and mechanical properties of lead-free solders and solders used in microelectronic applications, *IBM Journal of Research and Development*, 4/5(July/September), 2005.
676. Kang, S. K., Choi, W. K., Yim, M. J., and Shih, D. Y., Studies of mechanical and electrical properties of lead-free solder joints, *Journal of Electronic Materials*, 21(11), 1292–1299, 2002.

677. Subramanian, K. N., Lee, A., Choi, S., and Sonji, P., Materials issues in electronic interconnects and packaging, *Journal of Electronic Materials*, 30(4), 372–377, 2001.
678. Subramanian, K. N. and Lee, J. G., Physical metallurgy in lead-free electronic solder development, *Journal of Materials*, May, 26–32, 2003.
679. Wu, J. and Pecht, M., Fretting corrosion studies for lead-free alloy plated contacts, *Proceedings of 4th Electronics Packaging Technology Conference,* Singapore, December 10–12, pp. 20–31, 2002.
680. Gagnon, D. and Braunović, M., Effect of fretting in lead-free systems. In: A study of the physical characteristics of vibration-induced fretting corrosion, *Proceedings of 22nd International Conference on Electrical Contacts,* Seattle, USA, pp. 248–253, 2004.
681. Kamoshita, G.-I., Hirano, M., and Hara, N., Inhibiting effect of PBS additives to brown powder formation on Pd alloys, *Proceedings of the 3rd International Research Symposium on Electrical Contact Phenomena,* Orono, Japan, pp. 209–212, 1966.
682. Abbott, W. H., Frictional polymer formation on precious metal alloys, *Proceedings of 25th Holm Conference on Electrical Contacts,* Chicago, USA, pp. 11–16, 1979.
683. Reagor, B. T. and Seibles, L., The elucidation of frictional polymer structures using fourier transform infrared spectroscopy and pyrolysis gas chromatography, *Proceedings of 26th IEEE Holm Conference on Electrical Contacts,* Chicago, USA, pp. 95–102, 1980.
684. Crossland, W. A. and Murphy, P. M., The formation of insulating organic films on palladium–silver contact alloys, *IEEE Transactions on Parts, Hybrids and Packaging*, 10(1), 64–69, 1974.
685. Thwaites, C. J., The solderability of some tin, tin alloy and other metallic coatings, *Transactions of the Institute of Metal Finishing*, 36, 203–210, 1959.
686. Zakraysek, L., Intermetallic growth in tin-rich solders, *Welding Research Supplement*, November 537–546, 1972.
687. Unsworth, D. A. and Mackay, C. A., A preliminary report on growth of compound layers on various metal bases plated with tin and its alloys, *Transactions of the Institute of Metal Finishing*, 51, 85–91, 1973.
688. Tu, K. N., Interdiffusion and reaction in bimetallic Cu–Sn thin films, *Acta Metallurgica*, 27, 347–355, 1973.
689. Révay, L., Interdiffusion and formation of intermetallic compounds in tin–copper alloy surface coatings, *Surface Technology*, 5, 57–62, 1977.
690. Braunović, M., Effect of intermetallic phases on the performance of tin-plated copper connections and conductors, *Proceedings of 49th IEEE Holm Conference on Electrical Contacts,* Washington, USA, September 8–10, pp. 124–131, 2003.
691. Fields, R. J., Low, S. R. Physical and mechanical properties of intermetallics compounds commonly found in solder joints. *NIST Publication*, http://www.metallurgy.nist.gov
692. Urquhart, W., Interdiffusion studies on contact plating materials, *Proceedings of 22nd Holm Conference on Electrical Contacts,* Chicago, USA, pp. 185–189, 1976.
693. Braunović, M. and Gagnon, D., Formation of intermetallics in lead-free systems, *Proceedings of 50th IEEE Holm Conference on Electrical Contacts,* Montreal, Canada, pp. 267–273, 2004.
694. Lee, S.-H., Roh, H.-R., Chen, Z. G., and Kim, Y. -H, Contact resistance and shear strength of solder joints using Cu bumps capped with Sn or Ag/Sn layer, *Journal of Electronic Materials*, 34(11), 1446–1451, 2005.
695. Smits, F. M., Measurements of sheet resistivities with the four-point probe, *Bell System Technical Journal*, 37, 711–716, 1958.
696. Dirnfeld, S. F. and Ramon, J. J., Microstructure investigation of copper–tin intermetallics and the influence of layer thickness on shear strength, *Welding Research*, October, 373–380, 1990.
697. NIST. Database for solder properties with emphasis on new lead-free solders. http://www.boulder.nist.gov
698. Roubaud, P., Prasad, S., Bulwith, R., Kamath, S., and Garcia, A., Impact of intermetallic growth on the mechanical strength of lead-free BGA assemblies. *IPC SMEMA Council* 2001. Apex 2001:LF2-3 www.smema.org/smemastandards.htm.
699. Song, H. G., Ahn, J. P., Minor, A. M., and Morris, J. W., Au–Ni–Sn intermetallic relationships in eutectic Pb–Sn metallization, *Journal of Electronic Materials*, 30(4), 409–413, 2001.
700. Ho, C. E., Chen, W. T., and Kao, C. R., Interaction between solder and metallization during long-term aging of advanced microelectronic packages, *Journal of Electronic Materials*, 30(4), 379–386, 2001.

701. Islam, M. N. and Chan, Y. C., Interfacial reactions of Cu-containing lead-free solders with Au/NiP metallization, *Journal of Electronic Materials*, 34(5), 662–666, 2005.
702. Liao, C. N. and Wei, C. T., Effect of intermetallic compound formation on electrical properties of Cu/Sn interface during thermal treatment, *Journal of Electronic Materials*, 31(10), 1137–1142, 2004.
703. Yoon, J.-W., Lee, C.-B., and Jung, S.-B., Growth of an intermetallic compound layer with Sn–3.5Ag–5Bi on Cu and Ni–P/Cu during aging treatment, *Journal of Electronic Materials*, 32(11), 1195–1202, 2003.
704. Jang, G.-Y., Lee, J.-W., and Du, J.-Q., The nanoindenation characteristics of Cu6Sn5 Cu3Sn and Ni3Sn4 intermetallic compounds in the solder bump, *Journal of Electronic Materials*, 33(10), 1103–1110, 2004.
705. Chromik, R. R., Vinci, R. P., Allen, S. L., and Notis, M. R., *Journal of Materials Research*, 18, 2251–2257, 2003.
706. Atkinson, M., Origin of the size effect in indentation of metals, *International Journal of Mechanical Sciences*, 33(10), 843–849, 1991.
707. Maiocco, L., Smyers, D., Munroe, R., and Baker, I., Correlation between electrical resistance and microstructure in gold wire bonds on aluminum films, *IEEE Transactions on Components, Hybrids and Manufacturing Technology*, 13(3), 592–599, 1999.
708. Kashiwabara, M. and Hattori, S., Formation of Al–Au intermetallic compounds and resistance increase for ultrasonic AL wire bonding, *Review of the Electrical Communication Laboratory*, 17, 1001–1007, 1969.
709. Gerling, W., Electrical and physical characterization of gold-ball bonds on aluminum layers, *Proceedings IEEE Electronic Component Conference,* pp. 13–20, 1984.
710. Chen, G. K. C., On the physics of purple-plague formation and the observation of purple-plague in ultrasonically-joined gold–aluminum bonds, *IEEE Transactions PMP*, PMP-3(4), 149–155, 1967.
711. Morris, J. W., Goldstein, J. F., and Mei, Z., Microstructural influences on the mechanical properties of solids, In *The Mechanics of Solder Alloy Interconnects*, Frear, D., Morgan, H., Burchett, S., and Lau, J. H., Eds., ITP, New York, pp. 7–11, 1994.
712. Lau, J. H., Nakayama, W., Prince, J., and Wong, C. P., Electronic packaging: Design, materials, process and reliability, McGraw-Hill, New York, pp. 222–230, 1998.
713. Plumbridge, W. J., Gagg, C. R., and Peter, S., The creep of lead free solders at elevated temperatures, *Journal of Electronic Materials*, 30(9), 1178–1187, 2001.
714. Igoshev, V. I. and Kleiman, J. I., Creep phenomena in lead-free solders, *Journal of Electronic Materials*, 29(2), 244–251, 2000.
715. Bang, W. H., Oh, K. H., Pung, J. P., Morris, J. W., and Hua, F., The correlation between stress relaxation and steady state creep in eutectic Sn–Pb, *Journal of Electronic Materials*, 34(10), 1287–1293, 2005.
716. Homa, T. R., Cracking of electronic packaging joints due to creep-fatigue, *Electronic Packaging and Corrosion in Microelectronics*, ASM International, Metals Park, Ohio, USA, April 29–30, pp. 209–215, 1987.
717. Gerardin, M., *Comptes Rendus*, 53, 727–731, 1861.
718. Ho, P. S., d'Heurle, F. M., and Gangulee, A., Electro- and thermo-transport in metals and alloys, In, Hummel, R. E. and Huntington, H. B., Eds., AIME, New York, 1977.
719. Hummel, R. E., Electromigration of ionized cluster beam deposited aluminum metallizations. In *Proceedings of IEEE International Reliability Symposium,* pp. 207–213, 1989.
720. Christou, A., Ed, *Electromigration and electronic device degradation*, Wiley, New York, 1994.
721. Tu, K. N., Recent advances on electromigration in very-large-scale-integration of interconnects, *Journal of Applied Physics*, 94(9), 1559–5451, 2003.
722. Kwok, T., Electromigration and reliability in submicron metallization and multilevel interconnection, *Materials Chemistry and Physics*, 33, 176–182, 1993.
723. Shine, M. C. and d'Heurle, F. M., Activation energy for electromigration in aluminum films alloyed with copper, *IBM Journal of Research and Development*, September, 378–386, 1971.
724. Cho, J. and Thompson, C. V., Grain size dependence of electromigration induced failure in narrow interconnects, *Applied Physics Letters*, 54(25), 1582–2577, 1989.
725. Black, J. R., Mass transport of aluminum by momentum exchange with conducting electrons, *Proceedings of IEEE International Reliability Symposium,* pp. 147–156, 1967.

726. Park, C. W. and Vook, R. W., Electromigration-resistant Cu–Pd films, *Thin Solid Films*, 226, 238–246, 1993.
727. Chen, S.-W. and Chen, C.-M., Electromigration effects upon interfacial reactions, *Journal of Materials*, February 62–66, 2003.
728. Chen, S.-W. and Chen, C.-M., Electromigration effect upon the Sn/Ag and Sn/Ni interfacial reactions at various temperatures, *Acta Materialia*, 50, 2461–2470, 2002.
729. Gan, H., Choi, W. J., Xu, G., and Tu, K. N., Electromigration in solder joints, *Journal of Materials*, June 34–40, 2002.
730. Ye, H., Basaran, C., and Hopkins, D., Mechanical degradation of microelectronics solder joints under current stressing, *International Journal of Solids and Structures*, 40, 7269–7275, 2003.
731. Cobb, H. L., Cadmium whiskers monthly review, *American Electroplaters Society*, 33(2), 28–36, 1946.
732. Gaylon, G. T., Annotated tin whisker bibliography and anthology, *IEEE Transactions on Electronics Packaging Manufacturing*, 28(1), 94–101, 2005.
733. Osenbach, J. W., Shook, R. L., Vaccrao, B. T., Potteiger, B. D., Amin, A. N., Hooghan, K. N., Suratkar, P., and Ruengsinsub, P., Sn whiskers: Material, design, processing and post-plate reflow effects and development on an overall phenomenological theory, *IEEE Transactions on Electronics Packaging Manufacturing*, 28(1), 36–42, 2005.
734. Gaylon, G. T. and Palmer, L., An integrated theory of whisker formation: The physical metallurgy of whisker formation and the role of internal stresses, *IEEE Transactions on Electronics Packaging Manufacturing*, 28(1), 17–22, 2005.
735. Gaylon, G. T., Vo, N., and Smetana, J., Cause of tin whiskers remains elusive, *Lead-free Electronics*, November.
736. Fukuda, Y. and Osterman, M., Tin whiskers: What is the risk? *Lead-free Electronics*, July.
737. Sakamoto, I., Whisker test method of JEITA whisker growth mechanism for test method, *IEEE Transactions on Electronics Packaging Manufacturing*, 28(1), 10–17, 2005.
738. Special issue on tin whiskers, *IEEE Transactions on Electronics Packaging Manufacturing*, 28(1), 2005.
739. Chudnovski, B. H., Degradation of power contacts in industrial atmosphere. Silver corrosion and whiskers, *Proceedings of 48th IEEE Holm Conference on Electrical Contacts,* Orlando, USA, October 21–23, pp. 140–150, 2002.
740. Antler, M., Gold plated contacts: Effect of thermal aging on contact resistance, *Proceedings of 43rd IEEE Holm Conference on Electrical Contacts,* Philadelphia, USA, October 20–22, pp. 121–131, 1997.
741. Pinnel, M. R. and Bennett, J. E., Mass diffusion in polycrystalline copper/electroplated gold planar couples, *Proceedings of 17th Holm Seminar on Electrical Contacts,* Chicago, pp. 13–29, 1971.
742. Napp, D. T., Substitution of palladium for gold in IBM products, *Proceedings of 5th Plating Electron. Ind. Symp. American Electroplaters Society,* NY, pp. 28–35, 1975.
743. Schultz, D., *Connector Specifier*, February 2001.
744. Mroczkowski, R. S., The finish is just the beginning, *Connector Specifier*, October 2000.
745. Roos, J. R., Celis, J. P., and Vancoille, E., Investigation of nickel–indium electrodeposits for connectors, *Plating & Surface Finishing*, February 60–67, 1990.
746. Antler, M., Electronic connector contact lubricants: The polyether fluids, *IEEE Transactions on Components, Hybrids and Manufacturing Technology*, 10, 32–41, 1987.
747. Antler, M., Sliding studies of new connector contact lubricants, *IEEE Transactions on Components, Hybrids and Manufacturing Technology*, 10, 24–31, 1987.
748. Noel, S., Lecaude, N., Bodin, C., Tristani, L., and Zindine, E. M., Effect of heat treatment on electrical and tribological properties of hot-dipped tin separable contacts with fluorinated lubricant layers, *Proceedings of 20th International Conference on Electrical Contacts,* Stockholm, pp. 229–234, 2000.
749. Noel, S., Lecaude, Almarguy, D., and Tristani, L., Lubrication mechanisms of hot-dipped tin separable electrical contacts, *Proceedings of 47th IEEE Holm Conference on Electrical Contacts,* Montreal, Canada, September 25–27, pp. 197–202, 2001.
750. Myshkin, N. K., Tribological problems in electrical contacts, *Tribology International*, 24(1), 45–49, 1991.

751. Dijk, P., Contacts in Motion, *Proceedings of 19th International Conference on Electrical Contacts,* Nurenberg, Germany, September 21–23, pp. 123–127, 1998.
752. Saka, N., Llou, M. G., and Suh, N. P., The role of tribology in electrical contact phenomena, *Wear*, 100, 77–105, 1984.
753. Bryant, M. and Tewari, A., Wear rate reductions in carbon brushes conducting current and sliding against wavy copper surfaces, *Proceedings of 40th IEEE Holm Conference on Electrical Contacts,* Chicago, USA, October 17–19, pp. 229–238, 1994.
754. Kingsbury, H. E. R., Electrical contact lubrication, *Electrical Times*, 159(17), 14–15, 1971.
755. Brockman, I. H., Sieber, C. S., and Mroczkowski, R. S., The effects of the interaction of normal force and wipe distance on contact resistance in precious metal plated contacts, *Proceedings of 34th IEEE Holm Conference on Electrical Contacts,* San Francisco, USA, September 26–29, pp. 73–83, 1988.
756. Martens, R. and Pecht, M., The effects of wipe on corroded nickel contacts, *Proceedings of 42nd IEEE Holm Conference on Electrical Contacts,* Chicago, USA, September 16–20, pp. 342–551, 1996,
757. Abbott, W. H., The effects of design variables and surface films on the contact resistance of copper-copper contact interfaces, *Proceedings of 38th IEEE Holm Conference on Electrical Contacts*. Institute of Electric and Electronic Engineers, Inc. CHMT, Philadelphia, USA, October 18–21. pp.219–235, 1992.
758. Timsit, R. S., Bock, E., and Corman, N., Effect of surface reactivity of lubricants on the properties of aluminum electrical contacts, *IEEE Transactions on Components Packaging and Manufacturing Technology, Part A*, 21, 500–505, 1998.
759. Malucci, R. D. The effects of wipe contact resistance of aged surfaces, *Proceedings of 40th IEEE Holm Conference on Electrical Contacts*, Chicago, USA, October 17–19, pp. 131-144, 1994
760. Glossbrenner, E. W., Wear in sliding electrical contacts and its effects on performance—a physical model, *Proceedings of the Holm Seminar on Electrical Contacts,* pp. 65–72, 1970.
761. Pope, L. E. and Peebles, D. E., In city friction, wear and electrical contact resistance of precious metal alloys, *Tribology Transactions*, 31(2), 202–213, 1988.
762. Suh, N. P., An overview of the delamination theory of wear, *Wear*, 44(1), 1–16, 1977.
763. Rice, S. I., Nowotny, H., and Wayne, S. F., Formation of subsurface zones in impact wear, *ASLE Transactions*, 24, 261–268, 1980.
764. Soda, N., Kimura, V., and Tamaka, A., Wear of some F.C.C. metals during unlubricated sliding, Part I. Effects of load, velocity and atmosphere pressure, *Wear*, 33(1), 1–16, 1975.
765. Vook, R. W., Pope, L. E., and Rhode, R. W., The surface segregation of sulfur during oscillatory pin-on plate wear studies of precious metal electrical contact alloys—II, surface analysis, *Proceedings of 30th IEEE Holm Conference on Electrical Contacts,* Chicago, USA, September 17–21, pp. 513–518, 1984.
766. Pope, L. E. and Peebles, D. E., In situ examination of segregation and wear processes of precious metal electrical contact alloys, *IEEE Transactions on Components, Hybrids and Manufacturing Technology*, 10(1), 47–55, 1987.
767. Pope, L. E. and Peebles, D. E., Effects of composition and age hardening on precious metal electrical contacts, *Proceedings of 34th IEEE Holm Conference on Electrical Contacts,* San Francisco, USA, September 26–29, pp. 199–205, 1988.
768. Hammam, T., Tin coating techniques for copper-base alloys—the effects on friction, wear and electric properties, *Proceedings of 43rd IEEE Holm Conference on Electrical Contacts,* Philadelphia, USA, October 20–22, pp. 201–211, 1997.
769. Paulmier, D., Bouchoucha, A., and Zaidi, H., Influence of the electric current on wear in a sliding contact with copper/chrome steel, *Vacuum*, 41, 2213–2216, 1990.
770. Bouchoucha, A., Zaidi, H., Hounkponou, E., Robert, F., and Paulmier, D., Analysis of Metallic Transfer in Electrical Dynamic Contact Copper/Steel, *Proceedings of International Conference Nortrib '94*, Vol. 1, 163–170, 1994.
771. Senouci, A., Zaidi, H., Frene, J., Bouchoucha, A., and Paulmier, D., Damage of surfaces in sliding electrical contact copper/steel, *Applied Surface Science*, 144–145, 287–291, 1999.
772. Zhang, Y., Sun, I., Chen, Y., and Shangguan, B., Tribo-eIectric behaviors of copper under dry sliding against Cu–Cr alloys, *Proceedings of the 4th China International Symposium on Tribology,* Xi'an, China, pp. 35–40, 2004.

773. Chen, Z., Liu, P., Verhoeven, J. D., and Gibson, E. D., Electrotribological behavior of Cu–15 vol.% Cr in situ composites under dry sliding, *Wear*, 203–204, 28–35, 1997.
774. Liu, P., Bahadur, S., and Verhoeven, J. D., Electrical sliding friction and wear behavior of Cu–Nb in situ composites, *IEEE Transactions on Components, Packaging and Manufacturing Technology, Part A*, 17, 616–623, 1994.
775. Bouchoucha, A., Zaidi, H., Kadiri, E. K., and Paulmier, D., Influence of electric fields on the tribological behaviour of electrodynamical copper/steel contacts, *Wear*, 2003–2004, 434–441, 1997.
776. He, D. H., Manory, R. R., and Grady, N., Wear of railway contact wires against current collector materials, *Wear*, 215, 146–155, 1998.
777. He, D. H. and Manory, R., A novel electrical material with improved self-lubrication for railway current collectors, *Wear*, 249, 626–636, 2001.
778. Nagasawa, H. and Kato, K., Wear mechanism of copper alloy wire sliding against iron-base strip under electric current, *Wear*, 216, 179–183, 1998.
779. Zhao, H., Barber, G. C., and Liu, J., Friction and wear in high speed sliding with and without electrical current, *Wear*, 249, 409–414, 2001.
780. Chen, J. C. and Vook, R. W., Characterization of sliding Al–Cu electrical contacts, *Proceedings of 31st IEEE Holm Conference on Electrical Contacts,* Chicago, Illinois Institute Technology, USA, September 29–October 2, pp. 101–106, 1985.
781. Konchits, V. V., Influence of electric current on friction of metals, *Journal of Friction and Wear*, 2(1), 131–135, 1981.
782. Spurr, R. T., The ploughing contribution to friction, *British Journal of Applied Physics*, 7, 260–261, 1956.
783. Shan, H. S. and Pandey, P. C., Oxidation and wear behavior of carbide cutting tools, *Wear*, 37, 69–75, 1976.
784. Makel, D. D., Improved sliding electrical brush performance through the use of water lubrication, *Proceedings of 38th IEEE Holm Conference on Electrical Contacts,* Philadelphia, USA, October 18–21, pp. 149–155, 1992.
785. Vandemme, L. K. J., On the calculation of 1/f noise of contacts, *Journal of Applied Physics*, 11 89–96, 1976.
786. Vandamme, L. K. J. and Tioburg, R. P., 1/f noise measurements for characterizing multispot low-ohmic contacts, *Journal of Applied Physics*, 47(5), 2056–2058, 1976.
787. Vandamme, L. K. J., Contact noises as a diagnostic tool, *Proceedings of International Conference on Electrical Contact Phenomena*, VDE-Verlag GMBH, Berlin, Offenbach, Germany, June 7–11. pp .60–63. 1982.
788. Palenskis, V. and Shoblitskas, Z., Origin of 1/f noise, *Solid State Communications*, 43(10), 761–763, 1982.
789. Horton, J. C. and Radnlk, J. L., Electrical noise and mechanical wear characteristics of miniature slip rings, *Proceedings of Engineering Seminar on Electric Contacts, Milan,* pp. 185–206, 1965.
790. Mano K., Oguma T. The frequency characteristics of sliding precious metal contact noise, *Proceedings of 5th International Research Symposium on Electrical Contact Phenomena*. Munich, W. Germany. v. l. pp.297–300, 1990
791. Tsuchiya, K. and Tamai, T., Fluctuations of contact resistance in sliding contact, *Wear*, 16, 337–349, 1970.
792. Johnson, R. G. and George, R. I., Potentiometer contact noise source analysis: a case history, *Proceedings of 22nd Holm Conference on Electrical Contacts,* pp. 121–125, 1976.
793. Taniguchi, M., Inoue, T., and Mano, K., Frequency spectrum of electrical sliding contact noise and its waveform model, *Proceedings of 30th IEEE Holm Conference on Electrical Contacts,* Chicago, USA, September 17–21, pp. 491–498, 1984.
794. Lysonski, R., Haberl, J., Denton, L. R., File, D., Anderson, G., Williams, J., Morey, R., Reed, W., and Breindel, H., Test system for measurement of noise and coefficient of friction as a screen for potential lubricants in sliding electrical contacts, *Proceedings of 36th IEEE Holm Conference on Electrical Contacts,* Montreal, Canada, August 20–24, pp. 269–277, 1990.
795. Antler, M., Wear, friction and electrical noise phenomena in severe sliding systems, *ASLE Transactions*, 5(2), 297–307, 1962.

796. Bredel, L. J., Johnson, L. B., and Kuhlmann-Wilsdorf, D., Teaming measurements of the coefficient friction and of contact resistance as a tool for the investigation of sliding interfaces, *Wear*, 120, 161–173, 1987.
797. Tsuchiya, K. and Tamai, T., Noise spectrum for fluctuations of contact resistance and mechanism of noise generation in sliding contact, *Wear*, 19, 245–258, 1972.
798. Wilson, R. W., The contact resistance and mechanical properties of surface films on metals, *Proceedings of the Physical Society, Section B*, 429(9), 625–641, 1955.
799. Aronstein, J., Notes and bibliography on subjects pertinent to the investigation and design of separable electrical contacts, *IBM Technical Report TR22.874*, (October), 24–31, 1969.
800. Campbell, W. E. and Aronstein, J., Contact resistance and material transfer of soft metal microcontacts, *Proceedings of 16th Holm Seminar on Electrical Contacts,* Chicago, USA, pp. 163–176, 1970.
801. Valueva, N. A. and Myshkin, N. K., Influence of surfactant additive on properties of heat-resistant grease for electric contacts, *Soviet Journal of Friction and Wear*, 4(3), 143–145, 1983.
802. Lunn, B., Epilamen und mischreibung aus der sicht des metallkudlers, *VDI-Berichte*, 20, 41–46, 1957.
803. Furey, M. J., Metallic contact and friction between sliding surfaces, *ASLE Transactions*, 4(1), 1–11, 1961.
804. Myshkin, N. K., Belyi, V. A., and Konchits, V. V., Electrical properties of lubricant boundary layers, *ASLE Transactions*, 24(4), 505–508, 1981.
805. Mann, B., Kuhn, H., and Szantpaly, L., Tunneling through fatty acid monolayers and its relevance to photographic sensitization, *Chemical Physics Letters*, 8(1), 82–84, 1971.
806. Polymeropoulos, E. E., Electron tunneling through fatty-acid monolayers, *Journal of Applied Physics*, 48(6), 2404–2407, 1977.
807. Gundlach, K. H. and Kadles, J., The influence of the oxide film on the current in Al-Al oxide-fatty acid monolayer metal junction, *Chemical Physics Letters*, 25(2), 293–295, 1974.
808. Handy, R. M. and Scala, C., Electrical and structured properties of Langmuir films, *Journal of Electrochemical Society*, 113(2), 109–116, 1966.
809. Alamarguy, D., Schneegans, O., Noël, S., and Boyer, L., Correlation between the electrical and mechanical behaviours of a nanocontact with an alkanethiol monolayer, *Proceedings of 21st International Conference on Electrical Contacts,* Zurich, Switzerland, September 9–12, pp. 217–222, 2002.
810. Barkan, P. and Tuohy, E. J., Contact resistance theory for rough hemispherical silver contacrs in air and in vacuum, *IEEE Transactions on Power Apparatus and Systems (PAS)*, 84(12), 1132–1143, 1965.
811. Sommerfeld, A. and Bethe, H., In *Handbush der physic*, Geiger, H. and Shell, K., Eds., vol. 24(2), Springer, Berlin, p. 450, 1933.
812. Simmons, J. G., Potential barriers and emission-limited current flow between closely spaced parallel metal electrodes, *Journal of Applied Physics*, 35(8), 2472–2481, 1964.
813. Holm, R., Thermionic and tunnel currents in film-covered-symmetric contacts, *Journal of Applied Physics*, 39(7), 3294–3297, 1968.
814. Konchits, V. V. and Markova, L. V., Investigation of lubricant boundary layers by the probe methods, *Soviet Journal of Friction and Wear*, 12(6), 36–45, 1991.
815. Matsuoka, H. and Kato, T., An ultrathin liquid film lubrication theory—calculation method of solvation pressure and its applicatiion to EHL problem, *Transactions of ASME: Journal of Tribology*, 119, 217–226, 1997.
816. Hiraoka, N., Electric contact resistance between finely polished nickel plates with PEPE coating and its relation to friction, *Tribology International*, 33, 99–105, 2000.
817. Simmons, J. G., Generalized thermal J–U characteristic for the electrical tunnel effect, *Journal of Applied Physics*, 35(9), 2655–2658, 1964.
818. Konchits, V. V., Korotkevich, S. V., and Kim, C. K., Thermal effects and contact conductivity of boundary lubrication, *Lubrication Science*, 12(2), 145–168, 2000.
819. Campbell, W. E., The lubrication of electrical contacts, *IEEE Transaction on Components, Hybrids and Manufacturing Technology*, 1(1), 4–16, 1978.
820. Antler, M., The lubrication of gold, *Wear*, 6, 44–50, 1963.
821. Seubert, E., Kontaktschmierstoff und verhalten von schmierstoffen unter electrishen einflussen, *Schmicrstoffe und Scmierungstechnik*,17 54–60, 1967.

822. Antler, M., Organometallics in lubrication, *Industrial & Engineering Chemistry*, 51, 753–758, 1959.
823. Myshkin, N. K., Konchits, V. V., Kirpichenko, Y. E., and Markova, L. V., Wear of contact elements in electromechanical switches, *Wear*, 181–183, 691–699, 1995.
824. Belyi, V. A., Myshkin, N. K., and Konchits, V. V., Some aspects of the friction and wear of electrical sliding contacts under conditions of boundary lubrication, *Wear*, 77(1), 131–137, 1982.
825. Timsit, R. S. and Pelow, C. V., Shear strength and tribological properties of stearic acid films—Part I: On glass and aluminum-coated glass, *Journal of Tribology*, 114, 150–158, 1992.
826. Timsit, R. S., Bock, E., and Corman, N., Effect of surface reactivity of lubricants on the contact resistance of aluminum electrical contacts, *IEEE Transactions Components Packaging and Manufacturing Technology Part A*, 21, 500–505, 1998.
827. Keil, A., Lubrication of sliding contacts with higher mercaptans, *Proceedings of 9th International Conference on Electrical Contact Phenomena,* Chicago, USA, pp. 181–182, 1978.
828. Lewis, N., Reed, C. W., DeCorpo, J. J., and Wyatt, J. R., Lubrication quantity: Observations of the effects on gold sliding wear character and in-situ contamination formation, *Proceedings of 21st Holm Conference on Electrical Contacts,* Chicago, USA, pp. 129–134, 1975.
829. Brix, V. H., An electrical study of boundary lubrication, *Aircraft Engineering*, 19(223), 294–297, 1947.
830. Siripongese, C., Rogers, P. R., and Cameron, A., Thin film lubrication, *Engineering*, 186, 146–149, 1958.
831. Prashad, H., *Tribology in Electrical Environments*, Elsevier, Amsterdam, p. 1, 2006.
832. Guyetand, A., Contribution a 1′etude des contacts electriques separables: synthese bibliographique, *Revue General de I'Electricite*, 83(1), 3–26, 1974.
833. Uda, S., Higaki, T., Funami, H., and Mano, K., Contact lubricants and vapor lubrication system, *Proceedings of International Symposium on Electrical Contacts. Theory and Applications (ISECTA'93),* pp. 268–277, 1993.
834. Smith, E. F., Klein, A., Ney, J. M., Lysonski, R., Agopovich, J. W., and Dentob, R., Screening contact materials for low speed slip ring assemblies, *Proceedings of 39th IEEE Holm Conference on Electrical Contacts,* Pittsburg, USA, September 27–29, pp. 157–170, 1993.
835. Rice, D. W., Bredfeldt, K., and Kral, J., Corrosion inhibiting lubricants for separable connectors, *IEEE Transaction on Components, Hybrids and Manufacturing Technology*, 8(4), 546–549, 1985.
836. Bickerstaff, A. E., Contact resistance of carbon brushes, *Proceedings of the 3rd Conference on Industrial Carbons and Graphite*, Society of Chemical Industry, London, pp. 555–561, 1970.
837. Turner, J. B., Current collecting in direct current machines, *Journal of Science and Technology*, 36(3), 316–318, 1966.
838. Shobert, E. I., Electrical resistance of carbon brushes, *Transactions of the AIEE: Part III*, B(13), 788–798, 1954.
839. Holm, E., Contribution to the theory of the contact between a carbon brush and a copper collector ring, *Journal of Applied Physics*, 28(10), 1171–1176, 1957.
840. Senouci, A., Frene, J., and Zaidi, H., Wear mechanism in graphite–copper electrical sliding contact, *Wear*, 225–229, 949–953, 1999.
841. Belyi, V. A. and Savkin, V. G., Peculiarities of formation and properties of metal-polymer sliding electrical contacts, *Wear*, 47, 329–334, 1978.
842. Liu, D. R. and McCarthy, S., Resistance change at copper contacts with thin and thick oxide films under a zero force liquid gallium probe, *Proceedings of 46th IEEE Holm Conference on Electrical Contacts*, Institute of Electric and Electronic Engineers, Inc. CPMT, Chicago, USA, September 25–27. pp. 183–190, 2000.
843. Holm, E., Dependence of the conduction mechanism on polarity in stationary and sliding contact when high-resistivity film is present in the contact, *IEEE Transactions Personalized Abstract Search Service*, 4(5), 65–75, 1965.
844. Ueno, T. and Sawa, K., Characteristics of surface film on slip ring in the low atmospheric pressure. *Proceedings of 45th IEEE Holm Conference on Electrical Contacts*, Institute of Electric and Electronic Engineers, Inc. CPMT, Pittsburg, USA, October 4–6. pp. 169–174.
845. Schreurs, J., Johnson, L., and McNab, I. R., Characterization of thick films on slip rings during high current density operation, *IEEE Transactions on Components, Hybrids and Manufacturing Technology*, 4(1), 30–35, 1981.

846. Dillich, S. and Kulhmann-Wilsdorf, D., Two regimes of current conduction in metal-graphite electrical brushes and resulting instabilities, *IEEE Transactions on Components, Hybrids and Manufacturing Technology*, 6(1), 45–54, 1983.
847. Ueno, T. and Sawa, K., Study on sliding contact phenomena and surface film in low oxygen contents, *Proceedings of 20th International Conference on Electrical Contacts,* Stockholm, Sweden, June 19–23, pp. 209–214, 2000.
848. Belyi, V. A., Konchits, V. V., and Savkin, V. G., Polar effect within the sliding contact of metal-containing brushis, *Wear*, 25(3), 346–348, 1982.
849. Fisher, J., Campbell, K. J., and Quinn, T. F. J., The effect of current on the lubrication of sliding electrical contacts, *ASLE Transactions*, 15(3), 192–200, 1972.
850. Houkponou, E., Nery, H., Pauilmier, D., and Zaidi, H., Tribological behavior of dynamic electrical contact graphite–graphite, *Proceedings of 5th Nordic Symposium on Tribology (Nortrib'92)*, Helsinki, Finland, June 8–11, vol. 2, pp. 157–162, 1992.
851. Paulmier, D., Mansori, M., and Zaidi, H., Study of magnetized or electrical sliding contact of a steel XC48/graphite couple, *Wear*, 2003–2004, 148–154, 1997.
852. Mansori, M., Schmitt, M. S., and Paulmier, D., Friction behavior of a magnetized steel-graphite dynamic electric contact, *Proceedings of the 8th International Conference on Tribology (Nortrib'98),* Aarhus, Denmark, pp. 105–112, 1998.
853. Demkin, N. B., Izmailov, V. V., and Uzikova, T. I., Study of tribological characteristics of cermet electric brushes at low sliding velocities, *Soviet Journal of Friction and Wear*, 1(3), 24–29, 1980.
854. Holm, E., Friction in graphite brush contact as a function of the temperature in the contact spots, *Journal of Applied Physics*, 33, 156–163, 1962.
855. Meyeur, R., Contribution a l'etude des contacts glissants, *Revue General de l'Electricity*, 64(1), 213–222, 1955.
856. Lancaster, J. K., The influence of the conditions of sliding on the wear of electrographite brushes, *British Journal of Applied Physics*, 13(3), 468–477, 1962.
857. Clark, W. T., Connoly, A., and Hirst, W., The friction and wear of electrographite, *British Journal of Applied Physics*, 14(1), 20–27, 1963.
858. Mansori, M., Paulmier, D., Ginsztler, J., and Horvath, M., Lubrication mechanisms of sliding contact by simultaneous action of electric current and magnetic field, *Wear*, 225–229, 1011–1016, 1999.
859. Lancaster, J. K., Elastic deformation and wear of electrographite, *Nature*, 196, 368–380, 1962a.
860. Schreurs, J., Johnson, J. L., and McNab, R., High-current brushes. Part VI: Evaluation of slip-ring surface films, *IEEE Transactions on Components, Hybrids and Manufacturing Technology*, 3(1), 83–88, 1980.
861. Savage, R. H., Graphite lubrication, *Journal of Applied Physics*, 19(1), 1–10, 1948.
862. Millet, Y., Behavior of carbon brushes in dry and wet atmosphere *Proceedings of the 4th Conference of Carbon,* New York, pp. 719–725, 1960.
863. Elsey, H. M., Treatment of high altitude brushes by application of metallic halides, AIEE Paper. No. TP45-108, June, (6) 1945.
864. Glossbrenner, E. W. and Witherspoon, B. K., Brushes containing molybdenum disulfide for slip rings in spacecraft application, *Proceedings of 33rd IEEE Holm Conference on Electrical Contacts,* Chicago, USA, September 21–23, pp. 253–259, 1987.
865. Rabinowicz, E. and Ross, A.Z., Compatibility effects in the sliding of graphite and silver-graphite brushes against various ring materials. *Proceedings of 30th IEEE Holm Conference on Electrical Contacts*, Illinois Institute of Technology, Chicago, USA, September 17–21, pp. 499–506. 1984.
866. Chichinadze, A. V. and Myshkin, N. K., Friction and wear of electric contacts, In *Tribology—Lubrication, Friction, and Wear*, Kragelsky, I. V. and Alisin, V. V., Eds., Prof. Eng. Publ. Lim., London and Bury St. Edmunds, pp. 874–893, 2001. Chapter 30.
867. Rabinowicz, E., The temperature rise at sliding electrical contacts, *Wear*, 78, 29–37, 1982.
868. Lancaster, J. K.,The influence of arcing on the wear of carbon brushes on copper, *Wear*, 6, 341–352, 1963a.
869. Casstevens, J. M., Rylander, H. G., and Eliezer, Z., Influence of high velocities and high current densities on the friction and wear behavior of copper–graphite brushes, *Wear*, 48(1), 121–130, 1978.
870. Casstewens, J. M., Rylander, H. G., and Eliezer, Z., Friction and wear characteristics of powder metallurgy copper graphite brushes at high sliding eeds, *Wear*, 49(1), 169–178, 1978.

871. Marshall, R. A., Reichner, P., and Slepian, R. M., Current collection systems for pulse power homopolar machines, *Proceedings of the 7th Symposium on Engineering Problems of Fusion Research,* IEEE Publication, 77CH1267-4-NPS, pp. 434–438, 1977.
872. Marshall, R. A., The mechanism of current transfer in high current sliding contacts, *Wear*, 37, 233–240, 1976.
873. Baker, R. M., Sliding contacts electrical characteristics, *Electrical Engineering*, 55(1), 94–100, 1936.
874. Sherar, P. M. and Spry, W. J., Effect of carbon structure on copper oxidation at a sliding electrical contact, *Proceedings of the 5th Conference on Carbon,* New York, pp. 553–560, 1962.
875. Lancaster, J. K., The relation between the wear of carbon brush materials and their elastic moduli, *British Journal of Applied Physics*, 14(8), 497–505, 1963.
876. Hessler, V. P., Abrasion, a factor in electrical brush wear, *Electrical Engineering*, 56, 8–12, 1937.
877. Lancaster, J. K., The wear of carbons and graphite, In *Treatise on Materials Science and Technology*, Scott, D., Ed., Vol. 13, Academic Press, New York, pp. 141–174, 1979.
878. Baker, R. M. and Hewitt, G. W., Brush wear in hydrogen and in air, *The Electrical Journal*, 33(6), 287–289, 1936.
879. McKee, D. W., Savage, R. H., and Gunnoc, G., Chemical factors in brush wear, *Wear*, 22(2), 193–214, 1972.
880. Johnson, J. L., *Sliding Monolithic Brush Systems for Large Currents Proceedings of 32nd IEEE Holm Conference on Electrical Contacts,* Boston, USA, October 27–29, pp. 3–17, 1986.
881. Bryant, M. D., Electrically and frictionally derived mound temperatures in carbon graphite brushes, *Proceedings of 34th IEEE Holm Conference on Electrical Contacts,* San Francisco, USA, September 26–29, pp. 229–238, 1988.
882. Bryant, M. D., A particle ejection mechanism for brush wear, *Proceedings of 36th IEEE Holm Conference on Electrical Contacts,* Montreal, Canada, August 20–24, pp. 285–291, 1990.
883. Dow, T. A. and Kannel, J. W., Thermomechanical effects in high current density electrical slip rings, *Wear*, 79, 93–105, 1982.
884. Spry, W. J. and Sherer, P. M., Copper oxide film formation at a sliding carbon copper interface, *Wear*, 4(2), 137–149, 1961.
885. Wagner, K., Lenz, R., Britschin, F., and Scheerbarth, H., Radioaktive Untersuchungen der Stoffubertragung Zwischen Kupfer-Graphit-Bursten und einem Kupferrotor, *Elekrtie*, 8, 248–252, 1964.
886. Lawson, D. K. and Dow, T. A., The sparking and wear of high current density electrical brushes, *Wear*, 102, 105–125, 1985.
887. Ueno, T., Morita, N., and Sawa, K., Influence of surface roughness on voltage drop of sliding contacts under various gases environment, *Proceedings of 49th IEEE Holm Conference on Electrical Contacts,* Washington, USA, September 8–10, pp. 59–64, 2003.
888. Swinnerton, B. R. G., Carbon fiber fringe brush, *Wear*, 78, 81–92, 1982.
889. Broniarek, C. A., Damping characteristics of solid brush current collection systems, *Wear*, 78, 233–242, 1982.
890. Bryant, M. and Lin, J.W., Reductions of wear rate and contact interface observations for carbon samples sliding against wavy and smooth copper surfaces. In *Effects of Mechanic& Stiffness and Vibration on Wear in Test Devices and Applications*, Bayer Raymond, G., Ed., ASTM SIP 1247, American Society for Testing and Materials, Philadelphia, 1995.
891. Oktay, S. T. and Suh, N. P., Wear debris formation and agglomeration, *Journal of Tribology*, 114, 379–393, 1992.
892. Antler, M., Contact resistance probing: development of a standard practice by the american society for testing and materials, *Proceedings of 10th International Conference on Electrical Contacts*, Vol. 1, Budapest, Hungary, pp. 13–21, 1980.
893. Sproles, E. S. and Drozdovicz, M. H., Development of an automatic contact resistance probe, *Proceedings of 14th International Conference on Electrical Contacts,* Paris, France, pp. 195–200, 1988.
894. Kataoka, K., Micro phenomena in low contact-force probing on aluminum, *Proceedings of 51st IEEE Holm Conference on Electrical Contacts,* Chicago, USA, pp. 259–264, 2005.
895. Vieweg, V., Die Messung der Schmierfahigkeit von Olen, *Techn. Mech. und Thermodynamik*, 1(3), 102–108, 1930.
896. Sviridenok, A. I., Myshkin, N. K., Kalmykova, T. F., and Kholodilov, O. V., *Acoustic and Electrical Methods in Triboengineering*, Allerton, New York, 1988.

897. Tonk, A., Martin, G. M., Kapsa, P., and Georges, J. M., Boundary lubrication with anti-wear additives: Study of interface film formation by electrical contact resistance, *Tribology International*, 10 209–212, 1979.
898. Mansot, J. L. and Martin, J. M., In-situ measurements of thickness variation of boundary films tunneling conductivity, *Proceedings of the 10th Leeds-Lyon Symposium on Tribology,* Lyon, France, pp. 114–211, 1983.
899. Nakashima, K. and Takafuji, K., Measurement of oil film state using two kinds of electrical circuit, *Proceedings of the JSLE International Tribogy Conference,* Tokyo, Japan, June 8–10, pp. 615–620, 1985.
900. Kragel'skii, I. V., Alekseev, N. M., Gitis, N. V., and Karasik, I. I., Experimental investigation of the film starvation effect, *Soviet Journal of Friction and Wear*, 3(3), 484–489, 1982.
901. Kostetskii, B. I. and Shul'ga, O. V., Resistivity of the surface layers of metals and the seizure mechanism, *Doklady Akademii Nauk SSSR*, 188(1), 80–82, 1969.
902. Lerner, Y. N. and Kraegel'skii, I. V., Measurement of electrical contact resistance to investigate plastic contacting of deformed and annealed specimens with preliminary displacement, *Soviet Journal of Friction and Wear*, 2(2), 226–230, 1981.
903. Czichos, H., Crimmer, M., and Mittmann, H., Rapid measuring techniques for electrical contact resistance applied to lubricant additives studies, *Wear*, 40(2), 265–271, 1976.
904. Hivart, P., Bricout, L. P., and Oudim, J., A new friction-seizure test for phosphate/stearate coatings using conductivity measurement, *Lubricating Engineering*, 49(11), 833–837, 1993.
905. Marui, E. and Endo, H., Significant of contact resistance in boundary lubrication, *Wear*, 156, 49–55, 1992.
906. Alliston-Greiner, A. F., Testing extreme pressure and anti-wear performance of gear lubricants, *Proceedings of the Institute of Mechanical Engineers*, 205, 89–101, 1991.
907. Savage, R. and Flom, D., *Annals of the New York Academy of Sciences*, 58, 946–950, 1954.
908. Antler, M., Auletta, L. V., and Conley, J., Automated contact resistance probe, *Review of Scientific Instruments*, 34(12), 1317–1322, 1963.
909. Chiarenzelli, R. V., Air pollution effects on contact materials, *Proceedings of Engineering Seminar on Electric Contacts,* Univeristy of Maine, Orono, Maine, June 14–18, pp. 63–102, 1965.
910. Konchits, V. V. and Savkin, V. G., Friction and current passing in sliding electric contact. Part I, *Soviet Journal of Friction and Wear*, 4(6), 6–14, 1983.
911. Konchits, V. V., Korotkevich, S. V., and Kim, C. K., Formation and friction properties of boundary lubricating and surface modified layers at elevated temperatures, *Lubrication Science*, 14–4, 455–469, 2002.
912. Shhnable, R. and Beeker, H., Microprocessor Controlled Contact Resistance Probe for Manufacturing Control and Development, *Proceedings of 27th IEEE Holm Conference on Electrical Contacts,* Chicago, USA, pp. 131–137, 1981.
913. Voostrom, A., Augustus, L., Steinmentz, A., and Berg, G., Analysis of surface resistance and elemental composition of a reed contact, *Proceedings of 24th Holm Conference on Electrical Contacts,* Chicago, Illinois Institute of Technology, pp. 521–526, 1978.
914. Kasukabe, S., Harada, S., Maruyama, T., and Takagi, R., Contact properties of the spring probe for probing on a solder bump, *Proceedings of 38th IEEE Holm Conference on Electrical Contacts,* pp. 187–190, 1992.
915. Konchits, V. V. and Markova, L. V., Probe method of estimating electric conductivity and topography of surface, *Soviet Journal of Friction and Wear*, 10(4), 631–632, 1989.
916. Schneegans, O., Houze, A., Meyer, R., and Bayer, L., Study of the local electrical properties of metal surfaces using an a.f.m. with a conducting probe, *Proceedings of 42nd IEEE Holm Conference on Electrical Contacts,* Institute of Electric and Electronic Engineers, Inc. CPMT, Chicago, USA, September 16–20, pp. 205–211, 1996.
917. Courtney-Pratt, J. S. and Eisner, E., The effect of tangential force on the contact of metallic bodies, *Proceedings of the Royal Society of London*, 238(1215), 529–550, 1957.
918. Kawamura, M., Shiol, K., and Ninomiya, K., Electrical observations of surface being lubricated, *Proceedings of JSLE-ASLE International Lubrication Conference,* Tokyo, pp. 121–125, 1975.

919. Maekawa, K., Asanabe, S., Mitrutake, S., Cotton, K., Inenaga, N., and Motomura, O., Lubrication condition monitoring of piston ring and cylinder of large marine diesel engine, *Proceedings of the International Tribology Conference,* Yokohama, Japan, pp. 331–336, 1995.
920. Braginskii, A. P., Evseev, D. G., Zdan'ski, A. K., and Kukol, N. P., Investigation of running-in based on electrical and acoustic characteristics, *Soviet Journal of Friction and Wear*, 6(5), 812–820, 1985.
921. Karasik, I. I. and Kukol, N. P., Evaluation of friction regimes with imperfect lubrication from statistical electrical conduction characteristics, *Soviet Journal of Friction and Wear*, 2(3), 451–458, 1981.
922. Korndorf, S. F. and Podmasteiyev, K. V., Estimation of lubrication state in friction units by electrofluctuation methods, *Soviet Journal of Friction and Wear*, 10(4), 51–56, 1989.
923. Lerner, Y. N., Evaluation of microasperity deformation and surface film damage during predisplacement on the basis of contact electrical resistance measurements, *Soviet Journal of Friction and Wear*, 7(4), 84–90, 1986.
924. Ura, A. and Nakashima, A., Effect of deformation of the contact surface on wear and friction—a study on clarification of the mechanism of abrasive wear, *Wear*, 110, 409–418, 1986.
925. Lerner, Y., Strength of adhesive non-conducting films on metallic surfaces in friction, *Journal of Friction and Wear*, 25(3), 39–43, 2004.
926. Stott, F. H., Glascott, J., and Wood, G. S., The use of contact resistance measurements to study oxide films developed during high temperature sliding, *Journal of Physics D: Applied Physics*, 18, 541–556, 1985.
927. Markova, L. V., Konchits, V. V., and Myshkin, N. K., Experimental study of metallic contact spots formation, *Journal of Friction and Wear*, 16(2), 50–55, 1995.
928. Plint, A. G. and Plint, M. A., Test procedure for rapid assessment of frictional properties of engine oils at elevated temperatures, *Tribology International*, 17(4), 209–213, 1984.
929. Cann, P., Spikes, H. A., and Cameron, A., Thick film formation by zinc dialkyldithiophosphates, *ASLE Transaction*, 26, 48–52, 1983.
930. Cann, P. and Cameron, A., Studies of thick boundary lubrication—influence of ZDTP and oxidized hexadecane, *Tribology International*, 17(4), 205–207, 1984.
931. Konchits, V. V., Korotkevich, S. V., and Sautin, S. D., Lubricity of organic deposits on friction surface at elevated temperature, *Journal of Friction and Wear*, 23(2), 55–59, 2002.
932. Myshkin, N. K., Konchits, V. V., and Kim, C. K., Electrical probing in thermal tests of boundary layers, *Tribology Transactions*, 43(3), 514–520, 2000.
933. Konchits, V. V. and Markova, L. V., Estimation of lubricant interlayer shear strength under imperfect lubrication, *Tribotest Journal*, 4–4(June(4)), 367–375, 1998.
934. Tabor, D., The role of surface and intermolecular forces in thin film lubrication, In *Microscopical Aspects of Adhesion and Lubrication*, Georges, J.-M., Ed, pp. 651–679, 1982.
935. Homola, A. M., Israelachvili, J. N., McGuiggan, P. M., and Gee, M. J., Fundamental experimental studies in tribology: The transition from "interfacial" friction of undamaged molecularly smooth surfaces to "normal" friction wear, *Wear*, 136, 65–83, 1990.
936. Matveevskii, R. M., Boundary lubrication, In *Tribology in the U.S.A. and the Former Soviet Union: Studies and Applications*, Belyi, V. A., Ludema, K., and Myshkin, N. K., Eds., Allerton, New York, Part 44, pp. 287–303, 1994.
937. Myshkin, N. K., Evaluating thermal stability of materials and lubricants by electrical methods, *Soviet Journal of Friction and Wear*, 5(4), 744–747, 1984a.
938. Horn, J., Degner, W., Richter, G., and Fiedler, J., A device for studying the influence of tribomechanical and tribo-chemical phenomena on separable contacts and its use in testing tin–lead contact finishes, *Proceedings of International Conference on Electrical Contact Phenomena,* West Berlin, Germany, June 7–11, pp. 396–400, 1982.
939. Watanabe, Y., New instrument for measuring contact resistance developed for studying electrical contact phenomena, *Wear*, 112, 1–15, 1986.
940. Alley, D. M., Hagen, L. J., and Kuhlmann-Wilsdorf, D, Automated apparatus for long-term testing of electrical brushes, *Proceedings of 36th IEEE Holm Conference on Electrical Contacts,* Montreal, Canada, August 20–24, pp. 278–284, 1990.
941. Ueno, T. and Morita, N., An effect of gas adsorption and film formation on contact voltage drop of sliding contacts in various atmospheres, *Proceedings of 21st International Conference on Electrical Contacts,* Zurich, Switzerland, September 9–12, pp. 362–367, 2002.

942. Ztonkiewicz, Z., Computerized system to measure and analyze low current contact resistance, *Proceedings of 19th International Conference on Electrical Contacts,* Nuremburg, Germany, September 21–23, pp. 499–502, 1998.
943. Hubner-Obenland, F. and Minuth, J., A new test equipment for high dynamic real-time measuring of contact resistances, *Proceedings of 45th IEEE Holm Conference on Electrical Contacts*, Pittsburg, USA, October 4–6, pp. 193–202, 1999.
944. Taniguchi, M. and Takagi, T., Experimental study on the application of digital image measuring system to damage analysis of electrical sliding contact surface, *Proceedings of 19th International Conference on Electrical Contacts*, Institute of Electric and Electronic Engineers, Inc. CPMT, Nuremberg, Germany, September 21–23, pp. 111–115, 1998.
945. Myshkin N. K. Markova L. V, and Konchits V. V., Digital images of contact parameters and wear study in tribosystems, *Proceedings of the International Conference: Problems of Non-Conventional Bearing Systems, NCBS'99*, pp. 161–166, 1999.
946. Markova, L. V. and Konchits, V. V., A new approach to investigation of the interface between rubbing bodies and analysis of tribotests, *Journal of Friction and Wear*, 20(2), 78–83, 1999.
947. Belin, M. and Martin, J. M., Triboscopy, a new approach to surface degradation of thin films, *Wear*, 156, 151–160, 1992.
948. Belin, M., Triboscopy: a new quantitative tool for microtribology, *Wear*, 168, 7–12, 1993.
949. Pecht, M. G. and Nash, F. R., Predicting the reliability of electronic equipment, *Proceedings of the IEEE*, 82(7), 992–1004, 1994.
950. Mikron MikroScan 7600 PRO, http://www.irimaging.com
951. FLIR ThermaCAM® P60 IR Camera, http://www.flirthermography.com
952. Electrophysics EZTHERM PRO, http://www.electrophysics.com
953. Infrared Solution FLEXCAM, http://www.infraredsolutions.com
954. Lebold, J. Boldstar Infrared services, http://www.boldstarinfrared.com
955. Lischina, private communication.
956. Shape-memory temperature indicator. Furukawa Electric Co. Japanese. Patent 2-70218, 1990.
957. Shape-memory temperature indicator to monitor overheating of electric power cables. Tohoku Deneyoku KK-Fujikura Ltd. Japanese Patent 3-201313, 1991.
958. Vardorpe, J. (Leuven R&D). Shape-memory fire and temperature device. European Patent 0-128-601, 1984.
959. PhoneDucer, http://www.elwoodcorp.com
960. ndb Technologies, http://www.ndb.qc.ca
961. Sensorlink Corp., http://www.sensorlink.com
962. Snell, J. and Renowden, J. Improving results of thermographic inspections of electrical transmission and distribution lines. Paper presented at IEEE ESMO 2000, Paper 28C-TPC 17, Montreal, Canada, 2000.
963. USi Power Donut2, http://www.usi-power.com
964. Square D wireless temperature monitoring systems, http://www.squared.com
965. Omega Long range telemetry system, http://www.omega.com
966. Djuric, Z. and Frantlovic, M. Wireless CdTe-based temperature transmitter system. Private communication.
967. Wurzbach, R. N. A web-based cost benefit analysis method for predictive maintenance, http://www.mrgcorp.com
968. Buehler, W. J., Gilfrich, J. V., and Weiley, K. C., Effect of Low-Temperature Phase Changes on the Mechanical Properties of Alloys near Composition TiNi, *J. Appl. Phys.*, 34, 1475–1477, 1963.
969. Wayman, C. M. and Duerig, T. W., An introduction to martensite and shape-memory, In *Engineering Aspects of Shape-memory Alloys*, Duerig, T. W., Melton, K. N., Stoeckel, D., and Wayman, C. M., Eds., Butterworth-Heinemann, London, pp. 3–20, 1990.
970. Stoeckel, D. and Waram, T., Thermo-variable rate springs, Springs, 30(2), 1991.
971. Stoeckel, D., Shape-memory alloys — Prompt new actuator designs, *Adv. Mater. Processing*, 10, 33–38, 1990.
972. Wayman, C. M., Shape memory alloys, *MRS Bulletin*, 18(4), 49–56, 1993.
973. Stoeckel, D. and Yu, W., Superelastic Nickel–Titanium Wires, Technical Documentation, Raychem Corporation.

974. Stoeckel, D., Thermal Actuation with Shape-memory Alloys, Documentation technique, Raychem Corporation.
975. Mobereley, W. J. and Melton, K. N., Ni-Ti-Cu shape memory alloys, In *Engineering Aspects of Shape-Memory Alloys*, Duerig, T. W., Melton, K. N., Stoeckel, D., and Wayman, C. M., Eds., Butterworth-Heinemann, London, pp. 46–57, 1990.
976. Patoor, E. and Berveiller, M., Alliages à mémoire de forme, Hermes, 1990.
977. Wu, M. H., Cu-based shape memory alloys, In *Engineering Aspects of Shape-Memory Alloys*, Duerig, T. W., Melton, K. N., Stoeckel et, D., and Wayman, C. M., Eds., Butterworth-Heinemann, London, pp. 69–88, 1990.
978. Miyazaki, S., In *Thermal and Stress Cycling Effects and Fatigue Properties of Ni-Ti Alloys*, Duerig, T. W., Melton, K. N., Stoeckel et, D., and Wayman, C. M., Eds., Butterworth-Heinemann, London, pp. 394–413, 1990.
979. Kapgan, M. and Melton, K. N., Shape-memory alloy tube and pipe coupling, In *Engineering Aspects of Shape-memory Alloys*, Duerig, T. W., Melton, K. N., Stoeckel et, D., and Wayman, C. M., Eds., Butterworth-Heinemann, London, pp. 137–145, 1990.
980. Sydzyk, E., The design of electrical interconnection systems with shape-memory alloys, In *Engineering Aspects of Shape-memory Alloys*, Duerig, T. W., Melton, K. N., Stoeckel et, D., and Wayman, C. M., Eds., Butterworth-Heinemann, London, pp. 149–157, 1990.
981. Harrison, J. D. and Hodgson, D. E., Use of TiNi in mechanical and electrical connectors, In *Shape-memory Effects in Alloys*, Perkins, J., Ed., Plenum, New York, p. 517, 1990.
982. Guenin, G., Herubel, G., Bargain, R., and Demendez, M., (Souriau et Cie), Canadian Patent No. 1 250 631, 1989.
983. Krumme, J., Shape-memory alloy technology for high performance electrical connectors, *Electronic Progress*, 29(1), 2, 1989.
984. Waram, T., Design Considerations for Shape-memory Belleville Washers, Technical Documentation, Raychem Corporation.
985. Oberg, A. and Nilsson, S., Shape memory alloys for power connector applications, *Proc. 39th IEEE Conf. Elec. Contacts*, Pittsburgh, pp. 225–228, 1993.
986. Braunović, M. and Labrecque, C., Shape memory alloy mechanical contact devices, *Proc. 41st IEEE Conf. Elec. Contacts*, pp. 21–32, 1995.
987. Gordon, R. F., Design principles for Cu-Zn-Al alloys, In *Engineeriong Aspects of Shape-Memory Alloys*, Duerig, T. W., Melton, K. N., Stoceckel et, D., and Wayman, C. M., Eds., Butterworth-Heinemann, London, p. 245, 1990.
988. Furuya, Y. and Shimada, H., Shape-memory actuators for robotic applications, In *Engineering Aspects of Shape-Memory Alloys*, Duerig, T. M., Melton, K. N., Stoeckel et, D., and Wayman, C. M., Eds., Butterworth-Heinemann, London, pp. 338–355, 1990.
989. Stoeckel, D., Shape memory actuators for automotive applications, In *Engineering Aspects of Shape-Memory Alloys*, Duerig, T. W., Melton, K. N., Stoeckel et, D., and Wayman, C. M., Eds., Butterworth-Heinemann, pp. 283–294, 1990.
990. Furukawa Electric Co., Jap. Patent No. 2-70218, 1990.
991. Tohoku Denryoku KK- Fujikura Ltd., Jap. Patent No.3-201313, 1991.

Appendix 1: Methods of Description of Rough Surface

A.1.1 METHODS OF DESCRIPTION OF ROUGH SURFACE

Parametric method of description includes a number of parameters, some of which are given in Chapter 2. Here some further parameters are listed which are used in tribological theory and practice. As a rule, the parameters are determined in respect to mean line.

There are two methods of plotting the mean line: the *M*-system, or "mean-line system", and the *E* system or "envelope system".

The first method is recommended by ISO and by the standards of the majority of countries, e.g., UK, Holland, Russia, USA, etc., the second method is used in the standards of Germany, Italy, Switzerland and some other countries. According to the *M* system, the mean line is plotted using the method of least squares so that the sum of squared deviations of the profile curve from this line is minimal, meanwhile the shape of the mean line should coincide with the nominal (geometrical) profile. For example, it is a straight line for plane and cylinder along its generatrix, an arc for sphere and cylinder along its directrix, and so on.

The *E*-system implies the rolling of the real profile by a circle of sufficiently large radius (e.g., 25 mm in the German standard). The locus of the center of the circle is shifted by the circle radius giving the envelope, which is displaced into the profile curve by the depth of surface smoothing. As a result, we obtain the mean line consisting of the arcs of the rolling circle and approximately coinciding with the least-squares mean line.

The *M*- and *E*- systems differ insignificantly in practice. The mean line in these two systems is plotted within a sampling length *l*, which is the length of some elementary portion of the effective profile. The length is selected so that it becomes possible to exclude the irregularities of other types, waviness primarily. The sampling length is usually standardized.

High-spot count HSC is the number of complete profile peaks (with assessment length) projecting above the mean line, or a line parallel with the mean line (Figure A1.1, peaks 1–4). The parameter is insensitive to short wavelengths. In the case of profile mean line, it is identical to zero crossing density.

The degree of fullness K is a ratio of area of material (the area between the measured profile and a lower reference line, parallel to mean line) to area of enveloping rectangle.

There are parameters, which characterize the shape of a single asperity.

Mean peak radius of curvature r_p is defined as mean reciprocal curvature of all peaks in sampling length. *The peak curvature* c_p is the second derivative of profile equation $z(x)$ at the top of asperity and usually calculated by the central difference formula:

$$C_{pi} = (2z_i - z_{i-1} - z_{i+1})/l^2.$$

The mean radius of curvature is then determined from the formula:

$$r_p = \frac{1}{n-2} \sum_{i=1}^{n-2} \frac{1}{c_{pi}}.$$

where $n = L/l$, number of sampling points.

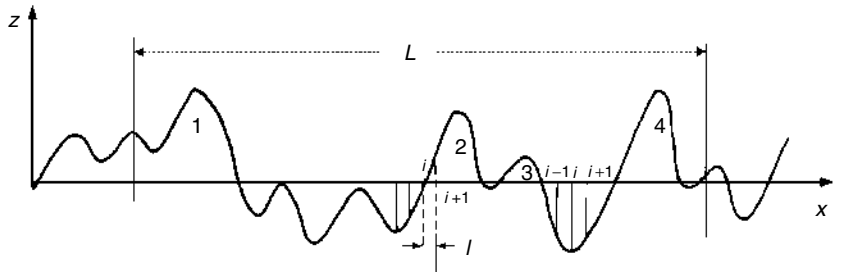

FIGURE A1.1 High-spot count and peak curvature.

There exist other methods to calculate the peak radius of curvature. For example, r_{pi} may be calculated from formula:

$$r_{pi} = \Delta l_i^2 / 8 h_i, \tag{A1.1}$$

where Δl_i is the length of the section of the asperity by the line equidistant to the mean line and spaced from the peak to a distance h_i. Here it is assumed that h_i is approximately equal to 0.3 R_a.

This list of roughness parameters currently in use is far from complete. The majority of the above parameters are included (or at least had been included) into national standards in various combinations (see Table A1.1 which includes the ISO standard for comparison).

Foreign standards should be used with specific caution because:

- the same parameter may be designated differently in different standards (these differences are specifically marked in Table A1.1, e.g., k_m instead of R_a in the Spanish standard);
- the same designation has different or differently assigned parameters. For example, unlike the above definition of R_z corresponding to Russian or British standard, the German standard determines this parameter as the average of the maximum peak-to-valley heights in five consecutive sampling lengths;
- different standards recommend different numbers of sample lengths to be used as the assessment length of one and the same parameter.

Probabilistic approach based on the probability theory and the random process theory is often used under the assumption that rough surfaces are Gaussian (normal).

TABLE A1.1
Some National Roughness Standards

R_a	R_z	R_{max}	R_p	t_p	S	S_m	Country
+	+						UK
+	+	+					Germany
k_m	H						Spain
+	+	+		+	+	+	Russia
+							USA
+	+	+		+			Sweden
+	R	+	+	$(T_p)C$	AR		France
+	+	+					Japan
+	+	+					ISO

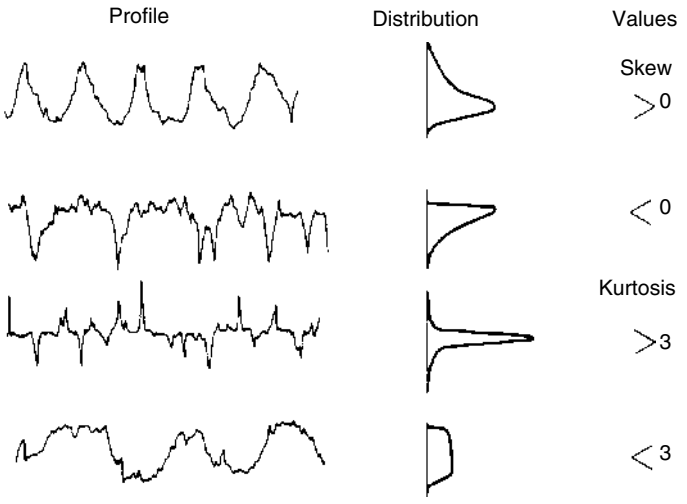

FIGURE A1.2 Skewness S_k and kurtosis K_s of real profile. (according to Thomas, T. R., *Precision Eng.*, 3, 97, 1971.)

Skewness S_k and *kurtosis* K_s are the parameters serving to assess the deviation of the real surface from the surface with symmetric distribution. The skewness S_k is a measure of deviation of the probability density from the symmetric shape (Figure A1.2). It is defined in the following manner:

$$S_k = \frac{1}{\sigma^3} \int_{-\infty}^{\infty} z^3 f(z) dz \tag{A1.2}$$

Symmetric distributions (for example, the Gaussian distribution) naturally possess zero skewness. The skewness is negative when profiles have worn peaks and deep scratches, while the skewness is positive for a surface with high peaks and/or shallow valleys filled up with debris.

The excess K_s characterizes the peakedness of the distribution and is defined as (Figure A1.2):

$$K_s = \frac{1}{\sigma^4} \int_{-\infty}^{\infty} z^4 f(z) \mathrm{d}z. \tag{A1.3}$$

The symmetric Gaussian distribution has the kurtosis equal to three. If the profile has comparatively few high peaks and deep valleys, e.g., as a result of surface turning with a sharp pointed tool, then $K_s < 3$ and the distribution is termed platikurtic. The distribution is termed leptokurtic, $K_s > 3$, in the opposite case when there is a large number of high peaks and deep valleys.

The probalistic approach is generalized by the approach based on the theory of random fields (processes).

It has been noted above that the surface roughness ordinate z is measured, say, from the mean plane. The coordinate is treated as a random function of two variables $z = z(x, y)$. According to the theory of random fields, in case the field z is homogenous and normal, as it is commonly assumed when analyzing rough surfaces, it is fully determined by its correlating function:

$$K(x, y) = \lim_{L_1, L_2 \to \infty} \frac{1}{4L_1 L_2} \int_{-L_1}^{L_1} \int_{-L_2}^{L_2} z(x_1, y_1) z(x_1 + x, y_1 + y) \mathrm{d}x_1 \mathrm{d}y_1.$$

Practically any problem of determination of field characteristics (some of them are listed below) can be solved. Still, it is frequently convenient to apply Fourier transformation to the correlation function:

$$\Phi(k_x, k_y) = \frac{1}{4\pi^2} \int_{-\infty}^{\infty} \int K(x, y)\exp[-i(xk_x + yk_y)]\mathrm{d}x\mathrm{d}y,$$

which is termed as the spectral density. Here k_x, k_y are the components of the wave vector k.

The moments of spectral density are intensively used in the subsequent analysis:

$$m_{pq} = \int_{-\infty}^{\infty} \int \Phi(k_x, k_y)k_x^p k_y^q \mathrm{d}k_x \mathrm{d}k_y$$

For isotropic surfaces it is easy to demonstrate that

$$\begin{aligned} m_{20} = m_{02} = m_2, \qquad m_{11} = m_{13} = m_{31} = 0 \\ m_{00} = m_0, \qquad 3m_{22} = m_{40} = m_{04} = m_4, \end{aligned} \tag{A1.4}$$

where m_0, m_2, m_4 are the moments of the spectral density of the profile.

The moments are practically determined from the surface profilograms using the Longuet-Higgins formulas for the densities of zeroes $D_{z,0}$ and extrema (maxima and minima) $D_{e,0}$:

$$D_{z,0} = \frac{1}{\pi}\left(\frac{m_2}{m_0}\right)^{1/2}, \tag{A1.5}$$

$$D_{e,0} = \frac{1}{\pi}\left(\frac{m_4}{m_2}\right)^{1/2}. \tag{A1.6}$$

Whence it is determined that

$$m_2 = \pi^2\sigma^2 D_{z,0}^2, \tag{A1.7}$$

$$m_4 = \pi^4\sigma^2 D_{z,0}^2 D_{e,0}^2, \tag{A1.8}$$

where the standard deviation σ equal to $(m_0)^{1/2}$ is also determined from the profilogram. Available modern measuring instruments allow us to determine the densities of zeroes and extrema automatically.

In order to determine a number of characteristics of a rough surface it may be enough to use the joint probability density of the random function and its first two derivatives:

$$\xi_1 = z(x, y), \qquad \xi_2 = \frac{\partial z(x, y)}{\partial x}, \qquad \xi_3 = \frac{\partial z(x, y)}{\partial y},$$

$$\xi_4 = \frac{\partial^2 z(x, y)}{\partial x^2}, \qquad \xi_5 = \frac{\partial^2 z(x, y)}{\partial x \partial y}, \qquad \xi_6 = \frac{\partial^2 z(x, y)}{\partial y^2}.$$

It is assumed that these random variables satisfy the general conditions of the central limit theorem, so their joint probability density is written as

$$p(\xi_1, \xi_2, \ldots, \xi_6) = \frac{1}{8\pi^3 \Delta^{1/2}} \exp\left(-\frac{1}{2}\vec{\xi}^T M \vec{\xi}\right), \tag{A1.9}$$

where $\vec{\xi}$ is the column vector of values ξ_j ($j = 1, 2, \ldots, 6$); T, the symbol of transposition; M, the quadratic matrix 6×6 inverse with the matrix N:

$$N = \begin{pmatrix} \overline{\xi_1^2} & \overline{\xi_1\xi_2} & \overline{\xi_1\xi_3} & \cdots & \overline{\xi_1\xi_6} \\ \overline{\xi_2\xi_1} & \overline{\xi_2^2} & \overline{\xi_2\xi_3} & \cdots & \overline{\xi_2\xi_6} \\ \bullet & \bullet & \bullet & \bullet & \bullet \\ \overline{\xi_6\xi_1} & \overline{\xi_6\xi_2} & \overline{\xi_6\xi_3} & \cdots & \overline{\xi_6^2} \end{pmatrix},$$

where the bar above symbols is the averaging of them.

Transformation of the matrix N with the allowance for Equation A1.4 yields the following expression for the isotropic surface:

$$M = \begin{pmatrix} \frac{2m_4}{\Delta_1} & 0 & 0 & \frac{3m_2}{2\Delta_1} & 0 & \frac{3m_2}{2\Delta_1} \\ 0 & \frac{1}{m_2} & 0 & 0 & 0 & 0 \\ 0 & 0 & \frac{1}{m_2} & 0 & 0 & 0 \\ \frac{3m_2}{2\Delta_1} & 0 & 0 & \frac{9\Delta_2}{4m_4\Delta_1} & 0 & -\frac{3\Delta_3}{4m_4\Delta_1} \\ 0 & 0 & 0 & 0 & \frac{1}{m_2} & 0 \\ \frac{3m_2}{2\Delta_1} & 0 & 0 & -\frac{3\Delta_3}{4m_4\Delta_1} & 0 & \frac{9\Delta_2}{4m_4\Delta_1} \end{pmatrix},$$

where $\Delta_1 = 2m_0m_4 - 3m_{22}$, $\Delta_2 = m_0m_4 - m_{22}$, $\Delta_3 = m_0m_4 - 3m_{22}$

Then the unknown joint probability density is written in the form:

$$p(\xi_1, \xi_2, ..., \xi_6) = \frac{1}{8\pi^3\sqrt{\Delta}} \exp\left(-\frac{1}{2}X\right) \tag{A1.10}$$

where $\Delta = \frac{4}{27}(m_2m_4)^2(2m_0m_4 - 3m_2^2)$;

$$X = \frac{2m_4}{\Delta_1}\xi_1^2 + \frac{9\Delta_2}{4m_4\Delta_1}(\xi_4^2 + \xi_6^2) + \frac{3}{m_4}\xi_5^2 + \frac{3m_2}{\Delta_1}\xi_1(\xi_4 + \xi_6) - \frac{3\Delta_3}{2m_4\Delta_1}\xi_4\xi_6 + \frac{1}{m_2}(\xi_2^2 + \xi_3^3).$$

Now it is the matter of techniques to determine various useful characteristics of the rough surface. For example, again leaving the details apart, let consider the distribution of the peaks. The surface has a summit (i.e., local maximum) in the point (x, y), providing the following conditions are satisfied:

$$\xi_2 = \xi_3 = 0, \qquad \xi_4 < 0, \qquad \xi_6 < 0, \qquad \xi_4\xi_6 - \xi_5^2 \geq 0.$$

If the point is within the elementary region dA above which the summit is disposed, the variables ξ_2, ξ_3 vary within the region

$$\mathrm{d}\xi_2\mathrm{d}\xi_3 = \left|\frac{\partial(\xi_2, \xi_3)}{\partial(x, y)}\right|\mathrm{d}A = |\xi_4\xi_6 - \xi_5^2|\mathrm{d}A.$$

Then the density of the summits with the ordinate ξ_1 is determined by integration:

$$P_{\text{sum}} = \iiint_V p(\xi_1, 0, 0, \xi_4, \xi_5, \xi_6)|\xi_4\xi_6 - \xi_5^2|\mathrm{d}\xi_4\mathrm{d}\xi_5\mathrm{d}\xi_6,$$

where the region of integration V is determined by the following inequalities:

$$\xi_4 < 0, \quad \xi_6 < 0, \quad \xi_4\xi_6 - \xi_{52} \geq 0.$$

With some experience and taste for non-trivial transformations it is easy to demonstrate that the last integral is taken in the finite form, after it is normalized for the density of the summits (the number of summits per square unit of area):

$$D = \frac{1}{6\pi\sqrt{3}}\frac{m_4}{m_2}. \tag{A1.11}$$

It is determined after transformations that the probability density of the summits is:

$$\begin{aligned} p(\xi_1^*) = \frac{\sqrt{3}}{2\pi}\Bigg\{ & \xi_1^*\left[\frac{3(2\alpha-3)}{\alpha^2}\right]^{1/2}\exp(-C_1\xi_1^{*2}) + \frac{3\sqrt{2\pi}}{2\alpha}(\xi_1^{*2}-1) \\ & \times\left[1+\operatorname{erf}\left(\xi_1^*\left(\frac{3}{2(2\alpha-3)}\right)^{1/2}\right)\right]\exp\left(-\frac{1}{2}\xi_1^{*2}\right) + \left[\frac{2\pi\alpha}{3(\alpha-1)}\right]^{1/2}, \\ & \times\left[1+\operatorname{erf}\left(\xi_1^*\left(\frac{\alpha}{2(\alpha-1)(2\alpha-3)}\right)^{1/2}\right)\right]\exp\left[\frac{-\alpha\xi_1^{*2}}{2(\alpha-1)}\right]\Bigg\} \end{aligned} \tag{A1.12}$$

where $\xi_1^* = \xi_1/m_0^{1/2}$; $\alpha = m_0m_4/m_2^2$; $C_1 = \alpha/(2\alpha-3)$.

This distribution was first derived by Nayak and below is referred to his name.

The distribution is degenerated in the normal one at $\alpha \to \infty$ and in the Rayleigh distribution at $\alpha \to 1.5$.

It is evident that Gaussian isotropic surface is adequately described by the moments m_0, m_2 and m_4, which are commonly found by processing the profilometer trace. In spite of this circumstance, a distinction needs to be drawn between statistics of surface (a random function of two variables) and statistics of profile (a random function of one variable, or a one-dimensional section of the surface). For example, it is well known that the probability density for the height of profile peaks is

$$p_{\text{peak}}(\xi_1^*) = \left(\frac{\alpha-1}{2\pi\alpha}\right)^{1/2}\left[\exp\left(-\frac{\alpha\xi_1^*}{2(\alpha-1)}\right) + \xi_1^*\left(\frac{\pi}{2(\alpha-1)}\right)\exp\left(-\frac{1}{2}\xi_1^{*2}\right)\left(1+\operatorname{erf}\frac{\xi_1^*}{\sqrt{2(\alpha-1)}}\right)\right].$$

Here by a peak is meant a maximum in the profilometer trace (profile) which does not need to be coincident with a maximum in the surface named a "summit".

A comparison of probability densities of summits and peaks (Figure A1.3) shows how the profile distors the surface. With the same parameter α the profile gives smaller amounts of high peaks and underestimates their height than there exist on surface. The reason is that the chance that stylus of profile-measuring instrument will travel over the summit is negligible. That is, the stylus,

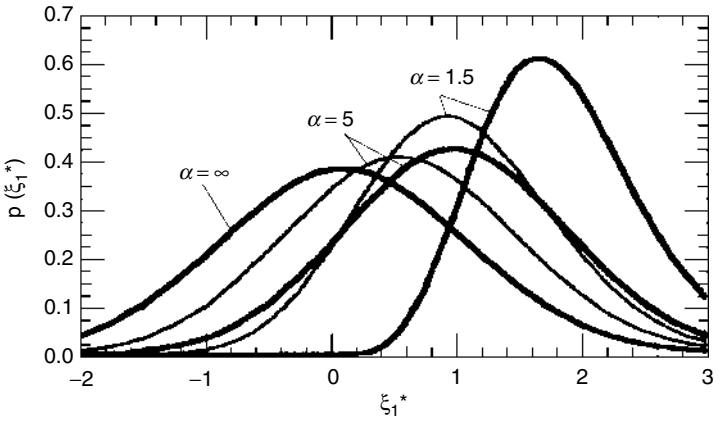

FIGURE A1.3 Probability densities for peak (thin lines) and summit (thick lines) heights.

as a rule, travels over the shoulder of an asperity. The distortion decreases when the parameter α varies from 1.5 (the greatest distortion) to ∞ (zero distortion).

Let us consider some other measures of surface roughness.

The surface gradient is defined by the variables (ξ_2, ξ_3), the joint probability density of which is found by the equation

$$p(\xi_2, \xi_3) = \frac{1}{2\pi m_2} \exp\left(-\frac{\xi_2^2 + \xi_3^2}{2m_2}\right). \tag{A1.13}$$

If we pass to the polar coordinates

$$(\xi_2, \xi_3) = (\xi \cos\theta, \sin\theta)$$

then with regard to the Jacobian

$$\left|\frac{\partial(\xi_2, \xi_3)}{\partial(\xi, \theta)}\right|$$

from Equation 2.11, we obtain

$$p(\zeta, \theta) = \frac{\zeta^2}{2\pi \Delta_2^{1/2}} \exp\left(-\frac{\zeta^2(m_{02}\cos^2\theta - 2m_{11}\cos\theta\sin\theta + m_{20}\sin 2\theta)}{2\Delta_2}\right)$$

Hence we may find the distribution density of the gradient modulus

$$p(\zeta) = \frac{\zeta}{\Delta_2^{1/2}} \exp\left(\frac{\zeta^2(m_{20} + m_{02})}{4\Delta_2}\right) I_0\left(\frac{\zeta^2(m_{20} - m_{02})}{4\Delta_2}\right) \tag{A1.14}$$

where $I_0(z) = (1/2\pi)\int_0^{2\pi} \exp(-z\sin\theta)d\theta$ is the Bessel function of the zero order for imaginary argument.

In deducing Equation A1.14 we suggested the axis X_1 coincides with the major direction, so that $m_{11} = 0$ and $m_{20} \geq m_{02}$. In the case of the isotropic roughness the gradient modulus has the

Rayleigh distribution

$$p(\zeta) = \frac{\zeta}{m_2}\exp(-\zeta^2/2m_2) \tag{A1.15}$$

Then the mean value of the gradient modulus is

$$\bar{\zeta} = \int_0^\infty \zeta p(\zeta)d\zeta = \left(\frac{\pi m_2}{2}\right)^{1/2} \tag{A1.16}$$

Surface curvature at summit is defined as follows. There are two major directions and the corresponding them principal curvatures K_1 and K_2 at each surface point. Their half-sum is the mean curvature $K_m = (K_1 + K_2)/2 = -(\xi_4+\xi_6)/2$. The joint probability density for summit heights ξ_1^* at the summit t_1 is

$$p(\xi_1^*, t) = \left(\frac{3C_1}{2\pi}\right)^{1/2}[t_1^2 - 2 + 2\exp(-t_{1/2}^2)]\exp(-C_1\xi_1^{*2})\exp\left[\frac{1}{2}(C_1t_1^2 + C_2t_1\xi_1^*)\right] \tag{A1.17}$$

Here $C_1 = \alpha/(2\alpha-3)$; $C_2 = C_1(12/\alpha)^{1/2}$; $t_1 = -K_m(3/m_4)^{1/2}$.
Then the expected value $\bar{K}_m(\xi_1^*)$ at the summit with the height ξ_1^* is

$$\bar{K}_m(\xi_1^*) = \left(\frac{m_4}{3}\right)^{1/2}\frac{I_3(\xi_1^*) - 2I_1(\xi_1^*) + 2I_5(\xi_1^*)}{I_2(\xi_1^*) - 2I_0(\xi_1^*) + 2I_4(\xi_1^*)}, \tag{A1.18}$$

where

$$I_0 = \left(\frac{\pi}{2C_1}\right)^{1/2}\exp\left(-\frac{1}{2}\xi_1^*\right)(1 + \operatorname{erf}\beta_1\xi_1^*),$$

$$I_1 = \frac{1}{C_1}\left[\exp(-C_1\xi_1^{*2}) + \pi^{1/2}\beta_1\xi_1^*\exp\left(-\frac{1}{2}\xi_1^{*2}\right)(1 + \operatorname{erf}\beta_1\xi_1^*)\right],$$

$$I_2 = \sqrt{2}C_1^{3/2}\left[\beta_1\xi_1^*\exp(-C_1\xi_1^{*2}) + \pi^{1/2}\left(\beta_1\xi_1^{*2} + \frac{1}{2}\right)\exp\left(-\frac{1}{2}\xi_1^{*2}\right)(1 + \operatorname{erf}\beta_1\xi_1^*)\right],$$

$$I_3 = \frac{2}{C_1^2}\left[(1 + \beta_1^2\xi_1^{*2})\exp(-C_1\xi_1^{*2}) + \pi^{1/2}\left(\beta_1\xi_1^{*3} + \frac{3}{2}\beta_1\xi_1^*\right)\exp\left(-\frac{1}{2}\xi_1^{*2}\right)(1 + \operatorname{erf}\beta_1\xi_1^*),\right.$$

$$I_4 = \left(\frac{\pi}{2(C_1+1)}\right)^{1/2}(1 + \operatorname{erf}\beta_2\xi_1^*)\exp\left[-\frac{\alpha\xi_1^{*2}}{2(\alpha-1)}\right],$$

$$I_5 = \frac{1}{C_1+1}\left[\exp(-C_1\xi_1^{*2}) + \pi^{1/2}\beta_2\xi_1^*(1 + \operatorname{erf}\beta_1\xi_1^*)\exp\left(-\frac{\alpha\xi_1^{*2}}{2(\alpha-1)}\right)\right],$$

$$\beta_1 = \left(\frac{3}{2(2\alpha-3)}\right)^{1/2}; \qquad \beta_2 = \left(\frac{\alpha}{2(2\alpha-1)(2\alpha-3)}\right)^{1/2}.$$

Analysis of dependence Equation A1.18 shows (Figure A1.4) the curvature radius at the summit is decreased with increase of the peak height (higher peaks is "more acute"), i.e., the curvature is increased.

Its increase depends on bandwidth parameter α: as $\alpha \to 1.5$ the mean curvature is directly proportional to the peak height $\bar{K}_m = -(2m_4/3)^{1/2}\xi_1$; as $\alpha \to 1.5$ it becomes independent of the peak height $\bar{K}_m = (8/3)(m_4/\pi)^{1/2}$.

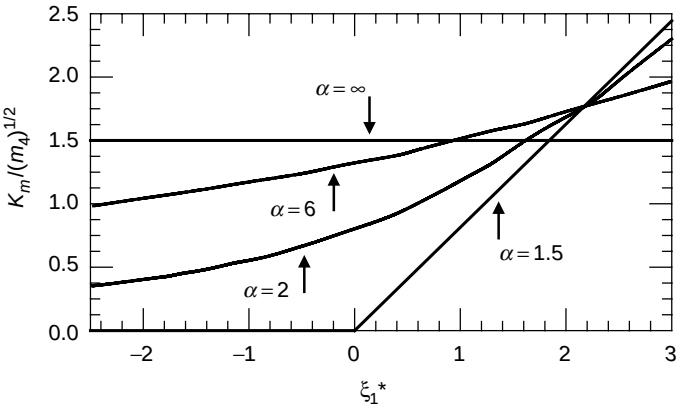

FIGURE A1.4 Mean curvature of summits for different values of α.

It is pertinent to note that the dimensionless peak curvature is calculated by the formula:

$$\frac{\bar{K}_{\text{peak}}(\xi_1^*)}{\sqrt{m_4}} = \beta\sqrt{\alpha}\frac{\xi\beta + \sqrt{\pi}\exp(\xi^2\beta^2)(1 + \text{erf}\,\xi\beta)(\xi^2\beta^2 + 0.5)}{1 + \xi\beta\sqrt{\pi}\exp(\xi^2\beta^2)(1 + \text{erf}\,\xi\beta)},$$

where $\beta = 1/[2(\alpha - 1)]^{1/2}$.

Comparison of peak and summit curvatures presented in Figure A1.5 shows that here, too, there is a distortion of the surface by the profile. This distortion is small for $\alpha > 2$ within the range, $0 \le \xi_1^* \le 3$ which is of interest to tribological calculation. It is notable that the profile gives both overestimated ($\alpha < 2.5$) and underestimated ($\alpha > 2.5$) values of peak curvature when compared to the summit curvature.

Average roughness $R_a^{'}$ is defined as mean value of absolute surface deviations from mean plane:

$$R_a^{'} = \frac{1}{A}\int\int_A |z(x, y)\mathrm{d}x\mathrm{d}y|$$

where A is the area of the domain under consideration.

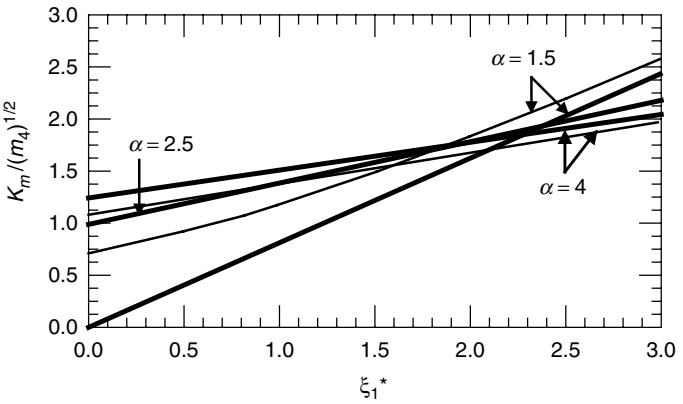

FIGURE A1.5 Comparison of peak (thin lines) and summit (thick lines) curvatures for $\alpha = 1.5$, 2.5 and 4.

Two first moments of functional $R_a^{'}$ are the mean

$$R_{\mathrm{a}}^{'} = \left(\frac{2}{\pi}\right)^{1/2} \sigma \tag{A1.19}$$

and the variance

$$DR_{\mathrm{a}}^{'} = \frac{4\sigma^2}{L_0^4} \sum_{k=1}^{\infty} \frac{1}{(2k)!} \left[\Phi^{(2k-1)(0)}\right]^2 \int_0^{L_0} \int \iint K^{2k}(r)\mathrm{d}x_1\mathrm{d}x_2\mathrm{d}y_1\mathrm{d}y_2$$

Here $\Phi^{(k)}(X)$ is the derivative of the Laplace function; $K(r)$ is the correlation function of the field.

Bearing area ratio is defined in the following manner. Let the surface $z = z\,(x, y)$ is intersected by horizontal plane parallel to the mean plane and far from it on some distance u. In this horizontal plane regions are cut out by surface z. Their summary area referred to unit of the nominal area is named the bearing area at level u and denoted by η_u. The mean value of the bearing area is

$$\eta_u = 1 - \Phi(u/\sigma), \tag{A1.20}$$

where

$$\Phi(x) = \frac{1}{(2\pi)^{1/2}} \int_{-\infty}^{\infty} \exp(-t^2/2)\mathrm{d}t.$$

The variance of functional η_u is

$$D\eta_u = \frac{1}{L_0^4} \sum_{k=1}^{\infty} \frac{1}{k!} \left[\Phi^{(k)}\left(\frac{u}{\sigma}\right)\right]^{1/2} \int_0^{L_0} \int \iint K^k(x_2 - x_1, y_2 - y_1)\mathrm{d}x_1\mathrm{d}x_2\mathrm{d}y_1\mathrm{d}y_2$$

The distribution of value η_u may be assumed nearly normal with the mathematical expectation $\bar{\eta}_u$ and variance $D\eta_u$.

Appendix 2: Shape-Memory Materials

A.2.1 GENERAL CHARACTERISTICS

The shape-memory effect (SME) refers to the ability of certain materials to "remember" a shape, even after severe deformation. When a material with shape-memory ability is cooled below its transformation temperature (martensite phase), it has a very low yield strength and can be deformed quite easily into a new shape. When heated above its transformation temperature, shape-memory material undergoes a change in crystal structure causing it to return spontaneously to its original shape (austenite phase). During this isotropic transformation process, as the atoms shift back to their original positions, a substantial amount of energy is released. A single 1 cm^3 of SME alloy can exert enough force to move an object weighing 4650 kg!

The SME was first observed as early as 1938, by A.B. Greninger and V.G. Mooridian, who showed that the martensite phase in brass could form and disappear with temperature change. At about the same time, G.V. Kurdyumov, a Russian metallurgist known for his early work on the crystallography of martensite transformations, particularly in steels, studied the phase relations in brass between the high-temperature β-phase and the martensite formed by rapid cooling.

It was not until 1962, however, that the shape-memory phenomenon came to worldwide attention with the announcement of the existence of this effect in a Ni-Ti alloy discovered by W.J. Buehler[968] of the U.S. Naval Ordonance Laboratory. The alloy was named "Nitinol" for (Ni)ckel–(Ti)tanium Naval Ordnance Laboratory (NOL). One of the first applications of the Nitinol alloy was developed by Raychem Corporation to solve the problem of coupling the hydraulic-fluid lines in the F-14 jet fighter built by Grumman Aerospace Corporation. With its wide experience in heat-shrinkable plastics, Raychem proposed a coupling in which a Nitinol alloy was shrunk to a tight fit by being raised above its martensite transformation temperature. The coupling maintained its gripping integrity down to −120EC so that its transformation temperature remained in the cryogenic region. Over one million such couplings have since been manufactured and installed in jet fighters and in marine and industrial piping connections without any reported failure.

The SME is a result of a thermoelastic martensitic transformation. In this phase transformation, a high-temperature parent phase (austenite) transforms to a low-temperature phase (martensite) by essentially homogeneous lattice shear strain and cooperative atomic movement. This transformation is displacive in nature and thus no diffusion processes are involved. Atoms are cooperatively rearranged into a new, more stable crystal structure, but without changing the chemical nature of the matrix. Furthermore, since no atomic motion is involved, this displacive transformation generally progresses in a time-independent mode and is dependent only on the temperature. The martensite structure is a zigzag or harmonica-type arrangement of lattice planes forming a so-called "twinned structure."[969]

The martensitic transformation is spontaneous and reversible occurring during cooling from the parent phase or austenite to the martensitic state or martensite. This phase transformation is a first-order displacive transformation in which a body-centre cubic phase (austenite), on cooling, transforms by a shear-like mechanism to martensite, which is both ordered and twinned. The martensitic transformation is diffusionless, i.e. it involves a cooperative rearrangement of atoms over a short distance into a new stable crystal structure without changing the chemical nature of the matrix. This process is illustrated in Figure A2.1a.[970]

The progress of the martensitic transformation may be followed by measuring such properties as electrical resistivity, length or volume changes as a function of temperature. Figure A2.1b illustrates typical property changes with temperature.[970] The martensitic transformation starts at temperature M_s (martensite start) during cooling and is completed at temperature M_f (martensite finish), when the austenitic phase has disappeared completely; the new phase formed is entirely martensitic. Upon heating, the reverse transformation starts at A_s (austenite start) when the martensite commences to disappear and at A_f (austenite finish) the transformation is completed.

The stress–strain curve of the martensitic NiTi can be divided into three well defined regions as seen in Figure A2.2.[970] An initial low plateau results from the stress-induced growth of one martensite orientation at the expense of an adjacent less-favorably oriented plate. This process, also called "detwinning", is fundamentally different from the conventional deformation by gliding in that the original shape can be recovered by thermally; in other words, by heating above the transformation temperature.

At higher stresses, there is a second region, which is usually linear, although not purely elastic. It is believed[968] that the deformation mechanism in this stage is a mixture of elastic deformation of the detwinned martensite, with the formation of new orientations of martensite intersecting those already present which, in turn, provides additional heat recoverable strain.

The transition to the third region is a result of the onset of irreversible plastic deformation and the material is plastically deformed in a conventional way. Depending on the alloy composition, its thermo-mechanical processing, testing direction and deformation mode, the length of the martensite plateau in the stress–strain curve extends typically 5–6%.

It should be noted that considerable hysteresis is associated with the martensitic transformation, since the transformation temperatures differ upon heating and cooling. The magnitude of this hysteresis depends on the alloy and is of great technological importance. Typical values are of

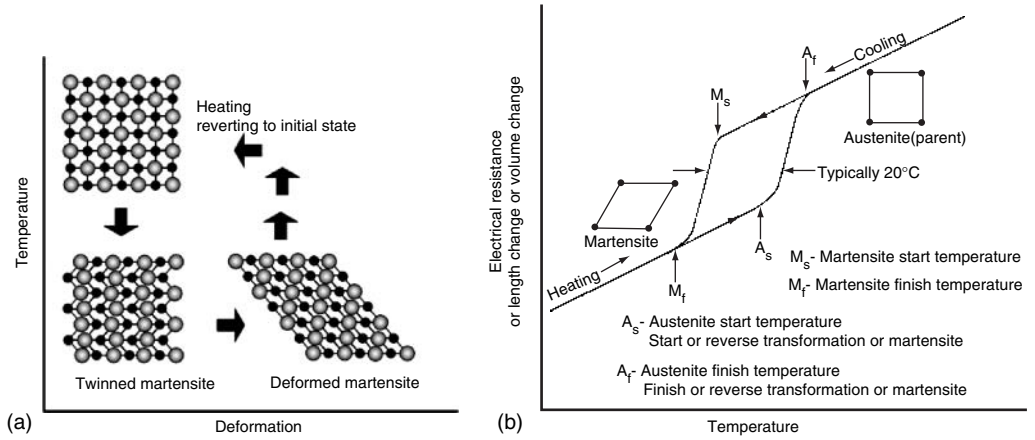

FIGURE A2.1 (a) Thermoelastic martensitic transformation and shape-memory effect and (b) Hypothetical plot of property change as a function of temperature for a martensitic transformation occurring in a shape-memory alloy.

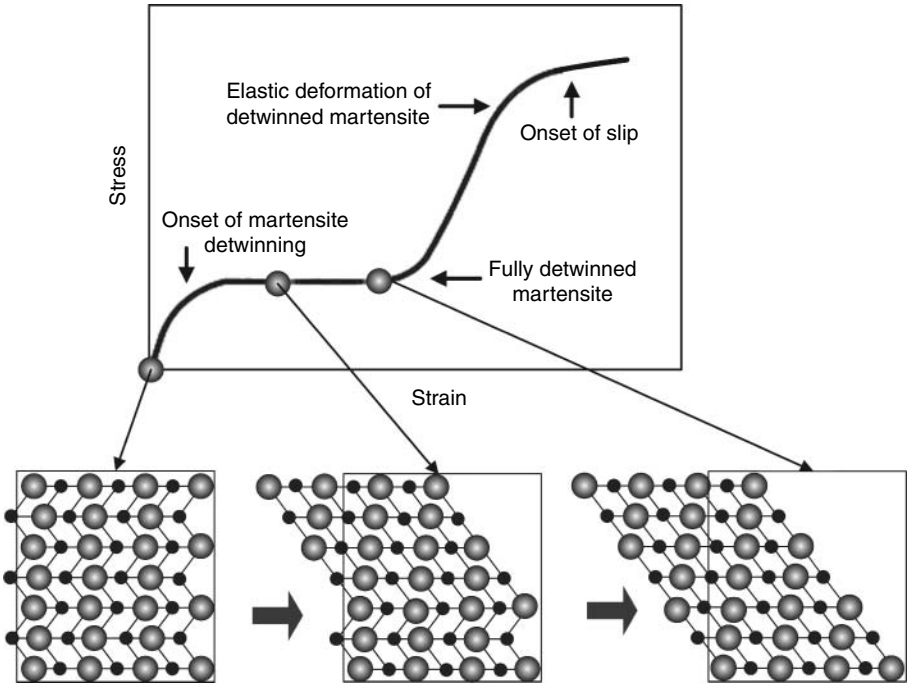

FIGURE A2.2 The stress-strain curve of NiTi alloy with corresponding structural changes.

the order 10–40EC, but by suitable thermo-mechanical treatment and selected alloy additions, values of 0–5EC (Ni-Ti "R" phase) or over 100EC can be attained (Figure A2.3).[970]

A.2.2 MANIFESTATIONS OF THE SHAPE-MEMORY EFFECT

A.2.2.1 One-Way Memory Effect

The one-way memory effect can be explained by invoking the following explanation. A straight SMA wire, fixed at one end (Figure A2.4a), is stretched or bent beyond its yield point at room temperature.[971,972] After unloading the wire will remain in the stretched or bent condition until it is heated to above the transformation temperature of the alloy (A_f). If no load is applied, it will return

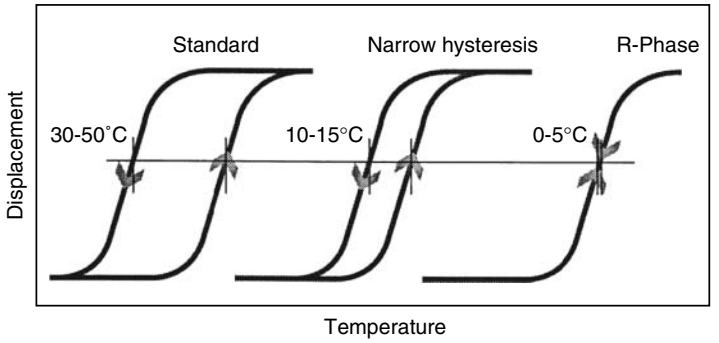

FIGURE A2.3 Motion-temperature hysteresis of different Ni-Ti alloys.

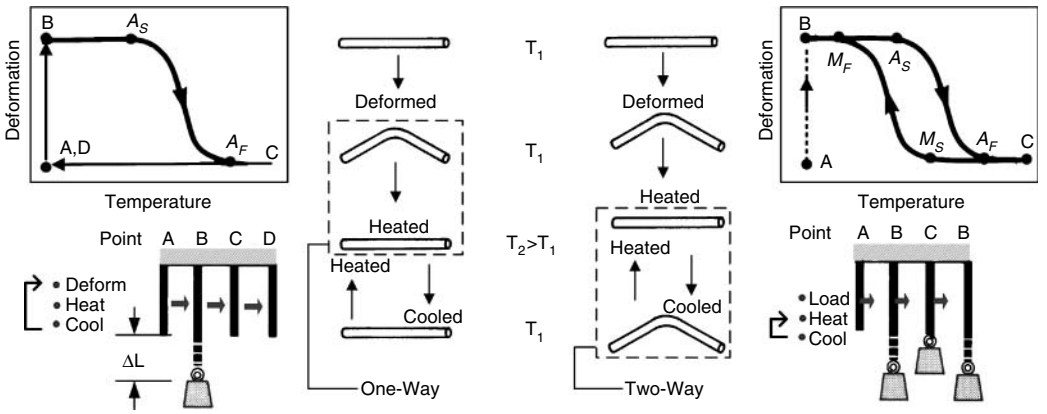

FIGURE A2.4 (a) One-way and (b) two-way shape memory effect.

to its original shape. Subsequent cooling below the transformation temperature (M_f) causes no macroscopic shape changes. It should be noted that although the one-way effect can be repeated many times, reactivation of the SME can only be realized by deforming the wire in the martensitic state. Since no special treatment is necessary, cyclic use of the one-way memory effect with external reset force in many instances is the more economic solution.

A.2.2.2 Two-Way Memory Effect

The two-way memory effect refers to the ability of SMA to assume one shape in the martensitic state (low temperature) and then spontaneously change to a second shape when heated to above A_f (high temperature) (Figure A2.4b).[971,972] This process can be cycled fairly reproducibly between different shapes by simply changing the temperature, providing the strain level involved is not excessive nor the exposure temperature too high. The two-way effect can only be produced by special thermomechanical treatment ("training") which comprises multiple heat/cool cycling under the same applied external force, thus allowing the material to "remember" the training process.

A.2.2.3 Pseudo-Elasticity (Superelasticity)

The Shape-memory effects described so far are "thermal memory" effects. Pseudo-elasticity or superelasticity can be considered a "mechanical memory" effect, in other words, a result of stress-induced martensite formation. The shape-memory material elongates plastically, as if permanently deformed, but when the stress is released, the martensite reverts to the parent phase and the SMA regains its original shape. Superelastic SMA can be elastically deformed up to 10% (Ni-Ti) or 6% (Cu-based alloys). The appearance of superelastic behavior is accompanied by heat release during stress-induced martensite formation and by heat absorption during stress removal. Figure A2.5 shows schematic stress–strain curves for a conventional material and and NiTi shape-memory alloy together with a comparison of microstructural changes occurring during elastic deformation.[973]

A.2.3 PRINCIPAL SHAPE-MEMORY ALLOYS

A.2.3.1 Nickel-Titanium Shape-Memory Alloys

Shape-memory alloys based on nickel and titanium provide the best combination of material properties for most commercial applications. In these alloys, the transformation temperature M_s (martensite start) is strongly dependent on the oxygen content and composition. For example,

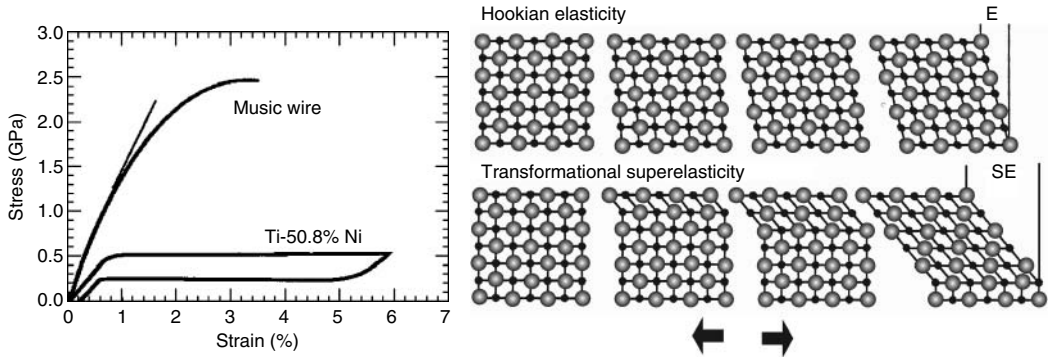

FIGURE A2.5 Stress–strain characteristics of steel and superelastic NiTi alloy wire and a comparison of microstructural changes occurring during elastic deformation.

increasing the oxygen content from 150 ppm (parts per million) to 450 ppm decreases the M_s temperature from 45°C to −5°C. The composition sensitivity of NiTi is of considerable practical importance and requires precise composition control during alloy preparation. Depending on the desired M_s, the necessary control is between 0.01 and 0.1%.[974]

Standard NiTi alloys show a hysteresis of 30–50°C but, with modifications, it is possible to either extend this to over 100°C or reduce it to about 10–15°C or even to 0–5°C in the case of some NiTi alloys with a premartensitic transformation, commonly known as the R-phase.

The addition of third or fourth elements to NiTi alloys provides a powerful tool to control transformation temperature, increase stability of M_s, control the hysteresis width, increase austenitic strength, reduce or increase martensitic strength and improve corrosion resistance. Additions of Cu, Nb and precious metals provide a useful combination of properties. For example, the addition of Cu can reduce the hysteresis width and composition sensitivity to the transformation temperature M_s and improve the fatigue resistance. Furthermore, the Cu-containing ternary NiTi alloy also has a martensite phase with a lower yield strength, thus requiring a lower reset force for some cyclic applications. Alloys with 10% Cu exhibit a two-step transformation and a corresponding two-step shape change.[974]

NiTi alloys have excellent corrosion resistance provided by a naturally formed thin oxide layer or "passive film". The stability of this film provides NiTi alloys with good resistance to many forms of corrosive attack. Consequently, the NiTi alloys are most appropriate for majority of applications in the actuator, electric connector and fastener fields. Different mechanical, physical and shape-memory properties of NiTi and Cu-based alloys are shown in Table A2.1.[976]

A.2.3.2 Copper-Based Shape-Memory Alloys

The early Cu-Based shape-memory alloys suffered from intergranular failure due to their intrinsic coarse grain structure. However, the recent development in the grain refining methods have significantly improved their mechanical properties thus making these fine-grain alloys more competitive than NiTi, bimetals and other low cost materials commonly used in conventional thermal and mechanical actuation applications.

Commercially available Cu-based shape-memory alloys derive from two base alloy systems: CuZn and CuAl. Both CuZn-based ternary alloys containing Al, Si, Sn, Ga or Mn and CuAl-based ternary alloys containing Ni, Be, Zn or Mn have been explored for their shape-memory properties. These studies have been extended to quaternary alloys of CuZnAlNi, CuZnAlMn and CuAlNiMn. The currently available alloys have been developed either in the form of ternary CuZnAl or CuAlNi, or in quaternary modifications containing Mn.[976,977]

TABLE A2.1
Properties of NiTi and Cu-Based Alloys

Property	Ni-Ti	Cu-Al-Ni	Cu-Zn-Al
Density (kg/m^3)	6500	7200	7800
Resistivity (μΩ m)	A - 1.0	A - 0.1	A - 0.07
	M - 0.8	M - 0.14	M - 0.12
Heat Capacity (J/kg EC)	470–620	400–480	390
Heat of Transformation (J/kg)	25,000	8000	8000
Young's Modulus (GPa)	70–98	80–100	70–100
Yield Strength (MPa)	M 200–800	M 150–300	M 150–300
	A 150–300		
Transformation Temperature (EC)	−200 /+100	−200/+200	−200 /+120
Max Operating Temperature (EC)	300	250	140
Damping (SDC %)	15	10	30
Shape-memory properties			
One-Way Strain (%)	20–30	20–30	10–20
Hysteresis (EC)	8	3–6	3–6
Two-Way Strain (%)	6	1–2	1–2

A.2.3.3 CuZnAl-Based Alloys

The -phase domain in these phases is found in the Cu-rich region, i.e. 68–80% Cu with 10–28% Zn and 2–6% Al. Addition of alloying elements affects the shape-memory properties of these alloys adjusting the martensitic transformation temperature and to optimizing the thermal-stability and mechanical properties. Small variations in the Zn or Al concentrations can change the martensitic transformation temperature M_s within the range $-200°C$ to $+200°C$.

Since the β-phase is metastable at room temperature, relatively rapid quenching from the betatizing temperature has to be used to retain this phase and avoid its decomposition. Stable transformation temperatures can be obtained by a post-quench aging treatment or by step-quenching. This calls for considerable precautions during the preparation and heat treatment of the alloy which, in turn, will assure a homogenous alloy composition and stability of the transformation temperature. Although the transformation temperatures of CuZnAl alloys can be manipulated over a wide temperature range, the practical upper limit is 120°C. This is because higher temperatures cause a rapid loss of the SME due to instability of the transformation temperatures.

The mechanical properties of these alloys are very temperature-sensitive and exhibit multistage yielding at temperatures approaching the transformation temperatures. The parent-phase has anomalous elastic properties and the pseudoelasticity (superelasticity) associated with stress-induced martensite-to-martensite transformation. Successive stress-induced martensite-to-martensite transformation can give rise to multistage pseudoelasticity which enables to obtain a recoverable strain of 17% in single crystals.

CuZnAl alloys are also very susceptible to dezincification, which appears preferentially at grain boundaries, surface defects and martensite interfaces. Dezincification is strongly influenced by the chemical composition and the phases present. At comparable Zn contents, martensitic alloys are more susceptible to dezincification than austenitic alloys. The alloy resistance to dezincification can be improved by additions of Al.

The CuZnAl alloys are also susceptible to stress-corrosion cracking, which results in intergranular failure. Although the surface coating may improve the resistance of these alloys to both dezincification and stress-corrosion cracking, it can also influence the SME. For most metallic

coatings, the permissible elastic strain is typically $<0.5\%$, too small to accommodate the shape-memory strain, which can be as high as 6%.

A.2.3.4 CuAlNi-Base Alloys

CuAlNi alloys containing 13–14% Al, 4–6% and the balance of Cu are generally used for high-temperature applications (up to 200°C) requiring high strength. The addition of Ni up to 4% reduces the transformation hysteresis, stabilizes the β-phase, decreases As to a reasonable value and improves the tensile strength. Adding Mn further improves the stability of transformation temperature and ductility of these alloys. Reducing the Al content to 12% suppresses brittle fracture due to precipitation of the brittle phase and significantly improves ductility.

These alloys have a very strong tendency to grain growth during the betatizing treatment that can be significantly reduced by adding Ti, B and Zr. Since refining is largely due to the formation of small insoluble particles which either assist grain nucleation or inhibit grain growth, these additives have only very slight effects on the transformation temperature.

A.2.3.5 Ferrous Shape-Memory Alloys

The FeMnSi alloys can exhibit a SME but are not strictly thermoelastic and have a weak pseudoelasticity. These shape-memory alloys are characterized by substantial, asymmetrical hysteresis, which limits their wider industrial use. These alloys are generally intended for applications where damping is of concern.

A.2.4 FABRICATION AND THERMOMECHANICAL TREATMENTS OF SHAPE-MEMORY ALLOYS

The fabrication of shape-memory alloys is no easy procedure. Close control of various stages of the melting and thermomechanical treatments is essential if the desired shape-memory properties, such as reproducibility, mechanical properties, fatigue resistance, transformation temperature stability etc., are to be obtained. The first stage of alloy preparation is melting generally carried out in an induction furnace but also in electric arc furnaces with consumable or nonconsumable electrodes. In the case of NiTi, melting is carried out under vacuum in a graphite crucible. [976,977]

Shaping of the SMAs is usually done using conventional forming methods such as rolling, drawing, swaging, etc. The selection of a method depends on the morphology of the end product. It should be noted that, for the same composition, the transformation temperatures as well as the aging characteristics can differ according to which forming method is used.

Other fabrication methods have recently been developed for shape-memory alloys. Among these, rapid solidification (melt spinning, melt extraction), powder metallurgy and sputtering are worth mentioning. To obtain the shape-memory properties, the material has to be in its β-phase, which is usually metastable at room temperature. Hence, to retain this phase, special thermomechanical treatment ("training") is required.

A.2.5 CHARACTERIZATION METHODS FOR SHAPE-MEMORY ALLOYS

The evolution of the SME in alloys can be followed by using different experimental techniques. The techniques generally used for metallurgical investigations such as optical and electron microscopy, X-ray or electron diffraction, microhardness, dilatometry etc., can be used to follow the structural changes caused by the martensitic transformations. However, other measuring techniques such as acoustic emission, differential scanning calorimetry (DSC), and electrical resistivity have been specifically developed and used to observe the structural changes in the SMA.

A.2.5.1 Electrical Resistivity

A change in electrical resistivity with temperature is a widely used simple measuring technique for monitoring transformation either in the absence or in the presence of deformation. The classical four-lead method is used to measure electrical resistivity changes. In the case of Cu-based alloys, the martensitic transformation causes a resistance rise of 25%. According to the law of solution, the resistivity of a two-phase alloy (austenite + martensite) is determined by the volume fractions of these phases present in the solution. This provides a means for determining the characteristic transformation temperatures and associated hysteresis. Figure A2.6 depicts a typical variation in the electrical resistivity with temperature.[969]

This technique yields very good, reproducible results when applied to Cu-based and iron-based alloys. However, caution must be exercised in the case of NiTi alloys, since the resistivity-temperature dependence of these alloys vary significantly according to the thermal history of the specimen. Hence, the use of this technique for characterizing the SME in NiTi alloys can only be used to obtain general information about the transformation temperatures and a more precise determination of these temperatures is very difficult. In addition, this technique offers a simple and reliable tool for monitoring the evolution (or defects) of the martensitic transformation and for quality control of an SMA element of practically any shape and thus it can be used industrially as a non-destructive method for the quality control of shape-memory alloys.

A.2.5.2 Differential Scanning Calorimetry (DSC)

Differential scanning calorimetry involves measuring the changes in specific heat during the transformation process. It is a very sensitive measuring technique which allows discrete events to be identified in the transformation range using samples as small as 10 mg and with minimal sample preparation. It also allows direct measurement of the transformation temperatures and energies as well as the fractions of alloys transformed as a function of temperature. Figure A2.7 shows typical DSC curves during martensitic transformation.[976]

There is a number of other experimental techniques developed based on the structural changes occurring during transformation. These techniques provide control measurement, feedback and quality for products as well as enable understanding of the shape-memory transformation process itself. Among the techniques developed around these changes, the following are particularly worthy of mention: thermal expansion, yield strength and Young's modulus, internal friction

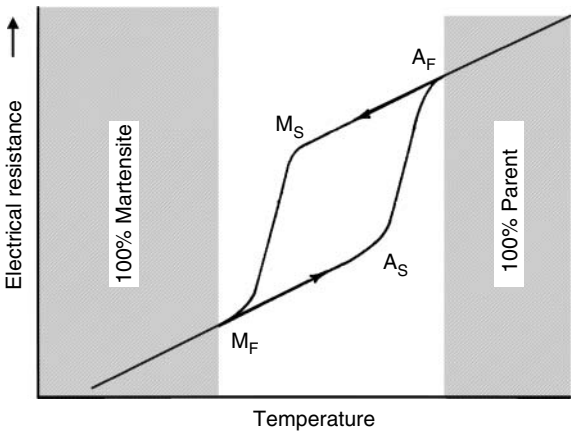

FIGURE A2.6 Changes of electrical resistivity with temperature associated with the martensitic transformation in a shape-memory alloy.

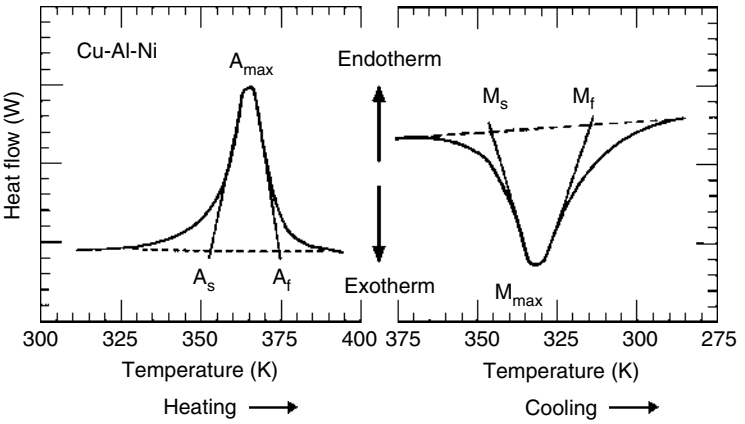

FIGURE A2.7 Evaluation of the transformation temperatures from a DSC curve.

and damping, magnetic susceptibility, thermoelectric power and the Hall effect coefficient, which are very sensitive to transformation changes and can be used for accurate monitoring of the SME in most alloys.

A.2.6 DEGRADATION OF SHAPE-MEMORY PROPERTIES

A major problem confronting the application of shape-memory alloys is the alteration in material characteristics induced either by cyclic deformation and phase changes or by aging at application temperatures.

A.2.6.1 Fatigue Resistance

The fatigue life of shape-memory alloys depends strongly on the cyclic-deformation mode, since the interfaces between different phases or between martensitic variants, grain boundaries, precipitates, grain size and other lattice defects all participate in the deformation process. Hence, in view of the large number of parameters exerting significant influence on the SME, improving the fatigue properties of SMA is very complex. In the case of polycrystalline Cu-based alloys, the strong anisotropy of the elastic properties and deformation results in intergranular fracture but in NiTi alloys it is much smaller and accounts for their superior fatigue resistance. Furthermore, the presence of a brittle phase at the grain boundaries significantly reduces the fatigue life of SMAs by facilitating crack propagation. Thus, improving the fatigue life imposes a reduction of the internal stresses at the grain boundaries and impedes the propagation of cracks. The enhancement can be achieved by:

- refining the grain and martensite plate sizes thus allowing for accommodation of deformation within the grain; powder metallurgy, rapid quenching or use of melting refiners can perform this task.
- creating the textured structures through rolling, for instance, thereby reducing the orientation difference between the grains as well as deformation incompatibility.

The use of single crystals can also improve the fatigue life of Cu-based alloys. Typical values of the fatigue life for the main shape-memory alloys are shown in Table A2.2.[976] These values can vary considerably, however, depending on the type of alloy and on the thermomechanical treatments.

TABLE A2.2
Typical Values for the Fatigue Resistance of Shape-Memory Alloys (P - Polycrystal, S - Single Crystal)

	Ni-Ti	Cu-Zn-Al	Cu-Al-Ni(P)	Al-Ni(S)
σ_{max} ($N = 10^5$ cycles)	250 MPa	75 MPa	100 MPa	150 MPa
ε_{max} One-way effect	8%	4%	5%	10%
$N = 10^3$	3%	2%	3%	6%
$N = 10^4$	2%	1%	2%	4%
ε_{max} Two-way effect	5%	2%	2%	
$N = 100$		1%	1.2%	
$N = 10^5$	1%	0.8%	0.8%	

A.2.6.2 Aging of Shape-Memory Alloys

The aging of SMA, often called amnesia, is manifested by changes in the transformation temperatures, increased hysteresis and stabilization of the martensitic phase, which entails loss of the SME. The rate at which aging progresses depends on the SMA application temperature. According to temperature, two aging effects can be distinguished: initial aging, in the martensitic phase, and long-term aging, in the austenitic phase. Initial aging corresponds to a diffusion-induced rearrangement of atoms that find their equilibrium state and thus stabilize the martensite and raise the transformation temperatures, M_s and A_s. The atom rearrangement is accelerated by the presence of a high concentration of quench-in vacancies. This can be eliminated or suppressed by step-quench which, in turn, will slow down the kinetics of this type of aging. [976–978]

The long term aging effect appears at higher temperatures where the austenitic phase is maintained. This type of aging is associated with decomposition of the austenitic phase at temperatures beyond their equilibrium temperatures. Depending on the temperature two possible mechanisms can be distinguished:

- Decomposition of the high-temperature phase and formation of more stable products (such as α-bianite in the case of Cu-based alloys) that are not characteristic of martensitic transformation.
- At lower temperatures, the formation of precipitates in the austenitic matrix changes the conditions for the formation of the martensitic phase.

Both processes are accelerated in the presence of a strain (strain-induced aging). The amnesia phenomenon affects also the two-way memory effect, as a result of which the characteristic microstructure produced by the training treatments is annihilated by the formation of stable precipitates and martensite plates.

A.2.7 APPLICATIONS OF SHAPE MEMORY ALLOYS

The SMA technology has not yet penetrated the electrical industry significantly, in part owing to a general lack of awareness as well as to the rather limited engineering data available about shape-memory materials. However, a steadily growing use of such materials in the electrical, automobile and mining industries, robotics, medicine and agriculture and in art indicates a wider recognition of the advantages and potential of the SMA technology.

Although initially the SME did not took attract worldwide attention, however, by the beginning of the 1970 diffusion of shape-memory alloys on a large industrial scale was under way.

TABLE A2.3
Shape-Memory Alloy Applications

1. Electrical Power Industry
   - Connectors
   - Circuit breakers
   - Fuses
   - Switches — switching devices
   - De-icing of transmission lines
   - Sagging of transmission lines
   - High-power heat engines
   - Robotic devices
   - Electrical/thermal actuators
   - Thermo-markers
   - Overcurrent protection
   - Overheating protection
   - Optical fiber splices
   - Contact bounce dampers
   - Nuclear power plant applications

2. Electronics Industry
   - IC connectors
   - ZIF connectors
   - DIP connectors
   - PGAP connectors
   - Micro-strip connectors
   - Locking rings for braided terminals
   - Disk drive lift/lower recording heads

3. Aerospace Industry
   - Hubble telescope
   - High-damping parts
   - Release mechanisms
   - Antenna release actuator
   - Hermetic seals
   - Explosive bolts
   - Vibration control devices
   - Sprag-type couplings
   - Ball-socket assemblies
   - Latching systems

4. Mechanical Engineering
   - Sealing rings
   - Valves
   - Tube/pipe couplings
   - Rock blasting
   - Springs
   - Washers
   - Force sensors
   - Filters

5. Automobile Industry
   - Cold starters
   - Fuel injection
   - Rattling-noise reduction
   - Temperature boost compensators
   - Shock absorbers
   - Climate control
   - Thermal valves
   - Fog lamp louvers
   - Windshield wipers

6. Domestic Appliance Industry
   - Fire detectors
   - Electric kettle switch
   - Automatic steam vent
   - Lamp robot
   - Greenhouse window opener
   - Air-conditioner actuator

7. Medical Applications
   - Eyeglass frames
   - Dental arch wires
   - Orthopedic implants
   - Catheter guide wires/coils
   - Clips for tubal sterilization
   - Interverter artificial joints

IC, integrated circuit; ZIF, zero-insertion force; DIP, dual in-line package; PGAP, pin grid array package.

More recently, the growth of SMA applications has experienced a remarkable acceleration in different fields of conventional and novel technologies as well as in medicine, biomedicine and orthodentistry. Table A2.3 shows an overview of identified SMA products developed and used in different domains of technology and medicine.

A.2.7.1 Joining Systems

The most widely exploited types of shape-memory alloys are those with a one-way SME in which an external constraint prevents the alloy from returning to its original shape on heating. In general,

their most successful uses are as fasteners or couplings for fluid piping and tubing, and also as electrical connectors. The main advantages of this type of coupling are:

- better alignment of the parts to be linked which, in turn, increases the coupling resistance to thermal cycling and mechanical vibrations;
- installation performed at much lower temperatures than conventional joining techniques such as brazing or welding;
- complete elimination of the deleterious effects a heat-affected zone.

A.2.7.2 Pipe and Tube Couplings

One of the first and still the most successful applications is for joining fluid piping and tubing. The first major commercial use of an SMA for this purpose was in 1969 by the Raychem Corporation which developed a Ni–Ti coupling (Cryofit) for joining titanium hydraulic control lines in the Grumman F-14 jet fighter. The coupling (Cryofit),[978] in the form of a sleeve with circular ribs on the interior circumference, is machined at room temperature, i.e. in austenitic condition, to have an inner diameter 4% smaller than the outer diameter of the tubes it is designed to join. After being cooled to liquid-nitrogen temperature (-196EC), i.e. well below its martensite transformation temperature, the coupling is expanded to a diameter 4% larger than the tube outer diameter, for overall an internal strain of 8%. The expanded coupling must be shipped and stored in liquid nitrogen to maintain the martensitic state.

Installation is completed by removing the coupling from the liquid nitrogen, inserting the sleeves with machined circular ribs, and then allowing the alloy to warm up and transform to austenite, causing the coupling to shrink tightly around the ends of the tubes. The high stress generated creates the joint and the effectiveness of the sealed joint depends on the geometry of the ribs and the mechanical properties of the tubing material and SMA. The joint can be disassembled by cooling it to below the martensite transformation temperature. The joining process is illustrated in Figure A2.8.

A.2.7.3 Electrical Connections

The second major application of shape-memory alloys is in electrical interconnection systems. The first SMA electrical connectors were developed by Raychem Corporation for electronic interconnection and electrical harnessing systems. These devices were primarily designed for commercial aerospace and military applications. When properly installed, their primary benefits are as follows:

- Zero insertion force allows mating of a connector with little, if any, frictional force.
- Extremely high-retention normal forces limit any relative movements between contacting members, which, in turn, prevents fretting and associated fretting corrosion.

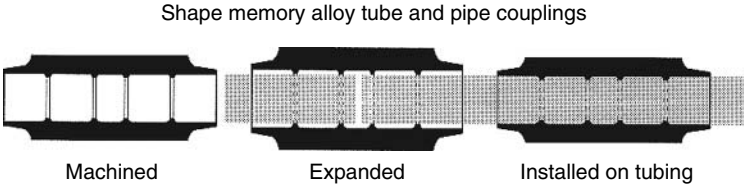

FIGURE A2.8 Principle of the shape-memory alloy coupling (Cryofit).

– They are impervious to environmentally induced degradation such as corrosion; this is due to high normal forces that make the contact zones "gastight", thus preventing the penetration of corrosive gases.
– They are free from chatter or contact bounce in severe shock or vibration environments.

They show a very stable contact resistance and/or voltage drop.

The first SMA connector, called Cryocon[980,981] was a pin-and-socket type developed by Raychem Corporation in the mid 1970s. The connector forms a high-compression fit that can be quickly released and recoupled. The design is in the form of a heavy walled tube referred to as a biasing spring (typically of made of Be-Cu alloy or other conductive spring material) and a ring made of Ni-Ti, called the driver. The socket of the Crycon connector consists of a Ni-Ti ring surrounding the outward-bending tangs of the gold-plated fork contact. The dimensions are such that the tangs exert a constant outward force on the ring. When cooled through its martensite transformation temperature range, the force exerted by the tangs causes the ring to expand, enabling insertion or retraction of the mating pin with zero force. As the assembly heats through the austenitic range, the Ni-Ti ring recovers its original diameter and closes the socket tightly around the pin, generating high retention forces. Figure A2.9 illustrates the Cryocon operation.

Since the Crycon connector is designed for room-temperature operation, the most important material consideration is that the transformation of a Ni-Ti alloy should occur within an appropriate temperature range. In other words, the austenitic transformation temperature (A_f) must be at or below normal service temperature, while that of the martensitic transformation (M_f) should be at or above the coolant temperature. The stresses developed by the Ni-Ti alloy ring during contraction cause the tangs of the socket to be held against the pin at extremely high pressures. Typically, forces exceeding 70 MPa (10 ksi) are generated at the contact interface causing small local deformation of the mating surfaces which, in turn, provides a very intimate contact between mating surfaces and reliable electrical contact characteristics.

Despite a number of advantages, the Crycon connector is somewhat complex and cumbersome in design. A more elegant and economical SMA connector has been developed by a French company Souriau using a Cu-Zn-Al alloy which is a good electrical conductor.[982] The Souriau connector is a pin-and-socket type and operates using the two-way memory effect. After training, the SMA (Cu-Zn-Al) socket can function in two states: open when cold and closed when hot (ambient temperature). The make/break operations can be performed many times without destroying the electrical continuity or mechanical strength of the connector. The gripping forces

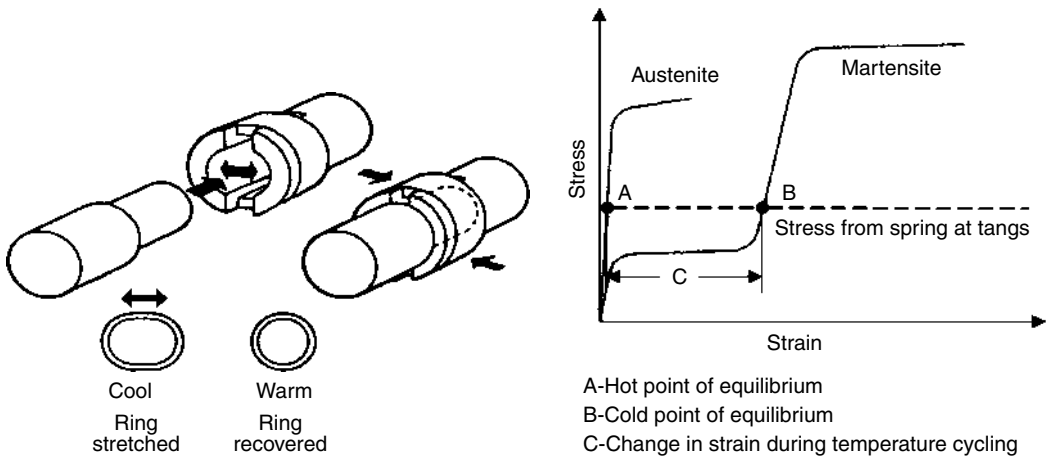

FIGURE A2.9 The Cryocon pin-and-socket connector with its stress–strain characteristics.

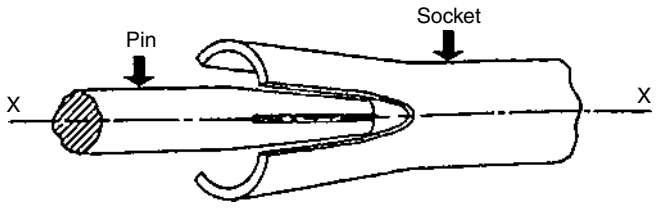

FIGURE A2.10 The Souriau pin-and-socket connector.

developed in the Souriau connector are five times higher than those exerted in a conventional connector thus providing good resistance to shock and vibration. A simplified schematic of the Souriau connector is seen in Figure A2.10.

The above discussion covers mainly the pin-and-socket types of microelectronic interconnections. These connectors have to comply with two contradictory requirements: high normal contact forces and low insertion forces. The latter can degrade contact forces, causing the connector resistance to become unacceptable whereas high insertion forces may damage the contact surfaces during assembling. In order to meet these requirements, an alternative type of connector has been developed by Beta Phase Inc., in Menlo Park, California.

The connector, known as Betaflex,[983] comprises a shape-memory element, a "closing" spring and a polyamide flexible circuit. A shape-memory alloy with a transformation temperature above $+125$EC was selected for operation in the range -55 to $+125$EC. Standard BeCu is used for "closing" spring to provide the contact forces in the connector. The heater, built into the flexible circuit and captured inside the connector, is powered by a low-voltage power supply. When activated, it causes the shape-memory element to recover its original flat memory shape, thus engaging and opening the contact "closing" spring. This "open" state allows board insertion and removal with zero force (ZIF). When the power is turned off, the connector closes, engaging the contacts with high normal forces. The rigid "backbone" design of the connector and the high normal forces maintained by SMA provide remarkable resistance to shock, vibration and fretting. Figure A2.11 illustrates the operation of the Betaflex connector.

The patents literature proposes many shape-memory connector designs. Although most of these designs were developed primarily for microelectronic interconnections, their basic operation and design principles can be used to develop power connectors and devices. However, no power connectors utilizing SMA could be found in either the patents or publications. This is due in part to the relatively high fabrication cost, complex processing metallurgy and thermomechanical treatments ("training") as well as the electric power industry's lack of awareness about SMA technology. Nevertheless, recent advances in the processing metallurgy, particularly in the field

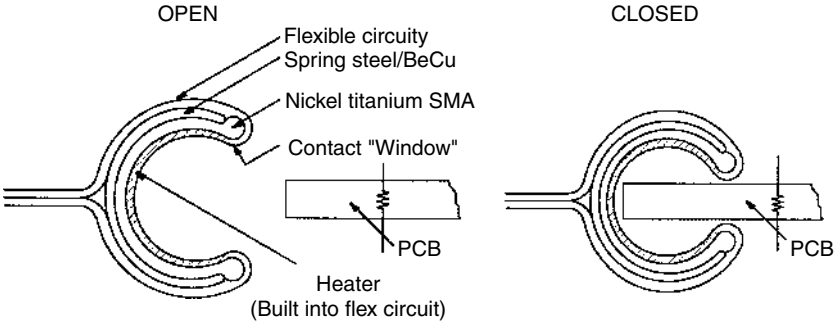

FIGURE A2.11 The principle of operation of the Betaflex multiple contact connector.

of powder metallurgy, and better control over SMA properties may change this situation and have a definite impact on their wider use in electric power connections.

A.2.7.4 Belleville (Disc-Spring) Washers

Deterioration of the electrical and mechanical integrity of a joint is usually accompanied by a temperature increase that can lead to stress relaxation, creep, fretting, thermoelastic ratcheting, accelerated oxidation/corrosion, etc. Furthermore, since the contact resistance is inversely proportional to the applied contact load, the loss of the latter during normal and/or overload conditions can further increase the contact temperature and accelerate the deterioration processes.

As shown in Mechanical Contact Devices 7.3.4, disc-spring (Belleville) washers combined with thick flat washers assure the most satisfactory mechanical stability of bolted joints under stress-relaxation and current-cycling conditions. Owing to their high sensitivity over a narrow temperature range the shape-memory alloys are ideal as Belleville washers. Figure A2.12 shows the load-deflection dependence of a NiTi shape-memory Belleville washer at 20 and 65EC.[984] Since the material at 20EC is fully martensitic, the load-deflection curve is nonlinear whereas at 65EC it is essentially linear indicating that the material is fully austenitic. This ability of an SMA washer to vary the shape of the load-deflection curve can be used to advantage in many applications.

The importance of this feature has been demonstrated in the case of a loosen bolted joint.[985,986] It was shown that even in improperly installed joints (low contact force), the heat, induced by the joint looseness, causes the Belleville washer to change its shape (become more arched) and increases the contact pressure. The net result is a stable joint with a low contact resistance.

A.2.7.5 Actuators

Actuators are devices that perform a task, such as moving an object, either on demand or in response to certain changes in temperature, pressure, current, etc. The intrinsic ability of the SMA to recover the total strain associated with martensitic transformation and simultaneously produce a reversion force, opens up new possibilities for intelligent designs of actuating systems or active structures. Owing to their extraordinary strength in response to temperature, SMA find widespread applications as alternatives to motors, solenoids, bimetallic actuators, fuse elements, washers, etc. Their use as actuators offer many advantages over conventional devices.

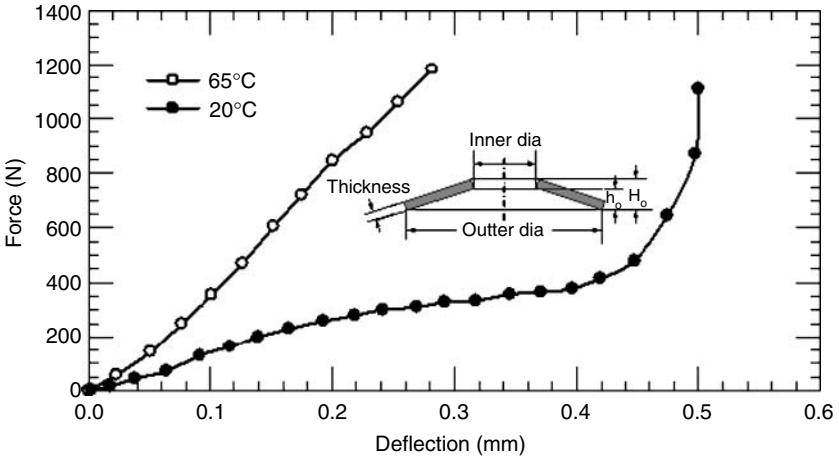

FIGURE A2.12 Load-deflection characteristics of a NiTi SMA Belleville washer at 20EC and 65EC.

Large amounts of recoverable strain can provide work densities up to 10 times higher than conventional approaches; applications where maximizing the work/volume or work/weight ratios of a device is of prime concern benefit greatly from the SMA approach. High electrical resistivity permits direct electrical actuation without extra parts and makes efficient use of available energy, thus enabling power supplies such as 5 and 12 V to be employed.

Depending on the temperature, the SME occurs almost instantaneously and causes martensitic transformation, instead of atom diffusion. The response characteristics of SMA actuators can be enhanced by improving the heat transmission properties. Large SMA strains permit extremely long strokes, a constant force during the stroke and a high starting force. SMA actuators can be linear, rotary or a combination of these.

Figure A2.13 illustrates a variety of SMA elements used in actuators.[987] These elements have their own set of unique operating characteristics. Most shape-memory actuator designs use SMA in the form of wires or coils, the main advantage of the latter being their ability to generate a large perceptible displacement out of a relatively small microscopic strain. However, since the stress distribution over the cross section of the coil is not constant, a greater volume of material is needed for generating the same force. On the other hand, when using wires, a uniform stress distribution or optimum use of material can be obtained.

The design of shape-memory actuators is generally based on the different stress-strain curves of the SMA in its austenitic and martensitic states. Although two-way shape-memory actuators are available, the one-way effect with an external reset force is used in most practical applications. A conventional steel spring provides a biasing force to reset the SMA spring at a lower temperature. Figure A2.14 shows a typical biased actuator and the force-displacement characteristics in both cold (martensite) and hot (austenite) states with the superimposed biasing-spring characteristics.[988] The actuator stroke is limited by the points at which the biasing-spring curve is intersected by the martensitic and austenitic SMA spring curves. For large deflections, nonlinear biasing springs are generally preferred.

Shape-memory actuators can be used in two ways: as electrical or thermal actuators. With electrical actuators, which serve to perform a function on demand, activation is achieved by passing a current through the device to heat it above A_s so that is recovers its shape. Thermal actuators convert thermal energy into mechanical energy; they combine the dual function of detection and actuation by reacting to temperature changes and changing the shape and/or generating a mechanical action.

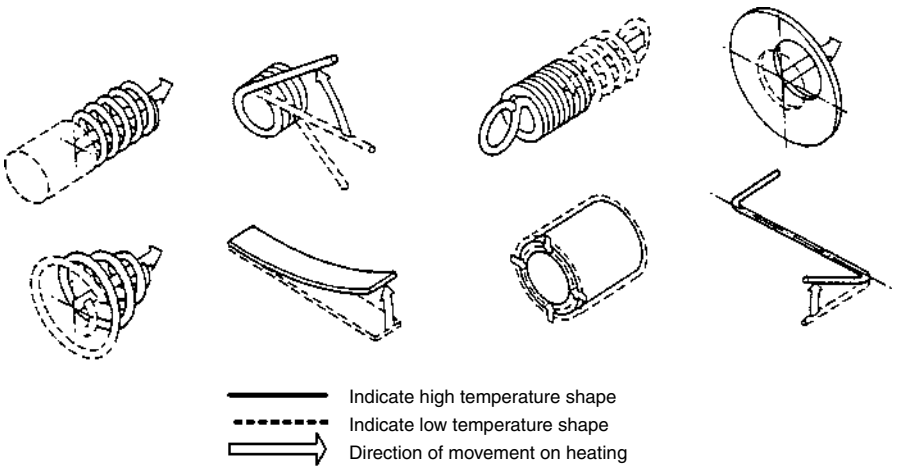

FIGURE A2.13 Various forms of shape-memory elements.

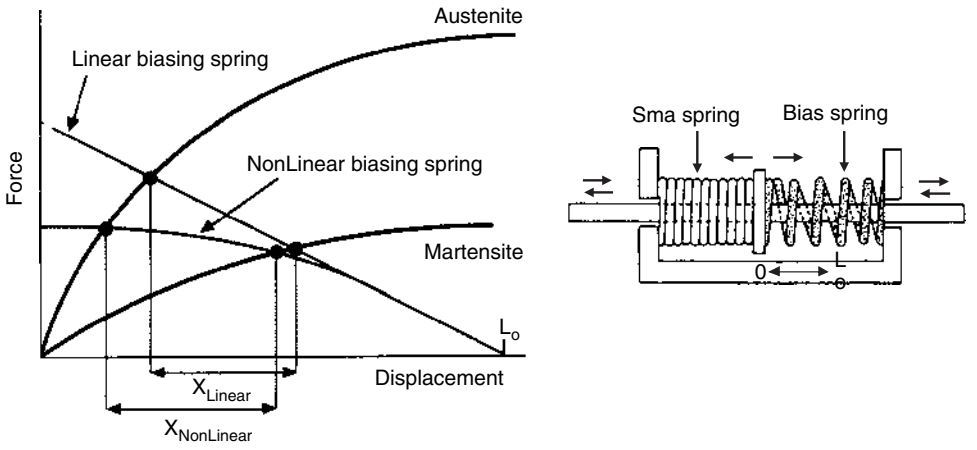

FIGURE A2.14 Type biased actuator and the force-displacement characteristics in both cold (martensite) and hot (austenite) states with the superimposed biasing-spring characteristics.

A.2.7.6 Electrical Actuators

These devices are generally used to perform tasks on demand and are designed to compete with servomotors, hydraulic systems, electrical motors and solenoids. The advantages of electrical actuators over motors and solenoids are their small size, noiseless operation, high work output and few mechanical parts. For instance, a 1-mm-thick wire made from Cu-Zn-Al alloy in the form of a 5-mm-diameter helicoidal spring with 100 turns can lift a load of 50 g to 1 m in height when energized by a current of 6 A at 12 V.[989]

The response time of an electrical actuator is controlled by its heat transmission property. By increasing the current density, very rapid activation can be achieved during heating, whereas cooling can only be affected by thermal conduction from the surface. The most common methods of increasing the rate of heat loss are to increase the surface area to volume ratio (via films, ribbons or the like), bond a heat-sinking material (such as silicone rubber or copper) to the wire or use cooling fluid instead of air. Combination of these methods can significantly reduce the response time of SMA actuators, although it should be borne in mind that use of these methods will inevitably increase the energy consumption of an actuator device. Hence, it is unrealistic to expect that these actuators can have a response time as fast as those of electric or hydraulic servo-systems. Nevertheless, the ability of electrical actuators to generate motion upon the passage of a current makes these devices very attractive for many applications in a variety of electrical.

The cycling nature of the operation of these devices and, hence, their fatigue life impose an obstacle to their wider use. Owing to their high electrical resistivity and longer fatigue life, NiTi alloys are generally preferred over Cu-based alloys. However, owing to their excellent thermal conductivity, electrical actuators made of Cu-based alloys have a much faster cooling response. Hence, the choice between those two materials is determined by the type and nature of the desired application equipment and systems.

A.2.7.7 Temperature Indicators

A very simple temperature indicator for monitoring excessive heating of bolted joints is shown in Figure A2.15a. It is a flat 5×40 mm by 0.2 mm thick strip of a Cu-based SMA that has been trained in such a way as to recover its original (austenitic) shape in the temperature range 95–105EC. When in its martensitic state (low temperature), the indicator, bent at 90E (position 1), is placed under

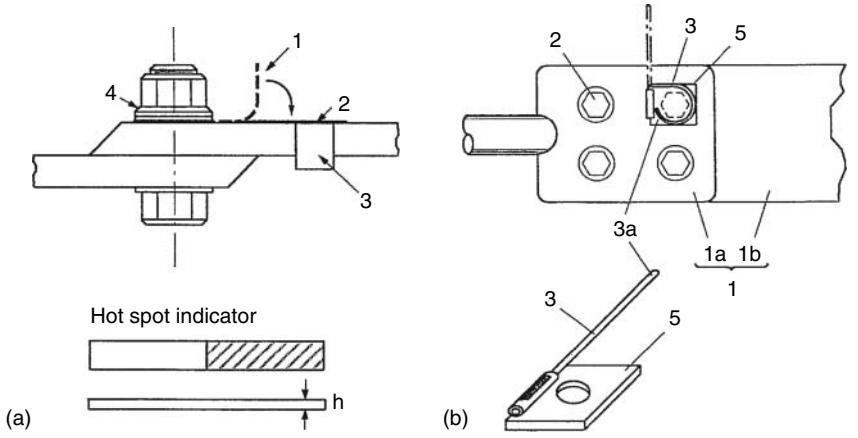

FIGURE A2.15 (a) Simple shape-memory over-temperature indicator and (b) Furukawa over-temperature indicator.

the flat washer and the joint is bolted. When the temperature of a bolted joint exceeds its transformation temperature (95–105EC), the indicator takes its austenitic shape, i.e. it flattens (position 2), thus providing a visible indication of excessive heating.

A similar temperature indicator,[990] shown in Figure A2.15b, is used to measure the temperature in a bolted joint between a terminal (1a) and bus bar (1b). Essentially, it is a short 0.1–1 mm thick SMA wire (3 and 3a) attached to a flat washer (5). When the bolt is assembled (low temperature), the wire is bent round the bolt head (2). As soon as the joint temperature exceeds the transformation temperature, usually above 100(C, the wire takes its straight (austenitic) shape, providing a visual signal of joint overheating.

The same operating principle was used to monitor overheating in electric power cables.[991] This is an SMA strip with a flag bent round the cable at low temperature (martensitic state). When the

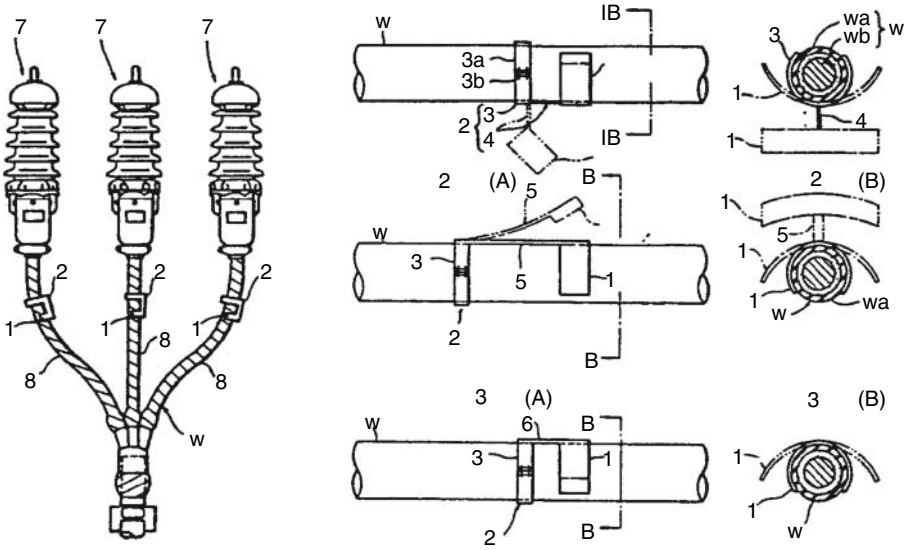

FIGURE A2.16 The Fujukura over-temperature SMA indicator.

cable reaches the transformation temperature of the SMA element, it expands and the flag pops up signaling cable overheating (Figure A2.16).

The advantage of this type of temperature indicator over infrared (thermographic) detection is the possibility of continuous supervision of the condition of the joints, electrical contacts of different units of power system equipment and devices, etc. The use of SMA temperature indicators with different transition temperatures offers a more detailed assessment of the state of various devices and contact junctions on the power system.

These problems compounded by the poor information and lack of engineering data for shape-memory alloys are probably the main cause for the slow penetration of SMA technology in the industry. It is indeed surprising that, despite some 10,000 patents issued world-wide on SMA covering the variety of devices and applications as well as the processing methods, so few large-scale applications exist.

Understanding the complex behaviour of SMA materials requires an open and intensive discussion between metallurgists, physicists and mechanical engineers and scientists, to improve our knowledge of the factors influencing the properties and behaviour of SMA materials. Combined fundamental and applied know-how will provide the necessary conditions for reproducible, cost-effective industrial processing and production of SMA materials.

Appendix 3: Electrical Contact Tables

TABLE A3.1A
Physical Properties of the Most Important Contact Materials

Material	Chemical Symbol	Atomic Number	Atomic Weight	Density (g cm^{-3})	Softening Temperature (°C)	Softening Voltage (Measured) (V)	Melting Point (°C)	Boiling Point (°C)	Melting Voltage (Measured) (V)	Melting Voltage (Calculated) (V)
Aluminum	Al	13	26.98	2.70	150	0.1	660	2,450	0.3	0.29
Antimony	Sb	51	121.75	6.7	0.2		630	1,380		0.28
Beryllium	Be	4	9.01	1.85			1,277	2,770		0.48
Bismuth	Bi	83	208.98	9.80			271	1,560		0.15
Cadmium	Cd	48	112.40	8.65			321	765		0.17
Carbon	C	6	12.01	2.3			(0)			
Chromium	Cr	24	52.00	7.19			1,875	2,480		0.67
Cobalt	Co	27	58.93	8.85			1,490	2,900		0.54
Copper	Cu	29	63.54	8.95	190	0.12	1,083	2,595	0.43	0.42
Gallium	Ga	31	69.72	5.91			30	2,237		0.04
Gold	Au	79	196.97	19.32	100	0.08	1,063	2,966	0.43	0.42
Indium	In	49	114.82	7.31			156	2,000		0.11
Iridium	Ir	77	192.20	22.5			2,450	4,600		0.86
Iron	Fe	26	55.85	7.87	500	0.19	1,537	2,750	0.6	0.57
Lead	Pb	82	207.19	11.36	200	0.12	327	1,750	0.19	0.17
Magnesium	Mg	12	24.31	1.74			650	1,120		0.28
Manganese	Mn	25	54.94	7.43			1,245	2,095		0.47

Mercury	Hg	80	200.59	13.55			−39	357		
Molybdenum	Mo	42	95.94	10.21	900	0.3	2,610	5,560	0.75	0.91
Nickel	Ni	28	58.71	8.90	520	0.16	1,453	2,800	0.65	0.54
Niobium	Nb	41	92.91	8.57			2,469	4,900		0.78
Osmium	Os	76	190.20	22.60			3,050	5,500		1.04
Palladium	Pd	46	106.40	12.02			1,552	3,170	0.57	0.57
Platinum	Pt	78	195.09	21.45	540	0.25	1,769	3,850	0.71	0.64
Rhenium	Re	75	186.20	21.04			3,180	5,900		1.09
Rhodium	Rh	45	102.91	12.41			1,966	3,900		0.70
Ruthenium	Ru	44	101.07	12.30			2,350	4,900		0.81
Silver	Ag	47	107.87	10.49	180	0.09	961	2,212	0.37	0.38
Tantalum	Ta	73	180.95	16.60	850	0.3	2,996	5,425		1.03
Tin	Sri	50	118.69	7.30	100	0.07	232	2,270	0.13	0.14
Titanium	Ti	22	47.90	4.51			1,668	3,280		0.61
Tungsten	W	74	183.85	19.32	1,000	0.4	3,410	5,930	1.1	1.16
Vanadium	V	23	50.94	6.10			1,900	3,400		0.68
Zinc	Zn	30	63.37	7.13	170	0.1	420	907	0.17	0.20
Zirconium	Zr	40	91.22	6.49			1,852	3,580		0.67

TABLE A3.1B
Physical Properties of the Most Important Contact Metals

Material	Elastic Modulus ($kNmm^{-2}$)	Heat of Fusion ($J\,g^{-1}$)	Vapor Pressure at Melting Point (Nm^{-2})	Heat of Vaporization ($J\,g^{-1}$)	Thermal Conductivity @20°C ($W\,m^{-1}\,K^{-1}$)	Thermal Expansion ($\times 10^{-6} K^{-1}$)	Volume Change at Solidification (%)	Specific Heat @20°C ($J\,g^{-1}\,K^{-1}$)	Electrical Resistivity ($\mu\Omega$ cm)	Temp. Coeff. of Resistivity ($\times 10^{-3\circ} K^{-1}$)
Aluminum	65	395	2.5×10^{-6}	10,470	222	23.6	−6.5	0.896	2.65	4.29
Antimony	56	160	24	1,970	21	9,5	+0.95	0.205	37.0	
Beryllium	298	1,090	4.3	24,700	147	11.6		1,892	4.0	25.0
Bismuth	33	52.3	6.5×10^{-4}	1,425	9	13.3	−0.33	0.12	106.8	4.0
Cadmium	57.5	55.3	16	879	92	29.8	−4.0	0.230	6.83	4.2
Carbon	5				50–300	0.6–4.3		0.670	6500	
Chromium	160	282	1030	5,860	67	6.2		0.461	14.95	3.0
Cobalt	216	245	190	6,680	71	13.8		0.415	6.24	6.6
Copper	115	212	5.2×10^{-2}	4,770	394	16.5	−4.2	0.385	1.65	4.3
Gallium	9.6	80.4	9.6×10^{-36}	3,895	33	18.0	+3.0	0.331	43.2	4.0
Gold	80	67.4	2.4×10^{-3}	1,550	297	14.2	−5.1	0.130	2.19	4.0
Indium	11	28.5	1.5×10^{-17}	2,970	25	33.0	−2.5	0.239	8.37	4.9
Iridium	548	144	1.5	3,310	59	6.8		0.130	5.3	4.1
Iron	208	274	7.3	6,385	75	11.8	−3.0	0.461	9.71	6.5
Lead	14.5	26.4	4.4×10^{-7}	858	33	29.3	−3.5	0.130	20.65	3.36

Magnesium	46	369	370	5,440	155	27.1	−4.1	1.026	4.45	16.5
Manganese	165	267	125	4,100	50	22.0	−1.7	0.482	185.0	0.5
Mercury		11.7	3.1×10^{-4}	292	9	60.8	−3.7	0.138	96.0	1.0
Molybdenum	347	292	3.6	5,610	142	4.9		0.276	5.2	4.7
Nickel	216	309	240	6,450	92	13.3	−2.5	0.439	6.84	6.8
Niobium	113	289	7.9×10^{-2}	7,790	54.7	3		0.272	10.6	3.9
Osmium	580	141	2.7	3,810	88	4.6		0.130	9.5	4.2
Palladium	117	143	1.3	3,475	72	11.8	−5.5	0.243	10.8	3.77
Platinum	154	113	3.2×10^{-2}	2,615	72	8.9	−6.0	0.130	10.6	3.93
Rhenium	480	178	3.5	3,420	72	6.7		0.138	19.3	4.6
Rhodium	386	211	6.5×10^{-1}	5,190	88	8.3	−10.8	0.247	4.51	4.4
Ruthenium	430	252	1.5	6,615	105	9.1		0.239	6.71	4.6
Silver	79	105	3.6×10^{-1}	2,387	419	19.7	−3.8	0.234	1.59	4.1
Tantalum	188	157	8×10^{-1}	4,315	54	6.5		0.142	12.45	3.5
Tin	47	60.7	6×10^{-21}	1,945	63	23	−2.8	0.226	11.6	4.6
Titanium	120	403	5.1×10^{-1}	8,790	17	8.4		0.519	41.6	5.5
Tungsten	360	193	4.4	3,980	167	4.6		0.138	5.55	4.8
Vanadium	136	330	3.2	10,260	29	8.3		0.498	26.0	3.9
Zinc	96	102	20	1,760	113	39.7	−4.7	0.385	5.92	4.2
Zirconium	98	224	1.7×10^{-3}	4,600	21	5.9		0.281	43.5	4.4

TABLE A3.1C
Physical Properties of Some Contact Metals at Their Melting Points

Material	Melting Point (°C)	Density (g cm^{-3})	Resistivity (μΩ cm)	Thermal Conductivity (W m^{-1} K^{-1})	Viscosity (Dynamic) ($\times 10^{-3}$ Nm^{-2} s)	Surface Tension (Jm^{-2})
Aluminum	660	2.39	20.0	92.7	4.5	0.86
Bismuth	271	10.06	128.1	11.0	1.68	0.39
Cadmium	321	8.02	33.7	44.0	1.4	0.67
Chromium	1,875	6.46		25.1	0.68	1.59
Copper	1,083	7.96	21.3	49.4	3.34	1.29
Gallium	30	6.2	26	33.5	2.04	0.74
Gold	1,063	17.32	30.8			0.75
Indium	156	7.03	33.1	41.9	1.69	0.56
Iridium	2,450	20.0				2.25
Iron	1,537	7.15	139		2.2	1.68
Lead	327	10.68	95.0	16.3	2.63	0.47
Magnesium	650	1.59	27.4	13.9	1.24	0.56
Mercury	values @a 20C	13.55	96	9	1.55	0.47
Molybdenum	2,610	9.34				2.25
Nickel	1,453	7.9	109			1.76
Palladium	1,552	10.7				1.5
Platinum	1,769	19.7				1.74
Rhodium	1,966	10.65				2.0
Silver	961	9.33	17.2		3.9	0.93
Tantalum	2,996	15.0				2.15
Tin	232	6.97	48.0	33.5	1.97	0.58
Titanium	1,668	4.13				1.51
Tungsten	3,410	17.6				2.31
Zinc	420	6.64	37.4	60.3	3.93	0.82

TABLE A3.2A
Physical Properties of Silver-Based Alloys

Material	Density (g cm^{-3})	Melting Temperature (°C)	Electrical Resistivity @20°C (μΩcm)	Temp. Coeff. Electrical Resistance ($\times 10^{-3}$ K^{-1})	Thermal Conductivity @ 20°C (Wm^{-1} K^{-1})	Elastic Modulus ($kNmm^{-2}$)	Hardness ($\times 10^2$ Nmm^{-2})
Ag	10.5	960	1.59	4.1	419	79	3–7
Ag - 10% Cd	10.3	910–925	4.3	1.4	150	60	3.6–10
Ag - 15% Cd	10.1	850–875	4.8	2	109	60	4.0–11.5
Ag - 3% Cu	10.4	900–934	1.92	3.2	385	85	4.5–9.5
Ag - 5% Cu	10.4	905–940	1.96	3	380	85	5–10
Ag - 10% Cu	10.3	779–875	2.08	2.8	335	85	6.5–12
Ag - 20% Cu	10.2	779–810	2.17	2.7	335	85	8–13
Ag - 2% Cu - Ni	10.4	940	1.92	3.5	385	85	5.5–10
Ag - 30% Pd	10.9	1150–1220	15.6	0.4	60	116	7–14
Ag - 40% Pd	11.1	1225–1285	20	0.36	46	134	7.5–15
Ag - 50% Pd	11.2	1290–1340	33.3	0.23	33.5	137	8–16
Ag - 60% Pd	11.4	1330–1385	41.7		29.3		10–18
Ag - 30% Pd - 5% Cu	10.8	1120–1165	15.4	0.37		108	9–17
Ag - 0.15% Ni	10.5	960	1.7	4	414	85	4.5–9
Ag - 10% Ni	10.2	960	2.0	3.5	310	84	5–11
Ag - 20% Ni	10.0	960	2.2	3.5	270	98	6–10.5
Ag - 30% Ni	9.8	960	2.4	3.4	240	115	6.5–11.5
Ag - 40%Ni	9.7	960	2.7	2.9	210	129	7.5–12
Ag - 50% Ni	9.6	960	3.1		185	145	7.5–13
Ag - 60% Ni	9.4	960	3.7		155	160	8–14
Ag - 70% Ni	9.3	960	4.0		140	170	8–15.5
Ag - 3% C	9.0	960	2.1	3.5	325		4.2
Ag - 5% C	8.5	960	2.3	3.3	318		4.0
Ag - 10% C	7.4	960	2.9				3.1
Ag - 15% C	6.5	960	4.5				2.6
Ag - 25% C	5.1	960	14.5				
Ag - 50% C	3.2	960	23				
Ag - 70% C	2.6	960	53				
Ag - 90% C	2.14	960	87				
Properties of Selected Sliding Contact Materials							
Ag - 5% Cu-10% C	6.8	905–940	4.7				
Ag - 48.5% Cu - 3% C	8.3	779–875	4.0				5.2
Ag - 47.5% Cu - 7% C	7.4	779–875	8.0				
Ag - 35% Cu - 30% C	4.2	779–815	63.6				
Ag - 69.75% Cu - 5% C	8.2	779–945	3.2				5.2
Ag - 72% Cu - 3% C	8.3	779–960	5.3				7.1

TABLE A3.2B
Physical Properties of Gold-Based Alloys

Material	Density (g cm^{-3})	Melting Temperature (°C)	Electrical Resistivity @20°C (μΩcm)	Temp. Coeff. Electrical Resistance ($\times 10^{-3}$ K^{-1})	Thermal Conductivity @ 20 °C (Wm^{-1} K^{-1})	Elastic Modulus ($kNmm^{-2}$)	Hardness ($\times 10^2$ Nmm^{-2})
Au	19.3	1063	2.19	4	297	80	2–7
Au - 8% Ag	18.1	1060	6.1			82	
Au - 10% Ag	17.8	1058	6.3	1.25	147	82	4–8.5
Au - 20% Ag	16.4	1036–1040	10	0.86	75	89	4–9.5
Au - 30% Ag	15.4	1025–1030	10.2	0.7			4.5–9.5
Au - 5% Ni	18.3	995–1010	13.3	0.71	52	83	11.5–16
Au - 5% Co	18.2	1010	6.2–55.5	0.68		88	9.5–16
Au - 10% Pt	19.5	1150–1190	12.2	0.98	54	95	8–10
Au - 25% Ag - 5% Cu	15.2	980	12.2	0.75			9–16
Au - 20% Ag - 0 10% Cu	15.1	865–895	13.7	0.52	66	87	12–19
Au - 26% Ag - 3% Ni	15.4	990–1020	11.4	0.88	59	114	9–14
Au - 25% Ag - 6% Pt	16.1	1060	15.9	0.54	46	93	6–11
Au - 14%Cu - 9% Pt – 4% Ag	16	955	14.3–25				19–27

TABLE A3.3
Physical Properties of Platinum- and Palladium-Based Alloys

Material	Density (g cm^{-3})	Melting Tempera-ture (°C)	Electrical Resistivity @20°C (μΩ cm)	Temp. Coeff. Electrical Resistance ($\times 10^{-3}$ K^{-1})	Thermal Conductivity @ 20°C (Wm^{-1} K^{-1})	Elastic Modulus ($kNmm^{-2}$)	Hardness ($\times 10^2$ Nmm^{-2})
Pt	21.4	1769	10.6	3.90	72	154	4–8.5
Pt - 5% lr	21.5	1774–1776	22		42	190	8.5
Pt - 10% Ir	21.6	1780–1785	17.9	2.00	29	220	10.5–17
Pt - 10% Ru	20.6	≈1800	33.3	0.83			235
Pt - 8% Ni	19.2	1670–1710	30	1.50		180	20–26
Pt 5% W	21.3	1830–1850	43.4	0.70		185	17–24
Pd	12.02	1552	10.8	3.80	72	117	4–9
Pd - 15% Cu	11.3	1370–1410	43.4	0.49	17	175	7–11
Pd - 40% Cu	10.4	1200–1230	33.3	0.28	38	175	8–12
Pd - 5% Ni	11.8	1455–1485	16.9	2.47	175		

TABLE A3.4A
Physical Properties of Copper-Based (Carrier) Alloy Materials

Material	Density (g cm^{-3})	Melting Temperature (°C)	Electrical Resistivity @20°C (μΩcm)	Temp. Coeff. Electrical Resistance ($\times 10^{-3}\ K^{-1}$)	Thermal Conductivity @ 20°C ($Wm^{-1}\ K^{-1}$)	Thermal Expansion ($\times 10^{-6}\ K^{-1}$)	Elastic Modulus ($kNmm^{-2}$)	Hardness ($\times 10^2$ Nmm^{-2})
Cu	8.96	1083	1.65	4.3	394	16.5	115	4–9
Cu - 10% Zn	8.79	1030–1043	4.0	108	184	18.2	125	6–11
Cu - 20% Zn	8.67	980–1000	5.3	1.5	142	18.8	120	6.5–15.5
Cu - 30% Zn	8.53	910–940	6.3	1.5	124	19.8	114	7–13
Cu - 40% Zn	8.41	895–900	6.7	1.7	117	20.3	103	8–14
Cu - 25% Ni	8.94	1150–1210	32.0	0.2	29	15.5	147	85
Cu - 0.1% Ag	8.89	1082	1.8	3.9	385	171	124	4–9
Cu - 2% Ag	9	1050–1075	2.0	3	330	17.5	123	5–13
Cu - 5% Ag - 1.8% Cd	9.1	920–1040	2.6	2.4	240	17.8	120	7–13.5
Cu - 1% Cd	8.94	1040–1080	2.2	3.4	320	17.0	124	9.5–14
Cu - 1% Cr	8.89	1070–1080	3.5	2.5	240	17.0	112	8–15
Cu - 0.5% Te	8.93	1050–1075	1.8	3.7	356	18.0	118	6–10

TABLE A3.4B
Physical Properties of Copper-Based (Spring) Alloy Materials

Material	Density (g cm^{-3})	Melting Temperature (°C)	Electrical Resistivity @20°C (μ Ωcm)	Temp. Coeff. Electrical Resistance ($\times 10^{-3}\ K^{-1}$)	Thermal Conductivity @ 20°C ($Wm^{-1}\ K^{-1}$)	Thermal Expansion ($\times 10^{-6}\ K^{-1}$)	Elastic Modulus ($kNmm^{-2}$)	Max. Spring Bending Strength (Nmm^{-1})
Cu	8.96	1083	1.65	4.3	394	16.5	115	230
Cu - 6% Sn - 0.2% P	8.93	910–1040	11.1	0.7	75	18.5	118	370–430
Cu - 8%Sn - 0.2% P	8.93	875–1025	13.3	0.7	67	18.5	115	390–480
Cu - 6% Sn - 6% Zn	8.86	900–1015	10.5	0.8	79	18.4	114	500
Cu - 9% Ni - 2% Sn	8.93	1060–1120	16		48	16	132	500
Cu - 18% Ni - 20% Zn	8.71	1025–1100	29	3	27	17	132	390–550
Cu - 1.7% Be - 0.2% Co	8.4	890–1000	5		95	17	130	780–1000
Cu - 2% Be - 0.2% Co	8.3	870–980	5	1	95	17	130	850–1050
Cu - 0.5% Be - 2.5% Co	8.8	1030–1070	3.6				132	370–650

TABLE A3.5
Properties of Typical Spring and Carrier Materials

Material	Density (g cm^{-3})	Melting Temperature (°C)	Electrical Resistivity @20°C ($\mu\ \Omega$cm)	Thermal Conductivity @ 20°C ($Wm^{-1}K^{-1}$)	Thermal E×pansion ($\times 10^{-6}\ K^{-1}$)	Elastic Modulus ($kNmm^{-2}$)	Hardness ($\times 10^2$ Nmm^{-2})
1100 Al (99% Al)	2.71	643–655	2.9	222	23.6	65	2.3–4.4
3003 Al (Al-Mn Alloy)	2.73	643–655	4.2	193	23.3	65	2.8–5.5
5052 Al (Al- Mg Alloy)	2.68	607–650	4.9	131	23.75	65	4.6–7.7
6101 Al (Al-0.6% Mg-0.5% Si)	2.69	620–655	3.02	218	23.5	69	7.1
Inconel (Ni-Cr- Fe Alloy)	8.5	1355–1413	98.0	26	12.9	207	~9.0
Constantan (55% Cu - 45 % Ni)	8.8	1225–1300	50.0	23	14.9	170	8–20
Monel (67% Ni - 30% Cu)	8.8	1300	48.2	25	14.0	179	
Invar (64% Fe - 36% Ni)	8.0	1427	80.0	1.2	<0.1	141	
301 stainless steel	7.9	1400–1420	71.0	16	17.0	190	~16
302 stainless steel	7.9	1400–1420	72.0	16	17.5	190	
304 stainless steel	7.9	1400–1455	70.0	16	17.5	190	
305 stainless steel	8.0	1400–1555	72.0	16	17.5	190	
430 stainless steel	7.7	1425–1510	60.0	26	10.5	196	

TABLE A3.6
SI Units and Other Commonly Used Units

SI units

Length	meter	m	
Mass	kilogram	kg	
Time	second	s	
Electric current	ampere	A	
Thermodynamic	degree	K	
Temperature	kelvin		
Amount of	mole	mol	
Substance			
Frequency	hertz	Hz	s^{-1}
Force	newton	N	$m \cdot kg/s^2$
Pressure	pascal	Pa	N/m^2
Energy, work	joule	J	N.m
Heat flu x density			W/m^2
Power,	watt	W	J/s
Radiant flu x			
Quantity of electricity	coulomb	C	$A \cdot s$
Elementary charge		e	
Electric potential	volt	V	W/A
Capacitance	farad	F	C/V
Electric resistance	ohm	Ω	V/A
Conductance	siemens	S	AV
Magnetic flux	weber	W	$V \cdot s$
Magnetic flux	tesla	T	Wb/m^2
Density			Kg/m^3
Magnetic field strength	amperes/ meter		A/m
Magnetomotive Force	ampere		A
Inductance	henry	H	$V \cdot s/A$
Thermal conductivity			W/(m K)
Diffusion coefficient			m^2/s

Other Commonly Used Units

Angstrom	A
bar	bar
British Thermal Unit	Btu
Calorie	cal
cycles per second	c/s
day	d
degree	°
degree Celsius	C
degree Fahrenheit	F
electron volt	eV
foot	ft
Gauss	G
gram	g, gm
horse power	hp
hour	h, hr
inch	in
liter	l
minute of time	min
ounce	oz
pond	p
pound	lb
relative humidity	rh
revolution	rev
standard atmosphere	atm
standard temperature and pressure @ 273 K & 1 atm	STP
torr	torr
year	yr
poise	P

TABLE A3.7
Miscellaneous Conversion Tables

Length	m	meter	
	cm	centimeter	100 cm $= 1$ m
	mm	millimeter	1000 mm $= 1$ m
	μm	micrometer	10^6 μm $= 1$ m
	in	inch	1 inch $= 25.4$ mm
	μin	microinch	1 μ in $= 0.0254$ μm
	Å	Angstrom	1 Å $= 10^{-10}$ m
Mass	g	gram	1 g $= 10^{-3}$ kg
	kg	kilogram	
	lb	pound	1 lb $= 0.454$ kg
	oz	ounce (avdp)	1 oz $= 28.35$ g
	oz	ounce (troy)	1 oz $= 31.1$ g
Force	N	newton	
	p	pound (gram force, gF)	1 kp $= 9.81$ N
	lbf	pound force	1 lbf $= 4.45$ N
Pressure	Pa	pascal	1 Pa $= 1$ Nm^{-2}
	bar	barr	1 bar $= 10^5$ Pa
	atm	atmosphere	1 atm $= 1.013$ bar
	torr	torr (mm of Hg)	1 torr $= 1$ atm /760
	lbf/in^2	pound/square inch	1 lbf in$^{-2} = 6.9\times10^3$ Pa
Energy	J	Joule	1 J $= 1$ N m^{-2}
	kWh	kilowatt hours	1 kWh $= 3.6\times10^6$ J
	ft lb	foot pounds	1 lbf in$^{-2} = 6.9\times10^3$ Pa
	eV	electron volts	1 eV $= 1.6\times10^{-19}$ J
Heat	cal	calories	1 cal $= 4.189$ J
	Btu	British thermal units	1 Btu $= 1055$ J
Power	W	watt	1 W $= 1$ J s
	hp	horse power	1 hp $= 746$ W
			1 hp $= 550$ ft lb s^{-1}
	ft lb/s	foot pounb/second	1 ft lb s$^{-1} = 1.36$ W
Charge	C	coulomb	1 C $= 1$ A s
		1 electron charge	1.6×10^{-19} C
Temperature	°C	degree celsius	°C $=$ K $- 273$
	F	degrees frenheit	F $= (9$°C$/5) + 32$
Volume	l	liter	1 l $= 10^3$ cm^3
		gallon (US)	3.785 l

TABLE A3.8
Some Fundamental Constants

Speed of light in vacuum	c	3×10^{8} m s^{-1}
Elementary charge	e	1.6×10^{-19} C
Electron rest mass	m_e	9.11×10^{-31} kg
Proton rest mass	m_P	1.67×10^{-27} kg
Neutron rest mass	m_n	1.68×10^{-21} kg
Permittivity constant	ε_0	8.85×10^{-12} F m^{-1}
Permeability constant	μ_0	1.26×10^{-6} H m^{-1}
Plank constant	h	6.63×10^{-34} J s
Molar gas constant	R	8.31 J mol^{-1} k^{-1}
Avogadro constant	N_A	6.02×10^{23} mol^{-1}
Boltzman constant	K	1.38×10^{-23} J K^{-1}
Stefan-Boltzman constant	σ	5.67×10^{-8} Wm^{-2} K^{-4}
Molar volume of an ideal gas at STP	V_m	2.24×10^{-2} m^3 mol$^-$